



Paul Bossart
Alan Geoffrey Milnes
Editors

Mont Terri Rock Laboratory, 20 Years

Two Decades of Research
and Experimentation on
Claystones for Geological Disposal
of Radioactive Waste

Swiss Journal of Geosciences Supplement

More information about this series at <http://www.springer.com/series/5422>

Paul Bossart · Alan Geoffrey Milnes
Editors

Mont Terri Rock Laboratory, 20 Years

Two Decades of Research
and Experimentation on Claystones
for Geological Disposal of Radioactive Waste

Previously published in *Swiss Journal of Geosciences*, Volume 110, Issue 1,
Pages 1–411, 2017

Editors

Paul Bossart
Swiss Geological Survey Swisstopo
Wabern
Switzerland

Alan Geoffrey Milnes
Swiss Federal Institute of Technology
ETH Zurich
Zurich
Switzerland

ISSN 2297-508X ISSN 2297-511X (electronic)
Swiss Journal of Geosciences
ISBN 978-3-319-70457-9

Library of Congress Control Number: 2017957688

© Springer International Publishing AG 2018

This work is subject to copyright. All rights are reserved by the Publisher, whether the whole or part of the material is concerned, specifically the rights of translation, reprinting, reuse of illustrations, recitation, broadcasting, reproduction on microfilms or in any other physical way, and transmission or information storage and retrieval, electronic adaptation, computer software, or by similar or dissimilar methodology now known or hereafter developed.

The use of general descriptive names, registered names, trademarks, service marks, etc. in this publication does not imply, even in the absence of a specific statement, that such names are exempt from the relevant protective laws and regulations and therefore free for general use.

The publisher, the authors and the editors are safe to assume that the advice and information in this book are believed to be true and accurate at the date of publication. Neither the publisher nor the authors or the editors give a warranty, express or implied, with respect to the material contained herein or for any errors or omissions that may have been made. The publisher remains neutral with regard to jurisdictional claims in published maps and institutional affiliations.

Cover illustration: balanced geological profile along the Mont Russelin and Mont Terri tunnels, taken from Bossart et al. (2017): Mont Terri rock laboratory, 20 years of research: introduction, site characteristics and overview of experiments. *Swiss Journal of Geosciences*, 110. doi: 10.1007/s00015-016-0236-1.

Printed on acid-free paper

This book is published under the trade name Birkhäuser (www.birkhauser-science.com)
The registered company is Springer International Publishing AG
The registered company address is: Gewerbestrasse 11, 6330 Cham, Switzerland

Contents

Editorial: Mont Terri rock laboratory 20 years of experimentation and applied research	1
Mont Terri Rock Laboratory, 20 Years of Research: Introduction, Site Characteristics and Overview of Experiments <i>Paul Bossart, Frédéric Bernier, Jens Birkholzer, Christophe Bruggeman, Peter Connolly, Sarah Dewonck, Masaaki Fukaya, Martin Herfort, Mark Jensen, Jean-Michel Matray, Juan Carlos Mayor, Andreas Moeri, Takahiro Oyama, Kristof Schuster, Naokata Shigeta, Tim Vietor and Klaus Wieczorek</i> Swiss Journal of Geosciences 2017, 2017:110(21, February 2017) DOI 10.1007/s00015-016-0236-1	3
Litho- and Biostratigraphy of the Opalinus Clay and Bounding Formations in the Mont Terri Rock Laboratory (Switzerland) <i>Bernhard Hostettler, Achim G. Reisdorf, David Jaeggi, Gaudenz Deplazes, Hansruedi Bläsi, Alain Morard, Susanne Feist-Burkhardt, Anton Waltschew, Volker Dietze and Ursula Menkveld-Gfeller</i> Swiss Journal of Geosciences 2017, 2017:110(25, February 2017) DOI 10.1007/s00015-016-0250-3	23
Tectonic Evolution Around the Mont Terri Rock Laboratory, Northwestern Swiss Jura: Constraints from Kinematic Forward Modelling <i>Christophe Nussbaum, Armelle Kloppenburg, Typhaine Caër and Paul Bossart</i> Swiss Journal of Geosciences 2017, 2017:110(28, January 2017) DOI 10.1007/s00015-016-0248-x	41
Tectonic Structure of the “Main Fault” in the Opalinus Clay, Mont Terri Rock Laboratory (Switzerland) <i>David Jaeggi, Ben Laurich, Christophe Nussbaum, Kristof Schuster and Peter Connolly</i> Swiss Journal of Geosciences 2017, 2017:110(17, January 2017) DOI 10.1007/s00015-016-0243-2	69
Comparative Study of Methods to Estimate Hydraulic Parameters in the Hydraulically Undisturbed Opalinus Clay (Switzerland) <i>Catherine Yu, Jean-Michel Matray, Julio Gonçalves, David Jaeggi, Werner Gräsle, Klaus Wieczorek, Tobias Vogt and Erik Sykes</i> Swiss Journal of Geosciences 2017, 2017:110(25, February 2017) DOI 10.1007/s00015-016-0257-9	87

Geochemical Signature of Paleofluids in Microstructures from Main Fault in the Opalinus Clay of the Mont Terri Rock Laboratory, Switzerland	
<i>Norbert Clauer, Isabelle Techer, Christophe Nussbaum and Ben Laurich</i>	
Swiss Journal of Geosciences 2017, 2017:110(19, January 2017)	
DOI 10.1007/s00015-016-0253-0	107
Pore-Water Evolution and Solute-Transport Mechanisms in Opalinus Clay at Mont Terri and Mont Russelin (Canton Jura, Switzerland)	
<i>Martin Mazurek and Antoine de Haller</i>	
Swiss Journal of Geosciences 2017, 2017:110(21, February 2017)	
DOI 10.1007/s00015-016-0249-9	131
Geomechanical Behaviour of Opalinus Clay at Multiple Scales: Results from Mont Terri Rock Laboratory (Switzerland)	
<i>Florian Amann, Katrin M. Wild, Simon Loew, Salina Yong, Reto Thoeny and Erik Frank</i>	
Swiss Journal of Geosciences 2017, 2017:110(16, February 2017)	
DOI 10.1007/s00015-016-0245-0	153
Hydro-Mechanical Evolution of the EDZ as Transport Path for Radionuclides and Gas: Insights from the Mont Terri Rock Laboratory (Switzerland)	
<i>Paul Marschall, Silvio Giger, Rémi De La Vassière's, Hua Shao, Helen Leung, Christophe Nussbaum, Thomas Trick, Bill Lanyon, Rainer Senger, Andrea Lisjak and Andrés Alcolea</i>	
Swiss Journal of Geosciences 2017, 2017:110(17, February 2017)	
DOI 10.1007/s00015-016-0246-z	175
Coupled Hydraulic-Mechanical Simulation of Seasonally Induced Processes in the Mont Terri Rock Laboratory (Switzerland)	
<i>Gesa Ziefle, Jean-Michel Matray, Jobst Maßmann and Andreas Möri</i>	
Swiss Journal of Geosciences 2017, 2017:110(17 https://c5.rgstatic.net/m/4951093203564/images/template/default/profile/profile_default_s.jpg , February 2017)	
DOI 10.1007/s00015-016-0252-1	197
High-Resolution Mini-Seismic Methods Applied in the Mont Terri Rock Laboratory (Switzerland)	
<i>Kristof Schuster, Florian Amann, Salina Yong, Paul Bossart and Peter Connolly</i>	
Swiss Journal of Geosciences 2017, 2017:110(22, February 2017)	
DOI 10.1007/s00015-016-0241-4	215
Seismotectonic Analysis Around the Mont Terri Rock Laboratory (Switzerland): A Pilot Study	
<i>Martinus Abednego, Patrick Blascheck, Senecio Schefer, Christophe Nussbaum, Manfred Joswig, Paul Bossart and Jon Mosar</i>	
Swiss Journal of Geosciences 2017, 2017:110(17, February 2017)	
DOI 10.1007/s00015-017-0263-6	235
In-situ Experiments on Bentonite-Based Buffer and Sealing Materials at the Mont Terri Rock Laboratory (Switzerland)	
<i>Klaus Wieczorek, Irina Gaus, Juan Carlos Mayor, Kristof Schuster, José-Luis García-Siñeriz and Toshihiro Sakaki</i>	
Swiss Journal of Geosciences 2017, 2017:110(20, February 2017)	
DOI 10.1007/s00015-016-0247-y	255

Performance of the Opalinus Clay Under Thermal Loading: Experimental Results from Mont Terri Rock Laboratory(Switzerland)	
<i>Antonio Gens, Klaus Wieczorek, Irina Gaus, Benoit Garitte, Juan Carlos Mayor, Kristof Schuster, Gilles Armand, José-Luis García-Siñeriz and Thomas Trick</i>	
Swiss Journal of Geosciences 2017, 2017:110(16, February 2017)	
DOI 10.1007/s00015-016-0258-8	271
Implementation of the Full-Scale Emplacement (FE) Experiment at the Mont Terri Rock Laboratory	
<i>Herwig R. Müller, Benoit Garitte, Tobias Vogt, Sven Köhler, Toshihiro Sakak, Hanspeter Weber, Thomas Spillmann, Marian Hertrich, Jens K. Becker, Niels Giroud, Veerle Cloet, Nikitas Diomidis and Tim Vietor</i>	
Swiss Journal of Geosciences 2017, 2017:110(16, February 2017)	
DOI 10.1007/s00015-016-0258-8	289
5-Year Chemico-Physical Evolution of Concrete–Claystone Interfaces, Mont Terri Rock Laboratory (Switzerland)	
<i>Urs Mäder, Andreas Jenni, Cathérine Lerouge, Stephane Gaboreau, Satoru Miyoshi, Yukinobu Kimura, Veerle Cloet, Masaaki Fukaya, Francis Claret, Tsubasa Otake, Masahito Shibata and Babara Lothenbach</i>	
Swiss Journal of Geosciences 2017, 2017:110(16, February 2017)	
DOI 10.1007/s00015-016-0240-5	309
Corrosion of Carbon Steel in Clay Environments Relevant to Radioactive Waste Geological Disposals, Mont Terri RockLaboratory (Switzerland)	
<i>Sophia Necib, Nikitas Diomidis, Peter Keech and Masashi Nakayama</i>	
Swiss Journal of Geosciences 2017, 2017:110(21, February 2017)	
DOI 10.1007/s00015-016-0259-7	331
Fifteen Years of Microbiological Investigation in Opalinus Clay at the Mont Terri Rock Laboratory (Switzerland)	
<i>Olivier X. Leupin, Rizlan Bernier-Latmani, Alexandre Bagnoud, Hugo Moors, Natalie Leys, Katinka Wouters and Simcha Stroes-Gascoyne</i>	
Swiss Journal of Geosciences 2017, 2017:110(24, February 2017)	
DOI 10.1007/s00015-016-0255-y	345
Impact of the Electron Donor on in situ Microbial Nitrate Reduction in Opalinus Clay: Results from the Mont Terri Rock Laboratory (Switzerland)	
<i>Nele Bleyen, Steven Smets, Joe Small, Hugo Moors, Natalie Leys, Achim Albrecht, Pierre De Cannière, Bernhard Schwyn, Charles Wittebroodt and Elie Valcke</i>	
Swiss Journal of Geosciences 2017, 2017:110(24, February 2017)	
DOI 10.1007/s00015-016-0256-x	357
Natural Gas Extraction and Artificial Gas Injection Experiments in Opalinus Clay, Mont Terri Rock Laboratory (Switzerland)	
<i>Agnès Vinsot, C. Anthony J. Appelo, Mélanie Lundy, Stefan Wechner, Cristelle Cailteau-Fischbach, Philippe de Donato, Jacques Pironon, Yanick Lettry, Catherine Lerouge and Pierre De Cannière</i>	
Swiss Journal of Geosciences 2017, 2017:110(23, February 2017)	
DOI 10.1007/s00015-016-0244-1	377

Exploring Diffusion and Sorption Processes at the Mont Terri Rock Laboratory (Switzerland): Lessons Learned from 20 Years of Field Research <i>Olivier X. Leupin, Luc R. Van Loon, Thomas Gimmi, Paul Wersin and Josep M. Soler</i> Swiss Journal of Geosciences 2017, 2017:110(7, March 2017) DOI 10.1007/s00015-016-0254-z	393
Twenty Years of Research at the Mont Terri Rock Laboratory: What We Have Learnt <i>Paul Bossart</i> Swiss Journal of Geosciences 2017, 2017:110(7, March 2017) DOI 10.1007/s00015-017-0267-2	407
Author Index	415

Editorial: Mont Terri rock laboratory 20 years of experimentation and applied research

© Swiss Geological Society 2017



Paul Bossart, director of the Mont Terri project, discussing the properties of the Opalinus Clay exposed in a tunnel window in the Mont Terri rock laboratory in front of a group of visiting scientists (Photo: Benedikt Galliker)

To celebrate the 20th anniversary of the Mont Terri rock laboratory, representatives from science, politics, and authorities met on 19 May, 2016, at the laboratory headquarters at St. Ursanne. Bundesrat Guy Parmelin, head of the Federal Department of Defence, Civil Protection, and Sport, opened the ceremony. He stressed the importance of the rock laboratory for the Swiss Confederation on the issue of safe nuclear disposal in Switzerland. In his words, “The rock laboratory in St. Ursanne, Canton Jura, plays a central role for the safety and construction of a deep geological repository in clay formations worldwide”.

In 2016 exactly 20 years have passed since what was then the SNHGS (Swiss National Hydrological and Geological Survey) launched a small project to characterize the Opalinus Clay in the Mont Terri exploration tunnel near St. Ursanne. Previously, the Canton of Jura had granted permission to open eight small niches to install measuring instruments. The project was initially intended to run for a maximum of three years. The aim was to clarify whether the Opalinus Clay, as an alternative to crystalline rock, could be considered for a deep geological repository of radioactive waste.

Twenty years later, the small exploration project has now become an international platform for applied research in the field of radioactive waste disposal, as well as in the field of carbon capture and sequestration (for instance, as CO₂). Sixteen partners from 8 countries, including the USA, Canada, and Japan, are participating in the research at Mont Terri. Some 140 experiments have been carried out since 1996, almost 50 are still running. The question of whether Opalinus Clay is suitable as a host rock for a repository was definitively answered in 2011: investigations conducted by Nagra, and their verification by ENSI, show that Opalinus Clay is the only viable host rock for the deep geological storage of highly radioactive waste in Switzerland. This led to the main decision on Stage 1 (Selection of Geological Siting Areas) of the Sectoral Plan for Deep Geological Repositories. The Mont Terri research project contributed significantly to reaching this conclusion, and of this we are very proud.

Considering this contribution to Swiss research on the host rock for a permanent repository alone, however, would underestimate the full impact of the Mont Terri research. Together with its international research partners, the project has developed new measurement and evaluation methods and brought them to maturity. Among many, it has advanced the determination of rock parameters using


innovative borehole geophysics, improved the methodology for characterization pore-water and microbial activity in claystones, and gained a new understanding of diffusion and retention processes of radionuclides in and through claystones. These methods are also applicable to low-permeability rocks at other sites. Moreover, the many technicians and scientists who are involved, exchange data and knowledge with each other. In this way, the partners gain a substantial added value on their investments.

This special issue gives an selection of research results achieved over the last 20 years. On the occasion of the Technical Meeting TM-34 on 10–11 February, 2016, in the Jesuit Church in Porrentruy, 150 scientists, technicians and managers communicated and discussed these research results, and produced scientific publications from their investigations. These papers are now presented in this Special Issue of the Swiss Journal of Geosciences, offering a representative cross-section of the research at the Mont Terri rock laboratory over the last 20 years.

Paul Bossart
Associate Editor, Swiss Journal of Geosciences
Director, International Mont Terri Project

Alan Geoffrey Milnes
Scientific Editor, Swiss Journal of Geosciences

Mont Terri rock laboratory, 20 years of research: introduction, site characteristics and overview of experiments

Paul Bossart¹  · Frédéric Bernier² · Jens Birkholzer³ · Christophe Bruggeman⁴ · Peter Connolly⁵ · Sarah Dewonck⁶ · Masaaki Fukaya⁷ · Martin Herfort⁸ · Mark Jensen⁹ · Jean-Michel Matray¹⁰ · Juan Carlos Mayor¹¹ · Andreas Moeri¹ · Takahiro Oyama¹² · Kristof Schuster¹³ · Naokata Shigeta¹⁴ · Tim Vietor¹⁵ · Klaus Wiczorek¹⁶

Received: 28 April 2016 / Accepted: 9 December 2016 / Published online: 21 February 2017
© The Author(s) 2017. This article is published with open access at Springerlink.com

Abstract Geologic repositories for radioactive waste are designed as multi-barrier disposal systems that perform a number of functions including the long-term isolation and containment of waste from the human environment, and the attenuation of radionuclides released to the subsurface. The rock laboratory at Mont Terri (canton Jura, Switzerland) in the Opalinus Clay plays an important role in the development of such repositories. The experimental results gained in the last 20 years are used to study the possible evolution of a repository and investigate processes closely related to

the safety functions of a repository hosted in a clay rock. At the same time, these experiments have increased our general knowledge of the complex behaviour of argillaceous formations in response to coupled hydrological, mechanical, thermal, chemical, and biological processes. After presenting the geological setting in and around the Mont Terri rock laboratory and an overview of the mineralogy and key properties of the Opalinus Clay, we give a brief overview of the key experiments that are described in more detail in the following research papers to this Special Issue of the Swiss Journal of Geosciences. These experiments aim to characterise the Opalinus Clay and estimate safety-relevant parameters, test procedures, and technologies for repository construction and waste emplacement. Other aspects covered are: bentonite buffer emplacement, high-pH concrete-clay interaction experiments, anaerobic steel corrosion with hydrogen formation, depletion of hydrogen by microbial activity, and finally, release of radionuclides

Editorial handling: A. G. Milnes.

This is the introductory paper (including a list of abbreviations and acronyms) to accompany the 20 research papers (papers 1–20) included in the Special Issue.

Electronic supplementary material The online version of this article (doi:10.1007/s00015-016-0236-1) contains supplementary material, which is available to authorized users.

✉ Paul Bossart
paul.bossart@swisstopo.ch

¹ Federal Office of Topography swisstopo, Seftigenstrasse 264, 3084 Wabern, Switzerland

² Federal Agency for Nuclear Control FANC, Rue Ravenstein 36, 1000 Brussels, Belgium

³ Lawrence Berkeley National Laboratory, Berkeley, CA 94720, USA

⁴ Belgian Nuclear Research Centre SCK.CEN, Boeretang 200, 2400 Mol, Belgium

⁵ CHEVRON, Rock Mechanics Team, Chevron ETC, 1500 Louisiana Street, Houston, TX 77002, USA

⁶ Agence Nationale pour la Gestion des Déchets Radioactifs ANDRA, Centre de Meuse Haute-Marne, RD 960, 55290 Bure, France

⁷ Nuclear Facilities Division, Nuclear Waste Technology Department, OBAYASHI Corporation, 2-15-2, Konan, Minato-ku, Tokyo 108-8502, Japan

⁸ Swiss Federal Nuclear Safety Inspectorate ENSI, Industriestrasse 19, 5200 Brugg, Switzerland

⁹ Nuclear Waste Management Organization (NWMO), 22 St. Clair Ave. E., Toronto, ON, Canada

¹⁰ Institut de Radioprotection et de Sécurité Nucléaire, 31, Avenue de la Division Leclerc, 92260 Fontenay-aux-Roses, France

¹¹ Empresa Nacional de Residuos Radiactivos S.A. ENRESA, Calle de Emilio Vargas, 7, 28043 Madrid, Spain

¹² Geosphere Environmental Science Department, Abiko Research Laboratory, Central Research Institute of Electric Power Industry CRIEPI, 1646, Abiko, Chiba 270-1194, Japan

into the bentonite buffer and the Opalinus Clay barrier. In the case of a spent fuel/high-level waste repository, the time considered in performance assessment for repository evolution is generally 1 million years, starting with a transient phase over the first 10,000 years and followed by an equilibrium phase. Experiments dealing with initial conditions, construction, and waste emplacement do not require the extrapolation of their results over such long timescales. However, experiments like radionuclide transport in the clay barrier have to rely on understanding long-term mechanistic processes together with estimating safety-relevant parameters. The research at Mont Terri carried out in the last 20 years provides valuable information on repository evolution and strong arguments for a sound safety case for a repository in argillaceous formations.

Keywords Underground research laboratory (URL) · International research programme · Nuclear waste disposal · Repository evolution · In situ experiments · THMC processes · Switzerland

1 Introduction

1.1 Objectives of underground rock laboratories

An underground rock laboratory (URL) is a research facility in which site characterisation and testing activities are carried out, along with technology development and demonstration activities in support of the development of deep geological repositories for disposal of radioactive waste (OECD 2013). Therefore, the prime objectives of investigation programs in rock laboratories are to acquire data that will provide in-depth understanding of long-term performance of repository components in a geological environment, and to obtain data that will be used as a starting-point for development and testing of safety assessment models. A further objective is to demonstrate and optimise key components of the engineered barrier system (e.g. testing of canister and backfilling materials and its interaction with the host rock). An important

contribution of a rock laboratory is to investigate the selected geological environment and to test models at more appropriate scales and conditions than can be achieved at the surface. A final objective is the evaluation of transferability of individual parameters, investigation techniques, data evaluation methods, process understanding, and conceptual models to reach high-level conclusions (e.g. engineering feasibility, safety aspects) relevant to a safety case¹ for a future repository program (Mazurek et al. 2008; Blechschmidt and Vomvoris 2010; Delay et al. 2014; Alexander et al. 2015).

There are two types of URL: generic and site-specific. Generic URLs are independent of final disposal sites and comprise facilities that are developed for research and testing purposes at a site that will not be used for waste disposal. Site-specific URLs are located in the host rock in an area that is considered as a potential future repository. They include facilities that are developed for specific investigations at the given site and may, indeed, be a forerunner to the development of a repository at that site. During the last 40 years, about 30 generic and site-specific URLs have been constructed and about half of them are still in operation (Blechschmidt and Vomvoris 2010). Many of these URLs were constructed in granitic (40%) but the majority (60%) in sedimentary rocks, such as bedded salt and salt domes, clays, tuffs, limestones, and diatomite. There are three major URLs in claystones: (1) the site-specific Meuse/Haute Marne URL, located in the Paris basin in France at a depth of 490 m in the stiff Callovian-Oxfordian clay formation, and operated by ANDRA; (2) the site-specific Hades URL at a depth of 225 m in the plastic Boom Clay in Belgium at a depth of 225 m, operated by SCK.CEN; and (3) the generic Mont Terri rock laboratory, located in the canton Jura in Switzerland at a depth of 280 m in the stiff Opalinus Clay, operated by the Swiss Geological Survey at swisstopo (Swiss Federal Office of Topography). This Special Issue of the Swiss Journal of Geosciences presents 20 papers describing the key experiments that have been carried out during the last 20 years of applied research at the generic Mont Terri rock laboratory. In this introductory paper, we give an overview of the papers comprising this Special Issue and placing them within a conceptual scheme of repository evolution.

¹³ Federal Institute for Geosciences and Natural Resources BGR, Stilleweg 2, 30655 Hannover, Germany

¹⁴ Japan Atomic Energy Agency JAEA, 432-2 Hokushin, Horonobe-cho, Hokkaido 098-3224, Japan

¹⁵ National Cooperative for the Disposal of Radioactive Waste NAGRA, Hardstrasse 73, 5430 Wetingen, Switzerland

¹⁶ Gesellschaft für Anlagen- und Reaktorsicherheit (GRS) GmbH, Process Analysis Department, Final Repository Safety Research Division, Theodor-Heuss-Strasse 4, D-38122 Braunschweig, Germany

¹ A safety case is a structured argument, supported by evidence, intended to justify that a system is acceptably safe. According to the IAEA (2012), it is "...the collection of scientific, technical, administrative and managerial arguments and evidence in support of the safety of a disposal facility, covering the suitability of the site and the design, construction and operation of the facility, the assessment of radiation risks and assurance of the adequacy and quality of all of the safety related work associated with the disposal facility".

1.2 Research in the Mont Terri rock laboratory

The Mont Terri rock laboratory lies north of the town of St-Ursanne in the canton of Jura. The research facilities are located at a depth of 280 m below the surface and are accessed through the security gallery of the Mont Terri tunnel of the A16-Transjura highway, which passes through the Jura mountain range. The research galleries in the Opalinus Clay layer have a total length of ca. 700 m.

The major aims of the international Mont Terri research project are to investigate and analyse the hydrogeological, geochemical, and rock mechanical properties of argillaceous formations. The Mont Terri rock laboratory offers a scientific and technical platform for international collaboration in the field of deep geological disposal. In the Mont Terri rock laboratory, experiments are dedicated to investigate the properties of a pristine claystone, the Opalinus Clay, its perturbation when an underground opening is constructed, the early and late time interplay of engineered barriers and the natural claystone barrier, and ultimately the understanding of the migration of radionuclides at varied length (near and far-field) and timescales. The latter experiments lead to an increase in confidence in estimating radionuclide mass transport through engineered and natural barriers and improving the reliability of the predictive numerical tools. Understanding mass transport processes is central to a repository safety case.

The Swiss Geological Survey at swisstopo is responsible for operation of the facility and directs the international Mont Terri project. Sixteen organisations from Belgium, Canada, France, Germany, Japan, Spain, Switzerland, and the USA, all of which are considering clay formations as potential host rocks for deep geological disposal of radioactive waste, are involved in the underground (in situ) experiments.

The Opalinus Clay has been selected in Switzerland as the preferred host rock for disposal of high-level waste (HLW) and is among the possible host rocks for low- and intermediate-level radioactive waste (LLW, ILW). A sectoral plan process, led by the Swiss Federal Office of Energy (SFOE), is now underway with the objective of selecting sites for deep geological repositories (SFOE 2008). However, the Mont Terri rock laboratory is first and foremost a research facility for international implementers and safety organisations to conduct collaborative international science and research projects in a low-permeability, smectite-rich claystone with self-sealing (swelling) properties. In this sense, the Mont Terri rock laboratory can be considered as a generic underground rock laboratory. Disposal of radioactive waste will not be considered here. However, some of the experiments at the Mont Terri rock lab should be seen in the context of a potential repository in Opalinus Clay at other locations in northern Switzerland

(Nagra 2002, 2010). These include experiments dealing with the horizontal emplacement of waste canisters and demonstration of selected aspects of the Swiss multi-barrier concept.

This introductory paper gives an overview of the geology in and around the Mont Terri rock laboratory (Sect. 2). In Sect. 3, we outline all the experiments that have been carried out over the last 20 years, and give an overview of the papers in this Special Issue and correlate them with the evolution of a potential repository in the Opalinus Clay. In Appendix, we list abbreviations and acronyms which are used throughout the Special Issue with their explanations. For a glossary of technical terms, we refer to Alexander et al. (2015), and to the IAEA-website: <http://www-pub.iaea.org/books/IAEABooks/6682/Radioactive-Waste-Management-Glossary>.

In the Electronic Supplementary Material attached as Online Resources 1–9 to the present paper, we give additional information about the Mont Terri research project for consultation online (Online Resource 1: explanatory text. Online Resources 2–9: figures and tables). There, we present the partner organisations that are involved in the research project together with their key persons, a retrospective historical overview over the last 30 years, the financial investments, and the project organisation between research partners, operator and owner of the facility. Furthermore, we present a complete list of performed and ongoing experiments since 1996, together with a map of the rock laboratory showing where these experiments are localised.

2 Site characteristics

The canton of Jura, where the Mont Terri rock laboratory is located, lies within the Jura mountain belt (Fig. 1). Stratigraphically, this mountain belt encompasses the period from Late Palaeozoic to Quaternary, but the majority of the rocks belong to the “Jurassic” time period. Tectonically, it can be divided into the Folded Jura, an arcuate fold-and-thrust belt located to the northwest of the Alpine arc and its foreland basin, extending from Lake Annecy in eastern France to the Zurich area in northern Switzerland and further into southern Germany, and the more external Tabular Jura with undeformed Mesozoic sediments (Fig. 1). The fold-and-thrust belt of the Folded Jura is surrounded by Tertiary basins of different types, to the north the Rhine Graben, to the west the Bresse Graben, and to the southeast the Swiss Molasse Basin. The Rhine and Bresse Grabens are associated with the Oligocene West-European rift system, whereas the Molasse Basin corresponds to an Oligo-Miocene foreland basin, which developed in front of the Alpine orogeny (Sommaruga 1999).

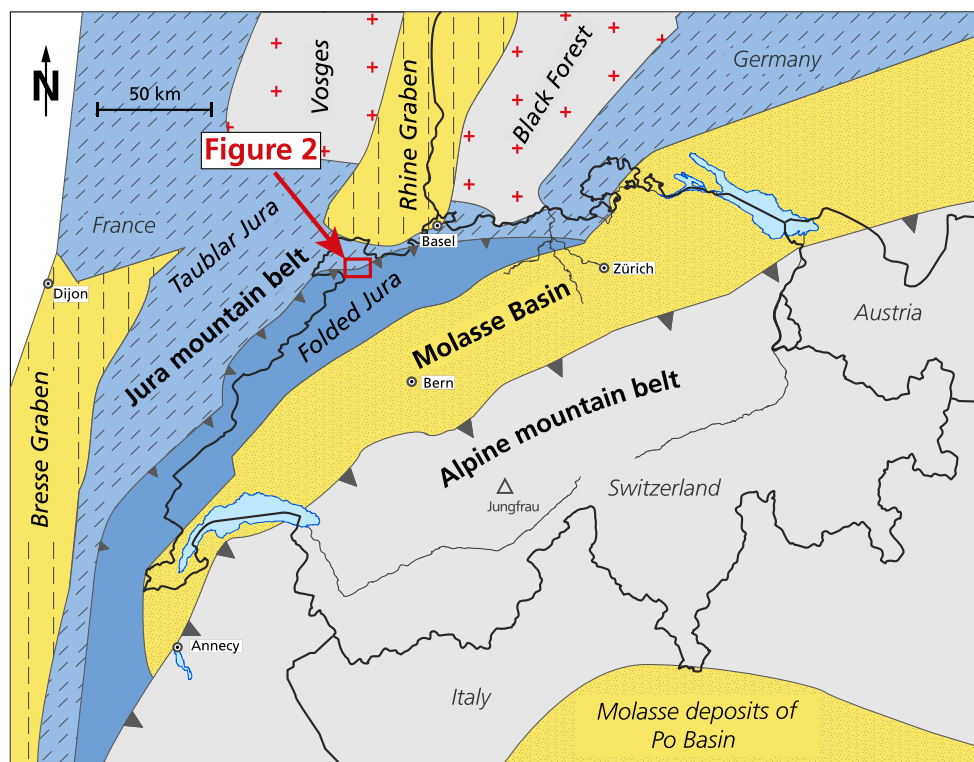


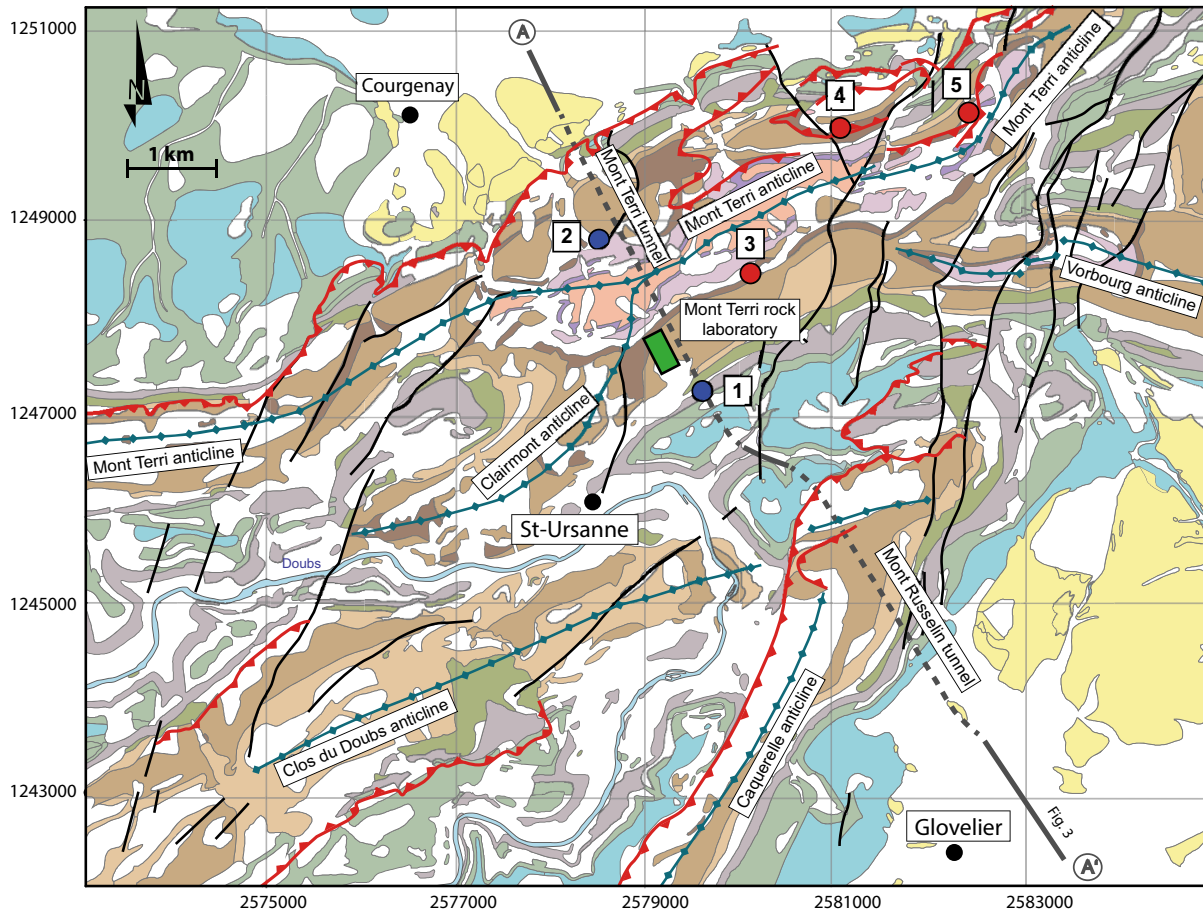
Fig. 1 Sketch map of tectonic units in Switzerland and neighbouring States. The Mont Terri rock laboratory is located in the Canton of Jura besides the Mont Terri motorway tunnel along the A16 Transjurane, in the Folded Jura. The *inset* refers to the geologic map of Fig. 2

The region of St-Ursanne, where the Mont Terri rock laboratory is located, lies within the Folded Jura, and comprises sedimentary rocks ranging in age from Carboniferous to Quaternary (Fig. 2). The Late Palaeozoic clastic sediments are unconformably overlain by almost 1600 m of Mesozoic limestones, marls and shales, around 400 m of Tertiary Molasse, and, locally, Quaternary fluvio-glacial sediments. Of special interest are the Liassic–Dogger units, which comprise several shallowing-upward regressive cycles, starting with the Opalinus Clay and ending with shallow-water carbonates (Blaesi 1987). The Opalinus Clay² consists of a monotonous sequence of dark grey, silty, micaceous clays and sandy shales, deposited around 174 Ma ago. This age is based on a new stratigraphic investigation in a deep borehole cutting the Opalinus Clay and adjacent formations near the rock laboratory

² Definition and usage of the term “Opalinus Clay”: it is regarded in this and following papers as a lithostratigraphic formation, the latter defined as a rock of similar mineralogical and petrophysical properties, which is clearly discernible and mappable as a distinct rock unit in the field. Unweathered, fresh Opalinus Clay is a monotonous succession of dark grey, mica bearing clay and silty marl, with carbonate and sandy lenses that become more abundant towards the top (<http://www.strati.ch>). According to Wetzler and Alia (2003) the thickness of this formation varies between 60 and 150 m. Its age is of late Toarcian to early Aalenian (~ 174 Ma). An update of its litho- and biostratigraphy is given in Hostettler et al. (2017).

Fig. 2 Geologic map of the folded and tabular Jura in the region of St-Ursanne, Canton of Jura. The A16 tunnels of Mont Russelin and Mont Terri are projected onto the map and provide the profile trace for Fig. 3. The Mont Terri rock laboratory is located in the southern limb of the Mont Terri anticline. In this large anticlinal fold, two deep boreholes (numbers 1–2) and 3 important surface outcrops (numbers 3–5) are indicated. Surface outcrops of Opalinus Clay are rare and altered due to weathering. The traces of the axial planes of the Mont Terri, Caquerelle, and Clairemont anticlines and the sinistral strike-slip faults are shown as the key tectonic structures of this map. The Paleogene and Neogene deposits comprise the following formations: Porrentury conglomerates, Terres jaunes, Meeresand, Septarionton, Alsace Molasse, Upper Marine Molasse (red marls and gonpholites), and Upper Freshwater Molasse (Formation du Bois de Raube, Vogesenschotter). Further details are given in the legend. This map is based on the Geological Atlas of Switzerland 1:25,000, map No. 40 “St-Ursanne,” (Laubscher 1963), available through swisstopo online under <https://map.geo.admin.ch>

(Hostettler et al. 2017). The Opalinus Clay is overlain by the Passwang Formation of sandy limestones, shales and oolitic ironstones, and underlain by the Staffelegg Formation consisting of limestones, marls, and shaly intercalations (see geologic map of Fig. 2 and vertical profile of Fig. 3). At Mont Terri and adjacent areas, the Opalinus Clay is barely exposed at the surface. One of the first lithological descriptions of the Opalinus Clay was given by Schmidt et al. (1924) from a borehole near Buix, located about 20 km to the NW of Mont Terri, where a total



Legend

Quaternary	Quaternary deposits	
Neogene Paleogene	Paleogene and Neogene deposits	
Jurassic	Kimmeridgian	Reuchenette Formation
	Oxfordian	Vellerat + Courgenay Formations
		St-Ursanne Formation + (Vorbourg Mb)
		Barschwil Formation
	Callovian	Ifenthal Formation
	Bathonian	Hauptrogenstein
	Bajocian	Passwang Formation
	Aalenian	Opalinus Clay
	Toarcian	Staffelegg Formation
	Pliensbachian	Klettgau Formation
	Sinemurian	Bänkerjoch Formation
	Hettangian	Schinznach Formation
Triassic	Rhaetian	Zeglingen Formation
	Norian	Kaiseraugst Formation
	Carnian	} Not exposed
	Ladinian	
	Anisian	

Symbols

- Thrust planes
- Anticlines
- Cross faults (extensional / strike-slip)
- Cross section (Fig. 3)
- Boreholes:
 - 1** BDB-1 (from tunnel)
 - 2** BDS-5 (from surface)
- Outcrops / Formations (coordinates):
 - 3** Sous les roches / Passwang Formation (2'580'224/1'248'480)
 - 4** La Malcôte / Passwang Formation (2'580'915/1'249'982), La Malcôte / Hauptrogenstein (2'581'102/1'249'886)
 - 5** Côte de boulet / Passwang Formation (2'582'296/ 1'249'995)

thickness of 157.5 m was encountered. The present thickness of the Opalinus Clay in the Mont Terri rock laboratory has been estimated to be 131 m. This corresponds to a sedimentary thickness of about 120 m when corrected for tectonic overthrusting (Hostettler et al. 2017). The Opalinus Clay at Mont Terri is an overconsolidated claystone. The maximum burial is estimated to have been 1350 m. This results in an overconsolidation ratio of almost 5, assuming a present-day mean overburden of 280 m.

2.1 Regional tectonic setting

Nussbaum et al. (2011) describe the regional geologic-tectonic setting in detail, which we summarise here. Pre-existing fault systems together with Permo–Carboniferous grabens and the Rhine–Bresse transfer zone (where the region of St-Ursanne is located) have largely influenced the thrust-and-fold-belt geometry of the Jura Mountains, resulting in complex interference structures such as cross-folds and strike-slip fault zones. Cross-folds occur with different trends, for example, the Caquerelle and Mont Terri anticlines and the divergence of the Mont Terri anticline at its western margin (Figs. 1, 2). During the Jura thrusting phase, inherited transcurrent faults from the European Cenozoic intra-continental rifting phase triggered development of both frontal and oblique ramps, depending on fault orientation with respect to transport direction. Consequently, the Mont Terri anticline can be considered as a non-cylindrical domal anticline. Its north-eastern border is cut by inherited sinistral strike-slip faults, and its southwestern end is interpreted as the result of cross folding. The detailed kinematic evolution of this structure is described in Nussbaum et al. (2017).

2.2 Local geology of the Mont Terri rock laboratory

2.2.1 Lithofacies

During construction of the Mont Terri tunnel system in the late 1980s, the reconnaissance gallery of the Mont Terri highway tunnel revealed fresh and high-quality exposures of Opalinus Clay. This led to more detailed lithostratigraphic, hydrogeological, and geochemical descriptions of this formation (Schaeren and Norbert 1989; Tripet et al. 1990; Blaesi et al. 1991, 1996; Gautschi et al. 1993; Hostettler et al. 2017). Not only the discovery of the Opalinus Clay at this locality, but also the simple geometry (limited thrust zones and imbricates) and the possibility of horizontal access, led to establishing the Mont Terri rock laboratory. The laboratory is located entirely in the Opalinus Clay, which can be subdivided into five units and comprises three lithofacies types (Fig. 4). At the bottom there is a shaly facies consisting of mica-bearing marly shales with nodular zones or mm-thick layers of quartz in the silt fraction. Above this there is a sharp transition to a thin carbonate-rich sandy facies, which is characterised by quartz-bearing calcareous biotrititic layers up to 10 cm thick. Then a sandy facies follows with calcareous silty claystones, and above this a dark-grey, mica-bearing, and slightly silty claystone, which is attributed to the shaly facies. The uppermost unit of the Opalinus Clay consists again of sandy facies, a light-grey silty claystone with lenses of laminated silt and lenses of bioclastic material. Schaeren and Norbert (1989) and Blaesi et al. (1991) defined the base of the Opalinus Clay as a lithological transition of argillaceous sediments to more marly sediments. The latter have been identified as the Gross Wolf

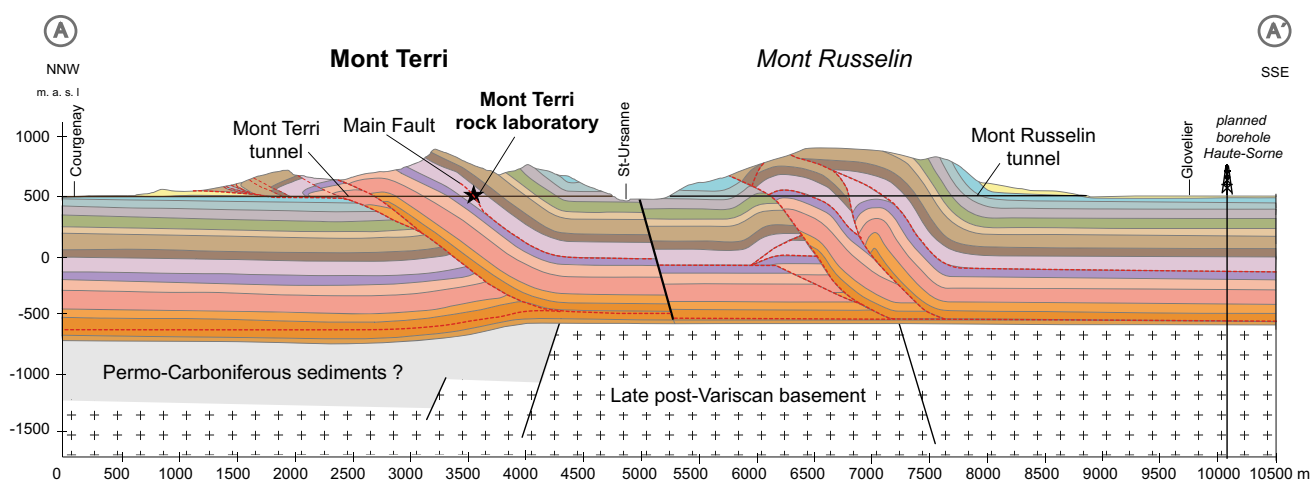


Fig. 3 Balanced geological profile along the Mont Russelin and Mont Terri tunnels. The profile trace is indicated in Fig. 2. These profiles are based on Schaeren and Norbert (1989), Freivogel and Huggenberger (2003), Caër et al. (2015), and Nussbaum et al. (2017).

The latter reference gives the kinematic evolution of this cross-section. Note the simple geometry of the Opalinus Clay in the Mont Terri rock laboratory compared to the Opalinus Clay of the other tunnel outcrops (i.e. Mont Russelin)

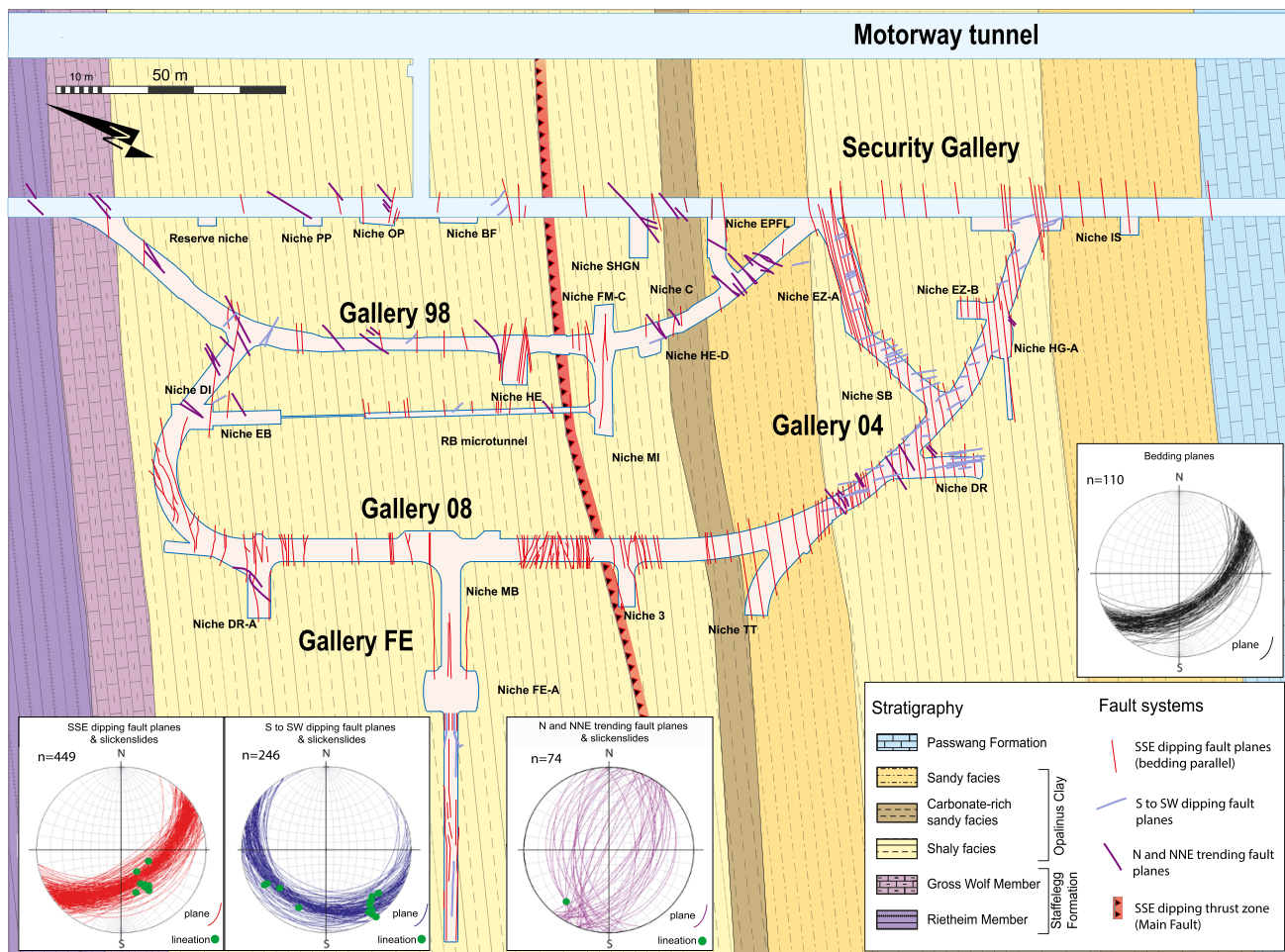


Fig. 4 Geologic–tectonic map of the Mont Terri rock laboratory. The Opalinus Clay is sandwiched between the Staffelegg Formation (*base*) and the Passwang Formation (*top*). There are three different facies of Opalinus Clay: shaly, carbonate-rich sandy, and sandy

facies. The mapped tectonic faults can be assigned to one of three fault systems as shown on the stereoplots (*bottom left*, lower hemisphere Wulff projections). The rock laboratory is intersected by a major fault, called the “Main Fault”

Member of the Staffelegg Formation (Reisdorf et al. 2011; Hostettler et al. 2017). The upper boundary of the Opalinus Clay is defined by a distinct hardground of chamositic crusts (Blaesi et al. 1991) and iron oolites.

2.2.2 Structural relations

A prominent tectonic overprint of the Opalinus Clay in sections of the Mont Terri and Mont Russelin is confirmed by numerous studies on structural data conducted during the evolution of the rock laboratory (e.g. Nussbaum et al. 2011). The Mont Terri rock laboratory is located in the southern limb of the Mont Terri anticline (Figs. 2, 3). The present overburden varies between 250 and 320 m and the strata dip with an angle between 30° and 50° towards SSE in the northern and southern part of the Mont Terri rock laboratory, respectively. The Mont Terri anticline

developed between 10 and 2 Ma ago at the junction of the frontal part of the Jura thrust-and-fold belt and the Rhine–Bresse transfer zone. The geometry is an imbricate fault-bend fold with a component of trishear (Nussbaum et al. 2017). In the Mont Terri rock laboratory, three different fault systems are identified that correlate with regional-scale tectonic structures. The three fault systems are shown in the stereoplots of Fig. 4. They comprise (1) N to NNE-striking steeply inclined normal faults of the Rhine–Bresse graben system reactivated in sinistral strike-slip mode during the Late Miocene Jura thrusting phase, (2) SSE-dipping faults subparallel to bedding initiated during the late stage of reverse faulting and anticline folding by flexural slip, and (3) SW-dipping, sub-horizontal faults resulting from lateral extension during thrusting of the Mont Terri anticline above the frontal ramp. The largest tectonic feature in the rock laboratory is the so-called Main

Fault, a thrust fault zone, which at the rock lab level dips on average about 15° steeper than bedding planes and exhibits a similar strike direction (Figs. 2, 3).

2.3 Mineralogy of Opalinus Clay

The mineral composition of the Opalinus Clay has been analysed by various groups (e.g. Mazurek 1999). In general, the shaly and sandy lithofacies display a qualitatively similar mineral composition. The shaly facies contains more clay minerals and less quartz compared to the sandy facies. The carbonate-rich sandy facies contains more calcite and quartz, but less clay minerals. Observed minerals are quartz, illite and mixed-layer illite–smectites, kaolinite, chlorite, biotite and muscovite, calcite, aragonite, siderite, dolomite and/or ankerite, albite and/or plagioclase, K-feldspar, pyrite, organic matter, and other accessory minerals such as apatite, celestine, zircon, and monazite. The total dry wt% of illite, chlorite and kaolinite varies between 8 and 80%, and the mixed-layer illite–smectites varies between 3 and 20% (Table 1). A best estimate of the total clay content is 66%, with mixed-layer illite-smectites of 10%. Quartz varies between 10 and 44%, with a best estimate of 14% and carbonate minerals vary between 4 and 57% with a best estimate of 13%. The best estimate for pyrite is 1.1% and that for organic carbon is 0.8%. Some secondary minerals have also been detected but not quantified, including celestine and barite in veins, and elemental sulphur. Other phases, namely gypsum and traces of jarosite, have been detected only in material that has been altered by oxidation. The bulk of organic material in the Opalinus Clay is kerogen or other uncharacterised material of terrestrial detrital origin. Organic geochemical indices and biomarkers show that the Opalinus Clay in the Mont

Terri section is thermally immature, having experienced maximum burial temperatures of about 80 °C during Cretaceous burial (Mazurek et al. 2006), and shows low hydrocarbon source-rock potential.

2.4 Other key properties of Opalinus Clay

The Opalinus Clay is an anisotropic material with different properties perpendicular and parallel to bedding. Properties for the shaly and sandy facies are given in Table 2, taking into account parameter values perpendicular and parallel to bedding. These properties were derived from Opalinus Clay at the level of the rock laboratory (280 m below surface).

From a hydraulic point of view, the Opalinus Clay is characterized by a very low hydraulic conductivity of $2 \times 10^{-13} \text{ m s}^{-1}$. Solute transport is, therefore, mainly controlled by molecular diffusion. This is also confirmed by measured natural chloride and helium (^4He) concentrations in the pore-water (Pearson et al. 2003). Chloride and helium concentrations in the pore-waters of Opalinus Clay and its bounding aquifer formations show smooth, regular profiles with depth, with some profiles being more symmetric than the others. When modelling these profiles taking into account the local erosion pattern, it was assumed that the upper aquifer in the Passwang formation was activated first, followed by the lower aquifer in the Staffelegg formation. The best interpretation, which includes this concentration pattern, is the process of molecular diffusion whereby solutes in the Opalinus Clay have diffused into the bounding aquifers (Mazurek and de Haller 2017). Also migration experiments with artificial non- to low-sorbing radionuclides in the Mont Terri rock laboratory confirm solute transport by molecular diffusion,

Table 1 Mineralogy of Opalinus Clay

Mineralogy	Shaly facies (wt%)	Sandy facies (wt%)	Carbonate-rich sandy facies (wt%)
Clay minerals			
Illite, chlorite, kaolinite	39–80	29–70	8–45
Illite/smectite mixed-layers	5–20	5–15	3–8
Quartz	10–27	22–44	22–36
Carbonates			
Calcite, dolomite, aragonite, ankerite, siderite	4–35	11–25	34–57
Feldspars			
Albite, K-feldspar	0.3–5	0.2–6	3–11
Pyrite	0.9–1.4	1–1.2	0.2–0.5
Organic matter	0.8–1.4	–	–
Accessory minerals			
Apatite, celestine, zircon, monazite	<0.1	<0.1	<0.1

The mineral compositions are presented for the shaly, sandy, and the carbonate-rich sandy facies. Values are given in wt%

Table 2 Selected in-situ and laboratory-derived key parameters for the Opalinus Clay in and around the Mont Terri rock laboratory (after Jaeggi and Bossart 2014)

Parameter	Shaly facies ^a		Sandy facies	
	Range	Best estimate	Range	Best estimate
Density (humid) [g/cm ³]	2.40-2.53 ^a (239)	2.45	2.42-2.63 ^d (65)	2.52
Total (physical) porosity [Vol %]	14-25 ^a (17)	18	5.3-17.7 ^d (17)	11.1
Water loss porosity [Vol %]	13-21 ^a	16	4.9-17.5 ^d (19)	10.5
Water content [weight %]	5.0-8.9 ^a (22)	6.6	2-6 ^e (112)	4
Seismic P-wave velocity V _p (N) [m/s]	2220-3020 ^a (48)	2620	1470-4610 ^e (61)	3280
Seismic P-wave velocity V _p (P) [m/s]	3170-3650 ^a (111)	3410	2870-5940 ^e (112)	3860
Hydraulic conductivity (N) [m/s]	2E-14 - 1E-12 ^a (57)	2E-13	1E-13-5E-12 ^f (10)	1E-12
Specific storage [m ⁻¹]	1E-7 - 1E-4 ^a (6)	2E-6	1E-6 - 1E-5 ^g (4)	7E-6
Effective diffusion coefficient (P) - Tritiated water HTO [m ² /s] - Iodine [m ² /s]	4.0E-11 – 6.8E-11 ^b (5) 1.0E-11 – 3.0E-11 ^b (5)	5.4E-11 2.0E-11	-	-
Effective diffusion coefficient (N) - Tritiated water HTO [m ² /s] - Iodine [m ² /s]	7.1E-12 – 1.1E-11 ^b (2) 2.3E-12 – 4.2E-12 ^b (2)	1.0E-11 3.0E-12	-	-
Effective porosity - Tritiated water HTO [%] - Iodine [%]	12.0 – 16.4 ^b (5) 5.0 – 12.5 ^b (2)	15.0 8.5	-	-
Uniaxial compressive strength, UCS (N) [MPa]	5-10 ^c (19)	7	6-37 ^c (51)	16
Uniaxial compressive strength, UCS (P) [MPa]	4-17 ^a (22)	10.5	4-37 ^c (60)	18.0
Elastic module, E-module (N) [GPa]	2.1-3.5 ^a (34)	2.8	0.4-19.0 ^c (51)	6.0
Elastic module, E-module (P) [GPa]	6.3-8.1 ^a (39)	7.2	2.0-36.7 ^c (60)	13.8
Poisson ratio (N) [-]	0.28-0.38 ^a (73)	0.33	0.06-0.42 ^c (51)	0.22
Poisson ratio (P) [-]	0.16-0.32 ^a (73)	0.24	0.13-1.23 ^c (59)	0.44
Thermal conductivity (N) [Wm ⁻¹ K ⁻¹]	1.0-3.1 ^a (9)	1.2	-	-
Thermal conductivity (P) [Wm ⁻¹ K ⁻¹]		2.1	-	-
Heat capacity [JKg ⁻¹ K ⁻¹]	-	1000 ^h	-	-
Porewater composition	Na-Cl-SO ₄ pore water with TDS of 18.3 g/l ⁱ			
Total cation exchange capacity CEC (Co-Hexamine, Ni-en in bold) [meq/100 g rock]	9.4-13.4^a (24) -	11.1 16 (24)	7.3-21.9 ^j (13)	14.4
Gas entry pressure [MPa]	1.2-3.2 ^k (11)	1.8-2.5	-	-

The table is ordered into petrophysical (orange), hydraulic (blue), rock-mechanical (grey), thermal (red), and geochemical parameters (yellow, green). Parameters are provided for the ranges and best estimates for the shaly and sandy facies. The number of parameter values, if available, are indicated in parenthesis. Note that currently not all parameters are available for both facies types, e.g. molecular diffusion and thermal parameters are only available for the shaly facies.

Parameters are distinguished for anisotropy by (N) samples normal to bedding, and (P) samples parallel to bedding. The petrophysical and rock-mechanical parameters originate mainly from drillcore measurements in the laboratory. Parameter values for the shaly facies are partly derived from ^a Bossart et al. (2008). The effective diffusion coefficients and effective porosities of the shaly facies are derived in situ and come from ^b Leupin et al. (2017a). The uniaxial compressive strength (UCS) values of the shaly facies normal to bedding come from ^c Amann et al. (2011a, b). The petrophysical and rock-mechanical parameters of the sandy facies come from ^d Peters et al. (2011) and ^e Gschwind (2013). In-situ derived hydraulic conductivities of the sandy facies come from ^f Lavanchy and Mettier (2012). The specific storage for the sandy facies are derived from ^g Yu et al. (2017). The heat capacity for the shaly facies come from ^h Garitte et al. (2014). Pore-water compositions with total dissolved solids originate from ⁱ Pearson et al. (2003). The total cation exchange capacity for the sandy facies has been derived by ^j Lerouge et al. (2011). The in-situ derived gas-entry pressure of the shaly facies originates from ^k Mische et al. (2010). The seismic P-wave velocity values in this table were derived from drillcore measurements in the laboratory; in-situ derived P-wave velocities are provided by Schuster et al. (2017)

providing diffusion parameters such as diffusion coefficients parallel and normal to bedding, effective porosities, and retardation parameters for sorbing radionuclides (Leupin et al. 2017a). As indicated in Table 2, these diffusion parameters can vary considerably and have to be evaluated separately for every species. This can be illustrated when comparing the parameters of non-sorbing tritiated water (HTO) and iodine: the effective diffusion coefficient of HTO parallel to bedding is $5.4 \times 10^{-11} \text{ m}^2 \text{ s}^{-1}$, with an effective porosity of 15%, which is about equal to the water loss porosity of 16%. The effective diffusion coefficient of iodide parallel to bedding is $2.0 \times 10^{-11} \text{ m}^2 \text{ s}^{-1}$ (less than half of that of HTO), with an effective porosity of only 8.5%, which is about half of the water-loss porosity. One reason for these different parameter values lies in the pore-space geometry of Opalinus Clay. The mean pore diameter is 40 nanometres, and the rather large iodine ions can access only about half of the total pore-space, whereas the rather small HTO molecules can access almost the whole pore-space.

From a rock-mechanical point of view, the Opalinus Clay can be considered as a transverse isotropic material (Bock 2009) with a best estimate of uniaxial compressive strength (UCS) for the shaly facies, parallel to bedding of 10.5 MPa, Poisson ratio of 0.24, and Young's modulus of 7.2 GPa. These mechanical parameters show rather different values in the sandy facies (Table 2). Generally, Opalinus Clay exhibits a quite complex rheological behaviour, which includes anisotropy, plasticity, and damage (Parisio 2016).

Thermal parameters were estimated only for the shaly facies. With a relatively low mean thermal conductivity of $1.8 \text{ W m}^{-1} \text{ K}^{-1}$ and a heat capacity of $1000 \text{ J kg}^{-1} \text{ K}^{-1}$ (Garitte et al. 2014), increased geothermal gradients are observed between bottom and top of the Opalinus Clay.

From a geochemical point of view, the pore-water is of Na-Cl-SO₄ type with a maximum of total dissolved solids (TDS) of 18.3 g l^{-1} , exhibiting a sea-water signature on the Cl⁻/Br⁻ plot and a cation exchange capacity CEC (Nien) of 11.1 meq/100 g rock (Table 2). The age of this marine pore-water in the region of the Mont Terri anticline is much younger than the sedimentation age of Opalinus Clay (174 Ma). Researchers applied two approaches to date pore-waters: Clauer et al. (2017) interpreted strontium isotope ratios of calcite from the matrix, veins, and fault gouges of the Opalinus Clay to yield an upper Eocene age of 38–36 Ma; Mazurek and de Haller (2017) analysed data on the geochemical evolution of pore-waters in and around Mont Terri giving a slightly younger age, close to the Oligocene/Miocene boundary at ca. 23 Ma. Both teams interpret these findings as marine incursions into the region of the future folded Jura of upper Eocene and Oligocene/Miocene ages, respectively.

Opalinus Clay also has the property of self-sealing, which means that cracks and fissures of the excavation damaged zone (EDZ) close when moisture is provided. Fractures in the EDZ, stress or anisotropy-induced, have the potential to act as preferential flow paths for radionuclides from the repository site to the biosphere. Thus, sealing of these fractures, especially when exhibiting an interconnected fracture network, is essential in order to reduce transmissivity of the EDZ network and thus to prevent any advective flow from the repository to the biosphere. This self-sealing propriety is mainly due to the mixed-layer illite-smectite clay minerals, which are present in both the shaly and sandy facies, and which swell when moisture is provided. This might be not true for the carbonate-rich sandy facies, where mixed-layer illite-smectite contents are small (Table 1). More detailed information about the parameters of the Opalinus Clay is given in Bossart and Thury (2008).

3 Thematic overview of experiments

3.1 Research topics focussed from 1996 to 2016

The Mont Terri research programme between 1996 and 2016 consists of 138 individual experiments; 93 experiments were successfully completed by mid-2016, and 45 experiments are still in progress (a compilation of these 138 experiments is presented in Online Resources 8 and 9). The three basic aims of these 138 experiments were and are: (1) understanding the characteristics, processes and mechanisms in undisturbed claystones, (2) understanding the repository-induced perturbations, and (3) performing experiments related to the demonstration of repository implementation technology. It is important to note that these experiments provide data and arguments that are relevant for the performance assessment of a repository and its safety case, but the performance of a repository cannot be directly tested in a generic rock laboratory like Mont Terri.

3.1.1 Experiments on characteristics, processes and mechanisms in undisturbed claystones

These experiments include:

- improving drilling and excavation technologies, and testing and sampling methods with the aim of minimising rock perturbations,
- estimating hydrogeological, rock mechanical, and geochemical parameters of the undisturbed Opalinus Clay, including upscaling parameters from laboratory to in situ scale (m to 100 m range),

- identifying geochemistry of pore-water and natural gases; gaining a better understanding of pore-water origin, dating, and its evolution over geological time-scales; and assessment of long-term hydraulic transients associated with basin inversion, erosion, and thermal scenarios,
- experimental work associated with understanding diffusive mass transport in the far-field (kilometre scale, timescale of several millions of years), mainly by measuring and interpreting natural tracer profiles in and around the Mont Terri rock laboratory,
- experimental work associated with the evaluation of diffusion and retention parameters for long-lived radionuclides in the near-field (centimetre to decimetre scale, timescale of 1–5 years), by artificially placing radionuclides into boreholes, letting them diffuse into the borehole wall, and then analysing the distribution of radionuclides in the overcores.

The latter two points are crucial to assessing the significance of mass transport and they also provide evidence on the degree to which this is diffusion dominated. A transport regime that is diffusion dominated is preferred for

long-term radioactive waste isolation and containment. Our strong evidence that mass transfer in a natural claystone barrier such as the Opalinus Clay is diffusion dominated provides an important argument supporting the safety case of a repository in this lithology.

3.1.2 Experiments on repository-induced perturbations

These include:

- hydro-mechanical coupled processes (e.g. stress redistributions and pore pressure evolution during mine-by testing),
- thermo-hydro-mechanical-chemical coupled processes (e.g. heating of bentonite and host rock),
- self-sealing processes in the excavation damaged zone, from small scale to repository scale,
- gas-induced transport of radionuclides in pore-water, gas transport along interfaces in the engineered barrier system,
- influence of cement rock liner on the bentonite backfill, buffering potential of the claystone in the near field, and its geochemical and kinetic processes.

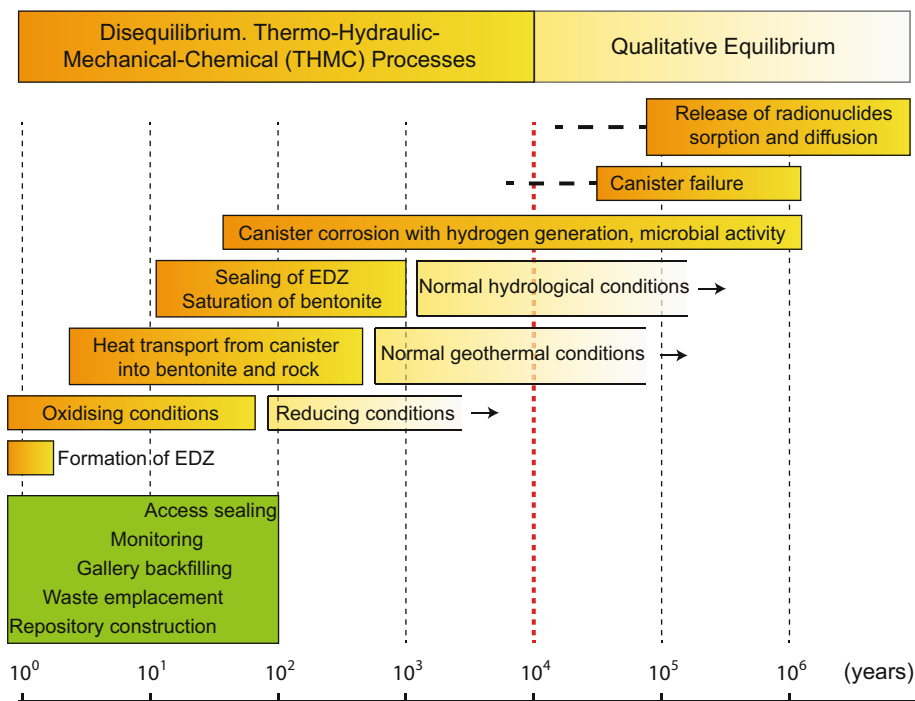
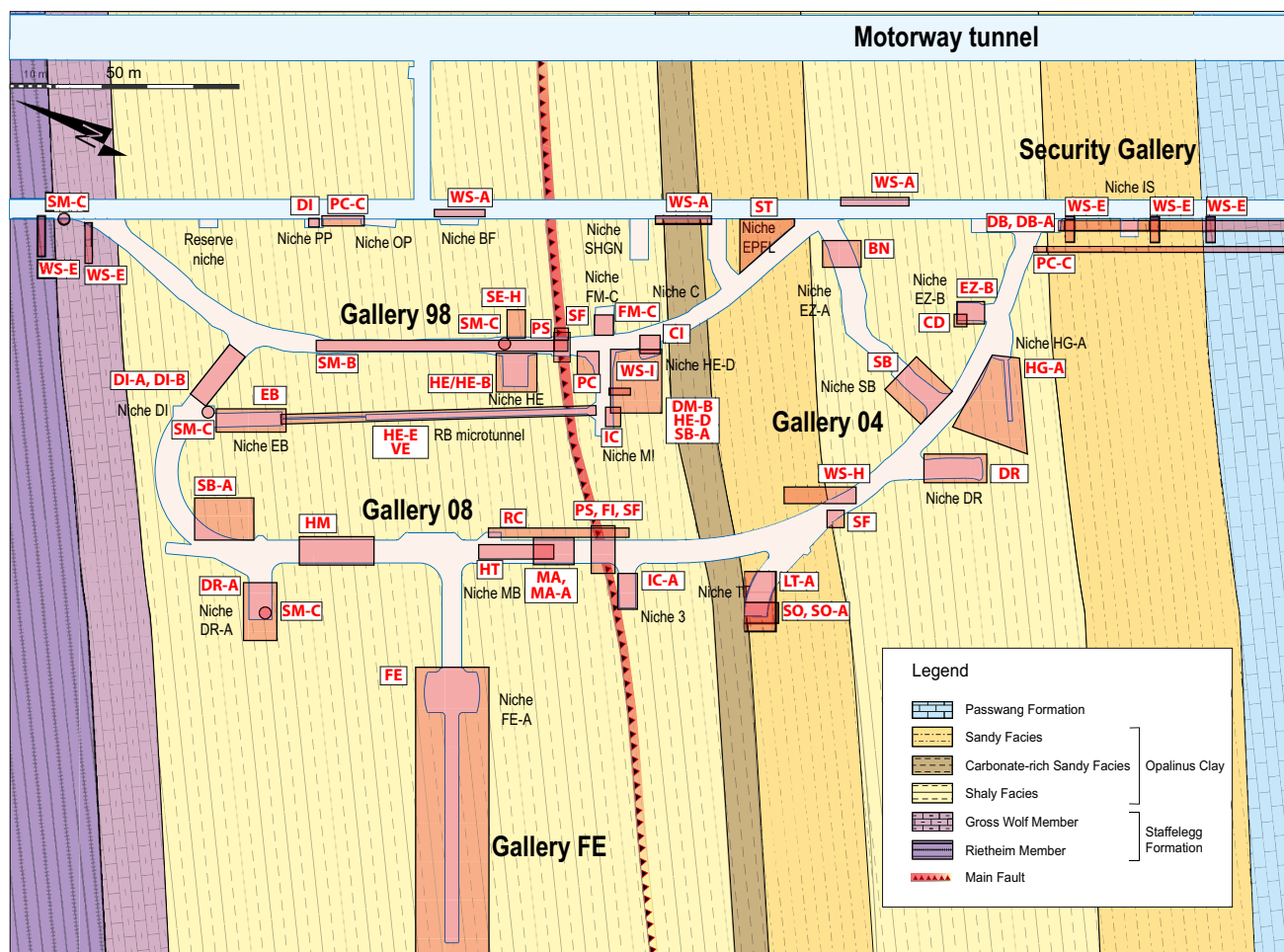


Fig. 5 The possible evolution of a potential high-level waste repository in the Opalinus Clay based on the Swiss disposal concept. Indicated in *green* are the human engineering activities starting with the construction of a repository until its sealing at the end (the time periods are best estimates and may differ considerably, depending on future decisions by the implementer, safety organisation, and

authorities). The expected processes during the lifespan of a repository are given in *orange* (disequilibrium) grading to *yellow* (equilibrium), starting with the formation of the excavation damaged zone (EDZ) and ending with the release of radionuclides from breached canisters. Thermo-hydraulic-mechanical and chemical equilibrium is assumed to occur after 10,000 years (see *red line*)



Experiments discussed in Special Issue

BN	Bitumen-nitrate-clay interaction	HT	Hydrogen transfer
CD	Cyclic deformations	IC	Iron corrosion of Opalinus Clay
CI	Cement-clay interaction	IC-A	Corrosion of iron in bentonite
DB	Deep inclined borehole through the Opalinus Clay	LP-A	Long-term monitoring of parameters (porewater pressures)
DB-A	Porewater characterisation-Benchmarking	LT-A	Clay properties, analyses of labtesting
DI	Diffusion in rock	MA	Microbial activity in Opalinus Clay
DI-A	Long-term diffusion	MA-A	Modular platform for microbial studies
DI-B	Long-term diffusion	PC	Porewater chemistry
DM-B	Long-term deformation measurements	PC-C	Gas porewater equilibrium
DR	Diffusion and retention experiment	PS	Petrofabric and strain determination
DR-A	Diffusion, retention and perturbations	RC	Rock mass characterisation
EB	Engineered barriers	SB	Selfsealing barriers clay - sand mixtures
EZ-B	Fracture generation	SB-A	Borehole sealing experiment
FE	Full scale emplacement demonstration	SE-H	Self-sealing with heat (Timodaz)
FI	Fluid-mineral interactions in Opalinus Clay during natural faulting and heating	SF	Self-sealing of tectonic faults
FM-C	Flow mechanism (tracer)	SM-B	High resolution seismic monitoring
HE/HE-B	Heater experiments I and II	SM-C	Permanent nanoseismic monitoring
HE-D	THM behaviour of host rock (heater test)	SO	Sedimentology of Opalinus Clay
HE-E	In-situ heater test in VE microtunnel	SO-A	Palynology of the Opalinus Clay
HG-A	Gas path host rock & seals	ST	Seismic transmission measurements
HM	Experimental lab investig. on HM-coupled properties & behavior Opalinus Clay	VE	Ventilation test
		WS-A/E/H/I	Porewater profiles, wet spots

◀**Fig. 6** Compilation of the 43 key experiments in the Mont Terri rock laboratory treated in the following papers of this Special Issue. The sites are shown in the map above and titles and abbreviations of the corresponding experiments are listed below. Only a subset of the Mont Terri experimental portfolio (138 experiments) is shown here. The complete experiment portfolio is presented in the electronic supplementary material (Online Resources 8 and 9)

3.1.3 Experiments related to the demonstration of repository implementation technology

These experiments comprise:

- construction and installation of engineered barriers on a 1:1 scale,
- horizontal emplacement of canisters and bentonite buffer of the space between canister and claystone,
- evaluation of corrosion rate of container materials, resaturation of bentonite buffer under decreasing heat transport from the canister, and long-term geochemical and microbial evolution of engineered barriers,
- sealing of boreholes and repository access tunnels and shafts, and long-term monitoring of the repository.

We emphasise that not all experiments can be strictly assigned to these three research aims. Some experiments come under two or even three of the aims, depending on the experiment objectives and concepts, and also on the temporal evolution of the experiment.

3.2 Overview of research and topics presented in the following papers

3.2.1 Potential repository evolution

Experimental results provide input for assessing different phases of repository evolution and performance. A potential repository evolution with causes and effects is shown in Fig. 5, and this will be used to organise the presentation of papers and experiments in the following section (Sect. 3.2.2). This evolution is based on the Swiss concept for high-level radioactive waste disposal in the Opalinus Clay (cf. Nagra 2002). We would like to emphasise that other countries may develop other repository evolution systems based on their own disposal concepts and construction and safety requirements. In the potential repository evolution shown in Fig. 5, we distinguish a transient disequilibrium phase and a qualitative equilibrium phase. Qualitative equilibrium does not mean a thermodynamic equilibrium, but rather an equilibrium that can be compared to the one before the repository was constructed. During construction of a repository (a time period of several years), stress redistribution leads to formation of an excavation damaged zone (EDZ) around the access and emplacement galleries. During the operational phase

(waste emplacement, buffer emplacement and backfilling, monitoring and sealing: a time period of up to 100 years, green box in Fig. 5), an unsaturated zone will evolve in the near-field due to ventilation, and redox conditions will become oxidizing. In the first few 100 years after closure, significant changes in the repository will occur, including heat transport from the canisters across the bentonite towards the rock, with canister surface temperatures up to 150 °C, and temperatures reaching ca. 90 °C at the bentonite-rock interface (Nagra 2002). Heat transport into the rock may cause excess pore-water pressures and reduction of effective stresses in the near-field, simply due to the fact that expansion of pore-water is higher than expansion of the rock fabric. As time advances, heat-flow will decrease leading to enhanced saturation in the near-field and swelling of the bentonite buffer. These processes take place concurrently with self-sealing of the EDZ fractures. Both swelling of clay minerals in the EDZ fractures and mechanical fracture closure (swelling bentonite) contribute to self-sealing. Redox conditions in the near-field become clearly reducing and anaerobic corrosion of the steel canisters prevails together with hydrogen production. During this period, microbial activity becomes important: bacteria are involved in redox reactions, degrading hydrogen (pore-water sulphates are reduced to sulphides such as H₂S). A sufficiently dense bentonite backfill is used to protect steel canisters from microbial-assisted corrosion. Finally, release of nuclides from the canisters is not expected to occur before some 10,000 years after emplacement. By this time, equilibrium conditions in the claystone are already re-established and hydraulic and thermal conditions are comparable to those before the repository was constructed. Radionuclide sorption and diffusion into the bentonite and the natural clay barrier is then the final process in the repository evolution, whereby 80% of the nuclides will be immobilized in the immediate vicinity of the canister.

3.2.2 The 20 papers and their relation to repository evolution

The papers in this Special Issue can be linked to the scheme of potential repository evolution shown in Fig. 5 and discussed in the previous section. Altogether, 43 experiments are outlined in the papers, and the location of these is shown in Fig. 6. The results of these experiments are combined and presented in the form of 20 scientific papers according to different themes, often including results from different experiments. The structure of this Special Issue, with the 20 papers organised according to their relevance for different periods of the repository evolution, is shown in Fig. 7. The sequence of the papers as they appear in this issue is given in Table 3, together with their titles and first authors. Figure 6 (location of

Repository evolution

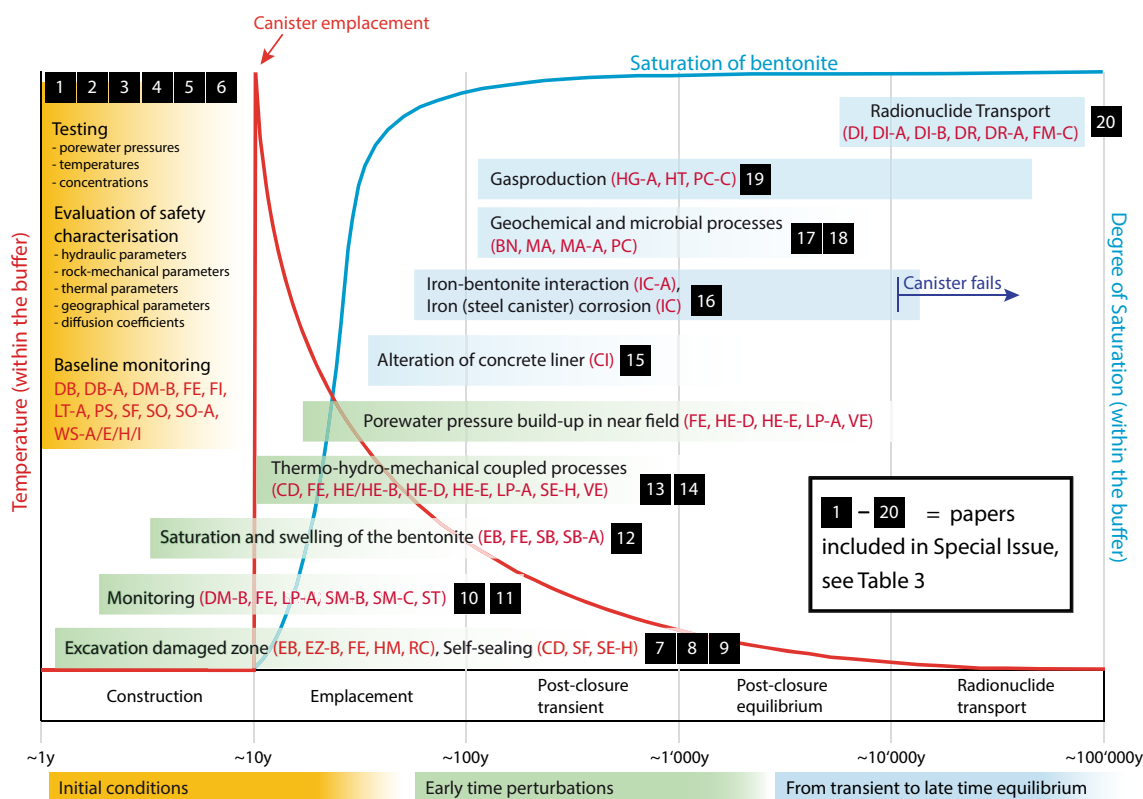


Fig. 7 Repository evolution, key experiments, and related publications in this Special Issue. The repository evolution can be divided into three periods: (1) initial conditions before repository construction (*orange*), (2) early time perturbations during and shortly after construction (*green*), and (3) transient to late time (post-closure) equilibrium (*blue*). The 43 key experiments are indicated as

abbreviations and refer to Fig. 6, which shows the complete titles of the key experiments together with their sites. The related publications are shown as *black numbers 1–20*. An overview of these publications is given in Table 3. This figure also indicates the temperature (*red curve*) and degree of saturation (*blue curve*) within the buffer

experiments in the rock laboratory) and Fig. 7 (linking corresponding papers to repository evolution) are thus the key figures and, with Table 3 (paper titles, key experiments, and first authors), they provide a guide and continuous thread for the following 20 papers.

From a practical point of view, only a subset of 43 of the total of 138 experiments is considered here and discussed in this Special Issue. However, this subset of 43 key experiments is characteristic for the total 138 completed and ongoing experiments and gives a comprehensive picture of the whole Mont Terri research programme. The other experiments are documented in internal technical notes, technical reports, and publications. For a complete overview, we refer to the electronically provided supplementary material (Online Resources 8 and 9).

As stated above, we chose the following 20 papers to reflect the different stages of the evolution of a potential repository. This compilation is shown in Fig. 7, where the 43 key experiments in the Mont Terri rock laboratory are

related to the three repository phases: initial conditions (*orange*), early time perturbations (*green*), and the transient to late time equilibrium phase (*blue*). The papers in this Special Issue are indicated with black boxes with white numbers and are repeated with the titles and authors in Table 3. Figure 7 also shows two features that are important for the repository evolution: (1) temporal temperature variations in the buffer (*red curve*), indicating the thermal loading of the disposal system by canister emplacement of highly radioactive waste with a temperature peak and its subsequent temperature decrease, and (2) temporal variations in the degree of buffer saturation (*blue curve*), indicating the continuous saturation of the bentonite buffer until the time when complete saturation of the buffer and Opalinus Clay in and around the emplacement tunnels is reached.

Alternatively, the 43 key experiments shown in Table 3 and Fig. 6 can be divided into observations over relevant timescales and experiments outside the

Table 3 List of scientific papers in this Special Issue and abbreviations of key experiments referred to in each paper, numbered in sequence, as shown in Fig. 7 (the detailed key experiment titles and its locations are given in Fig. 6)

#	Paper title	Key experiments	First author
Initial conditions			
1	Litho- and biostratigraphy of the Opalinus Clay and bounding formations in the Mont Terri rock laboratory (Switzerland)	SO, SO-A	Bernhard Hostettler (2017)
2	Tectonic evolution around the Mont Terri rock laboratory, northwestern Swiss Jura: constraints from kinematic forward modelling	-	Christophe Nussbaum (2017)
3	Tectonic structure of the “Main Fault” in the Opalinus Clay, Mont Terri rock laboratory (Switzerland)	PS	David Jaeggi (2017)
4	Comparative study of methods to estimate hydraulic parameters in the hydraulically undisturbed Opalinus Clay (Switzerland)	DB, DB-A	Catherine Yu (2017)
5	Geochemical signature of paleofluids in microstructures from Main Fault in the Opalinus Clay of the Mont Terri rock laboratory, Switzerland	FI, SF	Norbert Clauer (2017)
6	Pore-water evolution and solute-transport mechanisms in Opalinus Clay at Mont Terri and Mont Russelin (Canton Jura, Switzerland)	WS-A/E/H/I, SF	Martin Mazurek (2017)
Early time perturbations			
7	Geomechanical behaviour of Opalinus Clay at multiple scales: results from Mont Terri rock laboratory (Switzerland)	EZ-B, HM	Florian Amann (2017)
8	Hydro-mechanical evolution of the EDZ as transport path for radionuclides and gas: insights from the Mont Terri rock laboratory (Switzerland)	HG-A, EZ-B, SE-H	Paul Marschall (2017)
9	Coupled hydraulic-mechanical simulation of seasonally induced processes in the Mont Terri rock laboratory (Switzerland)	CD, LP-A	Gesa Ziefle (2017)
10	High-resolution mini-seismic methods applied in the Mont Terri rock laboratory (Switzerland)	DM-B, EB, EZ-B, HE/HE-B, LT-A, RC, ST	Kristof Schuster (2017)
11	Seismotectonic analysis around the Mont Terri rock laboratory (Switzerland): a pilot study	SM-B, SM-C	Martinus Abednego (2017)
12	In-situ experiments on bentonite-based buffer and sealing materials at the Mont Terri rock laboratory (Switzerland)	EB, HE-D, HE-E, SB, SB-A	Klaus Wiczorek (2017)
13	Performance of the Opalinus Clay under thermal loading: experimental results from Mont Terri rock laboratory (Switzerland)	HE/HE-B, HE-D, HE-E, VE	Antonio Gens (2017)
14	Implementation of the full-scale emplacement (FE) experiment at the Mont Terri rock laboratory (Switzerland)	FE	Herwig Mueller (2017)
From transient to late time equilibrium			
15	5-Year chemo-physical evolution of concrete-claystone interfaces, Mont Terri rock laboratory (Switzerland)	CI	Urs Maeder (2017)
16	Corrosion of carbon steel in clay environments relevant to radioactive waste geological disposals, Mont Terri rock laboratory (Switzerland)	IC, IC-A	Sophia Necib (2017)
17	Fifteen years of microbiological investigation in Opalinus Clay at the Mont Terri rock laboratory (Switzerland)	MA, MA-A, PC, PC-	Olivier X. Leupin (2017)
18	Impact of the electron donor on in situ microbial nitrate reduction in Opalinus Clay: results from the Mont Terri rock laboratory (Switzerland)	BN	Nele Bleyen (2017)
19	Natural gas extraction and artificial gas injection experiments in Opalinus Clay Mont Terri rock laboratory (Switzerland)	HT, PC-C	Agnès Vinsot (2017)
20	Exploring diffusion and sorption processes at the Mont Terri rock laboratory (Switzerland): lessons learned from 20 years of field research	DI, DI-A, DI-B, DR, DR-A, FM-C	Olivier X. Leupin (2017)

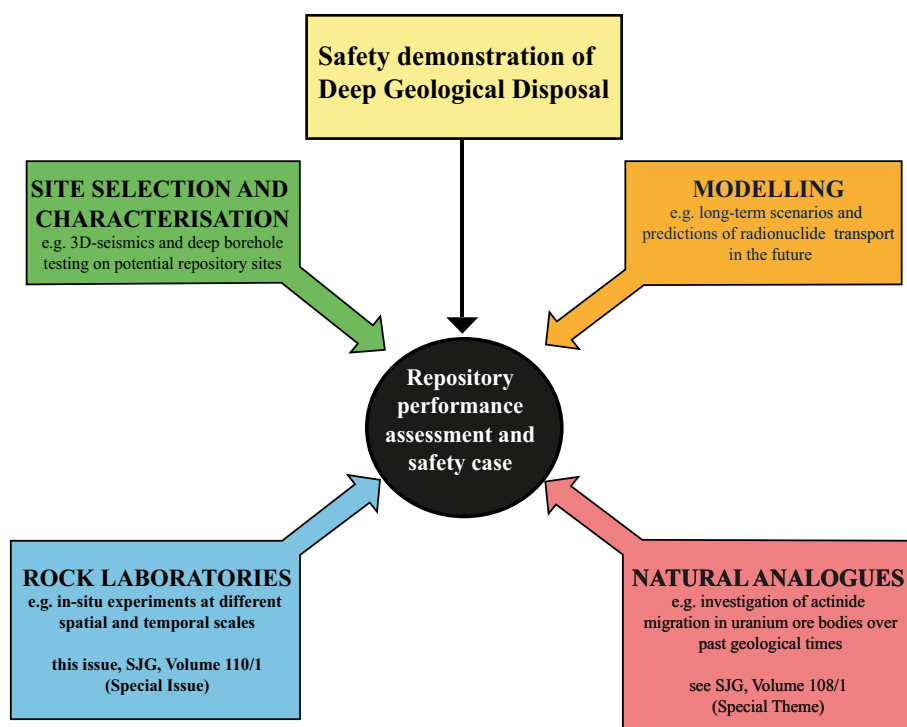
The first authors of the corresponding papers are indicated in the last column

observation window. To the first group belong experiments dealing with “initial conditions” such as host-rock characterisation, baseline monitoring, and feasibility experiments, such as construction of emplacement galleries and demonstration of full-scale emplacement. To the second group belong experiments designed to investigate long-term processes on timescales that are not directly accessible through conventional laboratory work. Good examples of this type are diffusion experiments where migration of radionuclides is studied under in situ conditions. The results yield robust transport parameters that are used to calibrate numerical models that simulate mass transport (advective–dispersive–diffusive and reactive transport). Once calibrated, these models can be used to make predictions of radionuclide migration released from a geological repository.

3.2.3 Rock laboratory and performance of geological repository

The question whether a rock laboratory like Mont Terri alone is sufficient to assess the performance of a geological repository at a real site can be clearly answered in the negative. As the geological situation at the proposed sites in northern Switzerland will be different (e.g. flat-lying Opalinus Clay with very few faults, different sub-units, confining rocks, stress situation, burial history etc.), additional site-specific investigations are required for developing a repository safety case. The Mont Terri project can, however, deliver strong arguments for a safety case through confident characterisation of properties governing repository evolution, such as the confirmation of diffusive mass transport as the governing transport mechanism in the

Fig. 8 Diagram showing the four principal contributors to the safety demonstration of a deep geological disposal



Opalinus Clay over different space and time scales. More information and investigations would be needed for an actual safety case, as e.g. the study of natural analogues (e.g. Alexander et al. 2015), testing of specific sites [with the intention of realising a repository, e.g. Nagra (2002, 2008)], and the entire palette of modelling to evaluate long-term scenarios and assess system performance (Fig. 8). Integrating all available information from real and analogue sites, including experimental results obtained from site-specific and generic rock laboratories, is thought to lead to reliable safety demonstrations for deep geological disposal and the development of an appropriate safety case.

Acknowledgements The authors would like to thank the 16 Mont Terri Partner organisations and the European Union for their financial investment into the Mont Terri Project over the past 20 years. The Republic and Canton of Jura as owner of the Opalinus Clay and landlord of the rock laboratory is warmly thanked, especially the Ministers Pierre Kohler, Laurent Schaffter, Philippe Receveur, and David Eray, who all supported the project. The cantonal “Commission de suivi” with its experts, especially Pascal Mertenat, Marcos Buser and Thomas Flüeler, are thanked for lively discussions and for providing us the yearly authorisations. We also thank the three reviewers, Philippe Schaub (SFOE), Russell Alexander (Bedrock Geosciences, Switzerland), and Geoffrey Milnes (Scientific Editor of the SJG) for significantly improving the manuscript. Roy Freeman reviewed the English of the manuscript. Last but not least, we thank

Marc Thury for his foresight and initiative in the early 1990s, which led to the founding of the Mont Terri Project 20 years ago.

Open Access This article is distributed under the terms of the Creative Commons Attribution 4.0 International License (<http://creativecommons.org/licenses/by/4.0/>), which permits unrestricted use, distribution, and reproduction in any medium, provided you give appropriate credit to the original author(s) and the source, provide a link to the Creative Commons license, and indicate if changes were made.

Appendix

Explanation of acronyms and abbreviations, which are used in this Special Issue.

Acronyms and abbreviations	Explanation
A	
ANDRA	Agence Nationale pour la gestion des Déchets Radioactifs, France (French National Radioactive Waste Management Organisation)
APHA	American Public Health Association
API	American Petroleum Index
AWWA	American Water Works Association

Acronyms and abbreviations	Explanation	Acronyms and abbreviations	Explanation
B		G	
BDZ	Borehole damaged zone	Ga08	Gallery 2008 (Mont Terri rock laboratory)
BdZ	Borehole disturbed zone	Ga98	Gallery 1998 (Mont Terri rock laboratory)
BGR	Bundesanstalt für Geowissenschaften und Rohstoffe, Deutschland (Federal Institute for Geosciences and Natural Resources, Germany)	GBM	Granulated Bentonite Mixture, but also Granular Backfill Material
BIB	Broad ion beam	GI Ltd.	Geotechnical Institute Limited, Switzerland
BRGM	Bureau de Recherches Géologiques et Minières, France (French Geological Survey)	GPa	Gigapascal
C		GR	Gamma ray
CEC	Cation exchange capacity	GRS	Gesellschaft für Anlagen- und Reaktorsicherheit gGmbH, Germany
Chevron	Chevron Corporation, USA	H	
CRIEPI	Central Research Institute of Electric Power Industry, Japan	HDO	Hydrodeuteriumoxid
D		HLW	High level (radioactive) waste
DAS	Data acquisition system	HM	Hydro-mechanical
DECOVALEX	Development of Coupled Models and their Validation against Experiments (project name)	HSK/ENSI	Hauptabteilung für die Sicherheit der Kernanlagen (until 2008), Eidgenössisches Nuklearsicherheitsinspektorat (Swiss Federal Nuclear Safety Inspectorate, since 2009)
DOE/LBNL	Department of Energy/Lawrence Berkeley National Laboratory, USA	HTO	Tritiated Water
E		I	
EBS	Engineered barrier system	IAEA	International Atomic Energy Agency, Austria
EDZ	Excavation damaged zone	IC	Ion chromatography
EdZ	Excavation disturbed zone	ICP-AES	Inductively coupled plasma-atomic emission spectroscopy
EMPA	Eidgenössische Materialprüfungs- und Forschungsanstalt, Schweiz (Swiss Federal Laboratories for Materials Science and Technology)	ICP-MS	Inductively coupled plasma-mass spectrometry
ENRESA	Empresa Nacional de Residuos Radiactivos S.A., España (Spanish National Radioactive Waste Management Organisation)	ICP-OES	Inductively COUPLED PLASMA-OPTICAL EMISSION SPECTROSCOPY
ENSI	Eidgenössisches Nuklearsicherheitsinspektorat, Schweiz (Swiss Federal Nuclear Safety Inspectorate, Switzerland)	ILW	Intermediate level (radioactive) waste
EPFL	École Polytechnique Fédérale de Lausanne, Suisse (Swiss Federal Institute of Technology, Lausanne, Switzerland)	IRSN	Institut de Radioprotection et de Sûreté Nucléaire, France (French Institute for Radiological Protection and Nuclear Safety)
ESDRED	Engineering Studies and Demonstration of Repository Designs (EC project)	ISRM	International Society for Rock Mechanics
ESM	Electronic Supplementary Material	IVM	Interval velocity measurements
ETH	Eidgenössische Technische Hochschule in Zürich, Schweiz (Swiss Federal Institute of Technology, Zurich, Switzerland)	J	
EURATOM	European Atomic Energy Community	IAEA	Japan Atomic Energy Agency, Japan
F		JU	Jura (Canton)
FANC	Federal Agency for Nuclear Control, Belgium	JU-cant. chemistry	Laboratoire cantonal jurassien accrédité (Chemical Laboratory of Canton of Jura, Switzerland)
FEDRO	Federal Roads Office, Switzerland	JU-ENV	Office de l'Environnement, Canton du Jura (Office for the Environment, Canton of Jura, Switzerland)
FIB	Focused ion beam	JU-OEPN	Office des Eaux et de la Protection de la Nature, Canton du Jura (Office for Water and Protection of Nature, Canton of Jura, Switzerland)
FORGE	Fate of Repository Gases (EC project)	JU-SIN	Service des Infrastructures, Canton du Jura (Office for Infrastructure, Canton of Jura, Switzerland)
FOWG	Federal Office for Water and Geology, Switzerland (until 2005)	K	
		kPa	Kilopascal
		L	

Acronyms and abbreviations	Explanation	Acronyms and abbreviations	Explanation
LLW	Low-Level (radioactive) waste	TH	Thermo-hydraulic
LUCOEX	Large Underground Concept Experiments (EC project)	THM	Thermo-hydro-mechanical
M		THMC	Thermo-hydro-mechanical-chemical
Ma	Million years	TIC	Total inorganic carbon
meq%	Milliequivalent %	TIMODAZ	Thermal Impact on the Damaged Zone (EC project)
MPa	Megapascal	TOC	Total organic carbon
Myr	Million years (duration)	U	
N		URF	Underground Research Facility
Nagra	Nationale Genossenschaft für die Lagerung radioaktiver Abfälle, Schweiz (National Cooperative for the Disposal of Radioactive Waste, Switzerland)	URL	Underground Research Laboratory
Ni-en	Nickelethylenediamine solution	V	
NNL	National Nuclear Laboratory, UK	W	
NWMO	Nuclear Waste Management Organisation, Canada	wt%	Weight percent
O		X	
OBI	Optical borehole imager	XRD	X-ray diffraction
OECD-NEA	Organisation for Economic Co-operation and Development-Nuclear Energy Agency	XRF	X-ray fluorescence
OPC	Ordinary Portland cement	Z	
P		ZH-AWEL	Amt für Abfall, Wasser, Energie und Luft, Kanton Zürich (Office for the Environment, Canton of Zurich, Switzerland)
PEPS	Long-term performance of the Engineered Barrier Systems (EC project)		
Q			
R			
RH	Relative humidity		
RWTH-Aachen	Rheinisch-Westfälische Technische Hochschule—Aachen, Deutschland (Technical University, Aachen, Germany)		
S			
SCK.CEN	Studiecentrum voor Kernenergie, Belgium (Belgian Nuclear Research Centre)		
SEM	Scanning electron microscopy		
SF/HLW	Spent Fuel/high level waste		
SFOE	Swiss Federal Office of Energy		
SGR	Spectral Gamma ray		
SGS	Swiss Geological Survey		
SJG	Swiss Journal of Geosciences		
SNHGS	Service National Hydrologique et Géologique, Suisse (former Swiss Geological Survey, until 2005)		
SRB	Sulphate-reducing bacteria		
STP	Standard temperature and pressure		
swisstopo	Bundesamt für Landestopografie (Federal Office of Topography, Switzerland)		
T			
TDR	Time-domain reflectometry		
TDS	Total dissolved solids		
TEM	Transmission electron microscopy		

References

- Abednego, M., Blascheck, P., Schefer, S., Mosar, J., Nussbaum, C., Joswig, M., & Bossart, P. (2017). Seismotectonic analysis around the Mont Terri rock laboratory (Switzerland): a pilot study. *Swiss Journal of Geosciences*, 110. doi:10.1007/s00015-017-0263-6 (this issue).
- Alexander, W. R., Reijonen, H. M., & McKinley, I. G. (2015). Natural analogues: Studies of geological processes relevant to radioactive waste disposal in deep geological repositories. *Swiss Journal of Geosciences*, 108, 75–100.
- Amann, F., Button, E., Evans, K., Gischig, V., & Blümel, M. (2011a). Experimental study of the brittle behavior of clay shale in rapid unconfined compression. *Rock Mechanics and Rock Engineering*, 44(4), 415–430.
- Amann, F., Kaiser, P., & Button, E. (2011b). Experimental study of brittle behavior of clay shale in rapid triaxial compression. *Rock Mechanics and Rock Engineering*, 45(1), 21–33.
- Amann, F., Wild, K. M., Loew, S., Yong, S., Thoeny, R., & Frank, E. (2017). Geomechanical behaviour of Opalinus Clay at multiple scales: results from Mont Terri rock laboratory (Switzerland). *Swiss Journal of Geosciences*, 110. doi:10.1007/s00015-016-0245-0 (this issue).
- Blaesi, H.-R. (1987). Lithostratigraphie und Korrelation der Dogger Sedimente in den Bohrungen Weiach, Riniken und Schafisheim. *Eclogae Geologicae Helveticae*, 80, 415–430.
- Blaesi, H.-R., Moeri, A., Bossart, P. (1996). Results of the Phase 1 drilling campaign. *Mont Terri Technical Report*, TR 96-01, p. 54. Federal Office of Topography (swisstopo), Wabern, Switzerland. <http://www.mont-terri.ch>.
- Blaesi, H.-R., Peters, T. J., & Mazurek, M. (1991). Der Opalinus Clay des Mont Terri (Kanton Jura): Lithologie, Mineralogie und physiko-chemische Gesteinsparameter. *Nagra Interner Bericht*, 90–60. Nagra, Wettingen, Switzerland. <http://www.nagra.ch>.

- Blechs Schmidt, I., & Vomvoris, S. (2010). Underground research facilities and rock laboratories for the development of geological disposal concepts and repository systems. In J. Ahn, M. J. Apted, et al. (Eds.), *Geological repository systems for safe disposal of spent nuclear fuels and radioactive waste* (pp. 83–118). Sawston: Woodhead Publishing Limited.
- Bleyen, N., Smets, S., Small, J., Moors, H., Leys, N., Albrecht, A., De Cannière, P., Schwyn, B., Wittebroodt, C., & Valcke, E. (2017). Impact of the electron donor on in situ microbial nitrate reduction in Opalinus Clay: results from the Mont Terri rock laboratory (Switzerland). *Swiss Journal of Geosciences*, 110. doi:10.1007/s00015-016-0256-x (this issue).
- Bock, H. (2009). RA experiment: Updated review of the rock mechanics properties of the Opalinus Clay of the Mont Terri URL based on laboratory and field testing. *Mont Terri Technical Report*, TR 08-04, p. 66. Federal Office of Topography (swisstopo), Wabern, Switzerland. <http://www.mont-terri.ch>.
- Bossart, P., & Thury, M. (2008). Mont Terri Rock Laboratory. Project, Programme 1996–2007 and results. *Reports of the Swiss Geological Survey*, No. 3, p. 445. Federal Office of Topography (swisstopo), Wabern, Switzerland. <http://www.mont-terri.ch>.
- Caër, T., Maillot, B., Souldoumiac, P., Leturmy, P., Frizon de Lamotte, D., & Nussbaum, C. (2015). Mechanical validation of balanced cross-sections: The case of the Mont Terri anticline at the Jura front (NW Switzerland). *Journal of Structural Geology*, 75, 32–38.
- Clauer, N., Techer, I., Nussbaum, C., & Laurich, B. (2017). Geochemical signature of paleofluids in microstructures from Main Fault of the Opalinus Clay of the Mont Terri rock laboratory, Switzerland. *Swiss Journal of Geosciences*, 110. doi:10.1007/s00015-016-0253-0 (this issue).
- Delay, J., Bossart, P., Ling, L. X., Blechs Schmidt, I., Ohlsson, M., Vinsot, A., et al. (2014). Three decades of underground research laboratories: What have we learned? *Geological Society London Special Publications*, 400(1), 7–32.
- Freivogel, M., & Huggenberger, P. (2003). Modellierung bilanzierter Profile im Gebiet Mont Terri—La Croix (Kanton Jura). In: P. Heitzmann, & J.-P. Tripet (Eds.), *Mont Terri Project—geology, paleohydrology and stress field of the Mont Terri region* (pp. 7–44). Bern: OFEG Report, Geology Serie, No. 4. Federal Office of Topography (swisstopo), Wabern, Switzerland. <http://www.mont-terri.ch>.
- Garitte, B., Gens, A., Vaunat, J., & Armand, G. (2014). Thermal conductivity of argillaceous rocks: Determination methodology using in situ heating tests. *Rock Mechanics and Rock Engineering*, 47(1), 111–129.
- Gautschi, A., Ross, C., & Scholtis, A. (1993). Pore water—groundwater relationships in Jurassic shales and limestones of northern Switzerland. In D. A. C. Manning, P. L. Hall, & C. R. Hughes (Eds.), *Geochemistry of clay—pore fluid interactions* (pp. 412–422). London: Chapman Hall.
- Gens, A., Wiczorek, K., Gaus, I., Garitte, B., Mayor, J.C., Schuster, K., Armand, G., García-Siñeriz, J-L., & Trick, T. (2017). Performance of the Opalinus Clay under thermal loading: experimental results from Mont Terri rock laboratory (Switzerland). *Swiss Journal of Geosciences*, 110. doi:10.1007/s00015-016-0258-8 (this issue).
- Gschwind, S. (2013). The relationship between failure behavior and sedimentary subfacies types in the sandy facies of Opalinus Clay. *Master Thesis*, Swiss Federal Institute of Technology in Zurich (ETH Zurich), Zurich, Switzerland, p. 170.
- Hostettler, B., Reisdorf, A. G., Jaeggi, D., Deplazes, G., Bläsi, H.-R., Morard, A., Feist-Burkhardt, S., Waltschew, A., Dietze, V., & Menkveld-Gfeller, U. (2017). Litho- and biostratigraphy of the Opalinus Clay and bounding formations in the Mont Terri rock laboratory (Switzerland). *Swiss Journal of Geosciences*, 110. doi:10.1007/s00015-016-0250-3 (this issue).
- IAEA. (2012). The safety case and safety assessment for the disposal of radioactive waste. IAEA Safety Standards Series, Specific Safety Guide No. SSG-23, STI/PUB/1553. International Atomic Energy Agency, Vienna, Austria.
- Jaeggi, D., & Bossart, P. (2014). Kompilation der lithologischen Variabilität und Eigenschaften des Opalinus-Ton im Felslabor Mont Terri. *Expert Report for ENSI, 09-08*, 66 pp. Federal Office of Topography (swisstopo), Wabern, Switzerland. <http://www.swisstopo.admin.ch>.
- Jaeggi, D., Laurich, B., Nussbaum, C., Schuster, K., & Connolly, P. (2017). Tectonic structure of the “Main Fault” in the Opalinus Clay, Mont Terri rock laboratory (Switzerland). *Swiss Journal of Geosciences*, 110. doi:10.1007/s00015-016-0243-2 (this issue).
- Laubscher, H. P. (1963). *Geologischer Atlas der Schweiz, Atlasblatt 40, 1085 St. Ursanne—Erläuterungen*. Basel: Schweizerische Geotechnische Kommission. Federal Office of Topography (swisstopo), Wabern, Switzerland. <http://www.mont-terri.ch>.
- Lavanchy, J. M., & Mettler, R. (2012). HA (Hydrogeological analysis) Experiment: Hydraulic database, Phases 1–16, Version 1.0. *Mont Terri Technical Note*, TN 2010-74, p. 22. Federal Office of Topography (swisstopo), Wabern, Switzerland. <http://www.mont-terri.ch>.
- Lerouge, C., Blanc, P., Gaboreau, S., Decouchon, E., Guerrot, C., Wille, C., Jean-Prost, E., & Haas, H. (2011). PC-C experiment: Mineralogy and geochemistry of cores of the BPC-C2 borehole Mont Terri Rock Laboratory—phase II, Final report. *Mont Terri Technical Note*, TN 2010-05 (rev), p. 61. Federal Office of Topography (swisstopo), Wabern, Switzerland. <http://www.mont-terri.ch>.
- Leupin, O.X., Bernier-Latmani, R., Bagnoud, A., Moors, H., Leys, N., Wouters, K., & Stroes-Gascoyne, S. (2017a). Fifteen years of microbiological investigation in Opalinus Clay at the Mont Terri rock laboratory (Switzerland). *Swiss Journal of Geosciences*, 110. doi:10.1007/s00015-016-0255-y (this issue).
- Leupin, O.X., Van Loon, L.R., Gimmi, T., Wersin, P., & Soler, J.M. (2017b). Exploring diffusion and sorption processes at the Mont Terri rock laboratory (Switzerland): lessons learned from 20 years of field research. *Swiss Journal of Geosciences*, 110. doi:10.1007/s00015-016-0254-z (this issue).
- Maeder, U., Jenni, A., Lerouge, C., Gaboreau, S., Miyoshi, S., Kimura, Y., Cloet, V., Fukaya, M., Claret, F., Otake, T., Shibata, M., & Lothenbach, B. (2017). 5-Year chemico-physical evolution of concrete-claystone interfaces, Mont Terri rock laboratory (Switzerland). *Swiss Journal of Geosciences*, 110. doi:10.1007/s00015-016-0240-5 (this issue).
- Marschall, P., Giger, S., De La Vassière, R., Shao, H., Leung, H., Nussbaum, C., Trick, T., Lanyon, B., Senger, R., Lisjak, A., & Alcolea, A. (2017). Hydro-mechanical evolution of the EDZ as transport path for radionuclides and gas: insights from the Mont Terri rock laboratory (Switzerland). *Swiss Journal of Geosciences*, 110. doi:10.1007/s00015-016-0246-z (this issue).
- Mazurek, M. (1999). Mineralogy of the Opalinus Clay. In: M. Thury, & P. Bossart (Eds.), *Mont Terri Rock Laboratory. Results of the hydrogeological, geochemical and geotechnical experiments performed in 1996 and 1997*. Geological Reports No. 23. Federal Office of Topography (swisstopo), Wabern, Switzerland. <http://www.mont-terri.ch>.
- Mazurek, M., & de Haller, A. (2017). Pore-water evolution and solute-transport mechanisms in Opalinus Clay at Mont Terri and Mont Russelin (Canton Jura, Switzerland). *Swiss Journal of Geosciences*, 110. doi:10.1007/s00015-016-0249-9 (this issue).
- Mazurek, M., Gautschi, A., Marschall, P., Vigneron, G., Lebon, P., & Delay, J. (2008). Transferability of geoscientific information

- from various sources (study sites, underground rock laboratories, natural analogues) to support safety cases for radioactive waste repositories in argillaceous formations. *Physics and Chemistry of Earth Parts A/B/C*, 33, 95–105.
- Mazurek, M., Hurford, A. J., & Leu, W. (2006). Unravelling the multi-stage burial history of the Swiss Molasse Basin: Integration of apatite fission track, vitrinite reflectance and biomarker isomerisation analysis. *Basin Research*, 18(1), 27–50.
- Miehe, R., Czaikowsk, O., & Wieczorek, K. (2010). Barrier Integrity of the Isolation Rock Zone in Clay Formations. *Mont Terri Technical Note*, TN 2010-82, 97 pp. Federal Office of Topography (swisstopo), Wabern, Switzerland. <http://www.mont-terri.ch>.
- Müller, H. R., Garitte, B., Vogt, T., Köhler, S., Sakaki, T., Weber, H., Spillmann, T., Hertrich, M., Becker, J. K., Giroud, N., Cloet, V., Diomidis N., & Vietor, T. (2017). Implementation of the full-scale emplacement (FE) Experiment at the Mont Terri rock laboratory (Switzerland). *Swiss Journal of Geosciences*, 110. doi:10.1007/s00015-016-0251-2 (this issue).
- Nagra. (2002). Projekt Opalinuston: Konzept für die Anlage und den Betrieb eines geologischen Tiefenlagers: Entscheidungsnachweis für abgebrannte Brennelemente, verglaste hochaktive sowie langlebige mittelaktive Abfälle. *Nagra Technical Report*, 02-02, p. 24. Nagra, Wettingen, Switzerland. <http://www.nagra.ch>.
- Nagra. (2008). Entsorgungsprogramm 2008 der Entsorgungspflichtigen. *Nagra Technical Report*, 08-01, p. 134. Nagra, 5400 Wettingen, Switzerland. <http://www.nagra.ch>.
- Nagra. (2010). Beurteilung der geologischen Unterlagen für die provisorischen Sicherheitsanalysen in SGT Etappe 2. Klärung der Notwendigkeit ergänzender geologischer Untersuchungen. *Nagra Technical Report*, 10-01, p. 44. Nagra, Wettingen, Switzerland. <http://www.nagra.ch>.
- Necib, S., Diomidis, N., Keech, P., & Nakayama, M. (2017). Corrosion of carbon steel in clay environments relevant to radioactive waste geological disposals, Mont Terri rock laboratory (Switzerland). *Swiss Journal of Geosciences*, 110. doi:10.1007/s00015-016-0259-7 (this issue).
- Nussbaum, C., Bossart, P., Amann, F., & Aubourg, C. (2011). Analysis of tectonic structures and excavation induced fractures in the Opalinus Clay, Mont Terri underground rock laboratory (Switzerland). *Swiss Journal of Geosciences*, 104, 187–210.
- Nussbaum, C., Kloppenburg, A., Caër, T., & Bossart, P. (2017). Tectonic evolution around the Mont Terri rock laboratory, northwestern Swiss Jura: constraints from kinematic forward modelling. *Swiss Journal of Geosciences*, 110. doi:10.1007/s00015-016-0248-x (this issue).
- OECD (2013). Underground Research Laboratories (URL). *Radioactive Waste Management, NEA/RWM/R(2013)2*, p. 53. Co-operation and Organisation for Economic Development, Paris, France.
- Parisio, F. (2016). Constitutive and numerical modelling of anisotropic quasi-brittle shales. *PhD Thesis*, Swiss Federal Institute of Technology in Lausanne (EPFL), Lausanne, Switzerland, p. 260.
- Pearson, F. J., Arcos, D., Bath, A., Boisson, J.-Y., Fernandez, A., Gaebler, H.-E., Gaucher, E., Gautschi, A., Griffault, L., Hernan, P., & Waber, H. N. (2003). Geochemistry of Water in the Opalinus Clay Formation at the Mont Terri Rock Laboratory (Synthesis Report). *Geological Report*, No. 5, p. 321. Federal Office of Topography (swisstopo), Wabern, Switzerland. <http://www.mont-terri.ch>.
- Peters, M., Mazurek, M., Jaeggi, D., & Müller, H. R. (2011). WS-H Experiment: Heterogeneities in the sandy facies of Opalinus Clay on a scale of millimeters to centimeters, *Mont Terri Technical Note*, TN 2010-76, p. 18. Federal Office of Topography (swisstopo), Wabern, Switzerland. <http://www.mont-terri.ch>.
- Reisdorf, A. G., Wetzel, A., Schlatter, R., & Jordan, P. (2011). The Stafflegg formation: A new stratigraphic scheme for the Early Jurassic of northern Switzerland. *Swiss Journal of Geosciences*, 104, 97–146.
- Schaeren, G., & Norbert, J. (1989). Tunnels du Mont Terri et du Mont Russelin—La traversée des “roches à risques”: Marnes et marnes à anhydrite. *Juradurchquerungen aktuelle Tunnelprojekte im Jura Mitteilungen der Schweizerischen Gesellschaft für Boden- und Felsmechanik*, 119, 19–24.
- Schmidt, C., Braun, L., Paltzer, G., Mühlberg, M., Christ, P., & Jacob, F. (1924). Die Bohrungen von Buix bei Pruntrut, und Allschwil bei Base. *Beiträge zur Geologie der Schweiz, Geotechnische Serie* (Vol. 10, p. 74). Zurich: Aschmann & Scheller.
- Schuster, K., Amann, F., Yong, S., Bossart, P., & Connolly, P. (2017). High-resolution mini-seismic methods applied in the Mont Terri rock laboratory (Switzerland). *Swiss Journal of Geosciences*, 110. doi:10.1007/s00015-016-0241-4 (this issue).
- SFOE. (2008). Sectorial Plan for Deep Geological Repositories, Conceptual Part. *Swiss Federal Office of Energy (SFOE) Report*, p. 99. Federal Office of Energy, Ittigen, Switzerland. <http://www.bfe.admin.ch>.
- Sommaruga, A. (1999). Décollement tectoniques in the Jura foreland fold and thrust belt. *Marine and Petroleum Geochemistry*, 16(2), 111–134.
- Tripet, J. P., Brechbühler, Y. A., Haarpaintner, R. T., & Schindler, B. (1990). Hydrogéologie des milieux à faible perméabilité: Étude des Marnes aaléniennes dans la galerie de des milieux à faible perméabilité: Étude des Marnes aaléniennes dans la galerie de reconnaissance du Mont Terri (Canton du Jura). *Bulletin de la Société Neuchâteloise des Sciences Naturelles*, 113, 179–189.
- Vinsot, A., Appelo, C. A. J., Lundy, M., Wechner, S., Cailteau-Fischbach, C., de Donato, P., Pironon, J., Lettry, Y., Lerouge, C., & De Cannière, P. (2017). Natural gas extraction and artificial gas injection experiments in Opalinus Clay, Mont Terri rock laboratory (Switzerland). *Swiss Journal of Geosciences*, 110. doi:10.1007/s00015-016-0244-1 (this issue).
- Wetzel, A., & Allia, V. (2003). Der Opalinuston in der Nordschweiz: Lithologie und Ablagerungsgeschichte. *Eclogae Geologicae Helvetiae*, 96(3), 451–469.
- Wieczorek, K., Gaus, I., Mayor, J. C., Schuster, K., García-Siñeriz, J.-L., & Sakaki, T. (2017). In-situ experiments on bentonite-based buffer and sealing materials at the Mont Terri rock laboratory (Switzerland). *Swiss Journal of Geosciences*, 110. doi:10.1007/s00015-016-0247-y (this issue).
- Yu, C., Matray, J.-M., Gonçalvès, J., Jaeggi, D., Gräsle, W., Wieczorek, K., Vogt, T., & Sykes, E. (2017). Comparative study of methods to estimate hydraulic parameters in the hydraulically undisturbed Opalinus Clay (Switzerland). *Swiss Journal of Geosciences*, 110. doi:10.1007/s00015-016-0257-9 (this issue).
- Ziefle, G., Matray, J.-M., Maßmann, J., & Möri, A. (2017). Coupled hydraulic-mechanical simulation of seasonally induced processes in the Mont Terri rock laboratory (Switzerland). *Swiss Journal of Geosciences*, 110. doi:10.1007/s00015-016-0252-1 (this issue).

Litho- and biostratigraphy of the Opalinus Clay and bounding formations in the Mont Terri rock laboratory (Switzerland)

Bernhard Hostettler¹ · Achim G. Reisdorf^{1,2} · David Jaeggi³ · Gaudenz Deplazes⁴ · Hansruedi Bläsi⁵ · Alain Morard³ · Susanne Feist-Burkhardt^{6,7} · Anton Waltschew⁸ · Volker Dietze⁹ · Ursula Menkveld-Gfeller¹

Received: 14 March 2016 / Accepted: 9 December 2016 / Published online: 25 February 2017
© Swiss Geological Society 2017

Abstract A 250 m-deep inclined well, the Mont Terri BDB-1, was drilled through the Jurassic Opalinus Clay and its bounding formations at the Mont Terri rock laboratory (NW Switzerland). For the first time, a continuous section from (oldest to youngest) the topmost members of the Staffelegg Formation to the basal layers of the Hauptrogenstein Formation is now available in the Mont Terri area. We extensively studied the drillcore for lithostratigraphy and biostratigraphy, drawing upon three sections from the Mont Terri area. The macropaleontological, micropaleontological, and palynostratigraphical data are complementary, not only spatially but they also cover almost all biozones from the Late Toarcian to the Early Bajocian. We ran a suite of geophysical logs to determine formational

and intraformational boundaries based on clay content in the BDB-1 well. In the framework of an interdisciplinary study, analysis of the above-mentioned formations permitted us to process and derive new and substantial data for the Mont Terri area in a straightforward way. Some parts of the lithologic inventory, stratigraphic architecture, thickness variations, and biostratigraphic classification of the studied formations deviate considerably from occurrences in northern Switzerland that crop out further to the east. For instance, with the exception of the Sissach Member, no further lithostratigraphic subdivision in members is proposed for the Passwang Formation. Also noteworthy is that the ca. 130 m-thick Opalinus Clay in the BDB-1 core is 20 m thinner than that equivalent section found in the Mont Terri tunnel. The lowermost 38 m of the Opalinus Clay can be attributed chronostratigraphically solely to the Aalensis Zone (Late Toarcian). Deposition of the Opalinus Clay began at the same time farther east in northern Switzerland (Aalensis Subzone, Aalensis Zone), but in the Mont Terri area the sedimentation rate was two or three orders of magnitude higher.

Editorial handling: P. Bossart and A. G. Milnes.

This is paper #1 in the Mont Terri Special Issue of the Swiss Journal of Geosciences (see Bossart et al. 2017, Table 3 and Fig. 7). It is a short version of Mont Terri Technical Report, TR 16-02 (Reisdorf et al. 2016).

Electronic supplementary material The online version of this article (doi:10.1007/s00015-016-0250-3) contains supplementary material, which is available to authorized users.

✉ Ursula Menkveld-Gfeller
menkveld@nmb.ch

- ¹ Naturhistorisches Museum der Burggemeinde Bern, Bernastrasse 15, 3005 Bern, Switzerland
- ² Geologisch-Paläontologisches Institut, Universität Basel, Bernoullistrasse 32, 4056 Basel, Switzerland
- ³ Federal Office of Topography swisstopo, Seftigenstrasse 264, 3084 Wabern, Switzerland
- ⁴ National Cooperative for the Disposal of Radioactive Waste (Nagra), Hardstrasse 73, 5430 Wettingen, Switzerland

Keywords Early–Middle Jurassic · Geophysical logging · Clay content · Ammonites · Microfossils · Palynomorphs

- ⁵ Institut für Geologie der Universität Bern, Baltzerstrasse 1+3, 3012 Bern, Switzerland
- ⁶ SFB Geological Consulting and Services, Odenwaldstraße 18, 64372 Ober-Ramstadt, Germany
- ⁷ Department of Earth Sciences, University of Geneva, 13 Rue des Maraîchers, 1205 Geneva, Switzerland
- ⁸ Steinplattenweg 55a, 90491 Nuremberg, Germany
- ⁹ Meraner Straße 41, 86720 Nördlingen, Germany

1 Introduction

1.1 Outline and aim of this study

The Opalinus Clay in Switzerland has been studied in detail as a potential host rock for the deep geological disposal of high-level radioactive waste (for overviews see Bossart et al. 2008; Bossart et al. 2017). Since 1996, numerous experiments have been conducted on the Opalinus Clay in the Mont Terri rock laboratory (Canton of Jura (NW Switzerland)) as part of the international research programme of the Mont Terri Consortium (Fig. 1). In 1989, the security gallery of the Mont Terri A16 highway tunnel was built and revealed that the Opalinus Clay has a total horizontal length of almost 250 m yielding a thickness of ca. 150 m at rock lab level (e.g. Bläsi et al. 1991, 1996; Bossart and Thury 2008) at this location. The rock lab offers unique access to the Opalinus Clay 300 m below the surface. Over the last 20 years, the Mont Terri rock laboratory has evolved into a system of galleries and niches exceeding 600 m in total length, with numerous experiment sites and more than 1000 boreholes. After initial lithostratigraphic studies were carried out in the galleries of the rock laboratory (e.g. Bläsi et al. 1996), there followed a long period focusing mainly on structural studies, summarized in Nussbaum et al. (2011). In 2010, the 217 m-deep BDS-5 borehole was drilled from the surface into the northern limb of the Mont Terri anticline (Jaeggi et al. 2012). In 2013, Reisdorf et al. 2014 initiated a biostratigraphic study of the Opalinus Clay under the framework of the SO (Sedimentology of Opalinus Clay) experiment, which was based on existing boreholes and outcrops within the Mont Terri rock laboratory. Ammonites found in the basal part of the Opalinus Clay supported dating this formation to the Aalensis Subzone (Aalensis Zone). Thus, sedimentation of the Opalinus Clay at Mont Terri had already begun during the Late Toarcian.

From December 2013 to January 2014, the 247.5 m-deep inclined borehole BDB-1 (Swiss coord. 2 579 515/1 247 412; Yu et al. 2017) was drilled with a downward inclination of 45° in order to achieve an orientation perpendicular to the bedding in the target interval, the Opalinus Clay. The borehole started in the lower part of the Hauptrogenstein (Bajocian) with beds dipping 65° towards the SSE, then penetrated the entire Passwang Formation and the Opalinus Clay with beds dipping around 45°, and ended in the upper (Toarcian) part of the Staffelegg Formation [Figs. 1, 2 (s. fold-out plate at the end of the issue or the electronic supplementary material under DOI 10.1007/s00015-016-0250-3); Table 1]. The borehole was drilled within the framework of the DB (Deep borehole) experiment, which aims to (1) study the hydraulic head profile through the Opalinus Clay and its adjacent bounding formations, (2) assess continuous profiles of petrophysical and

geochemical parameters on core material and in the borehole itself, and (3) constrain stratigraphy, variability of facies distribution and structure of the Opalinus Clay in an undisturbed continuous section.

1.2 Borehole BDB-1

The present study focuses on the third aim, the stratigraphy of borehole BDB-1. The borehole was drilled in two separate phases. In December 2013, the upper part ranging from 0 to 97.3 m measured depth was drilled with water, beginning in the lower part of the Hauptrogenstein and reaching up to ca. 9 m above the base of the Passwang Formation. After geophysical logging of the first part by Terratec geophysical services (Fischer 2014), the drill team cemented in a steel casing. Using air as a flushing medium, drilling was continued through the entire Opalinus Clay and into the uppermost 10 m of the Staffelegg Formation in January 2014. Drilling was then stopped at a water-bearing fracture within the Rietheim Member at a final measured depth of 247.5 m. The borehole yielded continuous core material of excellent quality. The core diameter was 101 mm in the upper section and 85 mm in the lower section. The present study includes the lithostratigraphic description and biostratigraphic subdivision based on ammonites, palynomorphs, ostracodes, and foraminifers (Chapters 3–6), as well as the interpretation of selected geophysical logs (see Suppl. Chapter 4).

1.3 Geological framework

At Mont Terri and directly adjacent areas, the Opalinus Clay is rarely exposed at the surface. One of the first lithological descriptions of the Opalinus Clay was given by Schmidt et al. (1924) from a borehole near Buix, located about 20 km to the NW of Mont Terri, where they encountered a total thickness of 157.5 m. Within the security gallery of the Mont Terri highway tunnel, the thickness of the Opalinus Clay was measured at 150 m (Schaeren and Norbert 1989; Bläsi et al. 1991, 1996). Bläsi et al. (1991) provided a detailed lithostratigraphic description of the Opalinus Clay located in a reconnaissance gallery at Mont Terri.

The entire Mont Terri rock laboratory is situated within the Opalinus Clay. This Formation can be subdivided into five units comprising three lithofacies types (Figs. 1, 2). From bottom to top, these are (1) a shaly facies consisting of mica-bearing calcareous claystones with lenses or with mm-thick layers of quartz in the silt fraction, (2) a sharp transition to a thin carbonate-rich sandy facies, characterized by quartz-bearing calcareous biotrititic layers of up to 10 cm thickness, (3) a sandy facies with calcareous

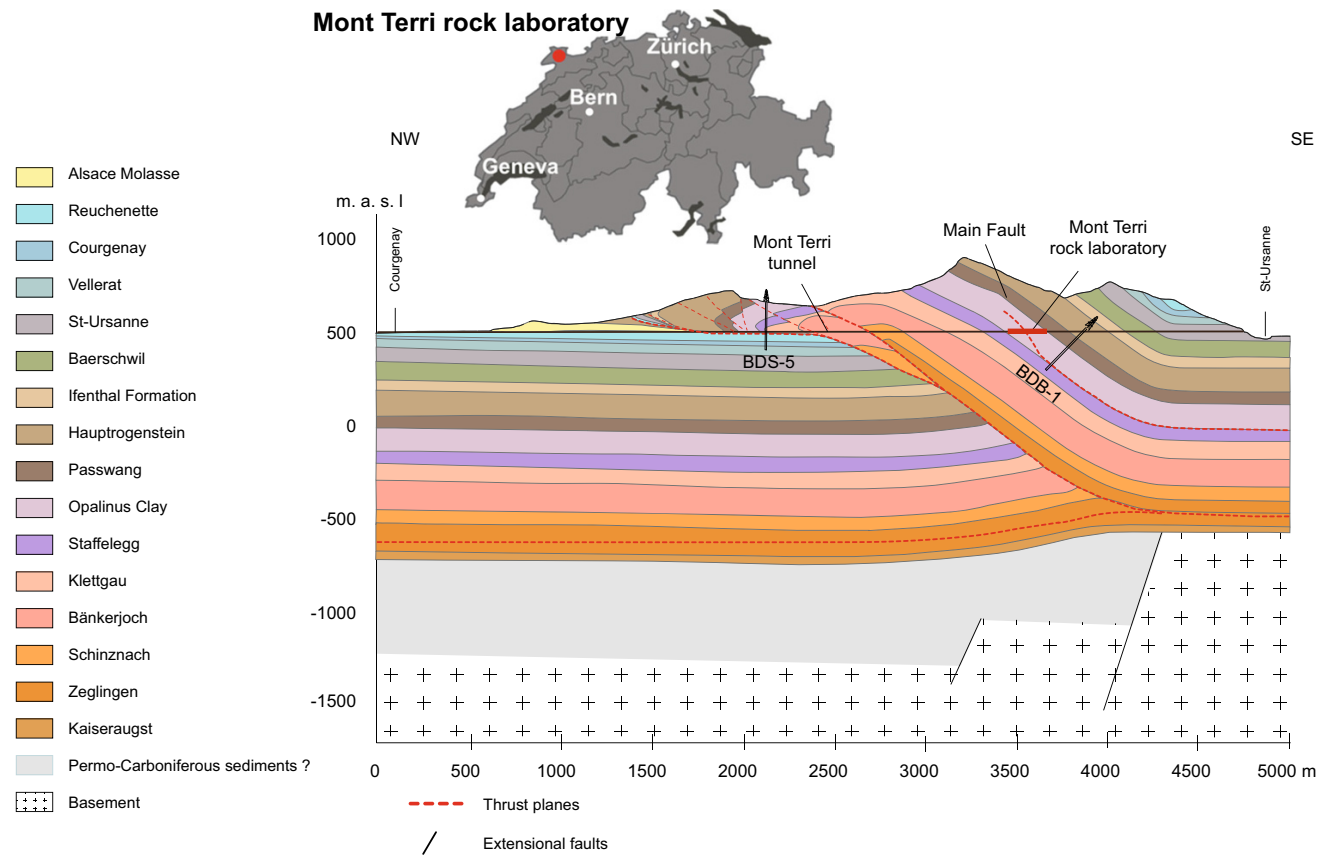


Fig. 1 Location of the Mont Terri rock laboratory within the Mont Terri anticline and geological situation of BDB-1 borehole (adapted from Caër et al. 2015). For comparison, the location of borehole BDS-5 is also displayed

silty claystones, which is then overlain by (4) a dark grey mica-bearing and slightly silty claystone attributed to the shaly facies. Finally, (5) the uppermost unit of the Opalinus Clay consists again of a sandy facies, a light grey silty claystone with laminated silt lenses, and lenses of bioclastic material.

Schaeren and Norbert (1989) and Bläsi et al. (1991) defined the base of the Opalinus Clay as a lithological transition of argillaceous sediments to more calcareous sediments. The latter have been identified as the “Jurensis-Mergel” (=Gross Wolf Member of the Staffelegg Formation, after Reisdorf et al. 2011a; see Table 1). The upper boundary of the Opalinus Clay is defined in the Mont Terri area by a distinct hardground of chamositic crusts and Fe-oolithes (this study). Bläsi et al. (1991) described this horizon with chamositic crusts, but set the top of Opalinus Clay in the Mont Terri rock laboratory ca. 7 m further upsection. A prominent tectonic overprint of the Opalinus Clay is confirmed by numerous studies on structural data conducted during the evolution of the rock laboratory (e.g. Nussbaum et al. 2011). The Mont Terri rock laboratory is located in the southern limb of the Mont Terri anticline (see Bossart et al. 2017: Fig. 1); the overburden varies between 230 m and 320 m and the stratal dip has an angle

between 30° and 50° towards the SSE in the northern and southern parts, respectively. The Mont Terri anticline developed in during 12–3 Ma at the junction between the frontal part of the Jura thrust-and-fold belt and the Rhine-Bresse transfer zone (Nussbaum et al. 2011). The geometry is a fault-bend fold that developed above a frontal ramp featuring an overturned forelimb with a detachment in the Triassic evaporites. The maximal overburden is estimated to be 1350 m, resulting in a maximum temperature of 85 °C during Cretaceous burial (Mazurek et al. 2006). At Mont Terri, three different fault systems are identified that correlate with regional-scale tectonic structures: (1) N- to NNE-striking normal faults of the Rhine-Bresse graben system that were reactivated in sinistral strike-slip mode during the Late Miocene Jura thrusting phase, (2) SSE-dipping faults parallel to bedding that were initiated during the late stage of reverse faulting, and (3) anticline folding by flexural slip and SW-dipping sub-horizontal faults that resulted from lateral extension during the thrusting of the Mont Terri anticline above the frontal ramp. The largest tectonic feature of the rock lab is the so-called Main Fault, a thrust fault, which at rock lab level dips on average about 15° steeper than the bedding planes but exhibits a similar strike direction (Nussbaum et al. 2011).

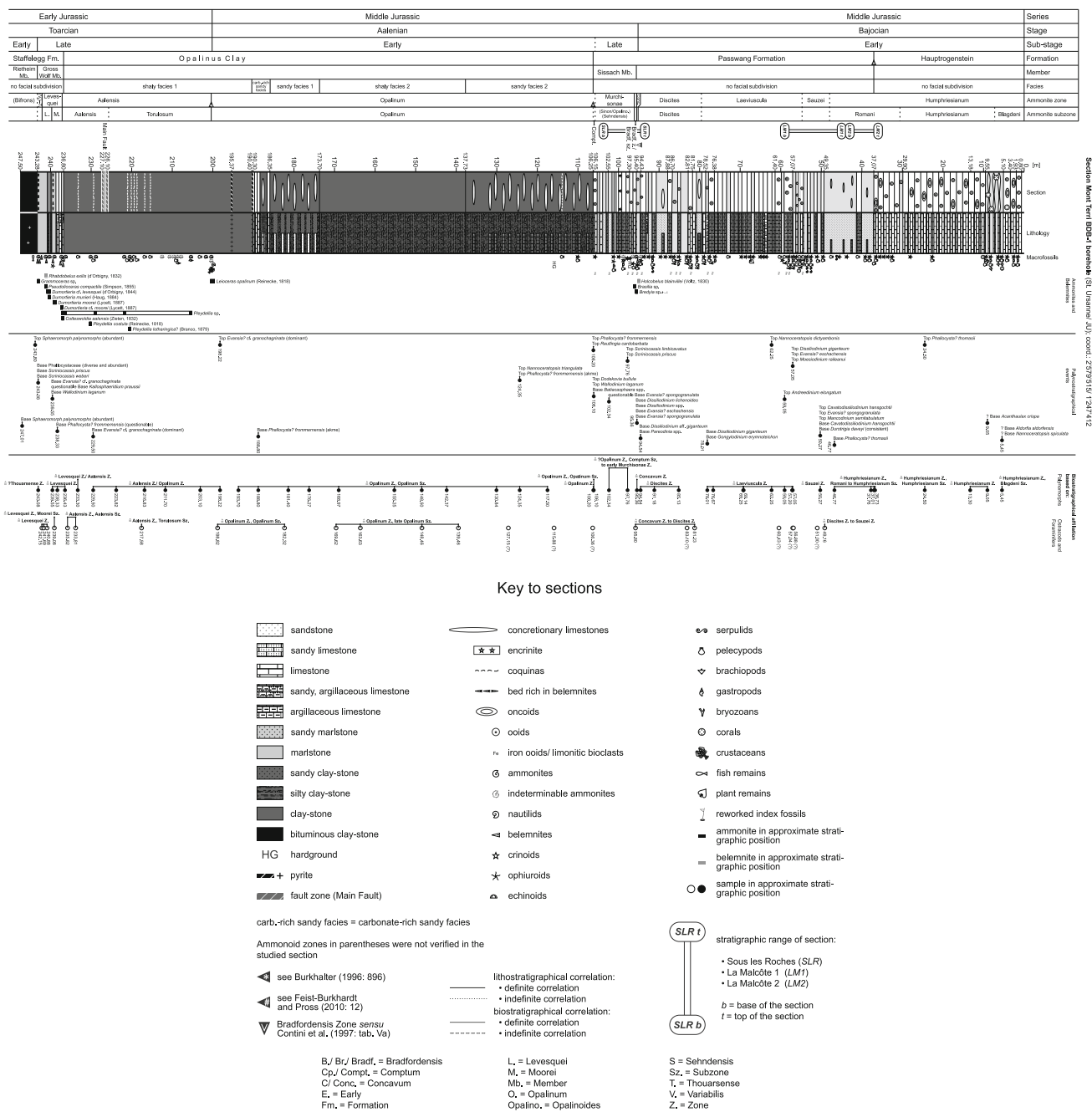


Fig. 2 Detailed section of the Early and Middle Jurassic strata of the Mont Terri BDB-1 core. Plotted next to the section are the position of macrofossil finds, selected palynological events in the section used for palynostratigraphical age dating, and the biostratigraphic interpretation and age assignment of samples to ammonite zones/subzones

2 Materials and methods

We processed the paleontological inventory with the goal of undertaking a detailed biostratigraphic subdivision of the studied formations. The latter was compiled on the basis of ammonites, ostracodes, foraminifera, and palynomorphs. Micropaleontological dating was based on 24

outwash samples and 47 samples extracted from the drill-core BDB-1 and processed for quantitative palynological analysis. The methodology used for the micropaleontological and quantitative palynological analysis is described in Reisdorf et al. (2016) and Feist-Burkhardt (2014). We present the geophysical logs and clay content estimates in Chapter 4 of the Supplement.

Three partial sections of the Passwang Formation and the basal Hauptrogenstein located in the vicinity of the BDB-1 drilling site were logged [see Supplementary Chapters 1 to 3: *Sous les Roches*, *La Malcôte 1*, and *La Malcôte 2* (see Bossart et al. 2017: Fig. 2)]. Correlating these partial sections with the BDB-1 log allowed us to cross-check the bio- and lithostratigraphy with the drillcore (Suppl. Figures 1 to 2). The macrofossils obtained from the BDB-1 drillcore and the outcrop samples have been deposited at the Naturhistorisches Museum der Burgergemeinde Bern.

3 Lithostratigraphy of the Mont Terri BDB-1 core

3.1 Staffelegg Formation (247.50–236.80 m)

The stratigraphically lowermost part of the core (247.50–243.28 m) comprises thinly bedded, brownish-black, bituminous, silty mudstones of the Rietheim Member (Fig. 2; Table 1). Above this follows the Gross Wolf Member (243.28–236.80 m) containing grey clayey marls and light grey marls, argillaceous limestones with filamentous bivalves and occasional layers rich in belemnites. These layers feature cone-in-cone calcite. The top of the Staffelegg Formation is defined by the last argillaceous limestone bed.

3.2 *Opalinus clay* (236.80–106.25 m)

From bottom to top, we classify the 130.55 m thick *Opalinus Clay* in the BDB-1 core into five subunits of specific facies:

1. Shaly facies 1 (236.80–190.40 m): dark grey calcareous, silty-sandy claystones containing mica and pyrite. It features numerous white, mm thin to max. 3 cm thick calcite lenses, consisting of cone-in-cone calcite.
2. Carbonate rich sandy facies (190.40–186.35 m): dark grey, calcareous, silty-sandy claystone layers alternating with light-grey calcareous lenses and dm-size layers. These latter consist of silt- to fine-sand-size grains and biogenic components derived mainly from bivalves and echinoderms up to 2 cm in size.
3. Sandy facies 1 (186.35–173.70 m): calcareous, silty-sandy claystones interspersed with numerous light-grey, thinly bedded sandstone lenses. The latter features small ripple and bioturbation structures with a lens-like shape due to compaction.
4. Shaly facies 2 (173.70–137.73 m): dark grey, mostly mica and pyrite containing calcareous silty-sandy claystones.
5. Sandy facies 2 (137.73–106.25 m): calcareous, silty-sandy claystones with numerous light-grey, laminated sandstone lenses. The latter feature small ripples,

occasionally lens-like due to compactional overprinting. Additionally, several bioclast-rich lenses and layers occur in this facies.

3.3 Passwang formation (106.25–37.07 m)

In the Mont Terri area, the base of the Passwang Formation begins with the first bed containing chamositic iron ooids and lithoclasts. In the borehole we measured upwards nearly 70 m of silty to fine-sandy marls, quartz sand and limestones with biotritus in the sand fraction, ferruginous limestones, and iron oolitic marls and limestones. This section between 106.25 and 76.38 m is very heterogeneous: grey, silty to fine sandy marls, with thin sandstone lenses, of which one part is rich in quartz sand, the other rich in calcareous biotritus. Within this marl series, rust-red limonitic and sandy limestone beds are repeatedly interspersed. They contain limonitic bioclasts and occasional iron ooids. This lower stratigraphic sequence of the Passwang Formation can be attributed to the Sissach Member (106.25–95.40 m; cf. Burkhalter 1996: 900). In the drillcore, the topmost beds of the Sissach Member (97.90–95.40 m) are represented by iron oolitic limestones with lithoclasts. The beds overlying the Sissach Member can be clearly distinguished from the members of the Passwang Formation sensu Diebold et al. (2006) and Jordan et al. (2008) and, as defined in the area of geographical extension (Burkhalter 1996: 908-916), by their lithology and stratigraphic architecture. A subcategorization of these sediments into members of the Passwang Formation sensu Jordan et al. (2008) is therefore not possible (Fig. 2; Table 1).

The section 76.38–61.40 m comprises alternating beds of light-grey, partially laminated and crossbedded sandy limestones alternating with thin marl layers. In several of the sandy limestones, quartz-sand-rich laminae alternate with bioclast-rich laminae. The core section 61.40–57.07 m is dominated by coarse, sparitic and biotrital sandy limestone beds featuring rust-red bioclasts (bryozoans, bivalves, and echinoderms) as well as limonitic intraclasts. The sandy limestone beds alternate with biotritus-rich marls.

The uppermost part of the Passwang Formation (57.07–37.07 m) begins with slab-shaped, fine-sandy, biotrital limestones alternating with fine-sandy marls. Above, silty to fine-sandy marls with mm-thin sandstone lenses follow. Both the limestones and marls are occasionally rich in ferruginous dolomite.

3.4 Hauptrogenstein (37.07–0 m)

The base of the Hauptrogenstein is the first oolitic limestone. The entire section of the core measured between

Table 1 Names of the Mesozoic rocks in the Mont Terri area and the subunits previously in use, the units of the BDB-1 borehole are highlighted in grey

Formation	Member	Old names
Reuchenette		<i>Kimméridgien, Ptérocérien</i>
	Vabenau	<i>Calcaires à Ptérocères inférieurs</i>
Courgenay		<i>Séquanien, Humeralis-Kalk</i>
	Porrentruy	<i>Séquanien supérieur</i>
	La May	<i>Calcaires à Térébratules</i>
Vellerat		<i>Séquanien, Couches d'Angolat</i>
	Bure	<i>Humeralis-Mergel</i>
	Hauptmumienbank	<i>Oolithe nuciforme, Oolithe pralinée, Oolithe grossière</i>
	Röschenz	<i>Séquanien inférieur, Natica-Mergel</i>
	Vorbourg	<i>Séquanien inférieur, Plattige Kalke, Couches du Vorbourg</i>
St-Ursanne		<i>Rauracien</i>
	Buix	<i>Calcaires crayeux ou corallien</i>
	Chestel	<i>ex Membre de Delémont, Oolithe corallienne, Pisolite de la Caquerelle</i>
Bärschwil		
	Liesberg	<i>Liesberg Schichten, Couches de Liesberg</i>
	Sornetan	<i>Terrain à Chailles</i>
	Renggeri	<i>Renggeriton, Marnes oxfordiennes</i>
Ifenthal		<i>Calcaire roux sableux-Callovien</i>
	Herznach	<i>Anceps-Athleta-Schichten</i>
	Bollement	<i>Dalle nacrée</i>
	Ängistein	<i>équivalent Dalle nacrée</i>
	Saulcy	<i>Callovien-Ton, Marnes calloviennes</i>
	Châtillon	<i>Makrocephalen-Kalke</i>
	St-Brais	<i>Calcaire roux sableux</i>
Hauptrogenstein		
	Pierre Blanche	
	Movelier	<i>Movelier Schichten</i>
	Oberer Hauptrogenstein	<i>Grande Oolithe, Oolithe supérieure</i>
	(Obere) Acuminata-Mergel	<i>Homomya-Mergel, Marnes à Ostrea acuminata</i>
Unterer Hauptrogenstein	<i>Oolithe subcompacte, Oolithe inférieure</i>	
Passwang		<i>Unterer Dogger/Blaukalk</i>
	undiff.	
	Sissach	<i>Murchisonae-Schichten</i>
Opalinus Clay		<i>Lias, Marnes aalenienes, Lias supérieur</i>
Stafflegg		<i>Lias, unterer und mittlerer Lias</i>
	Gross Wolf	<i>Jurensis-Mergel/-Schichten</i>
	Rietheim	<i>Posidonienschiefer, Schistes cartons, Schistes à Posidonies</i>
	?Rickenbach	<i>Mittlerer Lias?</i>
	Breitenmatt	<i>Mittlerer Lias?</i>
	Mont Terri	<i>Obliqua-Schichten? und Mittlerer Lias?</i>
Beggingen	<i>Gryphitenkalk</i>	
Klettgau		<i>Rhät und (oberer) Mittlerer Keuper</i>
	Belchen	<i>Rhät sandstein, Rhétien</i>
	Gruhalde	<i>Oberster Keuper, Marnes bigarrées supérieures</i>
	Gansingen	<i>Hauptsteinmergel, Gansinger Dolomit</i>
	Ergolz	<i>Untere Bunte Mergel und Schilfsandsteinstufe, grès à roseaux</i>
Bänkerjoch		<i>unterer Mittlerer Keuper, Gipskeuper, Marnes à anhydrite</i>
Schinznach		<i>Oberer Muschelkalk und Unterer Keuper (Lettenkohle)</i>
	Asp	<i>Unterer Keuper, Lettenkohle</i>
	Stamberg	<i>Trigonodusdolomit</i>
	Liedertswil	<i>Plattenkalk</i>
	Kienberg	<i>Oberer Trochitenkalk</i>
	Leutschenberg	<i>Unterer Trochitenkalk</i>
Zeglingen		<i>Mittlerer Muschelkalk; Anhydrit-Formation, Anhydrit-Gruppe</i>
	"Dolomitzone" (der Anhydritgruppe)	<i>Anhydritdolomit</i>

37.07 and 0 m belongs to the lower part of the Hauptrogenstein (=“Lower Oolitic Series”; Gonzalez and Wetzel 1996). The lowermost layers (37.07–29.90 m) consist of grey, oolitic, oncolithic and bioclastic micrites. Upsection (29.90–13.18 m), there are well-defined, coarse-grained, beige and light grey calcarenites, in which oncosparites clearly dominate. In the interval above (13.18–5.10 m), coral-containing, bioclast-rich marls follow, then oncomitic and oncosparitic limestones reappear.

4 Macrofossils and biostratigraphy of the Mont Terri BDB-1 core

The timeframe of the lithological succession in the core ranges from the Late Toarcian (Early Jurassic) to the Early Bajocian (Middle Jurassic) and can be fixed with certainty by means of ammonite biostratigraphy. Furthermore, we list fossils (bivalves, corals) that are characteristic of specific stratigraphic levels and provide clues to the stratigraphic correlation (see also Suppl. Chapter 3). The complete documentation for the macrofossils at the studied localities can be found in Reisdorf et al. (2016).

The BDB-1 core provides no evidence of the Variabilis Zone, nor did our assessment of microfauna or paly-nomorphs provide any such evidence. A fragment of a *Grammoceras* sp. recovered from the core at depth 243.23–243.28 m represents the oldest datable finding (Fig. 2). Its stratigraphic position within the Gross Wolf Member permits a tentative dating of the sediments to the Thouarsense Zone (Late Toarcian). As expected, the presence of *Cotteswoldia aalensis* (ZIETEN, 1832) a few cm below the topmost bed of the Gross Wolf Member indicates Aalensis Subzone age (Aalenis Zone, Late Toarcian; cf. Reisdorf et al. 2011a).

Numerous *Pleydellia* sp. specimens and a specimen of *Pleydellia lotharingica?* (BRANCO, 1879) were found in the basal strata of the Opalinus Clay. This fauna of late Toarcian age in sediments with typical (shaly) facies of the Opalinus Clay confirm the result of our initial study undertaken at the Mont Terri rock laboratory according to which the lithostratigraphic boundary between the Staffelegg Formation and the Opalinus Clay deviates by many m from the biostratigraphic boundary between the Toarcian (Early Jurassic) and the Aalenian (Middle Jurassic) (Reisdorf et al. 2014). The *Pleydellia lotharingica?* (BRANCO, 1879) specimen provides evidence to substantiate the Torulosum Subzone dating (Late Aalensis Zone) (cf. Ohmert and Rolf 1994, Feist-Burkhardt and Pross 2010). In the BDB-1 core, the Early–Middle Jurassic boundary is determined by the first occurrence of *Leioceras opalinum* (REINECKE, 1818) within the shaly facies of the Opalinus Clay at 200.37 m.

The next ammonite findings do not appear again until the Sissach Member (Passwang Formation). The first biostratigraphically useful finds permit an allocation to the genus *Brasilia*. Four specimens date the level at 95.95 m to the Bradfordensis Zone (Late Aalenian; cf. Burkhalter 1996: 900). Moreover, the finding of a *Bredya* sp. at 95.50–95.55 m is noteworthy; this specimen was found at the top of an approx. 50 cm-thick, iron ooid-bearing layer sequence embedded in a lithoclast. Numerous specimens of *Bredya* sp. preserved in this way were also found in the Sous les Roches section in similar sediments of Bradfordensis Zone age (see Supplement Chapter 2.1). The sedimentological context of these findings indicates reworking processes within a condensed layer sequence during the Bradfordensis Zone (cf. Dietze et al. 2014).

5 Invertebrate microfossils and biostratigraphy

5.1 Results

The complete documentation for the microfossils of the BDB-1 core can be found in Reisdorf et al. (2016).

5.1.1 Gross Wolf Member (Staffelegg Formation)

The four samples taken from the Gross Wolf Member of the BDB-1 core contain several ostracode species that are characteristic for the Late Toarcian: *Cytherella apostolescui* AINSWORTH, 1986; *Cardobairdia toarcensis* AINSWORTH, 1986; *Cytheropteron groissi* KNITTER, 1984; *Supratoarcina supratoarcensis* KNITTER and RIEGRAF, 1984; *Kinkelinella costata* KNITTER, 1983 and *Ektypocythere furcata* (WIENHOLZ, 1967). The last one is an index species for the Latest Dispansum Subzone (Insigne Zone) up to the Earliest Aalensis Subzone (Aalensis Zone) in southern Germany. In sample 4 (239.08 m) *Praeschuleridea ventriosa* (PLUMHOFF, 1963), the most important index species for the Late Toarcian and Aalenian, has its first appearance (Table 2). Some typical Late Toarcian foraminifera have a maximal abundance in these four samples as well: *Thurammina jurensis* (FRANKE, 1936), *Lenticulina helios* (TERQUEM, 1870) and *Palmula jurensis* (FRANKE, 1936) (Table 3).

5.1.2 Opalinus Clay

At the base of the Opalinus Clay (sample 5 at 235.82 m), there is evidence of a faunal change. *Aphelocythere kuhni* TRIEBEL and KLINGLER, 1959 occurs here for the first time (Table 2). This ostracode species is the only reliable marker for the Toarcian–Aalenian transition range (but not for the exact Toarcian–Aalenian boundary).

Table 2 Stratigraphical occurrence and frequency of ostracoda in the BDB-1 section, light grey = seldom (1–3 specimens/3 trays), medium grey = not seldom (4–10), black = abundant (>10)

Formation	Stafflegg			Opalinus Clay													Passwang							
	Gross Wolf			Levesquei			Aalensis		Opalinum					?	?	?	Concavum to Discites		?	?	?	?	Discites to Shuzeli	
Member				Moorei	Aalensis		Tenulosum	Opalinum																
Ammonite Zone																								
Ammonite Subzone																								
Drill core depth [m]	242.15	241.69	240.88	239.08	235.82	233.81	217.58	198.82	182.32	169.62	163.63	148.46	139.46	127.15	115.88	106.36	95.80	83.10	81.23	60.43	57.04	56.88	51.00	49.16
Sample no.	1	2	3	4	5	6	7	8	9	10	11	12	13	14	15	16	17	18	19	20	21	22	23	24
Ostracodes																								
<i>Cytherella apostolescui</i> ANSWORTH, 1986																								
<i>Cytherella callosa ampla</i> BRAUN in DILGER, 1963																								
<i>Cytherelloidea cadomensis</i> BUZON, 1960																								
<i>Bairdia hilda</i> JONES, 1884																								
<i>Bairdiacypris</i> sp.																								
<i>Cardobairdia toarcensis</i> ANSWORTH, 1986																								
<i>Bythocypris dorisae</i> KNITTER, 1984																								
<i>Cytheropteron grossi</i> KNITTER, 1984																								
<i>Cytheropteron supraliassicum</i> (HERRIG, 1981)																								
<i>Cytheropterna alafastigata</i> (FISCHER, 1962)																								
<i>Cytheropterna cribra</i> (FISCHER, 1962)																								
<i>Bythoceratina scrobiculata</i> (TRIEBEL and BARTENSTEIN, 1938)																								
<i>Monoceratina unguina</i> TRIEBEL and BARTENSTEIN, 1938																								
<i>Otocythere callosa</i> TRIEBEL and KLINGLER, 1959																								
<i>Pleurocythere? kirtonensis</i> BATE, 1963																								
<i>Kirtonella plicata</i> BATE, 1963																								
<i>Eucytherura angulocostata</i> KNITTER, 1983																								
<i>Eucytherura liassica</i> BATE and COLEMAN, 1975																								
<i>Eucytherura?</i> sp. 1																								
<i>Rutlandella transversiplicata</i> BATE and COLEMAN, 1975																								
<i>Procytherura</i> sp. 1																								
<i>Procytherura</i> sp. 2																								
<i>Aalenella reticulata</i> KNITTER, 1983																								
<i>Aalenella</i> sp. 1																								
<i>Aalenella?</i> sp.																								
<i>Supratoarcina supratoarcensis</i> KNITTER and REICRAF, 1984																								
<i>Kinkelina costata</i> KNITTER, 1983																								
<i>Kinkelina fischeri</i> MALZ, 1966																								
<i>Kinkelina sermoisensis</i> (APOSTOLESU, 1959)																								
<i>Kinkelina</i> sp. A CHMERT, 1988																								
<i>Ektyphocythere furcata</i> (WIENHOLZ, 1967)																								
<i>Praeschuleridea gallemanica</i> MALZ, 1966																								
<i>Praeschuleridea punctulata</i> (PLUMHOFF, 1963)																								
<i>Praeschuleridea ventriosa</i> (PLUMHOFF, 1963)																								
<i>Praeschuleridea? pinguis</i> (PLUMHOFF, 1963)																								
<i>Praeschuleridea decorata</i> BATE, 1968																								
<i>Praeschuleridea subtrigona</i> (JONES and SHERBORN, 1888)																								
<i>Acrocythere pumila</i> PLUMHOFF, 1963																								
<i>Aphelocythere asymmetrica</i> FRANZ et al., 2009																								
<i>Aphelocythere kuhni</i> TRIEBEL and KLINGLER, 1959																								
<i>Aphelocythere hamata</i> PLUMHOFF, 1963																								
<i>Aphelocythere pygmaea</i> PLUMHOFF, 1963																								
<i>Aphelocythere</i> sp. 1 PLUMHOFF, 1963																								
<i>Campocythere gracilis</i> PLUMHOFF, 1963																								
<i>Campocythere modesta</i> TRIEBEL, 1959																								
<i>Fuhrbergiella sauzei</i> BRAND and MALZ, 1962																								
<i>Paracypris</i> sp.																								

Table 3 Stratigraphical occurrence and frequency of foraminifera in the BDB-1 section, light grey = seldom (1–3 specimens/3 trays), medium grey = not seldom (4–10), black = abundant (>10)

Formation	Staffelegg							Opalinus Clay									Passwang										
	Gross Wolf																Silesach										
Ammonite Zone	Levesquei							Aalensis			Opalinum						?	?	?	Concavum to Discites			?	?	?	?	Discites to Sauzei
	Ammonite Subzone				Moorei	Aalensis		Torulolum	Opalinum																		
Drill core depth [m]		242.15	241.69	240.88	239.08	235.82	233.81	217.58	198.82	182.32	169.62	163.63	148.46	139.46	127.15	115.88	106.36	95.80	83.10	81.23	60.43	57.04	56.88	51.00	49.16		
Sample no.	1	2	3	4	5	6	7	8	9	10	11	12	13	14	15	16	17	18	19	20	21	22	23	24			
Foraminifers																											
<i>Reophax metensis</i> FRANKE, 1936																											
<i>Thuramina jurensis</i> (FRANKE, 1936)																											
<i>Ammobaculites coprolithiformis</i> (SCHWAGER, 1867)																											
<i>Ammobaculites fontinensis</i> (TERQUEM, 1870)																											
<i>Lingulina spatulata</i> TERQUEM, 1870																											
<i>Froncularia oolithica</i> TERQUEM, 1870																											
<i>Pseudonodosaria vulgata</i> (BORNEMANN, 1854)																											
<i>Nodosaria fontinensis</i> TERQUEM, 1870																											
<i>Nodosaria sexcostata</i> TERQUEM, 1858																											
<i>Nodosaria striatjurensis</i> KLÄHN, 1923																											
<i>Marginulina oolithica</i> (TERQUEM, 1870)																											
<i>Lenticulina dictyodes</i> (DEECKE, 1884)																											
<i>Lenticulina dorbignyi</i> (ROEMER, 1839)																											
<i>Lenticulina helios</i> (TERQUEM, 1870)																											
<i>Lenticulina muensteri</i> (ROEMER, 1839)																											
<i>Lenticulina prima</i> (D'ORBIGNY, 1850)																											
<i>Lenticulina varians</i> (BORNEMANN, 1854)																											
<i>Subhercynella paucinodula</i> BARTENSTEIN and LUPPOLD, 2005																											
<i>Astacolus suprajurassicus</i> (SCHWAGER, 1865)																											
<i>Planularia cordiformis</i> (TERQUEM, 1863)																											
<i>Palmula deslongchampsii</i> (TERQUEM, 1863)																											
<i>Palmula jurensis</i> (FRANKE, 1936)																											
<i>Citharina infraopalina</i> BRAND, 1962																											
<i>Reinholdella dreheri</i> (BARTENSTEIN, 1937)																											
<i>Reinholdella traubensis</i> OHM, 1967																											
<i>Spirillina oolithica</i> (SCHWAGER, 1867)																											
<i>Spirillina polygyrata</i> GUMBEL, 1862																											

The microfauna in sample 7 (217.58 m) is dominated by two foraminiferal species: *Reinholdella dreheri* (BARTENSTEIN, 1937) and *Reinholdella traubensis* OHM, 1967. *Aphelocythere kuhni* TRIEBEL and KLINGLER, 1959 has its last occurrence in sample 10 (169.62 m). *Aphelocythere pygmaea* PLUMHOFF, 1963, *Aphelocythere hamata* PLUMHOFF, 1963 (both in samples 10–13), and *Acrocythere pumila* PLUMHOFF, 1963 (in sample 13 only) were introduced by PLUMHOFF (1963) as index species of the Sinon to Staufensis Subzones (Murchisonae

Zone). In sample 13 (139.46 m), *Cytherelloidea cadomensis* BIZON, 1960; *Cytheropterina cribra* (FISCHER, 1962), and *Aaleniella reticulata* KNITTER, 1983, all remnant Toarcian species, have their last occurrence. Thus, a faunal break is evident at the top of this sequence, with several new species arising in higher stratigraphic levels (Tables 2, 3). Only a few species like *Kinkelinella sermoisensis* (APOSTOLESCU, 1959) and *Praeschuleridea punctulata* (PLUMHOFF, 1963) cross this chronostratigraphic boundary.

5.1.3 Passwang Formation

Samples 17 (95.80 m) and 19 (81.23 m) contain an almost identical and rich microfauna. The foraminiferal species *Lenticulina dictyodes* (DEECKE, 1884) makes its first appearance in sample 19. Its biostratigraphical range is from the Discites to the Humphriesianum Zone. Several ostracode index species appear for the first time in core samples from this range: *Cytherella callosa ampla* BRAUN in DILGER, 1963 and *Praeschuleridea decorata* BATE, 1968 (in sample 17 only), *Praeschuleridea? pinguis* (PLUMHOFF, 1963); *Camptocythere gracilis* PLUMHOFF, 1963; *Camptocythere modesta* PLUMHOFF, 1963; *Kinkelinella* sp. A OHMERT, 1988 (all in samples 17 and 19); *Praeschuleridea subtrigona* (JONES and SHERBORN, 1888) and *Aphelocythere asymmetrica* FRANZ et al., 2009 (both in sample 19). The biostratigraphical range of these ostracode species, as stated in the literature, seems somewhat controversial (for more details see Reisdorf et al. 2016). Summarising our findings, we deem a dating between the Murchisonae- and Discites Zone to be most appropriate. Sample 24 (49.16 m) yielded a rather rich and diverse fauna and several ostracode species appear for the first time in the BDB-1 core samples: *Bairdia hilda* JONES, 1884; *Bairdiacypris* sp.; *Pleurocythere? kirtonensis* BATE, 1963; *Kirtonella plicata* BATE, 1963; *Eucytherura? sp. 1*; *Procytherura sp. 1*; *Procytherura sp. 2*; *Aalenella? sp.*; *Aphelocythere sp. 1* PLUMHOFF, 1963, as well as *Fuhrbergiella sauzei* BRAND and MALZ, 1962. In England *Bairdia hilda* JONES, 1884; *Kirtonella plicata* BATE, 1963 and *Pleurocythere? kirtonensis* BATE, 1963 are reported from the Discites Zone (Bate 1963), the latter also from the Discites- to Laeviuscula Zone in southwestern Germany (Ohmert 1988). *Fuhrbergiella sauzei* BRAND and MALZ, 1962 appears first in the Early Bajocian and is most abundant in the Sauzei Zone. Of the foraminifera, *Ammobaculites coprolithiformis* (SCHWAGER, 1867) is a characteristic component of the fauna.

5.2 Interpretation

Based on the range charts of certain ostracode species, we can make a biostratigraphical subdivision of the BDB-1 drillcore (Table 2; Fig. 2). There is a basal unit of “Toarcian character” (in quotes because of its onset in the Late Toarcian with no relevant change at the Toarcian–Aalenian boundary) ranging from 242.15 to 198.82 m. After a faunal depletion in the lower sandy facies of the Opalinus Clay (184–171 m), a second biostratigraphic interval from 169.62 to 139.46 m is characterized by the continuing occurrence of Toarcian taxa, with some newly appearing index species of the Sinon to Staufensis Subzone (Murchisonae Zone) as known from NW Germany (where the Comptum Subzone of the Opalinus Zone is missing;

Plumhoff 1963). Separated by a further faunal hiatus in the upper sandy facies of the Opalinus Clay (127.15–106.36 m), the stratigraphic interval from 95.80 to 81.23 m exhibits a significant faunal change with index species for the Concavum to Discites zones. Up to 51.00 m the microfauna again diminishes, but the sample from 49.16 m contains further new ostracode taxa typical for the Discites to Sauzei zones. The extension and the limits of these biostratigraphical intervals of the BDB-1 core are somewhat uncertain because of the restricted number and distribution of the collected samples.

We can achieve a finer subdivision of the “Toarcian character” in the basal interval. The interval from 242.15 to 240.88 m with *Ektyphocythere furcata* (WIENHOLZ, 1967) and the absence of *Praeschuleridea ventriosa* (PLUMHOFF, 1963) could represent the Levesquei to Early Moorei subzones (Levesquei Zone). According to Knitter (1983), *Praeschuleridea gallemanica* MALZ, 1966 disappears in the Earliest Aalensis Subzone (Aalensis Zone); its last occurrence in the BDB-1 core is in sample 6 (233.81 m). With *Aphelocythere kuhni* TRIEBEL and KLINGLER, 1959 at 235.82 m, the Toarcian–Aalenian boundary should be expected somewhat higher (but not lower) in the section. Based on foraminifera in the Wittnau section (SW Germany), Ohmert (1996) established a Traubensis Zone crossing the Toarcian–Aalenian boundary, and a Dreheri Zone covering the Torulosum- and Opalinum Subzones (Late Aalensis to Early Opalinum zones). In the BDB-1 section *Reinholdella traubensis* OHM, 1967 is found at 217.58 m (Table 3). The exact position of the Toarcian–Aalenian boundary cannot be determined by means of microfossils, but a transition range is suspected between 230 and 199 m.

6 Palynomorphs and palynostratigraphy

Whereas biostratigraphic resolution of pollen and spores is limited in Jurassic assemblages, it is possible to perform high-resolution biostratigraphy based on dinoflagellate cyst occurrences. Indeed, dinoflagellate families show numerous first appearances (FAD = first appearance date) during the Early Jurassic followed by a diversification within families. In the past few years, dinoflagellate cyst assemblages have been identified from outcrops and boreholes in southern Germany and northern Switzerland (see Feist-Burkhardt and Wille 1992; Feist-Burkhardt and Pross 2010). These works form the basis for a Composite Standard developed by Feist-Burkhardt (unpublished) for the Early to Middle Jurassic that serves as a reference for validating the new biostratigraphic scheme of the Mont Terri area, adapted primarily on ammonite zonation.

6.1 Results

The studied samples yielded a well-preserved, rich, and diverse palynoflora. The palynomorph assemblages are composed mainly of dinoflagellate cysts (93 taxa in total). Pollen and spores (51 taxa) also occur, as well as minor components (24 taxa), among which are prasinophytes, acritarchs, fungal remains, foraminiferal test linings, and green algae. Feist-Burkhardt (2014 in Reisdorf et al. 2016) presents a range chart with quantitative stratigraphic distribution of palynomorphs together with proposed age assignments, as well as age and depth/age plots.

Fourteen stratigraphic intervals were identified based on their palynological content (mainly dinoflagellate cysts), ranging from the Early Toarcian to Early Bajocian. Table 4 summarises the palynostratigraphic subdivision and assigns each interval to the corresponding ammonite zone and occurrence within the lithostratigraphic unit.

6.2 Interpretation

At its lowermost level, the borehole reached the typical facies of the Rietheim Member of the Staffelegg Formation

(“Posidonienschiefer”; see Table 1), containing almost exclusively amorphous organic matter and small sphaeromorph palynomorphs. This bituminous facies is considered to be of Early Toarcian age.

Uphole, the first rich palynoflora comprising abundant pollen, spores, and dinoflagellate cysts occurs at 243.08 m. This sample dates from the Late Toarcian, probably Thouarsense Zone (occurrence of diverse and abundant Phallocystaceae and Valvaeodiniaceae, in particular *Scriniocassis priscus* (GOCHT, 1979) BELOW, 1990. The uppermost part of the Staffelegg Formation (Gross Wolf Member) was deposited during the Levesquei Zone or Aalensis Zone.

The lowermost samples from the Opalinus Clay (at 236.43 m and 233.30 m) confirm that the deposition of this formation already began during the Late Toarcian (Levesquei to Aalensis Zones) in the Mont Terri area (Reisdorf et al. 2013, 2014).

Based on palynostratigraphy, the position of the Toarcian–Aalenian boundary interval (occurrence acme of *Evansia?* cf. *granochagrinata* BELOW, 1990 between 229.50 m and 198.22 m) is in good accordance with the results obtained from ammonite biostratigraphy (first

Table 4 Palynostratigraphic subdivision of the BDB-1 borehole into 14 intervals, with assignment to the corresponding ammonite zone and chronostratigraphy. The general lithostratigraphic scheme is given on the right side

Chronostratigraphy		Biostratigraphy		Palynostratigraphy		Remarks (resp. units in Feist-Burkhardt & Pross 2010)	Lithostratigraphy	
Stage	Substage	Zone	Subzone	Depth [m]	Nr.		Member	Formation
Bajocian	Middle	Humphriesianum	Blagdeni	5.45	14	FAD of <i>Aldorfia aldorfensis</i>	Hauptrogenstein	
			<i>undifferentiated</i>	13.30 – 9.05	13	FAD of <i>Acanthaulax crista</i> and <i>Meiourougonyaulax</i> spp.		
			Humphriesianum	46.77 – 24.50	12	rich in fungal remains and <i>Sentusidinium</i> spp.		
			Romani			rich in foraminiferal test linings, FAD of <i>Phallocysta thomasii</i>		
	Early	Sauzei		50.27	11	extremely abundant foraminiferal test linings, LAD of <i>Cavatodissiliodinium hansgochti</i>	Passwang	
		Laeviuscula		78.01 – 57.05	10	abundant and diverse		
		Discites		94.54 – 85.13	9	<i>Dissiliodinium</i> spp.		
Aalenian	Late	Concavum		95.36	8	FAD of <i>Evansia? eschachensis</i>	Sissach	Opalinus Clay
		Murchisonae						
	Early	Opalinus	Comptum		102.34 – 97.76	7	strongly reduced diversity of Phallocystaceae	
					106.10	6	unit D	
			Opalinus		193.70 – 106.20	5	units B and C	
					229.50 – 198.22	4	acme of <i>Evansia?</i> cf. <i>granochagrinata</i> (unit A)	
Late	Aalensis							
	Levesquei		239.55 – 233.30	3	further diversification (Phallocystaceae and Valvaeodiniaceae)			
	Thouarsense		243.08	2	first rich palynoflora			
	Variabilis							
Early	Bifrons					Gross Wolf	Staffelegg	
	Falciferum		247.01 – 243.80	1	typical bituminous facies (AOM and sphaeromorphs)	Rietheim		

occurrence of *Leioceras opalinum* (REINECKE, 1818) at 200.50 m, see Chapter 4).

The overlying and major part of the Opalinus Clay was deposited during the Opalinus Subzone.

The base of the Passwang Formation dates from the Opalinus Subzone as well (samples at 106.20 and 106.10 m) whereas the top dates from the Humphriesianum Zone. Pollen and spores are relatively more abundant here than in the surrounding levels (especially the sporomorph taxon *Perinopollenites elatoides* COUPER, 1958). The Comptum Subzone, Concavum Zone, Discites Zone, Laeviuscula Zone and Sauzei Zone are also documented palynostratigraphically.

The base of the Hauptrogenstein is dated palynostratigraphically as Romani Subzone to Humphriesianum Subzone (Humphriesianum Zone, based on the occurrence of the dinoflagellate cyst *Phallocysta thomasi* SMELROR, 1991). It is also characterized by its richness in fungal remains and *Sentusidinium* spp.

In conclusion, in combination with the revised ammonite and microfossil zonations, the present palynostratigraphic analysis provides a solid biostratigraphic framework for the Opalinus Clay and bounding formations in the Mont Terri area.

7 Discussion and concluding remarks

The BDB-1 drillcore provided a multitude of significant stratigraphic and geophysical data on the Mont Terri area. This data permits a straightforward subdivision of the sampled core into a lithostratigraphic resolution of individual formations (Fig. 2). Of particular significance is the fact that we have recorded a continuous section from the upper part of the Staffelegg Formation to the basal beds of the Hauptrogenstein in detail for the first time. It has proven useful to compare the BDB-1 core with the three studied sections close to the Mont Terri rock laboratory; nearly half of the encountered beds of the Passwang Formation, including the basal beds of the Hauptrogenstein, are covered stratigraphically by these partial sections (Fig. 2, Suppl. Figure 3 and Suppl. Figure 2). The outcrops that were referenced before the initiation of drilling had already served as suitable stratigraphic aids for orientation purposes during the drilling campaign, e.g. anticipation of the boundary between the Passwang Formation and the Hauptrogenstein.

A key result of the present study is that the lithological succession of the core, and also of the near-by outcrops, is at the formation level, clearly correlatable with the lithostratigraphical units that were defined in their type regions lying farther east.

This holds true for the Staffelegg Formation, of which only the upper part consisting of the Rietheim and Gross

Wolf Members were encountered (cf. Reisdorf et al. 2011a). Aside from that, the basal strata of the Passwang Formation can be identified as the Sissach Member (cf. Burkhalter 1996). The “Lower Oolitic Series” is developed as an informal lithostratigraphic unit of the Hauptrogenstein in the study area (Gonzalez and Wetzel 1996).

On the other hand, the facial configuration and stratigraphic architecture of the Opalinus Clay and the Passwang Formation in the study area deviate to a greater or lesser degree from the occurrences that are situated farther east in northern Switzerland (Bläsi et al. 1996; Burkhalter 1996; Wetzel and Allia 2003; Jordan et al. 2008). As expected, the several m thick, relatively carbonate-rich sandy facies variations of the Opalinus Clay (Bläsi et al. 1991, 1996) typical of the Mont Terri region, are also traceable in the BDB-1 core. The subdivisions of the Opalinus Clay also correlate with the geophysical logs (Supplement Chapter 4). These geophysical logs observed in outcrops and boreholes in the Mont Terri rock laboratory are important to help better define transitional lithostratigraphic boundaries. Especially the intraformational transitions between sandy and shaly facies of the Opalinus Clay can be well constrained using geophysical criteria.

Of greater significance for the current stratigraphic nomenclature of northern Switzerland is the facial configuration of the beds of the Passwang Formation above the Sissach Member (see Supplement Chapter 1). No member of the Passwang Formation as defined in the extended area compares with the lithologies encountered in the Mont Terri area (cf. Burkhalter 1996: 908–916, Figs. 18 to 21; Jordan et al. 2008). We think that a definition of new lithostratigraphic units (members) to accommodate the local facial features would be desirable in this context, but this lies beyond the scope of the present work. However, comparing the BDB-1 core with the outcrops of Sous les Roches, La Malcôte 1 and La Malcôte 2, all close to the Mont Terri rock laboratory, suggests that distinct facies changes occur in the Mont Terri area over short distances thereby giving rise to more-or-less intense variations in the thickness of individual layers. For example, the marl following the Sissach Member, measured in the BDB-1 core, is 1.03 m thick whereas in the section Sous les Roches the marl is clearly more than 1.5 m thick. In the case of the sections described in this study, opportunities for correlation are limited to only a few stratigraphic levels (Fig. 2, Suppl. Figure 1 and Suppl. Figure 2).

A further essential finding from the BDB-1 borehole is the significant deviation of the total thickness of the Opalinus Clay from the most recent thickness calculations: the BDB-1 core thickness measured at ca. 130 m is 20 m thinner than that calculated for the Mont Terri rock laboratory (cf. e.g. Reisdorf et al. 2014). The Mont Terri mountain is built of a

structurally complicated anticlinal feature and numerous, mostly layer-parallel, faults are interspersed throughout the rock laboratory section as well as in the borehole. Thus for the time being, we cannot determine whether (1) one of the two thickness values represents a true thickness; (2) the lesser thickness in the drillcore was produced by shearing and/or squeezing; or (3) a doubling of the thickness of certain strata is present in the rock laboratory section and thus is responsible for a total thickness of 150 m.

The stratigraphic architecture and facies configuration of the Opalinus Clay (including two thin, horizon-stable pyrite horizons; see Reisdorf et al. 2014), typically developed in both sections for the Mont Terri area, does not permit us to decide on one thickness value or the other. Additionally, neither in the rock laboratory section nor in the drillcore are tectonically based doublings of strata, or gaps in strata, evident (see below). In the end, the stratigraphic position of the Main Fault in the drillcore, which deviates from that in the rock laboratory section, does not—according to the present state of understanding—contribute to solving the problem.

The independently derived macro- and micropaleontological findings from the studied core material are in themselves consistent in a noteworthy manner. The individual methods (ammonite, ostracode, foraminiferal biostratigraphy, and palynostratigraphy) supplement one another, not only spatially, but they also provide evidence for nearly all relevant biozones in a time period that extends from the Bifrons Zone (Early Toarcian) to the Humphriesianum Zone (Early Bajocian) (Fig. 2). The obtained biostratigraphic data thereby permit the following statements and conclusions:

1. the ammonite findings of Toarcian age in sediments with typical facies of the Opalinus Clay (shaly facies) confirm the conclusion of our first study (Reisdorf et al. 2014), according to which the lithostratigraphic boundary between the Staffelegg Formation and the Opalinus Clay deviates by several m from the chronostratigraphic boundary between the Toarcian (Early Jurassic) and the Aalenian (Middle Jurassic);
2. in terms of micropaleontology, the Torulosum Subzone (Late Aalensis Zone) was substantiated in the drillcore for the first time in the study area. In particular we emphasize that when applying the currently valid European Standard ammonite biostratigraphy, the Torulosum Subzone should be allocated to the Aalensis Zone, and thereby to the Latest Toarcian (Early Jurassic) (Feist-Burkhardt and Pross 2010; Reisdorf et al. 2014). The stratigraphic position of the extracted rock sample of Torulosum Subzone age and the first appearance of *Leioceras opalinum* (REINECKE, 1818) in BDB-1 core material suggests a minimum thickness of 17 m, respectively a maximum thickness of ca. 25 m for sediments of a Torulosum Subzone age. These thickness relations correspond to the orders of magnitude that occur in Wittnau (south of Freiburg i. Br., Germany), featuring nearly 23 m of strata of the same age and configured similarly in terms of facies (cf. Geologisches Landesamt Baden-Württemberg 1996; note the stratigraphic correlation in Reisdorf et al. 2014: Figs. 5-1 and 5-2).
3. The chronostratigraphic boundary between the Toarcian (Early Jurassic) and the Aalenian (Middle Jurassic) lies in the shaly facies 1 of the Opalinus Clay. Approx. 38 m-thick strata in the typical Opalinus Clay facies (shaly facies 1) are chronostratigraphically attributable to the Late Toarcian (Aalensis Zone inclusive of the Torulosum Subzone). We would like to emphasise this result as derived from the present study, since occurrences in sediments of the same age in typical Opalinus Clay facies situated farther to the east are at most only a few cm thick (Etter 1990; Reisdorf 2001; Reisdorf et al. 2011b). Moreover, farther to the east, the Aalensis Zone is most notably represented by sediments up to a few m thick and these can be attributed to the upper strata of the Gross Wolf Member (Staffelegg Formation) (Etter 1990, Nagra 1992; Reisdorf et al. 2011a, b).
4. The oldest sediments of the Opalinus Clay in the Mont Terri area were deposited during the Aalensis Subzone (Aalensis Zone, Late Toarcian). This also applies to many of the Opalinus Clay occurrences to the east of northern Switzerland and neighboring areas in southern Germany (Etter 1990; Reisdorf et al. 2011a, b, 2014: 17). Only a few deviating findings from northern Switzerland have been documented: Bläsi (1987: 417) and Etter (1990: Fig. 8) reported *Leioceras opalinum* from the uppermost part of the “Jurensis-Mergel” (=Gross Wolf Member) of the Riniken borehole, the Weiach borehole, and in the Siblingen section.
5. Sedimentation of the Opalinus Clay initiated in northern Switzerland and SW Germany mostly during the same time period (Aalensis Subzone, Aalensis Zone, Late Toarcian), but in the Mont Terri area with a considerably higher sedimentation rate.
6. Biostratigraphic data derived from outcrops by means of ammonites are better suited to chronostratigraphically comprehend the entire index-fossil-poor strata of the Passwang Formation in the BDB-1 core. Overall, these data suggest that sedimentation of the Sissach Member starts at the Opalinum to Comptum Subzone (Opalinum Zone) boundary and continues up to the Concavum Zone. The latest dating confirms the chronostratigraphic coverage as compared to the area of extension of the Sissach Member (cf. Burkhalter

1996: 900; note: the Bradfordensis Subzone has, in the meantime, been added to the independent Bradfordensis Zone, see e.g. Chandler and Callomon 2009; Contini et al. 1997).

7. According to our findings from the BDB-1 core and the La Malcôte 2 section in the Mont Terri area, deposition of the “Lower Oolitic Series” of the Hauptrogenstein began as early as within the Humphriesianum Subzone (Humphriesianum Zone) (for the stratigraphic subdivision of the Hauptrogenstein see Gonzalez and Wetzel 1996, Jordan et al. 2008), in contrast to the occurrences of the formation situated farther to the east. Sediments of the same age are represented farther east in the lithology of the Brüggli Member and the Rothenfluh Member (both belonging to the Passwang Formation; see Diebold et al. 2006). Accretion of ooids in the “Lower Oolitic Series” took place later (Niortense Zone) in the easterly occurrences. This confirms the west to east progradation of this carbonate platform (cf. Gonzalez and Wetzel 1996).
8. In most cases, the chronological precision of the resolution for the sections we studied and the drillcore material of BDB-1 are in the scope of a biozone. Consequently, these data do not permit substantiating possible stratigraphic gaps below this resolution. In any case, lithoclasts, in which ammonites of the genus *Bredya* are embedded, definitively demonstrate reworking processes in sediments of Late Aalenian age during the Bradfordensis Zone.

Acknowledgements The Mont Terri Project Partners BGR, GRS, IRSN, Nagra, NWMO, and swisstopo financially contributed to the drilling of the BDB-1 borehole. The operator of the Mont Terri rock laboratory swisstopo managed the drilling of the BDB-1 borehole and provided the facilities of the Mont Terri rock laboratory. This study was financially supported by the Mont Terri Consortium in the framework of the SO (Sedimentology of Opalinus Clay) experiment. All these contributions are gratefully acknowledged. We furthermore thank all the involved contractors and especially Entrepose Drilling SA for their great on-site operation, which yielded core material of excellent quality. In a first phase Sue Turner (Brisbane) helped to improve the English. To complete, Roy Freeman (Lucerne) reviewed the English text. The authors are much obliged to the constructive reviews of Reto M. Burkhalter, Robin Allenbach, Paul Bossart, and Alan G. Milnes, all of which enhanced the character of the final paper.

References

- Bate, R. H. (1963). Middle Jurassic Ostracoda from North Lincolnshire. *Bulletin of the British Museum (Natural History) Geology*, 8, 176–219.
- Bläsi, H.-R. (1987). Lithostratigraphie und Korrelation der Dogger Sedimente in den Bohrungen Weiach, Riniken und Schafisheim. *Eclogae Geologicae Helveticae*, 80, 415–430.
- Bläsi, H.-R., Moeri, A., & Bossart, P. (1996). *Results of the Phase I drilling campaign*. Mont Terri technical report, TR 96-01, 54 pp. Federal Office of Topography (swisstopo), Wabern, Switzerland. www.mont-terri.ch.
- Bläsi, H.-R., Peters, T. J., & Mazurek, M. (1991). Der Opalinus Clay des Mont Terri (Kanton Jura): Lithologie, Mineralogie und physiko-chemische Gesteinsparameter. *Nagra interner Bericht*, 90–60, Nagra, Wettingen, Switzerland. www.nagra.ch.
- Bossart, P., Bernier, F., Birkholzer, J., Bruggeman, C., Connolly, P., Dewonck, S., Fukaya, M., Herfort, M., Jensen, M., Matray, J.-M., Mayor, J. C., Moeri, A., Oyama, T., Schuster, K., Shigeta, N., Vietor, T., & Wieczorek, K. (2017). Mont Terri rock laboratory, 20 years of research: introduction, site characteristics and overview of experiments. *Swiss Journal of Geosciences*, 110. doi:10.1007/s00015-016-0236-1 (this issue).
- Bossart, P., & Thury, M. (2008). *Mont Terri Rock Laboratory. Project, programme 1996 to 2007 and results*. Reports of the Swiss Geological Survey, No. 3, Federal Office of Topography (swisstopo), Wabern, Switzerland. www.mont-terri.ch.
- Burkhalter, R. M. (1996). Die Passwang-Alloformation (unteres Aalénien bis unteres Bajocien) im zentralen und nördlichen Jura. *Eclogae Geologicae Helveticae*, 89, 875–934.
- Caër, T., Maillot, B., Souloumiac, P., Leturmy, P., Frizon De Lamotte, D., & Nussbaum, C. (2015). Mechanical validation of balanced cross-sections: The case of the Mont Terri anticline at the Jura front (NW Switzerland). *Journal of Structural Geology*, 75, 32–48.
- Chandler, R., & Callomon, J. (2009). The Inferior Oolite at Coombe Quarry, near Mapperton, Dorset, and a new Middle Jurassic ammonite faunal horizon, Aa-3b, *Leioceras comptocostosum* n. biosp. In the Scissum Zone of the Lower Aalenian. *Proceedings of the Dorset Natural History and Archaeological Society*, 130, 99–132.
- Contini, D., Elmi, S., Mouterde, R., & Rioult, M. (1997). 5 Aalénien. In E. Cariou & P. Hantzpergue (Eds.), *Biostratigraphie du Jurassique Quest-Européen et Méditerranéen. Zonations parallèles et distribution des invertébrés et microfossiles* (pp. 37–40). Pau Cedex: Elf Exploration Production.
- Diebold, P., Bitterli-Brunner, P., & Naef, H. (2006). Blatt 1069/1049 Frick-Laufenburg. *Geologischer Atlas der Schweiz 1:25000 Erläut.*, 110, 1–136.
- Dietze, V., Rieber, H., Auer, W., Franz, M., Schweigert, G., Chandler, R. B., et al. (2014). Aalenian (Middle Jurassic) ammonites and stratigraphy of the Geisingen clay pit (SW Germany). *Palaeodiversity*, 7, 61–127.
- Etter, W. (1990). *Paläontologische Untersuchungen im Unteren Opalinuston der Nordschweiz*. Ph.D. dissertation, University of Zürich, Zürich, Switzerland.
- Feist-Burkhardt, S. (2014). *SO-A experiment: Palynological analyses of samples from the BDB-1 borehole*. Mont Terri technical note, TN 2014-61, 11 pp. Federal Office of Topography (swisstopo), Wabern, Switzerland. www.mont-terri.ch.
- Feist-Burkhardt, S., & Pross, J. (2010). Dinoflagellate cyst biostratigraphy of the Opalinuston Formation (Middle Jurassic) in the Aalenian type area in southwest Germany and north Switzerland. *Lethaia*, 43, 10–31.
- Feist-Burkhardt, S., & Wille, W. (1992). Jurassic palynology in southwest Germany - state of the art. *Cahiers de Micropaléontologie*, 7, 141–164.
- Fischer, D. (2014). *Borehole Logging Mont Terri Test Site, in the borehole BDB-1*. Mont Terri Technical Note, TN2014-29, 23 pp. Federal Office of Topography (swisstopo), Wabern, Switzerland. www.mont-terri.ch.
- Geologisches Landesamt Baden-Württemberg (1996, ed.): Die Grenzziehung Unter-/Mitteljura (Toarcium/Aalenium) bei Wittnau und Fuentelsaz. - Beispiele interdisziplinärer

- geowissenschaftlicher Zusammenarbeit. *Informationen Geologisches Landesamt Baden-Württemberg*, 8, 52 pp. Freiburg i. Br.
- Gonzalez, R., & Wetzel, A. (1996). Stratigraphy and paleogeography of the Hauptrogenstein and Klingnau Formations (middle Bajocian to late Bathonian), northern Switzerland. *Eclogae Geologicae Helveticae*, 89, 695–720.
- Jaeggi, D., Müller, P., & Nussbaum, C. (2012). *DS (determination of stress) Experiment: Report about the drilling activities and the geology/hydrogeology encountered at borehole BDS-5*. Mont Terri Technical Report, TR 12-05, 42 pp. Federal Office of Topography (swisstopo), Wabern, Switzerland. www.mont-terri.ch.
- Jordan, P., Wetzel, A., & Reisdorf, A. G. (2008). Jurassic. Swiss Jura Mountains. In T. McCann (Ed.), *The Geology of Central Europe. Volume 2: Mesozoic and Cenozoic* (Vol. 2, pp. 880–889). London: Geological Society.
- Knitter, H. (1983). Biostratigraphische Untersuchungen mit Ostracoden im Toarcien Süddeutschlands. *Facies*, 8, 213–262.
- Mazurek, M., Hurford, A. J., & Leu, W. (2006). Unravelling the multi-stage burial history of the Swiss Molasse Basin: integration of apatite fission track, vitrinite reflectance and biomarker isomerization analysis. *Basin Research*, 18, 27–50.
- Nagra. (1992). Sondierbohrung Schafisheim Untersuchungsbericht (Gemeinde Schafisheim, Kanton Aargau, Schweiz), Nagra Technischer Bericht, NTB 88-11. In Swiss Geotechnical Commission (Ed.), *Beiträge zur Geologie der Schweiz, Geotechnische Serie, Lieferung 84* (pp. 1–183). www.swisstopo.ch.
- Nussbaum, C., Bossart, P., Amann, F., & Aubourg, C. (2011). Analysis of tectonic structures and excavation induced fractures in the Opalinus Clay, Mont Terri underground rock laboratory (Switzerland). *Swiss Journal of Geosciences*, 104, 187–210.
- Ohmert, W. (1988). The Ovalis Zone (Lower Bajocian) in the Type Area, Southwestern Germany. In *2nd international symposium on Jurassic stratigraphy* (pp. 255–268). Lisboa.
- Ohmert, W. (1996). Mikrofossilien. In: Geologisches Landesamt Baden-Württemberg (Ed.), *Die Grenzziehung Unter-/Mitteljura (Toarcium/Aalenium) bei Wittnau und Fuentelsaz – Beispiele interdisziplinärer geowissenschaftlicher Zusammenarbeit* (pp. 36–42). Freiburg i.Br.: Informationen Geologisches Landesamt Baden-Württemberg, 8.
- Ohmert, W., & Rolf, C. (1994). The Aalenian boundary at Wittnau (Oberrhein area, south-west Germany). *Miscellanea del Servizio Geologico Nazionale*, 5, 33–62.
- Plumhoff, F. (1963). Die Ostracoden des Oberaalenum und tiefen Unterbajocium (Jura) des Gifhorner Troges, Nordwestdeutschland. *Abhandlungen der Senckenbergischen Naturforschenden Gesellschaft*, 503, 1–100.
- Reisdorf, A. (2001). Neue Lias-Profile entlang der Transitgasleitung der TRG 3: Wirbligen (BL) und Titterten (BL). *Archäologie und Museum, Berichte aus Archäologie und Kantonsmuseum Basel-land*, 43, 43–48.
- Reisdorf, A. G., Maisch, M. W., & Wetzel, A. (2011a). First record of the leptonectid ichthyosaur *Eurhinosaurus longirostris* from the Early Jurassic of Switzerland and its stratigraphic framework. *Swiss Journal of Geosciences*, 104, 211–224.
- Reisdorf, A. G., Wetzel, A., Schlatter, R., & Jordan, P. (2011b). The Staffelegg formation: a new stratigraphic scheme for the Early Jurassic of northern Switzerland. *Swiss Journal of Geosciences*, 104, 97–146.
- Reisdorf, A. G., Hostettler, B., Waltschew, A., Jaeggi, D., & Menkveld-Gfeller, U. (2013). Chrono- and Biostratigraphy of the Opalinus Clay of the Mont Terri Rock Laboratory, Canton Jura, Switzerland. *Abstract Volume, 11th Swiss Geosciences Meeting*, Lausanne, p. 161.
- Reisdorf, A. G., Hostettler, B., Waltschew, A., Jaeggi, D., & Menkveld-Gfeller, U. (2014). *SO (Sedimentology of the Opalinus Clay), Biostratigraphy of the Basal Part of the Opalinus-Ton at the Mont Terri rock laboratory, Switzerland*. Mont Terri technical report, TR 14-07. Federal Office of Topography (swisstopo), Wabern, Switzerland. www.mont-terri.ch.
- Reisdorf, A. G., Hostettler, B., Jaeggi, D., Deplazes, G., Bläsi, H.-R., Morard, A., et al. (2016). *SO (Sedimentology of the Opalinus Clay) Experiment: Litho- and biostratigraphy of the 250 m deep Mont Terri BDB-1 borehole through the Opalinus Clay and bounding formations, St. Ursanne, Switzerland*. Mont Terri technical report, TR 16-02, Federal Office of Topography (swisstopo), Wabern, Switzerland. www.mont-terri.ch.
- Schaeren, G., & Norbert, J. (1989). Tunnels du Mont Terri et du Mont Russelin—La traversée des « roches à risques » : marnes et marnes à anhydrite. In *Juradurchquerungen - aktuelle Tunnelprojekte im Jura. Mitteilungen der Schweizerischen Gesellschaft für Boden- und Felsmechanik*, 119, 19–24.
- Schmidt, C., Braun, L., Paltzer, G., Mühlberg, M., Christ, P., & Jacob, F. (1924). Die Bohrungen von Buix bei Pruntrut, und Allschwil bei Basel. *Beiträge zur Geologie der Schweiz, Geotechnische Serie, 10*, 74 pp. Zurich: Aschmann & Scheller.
- Wetzel, A., & Allia, V. (2003). Der Opalinuston in der Nordschweiz: Lithologie und Ablagerungsgeschichte. *Eclogae Geologicae Helveticae*, 96, 451–469.
- Yu, C., Matray, J.-M., Gonçalves, J., Jaeggi, D., Gräsele, W., Wiczorek, K., et al. (2017). Comparative study of methods to estimate hydraulic parameters in the hydraulically undisturbed Opalinus Clay, Mont Terri rock laboratory (Switzerland). *Swiss Journal of Geosciences*, 110. doi:10.1007/s00015-016-0257-9 (this issue).

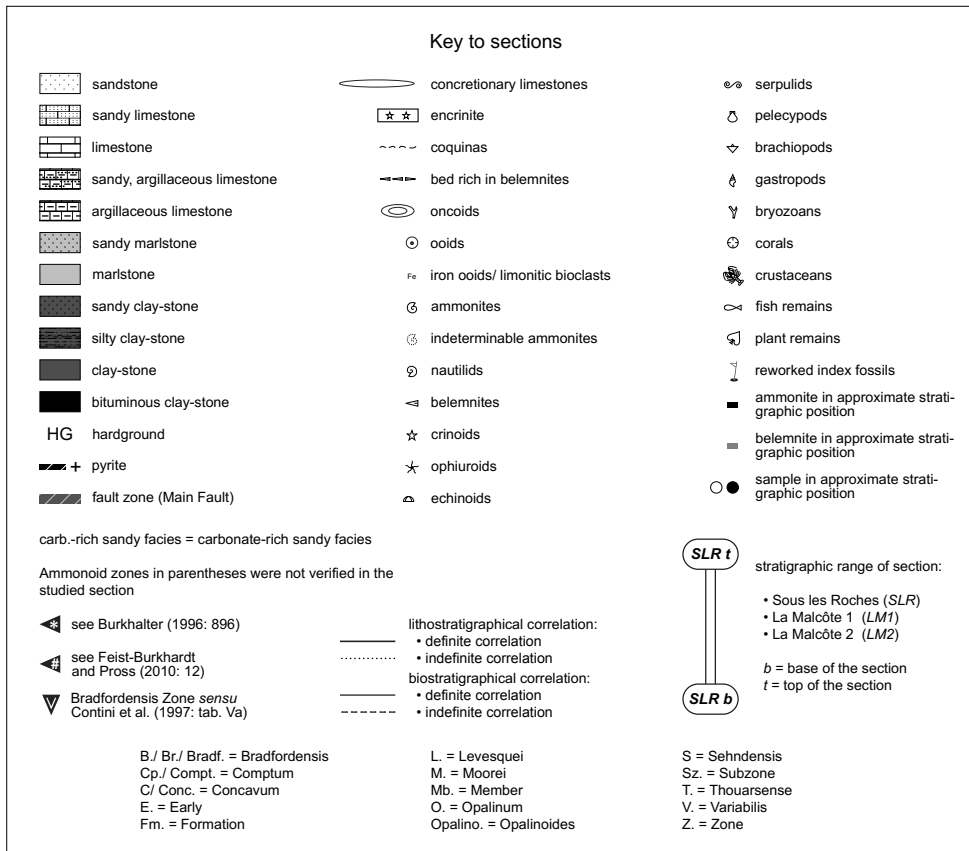


Fig. 2 Detailed section of the Early and Middle Jurassic strata of the Mont Terri BDB-1 core. Plotted next to the section are the position of macrofossil finds, selected palynological events in the section used for palynostratigraphical age dating, and the biostratigraphic interpretation and age assignment of samples to ammonite zones/subzones based on palynomorphs, and ostracods and foraminifers respectively. A high-resolution version of this figure is published as Electronic Supplementary Material with the online version of this paper. In the printed version, Fig. 2 is included as an A3-size foldout.

Tectonic evolution around the Mont Terri rock laboratory, northwestern Swiss Jura: constraints from kinematic forward modelling

Christophe Nussbaum¹ · Armelle Kloppenburg² · Typhaine Caër³ · Paul Bossart¹

Received: 10 April 2016 / Accepted: 9 December 2016 / Published online: 28 January 2017
© The Author(s) 2017. This article is published with open access at Springerlink.com

Abstract We propose a geometrically, kinematically, and mechanically viable thin-skinned kinematic forward model for a cross section intersecting the Mont Terri rock laboratory in the frontal-most part of the Jura fold-and-thrust belt, Switzerland. In addition to the available tunnel, borehole, and surface data, initial boundary conditions are crucial constraints for the forward modelling scenarios, especially the inherited topography of the basement and any pre-compressional offset within the Mesozoic sediments. Our kinematic analysis suggests an early-stage formation of the Mont Terri anticline located above ENE-trending, Late Paleozoic extensional faults, followed by back-stepping of the deformation developing the Clos du Doubs and Caquerelle anticlines further south. In this model, the thrust sequence was dictated by the inherited basement faults, which acted as nuclei for the ramps, detached along the basal décollement within the Triassic evaporites. The mechanical viability of both the thrust angles and thrust sequence was demonstrated by applying the limit analysis theory. Despite numerous subsurface geological data, extrapolation of structures to depth remains largely

under-constrained. We have tested an alternative model for the same cross section, involving an upper detachment at the top of the Staffelegg Formation that leads to duplication of the sub-Opalinus Clay formations, prior to detachment and thrusting on the Triassic evaporites. This model is geometrically and kinematically viable, but raises mechanical questions. A total displacement of 2.9 and 14.2 km are inferred for the classical and the alternative scenarios, respectively. In the latter, forward modelling implies that material was transported 10.8 km along the upper detachment. It is not yet clear where this shortening might have been accommodated. Despite the differences in structural style, both models show that pre-existing basement structures might have interfered in time and space. Both styles may have played a role, with lateral variation dictated by basement inherited structures.

Keywords Jura mountains · Structural geology · Multiple detachments · Forward modelling · Inherited basement faults · Mechanical analysis

Editorial handling: P. Bossart and A. G. Milnes.

This is paper #2 of the Mont Terri Special Issue of the Swiss Journal of Geosciences (see Bossart et al. 2017, Table 3 and Fig. 7).

✉ Christophe Nussbaum
christophe.nussbaum@swisstopo.ch

¹ Swiss Geological Survey, Federal Office of Topography
Swisstopo, Seftigenstrasse 264, 3084 Wabern, Switzerland

² 4DGeo/Structural Geology, Daal en Bergselaan 80,
2565 AH The Hague, The Netherlands

³ Géosciences et Environnement Cergy (GEC), Université de
Cergy-Pontoise, rue Descartes, 95031 Cergy-Pontoise Cedex,
France

1 Introduction

This study addresses the tectonic evolution of the region around the Mont Terri underground rock laboratory where experiments are dedicated to investigating the hydrogeological, geochemical, and rock mechanical properties of a pristine undisturbed claystone, the Opalinus Clay of Toarcian-Aalenian age (Bossart and Thury 2008; Bossart et al. 2017). The generic Mont Terri underground rock laboratory offers a scientific and technical platform for international collaboration in the field of geological disposal providing a unique opportunity to study the performance of a repository. The Mont Terri rock laboratory is located in the northern part of the Jura fold-and-thrust belt at the southern tip of the Upper Rhine Graben (Nussbaum et al. 2011).

The arcuate Jura mountain range is considered as a type example of a thin-skinned fold-and-thrust belt that propagates into the northern foreland of the Alpine orogeny along a basal décollement horizon formed by the mechanically weak Middle and Upper Triassic stratigraphic units (Buxtorf 1907; Laubscher 1961; Burkhard 1990; Guellec et al. 1990; Jordan 1992; Philippe 1995; Sommaruga and Burkhard 1997; Becker 2000). Thin-skinned deformation along this basal detachment is considered to have started not earlier than the Serravallian (Middle Miocene) and to have ceased in the Early Pliocene (e.g. Laubscher 1992; Becker 2000). Many authors postulate a late transition (post-early Pliocene) to thick-skinned tectonics (e.g. Mosar 1999; Ustaszewski and Schmid 2007; Madritsch et al. 2008) based on field observation and interpretation of seismic reflection data. Already in 1990, Guellec et al. proposed a transition from thin-skinned to thick-skinned deformation involving basement thrusts beneath the Internal Jura at Champfromier (south to Oyonnax) to explain a basement high interpreted on a seismic profile. The Jura has often been considered a foreland fold-and-thrust belt propagating from south to north. Nevertheless, this classical view is a matter of debate and certain authors, such as Cederboom et al. (2011), convincingly showed that the subalpine Molasse has been active after 5 Ma demonstrating “out-of-sequence” thrust chronology. By analogue modelling, Smit et al. (2003) suggested that the order of thrusts depends on many factors such as basal wedge angle, shortening rate, and coupling between basement and cover.

Over the last four decades, foreland fold-and-thrust belts have been modelled as critically tapered wedges (Chapple 1978; Boyer and Elliot 1982). The geometry of a critical wedge is defined by its surface slope and the dip of the basal décollement. Both depend on basal friction and material of the wedge, its density, and shear strength (Chapple 1978; Davis et al. 1983; Dahlen 1990). As a consequence, tectonic evolution and kinematics of thin-skinned fold-and-thrust belts are strongly controlled by the thickness of the sedimentary cover overlying the basal décollement, eventually modified by syn-tectonic erosion or sedimentation as well as aspects influencing the basal friction of the décollement, such as fluid pressure and fracture strength (Sommaruga and Burkhard 1997; Hindle 2008; von Hagke et al. 2014). In addition to these principal controlling mechanisms, localisation and development of contractional structures in thin-skinned foreland fold-and-thrust belts is known to be commonly influenced by pre-existing structures (i.e. Butler et al. 2006; Giambiagi et al. 2003). Deformation events predating thrust-belt initiation affect the geometry of the basal décollement horizon, potentially even offsetting it, and lead to the formation of fractures and faults that can act as pre-existing zones of

mechanical weakness during thrust-belt formation (Laubscher 1985, 1987; Homberg et al. 2002; Ustaszewski and Schmid 2007; Madritsch et al. 2008).

In 2003, Freivogel and Huggenberger proposed an initial interpretation of the deep structures beneath the Mont Terri rock laboratory based on a balanced cross section of the Mont Terri anticline along the Mont Terri motorway tunnel. They interpreted the Mont Terri anticline as a NNW-vergent imbricate fault-bend fold, with a total shortening estimated by area balancing to be approximately 2.1 km. Later, Caër et al. (2015) proposed two alternative 2D kinematic models for the same structure, interpreting it as the result of various combinations of fault-bend folding, fault-propagation folding, and detachment folding. Their interpretation is significantly different, since they considered inherited basement normal faults to play an active role during folding (thick-skinned deformation). They estimated a total shortening of 1.2–1.3 km for the Mont Terri anticline. They validated the mechanical viability of the sections by a mechanical approach using limit analysis theory described below in Sect. 6.1.

Here, we present new insights into the tectonic evolution of the region around the Mont Terri rock laboratory based on a combined analysis of geological maps, available data collected during the excavation of the Mont Terri and Mont Russelin tunnels, drilling of the reconnaissance boreholes, cross section area balancing techniques, and kinematic forward modelling. Whereas the rock laboratory and the tunnels provide a unique access to fresh and continuous outcrops, the underlying structure remains under-constrained. There are few seismic profiles available for the study region but their resolution, especially at the base of Mesozoic sequence, is insufficient for any interpretation of deep structures. Therefore, sequential restoration of cross sections is not possible, and any kinematic modelling must be concept-driven, starting from the available geological constraints. We propose here a kinematic forward model using the available data augmented by limiting constraints at depth. The aim of the kinematic modelling is to understand the dominant structural style, the sequence of thrusts and the kinematic relationships of the structural elements that are exposed and have been mapped around the Mont Terri rock laboratory.

2 Regional geological setting

2.1 Inherited Palaeozoic and Paleogene basement structures

The study region near the Mont Terri rock laboratory is characterized by a complex tectonic setting resulting from the junction of the northernmost part of the Folded Jura

with the southern end of the Upper Rhine Graben (URG) (top right inset in Fig. 1). At least two major inherited basement structures have affected the thin-skinned deformation of the Jura fold-and-thrust belt emplaced during Late Miocene-Early Pliocene times. The first inherited basement structure is related to Late Palaeozoic ENE-to NE-oriented basement faults from the Variscan orogeny and subsequent (Late Carboniferous to Permian) post-orogenic extension (Laubscher 1985; Ziegler 1992; Schumacher 2002). The second inheritance mainly re-used the Late Paleozoic basement structures and is associated with the Paleogene intra-continental rifting phase leading to the opening of the Upper Rhine Graben that evolved to the south along a major continental transfer zone, called the Rhine-Bresse Transfer Zone (RBTZ, Fig. 1a). This latter is localised by the Late Palaeozoic ENE-striking inherited basement faults. The RBTZ linked the simultaneous opening of the Upper Rhine Graben in the NE and Bresse Graben in the SW by sinistral transtensive reactivation of ENE-oriented basement faults of the pre-existing Permo-Carboniferous trough system (Laubscher 1972, 1973; Bergerat and Chorowicz 1981; Illies 1981; Ziegler 1992; Lacombe et al. 1993). Rifting in the southern Upper Rhine Graben began in the Upper Priabonian and persisted until Late Oligocene to Early Miocene under regional WNW-ESE extension, roughly perpendicular to the graben axis (Pflug 1982). This led to the formation of NNE-trending growth faults delimiting half grabens (e.g. Ferrette half-graben) and numerous associated extensional faults paralleling the southern Upper Rhine Graben. The trend of this set of faults is commonly termed “Rhenish” in the literature. Simultaneously, ENE-trending extensional flexures evolved in the sedimentary cover above reactivated basement faults; this trend is referred to as “Permo-Carboniferous” (Ustaszewski et al. 2005; Ustaszewski and Schmid 2006).

2.2 Overprint of the Late Miocene-Early Pliocene thin-skinned deformation

In the study area, the Folded Jura front is characterised by a significant change of orientation (Fig. 1). From the west to east, it follows an E-W, then an ENE-orientation, and then rotates into a NNE-trending fault zone connecting up the Ferrette fault further north.

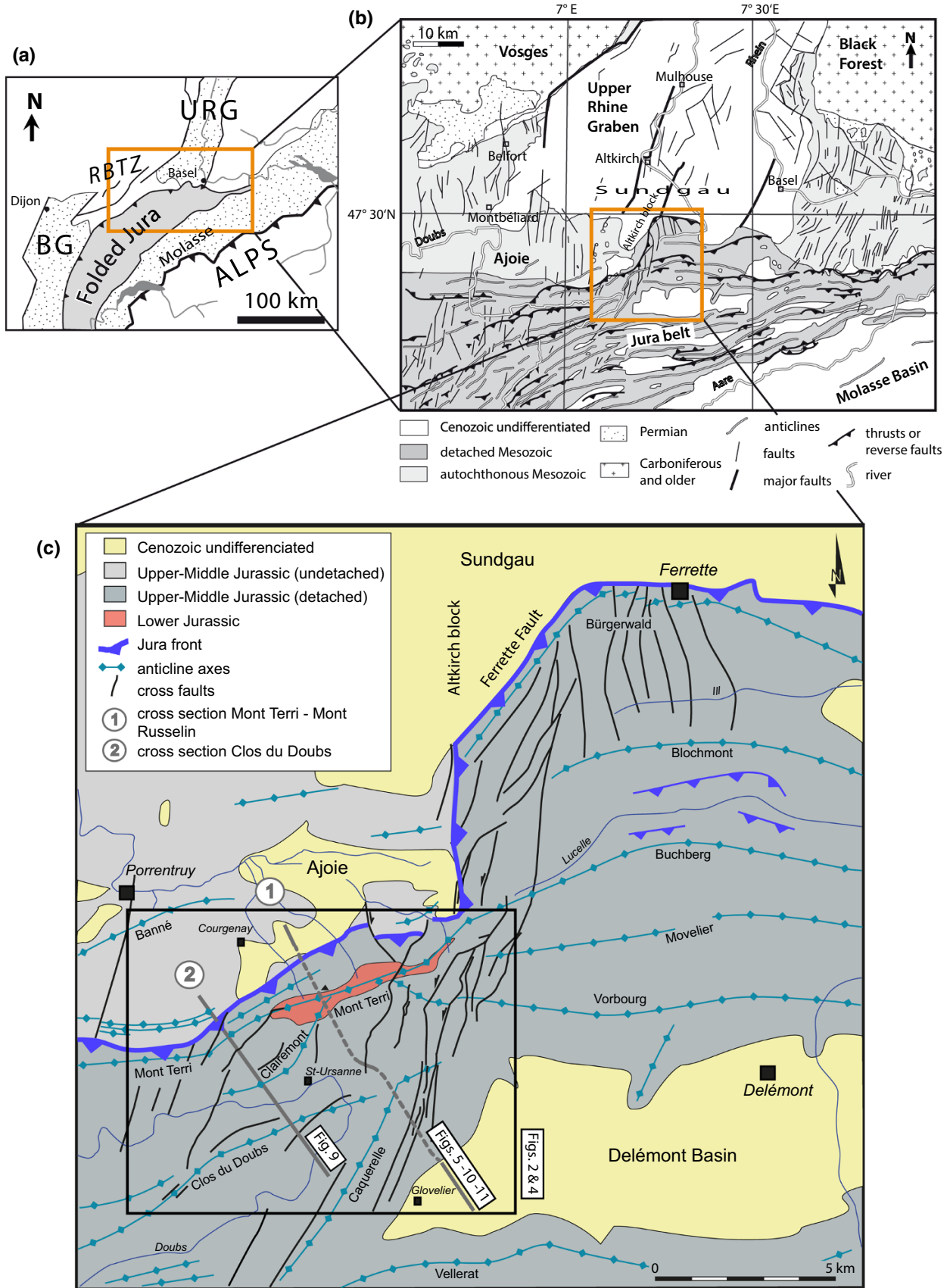
Furthermore, the study region is characterised by the NNE-orientated Caquerelle anticline that closes the Delémont Basin westwards (Figs. 1, 2, 3). This unexpected orientation suggests the presence of inherited basement normal faults at depth as suspected by Laubscher (1963a, b). This fault system is considered to dip to the east. The focal mechanism of the M_L 3.7 earthquake that occurred on December 11th 1987 in Glovelier (47.313N,

7.161E) at a depth of 9 km indicates a left-lateral strike-slip fault on a steeply E-dipping fault plane (Deichmann 1990). This fault presents the same orientation as the Ferrette fault located further north. The Ferrette Fault dips to the west and forms the eastern boundary of the Eo-Oligocene Ferrette half-graben. Based on seismic profiles interpreted by Ustaszewski et al. (2005), throw on this faults varies along strike, ranging from ca. 500 m in its central part and decreasing to 170 m in the south, suggesting a termination of the Ferrette Fault in the north-eastern part of the Mont Terri region. Therefore, we consider that the Ferrette fault evolved to the south into a diffuse transfer zone characterised by the superposition of “Rhenish” NNE-trending faults and reactivated ENE-striking Permo-Carboniferous faults.

2.3 Litho- and mechanical stratigraphy

In order to construct cross sections that define the end state of the forward models presented in Sect. 5, a locally valid stratigraphic column that included the thickness of the Mesozoic units was set up using the stratigraphic subdivisions and formation names according to the nomenclature defined by the Lithostratigraphic Lexicon of Switzerland (www.strati.ch). In all figures of this paper, the formations are illustrated by the official colours as defined by the Lithostratigraphic Lexicon. The formation thicknesses in the region of St-Ursanne were adapted after Laubscher (1963a, b) and complemented by the recent borehole BDB-1 for the thicknesses of the Opalinus Clay and Passwang Formation (Hostettler et al. 2017).

Above the basement evidencing some Late Paleozoic clastic sediment, several hundred meters of Triassic limestone, dolomites, marls, and evaporites follow, mark a depositional change from marine to continental environments. The dolomitic marls, dolomites, and evaporites of the Klettgau Formation belonging to the Keuper are the oldest rocks that crop out in the region of St-Ursanne (Fig. 2). During the Early Jurassic, a fully marine environment with successively increasing water depth developed, leading to the formation of calcareous, marly, and argillaceous rocks denoted as the Staffelegg Formation (Reisdorf et al. 2011). Together with rocks of the Keuper, these rocks form the core of the Mont Terri anticline. They are visible at the surface and were mapped in the Mont Terri area by several authors (Laubscher 1963a, b; Freivogel and Huggenberger 2003). The Staffelegg Formation, which reaches a thickness of up to 70 m, is followed by the 130 m thick Opalinus Clay, a monotonous succession of dark argillaceous rocks with some sandy or carbonate-rich facies variations (e.g. Schaeren and Norbert 1989; Bläsi et al. 1991; Wetzel and Allia 2003; Bossart and Thury 2008). Since the beginning of 2014, a continuous



◀ **Fig. 1** **a** Tectonic map with the main units of the northern Alpine region. *BG* Bresse Graben, *RBTZ* Rhine–Bresse Graben transfer zone, *URG* Upper Rhine Graben. **b** Large scale tectonic map of the junction between the Jura belt and the Upper Rhine graben. **c** Overview tectonic map of northwestern Folded Jura (modified after Laubscher 1963a, b), with the location of the Mont Terri–Mont Russelin section indicated

geological profile of the Opalinus Clay from the Mont Terri rock laboratory is available from the 250 m deep inclined borehole BDB-1 (Fig. 5). Three main lithofacies types were encountered. From bottom to top, the borehole drilled through 33 m of a shaly facies of Toarcian age with large amounts of bioclastic material followed by 15 m of a shaly facies with many ammonites. The transition to this upper part marks the Toarcian/Aalenian boundary, which was thoroughly biostratigraphically investigated in Hostettler et al. (2017). Further upwards, the borehole encountered 6 m of sandy carbonate-rich facies with several distinct bioclastic limestone beds. At the bottom of this facies, two conspicuous pyrite horizons are present. The carbonate-rich sandy facies is followed by 14 m of sandy facies with a large amount of bioclastic lenses, 35 m of monotonous shaly facies, and an upper sandy facies with marly, sometimes sideritic and sandy nodules. The top of the Opalinus Clay consists of a calcareous hardground with reworked limonitic intraclasts. The next lithostratigraphic unit, the Passwang Formation, is composed of a series of parasequences reflecting a shallow, mixed siliciclastic, and carbonate depositional environment (Burkhalter 1996) with a total thickness of about 70 m. The upper part of the drillhole comprises the Hauptrogenstein, consisting of shallow-water oolitic carbonates with some distinct coral horizons. Gonzalez and Wetzel (1996) described three shallowing-upward successions. These generally start with fine-grained marly beds and end with a maximum flooding surface or a hardground on top of oolitic or sparry bioclastic limestone. The Hauptrogenstein exhibits a total thickness of about 125 m and crops out in the northern overturned limb of the Mont Terri anticline just north of the drilling site. The end of the Middle Jurassic is characterized by shallow-water deposits and iron-oolitic beds of the Ifenthal Formation (Bitterli 2012). The thickness of these deposits is estimated at 55 m in the region of the Mont Terri. It is overlain by deeper-water clays (Gygi 1969) and nodular marls of the Bärschwil Formation, which mark the beginning of the Late Jurassic (Oxfordian). The overlying coral horizons and oolitic limestone with oncoids and patch reefs are remnants of a prograding reefal belt that extended over large areas. Well-bedded platy limestone and oncolitic beds of the Vellerat Formation indicate shallow-water conditions exhibiting a continental influence. Later, a shallow, fully marine carbonate platform evolved and led

to the 30 m-thick succession of micritic limestone of the Courgenay Formation. A total thickness of about 250 m can be attributed to the Oxfordian. During the Kimmeridgian, the platform intermittently emerged and water depth varied between 0 and 100 m. Numerous traces of dinosaurs have been found in the micritic and oolitic limestone of the Reuchenette Formation (Marty 2008; Comment et al. 2011).

We identify four levels of relative mechanical weakness that could form potential detachment levels (Fig. 3). The main and basal detachment level occurs within the Middle Triassic evaporites of the Zeglingen Formation. For the forward modelling, we defined the basal detachment as one discrete plane located in the middle of this formation. We realise that this may be an oversimplification and that the detachment may have finite width. A second, less important but still regionally significant detachment, is formed by the bituminous Posidonia shales at the top of the Staffelegg Formation. Drillcore analysis of the BDB-1 borehole (location shown in Fig. 6) revealed a 10 m-thick deformation zone within the Rietheim Member that together with the Gross Wold Member comprises the top of the Staffelegg Formation. We used this horizon as an upper detachment in the forward modelling presented in Sect. 5. In fact, we found no structural evidences in the drillcores and in the galleries for a detachment directly within the Opalinus Clay Formation. Two other minor detachment levels are the relatively weak shales of the Bärschwil Formation and those at the base of the Vellerat Formation. These latter were not used in the modelling for the sake of simplicity. This decision is justified at the regional scale. A model integrating all minor detachments is beyond the scope of this contribution.

3 Observations and existing data

3.1 Constraints from the geological map

The geological map of St-Ursanne (Laubscher 1963a, b) provides an important data source (Fig. 2). Based on the geological map, we present a tectonic map of the same region (Fig. 4). In order to better understand the relationships between the faults and the relief, we have drawn the faults over a hillshade model that illustrates the terrain topography (digital terrain model from Swisstopo 2011). It shows the main structural elements and includes a series of typically ENE-trending anticlinal axial traces mapped mostly as related to thrusts (as hangingwall anticlines), and a set of (N)NE-trending cross faults mostly with sinistral strike-slip component but some with normal displacement. Note the interplay between ENE and NNE-trending anticlinal axes, thrusts, and cross faults, and the

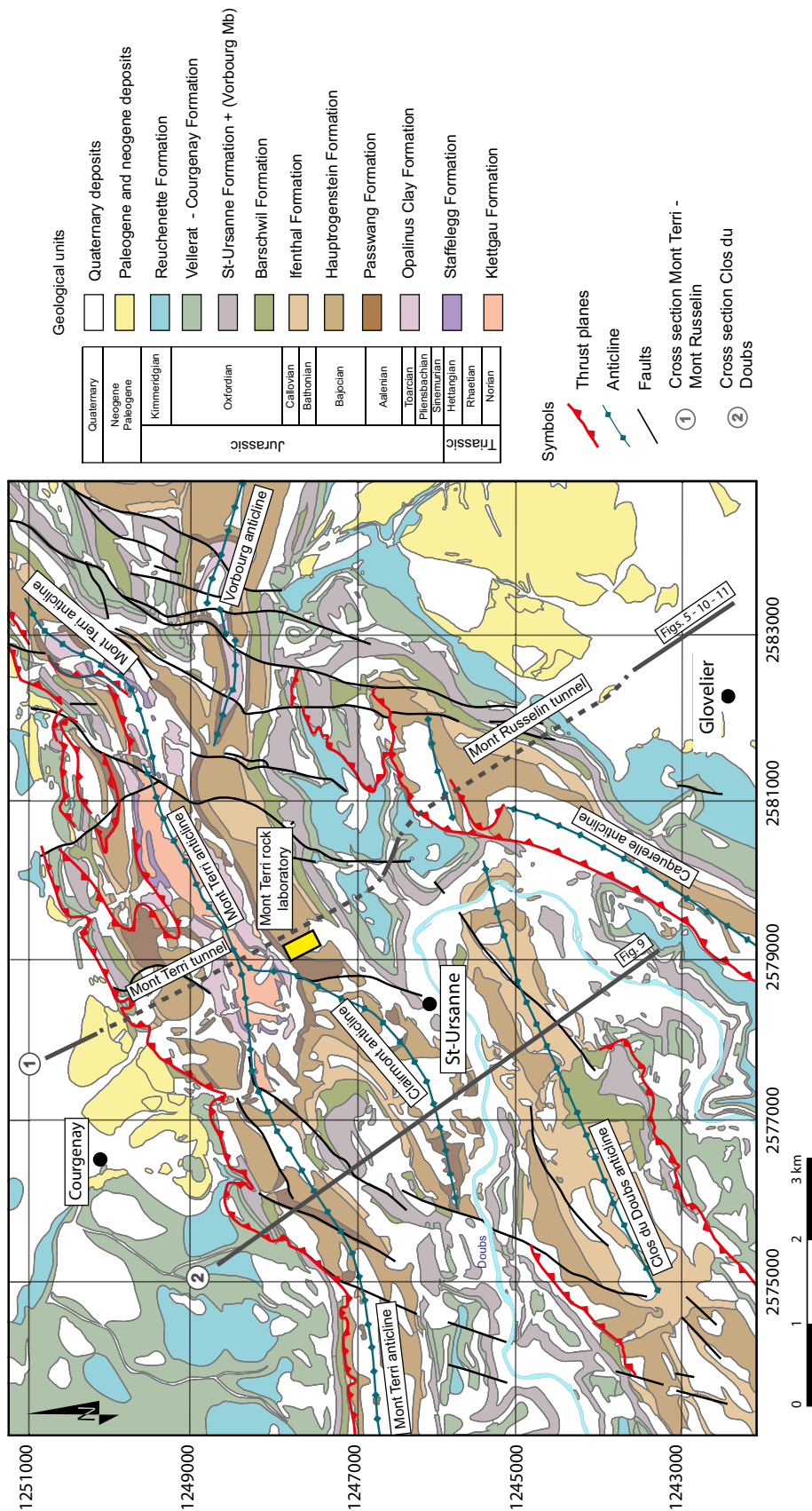


Fig. 2 Geological map of the St-Ursanne area, modified from GeoCover (Swisstopo 2012) and the Geological Atlas 1:25,000 (Laubscher 1963a, b). The formations are illustrated by the official colors as defined by the Lithostratigraphic Lexicon of Switzerland (www.strati.ch). The Paleogene and Neogene deposits encompass the following formations: Conglomerates of Porrentruy, Terres jaunes, Meeresand, Septarionton, Alsace Molasse, Upper Marine Molasse (marnes rouges & Gompfolites), Upper Freshwater Molasse (Formation du Bois de Raube, Vogesenschotter). Note the oldest exposed geological unit belongs to the Klettgau formation (Keuper) in the core of the Mont Terri anticline

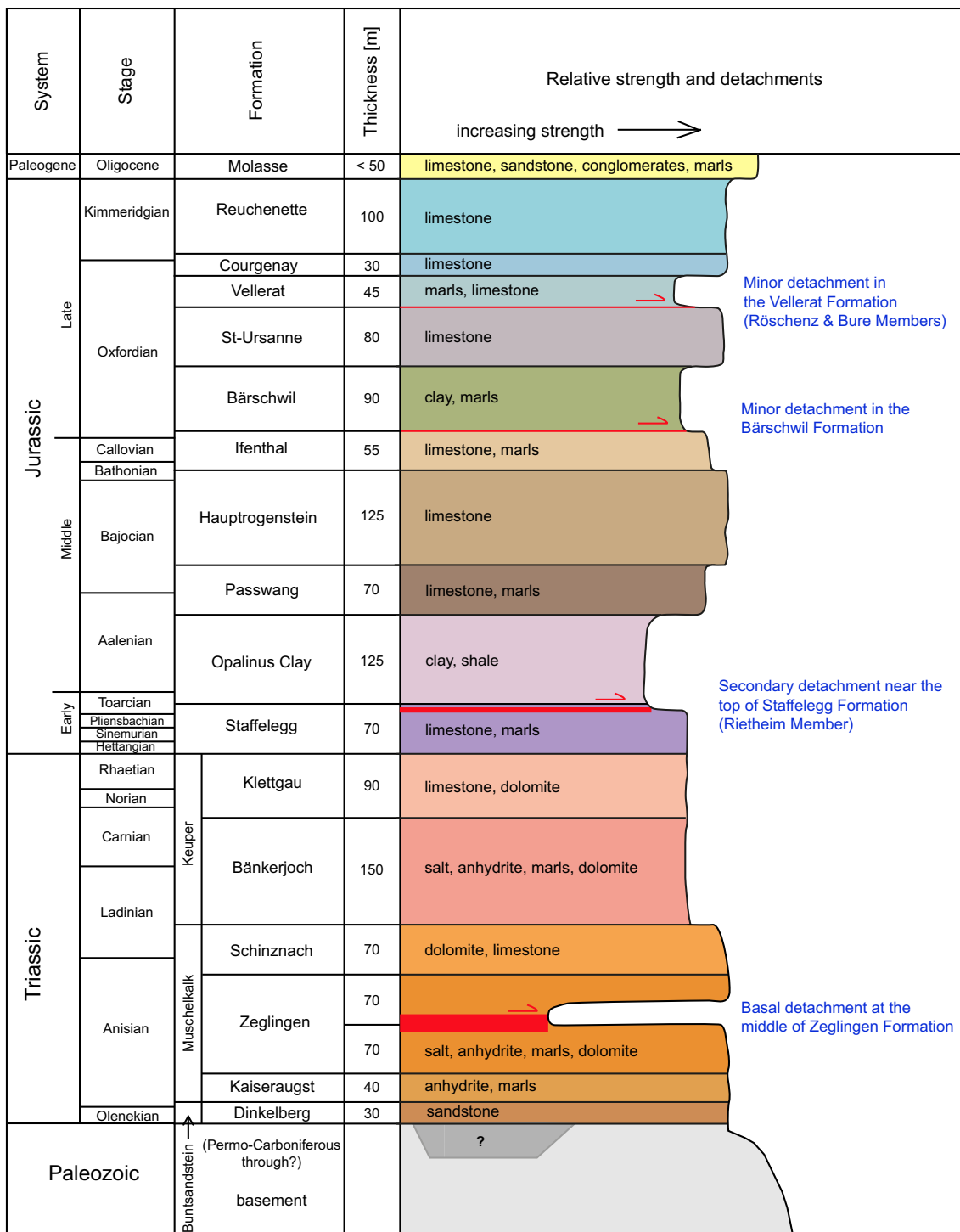


Fig. 3 Compiled stratigraphy of the Mesozoic cover and relative strength and detachments. Thickness of units adapted from Laubscher (1963a, b) and from the Lithostratigraphic Lexicon of Switzerland (www.strati.ch)

intersection with both cross sections presented in Figs. 9, 10, and 11. The anticlines appear to be offset by the NNE-trending thrusts, with complexity added by the Caquerelle anticline that is parallel to the NNE-trending thrust in front.

Most of the NNE-trending cross faults cutting through the anticlines present abrupt variations of the anticlinal traces (Fig. 4, location A). We interpret these faults to have acted as lateral ramps in a sinistrally transpressive mode during the Jura thin-skinned deformation phase. Some of

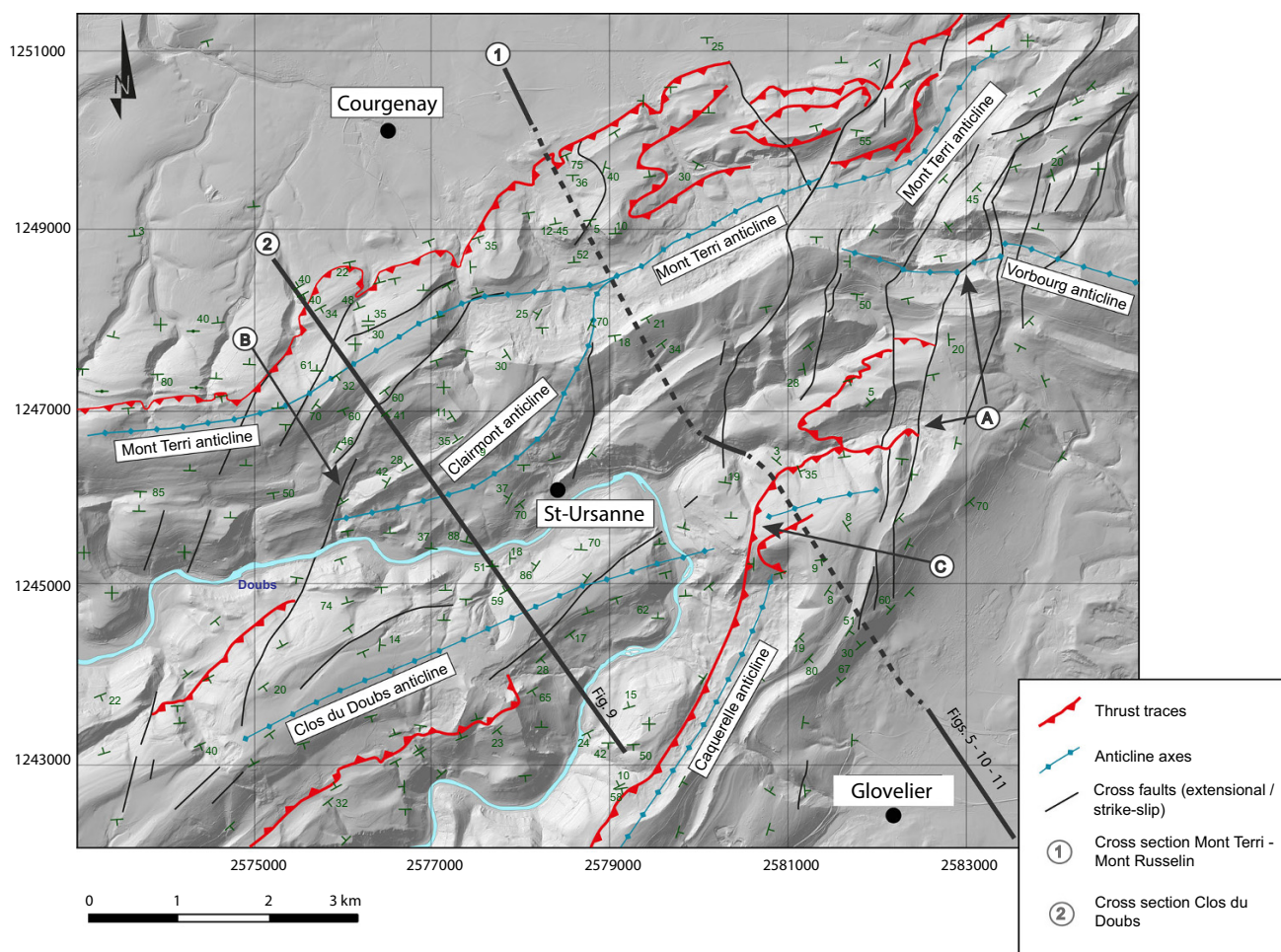


Fig. 4 Tectonic map of the St-Ursanne area, modified from Laubscher (1963a, b). Dip data are taken from Swisstopo (2012). The map overlies a hillshade model that illustrates the topography of the terrain (digital terrain model from Swisstopo 2011). Note the interplay between ENE and NNE-trending anticlinal axes, thrusts, and cross faults, and the intersection with both cross sections. A NNE-trending

faults typically cut across and sinistrally offset anticlinal traces, B NNE-trending faults typically cut across and sinistrally offset anticlinal traces and C The La Caquerelle thrust and anticline offsetting the Clos du Doubs anticline and interfering to form the Mont Russelin culmination

the NNE-trending faults have normal components of displacement (Fig. 4, location B). The nature of NNE-trending extensional faults is a subject of discussion, and is addressed in the forward modelling. One of the NNE-trending faults is the Caquerelle thrust. We interpret this thrust to have formed last, cutting obliquely across the ENE-trending folds and thrusts to form the Mont Russelin culmination (Fig. 4, location C). The Mont Russelin culmination is interpreted to be the result of the superposition of two anticlines (ENE-trending Clos du Doubs plunging eastwards beneath the NNE-trending Caquerelle). The NNE-orientation of the Caquerelle anticline, which is unusual in the northern part of the Jura belt, supports formation in situ above an inherited Rhenish basement-rooted fault. In the case of a forward-propagating sequence of the thrust front, this anticline would have been transported further north and the inherited fault that had served as

nuclei should be found further to the south, which is not observed on the geological map.

Triassic sediments form the core of the Mont Terri anticline. This is of particular interest because outcrop of Triassic sediments is not common along the trend. This exposure, even if not unique in the Jura belt, may indicate that local structural complexities occurred at depth, which locally uplifted the oldest sediments of the detached Mesozoic to the surface.

3.2 Constraints from tunnel mapping and drillcore observations

In Fig. 5, we present a compilation of all available data from the Mont Terri and Mont Russelin tunnels along a cross section that will serve as a basis for the forward models described in Sect. 5. The data consist of geological

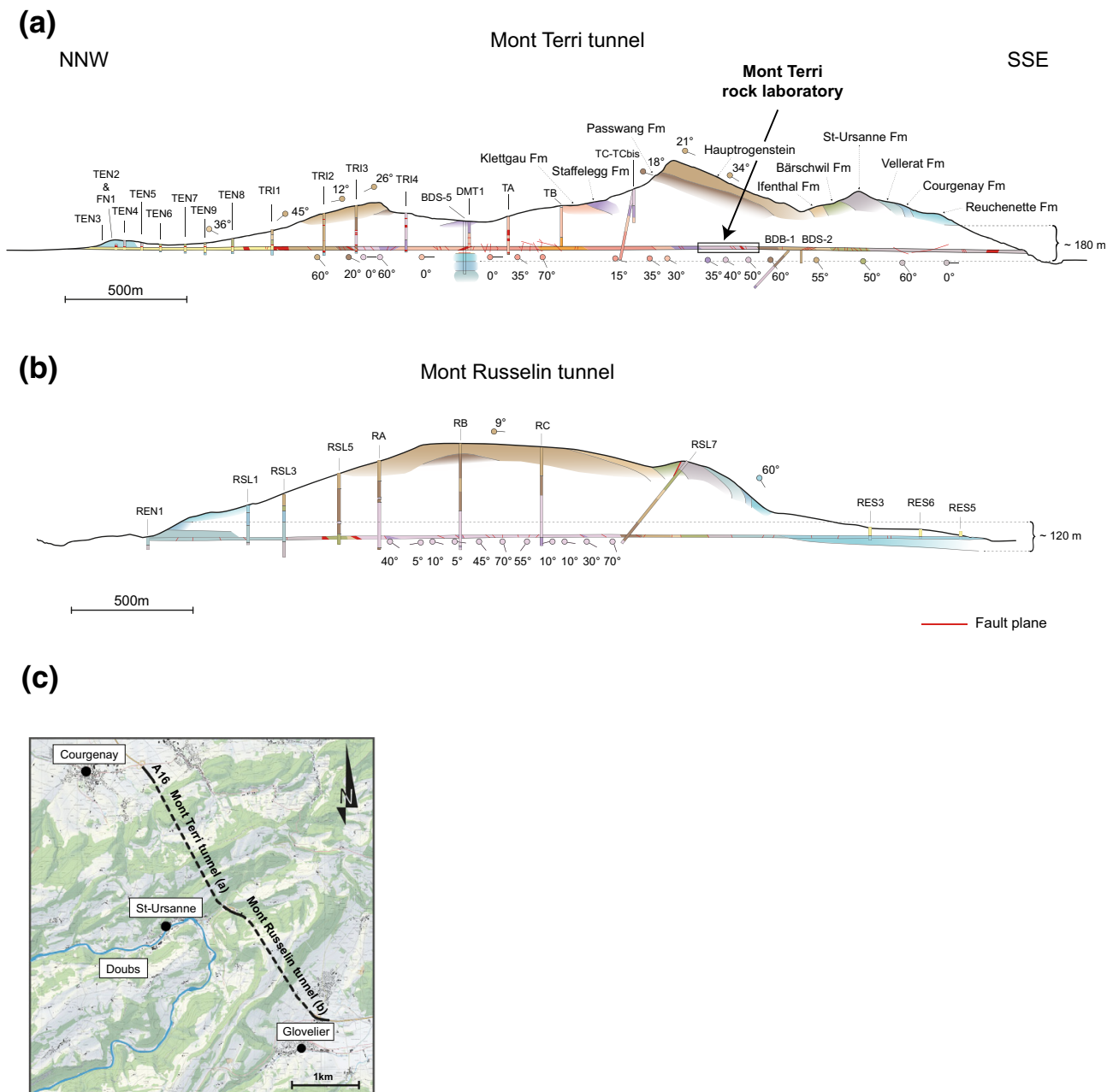


Fig. 5 Sub-surface cross section along the Mont Terri tunnel (a) and Mont Russelin tunnel (b). Compilation of field data acquired during the excavation of both tunnels and from the drillcore mapping of reconnaissance boreholes by Bureau Technique Jean Norbert

Geologues SA (1992), Bureau Technique Norbert Geologues-Conseils SA (1993), respectively. Surface data are taken from GeoCover (Swisstopo 2012). Site map of both tunnel from swisstopo (c). Mapped underground fractures in red

documentation of reconnaissance boreholes drilled and cored for the construction of the Mont Terri and Mont Russelin tunnels, geological mapping from excavation of both tunnels (Bureau Technique Jean Norbert Géologues SA 1992; Bureau Technique Norbert Géologues-Conseils SA 1993), and surface data from the geological map shown in Fig. 2. We have also integrated key boreholes (i.e. BDS-5, BDB-1 and BDS-2) drilled in the framework of the Mont Terri research programme (i.e. Jaeggi and Bossart 2016;

Hostettler et al. 2017). Stratigraphic and structural constraints, with dips and dip azimuths of bedding and structures, were taken from the tectonic map (Fig. 4) and projected onto Fig. 5.

The main structural observations constraining the forward modelling include (also refer to Sect. 5):

- The structural level of the stratigraphic sequence in the hangingwall syncline between the Mont Terri and Caquerelle anticlines, taken to indicate a relative uplift

of stratigraphy of ca. 180 m compared to the footwall and the presumed regional and reference level to the north in the Ajoie plain. Any forward model will need to explain this locally elevated level.

- The conspicuous subhorizontal fault, the shallow-dipping Mont Terri thrust, that surfaces near the northern entrance of the Mont Terri tunnel and that separates the strongly folded hangingwall from the flat-lying and largely undeformed footwall;
- The strongly folded and locally overturned nature of the hangingwall of the Mont Terri anticline.
- The backlimb of the Mont Terri anticline that presents a mean dip of 30° to the SSE. However, in the vicinity of NNE-trending cross faults, the strata are steepened and plunge with larger dips (50° – 60°). For the forward modelling, we applied the mean dip and for the present ignored the local perturbations, because they are likely to result from a different set of structures.
- The structural level of the stratigraphic sequence in the hangingwall syncline between the Mont Terri and Caquerelle anticlines is taken to indicate relative uplift of stratigraphy of ca. 120 m compared to the hangingwall and presumed regional and reference level to the south in the Delémont Basin close to Glovelier. A 2° dip of the basement surface to the SE enables us to explain the level difference of the stratigraphic sequence without invoking any basement bump.
- The stratigraphic and structural constraints, applied taking dips and dip azimuths of bedding and structures from the map, and projected onto the sections.

Figure 6 illustrates a subsurface cross section around the Mont Terri rock laboratory. This section integrates all available geological data from the Mont Terri tunnel and the relevant boreholes to define the stratigraphic formation boundaries. The different galleries of the Mont Terri rock laboratory, as well the security and Mont Terri motorway tunnels, are all intersected by a second-order thrust zone (1.0-to-4.2 m thick), called “Main Fault”. Close observation and structural analysis of outcrops in the galleries suggest that the Main Fault formed as a simple-shear fault-bend fold (Nussbaum et al. 2011). The beds of the hangingwall dip less than the fault ramp, which is in this case the shear-zone boundary, dipping 50° – 60° SSE. The angular difference of beds between the footwall (30° – 35°) and the hangingwall (40° – 45°) ranges from 10° to 15° . These geometric relationships favor an interpretation as a shear fault-bend fold (Suppe et al. 2004), in contrast with a classical fault-propagation fold or fault-bend fold where backlimb dips are parallel to the fault ramp.

4 Methodology

4.1 Kinematic forward modelling

4.1.1 Methodology and workflow

Two sections, one through the Mont Terri and the Mont Russelin tunnels, and one through the Clos du Doubs area, were set up in 3D digital space using MoveTM (see Fig. 2). Even though the section construction and kinematic analyses were done in 2D, it was important to analyse the sections in the 3D context of a regional Digital Elevation Model (swissALTI3D, Swisstopo 2011) with draped geological maps (Geological Atlas, GeoCover, swisstopo), since this provided context and additional constraints on bedding and fault geometry, particularly faults that were not at right angles to the section. First-order faults that crossed the sections were constructed as 3D wireframes from a selection of planar fault segments, constructed by solving local three-point-problems constrained by surface trace geometry and topography. The section interpretation was extended to depth by iterative kinematic forward modelling following the two end-member concepts to be tested (see Sect. 4.1.2).

We performed kinematic forward modelling of deformation, including folding and faulting, using MoveTM. This software provides a range of algorithms that mimic rock deformation styles including algorithms for fault-bend folding (Suppe 1983), and fault-propagation folding (Suppe and Medwedeff 1990) and Trishear (Erslev 1991). Kinematic forward modelling goes beyond the traditional line-length and area-balancing tests in 2D and 3D by including constraints on the sequence of deformation events and the mechanism by which deformation took place. As such it allows testing and quantification of not only the deformation style but also the order of faulting through time, and the geometry of horizons and faults at sequential steps in time. It is of particular use in data-poor studies where sequential restoration is under-constrained.

Typically, forward modelling is an iterative process where forward-modelled geometries are compared and contrasted to observed geometries and cross-cutting relationships, and modelling variables are adjusted accordingly.

Our approach comprised the following steps with the iterative process visualised in Fig. 7:

1. Data Integration: we took existing sections by Freivoegel and Huggenberger (2003) and Caër et al. (2015) as a starting point, organized available field-, tunnel, and drilling data and interpretations, and integrated in 3D georeferenced space including maps of various vintages, topography, and additional sections.

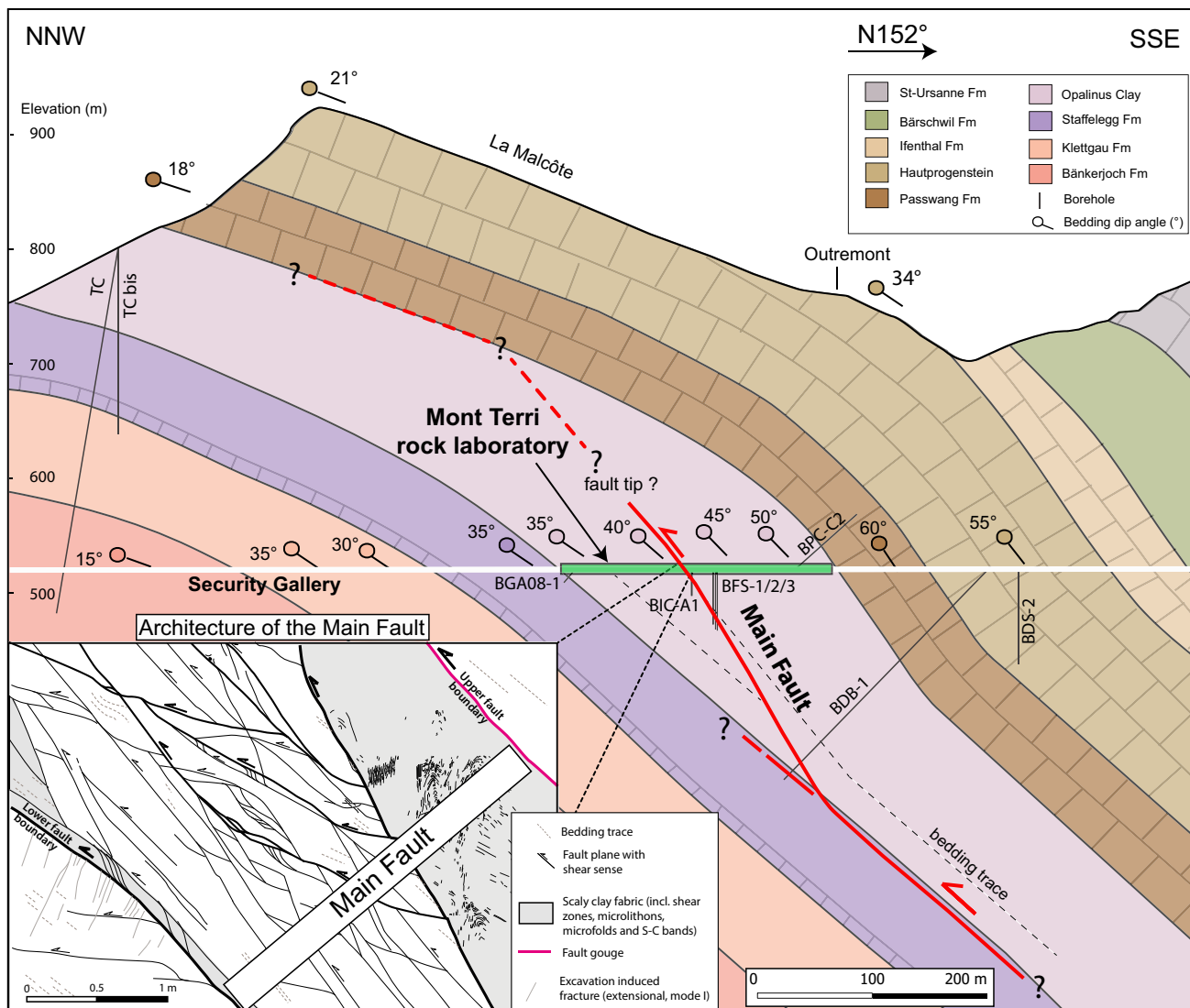


Fig. 6 Sub-surface cross section based on tunnel and borehole data collected within and in the vicinity of the Mont Terri rock laboratory. The main tectonic structure intersecting the rock laboratory is the 1–6 m wide “Main Fault” and is described in Nussbaum et al. (2011)

and Jaeggi et al. (2017). The significance of the fault for this study is that it is considered as being detached from the upper detachment at the top of the Staffelegg Formation. Surface data are taken from GeoCover (Swisstopo 2012)

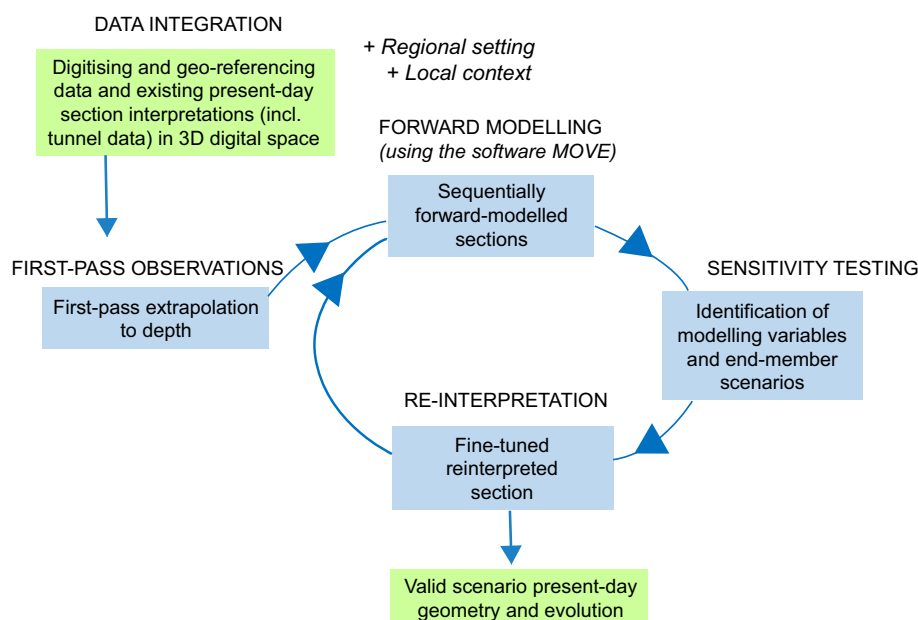
2. First-pass observations and structural constraints (described in Sect. 3) then led to an extrapolation of the interpretation of faults and fault block geometries to depth, following the two structural concepts to be tested.
3. Forward modelling then tested these first-pass geometries by applying fault displacements starting with a layer-cake stratigraphic sequence including a regional tilt.
4. For both scenarios, we identified the key modelling variables, determined the sensitivity of the results to the various settings, compared the resulting geometries and contrasted these with near-surface constraints, and selected an optimum set of parameters for each scenario (listed for each scenario in Sect. 5.2, Fig. 8).

The final iteration of our (re-)interpretations led us to select one optimum scenario (described in Sects. 5.2, 5.3, and visualised in Figs. 10, 11).

4.1.2 Initial boundary conditions and modelling constraints

We chose the section through the Mont Terri and Mont Russelin tunnels because of the abundance of available data acquired by the geological mapping of the fresh outcrops in both tunnels. Our section trace is not straight but steps in order to connect the trajectories of both tunnels as shown in Figs. 1 and 2. The dog-legged section is “rolled-out” to work in 2D view; this preserves the line length

Fig. 7 Kinematic forward modelling workflow with iterative steps, using first-pass extrapolations to depth as target geometries in the sequential forward modelling. Modelling variables and tested scenarios are shown in Fig. 8



going from the section in 3D to 2D, but may lead to overestimating length in a particular transport direction. During the ongoing analysis, we found that part of the late development involved tectonic transport that was not parallel to the Mont Terri section. This meant that the forward modelling in 2D for this particular step was limited. As such, we could not produce all geometries purely by using deformation algorithms. This is further discussed below in Sect. 5.

We assumed stratigraphic thicknesses to be constant for the units on top of the basement and on top of the post-Permo-Carboniferous sediments, even though the presence of mechanically weaker units are expected to have formed local, second, or third order structural duplications and/or omissions. We also assigned a general pre-folding SSE regional tilt for the stratigraphic sequence with a 2.0° instead of a 2.5° dip (Laubscher 2003). This decision was motivated by analysis of the reflexion seismic lines 73-BE5 and 74-BE10 acquired in 1973 and 1974 by Jura Bernois Pétrole SA, partly published by Suter (1978). These seismic lines show that the main stratigraphic horizons plunge to SSE with a dip of 2.0° .

As described in Sect. 3.1, we took the structural level of the stratigraphic sequence in the hangingwall syncline between the Mont Terri and Caquerelle anticlines to indicate relative uplift of stratigraphy of ca. 180 m compared to the footwall and presumed regional and reference level to the north in the Ajoie plain. This structural high is an important geological constraint and we integrated this as an initial condition in the forward modelling. Such local uplifts can be tentatively related to at least three different tectonic styles: (1) presence of inherited basement normal

faults creating a basement topographic high in the form of a horst (i.e. Guellec et al. 1990), (2) partial duplication of the Mesozoic sedimentary sequence along an upper detachment as proposed by Schori et al. (2015), or (3) thick-skinned tectonics involving fault reactivation and the creation of basement ramps as proposed by various authors for different regions in the Jura belt (i.e. Guellec et al. 1990; Pfiffner et al. 1997). In the study region, there were no available field data on the basement structure below the Mont Terri and Caquerelle anticlines to allow us to prefer one tectonic style over the other ones.

Considering the regional tectonic setting and available seismic data further north in the Ferrette half-graben (Rotstein et al. 2005; Ustaszewski et al. 2005; Ustaszewski and Schmid 2007), we favoured the presence of inherited basement normal faults and a horst to construct our generic model (Fig. 10). As initial boundary conditions, we assumed that the level difference (+180 m) between the Ajoie Plain and St-Ursanne is related to the presence of NNW-dipping normal faults lowering the basement below the future position of the Mont Terri anticline. We interpreted these as inherited Permo-Carboniferous faults. It is not clear if these inherited faults have also affected the sedimentary cover or not. Certain steep faults observed in the geological map (Fig. 2) could be interpreted as pre-existing normal faults formed during the Oligocene rifting phase. The available geological data along the Mont Terri and Mont Russelin tunnels are not convincing enough to introduce inherited normal faults dissecting the sedimentary sequence at the initial stage (see later below Fig. 10, step 1). For this reason, in setting up the model we assumed a NNW-vergent flexure of the sedimentary cover (and no

cross-cutting of the sediments) above suspected inherited basement faults. Furthermore, we questioned the presence of an eventual Permo-Carboniferous trough north of the section below the Ajoie plain. This possibility has already been addressed by Ustaszewski et al. (2005). Recent unpublished gravimetric data acquired by Geo-Energie Suisse AG for the geothermal project Haute-Sorne also suggest an important negative Bouguer anomaly below the Ajoie plain. Even if there are no available data, such as subsidence curves, we envisaged differential compaction in addition to extensional faults to explain the postulated NNW-vergent flexure. We did not introduce any additional basement fault south of the section to explain the stratigraphic difference level between St-Ursanne and Glovelier (−120 m) as shown in Fig. 5. The unpublished E-W-oriented seismic line 74-BE10 suggests the presence of two E-dipping faults affecting the Mesozoic sedimentary sequence and the pre-Triassic basement. There are also the Develier and Viques faults located further to the east of the Delémont Basin. By contrast, due to the poor resolution of this seismic line, we could not identify any basement fault below the Caquerelle anticline. This justified our decision to use the general 2.0° basement tilt to the SSE to explain the altitude difference.

The alternative scenario involved a partial duplication of the sedimentary sequence. In this model, we assumed a flat topography of the basement surface (see later below Fig. 11, step 1). This model does not imply the absence of basement faults but rather that they create no significant offsets within the sedimentary units.

5 Kinematic forward models

5.1 Modelling variables and proposed scenarios

We tested iteratively both classic and alternative scenarios for the section interpretations: the classical scenario with the basal detachment at Triassic evaporites level, and the alternative scenario in which displacement was on combined detachments within the Triassic evaporites and top of the Staffelegg Formation that led to the partial duplication of the sedimentary sequence. We considered the following five modelling variables (see Fig. 8).

1. Dip angles: the stratigraphic sequence was set up with a 2° regional tilt towards the hinterland. We constructed thrust-ramp angles at 25° (apart from those of the Caquerelle thrust, which are expected to be steeper due to their interpreted nature as sidewall ramps with oblique slip displacement; these are drawn with a 60° angle, an apparent dip because of the section angle).

2. Sequence of thrusting: we varied this to test whether a simple in-sequence order would suffice to explain the observed geometries.
3. Active detachment level(s) and linkages of detachments: we tested whether one single detachment level, or a combination of detachments levels with duplication of part of the sequence, are possible. We know what the dominant regional detachment is; in addition, we know which theoretically weaker stratigraphic units can be expected to have formed additional detachments.
4. Dominant representative deformation algorithm(s): the “duplication scenario” used fold-bend-folding as the dominant deformation algorithm, the “classical scenario” used the Trishear algorithm (Erslev 1991; Allmendinger 1998) for the main displacement. Both scenarios relied on the use of the Trishear algorithm (Erslev 1991; Allmendinger 1998) to produce the overturned frontal limb of the Mont Terri Anticline.
5. Role of basement structures in the initiation of thrusts, development of the local high in the Mont Terri hangingwall, and lateral (dis)continuity of thrusts and folds: we will discuss both scenarios below.

5.2 Lateral structural variability

The large lateral variability of structures, such as significant variations of anticline axes and thrust orientations as observed on the map in Fig. 4, require 3D analyses that will be realised in the future. For this study, we have built an additional cross section to the west of the main section (labelled 2 in Figs. 2, 3), intersecting the Clos du Doubs anticline (Figs. 8,9). The aim of this section is to verify if the same thrust sequence can be derived as that from the main section (Figs. 10, 11), and to understand how the structures evolved laterally and interfere with each other. The forward model presented in Fig. 9 suggests an out-of-sequence order of thrusts. This sequence comprises (1) ca. 90 m displacement due to pre-thrusting normal faulting in the Oligocene rifting phase (Fig. 9, step 2), (2) 100 m displacement due to fault-bend folding and 400 m trishear together comprising the Mont Terri thrust displacement (Fig. 9, step 2), (3) 700 m + 500 m of fault-bend folding with back-stepping of deformation and initiation of two wedges: Clairmont (Fig. 9, step 3) and Clos du Doubs (Fig. 9, step 4). The overturned limb of the Mont Terri anticline required that we add 400 m trishear displacement implying an important bed-thickness change. The hangingwall of the Mont Terri anticline (Fig. 10, step 4) is affected by important NNE-trending faults marking the spot where the E-W trend changes to NE (Fig. 4). This suggests that the NNE-trending faults are cross faults

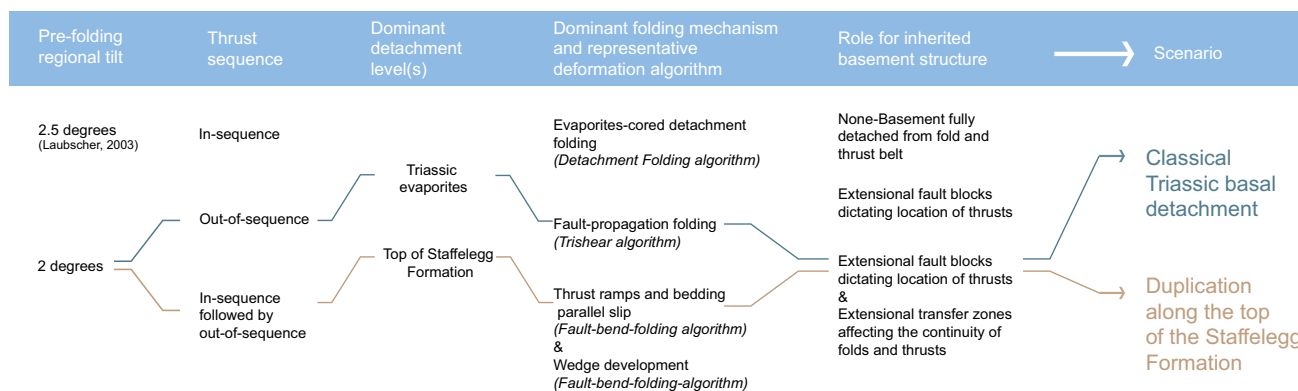


Fig. 8 Forward-modelling variables, range of considered options for each variable, and selected options for the two alternative scenarios that are considered in this study

accommodating sinistral NNE-displacement and causing an out-of-section displacement. We interpret these cross faults as inherited normal faults reactivated during Eo-Oligocene rifting. A pre-thrusting displacement of ca. 90 m is implemented (Fig. 9, step 1). This is in accordance with the amount of throw along the Eo-Oligocene faults estimated by Ustaszewski et al. (2005) to be on the order of 80–90 m based on the interpretation of seismic profiles located further north. We estimate the total shortening accommodated along the whole section to be 2.7 km.

5.3 Scenario with classical basal detachment

5.3.1 Thrust sequence

The cross sections shown in Fig. 10 illustrate our geological interpretation of first-order structures observed in and around the Mont Terri and Mont Russelin tunnels. We have integrated data from mapping of both tunnels and from surrounding reconnaissance boreholes drilled in preparation for the tunnel construction (Bureau Technique Jean Norbert Géologues SA 1992; Bureau Technique Norbert Géologues-Conseils SA 1993). For the purpose of this modelling study we considered only first-order thrusts and faults in the cross section.

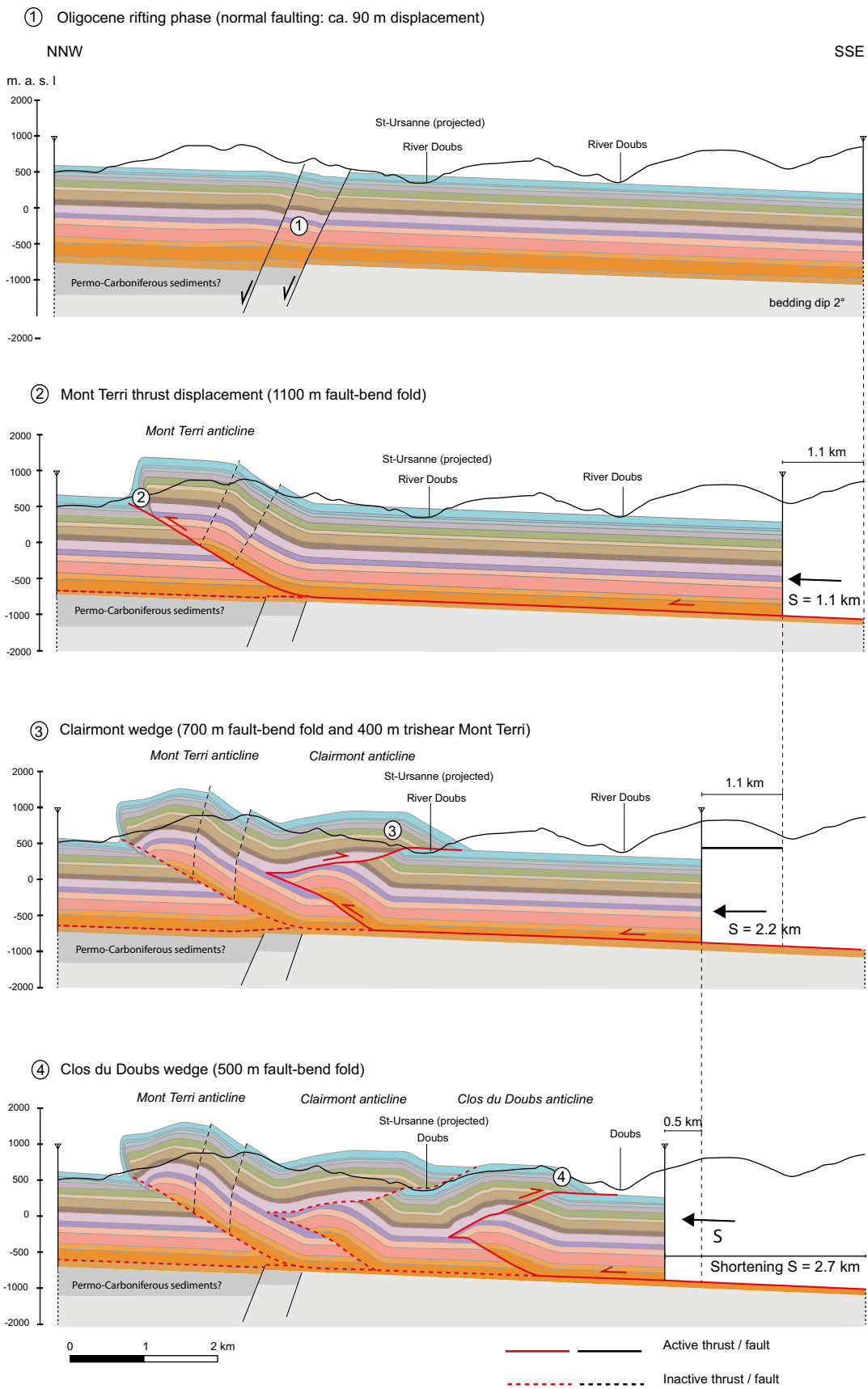
We found that a thrust sequence propagating purely forward from south to north to be inconsistent with the cross-cutting relationship as interpreted from the tectonic map (Fig. 4). An in-sequence thrust sequence failed to reproduce the present-day geometry of the geological data compiled in Fig. 5. After several iteration runs, it became clear that the folds and thrusts of the Mont Terri anticline developed first (Fig. 10, steps 2, 3 and 4), followed by those of the Clairmont anticline (visible only in Fig. 9) and the structures of the Clos du Doubs (Fig. 10, step 6). The Mont Terri thrust developed initially with 900 m displacement as fault-bend fold (Fig. 10, step 2). The

Fig. 9 Forward-modelled cross section of the Clos du Doubs to constrain and validate the thrust sequence of the forward models for the Mont Terri–Mont Russelin section (Fig. 10). Section trace is shown in Figs. 1, 2, and 4. Initial basement-related extensional faults are offset by an out-of-sequence series of thrust-wedges that connected the basal detachment to the detachment in the overlying Staffelegg Formation to form a tectonic wedge and a presently surfacing back-thrust. The final-stage geometry shown under (4) was not modelled in detail to fit with the present-day geometry. The stratigraphic units are described in Figs. 2 and 3

observed overturned forelimb formed during trishear development of the Mont Terri anticline (Fig. 10, step 3). The Mont Terri thrust comprises a master thrust associated with smaller thrusts in the hangingwall. These smaller thrusts are folded because of progressive displacement on the master thrust (Fig. 10, step 4).

The Clos du Doubs thrust followed the development of the Mont Terri thrust (Fig. 10, step 6). This thrust also detached along Triassic evaporites but rather than cutting across to the surface, it connected to the top of the Staffelegg Formation to form a wedge that, paired with the associated backthrust, jacked up and folded the overlying units (Fig. 10, step 6). Prior to forming the wedge, the thrust propagated to the north and the Main Fault (as observed in the Mont Terri rock laboratory) developed in the hangingwall as a second-order structure detaching within the top of the Staffelegg Formation (Fig. 10, step 5).

A pair of thrusts developed on the back of the Clos du Doubs wedge (Fig. 10, steps 8 and 9). Similar to the Mont Terri thrust, these connected the Triassic evaporite detachment to the surface, but they show complex deformation at the top of the Staffelegg Formation level as well. Offsets of the deeper units are larger than those of the younger overlying units. The 60°–80° dip of these thrusts is unusually steep for thrust structures. Also, these structures trend NN at the surface and comprise part of the Caquerelle fault exhibiting a “Rhenish” trend. This suggests an



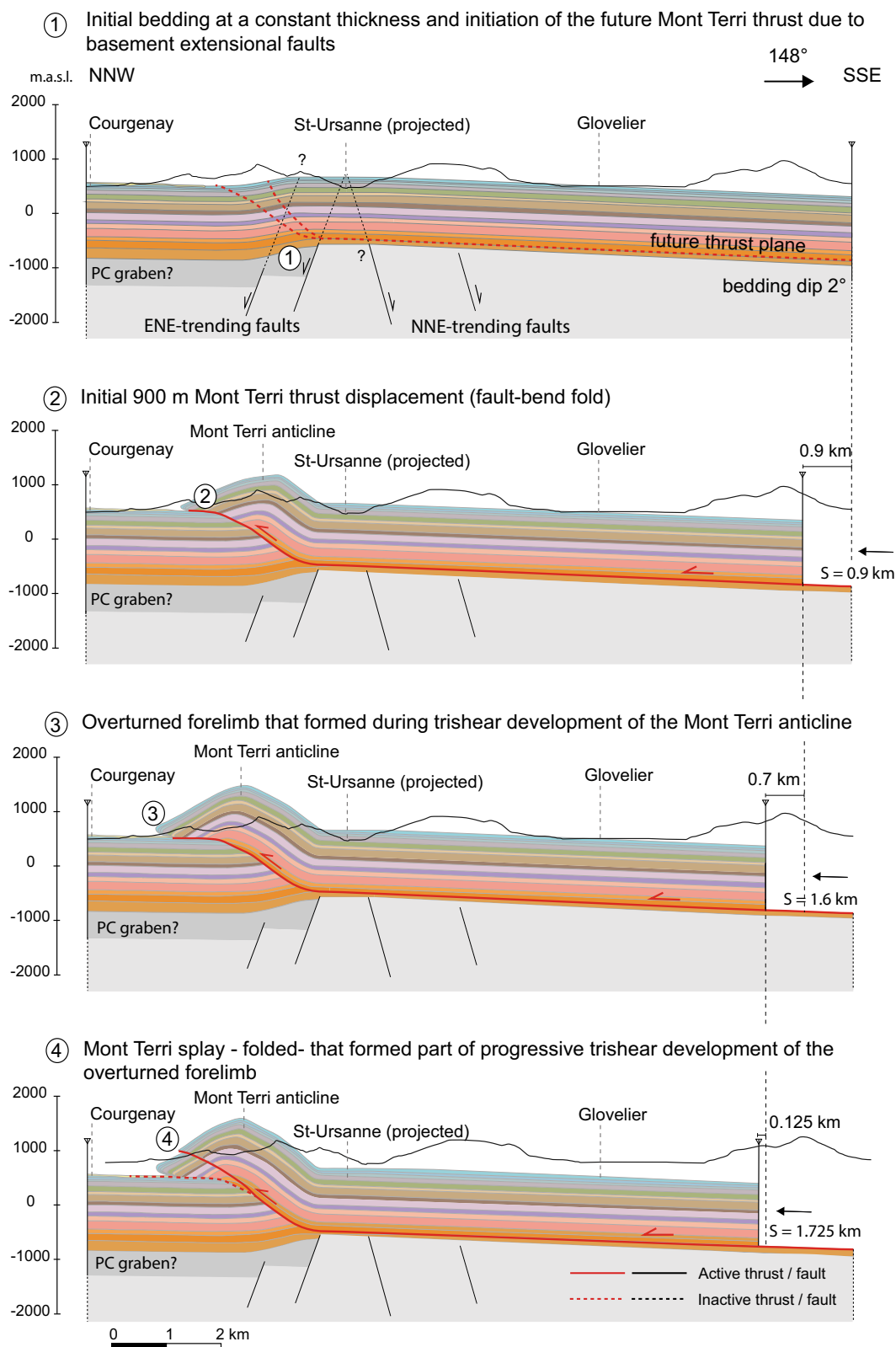


Fig. 10 Forward-modelled cross section of the Mont Terri and Mont Russelin using the classical scenario with a basal detachment. The syncline that is above regional between Mont Terri and Clos du Doubs anticlines relies on a local high formed by a basement horst.

The initial Clos du Doubs anticline is formed by a thrust wedge (like in the Clos du Doubs section, see Fig. 9), but is enhanced by a series of NNE-trending steep thrusts. Section trace is shown in Figs. 2 and 4 and stratigraphic legend from Figs. 2 and 3

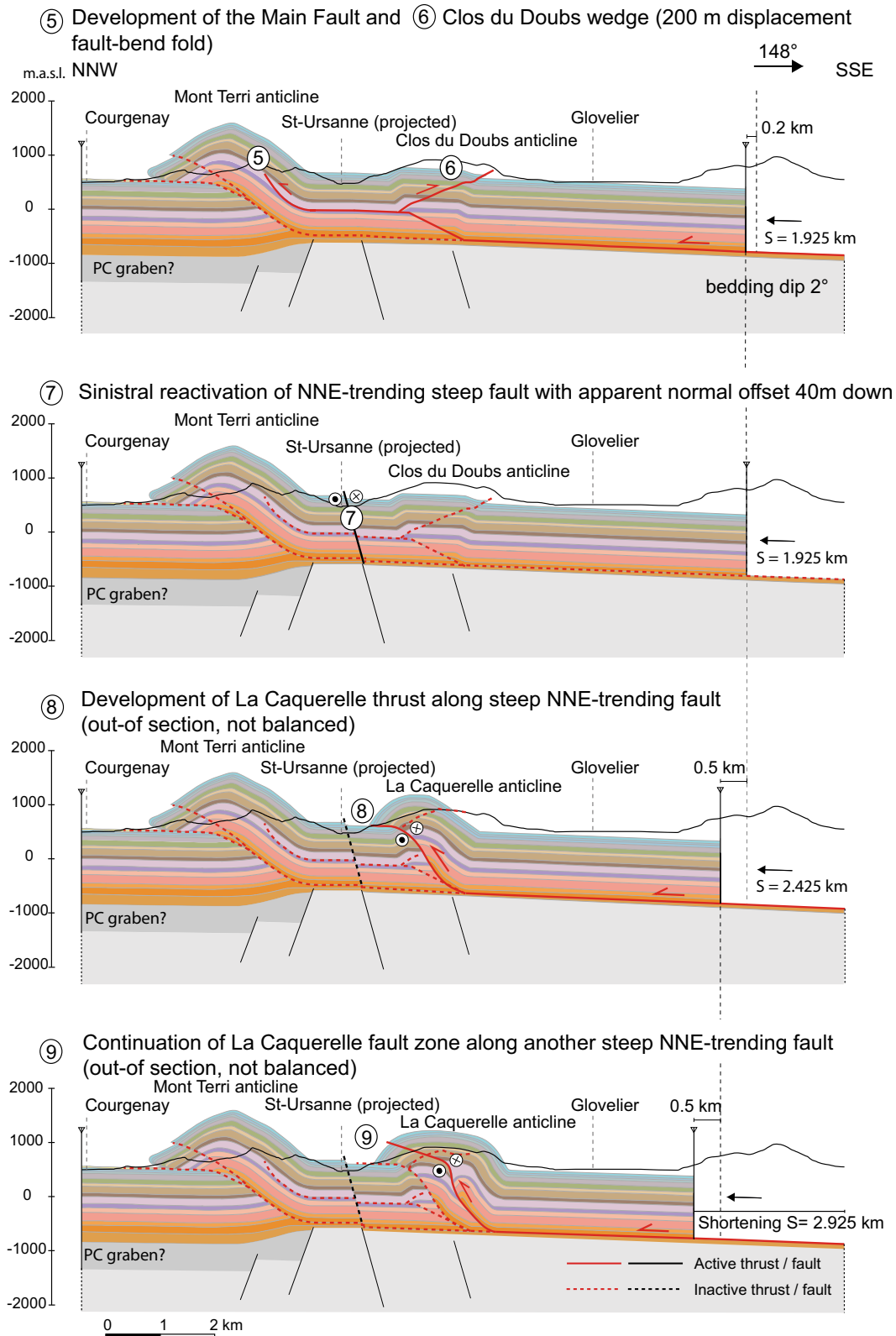


Fig. 10 continued

influence from basement faults in determining their location and geometry. The Caquerelle fault is interpreted to have acted as a sidewall ramp and have a significant oblique slip component that adds complexity to calculating the displacements. For our section, this is an out-of-plane tectonic transport, potentially causing offsets to be apparent offsets and limiting the use of the kinematic modelling algorithms.

One fault in the centre of the section shows normal offset (Fig. 10, step 7). It is interpreted as an isolated steep fault related to a possible underlying basement fault. The actual displacement or kinematics is unknown. Its timing is unconstrained by overprinting relationships with the thrusts.

5.3.2 Folding mechanism

The first 900 m displacement on the Mont Terri thrust was modelled with a fold-bend-fold algorithm, in which the development of the hangingwall anticline follows purely from the shape of the underlying fault (Fig. 10, step 2). The subsequent 1600 m offset was modelled with a Trishear algorithm, which combined discrete offset along the fault at depth with folding in a triangular zone near the surface. A trishear zone with a 30° angle was used with the lower side parallel to an erosional intra-Reuchenette surface (at 2° dip to SSE), which, combined with a small (0.1) propagation/slip ratio, caused the subtle overturned frontal limb with overturned angles reflecting those measured in the youngest units in outcrop today (Fig. 10, step 3). At that stage, it was likely that the flat-lying Mont Terri thrust had become less favourable for slip, and that the small thrust in the hangingwall of the Mont Terri thrust took over the displacement (Fig. 10, step 4). It was modelled using the fault-bend-fold algorithm and a 125 m displacement. Today, this thrust is slightly folded and we envisage that the fold-nose and the internal structures developed progressively, not in discrete steps.

The initiation of the Mont Russelin culmination started with the development of the Clos du Doubs thrust, which did not propagate to the surface, but connected to the upper detachment (top of Staffelegg Formation) to form a wedge (Fig. 10, step 6). This wedge was cut by a set of two Caquerelle thrusts that formed steep slopes and propagated through to the surface (Fig. 10, steps 8 and 9). Note that in this scenario the upward bend of the beds just below the Caquerelle thrust are not caused by drag due to thrusting, but by folding due to movement over the Clos du Doubs thrust and wedge emplacement.

The Caquerelle thrusts have a NNE-trend and are interpreted to have a large component of oblique displacement. The trend of the structures and the azimuth of displacement are not within the plane of section and hence

the deformation algorithms in 2D are not sufficient to model these structures, which would require a 3D forward model. The geometries of this step in section are constructed and not forward modelled. Based on current observations at the surface and in the tunnel, we interpret the structures to detach along the Triassic evaporites, but with significant deformation within the Opalinus Clay causing local thickness increase.

5.3.3 Role of inherited basement architecture

In the classic scenario, inherited basement structures are expected to play a significant role in dictating the location of both thrusts and oblique (cross) faults. Structures of both Mont Terri and Mont Russelin are thought to be triggered by relief in basement blocks, first recognised by Laubscher (1985). Fractures and faults in the overlying units may result from basement faults by either differential compaction of the (Permo-Carboniferous?) graben fills, or by possible reactivation (inversion, or strike slip) of the basement faults. These fractures and faults form weaknesses that cause nucleation of thrusts. In our current view, both Mont Terri and Mont Russelin are located just NW of interpreted basement faults, north of which compaction of the graben fill may have caused sag and a local draping tilt and/or small-scale extensional faulting of the overlying sediments (Fig. 10, step 1). This differential compaction and/or extensional fractures may explain the 180 m difference between the level of the units in the hangingwall of the Mont Terri thrust and the regional reference level (see Fig. 5).

5.3.4 Shortening estimates

The shortening (expressed as S in Fig. 10) along this section associated with the development of the Mont Terri and the Clos du Doubs thrusts is 1.725 km and 0.2 km, respectively. The development of the Caquerelle (out-of-section) thrust indicates at least another 1.0 km of shortening. The total shortening of this section amounts to 2.925 km.

5.4 Alternative scenario with duplication of sub-Opalinus Clay formations

Inspired by the recent study of Schori et al. (2015), we also propose an alternative model using multiple detachments within both the Triassic evaporites (basal detachment) and the Rietheim Member, which belongs to the top of the Staffelegg Formation (upper detachment). The presence of regional structural uplifts in the Jura, specifically in the Chasseral area of the Haute Chaîne, led Schori et al. (2015) to propose an alternative scenario to the classical view that

associates basement highs with thick-skinned tectonics (e.g. Guellec et al. 1990; Pfiffner et al. 1997), or with inherited basement normal faults causing a basement topography in horsts and grabens. They interpreted the overall structure of the Chasseral to be the result of the combination of displacements along the basal décollement in Middle Triassic evaporites and along an upper detachment at the base of the Opalinus Clay. In combination with an excess-area graphical approach and kinematic forward modelling, they argued that structural highs could have been formed during the main thin-skinned deformation, without the need for subsequent thick-skinned reactivation of pre-Triassic basement or detachment folding with thickening of anticline cores by flow of Triassic evaporites. Stratigraphic duplication by thrusting along the basal detachment that steps up to connect to a shallower detachment could explain the 180 m uplift from the regional level of the units in the Mont Terri hangingwall. Similarly, we consider here an alternative scenario involving an upper detachment within the Rietheim Member of the Staffelegg Formation (see Fig. 3). This member is composed of bituminous, predominantly thinly bedded shale and marl layers, offering a potentially good detachment layer.

5.4.1 Thrust sequence

In the duplication scenario, the thrust sequence is *overall* similar to that of the classic scenario and to the cross-cutting relationships as interpreted from the tectonic map (Fig. 4). The structures of the Mont Terri developed first, followed by the structures that formed the Mont Russelin, in an out-of-sequence fashion (Fig. 11). However, in contrast to the classic scenario, this scenario involves an initial 10.5 km duplication of the units below the Opalinus Clay formations, representing material that moved out of the section above the upper detachment, expressed as d (km) in Fig. 11. This duplication developed by displacement along the Triassic evaporites detachment that ramped up to connect to the top of the Staffelegg Formation, possibly initiated at where the Vellerat anticline now lies, bordering the southern part of the Delémont Basin (Fig. 11, step 1). After some 10.8 km of shortening (Fig. 11, step 2), two horses developed in front of this duplication (Fig. 11, step 3), followed by the development of the Mont Terri thrust (Fig. 11, step 4). Initially, the Mont Terri thrust detached along the lower Staffelegg Formation (Fig. 11, step 5), but with time the detachment stepped down to the Triassic evaporites again, through a ramp some 3 km to the SE (Fig. 11, step 6). This ramp formed the initial structure below what is now Mont Russelin. This is in contrast to the classic scenario where the initial structure is formed by a wedge and backthrust. The proto-Clos du Doubs

culmination (Fig. 11, step 7) is then enhanced by the development of the two oblique thrusts related to the Caquerelle structural trend that induced additional shortening on the Mont Terri anticline, uplifting the Upper Triassic sediments to the surface (Fig. 11, step 8).

5.4.2 Folding mechanism

The dominant cause for folding in the duplication scenario is thrusting and hangingwall folding above a ramp. The corresponding deformation algorithm used in the forward modelling is fault-bend-folding. In addition, for the Mont Terri Thrust and associated hangingwall fold, a trishear mechanism is interpreted to have caused the overturned forelimb, similar to that of the classic scenario.

5.4.3 Roles of basement architecture and cross faults

Similar to the classic scenario, basement horst and grabens, and associated faults are interpreted to have initiated the development of thrust in the overlying units. Development of Caquerelle is here interpreted to be soft-linked to the basement faults, detaching in the Top Staffelegg, consistent with the interpreted weakness of this detachment. However, geometrically the Caquerelle faults could equally well have detached along the Triassic evaporites and be linked to basement faults. With the duplication of the units below the Opalinus Clay, there is no need for 180 m differential compaction or extensional fault displacement at basement level in front of the Mont Terri Thrust.

5.4.4 Shortening estimates

The shortening (expressed as S in Fig. 11) along this section, associated with the development of the Mont Terri and the proto-Clos du Doubs thrusts, is 12.9 and 0.5 km, respectively. Significantly, there is here more than ca. 2 km shortening compared to the classic scenario. Similar to the classic scenario, the ca. 800 m shortening along the Caquerelle thrust is a minimum estimate due to out-of-section displacement along this oblique structure. Displacement along the upper detachment (d) amounts to 10.8 km (Fig. 10, steps 3–4). The minimum shortening measured in this cross section amounts to 14.2 km.

6 Discussion

6.1 Mechanical viability

When a cross section is geometrically and kinematically viable, it does not mean that it is mechanically viable. Therefore, we undertook an initial mechanical analysis,

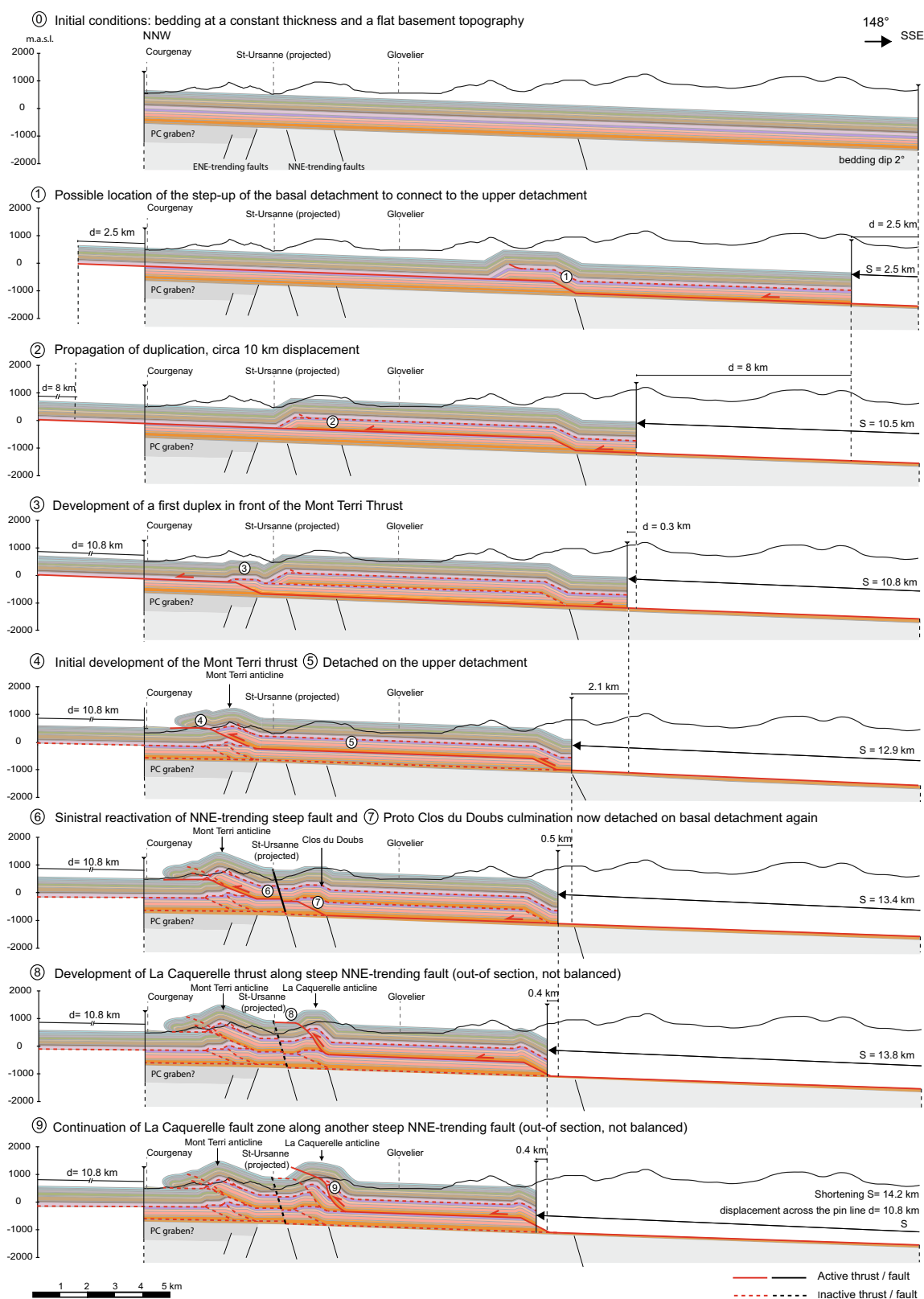


Fig. 11 Alternative forward-modelled cross section of the Mont Terri and Mont Russelin using the duplication scenario with multiple detachments: one basal detachment within the Triassic evaporites and an upper detachment at the top of the Staffelegg Formation.

Section trace is shown in Figs. 2 and 4 and stratigraphic legend from Figs. 2 and 3. S and d express respectively the shortening and the displacement

based on simple prototypes, for the classical scenario presented in Fig. 10. For this we used the kinematic approach of limit analysis theory (Salençon 2002) with the OptumG2 software (OptumG2 2014; Krabbenhøft and Damilke 2003; Krabbenhøft et al. 2005; Lyamin et al. 2005; Souloumiac et al. 2009, 2010). The method consists in searching the velocity field, and therefore the location of the deformation, that requires the minimum tectonic force (Maillot and Leroy 2006). The objective is to test the mechanical viability of the thrust sequence, characterised by an out-of sequence thrusting that forms the Caquerelle anticline.

We ran a first experiment to determine the range of friction angle values on the décollement needed to initiate the Mont Terri ramp far away from the southern existing structures, i.e. Vellerat anticline (Fig. 1). In a second experiment, we assumed that some relief forms above the Mont Terri ramp and we determined the range of friction values on this ramp necessary to abandon it and initiate a new ramp southward, which would correspond to the Clos du Doubs/Caquerelle thrust.

The prototype for the first experiment corresponds to the situation at the end of the formation of the Vellerat anticline to the south (Fig. 12a). We simplified this structure giving it a 10° topographic slope and filling it with homogeneous material. North of the Vellerat structure, the sedimentary cover is modelled as flat and lying above the basement represented by homogeneous material. The topographic slope has $\alpha = 2^\circ$ due to the presence of Cenozoic molasse (not represented on the geometrical evolution). The Triassic décollement is modelled by a horizontal plane at the base of the sedimentary cover and is disrupted by two normal faults, as in the geometrical model (Fig. 12a). We applied a compressive force along the southern wall of the prototype from the surface to the depth of the Triassic décollement. The software optimizes the value of this force by finding the geometry of failure that yields the minimum possible force. We varied the friction on the décollement Φ_d between 0° and 25° . For $\Phi_d \leq 5^\circ$, deformation propagates beyond the northernmost normal fault, despite the disruption of the décollement level (case A in Fig. 12b, c). For $6^\circ \leq \Phi_d \leq 7^\circ$, the northern normal fault localizes the ramp (case B in Fig. 12b, c), as assumed by the geometrical scenario. For $8^\circ \leq \Phi_d \leq 9^\circ$, the southernmost normal fault localizes the ramp (case C in Fig. 12b, c). For $\Phi_d \geq 9.5^\circ$, deformation does not propagate far enough along the décollement level to be consistent with the geometrical hypothesis presented in this paper (case D in Fig. 12b, c). In a second experiment, we choose $\Phi_d = 7^\circ$, i.e. in the range that gives the expected result (case B Fig. 12b, c) for the first experiment. The prototype for the second experiment corresponds to the situation after ca. 2.5 km of shortening has been accommodated by sliding on the Mont Terri ramp, assuming arbitrary erosion.

The mechanical test consisted in varying the friction on the part of the ramp that is in contact with the Triassic evaporites, Φ_r (purple dashed line called “Ramp part 2”, Fig. 13a). The other part has a friction fixed to $\Phi_R = 18^\circ$ (blue dashed line called “Ramp part 1”, Fig. 13a). We obtained two different results. For $\Phi_r \leq 8^\circ$, the Mont Terri ramp stays active (case B in Fig. 13c). For $\Phi_r \geq 9^\circ$, the Mont Terri ramp is abandoned and a new ramp develops southward (case C in Fig. 13c). This last case corresponds to the hypothesis of the geometrical scenario.

These two experiments show that two main steps of the geometrical scenario are mechanically viable using our calculation procedure. The first step requires friction on the Triassic décollement that is low enough to propagate the deformation northward up to the northern normal fault, but high enough to prevent the propagation of the deformation beyond this normal fault. The results of the second experiment show that if the friction on the ramp is high enough, this ramp can be abandoned in favour of the development of a new ramp in the south. It is interesting to note that if the friction angle on the ramp is around the limit (8° or 9°), it is likely that both Mont Terri and Caquerelle structures grew simultaneously since the results suggest that the force necessary to develop the solutions B and C (Fig. 13) is almost the same. The values determined here should not be considered as absolute values, because of the many simplifications done in these models, but they have relative significance. We note, however, that the low friction values obtained here for the Triassic décollement are in accordance with those obtained by von Hagke et al. (2014) for the Triassic evaporites and shales.

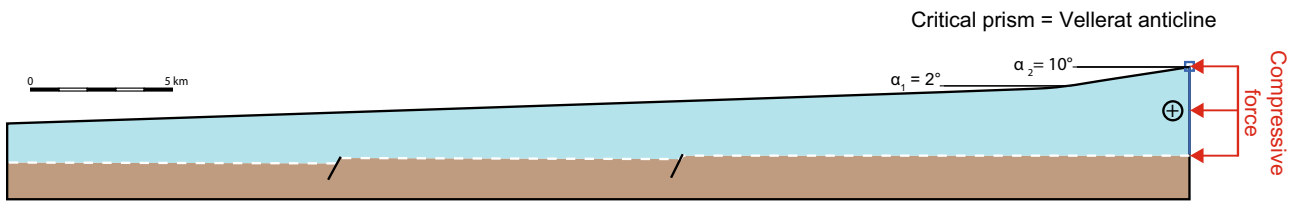
Step (b) of the duplication scenario is shown in Fig. 11 (step 2). We ran an initial test to check mechanical viability and the first results show that the proposed kinematics require lower friction on the Triassic décollement than on the Staffelegg décollement, which, at first glance, is not consistent with the rheology. However, some additional factors, for instance fluid pressure, could have lowered the friction along the Staffelegg décollement. Their integration in the mechanical analysis would be an important improvement to better simulate activation of the upper detachment, which was beyond the scope of this study.

6.2 Comparison with field data and improving the kinematic forward models

In Fig. 14, we compare the modelled section for the classical scenario (Fig. 10) with the field data shown in Fig. 5. In general, the match between the data and the model is acceptable, especially for the position of the first-order thrusts and faults. The observed offset of the stratigraphic units along the Mont Terri and Mont Russelin, when present, never exceeds 100 m. At that stage, it should be

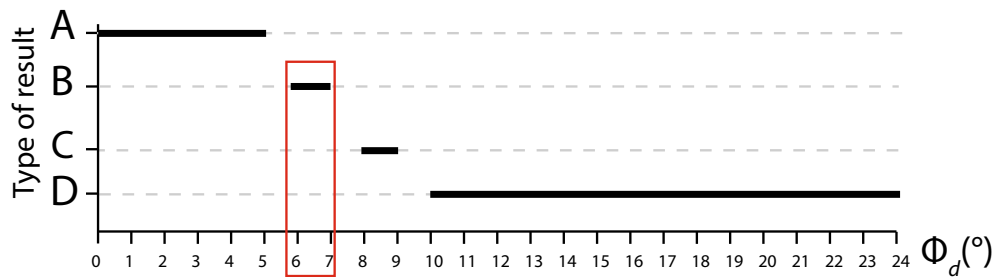
(a) NNW

SSE

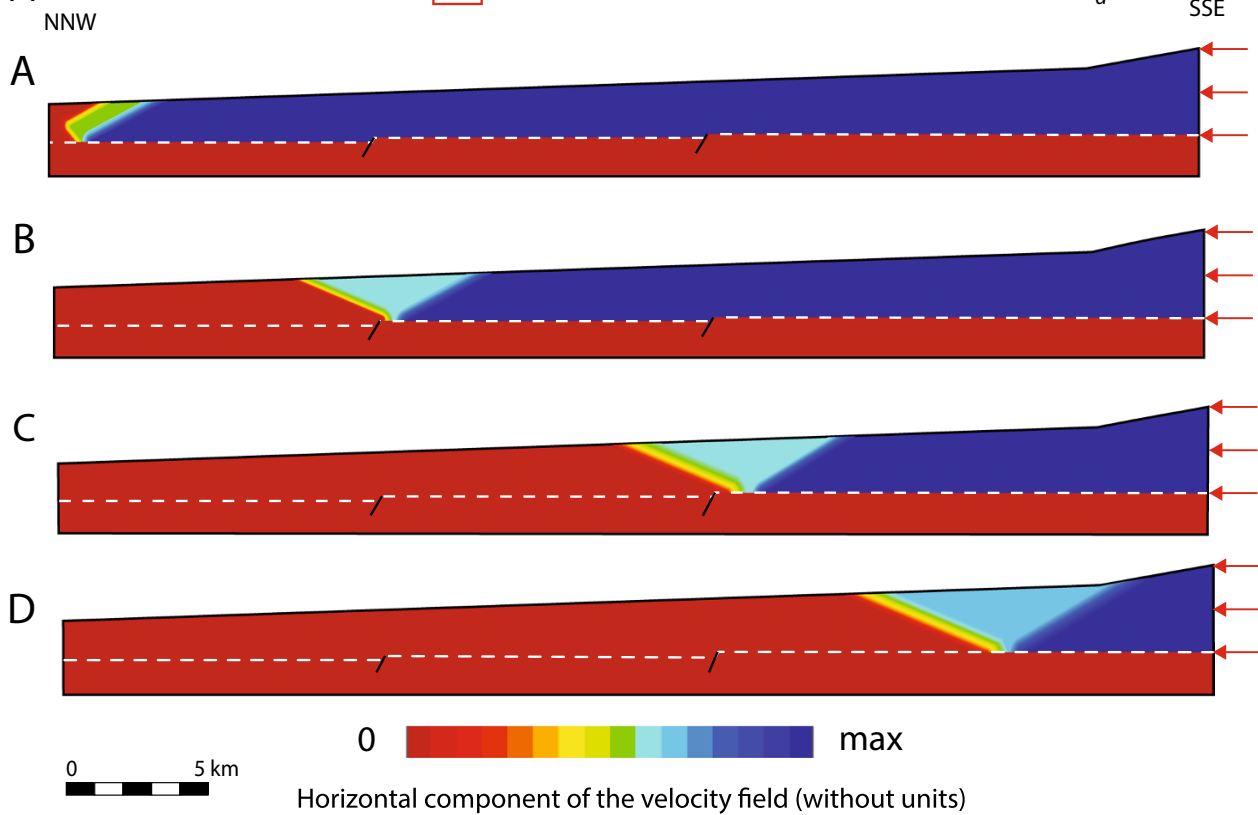


Legend	Geological units	Friction angle Φ (°)	Cohesion c (MPa)	Density ρ (kg/m ³)
Sedimentary cover undifferentiated		40	5	2300
Middle Triassic detachment		variable	-	2300
Basement undifferentiated		45	5	2300
Extensional fault		20	-	2300

(b)



(c)



◀ **Fig. 12** Results of the first geo-mechanical experiment: emplacement of the Mont Terri ramp. **a** Prototype composed of a Meso-Cenozoic sedimentary cover on top of a Triassic evaporitic décollement (*white dashed line*), lying above the basement. **b** Graph of the results obtained after applying a compressive force on the southern wall depending on the friction angle on the Triassic décollement. The *red rectangle* highlights the range of friction angles on the décollement for which the result obtained is the one expected by the geometrical scenario. **c** Illustration of the different results obtained and presented in **(b)**. See text for further explanation

recalled that our model includes all geological formations individually, insuring the maximum possible detail. A grouping of certain formations together (i.e. Early-, Middle-Late Triassic, Early-, Middle-, Late Jurassic) would help to better fit the data. Another observation concerns the backlimb of the Mont Terri anticline, which is not steep enough in our modelled section. We have considered only the first-order thrusts and faults in the cross section for the purpose of this modelling study; an underestimation of the role of backthrusts could explain this discrepancy.

The use of the Trishear algorithm to model folds produces considerable thickness variations of beds that initially had a constant thickness. This is particularly clear in the forward model presented in Fig. 9. We used this algorithm to try to reproduce the present-day geometry of the overturned forelimb of the Mont Terri anticline. Field data do not support thickness thinning in the competent limestone units which are still intensively fractured. By contrast, incompetent marl units, often hidden by Quaternary sediments, show thickness changes. We suspect that the position of the present-day Folded Jura front to the north of the Mont Terri region was dictated by ENE-trending north-vergent extensional flexures (as assumed in Fig. 10, step 1) caused by the Eo-Oligocene reactivation of Permo-Carboniferous basement faults that accommodated sinistral movements in addition to the throw. Introduction of this pre-thrusting flexure in the forward model may have a positive effect by promoting development of the overturned forelimb. This would improve the geometry of the hangingwall of the Mont Terri anticline by reducing the trishear component in the modelling, thus keeping the bed thicknesses more constant as observed in the field. The use of the Trishear algorithm may not be fully appropriate in this case.

6.3 Kinematic evolution

The kinematic approach suggests an early-stage formation of the Mont Terri thrust followed by back-stepping of the deformation to develop the Caquerelle thrust further to the south. In our interpretation, possible pre-existing inherited structures may have controlled the localisation of the front of the Folded Jura. When deformation propagated to the north, it may have localised along a suspected north-dipping ENE-trending extensional flexure, perhaps caused by

the Eo-Oligocene reactivation of Permo-Carboniferous faults. This gentle flexure might be a mechanical reason for the interruption of the northwards propagation of the deformation and the initiation of the Mont Terri thrust ramp that forms the present-day front of the Folded Jura. Finally, oriented at high angle from the transport direction, the oblique NNE-trending Rhenish fault beneath the Mont Russelin triggered the development of Caquerelle anticline.

In both the classical and the alternative models presented in this paper, the branch points (referring to the location at which a thrust branches off the detachment horizon) are supposed to be located above inherited basement faults. We suggest that these pre-existing faults have triggered the formation of wedges (Clairmont and Clos du Doubs) and have served as nuclei for the ramps related to the deep duplexes during a purely thin-skinned deformation. The basement topography may be either flat or offset by these inherited faults.

6.4 Open questions and recommendations for future work

The structural level of the stratigraphic sequence in the hangingwall syncline between the Mont Terri and Caquerelle anticlines is taken to indicate relative uplift of stratigraphy of ca. 180 m compared to the footwall and the presumed regional reference level to the north in the Ajoie plain. It remains questionable if this tectonic high is due to an extensional flexure above reactivated ENE-striking inherited faults during Eo-Oligocene and/or to differential compaction of the supposed Permo-Carboniferous sediments. This was the initial condition used for the construction of our classical model. Alternatively, the structural high might be explained by the duplication of a part of the sedimentary sequence (Middle Triassic-Liassic formations), by activation of an upper detachment located at the top of the Staffelegg Formation. We used this assumption to construct the alternative scenario for which the basement topography is supposed to be flat. Both scenarios propose a geometrical and viable kinematic solution.

Forward modelling of the alternative model implies that material was transported 10.5 km along the upper detachment. It is not yet clear where this shortening might have been accommodated. According to Burkhard (1990), the total shortening cumulated over the Central Jura is in the order of 25 km, based on the classical scenario with one single basal detachment. Already half of this shortening would be accommodated by our alternative model that involves only the last two anticlines of the Jura belt. The alternative model should be tentatively extended to the whole Central Jura from the Molasse Basin to the Folded Jura front to the north. As our study has shown, the basement inheritance led to a complex 3D fault and fold pattern. High-seated anticlines found everywhere in the

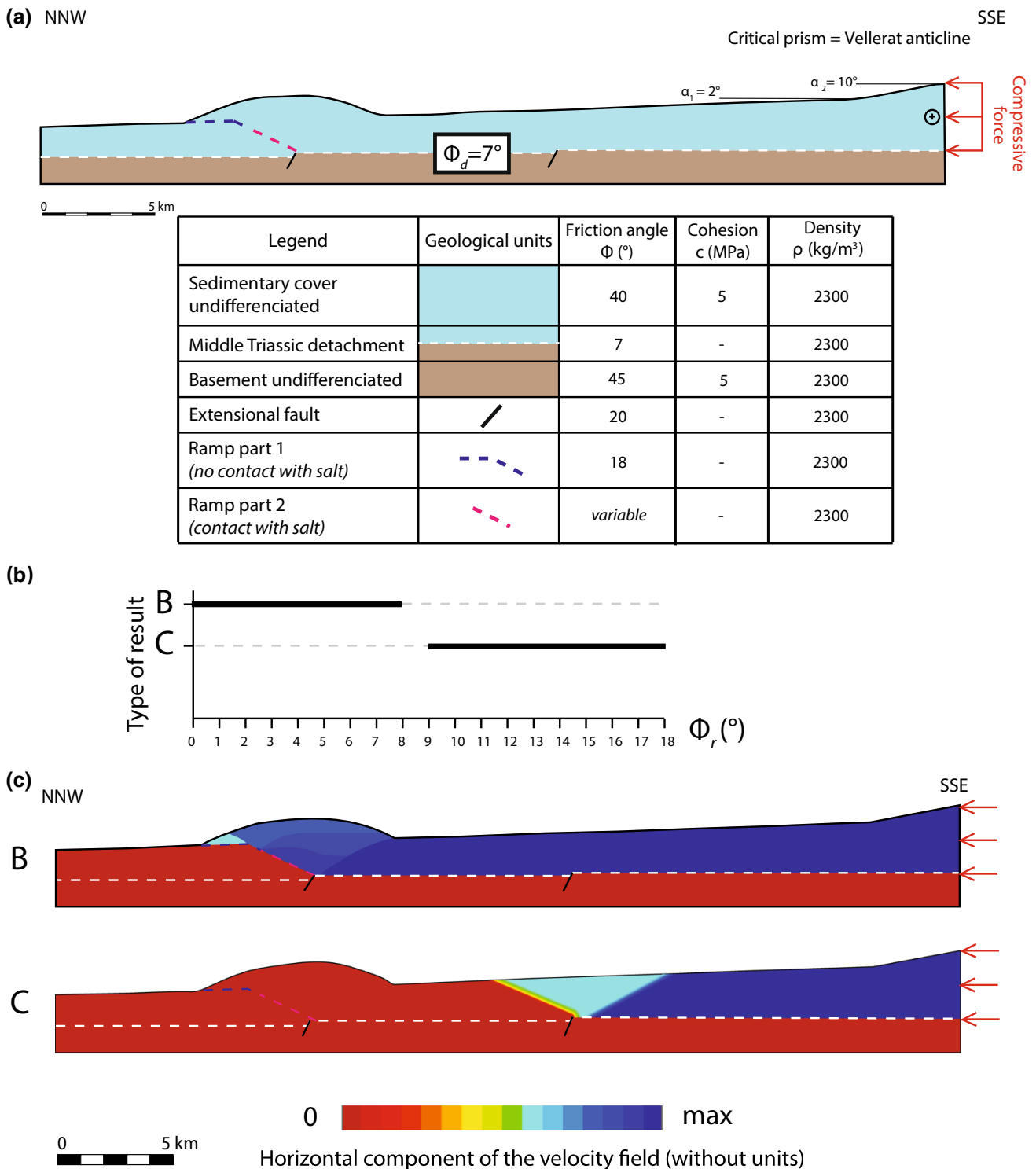


Fig. 13 Results of the second geo-mechanical experiment: emplacement of the Clos-du-Doubs Caquerelle structure by abandonment of the Mont Terri ramp. **a** Same prototype as in Fig. 10 after about 2.5 km of shortening accommodated on the Mont Terri ramp. **b** Graph

of the results obtained after applying a compressive force on the southern wall depending on the friction angle on the part of the ramp in contact with the Triassic evaporites. **c** Illustration of the different results obtained and presented in (b)

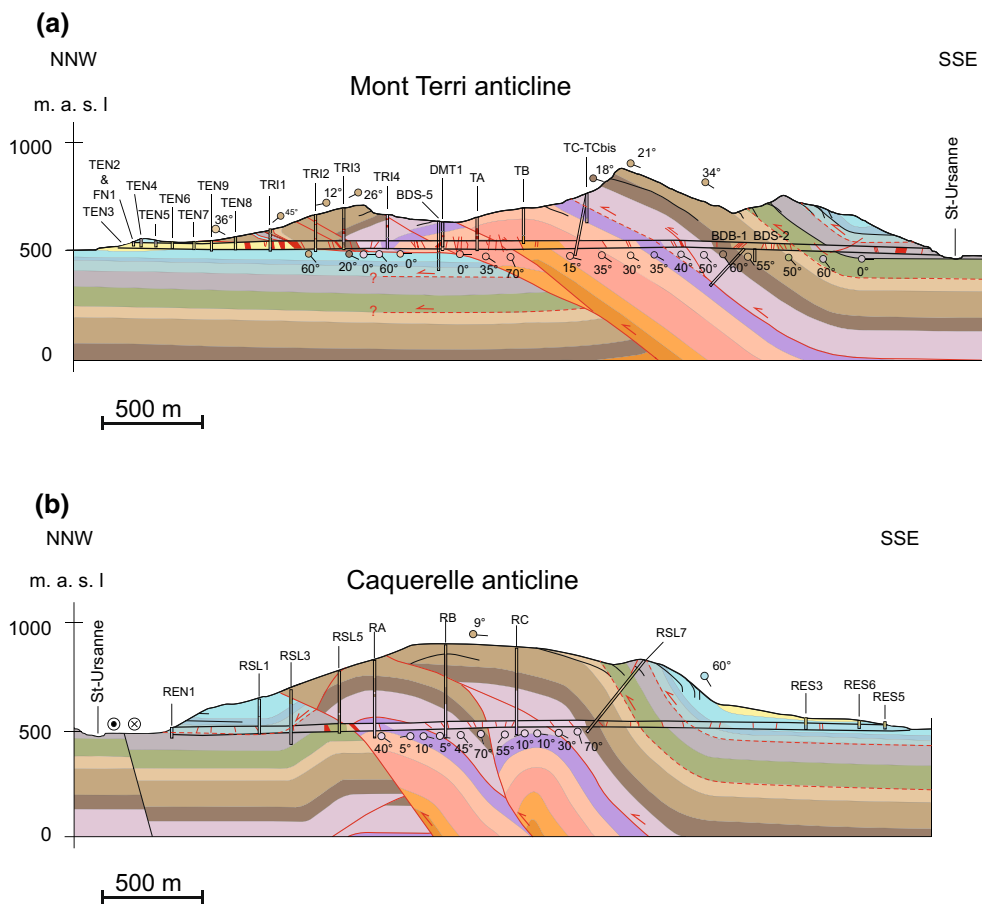


Fig. 14 Comparison of observed and forward modelled geometry, showing superposition of the tunnel, borehole and surface data (refer to Fig. 5) onto the forward modelled section shown in Fig. 10

Haute-Chaîne Folded Jura require attention and are here tentatively correlated with upper detachment levels. We suspect that any duplications are laterally controlled, segmented, and limited by NNE-trending faults or ENE-trending towards the Jura front. This may open the field for additional forward modelling. Finally, the integration of earthquake data and analysis of focal mechanisms in the forward models will help to constraint them by checking if the spatial distribution of the recent seismicity correlate with the thrusts. Both models show that subtle relationships with pre-existing basement structures might have interfered in time and in space. Both may have played a role, with lateral variation being most important.

7 Conclusions

Combining the available geological data collected in the Mont Terri and Mont Russelin tunnels, reconnaissance boreholes, cross section area balancing techniques, and kinematic forward modelling, we propose a sequential kinematic model of the region around the Mont Terri rock laboratory. Our preferred model is based on the classical

interpretation along two distinct profiles involving the basal detachment within the Triassic evaporites as single décollement. This model is in good agreement with the available subsurface data. We also present an alternative model using multiple detachments: within the Triassic evaporites (basal detachment) and within the Rietheim Member belonging to the top of the Staffelegg Formation (upper detachment).

7.1 Kinematic evolution

For both scenarios, the kinematic analysis suggests an early-stage formation of the Mont Terri anticline followed by back stepping of the deformation to the south with the development of wedges (classical scenario) or deep duplexes (alternative scenario), and finally the Caquerelle thrusts which developed out-of-section.

7.2 Structural style

In the classical scenario, both anticlines (Clairmont and Clos du Doubs) located south of the Mont Terri anticline

are interpreted as wedges composed of a major foreland-facing thrust rooting in the Triassic evaporites and a backthrust rooting in the top of the Staffelegg formation, pointing towards the importance of secondary detachments. This geometry may result from the early-stage formation of the Mont Terri anticline to the north, which may have influenced the deformation style in the hinterland. We interpret the thrust sequence obtained by forward modelling to indicate the presence of at least two different sets of inherited basement faults that might have acted as nuclei for the main ramps (Mont Terri and Caquerelle thrusts) and have triggered the formation of wedges (Clairmont and Clos du Doubs). The Mont Terri anticline is interpreted to have developed above ENE-trending faults of Late Palaeozoic origin that were subsequently reactivated during the Eo-Oligocene rifting phase associated with the opening of the Rhine and Bresse graben systems. In contrast, we interpret the Caquerelle thrust to have been triggered by an E-dipping, NNE-trending fault related to the opening of the Paleogene Upper Rhine Graben. The NNE orientation of Caquerelle anticline suggests an “in situ” formation above a pre-existing structure. The anticline axis is largely oblique with respect with the NNW-shortening direction, leading to lateral displacement of material, and making it impossible to balance the cross section.

In the alternative scenario, the Mont Terri anticline and Caquerelle thrust developed above deep duplexes composed of sub-Opalinus Clay formations, the Clos du Doubs anticline being one of them. Here again, we suggest that duplex ramps might have been triggered by inherited basement faults. We note that we have supposed these inherited basement faults, they have to date not been evidenced by any field data.

7.3 Shortening estimates

The forward model for the classical scenario reveals a total shortening of 2.9 and 1.7 km for the Mont Terri anticline itself. The cross section is not totally balanced due to the lateral displacement of the Caquerelle thrust and thus the total estimated shortening represents a minimum value. The shortening found for the Mont Terri anticline lies in the range estimated to be 2.1 and 1.3 km by Freivogel and Huggenberger (2003) and Caër et al. (2015), respectively. The forward model for the alternative scenario indicates a total shortening of 14.2 km, whereby only 2.9 km are needed to form the fault-bend folds of the Mont Terri and Caquerelle. Forward modelling suggests that material was transported 10.8 km along the upper detachment. Only a limited part of this shortening could be accommodated in-section further north in the Tabular Jura where some folding is observed. It is not clear where the main part of

the shortening might have been accommodated. This makes this scenario highly questionable.

7.4 Mechanical viability

We tested the mechanical viability of the thrust sequence scenario resulting from the kinematic forward modelling by applying the limit analysis mechanical approach to both the classical scenario with the basal detachment within the Middle Triassic evaporites and the alternative scenario with multiple detachments. We could validate the mechanical viability of the classic scenario. The mechanical viability of both the thrust angles and thrust sequence was demonstrated by applying the limit analysis theory. Preliminary results testing the alternative scenario show that the out-of-sequence thrust order requires lower friction along the Triassic detachment than on the Staffelegg detachment. At first glance, this is not consistent with the rheology. However, some additional factors, like fluid pressure, could have lowered the friction on the Staffelegg décollement. Their integration in the mechanical analysis would be an important improvement to better simulate the activation of the upper detachment, which was beyond the scope of this study.

Acknowledgements The authors would like to thank the Mont Terri Project Partners and especially swisstopo for their financial contribution. Both reviewers Jon Mosar and Urs Eichenberger provided useful comments and helped to improve the manuscript. Many geologists (i.e. David Jaeggi, Nicolas Badertscher, Herfried Madritsch, Andrea Lisjak) have contributed to the geological mapping of tectonic structures in the Mont Terri rock laboratory. We thank Caroline Hirsiger and Emilie Carrera for creating and improving the figures of this study, and Roy Freeman who did the English proofreading of the final version.

Open Access This article is distributed under the terms of the Creative Commons Attribution 4.0 International License (<http://creativecommons.org/licenses/by/4.0/>), which permits unrestricted use, distribution, and reproduction in any medium, provided you give appropriate credit to the original author(s) and the source, provide a link to the Creative Commons license, and indicate if changes were made.

References

- Allmendinger, R. W. (1998). Inverse and forward numerical modeling of trishear fault propagation folds. *Tectonics*, 17, 640–656.
- Becker, A. (2000). The Jura Mountains: an active foreland fold-and-thrust belt? *Tectonophysics*, 321, 381–406.
- Bergerat, F., & Chorowicz, J. (1981). Etude des images Landsat de la zone transformante Rhin-Saône (France). *Geologische Rundschau*, 70(1), 354–367.
- Bitterli, P. (2012). Die Ifenthal-Formation im nördlichen Jura. *Swiss Bulletin for Applied Geology*, 17(2), 93–117.
- Bläsi, H. R., Peters, T. J., & Mazurek, M. (1991). *Der Opalinus Clay des Mont Terri (Kanton Jura): Lithologie, Mineralogie und*

- physiko-chemische Gesteinsparameter*. Nagra Interner Bericht, 90-60, 44 pp. Nagra, Wettingen, Switzerland. www.nagra.ch.
- Bossart, P., Bernier, F., Birkholzer, J., Bruggeman, C., Connolly, P., Dewonck, S., Fukaya, M., Herfort, M., Jensen, M., Matray, J.-M., Mayor, J. C., Moeri, A., Oyama, T., Schuster, K., Shigeta, N., Vietor, T., & Wiczorek, K. (2017). Mont Terri rock laboratory, 20 years of research: introduction, site characteristics and overview of experiments. *Swiss Journal of Geosciences*, 110. doi:10.1007/s00015-016-0236-1 (this issue).
- Bossart, P., & Thury, M. (2008). *Mont Terri rock laboratory. Project, programme 1996–2007 and results*. Reports of the Swiss Geological Survey, No. 3, 445 pp. Federal Office of Topography (swisstopo), Wabern, Switzerland. www.mont-terri.ch.
- Boyer, S. E., & Elliot, D. (1982). Thrust systems. *American Association of Petroleum Geologists Bulletin*, 66, 1196–1230.
- Bureau Technique Norbert Geologues-Conseils SA. (1993). *Tunnel du Mont Terri Russelin—Dossier géologie après exécution*. Internal report.
- Bureau Technique Jean Norbert Geologues SA, Frutiger, J.-J., Schaaeren, G., & Neipp, S. (1992). *Tunnel du Mont Russelin—Notice d'accompagnement au profil géologique 1:5000 après exécution*. Internal report.
- Burkhalter, R. M. (1996). Die Passwang-Alloformation (unteres Aalénien bis unteres Bajocien) im zentralen und nördlichen Jura. *Eclogae Geologicae Helveticae*, 89(3), 875–934.
- Burkhard, M. (1990). Aspects of the large scale Miocene deformation in the most external part of the Swiss Alps (Subalpine Molasse to Jura fold belt). *Eclogae Geologicae Helveticae*, 83, 559–583.
- Butler, R. W. H., Tavarnelli, E., & Grasso, M. (2006). Structural inheritance in mountain belts: An Alpine-Apennine perspective. *Journal of Structural Geology*, 28, 1893–1908.
- Buxtorf, A. (1907). Zur Tektonik des Kettenjura. Berichte über die Versammlungen des Oberrheinischen. *Geologischen Vereins*, 40, 29–38.
- Caër, T., Maillot, B., Souloumiac, P., Leturmy, P., Frizon de Lamotte, D., & Nussbaum, C. (2015). Mechanical validation of balanced cross sections: The case of the Mont Terri anticline at the Jura front (NW Switzerland). *Journal of Structural Geology*, 75, 32–48.
- Cederboom, C. E., van der Beek, P., Schlunegger, F., Sinclair, H. D., & Oncken, O. (2011). Rapid extensive erosion of the North Alpine foreland basin at 5–4 Ma. *Basin Research*, 23(5), 528–550.
- Chapple, W. M. (1978). Mechanics of thin-skinned fold-and-thrust belts. *Geological Society of America Bulletin*, 89, 1189–1198.
- Comment, G., Ayer, J., & Becker, D. (2011). Deux nouveaux membres lithostratigraphiques de la Formation de Reuchenette (Kimméridgien, Ajoie, Jura Suisse)—Nouvelles données géologiques et paléontologiques acquises dans le cadre de la construction de l'autoroute A16 (Transjurane). *Swiss Bulletin for Applied Geology*, 16(1), 3–24.
- Dahlen, F. A. (1990). Critical taper model of fold-and-thrust belts and accretionary wedges. *Annual Review of Earth and Planetary Sciences*, 18, 55–99.
- Davis, D., Suppe, J., & Dahlen, F. A. (1983). Mechanics of fold-and-thrust belts and accretionary wedges. *Journal of Geophysical Research*, 88, 1153–1172.
- Deichmann, N. (1990). *Seismizität der Nordschweiz, 1980–1988, und Auswertung der Erdbebenserien von Günsberg, Läuelfingen und Zeglingen*. Nagra Technischer Bericht, 90-46, 90 pp. Nagra, Wettingen, Switzerland. www.nagra.ch.
- Erslev, E. A. (1991). Trishear fault-propagation folding. *Geology*, 19, 617–620.
- Freivogel, M., & Huggenberger, P. (2003). Modellierung bilanzierter Profile im Gebiet Mont Terri-La Croix (Kanton Jura). In P. Heitzmann & J.-P. Tripet (Eds.), *Mont Terri Project-geology, paleohydrology and stress field of the Mont Terri region* (pp. 7–44). Federal Office for Water and Geology (FOWG), Geology Series, No. 5, 319 pp. www.mont-terri.ch.
- Giambiagi, L. B., Alvarez, P. P., Godoy, E., & Ramos, V. A. (2003). The control of pre-existing extensional structures on the evolution of the southern sector of the Aconcagua fold and thrust belt, southern Andes. *Tectonophysics*, 369, 1–19.
- Gonzalez, R., & Wetzell, A. (1996). Stratigraphy and paleogeography of the Hauptrogenstein and Klingnau Formations (middle Bajocian to late Bathonian), northern Switzerland. *Eclogae Geologicae Helveticae*, 89(2), 695–720.
- Guellec, S., Mugnier, J., Tardy, M., & Roure, F. (1990). Neogene evolution of the western Alpine foreland in the light of ECORS data and balanced cross sections. *Mémoires de la Société géologique de France*, 156, 165–184.
- Gygi, R. A. (1969). Zur Stratigraphie der Oxford-Stufe (oberes Jura-System) der Nordschweiz und des süddeutschen Grenzgebietes. *Beiträge zur Geologischen Karte der Schweiz*, 136, 1–123.
- Hindle, D. (2008). How hard were the Jura mountains pushed? *Swiss Journal of Geosciences*, 101, 305–310.
- Homberg, C., Bergerat, F., Philippe, Y., Lacombe, O., & Angelier, J. (2002). Structural inheritance and cenozoic stress fields in the Jura fold-and-thrust belt (France). *Tectonophysics*, 357, 137–158.
- Hostettler, B., Reisdorf, A. G., Jaeggi, D., Deplazes, G., Bläsi, H. R., Morard, A., Feist-Burkhardt, S., Waltschew, A., Dietze, V., & Menkveld-Gfeller, U. (2017). Litho- and biostratigraphy of the Opalinus Clay and bounding formations in the Mont Terri rock laboratory (Switzerland). *Swiss Journal of Geosciences*, 110. doi:10.1007/s00015-016-0250-3 (this issue).
- Illies, J. H. (1981). Mechanism of Graben formation. *Tectonophysics*, 73, 249–266.
- Jaeggi, D., & Bossart, P. (2016). *Borehole BDS-5 near Derrière-Monterri, Courgenay, Switzerland*. Report of the Swiss Geological Survey No. 6. Federal Office of Topography (swisstopo), Wabern, Switzerland. www.mont-terri.ch. 189 pp.
- Jaeggi, D., Laurich, B., Nussbaum, C., Schuster, K., & Connolly, P. (2017). Tectonic structure of the “Main Fault” in the Opalinus Clay, Mont Terri rock laboratory (Switzerland). *Swiss Journal of Geosciences*, 110. doi:10.1007/s00015-016-0243-2 (this issue).
- Jordan, P. (1992). Evidence for large-scale decoupling in the Triassic evaporites of Northern Switzerland—An overview. *Eclogae Geologicae Helveticae*, 85, 677–693.
- Krabbenhøft, K., & Damkilde, L. (2003). A general non-linear optimization algorithm for lower bound limit analysis. *International Journal for Numerical Methods in Engineering*, 56, 165–184.
- Krabbenhøft, K., & Lyamin, A. V. (2014). Optum G2. *Optum Computational Engineering*. www.optumce.com.
- Krabbenhøft, K., Lyamin, A. V., Hjiat, M., & Sloan, S. W. (2005). A new discontinuous upper bound limit analysis formulation. *International Journal for Numerical Methods in Engineering*, 63, 1069–1088.
- Lacombe, O., Angelier, J., Byrne, D., & Dupin, J. (1993). Eocene-Oligocene tectonics and kinematics of the Rhine-Saone continental transform zone (Eastern France). *Tectonics*, 12, 874–888.
- Laubscher, H. P. (1961). Die Fernschubhypothese der Jurafaltung. *Eclogae Geologicae Helveticae*, 54, 221–280.
- Laubscher, H. P. (1963). *Erläuterungen zum Geologischen Atlasblatt “1085 St-Ursanne, 1:25'000”*. Basel: Schweizerische Geologische Kommission. Federal Office of Topography (swisstopo), Wabern, Switzerland.
- Laubscher, H. P. (1963). *Geologischer Atlas der Schweiz, Atlasblatt 40, 1085 St. Ursanne—Erläuterungen*. Basel: Schweizerische Geotechnische Kommission. Federal Office of Topography (swisstopo), Wabern, Switzerland. www.mont-terri.ch.

- Laubscher, H. P. (1972). Some overall aspects of Jura dynamics. *American Journal of Science*, 272, 293–304.
- Laubscher, H. P. (1973). Faltenjura und Rheingraben: zwei Grossstrukturen stossen zusammen. *Jahresberichte und Mitteilungen des Oberrheinischen Geologischen Vereins*, 55, 145–158.
- Laubscher, H. P. (1985). *The eastern Jura: Relations between thin-skinned and basement tectonics, local and regional*. Nagra Technischer Bericht, 85-53, 30 pp. Nagra, Wettingen, Switzerland. www.nagra.ch.
- Laubscher, H. P. (1987). Die tektonische Entwicklung der Nordschweiz. *Eclogae Geologicae Helveticae*, 80, 287–303.
- Laubscher, H. P. (1992). Jura kinematics and the Molasse Basin. *Eclogae Geologicae Helveticae*, 85, 653–675.
- Laubscher, H. P. (2003). Balanced sections and the propagation of décollement: A Jura perspective. *Tectonics*, 22(6). doi:10.1029/2002TC001427.
- Lyamin, A., Sloan, S., Krabbenhöft, K., & Hjiij, M. (2005). Lower bound limit analysis with adaptive remeshing. *International Journal for Numerical Methods in Engineering*, 63, 1961–1974.
- Madritsch, H., Schmid, S. M., & Fabbri, O. (2008). Interactions between thin- and thick-skinned tectonics at the northwestern front of the Jura fold-and-thrust belt (eastern France). *Tectonics*, 27(5), 1–31.
- Maillot, B., & Leroy, Y. (2006). Kink-fold onset and development based on the maximum strength theorem. *Journal of the Mechanics and Physics of Solids*, 54, 2030–2059.
- Marty, D. (2008). *Sedimentology, taphonomy, and ichnology of Late Jurassic dinosaur tracks from the Jura carbonate platform (Chevenez—Combe Ronde tracksite, NW Switzerland): Insights into the tidal-flat palaeoenvironment and dinosaur diversity, locomotion, and palaeoecology*. Ph.D. dissertation, University of Fribourg, Fribourg, Switzerland, 278 pp.
- Mosar, J. (1999). Present-day and future tectonic underplating in the western Swiss Alps: Reconciliation of basement/wrench-faulting and décollement folding of the Jura and Molasse basin in the Alpine foreland. *Earth and Planetary Science Letters*, 173(3), 143–155.
- Nussbaum, C., Amann, F., Aubourg, C., & Bossart, P. (2011). Analysis of tectonic structures and excavation induced fractures in the Opalinus Clay, Mont Terri underground rock laboratory (Switzerland). *Swiss Journal of Geosciences*, 104, 187–210.
- Pfiffner, O., Erard, P. F., & Stäubli, M. (1997). Two cross sections through the Swiss Molasse Basin (line E4–E6, W1, W7, W10). In O. A. Pfiffner, P. Lehner, P. Heitzmann, S. Müller, & A. Steck (Eds.), *Deep structure of the Swiss Alps, results of NRP 20* (pp. 64–72). Basel: Birkhäuser GmbH.
- Pflug, R. (1982). *Bau und Entwicklung des Oberrheingrabens (Erträge der Forschung)*. Darmstadt: Wissenschaftliche Buchgesellschaft.
- Philippe, Y. (1995). *Rampes latérales et zones de transfert dans les chaînes plissées: Géométrie, conditions de formation et pièges structuraux associés*. Ph.D. dissertation, Université de Savoie, Chambéry, France, 272 pp.
- Reisdorf, A. G., Wetzel, A., Schlatter, R., & Jordan, P. (2011). The Stafflegg formation: a new stratigraphic scheme for the Early Jurassic of northern Switzerland. *Swiss Journal of Geosciences*, 104(1), 97–146.
- Rotstein, Y., Schaming, M., & Rousse, S. (2005). Tertiary tectonics of the Dannemarie Basin, upper Rhine graben, and regional implications. *Internal Journal of Earth Sciences (Geologische Rundschau)*, 94, 669–679.
- Salençon, J. (2002). *De l'élastodéplasticité au calcul à la rupture*. Paris: Editions Ecole Polytechnique.
- Schaeren, G., & Norbert, J. (1989). Tunnels du Mont Terri et du Mont Russelin —La traversée des « roches à risques » : marnes et marnes à anhydrite. *Juradurchquerungen—aktuelle Tunnelprojekte im Jura. Mitteilungen der Schweizerischen Gesellschaft für Boden- und Felsmechanik*, 119, 19–24.
- Schori, M., Mosar, J., & Schreurs, G. (2015). Multiple detachments during thin-skinned deformation of the Swiss central Jura: a kinematic model across the Chasseral. *Swiss Journal of Geosciences*, 108, 327–343.
- Schumacher, M. E. (2002). Upper Rhine Graben: Role of preexisting structures during rift evolution. *Tectonics*, 21, 1006–1022. doi:10.1029/2001TC900022.
- Smit, J. H. W., Brun, J. P., & Sokoutis, D. (2003). Deformation of brittle-ductile thrust wedges in experiments and nature. *Journal of Geophysical Research*, 108(B10), ETG9-1.
- Sommaruga, A., & Burkhard, M. (1997). Seismic sections through the Alpine foreland—Jura Mountains. In O. A. Pfiffner, P. Lehner, P. Heitzmann, S. Müller, & A. Steck (Eds.), *Results of NRP 20—Deep structure of the Swiss Alps* (pp. 45–53). Basel: Birkhäuser GmbH.
- Souloumiac, P., Krabbenhöft, K., Leroy, Y., & Maillot, B. (2010). Failure in accretionary wedges with the maximum strength theorem: Numerical algorithm and 2D validation. *Computational Geosciences*, 14(4), 793–811.
- Souloumiac, P., Leroy, Y.-M., Krabbenhöft, K., & Maillot, B. (2009). Predicting stress in fault-bend fold by optimization. *Journal of Geophysical Research*, 114.
- Suppe, J. (1983). Geometry and kinematics of fault-bend folding. *American Journal of Science*, 283, 684–721.
- Suppe, J., Connors, C. D., & Zhang, Y. (2004). Shear fault-bend folding. In K. R. McClay (Ed.), *Thrust tectonics and hydrocarbon systems: AAPG Memoir 82* (pp. 303–323). Tulsa: American Association of Petroleum Geologists.
- Suppe, J., & Medwedeff, D. A. (1990). Geometry and kinematics of fault-propagation folding. *Eclogae Geologicae Helveticae*, 83, 409–459.
- Suter, M. (1978). Geologische Interpretation eines reflexionsseismischen W-E-Profiles durch das Delsberger Becken (Faltenjura). *Eclogae Geologicae Helveticae*, 71, 267–275.
- Swisstopo. (2011). *Digital elevation model swissALTI3D*. Federal Office of Topography (swisstopo), Wabern, Switzerland. www.swisstopo.ch.
- Swisstopo. (2012). *GeoCover-geological vector data*. Federal Office of Topography (swisstopo), Wabern, Switzerland. www.map.geo.admin.ch.
- Ustaszewski, K., Schuhmacher, M. E., & Schmid, S. (2005). Simultaneous normal faulting and extensional flexuring during rifting: An example from the southernmost Upper Rhine Graben. *International Journal of Earth Sciences*, 94, 680–696.
- Ustaszewski, K., & Schmid, S. M. (2006). Control of pre-existing faults on geometry and kinematics in the northernmost part of the Jura fold-and-thrust belt. *Tectonics*, 25, TC5003. doi:10.1029/2005TC001915.
- Ustaszewski, K., & Schmid, S. (2007). Latest Pliocene to recent thick-skinned tectonics at the Upper Rhine Graben—Jura Mountains junction. *Swiss Journal of Geosciences*, 100, 293–312.
- von Hagke, C., Oncken, O., & Evseev, S. (2014). Critical taper analysis reveals lithological control of variations in detachment strength: An analysis of the Alpine basal detachment (Swiss Alps). *Geochemistry Geophysics Geosystems*, 15(1), 176–191.
- Wetzel, A., & Allia, V. (2003). Der Opalinuston in der Nordschweiz: lithologie und Ablagerungsgeschichte. *Eclogae Geologicae Helveticae*, 96, 451–469.
- Ziegler, P. A. (1992). European Cenozoic rift system. *Tectonophysics*, 208, 91–111.

Tectonic structure of the “Main Fault” in the Opalinus Clay, Mont Terri rock laboratory (Switzerland)

David Jaeggi¹  · Ben Laurich² · Christophe Nussbaum¹ · Kristof Schuster³ · Peter Connolly⁴

Received: 11 April 2016 / Accepted: 9 December 2016 / Published online: 17 January 2017
© Swiss Geological Society 2017

Abstract Over the last 18 years we have extensively studied an intra-Opalinus Clay fault zone that crops out within the Mont Terri rock laboratory in NW-Switzerland. We performed micro- and macrostructural characterization on four outcrops of this so-called “Main Fault”, which crosscuts the entire Mont Terri rock laboratory. Combining detailed structural mapping, analysis down to the nanometer-scale, and geophysical investigations leads to a better understanding of fault zones within clay-dominated lithologies. The multi-scale, multi-technique approach that we applied in this study on four individual outcrops is critical for describing such a complex system. In these four outcrops, we differentiate five macroscopic structural elements of the Main Fault and have studied their occurrence and spatial distribution. In general, scaly clay, including S–C bands (S = “schistosité” = cleavage, C = “cisaillement” = shear parallel to shear zone boundaries) and microfolds, occurs in isolated, sharply bound lenses and in larger zones at the top and bottom of the Main Fault. A cm-

thin, continuous layer of gouge runs along the upper boundary of the fault zone. The non-scaly part shows rather low strain and consists of rhombohedral blocks of undeformed rock (horses), bound by slickensides. The μm -thin shear zones are considered to be elementary building blocks for the structural elements of the Main Fault. Direct comparison of the four studied outcrops to each other highlights the significant lateral variability of the Main Fault. In addition to a reduction in thickness from west to east, size and distribution of structural elements are highly variable. Correlation of these structural elements between closely spaced outcrops is not possible. Fortunately, the upper and lower boundary of the Main Fault, as well as thicker sheets of scaly clay, can be recognized using seismic attributes and thus yield indirect information about size and internal structure of fault zones in clay.

Keywords Mont Terri rock laboratory · Structural elements · Scaly clay · Microstructure · Clay gouge · p-wave velocity

Editorial handling: P. Bossart and A. G. Milnes.

This is paper #3 of the Monte Terri Special Issue of the Swiss Journal of Geosciences (see Bossart et al. 2017, Table 3 and Fig. 7)

✉ David Jaeggi
david.jaeggi@swisstopo.ch

¹ Federal Office of Topography swisstopo, Seftigenstrasse 264, 3084 Wabern, Switzerland

² Institute for Structural Geology, Tectonics and Geomechanics, RWTH-Aachen, Aachen, Germany

³ Federal Institute for Geosciences and Natural Resources BGR, Stilleweg 2, 30655 Hannover, Germany

⁴ CHEVRON, Rock Mechanics Team, Chevron ETC, 1500 Louisiana Street, Houston, TX 77002, USA

1 Introduction

The Mont Terri Project is an international research organisation, which aims to investigate and analyse the hydrogeological, geochemical and rock mechanical properties of the argillaceous Opalinus Clay Formation. This formation has been selected in Switzerland as the preferred host rock for the disposal of high-level radioactive waste. Furthermore its properties, described in detail in Bossart and Thury (2008) and Bossart et al. (2017), are ideal for experiments dealing with borehole integrity and CO₂ sequestration. Beside the inherent properties of the host rock, e.g. low permeability, high retention capacity for

radio-nuclides, and self-sealing of artificially induced fractures, faults and fault zones are important elements that might influence the evolution of a repository. Examples of large-scale fault settings in shales exist from studies of décollement zones of clay-rich accretionary prisms and tectonic mélanges: in the Barbados e.g. Housen et al. (1996), Labaume et al. (1997), and more recently in the Tohoku subduction zone e.g. Chester et al. (2013) and in the Alps e.g. Dielforder et al. (2015). Recent work focusing on the small-scale geometry and petrophysical properties of a fault zone in shale is available from the Tournemire site, e.g. Dick et al. (2016). These authors show that strain inferred from anisotropy of magnetic susceptibility indicate heterogeneous structural fabrics within the fault core. In the Opalinus Clay, faults and fault zones were investigated hydraulically by Marschall et al. (2004; 2005) who showed that permeability of faulted Opalinus Clay does not differ significantly from the undisturbed rock.

Faults and fault zones have a significant influence on the stability of galleries and the geometry of the excavation damaged zone (EDZ) (Yong et al. 2010; Thoeny 2014). The EDZ develops during the excavation of new galleries and is a zone where stress redistribution and subsequent rock convergence result in a network of unloading fractures. Geophysical investigations, e.g. ultrasonic measurements, have aided in the detection of high fault densities and fault zones (Schuster 2012). Further investigations have concentrated on macroscopic structure and the evolution of the faults and fault zones in the local and regional tectonic setting (Nussbaum et al. 2001, 2011). Recently, within the framework of the PS (Petrofabric and Strain) experiment, work focused on pore structure (Houben et al. 2013) and assessment of microscale to nanoscale characterisation of faults and fault zones. Laurich et al. (2014) found that the elementary building blocks of the Main Fault are thin localized shear zones of <4 μm width. They also found that with progressive deformation, number and density of slickenside shear surfaces increases, generating tectonically derived scaly clay and more homogeneous gouge. In all deformed elements of the Main Fault porosity is reduced compared to undeformed Opalinus Clay, resulting in local permeability barriers for pore water pressure dissipation. During the formation/activity of the Main Fault, such permeability barriers could have led to differential pore water pressures, which in turn could have controlled the evolution and distribution of structural elements.

The present study integrates the microstructural knowledge from the comprehensive work of Laurich (2015) with the macroscopic structure observed at the outcrop-scale (Nussbaum et al. 2001, 2011) in order to generate a synthetic geometrical model of a fault zone in Opalinus Clay. The final part of this study attempts to correlate the observed structural elements with ultrasonic

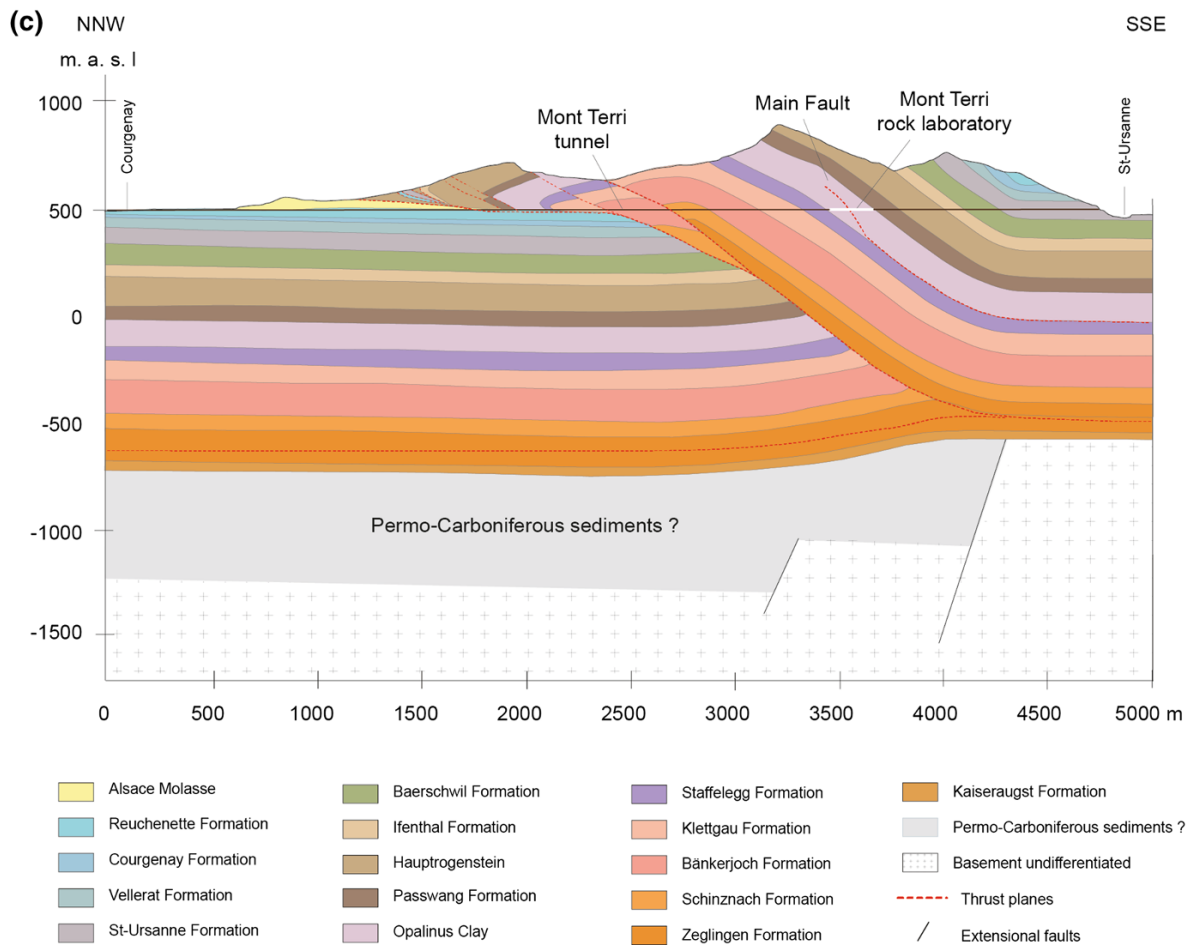
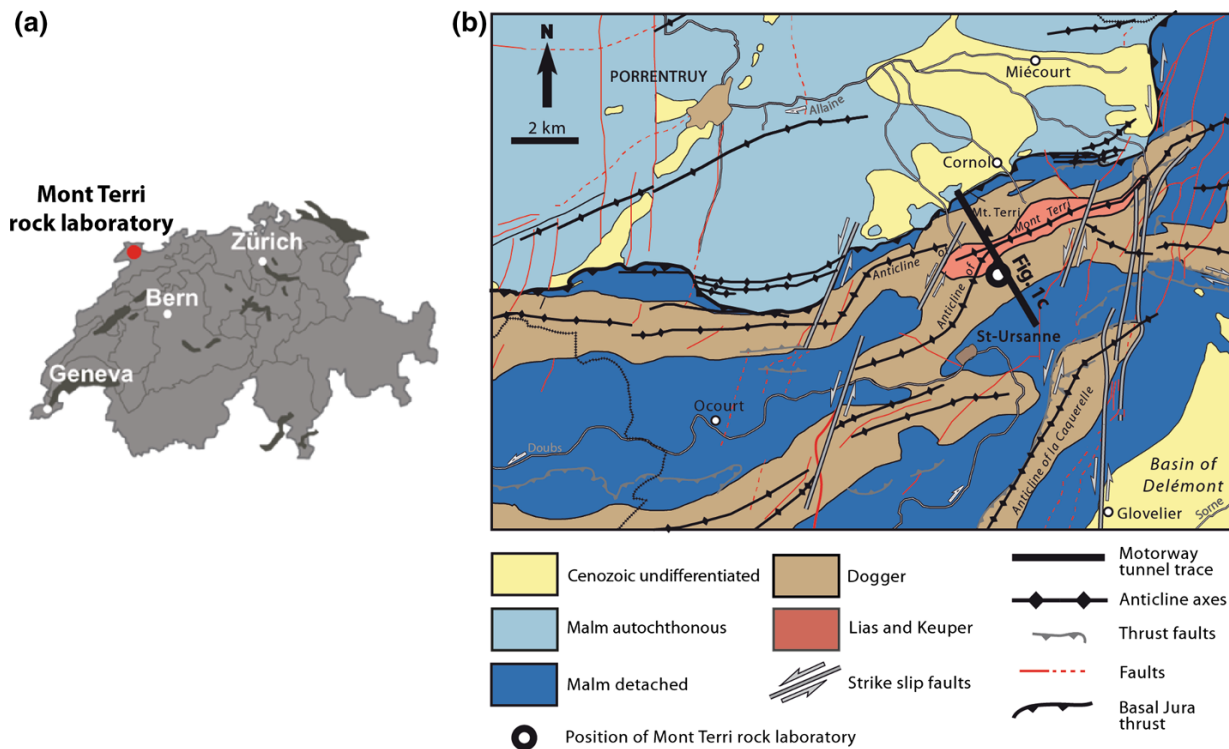
Fig. 1 **a** Location of Mont Terri rock laboratory, **b** tectonic overview of the Mont Terri area, **c** location of the Mont Terri rock laboratory on the geological cross section

and structural data from a borehole crossing the Main Fault close to one of the studied outcrops. Characterising the lateral variation and distribution of structural elements within a fault zone and recognising their signature on geophysical logs is critical for understanding overall rock-mass behaviour and repository evolution.

2 Geological setting

The Mont Terri rock laboratory is located in the Toarcian–Aalenian Opalinus Clay in the southern limb of the Mont Terri anticline about 300 m below the surface. The Opalinus Clay can be divided into a shaly facies, a sandy facies, and a carbonate-rich sandy facies (Blaesi et al. 1996; Bossart and Thury 2008; Hostettler et al. 2017) with varying contents of clay minerals, quartz, and carbonate. Bedding dips SSE between 50° in the southern part to 30° in the northern part. The anticline, which formed in the Late Miocene and Pliocene, is regarded as a fault-bend fold developed above a frontal ramp and features an overturned forelimb. This forelimb is affected by a complex pattern of thrust faults, extensional faults, and strike-slip faults (Nussbaum et al. 2011). The main detachment is located within the Middle Triassic evaporites; Zeglingen Formation (Fig. 1). Towards the WNW, the fold axis is approximately perpendicular to the SSE > NNW principal horizontal stress direction, present during the Middle Miocene Jura thrusting phase. Towards the WSW, the anticline bifurcates into two anticlines, of which the northern branch is intersected by a sinistral strike-slip fault. The two branches form a lateral or oblique ramp towards the west. Three major fault systems are present in the Mont Terri rock laboratory: SSE-dipping faults that run parallel or sub-parallel to the bedding, flat to SW-dipping faults, and steep N-NE-striking faults (Fig. 2).

The most prominent tectonic feature of the rock laboratory is the so-called Main Fault, a thrust fault located in the shaly facies of the Opalinus Clay with shear movement towards NNW. The Main Fault crosses the two galleries Ga08 and Ga98 at almost right angles (Fig. 2). These two galleries are trending SSE–NNW and are oriented approximately perpendicular to fold axis and strike of bedding. According to Nussbaum et al. (2011), the Main Fault zone consists of several architectonic elements: fault gouge, S–C bands (S = “schistosité” = cleavage, C = “cisaillement” = shear parallel to shear zone boundaries), meso-scale folds, microfolds, numerous fault planes, and apparently undeformed segments. The thickness of the fault zone varies laterally between 1 and 4.5 m.



Upper and lower fault boundaries dip 40° – 45° towards SSE in Ga08 and 50° – 55° towards SSE in Ga98. In the footwall of the fault, mainly subhorizontal fault planes are present, whereas SW-dipping faults are found in the hanging wall. For more detailed information about the geological context the reader is referred to Nussbaum et al. (2011) and Hostettler et al. (2017).

3 Materials and methods

3.1 Structural mapping of outcrops

We investigated the outcrops by structural small-scale mapping. Mapping was aided by applying a grid overlay to each exposure. The size of the grid elements ranged from 1.0 to 0.2 m depending on the exposure's surface area (size). Before mapping, the rock surface was carefully cleaned of dust and shotcrete patches. We photographed the entire outcrop surface and directly marked structural features on the photos. For easier comparison of size,

variability and distribution of structural elements, the outcrop images are all presented at the same scale and are viewed from SW to NE. Thus, outcrops on the eastern side of the gallery are viewed from the gallery (“view towards rock”) and outcrops on the opposite, western, side of the gallery are viewed from within the rock (“view towards gallery”). Their maps are, by necessity, horizontally mirrored. The outcrops on opposite sides of a gallery are 4 m apart and the two galleries Ga98 and Ga08 are 40 m apart.

3.2 Microscopic analysis

We extracted resin-stabilized drillcores and hand specimens from the different outcrops of the Main Fault. Exact sampling locations and detailed descriptions of the applied methods are given in Laurich et al. (2014) and Laurich (2015). Samples were investigated by optical and scanning electron microscopy (SEM) in surface (i.e. looking on the fault plane) and section views. Samples were split along slickensides, cut by hand, polished and water-immersed for 2 s. Water immersion results in a fine decoration of the

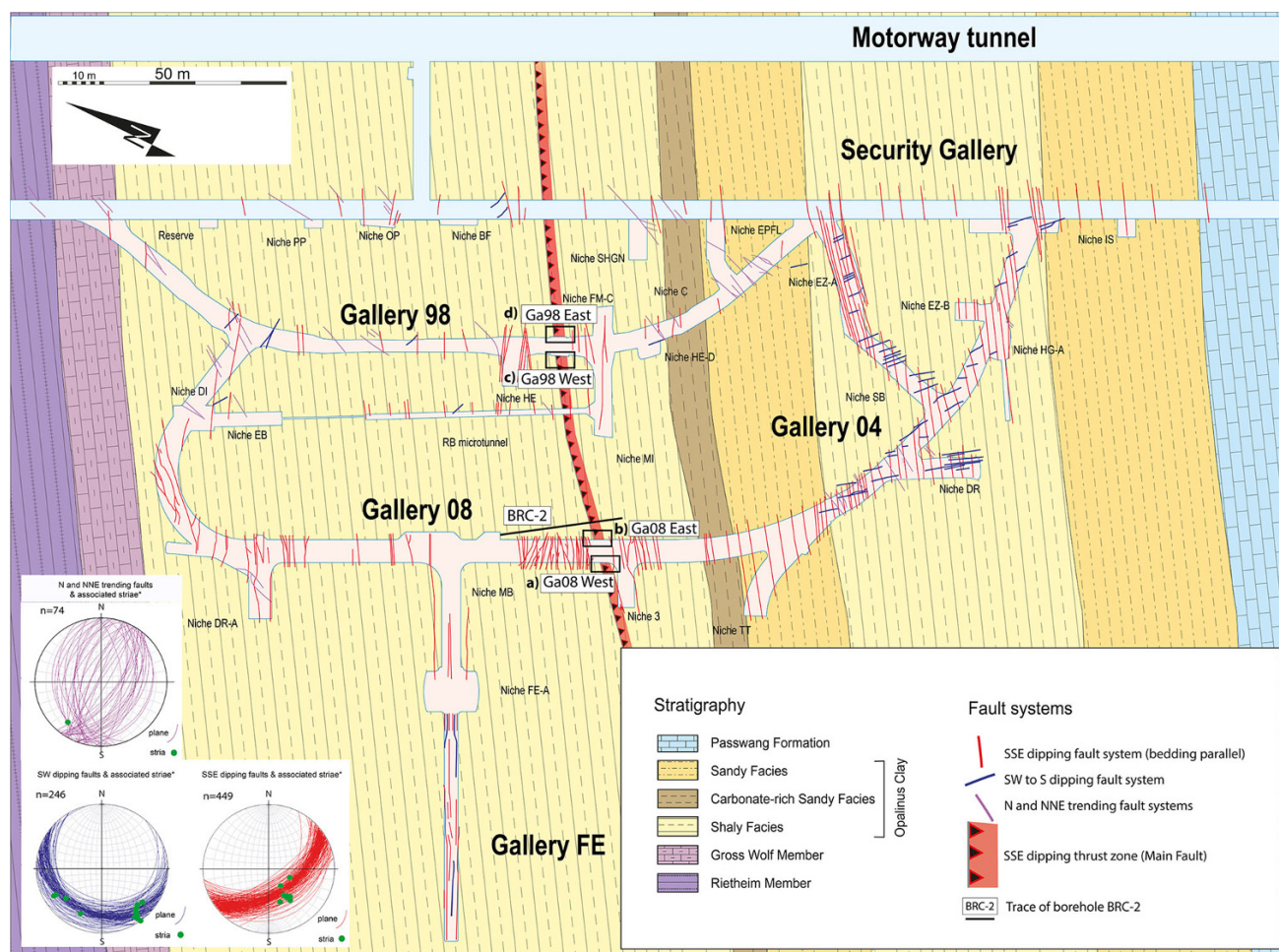


Fig. 2 Horizontal view of the Mont Terri rock laboratory with locations of the four investigated outcrops *a–d* and the trace of borehole BRC-2

foliation by the swelling clay matrix and thus helps to highlight fine structures. Ultra-thin sections followed by hand-polishing were produced. Finally, broad-ion beam polishing (BIB) and cutting transmission electron microscopy (TEM) lamellae by focused ion beam (FIB) were the methods used to investigate the microstructure.

3.3 Seismic characterization of fault zones by means of ultrasonic measurements

Continuous single-hole ultrasonic interval velocity measurements (IVM) were performed in borehole BRC-2 immediately after drilling. A BGR mini-sonic probe was utilized as shown in Fig. 3a. The centre frequency of the emitted signal was 50 kHz. The probe consists of four linearly distributed piezoelectric transducers. One transducer is used as the seismic source with the remaining three used as receivers at distances of 10, 20 and 30 cm from the source. Coupling of the transducers at the borehole wall was done using pneumatic cylinders. Measurements were conducted from top to bottom of the borehole and located at intervals of 10 cm. The borehole was oriented horizontally with an azimuth of 144°, consequently cutting the bedding at an angle of 40°. Inside the borehole the tool was orientated at 3 o'clock, thus measuring horizontally into the borehole wall towards Ga08 (Fig. 2).

Seismic velocities and amplitudes derived from initial p- and s-wave arrivals were calculated according to travel-times and distances, assuming straight ray propagation (Fig. 3b, c). As an unavoidable result of the drilling, we had to take into account a borehole disturbed zone (BdZ) with radial velocity gradients (Schuster et al. 2017). Therefore, these velocities are treated as apparent velocities. Differences between these apparent velocities allow

calculation of a BdZ corrected V_p , which enables investigation of the region beyond the BdZ. The BdZ-corrected V_p represents the V_p of the intact rock. The extent of the BdZ can reach several cm (Schuster 2012). Additionally, we calculated elastodynamic parameters like dynamic Young's modulus via receiver R3 (30 cm distance) data, which are generally very close to the BdZ-corrected parameters.

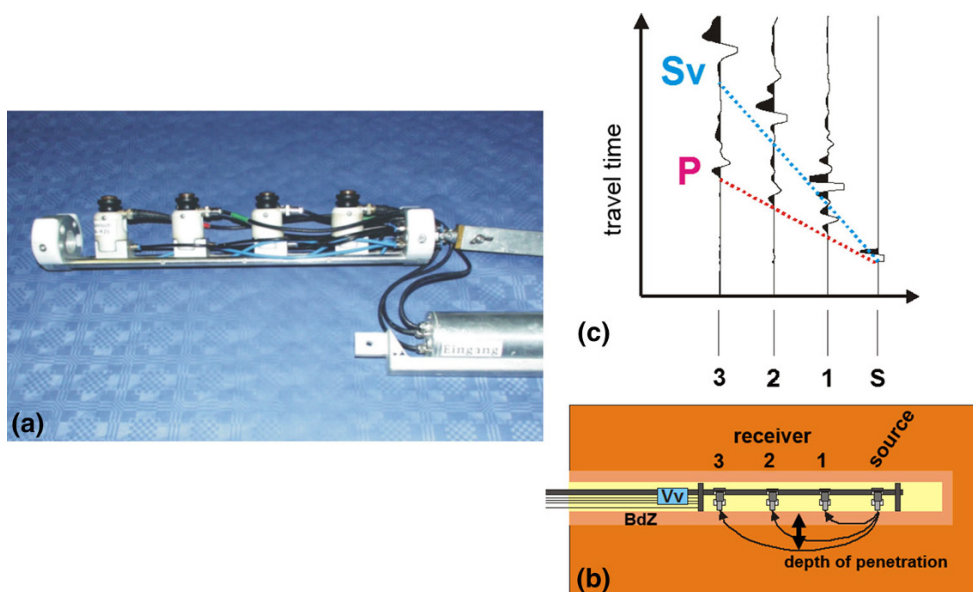
In the shaly facies of the anisotropic Opalinus Clay, V_p perpendicular to bedding is 2600 m/s and parallel to bedding 3400 m/s. With borehole orientation of BRC-2 perpendicular to the strike of the bedding and the tool measuring horizontally along the 40° dipping beds, a V_p of 2700 m/s is a good average value for undisturbed Opalinus Clay (Schuster et al. 2017). Any deviation from average values, is an indication of a change in elastic rock properties, such as micro- and macroscopic disturbances or damage, lithological changes and tectonised structures. Furthermore in strongly tectonised sections, such as scaly clay, the orientation of the foliation can change dramatically, which could in turn affect V_p .

4 Characteristics of the fault zones in the Mont Terri rock laboratory

4.1 Structural elements observed on the Main Fault and microscopic structure

Deformation in compacted clay sediments is usually localized in μm -thin shear zones and corresponding slickensides. Haines et al. (2013) describe the evolution of a thin shear zone with increasing shear. At the end of the linear part of the stress-strain curve, an echelon Riedel

Fig. 3 Principle of interval-velocity measurements (IVM). **a** BGR 4KUBS ultrasonic borehole probe, **b** seismic-ray propagation (schematic), **c** single shot section with P-wave arrivals (P) and vertically polarised shear-wave arrivals (S_v)



shears (R-shears) and shear-sense parallel Y-shears develop. These initially propagate towards the boundaries of the deformed layer and rotate further during post-peak stress or strain softening. During stable sliding at residual shear strength, where the material exhibits a perfectly plastic behaviour, a pervasive network of R-shears and Y-shears develops (Passchier and Trouw 1996). During further straining, the R-shears become undulatory and internal deformation occurs within the shear bounded packages. The rheology of shales appears to be scale dependent and thus phenomenological terms like “brittle” and “ductile” are a function of scale (Ismat 2013) and strain rate. Heterogeneities, such as larger pores or stiffer particles within the clay matrix act to localize early deformation. In the Opalinus Clay, fractures initiate mainly at grain boundaries and edges of coarse shell fragments (Klinkenberg et al. 2009). The mechanical behaviour of Opalinus Clay is strongly dependent on the content and distribution of bioclastic and detritic material. Furthermore, it is different for each lithofacies type. In the shaly facies, heterogeneities of bioclastic material act as nuclei for fracture growth and thus reduce the strength of the rock. In contrast, higher carbonate content in the sandy facies leads to increased rock-mechanical strength (Gschwind 2013). Laurich et al. (2014) found indicators for at least five different deformation mechanisms: (1) dissolution and precipitation creep, (2) rigid body rotation and particle sliding, (3) cataclasis, (4) intra-crystalline plasticity, and (5) new formation of clay minerals. In the next section, we describe the main structural elements observed in Opalinus Clay: isolated slickensides, gouges and scaly clay comprising microfolds, and S–C bands.

4.1.1 Slickensides (and thin shear zones)

Shiny, striated slickensided surfaces (sensu Blenkinsop 2000) occur especially in fault zones throughout the Opalinus Clay at Mont Terri (Fig. 2) and are present as smooth planar surfaces (Fig. 4a, b). Magnifications of up to 100 kx SEM show sub- μm to nm-sized clay particles aligned parallel to slickensides in section view (Fig. 4c, d). According to Clauer et al. (2017), chemical and isotopic analyses suggest that some of these clay particles can be interpreted as newly formed illite. The lateral extent of the slickensides ranges between μm and 1 m. Laurich (2015) presented eight slickenside kinematic indicators, such as different kinds of grooves, steps, and striae, all of which are consistent with a compressive regime. With increasing spatial frequency of slickensides, they become more curved and undulating, forming microfolds, S–C shear bands, and crenulation cleavage (sensu Passchier and Trouw 1996) in scaly clay aggregates. In section, slickensides are associated with μm -wide shear zones of parallel-aligned clay

particles (Fig. 4c, d). There, the shear zone internal porosity is drastically reduced when compared to the undeformed host rock.

Slickensides exhibit polished, dark, and shiny areas as well as more bright, ragged, and dull parts. These spatial variations are caused by variation in calcite content, which is low in restraining and high in releasing parts of the slickensided surfaces (Laurich et al. 2014; Laurich 2015). The latter manifest as risers of slickenside steps (Doblas et al. 1997), at which patches of calcite form (Fig. 4a). Occasionally slickensides and concentric growth patterns can be seen, indicating syntectonic calcite growth. Furthermore, aligned clay particles usually cover the calcite patches, suggesting movement along μm -shear zones made of clay, while the calcite forms in a crack-seal manner (Koehn and Passchier 2000). Despite the patches, calcite and, more rarely celestite veins are often associated with slickensides. Conversely, wide-aperture veins within the Main Fault are rare and crosscutting relationships are not observed. In addition to calcite precipitations, agglomerations of pyrite can be found along the shear zones. According to Laurich (2015), micron-wide shear zones (Fig. 4c, d) and nano particles on slickensides are common structures and shear zones probably initiated and evolved as en-echelon networks of shear fractures.

4.1.2 Fault gouge

Fault gouge is found in up to 2 cm-thick continuous bands along the upper boundary of the Main Fault. Furthermore, it occurs as less prominent thin discontinuous bands and lenses in other parts of the Main Fault, but always related to scaly clay (Fig. 4e, f). Fault gouge is known to accommodate high strain particularly in parts with high offset. In the Opalinus Clay, the dark colour of gouge compared to the host rock is conspicuous. Based on microscopic analysis Laurich et al. (2014) found that the darker colour originates from decreased calcite content, finer particle size, and reduced porosity (Fig. 4e). Polished and shiny slickensides are often present at the gouge-wall rock boundary. We also found slickensides within the gouge. If the gouge material is crushed, it disintegrates into a fine powder along a set of anastomosing and overlapping shear zones (Laurich et al. 2014). The gouge is clearly depleted in calcite compared to the host rock or the neighbouring scaly clay. This is in marked contrast to non-gouge slickensides, where calcite is present at risers. Inside the gouge a P-foliation pattern with high fabric intensity is present. Laurich et al. (2014) differentiated gouge with a high angle between P-foliation and shear-zone dip (type 1) from gouge with almost parallel angle between P-foliation and shear zone dip (type 2). Veins are rare inside the gouge but they also occur frequently along the gouge boundary.

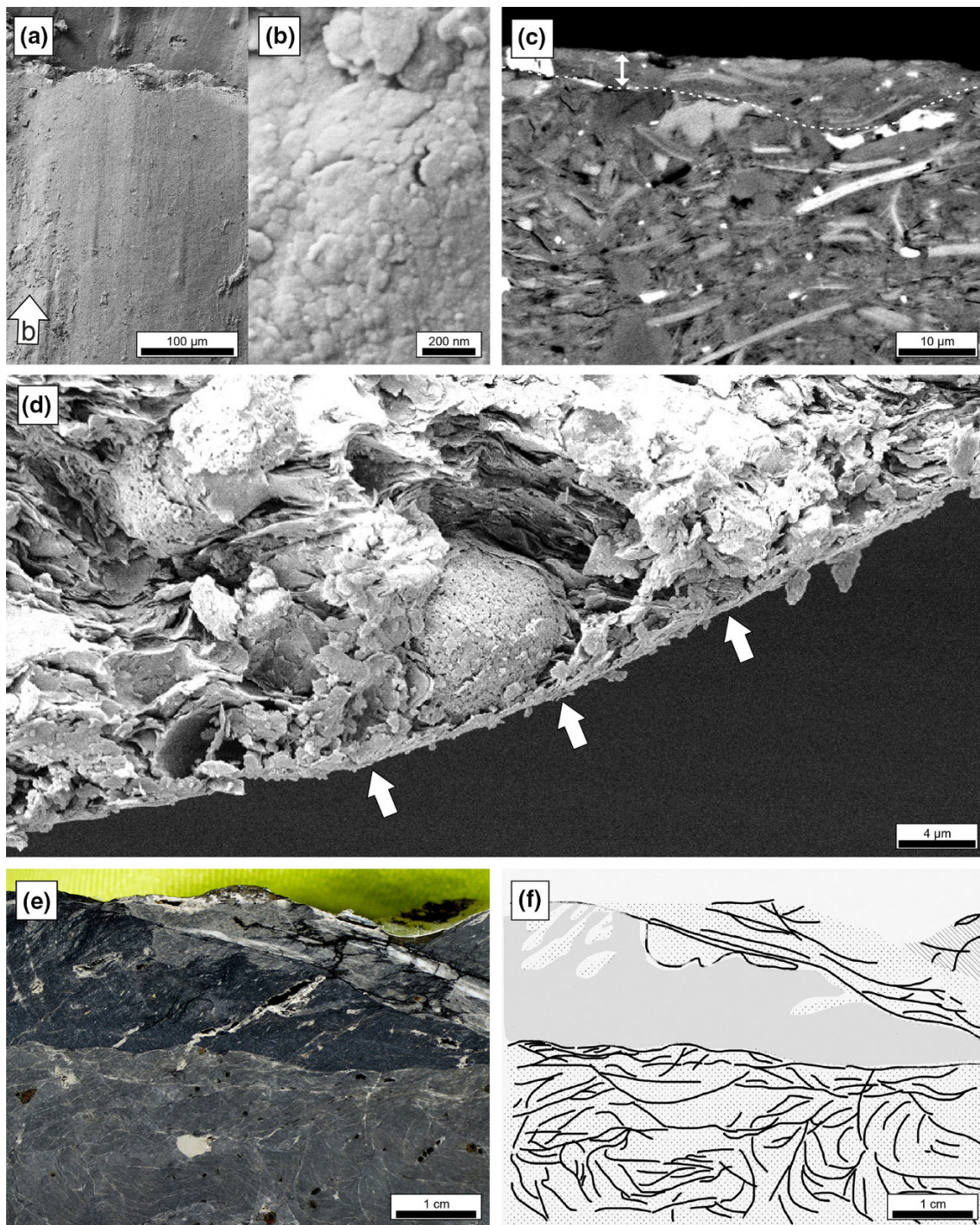


Fig. 4 a SEM micrograph of a polished surface with slickensides in top view. A slickenside riser perpendicular to shear direction can be seen in the upper part of the image with linear striae visible (arrow b) parallel to slip direction. b High-resolution SEM micrograph of a showing nm-wide, platy clay particles aligned parallel to the slickensided surface. c BIB-SEM micrograph of a μm -thin shear zone in side view (above dashed line). Note the shear zone-parallel alignment of clay minerals. Authigenic illite can be seen as thin curvy

fibres above the dashed line. Location of micrograph is given in Fig. 5d. d SEM image showing side view of a slickenside with a nano-sized thin band of clay particles (indicated by arrows), possibly authigenic illite. e Photograph and f sketch of a gouge band from the upper boundary of the Main Fault. The darker gouge is sharply separated by μm -thin shear zones from bordering scaly clay. Note the brighter clasts of scaly clay within the gouge. Dark lines in f are traced shears

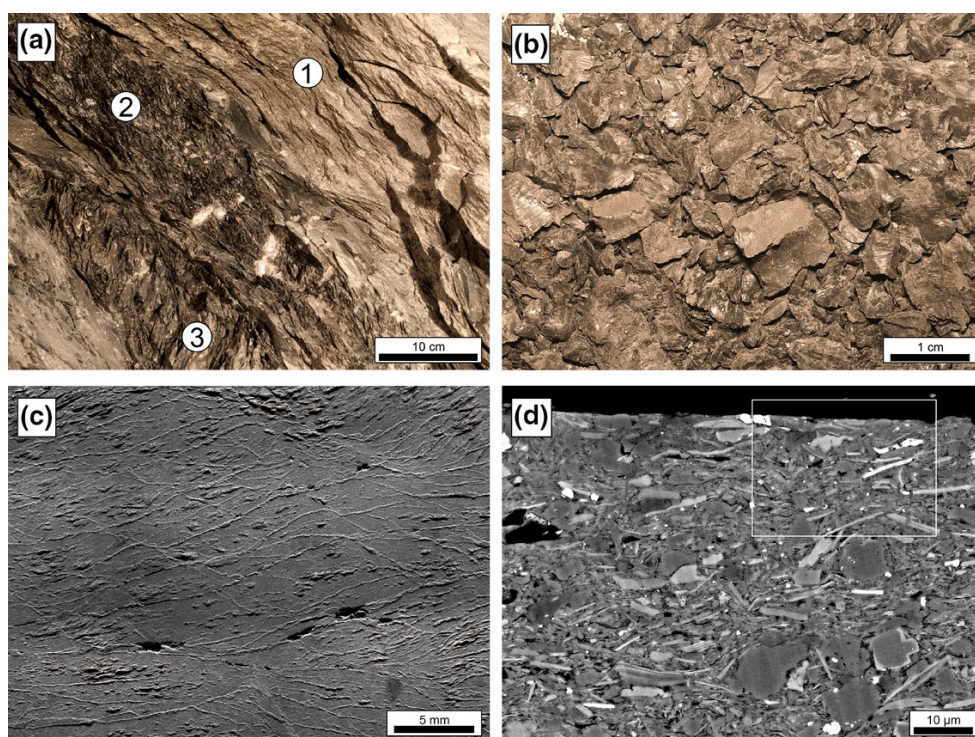


Fig. 5 **a** Photograph of outcrop in gallery 98, view direction towards ENE. 1 Mostly undeformed Opalinus Clay sectioned by solitary slickensides, 2 highly fissile scaly clay (=high degree of “scaliness”), 3 S–C band, width up to 10 cm. **b** Photograph of loose scaly clay microlithons with shiny polished surfaces. **c** Photograph of a water-

immersed sample showing the anastomosing shear-zone network that encapsulates microlithons of various sizes. **d** BIB–SEM micrograph of the internal structure of a microlithon. The fabric resembles that of undeformed shaly Opalinus Clay. White inset is shown in Fig. 4c

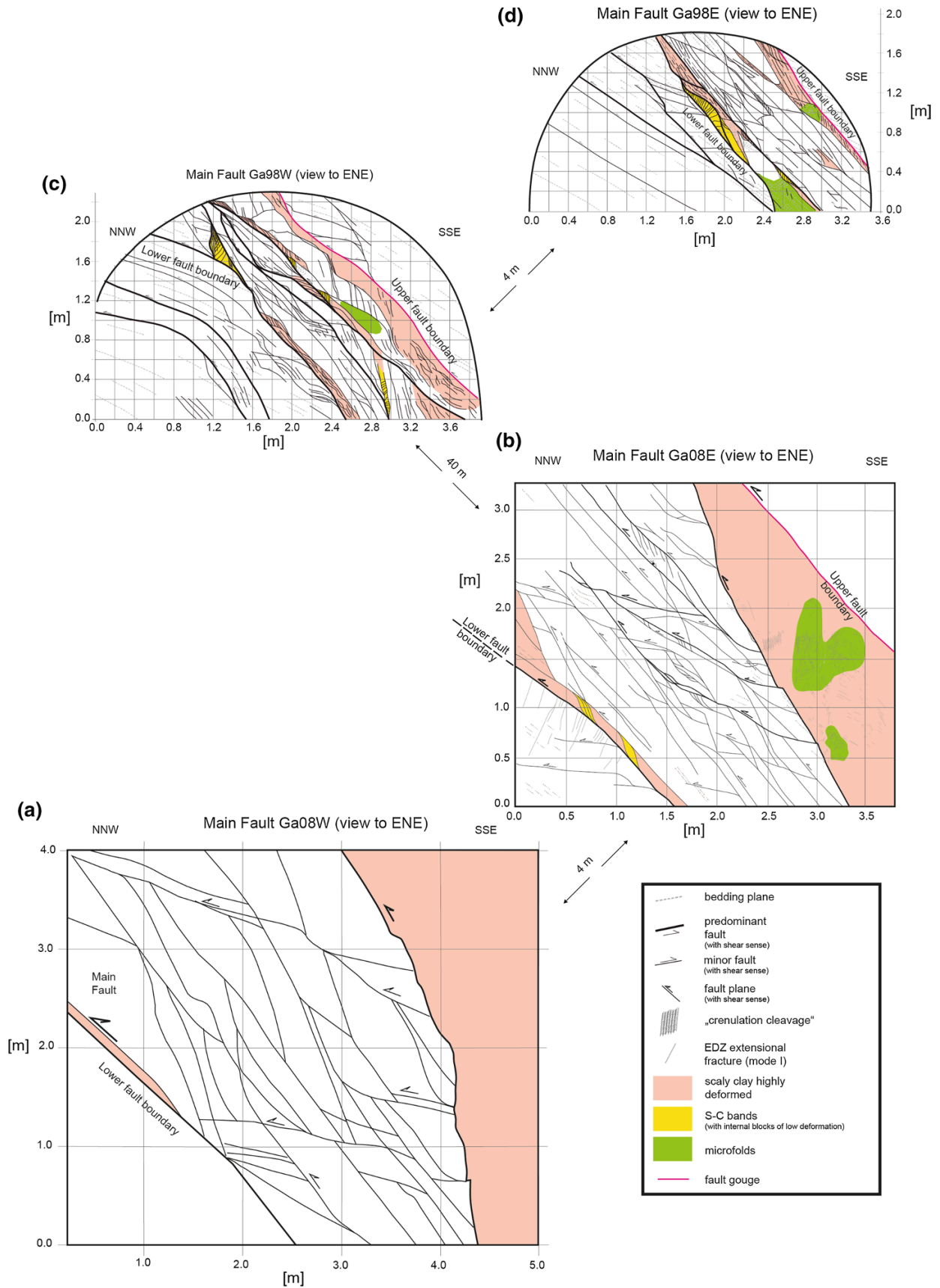
Laurich et al. (2014) analyzed 8 gouge samples with XRD. All samples revealed a significant reduction in calcite content, while all other mineral phases remain comparable to the host rock.

Gouge microstructures revealed indicators for cataclastic evolution accompanied by calcite pressure solution, strong particle reorientation, and formation of internal thin shear zones, presumably at later stages of gouge formation (Laurich et al. 2014). The occurrence of frequently healed and occasionally strained calcite veins in the surrounding of gouge indicates that during the evolution of the gouge, the deformation mechanism changed from purely frictional cataclasis to frictional-viscous pressure solution. The sharp boundaries of gouge are explained by intensive straining of the μm -thin shear zones that border the gouge, leading to abrasion and calcite dissolution of a thin layer of wall rock. We hypothesise that the decreased grain size within the gouge amplifies pressure-solution compared to the host rock (Gratier et al. 2014) and that the calcite re-precipitated as veins in the gouge surroundings. However, recent isotope analysis indicates that gouge-associated fluids might also have played a role in calcite dissolution (Clauer et al. 2017).

4.1.3 Scaly clay (microfolds, S–C bands)

Highly strained Opalinus Clay aggregates from the Main Fault can be broken by hand into progressively smaller lensoid flakes that are bound by shiny polished slickensided surfaces (Fig. 5b). This fabric is called scaly clay (sensu Vannucchi et al. 2003). According to Laurich (2015), it consists of a tangled, interconnected web of slickensides that bound largely unaltered microlithons (Figs. 4c, 5d). Thus, the scaly clay formed by finely distributed shear, leaving a ductile impression of microfolds and S–C bands at the macroscopic scale (Fig. 5a). The retrieval of scaly clay samples that maintain their integrity is difficult and rarely achieved. Within the rock mass, scaly clay is subjected to in situ stress, where at rock lab level sigma 1 is controlled by the overburden. Once samples of scaly clay are extracted from the rock mass, stress relief and desiccation lead to fast decomposition of the material. Subjected to the in situ stress, scaly clay, and fault zones in general exhibit a hydraulic permeability, which does not differ significantly from the host rock (Marschall et al. 2004).

Zones with scaly clay fabric range from 0.01 to 1 m thickness. Scaly clay aggregates are sharply separated from



◀**Fig. 6** Comparison of macrostructures observed at four different outcrops of the Main Fault. Views are drawn at the same scale and oriented the same way for comparison with fault dip from *upper left towards lower right*. **a** Main Fault Ga08W (view towards tunnel), note that upper fault boundary is just *above the right corner* behind shotcrete, **b** Main Fault Ga08E (view towards rock), **c** Main Fault Ga98W (view towards tunnel), **d** Main Fault Ga98E (view towards rock)

the non-scaly fault parts by μm -thin shears. The formation of scaly clay is interpreted as a product of continuous deformation within local relays of linking shear zones (Laurich 2015). Three macroscopically different appearances of scaly clay can be observed: (1) anastomosing fabric with branching shears mostly subparallel to the borders of the fault zone with internal rotation of bedding foliation (Fig. 5c), (2) S–C fabrics, where particle reorientation between two opposite single shears led to prominent sigmoidal structures (Fig. 5a), and (3) microfolds (Fig. 6b). Many of these S–C fabrics show internal rigid blocks with larger undeformed domains. Calcite veins are commonly present in scaly clay, occurring as intact, fractured and strained morphologies suggesting early to syn-tectonic vein precipitation. By means of $^{87}\text{Sr}/^{86}\text{Sr}$ isotopic analysis, Clauer et al. (2017) could show that some of the veins observed in Opalinus Clay formed before the development of the Mont Terri anticline. Furthermore, from studies of accretionary prisms it is known that the combined effects of compaction and calcite cementation in overpressured and mechanically weak rocks, such as a shale, can lead to coseismic formation of veins (Dielforder et al. 2015).

As discussed above, due to shearing, the thin shear zones are less porous, thus reducing porosity. In a rock with very low permeability, where on the short-term pore water cannot escape, further shearing leads to localized increase of pore water pressure. This localized pressure build-up can hypothetically be a cause for the development of a dense shear zone network, while in other parts of the Main Fault there is no scaly clay, even where the mineralogy is very similar.

4.2 Macroscopic structural description of the Main Fault in Ga08

4.2.1 Outcrop in Ga08 Western side (view towards tunnel)

The windowed exposure on the western side of Ga08 does not contain the entire Main Fault since the upper fault boundary is now behind shotcrete. Fortunately, the upper fault boundary can be extrapolated from neighbouring windows quite precisely to the upper SSE-corner of the main window (Fig. 6a). The rectangular window is 5 m wide and 4 m high. The approximately 4.5 m thick Main Fault covers about 85% of the window, showing scaly clay and a zone of isolated slickensides. The upper part mainly consists of scaly clay with anastomosing structures, with no clear signs of microfolding or S–C bands. This zone exhibits a thickness of more than 2 m and covers about 53% of the area of the entire Main Fault (Table 1). The lower boundary, towards the zone of isolated slickensides, shows a reduction in dip from bottom to top of the window from 80° to 60° , respectively. The lower part (47%) of the Main Fault in this westernmost outcrop consists of a broadly spanned network of slickensides building rhombohedral and internally undeformed blocks of 0.1–1 m size. This zone exhibits a thickness varying from 2 m at the lower part to 3 m in the upper part of the outcrop. The lower fault boundary has an average dip of 46° . In the NW-part of the lower boundary a 10 cm-thick non-continuous band of scaly clay is present.

4.2.2 Outcrop in Ga08 Eastern side (view towards rock)

The outcrop in Ga08 Eastern side is located about 4 m eastwards. The window covers an area of 3.8×3.3 m and shows the entire Main Fault. Lower and upper fault boundaries dip with 40° – 45° to the SSE. The beds in the hanging wall and the footwall dip less than the shear-zone boundary. The thickness of the Main Fault here is about 2.7 m, significantly less than on the western side of the gallery 4 m away. At the eastern exposure we differentiate

Table 1 Relative-area percentages of structural elements for the four different outcrops of the Main Fault in the Mont Terri rock laboratory

Outcrop	Fault zone width (m)	Scaly clay (incl. microfolds + S–C bands) (%)	Isolated slickensides (%)	Microfolds (%)	S–C bands (%)
Ga08 W	4.5	53	47	–	–
Ga08 E	2.7	42	58	5	1
Ga98 W	1.0	37	63	2	4
Ga98 E	0.9	20	80	4	3

The entire area of the Main Fault at individual outcrops is equal to 100%. Percentage of scaly clay area includes anastomosing scaly clay and the inherent zones of microfolding and S–C bands. For the outcrop in Ga08W, the non-visible part of the Main Fault was included in the total surface area for consistency

five structural elements (Fig. 6b). The upper fault boundary consists of a cm-thick gouge marking the sharp transition from undeformed host rock to highly deformed scaly clay. The fault gouge is continuous and the internal structure is macroscopically poorly visible. Further into the Main Fault, there is a 1–1.5 m-thick zone of scaly clay, which is separated from the lower part by a distinctive reverse fault. The internal structure of the scaly clay is mainly anastomosing, evidencing occasional regions of microfolds with folded axes. Microfolds compose approximately 5% of the entire Main Fault area in this exposure (Table 1). Crenulation cleavage is also present. The next lower 1.5–2 m of the Main Fault is characterised by 0.01–0.1 m-scale rhombohedral undeformed blocks bounded by single sinistral slickensides. At some locations the morphologies expressed resemble incipient S–C bands, with some P-shears. No scaly clay occurs in this section of the Fault. Below the intra-fault section adjacent to the footwall, the outcrop consists of a 10 cm-thick continuous band of scaly clay with a sharp transition to the undeformed footwall. Here, the scaly clay exhibits zones with sigmoidal shapes indicating S–C banding.

In summary, shear bands comprise less than 1% of the entire Main Fault surface. Scaly clay, including shear bands and microfolds, covers about 42% of the entire Main Fault surface and isolated slickensides building rhombohedral blocks cover about 58%.

4.3 Macroscopic structural description of the Main Fault in Ga98

4.3.1 Outcrop in Ga98 Western side (view towards tunnel)

This horseshoe-shaped outcrop has the most complicated internal structure of the Main Fault exposed in the Mont Terri rock laboratory. The outcrop is 3.9 m wide and 2.3 m high with the Main Fault zone approximately 1.0 m thick representing undulating upper and lower boundaries. The upper fault boundary dips at 45° whilst the lower one dips at 52°. The lower fault boundary appears to flatten out towards the NNW (Fig. 6c). Bedding in the footwall is less inclined (30°–35°) than in the hanging wall (42°–46°). The upper fault boundary is characterised by a cm-thick gouge that occurs on top of a continuous band of scaly clay. The thickness of this scaly-clay band varies between 5 and 20 cm. Internally, other than an anastomosing fabric, we detect no specific features. Below, there is a 60–70 cm-thick heterogeneous zone of undeformed, mostly rhombohedral, 0.01–0.1 m-scale blocks bound by slickensides. Two major internal faults sub-parallel to the fault zone boundaries and a third interconnecting fault are also present. Unlike the Ga08 exposure, scaly clay occurs within this central part and includes regions of microfolding and S–C bands. Scaly clay is mainly concentrated along the

internal major faults emphasising the importance of these internal major faults. Towards the footwall, the Main Fault zone is bordered by discontinuous scaly clay. In the upper left corner, a well-developed S–C band occurs, where the lower fault boundary bifurcates into two faults, one with a 20° dip and the other exhibiting 60° dip. This geometry is interpreted to result from the indentation of an undeformed wedge, which led to increased strain at the triple point and consequently the development of the S–C band. S–C bands comprise up to ca. 4% of the Main Fault area, and microfolds approximately 2% (Table 1). Scaly clay, including shear bands and microfolds, represents an area of 37%. The rest of the Main Fault consists of rhombohedral blocks bound by slickensides.

4.3.2 Outcrop in Ga98 Eastern side (view towards rock)

The horseshoe-shaped easternmost outcrop is 3.5 m wide and about 1.8 m high, has lower and upper fault boundaries with 55°–60° dip to the SSE and a thickness of the Main Fault of approximately 0.9 m (Fig. 6d). At the upper fault boundary there is a distinct cm-thick continuous fault gouge. Then, a max. 20 cm-thick zone of scaly clay occurs, generally with an anastomosing internal fabric and occasional regions of microfolding. In the lower right part of the scaly clay, slickensides with P-shear orientations are present, whereas in the upper part Y-shears seem to dominate. Below, a 50–60 cm-thick zone of isolated slickensides forming rhombohedral undeformed blocks of 0.01–0.1 m-scale occurs. At one location ($x/y = 2.5/1.2$ m), scaly clay from the upper part of the Main Fault branches into the zone of isolated slickensides. The scaly clay here encompasses a large internally undeformed block, which acted again as an indenter. At some other locations (e.g. $x/y = 3.1/0.5$ m) strain seems high enough for the formation of incipient scaly clay. The bottom part of the Main Fault comprises 20 cm-thick scaly clay. This band is interrupted by undeformed blocks. The region close to the undeformed footwall exhibits well-developed microfolds and a 0.8 m-long S–C band. This shear band has an internal structure with undeformed blocks (microlithons) bounded by sigmoidal slickensides. S–C bands and microfolds occupy 3 and 4% of the entire Main Fault, respectively (Table 1). Scaly clay, including microfolds and S–C bands, represents about 20% of the entire area. Rhombohedral blocks bound by isolated slickensides comprise the largest area of the fault.

4.4 Seismic parameter responses of fault zones in Opalinus Clay

Interval velocity measurements (IVM) react very sensitively to the occurrence and generation of microcracks (Schuster et al. 2017). Furthermore in strongly tectonised

sections, such as scaly clay, orientation of foliation and thus orientation relative to the anisotropic material can change dramatically, which could also affect V_p . We therefore assume that many of the structural elements identified within the Main Fault (scaly clay, shear bands, microfolds) modify this geophysical signal since they are small-scale discontinuities.

4.4.1 Borehole BRC-2

We analysed seismic responses (V_p , amplitude) along the BRC-2 borehole placing emphasis on the section crossing the Main Fault (Fig. 2). Borehole BRC-2 was drilled in April 2008 at GM94.5 along Gallery 08. The 131 mm-diameter borehole trends almost horizontally towards 152° with a slight dip of 1° . The 29.2 m long borehole crosses bedding at an angle of ca. 40° and is located ca. 3.5–4.0 m behind the Ga08E outcrop of the Main Fault. The Main Fault is encountered between drilling depths 18.3 and 21.5 m and has a dynamic Young's Modulus of $<5\text{GPa}$ and a fault frequency of 20 faults/m (Thoeny 2014). Intact Opalinus Clay in the direction of borehole BRC-2 typically has a V_p of 2700 m/s (Schuster et al. 2017). V_p along the BRC-2 borehole varies between 2500 and 2700 m/s corresponding in general to undisturbed rock with a maxima of 2800 m/s and minima of 1900 m/s. Thoeny (2014) and Baur (2014) correlated the minima to single faults or fault zones. The maxima could, however, at least partly be correlated to accumulations of carbonate sands, containing bioclastic material (mostly bivalve debris). Periodic decrease of V_p by several hundreds of m/s and over several m length could be related to an upwards decrease in carbonate particle size and abundance. It is known from other boreholes crossing the sandy or carbonate-rich sandy facies that V_p can reach values of 4500 m/s due to increased stiffness associated with mineralogy, different sedimentary fabric, and cementation (Schuster et al. 2017). In core material, detection of major fault zones is sometimes challenging and not always clear. However, direct correlation of the borehole to the large outcrop of the Main Fault in Ga08E, just 3.5–4.0 m apart, is a unique opportunity to study the seismic behaviour in fault zones in more detail.

4.4.2 Correlation of seismic parameters in response to structural elements

With the unique configuration of a borehole located close and sub-parallel to a well-described fault zone, more detailed analysis of fault structure and fault geometry is possible than from core description or optical borehole images alone. Figure 7 shows V_p and the common offset gather (COF) including travel times and colour coded amplitudes of borehole BRC-2 in comparison with the

structural map of the outcrop in Ga08E. Borehole BRC-2 is located about 3.5–4.0 m behind the outcrop at a projected level of about 2.1 m in the gallery. On core material and optical borehole imager, the Main Fault was encountered between 18.3 and 21.5 m depth. Two zones of scaly clay could be detected. A thin zone at the basis extends from 18.3 to 18.5 m and a second thicker one at the top of the Main Fault from 19.5 to 21.5 m. In the middle part, undisturbed blocks bound by single slickensides are present. Before considering V_p values, we note that BdZ-corrected V_p accounts for the stronger attenuation of V_p due to the enhanced pore space in the near field of the borehole. The corrected or improved V_p signal simultaneously allows for a higher penetration depth per time increment. Treated accordingly, the V_p signal of undisturbed Opalinus Clay yields values between 2400 and 2700 m/s at an angle of 40° between borehole and bedding planes. Between 18.3 and 18.5 m, a sudden decrease towards 2200 m/s is present. By investigating core material we were able to identify this as scaly clay that builds the lower fault boundary of the Main Fault. Below from 18.5 to 19.5 m single slickensides could be detected on core material, which yield a V_p of 2400 m/s. Then between 19.5 and 21.5 m, V_p is again mostly low, reaching values below 2000 m/s. On core material this zone can be attributed to a thick zone of scaly clay, which comprises the upper part of the Main Fault. On the COF the strong attenuation of the amplitude within these two zones of scaly clay is clearly highlighted (Fig. 7). At outcrop Ga08E, we can differentiate six different domains: undeformed foot- and hanging wall rock, scaly clay, S–C bands, microfolds, rhombohedral blocks bound by slickensides, and fault gouge. Scaly clay in the top part of the Main Fault of this outcrop is more than a metre thick and thus a prominent structural element. Furthermore, scaly clay of the lower fault boundary can also be identified clearly on IVM data. Microfolds, S–C bands, and gouges are too small and too patchy for reliable correlation to seismic responses.

Comparing borehole and outcrop data shows that fault boundaries and main structural elements can be correlated over a distance of 3.5–4.0 m. Within the Main Fault, the order of structural elements persists with a thin zone of scaly clay at the basis and a thick zone of scaly clay at the top with a separating zone of rhombohedral blocks in between, but their thicknesses varies considerably. Even though direct correlation of structural elements from an outcrop to a borehole located nearby seems to be simple, we note that the Main Fault features are highly non-planar. This is especially true for scaly clay, S–C bands, and microfolds. Patchy occurrence and lateral boudinage are quite common. A comparison of the Ga08E outcrop with the Ga08W outcrop (Fig. 6) shows the pronounced lateral variability that occurs along the Main Fault. Despite these restrictions, we

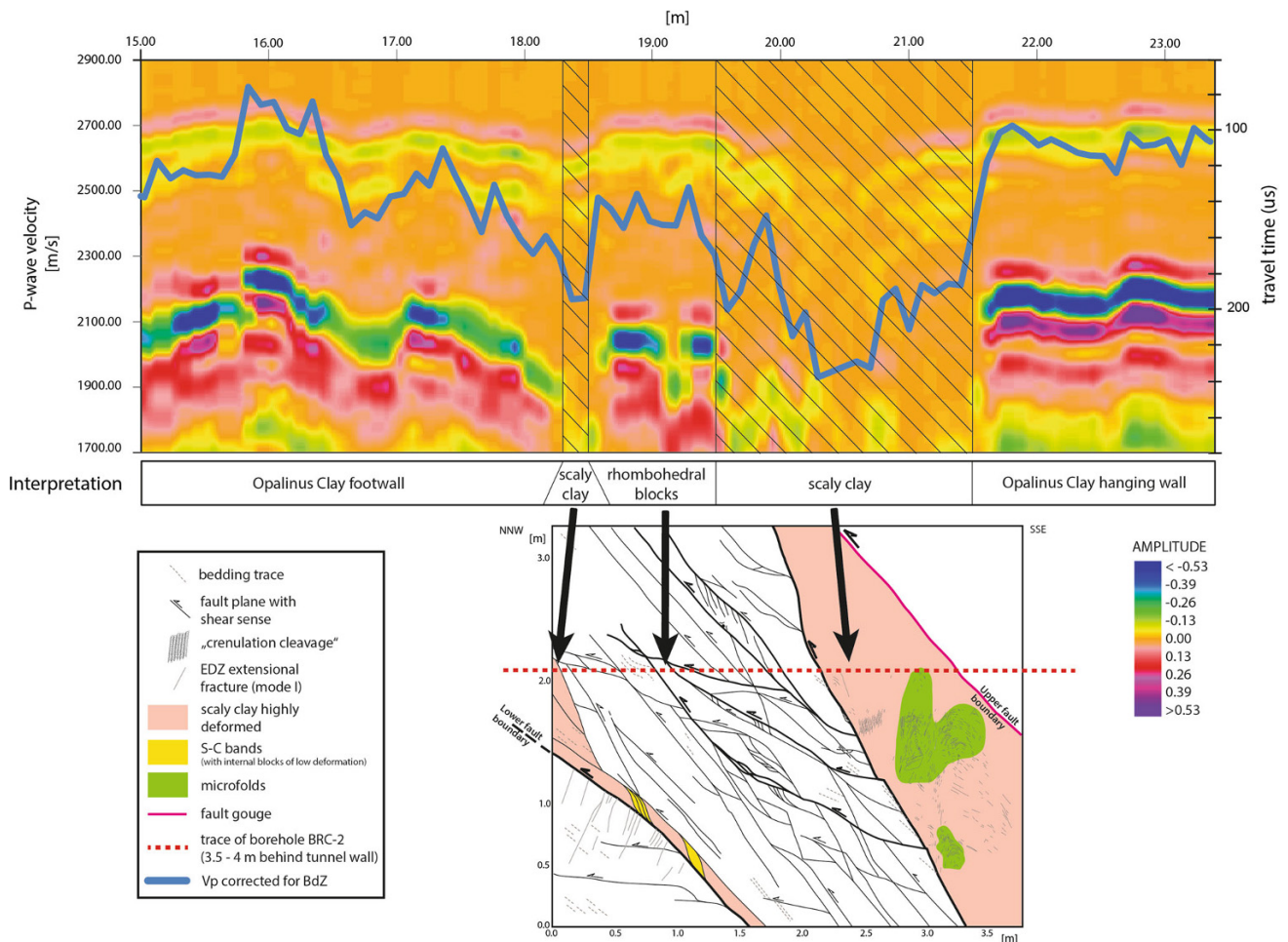


Fig. 7 Signal of BdZ-corrected Vp along trace of borehole BRC-2 correlated to structural elements of Main Fault Ga08E. The trace of BRC-2 is located ca. 3.5–4.0 m behind the tunnel wall. The BdZ-corrected Vp uses different emitter-receiver spacings, which represents

a larger depth of penetration (Vp on left vertical axis). Upper horizontal axis marks borehole metre of BRC-2. In the background, a common offset gather (COF) is given, showing traveltimes (us) on the right vertical axis and relative colour coded amplitudes

can make some important findings: Vp, normalised amplitudes and elastodynamic parameters within the Main Fault are clearly reduced compared to undeformed Opalinus Clay. Also, upper and lower boundaries of the Main Fault can be recognised on the ultrasonic log. Thick zones of scaly clay (>0.2 m) exhibit lower Vp than the zone of rhomboidal blocks bound by slickensides. Consequently, at least for the Main Fault in Ga08, resolution of the ultrasonic measurements is sufficient for detection of internal boundaries within the Main Fault structure.

5 Interpretation and discussion

5.1 Structural elements of the Main Fault

The four outcrops of the Main Fault in the Mont Terri rock laboratory exhibit five macroscopic structural elements characterizing this Opalinus Clay fault zone. These are (1)

scaly clay with (2) microfolds and (3) S–C bands, (4) gouge, and (5) rhomboidal blocks bound by slickensides. Slickensides are found in all the five structural elements and thus represent a major part of such fault zones. Slickensides are characterised by reduced porosity, aligned clay particles and patchy calcite as well as risers (Laurich 2015). Indicators of pressure solution are present at steps (e.g. truncated shell fragments).

Scaly clay is interpreted to be a product of continuous strain at geometrically locked positions, which occur within relays of two linking shears. Laurich (2015) showed that shear zone density increases with increasing strain. We observe no mineralogical change compared to the host rock. Scaly clay represents the highest strained parts of the Main Fault and occurs on all four outcrops especially at the upper and lower fault boundary. For the Main Fault, this geometrical occurrence of scaly clay at the fault boundaries implies that the fault core with highest strains is located at fault boundaries; whereas the central parts have

accommodated much less strain. Investigations performed on the Tournemire shale support this observation (Dick et al. 2016). Those authors reported that strain inferred from anisotropy of magnetic susceptibility measurements on a 1.5 m-thick fault zone indicated heterogeneous structural fabrics within the core of the fault zone. This core also exhibits subparallel, strongly deformed zones, such as gouge bands and scaly clay with isolated lenses of undeformed rock. A comparison of fault zone geometry between siliclastic sediments and siltstones yielded thinner deformation bands in the siltstones (Johansen and Fossen 2008). These authors furthermore reported that deformation bands, such as gouges or scaly clay, are unevenly distributed throughout the damage zone. At the outcrops in Ga98, scaly clay is present in the inner part of the fault. The abundance of scaly clay reduces gradually from the westernmost outcrop Ga08W (53%) to the outcrop Ga98E (20%). Table 1 clearly shows the correlation between thickness of the fault zone and areal coverage by scaly clay. The thinner the fault zone, the less abundant the scaly clay. This observation is somewhat contradictory for outcrops that are only 50 m apart and which should contain the same fault zone. Thus if similar strain rates or offsets for all four outcrops are assumed, the strain could, for instance, be more localized in the fault-gouge layers. Fault gouge might contribute differently to strain accommodation from one outcrop to the other. Alternatively, strain and total offset could decrease from western to eastern outcrops and partly be accommodated by rock matrix or by faults or fault zones parallel to the Main Fault. Different fault zone widths and area percentages of scaly clay suggest that (1) the major offset is accommodated by the thin gouge band leaving a highly variable macroscopic strain and (2) there are unrecognized, Main Fault parallel, fault zones in Ga98 that partly accommodate the offset. These deductions agree with observations in other galleries and boreholes where it is difficult to correlate the Main Fault over even short distances. At several locations in the rock lab (e.g. Gallery FE; Jaeggi et al. 2013) and in borehole BFE-E5 (Jaeggi et al. 2014), comparable fault zones with identical orientations and structural elements have been found, although it was impossible to correlate them laterally over larger distances. We postulate that fault zones in clay rocks exhibiting low stiffness and pronounced bedding anisotropy are inherently discontinuous and probably distribute offset along several parallel fault strands, each with a highly variable internal structure. At this larger scale, clay/shale fault zones probably have similar internal structures compared to those observed within the Mont Terri Main Fault, i.e. they consist of higher and lower-strained regions bounded by slickenside-dominated shear surfaces.

Scaly clay includes *S-C bands* and *microfolds*. Comparing the four outcrops shows that with reducing thickness

of the fault zone, complexity of internal structure increases. In contrast, scaly clay in Ga08W exhibits only an anastomosing network of slickensides. We can detect no preferred orientation of the shears. Microfolds and *S-C bands* are present in the thinner exposures further east. Laurich (2015) showed that scaly clay internal microlithons are largely undeformed. Generally, scaly clay and its associated microfolds and shear bands occur at the upper and lower boundary of the fault zone. The Ga98W exposure presents an exception, where these structural elements are present within the central zone of rhombohedral blocks bound by slickensides. This exposure has three major internal faults subparallel to the Main Fault boundaries, and the internal structure is much more undulating, where it is difficult to determine the lower fault boundary. We postulate that the undulating behaviour together with the internal major faults parallel to the boundaries led to geometric locking with subsequent strain concentrations at internal locations. This enabled the formation of scaly clay and associated deformation structures.

Fault gouge is associated with the scaly clay and is commonly located at the upper boundary of the Main Fault (hanging wall) with highest strain occurring in very narrow bands. Microscopic investigations by Laurich (2015) have shown that the dark colour of the gouge results from grain size reduction, reduced porosity, and calcite depletion. Veins inside the gouge are rare, but occur frequently along gouge boundaries. This could indicate that gouge acts as a low permeability zone (permeability barrier) during formation of fault zones. Furthermore, Laurich (2015) demonstrated that these veins are frequently healed and occasionally strained, suggesting a frictional-viscous deformation mechanism assisted by pressure solution. Macroscopically, only fault gouges at the upper boundary of the Main Fault are mappable. Microscopically, gouge is also found in scaly clay samples far from fault zone boundaries (Laurich 2015).

In their work on the Barbados prism, Housen et al. (1996) proposed that most strain in the décollement has been accumulated by the volumetrically minor component of shear zones. We can confirm this statement at Mont Terri on a much smaller scale, where we observe the occurrence of a low area percentage of highly deformed scaly clay and gouge compared to zones of undeformed host rock within the Main Fault. At Mont Terri, the internal zones of the Main Fault are characterized by mostly undeformed *rhombohedral blocks* bound by μm -thick slickensides. A comparison of the different outcrops clearly shows reduction of block size from the largest in Ga08W towards those in Ga98. Furthermore, the area percentage of the zone with isolated slickensides clearly increases with decreasing thickness of the fault zone: 47% for Ga08W vs. 80% for Ga98E. The abundance of scaly clay in turn

decreases. This behaviour is not straightforward since the zone with blocks bound by slickensides accommodates much less strain than scaly clay. However, the reduction in block size with decreasing thickness of the fault zone can be explained by strain accommodated across a much thinner zone. We note that the mapping detail possible at Ga08W was less than for the other exposures, which could at least partly explain the larger block size of the internal zone.

Calcite veins, μm -shear zones, and gouge show decreased porosity and are thought to act as local seals during evolution of the fault zone (Laurich et al. 2014; Laurich 2015). In a rock with very low-permeability where on the short-term pore water cannot escape, further shearing leads to localized increase of the pore water pressure. An increase in pore-water pressure shifts the Mohr's stress circle to the left or towards failure at smaller normal stresses, favouring generation of new shears (Gudmundsson 2001). This localized pressure build-up can hypothetically cause development of a dense shear zone network, as for scaly clay (Vannucchi et al. 2003). Thus in parts of the Main Fault, these seals might have led to intra-fault pore pressure increase that finally caused formation of the complex anastomosing shear zone network of scaly clay. Laurich et al. (2016) propose a model to explain the progressive formation of a self-similar network of anastomosing thin shear zones during continuous deformation. According to these authors, evolution of the initial segments of the Main Fault can be explained by localized deformation that has interacted with slip along rotated bedding foliation. Due to fault geometry, geometric locking leads to stress concentrations, initiating new shear zones. Laurich et al. (2016) propose that these initial shear zone networks develop into fault segments, which coalesce during further fault movement. Such an evolution leads inevitably to the assumed heterogeneous strain distribution across the Main Fault. Based on our geometrical observations on the Main Fault with varying fault zone thickness and strain localization in structural elements such as gouge and scaly clay, we furthermore propose that geometric locking leads to microcracking and dilatancy, which provoked intermittent local pore pressure drops. During such pressure drops, lateral stress transfer across the undeformed rock matrix to domains out of the mapped Main Fault zone could have occurred. There again similar fault geometries could have developed at parallel fault strands initiated by bedding-parallel slip combined with rotation of bedding foliation.

P-wave velocity (V_p) of borehole BRC-2 can clearly be correlated to the internal structure of the Main Fault in Ga08. From 18.3 to 21.5 m V_p is consistently reduced with respect to undeformed Opalinus Clay (Fig. 7). The scaly clay at the lower fault boundary (footwall) leads to

a pronounced decrease of V_p and a change in the COF trace plot. Geophysical investigations can therefore resolve scaly clay of 20 cm thickness in borehole BRC-2, which probably is close to the theoretical upper limit of resolution. Rhombohedral blocks bound by slickensides are damping amplitude and decreasing seismic velocity when compared to the undeformed host rock. However, V_p is still higher than in scaly clay. It is not surprising that the thick zone of scaly clay with highest density of slickensides in various orientations exhibits the lowest seismic velocities. The anastomosing, uncemented structure attenuates ultrasonic waves, despite decreased porosity. In addition to mineralogy and cementation, fabric has a major influence on ultrasonic signals (Schuster et al. 2017). We postulate that thicker zones of scaly clay (>0.2 m) and rhombohedral blocks bound by slickensides can be detected and distinguished with ultrasonic measurement. Thus, under ideal circumstances these geophysical tools can resolve the internal structure of the Main Fault.

5.2 Generic block model of the Main Fault at Mont Terri

Macroscopic comparison of the four exposures combined with microscopic investigations by Laurich (2015) enables us to derive a generic model for the Main Fault of the Mont Terri rock laboratory. The block model shows the most important features of the Main Fault (Fig. 8). It is representative for the Main Fault in Ga08 and Ga98E. Ga98W is more complex with a slightly different spatial distribution of structural elements. Upper and lower fault boundaries are bound by structural elements, which probably accommodated most of the strain. The gouge at the top of the Main Fault is continuous. Microscopic investigations of different exposures of gouge have shown sharp boundaries with the host rock emphasising host rock abrasion and calcite dissolution in a μm -thin, gouge-bounding Y-shear. Two types of gouge have been found, differing in P-foliation angle. The type with P-foliation subparallel to the shear zone dip is inferred to represent a mature gouge, while the type with P-foliation oblique to the shear zone dip is interpreted as young gouge. In agreement with this interpretation, the latter type has more unreworked host rock clasts than the first type. Scaly clay is always adjacent to gouge, occasionally in aggregates as thick as 1 m. It is appealing to hypothesise that gouge has formed by ongoing deformation of the scaly clay. Apart from rather small regions of microfolds and S-C bands, anastomosing networks of shear zones dominate the internal structure of scaly clay. For all these structural elements, slickensides are the elementary building blocks. Except for the thick upper zone of scaly clay in Ga08, there is a much thinner

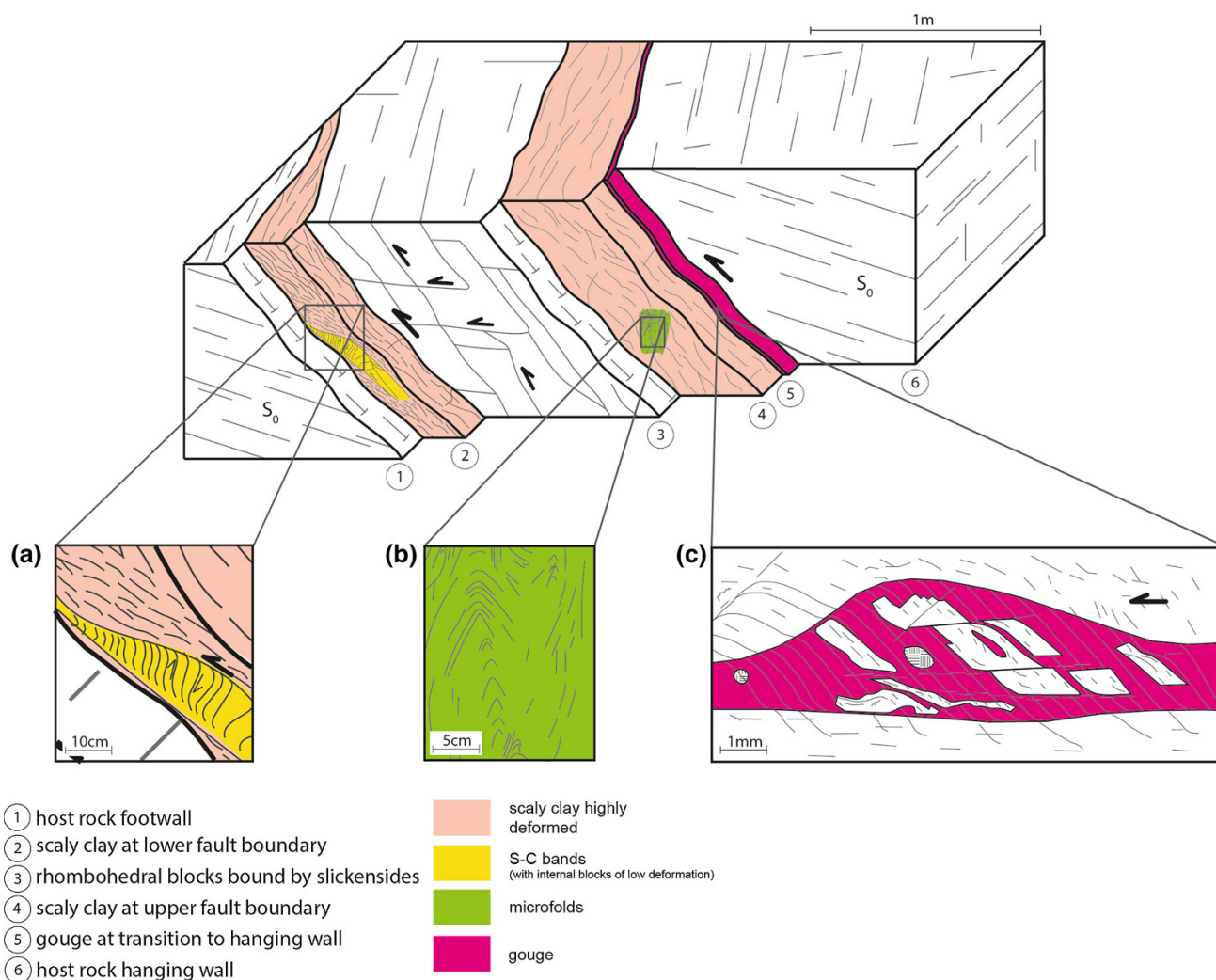


Fig. 8 Generic block model of the Main Fault in the Opalinus Clay of the Mont Terri rock laboratory showing the structural elements and their distribution. Close-ups: **a** S–C bands with internal sigmoidal

(<20 cm) zone of scaly clay at the lower boundary of the Main Fault. At the base (footwall) of the Main Fault, S–C bands are common and contain internal, largely undeformed microlithons. Again, except for the exposure in Ga08W this lower band of scaly clay seems to be continuous. The colours of the model (Fig. 8) highlight the amount of strain accommodated, which is highest for the dark red (gouge), intermediate to high for light red (scaly clay and associated microfolds and S–C bands), and lowest for the uncoloured parts, such as rhombohedral blocks bound by slickensides and the undeformed wall rock.

6 Conclusions

We can identify five structural elements at outcrop scale and have established a generic block model that encompasses the observed macroscopic features of a fault zone

structure, **b** microfolds within scaly clay, **c** gouge as observed at upper boundary of Main Fault (adapted after Laurich 2015)

within the Opalinus Clay. Scaly clay is observed as isolated aggregates within the Main Fault and at its upper (hanging wall) and lower (footwall) boundaries. Scaly clay includes microfolds and S–C bands. A continuous gouge band of up to 2 cm thickness runs along the upper boundary of the Main Fault. The non-scaly, inner part of the Main Fault consists of rhombohedral blocks bound by slickensides.

We found identical orientations and structural elements throughout the rock laboratory. However, lateral correlation of structural elements over larger distances is impossible. Comparison of relative area percentages of structural elements among the four exposures analysed shows that with decreasing fault zone thickness, the area percentage of the zone with isolated slickensides increases, whilst the abundance of scaly clay decreases. Reduction of block size with decreasing thickness of the fault zone can be explained by the amount of strain accommodated across a much thinner zone.

We postulate that fault zones in clay rocks with low stiffness and pronounced bedding anisotropy are inherently discontinuous and probably distribute offset along several parallel fault strands, each with a highly variable internal structure. A model for the evolution of such fault zones, which is consistent with our observations on fault geometry and distribution of structural elements, is proposed by Laurich et al. (2016).

Correlation of V_p with structural elements of the Ga08E outcrop shows a clear relationship to the internal structure of the Main Fault. Given the strong correlation between outcrop and geophysical borehole data, we can use ultrasonic geophysical measurements to deduce the internal structure of the Mont Terri Main Fault to a high degree of fidelity.


Acknowledgements The authors would like to thank the Mont Terri Project Partners swisstopo and Chevron for their financial contribution to the PS (Petrofabric and Strain) experiment. Both reviewers Marco Herwegh from University of Bern and Reto Thöny from AF Consult provided useful comments and helped to improve the manuscript. We thank Fabian Jäggi, Solothurn, for creating and improving the figures of this work.

References

- Baur, S. (2014). *Geological, Petrophysical and Geochemical Investigations of the Opalinus Clay Formation of the Underground Rock Laboratory Mont Terri, Switzerland*. Master thesis, Albert-Ludwigs-University of Freiburg, Freiburg in Breisgau, Germany.
- Blaesi, H. R., Moeri, A., & Bossart, P. (1996). *Results of the Phase I drilling campaign*. Mont Terri Technical Report, TR96-01. Federal Office of Topography (swisstopo), Wabern, Switzerland. <http://www.mont-terri.ch>.
- Blenkinsop, T. G. (2000). *Deformation microstructures and mechanisms in minerals and rocks* (p. 150). Dordrecht: Kluwer Academic Publishers.
- Bossart, P., Bernier, F., Birkholzer, J., Bruggeman, C., Connolly, P., Dewonck, S., et al. (2017). Mont Terri rock laboratory, 20 years: Introduction, site characteristics and overview of experiments. *Swiss Journal of Geosciences*, 110. doi:10.1007/s00015-016-0236-1.
- Bossart, P., & Thury, M. (2008). *Mont Terri Rock Laboratory. Project, programme 1996 to 2007 and results. Reports of the Swiss Geological Survey*, 3. Federal Office of Topography (swisstopo), Wabern, Switzerland. <http://www.mont-terri.ch>.
- Chester, F. M., Rowe, C., Ujiie, K., Kirkpatrick, J., Regalla, C., Remitti, F., et al. (2013). Structure and composition of the plateboundary slip zone for the 2011 Tohoku-Oki earthquake. *Science*, 342, 1208–1211.
- Clauer, N., Techer, I., Nussbaum, C., & Laurich, B. (2017). Geochemical signatures of paleofluids in microstructures from Main Fault of the Opalinus Clay, Mont Terri rock laboratory (Switzerland). *Swiss Journal of Geosciences*, 110 (this issue).
- Dick, P., Wittebroodt, C., Courbet, C., Sammaljärvi, J., Estève, I., Matray, J.-M., et al. (2016). The internal architecture and permeability structures of faults in shale formations. *The Clay Minerals Society Workshop Lectures Series*, 21(17), 227–242.
- Dielforder, A., Vollstaedt, H., Vennemann, T., Berger, A., & Herwegh, M. (2015). Linking megathrust earthquakes to brittle deformation in a fossil accretionary complex. *Nature Communications*, 6, 7504.
- Doblas, M., Mahecha, V., & Hoyos, M. (1997). Slickenside and fault surface kinematic indicators on active normal faults of the Alpine Betic cordilleras, Granada, southern Spain. *Journal of Structural Geology*, 19, 159–170.
- Gratier, J.-P., Renard, F., & Vial, B. (2014). Postseismic pressure solution creep: Evidence and time-dependent change from dynamic indenting experiments. *Journal of Geophysical Research Solid Earth*, 119, 2764–2779.
- Gschwind, S. (2013). *The Relationship between Failure Behavior and Sedimentary Subfacies Types in the Sandy Facies of Opalinus Clay*. Master thesis, Swiss Federal Institute of Technology in Zurich (ETH Zurich), Zurich, Switzerland.
- Gudmundsson, A. (2001). Fluid overpressure and flow in fault zones: Field measurements and models. *Tectonophysics*, 336, 183–197.
- Haines, S. H., Kaproth, B., Marone, C., Saffer, D., & van der Pluijm, B. (2013). Shear zones in clay-rich fault gouge: A laboratory study of fabric development and evolution. *Journal of Structural Geology*, 51, 206–225.
- Hostettler, B., Reisdorf, A. G., Jaeggi, D., Deplazes, G., Blaesi, H. R., Morard, A., et al. (2017). Litho- and biostratigraphy of the Opalinus Clay and bounding formations in the Mont Terri rock laboratory (Switzerland). *Swiss Journal of Geosciences*, 110. doi:10.1007/s00015-016-0250-3
- Houben, M. E., Desbois, G., & Urai, J. L. (2013). Pore morphology and distribution in the Shaly facies of Opalinus Clay (Mont Terri, Switzerland): Insights from representative 2D BIB–SEM investigations on mm to nm scale. *Applied Clay Science*, 71, 82–97.
- Housen, B. A., Tobin, H. J., Labaume, P., Leitch, E. C., & Maltman, A. J. (1996). Strain decoupling across the decollement of the Barbados accretionary prism. *Geology*, 24, 127–130.
- Ismat, Z. (2013). Block-supported cataclastic flow within the upper crust. *Journal of Structural Geology*, 56, 118–128.
- Jaeggi, D., Lisjak, A., Gisiger, J., & Becker, J. (2013). FE-C experiment: Engineering part of full-scale emplacement experiment. Geological and structural mapping of the FE-tunnel including a photogrammetric method. *Mont Terri Technical Note*, TN2012-82. Federal Office of Topography (swisstopo), Wabern, Switzerland. <http://www.mont-terri.ch>.
- Jaeggi, D., Wymann, L., Burrus, F., Becker, J., & Bossart, P. (2014). FE-E (EDZ-characterization in the vicinity of the FE-gallery) experiment. Synthesis of the excavation damaged zone (EDZ). *Mont Terri Technical Note*, TN2014-33. Federal Office of Topography (swisstopo), Wabern, Switzerland. <http://www.mont-terri.ch>.
- Johansen, T. E. S., & Fossen, H. (2008). Internal geometry of fault damage zones in interbedded siliciclastic sediments. In C. A. J. Wibberley, W. Kurz, J. Imber, R. E. Holdsworth, & C. Collettini (Eds.), *The internal structure of fault zones: Implications for mechanical and fluid-flow properties* (pp. 35–56). London: The Geological Society of London.
- Klinkenberg, M., Kaufhold, S., Dohrmann, R., & Siegesmund, S. (2009). Influence of carbonate microfibrils on the failure strength of claystones. *Engineering Geology*, 107, 42–54.
- Koehn, D., & Passchier, C. W. (2000). Shear sense indicators in striped bedding-veins. *Journal of Structural Geology*, 22, 1141–1151.
- Lablaume, P., Maltman, A. J., Bolton, A., Tessier, D., Ogawa, Y., & Takizawas, S. (1997). Scaly fabrics in sheared clays from the decollement zone of the Barbados accretionary prism. In T. R. Shipley, Y. Ogawa, P. Blum, J. M. Bahr (Eds.), *Proceedings of the ocean drilling program* (pp. 59–77). USA: Texas A&M University.

- Laurich, B. (2015). *Evolution of microstructure and porosity in faulted Opalinus Clay*. PhD thesis, RWTH Aachen University, Aachen, Germany.
- Laurich, B., Urai, J. L., Desbois, G., Vollmer, C., & Nussbaum, C. (2014). Microstructural evolution of an incipient fault zone in Opalinus Clay: Insights from optical and electron microscopic study of iron-beam polished samples from the Main Fault in the Mont Terri underground research laboratory. *Journal of Structural Geology*, 67, 107–128.
- Laurich, B., Urai, J. L., & Nussbaum, C. (2016). Microstructures and deformation mechanisms in Opalinus Clay: Insights from scaly clay from the Main Fault in the Mont Terri Rock Laboratory (CH). *Journal Solid Earth*. doi:10.5194/se-2016-94.
- Marschall, P., Croisé, J., Schlickenrieder, L., Boisson, J.-Y., Vogel, P., & Yamamoto, S. (2004). Synthesis of hydrogeological investigations at the Mont Terri Site (phases 1 to 5). In P. Heitzmann (Ed.), *Mont Terri Project—Hydrogeological synthesis—Osmotic flow*. Bern: Reports of the Federal Office for Water and Geology, Geology Series, 6.
- Marschall, P., Gimmi, T., & Horseman, S. (2005). Characterisation of gas transport properties of the Opalinus Clay. *Oil & Gas Science and Technology*, 60, 121–139.
- Nussbaum, C., Bossart, P., Amann, F., & Aubourg, C. (2011). Analysis of tectonic structures and excavation induced fractures in the Opalinus Clay, Mont Terri underground rock laboratory (Switzerland). *Swiss Journal of Geosciences*, 104, 187–210.
- Nussbaum, C., Bossart, P., Zingg, A., Inderbitzin, L., & Steiger, H. (2001). *Géométrie et cinématique d'une zone de chevauchement („Main Fault“) recoupant les Argiles à Opalinus dans le laboratoire souterrain du Mont Terri*. Mont Terri Technical Report, TR2001-04. Federal Office of Topography (swisstopo), Wabern, Switzerland. <http://www.mont-terri.ch>.
- Passchier, C. W., & Trouw, R. A. J. (1996). *Microtectonics*. Berlin: Springer.
- Schuster, K. (2012). Detection of borehole disturbed zones and small scale rock heterogeneities with geophysical methods. In X. Li, L. Jing, & P. Blaser (Eds.), *Proceedings of the EC-TIMODAZ-THERESA International Conference, Impact of thermo-hydro-mechanical chemical (THMC) processes on the safety of underground radioactive waste repositories, Luxembourg, 29 Sep.–1 Oct. 2009* (pp. 135–145). Publications Office, 2012.
- Schuster, K., Amann, F., Yong, S., Connolly, P., & Bossart, P. (2017). High-resolution mini-seismic methods applied in the Mont Terri rock laboratory (Switzerland). *Swiss Journal of Geosciences*, 110. doi:10.1007/s00015-016-0241-4.
- Thoeny, R. (2014). *Geomechanical analysis of excavation-induced rock mass behavior of faulted Opalinus Clay at the Mont Terri Underground Rock Laboratory (Switzerland)*. PhD thesis, Swiss Federal Institute of Technology in Zurich (ETH Zurich), Zurich, Switzerland.
- Vannucchi, P., Maltman, A., Bettelli, G., & Clennell, B. (2003). On the nature of scaly fabric and scaly clay. *Journal of Structural Geology*, 25, 673–688.
- Yong, S., Kaiser, P. K., & Loew, S. (2010). Influence of the tectonic shears on tunnel-induced fracturing. *International Journal of Rock Mechanics and Mining Sciences*, 47, 894–907.

Comparative study of methods to estimate hydraulic parameters in the hydraulically undisturbed Opalinus Clay (Switzerland)

Catherine Yu^{1,2}  · Jean-Michel Matray¹ · Julio Gonçalves² · David Jaeggi³ · Werner Gräsele⁴ · Klaus Wiczorek⁵ · Tobias Vogt⁶ · Erik Sykes⁷

Received: 11 March 2016 / Accepted: 17 December 2016 / Published online: 25 February 2017
© The Author(s) 2017. This article is published with open access at Springerlink.com

Abstract The deep borehole (DB) experiment gave the opportunity to acquire hydraulic parameters in a hydraulically undisturbed zone of the Opalinus Clay at the Mont Terri rock laboratory (Switzerland). Three methods were used to estimate hydraulic conductivity and specific storage values of the Opalinus Clay formation and its bounding formations through the 248 m deep borehole BDB-1: application of a Poiseuille-type law involving petrophysical measurements, spectral analysis of pressure time series and in situ hydraulic tests. The hydraulic conductivity range in the Opalinus Clay given by the first method is 2×10^{-14} – 6×10^{-13} m s⁻¹ for a cementation factor ranging between 2 and 3. These results show low

vertical variability whereas in situ hydraulic tests suggest higher values up to 7×10^{-12} m s⁻¹. Core analysis provides economical estimates of the homogeneous matrix hydraulic properties but do not account for heterogeneities at larger scale such as potential tectonic conductive features. Specific storage values obtained by spectral analysis are consistent and in the order of 10^{-6} m⁻¹, while formulations using phase shift and gain between pore pressure signals were found to be inappropriate to evaluate hydraulic conductivity in the Opalinus Clay. The values obtained are globally in good agreement with the ones obtained previously at the rock laboratory.

Keywords Argillaceous formation · Hydraulic well tests · Poiseuille-type law · Harmonic tidal analysis · Hydraulic conductivity · Specific storage · Nuclear waste disposal

Editorial handling: P. Bossart and A. G. Milnes.

This is paper #4 in the Mont Terri Special Issue of the Swiss Journal of Geosciences (see Bossart et al. 2017, Table 3 and Fig. 7).

✉ Catherine Yu
catherine.jiyu@irsn.fr

- ¹ Institut de Radioprotection et de Sûreté Nucléaire, 31 Allée du Général Leclerc, 92260 Fontenay-aux-Roses, France
- ² Aix Marseille Université UMR 6635 CEREGE Technopôle Environnement Arbois-Méditerranée, BP80, 13545 Aix-en-Provence Cedex 4, France
- ³ Federal Office of Topography Swisstopo, Seftigenstrasse 264, 3084 Wabern, Switzerland
- ⁴ Federal Institute for Geosciences and Natural Resources (BGR), Stilleweg 2, 30655 Hannover, Germany
- ⁵ Global Research for Safety (GRS), Schwertnergasse 1, 50667 Cologne, Germany
- ⁶ National Cooperative for the Disposal of Radioactive Waste (Nagra), Hardstrasse 73, 5430 Wettingen, Switzerland
- ⁷ Nuclear Waste Management Organization, 22 St. Clair Ave. E., Toronto, ON, Canada

1 Introduction

Based on favourable confining properties, such as low permeability, strong retention and self-sealing capacities, clay formations are the preferred host rock option for a deep geological repository of long-lived, intermediate and high level radioactive waste in several countries including France, Belgium and Switzerland. In the latter country, the Opalinus Clay (OPA) has been selected as a potential host rock for a disposal facility (Nagra 2002) and has been studied at the Mont Terri rock laboratory since 1996. The laboratory is located at a depth of ca. 280 m, in the security gallery of the A16 Transjurane motorway, which crosses the Jura Mountains in north-western Switzerland.

The accurate hydraulic characterisation of low permeability formations is of high importance to ensure the safety of a geological repository. Hydraulic properties can be estimated by various laboratory and field experiments (Van

der Kamp 2001; Yu et al. 2013), including empirical methods based on the rock matrix properties (Chapuis and Aubertin 2003), falling head or constant head permeameter tests in laboratory (Boulin et al. 2012), and in situ field tests that rely on measurement of pore pressure or water level changes due to tidal natural loading (Bredehoeft 1967; Merritt 2004; Jiang et al. 2013) or artificial application of an hydraulic pressure different from the static formation pressure (Neuzil 1982; Butler 1998; Mejías et al. 2009). As these methods are carried out from sub-millimetre to hectometre investigation scales, scale dependency can affect the results (Keller et al. 1989; Neuzil 1994).

This paper compares three different techniques to estimate hydraulic properties of the Opalinus Clay: application of a Poiseuille-type law involving petrophysical measurements, in situ packer tests and spectral analysis of pore pressure time series.

2 Geological setting

The Opalinus Clay at the Mont Terri site is an overconsolidated claystone of Aalenian-Toarcian age, overlain by 800 m of Middle to Late Jurassic limestones, marls and shales, and underlain by 400 m of Early Jurassic to Triassic marls and limestones, dolomites and anhydrites (Fig. 1). The thickness

of the Opalinus Clay in the Mont Terri anticline varies between 130 m in the BDB-1 borehole and 160 m at rock laboratory level, depending on the tectonic contribution. This corresponds to a sedimentary thickness of about 120 m, when corrected for tectonic overthrusting. The Opalinus Clay reached a burial depth of 1350 m about 120 Ma ago during early Cretaceous, which resulted in a maximum temperature of 80–90 °C (Mazurek et al. 2006). A period of marine regression occurred between 100 and 40 Ma, leading to a subaerial exposure of the top of the Malm limestone. Starting about 40 Ma, the rifting of the Rhine Graben affected Northern Switzerland, resulting in considerable subsidence of the area in the mid-Tertiary, which brought the Opalinus Clay sequence back to about 500 m depth. Two sea invasions into the Mont Terri area took place during Priabonian (37–34 Ma) and during the Rupelian (34–28 Ma) (Clauer et al. 2017). Late Alpine folding during the late Miocene to Pliocene (about 12–3 Ma) formed the Folded Jura. Erosion exposed the core of the Mont Terri anticline towards 2.5 Ma, and allowed fresh water infiltration to the Middle Jurassic limestones. Similarly, infiltration to the Early Jurassic limestones would have started in the Quaternary, around 350 thousand years ago (Pearson et al. 2003).

Three main facies were identified within the Opalinus Clay (Blaesi et al. 1991): a shaly facies in the lower part of the sequence, a thin carbonate-rich sandy facies in the

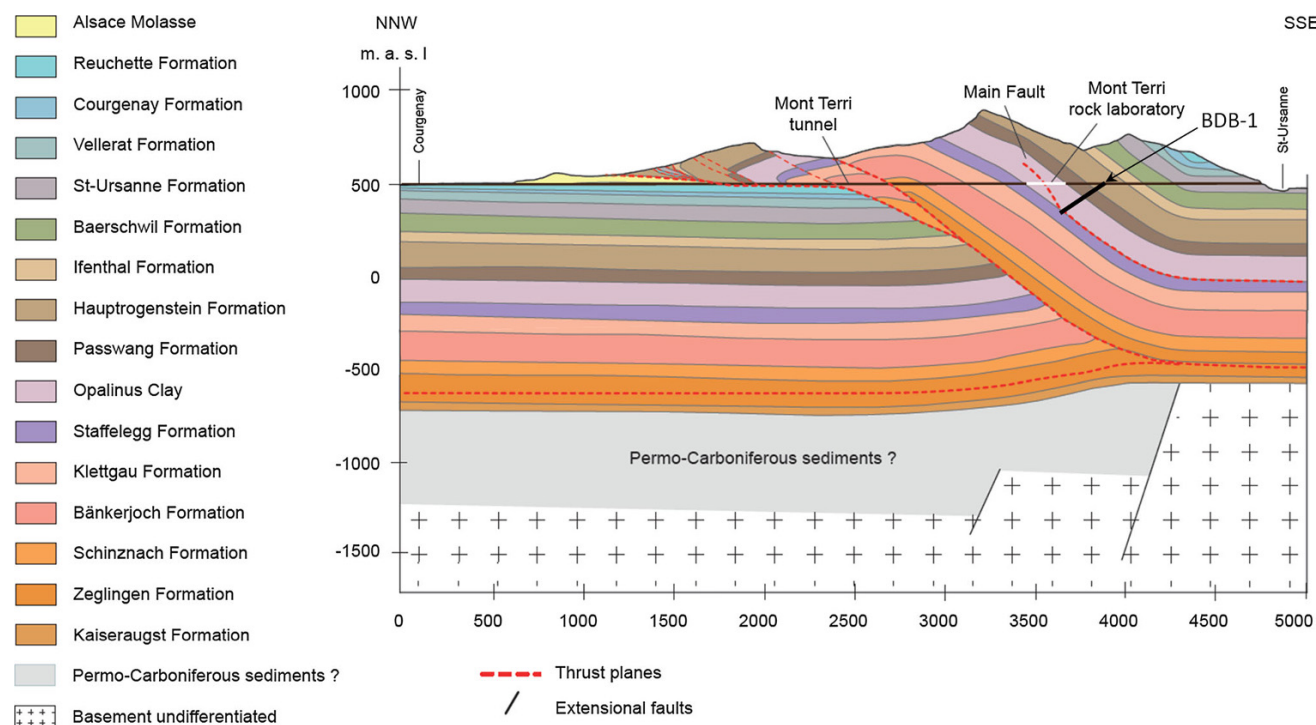


Fig. 1 Geological cross-section of the Mont Terri anticline. Location of the rock laboratory is indicated by a *white line*. The BDB-1 deep borehole, represented by a *thick black line*, crosses the *lower part*

of the Dogger aquifer, the entire Opalinus Clay formation and the *upper part* of the Liassic marls (adapted from Nussbaum et al. 2017)

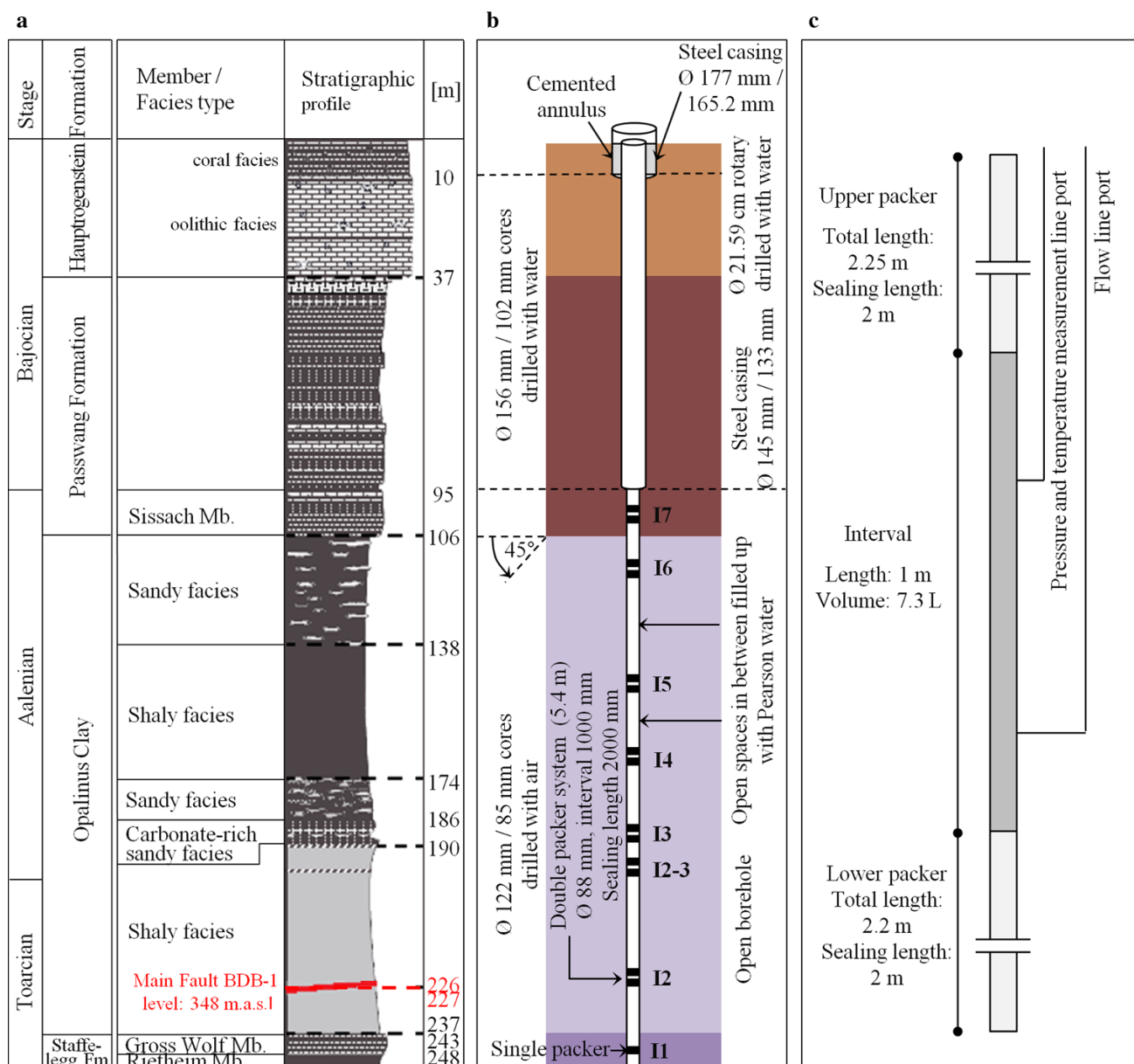


Fig. 2 a Stratigraphic sequence along the BDB-1 borehole; b BDB-1 borehole layout; c Layout of double packer elements (adapted from Hostettler et al. 2017)

middle part of the formation, and a sandy facies interstratified with shaly facies in the upper sequence. The shaly facies mineral composition includes 27–78% of clay minerals (illite, chlorite, kaolinite and illite–smectite mixed layers), 4–29% of carbonates, 10–32% of quartz, and accessory feldspars, pyrite and organic matter (Bossart and Thury 2008).

Several minor tectonic faults and a larger fault zone called “Main Fault” can be observed in the Opalinus Clay (Nussbaum et al. 2011). Nagra’s investigations in deep boreholes at Riniken, Weiach, Schafisheim and Benken revealed that the tectonically disturbed zones are hydraulically similar to the undeformed matrix (Johns et al.

1995; Gautschi 2001). Based on permeameter tests and in situ packer tests, hydraulic conductivity values in tectonically disturbed zones are in the range of 2×10^{-14} to $2 \times 10^{-12} \text{ m s}^{-1}$, and specific storage ranges from 2×10^{-7} to $1.7 \times 10^{-4} \text{ m}^{-1}$ (Marschall et al. 2005).

3 BDB-1 deep borehole

The deep borehole experiment (DB) aims at evaluating the hydrogeological properties and processes of undisturbed Opalinus Clay at the Mont Terri rock laboratory. For the

Table 1 Specifications of the pressure and temperature sensors installed in BDB-1 borehole

Sensor type	Temperature	Pore pressure
Model	IST AG PT1000	Keller AG PAA-33X
Validity range	-50 to 650 °C	0-50 bars (absolute)
Accuracy	± (0.15 + 0.002 T) °C	0.05% FS

first time in this laboratory, a 247.5 m long 45° downward inclined borehole has been drilled through the Opalinus Clay and the bounding formations. The stratigraphic sequence crossed by the borehole is presented in Fig. 2a and is described in detail in Hostettler et al. (2017). The borehole was entirely cored for stratigraphic, petrophysical, mineralogical and geochemical studies. The Opalinus Clay section was drilled with air as drilling fluid. Drilling was immediately followed by the installation of a multi-packer system (Fierz and Rösli 2014) consisting in five double packer measuring intervals and an interval port within the Opalinus Clay, a single packer in the Staffelegg Formation at the bottom of the borehole, and a further double packer interval isolating the lowermost zone of the Passwang Formation (Fig. 2b, c). Intervals were equipped with sensors that enable long term monitoring of pressure and temperature (Table 1). Pressure sensors are located at the surface and connected by stainless steel lines to the interval fluids, whereas temperature sensors are located downhole inside the intervals.

4 Techniques for hydraulic parameters evaluation

4.1 Petrophysical model

Assuming a plane-parallel geometry, the intrinsic permeability can be computed across an argillaceous formation using a semi-empirical Poiseuille-type law (Kostek et al. 1992; Pape et al. 1999; Tremosa 2010):

$$k = \frac{b^2}{3F}, \quad (1)$$

where k is the intrinsic permeability [m^2], b is the half-pore size [m] and F is the formation factor [-], which accounts for the tortuosity of the porous media and can be determined using the Archie's law (Archie 1942):

$$F = \omega^{-m}, \quad (2)$$

where ω is the porosity [-] and m is the cementation factor. The formation factor can also be related to diffusion parameters (Boving and Grathwohl 2001; Van Loon and Mibus 2015) or electrical properties (Archie 1942), following Eqs. (3) and (4):

$$F = \frac{D_w}{D_e}, \quad (3)$$

where D_w is the diffusion coefficient in pure water [$\text{m}^2 \text{s}^{-1}$] and D_e is the effective diffusion coefficient [$\text{m}^2 \text{s}^{-1}$].

$$F = \frac{R_0}{R_w}, \quad (4)$$

where R_0 is the rock resistivity [ohm m] saturated with a brine of resistivity R_w [ohm m].

The half-pore size can be computed from petrophysical parameters according to the following relation based on a mass balance equation (Neuzil 2000; Altinier 2006):

$$b = \frac{\omega}{(1 - \omega)\rho_s A_s}, \quad (5)$$

where b is the half-pore size [m], ω is the porosity [-], ρ_s is the grain density [g m^{-3}] and A_s is the specific surface area [$\text{m}^2 \text{g}^{-1}$].

Intrinsic permeability and hydraulic conductivity are linked according to:

$$K = \frac{k\rho_f g}{\mu_f}, \quad (6)$$

where K is the hydraulic conductivity [m s^{-1}], ρ_f is the fluid density [kg m^{-3}], g is the gravity acceleration [m s^{-2}] and μ_f is the fluid dynamic viscosity [Pa s].

Fluid dynamic viscosity was estimated according to Mercer et al. (1975):

$$\mu_f = (5.38 + 3.8A - 0.26A^2) \times 10^{-3} \text{ Pa s}, \quad (7)$$

with

$$A = \frac{T - 150}{100}, \quad (8)$$

where μ_f is the fluid dynamic viscosity [Pa s] and T is the temperature [°C].

The Unesco equation of state (1981) was used to determine the fluid density as a function of salinity, temperature and pressure.

Determination of petrophysical parameters were performed in laboratory on representative element volume samples taken from the central part of BDB-1 drillcores. Porosity and water contents were determined by weighing before and after oven-drying at 105 °C until mass stabilisation. Density and degree of saturation were calculated based on Archimede's principle after sample immersion into kerdane following the experimental protocol first proposed by Monnier et al. (1973) and later adapted by Matray et al. (2007) for argillite samples. Grain density was evaluated using a helium pycnometer (Micromeritics® AccuPyc II 1340) on oven-dried samples and also recalculated from results of X-Ray diffraction measurements on bulk samples.

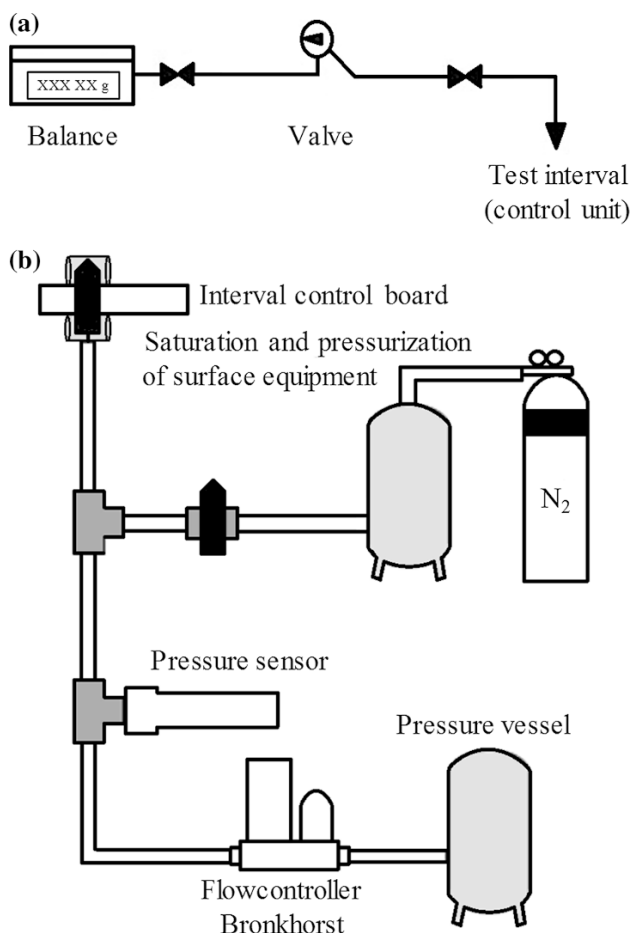


Fig. 3 Experimental set up for: **a** pulse withdrawal tests; **b** constant rate pumping tests performed on BDB-1 borehole (©Solexperts)

4.2 In-situ hydraulic testing experiments

Hydraulic in situ testing in boreholes, also referred as well testing, is the most common method used in groundwater and oil industries to acquire the hydraulic properties of geological formations. Pulse withdrawal tests and constant

rate withdrawal tests were conducted in BDB-1 borehole, from March 11th to November 16th 2015. During a withdrawal pulse test, pressure is lowered abruptly by opening and closing the downhole shut-in valve (Bredehoeft and Papadopoulos 1980; Neuzil 1982). These tests are preferred as initial phase because they give an immediate measurement of the system compressibility and generally require shorter time frame than pumping tests. Given its quick hydraulic response, performing more pulse tests on interval 1 (Staffellegg Formation, Fig. 2b) was possible, whereas two pulse tests were carried out on each of the other intervals.

Constant rate withdrawal test parameters such as flow rate and flow duration must be chosen with caution. In low permeability media, high flow rates can lead to desaturation of the measuring intervals and extreme drops in pressure. Therefore, a flowmeter able to sustain a very low pumping rate of 0.3 g h⁻¹ for several days (Bronkhorst® μ-flow L01) was used to test intervals 2 to 7 (Fig. 2b), for which the hydraulic responses to pulse testing were the slowest. Interval 1 was tested with a higher flow rate of 5 ml min⁻¹ using a Bronkhorst® Liqui-Flow L10. Experimental setups for both kind of tests and associated hydraulic responses are respectively reported in Figs. 3 and 4. Flowmeter failed during the testing of intervals 2 and 6 and approximately two months of pressure recovery were required before performing a second test on these test chambers.

Hydraulic test data were analysed using the well-test interpretation program nSIGHTS, which was developed by INTERA for Sandia National Laboratories (Beauheim and Roberts 2004). The code is based on Barker’s equation (1988), which describes flow in an n-dimensional space, and does not restrict to integer dimensions (Beauheim et al. 2004).

$$S_s \frac{\partial h}{\partial t} = \frac{K}{r^{n-1}} \frac{\partial}{\partial r} \left(r^{n-1} \frac{\partial h}{\partial r} \right), \quad (9)$$

where S_s is the specific storage coefficient [m⁻¹], h is the hydraulic head [m], t is the elapsed time [s], K is the

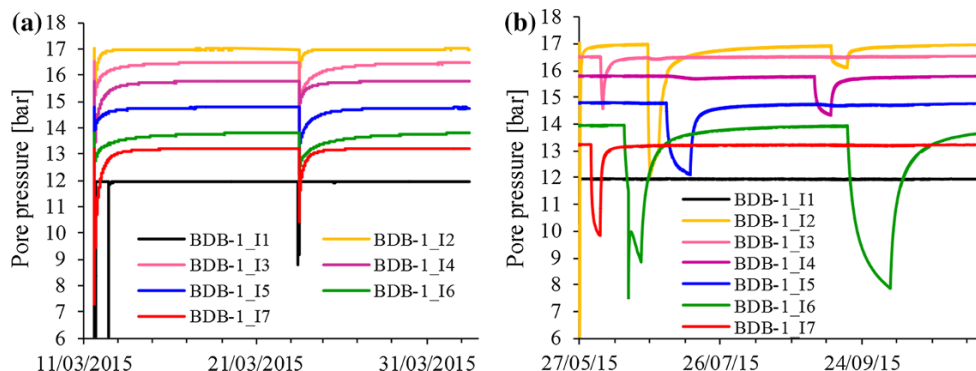


Fig. 4 Records of pore pressure responses in the seven intervals of BDB-1 borehole to: **a** pulse tests; **b** constant rate withdrawal tests

Table 2 Plausibility ranges set in nSIGHTS for fitted parameters

Fitted parameter	Plausibility range
K [m s ⁻¹]	
Interval 1	10 ⁻¹³ –10 ⁻⁸
Interval 2 to 7	10 ⁻¹³ –10 ⁻¹¹
S _s [m ⁻¹]	10 ⁻⁸ –10 ⁻⁴
Flow dimension [–]	1–3.5
Skin thickness [cm]	0.5–30
External boundary radius [m]	0–5

K stands for hydraulic conductivity and S_s for specific storage. Skin zone conductivity ranges were set one order of magnitude higher compared to intact rock

hydraulic conductivity [m s⁻¹], r is the radial distance from borehole [m], and n is the flow dimension [–].

The flow area is defined as

$$A(r) = b^{3-n} \frac{2\pi^{n/2}}{\Gamma^{n/2}} r^{n-1}, \quad (10)$$

where b is the extent of the flow zone [m], and Γ is the gamma function [–].

nSIGHTS is able to take account of borehole inclination by adjusting parameters such as formation thickness or capacitive effect. Equations are programmed as functions of pressure and the code uses unsensitively pressure or hydraulic head data according to user configuration. Flow is simulated in saturated conditions under a pressure gradient between the well and the external boundary of the model following Dupuit conditions. Density effects do not intervene directly in the equation system, as density is considered constant in the test interpretation.

Uncertainties associated with the fitted parameters are evaluated by performing random perturbation analyses. Plausibility ranges for fitted parameters were defined prior to the parameter optimisation procedure (Table 2). During the inverse parameter estimation, nSIGHTS provides best-fit results within these pre-defined ranges. Optimisation was performed using a simplex approach. Uncertainties associated with the fitted parameters are evaluated by performing random perturbation analyses (not detailed in this paper).

4.3 Tidal analysis on pore pressure time series

Rotational and gravitational forces exerted by the sun and the moon on the Earth induce latitudinal and longitudinal strains within the solid matrix and cause deformations with two dominant periods: diurnal and semi-diurnal. The tidal gravitational potential can be resolved into a finite set of tidal components described as harmonics, which are sinusoidal functions of given amplitude and frequency (Doodson and Warburg 1941; Cutillo and Bredehoeft

2011). Five main components account for about 95% of the tidal potential: the M₂ and N₂ semidiurnal lunar tides, the S₂ semidiurnal solar tide, the O₁ diurnal lunar tide, and the K₁ diurnal lunar-solar tide.

Seasonal or climatic variations, anthropogenic activities and tidal forces induce hydraulic pressure changes in geological formations. The amplitude of the pressure response depends on the poroelastic response of the aquifer matrix. Pressure signal can therefore be analysed to determine hydrogeological properties, such as specific storage, effective porosity and hydraulic conductivity. The models used in this work are based on Terzaghi's (1936) effective stress concept, which assumes a constant total stress distributed between grains and fluid stress. Bredehoeft (1967) related tidal strain to specific storage:

$$S_s = \frac{|\Delta\varepsilon|}{|\Delta h|}, \quad (11)$$

where S_s is the specific storage [m⁻¹], $|\Delta\varepsilon|$ is the amplitude of volumetric strain fluctuation fixed at 2×10^{-8} for the M₂ tide (Melchior 1978), and $|\Delta h|$ is the amplitude of relative pressure head fluctuations [m].

Jacob's (1940) formula was used to compute the porosity:

$$\omega = \frac{E_W S_s B}{\rho_f g}, \quad (12)$$

where ω correspond to the porosity [–], E_W is the stiffness modulus of water, equal to 2.05 GPa, S_s is the specific storage [m⁻¹], B is the barometric efficiency [–], which reflects the elastic response of the system, ρ_f is the fluid density, and g is the gravity acceleration equal to 9.81 m s⁻².

Hydraulic conductivity was estimated with formulations using the M₂ harmonic amplitude and phase shift (Boldt-Leppin and Hendry 2003; Timms and Acworth 2005), measured at two depths, z_1 and z_2 [m]:

$$K_v^{Amp}(f_{M_2}) = S_s(f_{M_2}) \frac{(z_1 - z_2)^2}{(f_{M_2})^{-1}} \left[\ln \left(\frac{A_{z_1}(f_{M_2})}{A_{z_2}(f_{M_2})} \right) \right]^{-2} \quad (13)$$

$$K_v^{Amp}(f_{M_2}) = S_s(f_{M_2}) \frac{(z_1 - z_2)^2}{(f_{M_2})^{-1}} \left[\ln \left(\frac{A_{z_1}(f_{M_2})}{A_{z_2}(f_{M_2})} \right) \right]^{-2}, \quad (14)$$

where K_v^{Amp} is the “amplitude effective hydraulic conductivity”, A_{z_1} and A_{z_2} [kPa], are the M₂ earth tide amplitude associated to the sensors, S_s [m⁻¹] is the arithmetic mean of the effective specific storage coefficients obtained individually for the two sensors, f_{M_2} [s⁻¹] is the frequency of the M₂ earth tide equal to 2.236×10^{-5} Hz, $K_v^{\Delta\varphi}$ [m s⁻¹] is the “phase effective hydraulic conductivity”, and $\Delta\varphi$ [rad] is the spectral phase shift between the sensors.

Spectral analysis of BDB-1 borehole pressure dataset was performed using the Multi-Statistical Analysis Tool (MuSTAT v1), jointly developed by the Institut de

Radioprotection et de Sûreté Nucléaire and the Institut National Polytechnique de Toulouse (Fatmi et al. 2008; Ababou et al. 2012; Bailly et al. 2014). Consisting in a Python code associated with toolboxes programmed in Matlab, the package provides automatic features: (a) pre-processing of time series, that enables the detection of time gaps and spurious values, as well as data reconstruction by autoregressive first order process; (b) processing of a single time series; (c) cross-analysis of two time series.

5 Results at various scales of investigation

5.1 Sub-millimeter to centimeter scale

5.1.1 Petrophysical parameters

The petrophysical parameters necessary for the computation of intrinsic permeability are presented in Fig. 5 as a function of distance along BDB-1 borehole.

The mean water accessible porosity is 13.0% in the Opalinus Clay, with a lower average porosity of 12.0% in the sandy facies compared to the shaly facies, which exhibit a mean porosity of 13.5%. These values are lower than the mean value of 18% suggested by previous studies performed at the Mont Terri tunnel level. The Passwang

Formation presents slightly lower porosity values ranging between 8.1 and 14.6% with a mean value of 12.2%. The Hauptrogenstein is characterised by the lowest porosity with a mean value of 3.9%.

Grain densities obtained by helium pycnometry have a mean value of 2.74 g cm^{-3} in the Opalinus Clay overlying formations and of 2.72 g cm^{-3} in the argillaceous layer. The lowest grain densities are found in the bituminous Rietheim Member of the Staffelegg Formation (see Fig. 1a), ranging between 2.3 and 2.4 g cm^{-3} . These low values are probably linked to the presence of organic matter.

The Passwang Formation, which directly overlays the Opalinus Clay, does not reveal clear petrophysical discrepancies with the clay formation except for the specific surface area. This parameter has an average value of $13 \text{ m}^2 \text{ g}^{-1}$ in the carbonated section of the borehole and shows significant fluctuations linked to the marly composition of the Passwang Formation. A higher mean value of $29 \text{ m}^2 \text{ g}^{-1}$ characterises the Opalinus Clay.

The Opalinus Clay is also characterised by a low pore size. Analyses of nitrogen adsorption and desorption isotherms show that 70 to 93% of the connected porous network is constituted of mesopores (pore diameter between 2 and 50 nm), with a mean size of 13 nm. Calculation of the half-pore size from petrophysical parameters, following

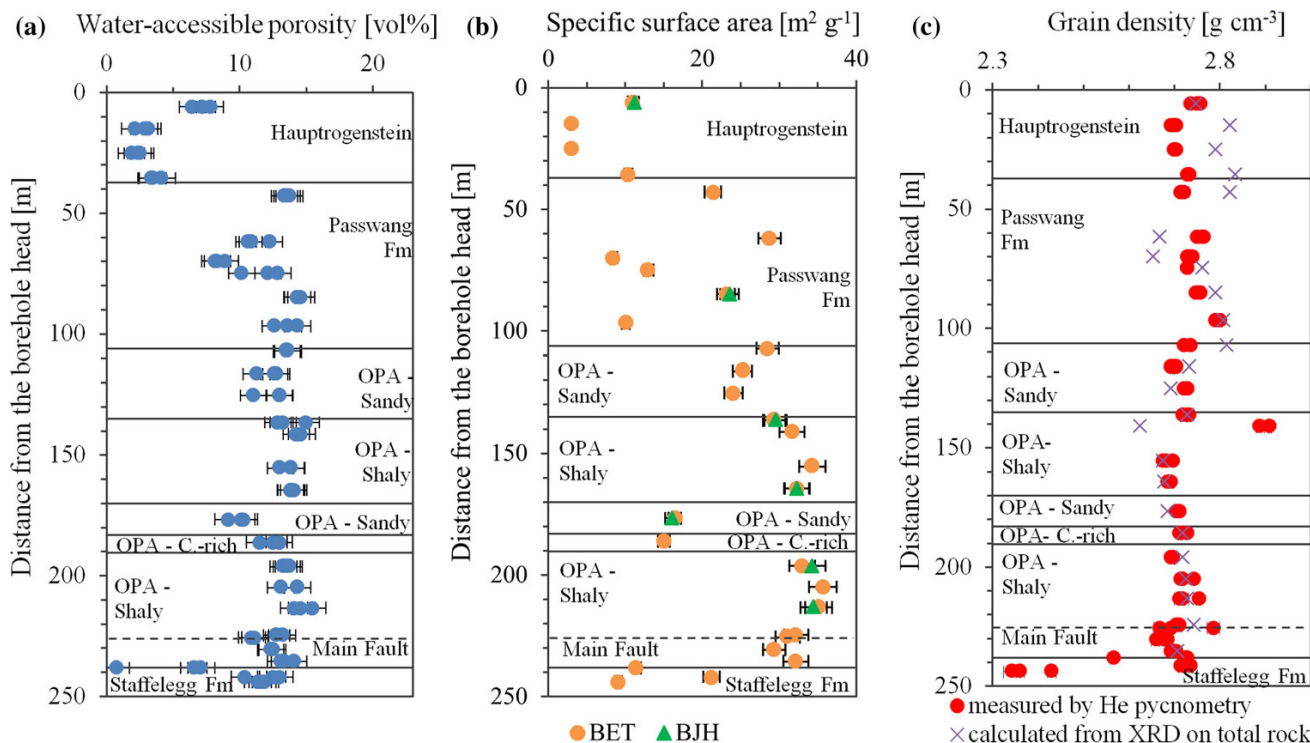


Fig. 5 Petrophysical parameters acquired along BDB-1 borehole: **a** Water accessible porosity acquired by oven-drying at $105 \text{ }^\circ\text{C}$; **b** Specific surface area obtained by BJH and BET methods; **c** Grain density estimated by helium pycnometry on oven dried samples

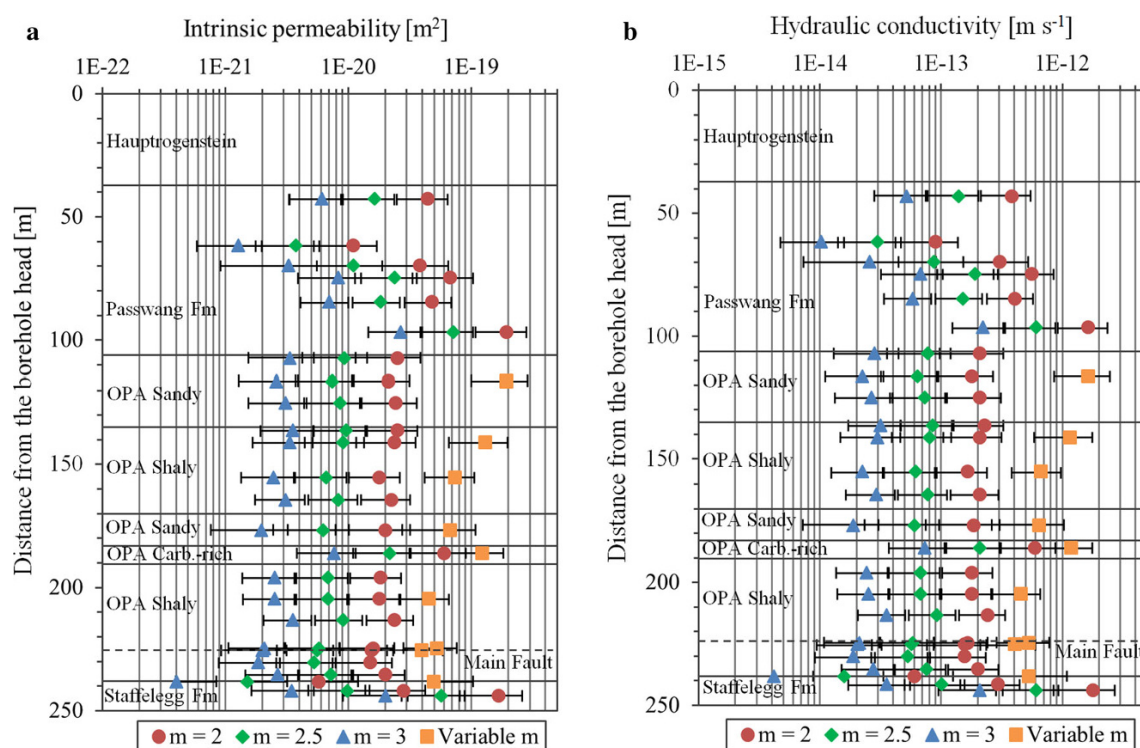


Fig. 6 **a** Intrinsic permeability profile and **b** hydraulic conductivity profile computed across the Opalinus Clay (OPA) and the Passwang Formation for cementation factor (m) of 2, 2.5 and 3. *Square symbols*

Eq. (5), gives mean pore sizes in the range of 3.1 to 7.3 nm.

Ranging between 1.3 and 5.4 (Horseman et al. 1996), the cementation factor was estimated to be close to 2 for compacted and deeply buried sediments (Ullman and Aller 1982; Tremosa 2010). Van Loon et al. (2003) related the effective diffusion coefficient of tritium measured in the Opalinus Clay to its porosity using a cementation factor of 2.5. An attempt was made to compute cementation factors from conductivity values obtained by borehole logging in BDB-1 and water-accessible porosity determined at laboratory scale. No real conductivity of formation fluid was acquired in the Opalinus Clay, as this part of the borehole was drilled with air. Therefore, fluid conductivity values were estimated based on chlorinity data acquired on BDB-1 core samples (not detailed in this paper). Low values of cementation factors are thus obtained and range between 0.9 and 1.7.

5.1.2 Intrinsic permeability and hydraulic conductivity

The intrinsic permeability profiles (Fig. 6a) show a low vertical variability through the Opalinus Clay, where it ranges between 1.8×10^{-21} and 6.1×10^{-20} m² if a cementation factor varying between 2 and 3 is taken. For a

represent values for variable m computed based on conductivity logging measurements across the Opalinus Clay

cementation factor of 2.5, the mean intrinsic permeability is 7.7×10^{-21} m² for the Opalinus Clay shaly facies and 7.9×10^{-21} m² for its sandy facies. These values are in good agreement with the range of 1×10^{-21} and 6×10^{-20} m² obtained by gas injection experiments performed at the Mont Terri laboratory (Marschall et al. 2005). Based on the same cementation factor, difference can be seen in the carbonate-rich sandy facies, where values are about three times higher than in the shaly and the sandy facies. With a higher exponent $m = 3$, the resulting intrinsic permeability has a mean value of 7.6×10^{-21} m² and no clear distinction arises between the different facies. The intrinsic permeability values computed in the Passwang Formation and the Staffelegg Formation are much more heterogeneous and vary between 1.5×10^{-21} and 5.8×10^{-20} m².

The corresponding hydraulic conductivity profiles are presented in Fig. 6b and show similar trends compared with the intrinsic permeability profiles. The hydraulic conductivity obtained for the Opalinus Clay ranges between 1.9×10^{-14} and 5.8×10^{-13} m s⁻¹ for a cementation factor varying between 2 and 3. For a cementation factor of 2.5, the formation is characterised by a mean hydraulic conductivity of 8.3×10^{-14} m s⁻¹. No clear discrepancy between the shaly facies and the sandy

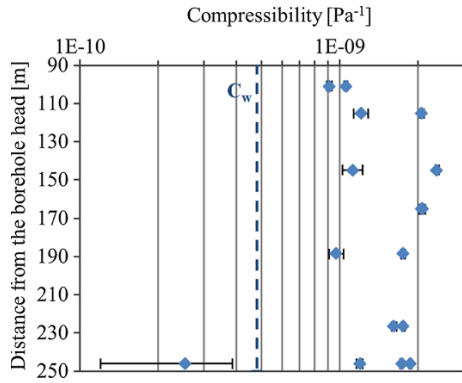


Fig. 7 System compressibility computed from pulse testing in BDB-1 borehole. *Dashed line* represents the water compressibility at 10 °C. The outlier in the *lower* part of the borehole is due to a very low withdrawn volume

facies is revealed, with respective mean values of 7.3×10^{-14} and $6.9 \times 10^{-14} \text{ m s}^{-1}$. These values are consistent with the range of 2×10^{-14} – $1 \times 10^{-12} \text{ m s}^{-1}$ reported in previous studies (Bossart and Thury 2008). The Passwang Formation and the Staffelegg Formation present a various range of hydraulic conductivities between 1.6×10^{-14} and $6.1 \times 10^{-13} \text{ m s}^{-1}$.

The computation of intrinsic permeability using variable cementation factors in the Opalinus Clay gives higher values in the range of 4.0×10^{-20} to $1.9 \times 10^{-19} \text{ m}^2$, corresponding to hydraulic conductivity values in the range of 4.1×10^{-13} – $1.7 \times 10^{-12} \text{ m s}^{-1}$.

5.2 Decimeter to meter scale: in situ hydraulic tests results

Pore pressure should be fully recovered from artificial disturbance induced by the installation procedure (e.g., drilling, logging, equipment installation) before starting a hydraulic test. Steady state was considered to be reached when the tidal components were detected on all pore pressure time series acquired in BDB-1 borehole, which indicate that the system is fully pressurised and saturated (see Sect. 5.3.1).

The observed compressibility of the test zone (C_{tz}) was deduced from pulse tests and computed according to:

$$C_{tz} = \frac{1}{V_{tz}} \frac{dV}{dP}, \quad (14)$$

where $V_{tz} [\text{m}^3]$ is the shut-in volume, $dV [\text{m}^3]$ is the withdrawn volume and $dP [\text{Pa}]$ is the pressure variation. Test zone compressibility in BDB-1 borehole varies 9.1×10^{-10} and $2.4 \times 10^{-9} \text{ Pa}^{-1}$ (Fig. 7), approximately up to a factor of 5 larger than water compressibility, which is equal to $4.8 \times 10^{-10} \text{ Pa}^{-1}$ at 10 °C (Kell 1975). The

discrepancy can be attributed to the mechanical compliance of the equipment.

Semi-logarithmic plots presented in Fig. 8 give a qualitative comparison of the hydraulic behaviours characterising the different tested intervals. Degree of pore pressure dissipation (U) and normalised drawdown pressure (U_{norm}) are respectively defined by the following equations:

$$U = \frac{U_t - U_0}{U_{min} - U_0} \quad (15)$$

$$U_{norm} = \frac{U_t - U_{min}}{U_0 - U_{min}}, \quad (16)$$

where U_t [kPa] is the pore pressure at time t , U_0 [kPa] is the hydrostatic pore pressure in situ and U_{min} [kPa] is the pore pressure reached after pulse application or at the end of the pumping phase.

Discrepancies in the degree of dissipation can be observed between tests performed on a same interval (Fig. 8a). Constant rate withdrawal tests were carried out using the same flow rate of 0.3 g h^{-1} for different durations. To compare the evolution of pore pressures in the measuring intervals during pumping phase, P_{min} was taken to correspond to the shortest pumping duration in the calculation of U_{norm} . If specific storage is assumed homogeneous through the Opalinus Clay, the order from left to right on Fig. 8b gives an indication of decreasing permeability.

The application of a composite model, which takes into account a damaged skin zone, was required for most of the test numerical interpretations. Taking as an example the first pulse test carried out on BDB-1 Interval 2, Fig. 9 shows a comparison of the residuals (measured value minus simulated value) to that of a normal distribution, using a homogeneous model and a composite one. The homogeneous model appears to be unsatisfactory because the residuals are not normally distributed, which indicates the presence of a systematic error.

Pulse tests and constant rate pumping tests results are respectively compiled in Table 3. Pulse testing revealed the highest hydraulic conductivity values in the Staffelegg Formation (Interval 1, see Fig. 2b) with best fit values ranging from 2.1×10^{-10} to $5.9 \times 10^{-10} \text{ m s}^{-1}$. Located in the basal shaly facies of Opalinus Clay (Interval 2), the bottom part of the main fault zone is characterised by conductivity values from 3.1×10^{-12} to $7.3 \times 10^{-12} \text{ m s}^{-1}$ and do not differ from the upper shaly facies represented by Interval 4 and 5 (Fig. 10), whose best estimates are up to $4.2 \times 10^{-12} \text{ m s}^{-1}$. The lowest values are found in the sandy facies (Interval 6, best fit values up to $2.7 \times 10^{-13} \text{ m s}^{-1}$), and the carbonate-rich sandy facies (Interval 3, best fit values up to $5.1 \times 10^{-13} \text{ m s}^{-1}$). The basal part of the Passwang

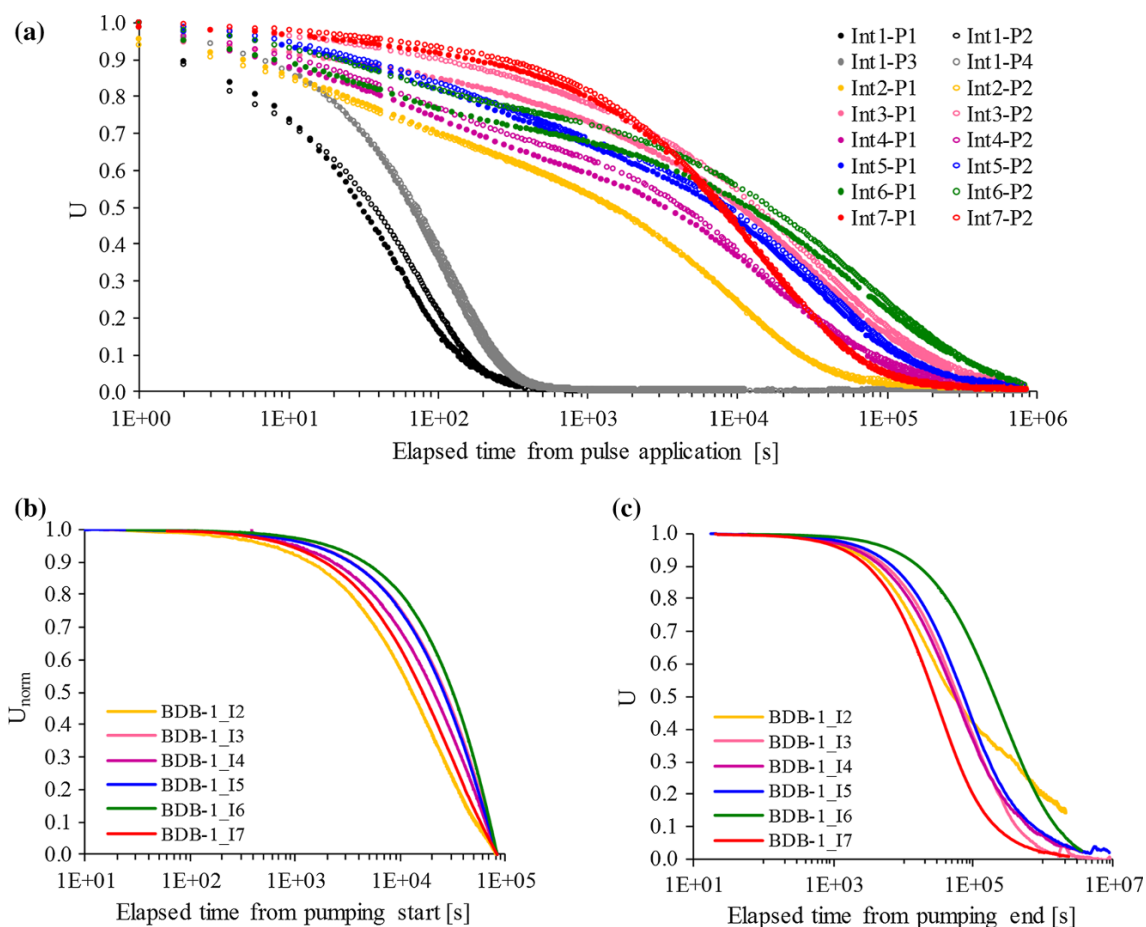


Fig. 8 Comparison of the different tests performed on BDB-1 borehole: **a** degree of dissipation associated to the recovery phases of pulse withdrawal tests; **b** normalised pressure drawdown during

constant rate withdrawal tests and **c** degree of dissipation following the end of the withdrawal phase

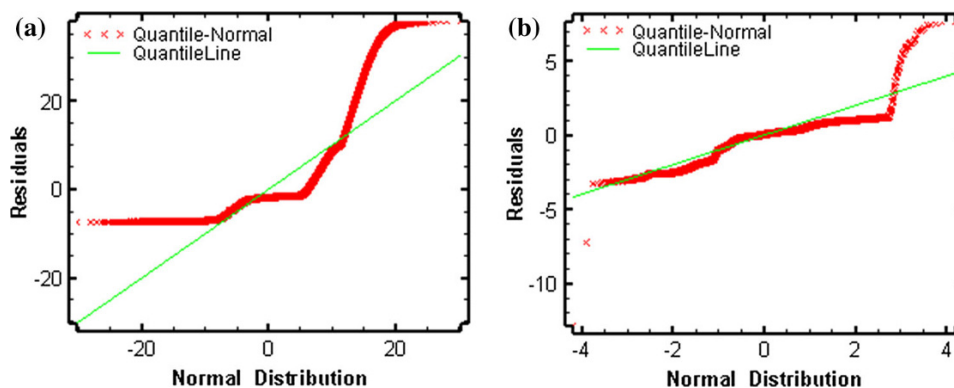


Fig. 9 Example of residual plots for the optimization of Interval 2 (Opalinus Clay shaly facies) pulse sequence fit to the Cartesian pressure response using **a** a homogeneous model and **b** a composite model with skin

Formation, represented by Interval 7, shows similar hydraulic conductivity values to Opalinus Clay (5.8×10^{-13} – 1.4×10^{-12} m s⁻¹).

The analyses results of the constant flowrate withdrawal tests are quite consistent with those obtained from pulse tests. Indeed, a similar trend can be observed with slightly

Table 3 Parameter estimates from BDB-1 borehole pulse withdrawal tests and constant rate (CR) withdrawal tests (K [m s⁻¹]: hydraulic conductivity; S_s [m⁻¹]: specific storage; n: flow dimension; t_s [cm]: skin thickness)

Test	Interval	T _s [cm]	K [m s ⁻¹]			S _s [m ⁻¹]			n	
			Formation		Skin	Formation		Skin	Range	Best fit
			Range	Best fit	Best fit	Range	Best fit	Best fit		
Pulse										
C1-1	I ₁	-	1 × 10 ⁻¹⁰ -3.5 × 10 ⁻¹⁰	2.1 × 10 ⁻¹⁰	-	6 × 10 ⁻⁹ - 6.3 × 10 ⁻⁸	1.4 × 10 ⁻⁸	-	1.9-2.7	2.2
C1-2	I ₁	-	1 × 10 ⁻¹¹ -1 × 10 ⁻⁷	4.2 × 10 ⁻¹⁰	-		1.4 × 10 ⁻⁶	-		2.0
C1-3	I ₁	-	1 × 10 ⁻¹¹ -1 × 10 ⁻⁷	5.6 × 10 ⁻¹⁰	-		6.3 × 10 ⁻⁸	-		2.4
C1-6	I ₁	-	3 × 10 ⁻¹¹ -1 × 10 ⁻⁸	5.9 × 10 ⁻⁹	-		8.3 × 10 ⁻⁷	-		2.0
C2-1	I ₂	0.5	2 × 10 ⁻¹² -3 × 10 ⁻¹¹	3.1 × 10 ⁻¹²	7.8 × 10 ⁻¹²	1 × 10 ⁻⁷ - 3 × 10 ⁻⁵	5.2 × 10 ⁻⁶	4.3 × 10 ⁻⁵	1.8-3.0	2.8
C2-2	I ₂	0.5	2 × 10 ⁻¹² -1 × 10 ⁻¹⁰	7.3 × 10 ⁻¹²	1.0 × 10 ⁻¹¹	1 × 10 ⁻⁷ - 2 × 10 ⁻⁵	3.0 × 10 ⁻⁶	4.7 × 10 ⁻⁵	1.4-2.9	2.0
C3-1	I ₃	0.5	1 × 10 ⁻¹³ -3 × 10 ⁻¹²	5.1 × 10 ⁻¹³	1.6 × 10 ⁻¹²	5 × 10 ⁻⁷ - 3 × 10 ⁻⁵	3.7 × 10 ⁻⁶	1.2 × 10 ⁻⁵	1.4-3.1	2.1
C3-2	I ₃	0.5	2 × 10 ⁻¹³ -2 × 10 ⁻¹²	4.9 × 10 ⁻¹³	1.6 × 10 ⁻¹²	2 × 10 ⁻⁶ - 3 × 10 ⁻⁵	1.1 × 10 ⁻⁵	1.5 × 10 ⁻⁵	1.4-3.4	2.5
C4-1	I ₄	0.5	1 × 10 ⁻¹² -9 × 10 ⁻¹²	2.3 × 10 ⁻¹²	5.7 × 10 ⁻¹²	2 × 10 ⁻⁶ - 1 × 10 ⁻⁵	6.4 × 10 ⁻⁶	5.5 × 10 ⁻⁵	1.7-3	2.3
C4-2	I ₄	2.0	7 × 10 ⁻¹³ -1 × 10 ⁻¹¹	4.2 × 10 ⁻¹²	2.7 × 10 ⁻¹¹	1 × 10 ⁻⁶ - 2 × 10 ⁻⁵	2.2 × 10 ⁻⁶	9.7 × 10 ⁻⁶	1.5-3	2.0
C5-1	I ₅	0.5	4 × 10 ⁻¹³ -4 × 10 ⁻¹²	1.6 × 10 ⁻¹²	1.4 × 10 ⁻¹²	3 × 10 ⁻⁷ - 8 × 10 ⁻⁶	1.0 × 10 ⁻⁶	2.6 × 10 ⁻⁵	1.8-2.9	1.9
C5-2	I ₅	0.5	4 × 10 ⁻¹³ -3 × 10 ⁻¹²	1.0 × 10 ⁻¹²	2.7 × 10 ⁻¹²	1 × 10 ⁻⁶ - 3 × 10 ⁻⁵	8.5 × 10 ⁻⁶	4.7 × 10 ⁻⁵	1-3	2.5
C6-1	I ₆	1.5	8 × 10 ⁻¹⁴ -8 × 10 ⁻¹³	1.9 × 10 ⁻¹³	1.4 × 10 ⁻¹¹	8 × 10 ⁻⁷ - 1 × 10 ⁻⁵	6.6 × 10 ⁻⁶	6.6 × 10 ⁻⁶	1.7-3	2.6
C6-2	I ₆	0.5	2 × 10 ⁻¹³ -6 × 10 ⁻¹³	2.7 × 10 ⁻¹³	5.4 × 10 ⁻¹²	1 × 10 ⁻⁶ - 2 × 10 ⁻⁵	1.7 × 10 ⁻⁵	2.9 × 10 ⁻⁵	1.7-3	2.8
C7-1	I ₇	0.5	3 × 10 ⁻¹³ -4.5 × 10 ⁻¹²	5.8 × 10 ⁻¹³	3.7 × 10 ⁻¹³	4 × 10 ⁻⁷ - 2 × 10 ⁻⁵	3.7 × 10 ⁻⁶	1.9 × 10 ⁻⁶	1.9-3.5	3.0
C7-2	I ₇	0.5	4 × 10 ⁻¹³ -2 × 10 ⁻¹²	1.4 × 10 ⁻¹²	8.6 × 10 ⁻¹²	10 ⁻⁹ - 2 × 10 ⁻⁵	1.2 × 10 ⁻⁶	9.4 × 10 ⁻⁷	2.1-2.6	2.3
CR										
C1-7	I ₁	4.3	1 × 10 ⁻¹⁰ -1 × 10 ⁻⁹	5.0 × 10 ⁻¹⁰	5.7 × 10 ⁻⁹	1 × 10 ⁻⁸ - 1 × 10 ⁻⁴	8.2 × 10 ⁻⁶	6.2 × 10 ⁻⁵	2.0-3.0	2.1
C2-2	I ₂	14.2	4 × 10 ⁻¹³ -8 × 10 ⁻¹¹	3.9 × 10 ⁻¹²	3.5 × 10 ⁻¹¹		1.2 × 10 ⁻⁶	9.0 × 10 ⁻⁵	1.4-2.7	1.95
C3-3	I ₃	0.7	1 × 10 ⁻¹³ -2 × 10 ⁻¹²	9.9 × 10 ⁻¹³	1.6 × 10 ⁻¹²	3 × 10 ⁻⁸ - 6 × 10 ⁻⁵	1.5 × 10 ⁻⁵	4.9 × 10 ⁻⁵	1.5-3.0	1.9
C4-3	I ₄	1.4	4 × 10 ⁻¹⁴ -5 × 10 ⁻¹²	2.4 × 10 ⁻¹²	3.0 × 10 ⁻¹²	4 × 10 ⁻⁸ - 3 × 10 ⁻⁴	1.2 × 10 ⁻⁵	4.0 × 10 ⁻⁵	1.9-3.0	2.1
C5-3	I ₅	1.8	7 × 10 ⁻¹⁴ -9 × 10 ⁻¹²	8.1 × 10 ⁻¹³	1.5 × 10 ⁻¹¹	1 × 10 ⁻⁷ - 3 × 10 ⁻⁵	8.9 × 10 ⁻⁵	2.4 × 10 ⁻⁵	1.9-3.0	2.3
C6-3	I ₆	0.5	1 × 10 ⁻¹⁴ -4 × 10 ⁻¹²	2.2 × 10 ⁻¹³	1.1 × 10 ⁻¹²	1 × 10 ⁻⁷ - 2 × 10 ⁻⁵	7.7 × 10 ⁻⁶	9.9 × 10 ⁻⁵	1.5-2.9	2.5
C7-3	I ₇	0.6	1 × 10 ⁻¹³ -1 × 10 ⁻¹²	4.4 × 10 ⁻¹³	8.2 × 10 ⁻¹³	3 × 10 ⁻⁸ - 4 × 10 ⁻⁶	8.5 × 10 ⁻⁶	2.3 × 10 ⁻⁵	2.1-3.0	2.7

Shaded cells represent unrealistically wide range of uncertainties

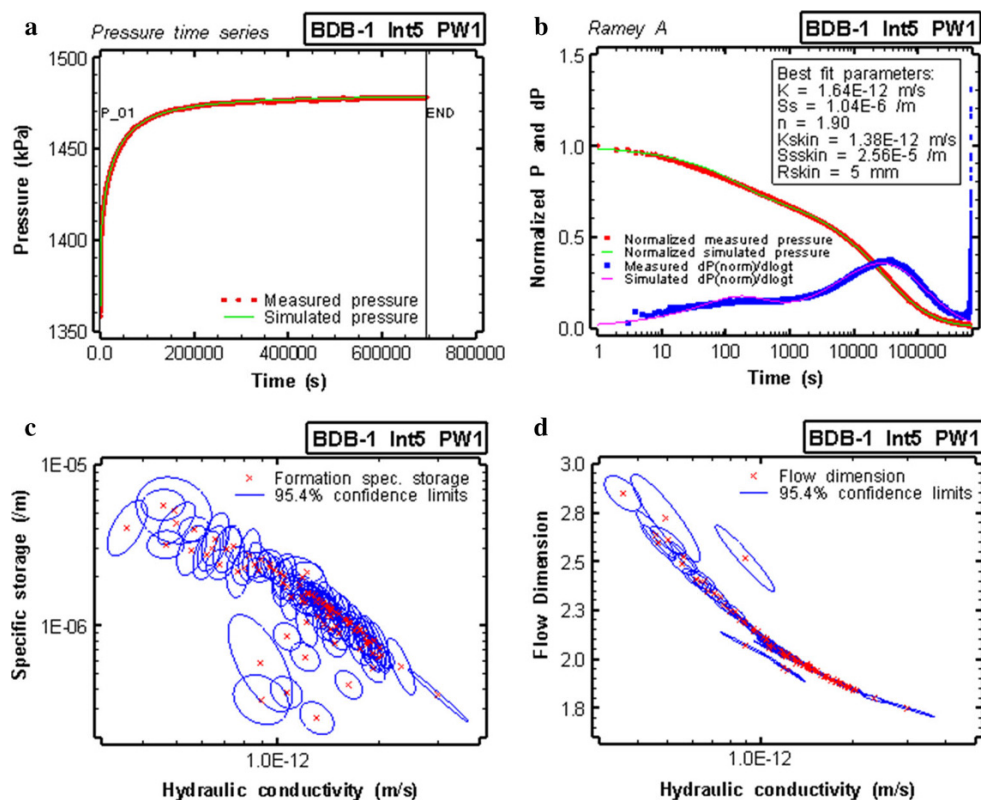


Fig. 10 a Simulation of a pulse test performed on BDB-1 Interval 5 located in the upper shaly facies of Opalinus Clay and b associated Ramey A plot with best fit parameters. Results of 200 perturbation analyses and their confidence regions (c and d)

higher permeability values in the shaly facies than in the sandy facies of Opalinus Clay.

Specific storage and flow dimension estimates are highly variable. One issue with single well hydraulic testing is that the volume of tested rock is limited to the immediate vicinity of the well.

5.3 Hectometer scale: tidal analysis

5.3.1 Tidal identification in BDB-1 pore pressure series

Detection of tidal components was performed on the pore pressure time series monitored by the sensors placed in BDB-1 borehole, with an acquisition time step set at 15 min. The four largest amplitude tidal components, O_1 , K_1 , S_2 and M_2 appear on all processed signals at the exact expected frequencies for time series between September 1st 2014 and March 10th 2015 (Fig. 11).

The form ratio is defined as the sum of the two main diurnal component amplitudes, K_1 and O_1 , divided by the sum of the two main semi-diurnal component amplitudes, M_2 and S_2 (Wiegel 1964). Tidal deformation through the Opalinus Clay at Mont Terri is characterised by a form ratio varying between 0.84 and 1.04, which indicates a

Fig. 11 Estimated Root Mean Square spectrum of pore pressure time series measured in BDB-1 borehole between 01/09/2014 and 10/03/2015. The following tides are observable: principal lunar semi-diurnal tide M_2 (2.236×10^{-5} Hz) and solar semi-diurnal tide S_2 (2.315×10^{-5} Hz), lunar diurnal tides K_1 (1.161×10^{-5} Hz) and O_1 (1.076×10^{-5} Hz), and the solar diurnal components S_1 (1.157×10^{-5} Hz) and P_1 (1.154×10^{-5} Hz)

mixed, mainly semi-diurnal tide (Table 4). The maximum value is found in the interval located in the Passwang Formation, for which the diurnal components have slightly higher amplitudes than the semi-diurnal ones. Except for this interval, the M_2 tide presents the highest amplitude among the four major tides.

5.3.2 Hydraulic parameters computation

The results of specific storage coefficient computation are given in Table 5. Specific storage values are ranging between 1.1×10^{-6} and $1.6 \times 10^{-6} \text{ m}^{-1}$ in the Opalinus Clay and are higher for the adjacent formations ($2.4 \times 10^{-6} \text{ m}^{-1}$ for the Lower Dogger limestone and $3.1 \times 10^{-6} \text{ m}^{-1}$ for the Staffelegg Formation). These estimates are consistent with the range given in the literature, deduced from in situ packer tests and permeameter

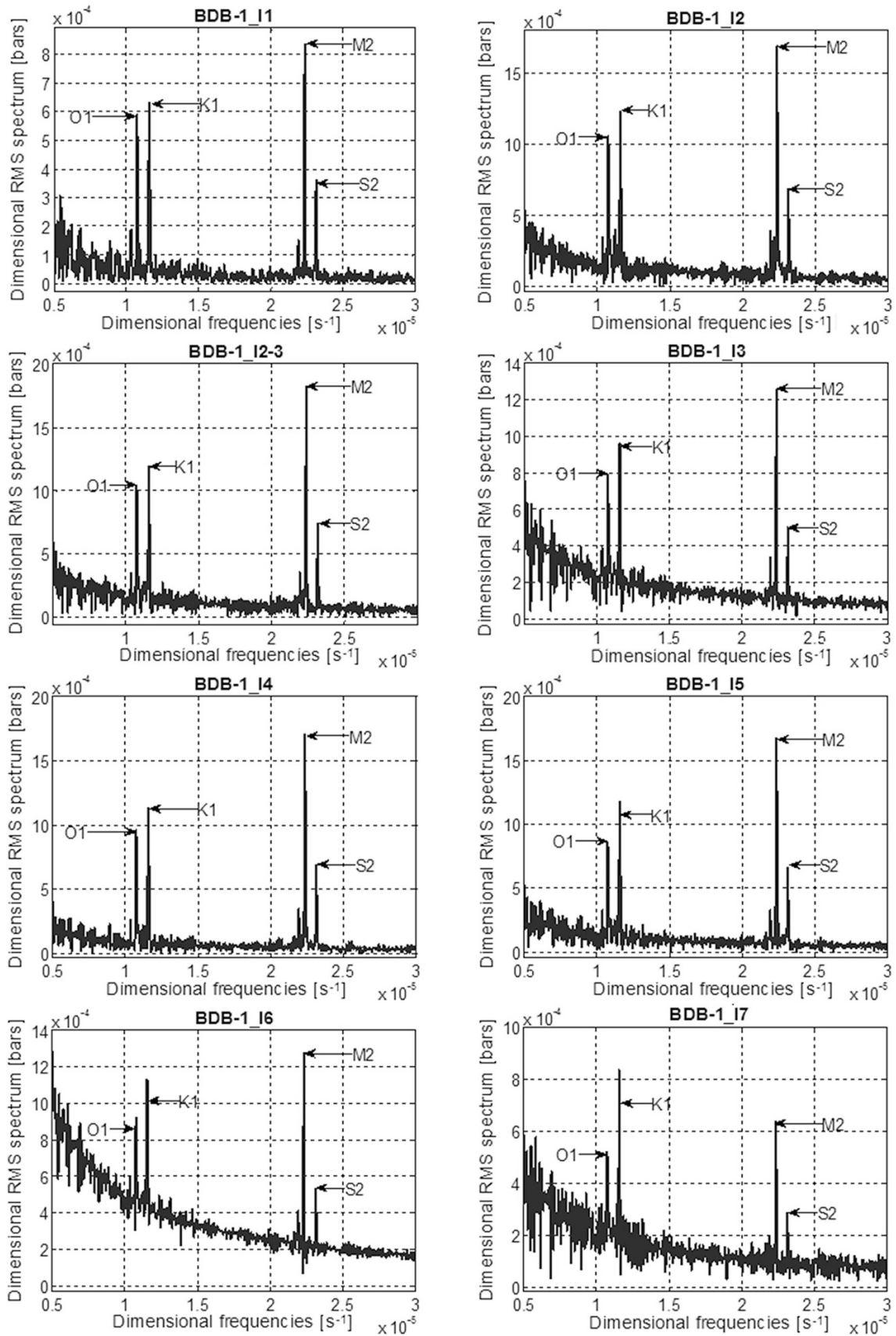


Table 4 Amplitudes of the tidal components with associated frequencies observed on BDB-1 pore pressure time series between 01/09/2014 and 10/03/2015

Formation/associated chamber	Amplitude on the RMS spectrum [bars]				Form ratio
	O ₁ (1.076 × 10 ⁻⁵ Hz)	K ₁ (1.161 × 10 ⁻⁵ Hz)	S ₂ (2.315 × 10 ⁻⁵ Hz)	M ₂ (2.236 × 10 ⁻⁵ Hz)	
Staffelegg formation/I ₁	5.886 × 10 ⁻⁴	6.326 × 10 ⁻⁴	3.606 × 10 ⁻⁴	8.353 × 10 ⁻⁴	1.02
OPA-shaly facies/I ₂	1.054 × 10 ⁻³	1.230 × 10 ⁻³	6.848 × 10 ⁻⁴	1.696 × 10 ⁻³	0.96
OPA-shaly facies/I ₂₋₃	1.041 × 10 ⁻³	1.192 × 10 ⁻³	7.390 × 10 ⁻⁴	1.823 × 10 ⁻³	0.87
OPA-carbonate-rich facies/I ₃	7.905 × 10 ⁻⁴	9.553 × 10 ⁻⁴	5.014 × 10 ⁻⁴	1.255 × 10 ⁻³	0.99
OPA-shaly facies/I ₄	9.560 × 10 ⁻⁴	1.133 × 10 ⁻³	6.838 × 10 ⁻⁴	1.701 × 10 ⁻³	0.88
OPA-shaly facies/I ₅	8.591 × 10 ⁻⁴	1.084 × 10 ⁻⁴	6.546 × 10 ⁻⁴	1.670 × 10 ⁻³	0.84
OPA-sandy facies/I ₆	8.637 × 10 ⁻⁴	1.205 × 10 ⁻³	5.329 × 10 ⁻⁴	1.278 × 10 ⁻³	1.04
Passwang formation/I ₇	5.200 × 10 ⁻⁴	7.206 × 10 ⁻⁴	2.825 × 10 ⁻⁴	6.360 × 10 ⁻⁴	1.35

Table 5 Specific storage coefficients (S_s) estimated from absolute pore pressure signals for BDB-1 borehole measuring intervals with corresponding formations and amplitudes of pressure head fluctuations Δh

Formation	Chamber	Δh [bar]	Δh [m]	S _s [m ⁻¹]
Upper toarcian-staffelegg formation	I ₁	8.353 × 10 ⁻⁴	8.52 × 10 ⁻³	2.4 × 10 ⁻⁶
Upper toarcian/lower aalenian-opalinus clay-shaly facies	I ₂	1.696 × 10 ⁻³	1.73 × 10 ⁻²	1.2 × 10 ⁻⁶
Upper toarcian/lower aalenian-opalinus clay-shaly facies	I ₂₋₃	1.823 × 10 ⁻³	1.86 × 10 ⁻²	1.1 × 10 ⁻⁶
Lower aalenian-opalinus clay-carbonate-rich facies	I ₃	1.255 × 10 ⁻³	1.28 × 10 ⁻²	1.6 × 10 ⁻⁶
Lower aalenian opalinus clay-shaly facies	I ₄	1.701 × 10 ⁻³	1.73 × 10 ⁻²	1.2 × 10 ⁻⁶
Middle aalenian-opalinus clay-shaly facies	I ₅	1.670 × 10 ⁻³	1.70 × 10 ⁻²	1.2 × 10 ⁻⁶
Upper aalenian-opalinus clay-sandy facies	I ₆	1.278 × 10 ⁻³	1.32 × 10 ⁻²	1.5 × 10 ⁻⁶
Upper aalenian-passwang formation	I ₇	6.360 × 10 ⁻⁴	6.49 × 10 ⁻³	3.1 × 10 ⁻⁶

Table 6 Spectral coherence function (Coh), arithmetic mean of the specific storativity coefficient (\tilde{S}_s), amplitude of the pore pressure signal 1 (A_{z1}), and of the pore pressure signal 2 (A_{z2}), vertical effective amplitude hydraulic conductivity (\tilde{K}_v^{Amp}) and vertical effective phase hydraulic conductivity ($\tilde{K}_v^{\Delta\varphi}$), effective dynamic porosity (ω) obtained for the M₂ earth tide for different couples of sensors in BDB-1 borehole

Chamber	Coh	\tilde{S}_s	A _{z1}	A _{z2}	Δφ	\tilde{K}_v^{Amp}	$\tilde{K}_v^{\Delta\varphi}$	B	ω	ω _{water loss}
	[-]	[m ⁻¹]	[bar]	[bar]	[rad]	[m s ⁻¹]	[m s ⁻¹]	[-]	[-]	[-]
I ₁ vs. I ₂	0.9985	1.8 × 10 ⁻⁶	8.35 × 10 ⁻⁴	1.70 × 10 ⁻³	-0.18220	4.7 × 10 ⁻⁸	7.2 × 10 ⁻⁷	0.2520	0.09	0.18
I ₂ vs. I ₂₋₃	0.9992	1.1 × 10 ⁻⁶	1.70 × 10 ⁻³	1.82 × 10 ⁻³	0.03573	2.5 × 10 ⁻⁶	1.0 × 10 ⁻⁵	1.0350	0.24	0.15
I ₂₋₃ vs. I ₃	0.9986	1.3 × 10 ⁻⁶	1.82 × 10 ⁻³	1.26 × 10 ⁻³	0.07658	1.4 × 10 ⁻⁷	3.3 × 10 ⁻⁶	0.3949	0.11	0.13
I ₃ vs. I ₄	0.9977	1.4 × 10 ⁻⁶	1.26 × 10 ⁻³	1.70 × 10 ⁻³	-0.06768	2.9 × 10 ⁻⁷	5.8 × 10 ⁻⁶	4.6810	1.33	0.12
I ₄ vs. I ₅	0.9930	1.2 × 10 ⁻⁶	1.70 × 10 ⁻³	1.67 × 10 ⁻³	0.02158	5.7 × 10 ⁻⁵	4.1 × 10 ⁻⁶	0.4758	0.12	0.14
I ₅ vs. I ₆	0.9965	1.4 × 10 ⁻⁶	1.67 × 10 ⁻³	1.28 × 10 ⁻³	-0.05037	6.4 × 10 ⁻⁷	1.8 × 10 ⁻⁵	0.2889	0.08	0.13
I ₆ vs. I ₇	0.9965	2.3 × 10 ⁻⁶	1.28 × 10 ⁻³	6.36 × 10 ⁻³	0.50810	3.9 × 10 ⁻⁸	7.3 × 10 ⁻⁸	1.6290	0.79	0.13

Mean water-loss porosity (ω_{water loss}) is given for comparison purposes

Shaded cells indicate spurious values

tests for the Opalinus Clay shaly facies: between 1×10^{-7} and $1 \times 10^{-4} \text{ m}^{-1}$, with a best estimate at $2 \times 10^{-6} \text{ m}^{-1}$ (Bossart and Thury 2008).

Effective dynamic porosity values obtained using the M₂ tide (Table 6) are globally in well agreement with those obtained from petrophysical measurements. Indeed,

coherent values between 8 and 24% are obtained by cross-analyses of measuring intervals located in the Opalinus Clay. Statistical analysis carried out in previous studies on Mont Terri samples (Fatmi 2009; Bailly and Matray 2015) revealed very low range values between 1 and 4% at the tunnel level. These unexplained low values could be

related to the hydraulically disturbed state of the studied area and desaturation phenomena.

Hydraulic conductivity values obtained in the saturated part of the claystone by cross-analysis (Table 6) are much higher than those obtained by other techniques. Indeed, high conductivities ranging between 5.7×10^{-5} and $1.4 \times 10^{-7} \text{ m s}^{-1}$ are found in the Opalinus Clay. These values are 6 to 8 orders of magnitude higher than the range expected from literature data, suggesting that the method is not appropriate for this formation. Discrepancies up to three orders of magnitude between laboratory hydraulic conductivity results and tidal analysis results were also reported by Boldt-Leppin and Hendry (2003) who studied the King site claystone formation (Canada). These discrepancies were explained by scale factor effects and the presence of fractured area.

Bailly and Matray (2015) performed statistical analysis on pore pressure time series acquired in the BCD-3 borehole located at the Mont Terri tunnel level. They obtained hydraulic conductivities ranging between 1.9×10^{-10} and $7.5 \times 10^{-11} \text{ m s}^{-1}$ in the unsaturated part of the Opalinus Clay by applying the same method on the S_1 solar diurnal tide. The M_2 tide was not found in the studied pore pressure time series due to suction conditions associated to the rock laboratory level. The study also suggested that the structures observed in this borehole were hydraulically conductive, meaning that the Opalinus Clay true permeability should be even lower than the range given by tidal analysis.

6 Discussion

6.1 Comparability of laboratory tests and in situ tests results

Reliable estimates of permeability and specific storage that describe the bulk hydraulic behaviour are needed for the evaluation of radionuclide transport in geological formations. Linking the results of laboratory tests to bulk characteristics at the regional scale is not straightforward and the meaning of measured values has to be interpreted. Sedimentary rocks are generally associated with anisotropic properties such as permeability, diffusion coefficient and mechanical features. In the Opalinus Clay, which is an overconsolidated clay, a moderate permeability anisotropy ratio of 5.5 was estimated based on laboratory permeameter tests (Muñoz et al. 2003; Croisé et al. 2004; Fernández-García et al. 2007).

The petrophysical model is based on a conceptual parallel plane geometry which would be associated to a flow orientation parallel to bedding planes. Since BDB-1 borehole was drilled perpendicular to bedding plane, the main solicited direction for fluid flow during hydraulic testing is

also parallel to stratification. For its part, tidal analysis is mainly based on gravitational forces that propagate radially from the center of the Earth and should result, given the setting of the Mont Terri anticline, in composite values of parallel and perpendicular to bedding permeabilities.

Although the petrophysical model may be unsuited to carbonated formations, calculation was also performed on the Passwang Formation and the Staffelegg Formation, which shows similar petrophysical parameters. Another questionable point is the use of a constant value for the Archie's exponent since this parameter depends on the nature of the porous medium. Consequently, adapted values should be taken in the future according to the evolution of rock facies along the stratigraphic sequence. Conductivities values obtained in BDB-1 with variable cementation factor (Fig. 12a) are only indicative and not quality-assured, given the uncertainties linked to data acquisition. Indeed, the Opalinus Clay was in the air-drilled section of the borehole, giving constraints for in situ determination of cementation factor.

Fitting the cementation factor by comparing petrophysical results and estimates from hydraulic tests can be debatable. Indeed, the volume of solicited rock is higher in the latter case and takes greater account of formation heterogeneities and local potentially open fractures. This point is clearly illustrated by the discrepancies observed for the Staffelegg Formation, in which many fractures were evidenced by drillcore mapping. Indeed, petrophysical measurements on centimetre-scale samples do not take into account these hydraulically conductive structures and underestimate the values of bulk properties.

Archie's law is rigorously an empirical relationship that links the electrical resistivity of saturated clay-free rocks and their porosity. However, an analogy can be made between the electrical potential and the concentration. It has been shown that effective diffusion coefficient could be predicted by this relationship in a variety of clays and shales with a cementation factor ranging between 2 and 3 (Boving and Grathwohl 2001; Van Loon et al. 2003; Mazurek et al. 2009). Best fit values of hydraulic conductivity obtained from hydraulic testing are generally higher than those computed with the petrophysical law (Fig. 12a). Hydraulic conductivities higher than $10^{-12} \text{ m s}^{-1}$ found in the Opalinus Clay shaly facies would be associated to illogical values of cementation factor inferior to 1.3, which was given for clean unconsolidated sand packs by Archie (1942).

Whether it be for pulse or constant withdrawal tests, the numerical interpretation of hydraulic tests suggests rather wide and unrealistic ranges of uncertainties for hydraulic conductivity and specific storage. Covering several orders of magnitude and not tightly around the best estimates (Table 3), these uncertainties are probably linked to the

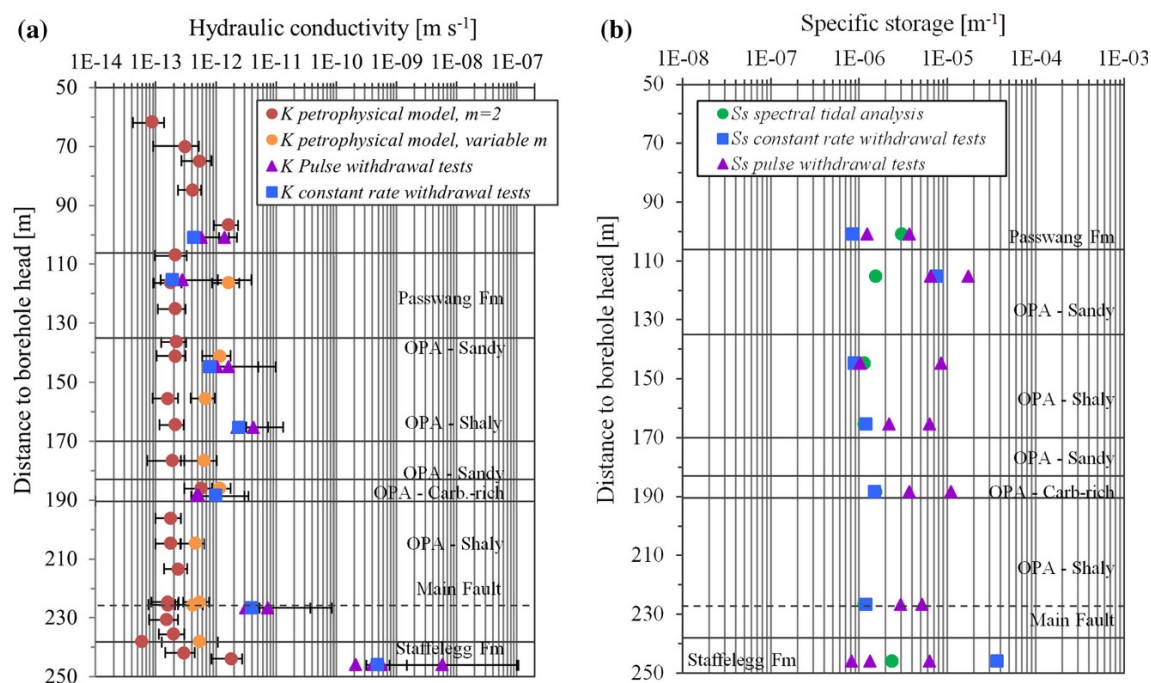


Fig. 12 Comparison of results obtained by petrophysical analysis, in situ hydraulic testing and tidal spectral analysis performed on BDB-1 borehole: **a** hydraulic conductivity **b** specific storage

large number of fitted parameters. Tidal analysis may be more representative than single well hydraulic testing for specific storage estimation (Fig. 12b), since the tidal deformation is applied to the entire rockmass. The highest values for specific storage obtained from pulse testing should be taken with caution since the sensitivity to this parameter is low for this kind of test (Cooper et al. 1967).

6.2 Consistency with previous results

Numerous in situ and laboratory investigations have been carried out at the Mont Terri rock laboratory to characterize the hydraulic properties of the Opalinus Clay. Laboratory permeameter tests revealed conductivity values ranging from 6 to $12 \times 10^{-14} \text{ m s}^{-1}$ with high associated storage coefficient of $4.8 \times 10^{-4} \text{ m}^{-1}$ (Croisé et al. 2004). Figure 13 shows a compilation of hydraulic conductivity results obtained from packer tests (pulse, constant head and constant rate) performed previously at the Mont Terri site (Lavanchy and Mettier 2012), along with data collected in BDB-1 borehole. Tests were mainly performed in boreholes oblique or normal to bedding drilled in area unaffected by the excavation damaged zone of the tunnel. Previous permeability values measured at the rock laboratory level range from 1.5×10^{-14} to $1.1 \times 10^{-9} \text{ m s}^{-1}$ with 55% of the values in the order of $10^{-13} \text{ m s}^{-1}$. The high values above $1.1 \times 10^{-10} \text{ m s}^{-1}$ of the shaly facies from previous studies might be affected by the excavation

damaged zone (EDZ) and are not quality assured. The best fit values obtained from BDB-1 hydraulic testing fall virtually in the expected range with higher values in the order of $10^{-12} \text{ m s}^{-1}$ characterising the Opalinus Clay shaly facies.

Specific storage coefficients obtained by tidal analysis are rather homogeneous within the Opalinus Clay with values in the order of 10^{-6} m^{-1} , which are comparable to the range of 2×10^{-6} to $5 \times 10^{-6} \text{ m}^{-1}$ found by Bailly and Matray (2015).

No significant correlation between the hydraulic conductivity and the different lithological facies was highlighted by Croisé et al. (2004), Nussbaum and Bossart (2004) and Lavanchy and Mettier (2012) due to a lack of data from the sandy facies. Although best fit values obtained from BDB-1 borehole indicate higher values in the shaly facies, uncertainty ranges make it difficult to conclude on a possible contrast. Numerical simulations show that sandstone lenses embedded in clay rich strata do not compromise the barrier function of the Opalinus Clay since low hydraulic conductivity values characterise the entire formation. Furthermore, Opalinus Clay sandy layers are better cemented and display lower porosities (Fig. 5a). Microscopic observations in the sandy facies revealed precipitation of authigenic quartz, carbonates and kaolinite (Peters et al. 2011). On the other hand, porosity values measured in BDB-1 borehole are globally lower than those obtained at the rock laboratory tunnel level and may reflect

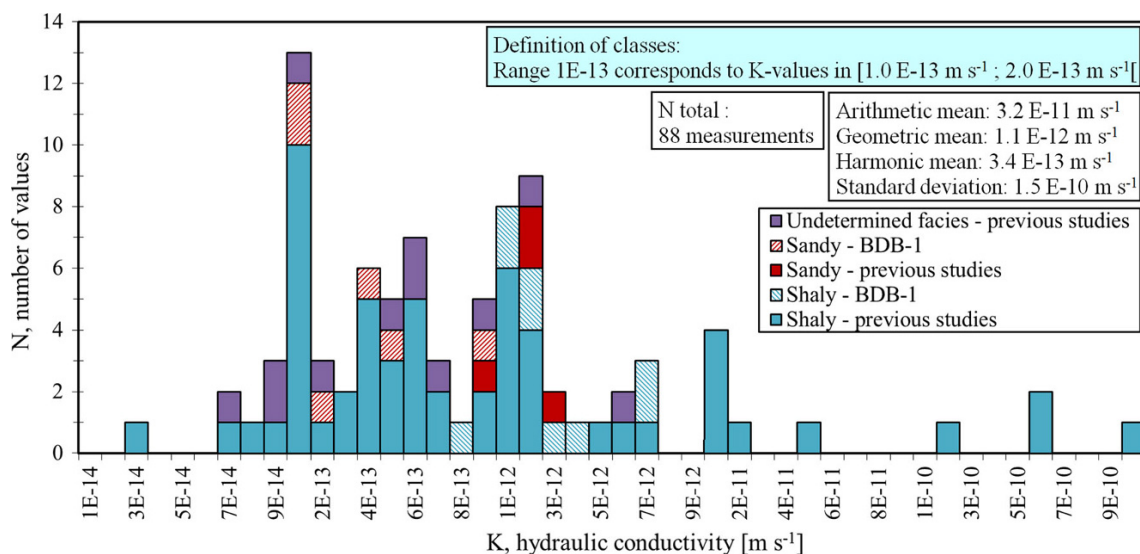


Fig. 13 Compilation of results from hydraulic borehole packer tests performed on the Opalinus Clay at the Mont Terri rock laboratory. The high values of the shaly facies from previous studies might be

the deconfinement and relaxation of stresses occurring at the latter location.

The Main Fault that intersects the laboratory does not impact the barrier function of the Opalinus Clay. Indeed, the sealing of fault planes by calcite shear fibres and clay minerals induce small effect of tectonic deformation on the hydraulic properties of the Opalinus Clay (Nussbaum et al. 2011). This observation is supported by the consistency between the hydraulic tests performed in the intact shaly facies and those carried out in the interval crossing the fault zone. Similarly, no contrast can be identified on the different profiles obtained with the petrophysical model.

7 Conclusions

The deep borehole (DB) experiment enabled the acquisition of data in a fresh borehole penetrating the entire hydraulically undisturbed Opalinus Clay at Mont Terri. Therefore, the presented results are unique, because other hydraulic data at Mont Terri are or might be influenced by tunneling and experimental activities. Three methods with different investigation volumes were carried out and compared.

A model that links intrinsic permeability to petrophysical parameters gives intrinsic permeability values ranging between 2×10^{-21} and 6×10^{-20} m² for a cementation factor varying between 2 and 3, corresponding to hydraulic conductivities between 2×10^{-14} and 6×10^{-13} m s⁻¹. Tidal analysis revealed itself not to be an appropriate method to compute hydraulic conductivity in our study, giving values overestimated of several orders of

affected by the EDZ and are not quality assured (modified from Lavanchy and Mettier 2012)

magnitudes. However, this approach gives reasonable values for specific storage and effective porosity. As a third method, in situ hydraulic testing was performed using the multipacker system installed in BDB-1 borehole. Hydraulic conductivity values obtained by numerical inversion from pulse tests are consistent with those deduced from constant rate withdrawal tests, and suggest a slight vertical variability across the formation in the range of 1×10^{-13} to 7×10^{-12} m s⁻¹, possibly due to local variations of the matrix structure, composition and cementation, or the presence of fractures. In conclusion, the hydraulic conductivity values of the deep borehole (DB) experiment agree well with previous hydraulic testing results performed in the hydraulically disturbed Opalinus Clay around the Mont Terri rock laboratory. Therefore, future hydraulic testing in the laboratory outside the excavated damaged zone can be rated as comparable to undisturbed conditions. However, results obtained in BDB-1 borehole show higher values (in the order of 10^{-12} m s⁻¹) for the Opalinus Clay shaly facies than its sandy facies (in the order of 10^{-13} m s⁻¹), which is consistent with previous microscopic observations (Peters et al. 2011). Further laboratory experiments using Hassler cells will be performed to characterise the Opalinus Clay permeability anisotropy in the future.

Petrophysical analysis of drillcores and time-series analyses are complementary to hydraulic testing. These techniques involve different volumes of investigation. Core analysis, as well as laboratory permeameter tests, give the homogeneous matrix hydraulic properties but do not account for larger scale heterogeneities such as sedimentary and tectonic features. Moreover, analyses on core

samples might be influenced by deconfining and alteration of the core material, thus resulting in biased values. Therefore, hydraulic testing in a fresh borehole is the recommended method for determination of hydraulic conductivity in overconsolidated clays. However, the pressure perturbations e.g., induced by drilling activities have to be taken into account for design and analyses of hydraulic testing. The dissipation of drilling and installation of instrumentation induced pressure perturbations can be identified by the tidal components in the pore pressure time series. Our study showed that drilling the BDB-1 borehole with air as drilling fluid and a saturation with artificial pore-water was an appropriate choice for our application, because: (1) no mud-cake was created, (2) no artificial osmotic effects and borehole convergence were observed so far, (3) future water sampling can be carried out since there was no contamination with drilling mud, and (4) we reached fully undisturbed formation pressures after several months. The latter was possible to do so in an underground laboratory experiment, due no time and financial constraints, which are limiting factors on drill site for exploration boreholes. Therefore, in clay formations, particular care should be taken in the choice of drilling method and drilling fluid as well as borehole instrumentation materials, in order to obtain accurate hydraulic parameters.

Acknowledgements This study was performed in the framework of the deep borehole (DB) experiment, financed by six partners of the International Mont Terri Consortium (swisstopo, NAGRA, BGR, GRS, NWMO, IRSN). The authors would like to thank Karam Kontar and Jocelyn Gisiger (Solexperts AG) for their technical support and realisation of hydraulic testing, as well as Christelle Courbet (IRSN) and Benoît Paris (INTERA) for advices on numerical interpretation. The MuStat v1 package used in this paper is the result of previous works respectively done by: Alain Mangin (CNRS, Laboratoire d'écologie des hydrosystèmes de Moulis), David Labat (Géosciences Environnement Toulouse), Rachid Ababou (CNRS/INPT/IMFT), Hassane Fatmi (PhD at IRSN and CNRS/INPT/IMFT) and David Bailly (TREES Institute). The constructive and careful reviews of Prof. Z. Jiang (Queensland University of Technology, Brisbane, Australia) and Prof. P. Cosenza (University of Poitiers, France) contributed to improve the initial version of this article and are greatly acknowledged.

Open Access This article is distributed under the terms of the Creative Commons Attribution 4.0 International License (<http://creativecommons.org/licenses/by/4.0/>), which permits unrestricted use, distribution, and reproduction in any medium, provided you give appropriate credit to the original author(s) and the source, provide a link to the Creative Commons license, and indicate if changes were made.

References

- Ababou, R., Fatmi, H., Matray, J. M., Nussbaum, C., & Bailly, D. (2012). Statistical analyses of pore pressure signals in claystone during excavation works at the Mont Terri Underground Research Laboratory. In R. Abdel Rahman (Ed.), *Radioactive waste* (pp. 373–430). Publisher: InTech.
- Altinier, M. V. (2006). Etude de la composition isotopique des eaux porales de l'argilite de Tournemire : intercomparaison des méthodes de mesure et relations avec les paramètres pétrophysiques. Ph. D. dissertation, Université Paris-Sud, Orsay, France, pp. 200
- Archie, G. E. (1942). The electrical resistivity log as an aid in determining some reservoir characteristics. *Transactions of the American Institute of Mining Metallurgical, and Petroleum Engineers*, 146, 54–62.
- Bailly, D., Matray, J. M., & Ababou, R. (2014). Temporal behavior of a ventilated claystone at the Tournemire URL: Cross-spectral analyses focused on daily harmonics. *Engineering Geology*, 183, 137–158.
- Bailly, D., & Matray, J.-M. (2015). LP-A Experiment: Phase 20, Statistical analysis of time series acquired in the EZ-B Niche and at the Main fault. Mont Terri Technical Note, TN 2014-59, 79 pp. Federal Office of Topography (swisstopo), Wabern, Switzerland. www.mont-terri.ch.
- Barker, J. A. (1988). A generalized radial-flow model for hydraulic tests in fractured rock. *Water Resources Research*, 24(10), 1796–1804.
- Beauheim, R. L., Roberts, R. M., & Avis, J. D. (2004). Well testing in fractured media: flow dimensions and diagnostic plots. *Journal of Hydraulic Research*, 42, 69–76.
- Beauheim, R. L., & Roberts, R. M. (2004). Well-test analysis techniques developed for the Waste Isolation Pilot Plant. In Proceedings of the 66th EAGE Conference and Exhibition, Paris, France.
- Blaesi, H.-R., Peters, T. J., & Mazurek, M. (1991). Der Opalinus-Ton des Mt. Terri (Kanton Jura): Lithologie, Mineralogie und physiko-chemische Gesteinsparameter. Nagra Interner Bericht, (pp. 90–60). Nagra, Wettingen, Switzerland. www.nagra.ch.
- Boldt-Leppin, B. E. J., & Hendry, J. (2003). Application of Harmonic Analysis of Water Levels to Determine Vertical Hydraulic Conductivities in Clay-Rich Aquitards. *Ground Water*, 41(4), 514–522.
- Bossart, P., & Thury, M. (2008). Mont Terri Rock Laboratory. Project, Programme 1996 to 2007 and Results. Reports of the Swiss Geological Survey, No. 3, p 445. Federal Office of Topography (swisstopo), Wabern, Switzerland. www.mont-terri.ch.
- Bossart, P., Bernier, F., Birkholzer, J., Bruggeman, C., Connolly, P., Dewonck, S., Fukaya, M., Herfort, M., Jensen, M., Matray, J.-M., Mayor, J. C., Moeri, A., Oyama, T., Schuster, K., Shigeta, N., Vietor, T., & Wiczorek, K. (2017). Mont Terrirock laboratory, 20 years of research: introduction, site characteristics and overview of experiments. *Swiss Journal of Geosciences*, 110. doi:10.1007/s00015-016-0236-1 (this issue).
- Boulin, P. F., Bretonnier, P., Gland, N., & Lombard, J. M. (2012). Contribution of the steady state method to water permeability measurement in very low permeability porous media. *Oil and Gas Science and Technology*, 67, 387–401.
- Boving, T. B., & Grathwohl, P. (2001). Tracer diffusion coefficients in sedimentary rocks: correlation between porosity and hydraulic conductivity. *Journal of Contaminant Hydrogeology*, 53(1), 85–100.
- Bredehoeft, J. D. (1967). Response of well-aquifer systems to Earth tides. *Journal of Geophysical Research*, 72(12), 3075–3087.
- Bredehoeft, J. D., & Papadopoulos, S. S. (1980). A method for determining the hydraulic properties of tight formations. *Water Resources Research*, 16(1), 233–238.
- Butler, J. J. (1998). *The design and performance, and analysis of slug tests* (p. 252). Boca Raton: Lewis Publishers (imprint of CRC Press LLC).

- Chapuis, R. P., & Aubertin, M. (2003). *Predicting the Coefficient of Permeability of Soils Using the Kozeny-Carman Equation* (p. 35). Montréal: Ecole Polytechnique de Montréal.
- Clauer, N., Techer, I., Nussbaum, C., & Laurich, B. (2017). Geochemical signature of paleofluids in microstructures from “Main Fault” in the Opalinus Clay of the Mont Terri rock laboratory, Switzerland. *Swiss Journal of Geosciences*, 110. doi:10.1007/s00015-016-0253-0 (this issue).
- Cooper, H. H., Bredehoeft, J. D., & Papadopulos, I. S. (1967). Response of a finite-diameter well to an instantaneous charge of water. *Water Resource Research*, 3, 263–269.
- Croisé, J., Schilckenrieder, L., Marschall, P., Boisson, J. Y., Vogel, P., & Yamamoto, S. (2004). Hydrogeological investigations in a low permeability claystone formation: the Mont Terri Rock Laboratory. *Physics and Chemistry of the Earth*, 29, 3–15.
- Cuttillo, P. A., & Bredehoeft, J. D. (2011). Estimating aquifer properties from the water level response to earth tides. *Ground Water*, 49(4), 600–610.
- Doodson A. T., & Warburg, H. D. (1941). Admiralty manual of tides. Her Majesty’s Stationary Office, London, xii, p 270.
- Fatmi, H. (2009). *Méthodologie d’analyse des signaux et caractérisation hydrogéologique: application aux chroniques de données obtenues aux laboratoires souterrains du Mont Terri, Tournemire et Meuse/Haute-Marne*. Ph.D. dissertation (p. 249). Toulouse: Université de Toulouse.
- Fatmi, H., Ababou, R., & Matray, J.-M. (2008). Statistical pre-processing analyses of hydrometeorological time series in a geological clay site (methodology and first results for Mont Terri’s PP experiment). *Journal of Physical Chemistry Letters A/B/C*, 33, S14–S23.
- Fernández-García, D., Gómez-Hernández, J. J., & Mayor, J. C. (2007). Estimating hydraulic conductivity of the Opalinus Clay at the regional scale: Combined effect of desaturation and EDZ. *Physics and Chemistry of the Earth, Parts A/B/C*, 32(8), 639–645.
- Fierz, T., & Rösli, U. (2014). Mont Terri DB Experiment: Installation of a 7-interval multi-packer system into borehole BDB-1. Instrumentation Report. Mont Terri Technical Note, TN 2014-23. p 37. Federal Office of Topography (swisstopo), Wabern, Switzerland. www.mont-terri.ch.
- Gautschi, A. (2001). Hydrogeology of a fractured shale (Opalinus Clay): Implications for the deep disposal of radioactive wastes. *Hydrogeology Journal*, 9, 97–107.
- Horseman, S. T., Higgo, J. J. W., Alexander, J., & Harrington, J. F. (1996). Water, Gas and Solute Movement Through Argillaceous Media. Nuclear Energy Agency Rep., CC-96/1, OECD, Paris, p 306.
- Hostettler, B., Reisdorf, A. G., Jaeggi, D., Deplazes, G., Bläsi, H.-R., Morard, A., Feist-Burkhardt, S., Waltschew, A., Dietze, V., & Menkveld-Gfeller, U. (2017). Litho- and biostratigraphy of the Opalinus Clay and bounding formations in the Mont Terri rock laboratory (Switzerland). *Swiss Journal of Geosciences*, 110. doi:10.1007/s00015-016-0250-3 (this issue).
- Jiang, Z., Martiethoz, G., Taulis, M., & Cox, M. (2013). Determination of vertical hydraulic conductivity of aquitards in a multi-layered leaky system using water-level signals in adjacent aquifers. *Journal of Hydrology*, 500, 170–182.
- Johns, R. T., Vomvoris, S. G., & Löw, S. (1995). *Review of hydraulic field tests in the Opalinus Clay of Northern Switzerland*. Nuclear Energy Agency: Hydraulic and hydrochemical characterisation of argillaceous rocks.
- Kell, G. S. (1975). Volume properties of ordinary water. In R. C. Weast (Ed.), *Handbook of chemistry and physics* (56th ed.). Cleveland: CRC Press.
- Keller, C. K., Van der Kamp, G., & Cherry, J. A. (1989). A multiscale study of the permeability of a thick clayey till. *Water Resources Research*, 25(11), 2299–2317.
- Kostek, S., Schwartz, L., & Johnson, D. (1992). Fluid permeability in porous media: Comparison of electrical estimates with hydrodynamical calculations. *Physical Review B*, 45(1), 186–194.
- Lavanchy, J. M., & Mettier, R. (2012). HA (Hydrogeological analysis) Experiment: Hydraulic database, Phases 1-16, Version 1.0. Mont Terri Technical Note, TN 2010-74, p 22. Federal Office of Topography (swisstopo), Wabern, Switzerland. www.mont-terri.ch.
- Marschall, P., Horseman, S., & Gimmi, T. (2005). Characterisation of gas transport properties of the Opalinus Clay, a potential host rock formation for radioactive waste disposal. *Oil and Gas Science and Technology*, 60(1), 121–139.
- Matray, J.-M., Savoye, S., & Cabrera, J. (2007). Desaturation and structure relationships around drifts excavated in the well-compacted Tournemire’s argillite (Aveyron, France). *Engineering Geology*, 90, 1–16.
- Mazurek, M., Hurford, A., & Leu, W. (2006). Unravelling the multi-stage burial history of the Swiss Molasse Basin: integration of apatite fission track, vitrinite reflectance and biomarker isomerisation analysis. *Basin Research*, 18, 27–50.
- Mazurek, M., Alt-Epping, P., Bath, A., Gimmi, T., & Waber, H. N. (2009). *Natural tracer profiles across argillaceous formations: The CLAYTRAC Project* (p. 365). Paris: Nuclear Energy Agency report, OECD.
- Mejías, M., Renard, P., & Glenz, D. (2009). Hydraulic 652 testing of low-permeability formations: A case study in the granite of Cadalso de los Vidrios, Spain. *Engineering Geology*, 107, 88–107.
- Melchior, P. (1978). *The tides of the planet Earth* (p. 609). Oxford: Pergamon Press.
- Mercer, J. W., Pinder, G. F., & Donalson, I. G. (1975). A Galerkin-finite element analysis of the hydrothermal system at Wairakei, New-Zealand. *Journal of Geophysical Research*, 80, 2608–2621.
- Merritt, M. L. (2004). Estimating hydraulic properties of the Floridan aquifer system by analysis of earth-tide, ocean-tide, and barometric effects. Collier and Hendry Counties, Florida. U.S. Geological Survey Water-resources investigations Report 03-4267, p 70.
- Monnier, G., Stengel, P., & Fies, J. C. (1973). Une méthode de mesure de la densité apparente de petits agglomérats terreux. Application à l’analyse de système de porosité du sol. *Annales Agronomiques*, 24, 533–545.
- Muñoz, J. J., Lloret, A., & Alonso, E. (2003). Laboratory Report: Characterization of hydraulic properties under saturated and non saturated conditions. Project Deliverable, 4.
- Nagra (2002). Projekt Opalinuston: Konzept für die Anlage und den Betrieb eines geologischen Tiefenlagers: Entsorgungsnachweis für abgebrannte Brennelemente, verglaste hochaktive sowie langlebige mittelaktive Abfälle. Nagra Technical Report, 02-02, p 24. Nagra, Wettingen, Switzerland. www.nagra.ch.
- Neuzil, C. E. (1982). On conducting the modified ‘slug’ test in tight formations. *Water Resources Research*, 18(2), 439–441.
- Neuzil, C. E. (1994). How permeable are clays and shales? *Water Resources Research*, 30(2), 145–150.
- Neuzil, C. E. (2000). Osmotic generation of “anomalous” fluid pressures in geological environments. *Nature*, 403, 182–184.
- Nussbaum, C., & Bossart, P. (2004). Compilation of K-values from packer tests in the Mont Terri rock laboratory. Mont Terri Technical Note, TN 2005-10, p 29. Federal Office of Topography (swisstopo), Wabern, Switzerland.
- Nussbaum, C., Bossart, P., Amann, F., & Aubourg, C. (2011). Analysis of tectonic structures and excavation induced fractures in the Opalinus Clay, Mont Terri underground rock laboratory (Switzerland). *Swiss Journal of Geosciences*, 104, 187–210.
- Nussbaum, C., Kloppenburg, A., Caer, T. & Bossart, P. (2017). Tectonic evolution of the Mont Terri anticline based on forward

- modelling. *Swiss Journal of Geosciences*, 110. doi:10.1007/s00015-016-0248-x (this issue).
- Pape, H., Clauser, C., & Iffland, J. (1999). Permeability prediction based on fractal pore-space geometry. *Geophysics*, 64, 1447–1460.
- Pearson, F. J., Arcos, D., Boisson, J-Y., Fernández, A. M., Gäbler, H.E., Gaucher, E., Gautschi, A., Griffault, L., Hernán, P., & Waber, N. (2003). Mont Terri Project-Geochemistry of water in the Opalinus Clay Formation at the Mont Terri Rock Laboratory. Reports of the Swiss Geological Survey, No. 5, p 143. Federal Office of Topography (swisstopo), Wabern, Switzerland. www.mont-terri.ch.
- Peters, M., Mazurek, M., Jaeggi, D., & Müller, H. (2011). WS-H Experiment: Heterogeneities in the sandy facies of Opalinus Clay on a scale on millimetres to centimeters. Mont Terri Technical Note, TN 2010-76, p 66. Federal Office of Topography (swisstopo), Wabern, Switzerland.
- Terzaghi, V. K. (1936). The shearing resistance of saturated soils and the angle between the planes of shear. *First International Conference of Soil Mechanics*, Harvard University Press, 1, 54–56.
- Timms, W. A., & Acworth, R. I. (2005). Propagation of pressure change through thick clay sequences: an example from Liverpool Plains, NSW, Australia. *Hydrogeology Journal*, 13(5–6), 858–870.
- Tremosa, J. (2010). Influence of osmotic processes on the excess-hydraulic head measured in the Toarcian/Domerian argillaceous formation of Tournemire. Ph.D. dissertation (p. 322). Paris: Université Pierre et Marie Curie.
- UNESCO. (1981). Tenth report on the joint panel on oceanographic tables and standard. *UNESCO Technical Paper in Marine Science*, 36, 28.
- Ullman, W. J., & Aller, R. C. (1982). Diffusion coefficients in nearshore marine sediments. *Limnology and Oceanography*, 27, 552–556.
- Van Loon, L. R., & Mibus, J. (2015). A modified version of Archie's law to estimate effective diffusion coefficients of radionuclides in argillaceous rocks and its application in safety analysis studies. *Applied Geochemistry*, 59, 85–94.
- Van Loon, L. R., Soler, J. M., Jakob, A., & Bradbury, M. H. (2003). Effect of confining pressure on the diffusion of HTO, $^{36}\text{Cl}^-$ and $^{125}\text{I}^-$ in a layered argillaceous rock (Opalinus Clay): diffusion perpendicular to the fabric. *Applied Geochemistry*, 18, 1653–1662.
- Van der Kamp, G. (2001). Methods for determining the in situ hydraulic conductivity of shallow aquitards—an overview. *Hydrogeology Journal*, 9, 5–16.
- Wiegel, R. L. (1964). *Tsunamis, storm surges, and harbour oscillations*. In *Oceanographical Engineering* (pp. 95–127). Englewood Cliffs: Prentice Hall.
- Yu, L., Rogiers, B., Gedeon, M., Marivoet, J., Craen, M. D., & Mallants, D. (2013). A critical review of laboratory and in situ hydraulic conductivity measurements for the Boom Clay in Belgium. *Applied Clay Science*, 75, 1–12.

Geochemical signature of paleofluids in microstructures from Main Fault in the Opalinus Clay of the Mont Terri rock laboratory, Switzerland

Norbert Clauer¹ · Isabelle Techer² · Christophe Nussbaum³ · Ben Laurich^{4,5}

Received: 6 March 2016 / Accepted: 9 December 2016 / Published online: 19 January 2017
© Swiss Geological Society 2017

Abstract The present study reports on elemental and Sr isotopic analyses of calcite and associated celestite infillings of various microtectonic features collected mostly in the Main Fault of the Opalinus Clay from Mont Terri rock laboratory. Based on a detailed microstructural description of veins, slickensides, scaly clay aggregates and gouges, the geochemical signatures of the infillings were compared to those of the leachates from undeformed Opalinus Clay, and to the calcite from veins crosscutting Hauptrogenstein, Passwang and Staffelegg Formations above and below the Opalinus Clay. Vein calcite and celestite from Main Fault yield identical $^{87}\text{Sr}/^{86}\text{Sr}$ ratios that are also close to those recorded in the Opalinus Clay matrix inside the Main Fault, but different from those of the diffuse Opalinus Clay calcite outside the fault. These varied $^{87}\text{Sr}/^{86}\text{Sr}$ ratios of the diffuse calcite evidence a

lack of interaction among the associated connate waters and the flowing fluids characterized by a homogeneous Sr signature. The $^{87}\text{Sr}/^{86}\text{Sr}$ homogeneity at 0.70774 ± 0.00001 (2σ) for the infillings of most microstructures in the Main Fault, as well as of veins from nearby limestone layer and sediments around the Opalinus Clay, claims for an “infinite” homogeneous marine supply, whereas the gouge infillings apparently interacted with a fluid chemically more complex. According to the known regional paleogeographic evolution, two seawater supplies were inferred and documented in the Delémont Basin: either during the Priabonian (38–34 Ma ago) from western Bresse graben, and/or during the Rupelian (34–28 Ma ago) from northern Rhine Graben. The Rupelian seawater that yields a mean $^{87}\text{Sr}/^{86}\text{Sr}$ signature significantly higher than those of the microstructural infillings seems not to be the appropriate source. Alternatively, Priabonian seawater yields a mean $^{87}\text{Sr}/^{86}\text{Sr}$ ratio precisely matching that of the leachates from diffuse calcite of the Opalinus Clay inside the Main Fault, as well as that of its microstructures and the same features of the sediments above and below. To envision a Priabonian seawater supply, there is a need for its storage without a significant evolution in its Sr isotopic composition until the final deformation of the area. The paleo-hydrogeological context calls for a possible infiltration of the seawater into a limestone karst located above the Opalinus Clay that could have acted as the storage reservoir. The karstic nature of this reservoir also explains why the $^{87}\text{Sr}/^{86}\text{Sr}$ of the fluids was not modified significantly until expulsion. An alternative storage could have been provided by the regional faulting system that developed during the contemporary regional rifting of the Rhine Graben. The fluid expulsion started along these extensional faults during the further Upper Eocene–Lower Oligocene rifting phase. Later, the thin-

Editorial handling: P. Bossart and A. G. Milnes.

This is paper #5 in the Mont Terri Special Issue of the Swiss Journal of Geosciences (see Bossart et al. 2017, Table 3 and Fig. 7)

✉ Norbert Clauer
nclauer@unistra.fr

- ¹ Laboratoire d’Hydrologie et de Géochimie de Strasbourg (CNRS-UdS), 1 rue Blessig, 67084 Strasbourg, France
- ² Equipe Associée 7352 CHROME, Université de Nîmes, rue du Dr. Georges Salan, 30021 Nîmes, France
- ³ Swiss Geological Survey, Federal Office of Topography Swisstopo, Seftigenstrasse 264, 3084 Wabern, Switzerland
- ⁴ Structural Geology, Tectonics and Geomechanics, RWTH Aachen University, Lochnerstrasse 4-20, 52056 Aachen, Germany
- ⁵ Federal Institute for Geosciences and Natural Resources BGR, Stilleweg 2, 30655 Hannover, Germany

skinned deformation of the Jura Belt affected the Mont Terri region in the form of the Main Fault, probably between approximately 9 and 4 Ma on the basis of preliminary K–Ar ages of nanometer-sized authigenic illite crystals recovered from gouge samples.

Keywords Microtectonic features · Calcite infillings · Elemental and $^{87}\text{Sr}/^{86}\text{Sr}$ geochemistry · Regional geological evolution · Fluid diffusion vs. fluid flow · Past seawater vs. present-day free water

1 Introduction

Petrophysical characteristics of argillaceous sediments are critically important for a reliable evaluation of their abilities to safely confine buried wastes, especially those of the nuclear industry. Low porosity/permeability properties of such potential repositories represent parameters of prime importance as they depend on the intensity of their compaction/cementation (Worden and Morad 2003; Burley and Worden 2003), but also on their structural evolution that can develop post-deposition features able to favor fluid migrations, interactions with the rock materials (Urai and Wong 1994; Mitra and Ismat 2001; Warr and Cox 2001; Milliken and Reed 2010; Buatier et al. 2012), and exportation of released radionuclides. In this context, the Opalinus Clay of the Mont Terri rock laboratory has been selected as a case study for evaluation of its intrinsic storage characteristics. In this context, the occurrence of the well-exposed Main Fault thrust zone provides an excellent opportunity to identify and describe the varied microstructural features (Laurich et al. 2014, 2016; Jaeggi et al. 2017) in order to evaluate their impact on the initial and future porosity/permeability characteristics of the host sediments.

Much has been published about physical deformation induced by tectonic activity in clay-rich shear zones (e.g. Agar et al. 1989; Labaume et al. 1997; Dehandschutter et al. 2005; Eiichi 2012; Ujiie et al. 2013) that can lead to the formation of gouge clusters (e.g. Rutter et al. 1986; Logan et al. 1992; Haines et al. 2013). Of interest here is the occurrence of such features in the Main Fault that potentially facilitate fluid flows interacting with varied host minerals, therefore implying chemical signatures depending on the type of fluids, as well as their temperature and chemical composition. In fact, such geochemical and isotopic tracing and dating information remains of limited application in fold/fault zones, mainly because of challenging sampling aspects (e.g. Schleicher et al. 2006; Sasseville et al. 2008). The sampling constraints are mainly due to the very fine size and therefore to the fragile fabric of the constitutive crystals (e.g. Vrolijk and van der Pluijm 1999; Warr et al. 2014).

A specific study was designed in the frame of Mont Terri scientific research projects to report on a combined geochemical and strontium (Sr) isotopic analysis of calcite and celestite intimately associated in varied microstructural features precisely located in the Main Fault of the Opalinus Clay in the Mont Terri rock laboratory (Techer et al. 2017). These varied microstructures identified and described by Laurich et al. (2014) represent drains that were used once by migrating fluids, as they contain infillings consisting mostly of calcite, but also of celestite. On the basis of electron microscope observations, these authors discussed their impact on the physical rock properties and deduced underlying deformation mechanisms. The objectives of the present geochemical and isotopic study became then a precise collection of these microstructures and a chemical identification of associated calcite and celestite infillings, in order to discuss the origin and nature of the interacting fluids, the extent of their interactions with the host minerals in and next to the microstructures of the Main Fault, as well as in those observed in the associated surrounding undeformed Opalinus Clay matrix and in the Hauptrogenstein, Passwang and Staffelegg Formations from above and below the Opalinus Clay, all taken as references. Clearly, the aim here is not examining the effects of fluid diffusion into the rock mass of the Opalinus Clay, but tracing potential fluid flows that could have migrated in the microstructures of the Opalinus Clay and the sedimentary formations around, with a special emphasis for the rock structures affected tectonically within the Main Fault and nearby.

2 Summary of the geological setting

The geological setting and structural evolution of the Mont Terri region is described in detail in Bossart et al. (2017), and Nussbaum et al. (2017). The Opalinus Clay of interest here consists of incompetent, silty and sandy shales of Aalenian/Toarcian stratigraphic age (ca. 174 Ma). It became a formation of major interest since it was selected for preliminary studies in the search of potential nuclear waste disposal sites in Switzerland, along with the excavation of the Mont Terri rock laboratory (Bundesamt für Energie 2008; Fig. 1a, b). Its argillaceous materials typically yield natural characteristics that appeared suitable for radioactive waste confinement with especially an extremely low hydraulic conductivity, low diffusion coefficients, and a fair retention ability of radionuclides (e.g. Hoth et al. 2007).

Also of concern here is the fact that the Mont Terri rock laboratory is intersected by a 0.8–5 m wide thrust zone called “Main Fault” that outcrops at different underground places in the laboratory. This blind thrust fault has been interpreted to result from a detachment at the base of the Opalinus Clay along the Rietheim Member of the

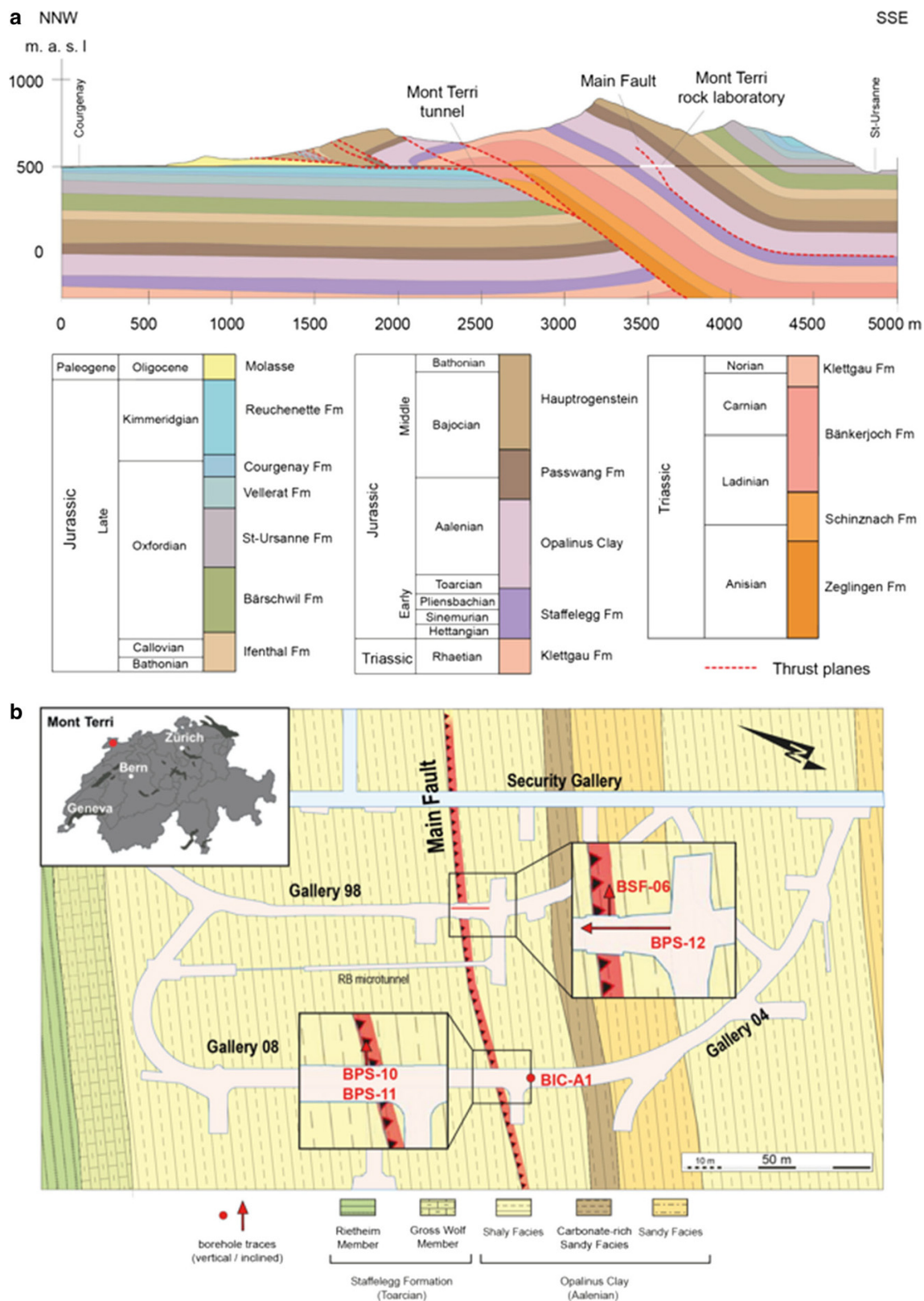


Fig. 1 Geologic context of the Mont Terri underground rock laboratory: **a** regional cross-section of the Mont Terri anticline and the Main Fault with the location of the rock laboratory (from

Nussbaum et al. 2017); **b** geological map with the location of the boreholes from which cores were taken

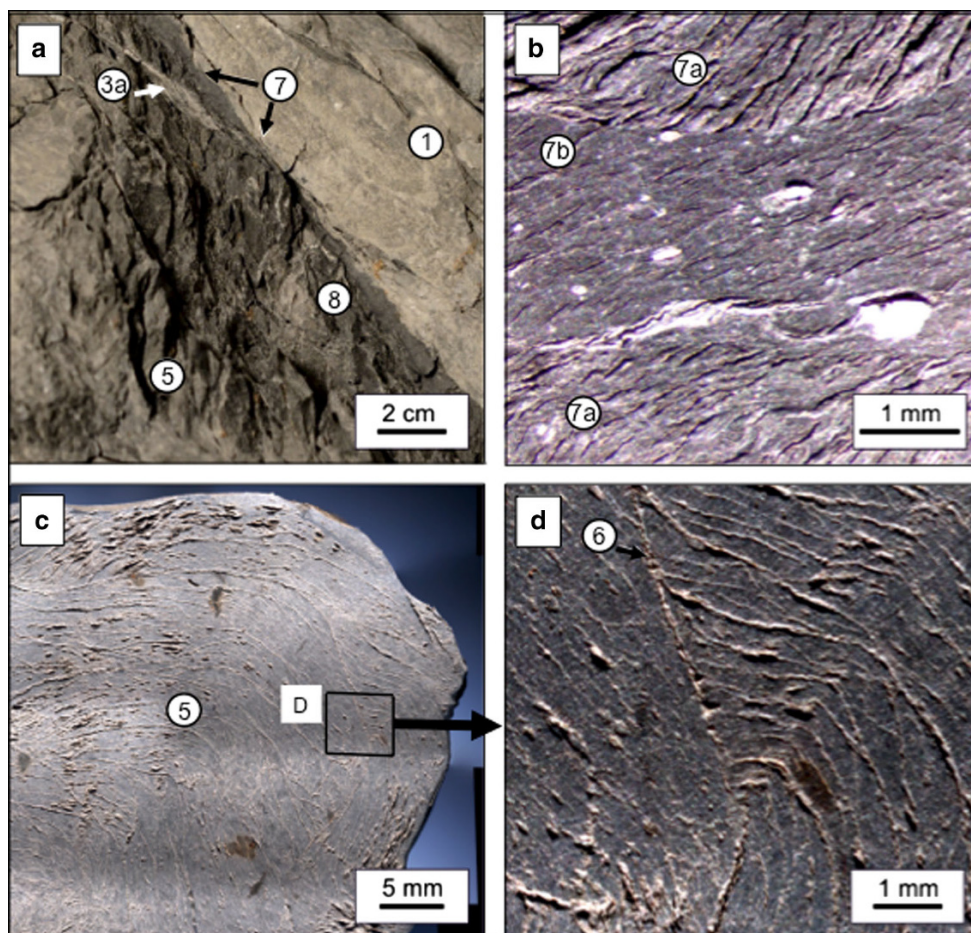


Fig. 2 **a** Photograph showing a detail from upper fault zone boundary of the Main Fault. The picture was taken at the outcrop in gallery 98 (viewing direction ENE). Numbers refer to samples types as given in Fig. 6. Note the thin, continuous dark band of gouge (7) next to brighter undeformed material (1) and the scaly clay next to (8) and away from the gouge (5). **b** Photograph (*shaded light*) of a water immersed gouge sample taken from the Main Fault outcrop in gallery 98. Due to the water immersion, the foliation stands out,

illustrating two different gouge types (7a and 7b). The foliation also suggests high fabric intensity within the gouge. Note the sharp boundary between both types. **c** Photograph (*shaded light*) of a water immersed scaly clay sample from the Main Fault outcrop in gallery 98. Note the high variability in foliation orientation. **d** Detail of **c** showing bend bedding foliation (micro-fold) and discordant shear zones (6)

Staffelegg Formation (Nussbaum et al. 2017; Fig. 1a). It provides an excellent opportunity to investigate incipient deformation and faulting, because of an easy access to extremely well preserved samples either cored into or outcropping at the gallery walls. This access allows a detailed evaluation of the impact of the microstructures on the natural confinement properties of the clay-rich mechanically deformed Opalinus Clay (e.g. Pearson et al. 2003; Bossart and Wermeille 2003; Nussbaum and Bossart 2008). The rocks of the fault zone consist of undeformed and highly strained volumes occurring next to each others (Laurich et al. 2014; Fig. 2a). Abundant in the outcrop of the Main Fault in the laboratory, the slickensides are associated with a network of micrometer-thin shear zones (Figs. 2, 3). They consist often of millimeter-sized calcite veins (Fig. 3), and more rarely of celestite veins.

Nanometer-sized particles, also of clay type, are abundant on the slickenside surfaces and visible within the micrometer-thin shear zones (Figs. 3, 5). An increasing density of the slickensides characterizes the scaly-clay fabric (*sensu* Vannucchi et al. 2003; Fig. 2c, d), comprising a tangled anastomosing network of thin shear zones that

Fig. 3 **a** Photograph of a slickenside surface (*top view*). **b** On such a surface, note the dark, polished parts and the bright, ragged parts, being respectively treads and risers of the slickenside steps (Laurich 2015). The arrow gives the movement direction of the missing block. **c** Photograph of **b** combined with a SEM-EDX Ca mapping picture showing the occurrence of calcite at the risers. This suggests that the risers are in the stress-releasing zones, where Ca precipitation took place. **d** Side view on a micrometer-thin shear zone in a broken sample. Note that the bedding foliation is continuous up to the thin shear zone. **e** Is an *inset* of **d** illustrating that the shear zone width can be as small as only 10th of nm

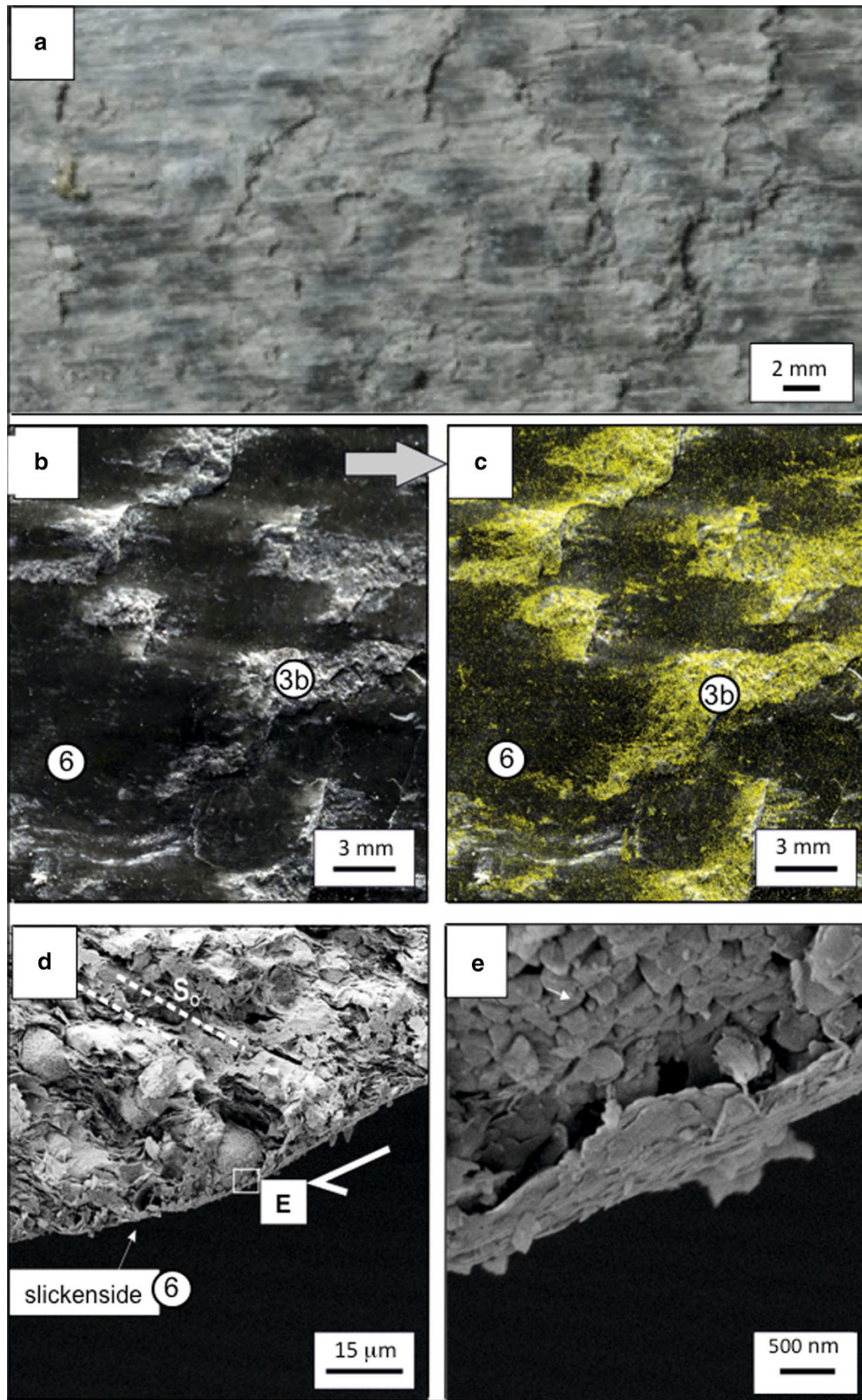
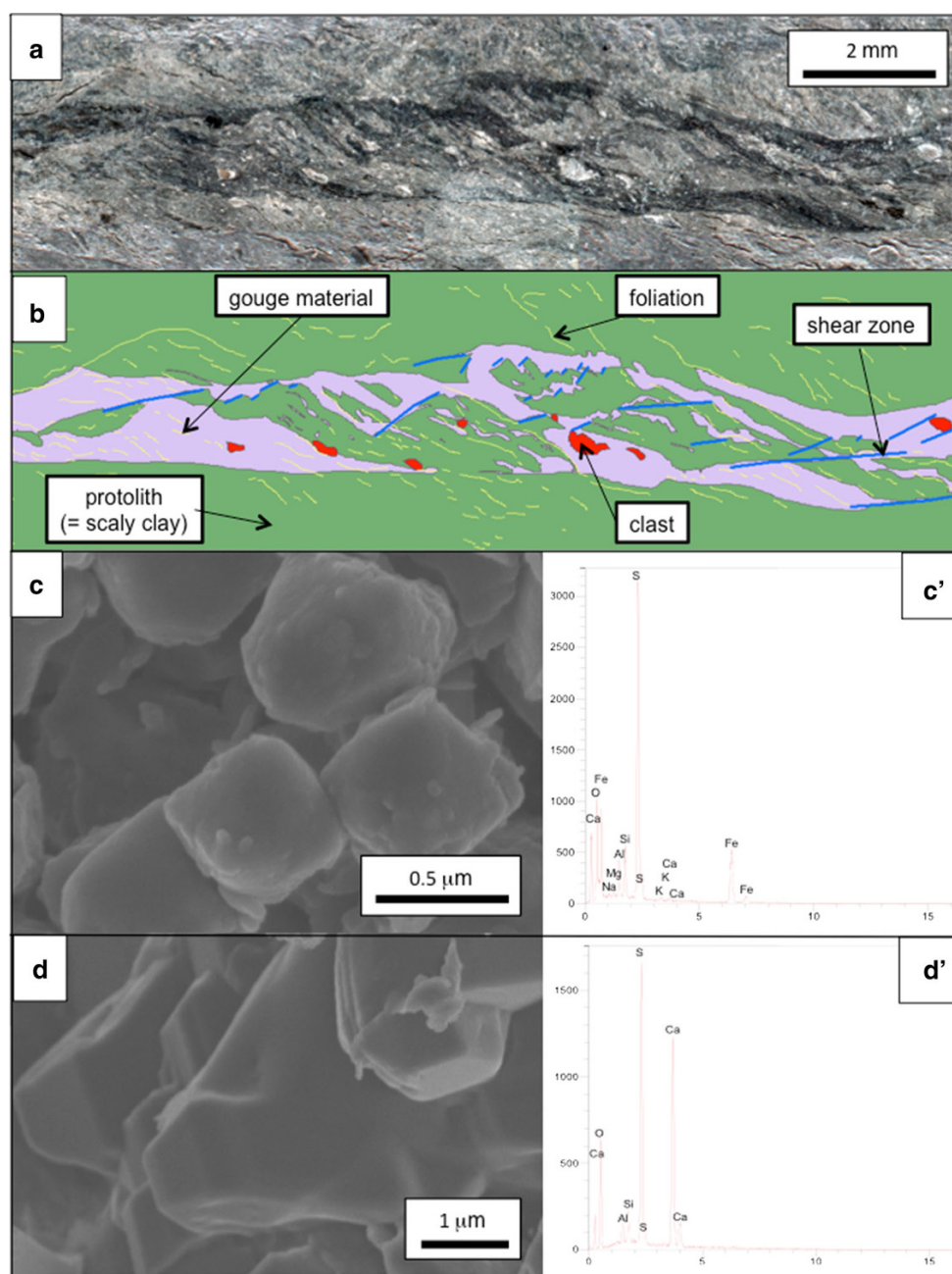


Fig. 4 a, b Photo and interpretative sketch of a water-immersed gouge sample showing gouge (dark black) internal shear zones and grains, as-well as brighter wall rock clasts. The pictured sample was collected in the gallery 08, at the limit between the upper and lower Main Fault segments (from Techer et al. 2017). c Slightly dissolved pyrite grains of the gouge. d Authigenic gypsum crystals of the gouge. The c', d' chemical spectra highlight the dominant occurrence of S in both and of Fe in the former and Ca in the latter



contain lens-shaped facies, almost undeformed microolithons (Laurich et al. submitted). The highest strain of the Opalinus Clay in the Main Fault is possibly localized in a thin (<2 cm) gouge layer at the upper fault zone boundary (Fig. 4a, b). This gouge layer is characterized by a strong foliation, isolated round clasts, grain-size reduction (Fig. 5a) and drastically lower calcite contents than in the nearby scaly clays (Laurich 2015).

Based on a description by Nussbaum et al. (2011) at a macro- and meso-scale, the following information is potentially relevant for the present review: (1) the tectonically undeformed rock fabric is heterogeneous and weakly foliated with a porosity of 8–24% (Nussbaum and Bossart

2008; Houben et al. 2013, 2014), (2) the fracture network and strain intensity are heterogeneous in the fault volume (Nussbaum et al. 2011), comprising zones with tiny fault gouges (<1 cm), shear bands, micro-folds, striated fault planes, all next to apparently undeformed materials, (3) based on paleo-stress analyses of slickenside striae, the kinematic analysis outlines sub-horizontal, striking NNW-SSE in a reverse faulting mode (Nussbaum et al. 2011), and (4) the paleo-fluid flux estimated from calcite and celestite veins in the Rock Laboratory (Pearson et al. 2003) suggests advective flows (Nagra 2008).

The geochemical information available in internal reports from partner organizations of the Mont Terri

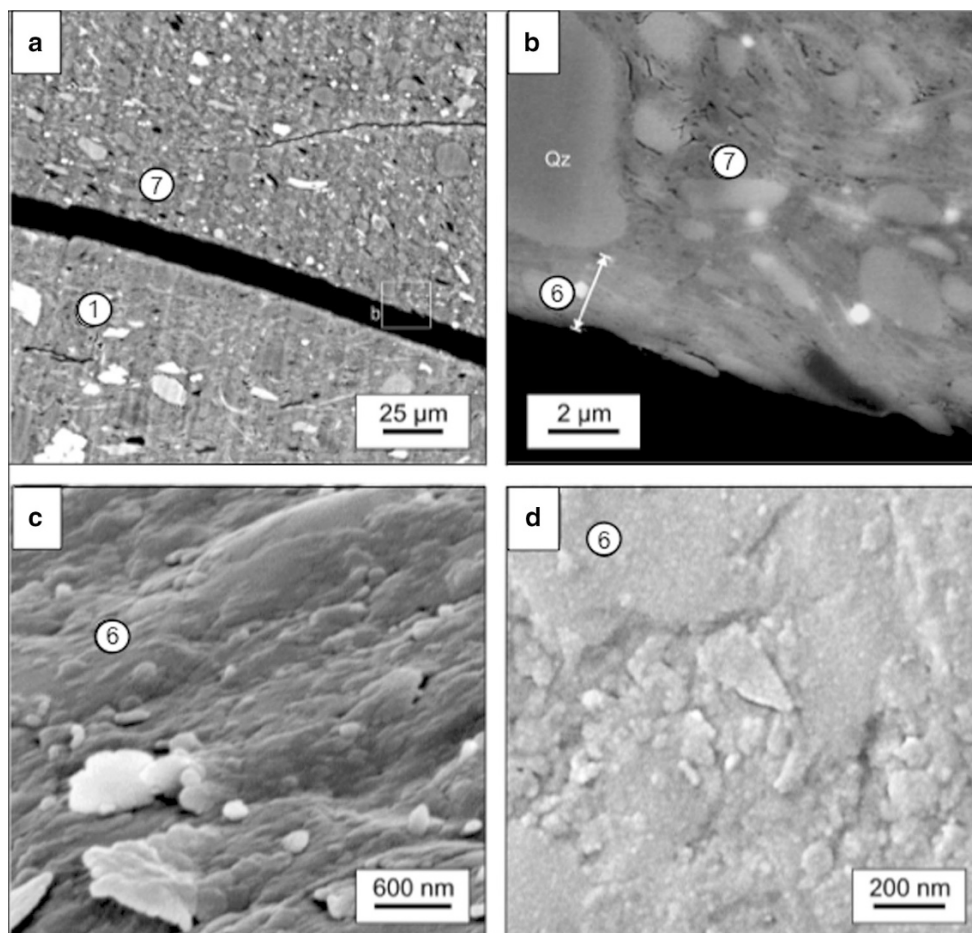


Fig. 5 **a** BIB-SEM micrograph showing a gouge (*upper sample part*) in contact with undeformed material (*lower part*) separated by an open void (=sampling artifact). Compared to undeformed material, the gouge has a smaller grain size, contains more rounded grains and yields higher fabric intensity. **b** Is a detail of the micrograph

a picturing the gouge's boundary to be a micrometer-thin shear zone of shears parallel to nanometer-sized clay particles. **c, d** High-resolution SEM micrographs of slickenside surfaces covered by clay particles having sizes of a few 10th of nanometers. **c** Oblique view of the same, and **d** top view

Consortium contains petrographic and geochemical results of vein infillings from the Main Fault, diffuse calcite from undeformed Opalinus Clay reference materials (Degueldre et al. 1998; Lancelot 2001; Pearson et al. 2001), and porewaters (Pearson et al. 2003). The calcite and celestite veins described by de Haller et al. (2014) within the whole Opalinus Clay matrix are thin (<1 mm thick) and yield fibrous crack-seal microstructures that indicate syntectonic precipitation. These authors consider that the Opalinus Clay acted as a seal for migrating fluid flows during most of its history except during the tectonic episode that developed the Main Fault.

3 Sampling and analytical context

Most sampling of the present study was completed in the fault zone, in a precise petrofabric context detailed by Laurich et al. (2014) with a summarizing view of the

selected features and their relationships, especially in the nearby BSF-06, BPS-12 and BIC-A1 cores (Fig. 1b). A synthetic sketch explaining the relationship among the features analyzed for their chemical characteristics by Techer et al. (2017; Fig. 6) has also been drafted, whereas further information about the core drillings is available in Nussbaum et al. (2006). Collection of the selected vein infillings consisting of calcite (CaCO_3) or celestite (SrSO_4) was as precise as possible by careful sorting out under a binocular. Characterized by different reactivity to acid leaching, calcite being easily dissolved even by a dilute acid and celestite being quite insoluble in acids, a sequential leaching procedure was applied to the picked-up crystals that were first crushed gently before acid reaction, for discrimination of their respective elemental and Sr isotopic data. The initial leaching consisted of a 1 N HAC leaching for 10 min to extract the soluble calcite phase, the leachate being recovered by centrifugation, split in two, and used for either Sr separation and isotope determination

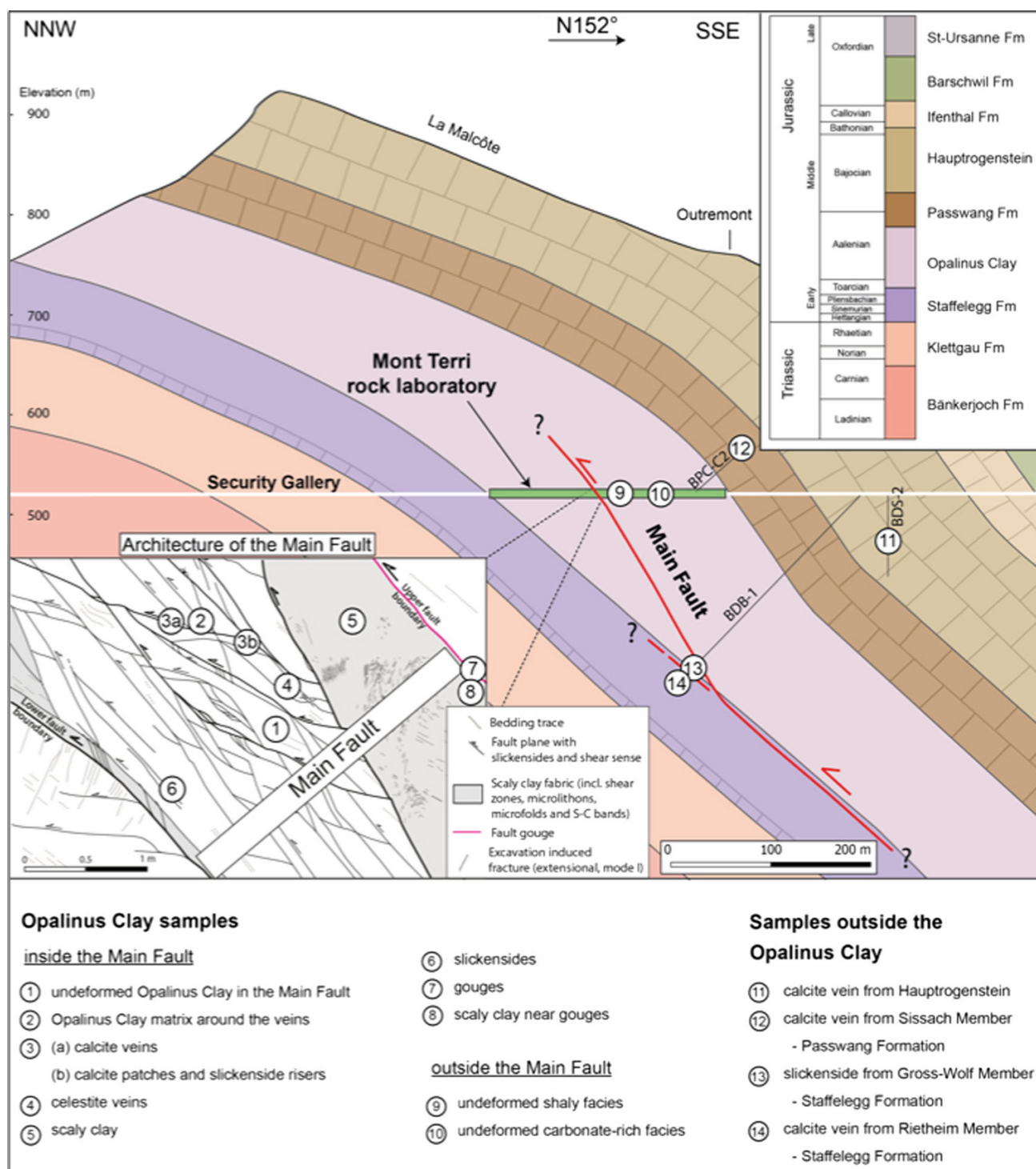
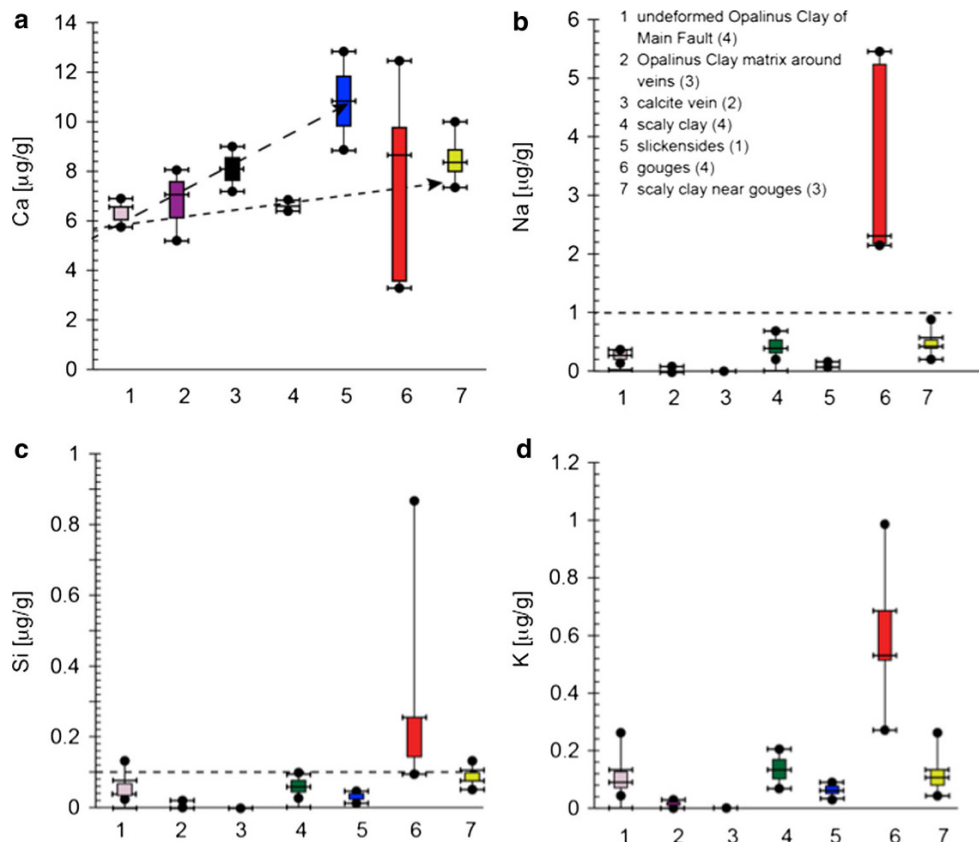


Fig. 6 Geological cross section around the Mont Terri rock laboratory. The Main Fault and the spatial, lithological and structural location of the 14 sample types analyzed by Techer et al. (2017) and discussed here is shown

or elementary analysis. In the case of the veins consisting of both calcite and celestite, the leftover celestite powder after gentle leaching was dissolved by a mixture of 7 N HNO₃, 6 N HCl and 12 N HF in a microwave equipment (ThermoFisher Thos One) at high temperature and under

pressure. All obtained solutions were evaporated and dissolved again in a few drops of HNO₃. It is probably appropriate to recall two methodological aspects at this point: (1) initial gentle acid leaching as used here for calcite dissolution does not affect the Sr isotopic system of

Fig. 7 Boxplot presentation of major elemental contents. The long central rectangles of the boxes represent 75% of their contents with a transversal bar for the average of these data, the highest and lowest values being outlined by the circles above and below. In the sample description, the numbers in brackets give the number of analyzed samples (from Techer et al. 2017)



potentially associated alkali-bearing minerals that therefore does not supply any radiogenic ^{87}Sr to the leachates (Clauer et al. 1993), and (2) leaching of the Opalinus Clay matrix dissolves the diffuse calcite but also removes chemical elements adsorbed potentially on the clay particles (Lerouge et al. 2010). However, this is not of a real concern here as the Sr adsorbed on the clay materials yields necessarily the same $^{87}\text{Sr}/^{86}\text{Sr}$ ratios as the calcite crystals, both deriving from the same connate fluids, and secondly the amount of Sr removed from clay particles is significantly lower than that of calcite, which is a main sedimentary Sr carrier.

The Sr separation was completed on Eichrom Sr-resin following Pin et al.'s (2003) procedure. After separation on a resin column, the $^{87}\text{Sr}/^{86}\text{Sr}$ isotopic ratios were measured by solid-source thermal ionization mass spectrometry. The contents of Ca and Sr, as well as of Si, Al, Mg, Fe, Mn, Ti, Na, K and P from various leachates were determined by ICP-AES/MS following Samuel et al.'s (1985) procedure.

4 Summary of the available geochemical database

Details of the elemental and $^{87}\text{Sr}/^{86}\text{Sr}$ results are available elsewhere (Techer et al. 2017); they were not duplicated here on purpose. In summary, significant variations of most

analyzed major elements were obtained for the dissolved calcite dispersed in the Opalinus Clay matrix, and for the infillings of the scaly clays, slickensides, veins and gouges. These varied contents suggest, together with the Ca/Sr ratios, different elemental compositions for the "initial" diffuse calcite of the undeformed Opalinus Clay in the Main Fault, and for that of the tiny structural features on one hand, and of the gouges on the other, for instance on the basis of the Ca, Na, Si and K contents (Fig. 7). The fluids that interacted with calcite of the veins are clearly different from those that interacted with the diffuse calcite of the undeformed Opalinus Clay matrix and with those of the gouge calcite that all outline specific chemical compositions. In summary, the fluids that flew through the gouges generated carbonates with a different striking chemical composition, even if their Ca/Sr ratios remain in the general range of the other studied features. For instance, the gouge leachates are significantly enriched in Si, Al and alkalis, especially Na, relative to those of the other features (Fig. 8). The infillings of the veins and the diffuse calcite of the Opalinus Clay matrix around them yield very low contents in K, whereas higher K contents were detected in diffuse calcite from undeformed matrix outside the Main Fault, in those of the slickensides and the scaly clays. The highest K contents were detected in the gouge leachates. Most Si and Al contents of the leached

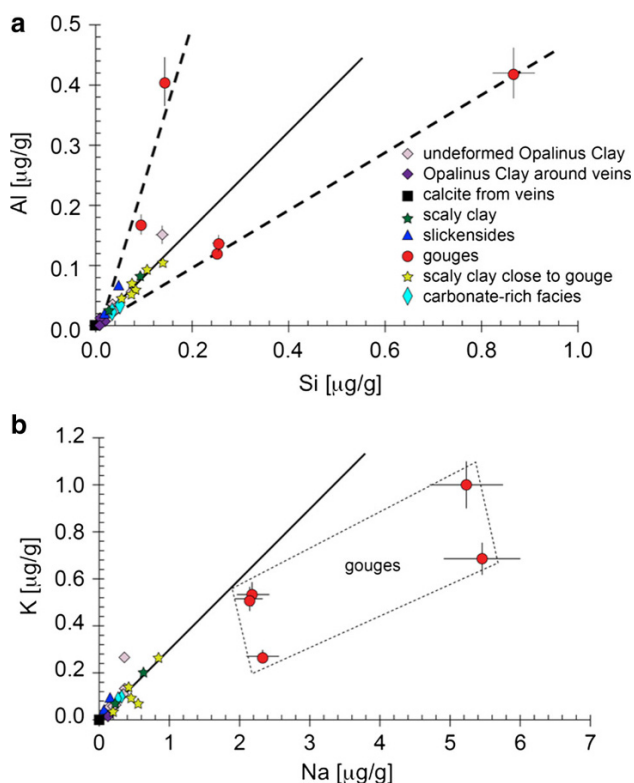


Fig. 8 Correlations between the Al and Si, and between the K and Na contents of the infillings from varied microtectonic structures. In the upper diagram, the full line outlines the Si–Al correlation for all infillings except those of the gouges, while the lower dashed line outlines the Si/Al ratio of potential illite authigenesis. In the lower K vs. Na diagram, the data points of the gouge infillings plot all outside the line including the data of the other infillings (from Techer et al. 2017)

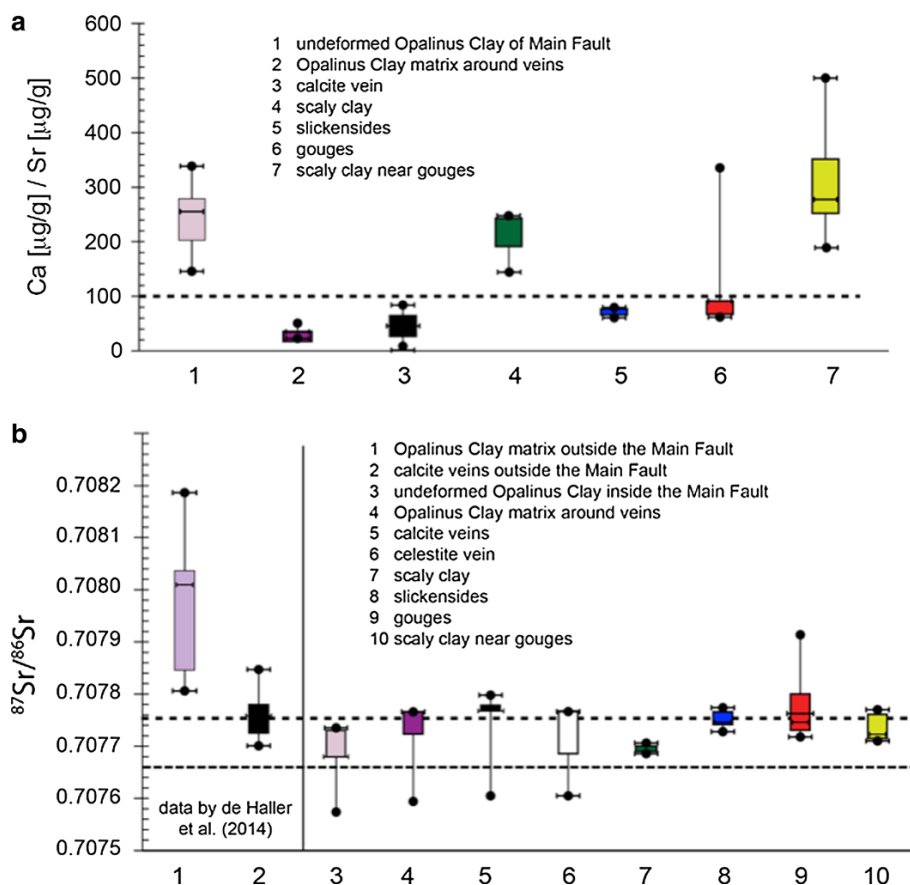
calcite of all features plot along a trend with a correlation factor of 1, whereas those of the gouges are clearly outside (Fig. 8). Noteworthy are also the data points of the Si and Al contents of the calcite from gouges that yield ratios identical to the theoretical Si/Al ratio of illite, making an authigenic crystallization plausible (Rieder et al. 1998), even if not yet precisely identified and described. Also, the diffuse calcite of the Opalinus Clay matrix sampled either away from microstructures, or in the scaly clays, yields significantly higher Ca/Sr ratios (>100) than the leachates of the “fluid-flow” sites, that is to say of the calcite from veins, matrix around the veins, slickensides and gouges (<100; Fig. 9a).

The distribution of the rare earth elements (REE) of a mineral or a rock is generally displayed relative to the same elements of a reference mineral or rock (e.g. Taylor and McLennan 1985). The observed variations of the individual REEs can then be calibrated to those of the chosen reference. If the ratio of each is then at 1, no fractionation occurred, while it did when the ratio is either below or above unity. In the former case, the considered REE is at a

lower amount than in the reference, and in the latter it is concentrated in the sample relative to the reference. Here, the REE contents of the infillings from varied microstructures are either enriched or depleted relative to the diffuse Opalinus Clay calcite. In sum, the contents display three shapes relative to that of the reference (Fig. 10a, b, d, e): (1) an almost flat distribution for some scaly clays and the carbonated sandy Opalinus Clay facies, meaning that no major fractionations occurred in these mineral phases; (2) an open “V” shaped distribution with a slightly decreasing repartition for the light REEs (LREEs) from La to Gd followed by an increase from Tb to Yb and Lu in the veins and slickensides, the Opalinus Clay matrix around the veins, as well as in the vein calcite of the sediments above and below the Opalinus Clay (Fig. 10c–e, underlined in blue), and (3) a pattern with ups and downs along a continuous increase of the LREEs from La to Sm, a decrease from Sm to Lu for the gouge samples, all characterized by various positive Sm anomalies, and for the diffuse calcite of two scaly clays collected close to a gouge (Fig. 10a, b, underlined in red). Varied fractionations obviously occurred in the samples corresponding to the cases 2 and 3. In summary, one type of fluid seems to have migrated through the tiny millimeter-sized structural features (veins and slickensides) of the Main Fault, also diffusing somehow into the matrix around the veins and the scaly clays. This is also the case for the veins of the sediments surrounding the Opalinus Clay that yield also a positive La anomaly. Conversely, the REE patterns of the gouges are clearly different with an intriguing positive Sm anomaly that is known to be lacking in the pure mineral world. Scaly clay aggregates yield REE patterns similar to those of the gouges when collected next to it, while scaly clays taken farer away from gouges yield patterns that are similar to those of the undeformed Opalinus Clay.

Comparing the $^{87}\text{Sr}/^{86}\text{Sr}$ ratios of the infillings from varied microstructural features of the Opalinus Clay used here and determined by Techer et al. (2017), to data of calcite separates from in- and outside the Main Fault published by Pearson et al. (2003) and de Haller et al. (2014) is of interest and importance for the global interpretation of the whole database (Fig. 9b). Almost all $^{87}\text{Sr}/^{86}\text{Sr}$ ratios from these two publications range narrowly between 0.70768 and 0.70778. Only those of the diffuse calcite of the matrix from outside the Main Fault are significantly above this overall narrow range. This repartition calls for two observations: (1) the $^{87}\text{Sr}/^{86}\text{Sr}$ ratios of the diffuse calcite from undeformed Opalinus Clay in the Main Fault are closer to the $^{87}\text{Sr}/^{86}\text{Sr}$ ratios of the microstructures, being even within the same range, than to those of the diffuse calcite from matrix outside the fault, and (2) the infillings of the veins from outside the Main Fault contain Sr with $^{87}\text{Sr}/^{86}\text{Sr}$ ratios that are within the dispersion range

Fig. 9 Boxplots of **a** the Ca/Sr ratio from infillings of the varied microtectonic structures, **b** the $^{87}\text{Sr}/^{86}\text{Sr}$ ratio of the same infillings and from those analyzed by de Haller et al. (2014). For the explanations of the boxplots, see Fig. 7 (from Techer et al. 2017)

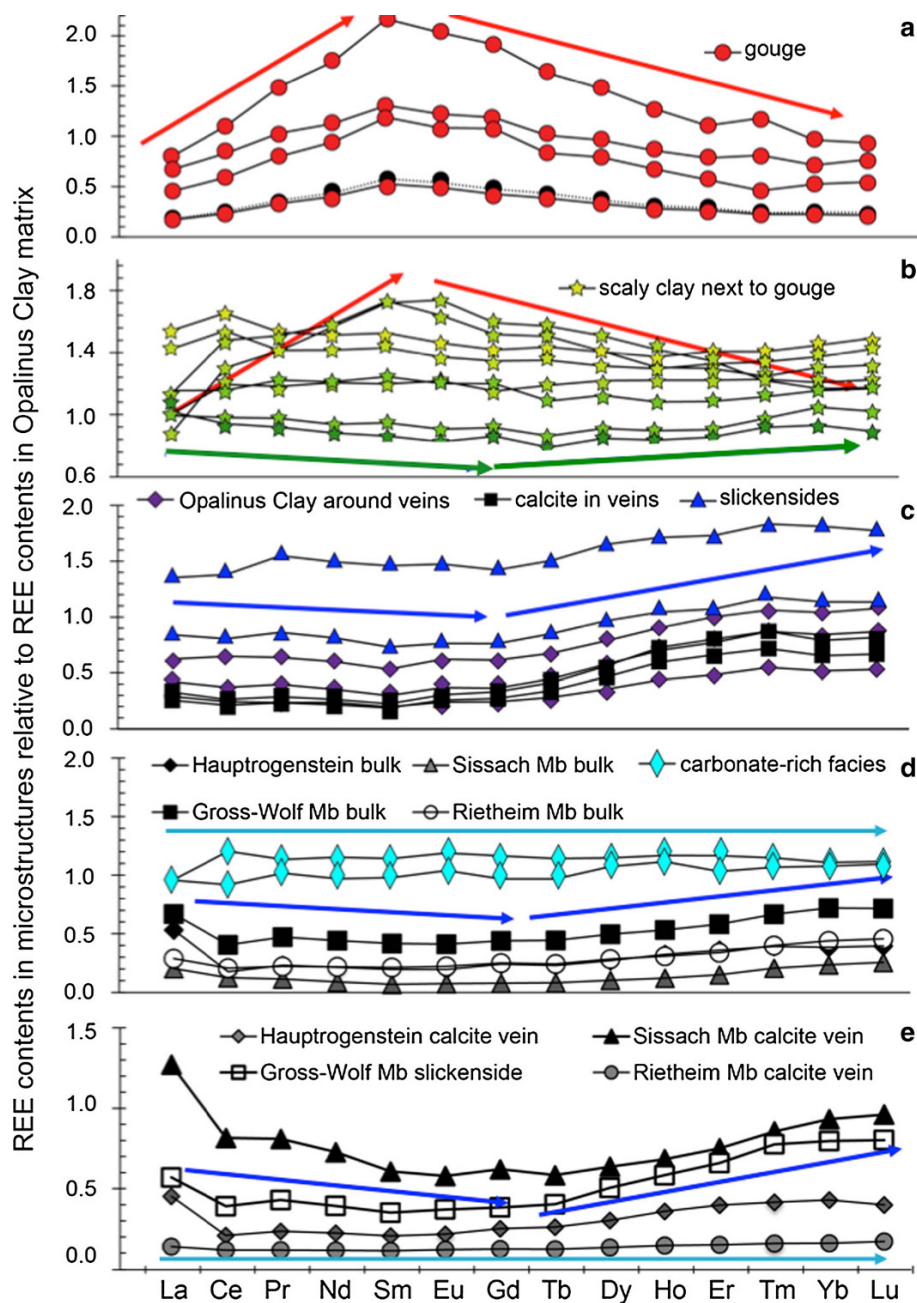


of those of the microstructural infillings within the fault. The undeformed Opalinus Clay within the Main Fault contains leachable $^{87}\text{Sr}/^{86}\text{Sr}$ ratios close to those of the microstructures of the fault itself, suggesting that the fluids that flew within the microstructures apparently diffused also discretely into the whole rock volume of the fault, somehow “contaminating” it locally. In fact, as already mentioned, leachates that include the diffuse calcite might also contain chemical elements adsorbed at the detrital silicates of the matrix and of the sediments below and above the Opalinus Clay. In fact, they yield $^{87}\text{Sr}/^{86}\text{Sr}$ ratios within the range of those from calcite infillings of the Main Fault microstructures.

The correlation between the $^{87}\text{Sr}/^{86}\text{Sr}$ and the Ca/Sr ratios (in wt%) of calcite veins, undeformed matrix close to and away from veins sketches a wide area (Fig. 11). This discrepancy between the narrowly ranging $^{87}\text{Sr}/^{86}\text{Sr}$ ratios of the leachable minerals of most microstructures and the widely scattered $^{87}\text{Sr}/^{86}\text{Sr}$ ratios of the diffuse calcite from undeformed Opalinus Clay was striking and unexpected. In fact, the conceptual hypothesis was rather based on the occurrence of a homogeneous sedimentary reservoir represented by the diffuse calcite from undeformed matrix and by a less homogeneous reservoir

external to the Opalinus Clay, mixing more or less with earlier calcite dissolved in the microstructures and recrystallizing after mixing. This is clearly not the case. The average $^{87}\text{Sr}/^{86}\text{Sr}$ ratio of the end-member characterizing the moving “fluid-flow” is at 0.70774 ± 0.00001 (2σ), which excludes any potential interference of porewaters with higher $^{87}\text{Sr}/^{86}\text{Sr}$ ratios, for instance from the Opalinus Clay host rocks or from older sedimentary systems, especially from Triassic Muschelkalk stratigraphic formation as stipulated elsewhere (de Haller et al. 2014). In fact, the secular variation of the seawater Sr of this Triassic epoch only yields a few values that are significantly scattered above 0.7078 (Fig. 13a; McArthur et al. 2001). Occurrence of Triassic evaporate-type sulfates to assess the observed celestite precipitation in the veins and slickensides can therefore be excluded. Also, none of the Sr from infillings of the varied microstructures of the Opalinus Clay could originate either from carbonate-rich layer, or from surrounding sediments. Also to be mentioned are the $^{87}\text{Sr}/^{86}\text{Sr}$ ratios of the vein infillings occurring in the sediments above and below the Opalinus Clay that are within the range of the $^{87}\text{Sr}/^{86}\text{Sr}$ ratios of the infillings from Opalinus Clay microstructures. This similarity suggests that the same fluids migrated also along the

Fig. 10 REE distribution patterns of the veins, the slickensides, the gouges, the scaly clays of the Opalinus Clay (OPA) and the surrounding sediments (from Techer et al. 2017)



tectonic features that were observed outside the Main Fault, which is confirmed, in turn, by the distribution of the REEs (Fig. 10).

5 Discussion

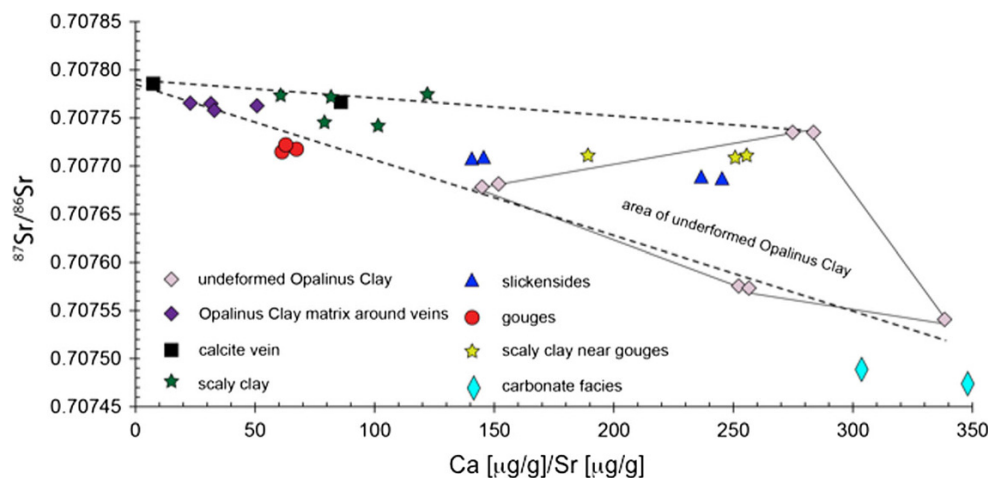
The goal set here is an integration of the chemical information into the microstructural description for a determining evaluation of the structural evolution of the Main Fault in the Opalinus Clay of the Mont Terri rock laboratory. This evaluation includes two aspects that will be addressed

successively and combined in a final wrap up, namely: (1) how useful can a geochemical database be in interpreting a structural context, and (2) when and how did the tectono-thermal event proceed on the basis of the combined stratigraphic, micro-structural and geochemical information.

5.1 The geochemical information

The relationship between the $^{87}\text{Sr}/^{86}\text{Sr}$ and Ca/Sr ratios of the leachable carbonates from undeformed Opalinus Clay matrix and from varied microstructures of the Main Fault was initially tested to provide new information about how

Fig. 11 Relationship between the $^{87}\text{Sr}/^{86}\text{Sr}$ and the Ca/Sr ratios of the infillings from microstructural features and matrices analyzed by Techer et al. (2017). The yellow diamonds to the right define the analytical area of the undeformed Opalinus Clay OPA (from Techer et al. 2017)



the fault evolved. This combination is quite complex, as a simple two end-member mixing cannot be applied straight: in fact, more than one linear trend can be drawn through the data points of the concerned diagram (Fig. 11). In fact, it is the diffuse calcite of the undeformed Opalinus Clay that yields an unexpectedly scattered $^{87}\text{Sr}/^{86}\text{Sr}$ ratio, making a mathematical evaluation difficult for a hypothetical mixing with Sr of the migrating fluids. This preliminary observation is confirmed by determinations published by de Haller et al. (2014; Fig. 9b) that showed dispersed $^{87}\text{Sr}/^{86}\text{Sr}$ ratios for the leachable undeformed Opalinus Clay from outside the Main Fault, and a narrowly ranging $^{87}\text{Sr}/^{86}\text{Sr}$ ratio for the vein infillings of the matrix similar to those analyzed by Techer et al. (2017) and discussed here.

The best evaluation of the geochemical input for a valuable explanation of the Main Fault structural processing starts with a comparison of the chemical composition from infillings of the different microstructures. As shown by the elemental contents in the leachates from undeformed matrix, slickensides, veins, scaly clays and gouges, fluids that interacted with the vein infillings are clearly different from those that interacted with the diffuse calcite of the undeformed Opalinus Clay, in addition to an even more specific composition for the leachates from gouges (Fig. 7). This difference calls for a preliminary statement, namely that water diffusion into the rock mass of the Opalinus Clay (=diffuse calcite in the undeformed matrix) and water percolation (advection) in the identified microstructures (=calcite infillings induced from interaction with the migrating fluids) result from different processes that probably occurred at different periods. Furthermore, the heterogeneous $^{87}\text{Sr}/^{86}\text{Sr}$ ratio of the diffuse calcite from Opalinus Clay clearly excludes any contribution of the associated connate waters to the flow waters of the microstructures. The analytical variation of their $^{87}\text{Sr}/^{86}\text{Sr}$ ratio being one hundred times higher, at 1×10^{-3} , than that of the homogeneous $^{87}\text{Sr}/^{86}\text{Sr}$ ratio of the flow fluids, which is only of 1×10^{-5} , no mixing of connate waters with such

variable Sr isotopic composition can provide a mixture characterized by a homogeneous Sr isotopic signature, whatever the envisioned mixing.

As already mentioned, the fluids flew in a different chemical context in the gouges than those of the other microstructures, being even possibly of another origin. These different fluids had a tendency to dissolve calcite instead of precipitating it, with the leftover having a different chemical composition, even if the Ca/Sr ratio that characterizes the mineral type rather than the origin of the fluids remained in the general area of all studied microstructures. The chemical compositions of the gouge infillings yield higher Al and Si contents than those of the infillings from any of the other microstructures (Fig. 8). The Si–Al data points of three gouge infillings plot also within the theoretical Si/Al ratio of illite, making its crystallization potentially plausible as postulated by Rieder et al. (1998). The second determining elemental information is in the Ca/Sr ratio of the gouge infillings that is lower than 100, which is the range of those from veins and slickensides, whereas the leachable undeformed Opalinus Clay sampled either away from microstructures or from scaly clays yields Ca/Sr ratios higher than 100 (Fig. 9a). The Ca/Sr ratio of the gouge leachates is also more widely scattered in a 1–5 range. On top of this chemical information tending to identify the occurrence of a different fluid, scanning-electron microscope observations also allowed identification of pyrite grains in the gouge rock chips that were clearly dissolved next to large patches of idiomorphic gypsum (Fig. 4c, d). Of course, it can always be argued that pyrite alters naturally by oxidation next to recent underground excavations and that it might facilitate precipitation of gypsum. In the present case, the samples were recovered from dry drillings away from gallery excavations, and the gypsum precipitation can be observed as large, idiomorphic and well-organized crystals.

The REE distribution patterns of the infillings from microstructures and those of the diffuse calcite from

undeformed Opalinus Clay support the fact that one type of fluid seems to have migrated through most tiny millimeter-sized structural features (veins and slickensides) of the Main Fault, also diffusing somehow into the matrix around the veins. The same fluids or of a similar type migrated also along the veins of the sediments occurring next to the Opalinus Clay, depositing identical infillings in similar features. Conversely, the REE patterns of the gouge infillings are noticeably different with an intriguing and variable positive Sm anomaly that has never been reported in pure minerals, to the best of our knowledge. This Sm anomaly is another index that external fluids had to intrude the gouges at a given time as such a Sm positive anomaly cannot develop in a closed chemical system of mineral origin. This additional fluid had to be mixed with those generated internally by an expected pressure-solution process. Interestingly, the REE patterns of the scaly clays are either similar to those of the diffuse calcite from matrix, or to those of the gouges, depending probably on their precise sampling location and their mineral composition. In any case, they confirm the occurrence of the just-mentioned supplementary external fluid. As the intimate details of the gouges are difficult to distinguish with a blank eye, it is most probable that the collected scaly clays consist, in fact, of more or less structurally undeformed Opalinus Clay that is more or less affected chemically. Depending on the impact of the migrating fluids, they might differ and their leachates mimic those from nearby gouges (Figs. 2b, 4, 5a).

5.2 Summary of the evolution of the Opalinus Clay matrix

The evolution of the Opalinus Clay integrates sedimentary, diagenetic and tectonic events since deposition in a marine environment about 174 Ma ago (Middle Jurassic), the successive events being identified and integrated into a summarizing sketch (Fig. 12). After deposition, the entire

sedimentary pile including the Opalinus Clay was progressively buried and subjected to a Late Jurassic subsidence about 150 Ma ago that resulted from a widespread rifting described all over Europe (e.g. Cathelineau et al. 2012 and references therein). After that subsidence, gentle burial continued until about 120 Ma (Early Cretaceous) ago to a sediment thickness of about 1350 m. A quiescent period followed until an uplift of the whole sedimentary sequence that led to the erosion of the Cretaceous and Late Jurassic sediments above the Opalinus Clay. At about 40–28 Ma ago (second half of the Paleogene), a new subsidence that did not necessarily affect all regionally dispersed basins resulted from a renewed rifting activity with a final uplift that brought the Opalinus Clay back to a depth of about 500 m (Mazurek et al. 2006). This subsidence was obviously only limited to some sub-basins, probably not reaching the study area. The Delémont Basin of interest here was most probably in a backbulge Alpine position, being only transgressed during the Lower Oligocene (Berger et al. 2005a).

5.3 Intricacy of the sedimentological evolution of and the geochemical signatures in the Opalinus Clay

During deposition of the Opalinus Clay, seawater and biologic remnants were trapped in the sediments with probable crystallization of a diffuse sedimentary calcite. Most of this seawater was expelled afterwards probably during progressive burial, while mineral and biologic relicts remained within the sediments. On the basis of the secular variation of the $^{87}\text{Sr}/^{86}\text{Sr}$ ratio of seawater (e.g. Veizer et al. 1999; McArthur et al. 2001), the $^{87}\text{Sr}/^{86}\text{Sr}$ ratio of the seawater contemporaneous to Opalinus Clay sedimentation during the Middle Jurassic was at about 0.70730 (Fig. 13b), which is in the analytical uncertainty with that of an echinoderm value of 0.70733, but significantly below that of bivalve shells at 0.70755 (de Haller

Era	Period	Epoch	Stage	Age (Ma)	Sea movements	Tectonic phases	Tectonic regime	Pore water dynamics	Microstructures of the Main Fault
Cenozoic	Quaternary	Holocene		0.02	last marine transgression			expulsion of pore water	
			Pleistocene	Upper					
		Middle		0.78					
		Calabrian		1.80					
			Gelasian	2.58					
	Neogene	Pliocene	Piacenzian	3.60					
			Zanclean	5.33					
		Miocene	Messinian	7.25					
	Tortonian		11.6						
	Serravallian		13.8						
		Langhian	16.0						
		Burdigalian	20.4						
		Aquitanian	23.0						
	Paleogene	Oligocene	Chattian	28.1					
Rupelian			33.9						
Eocene		Priabonian	37.8						
		Bartonian	41.2						
		Lutetian	47.8						
		Ypresian	56.0						
Paleocene		Thanetian	59.2						
		Selandian	61.6						
	Danian	66.0							
					initial rifting of the Rhine-Bresse system	extension	probable introduction of new pore water	slickensides + veins in the affected OPA matrix and sediments above and below (no Main Fault yet)	
				Hiatus (eroded or not deposited)			probable expulsion of initial pore water		

Fig. 12 Sketch summarizing the successive steps of the evolution of the Opalinus Clay (OPA) based on structural and petrographic observations and the herein obtained geochemical data. Further references are in the text

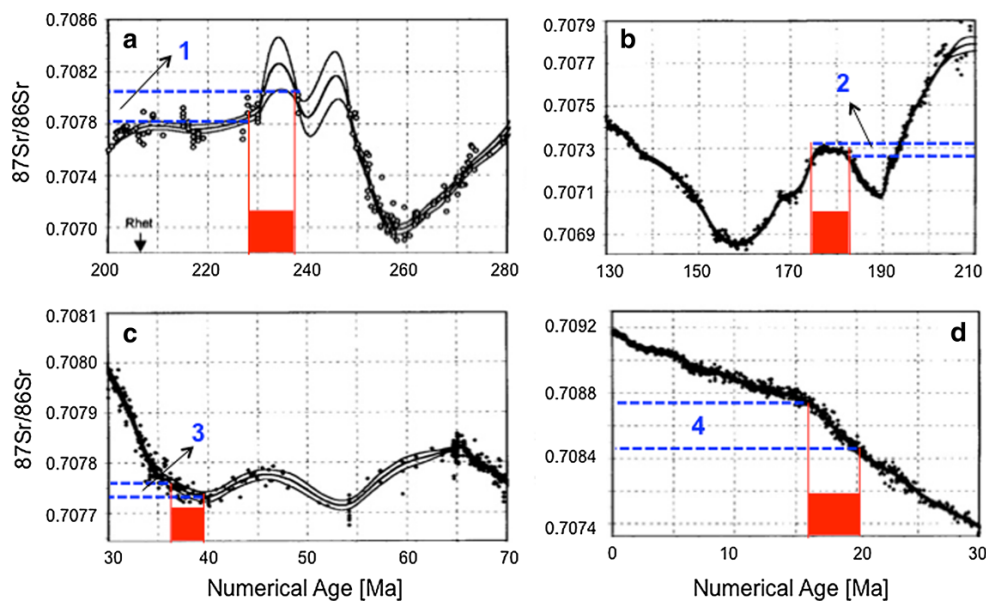


Fig. 13 Secular variation of the $^{87}\text{Sr}/^{86}\text{Sr}$ ratio from world seawater (adapted from McArthur et al. 2001): the sketch **a** outlines the period from 280 to 200 Ma with the specific period highlighted by a red sector that corresponds to the hypothetical $^{87}\text{Sr}/^{86}\text{Sr}$ ratio framed as zone 1 on the $^{87}\text{Sr}/^{86}\text{Sr}$ ratio that de Haller et al. (2014) speculated as the Triassic fluid supply to the Opalinus Clay (OPA) (see text for further explanation). The sketch **b** presents the period between 210 and 130 Ma including the deposition time of the Opalinus Clay

highlighted by the red sector that corresponds to the $^{87}\text{Sr}/^{86}\text{Sr}$ ratio outlined by the zone 2. The sketch **c** outlines the period from 70 to 30 Ma corresponding to the potential Priabonian marine seawater invasion outlined by the red sector with the corresponding $^{87}\text{Sr}/^{86}\text{Sr}$ ratio of the marine water in the zone 3. The sketch **d** outlines the most recent period between 30 and 0 Ma, giving the $^{87}\text{Sr}/^{86}\text{Sr}$ ratio of the Burdigalian seawater in the red sector with the corresponding $^{87}\text{Sr}/^{86}\text{Sr}$ ratio in the zone 4. More information is in the text

et al. 2014), as well as below those of the diffuse calcite of the matrix (de Haller et al. 2014; Techer et al. 2017). Fossils like those discussed here basically reflect seawater environments, as their $^{87}\text{Sr}/^{86}\text{Sr}$ ratios necessarily record the Sr signature of the seawater in which they were living. Therefore, the $^{87}\text{Sr}/^{86}\text{Sr}$ ratio of the calcite from one of them above that of the contemporaneous seawater indicates that it is no longer representative of the original marine environment, but necessarily of a further recrystallization episode (Faure 1986). The same most probably occurred for the initial sedimentary calcite of the Opalinus Clay that registered an increase of its $^{87}\text{Sr}/^{86}\text{Sr}$ ratio due to diagenetic recrystallization with interactions between pore-waters and fragile detrital minerals that potentially carry and exchange radiogenic ^{87}Sr with their environment (e.g. Clauer et al. 1975). Even if of limited intensity, such interactions may have induced release of small amounts of radiogenic ^{87}Sr by the altering minerals that increased the $^{87}\text{Sr}/^{86}\text{Sr}$ ratio of the diagenetically diffuse calcite from sediment matrix.

5.4 Some pending aspects

The heterogeneous $^{87}\text{Sr}/^{86}\text{Sr}$ ratio of the diffuse calcite of the undeformed Opalinus Clay matrix from outside and inside the Main Fault suggest limited exchanges in variably

small volumes during progressive burial, rather than flows of large volumes of fluids carrying isotopically homogeneous Sr and expected during sudden subsidence episodes by nearby tectonic activity. Other aspects need to be addressed further to possibly provide additional information useful for a concept of the regional evolution.

5.4.1 The variable $^{87}\text{Sr}/^{86}\text{Sr}$ signature of the diffuse calcite from undeformed Opalinus Clay matrix

Diagenetic interactions between seawater and fragile ^{87}Sr -bearing minerals do not explain why the Sr isotopic signature of the diffuse calcite from Opalinus Clay matrix is heterogeneous. Indeed, a regional evolution with limited uplift and subsidence episodes induces rather limited fluid migrations and mixings, therefore small but significant local variations of the $^{87}\text{Sr}/^{86}\text{Sr}$ ratio from diffuse calcite. It might also be that the final tectonic episode affecting the Opalinus Clay in the Main Fault was not penetrative enough to inject large amounts of fluids into the rock material beyond the microstructures, and therefore to erase potential records of successive fluid migrations. It can probably be assumed that most of the fluids with homogeneous $^{87}\text{Sr}/^{86}\text{Sr}$ ratios were generated during tectonic activity in the microstructures, mostly of the Main Fault. In fact, limited amounts of this “homogeneous” Sr from fluid

flows that potentially affected the original $^{87}\text{Sr}/^{86}\text{Sr}$ ratios of the diffuse calcite from matrix, and consequently the connate waters, seem to have diffused into the Opalinus Clay matrix of the fault volume, recorded for instance by the $^{87}\text{Sr}/^{86}\text{Sr}$ ratio of the diffuse calcite in the scaly clays and the matrix around the veins, the case of the gouges remaining different (Fig. 9).

5.4.2 Origin of the fluids that precipitated the infillings of the microstructures

The $^{87}\text{Sr}/^{86}\text{Sr}$ ratio of the fluids that flew within the microstructures of the Main Fault is very homogeneous at a mean 0.70774 ± 0.00001 (2σ) relative to a more widely scattered $^{87}\text{Sr}/^{86}\text{Sr}$ ratio of the diffuse calcite from undeformed Opalinus Clay of inside and outside the Main Fault (Fig. 9b). It is clear that the pore-waters of the Opalinus Clay and of the sediments below and above, as well as of the carbonate-rich sandy facies (CF1) close to the Main Fault could not contribute to the chemical composition of the fluids that migrated within the studied microstructures. The diffuse calcite of the sediments surrounding the Opalinus Clay is characterized by low $^{87}\text{Sr}/^{86}\text{Sr}$ ratios and high Ca/Sr values, the latter ratio making possible a potential Ca contribution to the migrating fluid(s), but not explaining their high Sr isotopic composition. In this context, the hypothesis promoted by de Haller et al. (2014) about Triassic fluids having moved upward during the tectonic activity of the Main Fault along the described microstructures appears debatable because of the inappropriate $^{87}\text{Sr}/^{86}\text{Sr}$ ratios of the potential initial fluid contributor(s). As already mentioned, the $^{87}\text{Sr}/^{86}\text{Sr}$ ratios of the Triassic seawater are quite scattered, from 0.7078 to 0.7081, above the reference value of 0.70774 (McArthur et al. 2001; Fig. 13a). Of course, it can be argued that a few values are below the 0.7078 limit and/or that the values provided by Veizer et al. (1999) fit better than those by McArthur et al. (2001), which is not necessarily a solid argument in the context. Also, as already stated, the connate waters of the Opalinus Clay matrix that precipitated the diffuse calcite could not contribute to the fluids from microstructures for two determining reasons because of their far too widely scattered $^{87}\text{Sr}/^{86}\text{Sr}$ ratio. It is known for long (Boger and Faure 1974) that a Sr isotopic signature of a fluid or mineral cannot become homogeneous by any kind of mixing with an additional component. The second reason is physical: the results discussed above have shown that the flowing fluids diffused into the host rocks, especially around the veins, which renders improbable any supply of pore fluids to the flows.

Alternatively, the uniform $^{87}\text{Sr}/^{86}\text{Sr}$ ratio of the calcite infillings from most microstructures suggests a large and unique reservoir for the interacting fluids, in order to insure

precisely that constant Sr isotope composition for the fluids that generated all visible infillings. In turn, such a large volume of fluids with a homogeneous $^{87}\text{Sr}/^{86}\text{Sr}$ ratio calls for seawater. However, the elemental composition of the fluids that generated the infilling precipitations was not quite homogeneous, which requires interactions with wall rocks of varied elemental compositions, but with identical $^{87}\text{Sr}/^{86}\text{Sr}$ ratios, pointing to minerals that are lacking radioactive ^{87}Rb , in fact essentially carbonates, salts, oxides, ... (Faure 1986). If the fluids that interacted with the carbonate and sulfate infillings with analytically identical $^{87}\text{Sr}/^{86}\text{Sr}$ ratios originated from an important reservoir, likely of marine origin, the $^{87}\text{Sr}/^{86}\text{Sr}$ ratio of this seawater was necessarily of 0.70774 ± 0.00001 , which is the mean $^{87}\text{Sr}/^{86}\text{Sr}$ ratio of the infillings from studied microstructures. This seawater $^{87}\text{Sr}/^{86}\text{Sr}$ signature identifies the Upper Eocene timing, between about 38 and 34 Ma ago, on the Sr isotope chronostratigraphic scale with a few older $^{87}\text{Sr}/^{86}\text{Sr}$ ratios that are identical but scattered, while those of the younger seawaters increase straight (McArthur et al. 2001; Fig. 13c, d). Considering all approximations and uncertainties of such modeling, it is necessary to evaluate also the paleogeographic investigations to identify marine invasion(s) that could have potentially invaded the Mont Terri region during the period of concern here. A possible marine invasion coming from western Bresse Graben along the Rhine-Bresse transfer zone was postulated to have reached an area close to the study region during the Upper Eocene Priabonian from 38 to 34 Ma ago (Sissingh 2006). A second marine incursion coming from southern Upper Rhine Graben during the Late Rupelian between 34 and 28 Ma ago was also documented in many studies (Berger et al. 2005b; Hinsken et al. 2007; Pirkenseer 2007).

Sediments recording the Priabonian marine transgression into the Delémont Basin were not reported so far in the literature. Most of the scientific community stands with the sedimentological description of only one regional seawater invasion during the Rupelian into the Mont Terri region that was characterized by two short transgressions coming from southern Upper Rhine Graben (e.g. Braillard 2006; Roussé 2006; Picot et al. 2008). The first of these two pulses is documented by deposition of the “Conglomérats de Porrentruy” in the nearby Ajoie Basin with a short and discrete seawater record at 33 Ma. The second invasion occurred slightly later at 32–30 Ma ago, with deposition of the “Meeressand and Septarienton” sediments in the Delémont Basin (Fig. 14). The next regional marine transgression has been set during the Burdigalian (20–16 Ma ago) with deposition of the “Upper Marine Molasse” (UMM) from Swiss Molasse Basin to the south. This last invasion can be discarded in our fluid-flow model, on the basis of its just mentioned significantly higher seawater $^{87}\text{Sr}/^{86}\text{Sr}$ ratios ranging from 0.7084 to 0.7087 (Fig. 13d; McArthur et al.

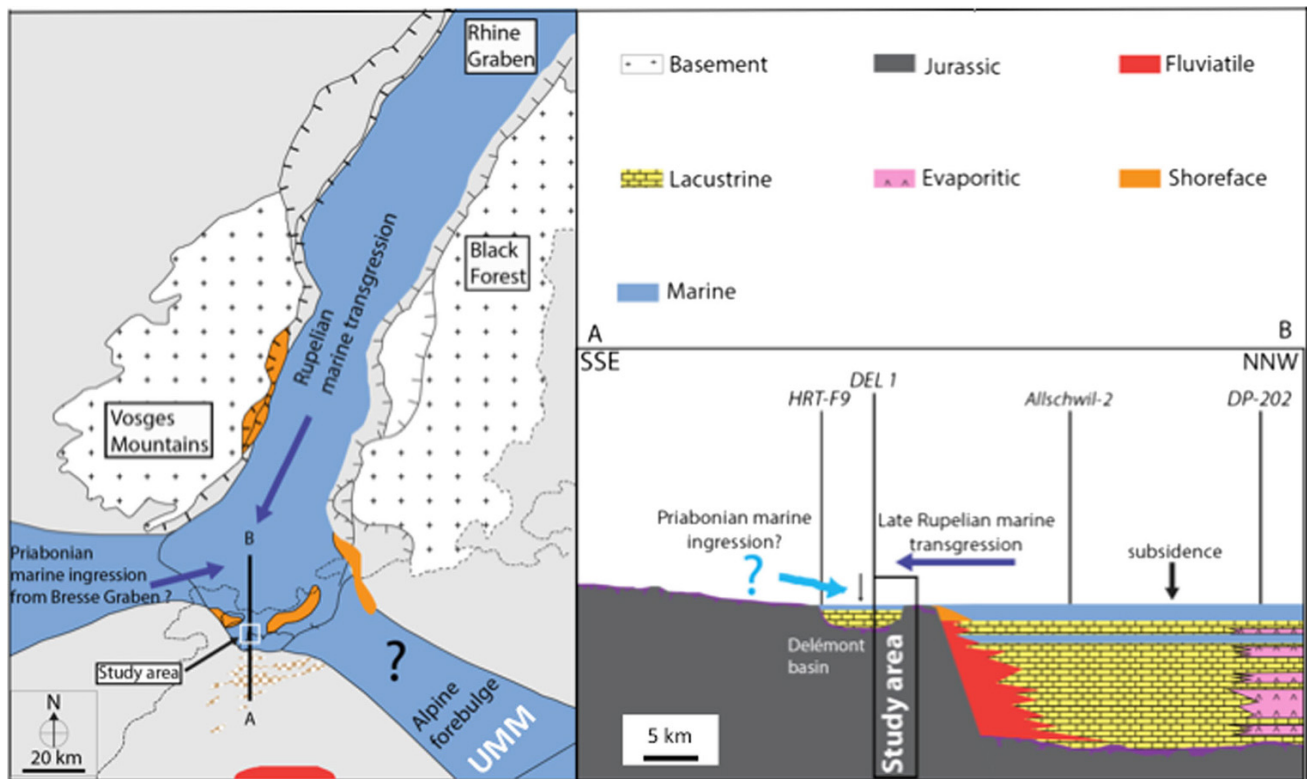


Fig. 14 A regional sketch of the paleo-structural situation of the Delémont Basin and its neighborhood during the Rupelian. On the left sketch are indicated the study area and the SSE-NNW cross-section

2001) that do not fit at all with those of the fluids responsible for the microstructural infillings. In summary, the Sr isotope chronostratigraphy points to a sea invasion into the Delémont Basin between 38 and 36 Ma, whereas the sedimentary records point to a younger episode from 32 to 30 Ma, with an additional discrete sea invasion slightly earlier at 33 Ma, all based on sediment records.

The purpose is not to start here a debate comparing the potentials of the two applied dating techniques. Both have solid but also weak aspects such as approximate age estimations for the Sr isotope chronostratigraphy, but with the certitude that the seawater Sr signature cannot record an invasion younger than 36 Ma because of the significant increase of the marine $^{87}\text{Sr}/^{86}\text{Sr}$ ratio afterwards, as discussed above. Conversely, the sedimentary biostratigraphic approach provides generally precise ages for the deposited marine sediments on the basis of their varied microfauna (e.g. foraminifera), which is not the case here because the biozones are long ranging. It has also the weakness to be only based on accessible deposits; dating becomes problematic if the necessary records were either not deposited or eroded meanwhile, which cannot be ignored. In the present case, a temporary marine connection was stipulated between the Mulhouse Basin and the Molasse Basin during the Upper Eocene (Sittler 1965). Sissingh (1998, 2006) postulated a

with the location of the drillings (vertical bars) on which the stratigraphic interpretation was based (modified from Pirkenseer 2007)

regional marine Priabonian transgression southwards from Upper Rhine Graben, obviously on the basis of foraminifera descriptions in drilling material described near the Fribourg/Brigau area by Ohmert (1993), but without records yet reported in the Delémont and Ajoie basins. As the potential Priabonian sea transgression occurred during a siderolithic episode on the continent, it could have interacted with the newly formed karstic system that was enhanced by contemporaneous extensional faulting of the Rhine-Bresse Graben transfer zone, rather than depositing sediments (Pirkenseer, pers. comm.). However, foraminifera have anyway to be described in the modified karst materials to support this hypothesis. At this point, the scenario still lacks occurrence of appropriate sediment relicts with determining microfossils.

As the contemporaneous rifting episode was mainly in an extension mode associated with a strike-slip component in the transfer zone linking the Bresse and Rhine grabens, no immediate expulsion of the seawater trapped in a reservoir to be identified occurred expectedly. However, it is needed to identify the potential reservoir that had to be outside the Opalinus Clay, as it did not favor significant interactions with either the early-crystallized calcite, or the detrital clay-type materials of the Opalinus Clay matrix. The constant $^{87}\text{Sr}/^{86}\text{Sr}$ ratio of the microstructural infillings

calls for a carbonate reservoir, which could have resulted precisely from Priabonian regional siderolithic episode between 37 and 34 Ma that facilitated formation of a karstic system (Braillard 2006) above the Opalinus Clay, when the thin-skinned deformation of the Jura front reached the Mont Terri region between approximately 10 and 3 Ma. Development of the Main Fault is associated with this deformation phase that expelled the fluids into the microtectonic structures of the Main Fault, inducing also the formation of discretely associated veins and slickensides in the sediments above and below the Opalinus Clay.

5.4.3 *The water-Opalinus Clay matrix interactions in the scaly clays and around the veins*

Expulsion of Priabonian seawater was probably synchronous with the vein and slickenside formation in the Opalinus Clay matrix and in the surrounding sediments due to folding of the Main Fault. This expulsion induced interactions between the fluids that precipitated calcite in the microstructures, as well as closely around these microtectonic features. These interactions around the veins outline a diffusion process into the undeformed Opalinus Clay based on the Ca/Sr ratio and REE distribution patterns (Figs. 10, 11). Consequently, the flowing fluids within the veins did not accommodate connate waters, as the pressure in the microstructures was such that they diffused into the host rocks and not the other way around.

The case of the scaly clays appears slightly more complex than that of the undeformed Opalinus Clay matrix around the veins, as they seem to result tectonically from shear bands deriving into meso- to micro-folds. Arch et al. (1988) demonstrated that high water contents lead to an increased complexity in the shear zone geometry of clay-type sediments. Such an interpretation supports the occurrence of fluid flows rather than limited interactions among almost immobile pore-waters and altering minerals. Also to be remembered is the fact that somehow static interactions between such waters and fragile minerals do probably not provide systematic homogeneous Sr isotopic and Sr/Ca ratios for the analyzed microstructural infillings. In fact, the $^{87}\text{Sr}/^{86}\text{Sr}$ ratio of the leached Sr from scaly clays is similar to those of the undeformed matrix close to the veins. However, the more scattered Ca/Sr ratios and REE distribution patterns of the scaly clays suggest varied compositions for the vein and gouge calcite relative to the diffuse calcite of the reference undeformed Opalinus Clay. This suggests also that the chemical signature of the analyzed infillings of the scaly clays are either more representative of the fluid-flow signatures like in the vein or gouge calcite and/or of those from diffuse calcite of the undeformed Opalinus Clay, depending on how sampling was made.

5.4.4 *What type of water-rock interactions in the gouges?*

Frictional sliding and abrasion are common processes in gouges, the constituting minerals being often smaller than those of their wall rocks. Indeed, the abundant nano-sized particles in gouges may result from combined cataclasis and pressure solution-precipitation that can occur by recrystallization of kinked and folded detrital clay particles (Solum 2003; Laurich 2015). From geochemical data, the interaction with fluid flows favoring illite neoformation has been described in larger gouges (e.g. Vrolijk and van der Pluijm 1999; Sasseville et al. 2008; Warr et al. 2014). Being considered as the most “evolved” micro-structural feature of the Main Fault (Laurich 2015), the gouges contain infillings with $^{87}\text{Sr}/^{86}\text{Sr}$ and Ca/Sr ratios, and REE distribution patterns suggesting the supply of an additional fluid necessarily external, relative to those that interacted with the calcite infillings of the veins and the slickensides. The strikingly high K and Na contents of the leachates from gouges point towards an increased alteration of some of the constitutive minerals of the gouge protolith (Fig. 8), especially if one considers that all other microstructures host infillings that apparently interacted with only one fluid flow. For instance, dissolution of salt grains observed by scanning electron microscope, which appear not to have been in contact with the fluids in most microstructures, could explain the increased K and Na contents together with unchanged $^{87}\text{Sr}/^{86}\text{Sr}$ ratios for the gouge leachates that remain identical to those of the veins and slickensides.

Clearly, the high Si/Al ratios and the high K contents of the leachates from gouges could not result from a “simple” solution-pressure process, as they would have also altered K-alumino-silicates, which seems not to have been the case. Alternatively, minerals such as quartz grains or illite-rich clay crystals that were described by Laurich (2015) are basically enriched in Si, Al and K, and could have precipitated in the gouges. In the case of the REE distribution patterns, the unexpected positive Sm anomaly has not yet, to the best of our knowledge, been reported in minerals like those studied here (Fig. 10; Piper and Bau 2013), inciting us to consider that its origin could be due to the occurrence of organics in the solutes of a supplementary fluid of external origin. In fact, the Rietheim Member of the Staffelegg Formation considered as the detachment horizon of the Main Fault (Nussbaum et al. 2017) consists here of “bituminous schists” that could have released fluids enriched in organics matured during the faulting. In addition to Sm supply to the diffuse leachates of the gouges, it is needed to point also to a higher P content for the same leachates (Techer et al. 2017), and the combination of these two geochemical changes clearly support a supply of organic-derived solutes that could definitely not originate within the gouge volumes.

In the detail, the gouges consist of a fine, distinct, dark-black microstructure that is characterized by a very homogeneous orientation of its clay particles. The gouge of the Main Fault consists of internal micrometer-wide shear zones, wider (50 μm) shear bands, brighter wall-rock clasts and grain clasts (Fig. 4; Laurich 2015). In fact, we aimed to sub-sample only the dark gouge from locations with little or no wall-rock clasts (7b in Fig. 2b). However, the $^{87}\text{Sr}/^{86}\text{Sr}$ and elemental signatures of the gouge leachates could have resulted from local interactions due to a variable “accessibility” of the fluids to the internal gouge features, as well as from variable interactions with local host minerals, relative to limited fluid/wall-mineral interactions in the microtectonic “drains” of the Main Fault. In summary, the different elemental compositions of the leachates from gouge samples could have resulted from interactions with limited volumes of fluids of varied origins at different timings relative to those recorded in the calcite and celestite of the veins. However, variations should have been detected in this case in the $^{87}\text{Sr}/^{86}\text{Sr}$ ratios of the calcite, due mainly to variable extents of the interactions and consequent varied addition of radiogenic ^{87}Sr released from altered minerals. These minerals could have been more sensitive to increased thermal conditions during folding, but they cannot amount for the volume necessary for all observed gouge infillings, moreover with homogeneous $^{87}\text{Sr}/^{86}\text{Sr}$ ratios.

5.4.5 What origin for the present-day free waters from Opalinus Clay?

Technical reports of research programs on the Mont Terri rock laboratory outline $^{87}\text{Sr}/^{86}\text{Sr}$ ratios, and Ca and Sr contents of “free” fluids recovered directly in rock segments isolated by packers after dry drillings (e.g. Pearson et al. 2003). Identified as “drill-hole fluids”, “pore-waters”

or “interstitial waters”, these fluids yield $^{87}\text{Sr}/^{86}\text{Sr}$ ratios that are surprisingly within the range of those of the infillings from studied microtectonic features (Table 1). This isotopic identity could, of course, be completely fortuitous, as these “free” waters appear not to have interacted with the calcite from undeformed Opalinus Clay matrix. If they would have, their $^{87}\text{Sr}/^{86}\text{Sr}$ ratio should be much more scattered, as are the same ratios of the diffuse matrix calcite. Alternatively, these present-day waters collected after drillings into the Opalinus Clay cannot correspond to older so-called “connate waters” from which the diffuse matrix calcite precipitated. Their $^{87}\text{Sr}/^{86}\text{Sr}$ ratios being identical to those of the microstructural infillings, they cannot derive from, nor can account for any kind of mixing with the pore-waters that generated the scattered $^{87}\text{Sr}/^{86}\text{Sr}$ ratios of the diffuse calcite.

The Priabonian seawater stored in a karstic reservoir closely above the Opalinus Clay, or in the fault system resulting from Rhine Graben rifting, had visibly no detectable interaction with minerals characterized by ^{87}Sr -enriched soluble mineral phases before the beginning of the fluid injections into the microstructures of the Main Fault, as well as into microstructures outside the fault. Clearly, the identity among the $^{87}\text{Sr}/^{86}\text{Sr}$ ratios of the present-day pore-waters and those of the calcite from microtectonic features was unexpected; it is even intriguing. Despite the still limited number of available pore-water analyses, the systematic proximity of their $^{87}\text{Sr}/^{86}\text{Sr}$ ratios with those of the calcite from most microstructures of the Main Fault points towards the possibility that these free waters are still able to circulate along the Opalinus Clay micrometer-thin shear zones and potentially along veins and slickensides. Alternatively, they seem not to diffuse into the undeformed matrix. The proximity of the $^{87}\text{Sr}/^{86}\text{Sr}$ ratios of the microtectonic features and the present-day free waters that are still “mobile” in the Opalinus Clay certainly needs

Table 1 The Ca and Sr concentrations, and the 1/Sr, Ca/Sr and $^{87}\text{Sr}/^{86}\text{Sr}$ ratios of pore-waters from boreholes into the Opalinus Clay from Mont Terri rock laboratory

Borehole	Sample ID	Sr ($\mu\text{g/g}$)	1/Sr	Ca ($\mu\text{g/g}$)	Ca/Sr	$^{87}\text{Sr}/^{86}\text{Sr}$ ($\pm 2\sigma$)	Origin data
						0.707705 (2)	This study
BWS-A1	A-1/4	35.5	0.028	570	16.1	0.707651 (22)	Pearson et al. (2003)
BWS-A2	A-2/1	21.5	0.047	43.2	2.01	0.707774 (36)	Pearson et al. (2003)
	A-2/18				8.64	0.707750 (?)	Pearson et al. (2003)
BWS-A3	A-3/4	31.6	0.032	283	8.96	0.707715 (20)	Pearson et al. (2003)
BHT1	HT2	47.8	0.021	650	13.6	0.707677(12)	A. Vinsot (Andra) pers com
	HT3	47.9	0.021	650	13.6	0.707751 (12)	A. Vinsot (Andra) pers com
	HT8	41.8	0.024	695	16.6	0.707651 (13)	A. Vinsot (Andra) pers com
	HT10	42.8	0.023	695	16.2	0.707770 (12)	A. Vinsot (Andra) pers com
BDS2	DS	0.77	1.30	67.1	87.1	0.707730 (10)	A. Vinsot (Andra) pers com
BPCC2	PPC	26.6	0.038	62.2	2.34	0.707730 (80)	A. Vinsot (Andra) pers com

? stands for Unknown result

more concerned interest about their origin(s). The most reasonable hypothesis to be formulated at this point is that the calcite infillings of the microstructures, rather than that of the undeformed matrix, seem to control the $^{87}\text{Sr}/^{86}\text{Sr}$ ratio of these present-day free waters that might interact with the identified infillings.

5.5 The origin of the fluid flows and the timing of their circulation(s)

On the basis of the homogeneous $^{87}\text{Sr}/^{86}\text{Sr}$ ratios of the vein calcite and celestite, the calcite associated with the slickensides of the Main Fault, the calcite from veins of the sediments above and below the Opalinus Clay, the Priabonian karstic reservoir or the contemporaneous regional fault system could have been progressively contracted, which initiated expulsion of the stored seawater into the microstructures of the progressively deformed matrix from Opalinus Clay, especially next to the Main Fault, and into those of the sediments around the Opalinus Clay. This seawater with stable $^{87}\text{Sr}/^{86}\text{Sr}$ ratios migrated along the microstructural drains that were built since the local rifting became active, especially along faults of the Rhine Graben rifting that reached the Jura region and more precisely the Mont Terri area during the Upper Eocene (Ustaszewski et al. 2005; Ustaszewski and Schmid 2007; Nussbaum et al. 2011). Tectonic activity appears to have been the driving force for the faulting and associated migration of specific seawater along microtectonic features that developed during the folding process.

As the gouges contain here less calcite (Fig. 7a), probably dissolved by fluids of sulfate and/or phosphate type, the former on the basis of pyrite dissolution and celestite authigenesis in the gouges and the latter being plausible on the basis of higher P contents of the leachates from the gouges (Techer et al. 2017), these fluids were different from those of the vein and slickenside drains. Also they cannot result from sole pressure-solution process, as they do not explain the increased contents of P and the Sm positive anomaly. These combined increases can best be explained by the addition of organic solutes released by the Rietheim Formation during sliding of the fault. It looks like successive fluid pulses could have been driven during the late tectonic event corresponding to the formation of the Jura thrust-and-fault belt between 10.5 and 3 Ma. From Sr isotopic information, it can be postulated that this late episode did not activate some contemporaneous marine reservoir, because the $^{87}\text{Sr}/^{86}\text{Sr}$ ratio of the gouge calcite remained identical to that of the other leachates, suggesting a further contribution of the same initial reservoir, either karstic or fault-systemic. Furthermore, the present-day free fluids yield the same $^{87}\text{Sr}/^{86}\text{Sr}$ ratio, which confirms no supplementary fluid supply since faulting.

5.6 What can still be improved?

Timing of most major episodes that impacted the Opalinus Clay since deposition lacks precise numerical dating with constrained uncertainties on top of the detailed available sedimentological reconstructions. Also, more elemental and isotopic determinations on infillings of microstructures around the Main Fault would definitely help detailing more the impact(s) of the successive tectonic episodes affecting the Opalinus Clay. In fact, a more precise dating of the Main Fault folding is potentially feasible on the basis of an appropriate extraction of the authigenic illite crystals, which occurrence appears plausible in the gouge volumes on the basis of electron-microscope observations (Laurich 2015) and elemental chemistry of the leachates (Techer et al. 2017). Indeed, direct isotopic dating becomes likely if a clean separation of pure authigenic illite crystals is feasible, for instance, on the basis of presently available sophisticated methods of separating nanometer-sized illite crystals from detrital counterparts. Separation of such nanometer-sized illite crystals is now well mastered (Środoń et al. 1992), and many direct isotopic dating of such small-sized separates of bentonites (e.g. Clauer et al. 1997, 2013; Środoń et al. 2009) and sandstones (Clauer et al. 2004; Blaise et al. 2015) are now available by the K–Ar and Rb–Sr methods. Nanometric separation of illite crystals and their isotopic dating have first been applied to bentonite beds, because these units lack detrital components, which facilitated interpretation of the isotopic ages. Since, the method has been applied to sandstones with variable success clearly depending on how separation of the authigenic fraction can be technically completed. Here, the attempt is applied for the first time, to the best of our knowledge, on $<0.02\ \mu\text{m}$ separates of discrete gouge samples from shales. The preliminary data show that complete separation of pure authigenic illite crystals has yet not been successful. However, on the basis of a fairly constrained identical age for the detrital illite, and of well-constrained K contents of the detrital (at about 3%) and authigenic illite separates (at about 5%), preliminary K–Ar ages for the authigenic illite crystals from gouge samples range between 9 and 4 Ma with uncertainties yet difficult to evaluate precisely, but which could be at a $\pm 10\%$ level. This age range represents a reasonable first estimation of the tectonic event responsible for folding of the Main Fault, formation of the associated microtectonic structures and precipitation of most infillings, especially of illite in the gouges. Independently, the authigenic illite from deeply buried Opalinus Clay near Kreuzlingen in northeastern Switzerland could have crystallized slightly earlier between 11 and 9 Ma, because linked to the diagenetic burial episode and not to the tectonic folding identified in the Main Fault.

A further pending question is about the origin of the present-day free waters, and about the extent of their interactions with the host rocks for which the envisioned interpretation has still to be tested, improved and consolidated, possibly on the basis of an enlarged analytical database.

6 Conclusions

Combined to a detailed observation and description of the microtectonic structures identified in the Main Fault that intersects the Opalinus Clay in the Mont Terri Rock Laboratory, this study focuses on an elemental and Sr isotopic investigation of associated micro-sampled calcite and celestite. Calcite and celestite crystallized at the same time in the microstructures of the Main Fault from a fluid either bi-carbonated or sulfated, but with analytically identical $^{87}\text{Sr}/^{86}\text{Sr}$ ratios. The undeformed Opalinus Clay matrix preserved as a relict within the Main Fault contains leachable $^{87}\text{Sr}/^{86}\text{Sr}$ ratios that are closer to those of the microtectonic infillings than to those of the undeformed Opalinus Clay outside the Main Fault, which $^{87}\text{Sr}/^{86}\text{Sr}$ ratios are unexpectedly varied. The Sr isotopic ratio of the diffuse calcite from undeformed matrix suggests that the rock volume within the fault has been slightly contaminated by the fluid flows that circulated in the microtectonic structures, diffusing discretely into the surrounding host rock. Therefore, the pore-waters that generated the calcite of the Opalinus Clay matrix could not contribute to the flowing fluids because: (1) flowing fluids diffused from veins at least into the host matrix, and (2) the widely varied $^{87}\text{Sr}/^{86}\text{Sr}$ ratios of the residual pore-waters cannot be accommodated into the narrow $^{87}\text{Sr}/^{86}\text{Sr}$ ratio of the flowing fluids.

The $^{87}\text{Sr}/^{86}\text{Sr}$ of the infillings from microtectonic structures of the Main Fault range very narrowly at 0.70774 ± 0.00001 (2σ), suggesting that the fluid flow(s) was (were) efficient enough to maintain such a chemical homogeneity in the different features, despite probable interactions with the wall rocks. The same homogeneous $^{87}\text{Sr}/^{86}\text{Sr}$ ratio was also determined in the calcite veins of the Toarcian Staffelegg and Dogger Passwang Formations located respectively above and below the Opalinus Clay. The present interpretation calls for a temporary storage of the fluids in a large homogeneous reservoir located slightly above the Opalinus Clay, like an "infinite" marine reservoir, with a specific $^{87}\text{Sr}/^{86}\text{Sr}$ ratio that points to Priabonian seawater supply (about 38–34 Ma ago) according to the Sr isotopic secular evolution of the seawater. This result is consistent with a possible sea incursion coming from western Bresse Graben through the Rhine-Bresse Graben transfer zone. However, this paleogeographic reconstruction is not yet unanimously accepted,

as it cannot be ultimately verified due to the absence of known Priabonian sediments in the Mont Terri region. The causes for these lacking deposits can be multiple: either they were not found so far, were not deposited, or were eroded during a contemporaneous siderolithic episode. Therefore, if assuming the Priabonian sea incursion, the infiltrated seawater could have been injected along veins and slickensides during the coeval rifting episode, resulting in the creation of the Rhine Graben and in associated extensional faults affecting the entire Mesozoic sedimentary sequence as well as the basement.

The chemical composition of the calcite infillings from the gouges calls for the supply, on top of a pressure-solution action, of an additional fluid that was different from those responsible for the crystallization of the vein and slickenside infillings, and also for that of the diffuse calcite of the Opalinus Clay matrix around the veins. The different chemical composition of the fluids that precipitated the carbonates from the gouges is especially visible in the Si and Al correlation of the leachates that suggests nanometer-sized illite-type crystallization. Calcite dissolution in the gouges seems to have been regulated by the dissolution of pyrite and concomitant precipitation of gypsum. Addition of this different fluid occurred most probably during the Main Fault folding and sliding in the most deformed gouge microstructures. The resulting fluid probably interacted with minerals, which induced changes in their elemental compositions, but not their Sr isotopic ratios. Tectonic activity along with the regional stress was obviously the driving force for migration/injection of fluids in the microstructures probably initiated during the final Eo-Oligocene rifting episode of the Upper Rhine Graben, before the ultimate thin-skinned deformation generated the Main Fault and the Mont Terri anticline about 9–4 Ma ago, as attested by preliminary K–Ar ages.

Acknowledgements We are especially thankful to Pierre De Canière (FANC-AFCN) and Claudius Pirkenseer (Paléontologie A16 and University of Fribourg) for their extremely detailed, constructive and improving reviews, to Paul Bossart (Mont Terri Consortium and swisstopo) for support and funding of the FI Experiment, and to Andreas Gautschi (Nagra) for his continuous interest and support for this research project. Special thanks are also due to Agnès Vinsot (Andra) who made available to us a pore-water sample and the dataset of those she studies in the frame of the HT Experiment. Sincere thanks are also due to Roy Freeman for his efforts to improve the English presentation.

References

- Agar, S. M., Prior, D. J., & Behrmann, J. H. (1989). Back-scattered electron imagery of the tectonic fabrics of some fine-grained sediments: Implications for fabric nomenclature and deformation processes. *Geology*, *17*, 901–904.
- Arch, J., Maltman, A. J., & Knipe, R. J. (1988). Shear-zone geometries in experimentally deformed clays: The influence of

- water content, strain rate and primary fabric. *Journal of Structural Geology*, 10, 91–99.
- Berger, J. P., Reichenbacher, B., Becker, D., Grimm, M., Grimm, K., Picot, L., et al. (2005a). Paleogeography of the Upper Rhine Graben (URG) and the Swiss Molasse Basin (SMB) from Eocene to Pliocene. *International Journal of Earth Sciences*, 94, 697–710.
- Berger, J. P., Reichenbacher, B., Becker, D., Grimm, M., Grimm, K., Picot, L., et al. (2005b). Eocene-Pliocene time scale and stratigraphy of the Upper Rhine Graben (URG) and the Swiss Molasse Basin (SMB). *International Journal of Earth Sciences*, 94, 711–731.
- Blaise, T., Clauer, N., Cathelineau, M., Boiron, M. C., Techer, I., & Boulvais, P. (2015). Reconstructing fluid-flow events in Lower-Triassic sandstones of the eastern Paris Basin by elemental tracing and isotopic dating of nanometric illite crystals. *Geochimica et Cosmochimica Acta*, 176, 157–184.
- Boger, P., & Faure, G. (1974). Strontium-isotope stratigraphy of a Red Sea core. *Geology*, 2, 181–183.
- Bossart, P., Bernier, F., Birkholzer, J., Bruggeman, C., Connolly, P., Dewonck, S., Fukaya, M., Herfort, M., Jensen, M., Matray, J.-M., Mayor, J. C., Moeri, A., Oyama, T., Schuster, K., Shigeta, N., Vietor, T., & Wiczorek, K. (2017). Mont Terri rock laboratory, 20 years of research: introduction, site characteristics and overview of experiments. *Swiss Journal of Geosciences*, 110. doi:10.1007/s00015-016-0236-1 (this issue).
- Bossart, P., & Wermeille, S. (2003). Paleohydrological study of the surroundings of the Mont Terri Rock Laboratory. In P. Heitzmann, J.P. Tripet (Eds.), *Mont Terri Project—Geology, Paleohydrology and Stress Field of the Mont Terri Region* (pp. 45–64). Wabern, Switzerland: Reports of the Swiss Geological Survey Federal Office of Topography (swisstopo). <http://www.mont-terri.ch>.
- Braillard, L. (2006). *Morphogenèse des vallées sèches du Jura tabulaire d'Ajoie (Suisse): rôle de la fracturation et étude des remplissages quaternaires*. Ph.D. dissertation, University of Fribourg, Switzerland.
- Buatier, M. D., Chauvet, A., Kanitpanyacharoen, W., Wenk, H. R., Ritz, J. F., & Jolivet, M. (2012). Origin and behavior of clay minerals in the Bogd fault gouge, Mongolia. *Journal of Structural Geology*, 34, 77–90.
- Bundesamt für Energie (2008). *Sachplan geologische Tiefenlager: Konzeptteil*. Bern, Schweiz: Bundesamt für Energie BFE. <http://www.bfe.admin.ch>.
- Burley, S. D., & Worden, R. (2003). *Sandstone diagenesis: Recent and ancient. Reprint series of the International Association of Sedimentologists* (p. 656). New York: Wiley.
- Cathelineau, M., Boiron, M. C., Fourcade, S., Ruffet, G., Clauer, N., Belcourt, O., et al. (2012). A major Late Jurassic fluid event at the basin/basement unconformity in western France: $^{40}\text{Ar}/^{39}\text{Ar}$ and K–Ar dating, fluid chemistry, and related geodynamic context. *Chemical Geology*, 322, 99–120.
- Clauer, N., Chaudhuri, S., Kralik, M., & Bonnot-Courtois, C. (1993). Effects of experimental leaching on Rb–Sr and K–Ar isotopic systems and REE contents of diagenetic illite. *Chemical Geology*, 103, 1–16.
- Clauer, N., Fallick, A. E., Eberl, D. D., Honty, M., Huff, W., & Aubert, A. (2013). K–Ar dating and $\delta^{18}\text{O}$ – δD characterization of nanometric illite from Ordovician K-bentonites of the Appalachians: Illitization and the Acadian-Alleghenian tectonic activity. *American Mineralogist*, 98, 2144–2154.
- Clauer, N., Hoffert, M., Grimaud, D., & Millot, G. (1975). Composition isotopique du strontium d'eaux interstitielles extraites de sédiments récents: un argument en faveur de l'homogénéisation isotopique des minéraux argileux. *Geochimica et Cosmochimica Acta*, 39, 1579–1582.
- Clauer, N., Rousset, D., & Środoń, J. (2004). Modeled shale and sandstone burial diagenesis based on the K–Ar systematics of illite-type fundamental particles. *Clays and Clay Minerals*, 52, 576–588.
- Clauer, N., Środoń, J., Francú, J., & Šucha, V. (1997). K–Ar dating of illite fundamental particles separated from illite/smectite. *Clay Minerals*, 32, 181–196.
- de Haller, A., Mazurek, M., Spangenberg, J., & Möri, A. (2014). *Self-sealing of faults (SF) project: Final report. Mont Terri Technical Report, TR 08-02*. Wabern, Switzerland: Federal Office of Topography (swisstopo). <http://www.mont-terri.ch>.
- Degueldre, C., Scholtis, A., Thomas, B. (1998). *WS-A experiment: Opalinus Clay groundwaters and colloids. A sampling and analysis exercise at Mont Terri (June/July 1997). Analytical results. Mont Terri Technical Note, TN 1997-20*. Wabern, Switzerland: Federal Office of Topography (swisstopo). <http://www.mont-terri.ch>.
- Dehandschutter, B., Vandycke, S., Sintubin, M., Vandenberghe, N., & Wouters, L. (2005). Brittle fractures and ductile shear bands in argillaceous sediments: Inferences from Oligocene Boom Clay (Belgium). *Journal of Structural Geology*, 27, 1095–1112.
- Eiichi, I. (2012). Microstructure and origin of faults in siliceous mudstone at the Horonobe Underground Research Laboratory site, Japan. *Journal of Structural Geology*, 34, 20–29.
- Faure, G. (1986). *Principles of isotope geology* (2nd ed., p. 608). New York: Wiley.
- Haines, S. H., Kaproth, B., Marone, C., Saffer, D., & van der Pluijm, B. (2013). Shear zones in clay-rich fault gouge: A laboratory study of fabric development and evolution. *Journal of Structural Geology*, 51, 206–225.
- Hinsken, S., Ustaszewski, K., & Wetzel, A. (2007). Graben with controlling syn-rift sedimentation: The Paleogene southern Rhine Graben as an example. *International Journal of Earth Sciences*, 96, 979–1002.
- Hoth, P., Wirth, H., Reinhold, K., Bräuer, V., Krull, P., Feldrappe H. (2007). *Einlagerung radioaktiver Abfälle in tiefen geologischen Formationen Deutschlands—Untersuchung und Bewertung von Tongesteinsformationen*. Hannover, Germany: Bundesanstalt für Geowissenschaften und Rohstoffe (BGR).
- Houben, M. E., Desbois, G., & Urai, J. L. (2013). Pore morphology and distribution in the Shaly facies of Opalinus Clay (Mont Terri, Switzerland): Insights from representative 2D BIB–SEM investigations on mm to nm scale. *Applied Clay Science*, 71, 82–97.
- Houben, M. E., Desbois, G., & Urai, J. L. (2014). A comparative study of representative 2D microstructures in shaly and sandy facies of Opalinus Clay (Mont Terri, Switzerland) inferred from BIB–SEM and MIP methods. *Marine and Petroleum Geology*, 49, 143–161.
- Jaeggi, D., Laurich, B., Nussbaum, C., Schuster, K., Connolly, P. (2017). Tectonic structure of the “Main Fault” in the Opalinus Clay, Mont Terri rock laboratory (Switzerland). *Swiss Journal of Geosciences*, 110. doi:10.1007/s00015-016-0243-2 (this issue).
- Labaume, P., Maltman, A.J., Bolton, A., Tessier, D., Ogawa, Y., Takizawa, S. (1997). Scaly fabrics in sheared clays from the décollement zone of the Barbados accretionary prism. In *Proceedings of the ocean drilling program. Scientific results* (pp. 59–77). Ocean Drilling Program.
- Lancelot, J. (Ed.). (2001). *WS-G experiment: Geochemical pore water characterisation of reference argillaceous samples from the Mont Terri Rock Laboratory. Mont Terri Technical Note, TN 1999-43*. Wabern, Switzerland: Federal Office of Topography (swisstopo). <http://www.mont-terri.ch>.
- Laurich, B. (2015). *Evolution of microstructure and porosity in faulted Opalinus Clay*. Ph.D. dissertation, Rheinisch-Westfälische Technische Hochschule (RWTH), Aachen, Germany.

- Laurich, B., Urai, J. L., Desbois, G., Vollmer, C., & Nussbaum, C. (2014). Microstructural evolution of an incipient fault zone in Opalinus Clay: Insights from an optical and electron microscopic study of ion-beam polished samples from the Main Fault in the Mont Terri Underground Research Laboratory. *Journal of Structural Geology*, *67*, 107–128.
- Laurich, B., Urai, J. L., & Nussbaum, C. (2016). Microstructures and deformation mechanisms in Opalinus Clay: Insights from scaly clay from the Main Fault in the Mont Terri Rock Laboratory (CH). *Journal of Geophysical Research: Solid Earth*. doi:10.5194/se-2016-94. (submitted).
- Lerouge, C., Gaucher, E. C., Tournassat, C., Négrel, P., Crouzet, C., Guerrot, C., et al. (2010). Strontium distribution and origins in a natural clayey formation (Callovian-Oxfordian, Paris Basin, France): A new sequential extraction procedure. *Geochimica et Cosmochimica Acta*, *74*, 2926–2942.
- Logan, J. M., Dengo, C. A., Higgs, N. G., & Wang, Z. Z. (1992). Fabrics of experimental fault zones: Their development and relationship to mechanical behavior. *International Geophysics Series*, *51*, 33–67.
- Mazurek, M., Hurford, A. J., & Leu, W. (2006). Unravelling the multi-stage burial history of the Swiss Molasse Basin: Integration of apatite fission track, vitrinite reflectance and biomarker isomerisation analysis. *Basin Research*, *18*, 27–50.
- McArthur, J. M., Howarth, R. J., & Bailey, T. R. (2001). Strontium isotope stratigraphy: LOWESS Version 3: Best fit to the marine Sr-isotope curve 0–509 Ma and accompanying look-up table for deriving numerical age. *The Journal of Geology*, *109*, 155–170.
- Milliken, K. L., & Reed, R. M. (2010). Multiple causes of diagenetic fabric anisotropy in weakly consolidated mud, Nankai accretionary prism, IODP Expedition 316. *Journal of Structural Geology*, *32*, 1887–1898.
- Mitra, G., & Ismat, Z. (2001). Microfracturing associated with reactivated fault zones and shear zones: What it can tell us about deformation history. *Geological Society of London, Special Publications*, *186*, 113–140.
- Nagra (2008). *Vorschlag geologischer Standortgebiete für das SMA- und das HAA-Lager. Nagra Technischer Bericht, 08-04*. Nagra, Wettingen, Switzerland. <http://www.nagra.ch>.
- Nussbaum, C., Amann, F., Aubourg, C., & Bossart, P. (2011). Analysis of tectonic structures and excavation induced fractures in the Opalinus Clay, Mont Terri underground rock laboratory (Switzerland). *Swiss Journal of Geosciences*, *104*, 187–210.
- Nussbaum, C., & Bossart, P. (2008). Geology. In M. Thury, & P. Bossart, (Eds.), *Mont Terri rock laboratory project, programme 1996 to 2007 and results* (pp. 29–37). Wabern, Switzerland: Federal Office of Topography (swisstopo). <http://www.mont-terri.ch>.
- Nussbaum, C., Kloppenburg, A., Caër, T., Bossart, P. (2017). Tectonic evolution around the Mont Terri rock laboratory, northwestern Swiss Jura: constraints from kinematic forward modelling. *Swiss Journal of Geosciences*, *110* (this issue).
- Nussbaum, C., Meier, O., Masset, O., Badertscher, N. (2006). *Self-sealing of fault (SF) experiment drilling of resin impregnated boreholes part of drilling campaign of phase 11 drilling data, drillcore mapping and photo documentation. Mont Terri technical note, TN 2006-22*. Wabern, Switzerland: Federal Office of Topography (swisstopo). <http://www.mont-terri.ch>.
- Ohmert, W. (1993). Eine obereozäne Foraminiferenfauna aus dem südlichen Oberrhein-Graben. *Zitteliana*, *20*, 323–329.
- Pearson, F. J., Acros, D., Bath, D., Boisson, J. Y., Fernández, A. M., Gäbler, H.-E., et al. (2003). *Mont Terri project: geochemistry of water in the opalinus clay formation at the Mont Terri rock laboratory*. Federal Office for Water and Geology (FOWG), Geology Series No. 5. <http://www.mont-terri.ch>.
- Pearson, F. J., Arcos, D., Jordi, B., Fernandez, A. M., Gaucher, E., Pena, J., et al. (2001). *Geochemical modelling and synthesis (GM) task: Compilation of aqueous geochemistry data collected during phases 4 and 5, rock property data from all phases and results of phase 5 geochemical modelling. Mont Terri technical note, TN 2000-36*. Wabern, Switzerland: Federal Office of Topography (swisstopo). <http://www.mont-terri.ch>.
- Picot, L., Becker, D., Cavin, L., Pirkenseer, C., LaPaire, F., Rauber, G., et al. (2008). Sédimentologie et paléontologie des paléoenvironnements côtiers rupéliens de la Molasse marine rhénane dans le Jura suisse. *Swiss Journal of Geosciences*, *101*, 483–513.
- Pin, C., Joannon, S., Bosq, C., Le Fèvre, B., & Gauthier, P. J. (2003). Precise determination of Rb, Sr, Ba and Pb in geological materials by isotope dilution and ICP-quadrupole mass spectrometry following selective separation of the analytes. *Journal of Analytical Spectrometry*, *18*, 135–141.
- Piper, D. Z., & Bau, M. (2013). Normalized rare earth elements in water, sediments, and wine: Identifying sources and environmental redox conditions. *American Journal of Analytical Chemistry*, *4*, 69–83.
- Pirkenseer, C. (2007). *Foraminifera, ostracoda and other microfossils of the southern Upper Rhine Graben: palaeoecology, biostratigraphy, palaeogeography and geodynamic implications*. Ph.D. dissertation, University of Fribourg, Switzerland.
- Rieder, M., Cavazzini, G., D’Yakonov, Y. S., Frank-Kamenetskii, V. A., Gottardi, G., Guggenheim, S., et al. (1998). Nomenclature of the micas. *Clays and Clay Minerals*, *46*, 586–595.
- Roussé, S. (2006). *Architecture et dynamique des séries marines et continentales de l’Oligocène moyen et supérieur du Sud du Fossé Rhénan: évolution des milieux de dépôts en contexte de rift en marge de l’avant-pays alpin*. Ph.D. dissertation, University Louis Pasteur, Strasbourg, France.
- Rutter, E. H., Maddock, R. H., Hall, S. H., & White, S. H. (1986). Comparative microstructures of natural and experimentally produced clay-bearing fault gouges. *Pure and Applied Geophysics*, *124*, 3–30.
- Samuel, J., Rouault, R., & Besnus, Y. (1985). Analyse multi-élémentaire standardisée des matériaux géologiques en spectrométrie d’émission par plasma à couplage inductif. *Analisis*, *13*, 312–317.
- Sasseville, C., Tremblay, A., Clauer, N., & Liewig, N. (2008). K–Ar time constraints on the evolution of polydeformed fold-thrust belts: the case of the Northern Appalachians (southern Québec). *Journal of Geodynamics*, *45*, 99–119.
- Schleicher, A. M., van der Pluijm, B. A., Solum, J. G., & Warr, L. N. (2006). Origin and significance of clay-coated fractures in mudrock fragments of the SAFOD borehole (Parkfield, California). *Geophysical Research Letters*, *33*, 1–5.
- Sissingh, W. (1998). Comparative Tertiary stratigraphy of the Rhine graben, Bresse graben and Molasse basin: correlation of Alpine foreland events. *Tectonophysics*, *300*, 249–284.
- Sissingh, W. (2006). Syn-kinematic palaeogeographic evolution of the West European platform: Correlation with Alpine plate collision and foreland deformation. *Geologie en Mijnbouw*, *85*, 131–180.
- Sittler, C. (1965). *Le Paléogène des fossés rhénan et rhodanien. Etudes sédimentologiques et paléo-climatiques*. Strasbourg: Université de Strasbourg, Centre National de la Recherche Scientifique, Institut de Géologie.
- Solum, J. G. (2003). Influence of phyllosilicate mineral assemblages, fabrics, and fluids on the behavior of the Punchbowl fault, southern California. *Journal of Geophysical Research*, *108*, 1–12.
- Środoń, J., Clauer, N., Huff, W., Dudek, T., & Banas, M. (2009). K–Ar dating of Ordovician bentonites from the Baltic Basin and the Baltic Shield: implications for the role of temperature and time in the illitization of smectite. *Clay Minerals*, *44*, 361–387.
- Środoń, J., Elsass, F., McHardy, W. J., & Morgan, D. J. (1992). Chemistry of illite/smectite inferred from TEM measurements of fundamental particles. *Clay Minerals*, *27*, 137–158.

- Taylor, S. R., & McLennan, S. M. (1985). *The continental crust: Its composition and evolution*. Oxford: Blackwell.
- Techer, I., Clauer, N., Laurich, B., Nussbaum, C., Urai, J. L. (2017). Origin and timing of fluid flows in discrete petrofabric features of the “Main Fault” in the Opalinus Clay (Mont Terri, Switzerland): Clues from elemental and Sr isotopic analyses. *Journal of Structural Geology* (**submitted**).
- Ujiie, K., Tanaka, H., Saito, T., Tsutsumi, A., Mori, J. J., Kameda, J., et al. (2013). Low co-seismic shear stress on the Tohoku-Oki megathrust determined from laboratory experiments. *Science*, 342, 1211–1214.
- Urai, J., & Wong, S. W. (1994). Deformation mechanisms in experimentally deformed shales. *Annales Geophysicae*, 12, C98.
- Ustaszewski, K., Schuhmacher, M. E., & Schmid, S. (2005). Simultaneous normal faulting and extensional flexuring during rifting: An example from the southernmost Upper Rhine Graben. *International Journal of Earth Sciences*, 94, 680–696.
- Ustaszewski, K., & Schmid, S. (2007). Latest Pliocene to recent thick-skinned tectonics at the Upper Rhine Graben-Jura Mountains junction. *Swiss Journal of Geosciences*, 100, 293–312.
- Vannucchi, P., Maltman, A., Bettelli, G., & Clennell, B. (2003). On the nature of scaly fabric and scaly clay. *Journal of Structural Geology*, 25, 673–688.
- Veizer, J., Ala, D., Azmy, K., Bruckschen, P., Buhl, D., Bruhn, F., et al. (1999). $^{87}\text{Sr}:^{86}\text{Sr}$, $\delta^{13}\text{C}$ and $\delta^{18}\text{O}$ evolution of Phanerozoic seawater. *Chemical Geology*, 161, 59–88.
- Vrolijk, P., & van der Pluijm, B. A. (1999). Clay gouge. *Journal of Structural Geology*, 21, 1039–1048.
- Warr, L. N., & Cox, S. (2001). Clay mineral transformations and weakening mechanisms along the Alpine Fault, New Zealand. *Geological Society, London, Special Publications*, 186, 85–101.
- Warr, L. N., Wojatschke, J., Carpenter, B. M., Marone, C., Schleicher, A. M., & van der Pluijm, B. A. (2014). A “slice-and-view” (FIB–SEM) study of clay gouge from the SAFOD creeping section of the San Andreas Fault at about 2.7 km depth. *Journal of Structural Geology*, 69, 234–244.
- Worden, R. H., & Morad, S. (2003). Clay minerals in sandstones: Controls on formation, distribution and evolution. In R.H. Worden, S. Morad (Eds.), *Clay mineral cements in sandstones*. (pp.3–41). International Association of Sedimentologists Special Publication no. 34, Blackwell, Oxford.

Pore-water evolution and solute-transport mechanisms in Opalinus Clay at Mont Terri and Mont Russelin (Canton Jura, Switzerland)

Martin Mazurek¹  · Antoine de Haller^{1,2}

Received: 17 March 2016 / Accepted: 9 December 2016 / Published online: 21 February 2017
© The Author(s) 2017. This article is published with open access at Springerlink.com

Abstract Data pertinent to pore-water composition in Opalinus Clay in the Mont Terri and Mont Russelin anticlines have been collected over the last 20 years from long-term in situ pore-water sampling in dedicated boreholes, from laboratory analyses on drillcores and from the geochemical characteristics of vein infills. Together with independent knowledge on regional geology, an attempt is made here to constrain the geochemical evolution of the pore-waters. Following basin inversion and the establishment of continental conditions in the late Cretaceous, the Malm limestones acted as a fresh-water upper boundary leading to progressive out-diffusion of salinity from the originally marine pore-waters of the Jurassic low-permeability sequence. Model calculations suggest that at the end of the Palaeogene, pore-water salinity in Opalinus Clay was about half the original value. In the Chattian/Aquitainian, partial evaporation of sea-water occurred. It is postulated that brines diffused into the underlying sequence over a period of several Myr, resulting in an increase of salinity in Opalinus Clay to levels observed today. This hypothesis is further supported by the isotopic signatures of SO_4^{2-} and $^{87}\text{Sr}/^{86}\text{Sr}$ in current pore-waters. These are not simple binary mixtures of sea and meteoric water, but their Cl^- and

stable water-isotope signatures can be potentially explained by a component of partially evaporated sea-water. After the re-establishment of fresh-water conditions on the surface and the formation of the Jura Fold and Thrust Belt, erosion caused the activation of aquifers embedding the low-permeability sequence, leading to the curved profiles of various pore-water tracers that are observed today. Fluid flow triggered by deformation events during thrusting and folding of the anticlines occurred and is documented by infrequent vein infills in major fault structures. However, this flow was spatially focussed and of limited duration and so did not markedly affect the bulk pore-water.

Keywords Geochemical evolution · Pore-water tracers · Sea-water evaporation · Diffusion · Fluid flow · Veins · Nuclear waste disposal

1 Introduction

The Mont Terri rock laboratory is currently looking back on 20 years of research dedicated to the hydrogeological, geochemical and geomechanical characterisation of Opalinus Clay (Thury and Bossart 1999; Bossart and Thury 2007; Bossart et al. 2017). With regard to geochemical studies, a suite of novel techniques have been developed to characterise the chemical and isotopic compositions of pore-waters. This became necessary because the pore-space architecture of Opalinus Clay is dominated by mean pore apertures in the range of nanometres, leading to extremely low hydraulic conductivity in the order of 1×10^{-13} m/s (Marschall et al. 2003; AF Consult 2012). Standard pore-water sampling techniques are generally not applicable to such low-permeability systems. Apart from other lines of evidence, this contribution is partially based

Editorial handling: P. Bossart and A. G. Milnes.

This is paper #6 in the Mont Terri Special Issue of the Swiss Journal of Geosciences (see Bossart et al., 2017, Table 3 and Fig. 7).

✉ Martin Mazurek
mazurek@geo.unibe.ch

¹ Institute of Geological Sciences, University of Bern, Bern, Switzerland

² Present Address: Earth and Environmental Sciences, University of Geneva, Geneva, Switzerland

Table 1 Major-ion and selected isotope data from water-sampling boreholes at Mont Terri and Mont Russelin

Borehole	Mont Terri BWS-A1	Mont Terri BWS-A2	Mont Terri BWS-A3	Mont Terri BWS-H2	Mont Terri BPC-C	Mont Terri BBB3	Mont Russelin deep ground- water (Staffelegg Fm.)
Sampling date	18.6.97	18.6.97	18.6.97	19.5.09	31.8.04	12.12.11	1991
Laboratory	PSI	BGS	PSI/BGS	Hydroisotop	Andra	Hydroisotop	BGS
Na ⁺ (mg/L)	5610	4315	2864	4430	6414	4880	
K ⁺ (mg/L)	65.3	130.0	40.6	51.8	69.6	59.5	
Mg ²⁺ (mg/L)	344	311	151	286	542	370	
Ca ²⁺ (mg/L)	570	43	283	455	774	547	
Sr ²⁺ (mg/L)	35.5	2.2	31.6	40.1	42.9 ^a		
F ⁻ (mg/L)	0.77	0.17	0.47	0.8			
Cl ⁻ (mg/L)	10,395	6067	4909	7420	11,628	8230	18,400
Br ⁻ (mg/L)	36.3	23.9	15.2	27.1		23.6	65
SO ₄ ²⁻ (mg/L)	1251	1903	1082	1050	1651	1480	
δ ¹⁸ O (H ₂ O) (‰v-SMOW)	-8.49	-8.70	-9.17	-9.18	-8.77 ^b	-8.17	-4.9
δ ² H (H ₂ O) (‰v-SMOW)	-52.7	-58.0	-63.6	-62.2	-47.9 ^b	-57.4	-28
δ ³⁴ S (SO ₄ ²⁻) (‰v-CDT)	21.88		21.01	22.5	21.3 ^a		
δ ¹⁸ O (SO ₄ ²⁻) (‰v-CDT)	11.97		12.28	11.9			
⁸⁷ Sr/ ⁸⁶ Sr	0.707651	0.707774	0.707715				
References	Pearson et al. (2003)	Pearson et al. (2003)	Pearson et al. (2003)	Müller and Leupin (2012)	Vinsot et al. (2008)	Vogt (2013)	Bureau Technique Norbert (1993)

Data refer to the first sampling campaign that yielded sufficient water for analysis

^a Sampled 8.10.05

^b Sampled 5.1.05

on published data collected in the frame of several projects conducted at Mont Terri, including WS, WS-H, WS-I (Ground- and pore-water sampling), PC (Pore-water chemistry), HT (Hydrogen transfer), SF (Self-sealing of faults) and NT (Natural tracers).

Pore-waters at Mont Terri were recognised as geochemical archives of palaeo-fluids and of the mechanisms by which they interacted with the embedding aquifers. The obtained data were used to constrain solute-transport processes in the low-permeability sequence and the evolution of pore-water since the formation of the Jura Fold and Thrust Belt (Pearson et al. 2003; Mazurek et al. 2011). Folding and thrusting occurred at about 9–4 Ma (Becker 2000). Further, the geochemical studies were extended beyond the Mont Terri rock laboratory, including data from the adjacent Mont Russelin tunnel profile (Koroleva et al. 2011).

Pore-waters were collected in situ by long-term sampling in dedicated short boreholes. These experiments yielded the most complete chemical and isotopic characterisation, but given the limited number of sampling locations, the spatial resolution was limited. These data were

augmented by various laboratory methods on drillcore samples, such as aqueous extraction, out-diffusion, squeezing, vacuum distillation and diffusive isotope exchange via the vapour phase. A large data set with good spatial resolution was obtained from these analyses. However, each laboratory method only yielded partial information on pore-water composition, and the representativity of the measurements for in situ conditions was an issue in some cases. Further information pertinent to pore-water evolution was obtained from the isotopic signatures of calcite and celestite occurring in veins that were formed during Jura thrusting (De Haller et al. 2014). These veins—in most cases thin veinlets—record the isotopic composition of water that migrated along fractures at that time. The sampling areas in the Mont Terri and Mont Russelin tunnels are indicated in the geological profiles shown in Fig. 1.

It has long been recognised that pore-waters at Mont Terri and Mont Russelin cannot be explained as simple binary mixtures of sea and meteoric water (see Pearson et al. 2003 and Sect. 5.2 below). The objective of this contribution is to integrate the chemical and isotopic information archived in

Fig. 1 Profiles across the Mont Terri and Mont Russelin anticlines, adapted from Freivogel and Huggenberger (2003) and Bureau Technique Norbert (1993). Blue bars in tunnels indicate sampled areas. Inset illustrates the concept of orthogonal distance (in metres) used to represent the spatial distribution of pore-water compositions

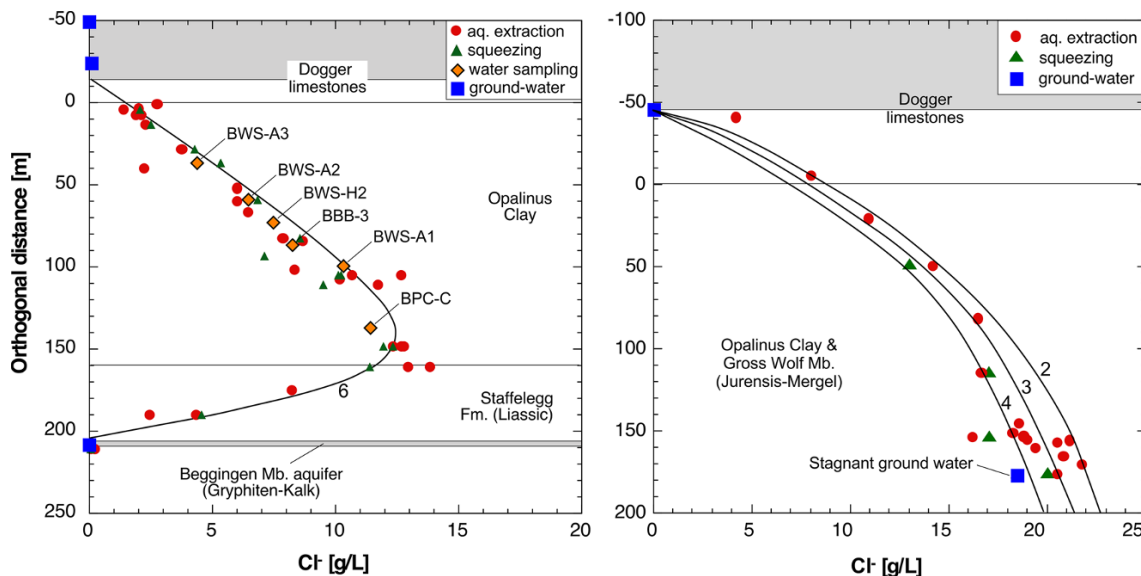
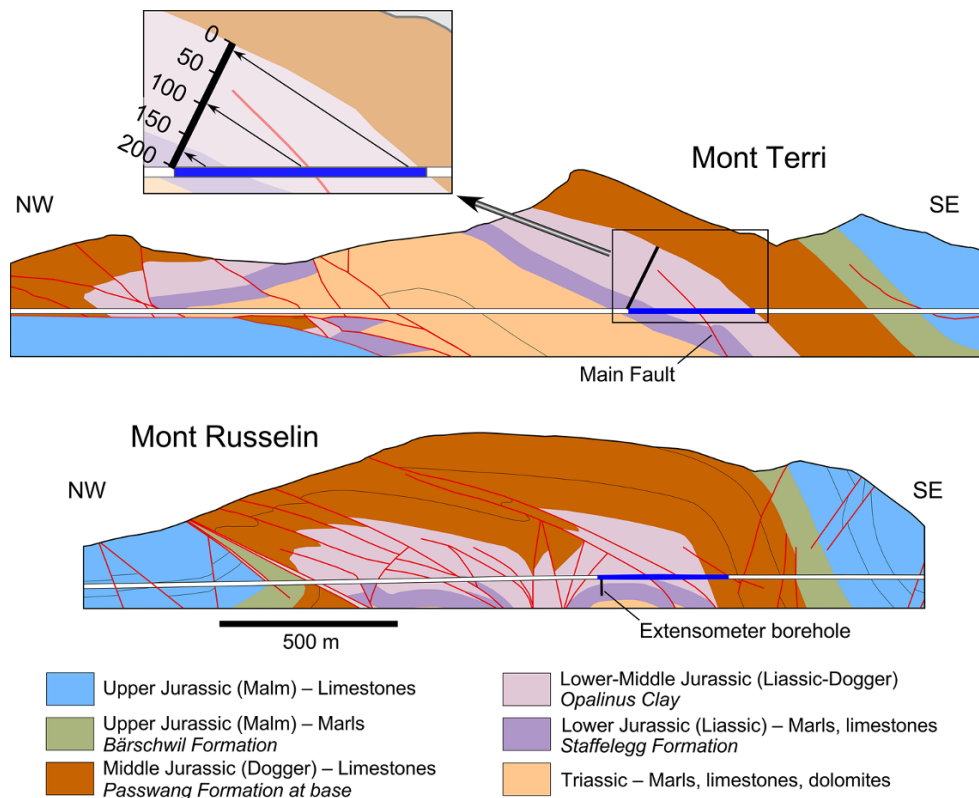


Fig. 2 Spatial distribution of Cl^- in pore-waters from Mont Terri and Mont Russelin. “Orthogonal distance” refers to distance from the top of Opalinus Clay in the direction normal to bedding. Numbers indicate total diffusion times in Myr. Data from Pearson et al. (2003)

and Koroleva et al. (2011), model fits from Mazurek et al. (2011) and Koroleva et al. (2011). References for water samples taken in situ see Table 1. Aquifers are shown in grey

pore-waters and in vein infills, together with independent information on the regional geological evolution, in order to constrain fluid provenance and the long-term geochemical evolution at Mont Terri prior to Jura thrusting. Pore-water

chemistry evolves over time in response to changing boundary conditions at the Earth’s surface (e.g. marine vs. continental periods) and the possible impact of fluid-flow events related to tectonic activity.

2 Pore-water sampling techniques in the Mont Terri rock laboratory: methods and results

2.1 Laboratory methods

A suite of methods were applied to quantify the chemical and isotopic composition of pore-waters at Mont Terri, including long-term sampling in dedicated boreholes, aqueous extraction, squeezing, diffusive exchange, vacuum distillation and out-diffusion (Rübel et al. 2002; Pearson et al. 2003). Most laboratory techniques applied on drill-cores only yield partial data on pore-water composition, mostly pertinent to conservative constituents such as halogens (Cl^- , Br^-), stable isotopes of water ($\delta^{18}\text{O}$, $\delta^2\text{H}$) and dissolved noble gases (He , $^3\text{He}/^4\text{He}$, Ar , $^{40}\text{Ar}/^{36}\text{Ar}$). At Mont Terri, a large number of drillcore samples were investigated over the entire clay-rich, low-permeability sequence, including the Opalinus Clay and the upper part of the Staffelegg Formation. This sequence is bounded by fractured limestone units at the top (Passwang Formation) and at the base (Beggingen Member of the Staffelegg Formation). These limestones have elevated permeabilities and constitute the hydrogeological boundaries of the clay-rich sequence. Even though they do not represent economically productive water resources, ground-water flow is dominated by advection, and they are termed aquifers in the following. At Mont Russelin, a similar campaign was conducted in the southeastern limb of the anticline (Fig. 1; Koroleva et al. 2011). Figure 2 illustrates the systematic spatial variability of Cl^- concentrations across both profiles, based on laboratory data and in situ sampling of pore and ground-waters. While sampling was made in short boreholes drilled from the tunnels, Fig. 2 represents the data as a function of orthogonal distance from the top of Opalinus Clay, i.e. data were projected to a plane perpendicular to stratification, as shown in the inset of Fig. 1. The orthogonal distance represents the minimum transport length for pore-water solutes to the bounding aquifer.

2.2 In-situ sampling of pore-water

The method of in situ sampling of pore-water in dedicated boreholes was first developed at Mont Terri in the frame of the WS experiment (Pearson et al. 2003). In contrast to most laboratory techniques, this approach potentially yields a complete data set on the major and trace element composition of the pore-water. Four boreholes were dry drilled with flushing by compressed air, and borehole sections at least 13 m away from the tunnel were isolated by single packers. The isolated intervals were filled with N_2 and held at a pressure of 0.5–0.8 bar over a total experimental period of about 4 years. Pore-water accumulated in the boreholes over time and was sampled recurrently. The total

volumes of water collected were about 23, 6 and 18 L for boreholes A1, A2 and A3 (all drilled upward and perpendicular to bedding), while borehole A6 (drilled parallel to bedding) remained dry. Within each borehole, the flow rates also varied greatly over time between zero and a maximum of 65 mL/d. Similarly, the chemical compositions of the collected waters showed some limited variability, which may partly be linked to excavation activities in the vicinity of the water-sampling boreholes.

Compositions of waters obtained during the first sampling campaign, 6–15 months after installation, are given in Table 1 and shown in Fig. 2. The A1 water, originating from the central parts of Opalinus Clay (100 m orthogonal distance from the top of the formation), has the highest salinity, corresponding to slightly more than half that of sea-water. The A2 and A3 waters, originating from the upper part of Opalinus Clay (about 60 and 35 m orthogonal distance, respectively), show decreasing salinities. While the major-ion and most of the isotope data obtained in the water-sampling boreholes over 4 years are considered reliable, data pertinent to pH and dissolved inorganic carbon [and therefore $\text{p}(\text{CO}_2)$] remain problematic (Pearson et al. 2003). Given the fact that pore-water degassed into the N_2 -filled sampling interval, the carbonate system was perturbed.

A series of further experiments have been conducted in more recent times, shedding further light into pore-water chemistry. The setup of the PC and PC-C experiments included improvements to minimise disturbances, such as drilling with N_2 rather than air. The concept of the PC experiment was diffusive equilibration between an artificial pore-water circulating in a borehole and the surrounding in situ pore-water. The goal of this experiment was to obtain better constraints on the carbonate system and $\text{p}(\text{CO}_2)$. However, it became evident during monitoring that the pore-water chemistry was disturbed by a leaking gel-electrode that triggered substantial microbial activity. This led, among others, to sulphate reduction and significant alteration of pore-water chemistry (Wersin et al. 2011). The concept of PC-C experiment was similar to that of the WS experiments but involved continuous flushing with argon in the test interval. The experiment yielded reliable and extensive analyses of seepage water after a transient phase (Vinsot et al. 2008). More recent experiments (WS-H and WS-I, Müller and Leupin 2012; Vogt 2013; Lorenz and Vogt 2014) were carried out to study inflow waters (wet spots), which were partly triggered by excavation activities. Chemical and isotopic analyses confirmed that these seepage waters correspond to local in situ waters because their compositions cannot be distinguished from those of the adjacent pore-waters. In particular, Cl^- and Br^- concentrations are consistent with the spatial distribution of these solutes as defined by Pearson

et al. (2003). In the HT experiment, the effect of gaseous hydrogen injected into a borehole was analysed (Vinsot et al. 2014). Extensive sulphate reduction was observed, induced by microbial activity in the borehole. Selected data from these experiments are shown in Table 1.

2.3 Stagnant ground-water at Mont Russelin

In the Mont Russelin anticline, a ground-water in the Beggingen Member of the Staffelegg Formation underlying Opalinus Clay could be sampled in an extensometer borehole (location shown in Fig. 1), during tunnel construction (Bureau Technique Norbert 1993). Because of some degree of contamination originating from the cementitious backfill of the borehole, only halogen and water-isotope data are considered reliable and are reported in Table 1. This water yielded among the highest salinities and the least negative δ values for water isotopes when compared to all other data from Mont Terri and Mont Russelin (Table 1, Fig. 2). This composition contrasts with that of the young and fresh water found in the same unit at Mont Terri. The difference is due to the fact that while erosion exhumed strata down to the Triassic at Mont Terri, leading to an active flow system, there was much less erosion at Mont Russelin, where the Staffelegg Formation does not crop out and is always covered by Opalinus Clay (as shown in the profiles in Fig. 1). The absence of in- and exfiltration areas and the protected position in the core of the anticline is taken as evidence that the ground-water of the Staffelegg Formation at Mont Russelin is a stagnant water body unaffected by processes postdating the thrusting and folding of the anticline but in diffusive equilibrium with the overlying clay-rich rocks. Therefore, Mazurek et al. (2011) and Koroleva et al. (2011) concluded that this water likely represents the composition of pore-waters that resided in the low-permeability sequence at the time of Jura thrusting and related vein formation.

3 Structural features and petrography of veins

Veins at Mont Terri occur in structures that can be attributed to thrust-fault systems that developed during the formation of the anticline (Nussbaum et al. 2011, 2017). In spite of substantial brittle deformation, veins in Opalinus Clay are infrequent and thin, indicating that fluid flow across the formation during deformation was limited. They consist of calcite, celestite and subordinate pyrite. Frequently, they are hardly visible in outcrop but can be identified in thin section. Within the Main Fault (shown in Fig. 1), the largest thrust fault within the Mont Terri rock laboratory (Nussbaum et al. 2011, 2017), veins are typically < 1 mm thick and also occur within a few metres

around the fault, documenting a diffuse pattern of deformation and vein precipitation.

In order to retrieve friable, cohesionless fault rock with as little mechanical disturbance as possible, a special drilling technique was used to minimise damage due to drilling. A steel device with guiding tubes was used to drill eight perforation holes (25 mm each) 60 cm into the Main Fault (Fig. 3a). The ring perforation was subsequently filled with epoxy resin. After polymerisation, the interval was overcored (143 mm), placed in an acrylic liner and further stabilised by filling the ring space with epoxy resin. A more detailed documentation of the drilling technique can be found in Nussbaum et al. (2006). Figure 3b shows a slice of the core obtained by this technique and provides a cross section across one of the major fault planes within

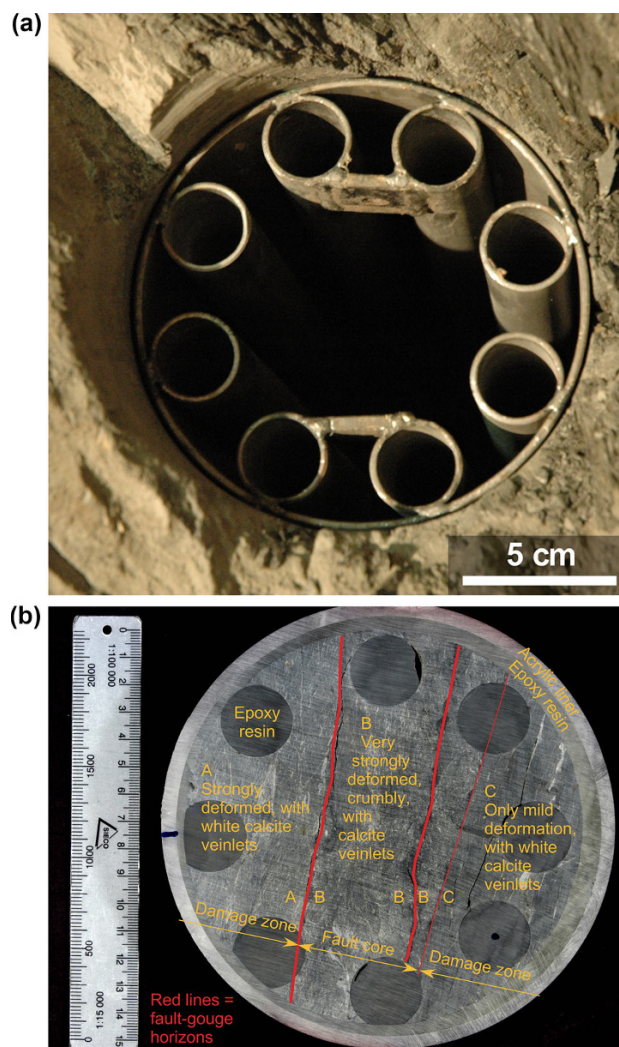


Fig. 3 Drilling procedure and structural features in retrieved core obtained from a borehole drilled into one of the main internal fault planes of the Main Fault at Mont Terri. Diameter of core is 14.3 cm. **a** Device with 8 tubes used as guides to drill a ring perforation around the core. **b** Cross section of retrieved core showing the structural elements of the penetrated fault segment

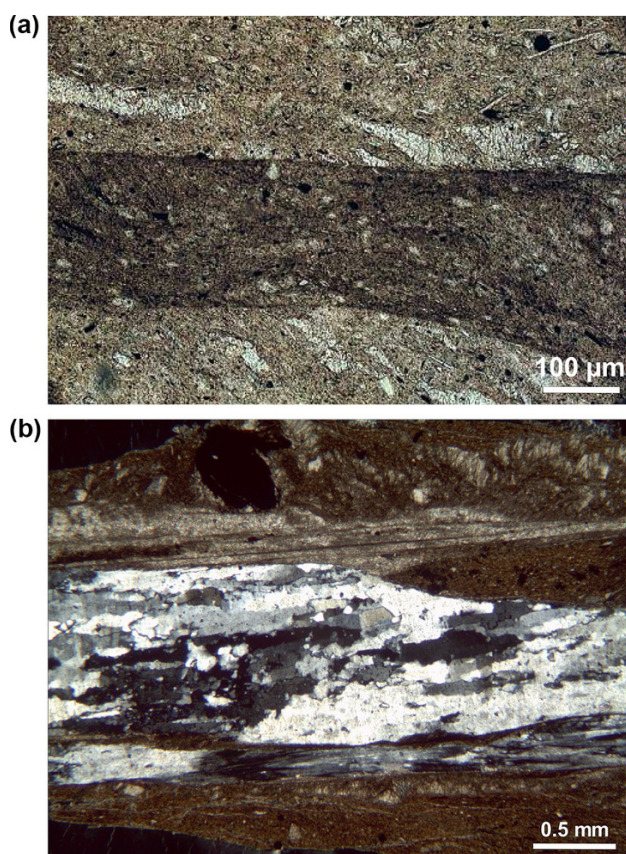


Fig. 4 Microscopic features of the Main Fault at Mont Terri. **a** Cohesionless fault-gouge horizon with sharp boundaries. Length of picture is 0.7 mm, parallel polars. **b** Celestite-calcite vein with fibrous texture, indicating syntectonic growth. Length of picture is 3.5 mm, crossed polars

the Main Fault. It consists of a fault core, which is bounded by mm-thick horizons of fault gouge (Fig. 4a), surrounded on both sides by a less strongly deformed damage zone. Veinlets are recognised mainly in the damage zone and less in the fault core (Fig. 3b). Microscopic investigations show that they are often fibrous, indicating syn-tectonic growth of both calcite and celestite (Fig. 4b). The youngest stage of vein formation occurred in microscopic pull-apart structures formed associated to the last shear movements. Outside the Main Fault, veinlets were separated by disaggregating the rock using the technique described in de Haller et al. (2014), followed by hand picking. Petrographically, these veins cannot be distinguished from those within the Main Fault.

4 Isotopic composition of vein infills, whole rocks and current pore-water

The sampling and analytical methods for pore-waters are documented in Pearson et al. (2003), those for isotopic measurements on minerals and rocks are described in de Haller et al. (2014).

4.1 Oxygen and carbon isotopes in calcite

As shown in Table 2 and Fig. 5, $\delta^{18}\text{O}$ of whole-rock carbonate varies in the range 23.4–29.1‰_{V-SMOW}, largely consistent with values for marine calcite at the time of deposition (Gomez et al. 2009; Korte et al. 2015). Vein calcite has consistently lower $\delta^{18}\text{O}$ values. Within the Main Fault, the average fractionation between whole-rock carbonate and vein calcite is 4.5‰_{V-SMOW}, suggesting that the veins precipitated at higher temperature and/or from waters with $\delta^{18}\text{O}$ values lower than that of sea-water. Vein calcite from Mont Russelin has $\delta^{18}\text{O}$ values of 17.1–17.4‰_{V-SMOW}, which is lower than the values at Mont Terri (19.3–22.9‰_{V-SMOW}).

4.2 Sulphur and oxygen isotopes in celestite and in current pore-water

Celestite was observed exclusively in veins hosted by Opalinus Clay, and the sulphate-isotope data are given in Table 2 and Fig. 6. Data for whole-rock gypsum or anhydrite from the underlying Triassic evaporites (Gipskeuper, Muschelkalk) are also included (data from Table 3). The isotopic composition of sulphate in current pore-water was obtained by long-term sampling in boreholes distant from any major deformation features (data in Table 1, Pearson et al. 2003; Müller and Leupin 2012) and is also shown in Fig. 6. Only data from the first sampling in each borehole are shown, while later samplings (after about a year) diverge in different directions, most probably due to microbially mediated redox reactions in the sampling interval.

4.3 $^{87}\text{Sr}/^{86}\text{Sr}$ in calcite, celestite, whole-rock carbonate and in current pore-water

Data for veins are shown in Table 2, and whole-rock data are given in Table 3. Further whole-rock carbonate data were obtained for the generally clay-rich units between the Passwang and Staffelegg Formations, including Opalinus Clay. However, Sr in acetic-acid leachates from such rocks may include significant contributions from clay minerals and possibly feldspars in addition to carbonate (see also Lerouge et al. 2010). Therefore, these data are not considered reliable and not reported here.

All data are shown in Fig. 7, together with data for current pore-water (Table 1; Pearson et al. 2003) and for Sr sorbed on clay minerals (from Lerouge et al. 2010). Vein calcite, vein celestite (including the two measurements from Mont Russelin) and current pore-water in Opalinus Clay occupy overlapping fields. The $^{87}\text{Sr}/^{86}\text{Sr}$ ratios in whole rocks from the Triassic as well as from the middle/late Dogger are within or close to the respective fields of

Table 2 Isotope data for veins at Mont Terri (MT) and Mont Russelin (MR)

Locality	Sample ID	Tunnel chaignage (m)	Unit	Mineral	$\delta^{34}\text{S}_{\text{sulphate}}$ (‰v.-CDT)	± 1 σ	$\delta^{18}\text{O}_{\text{sulphate}}$ (‰v.-SMOW)	± 1 σ	$^{87}\text{Sr}/^{86}\text{Sr}$	± 2 σ	$\delta^{13}\text{C}_{\text{carbonate}}$ (‰v.-PDB)	± 1 σ	$\delta^{18}\text{O}_{\text{carbonate}}$ (‰v.-SMOW)	± 1 σ
MT	MT-23	275.00	St-Ursanne Fm (Malm)	Calcite					0.707768	0.000038	-7.15	0.05	21.64	0.06
MT	BSF-004-8	870.00	Opalinus Clay (Dogger)	Celestite	22.6	0.3	16.1	0.3	0.707759	0.000022				
MT	BSF-004-8	870.00	Opalinus Clay (Dogger)	Celestite	24.8	0.3	18.6	0.3						
MT	BSF-004-8	870.00	Opalinus Clay (Dogger)	Celestite	24.7	0.3	17.5	0.3						
MT	UNIBE-124.20	914.50	Opalinus Clay (Dogger)	Calcite- celestite	22.4	0.3	17.0	0.2	0.707749	0.000022	-2.08	0.05	19.32	0.06
MT	UNIBE-123.5	915.20	Opalinus Clay (Dogger)	Calcite					0.707764	0.000022	-2.29	0.05	21.07	0.06
MT	UNIBE-118.25	920.45	Opalinus Clay (Dogger)	Calcite					0.707796	0.000028	-1.85	0.05	19.91	0.06
MT	UNIBE-116.25	922.45	Opalinus Clay (Dogger)	Calcite- celestite					0.707776	0.000037	-1.84	0.05	19.34	0.06
MT	BSF-006-13	923.00	Opalinus Clay (Dogger)	Calcite					0.707848	0.000026	-2.12	0.05	19.59	0.06
MT	MT-6	923.00	Opalinus Clay (Dogger)	Calcite					0.707783	0.000024	-2.05	0.05	19.88	0.06
MT	UNIBE-113.75	924.95	Opalinus Clay (Dogger)	Calcite					0.707701	0.000026	-2.37	0.05	19.96	0.06
MT	GM-64	967.00	Opalinus Clay (Dogger)	Celestite	22.5	0.2	18.5	0.3	0.707712	0.000020				
MT	GM-24	1003.00	Opalinus Clay (Dogger)	Celestite	28.4	0.4	17.8	1.4	0.707725	0.000028				
MT	GM-6.8	1010.00	Opalinus Clay (Dogger)	Calcite- celestite	28.1	0.4	17.9	0.5	0.707726	0.000024	0.56	0.05	22.87	0.06
MR	MR-SF7		Opalinus Clay (Dogger)	Calcite- celestite					0.707853	0.000022	-0.36	0.05	17.11	0.06
MR	BSF11 (13-15)		Opalinus Clay (Dogger)	Calcite- celestite	19.5	1.3	14.5	2.0	0.707804	0.000023	-0.28	0.05	17.39	0.06

 $^{87}\text{Sr}/^{86}\text{Sr}$ data in mixed calcite-celestite veins refer to celestite

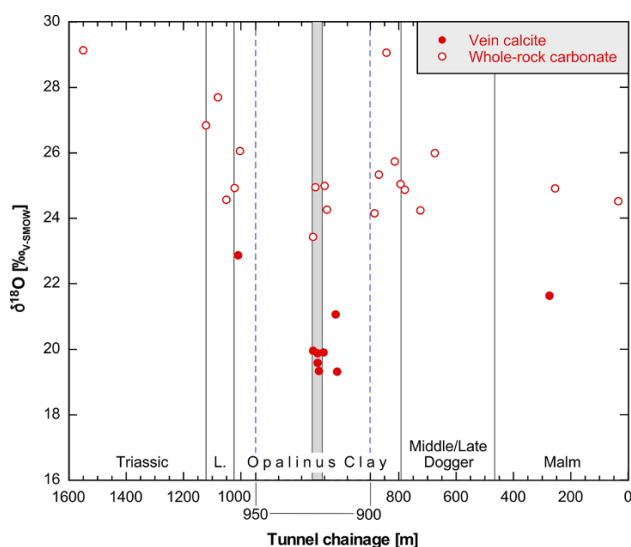


Fig. 5 $\delta^{18}\text{O}$ of vein calcite and whole-rock carbonate along the tunnel profile at Mont Terri. Note the expanded length scale in the region of the Main Fault (shown in grey). L. Liassic

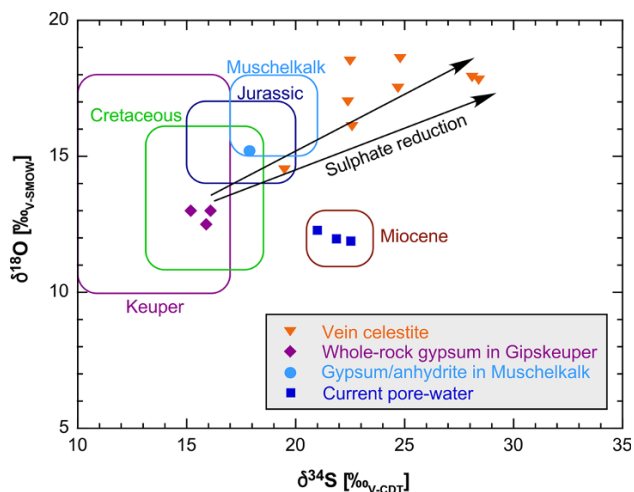


Fig. 6 Isotopic composition of sulphate in rocks, veins and pore-waters at Mont Terri. Fields are shown for marine sulphate during different geological periods (based on Claypool et al. 1980 and Balderer et al. 1991). Data for current pore-waters are from Pearson et al. (2003) and Müller and Leupin (2012)

contemporary sea-water according to the compilation of McArthur et al. (2012). On the other hand, all vein data as well as current pore-water in Opalinus Clay yield $^{87}\text{Sr}/^{86}\text{Sr}$ ratios that are substantially higher than late Toarcian/Aalenian sea-water according to McArthur et al. (2012), indicating an external component of Sr with a higher $^{87}\text{Sr}/^{86}\text{Sr}$ ratio. In principle, such a component can be derived either from the underlying Keuper, or from a Tertiary sea-water that may have infiltrated during the deposition of the Lower Freshwater Molasse (USM) or the Upper Marine Molasse (OMM).

5 Discussion

5.1 Main characteristics of pore-waters

Pore-water composition at Mont Terri and Mont Russelin is dominated by Na^+ , Cl^- and SO_4^{2-} (Table 1). The pore-waters span a wide range of salinities (Cl^- concentration profiles are shown in Fig. 2). At Mont Terri, total dissolved solids (TDS) increase with the distance from the fresh-water aquifer in the Passwang Formation and reach a maximum of 28 g/L before returning sharply to low values towards the underlying fresh-water aquifer in the Beggingen Member (Staffelegg Formation). At Mont Russelin, the upper part of the profile looks similar to that at Mont Terri, but in the lower part salinity keeps increasing, reflecting the fact that the aquifer in the Staffelegg Formation is stagnant and contains an old, saline water, and reaching a TDS value of 41 g/L, slightly higher than modern sea-water. Mazurek et al. (2011) and Koroleva et al. (2011) interpreted the regular distributions of Cl^- , $\delta^{18}\text{O}$, $\delta^2\text{H}$ and dissolved He as a consequence of diffusive exchange between pore-waters and aquifers since the time these were first flushed by fresh water. The observed spatial distributions of all tracers could be explained as diffusion profiles with modelled evolution times that are plausible from a geological perspective, in particular 6 Myr at Mont Terri and 2–4 Myr at Mont Russelin. (Note that in accordance with Aubry et al. (2009), Myr is used here to address duration, while Ma refers to absolute dates.)

The Cl^-/Br^- ratio of pore-waters both at Mont Terri and at Mont Russelin is consistently close to the current sea-water ratio of 290 g/g, independent of the salinity of the water (Fig. 8). This is also true for the sample of deep, stagnant ground-water in the Beggingen Member (Staffelegg Formation) of the Mont Russelin anticline. It is therefore concluded that all pore-waters have a marine component.

5.2 Provenance of pore-waters: evidence from the literature

Based on pore-water chemistry alone (Fig. 2 and Fig. 8), the pore-waters could be explained as binary mixtures of sea-water and meteoric water, i.e. as products of the diffusive exchange with the embedding fresh-water aquifers since the time these were exhumed and activated. However, this hypothesis does not fit with the evidence from stable isotopes of water. Considering binary mixing of sea and temperate- to warm-climate meteoric water, the fraction of the meteoric component obtained from the stable-isotope data is much higher when compared to that calculated from the Cl^- concentration (Fig. 9). This is also

Table 3 Isotope data for whole rocks at Mont Terri

Sample ID	Tunnel chainage (m)	Unit	Mineral	$\delta^{34}\text{S}$ (‰v.v.- CDT)	$\delta^{18}\text{O}_{\text{sulphate}}$ (‰v.v.-SMOW)	$^{87}\text{Sr}/^{86}\text{Sr}$	$\pm 2 \sigma$	$\delta^{13}\text{C}_{\text{carbonate}}$ (‰v.v.-PDB)	$\pm 1 \sigma$	$\delta^{18}\text{O}_{\text{carbonate}}$ (‰v.v.-SMOW)	$\pm 1 \sigma$
MT-25	35.00	St-Ursanne Fm (Malm)	carbonate			0.707094	0.000027	0.41	0.05	24.52	0.06
MT-24	255.00	St-Ursanne Fm (Malm)	carbonate			0.707090	0.000021	0.63	0.05	24.91	0.06
MT-21	675.00	Hauptrogenstein (Dogger)	carbonate			0.707203	0.000020	2.99	0.05	25.99	0.06
MT-22	725.00	Passwang Fm (Dogger)	carbonate					1.21	0.05	24.24	0.06
BWS- E1(3.40- 3.60)	779.40	Passwang Fm (Dogger)	carbonate					-0.16	0.05	24.87	0.06
BWS- E4(3.25- 3.45)	794.20	Opalinus Clay (Dogger)	carbonate					-0.09	0.05	25.04	0.06
BWS- E5(4.38- 4.50)	814.50	Opalinus Clay (Dogger)	carbonate					0.46	0.05	25.73	0.06
BWS- A3(28.00- 28.12)	843.50	Opalinus Clay (Dogger)	carbonate					2.34	0.05	29.06	0.06
MT-9	870.00	Opalinus Clay (Dogger)	carbonate					-0.29	0.05	25.33	0.06
BWS- A2(2.33- 2.48)	885.20	Opalinus Clay (Dogger)	carbonate					0.20	0.05	24.15	0.06
UNIBE- 119.75	918.95	Opalinus Clay (Dogger)	carbonate					-1.01	0.05	24.26	0.06
UNIBE- 118.75	919.95	Opalinus Clay (Dogger)	carbonate					-1.27	0.05	24.99	0.06
UNIBE- 114.75	923.95	Opalinus Clay (Dogger)	carbonate					-1.58	0.05	24.95	0.06
MT-7	925.00	Opalinus Clay (Dogger)	carbonate					-1.35	0.05	23.43	0.06
BWS- A6(19.55- 19.75)	1003.50	Opalinus Clay (Dogger)	carbonate					0.08	0.05	26.06	0.06
BWS- E6(5.00- 5.15)	1022.10	Staffelegg Fm, Gross Wolf Mb (Liassic)	carbonate					0.28	0.05	24.93	0.06
BWS- E7(4.95- 5.10)	1050.60	Staffelegg Fm, Rietheim Mb (Liassic)	carbonate					1.12	0.05	24.57	0.06
BWS- E8(4.70- 5.10)	1080.40	Staffelegg Fm, Mont Terri Mb (Liassic)	carbonate					0.13	0.05	27.70	0.06

Table 3 continued

Sample ID	Tunnel chainage (m)	Unit	Mineral	$\delta^{34}\text{S}$ (‰v.-CDT)	$\delta^{18}\text{O}_{\text{sulphate}}$ (‰v.-SMOW)	$^{87}\text{Sr}/^{86}\text{Sr}$	$\delta^{13}\text{C}_{\text{carbonate}}$ (‰v.-PDB)	$\delta^{18}\text{O}_{\text{carbonate}}$ (‰v.-SMOW)	± 1 σ	± 1 σ
BWS-E9(4.80-5.10)	1121.90	Staffellegg Fm, Beggingen Mb (Liassic)	carbonate				-3.18	26.84	0.05	0.06
MT-3	1150 ^a	Klettgau Fm, Belchen Mb (Triassic)	gypsum	16.1	0.3	0.4	0.707932	0.000030		
MT-3	1150 ^a	Klettgau Fm, Belchen Mb (Triassic)	gypsum	15.9	0.3	0.4				
MT-3	1150 ^a	Klettgau Fm, Belchen Mb (Triassic)	gypsum	15.2	0.3	0.4				
MT-20	1550	Schinznach Fm, Trigonodus-Dol. (Triassic) ^b	gypsum/ anhydrite; carbonate	17.9	0.3	0.4	0.707984	0.000033	0.05	0.06

^a Samples were collected on the surface (locality "La Gypsière"), tunnel chainage is based on a projection

^b $^{87}\text{Sr}/^{86}\text{Sr}$ refers to carbonate

illustrated by the ground-water sample from Mont Russelin, with a near-marine Cl^- concentration of 18.4 g/L but markedly negative $\delta^{18}\text{O}$ and $\delta^2\text{H}$ values of -4.9 and -28‰v.-SMOW , respectively.

The difficulty to explain the pore-waters at Mont Terri and Mont Russelin as mixtures of sea and meteoric water has already been discussed by Pearson et al. (2003). They considered interactions of pore-water with clay minerals, effects of ion filtration and differences in the diffusion coefficients for Cl^- and water as potential mechanisms to rationalise the provenance of the waters. On a qualitative level, they discarded the former two mechanisms and proposed that the discrepant mixing proportions could be due to the higher diffusion coefficient for the water molecule when compared to that for halogens. However, Mazurek et al. (2011) performed model calculations and showed that differences in the diffusion coefficients are insufficient to explain the observations. These authors concluded that the $\delta^{18}\text{O}$ and $\delta^2\text{H}$ values of the pore-water must have been negative at the time when diffusive exchange was initiated after flushing of the embedding aquifers with fresh meteoric water. They consider the deep ground-water from Mont Russelin as a good proxy of the water present in the system prior to the formation of the Jura Fold and Thrust Belt, even though its origin cannot be explained in a simple way.

5.3 Regional hydrogeological and hydrochemical evolution

A potentially better understanding of the early part of pore-water evolution can be obtained by considering current knowledge of palaeo-hydrogeology and hydrochemistry for times prior to the formation of the Jura Fold and Thrust Belt.

5.3.1 Jurassic to Cretaceous (201–66 Ma); chronostratigraphy according to Cohen et al. 2013)

Marine conditions prevailed in the area of interest during Jurassic and large parts of Cretaceous times, and sedimentation took place. It is therefore safe to say that pore-waters in the sedimentary pile had a composition close to that of sea-water. In the late Cretaceous, the basin was inverted, leading to exhumation and erosion.

5.3.2 Palaeogene (66–23 Ma)

Due to predominantly continental conditions and therefore long-term exposure to meteoric waters in the Palaeogene, karst formation occurred in the limestones of the Malm, which became a regional aquifer. In the area of interest, Palaeogene karstification is not known in the underlying

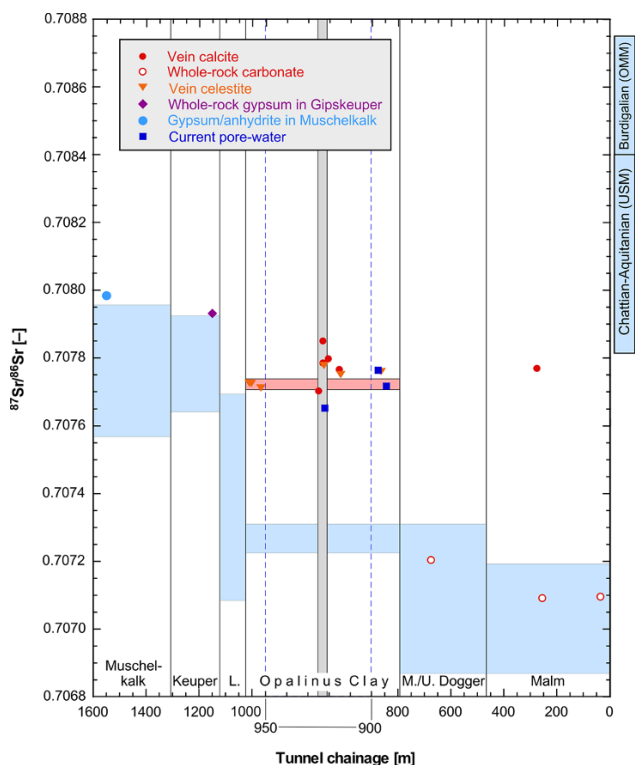


Fig. 7 $^{87}\text{Sr}/^{86}\text{Sr}$ ratios in vein minerals, whole-rock carbonate/sulphate and current pore-water at Mont Terri. Data for pore-water are from Pearson et al. (2003). Blue areas indicate $^{87}\text{Sr}/^{86}\text{Sr}$ values for contemporary sea-water according to McArthur et al. (2012). Pink bar shows range of $^{87}\text{Sr}/^{86}\text{Sr}$ for Sr sorbed on clay minerals in Opalinus Clay according to Lerouge et al. (2010). Grey bar indicates the Main Fault. Note the break in horizontal scale in the region of the Main Fault

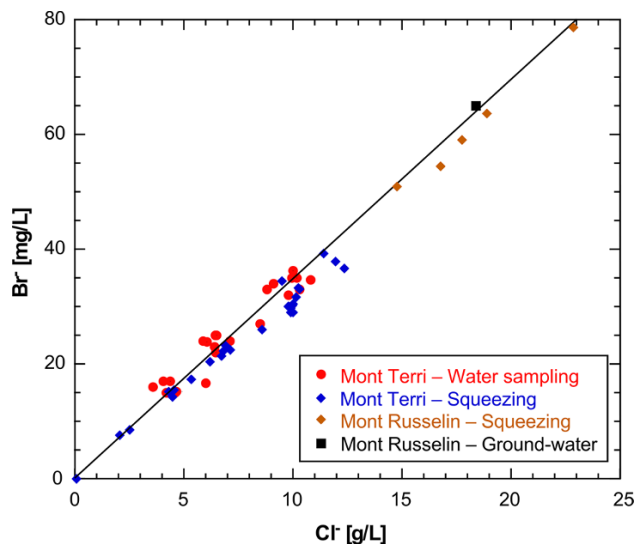


Fig. 8 Cl^- and Br^- concentrations in pore-waters at Mont Terri and Mont Russelin. Data are from Pearson et al. (2003) and Koroleva et al. (2011). Solid line indicates the Cl^-/Br^- ratio in modern sea-water

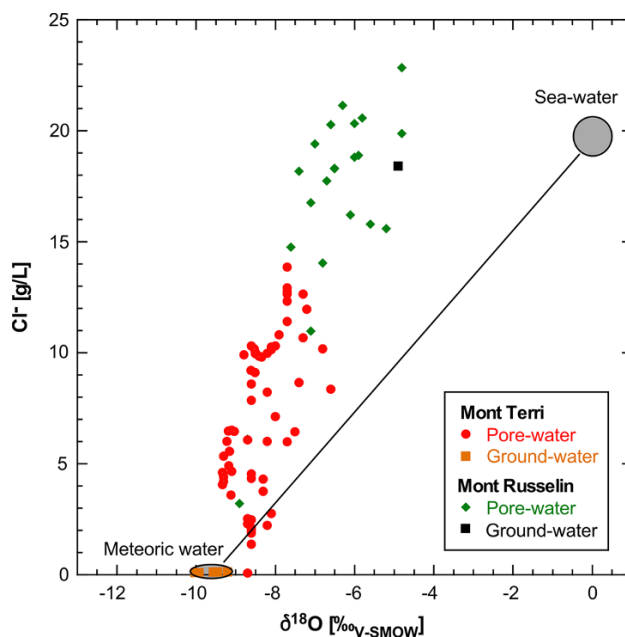


Fig. 9 Cl^- concentrations versus $\delta^{18}\text{O}$ in pore and ground-waters. Mixing line between sea-water and current meteoric water at Mont Terri is also shown

limestone units, such as the Hauptrogenstein (P. Jordan, pers. comm. Dec. 2015). Therefore, conceptually, the Malm aquifer can be considered as a fresh-water boundary leading to progressive out-diffusion of salinity from the underlying, largely clay-rich sequence.

While NaCl/KCl salts were deposited in the Rhine Graben during the Eocene, there is no evidence of marine environments at that time in the Mont Terri region (Pirkenseer et al. 2010). In the Oligocene, marine incursions of limited duration may have occurred from the Rhine Graben, even though the Mont Terri region was located along the southern shoreline (Picot et al. 2008; Pirkenseer et al. 2010, 2011, 2013). The possible presence of short brackish or marine stages does not change the fact that for most of the Palaeogene, the region was exposed to continental conditions.

5.3.3 Aquitanian (23–20 Ma)

In spite of the generally continental conditions in northern Switzerland (deposition of the Lower Freshwater Molasse (USM), 28–20.5 Ma), the region of the Folded Jura experienced marine episodes in the late Chattian and Aquitanian. Evaporites, mainly gypsiferous marls, were identified at several locations and interpreted as sabkha deposits (Kissling 1974; Mojon et al. 1985; Berger 1996; Weidmann et al. 2014). Kuhlemann and Kempf (2002) attribute these units to marine incursions from the north-west (Bresse-Rhône Graben, Rhine Graben). The potential

effects of brines on the surface on the composition of pore-waters in the underlying units are discussed below.

5.3.4 Burdigalian (20–16 Ma)

In the external parts of the Swiss Molasse Basin, the Burdigalian Upper Marine Molasse (OMM, 20.4–16 Ma) was deposited in a narrow channel between the Alpine front and the foreland bulge and records the last marine period (Kuhlemann and Kempf 2002). The extent of the OMM towards the northwest is not well known due to erosion in the Jura Mountains. In the early Burdigalian, the Mont Terri region was either continental with no sedimentation or marine deposits of this age were eroded (Berger 1996; Berger et al. 2005). In the late Burdigalian, the region was located close to the coast line, and the conditions were shallow marine to brackish (Berger et al. 2005; Becker and Berger 2004). Today, the nearest outcrops of the OMM are about 20 km to the southeast near Moutier (Pfirter et al. 1996). Thus, it is possible in principle but still remains unclear whether or not the Mont Terri area has been exposed to marine or brackish conditions over substantial time periods during the Burdigalian. There are no records of restricted environments in the OMM where sea-water evaporation may have played a major role. The Burdigalian OMM was the last marine stage in the region, and continental conditions have prevailed since then.

5.4 Partial evaporation of sea-water: a potential mechanism to rationalise observed pore-water compositions

Partial evaporation of sea-water apparently took place in the Aquitanian, meaning that the upper boundary condition for the low-permeability sequence changed drastically from meteoric to brine for some time. Sea-water evaporation is a process that results in distinct and non-linear effects on salinity and water-isotope composition. Below halite saturation, concentrations of halogens increase linearly with evaporation, while the evolution of water isotopes follows a more complex and non-linear scheme. The stable-isotope composition of evaporating sea-water depends on relative humidity (determining the relative contribution of kinetic effects of evaporation), on temperature (determining the fractionation factors) and ion concentrations (determining isotope fractionations between water in hydration shells of ions and free water). Laboratory experiments by Craig et al. (1963), Craig and Gordon (1965) and Gonfiantini (1965, 1986) indicate that $\delta^{18}\text{O}$ and $\delta^2\text{H}$ increase, even though less than what would be expected from a distillation process. The limited increase is due to the rapid exchange of water molecules between water and vapour, an effect that predominates over the

separation effect due to the removal of vapour (Craig et al. 1963; Lloyd 1966). The slope of the evaporation line in a $\delta^{18}\text{O}$ - $\delta^2\text{H}$ plot is close to that of the meteoric water line at high air humidity but becomes flatter under more arid conditions (see illustrations in Gonfiantini 1986). Once evaporation reduced the original mass of sea-water to about 20%, the $\delta^{18}\text{O}$ and $\delta^2\text{H}$ values loop back towards lower values due to the growing importance of water-ion interactions in the brine (Gonfiantini 1965; Clark and Fritz 1999). Based on surveys in natural salt pans, Lloyd (1966) concluded that $\delta^{18}\text{O}$ values of evaporating sea-water in humid coastal environments do not exceed 6‰_{V-SMOW}.

5.5 Scoping calculations exploring pore-water evolution

The preceding sections presented evidence for marine incursions followed by partial evaporation in the Aquitanian. Assuming that these brines were also present at Mont Terri and Mont Russelin, the question is if and how they could have infiltrated into the underlying low-permeability sequence. The brine had an elevated density (around 1.08 cm³/g at gypsum saturation, 1.22 cm³/g at halite saturation; based on calculations with PhreeQC), which may have triggered density-driven infiltration into the karst aquifer of the Malm. From there, diffusive exchange with the low-salinity pore-waters of the underlying low-permeability rocks may have taken place. In the following, an attempt is made to quantify these processes. The Malm aquifer is considered as the upper boundary, which overlies a low-permeability sequence in which transport is dominated by diffusion. The objective is to explore how pore-water composition is affected by chemical changes in the Malm aquifer. Given the fact that the palaeo-hydrogeological evolution is not known accurately and some assumptions needed for the calculations are speculative, the results must be considered as scoping calculations. They are suited to test the plausibility of working hypotheses but are less well constrained than the modelling efforts performed by Mazurek et al. (2011) for the youngest part of the evolution (post-Jura folding). In line with the discussion in the preceding section, the main model assumptions are summarised in Table 4. The calculations consider the time period between the end of the open-marine period (66 Ma, base Tertiary) and the onset of flushing of the hanging-wall aquifer (Dogger) with fresh water at 6 Ma. A pore-diffusion coefficient D_p (Cl^-) of 7×10^{-11} m²/s normal to bedding, typical of Opalinus Clay at Mont Terri (Van Loon and Soler 2003; Van Loon et al. 2005a, b), was used for the whole sequence. A modified version of the reactive transport code FLOTRAN (Lichtner 2007), in particular the TRANS90 module, was used. FLOTRAN is a finite-volume code capable of

Table 4 Overview of the assumed palaeo-hydrogeological evolution and values used for transport modelling of the time period between deposition of Opalinus Clay and the onset of flushing of the Dogger aquifer at 6 Ma

Time period	Age (Ma)	Model time (Myr)	Environment	Data used for modelling	Significance in model calculations
Jurassic-Cretaceous	201–66		Open marine	Cl^- at 66 Ma = 19.35 g/L, $\delta^{18}\text{O} = 0\text{‰}$ throughout the sequence	Initial and upper boundary condition
Palaeogene	66–23	0–43	Continental	Meteoric water ($\text{Cl}^- = 0$ g/L, $\delta^{18}\text{O} = -7.7\text{‰}$) circulating in Malm aquifer	Upper boundary condition
Aquitainian (and younger?)	23–a	43–b	Hypersaline (partial evaporation of sea-water)	$\text{Cl}^- = 70\text{--}190$ g/L, $\delta^{18}\text{O} = +6\text{‰}$ in Malm aquifer	Upper boundary condition
- Late Miocene	a–6	b–60	Continental	Meteoric water ($\text{Cl}^- = 0$ g/L, $\delta^{18}\text{O} = -8.6\text{‰}$) circulating in Malm aquifer	Upper boundary condition

a = 14.5 Ma/19.5 Ma, b = 51.5 Myr/46.5 Myr for model variants considering brine at gypsum saturation ($\text{Cl}^- = 70$ g/L)/brine at halite saturation ($\text{Cl}^- = 190$ g/L). For the model variant considering brine at gypsum saturation ($\text{Cl}^- = 70$ g/L), a = 14.5 Ma, b = 51.5 Myr. For the model variant considering brine at halite saturation ($\text{Cl}^- = 190$ g/L), a = 19.5 Ma, b = 46.5 Myr

describing two-phase flow and transport of water and gas phases coupled to multicomponent solute transport and reaction with aqueous gaseous species and solids in up to three spatial dimensions. Here, only diffusive transport is considered, and boundary conditions (concentrations or isotope ratios at the model boundaries) can be varied over time as required by the palaeo-hydrogeological scenarios under consideration.

The calculation starts at the beginning of the Tertiary (66 Ma), considering a marine Cl^- concentration throughout the sequence at that time. The whole Palaeogene is assumed to be a continental period characterised by negligible Cl^- concentration in the Malm aquifer. Therefore, out-diffusion of salinity will occur over this period. At the onset of the Aquitainian (23 Ma), a hypersaline upper boundary condition in the Malm aquifer is assumed. Sediments deposited during this period contain gypsum but no halite, suggesting that sea-water at that time evaporated to concentrations in the interval between gypsum and halite saturation. Calculations using the PHREEQC V3 code (Parkhurst and Appelo 2013) with the Pitzer data base indicate that this interval corresponds to Cl^- concentrations in the range 70–190 g/L. The duration of the hypersaline upper boundary condition is treated as a fit parameter, and model runs were performed in the range of 1–10 Myr, leaving all other parameters unchanged. Following the hypersaline stage, a meteoric environment is assumed until the late Miocene (6 Ma), at which time the limestone aquifer in the Passwang Formation has been activated due to exhumation following the formation of the Mont Terri anticline. The model calculations stop at this time, given the fact that the Pliocene and Pleistocene evolution is complex and has been modelled in detail by Mazurek et al. (2011).

The calculated Cl^- concentration profiles at the end of the model time (late Miocene, 6 Ma) considering a brine composition of 70 g/L for the hypersaline period are shown in Fig. 10a. In order to approach the Cl^- concentration of 18.4 g/L found in the stagnant ground-water in the Beggingen Member (Staffelegg Formation) at Mont Russelin, a duration for the hypersaline episode in the early Miocene of 8.5 Myr is required, i.e. it exceeds the duration of the Aquitainian. Assuming a brine composition corresponding to halite saturation shortens the best-fit time to 3.5 Ma (not shown). Figure 10b shows the modelled evolution of Cl^- in the model case considering a hypersaline boundary with $\text{Cl}^- = 70$ g/L in detail. During the Palaeogene (model time 0 Myr = 66 Ma), out-diffusion leads to progressively decreasing Cl^- concentrations. After 43 Myr (end of the Palaeogene), the Cl^- concentration at the depth level of Opalinus Clay was 9–11 g/L, about half the original value. This means that Cl^- concentration must have been increased at later stages to reach the maximum values observed today (14 g/L at Mont Terri, 22 g/L at Mont Russelin; see Fig. 2). This increase can be achieved by the propagation of a 8.5 Myr long hypersaline pulse to depth, as shown in Fig. 10b. The final profile after 60 Myr running time (late Miocene, 6 Ma) is rather flat.

The same model scenario that was used for Cl^- above can also be applied to $\delta^{18}\text{O}$ in pore-water (details in Table 4). A diffusion coefficient D_p (HTO) normal to bedding of 1.2×10^{-10} m²/s (Van Loon and Soler 2003; Van Loon et al. 2005a, b) was used. The upper boundary condition for the model calculations changed over time in response to evolving environmental conditions. Given the fact that Tertiary climate was warmer than today, the isotopic composition of precipitation had higher δ values. The time–temperature relationship of Zachos et al. (2008) and

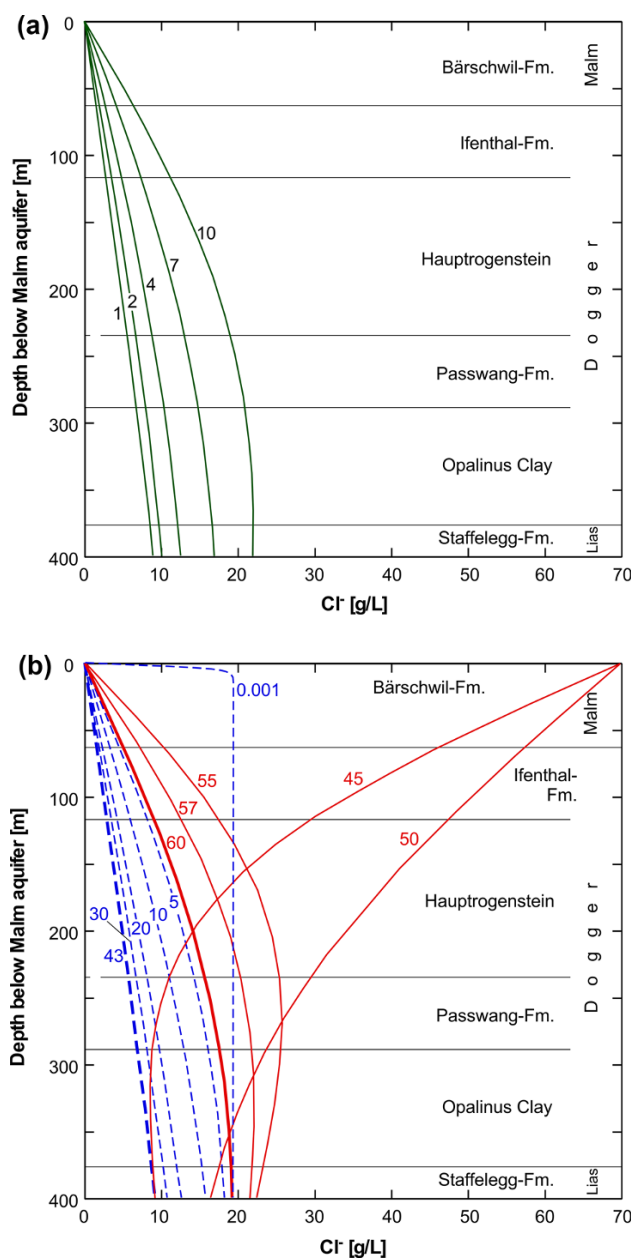


Fig. 10 Results of model calculations considering diffusive exchange of Cl^- between the Malm aquifer (upper boundary condition) and the underlying low-permeability sequence. The scenario considers a Cl^- concentration of 70 g/L at the upper boundary for the duration of the hypersaline period. Stratigraphic profile according to Freivogel and Huggenberger (2003). **a** Modelled final Cl^- concentrations in the late Miocene (6 Ma), considering different durations for the hypersaline upper boundary condition in the early Miocene. Numbers indicate the durations for this condition in Myr. **b** Evolution of Cl^- concentrations for a model considering a hypersaline stage lasting 8.5 Myr. Numbers indicate evolution times in Ma since the onset of the Tertiary (66 Ma). Broken blue lines represent the Palaeogene evolution, solid red lines refer to the Neogene

Hansen et al. (2013) indicates that mean global temperatures were 8.1 and 4.4 °C higher than today during the Palaeogene and the Neogene, respectively. Several authors

explored the dependence of $\delta^{18}\text{O}$ in meteoric water on surface temperature, mainly on the basis of noble-gas infiltration temperatures in ground-waters (Pearson et al. 1991; Stute and Schlosser 2000; overview in Mazurek et al. 2009, Appendix A4.1). For central Europe, Huneau (2000) and Philippot et al. (2000) obtained an average dependence of 0.24‰/°C. Based on this, $\delta^{18}\text{O}$ is estimated to be 1.95‰ and 1.05‰ higher than today for the Palaeogene and Neogene, respectively. Considering the current average $\delta^{18}\text{O}$ of recent ground-waters at Mont Terri and Mont Russelin ($-9.67\text{‰}_{\text{V-SMOW}}$) yields $\delta^{18}\text{O}$ of $-7.7\text{‰}_{\text{V-SMOW}}$ for the Palaeogene and $-8.6\text{‰}_{\text{V-SMOW}}$ for the Neogene. These values were used as the upper boundary condition for the model calculation during continental periods (Table 4). For the hypersaline stage, a $\delta^{18}\text{O}$ of $+6\text{‰}_{\text{V-SMOW}}$ was assumed on the basis of values measured in natural salt pans by Lloyd (1966), a topic further discussed in Sect. 5.4 above. The calculation considering hypersaline conditions over a period of 8.5 Myr yields $\delta^{18}\text{O} = -5.7$ to -5.2‰ at the end of the Palaeogene (after 43 Myr running time) for Opalinus Clay. After the total running time of 60 Myr (6 Ma), a $\delta^{18}\text{O}$ in the range -3.5 to -4.3‰ is obtained. This range shifts slightly (max. 0.5‰) towards more negative values when the duration of the hypersaline period is reduced to 3.5 Myr.

5.6 Plausibility of a Tertiary component in waters of the low-permeability sequence

Figure 11 illustrates the results of the model calculations, together with measured data and the assumed sea-water evaporated until gypsum saturation (point 2: $\text{Cl}^- = 70$ g/L, $\delta^{18}\text{O} = +6\text{‰}_{\text{V-SMOW}}$). The modelled Cl^- concentrations and $\delta^{18}\text{O}$ values for Opalinus Clay are shown as point 3 (end Palaeogene) and point 4 (upper Miocene, 6 Ma). Note that point 4 is slightly above the line connecting points 2 and 3, which is due to the different diffusion coefficients for Cl^- and $\delta^{18}\text{O}$. Point 4 is quite close to the value of the deep ground-water at Mont Russelin, supporting the hypothesis that this water can be rationalised as a mixture of pore-water residing in the formation at the end of the Palaeogene (point 3) and a partially evaporated sea-water that diffused down into the low-permeability sequence.

In principle, the proposed mechanism is capable of explaining the composition of the deep ground-water at Mont Russelin, which is considered to represent the pore-water composition prior to activation of the aquifers in the Passwang Formation and the Beggingen Member (Staffelegg Formation). The involvement of a component of evaporated sea-water is required to explain the departure of the Mont Russelin water from the mixing line between sea-water and meteoric water (see Fig. 11), and the calculated

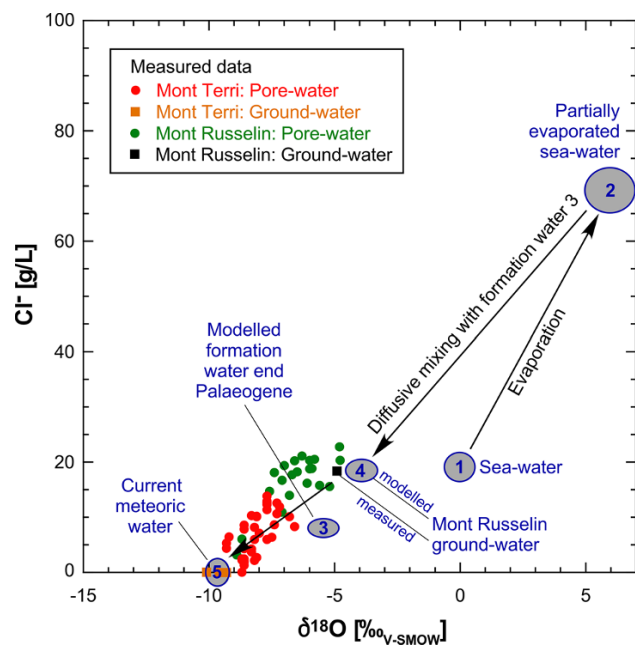


Fig. 11 Diagram of $\delta^{18}\text{O}$ versus Cl^- illustrating the hypothetical path of sea-water evaporated to gypsum saturation, later mixing with meteoric water

duration for the hypersaline period is 3.5–8.5 Ma when considering diffusive transport alone. The main question that remains is how the hypersaline water penetrated the low-permeability sequence. It is difficult at this stage to qualify the geological plausibility of a hypersaline episode lasting several Myr, even though it appears to lie within the possible spectrum.

While the model calculations assumed diffusion as the only process, the possibility exists that at least in limestones, such as the Hauptrogenstein, an advective component may have enhanced solute transport. Further, faults related to the Rhine Graben system were active at that time and may have provided at least transient short circuits. Such structures are also known in the Mont Terri rock laboratory (Nussbaum et al. 2011). An advective component at least in some units would lead to more rapid transport of salinity and so would shorten the calculated duration of the hypersaline event.

Further, there are independent arguments supporting the presence of a Tertiary marine component:

- The isotopic composition of SO_4^{2-} in pore-water at Mont Terri falls into the narrow field of Miocene sea-water (Fig. 6). It lies outside the ranges for Jurassic and Cretaceous sea-waters, and it also cannot be derived from these waters via partial reduction. Given the fact that most of the SO_4^{2-} present in the sediments at the time of deposition was lost by bacterial reduction during early diagenesis (uppermost decimetres of the sediment below the sea floor; see Raiswell and Canfield

2012) and precipitated as pyrite, the absence of a Jurassic isotope signature is plausible.

- The $^{87}\text{Sr}/^{86}\text{Sr}$ ratio in pore-water and that of Sr sorbed on clay minerals is substantially higher than the ratio of connate late Toarcian/Aalenian water (Fig. 7). However, it can be well explained as a mixture of connate water and a Tertiary sea-water component.

In conclusion, the suggested mixing of waters can explain the fact that the waters at Mont Terri and Mont Russelin have marine signatures on the one hand and the seemingly inconsistent mixing proportions of meteoric water on the other hand. The time needed to equilibrate the low-permeability sequence with a sea-water derived karst groundwater in the Malm is on the long end of what is plausible from a geological perspective. Possible advective transport at least in the competent limestone units would shorten transport times.

The late Chattian/Aquitainian marine incursions are known from the external parts of the Folded Jura but not from more eastern regions. It is worth noting that while Cl^-/Br^- ratios at Mont Terri and Mont Russelin are close to marine values (around 290 g/g), this is not the case for Opalinus Clay in the more eastern parts of northern Switzerland where values up to 1000 are observed (borehole Schlattingen: Mazurek et al. 2015; boreholes Weiach, Riniken, Schafisheim: Meier and Mazurek 2011). Here, the Cl^-/Br^- ratio points to non-marine components of salinity, e.g. originating from halite dissolution.

5.7 Vein infills as records of fluids circulating during the formation of the Jura Fold and Thrust Belt

The potential effects of the formation of the Jura Fold and Thrust Belt include (1) transient advective fluid flow triggered by deformation events, and (2) the creation of topography, leading to erosion, exhumation of aquifers and activation of fluid circulation in these. Transient syntectonic fluid flow is recorded by vein infills. There are only few and thin veins in Opalinus Clay at Mont Terri, most of them in and around the Main Fault. Flow was spatially focussed to discrete structures and to temporally limited time scales, most probably linked to seismo-tectonic movements along faults (see e.g. Cox 2005). At present, brittle structures at Mont Terri are hydraulically indistinguishable from the rock matrix (Meier et al. 2002), suggesting an efficient self-sealing mechanism (Bock et al. 2010; Fisher et al. 2013). Further, profiles of conservative pore-water tracers (Cl^- , Br^- , He, $\delta^{37}\text{Cl}$, $\delta^{18}\text{O}$, $\delta^2\text{H}$) do not show any evident perturbation near or within the Main Fault, further supporting the hydraulic irrelevance of this

structure at present time (Pearson et al. 2003; Mazurek et al. 2009, 2011).

5.7.1 Evidence based on isotopes of SO_4^{2-} and of the $^{87}Sr/^{86}Sr$ ratio

Figure 6 illustrates the available S and O isotope data from sulphate in celestite as well as pore-waters. It further shows the ranges of the global evolution of $\delta^{34}S$ and $\delta^{18}O$ in marine sulphate over geological time according to Claypool et al. (1980) and, for the Miocene, the values for northern Switzerland obtained by Balderer et al. (1991). The range of values for celestite from Mont Terri is outside the field of marine sulphate at all times at which sea-water was potentially present in the region, which means that the sulphate isotopes must have been affected by more recent processes, such as microbially mediated reactions. Figure 6 shows that the data can be explained by partial reduction of sulphate originating in the underlying evaporites of the Keuper, leading to enrichment of the heavy isotopes in the residual sulphate. The slope of this enrichment in a plot of $\delta^{34}S$ versus $\delta^{18}O$ varies as a function of various factors (bacterial vs. abiotic reduction, open vs. closed system, effects of Rayleigh distillation) but mostly lies in the range 0.25–0.4 (Pierre 1989; Clark and Fritz 1999). As shown in Fig. 6, a slope of 0.4 reasonably well fits the trend of vein celestite with sulphate originating in the Keuper evaporites. The importance of sulphate reduction prior or during vein formation is also documented by the occurrence of pyrite as vein infill.

As shown in Fig. 7, the $^{87}Sr/^{86}Sr$ ratio in veins coincides with the corresponding values for Sr sorbed on clay minerals as given by Lerouge et al. (2010), as well as with those in current pore-water (data from Pearson et al. 2003). It therefore appears likely that sulphate-rich waters migrating upwards from the Keuper during deformation events linked to the formation of the anticline reacted with Sr already present in Opalinus Clay, either in pore-water or on cation-exchange sites of clay minerals. It was suggested in Sect. 5.6 that this Sr is best interpreted as a mixture of connate Sr and Sr derived from a Tertiary sea-water.

5.7.2 Temperature of vein formation

The $\delta^{18}O$ values of vein calcite are lower when compared to whole-rock carbonate (Fig. 5). Provided the isotopic composition of the water from which vein calcite precipitation is known, the temperature of vein crystallisation can be determined. However, given the fact that current pore-water is strongly affected by diffusive exchange with the surrounding aquifer waters since Jura deformation (Mazurek et al. 2011), its composition at that time cannot be easily constrained. The best proxy for

such a water is considered to be the deep stagnant ground-water at Mont Russelin (see Sect. 2.3). Taking its $\delta^{18}O$ value of -4.9‰_{V-SMOW} , temperatures in the range 37–47 °C can be calculated for the precipitation of the calcite veins in and immediately around the Main Fault, using the fractionation factor of O'Neil et al. (1969). This range is below the maximum temperature of Miocene burial of 55 °C obtained by Mazurek et al. (2006). On the other hand, if one would assume the presence of sea-water ($\delta^{18}O = 0\text{‰}$) at the time of vein precipitation during folding and thrusting, the calculated temperature of vein formation would lie in the range 68–81 °C, i.e. well above the maximum burial temperature during the Miocene. On this basis, it is concluded that the water from which the veins precipitated must have had a negative $\delta^{18}O$ value.

Two measurements of $\delta^{18}O$ of vein calcite are also available from Mont Russelin, with even lower values of 17.1 and 17.4‰_{V-SMOW} (Table 2). Assuming precipitation from a water with $\delta^{18}O = -4.9\text{‰}_{V-SMOW}$ yields a temperature of 59–61 °C, close to the maximum temperature of Miocene burial.

Values for $\delta^{13}C$ of vein calcite show a wide range of variability (about -7 to 1‰_{V-PDB} , see Table 2). The values are close to or lower than those of whole-rock carbonate. In the Main Fault and its immediate surroundings, $\delta^{13}C$ of vein calcite is lower by 0.8‰ compared to whole-rock carbonate.

5.8 Effect of fluid related to vein precipitation on bulk pore-water

Sulphate isotopes in celestite and in current pore-water occupy different fields in Fig. 6 and appear to be genetically unrelated. The question arises to what degree fault-related fluid flow recorded in the veins affected the pore-water chemistry in the bulk rock matrix of Opalinus Clay. The movements related to thrusting were likely shallow seismo-tectonic events. Various authors characterised the hydrogeological consequences of such events (e.g. Muir-Wood and King 1993; Wang and Manga 2010). Fluid flow and geochemical disturbances have been observed over no longer than days to years. Further, self-sealing (Marschall et al. 2008; Bock et al. 2010; Fisher et al. 2013) is expected to occur in clay-rich lithologies containing swelling clay minerals, such as the low-permeability sequence at Mont Terri and Mont Russelin, suggesting that fluid pulses were likely short-lived.

In order to quantify the diffusive propagation of a geochemical perturbation from a permeable structure into the adjacent rock matrix, simple design calculations were made considering simple in-diffusion from a boundary with time-invariant composition into an infinite half-space. This

scenario can be explored using an analytical solution taken from Carslaw and Jaeger (1973)

$$\frac{C}{C_0} = \operatorname{erfc}\left(\frac{x}{2\sqrt{D_p t}}\right).$$

This equation relates concentration C at time t with the distance x from the boundary, with D_p = pore-diffusion coefficient and C_0 = invariant concentration at the boundary. Cl^- is taken as an example species, using a diffusion coefficient $D_p = 2 \times 10^{-10} \text{ m}^2/\text{s}$ parallel to bedding (Van Loon and Soler 2003). As shown in Fig. 12, even over 100 y the disturbance propagates only a few m into the rock. Given the scarcity of vein infills at Mont Terri and Mont Russelin, episodically permeable structures are infrequent and mostly linked to widely-spaced major faults. Therefore, spatially and temporally limited advection across Opalinus Clay affects only a minor volume fraction of the total volume of the formation. Once flow ceases and the fracture self-seals, the geochemical disturbance in the rock matrix will be obliterated by diffusion over geologically short time scales. It is concluded that limited fluid flow across discrete but infrequent structures is not expected to greatly affect the bulk composition of pore-water in the formation. This explains why sulphate isotopes of vein infills and current pore-water are unrelated, and why pore-waters have a marine signature today (Cl^-/Br^- ratio), in spite of later fluid flow during Jura deformation.

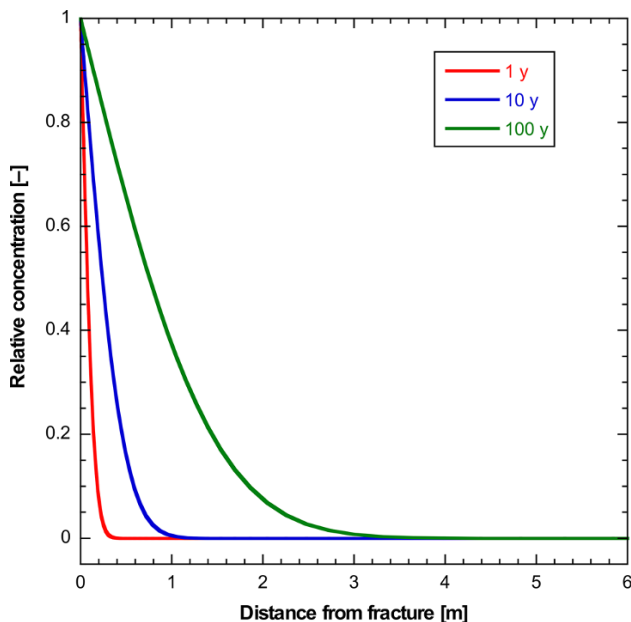


Fig. 12 Diffusive propagation of a geochemical perturbation from a fracture into the rock matrix

5.9 Evolution since Jura folding

Apart from geochemical disturbances localised in active faults, the formation of the Jura Fold and Thrust Belt created a substantial topography that enhanced erosion, in particular of the anticlinal structures. Erosion led to the exhumation of limestone aquifers at Mont Terri and, to a lesser degree, at Mont Russelin. Exhumation initiated the flushing of the aquifers with meteoric water, which established new geochemical boundary conditions on both sides (Mont Terri) or on top (Mont Russelin) of the low-permeability sequence. Diffusion since the time of aquifer flushing led to the curved tracer profiles that are observed today (e.g. Figure 2). Model calculations of Mazurek et al. (2011) successfully reproduced the present-day profiles considering diffusion alone, and the calculated evolution times were consistent with independent palaeo-hydrogeological evidence. The mixing process is illustrated by points 4 and 5 in Fig. 11.

6 Conclusions

Pore-waters in clay-rich aquitards are geochemical archives with a much longer memory than ground-waters in more permeable units. This is due to the fact that diffusion is the dominating mechanism of mass transport, leading to slow adjustment to changing conditions in the adjacent aquifers. At Mont Terri and Mont Russelin, pore-waters have a marine component, highlighted by the Cl^-/Br^- ratio and the isotopic composition of SO_4^{2-} . The marine signature probably reflects sea-water incursions at the Oligocene/Miocene boundary (about 23 Ma).

The most complete chemical and isotopic data set can be obtained from waters sampled in long-term in situ experiments, and it is complemented by laboratory data obtained from measurements on drillcores. While the latter are more numerous, they typically yield only partial information on pore-water composition. Isotopic data obtained from calcite and celestite in veins are another source of information, providing insights into the composition of the fluid at the time of vein formation. On the basis of this data set, together with independent knowledge on regional geology and hydrogeology, the following evolution is proposed:

- Deposition of the Jurassic-Cretaceous rocks occurred in a sedimentary basin under open-marine conditions. Pore-waters in the sedimentary pile were likely similar to sea-water. Diagenetic effects modified some components, e.g. SO_4^{2-} was reduced and is present as pyrite today.
- Towards the end of the Cretaceous, the basin was inverted, leading to continental conditions throughout the Palaeogene. Erosion removed Cretaceous rocks

completely and led to karstification in the limestones of the Malm (upper Jurassic), which became a regional aquifer. Given the existence of a fresh-water regime in the Malm over tens of Myr, out-diffusion of dissolved ions led to a decrease of salinity in the underlying low-permeability sequence. Model calculations indicate that at the level of the Opalinus Clay, salinity was about half that of sea-water at the end of the Palaeogene. This is less than in the most saline waters present today at Mont Terri and Mont Russelin, so an increase of salinity must have taken place at more recent times.

- During the deposition of the Lower Freshwater Molasse, marine incursions from the northwest occurred in the external parts of the Folded Jura and led to the deposition of gypsiferous evaporites (about 23 Ma, late Chattian/early Aquitanian). It is suggested that hypersaline waters derived from partially evaporated sea-water infiltrated the Malm aquifer and so drastically changed the upper boundary condition for the underlying pore-waters.
- Model calculations considering diffusive transport alone indicate that the time needed to attain the salinity level in Opalinus Clay observed today is in the range 3.5–8.5 Ma. There are no independent arguments in support of such a long duration for the brine regime at the upper boundary condition, so this mechanism remains hypothetical. Nevertheless, isotopes of SO_4^{2-} are consistent with a Miocene marine source and would be difficult to explain otherwise. The $^{87}\text{Sr}/^{86}\text{Sr}$ ratio is consistent with a mixture of connate and Miocene Sr. Further, the in-diffusion of partially evaporated sea-water potentially explains the observation that pore-waters at Mont Terri and Mont Russelin cannot be interpreted as simple binary mixtures of sea and meteoric water—the proportion of a meteoric component based on halogen concentrations is consistently lower than that obtained from stable water isotopes. During sea-water evaporation, the concentrations of halogens increase linearly until halite saturation is reached. In contrast, $\delta^{18}\text{O}$ and $\delta^2\text{H}$ behave non-linearly, depending on the climatic conditions.
- Following the hypersaline stage, meteoric conditions and therefore a fresh-water upper boundary prevailed until the onset of deformation related to the formation of the Jura Fold and Thrust Belt in the uppermost Miocene. At that time, limited and transient flow along active faults occurred and led to the formation of calcite-celestite veins. According to the isotopic signature of sulphate in celestite, the fluids originate in the underlying Triassic evaporites. SO_4^{2-} was partially reduced during transport, evidenced by the isotopic trends and the presence of pyrite in the veins. Veins are

scarce and mostly associated to major thrust structures. Flow in these structures was limited spatially and temporally and did not affect the bulk pore-water in the rock matrix. This is also highlighted by the preservation of a marine Cl^-/Br^- ratio in the pore-water as well as of its isotopic composition of SO_4^{2-} , which has a Miocene signature and differs substantially from that in vein celestite. Vein precipitation occurred at temperatures of 35–45 °C at Mont Terri, possibly at somewhat higher temperatures at Mont Russelin.

- After the formation of the anticlinal structures, erosion activated the aquifers above (Mont Terri, Mont Russelin) and below (only Mont Terri) the low-permeability sequence, where fresh-water conditions were established and are still present today. This last change in boundary conditions led to the development of the curved profiles of Cl^- , Br^- , $\delta^{18}\text{O}$, $\delta^2\text{H}$ and He that are observed today.
- While the proposed model of pore-water evolution is consistent with a range of independent lines of evidence, some uncertainty remains that cannot be further reduced at this stage. The main points include the composition and residence time of the Miocene brine that is suggested as a source of salinity for the underlying low-permeability sequence, and the isotopic composition of precipitation during the Tertiary.

Acknowledgements We thank Paul Wersin, Albert Matter (both Uni. Bern) and Andreas Gautschi (Nagra) for useful discussions. Detailed and constructive reviews by A. Bath (Intellisci, UK) and J. M. Matray (IRSN, France) helped to improve the manuscript.

Open Access This article is distributed under the terms of the Creative Commons Attribution 4.0 International License (<http://creativecommons.org/licenses/by/4.0/>), which permits unrestricted use, distribution, and reproduction in any medium, provided you give appropriate credit to the original author(s) and the source, provide a link to the Creative Commons license, and indicate if changes were made.

References

- Afconsult. (2012). HA-experiment: Hydraulic database phases 1-16. *Mont Terri Technical Note*, TN 2010-74, 20 pp. Federal Office of Topography (swisstopo), Wabern. www.mont-terri.ch.
- Aubry, M. P., Van Couvering, J. A., Christie-Blick, N., Landing, E., Pratt, B. R., Owen, D. E., et al. (2009). Terminology of geological time: Establishment of a community standard. *Stratigraphy*, 6, 100–105.
- Balderer, W., Pearson, F. J., & Soreau, S. (1991). Sulphur and oxygen isotopes in sulphate and sulphide. In F. J. Pearson, W. Balderer, H. H. Loosli, B. E. Lehmann, A. Matter, T. Peters, H. Schmassmann & A. Gautschi (Eds.), *Applied isotope hydrology: A case study in northern Switzerland* (pp. 227–242). Studies in Environmental Science, vol. 43. Amsterdam: Elsevier.
- Becker, A. (2000). The Jura Mountains—An active foreland fold-and-thrust belt? *Tectonophysics*, 321, 381–406.

- Becker, D., & Berger, J. P. (2004). Paleogeography of the Swiss Molasse Basin and the Upper Rhine Graben during the Late Burdigalian and Langhian. *Courier Forschungsinstitut Senckenberg*, 249, 1–13.
- Berger, J. P. (1996). Cartes paléogéographiques-palinspastiques du bassin molassique suisse (Oligocène inférieur-Miocène moyen). *Neues Jahrbuch für Geologie und Paläontologie-Abhandlungen*, 202, 1–44.
- Berger, J. P., Reichenbacher, B., Becker, D., Grimm, M., Grimm, K., Picot, L., et al. (2005). Paleogeography of the Upper Rhine Graben (URG) and the Swiss Molasse Basin (SMB) from Eocene to Pliocene. *International Journal of Earth Sciences*, 94, 697–710.
- Bock H., Dehandschutter, B., Martin, C. D., Mazurek, M., de Haller, A., Skoczylas, F., et al. (2010). Self-sealing of fractures in argillaceous formations in context with the geological disposal of radioactive waste. *OECD/NEA Report*, 6184, 310 pp. OECD, Paris, France. www.oecdbookshop.org.
- Bossart, P., Bernier, F., Birkholzer, J., Bruggeman, C., Connolly, P., Dewonck, S., Fukaya, M., Herfort, M., Jensen, M., Matray, J.-M., Mayor, J. C., Moeri, A., Oyama, T., Schuster, K., Shigeta, N., Vietor, T., & Wiczorek, K. (2017). Mont Terri rock laboratory, 20 years of research: introduction, site characteristics and overview of experiments. *Swiss Journal of Geosciences*, 110. doi:10.1007/s00015-016-0236-1 (this issue).
- Bossart, P., & Thury, M. (2007). Research in the Mont Terri rock laboratory: Quo vadis? *Physics and Chemistry of the Earth*, 32, 19–31.
- Bureau Technique Norbert. (1993). Tunnel du Mont Russelin—Profil en long géologique. *Unpublished document*.
- Carslaw, H. S., & Jaeger, J. C. (1973). *Conduction of heat in solids* (2nd ed.). Oxford: Clarendon Press.
- Clark, I., & Fritz, P. (1999). *Environmental isotopes in hydrogeology* (2nd printing, 328 pp.). Boca Raton: CRC Press.
- Claypool, G. E., Holser, W. T., Kaplan, I. R., Sakai, H., & Zak, I. (1980). The age curves of sulfur and oxygen isotopes in marine sulfate and their mutual interpretation. *Chemical Geology*, 28, 199–260.
- Cohen, K. M., Finney, S. C., Gibbard, P. L., & Fan, J. X. (2013). The ICS international chronostratigraphic chart. *Episodes*, 36, 199–204.
- Cox, S. F. (2005). Coupling between deformation, fluid pressure, and fluid flow in ore producing hydrothermal systems at depth in the crust. *Economic Geology*, 100, 39–75.
- Craig, H., & Gordon, L. I. (1965). Deuterium and oxygen-18 variations in the ocean and marine atmosphere. In E. Tongiorgi (Ed.), *Stable isotopes in oceanographic studies and paleotemperatures* (pp. 161–182). Pisa: Consiglio Nazionale delle Ricerche, Laboratorio de Geologia Nucleare.
- Craig, H., Gordon, L., & Horibe, Y. (1963). Isotopic exchange effects in the evaporation of water. *Journal of Geophysical Research*, 68, 5079–5087.
- De Haller, A., Mazurek, M., Spangenberg, J., & Möri, A. (2014). SF (Self-sealing of faults and paleo-fluid flow): Synthesis report. *Mont Terri Technical Report*, TR 08-02, 63 pp. Federal Office of Topography (swisstopo), Wabern, Switzerland. www.mont-terri.ch.
- Fisher, Q., Kets, F., & Crook, A. (2013). Self-sealing of faults and fractures: Evidence from the petroleum industry. *Nagra Arbeitsbericht*, NAB 13-06, 231 pp. Nagra, Wettingen. www.nagra.ch.
- Freivogel, M., & Huggenberger, P. (2003). Modellierung bilanzierter Profile im Gebiet Mont Terri—La Croix (Kanton Jura). In P. Heitzmann & J. P. Tripet (Eds.), *Mont Terri project—Geology, paleohydrology and stress field of the Mont Terri region* (pp. 7–44). Reports of the Federal Office for Water and Geology, Geology Series, No. 4. Federal Office of Topography (swisstopo), Wabern. www.mont-terri.ch.
- Gomez, J. J., Canales, M. L., Ureta, S., & Goy, A. (2009). Palaeoclimatic and biotic changes during the Aalenian (Middle Jurassic) at the southern Laurasian Seaway (Basque-Cantabrian Basin, northern Spain). *Palaeogeography, Palaeoclimatology, Palaeoecology*, 275, 14–27.
- Gonfiantini, R. (1965). Effetti isotopici nell'evaporazione di acque salate. *Atti della Società Toscana di Scienze Naturali, Serie A*, 72, 550–569.
- Gonfiantini, R. (1986). Environmental isotopes in lake studies. In P. Fritz & J. C. Fontes (Eds.), *Handbook of environmental isotope geochemistry* (Vol. 2, pp. 113–168). The terrestrial environment, B Burlington: Elsevier.
- Hansen, J., Sato, M., Russell, G., & Kharecha, P. (2013). Climate sensitivity, sea level and atmospheric carbon dioxide. *Philosophical transactions of the Royal Society A*, 371, 20120294.
- Huneau, F. (2000). *Fonctionnement hydrogéologique et archive paléoclimatique d'un aquifère profond méditerranéen*. Ph.D. dissertation, University of Avignon, Avignon.
- Kissling, D. (1974). *L'Oligocène de l'extrémité occidentale du bassin molassique suisse. Stratigraphie et aperçu molassique*. Ph.D. dissertation, Université de Genève, Genève.
- Koroleva, M., Alt-Epping, P., & Mazurek, M. (2011). Large-scale tracer profiles in a deep claystone formation (Opalinus Clay at Mont Russelin, Switzerland): Implications for solute transport processes and transport properties of the rock. *Chemical Geology*, 280, 284–296.
- Korte, C., Hesselbo, S. P., Ullmann, C. V., Dietl, G., Ruhl, M., Schweigert, G., et al. (2015). Jurassic climate mode governed by ocean gateway. *Nature Communications*. doi:10.1038/ncomms10015.
- Kuhlemann, J., & Kempf, O. (2002). Post-Eocene evolution of the North Alpine Foreland Basin and its response to Alpine tectonics. *Sedimentary Geology*, 152, 45–78.
- Lerouge, C., Gaboreau, S., Blanc, P., Guerrot, C., Haas, H., Jean-Prost, V., et al. (2010). PC experiment: Mineralogy and geochemistry of cores of the BPC935 borehole. *Mont Terri Technical Note*, TN 2010-05, 46 pp. Federal Office of Topography (swisstopo), Wabern. www.mont-terri.ch.
- Lichtner, P. C. (2007). FLOTRAN Users Manual: Two-phase non-isothermal coupled thermal-hydrologic-chemical (THC) reactive flow and transport code, Version 2. *LANL report*, LA-UR-01-2349, 173 pp. Los Alamos National Laboratory, Los Alamos, NM.
- Lloyd, R. M. (1966). Oxygen isotope enrichment of sea water by evaporation. *Geochimica et Cosmochimica Acta*, 30, 80–814.
- Lorenz, G. & Vogt, T. (2014). WS-I Experiment—Chemical analyses of BBB-3 water samples collected before pressure build up and during constant rate withdrawal hydro-testing. *Mont Terri Technical Note*, TN 2013-89, 4 pp. Federal Office of Topography (swisstopo), Wabern. www.mont-terri.ch.
- Marschall, P., Croisé, J., Schlickenrieder, L., Boisson, J. Y., Vogel, P., & Yamamoto, S. (2003). Synthesis of hydrogeological investigations at the Mont Terri site (phases 1 to 5). *Mont Terri Technical Report*, TR 2001-02, 116 pp. Federal Office of Topography (swisstopo), Wabern. www.mont-terri.ch.
- Marschall, P., Trick, T., Lanyon, G. W., Delay, J., & Shao, H. (2008). Hydro-mechanical evolution of damaged zones around a micro-tunnel in a claystone formation of the Swiss Jura Mountains. In *42nd US Rock Mechanics Symposium (USRMS)*, American Rock Mechanics Association.
- Mazurek, M., Alt-Epping, P., Bath, A., Gimmi, T., & Waber, H. N. (2009). Natural tracer profiles across argillaceous formations: The CLAYTRAC project. *OECD/NEA Report*, 6253, 361 pp. OECD Publishing, Paris. www.oecdbookshop.org.

- Mazurek, M., Alt-Epping, P., Bath, A., Gimmi, T., Waber, H. N., Buschaert, S., et al. (2011). Natural tracer profiles across argillaceous formations. *Applied Geochemistry*, *26*, 1035–1064.
- Mazurek, M., Hurford, A. J., & Leu, W. (2006). Unravelling the multi-stage burial history of the Swiss Molasse Basin: Integration of apatite fission track, vitrinite reflectance and biomarker isomerisation analysis. *Basin Research*, *18*, 27–50.
- Mazurek, M., Oyama, T., Wersin, P., & Alt-Epping, P. (2015). Pore-water squeezing from indurated shales. *Chemical Geology*, *400*, 106–121.
- McArthur, J. M., Howarth, R. J., & Shields, G. A. (2012). Strontium Isotope Stratigraphy. *The Geologic Time Scale*, *1*, 127–144.
- Meier, D. & Mazurek, M. (2011). Ancillary rock and pore-water studies on drillcores from northern Switzerland. *Nagra Arbeitsbericht*, NAB 10-21, 60 pp. Nagra, Wettingen. www.nagra.ch.
- Meier, P. M., Trick, T., Blümling, P., & Volckaert, G. (2002). Self-healing of fractures within the EDZ at the Mont Terri Rock Laboratory: Results after one year of experimental work. In N. Hoteit, K. Su, M. Tijani, & J. F. Shao (Eds.), *Proceedings of international workshop on geomechanics, hydromechanical and thermohydro-mechanical behaviour of deep argillaceous rocks: Theory and experiment* (pp. 267–274). Paris, France.
- Mojon, P. O., Engesser, B., Berger, J. P., Bucher, H., & Weidmann, M. (1985). Sur l'âge de la Molasse d'eau douce inférieure de Boudry, Neuchâtel. *Eclogae Geologicae Helveticae*, *78*, 631–667.
- Muir-Wood, R., & King, G. C. P. (1993). Hydrological signatures of earthquake strain. *Journal of Geophysical Research*, *98*, 22035–22068.
- Müller, H., & Leupin, O. (2012). WS-H (Investigation of wet spots): Observation, first experimental results, and a short presentation of possible hypotheses regarding the origin of these waters. *Mont Terri Technical Note*, TN 2012-96, 49 pp. Federal Office of Topography (swisstopo), Wabern. www.mont-terri.ch.
- Nussbaum, C., Bossart, P., Amann, F., & Aubourg, C. (2011). Analysis of tectonic structures and excavation induced fractures in the Opalinus Clay, Mont Terri underground rock laboratory (Switzerland). *Swiss Journal of Geosciences*, *104*, 187–210.
- Nussbaum, C., Kloppenburg, A., Caër, T., & Bossart, P. (2017). Tectonic evolution around the Mont Terri rock laboratory, northwestern Swiss Jura: Constraints from kinematic forward modelling. *Swiss Journal of Geosciences*, *110* (this issue).
- Nussbaum, C., Meier, O., Masset, O., & Badertscher, N. (2006). Self-sealing of fault (SF) Experiment—Drilling of resin impregnated boreholes. *Mont Terri Technical Note*, TN 2006-22, 36 pp. Federal Office of Topography (swisstopo), Wabern. www.mont-terri.ch.
- O'Neil, J. R., Clayton, R. N., & Mayeda, T. K. (1969). Oxygen isotope fractionation in divalent metal carbonates. *Journal of Chemistry and Physics*, *51*, 5547–5558.
- Parkhurst, D. L., & Appelo, C. A. J. (2013). Description of input and examples for PHREEQC version 3—A computer program for speciation, batch-reaction, one-dimensional transport, and inverse geochemical calculations. *U.S. Geological Survey Techniques and Methods*, Book 6, 497. <http://pubs.usgs.gov/tm/06/a43>.
- Pearson, F. J., Arcos, D., Bath, A., Boisson, J. Y., Fernandez, A. M., Gäbler, H. E., et al. (2003). Mont Terri project—Geochemistry of water in the Opalinus Clay formation at the Mont Terri Rock Laboratory (319 pp.). *Reports of the Federal Office for Water and Geology, Geology Series, No. 5*. Federal Office of Topography (swisstopo), Wabern. www.mont-terri.ch.
- Pearson, F. J., Balderer, W., Loosli, H. H., Lehmann, B. E., Matter, A., Peters, T., et al. (1991). *Applied Isotope Hydrogeology—A case study in northern Switzerland*. Amsterdam: Elsevier.
- Pfirtner, U., Antenen, M., Heckendorn, W., Burkhalter, R. M., Gürlér, B., & Krebs, D. (1996). *Geologischer Atlas der Schweiz 1:25'000, Blatt Moutier*. Federal Office of Topography (swisstopo), Wabern. www.map.geo.admin.ch.
- Philippot, A. C., Michelot, J. L., & Marlin, C. (2000). A paleohydrogeological study of the Mol site, Belgium (PHYMOL project). Rapport spécifique no. 3: Analyse des isotope et des gaz nobles. *European Commission Report*, DOC RTD/55/2000-FR.
- Picot, L., Becker, D., Cavin, L., Pirkenseer, C., Lapaire, F., Rauber, G., et al. (2008). Sédimentologie et paléontologie des paléoenvironnements côtiers rupéliens de la Molasse marine rhénane dans le Jura suisse. *Swiss Journal of Geosciences*, *101*, 483–513.
- Pierre, C. (1989). Sedimentation and diagenesis in restricted marine basins. In P. Fritz & J. C. Fontes (Eds.), *Handbook of environmental isotope geochemistry* (Vol. 3A, pp. 257–315). Burlington: Elsevier.
- Pirkenseer, C., Berger, J. P., & Reichenbacher, B. (2013). The position of the Rupelian/Chattian boundary in the southern Upper Rhine Graben based on new records of microfossils. *Swiss Journal of Geosciences*, *106*, 291–301.
- Pirkenseer, C., Spezzaferi, S., & Berger, J. P. (2010). Palaeoecology and biostratigraphy of the Paleogene Foraminifera from the southern Upper Rhine Graben and the influence of reworked planktonic Foraminifera. *Palaeontographica, Abteilung A: Palaeozoology-Stratigraphy*, *293*, 1–93.
- Pirkenseer, C., Spezzaferi, S., & Berger, J. P. (2011). Reworked microfossils as a paleogeographic tool. *Geology*, *39*, 843–846.
- Raiswell, R., & Canfield, D. E. (2012). The iron biogeochemical cycle past and present. *Geochemical Perspectives*, *1*, 1–220.
- Rübel, A. P., Sonntag, C., Lippmann, J., Pearson, F. J., & Gautschi, A. (2002). Solute transport in formations of very low permeability: Profiles of stable isotope and dissolved noble gas contents of pore water in the Opalinus Clay, Mont Terri, Switzerland. *Geochimica et Cosmochimica Acta*, *66*, 1311–1321.
- Stute, M., & Schlosser, P. (2000). Atmospheric noble gases. In P. G. Cook & A. L. Herczeg (Eds.), *Environmental tracers in subsurface hydrology* (pp. 349–377). Boston: Kluwer.
- Thury, M., & Bossart, P. (1999). The Mont Terri rock laboratory, a new international research project in a Mesozoic shale formation, in Switzerland. *Engineering Geology*, *52*, 347–359.
- Van Loon, L. R., Baeyens, B., & Bradbury, M. H. (2005a). Diffusion and retention of sodium and strontium in Opalinus clay: Comparison of sorption data from diffusion and batch sorption measurements, and geochemical calculations. *Applied Geochemistry*, *20*, 2351–2363.
- Van Loon, L. R., Müller, W., & Iijima, K. (2005b). Activation energies of the self-diffusion of HTO, $^{22}\text{Na}^+$ and $^{36}\text{Cl}^-$ in a highly compacted argillaceous rock (Opalinus Clay). *Applied Geochemistry*, *20*, 961–972.
- Van Loon, L. R., & Soler, J. M. (2003). Diffusion of HTO, $^{36}\text{Cl}^-$, $^{125}\text{I}^-$ and $^{22}\text{Na}^+$ in Opalinus Clay: Effect of confining pressure, sample orientation, sample depth and temperature. *Nagra Technical Report*, 03-07, 119 pp. Nagra, Wettingen. www.nagra.ch.
- Vinsot, A., Appelo, C. A. J., Cailteau, C., Wechner, S., Pironon, J., De Donato, P., et al. (2008). CO₂ data on gas and pore water sampled in situ in the Opalinus Clay at the Mont Terri rock laboratory. *Physics and Chemistry of the Earth*, *33*, S54–S60.
- Vinsot, A., Appelo, C. A. J., Lundy, M., Wechner, S., Lettry, Y., Lerouge, C., et al. (2014). In situ diffusion test of hydrogen gas in the Opalinus Clay. *Geological Society, London, Special Publications*, *400*(1), 563–578.
- Vogt, T. (2013). WS-I Experiment—Outflow measurements and hydrochemical analyses. *Mont Terri Technical Note*, TN 2013-01, 10 pp. Federal Office of Topography (swisstopo), Wabern. www.mont-terri.ch.
- Wang, C. Y., & Manga, M. (2010). *Earthquakes and water* (225 pp). Berlin Heidelberg: Springer.

- Weidmann, M., Engesser, B., Berger, J. P., Mojon, P. O., Ginsburg, L., Becker, D., et al. (2014). Paléontologie et biostratigraphie de la Molasse de l'Oligocène et du Miocène basal du Talent et d'autres localités du Plateau vaudois (Suisse). *Revue de Paléobiologie (Genève)*, 33, 463–531.
- Wersin, P., Leupin, O. X., Mettler, S., Gaucher, E. C., Mäder, U., De Cannière, P., et al. (2011). Biogeochemical processes in a clay formation in situ experiment: Part A—Overview, experimental design and water data of an experiment in the Opalinus Clay at the Mont Terri Underground Research Laboratory, Switzerland. *Applied Geochemistry*, 26, 931–953.
- Zachos, J. C., Dickens, G. R., & Zeebe, R. E. (2008). An early Cenozoic perspective on greenhouse warming and carbon-cycle dynamics. *Nature*, 451, 279–283.

Geomechanical behaviour of Opalinus Clay at multiple scales: results from Mont Terri rock laboratory (Switzerland)

Florian Amann¹  · Katrin M. Wild¹ · Simon Loew¹ · Salina Yong² · Reto Thoeny³ · Erik Frank⁴

Received: 5 April 2016 / Accepted: 9 December 2016 / Published online: 16 February 2017
© Swiss Geological Society 2017

Abstract The paper represents a summary about our research projects conducted between 2003 and 2015 related to the mechanical behaviour of Opalinus Clay at Mont Terri. The research summarized covers a series of laboratory and field tests that address the brittle failure behaviour of Opalinus Clay, its undrained and effective strength, the dependency of petro-physical and mechanical properties on total suction, hydro-mechanically coupled phenomena and the development of a damage zone around excavations. On the laboratory scale, even simple laboratory tests are difficult to interpret and uncertainties remain regarding the representativeness of the results. We show that suction may develop rapidly after core extraction and substantially modifies the strength, stiffness, and petro-physical properties of Opalinus Clay. Consolidated undrained tests performed on fully saturated specimens revealed a relatively small true cohesion and confirmed the strong hydro-

mechanically coupled behaviour of this material. Strong hydro-mechanically coupled processes may explain the stability of cores and tunnel excavations in the short term. Pore-pressure effects may cause effective stress states that favour stability in the short term but may cause longer-term deformations and damage as the pore-pressure dissipates. In-situ observations show that macroscopic fracturing is strongly influenced by bedding planes and faults planes. In tunnel sections where opening or shearing along bedding planes or faults planes is kinematically free, the induced fracture type is strongly dependent on the fault plane frequency and orientation. A transition from extensional macroscopic failure to shearing can be observed with increasing fault plane frequency. In zones around the excavation where bedding plane shearing/shearing along tectonic fault planes is kinematically restrained, primary extensional type fractures develop. In addition, heterogeneities such as single tectonic fault planes or fault zones substantially modify the stress redistribution and thus control zones around the excavation where new fractures may form.

Editorial handling: P. Bossart and A. G. Milnes.

This is paper #7 of the Mont Terri Special Issue of the Swiss Journal of Geosciences (see Bossart et al. 2017, Table 3 and Fig. 7).

✉ Florian Amann
florian.amann@erdw.ethz.ch

¹ Institute of Geology, Engineering Geology, Swiss Federal Institute of Technology, Zurich, Sonneggstrasse 5, 8092 Zurich, Switzerland

² Knight Piésold Ltd., Suite 1400 - 750 West Pender, Vancouver V6C 2T8, British Columbia, Canada

³ Grundwasserschutz und Entsorgung, AF-Consult Switzerland AG, Täferstrasse 26, 5405 Baden, Switzerland

⁴ Sektion Geologie (GEOL), Eidgenössisches Nuklear-Sicherheitsinspektorat (ENSI), Industriestrasse 19, 5200 Brugg, Switzerland

Keywords Clay shale · Excavation damaged zone · Undrained shear strength · Pore-pressure response · Suction · Tectonic structures · Nuclear waste disposal

1 Introduction

Our scientific research on the geomechanical behaviour of Opalinus Clay that we conducted in the past decade addresses fundamental behavioural aspects, associated with the short-term behaviour (i.e. the behaviour during the excavation) and the longer-term behaviour (i.e. the behaviour during the open drift phase) of the material in close

vicinity to a drift, and factors that influence the development of an excavation damaged zone (EDZ). The attempt was and is to contribute to an improved understanding of (1) the governing mechanical behaviour of Opalinus Clay, (2) the dependency of its geomechanical and petro-physical properties on the effective stress state, (3) its strength at a saturated state, (4) the short-term pore-pressure evolution during triaxial testing and tunnel excavation, (5) the processes and geological factors that control the formation of an EDZ, (6) the influence of tectonic structures at multiple scales on the EDZ, and (7) the influence of excess pore-pressures dissipation on the EDZ and tunnel deformations. The scale of investigations spans from laboratory experiments at the cm-to dm-scale to in situ experiments on the dm- to m-scale.

An overview of the experiments related to the conducted scientific research is given in Fig. 1. The work comprises a series of laboratory experiments, conducted to characterize the geomechanical properties and behaviour of intact Opalinus Clay, spanning from unconsolidated undrained (UU) shear tests (Amann et al. 2011, 2012a), unconfined compression and indirect tensile strength tests on specimens equilibrated at various relative humidity (RH) (Wild et al. 2015c), and consolidated undrained (CU) and drained (CD) triaxial tests on fully re-saturated specimens (Wild et al. 2015a). Furthermore, three in situ experiments were carried out. An overcoring experiment was used to study the evolution of a BDZ in intact rock in situ (Kupferschmied et al. 2015). Additionally, two mine-by experiments at the Mont Terri Rock laboratory were conducted, which focused on the interrelationships between pre-existing faults (i.e. faults planes and fault zones characterized by a high fault plane density) and excavation-induced damage at the macro and micro-scale (Yong et al. 2010, 2013; Thoeny 2014). These experiments included detailed structural and kinematic analysis using a broad range of in situ characterisation and monitoring methods, supplemented by 3D numerical modelling.

The focus of this contribution is on the characterization of the complex mechanical behaviour of Opalinus Clay, a

material at the transition between stiff soil and weak rock, by integrating the results gained in the various scientific experiments that were conducted over the past decade and have provided insights on the complexity of the geomechanical behaviour and factors that affect the development of an EDZ in the short and longer term.

2 Opalinus Clay at the Mont Terri Rock laboratory

Lithologically, Opalinus Clay at the Mont Terri Rock laboratory (Fig. 2) can be divided into several facies: carbonate-rich, sandy, and shaly (Thury and Bossart 1999). In this contribution, the shaly facies of Opalinus Clay at the Mont Terri Rock Laboratory is discussed. Opalinus Clay shows a pronounced micro-fabric of the clayey matrix, forming a distinct macroscopic bedding, which is related to a complex history of sedimentation, burial, physical compaction, development of diagenetic bonding, uplift, tectonic faulting, and erosion (Van Loon et al. 2004; Marschall et al. 2005). The maximum burial depth at the level of the Mont Terri Rock Laboratory was estimated to be 1350 m in the late Tertiary (Mazurek et al. 2006). The present overburden ranges from 230 to 330 m (Thury and Bossart 1999). The complex geological and tectonic history of Opalinus Clay caused a compact structure and inter-particle bonding. However, no diagenetic cements that fill the pore space (such as pyrite, siderite, or calcite cement) have been found in the shaly facies (Nagra 2002). Therefore, bonding is probably more related to recrystallization of clay particles and adhesion from molecular bonds.

Opalinus Clay from the shaly facies mainly consists of clay minerals (i.e. 27–78% clay minerals composed of 15–30% illite, 5–20% illite/smectite mixed layer phases, 3–18% chlorite, and 15–22% kaolinite), and non-clay minerals (e.g. 10–27% quartz, 0.3–5% feldspar, 0.9–1.4% pyrite, and 0.8% organic matter) with a variable range of grain sizes (Mazurek 1998; Thury and Bossart 1999; Nagra 2002; Klinkenberg et al. 2009). Furthermore, carbonate bioclasts are often found (13% carbonate content). The water loss porosity of the shaly facies is in the order of 15–19% (Bossart 2008; Amann et al. 2011, 2012a; Wild et al. 2015c).

Structurally, the bedding is well-developed and the most pronounced feature at the Mont Terri Rock Laboratory. It dips towards the southeast with an angle varying between 30° at the northernmost contact to 50° at the southernmost contact (Bossart et al. 2017). Prominent tectonic features at the Mont Terri Rock Laboratory consist of three minor tectonic fault planes and a larger thrust fault (Main Fault). A detailed analysis of the tectonic setting is given in Nussbaum et al. (2011).

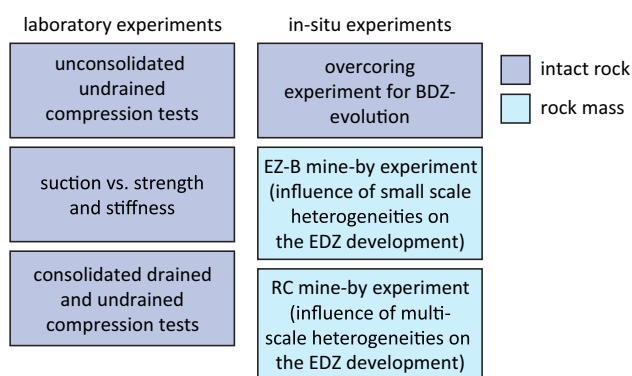


Fig. 1 Experiments conducted at the Chair of Engineering Geology at ETH Zurich in the past decade

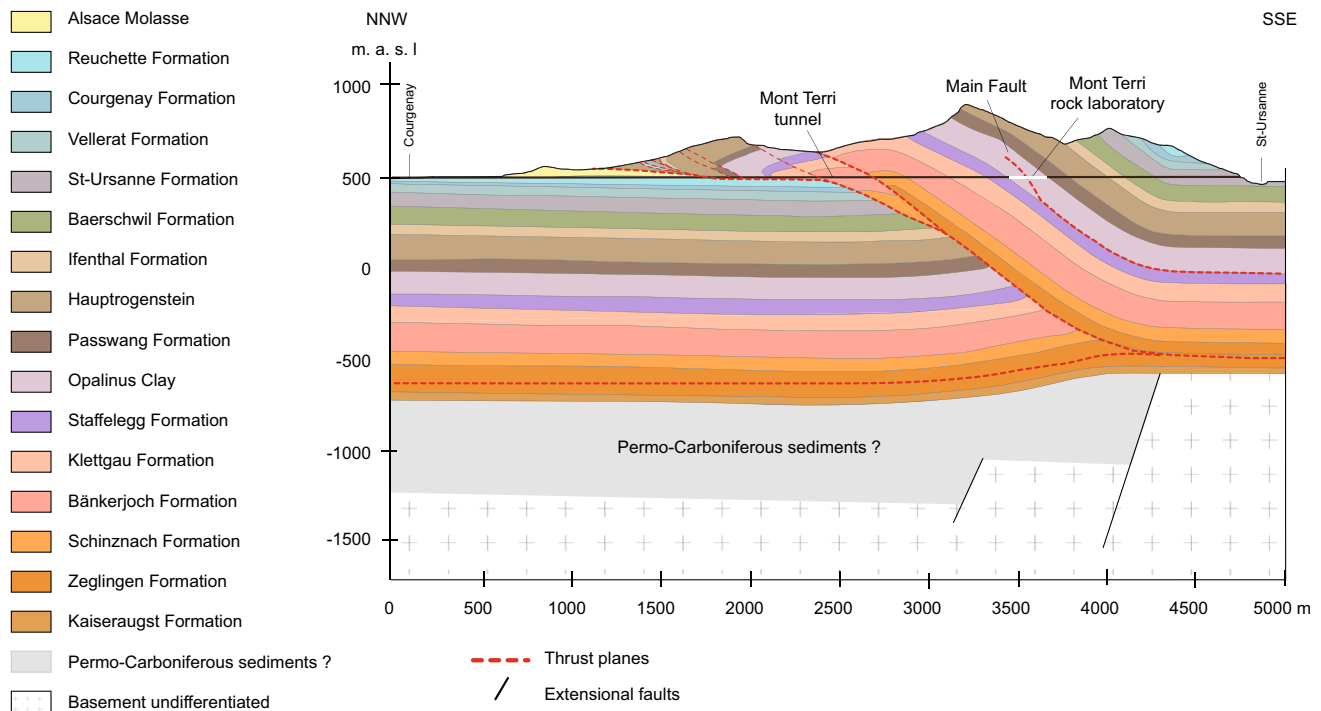


Fig. 2 Geological cross-section of the Mont Terri anticline and location of the Mont Terri rock laboratory (Nussbaum et al. 2017, this volume)

3 Laboratory experiments

Three series of laboratory experiments to characterize the hydro-mechanical behaviour and properties of Opalinus Clay have been carried out in the reporting period. A first series investigated the brittle failure behaviour of Opalinus Clay under unconsolidated undrained conditions. A second series focused on the influence of suction on petro-physical and mechanical properties. In a third series of laboratory tests, we analysed the hydro-mechanical coupled behaviour of Opalinus Clay utilizing consolidated undrained and drained tests including pore-pressure measurements.

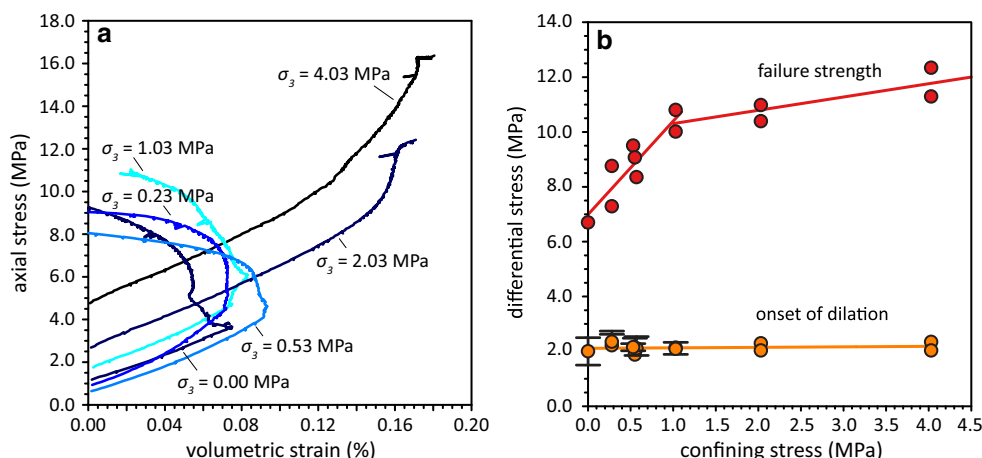
3.1 The undrained shear strength of Opalinus Clay

In 2010, we performed a series of unconsolidated undrained (UU) compression tests on Opalinus Clay specimens (Amann et al. 2011, 2012a). The study focused on the brittle failure behaviour of Opalinus Clay in a confining stress range that is relevant for the near field of tunnel excavations in Opalinus Clay at the Mont Terri Rock Laboratory (i.e. 0–4 MPa). Significant efforts were made to test the specimens as close as possible to the natural water content, which required a specimen preparation procedure that allowed testing approximately 30 min after core extraction from the vacuum-evacuated foil. The specimens were loaded normal to the bedding orientation (S-specimens). Both axial and radial strains were monitored at the specimen's surface. In

addition, micro-seismic emissions were captured during the unconfined compression tests utilizing four piezoelectric transducers. More details of the testing procedure and the laboratory set-up are given in Amann et al. (2011) and (2012a).

The study revealed essential insights into the behaviour of Opalinus Clay in UU tests that demonstrate that Opalinus Clay shares similarities with both brittle rocks and stiff soils. It was shown that the onset of yielding/dilatancy is associated with the formation of micro-cracks that emanate measurable micro-seismic signals. This behaviour is typical for brittle rocks. On the other hand, Opalinus Clay deforms in a highly non-linear fashion, indicating yielding of the material long before the differential stress reaches the peak strength. The non-linearity of the stress–axial strain curve starts at the onset of dilatancy, which is unusual for brittle rocks but typical for soils, in particular clays. However, dilatancy is suppressed at increasing confining stresses. At low confining stresses the volume of the specimens at peak strength was similar to the volume of the specimens at the start of the compression test (Fig. 3a). This behaviour is typical for both brittle rock types and over-consolidated clays. Furthermore, the differential stress at the onset of dilatancy was independent of the confining stress (Fig. 3b), indicating breaking of cohesive bonds that leads to the mobilization of frictional resistance. The independency of the differential stress at the onset of micro-cracking and the mobilization of frictional resistance at the onset of dilatancy have been observed for

Fig. 3 a Axial stress–volumetric strain curves before failure for different confining stresses. **b** Failure strength and onset of dilatancy in dependency of the confining stress. Adapted from Amann et al. (2012a), 27/30, copyright Springer-Verlag 2011, with permission of Springer



many brittle rock types (Martin 1997; Amann et al. 2011), but also for remoulded clays (Schmertmann and Osterberg 1960).

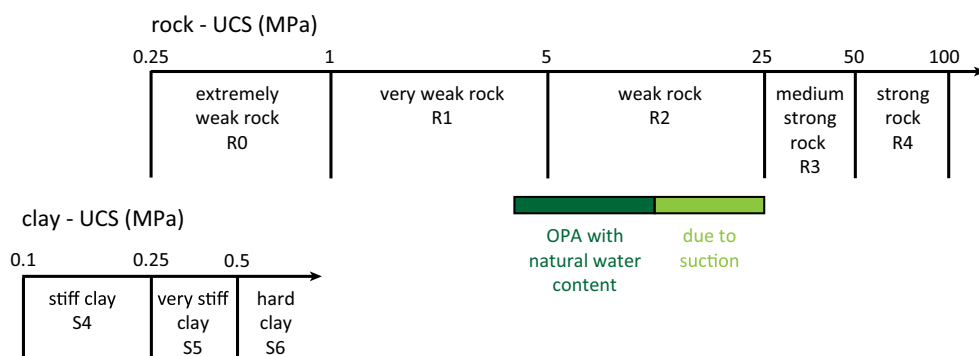
The study also revealed values of the unconfined compressive strength (*UCS*) of specimens loaded normal to bedding between 4.5 and 8.0 MPa (Amann et al. 2011). Further tests on specimens loaded parallel to bedding revealed *UCS* values between 9.0 and 11.0 MPa at natural water content (Wild et al. 2015c). Based on these values, Opalinus Clay at its natural water content can be classified as a very weak (R1) to weak (R2) rock according to ISRM classification (Fig. 4) (ISRM 1979).

A further outcome of this study was a strong non-linear failure envelope (Fig. 3b). The simplified bi-linear fit used by Amann et al. (2012a) revealed a high undrained friction angle of $\phi = 43^\circ$ and an apparent cohesion of 2 MPa at low confinement (i.e. <1 MPa). For higher confining stresses (i.e. >1 MPa), where dilatancy of the material was suppressed, the undrained friction angle was reduced to $\phi = 11^\circ$ and the apparent cohesion increased to 4 MPa.

Saturated clays often exhibit an undrained friction angle of zero degree. However, undrained friction angles $>0^\circ$ have been measured in UU tests and have been discussed in detail by Bishop and Eldin (1950), Golder and Skempton (1948) and for the specific data discussed above by Amann

et al. (2015). Bishop and Eldin (1950) proposed, based on theoretical considerations and experiments on sands, that two potential factors may account for a high undrained friction angles: (1) the specimens contain entrapped air, which increases the compressibility of the pore fluid substantially, and (2) excessive negative pore-pressure evolves under undrained shearing at low normal stresses due to the dilatant structure of the soil and causes pore-water cavitation. For the latter case, the undrained friction angle at low normal stresses is approximately the same as the effective friction angle (Bishop and Eldin 1950). At high normal stresses, cavitation does not occur and the failure envelope for typical soils indicates an undrained friction angle of 0° or a low undrained friction angle. The sharp transition from a high undrained friction angle to an undrained friction angle of zero depends, according to Bishop and Eldin (1950), on the undrained shearing resistance and the effective consolidation pressure. In addition, Amann et al. (2015) postulated that the concept of “ $\phi = 0^\circ$ ” applies only for soils and rocks where Skempton’s pore-pressure coefficient *B* is unity. For $B < 1$, as in the case of Opalinus Clay (Aristorenas 1992; Wild et al. 2015a), the undrained friction angle is larger than zero. Thus, for the Opalinus Clay specimens measured at low confining stresses in the series of UU tests described above, the frictional resistance

Fig. 4 ISRM classes based on the *UCS* of the material (according to ISRM 1979). The *UCS* for Opalinus Clay at its natural water content is shown in the dark blue box. The increase in *UCS* with increasing suction is shown in the light blue box



seems to be dominated by the strong dilatant behaviour that might be associated with the microstructure of Opalinus Clay. At high confining stresses, where dilatancy is strongly suppressed, the lower undrained friction angle of 11° could be associated with either a Skempton's B value smaller unity or an unsaturated state of the material.

Besides the uncertainties in interpreting the UU test results, a major problem with UU tests is associated with the initial effective stress state (i.e. the effective stress state before undrained loading) of the specimen. For an isotropic rock sample taken from a rock mass characterized by an isotropic stress state, the effective stress after core extraction remains constant and the results obtained from UU tests are representative for this initial effective stress. This is, however, not the case for an anisotropic material such as Opalinus Clay taken from an anisotropic stress field such as the one observed at the Mont Terri Rock Laboratory. Thus, in the series of UU tests performed by Amann et al. (2011) and (2012a), the initial effective stress state remains unknown. Since saturation was not re-established and pore-pressure was not measured during undrained loading in their study, the interpretation and applicability of the test results in terms of the undrained shear strength remains uncertain and partly speculative.

3.2 The influence of suction on the strength and stiffness of Opalinus Clay

Due to the potential influence of the initial effective stress state associated with partially saturated condition, Wild et al. (2015c) performed a large series of laboratory experiments aiming at providing relationships between total suction and the Young's Modulus (E), the Poisson's ratio (ν), the onset of dilatancy (CI), the Brazilian tensile strength (BTS), the UCS , and the P-wave velocity (v_p). Over a period of three years, specimens were equilibrated in desiccators at different levels of relative humidity (RH) ranging between 19 and 99%. The correspondent suction pressure was calculated according to Kelvin's relationship. After specimen equilibration, BTS and UCS tests were performed immediately after removing the specimens from the desiccators. Load was applied according to the ISRM suggested methods such that failure occurred within 5–10 min for the UCS specimens and within 1–3 min for the BTS specimens (ISRM 1978, 1979). The study revealed that total suction has a major influence on both the strength and stiffness of Opalinus Clay (Fig. 5). From 0 to 57 MPa total suction, UCS , CI , BTS and E increases almost linearly. For suction >57 MPa, both the strength and E remain constant except for the BTS parallel to bedding, which tends to drop to smaller numbers. E increases by a factor of 3–4 between a total suction of 13 and 57 MPa (Fig. 4a), CI by a factor of 4 (Fig. 5b), UCS for tests loaded parallel to the bedding orientation by a factor of 1.5

(Fig. 5b), and the BTS parallel and normal to bedding by a factor of 2–3 (Fig. 5c).

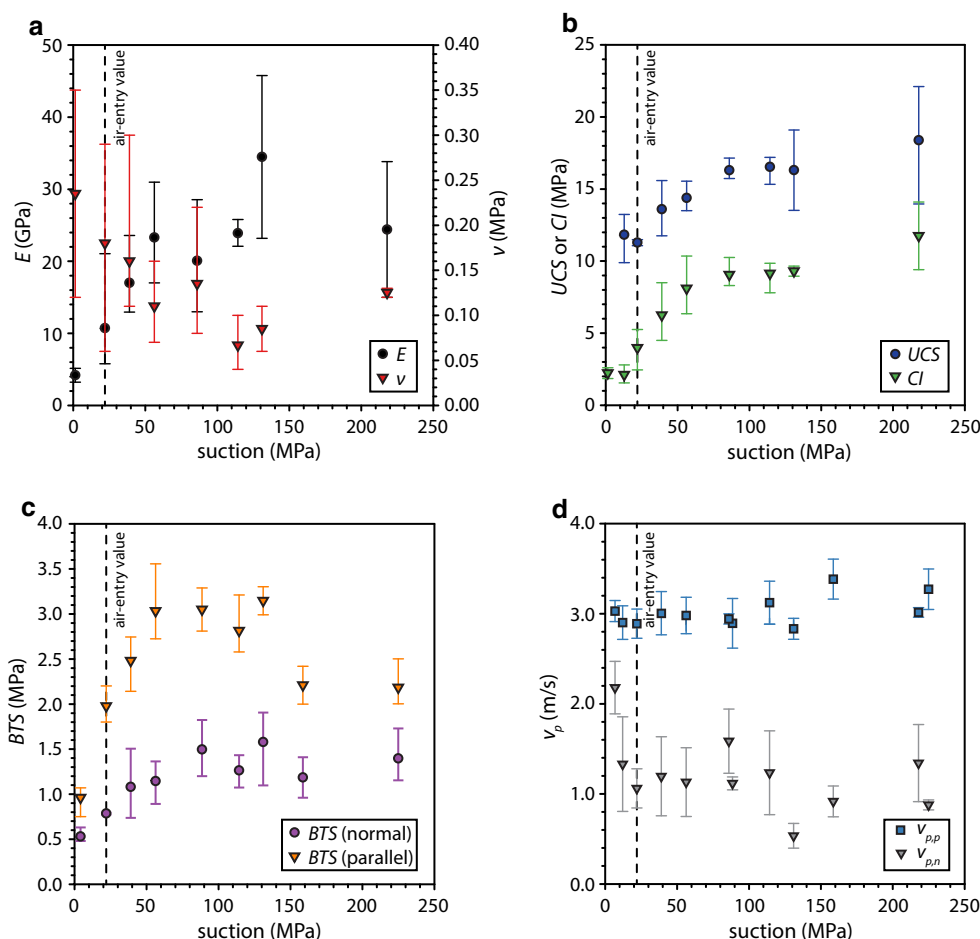
The increase in strength with decreasing water content (i.e. an increase in suction) was more pronounced for the BTS normal to bedding. Similar observations could be made by comparing the UCS values with data from tests on S-specimens (i.e. specimens loaded normal to bedding) conducted by Amann et al. (2011), Rummel and Weber (2004), and Schnier and Stührenberg (2007). The UCS for specimens loaded parallel to bedding increased from values between 9 and 11 MPa at water contents between 7.6 and 8.4% to values between 12 and 16 MPa for water contents between 4.8 and 5.0%. The UCS for specimens loaded normal to bedding showed an increase from 4–8 to 20–25 MPa for the same decrease in water content. Hence, Opalinus Clay with low water content (i.e. smaller than the natural water content due to drying) can be classified as a material somewhere between weak and medium strong rock according to the ISRM classification shown in Fig. 4.

Besides these unique relationships between total suction, water content and geomechanical properties, the study revealed that while the P-wave velocity parallel to bedding remained almost constant, the P-wave velocity normal to bedding dropped sharply upon desaturation until the air-entry value (found to be at 22 MPa suction) was reached (Fig. 5d). This drop is associated with desiccation cracks observed solely parallel to the bedding orientation. For suction larger than the air-entry value, the data suggest no further damage accumulation (i.e. the shrinkage limit is reached). Peron et al. (2009) showed experimentally for clays that the magnitude of the shrinkage limit and the air-entry value are similar. This supports the observations in our study and suggests that the majority of desiccation damage is associated with the early stage of desaturation where the suction increases from zero to approximately the air-entry value. For Opalinus Clay, the air-entry value and the shrinkage limit are reached within 30 min after core extraction from the vacuum-evacuated foil and exposure to the laboratory environment (Wild et al. 2015c). Thus, although unsaturated Opalinus Clay tends to behave more rock-like when considering the UCS , this finding shows again similarities to soil/clays, at least in the low suction regime. Despite this, this study generally suggests that in the context of an underground excavation, changes in brittle failure characteristics, stiffness and strength have to be expected when the rock is exposed to a tunnel environment characterized by a low RH.

3.3 Study on consolidated undrained (CU) and consolidated drained (CD) tests

As a consequence of the uncertainties associated with UU tests and the major influence of total suction on the strength

Fig. 5 Influence of total suction on **a** the Young's modulus (E), **b** the unconfined compressive strength (UCS) and the onset of dilation (CI), **c** the Brazilian tensile strength (BTS) normal and parallel to bedding, and **d** the P-wave velocity normal ($v_{p,n}$) and parallel ($v_{p,p}$) to bedding. adapted from Wild et al. (2015c), 433–436, copyright Springer, Wien 2014, with permission of Springer



and stiffness of Opalinus Clay, we performed a series of CU and CD tests. The specimens were re-saturated in a long-lasting (i.e. up to several weeks) procedure that involved a flushing and a backpressure phase. Afterwards, the specimens were consolidated to different effective confinements relevant for tunnel excavations at the Mont Terri Rock Laboratory (i.e. 0.5, 0.75, 1.0, 2.0, and 4.0 MPa) and sheared by applying a standard triaxial stress path. Great attempt was taken to ensure full saturation and complete consolidation. An axial strain rate that was slow enough to either allow a reliable measurement of the pore-pressure response during undrained shearing or to avoid pore-pressure changes during drained loading was chosen. For this study we utilized both P-specimens (load is applied parallel to bedding) and S-specimens (load is applied normal to bedding).

As for the UU tests, the test results of the CU and CD tests showed similarities with both soils and rocks such as for example the dependency of the Young's modulus on the confining stress, a suppressed dilatancy with increasing confinement, and a non-linearity of the stress–strain response before peak strength. The data set revealed a relatively low cohesion in the range of 1 MPa.

Generally, a strong hydro-mechanically coupled behaviour was observed during the CU tests. In the elastic range, the pore-pressure build-up is controlled by Skempton's pore-pressure parameters A and B (Skempton 1954). Wild et al. (2015a) found that B , the ratio between the pore-pressure change and the increase in confining stress, ranges between 0.67 and 0.97 and decreases with increasing effective confinement (Fig. 6). The decrease in B is consistent with the general increase in Young's modulus and therefore related to a decrease in compressibility of the rock.

Figure 7 shows typical effective stress paths from a CU test on a P- and a S-specimen (consolidated at 2 MPa effective stress). Also plotted is the theoretical elastic effective stress path for an isotropic specimen loaded under the same conditions. A linear pore-pressure build-up is measured for all specimens up to about 0.2–4.0 MPa differential stress (dependent on the confinement). A difference in the behaviour of P- and S-specimens can be identified (Wild et al. 2015a). At low differential stress, the stress path of the P-specimen lies on the right hand side of the theoretical stress path of an isotropic poroelastic material, which indicates a lower pore-pressure build-up

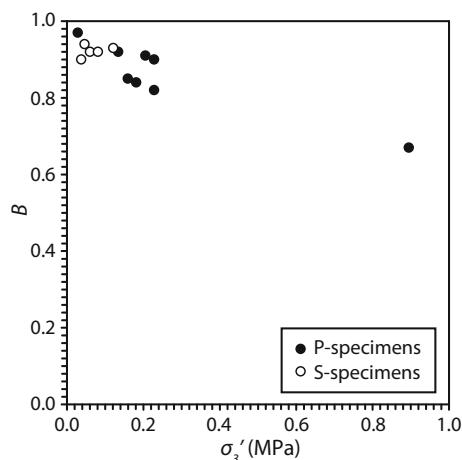


Fig. 6 Relationship between B value and effective confinement (σ_3'). Adapted from Wild et al. (2015a), San Francisco, CA, USA, 28 June to 1 July 2015, copyright 2015 ARMA, adapted with permission of American Rock Mechanics Association

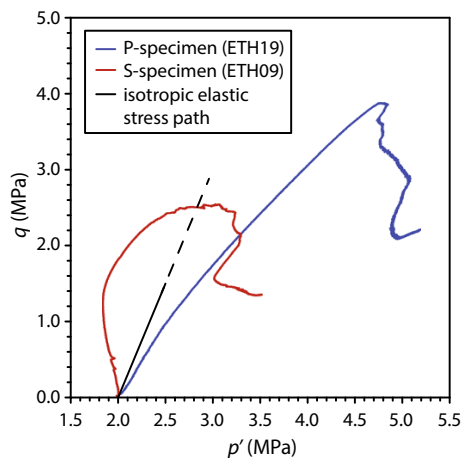


Fig. 7 Effective stress paths for a P- and a S-specimen using a standard triaxial stress path with 2.0 MPa initial effective confinement. The *black line* represents the theoretical elastic effective stress path for an isotropic specimen loaded under the same conditions

compared to an isotropic specimen. For a S-specimen, the stress path lies on the left hand side of the theoretical stress path, i.e. more pore-pressure is built-up. This observation is consistent with findings of Bellwald (1990), Aristorenas (1992), and Islam and Skalle (2013). The difference in excess pore-pressure and behaviour can be related to the transverse isotropy of the clay shale (Aristorenas 1992; Bobet et al. 1999; Einstein 2000; Islam and Skalle 2013). S-specimens exhibit a higher compliance leading to a higher pore-pressure build-up compared to an isotropic material. P-specimens are stiffer than an isotropic material and therefore less excess pore-pressure is built-up.

At differential stresses of about 0.2–4.0 MPa, the specimens start to dilate and the pore-pressure increase becomes smaller with each incremental increase in

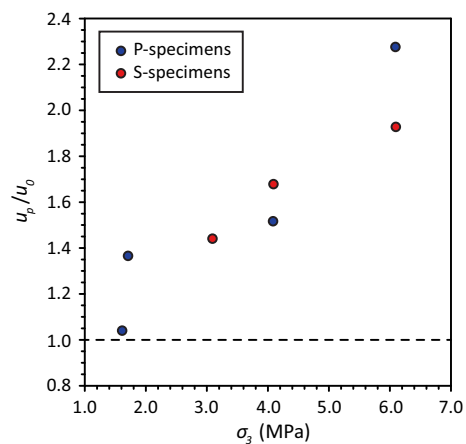


Fig. 8 Pore-pressure at peak (u_p) compared to the initial pore-pressure (u_0) vs. total confinement (σ_3) for P- and S-specimens. Adapted from Wild et al. (2015a), San Francisco, CA, USA, 28 June to 1 July 2015, copyright 2015 ARMA, adapted with permission of American Rock Mechanics Association

differential stress (Wild et al. 2015a). The confinement not only influences the point where dilation starts but also the amount of pore-pressure that is built-up until peak strength is reached. Whereas specimens tested at low confinement reach the peak pore-pressure before the peak strength, specimens tested at higher confining stresses show a pore-pressure increase until peak strength is reached and then drop as a consequence of the dilatancy that accompanies failure. Thus, the pore-pressure measured at peak (u_p) for specimens tested at low confining stresses is comparable to the initial pore-pressure (u_0) (Fig. 8). With increasing confinement, the ratio between pore-pressure at peak and initial pore-pressure increases.

Due to the low hydraulic conductivity of Opalinus Clay and the relatively high advance rate (2–20 m/day), the excavation process can be considered undrained. As a consequence, the strong hydro-mechanically coupled behaviour of Opalinus Clay can lead to significant pore-pressure changes around an underground excavation in the short-term, which influence the stability and behaviour of the rock mass. The excess pore-pressure that develops during excavation will dissipate in the longer term and may cause long-lasting deformations (e.g. swelling or consolidation) and progressive damage in the EDZ.

4 In-situ experiments

In the period 2003–2015 we performed three in situ experiments (i.e., EZ-B, RC and HM-B) to examine the hydro-mechanical behaviour and EDZ evolution of Opalinus Clay on the intact rock and the rock mass scale. On the intact rock scale we investigated the time-dependent

evolution of a borehole damaged zone that develops around a borehole drilled parallel to bedding. On the rock mass scale (i.e. tunnel scale), we focused on the influence of heterogeneities such as tectonic fault planes and fault zones on stress redistribution and on the kinematic freedom for shear dislocations along tectonic fault planes.

4.1 Time-dependent evolution of the damage zone around a borehole

In an attempt to better understand the evolution of the damage zone around underground excavations in intact Opalinus Clay, we performed an overcoring experiment in 2013. A pilot borehole (BHM-3) was drilled parallel to the bedding plane orientation in Gallery 08 (Kupferschmied et al. 2015). The location of the borehole is shown in Fig. 6 in Bossart et al. (2017). After core extraction, the borehole was left unsupported for 12 h and was then impregnated with a fluorescent resin (injected with a low injection pressure). After resin curing, the pilot borehole was overcored, using a 280 mm diameter bore core and the resin-impregnated section of about 1 m length was extracted. The core was cut into 30 mm thick slices that were then analysed macroscopically under UV-light and microscopically using thin sections from selected locations under a UV-light embedded microscope. The results of these analyses were used to gain detailed insight into the failure mechanism that control the short term around a circular opening in Opalinus Clay.

The BDZ was dominated by tangential shear fractures on opposing sides that intersect the pilot borehole (Fig. 9). In most of the slices, these initial bedding parallel fractures developed in only one direction (Fig. 9a). Occasionally, tangential fractures extending in the opposing directions were observed (Fig. 9b).

From the bedding parallel shear fractures tangential to the borehole wall, extensional type fractures (such as wing

cracks and horsetail splays) and secondary shear fractures emanated and propagated back toward the pilot borehole (Fig. 9). The detailed analysis of the structures revealed that the short-term BDZ is (1) dominated by shearing of bedding planes, which leads to the formation of branching fractures, is (2) localized, and is (3) only about half a pilot borehole radius deep.

Two further bedding parallel boreholes (BHG-B11 and BSE-3; for the location see Fig. 5, Bossart et al. 2017) were used to study both the evolution of BDZ structures and the extent of the BDZ with time. Borehole BHG-B11 was left unsupported for a total duration of 6 days before resin was injected and the borehole was overcored (Jaeggi et al. 2010), whereas borehole BSE-3 was left unsupported for 30 days (Badertscher et al. 2008). For the complete history of both boreholes the reader is referred to Kupferschmied et al. (2015). A comparison between the resin-impregnated BDZ structures of the different overcored boreholes delivered important insights into the development of the BDZ in relatively short durations. Within 6 days (i.e. observed in BHG-B11), the BDZ developed in both lateral and radial extent perpendicular to the bedding plane orientation and formed a chimney-like fracture network that extended at least one borehole diameter into the surrounding rock (Fig. 10a). For BSE-3, that was left unsupported for 30 days, the radial extension of the chimney like fracture network was larger than two borehole diameters (Fig. 10b). For further detailed information about the structures within the fracture network, the reader is referred to the description given in Kupferschmied et al. (2015).

The comparison between the initial and the longer-term BDZ suggests a transition from a locally damaged state characterized by shear fractures, horsetail splays, wing cracks and second order shears to a deep and delineated damage zone composed of buckled slabs in relatively short time and without further mechanical perturbation.

Fig. 9 Sketches obtained from the macroscopic analysis of the typical BDZ-structures around a circular opening drilled parallel to the bedding plane orientation (S_0): **a** dominating tangential fractures developed in only one direction (more often observed), **b** tangential fractures extending in opposing directions (occasionally observed). Adapted from Kupferschmied et al. (2015), 108, Copyright 2015 Elsevier Ltd., with permission from Elsevier

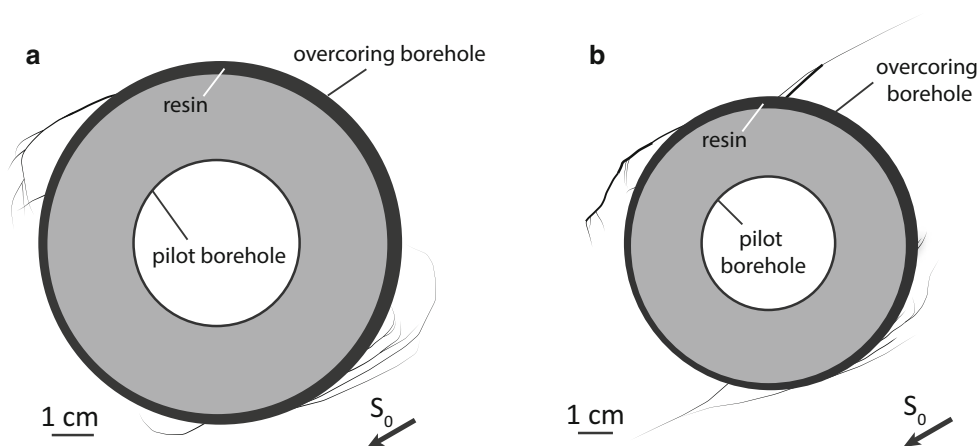
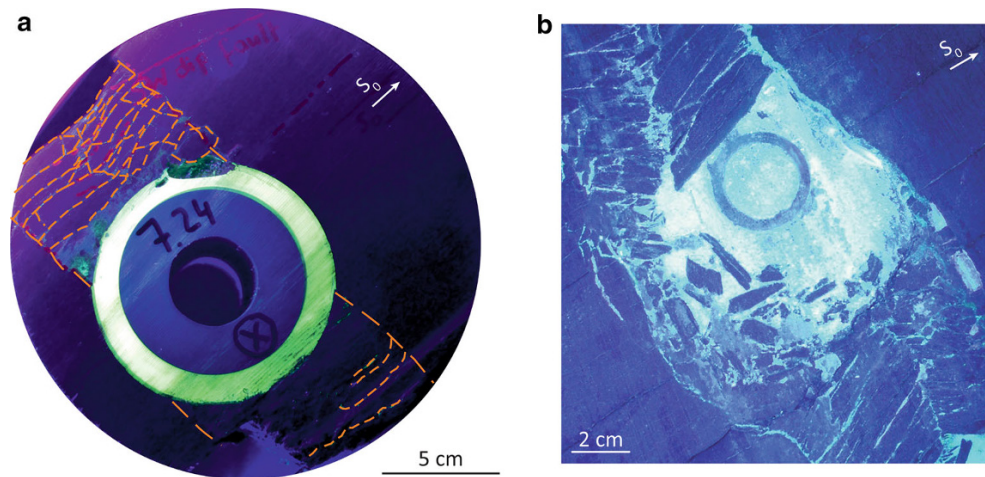


Fig. 10 BDZ in boreholes that were left unsupported for **a** 6 days and **b** 3 weeks. Adapted from Kupferschmid et al. (2015), 111, Copyright 2015 Elsevier Ltd., with permission from Elsevier



4.2 EDZ evolution around Gallery 04 and the EZ-B niche

All the above studies deal with behavioural aspects of the intact Opalinus Clay. This is, however, not the case for larger underground structures like galleries at the Mont Terri Rock Laboratory where a different behaviour due to the presence of geological heterogeneities and pre-existing tectonic features has to be anticipated. Therefore, we performed two mine-by experiments aiming at gaining a better understanding of such structures on the rock mass behaviour and the development of an EDZ at multiple scales (Yong 2007; Thoeny 2014).

A first in situ experiment, called the EZ-B experiment, involved the excavation of a short tunnel (EZ-B Niche) with a diameter of 3.8 m and in a direction normal to the strike of bedding but oblique to the Gallery 04 axis (Fig. 5 in Bossart et al. 2017). The EZ-B Niche is located in the shaly facies, which is locally oriented on average at $147/45^\circ$. Prior to excavation, seven boreholes (BEZ-B1 to B7) were drilled for geological and geophysical characterization (BEZ-B1 to B3) as well as pore-pressure monitoring (BEZ-B4 to B7). The 1.5-m long entrance was excavated with a road header while the remaining 5 m of the niche was completed with a pneumatic hammer in six steps over a period of 12 days (Fig. 11). Additional 12 boreholes (BEZ-B8 to B19) were drilled from the niche in two vertical and one horizontal planes. An extensive program of geological, geophysical and deformation measurements was made prior to, during and after the niche excavation (Yong 2007). These consisted of: (1) geological mapping and 3D panoramic laser scanning, (2) core logging as well as optical televiewer and single-hole ultrasonic logging of boreholes, and (3) pore-pressure monitoring.

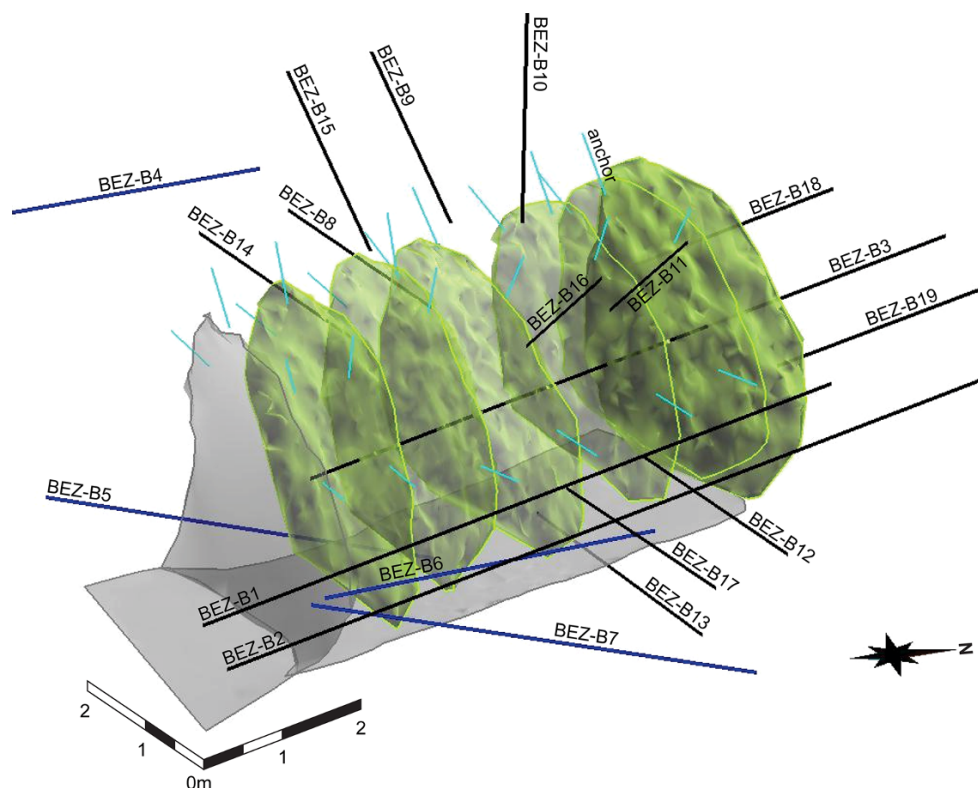
4.2.1 Macroscopic EDZ fracturing around Gallery 04

Detailed fracture mapping in the EZ-B niche entrance provided evidence that tectonic fault planes influenced the development of excavation-induced fracturing around Gallery 04 (Yong et al. 2010). In the west wall, the bedding-parallel fault planes were mobilized without interference from the sub-horizontal fault planes while mobilization of both sets were required to induce fracture growth parallel with the gallery wall in the east wall (Fig. 12). Numerical 2D and 3D elastic and elasto-plastic models demonstrated that if the tectonic structures (fault planes) are not kinematically restrained, their mobilization can play a key role in the development of the induced fracture network. In this case, the influence of such rock mass heterogeneity dominated over the rock matrix anisotropy of the persistently bedded Opalinus Clay that is prevalent at the Mont Terri Rock Laboratory. These results are consistent with observations made by Martin et al. (2004), Bossart et al. (2004) and Marschall et al. (2006).

4.2.2 Macroscopic and microscopic EDZ fracturing around the EZ-B niche

Damage around the completed EZ-B niche was investigated by fracture mapping on drillcores, televiewer images and ultrasonic logging in radial boreholes. These investigations revealed a thin inner zone of about 20 cm characterized by macroscopic fracturing and a lack of borehole instabilities (Fig. 13). This zone also coincided with the lowest P-wave amplitudes and velocities. An outer zone of increasing P-wave velocities and amplitudes was seen in the surrounding 50–70 cm. The thin macro-fractured zone was to be expected, according to a 3D numerical stress analysis that showed the rock mass most susceptible to spalling is found in the side-walls and upper western haunch, where the modelled stress

Fig. 11 Isometric view of the various EZ-B niche faces, boreholes, and roof anchors. Reprinted from Yong et al. (2013), 302, Copyright 2013 Elsevier Ltd., with permission from Elsevier



levels only just reached a minimum to maximum principal stress ratio (spalling limit) smaller than 0.05 in the inner zone.

Rock mass damage ahead of the progressively-excavated EZ-B niche was characterized through repeat single-hole ultrasonic velocity logging and optical televiewer imaging. Furthermore, three-dimensional elastic stress analyses were conducted (Yong et al. 2013). By integrating field and numerical data, geological structures (i.e. bedding and bedding-parallel tectonic fault planes) were shown to be most influential near the entrance but diminished in role as the niche deepened (Fig. 14) and the structures became more kinematically restrained. Damage ahead of the niche face accumulated progressively as the formerly compressed volume of rock unloaded during the excavation. Low minimum to maximum principal stress ratios coincided with the lowest seismic wave velocities and amplitudes. This was corroborated in recent laboratory studies by Amann et al. (2011), who defined the brittle failure process of Opalinus Clay under undrained and low confinement conditions and demonstrated that the volumetric behaviour in the pre-rupture stage is dependent on confining stress.

4.3 EDZ evolution around Gallery 08

Within the framework of the excavation of Gallery 08 at the Mont Terri Rock Laboratory, we performed a second mine-by experiment between GM 94.5 and GM 127 (RC

experiment), where Gallery 08 intersects the Main Fault of the Mont Terri Rock Laboratory (Fig. 5 in Bossart et al. 2017) and thus the rock mass exhibited a wide range of structural conditions ranging from almost massive to heavily faulted rock (Thoeny 2014). The 32.5 m long Gallery section was excavated full-face normal to the bedding plane strike in 23 steps using a road header. The bedding planes in the experimental section dip approximately 45° in the direction of the advancing tunnel face. The fracture network within the experimental tunnel section was characterized prior to and after excavation by integrating structural data from geological tunnel mapping and from 2 pre- (BRC-1 and BRC-2) and 2 post-excitation boreholes (BRC-3 and BRC-4) that were logged using an optical televiewer and geological core logging (the locations of the boreholes are given in Fig. 5 in Bossart et al. 2017). We used complementary geophysical methods including single-hole interval velocity measurements and seismic refraction tomography to quantify spatial variations in seismic velocities, rock mass properties, and the extent of the EDZ. Both displacements and deformations in the surrounding rock mass were monitored during and after completion of the excavation using borehole inclinometers, extensometers, deflectometers, high-resolution geodetic displacement monitoring, and laser scanning of excavation surfaces (Thoeny 2014).

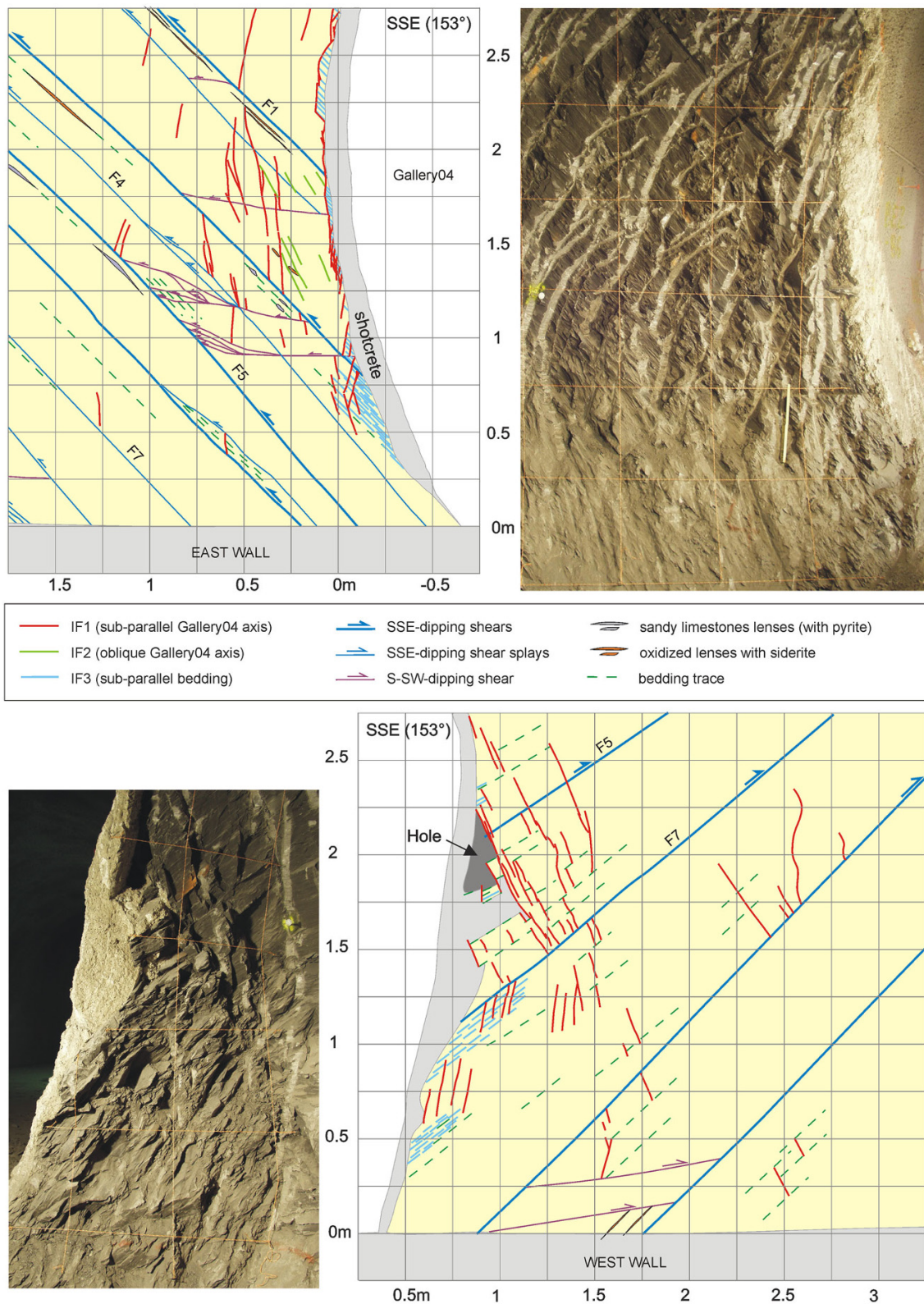


Fig. 12 Induced fracturing mapped and photographed in the east (top) and west (bottom) walls of the EZ-B Niche entrance, parallel view with Gallery04 (maps by Christophe Nussbaum and photos by

Frank Lemy). Tectonic fault planes are labelled, “F#”. Reprinted from Yong et al. (2010), 897, Copyright 2010 Elsevier Ltd., with permission from Elsevier

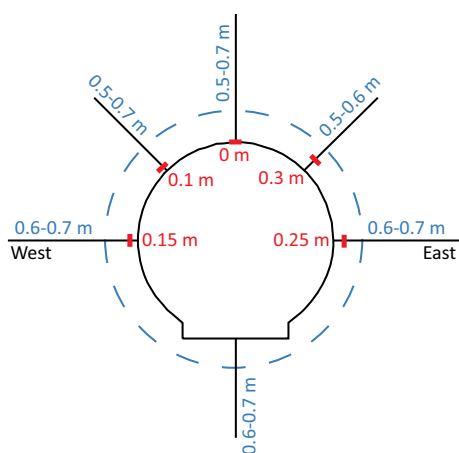


Fig. 13 EDZ around the EZ-B niche, as determined from borehole data integration (blue). Induced macro-fracturing is shown in red. (From Yong 2007)

The integration of various geological, geophysical and deformation monitoring methods provided a unique opportunity to better understand (1) structural and kinematic relationships between natural and excavation induced fractures, (2) the spatial and temporal evolution of the excavation-induced displacement field and (3) the stress redistribution around an excavation in an anisotropic and heterogeneous clay shale formation.

4.3.1 Structural and kinematic relationship between natural and excavation-induced fractures

A combination of geological and geophysical characterization techniques (i.e. geological mapping of the tunnel/niche surfaces, core logging, and seismic refraction tomography) on the tunnel and borehole scale was used to analyse the structural and kinematic influence of natural fractures on the characteristics and the spatial variation of excavation-induced damage (Thoeny 2014). The study revealed that the spatial variation in fault plane frequency along the tunnel axis has a strong influence on the rock mass strength and the deformability. This again affects the location and the radial extent of the induced damage at both borehole and tunnel scale. Based on the observations, a conceptual model of the EDZ around the mine-by section was established (Fig. 15). A strongly damaged inner zone with a radial extent of 0.5–1.5 m was observed which is unaffected by variations in fault plane density along the tunnel axis. Furthermore, a less damaged outer zone which changed in radial extent depending on the fault plane density was identified. Within the main fault, the radial extent of this outer zone reaches up to a distance of 4 m, whereas between fault zones the outer zone extends to

2–3 m. The EDZ around the RC section consists of reactivated fault planes and seven different types of induced fractures (IF) (Fig. 16):

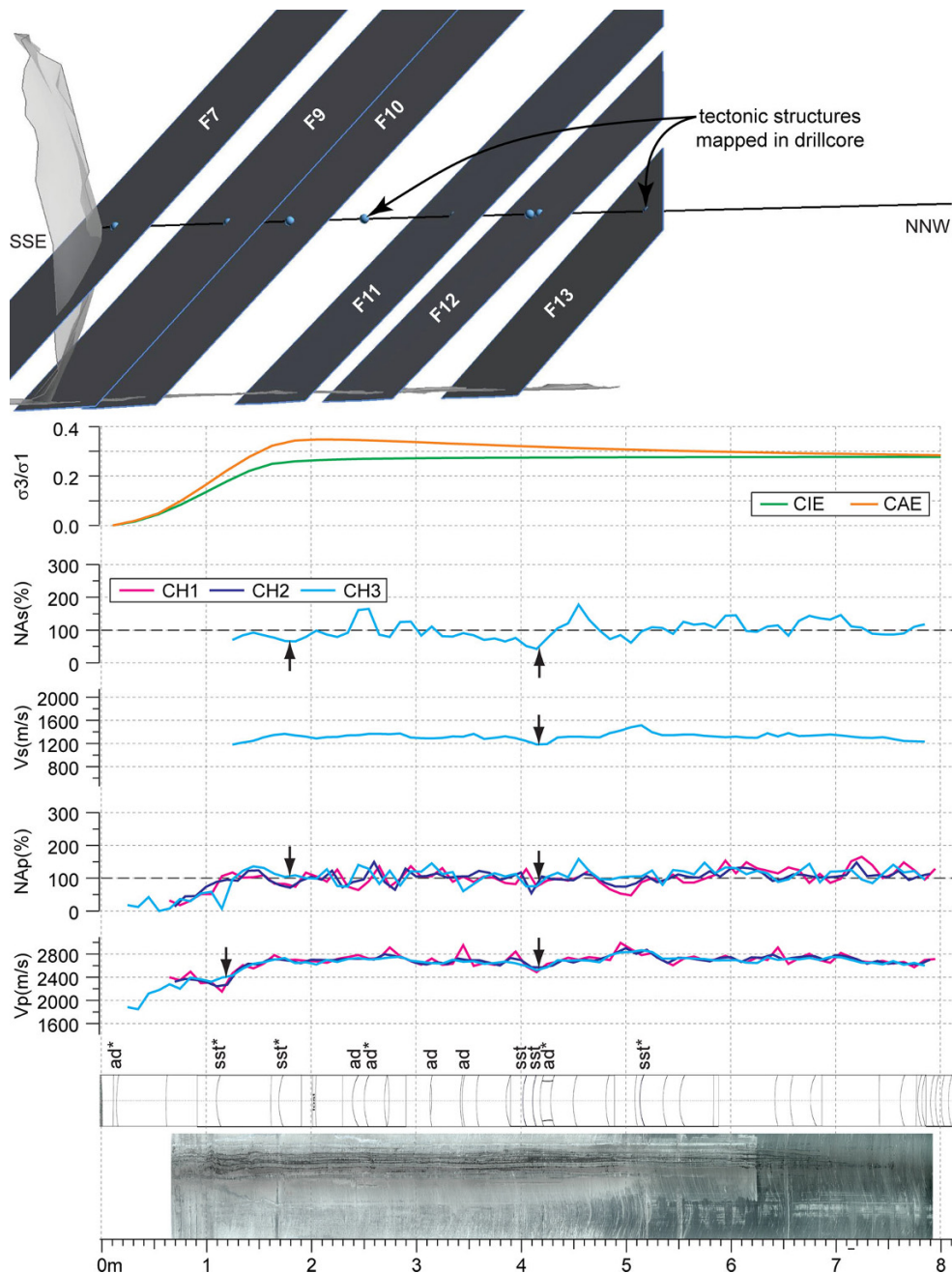
- (IF 1) extensional fractures parallel to the sidewalls
- (IF 2) extensional fractures oblique to the tunnel axis at the sidewalls
- (IF 3) sub-horizontal extensional fractures parallel to the tunnel invert
- (IF 4) extensional and/or shear fractures along bedding planes at the tunnel invert
- (IF 5) extensional fractures perpendicular to sheared bedding or reactivated fault planes at the tunnel invert
- (IF 6) shear fractures along bedding planes at the tunnel face
- (IF 7) extensional fractures sub-perpendicular to sheared bedding planes or reactivated fault planes at the tunnel face.

The failure mechanism, orientation, and frequency of these induced fractures are strongly influenced by the occurrence and characteristics of multi-scale tectonic fault planes. Extensional fracturing (IF1–IF2) dominated at the sidewalls where fault plane reactivation and bedding shear are constrained due to high normal stresses. Depending on the fault plane frequency, different IF were observed at the tunnel invert or tunnel face where fault plane reactivation and bedding plane shear are kinematically free. In sections where the rock mass is sparsely faulted (0–1 fault/m²), extensional brittle failure and shearing along bedding planes (IF3-IF4 at invert, IF6 at tunnel face) were observed. In sections where the rock mass shows a higher fault plane frequency (1–3 faults/m²), the EDZ is mainly composed of IF5 (invert) or IF7 (face) fractures. In sections with even higher fault plane density (>4 faults/m²), reactivation of densely spaced fault planes becomes more evident and macroscopic EDZ fractures described above diminish, which indicates a transition from extensional macroscopic failure to shearing.

4.3.2 Spatial and temporal evolution of the excavation-induced displacement field

The influence of pre-existing fault planes and fault zones on excavation induced displacements and deformation in the short and longer term was analysed on the fracture and tunnel scale (Thoeny 2014). On the borehole scale, vertical, radial, and longitudinal displacements were monitored using a TRIVEC, a deflectometer, and two extensometers. The data was recorded during the excavation phase as well as in the longer term (up to 2.5 years after installation). Additionally, laser scanning monitoring of the tunnel surface was used. The analysis of the data revealed that the overall rock mass response of faulted Opalinus Clay is mainly controlled by the rock anisotropy. Heaving

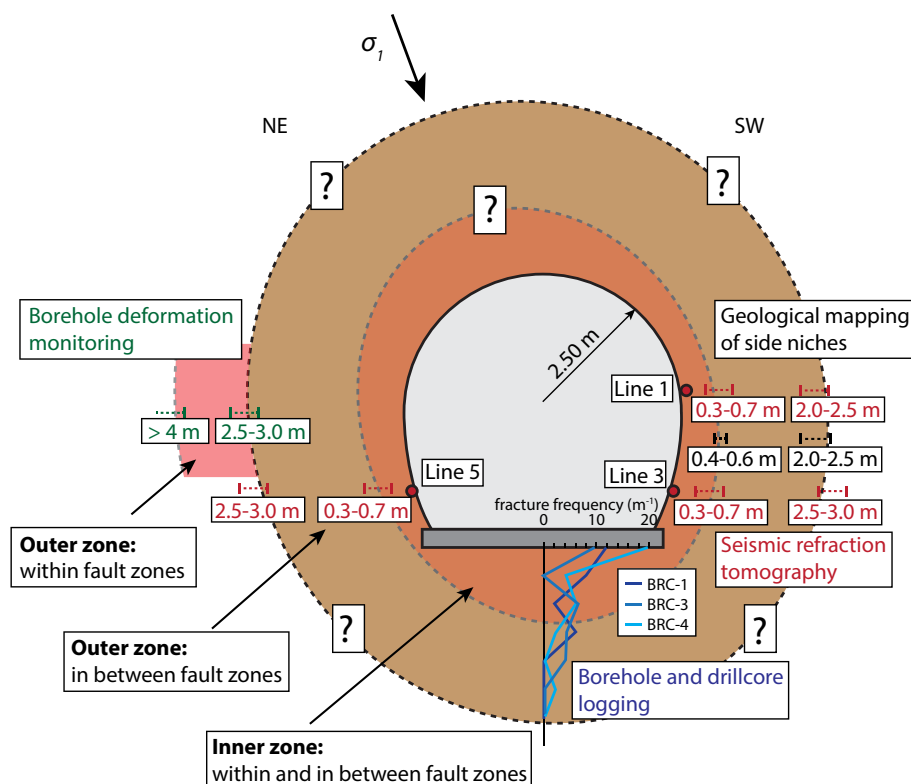
Fig. 14 BEZ-B3 borehole data with *asterisks* indicating drillcore structures mapped closest to projected intersections of bedding-parallel shears, represented by *arrows*. Reprinted from Yong et al. (2013), 306, Copyright 2013 Elsevier Ltd., with permission from Elsevier



observed at the lower sidewalls and below the tunnel invert as well as settlements at the tunnel crown and upper sidewalls suggest that the preferred displacement orientation is sub-perpendicular to the bedding. Furthermore, the displacement field and magnitude at the tunnel face, crown and invert is influenced by individual pre-existing fault planes. At the sidewalls, the orientation of the fault planes with respect to the tunnel is kinematically rather unfavourable for shearing along them and the response is dominated by extensional fracturing through the intact rock matrix. This results in the formation of slab-like structures behind the tunnel face associated with large displacements.

Continuous borehole monitoring by deflectometer and extensometers showed that longer-term rock mass deformations parallel to the rock anisotropy are substantially smaller than deformations occurring during the excavation phase. This is in contrast to the measurements of the inclinometer which indicate significantly larger displacements in the longer term compared to the short term, especially in the vertical direction, oblique to the bedding. Parallel to bedding, the short-term rock mass deformations are controlled by differential deformations along fault planes. The longer-term response, on the other hand, is not significantly affected by these large-scale heterogeneities

Fig. 15 Conceptual model of the excavation damaged zone based on borehole information, geological mapping, seismic tomography, borehole and drillcore logging and deformation measurements in BRC-2 (the location of the borehole is given in Fig. 5 of Bossart et al. 2017, this volume) (Figure modified from Thoeny 2014)



but rather related (especially in the tunnel invert) to the extent of the initial (short-term) EDZ.

4.3.3 Stress redistribution

Site-specific three-dimensional numerical models were used to investigate the influence of rock mass characteristics (i.e. large-scale deformability and strength heterogeneities related to multi-scale fault zones) on the excavation-induced stress redistribution during tunnel excavation and the associated short-term rock mass response (displacements) in the tunnel near-field (Thoeny 2014). Both the elastic and plastic response around the mine-by section was simulated using the commercial three-dimensional continuum code FLAC3D (Itasca 2009). The total stress approach was used and the short-term behaviour during excavation was assumed to be undrained. First, an elastic analysis with an isotropic and transversal isotropic model was conducted to identify the influence of the rock anisotropy (related to the bedding planes) and the rock mass heterogeneity (related to fault zones) on the stress and displacements. Afterwards, an elasto-plastic model was used to quantify the effect of the stress redistribution on the displacements and the extent of the EDZ. Further details to the models are given in Thoeny (2014).

The elastic models revealed that substantial stress concentration in the rock mass adjacent to fault zones can be related to large-scale heterogeneities in deformability (i.e.

caused by spatial variations in fault plane frequency; the contrasts in deformability were derived from single-hole interval velocity measurements which suggest various zones of similar P-wave velocities; it was assumed that the computed contrasts in the dynamic Young's modulus are the same for the static Young's modulus). The magnitude and extent of these stress concentrations are proportionally related to the stiffness contrast between fault zones and the intact rock mass. The study further showed that isotropic heterogeneous models with an average Young's modulus used for the intact rock mass can sufficiently represent the changes in stress magnitudes in a transversally isotropic rock mass, at least for the orientation of the tunnel is respect to the bedding plane orientation encountered in the RC experiment. Furthermore, the constitutive model (i.e. isotropic/transversely isotropic) only influences the orientation of the displacement vector but not its magnitude. Also the stress path is unaffected. Stress path analyses allowed to identify kinematic failure modes occurring during tunnel excavation. Generally, shearing along fault and bedding planes dominate at the face, invert and crown. This findings are consistent with Martin et al. (2004) and Nussbaum et al. (2011). However, differences in initiation of shearing and the associated type of faulting were observed. At the face, the reactivation of fault and bedding planes is initiated ahead of the face (2–3 m for faults, 0.5–1 m for bedding planes) and is consistently associated with normal faulting. At the invert/crown, the initiation of

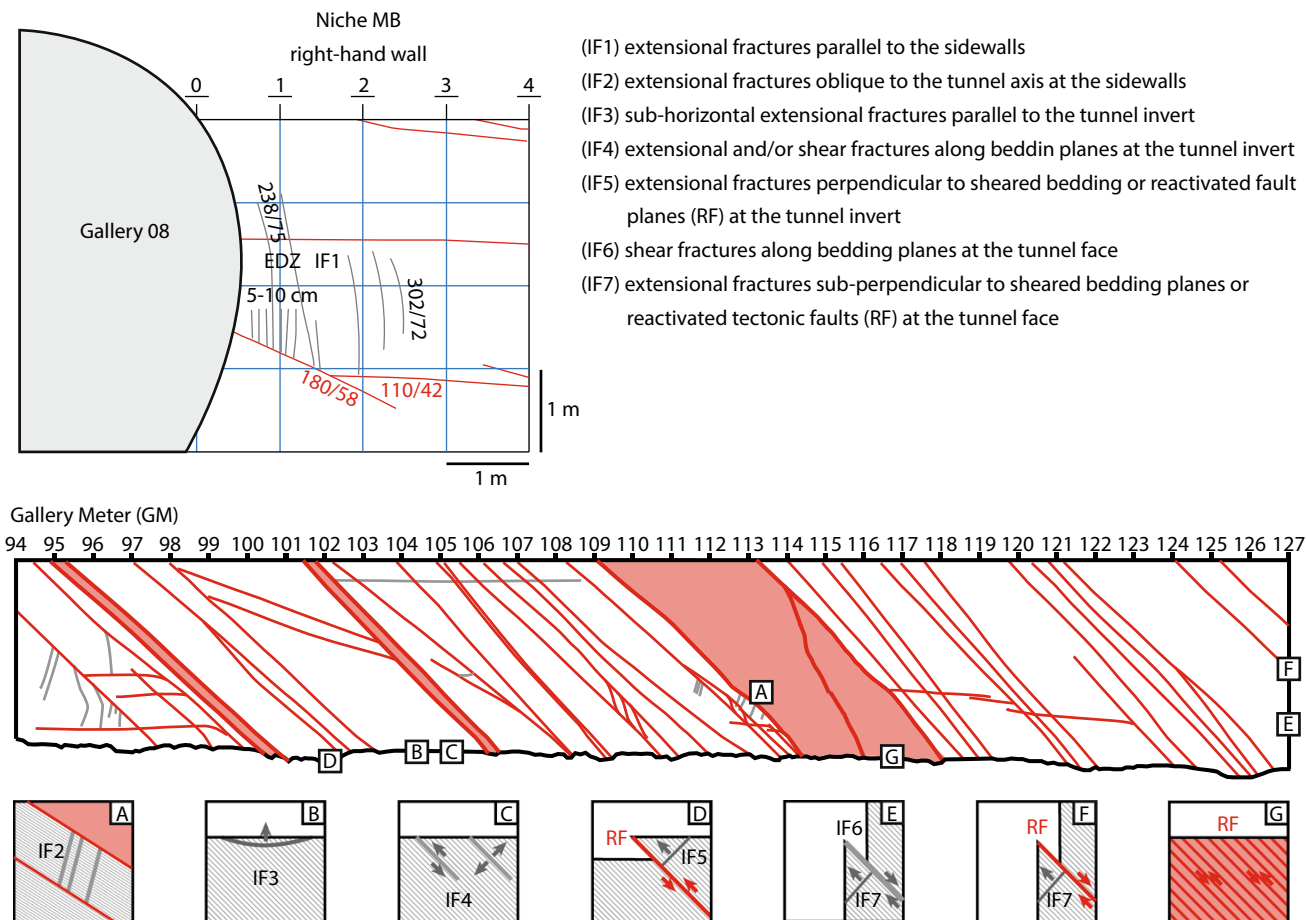


Fig. 16 Conceptual model that illustrates the structural and kinematic relationship between pre-existing tectonic fault planes and excavation induced fractures around the RC-mine-by section. (Figure modified from Thoeny 2014)

fault and bedding plane shear takes place behind the face and is associated with reverse faulting. Furthermore, extensional fracturing was identified as the primary failure mechanism at the sidewalls. Extensional fractures may also form sub-parallel to the tunnel face in the vicinity of fault zones where stresses are significantly augmented. All these findings are consistent with field observations.

The elasto-plastic models showed that variations in rock mass strength and deformability along the tunnel axis have a significant influence on the extent of the EDZ. The modelled radial extent and its variation are consistent with the conceptual model of the EDZ described above (Fig. 15). Furthermore, the spatial and temporal evolution of the displacement field as well as the measurable displacement magnitudes of the models are generally in good agreement with the measured values. The magnitudes are only not captured in zones where structural controlled instabilities (slab-like features) or major side-wall slabs associated with dilatant behaviour develop. Nevertheless, these zones correspond in extent and location to the maximum modelled plastic shear strain.

5 Discussion

5.1 The importance of the effective stress state on the stability of Opalinus Clay excavations

The relatively low cohesion tested in CU and CD test on back-saturated Opalinus Clay specimens would suggest that tunnel deformations at the Mont Terri Rock Laboratory may be large. For the stress state at the Mont Terri Rock Laboratory, significant squeezing of the rock mass into the tunnel excavation could be anticipated. However, excavation sidewall and faces are, except for instabilities which are associated with pre-existing tectonic structures or large side-wall slabs, stable or show only small to moderate short-term deformations [i.e. 1–2 cm in case of excavations normal to the bedding orientation (Thoeny 2014) and 2–4 cm parallel to the bedding orientation (Martin et al. 2011)]. The short-term stability is likely associated with the effective stress state that evolves as a consequence of tunnelling stress path, which may cause a short-term apparent cohesive strength component. This is

illustrated in the following, based on experience gained from the above experimental studies, theoretical considerations and conceptual numerical modelling.

5.1.1 Apparent cohesion in a bore core

The effective stress state in a bore core extracted at the Mont Terri Rock Laboratory can be illustrated with a simple model of a bore core that is unloaded from its in situ state of stress. At the Mont Terri Rock Laboratory, the mean total stress σ_m is 4.5 MPa according to Corkum and Martin (2007), the in situ pore-pressure P is approximately 2.0 MPa and thus the effective mean stress σ_m' is 2.5 MPa. Assuming isotropic elastic conditions, the pore-pressure drop can theoretically be estimated using the following expression, $\Delta P = B\Delta\sigma_m$, where B is Skempton's pore-pressure coefficient (Skempton 1954). Assuming B is at unity, the pore-pressure in the bore core is -2.5 MPa after core extraction although the effective stress remains constant. Thus, a substantial apparent cohesive strength component is to be anticipated which stabilizes the core until pore-pressures that develop in the short term dissipate. For the anisotropic stress state at the Mont Terri Rock Laboratory and for the assumption of a transversal isotropic material behaviour, the effective stress in the bore core depends significantly on the drilling orientation with respect to the principal stress components. We used a simplified numerical model to estimate the negative pore-pressure in a bore core with different orientations of the plane of anisotropy in respect to the stress state at the Mont Terri Rock Laboratory. The model consists of a single cell in FLAC3D (Itasca 2009) which is unloaded to atmospheric conditions from an in situ state of stress similar to the state of stress in the Mont Terri Rock Laboratory. The model geometry is shown in Fig. 17.

We used an elastic, transversal isotropic model that does not account for any plastic deformations. We analysed various orientation of the plane of anisotropy and we

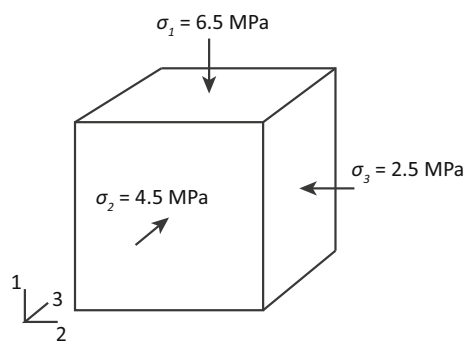


Fig. 17 Model geometry of the conceptual three-dimensional model conducted to estimate the negative pore-pressure in a bore core with different orientations of the plane of anisotropy

assumed different ratios between E_1 and E_3 (i.e. the Young's moduli normal and perpendicular to the bedding plane orientation) ranging between 0.5 and 3. Note that this model does not intent to capture the complexity associated with drilling and core extraction as for example described in detail in Pei (2003). The results are illustrated in Fig. 18 which shows the modelled pore-pressure in a sample that developed upon unloading for the assumption that the plane of anisotropy is rotated about axis 2 (Fig. 18a), axis 1 (Fig. 18b) and an axis that is 45° inclined from axis 1 (Fig. 18c). Fluid pressure between -0.5 and -3.5 MPa can be anticipated and suggest that the short-term stability of bore cores is primarily due to negative fluid pressures that evolve during bore core unloading and an associated apparent cohesive strength component.

5.1.2 Apparent cohesion around a borehole

Our overcoring experiment showed that the short-term damage zone that evolves around a borehole drilled parallel to the bedding directions is very localized and dominated by shearing along bedding planes that are tangential to the borehole wall and branching fractures. The extent of the initial BDZ (i.e. after 12 h) was in the order of 0.25 times the radius of the pilot borehole. After 6 days, the BDZ depth was about two diameters of the pilot borehole and twofold wider than the initial BDZ. Within only 30 days, an unsupported borehole collapsed and the BDZ increased rapidly in extend and depth. Kupferschmied et al. (2015) concluded that the limited extent of the BDZ in the short term is associated with an effective stress state that favours stability of the borehole and evolves as a consequence of unloading and dilatant failure immediately during drilling (i.e. negative excess pore-pressures develop that increase the effective stress).

The rapid development of the BDZ within 30 days could be related to different processes such as dissipation of excess pore-pressure, creep, and processes related to seasonal variations in climatic conditions (RH or temperature). However, the observations revealed that the evolution from an initial state to a longer-term state occurs relatively fast. This suggests that the evolution of the BDZ is likely controlled by pore-pressure dissipation, which destabilizes the borehole, rather than by creep or climatic variations. Destabilization is associated with a propagation of initial tangential shear fractures and the formation of further bedding parallel shear fractures deeper in the rock mass. These bedding parallel shears form slabs that tend to buckle into the borehole until collapse occurs. The hypothesis that excess pore-pressure dissipation dominates the long-term behaviour of underground excavations is in agreement with the conclusions from Martin et al. (2004), numerical findings performed by Amann et al. (2012b),

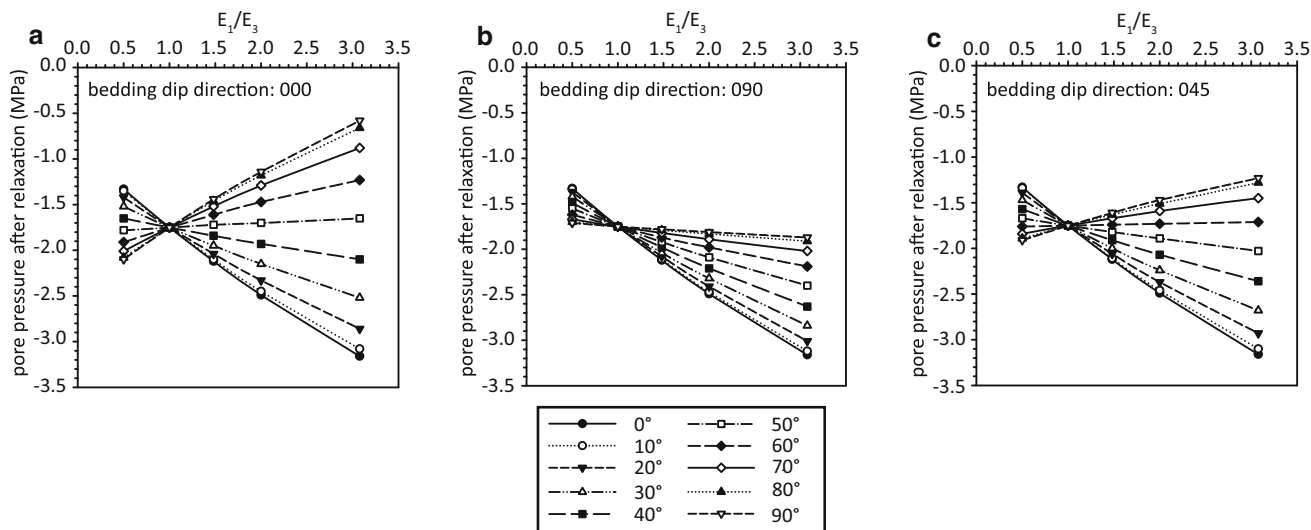


Fig. 18 Theoretical pore-pressure after relaxation of a bore core from an in situ state of stress equivalent to the state of stress at the Mont Terri Rock Laboratory. Dip direction is measured positive clockwise

in the horizontal plane from *axis 3* (Fig. 16), which is zero degrees in azimuth. Dip is measured positive down from the horizontal plane (*plane 2-3*)

experimental data reported by Neerdael et al. (1999), and theoretical considerations reported by Anagnostou (2009). While this conclusion seems plausible owing the measurements of the long-term excess pore-pressure dissipation in the Mont Terri Rock Laboratory (Masset 2006), the rapid increase in damage of unsupported openings was unexpected and fairly new.

5.1.3 Apparent cohesion around tunnel excavations

Similar to a bore core and a borehole, also the rock mass in the vicinity of an underground excavation experiences unloading. Test galleries constructed in Opalinus Clay at the Mont Terri Rock Laboratory have been used to characterize the hydro-mechanical coupled behaviour of Opalinus Clay during tunnel excavation (Martin et al. 2004; Corkum and Martin 2007; Popp et al. 2008; Vietor et al. 2010; Giger et al. 2015). The short-term pore-pressure response monitored during the construction of these test galleries revealed a pore-pressure rise ahead of the tunnel face followed by subsequent reduction of pore-pressures immediately around the tunnel or slightly ahead of the tunnel face. With increasing distance from the tunnel, pore-pressures appear unaffected by construction work in the short term (Corkum and Martin 2007; Vietor et al. 2010; Amann et al. 2011; Wild et al. 2015b; Giger et al. 2015). Close to the tunnel, the pore-pressure was substantially below the in situ pore-pressure. For the majority of pore-pressure measurements conducted during the excavation of tunnels at the Mont Terri Rock Laboratory, the minimum measured pore-pressure was 100 kPa, suggesting that a conductive excavation damaged zone formed, connecting

the monitoring interval with the tunnel. The pore-pressure measurements we performed in the framework of the EZ-B experiment (Fig. 19) showed a similar behaviour at sensor BEZ-B7, where the pore-pressure rose during excavation and fell quickly in two steps to a pressure close to the atmospheric pressure as the face passed the monitoring location. In contrast, sensors BEZ-B4 and BEZ-B5 recorded pore-pressures of 40–50 kPa below atmospheric pressure. These pore-pressure measurements demonstrated for the first time that sub-atmospheric pore-pressure could develop during the excavation of galleries in Opalinus Clay, which may provide a significant apparent cohesion, at least in the short term.

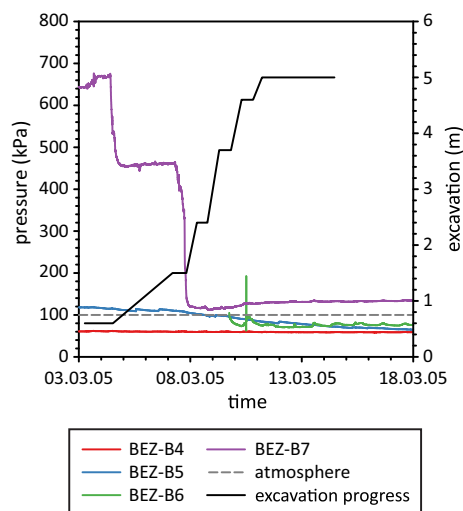


Fig. 19 Pore-pressure response monitored around the EZB-niche during niche excavation. Modified from (Yong 2007)

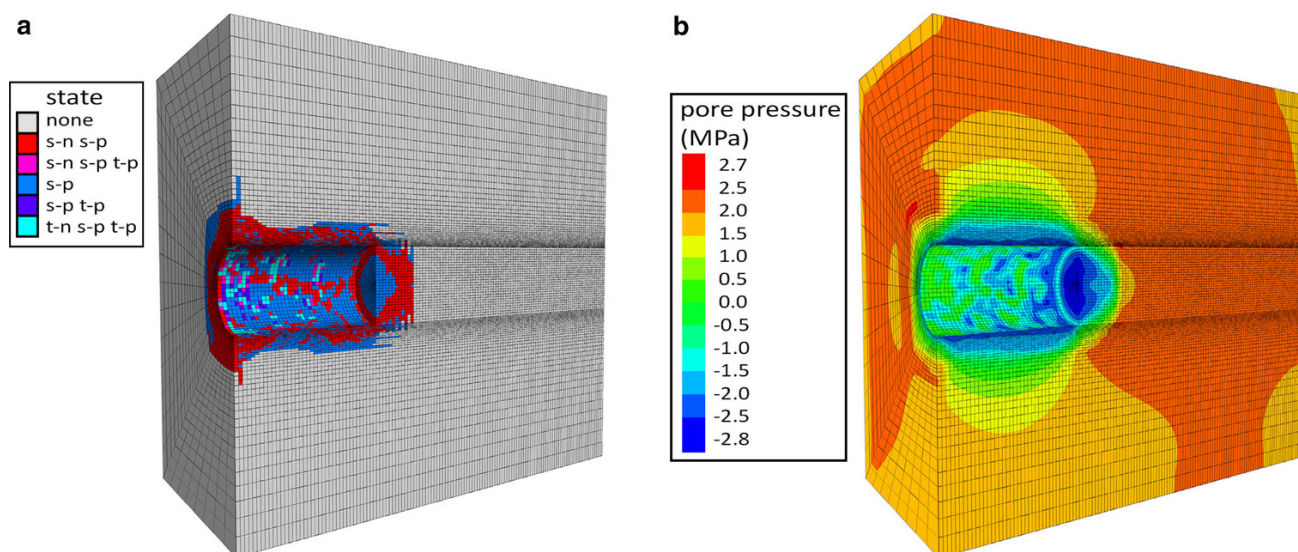


Fig. 20 **a** Excavation damaged zone and failure mechanism (*none* elastic behaviour, no failure; *s-n* shear now, *s-p* shear past, *t-n* tension now, *t-p* tension past). **b** Short-term pore-pressure response around the excavation

We used conceptual numerical models aiming at a better understanding of the pore-pressure response in the near-field of tunnels excavated in a low permeable clay shale (Wild et al. 2015b). For the numerical analysis we used FLAC3D (Itasca 2009) and assumed an unsupported, circular opening with a diameter of 4 m that is step-wise excavated. We utilized an isotropic stress state and a stress state with $K_0 = 0.5$ (where K_0 is the ratio between the horizontal and vertical stress), and an initial pore-pressure of 2 MPa. The principal stresses and pore-pressures that evolve as a consequence of tunnel excavation were monitored in the centre of the three-dimensional model at various radial distances from the tunnel. For the fully coupled analysis we assumed that the excavation process is undrained. For the constitutive behaviour we used (1) an elastic constitutive model that was either isotropic or transversal isotropic and (2) an isotropic elastic-brittle plastic model based on a linear Mohr–Coulomb failure criterion. For further details of the numerical model see Wild et al. (2015b). The model results suggested that the pore-pressure response typically observed at the Mont Terri Rock Laboratory is a consequence of (1) the anisotropic in situ state of stress, (2) the transversal isotropic stiffness of Opalinus Clay, (3) the anisotropy ratio, (4) the orientation of the tunnel axis relative to the in situ stress state, and (5) dilatancy accompanying failure. An important outcome of this numerical study was that pore-pressure changes associated with tunnel excavation can lead to absolute negative pore-pressures of up to -3 MPa in the short term (Wild et al. 2015b). In case of a transversal isotropic model, zones around the excavation with absolute negative pore-pressure are limited and the limitation depends on the assumption of the in situ stress state and the orientation of

the plane of anisotropy. In case of an elasto-plastic model, where an EDZ may develop ahead and around the advancing tunnel face (Fig. 20a), negative pore-pressures are to be anticipated within the EDZ (Fig. 20b). These negative pore-pressures are primarily related to the dilatancy that accompanies failure. The pore-pressure drop to sub-zero pore-pressures around the excavation contributes to the stability of the excavation. In the longer term, however, these negative excess pore-pressure dissipate and cause time dependent tunnel convergences. Note, however, that the rock mass close to the excavation might also dry as a consequence of the tunnel environment. This may cause an unsaturated zone with an apparent strength and stiffness significantly larger than the saturated rock, which can contribute to the stability of the excavation (Martin et al. 2004). Seasonal cyclic variations in RH may, however, cause a strength degradation and additional deformations (Walter 2015).

5.2 The influence of rock and rock mass anisotropy and heterogeneities on the EDZ development

Our in situ experiments showed that many fractures that form around underground excavations in Opalinus Clay are either directly or indirectly associated with bedding plane shearing or dislocations along pre-existing tectonic structures. These secondary fractures are either extensional type fractures such as horsetail splays or wing cracks or secondary shear fractures. Only when bedding plane shearing or shearing along tectonic structures was kinematically constrained, extensional type fractures initiated as primary fractures.

For a circular opening excavated parallel to the bedding plane strike (i.e. as anticipated for a repository in northern Switzerland and investigated in our study of the BDZ evolution) the behavior was dominated by bedding plane shearing and opening, and all observed extensional type fractures were secondary fractures (i.e. associated with shearing along bedding or buckling of slabs). Buckling of slabs into the unsupported boreholes developed in relatively short time and eventually borehole collapse occurred. Assuming that the behaviour observed for boreholes is representative for a mechanically excavated circular tunnel parallel to bedding, early installed rock support such as dense rock bolts covering the anticipated buckling zone, and/or shotcrete can largely prevent rock buckling and mitigate the development of large open fractures and overbreaks.

For excavations oriented normal to the bedding plane strike direction primary extensional type fractures were occasionally observed at the flat tunnel invert and at the sidewalls, where large spalls formed. Our research consistently showed that both bedding planes and tectonic fault planes dominate the formation of an EDZ.

Another important aspect that is associated with the presence of heterogeneities (i.e. tectonic fault planes, fault zones and related stiffness and strength contrasts) is the strong influence on stress redistribution around the excavation. Our numerical models demonstrate that even the presence of single tectonic fault planes substantially modify the redistributed stresses and the zone around an excavation where new fractures may evolve. Fault zones further modify the stress redistribution in both the radial and longitudinal tunnel directions. Due to stiffness contrasts between fault zones and the adjacent rock mass, large stress concentrations are to be anticipated on both sides of the fault zone. These stress concentrations lead to an intense fracturing and deformations of the rock in close vicinity to the fault zone. The zone of influence depends on the dimensions of the tunnel, the fault zone and the stiffness contrast between fault zone and the adjacent rock mass. In case of the RC mine-by experiment the zone of influence (i.e. the zone with significant modelled stress concentration) was approximately 2–3 m on both sides of the main fault.

6 Conclusions

The research conducted between 2003 and 2015 investigated the behaviour of intact and fractured Opalinus Clay. Our research comprised a series of laboratory experiments such as unconsolidated undrained shear tests, unconfined compression and indirect tensile strength tests on specimens equilibrated at various relative humidity and

consolidated undrained and drained triaxial tests on fully re-saturated specimens. Furthermore, three in situ experiments were carried out: an overcoring experiment and two mine-by experiments at the Mont Terri Rock Laboratory.

On the laboratory scale, we showed that even simple laboratory tests, such as unconsolidated undrained shear tests, are difficult to interpret and uncertainties remain in the representativeness of the test results. The observed shear strength, in particular the high undrained friction angle, and the bi-linear shape of the failure envelope resulting from the series of UU tests can be associated with a true material behaviour or a partly saturated state of the specimens. Partially saturated conditions are associated with suction. Our experimental studies showed that suction may develop rapidly after core extraction and substantially modifies the strength and the stiffness of the material.

Consolidated undrained tests performed on fully saturated specimens revealed a relatively small true cohesion and confirm the strong hydro-mechanical coupled behaviour of Opalinus Clay. This strong hydro-mechanical coupled behaviour, in particular pore-pressure changes that are associated with unloading stress path and the tendency of Opalinus Clay to dilate, may explain the stability of borecores and tunnel excavations in the short term. Pore-pressures develop which are below atmospheric pressure or rather absolute negative. This pore-pressure drop causes effective stress states that favour stability in the short term, but may cause longer-term deformations and a further development of the excavation damaged zone as the pore-pressure dissipates.

Our in situ experiment examined the formation and development of an EDZ that evolves around excavations which are excavated parallel or normal to the bedding plane orientation. Macroscopic fracturing is strongly influenced by the presence of bedding planes and tectonic fault planes. A transition from extensional macroscopic failure to shearing can be observed with increasing fault plane frequency in section where opening or shearing along bedding planes or tectonic fault planes is kinematically free. In sections where bedding plane shearing/shearing along tectonic fractures is kinematically constrained, primary extensional type fractures develop. In addition, heterogeneities such as single tectonic fault planes or fault zone substantially modify the stress redistribution and thus zones around the excavation where new fractures may form.

During our research program we observed behavioural aspect of Opalinus Clay that are either typical for rocks or soils. Due to the observed dependency of Opalinus Clay on the water content and therefore typical transitional character of the rock, our research suggests that the shaly facies of the Opalinus Clay at the Mont Terri Rock Laboratory can be classified as a, “soil-like” clay shale.

Acknowledgements Most of the funding of the projects described in this article was provided by the Swiss Federal Nuclear Safety Inspectorate (ENSI) with cost-sharing contributions from Swisstopo (Federal Office of Topography, Switzerland), BGR (Federal Institute for Geosciences and Natural Resources, Germany) and Chevron (USA). We also highly appreciate the scientific and technical contributions made by many partner organizations and scientists. Important partners of these projects have been ENSI (Martin Herfort, Meinert Rahn, Ernando Saraiva), BGR (Kristof Schuster, Torsten Tietz, Dieter Boeddener, Friedhelm Schulte, and Wilfried Stille), Swisstopo (Christophe Nussbaum, Nicolas Badertscher, Olivier Meier, David Jäggi, Claude Girardin, and Lukas Glur), University of Alberta at Edmonton (Derek Martin), CEMI (Peter Kaiser, Andrew Corkum), Queen's University (Mark Diederichs), the Technical Universities of Torino (Marco Barla), TU Graz (Manfred Blümel), the Geodetic Metrology and Engineering Geodesy Group of ETH Zurich (Stephan Schütz, Florence Vaudan), and many colleagues and students from the Department of Earth Sciences at ETH (Corrado Fidelibus, Keith Evans, Frank Lemy, Valentin Gischig, Jonas von Rütte, Jürgen Hansmann, Freddy Xavier Yugsi Molina, Christian Haug, Sophie Gschwind, Sebastian Zimmer, Linda Wymann, Nicolas Kupferschmid, Patric Walter, Matthew Perras, Claudio Madonna, and Hansruedi Maurer). We are grateful to the two reviewers (Prof. Derek Martin and Dr. Bill Lanyon) for their valuable comments.

References

- Amann, F., Button, E. A., Evans, K. F., Gischig, V. S., & Blümel, M. (2011). Experimental study of the brittle behavior of clay shale in short-term unconfined compression. *Rock Mechanics and Rock Engineering*, *44*(4), 415–430.
- Amann, F., Kaiser, P. K., & Button, E. A. (2012a). Experimental study of the brittle behavior of clay shale in rapid triaxial compression. *Rock Mechanics and Rock Engineering*, *45*(1), 21–33.
- Amann, F., Thoeny, R., & Martin, C. D. (2012b). Rock mechanical considerations associated with the construction of a nuclear waste repository in clay rock. In *Proceedings of the 46th US Rock Mechanics/Geomechanics Symposium 2012*, Chicago, American Rock Mechanics Association.
- Amann, F., Wild, K. M., & Martin, C. D. (2015). The role of capillary suction and dilatancy on the interpretation of the confined strength of clay shales. In *Proceedings of the 13th International Congress of Rock Mechanics/Shale Symposium, 2015, Montreal*, International Society for Rock Mechanics.
- Anagnostou, G. (2009). The effect of advance-drainage on the short-term behavior of squeezing rocks in tunneling. In *Proceedings of the International symposium on computational geomechanics, Juan-Les-Pins, France* (pp. 668–679).
- Aristorenas, G. V. (1992). *Time-dependent behavior of tunnels excavated in shale*. Ph.D. dissertation, Massachusetts Institute of Technology, Cambridge, Massachusetts, USA.
- Badertscher, N., Girardin, C., & Nussbaum, C. (2008). SE-H Experiment: EDZ structural analyses of resin impregnated sections from BSE-3 overcores. *Mont Terri Technical Note*, TN 2008-15. Federal Office of Topography (swisstopo), Wabern, Switzerland. www.mont-terri.ch.
- Bellwald, P. (1990). *A contribution to the design of tunnels in argillaceous rock*. Ph.D. dissertation, Massachusetts Institute of Technology, Cambridge, Massachusetts, USA.
- Bishop, A. W., & Eldin, G. (1950). Undrained triaxial tests on saturated sands and their significance in the general theory of shear strength. *Géotechnique*, *2*(1), 13–32.
- Bobet, A., Aristorenas, G., & Einstein, H. H. (1999). Feasibility analysis for a radioactive waste repository tunnel. *Tunnelling and Underground Space Technology*, *13*(4), 409–426.
- Bossart, P. (2008) Annex 4-12. In P. Bossart, & M. Thury (Eds.), *Mont Terri Rock Laboratory. Project, Programme 1996 to 2007 and Results*. Reports of the Swiss Geological Survey, No.3. Federal Office of Topography (swisstopo), Wabern, Switzerland. www.mont-terri.ch.
- Bossart, P., Bernier, F., Birkholzer, J., Bruggeman, C., Connolly, P., Dewonck, S., Fukaya, M., Herfort, M., Jensen, M., Matray, J.-M., Mayor, J. C., Moeri, A., Oyama, T., Schuster, K., Shigeta, N., Vietor, T., & Wiczorek, K. (2017). Mont Terri rock laboratory, 20 years of research: introduction, site characteristics and overview of experiments. *Swiss Journal of Geosciences*. doi:10.1007/s00015-016-0236-1 (this issue).
- Bossart, P., Trick, T., Meier, P. M., & Mayor, J.-C. (2004). Structural and hydrogeological characterisation of the excavation-disturbed zone in the Opalinus Clay (Mont Terri Project, Switzerland). *Applied Clay Science*, *26*, 429–448.
- Corkum, A. G., & Martin, C. D. (2007). Modelling a mine-by test at the Mont Terri rock laboratory, Switzerland. *International Journal of Rock Mechanics and Mining Sciences*, *44*, 846–859.
- Einstein, H. H. (2000). Tunnels in Opalinus Clayshale—A review of case histories and new developments. *Tunnelling and Underground Space Technology*, *15*(1), 13–29.
- Giger, A. B., Marschall, P., Lanyon, B., & Martin, C. D. (2015). Hydro-mechanical response of Opalinus Clay during excavation works—A synopsis from the Mont Terri ROCK LABORATORY. *Geomechanics and Tunneling*, *8*(5), 421–425.
- Golder, H. Q., & Skempton, A. W. (1948). The angle of shearing resistance in cohesive soils for tests at constant water content. In *Proceedings of the Second International Conference of Soil Mechanics and Foundation Engineering, Vol. 1*, (pp. 185–192).
- Islam, M. A., & Skalle, P. (2013). An experimental investigation of shale mechanical properties through drained and undrained test mechanisms. *Rock Mechanics and Rock Engineering*, *46*, 1391–1413.
- ISRM. (1978). Suggested methods for determining tensile strength of rock materials. *International Journal of Rock Mechanics and Mining Sciences & Geomechanical Abstracts*, *15*, 99–103.
- ISRM. (1979). Suggested methods for determining the uniaxial compressive strength and deformability of rock materials. *International Journal of Rock Mechanics and Mining Science & Geomechanical Abstracts*, *16*(2), 135–140.
- Itasca (2009). Fast Lagrangian Analysis of Continua in 3 dimensions, Version 4. *Itasca Consulting Group*, 438.
- Jaeggi, D., Nussbaum, C., Moeri, A., Shao, H., & Mueller, H. (2010). WS-H experiment: overcoring and structural analyses of the resin-impregnated BHG-B11 overcore under plane and UV light. *Mont Terri Technical Note*, TN 2010-32. Federal Office of Topography (swisstopo), Wabern, Switzerland. www.mont-terri.ch.
- Klinkenberg, M., Kaufhold, S., Dohrmann, R., & Siegesmund, S. (2009). Influence of carbonate microfabric on the failure strength of claystones. *Engineering Geology*, *107*, 42–54.
- Kupferschmid, N., Wild, K. M., Amann, F., Nussbaum, C., Jaeggi, D., & Badertscher, N. (2015). Time-dependent fracture formation around a borehole in a clay shale. *International Journal of Rock Mechanics and Mining Sciences*, *77*, 105–114.
- Marschall, P., Distinguin, M., Shao, H., Bossart, P., Enachescu, C., & Trick, T. (2006). Creation and evolution of damage zones around a microtunnel in a claystone formation of the Swiss Jura Mountains. In *SPE International Symposium and Exhibition on Formation Damage Control*, Society of Petroleum Engineers.
- Marschall, P., Horseman, S., & Gimmi, T. (2005). Characterisation of gas transport properties of the Opalinus Clay, a potential host rock formation for radioactive waste disposal. *Oil & Gas Science and Technology*, *60*(1), 121–139.

- Martin, C. D. (1997). Seventeenth Canadian Geotechnical Colloquium: The effects of cohesion loss and stress path on brittle rock strength. *Canadian Geotechnical Journal*, 34, 698–725.
- Martin, C. D., Lanyon, G. W., Bossart, P., & Blümling, P. (2004). Excavation disturbed zone (EDZ) in clay shale: Mont Terri. *Mont Terri Technical Report*, TR 01-01. Federal Office of Topography (swisstopo), Wabern, Switzerland. www.mont-terri.ch.
- Martin, C. D., Macciotta, R., Elwood, D., Lan, H., & Vietor T. (2011). Evaluation of the Mont Terri Mine-By response: Interpretation of results and observations. Report to Nagra (unpublished).
- Masset, O. (2006). Rock Laboratory pore pressure long term evolution. *Mont Terri Technical Note*, TN 2006-43. Federal Office of Topography (swisstopo), Wabern, Switzerland. www.mont-terri.ch.
- Mazurek, M. (1998). Mineralogical composition of Opalinus Clay at Mont Terri—A laboratory intercomparison. *Mont Terri Technical Note*, TN 98-41. Federal Office of Topography (swisstopo), Wabern, Switzerland. www.mont-terri.ch.
- Mazurek, M., Hurford, A. J., & Leu, W. (2006). Unravelling the multi-stage burial history of the Swiss Molasse Basin: integration of apatite fission track, vitrinite reflectance and biomarker isomerisation analysis. *Basin Research*, 18, 27–50.
- Nagra (2002). Projekt Opalinuston. Synthese der geowissenschaftlichen Untersuchungsergebnisse. *Nagra Technischer Bericht*, 20-03. Nagra, Wettingen, Switzerland. www.nagra.ch.
- Neerdael, B., DeBruyn, D., Mair, R. J., & Taylor, R. N. (1999). Geotechnical behavior of Boom Clay. Commission of the European Communities. *Nuclear Science and Technology, Pilot tests on radioactive waste disposal in underground facilities, EUR 13985*, 223–238.
- Nussbaum, C., Bossart, P., Amann, F., & Aubourg, C. (2011). Analysis of tectonic structures and excavation induced fractures in Opalinus Clay, Mont Terri underground Rock Laboratory (Switzerland). *Swiss Journal of Geoscience*, 104(2), 187–210.
- Nussbaum, C., Kloppenburg, A., Caër, T., & Bossart, P. (2017). Tectonic evolution around the Mont Terri rock laboratory, northwestern Swiss Jura: constraints from kinematic forward modelling. *Swiss Journal of Geosciences*, 110. doi:10.1007/s00015-016-0248-x (this issue).
- Pei, J. (2003). *Effect of sample disturbance in Opalinus Clay shales*. Ph.D. dissertation, Massachusetts Institute of Technology, Cambridge, Massachusetts, USA.
- Peron, H., Hueckel, T., Laloui, L., & Hu, L. B. (2009). Fundamentals of desiccation cracking of fine-grained soils: experimental characterization and mechanisms identification. *Canadian Geotechnical Journal*, 46, 7–1201.
- Popp, T., Salzer, K., & Minkley, W. (2008). Influence of bedding planes to EDZ-evolution and the coupled HM properties of Opalinus Clay. *Physics and Chemistry of the Earth*, 33, 374–387.
- Rummel, F., & Weber, U. (2004). RA experiment: rock mechanical testing and characterization on drillcores of boreholes BRA-1 and BRA-2. *Mont Terri Technical Note*, TN 2004-38. Federal Office of Topography (swisstopo), Wabern, Switzerland. www.mont-terri.ch.
- Schmertmann, J. H., & Osterberg, J. O. (1960). An experimental study of the development of cohesion and friction with axial strain in saturated cohesive soils. In *Research Conference on Shear Strength of Cohesive Soils* (pp. 643–694). American Society of Civil Engineers.
- Schnier, H., & Stührenberg, D. (2007). LT experiment: strength tests on cylindrical specimens, documentation and evaluation (Phases 8 & 9). *Mont Terri Technical Report*, TR 03-04. Federal Office of Topography (swisstopo), Wabern, Switzerland. www.mont-terri.ch.
- Skempton, A. W. (1954). The pore-pressure coefficients A and B. *Géotechnique*, 4(4), 143–147.
- Thoeny, R. (2014). *Geomechanical analysis of excavation-induced rock mass behavior of faulted Opalinus Clay at the Mont Terri Underground Rock Laboratory (Switzerland)*. Ph.D. dissertation, Swiss Federal Institute of Technology, Zürich, Switzerland.
- Thury, M., & Bossart P. (1999). Mont Terri rock laboratory, results of the hydrogeological, geochemical and geotechnical experiments performed in 1996 and 1997. *Landeshydrologie und -geologie, Geologischer Bericht No. 23*. Federal Office of Topography (swisstopo), Wabern, Switzerland. www.mont-terri.ch.
- Van Loon, L. R., Soler, J. M., Müller, W., & Bradbury, M. H. (2004). Anisotropic diffusion in layered argillaceous rocks: a case study with Opalinus Clay. *Environmental Science and Technology*, 38, 5721–5728.
- Vietor, T., Armand, G., Nyonoaya, S., Schuster, K., & Wiczorek, K. (2010). Excavation induced damage evolution during a mine-by experiment in Opalinus clay. In *Proceedings of the 4th Int. Meeting on Clays in Natural & Engineered Barriers for Nuclear Waste Confinement, Nantes, France*.
- Walter, P. (2015). *Environmental degradation of Opalinus Clay with cyclic variations in relative humidity*. Master thesis, Swiss Federal Institute of Technology, Zürich, Switzerland.
- Wild, K. M., Amann, F., & Martin, C. D. (2015a). Dilatancy of clay shales and its impact on pore pressure evolution and effective stress for different triaxial stress paths. In *Proceedings of the 49th US Rock Mechanics/Geomechanics Symposium*, American Rock Mechanics Association.
- Wild, K. M., Amann, F., & Martin, C. D. (2015b). Some fundamental hydromechanical processes relevant for understanding the pore pressure response around excavations in low permeable clay rocks. In *Proceedings of the 13th International Congress of Rock Mechanics*. International Society for Rock Mechanics.
- Wild, K. M., Wymann, L. P., Zimmer, S., Thoeny, R., & Amann, F. (2015c). Water retention characteristics and state-dependent mechanical and petro-physical properties of a clay shale. *Rock Mechanics and Rock Engineering*, 48, 427–439.
- Yong, S. (2007). *A three-dimensional analysis of excavation-induced perturbations in the Opalinus Clay at the Mont Terri Rock Laboratory*. Ph.D. dissertation, Swiss Federal Institute of Technology, Zürich, Switzerland.
- Yong, S., Kaiser, P. K., & Loew, S. (2010). Influence of tectonic shears on tunnel-induced fracturing. *International Journal of Rock Mechanics and Mining Sciences*, 47, 894–907.
- Yong, S., Kaiser, P. K., & Loew, S. (2013). Rock mass response ahead of an advancing face in faulted shale. *International Journal of Rock Mechanics and Mining Sciences*, 60, 301–311.

Hydro-mechanical evolution of the EDZ as transport path for radionuclides and gas: insights from the Mont Terri rock laboratory (Switzerland)

Paul Marschall¹ · Silvio Giger¹ · Rémi De La Vassière² · Hua Shao³ · Helen Leung⁴ · Christophe Nussbaum⁵ · Thomas Trick⁶ · Bill Lanyon⁷ · Rainer Senger⁸ · Andrea Lisjak⁹ · Andrés Alcolea¹⁰

Received: 29 March 2016 / Accepted: 9 December 2016 / Published online: 17 February 2017
© Swiss Geological Society 2017

Abstract The excavation damaged zone (EDZ) around the backfilled underground structures of a geological repository represents a release path for radionuclides, which needs to be addressed in the assessment of long-term safety. Additionally, the EDZ may form a highly efficient escape route for corrosion and degradation gases, thus limiting the gas overpressures in the backfilled repository structures. The efficiency of this release path depends not only on the shape and extent of the EDZ, but also on the self-sealing capacity of the host rock formation and the prevailing state conditions, such as in situ stresses and pore pressure. The hydro-mechanical and chemico-osmotic phenomena associated with the formation and temporal evolution of the EDZ are complex, thus precluding a detailed representation of the EDZ in conventional

modelling tools for safety assessment. Therefore, simplified EDZ models, able to mimic the safety-relevant functional features of the EDZ in a traceable manner are required. In the framework of the Mont Terri Project, a versatile modelling approach has been developed for the simulation of flow and transport processes along the EDZ with the goal of capturing the evolution of hydraulic significance of the EDZ after closure of the backfilled underground structures. The approach draws on both empirical evidence and experimental data, collected in the niches and tunnels of the Mont Terri rock laboratory. The model was benchmarked with a data set from an in situ self-sealing experiment at the Mont Terri rock laboratory. This paper summarises the outcomes of the benchmark exercise that comprises relevant empirical evidence, experimental data bases and the conceptual framework for modelling the evolution of the hydraulic significance of the EDZ around a backfilled tunnel section during the entire re-saturation phase.

Editorial handling: P. Bossart and A. G. Milnes.

The abbreviations EDB, EZ-A, EZ-B, FE, GP, GP-A, GS, HG-A, SE-H denote in situ experiments at the Mont Terri rock laboratory.

This is paper #8 of the Mont Terri Special Issue of the Swiss Journal of Geosciences (see Bossart et al. 2017, Table 3 and Fig. 7).

✉ Paul Marschall
paul.marschall@nagra.ch

¹ National Cooperative for the Disposal of Radioactive Waste NAGRA, Hardstrasse 73, 5430 Wettingen, Switzerland

² Agence Nationale Nationale pour la Gestion des Déchets Radioactifs ANDRA, Meuse Haute-Marne, Center RD 960, 55500 Bure, France

³ Federal Institute for Geosciences and Natural Resources BGR, Stilleweg 2, 30655 Hannover, Germany

⁴ Nuclear Waste Management Organization NWMO, 22 St. Clair Ave. E., Toronto, ON, Canada

⁵ Federal Office of Topography swisstopo, 3084 Wabern, Switzerland

⁶ Solexperts AG, Mettlenbachstrasse 25, 8617 Mönchaltorf, Switzerland

⁷ Fracture Systems Ltd., Tregurrian, Ayr, St Ives, Cornwall, UK

⁸ Intera Incorporated, 1933 Jadwin Avenue, Suite 130, Richland, WA 99354, USA

⁹ Geomechanica Inc., 90 Adelaide St W, Toronto, ON M5H 4A6, Canada

¹⁰ TK Consult AG, Mainaustrasse 30, 8008 Zurich, Switzerland

Keywords Thermo-hydro-mechanical (THM) processes · Excavation damaged zone (EDZ) · EDZ self-sealing · Opalinus clay · THM modelling · Geological disposal of nuclear waste

Abbreviations

DECOVALEX	Development of coupled models and their validation against experiments
DFN	Discrete fracture network
EDZ	Excavation damaged zone
EPM	Equivalent porous medium
FDEM	Finite discrete element method
FORGE	Fate Of Repository Gases–EURATOM Collaborative Project/7th Framework Programme
GI1, 2 and 3	Long-term gas injection experiments in the HG-A experiment
NFPRO	Understanding and physical and numerical modeling of the key processes in the near field–EURATOM Integrated Project/6th Framework Programme
SA	Safety assessment
SF/HLW	Spent fuel/high level waste
SATP	Standard ambient temperature and pressure conditions (25 °C, 101 kPa)
TDR	Time domain reflectometer
THMC	Thermo-hydro-mechanical-chemical coupled processes
TIMODAZ	Thermal impact on the damaged zone around a radioactive waste disposal in clay host rocks EURATOM Collaborative Project/6th Framework Programme
NNW, SSE	Strike directions of the main tectonic fracture systems at Mont Terri CODE_BRIGHT, FLAC3D, TOUGH2, T2GGM are academic and commercial codes for THM modelling

1 Introduction

The construction of the underground facilities of a geological repository for radioactive waste, the emplacement of wastes during the operational phase, and the closure operations in different parts of the repository will induce perturbations of state variables (e.g. stress, water pressure, temperature, saturation, chemical composition of the pore-water) in the host rock around the underground structures. These perturbations are associated with several coupled thermo-hydro-mechanical-chemical phenomena (THMC). Within the zone where these perturbations occur there may

exist a zone of damaged rock. According to Tsang et al. (2005), the excavation damaged zone (EDZ) is a zone around the underground structures with significant irreversible processes and significant changes in flow and transport properties. These changes include, for example, one or more orders of magnitude increase in flow permeability.

In the framework of safety assessment (SA), a balanced evaluation of the impact of repository-induced effects on long-term safety is required. Such evaluation includes, but is not limited to, the role of the EDZ around the backfilled underground structures. The hydraulic significance of the EDZ as viable release path for radionuclides serves as a quantitative input for dose calculations. Furthermore, the EDZ may contribute in a beneficial way to repository performance as it represents an efficient pathway for the escape of repository gases associated with the corrosion and degradation of the wastes (see Nagra (2008) and Nagra (2016) for further details).

Dose calculations for SA require simplified abstractions of the EDZ. These abstractions represent the water/gas transport capacity of the EDZ after backfilling and sealing of the underground structures in terms of effective parameters for the thickness, hydraulic conductivity and porosity of the EDZ. It is common to describe the EDZ as a homogeneous circular shell around the backfilled tunnels (e.g. Lanyon and Senger 2011). Yet, robust assessments require a rigorous analysis of the associated conceptual and parametric uncertainties. Such analysis includes a detailed evaluation of the complete history of the EDZ, comprising its creation during repository construction, its evolution during the operational period and the post closure behaviour after backfilling of the underground structures. The shape and the extent of the EDZ are mainly controlled by the geological setting, initial state conditions (e.g. pore pressure, stress state), the excavation procedures and the design of the tunnel support system. The hydraulic significance of the excavation-induced release paths is affected by the action of the THMC phenomena and processes during the operational times and after repository closure.

Excavation damaged and disturbed zones have been studied in a range of rocks since the 1980s (Wilson et al. 1983). An early conceptualization of the EDZ in a low porosity marl formation (Helvetic Marls at the Wellenberg site in Central Switzerland) was presented in Nagra (1997). A comprehensive appraisal was dedicated to the creation and evolution of the EDZ in the Opalinus Clay formation at a repository depth of 650 m (Nagra 2002). In the EURATOM Integrated Project “NFPRO”, a state-of-the-art report on the creation and evolution of the EDZ was compiled, comprising a synopsis of experience from investigations in hard rocks, rock salt and clay formations (Alheid et al. 2007). The overall achievements of the

“NFPRO” research programme were summarized in the Final Synthesis Report (Aranyosy et al. 2008). More recently, a review of studies on the EDZ around excavations in sedimentary rocks was presented by Lanyon (2011). So far, full-scale investigations on EDZ development in indurated clays have been limited to the underground laboratories of Mont Terri (Lanyon et al. 2014), Tournemire (Rejeb et al. 2008) and the Meuse/Haute Marne site (Armand et al. 2013a, b).

Over the last two decades, the EDZ-related research programmes at the Mont Terri rock laboratory (Fig. 1) have gained recognition in the geoscientific community worldwide. As a result, new insights on the creation and evolution of the EDZ in indurated clays have seen light:

- Empirical evidence, contributing to the characterisation of the shape and extent of the EDZ for a variety of geological conditions, different excavation methods and tunnel support designs.
- Dedicated THMC experiments with emphasis on the phenomena and coupled processes governing flow and transport along the EDZ.
- Integrated experimental programmes providing qualitative and quantitative evidence of the gas and water transport capacity of the EDZ along seal sections of underground structures during all evolutionary stages.
- Complementary modelling programmes, aimed at the development and validation of traceable modelling workflows and simplified EDZ abstraction schemes.

The synopsis presented here refers to the key experiments at the Mont Terri rock laboratory in the fields of

EDZ related research and summarises distinguished achievements.

2 EDZ related phenomena and processes

2.1 Basic considerations

The nature and magnitude of excavation-induced damage around the underground structures of a geological repository evolve over time according to the life phase of the disposal system. Alheid et al. (2007) identified four major evolutionary phases, with corresponding phenomena and processes, in the context of the EC-funded project NFPRO: (i) the excavation phase, associated with coupled hydro-mechanical processes in the rock mass in response to mechanical unloading, (ii) the operational phase, affected by the ventilation of the underground structures, drainage of the rock mass and various perturbations due to operations in the repository, (iii) the backfilling and sealing of emplacement rooms, leading to resaturation of the unsaturated zone, heating effects around the high level waste (HLW) emplacement tunnels and coupled THM phenomena, and (iv) the repository closure phase, characterised by progressive resaturation of the host rock around the repository and saturation of the underground facilities, what induces chemical loadings able to amplify the interaction between chemical and mechanical processes.

Indurated clays such as the Opalinus Clay form a class of rock between soft rocks and hard clays. The strength of these rocks is relatively low, but tunneling is still feasible

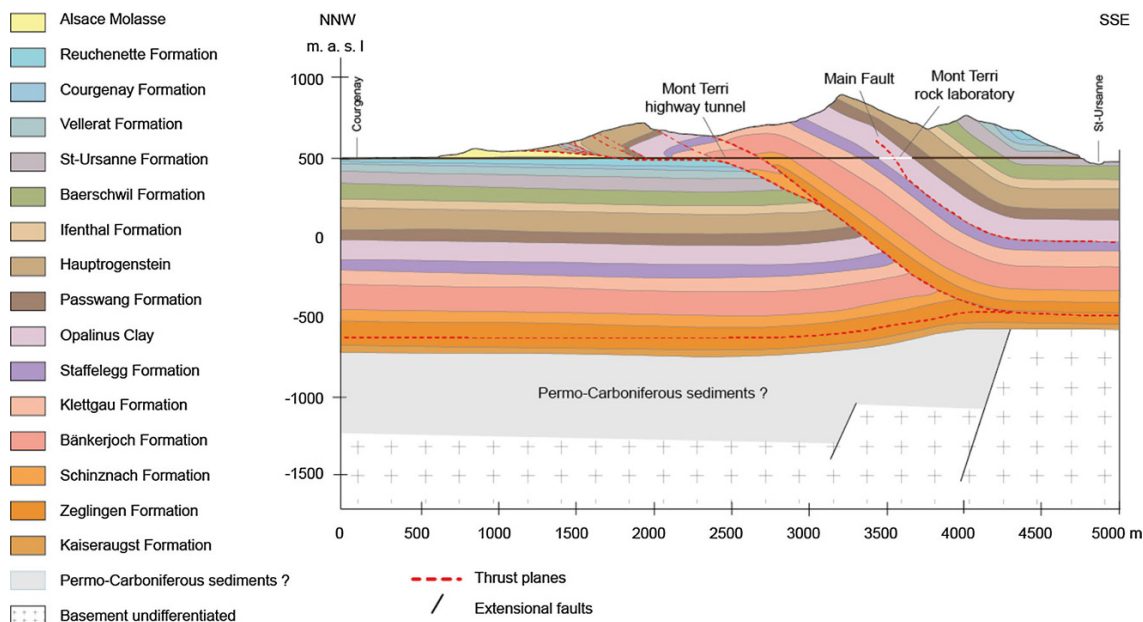


Fig. 1 Geological cross-section of the Mont Terri anticline and location of the Mont Terri rock laboratory (Nussbaum et al. 2017)

even with standard methods and low to medium support measures. The rock permeability is very low and even existing natural fractures do not show increased transmissivity as long as a significant normal stress is acting on the fracture surfaces. Similar to hard rocks (e.g. Martin et al. 2001) the stability of excavations can be considered under three classes:

- Structurally controlled failure (i.e. failure associated with reduced rock strength due to sedimentary and tectonic structures);
- Stress-controlled failure (i.e. failure associated with elevated deviator stress around the cavities);
- A combination of structure- and stress-controlled failure.

The application of such a failure classification scheme to clay-rich rocks is complicated by compaction processes, bedding-induced anisotropy and the influence of wetting. In this context, the following processes are of particular importance:

- Swelling, weakening and softening (see Steiner 1996 and Einstein 2002);
- Shrinkage during drying and loss of strength due to repeated wetting/drying cycles.

Structurally-controlled wedge-type failures can be managed by maintaining a compressive stress regime (Diederichs and Kaiser 1999) and identifying the relevant discontinuity sets. Yet, problems may occur at intersections

with other excavations or in regions with unexpected discontinuity orientations. Furthermore, within the repository, fault zones should be avoided in tunnel sections designated for seal emplacement. The focus for the EDZ-related studies is therefore on stress-controlled failure and combinations of stress/structure failure modes.

2.2 Phenomenology: empirical evidence

The creation and evolution of the EDZ around the openings is controlled by several factors, including the hydro-mechanical state conditions (e.g. stress, pore pressure, temperature), engineering design (e.g. configuration of the underground structures, size and shape of tunnel cross-sections, excavation technique, support system/lining) and the impacts on the system during the operational phase (e.g. ventilation, waste emplacement). The deformation behaviour is further complicated, amongst others, by (i) rock anisotropy (stiffness and strength), (ii) spatial variability of rock fabric (facies variability and tectonic features) and (iii) clay-specific hydro-mechanical couplings, giving rise to long-lasting time-dependent processes in the EDZ even after closure of the backfilled repository structures. Typical features of the rock mass fabric observed in the Opalinus Clay at Mont Terri are shown in Fig. 2. These include geostructural features observed at different scales, from the millimetre to the meter, and associated with both sedimentary and tectonic processes.

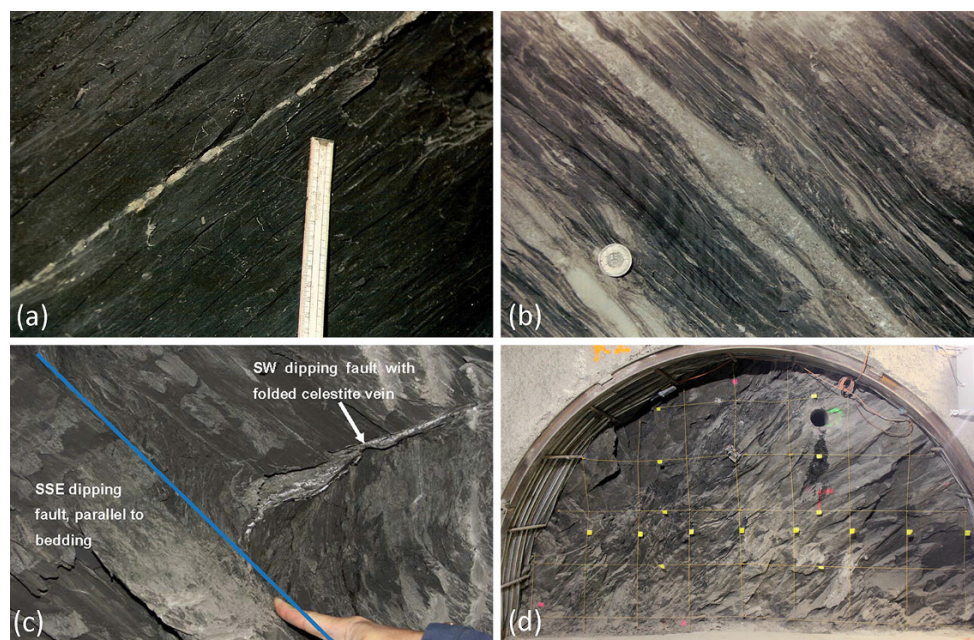


Fig. 2 Heterogeneity and anisotropy in the Opalinus Clay at Mont Terri (natural state): **a** dark grey silty, calcareous layers of the shaly facies with a vein of celestite; **b** silty to sandy marls of the sandy

facies with sandstone lenses cemented with carbonates; **c** SW dipping fault associated with a folded vein of celestite; **d** the Main Fault intersecting Gallery 98 in window through shotcrete

The inventory of brittle EDZ features (i.e., caused directly by the short-term excavation-induced unloading and loading) includes extensional fractures (Fig. 2a), spalling and buckling of the bedding planes (Fig. 2b, c), interactions with the existing tectonic features (Fig. 2b), bedding slip, single shear fractures and shear-bands (Fig. 3). Far reaching bounding shear bands delimit the EDZ and the intact rock zones (Blümling et al. 2007).

Further EDZ features can be attributed to the operational phase, such as desiccation cracks in response to tunnel ventilation and swelling-induced disaggregation of the rock matrix, when subjected to water-based fluids (e.g. cement water during the construction of the invert; water injections in boreholes, see Fig. 4a). In the Mont Terri rock laboratory, the prevailing ventilation conditions and the gravity driven pore-water drainage towards the tunnel system

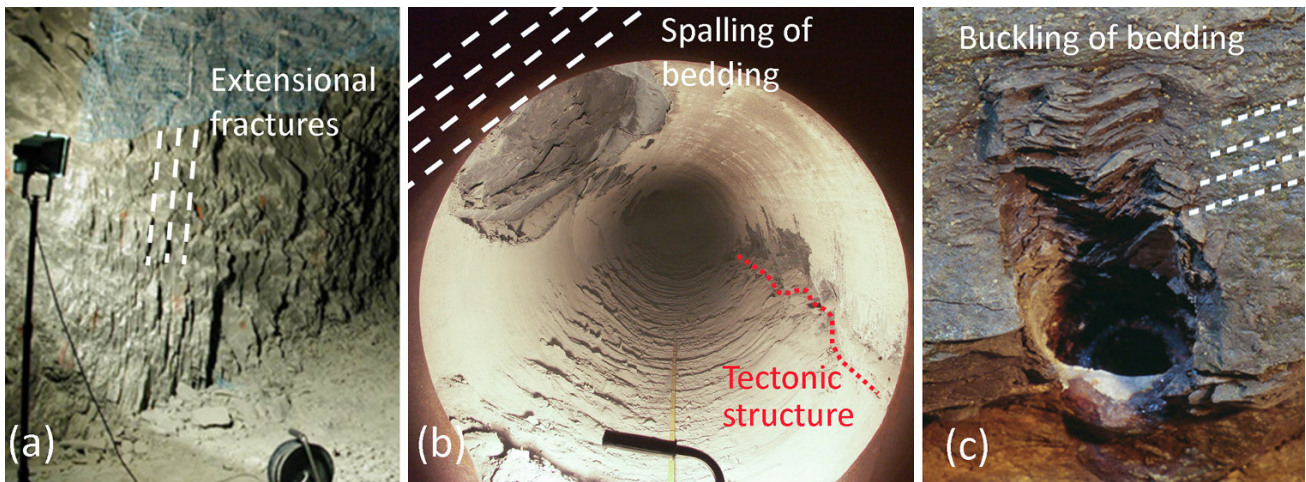


Fig. 3 Excavation-induced brittle features in Opalinus Clay (Mont Terri rock laboratory): **a** extensile fractures created during the excavation of Gallery 98 (Nagra 2002); **b** bedding related spalling processes in the crown of the HG-A microtunnel and interaction of

stress controlled failure at the lower right side wall with a tectonic structure (Marschall et al. 2006); **c** buckling of the bedding planes around a small borehole (Blümling et al. 2007)

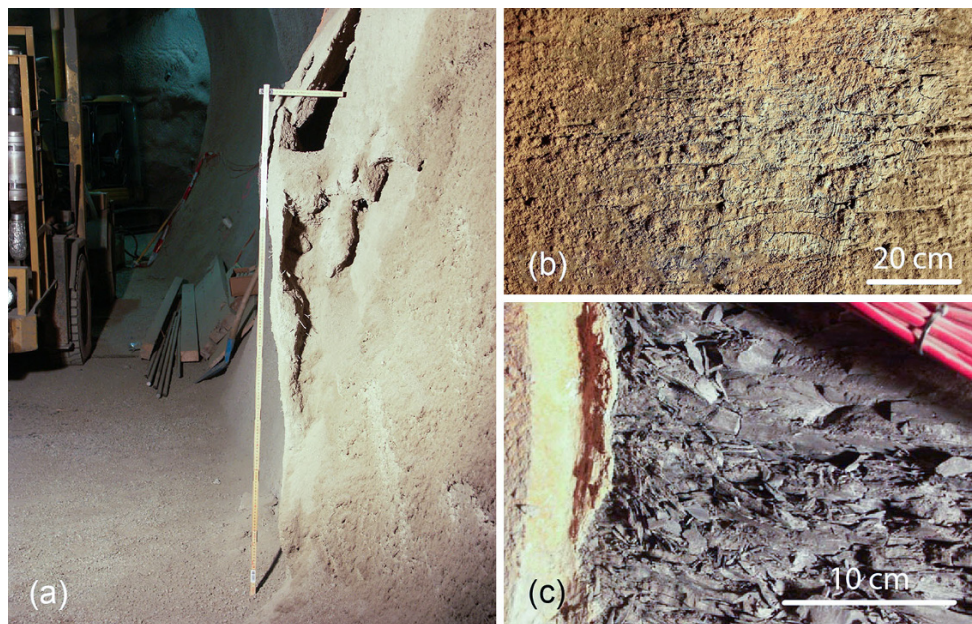


Fig. 4 EDZ-related phenomena in the Opalinus Clay during the operations phase of the Mont Terri rock laboratory: **a** damage of the shotcrete liner caused by swelling and creep processes; **b** desiccation cracks at the tunnel wall of the HG-A microtunnel in response to

tunnel ventilation; **c** degradation of the Opalinus Clay caused by water uptake at the contact zone between liner and rock (HG-A microtunnel)

cause a significant impact on the development of the EDZ. Cyclic deformation of the tunnel surface due to earth tides, as well as seasonal variations of barometric pressure, humidity and temperature lead to progressive degradation of the EDZ (Fig. 4b). Furthermore, monitoring and maintenance activities in support of the implementation of the in situ experiments may have increased the size of the EDZ in the long-term (e.g. water uptake during instrumentation of the HG-A tunnel; see Fig. 4c). In a real repository environment, there are further phenomena and processes, which may lead to a continuous weakening of the rock mass around the tunnel, such as ground motion associated with waste emplacement operations (successive excavation of emplacement tunnels, transportation of waste canisters, etc.). The weakening of the EDZ during the operational phase is associated predominantly with time-dependent ductile failure mechanisms (also termed “creep”), going along with a gradual loss of cohesion in the rock matrix and the development of fault gouges along fracture planes.

2.3 Extent of the EDZ and failure mechanisms

In the Mont Terri rock laboratory, the extent and shape of the EDZ have been characterized at various experimental sites using both geological and geophysical methods. Geological investigations include structural mapping of excavation surfaces (tunnel walls, niches and wallrock “windows”) and core mapping of boreholes drilled from the excavation (most commonly radial boreholes). Classification schemes were established to discriminate between natural (tectonic) fractures and faults, EDZ-related features and artificially induced fractures caused by drilling and core handling.

Structural mapping of the tunnel walls of the newly excavated cavities has been a routine procedure associated with all previous extensions of the Mont Terri rock laboratory. In addition, dedicated experimental programmes were initiated to characterise in a systematic way the shape and extent of the EDZ and to establish inventories of EDZ features for tunnel sections parallel and normal to bedding. A comprehensive compilation of the corresponding structural data bases is given in Lanyon et al. (2014), comprising structural maps and structural analyses of core samples from the EZ-A niche, Gallery 04, EZ-B niche, HG-A microtunnel, Gallery 08, Mine-By Experiment and the FE-Experiment. The compilation refers—amongst other aspects—to the detailed evaluation of EDZ fracture statistics by Yong (2007), which draws on elaborate analysis of fracture density from over 100 boreholes (see Fig. 5). Yong’s evaluations reveal that fracture count in the first 0.5 m can be as high as 10 (mean spacing of 5 cm between fractures) around some excavations but typically reduces to less than 2 between 2.5 and 3 m from the tunnel

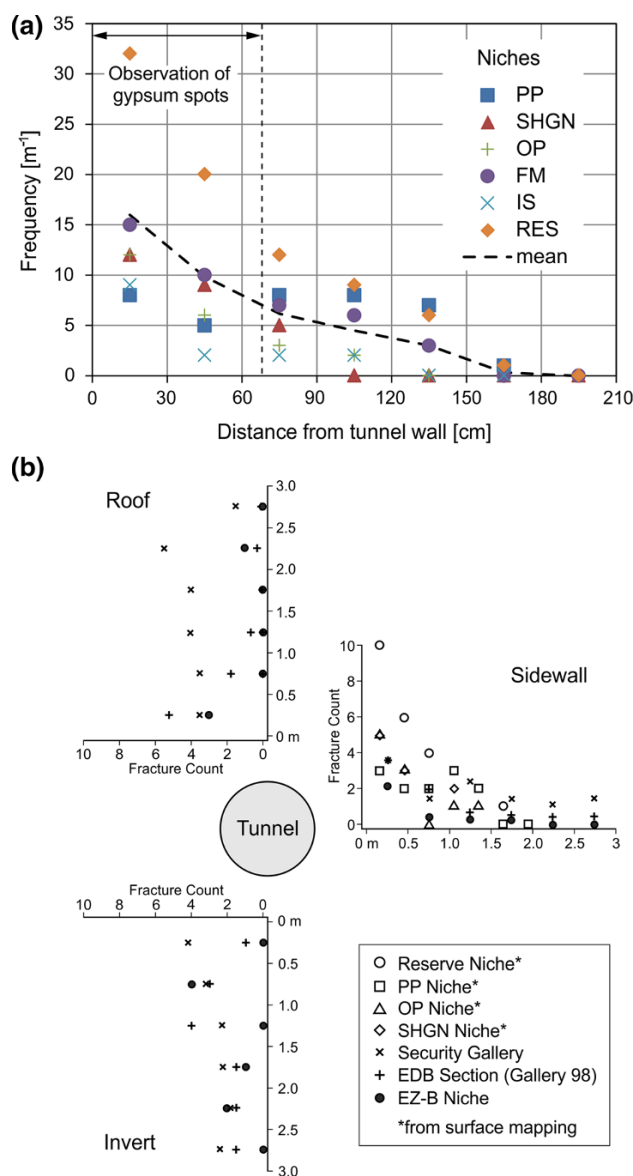


Fig. 5 Fracture statistics derived from tunnel mapping and borehole logging: **a** line-counted frequencies from the side walls of the niches in the security gallery (after Bossart et al. 2002) and **b** fracture counts in 0.5 m borehole intervals from the EZ-B Niche and previous sub-parallel excavations (from Yong 2007)

wall. Detailed investigation of macro-fracturing around the EZ-B niche suggested a much narrower zone of macro-fracturing with a thickness of ~ 20 cm and an outer zone extending to 70 cm characterised by a reduced seismic velocity. Almost all excavations show the highest fracture density close to the tunnel wall and significant drop in fracture frequency beyond 2 m from it.

Another method for core mapping developed at Mont Terri involves resin injection into a pilot hole followed by subsequent overcoring (Bossart et al. 2002, 2004). The resin injection method allows one to identify open (resin-impregnated) fractures within the EDZ and can give

information on the prevailing fracture mechanisms, reactivation of pre-existing features, connectivity and structural relationships. Labiouse and Vietor (2014) used this method in the context of the EC-funded TIMODAZ project (SE-H experiment) for analysing an overcore from a sub-horizontal 101 mm borehole, which had been used for a 3 year-long dilatometer test. Resin-impregnated core samples (Fig. 6a) corresponding to the test and packer sections show similar fracture patterns, indicating that the mechanisms leading to borehole collapse were similar and independent of the testing history. The sub-vertical buckling failure zones extend beyond the overcore (in excess of a borehole diameter).

The fracture mechanisms postulated by Labiouse and Vietor (2014) on the borehole scale exhibit distinct similarities with the conceptual model developed by Martin and Lanyon (2003) for the EDZ around the EDB section of Gallery 98. Extensional fractures formed in the excavation side-walls while the EDZ in the roof and floor was related to a region of potential bedding-slip and subsequent kink/buckling failures (see Fig. 6b). Blümling et al. (2007) further developed the model of Martin and Lanyon (2003), incorporating the observed buckling failure and through-going shears associated with bedding slip.

The aforementioned characterisation methods are complementary in the sense that different emphasis is placed on

various aspects of the EDZ and excavation orientation. In the past, numerous conceptual EDZ models have been developed for the Mont Terri rock laboratory, capable to explain the prevailing structural features and failure mechanisms for particular geological settings and a given excavation method. Thus, for excavations normal to bedding strike (i.e., sub-parallel to σ_{hmax}), Bossart et al. (2002) present a concept of “onion-like” extensile fractures forming an interconnected network within 1 m from the tunnel wall but tending to be isolated structures beyond this distance (Fig. 7a). For the same orientation of the excavation, Blümling et al. (2007) complement the concept of extensile fracturing by adding buckling and kink failures, commonly associated with zones of bedding slip and multiple through-going shears (Fig. 7b). Complex combinations of structural and stress induced failure (Fig. 7c) have been conceptualised by Marschall et al. (2006) for excavations along bedding strike (i.e., sub-parallel to σ_{hmin}).

The complexity of the geological setting (stress state, lithological variability, tectonic overprint) and the differences in the adopted excavation approaches makes it challenging to develop a generalised conceptual model of the EDZ at Mont Terri. Nevertheless, important conclusions can be drawn with respect to the inventory of characteristic EDZ features and the EDZ related phenomena and processes:

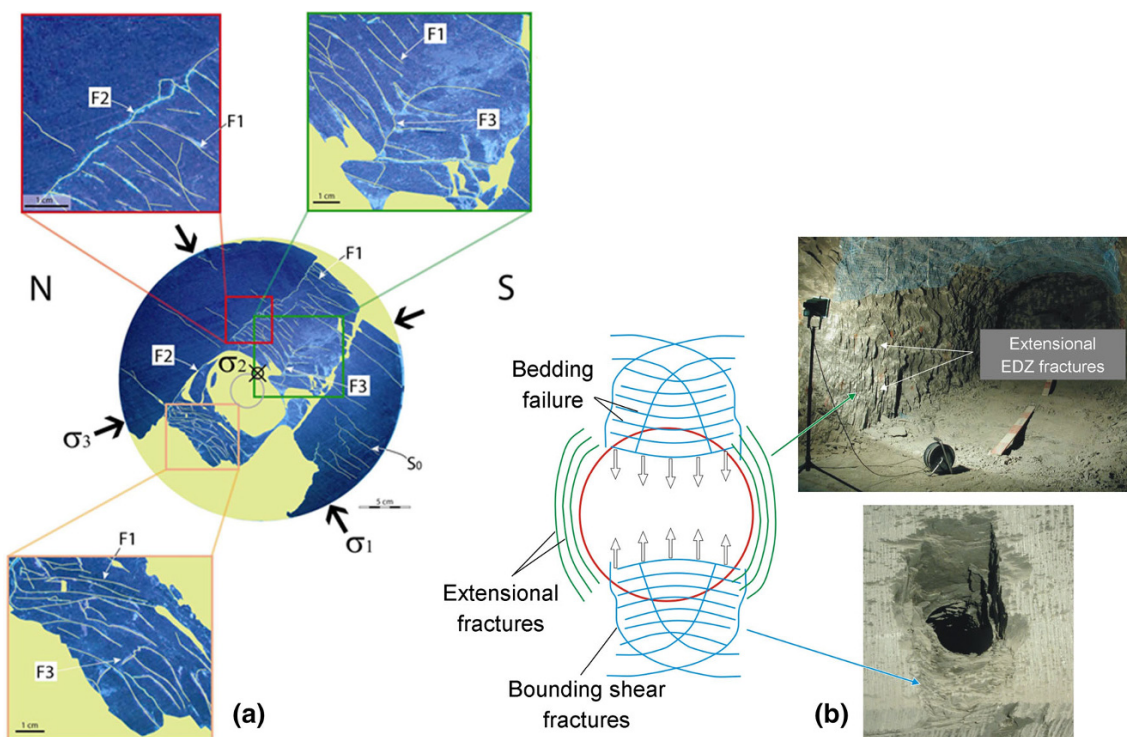


Fig. 6 Fracture mechanisms postulated by Labiouse and Vietor (2014): **a** analysis of resin impregnated core samples (SE-H project), **b** conceptual model of fracture mechanisms at the tunnel scale,

developed by Martin and Lanyon (2003) for the EDZ around the EDB section of Gallery 98

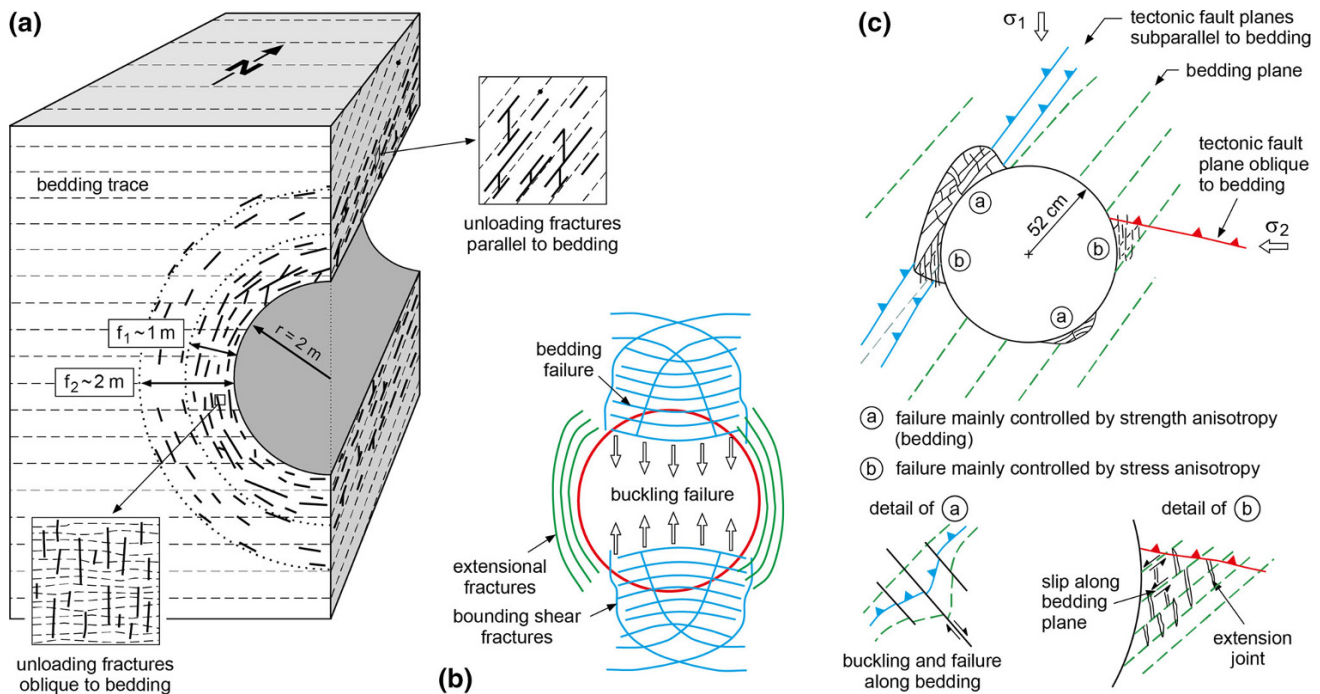


Fig. 7 Conceptual models of EDZ, derived in the framework of Mont Terri Project: **a** radial distribution of extensile fracturing (tunnel axis normal to bedding strike, sub-parallel to σ_{hmax} ; see also Bossart et al. 2002); **b** combined buckling failure and extensile fracturing (tunnel axis normal to bedding strike, sub-parallel to σ_{hmax} ; see also Blümling

et al. 2007); **c** schematic representation of the damage zone around the HG-A microtunnel, showing the key processes and features that affect borehole stability: slablike breakouts on the *upper left side* are caused by extensile failure along tectonic fractures and wedge-like breakouts on the *right side*

- Clear evidence was found, that the immediate (short-term) failure of the Opalinus Clay in response to the excavation process is brittle. The inventory of EDZ-related features can be classified as extensional fracturing, bedding parallel slip, buckling and kink failures, single shear fractures and shear bands and, eventually, reactivated tectonic features.
- The short-term response can be stress controlled, structurally controlled or a combination of both regimes.
- Governing parameters for stress controlled failure are the in situ stress tensor and the stress state ahead of the tunnel face. Thus, stress controlled failure is strongly related to the adopted excavation techniques and the progress of excavation.
- Structurally controlled failure is caused by sedimentary and tectonic structures. Variabilities in microstructure such as bedding or intercalations of sandy and clay-rich layers tend to create self-similar failure patterns (e.g. buckling), which are observed at scales ranging from small boreholes to the tunnel scale (see Fig. 3). In addition, reactivations of tectonic structures are highly irregular and, consequently, difficult to predict without detailed knowledge of the pre-existing fracture patterns.

- The long-term response of the rock during the operational phase in terms of tunnel convergence is largely associated with ductile failure mechanisms and can be conceptualised as a viscous component (termed “creep”) in the deformation behaviour of the rock.

2.4 Hydraulic characterisation of the EDZ

Representative transmissivity estimates of the EDZ fractures immediately after excavation are of high importance for the calibration of discrete fracture network models (DFN models; see Alcolea et al. 2016). To that end, small-scale in situ transmissivity measurements were carried out in radially oriented boreholes as part of the early EDZ related research programme (Bossart et al. 2002). The boreholes were equipped with multi-packer systems, isolating measurement intervals of 10–50 cm at various distances from the tunnel wall. Hydraulic pulse and constant head tests were conducted in the saturated part of the EDZ, whereas simple pneumatic tests were undertaken in the unsaturated rock in the immediate vicinity of the tunnel surface to investigate the local effective permeability. Figure 8 shows that permeability increases several orders of magnitude (up to 6–7) within 20–40 cm from the tunnel.

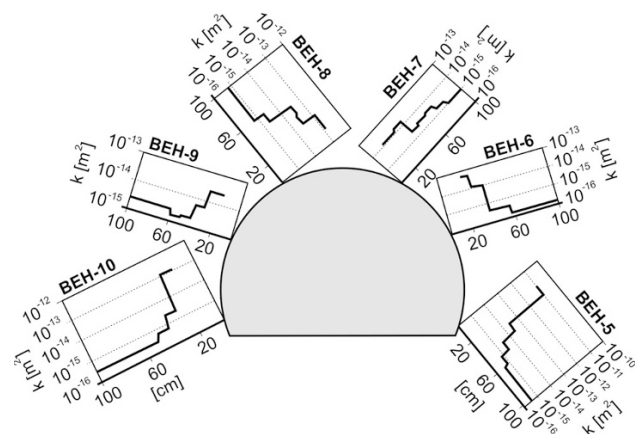


Fig. 8 Hydraulic characterisation of the EDZ features around excavations in the Mont Terri rock laboratory: in-situ permeability measurements conducted in Mont Terri experimental drift (from Bossart et al. 2002)

This zone coincides with that exhibiting high fracture density.

Several experiments were conducted to demonstrate the evolution of transmissivity of the excavation-induced fractures in the ventilated tunnel and after re-compaction of the EDZ in order to capture the time dependence of the self-sealing process. A long-term in situ experiment, conducted in the EDZ of an open tunnel section, indicated a significant reduction of the EDZ transmissivity over a period of 800 days from 5×10^{-7} to 2×10^{-9} m²/s (blue dots in Fig. 9). During the subsequent test phase, a load plate was installed and the EDZ was subjected to radial stresses between 1 and 5 MPa to simulate bentonite swelling pressures in a backfilled emplacement tunnel. A further drop in transmissivity of two orders of magnitude to 2×10^{-11} m²/s was observed (red dots in Fig. 9).

2.5 Investigation of fracture closure mechanisms

The dependence of fracture transmissivity on effective normal stress has been the issue of laboratory studies and in situ tests (Blümling et al. 2007). As part of the GS experiment (Gasfrac Self-sealing) at Mont Terri, hydraulic tests were performed in a borehole before and after a combined hydro- and gas-frac experiment (Marschall et al. 2005). The experiment was carried out in a test interval containing a hydrofrac with a well-defined fracture geometry. Interval transmissivity increased by 5–6 orders of magnitude when the injection pressure exceeded the effective normal stress on the fracture plane (Fig. 10). For low injection pressures, however, the interval transmissivity was close to that of the intact rock ($T \leq 10^{-12}$ m²/s). These findings can be explained by the dependence of fracture transmissivity (or hydraulic conductivity) on effective normal stress, which follows a hyperbolic fracture

closure law (see Nagra 2002). An effective mechanical self-sealing of the artificial fracture is observed already at moderate effective normal stresses in the order of 1–2 MPa (Fig. 10).

3 Modelling of water/gas flow along the EDZ

3.1 Background and rationale

The complexity of the hydro-mechanical phenomena associated with the creation and temporal evolution of the EDZ precludes a detailed representation of the EDZ with conventional modelling tools for safety assessment (SA). Therefore, quantitative analyses in support of the assessment of long-term radiological safety of geological repositories are often based upon simplified representations of the EDZ, assuming a configuration of concentric shells (single or double shell) with enhanced hydraulic conductivity (Fig. 11).

In recent years, several numerical EDZ abstraction approaches have been proposed for SA applications, referring to data bases from the Mont Terri rock laboratory. Lanyon and Senger (2011) developed a sequential modelling approach for indurated clay formations, based on a stochastic representation of the EDZ in terms of discrete fracture network (DFN) models. The underlying hydraulic DFN models, derived from structural mapping of tunnel walls and drillcores, were converted into equivalent porous medium (EPM) models with stochastic permeability distributions. Combined water and gas flow along stochastic realizations of the EDZ was simulated with the EPM models. Eventually, effective properties suitable for performance assessment were derived by inverse modelling of the results of stochastic modelling with a simple single shell representation of the EDZ. Senger et al. (2013) validated the aforementioned modelling approach with long-term monitoring data from the HG-A experiment (gas path through host rock and along seals) at Mont Terri.

Walsh et al. (2015) developed an EPM-based modelling framework which simulates two-phase flow with the T2GGM code (Suckling et al. 2012) and mechanical processes with FLAC3D (Itasca 2012). This coupled model predicted the evolution of the EDZ around the HG-A tunnel, and then modelled the EDZ permeability as a function of time (self-sealing) and packer pressure (hydro-mechanical coupling).

Alcoverro et al. (2014) developed a simplified hydro-mechanical modelling approach for SA applications using the THM-simulator CODE_BRIGHT (DIT-UPC 2000). The permeability of the EDZ was assumed to depend on deformation, allowing the simulation of self-sealing processes in the EDZ in response to re-saturation and stress

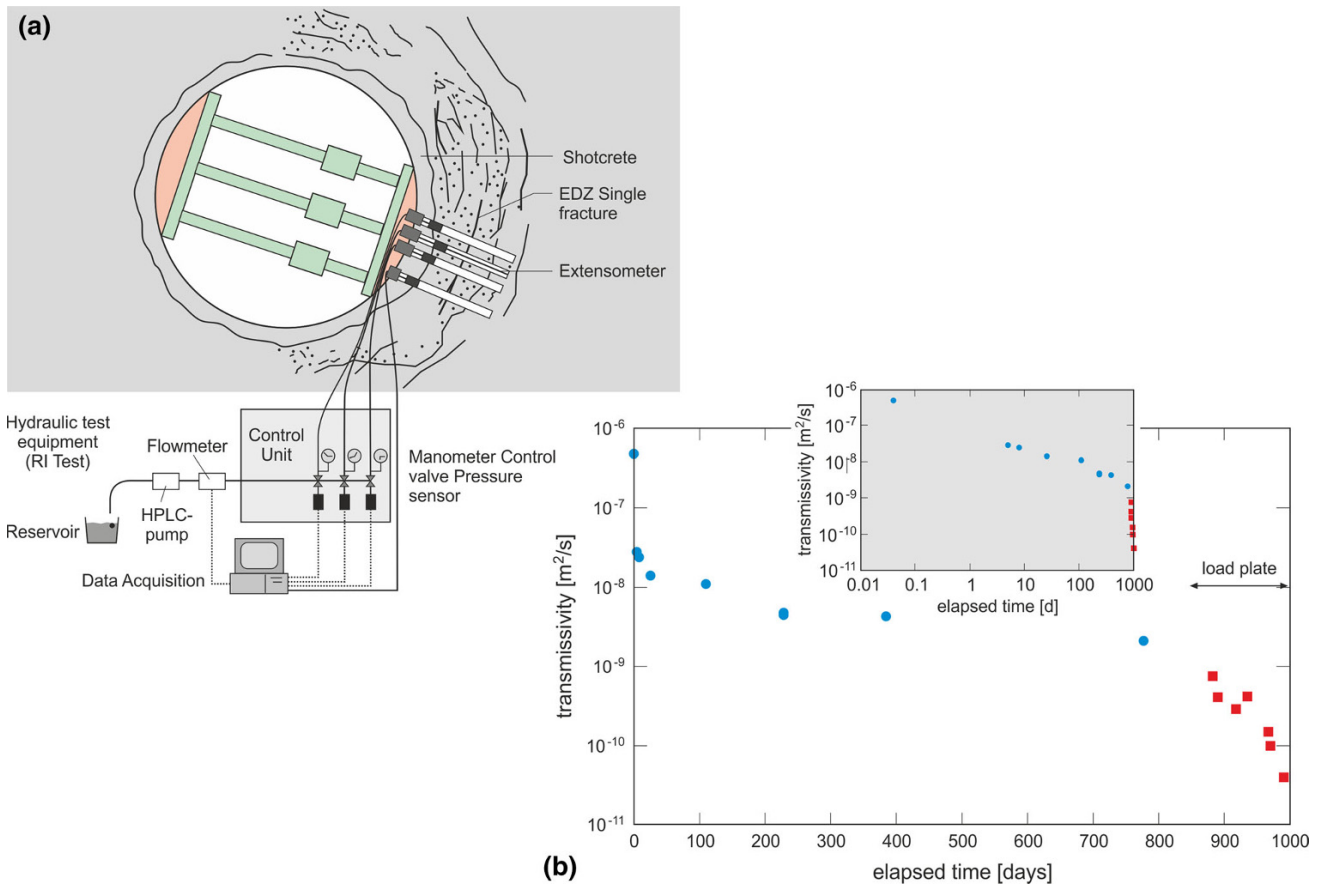
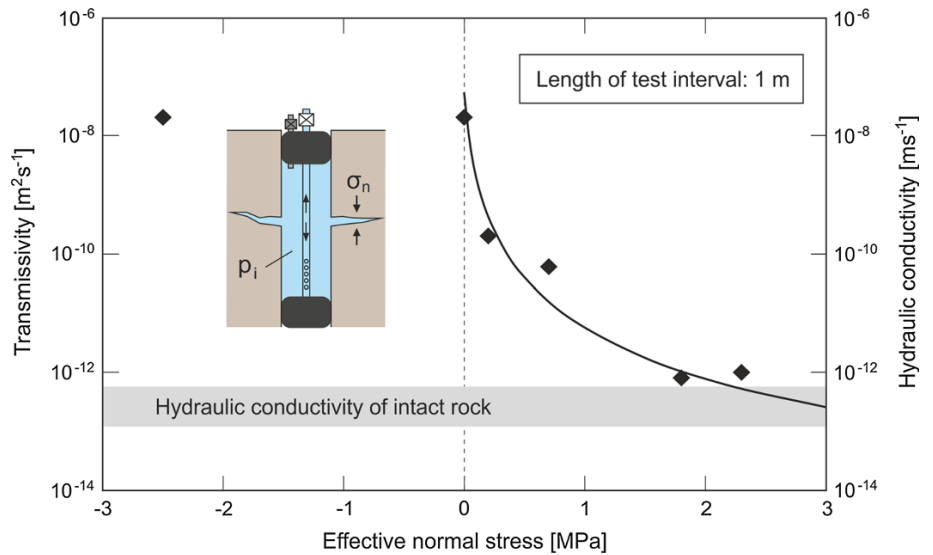


Fig. 9 Long-term changes in EDZ transmissivity in an open tunnel section at the Mont Terri rock laboratory: **a** sketch of the experimental set-up and **b** long-term monitoring of EDZ transmissivity. Initially, the EDZ was saturated for a period of 800 days (*blue dots*) and EDZ

transmissivity was monitored periodically. Afterwards, a load plate inducing a radial stress between 1 and 5 MPa was installed and the transmissivity measurements were repeated (EU Selfrac Project; Nagra 2002)

Fig. 10 Experimental evidence of sealing effects in Opalinus Clay at Mont Terri. Suggested hyperbolic relationship between interval transmissivity and effective normal stress, ($\sigma_n - p_i$), based on the investigation of fracture closure mechanisms in the so-called Gasfrac self-sealing (GS) experiment (after Nagra 2002). Hydraulic tests were conducted for different interval pressure values, p_i . The normal stress, σ_n (ca. 4.3 MPa), was derived from the shut-in pressure recorded during hydraulic fracturing



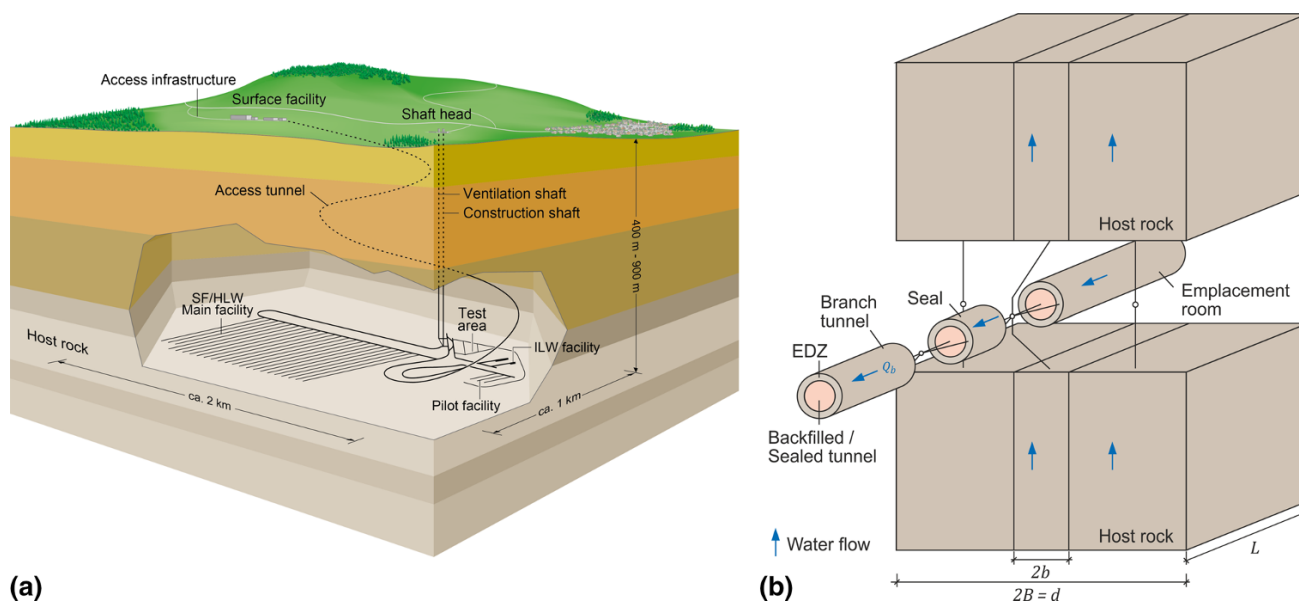


Fig. 11 Simulation of radionuclide release in safety assessment (SA): abstraction of the radionuclide release paths from the site descriptive model (*left*) towards a simplified representation in a numerical

recovery. The modelling approach was benchmarked extensively with long-term monitoring data from the HG-A experiment.

3.2 A novel EDZ abstraction approach

The aforementioned EDZ modelling approaches have successfully demonstrated their suitability for simulating the hydraulic behavior of the EDZ around backfilled tunnel sections and for the back-analysis of the self-sealing processes associated with the re-saturation and pressure recovery along the seal section of the HG-A experiment. A shortfall of these approaches is their limited ability to represent the mechanisms of fracture closure in response to pressure recovery in the EDZ, thus restricting the predictive capability of the models.

A novel numerical approach has been developed by Alcolea et al. (2016) with special emphasis on an adequate representation of the hydro-mechanical conditions in the EDZ, covering the full range of hydraulic regimes, from the fracture dominated, with localised pore-water flow during early times, to the matrix-dominated distributed flow in the late times. The workflow consists of three main steps carried out sequentially (Fig. 12). First, a hybrid finite-discrete element method (FDEM; Lisjak et al. 2016) is used to simulate the geometry and geomechanical conditions of the discrete fracture networks forming the EDZ (Fig. 12a). The FDEM simulations are purely mechanical and mimic the excavation and emplacement processes only. Second, the geometric properties simulated by the

transport code (*right*). The EDZ is implemented as a single shell model with effective properties in terms of cross-sectional area, porosity and hydraulic conductivity (modified after Poller et al. 2014)

FDEM are mapped onto a finite element mesh (Fig. 12b), which allows to solve the fluid motion equations in the excavation near-field. A salient feature of the suggested approach is that hydraulic parameters of both fracture and matrix evolve over time as a response to re-saturation of the tunnel surroundings. Finally, an abstraction of the complex model is made based on the late time behaviour (after full re-saturation) of the system (Fig. 12c). The main outputs of the model are the spatio-temporal distributions of hydraulic parameters and the corresponding specific fluxes towards the tunnel, with special emphasis on the late time behaviour. Finally, the abstraction of the EDZ is implemented by defining a piece-wise homogeneous “shell-like” model with hydraulic behaviour identical to that of the complex model.

3.3 Heuristic modelling concept of fracture self-sealing

Based on the presented empirical and experimental evidence (Sect. 2), the hydraulic significance of the EDZ during tunnel construction and its evolution during the operational phase and after backfilling of the underground structures can be formulated in terms of a heuristic EDZ closure model (Fig. 13). The creation of the EDZ is a brittle process, i.e., the increase of the void volume in the damaged rock zone around the excavation is solely attributed to fracture opening, whereas the porosity of non-fractured rock remains essentially unchanged during the early times after excavation. Initially, the newly created

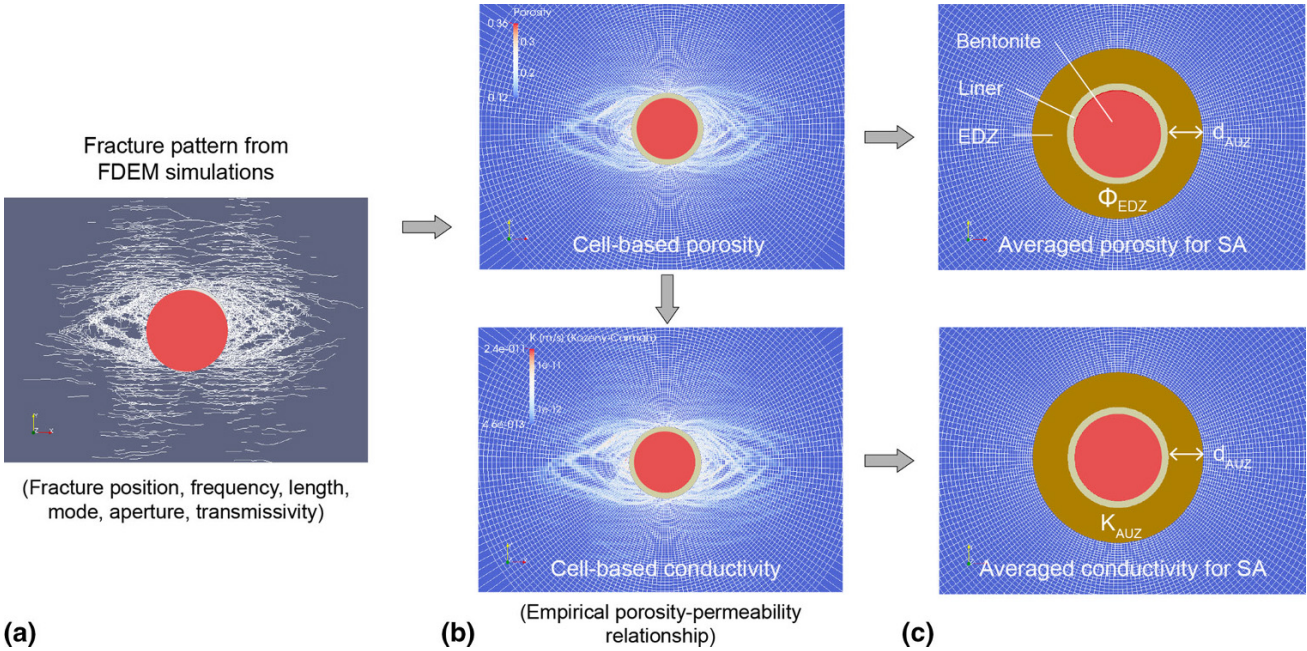


Fig. 12 Concept of the EDZ abstraction procedure for safety assessment (SA) applicable for a circular tunnel (after Alcolea et al. 2016): **a** representative fracture patterns are simulated for relevant repository configurations with a discrete element model (FDEM); **b** the discrete fracture patterns are converted in heterogeneous porosity and hydraulic conductivity distributions; **c** in a final abstraction process, the heterogeneous porosity and conductivity distributions are converted into a shell defined by a radius and homogeneous porosity and conductivity

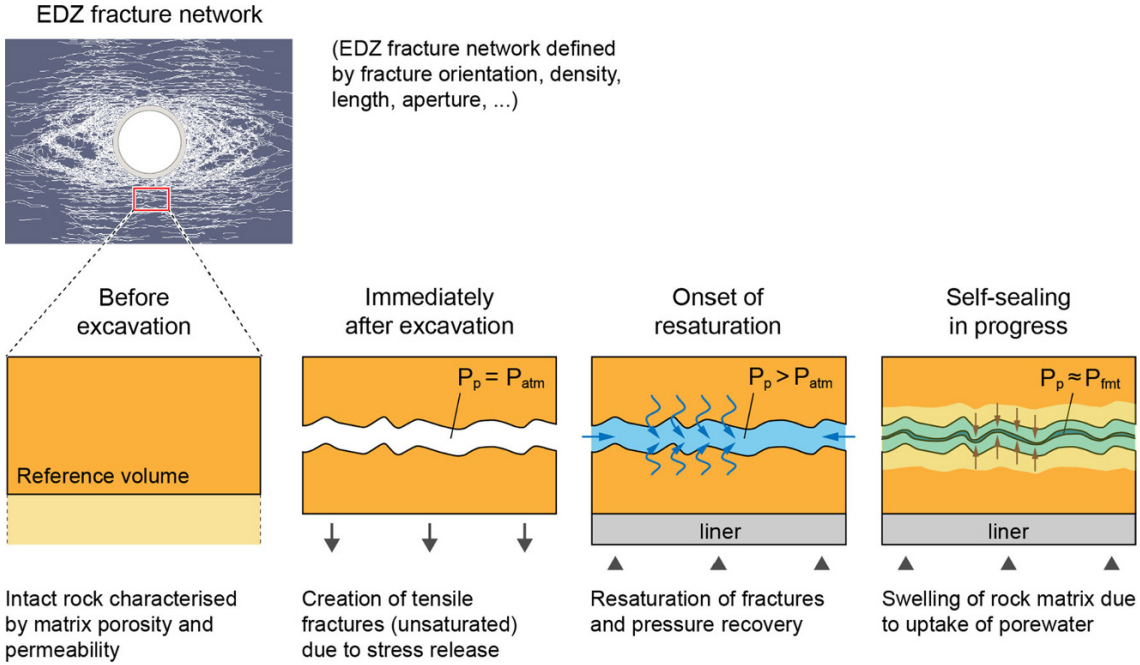


Fig. 13 Schematic sketch of the conceptual framework for EDZ fracture closure in Opalinus Clay, covering the key phenomena and features from the early post excavation phase until static formation pressure recovery

EDZ fractures are unsaturated and exposed to atmospheric pressure, whereas the non-fractured rock remains saturated and exhibits high matrix suction as a consequence of the high gas entry pressure of the Opalinus Clay (Ferrari et al.

2014). The initial transmissivity of the unsaturated EDZ fractures is controlled by the fracture aperture and can be very high. The matrix conductivity remains essentially unchanged, i.e., it is the same as the conductivity of the

intact rock. With time, the matric suction in the rock matrix decreases due to the uptake of pore-water from outer rock zones and the fractures start to resaturate. Pore-water uptake from the non-fractured rock zones is associated with swelling and consequently with an increase of matrix porosity. This porosity increase occurs at the expense of a decrease of fracture aperture (and correspondingly, of fracture transmissivity), i.e., fractures start to close and fracture transmissivity reduces drastically, whereas the hydraulic conductivity of the non-fractured matrix zones increases slightly as a consequence of the porosity increase. This process continues until the equilibrium of effective stresses is reached. This is essentially the case, when pore pressure reaches the static formation pressure.

Alcolea et al. (2016) implemented the heuristic EDZ closure model in a numerical workflow and subjected long-term monitoring data from the HG-A experiment at Mont Terri to a detailed back analysis. The results of this analysis are presented in the subsequent paragraphs.

4 Assessment of model performance

4.1 The role of the Mont Terri rock laboratory

The performance of a modelling approach is commonly evaluated by comparing model predictions with experimental evidence. Rigorous model validations require comprehensive benchmark exercises for the full range of intended model applications as part of a systematic prediction-evaluation process. In geoscientific modelling workflows rigorous validations are rarely achieved due to the lack of detailed knowledge concerning the actual state of the modelled geo-system and the limited amount of measurements of its temporal evolution. In this sense, the Mont Terri rock laboratory offers a unique opportunity to collect comprehensive geoscientific data bases for model validation not only from well-instrumented long-term in situ experiments, but also from general site characterisation activities such as structural mapping and borehole logging.

Modelling benchmarks for the simulation of the hydro-mechanical evolution of the EDZ have been carried out as part of the EC-funded FORGE project (Harrington et al. 2013; Shao et al. 2015) and in the framework of the DECOVALEX project (Xu et al. 2013; Nguyen and Le 2015). In both benchmark exercises, the HG-A in situ experiment at Mont Terri served as a key experiment for model calibration and validation.

4.2 The HG-A experiment

The HG-A experiment (gas path through host rock and along seal sections) was designed as an integrated

experimental programme to provide qualitative and quantitative evidence of the gas and water transport capacity of the EDZ along the sealed section of the HG-A microtunnel during all relevant evolutionary stages, comprising the excavation phase, a short ventilation period and the back-filling and sealing stages (Marschall et al. 2006, 2008; Lanyon et al. 2009, 2014). The test site is located in the southern part of the Mont Terri rock laboratory off Gallery 04 (Fig. 14). A 1 m diameter, 13 m long microtunnel was excavated during February 2005 from a niche in Gallery 04. The microtunnel was directed parallel to bedding strike and bedding parallel features run along the tunnel. Excavation was monitored by a borehole array containing piezometers and deformation gauges (clino-chain and chain deflectometers). The borehole array was subsequently augmented with additional piezometer boreholes and borehole stressmeters.

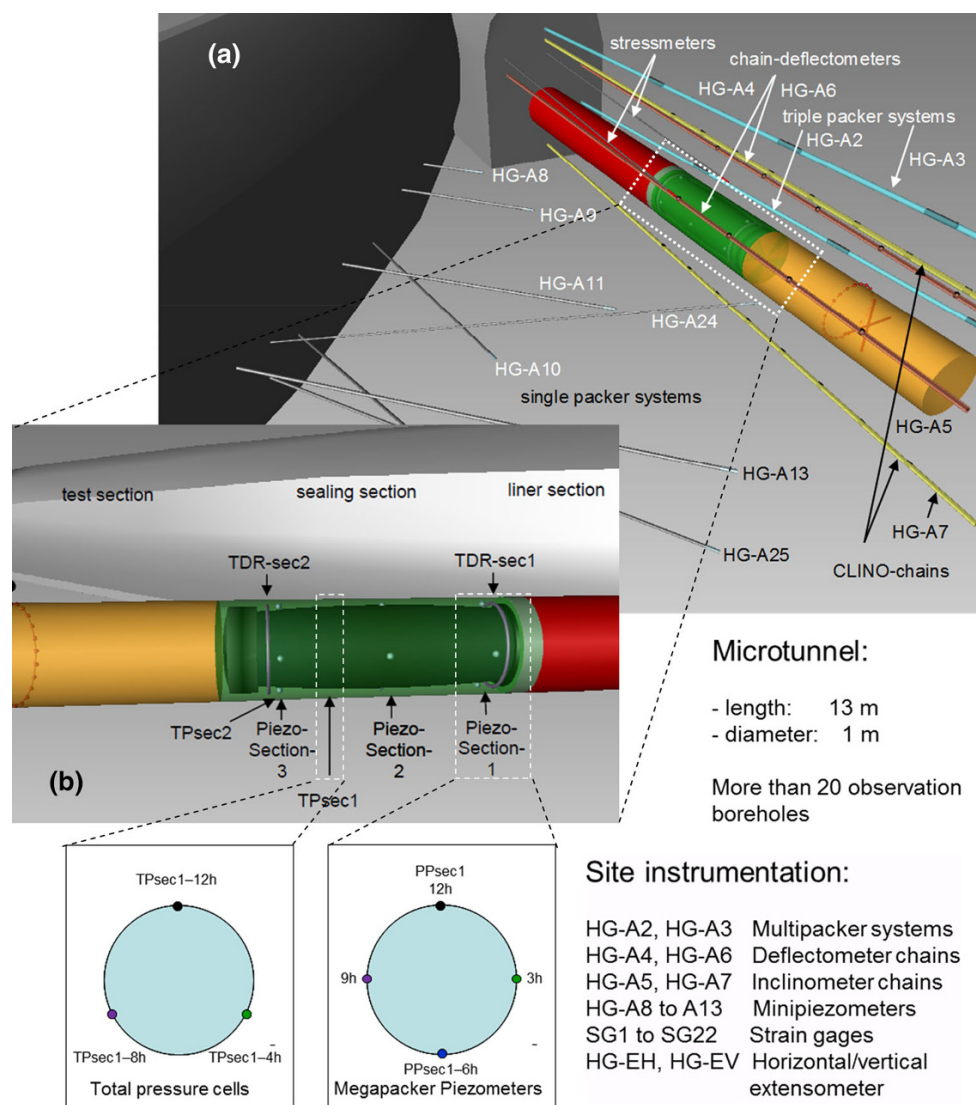
4.3 Creation of the EDZ

The excavation of the HG-A microtunnel was carried out using a steel auger (Marschall et al. 2006). No drilling fluid was used in order to avoid swelling and disaggregation of the clay during drilling. Immediately after termination of the drilling process, a steel liner was installed along the first 6 m of the microtunnel to stabilise the damage zone around the tunnel entrance. Detailed small scale geological mapping of the tunnel section between 6 and 13 m was carried out after emplacement of the liner. The facies in the microtunnel is composed of marly shales, which are locally intercalated with grey-white silty limestones and weakly cemented fine-grained brownish siderite layers. On the metre scale, the lithologies are quite homogeneous. However, a quite pronounced bedding anisotropy could be mapped (bedding traces in the microtunnel are almost horizontal, true bedding dip is 51°).

After completion of construction, the surface of the microtunnel was scanned with a tachymeter from 6 to 13 m along the tunnel axis (Fig. 15), which confirmed the results of structural mapping, indicating that breakouts occur mainly at locations where bedding is oriented tangential to the tunnel circumference.

The instantaneous brittle failure process during and immediately after excavation of the HG-A microtunnel exhibits the characteristic EDZ features around cylindrical cavities in claystone formations, such as massive breakouts, spalling and buckling phenomena. Instantaneous failure was caused by the combined effect of (i) the anisotropy in far-field stress, (ii) the anisotropy of geomechanical rock properties (stiffness and strength) and (iii) the heterogeneity of the rock mass (tectonic fracture systems and flaws in the rock fabric). The conceptualisation of the damage zone around the HG-A microtunnel (Marschall

Fig. 14 Schematic drawing of the HG-A microtunnel and the site instrumentation. *Colour coding* refers to the steel liner (red), the seal section (green) and the backfilled test section (orange)



et al. 2006) is given in Fig. 7c. The damage zones on the upper left side (9:00–11:00 o'clock) exhibit clear signatures of extensile fracturing such as plumose structures and disjoining of bedding planes. The breakouts are largely linked to the SSE dipping thrust system, which is oriented subparallel to the bedding planes and intersects the tunnel at a low angle. These fractures represent planes of weakness with reduced uniaxial compressive strength and are therefore preferential loci for failure initiation during the excavation process. In the upper zone between 10:00 and 11:00 o'clock, spalling and buckling phenomena create slab-like breakouts. Spalling occurs preferentially in the rear end of the tunnel at areas where SSW dipping fault planes phase out, whereas buckling dominates in the section with the most prominent breakouts between 6 and 9 m. In the lower zone between 9:00 and 10:00 o'clock, damage seems more and more stress controlled, i.e., onion-like extension joints associated with the minor in-plane

principal stress component tend to delimit the damage zones on the left side of the tunnel. Less distinct are the buckling phenomena along the tunnel floor (about 5:00 o'clock). No significant breakouts are formed in this zone, because the debris is kept in place due to gravity. Complementary extensometer records give clear indication for on-going tunnel convergence in the lower sidewall to the NNW.

4.4 Hydraulic and gas testing

Following a short ventilation phase of several months, the test section (9–13 m) and the seal section (6–9 m) of the microtunnel were instrumented with piezometers, extensometers, strain-gauges, total pressure cells and time domain reflectometers (TDRs) to measure pressure, deformation, total stress and water content. Finally, the megapacker was installed in June 2006. Saturation of the

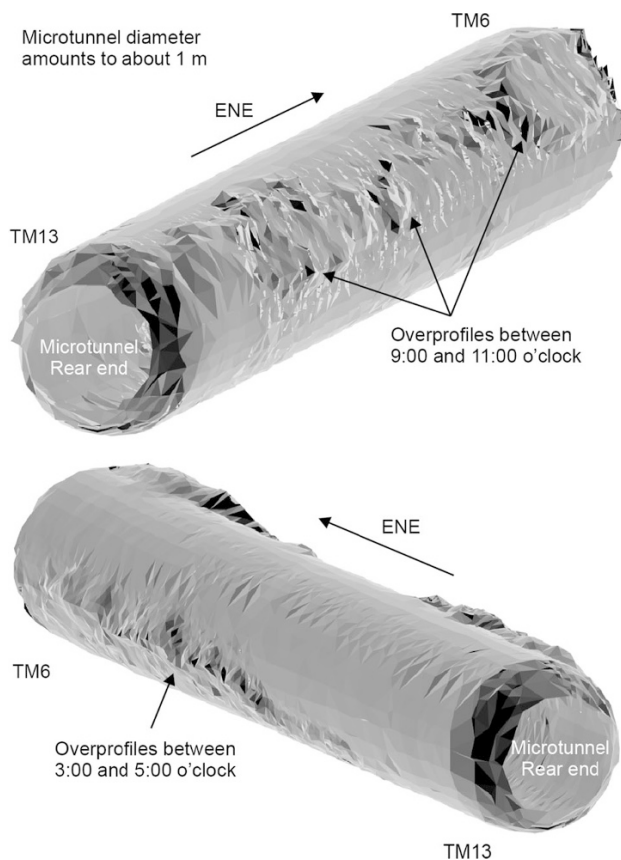


Fig. 15 Characterisation of the EDZ in the HG-A microtunnel: 3-D laser scan with a tachymeter. Views are from the rear end of the tunnel towards the SSE side wall (*top*) and the NNW side wall (*bottom*), respectively. The radial accuracy of the scans is ± 3 mm and the axial resolution varies between 5 and 10 cm

test section and surrounding rock started in November 2006 and comprised several saturation tests and a long-term multirate hydraulic test, starting in January 2008 (Fig. 16). This test continued until February 2010 and involved a series of constant rate injection steps, with stepwise reduced rates in the range between ca. 10 and 0.1 ml/min. The results from the hydraulic testing indicated progressive self-sealing (Lanyon et al. 2014). During hydraulic testing the effective stress conditions in the seal zone were altered by varying the megapacker pressure in the range between 2000 and 2600 kPa.

The gas injection phase included three separate nitrogen gas injections termed GI1, GI2 and GI3. Figure 16 displays the corresponding microtunnel sensor responses. After each gas injection, following a shut-in period, water was extracted from the test section and depressurized to remove trapped gas (gas–water exchange). The degassed water was then re-injected into the test section. This procedure provided a well-defined initial gas saturation in the test section pore-water for the subsequent gas injection. During gas injection a low constant rate (c. 0.02 ml/min) water

injection was maintained in the test section. Gas pressure during GI1 was limited to 1200 kPa, significantly below the minimum stress, to avoid coupled mechanical effects. After an initial 20 ml/min (SATP) injection, when pressure rose quickly, the injection rate was reduced to about 10 ml/min (SATP) to maintain an approximately constant pressure in the test section. During GI2 test section pressure rose more slowly than in GI1 and then peaked at around 1350 kPa. After the pressure breakdown, the test section pressure dropped over about a month by ca. 350–1000 kPa and then stabilized at about 1040 kPa. During GI3, test section pressure again peaked at 1350 kPa but with a broader peak than in GI2 and then dropped to about 850 kPa owing to an interruption in injection before recovering (after resumption of gas injection) and stabilised at about 1000 kPa.

4.5 Modelling of EDZ formation

Lisjak et al. (2016) carried out numerical simulations of the EDZ formation and compressive stress controlled sealing process around the HG-A microtunnel using a hybrid finite-discrete element method (FDEM). The model geometry consisted of a circular opening representing a 2D cross section of the HG-A microtunnel located along the seal section (Fig. 17). The influence of model boundaries on the excavation near-field was minimized by placing them at a distance of 10 m from the centre of the microtunnel. To maximize the model resolution in the EDZ while keeping the computation times within practical limits, a $4 \text{ m} \times 4 \text{ m}$ mesh refinement zone, with a nominal element size of 0.015 m, was adopted around the excavation boundary. In this zone, the mesh was pre-conditioned along the bedding direction by introducing a layering thickness of 0.05 m, as required to adopt the anisotropic fracture model. A transversely isotropic stiffness model coupled with a direction-dependent fracture criterion was adopted for the Opalinus Clay. The input values for the fracture model were derived from the FDEM back-analysis of the full-scale emplacement (FE) tunnel at the Mont Terri rock laboratory (Lisjak et al. 2015). The reference values of the principal stress components at Mont Terri ($\sigma_1 = 6.5$ MPa, $\sigma_2 = 4.5$ MPa, $\sigma_3 = 2.5$ MPa) were used to specify the in situ stress field in the HG-A model.

The simulation of the EDZ formation and recompaction process was accomplished with two separate model runs. The first run was intended to analyse the failure mechanisms and damage propagation associated with the EDZ formation process. The second run was dedicated to the recompaction of the EDZ in response to packer inflation, acting as a radial stress on the inner model boundary.

A total of 5 model variants were specified as part of a sensitivity analysis, aimed at assessing the impact of

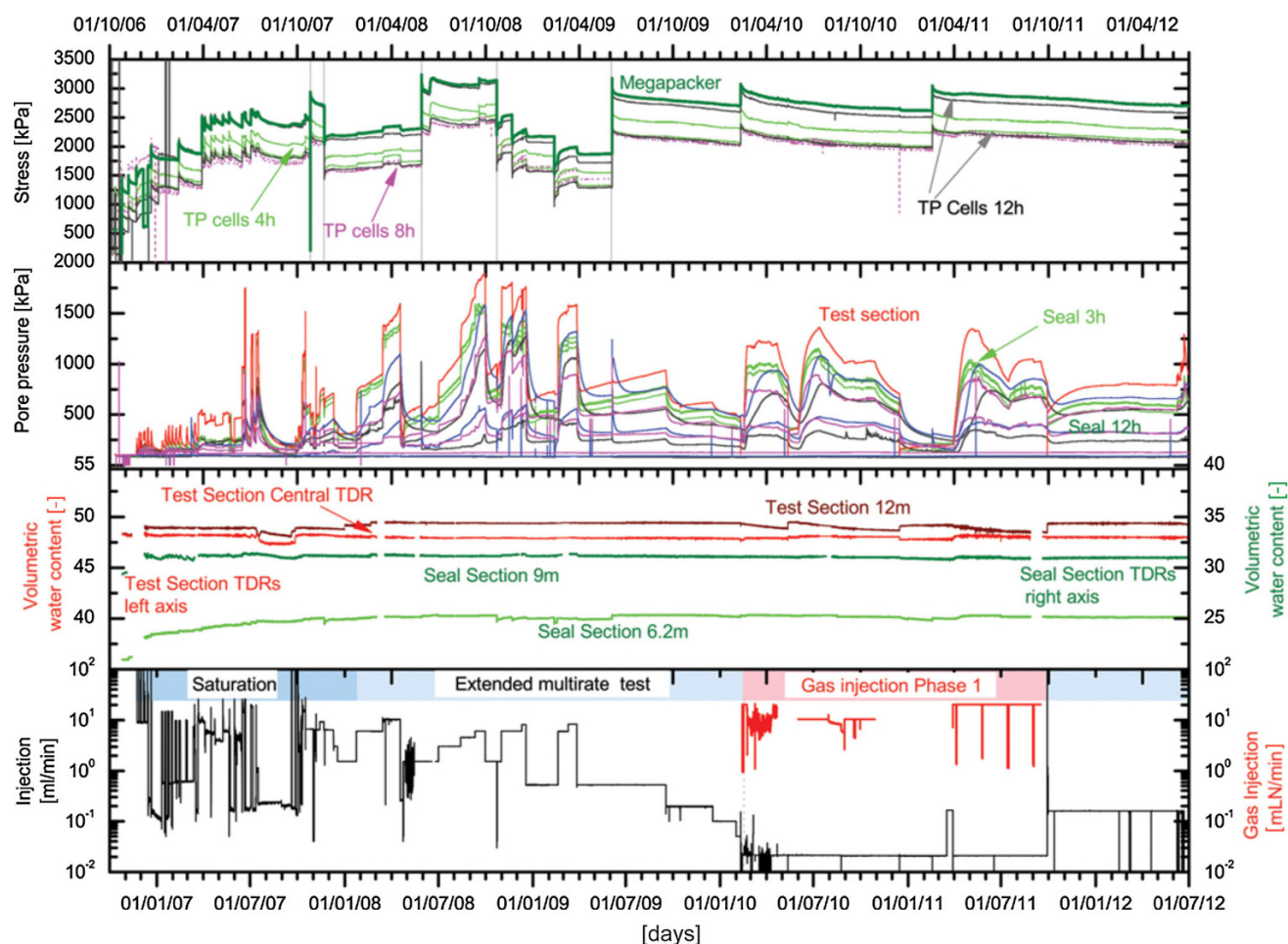


Fig. 16 Microtunnel stress, pore pressure, water content and flow rate measurements from start of saturation (from Lanyon et al. 2014)

parametric and conceptual uncertainties on the EDZ formation. Of particular interest was the effect of the tectonic fault (see Fig. 7c) on the development of the EDZ fracture pattern. The numerical results of the model variant with tectonic fault (model “HG-A-F”) indicate that damage starts to develop around the excavation boundary in response to the gradual softening of the excavation core (Fig. 17). Failure initiates in the form of shear (i.e., Mode II) fractures nucleating and growing along bedding planes approximately tangential to the tunnel walls (Fig. 17a,b). The distinctive location of these failure zones is caused by a combination of compressive stress concentration arising in the sidewalls and the low shear strength of the bedding planes. The impact of the tectonic discontinuity with fault plane oriented oblique to bedding affects the rock mass strength, fracturing behaviour, as well as the induced failure kinematics in the subsequent phases of damage propagation (Fig. 17c, d). A distinctive interaction can be observed between the pre-existing discontinuity in the right sidewall and the growing EDZ fractures. Particularly, the propagation of shear fractures nucleating at 270° – 360° ,

tends to be arrested at the intersection with the fault plane (Fig. 17c). As a result, the growth of shear fractures along the bedding direction tends to be inhibited in favor of new shorter bedding-parallel fractures nucleating along the fault plane direction (Fig. 17d).

The mechanical re-compaction of the EDZ in response to packer inflation was simulated by assigning a radial pressure of 3 MPa on the inner model boundary. As shown in Fig. 18a, a zone of high fracture aperture (corresponding to high fracture transmissivity) develops in the microtunnel sidewalls during the preceding EDZ formation process. In response to packer inflation a substantial fracture aperture reduction is simulated around the opening (Fig. 18b), indicating a 64% decay in the total fracture porosity value.

4.6 Hydraulic conductivity around the HG-A microtunnel

Drawing on the workflow described in Fig. 12, the FDEM based discrete fracture networks around the HG-A microtunnel were converted into cell-based distributions of

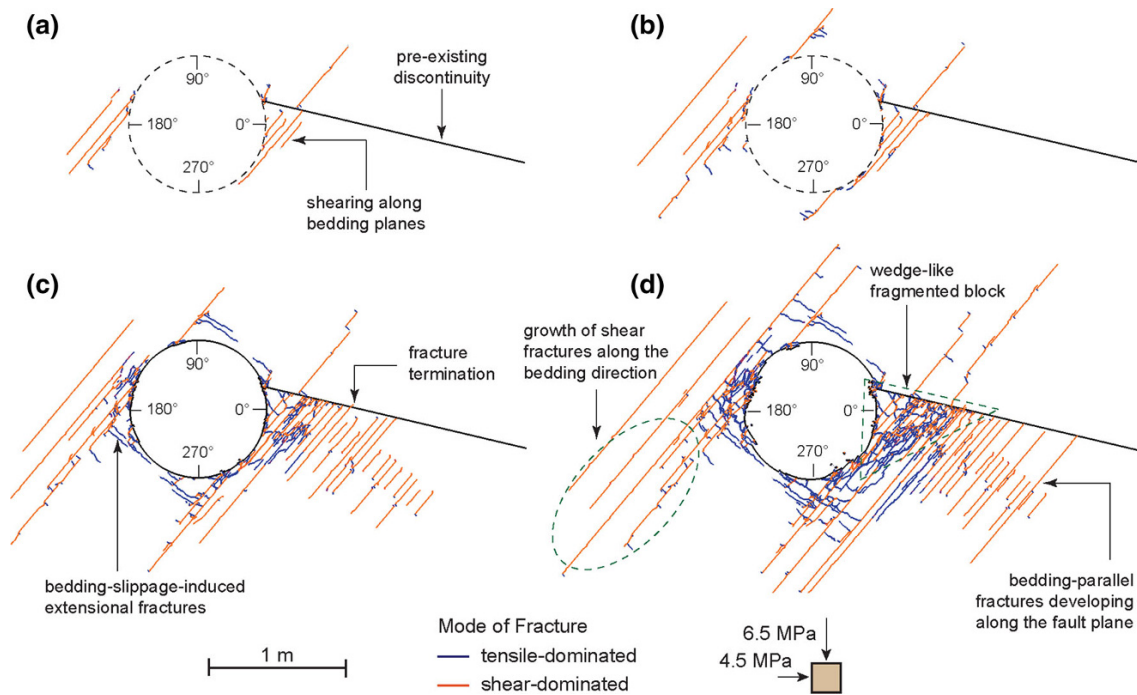
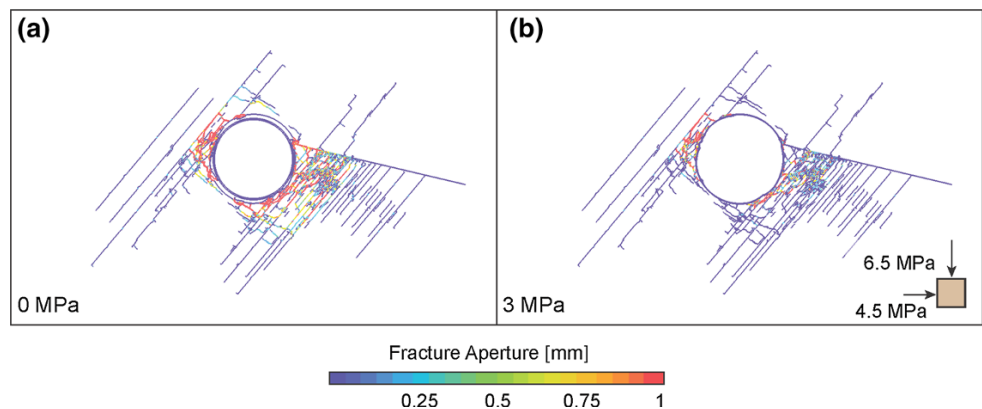


Fig. 17 Simulated EDZ formation process in a model that explicitly accounts for the presence of a sub-horizontal, SW-dipping tectonic fault in the right sidewall [FDEM model “HG-A-F” after Lisjak et al.

(2016)]: **a** 50,000 time steps, **b** 100,000 time steps, **c** 140,000 time steps, and **d** 200,000 time steps

Fig. 18 Spatial distribution of fracture aperture **a** at the time of packer installation and **b** after reaching equilibrium conditions under the effect of a 3 MPa radial pressure, in a model explicitly accounting for the presence of a sub-horizontal, SW-dipping tectonic fault (FDEM model “HG-A-F”; after Lisjak et al. 2015)



effective porosity and hydraulic conductivity (Alcolea et al. 2016). To this end, a finite element mesh was created over which the fracture traces and corresponding fracture characteristics (fracture mode, trace length, aperture) were mapped on the corresponding cells. Effective porosity and effective conductivity values were assigned to each cell by “box-counting” the contributions of the intact rock matrix and traces of the intersecting fractures. A porosity of 12% and a hydraulic conductivity of 4.5×10^{-14} m/s were assigned to the intact rock, representing the properties of the Opalinus Clay at the transition between shaly and sandy

facies. In the conceptual framework, self-sealing of the fractures in response to pore pressure changes (Fig. 13) was mimicked by a swelling mechanism. Thus, the increase of pore pressure from very low negative values (suction) during the unsaturated phase towards static formation pressures in the saturated state after full pore pressure recovery increases the porosity of intact matrix and reduces the aperture of the fracture traces. Based on the available experimental data (Fig. 10), a hyperbolic fracture closure mechanism (Barton-Bandis relationship) was adopted to simulate the reduction of fracture transmissivity in response to pore pressure

increase. Correspondingly, the increase of matrix conductivity associated with the swelling process was expressed in terms of a well-established porosity–permeability relationship (Kozeny–Karman relationship). Further details of the adopted models for simulating the self-sealing of the EDZ are found in Alcolea et al. (2016).

With the given approach, the initial distributions of effective porosity and conductivity around the HG-A microtunnel and their evolution with pore pressure recovery have been calculated for all FDEM fracture network realisations. At early times, when pore pressure in the fracture network is negative due to unsaturated conditions and efficient swelling of the intact matrix does not yet apply, the hydraulic conductance of the EDZ is dominated by the contribution of the highly transmissive fractures, displaying effective conductivities which are many orders of magnitude higher than the parameters of the intact rock (Fig. 19b). Conversely, when fractures are essentially closed after complete pore pressure recovery, the effective hydraulic conductivity of the EDZ is largely controlled by the matrix behaviour. Figure 18c, d display the late-time distributions of effective porosity and conductivity for the FDEM that

includes the tectonic fracture (Fig. 19a). Cell-based porosities in the immediate vicinity of the microtunnel range between 12 and 40%. Local conductivity values spread between 10^{-11} and 4.5×10^{-14} m/s, which is in general agreement with experimental evidence (see Lanyon et al. 2014).

4.7 Back analysis of water/gas injections: examples

The cell-based distributions of effective porosity and hydraulic conductivity around the HG-A microtunnel, in combination with the implemented self-sealing mechanism (i.e., pressure-controlled fracture closure and swelling of the intact matrix blocks) formed the input for back analyses of the long-term water injections and the gas injection tests.

The multi-rate water injection test described earlier (Fig. 16) was selected for assessing the self-sealing behaviour of the EDZ around the HG-A microtunnel. Pore pressure transients from the piezometer boreholes HG-A2 and HG-A3 (Fig. 14) were used to infer—via maximum likelihood optimization—the fracture closure parameter that controls the closure law (Barton–Bandis like) mimicking the long-term self-sealing of the EDZ. Two different

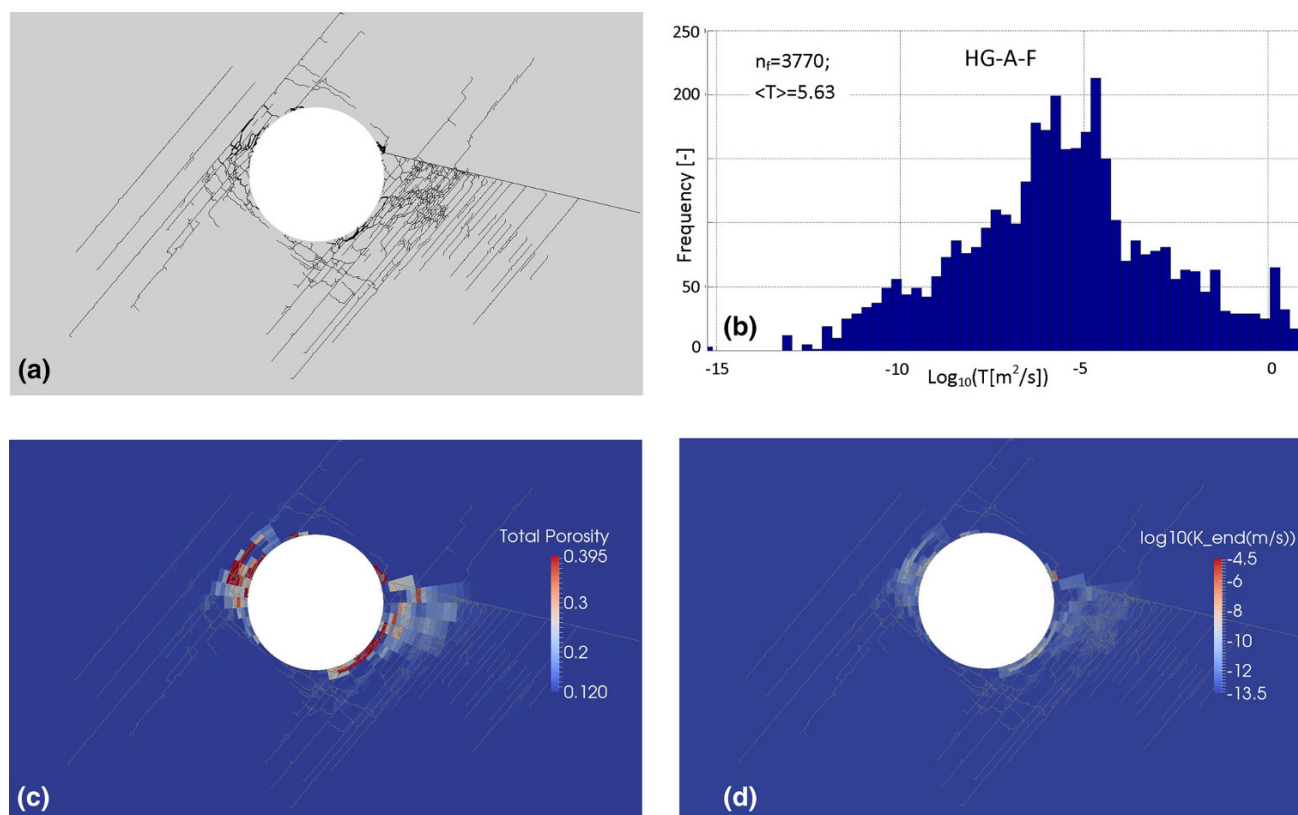


Fig. 19 Modelling of effective EDZ properties around the HG-A microtunnel: **a** FDEM fracture network model with tectonic feature (“HG-A-F”), **b** histograms of initial fracture transmissivity. In the

insets, $\langle T \rangle$ denotes the geometric mean of transmissivity, **c**, **d** equivalent porous medium properties on a finite element mesh: late time distributions (after Alcolea et al. 2016)

FDEM variants of the EDZ fracture network were considered, namely a variant without tectonic faults (FDEM model “HG-A”; see Lisjak et al. 2016) and a variant with a SW-dipping pre-existing discontinuity (Fig. 17; FDEM model “HG-A-F”). Even at early times, model HG-A is characterised by a low hydraulic conductance due to its relatively low fracture density, as compared to model HG-A-F. Figure 20a displays the pressure fits at observation borehole HG-A2 for both models. In spite of the simplistic representation of the model domain (2-D model geometry) and the hydro-mechanical boundary conditions (axisymmetric pressure field and plane stress conditions), the model exhibits relatively good fits of available measurements (see for instance, the time period 300–400 days, Fig. 20a) and captures the main trends of the measured pressure records at the piezometer boreholes in response to the multi-step water injection. Overall, model HG-A-F performs slightly better, suggesting that increased fracture density is more representative for the EDZ around the HG-A microtunnel than the sparse fracture network of the HG-A model.

Gas injection test GI-2 with a gas injection period of 5 months was selected for assessing the gas transport behaviour of the EDZ along the seal section. The simulations were executed with the two-phase flow code TOUGH2 (Pruess et al. 2012) using the FDEM fracture model HG-A-F and the fracture closure parameter determined after the analysis of the long-term water injection test. The simulated gas pressure build-up in the test zone of the HG-A microtunnel and the modelled pressure transients along the seal section are in good agreement with the monitored piezometer data. Clear evidence was seen for a preferential gas flow path, associated with the extended damage zone around the tectonic fault. Figure 20b displays the gas path along the seal section in terms of gas saturation at the time when the gas breakthrough to the Gallery 04 is observed. The modelling results were achieved without extensive calibration of the conductivity and porosity distributions, indicating a good performance of the applied model set-up. Further adaptations of the capillary pressure and relative permeability relationships (cubic scaling law instead of Leverett scaling; Grant gas permeability curve) provided further improvements of the data fits.

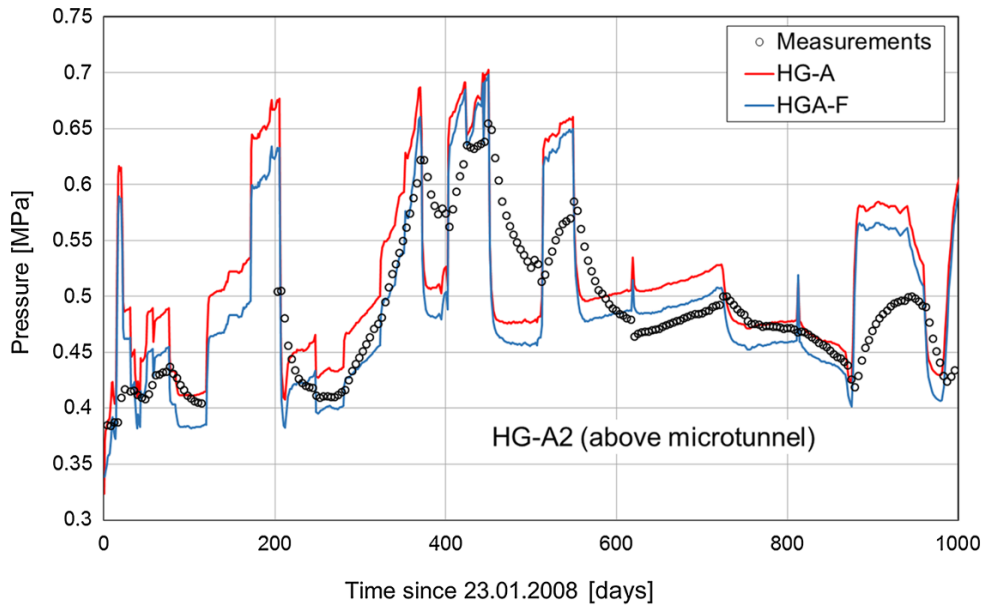
5 Conclusions

In the framework of the Mont Terri Project, new insights have been gained concerning the formation and evolution of the EDZ in indurated clays. Clear evidence was found,

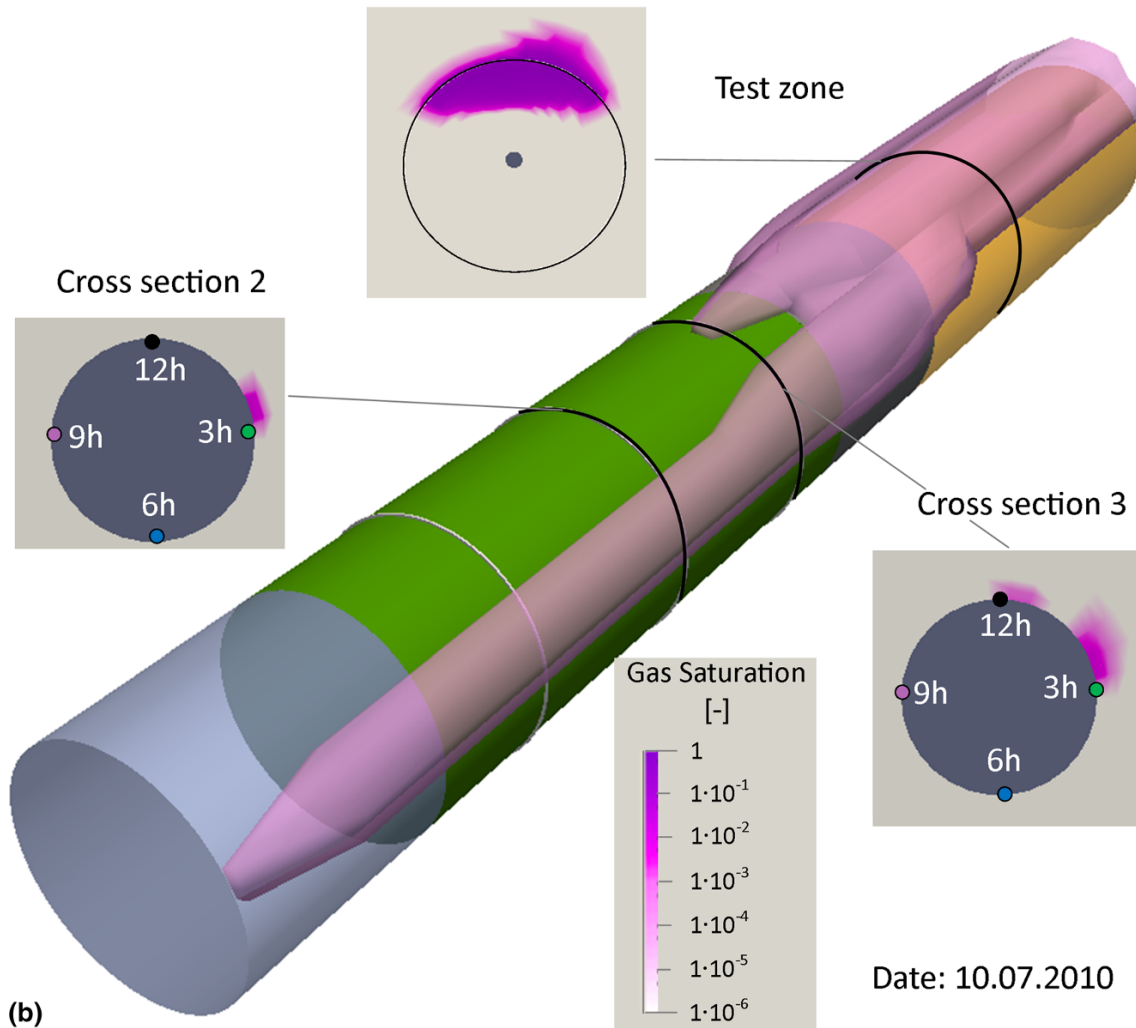
that the immediate (short-term) failure of the Opalinus Clay in response to the excavation process is brittle. The inventory of EDZ-related features comprises extensional fracturing, bedding parallel slip, buckling and kink failures, isolated shear fractures, shear bands and reactivated tectonic features. Multiple examples of stress controlled failure have been reported, all suggesting that the in situ virgin stress and the stress state ahead of the tunnel face govern the formation of the EDZ. As a consequence, the extent of stress controlled failure is strongly influenced by the choice of excavation technique and the progress of excavation. On the other hand, structurally controlled failure is related to the occurrence of sedimentary and tectonic structures. Variabilities in microstructure such as bedding or intercalations of sandy and clay-rich layers tend to create self-similar failure patterns (e.g. buckling), which are observed at scales ranging from small boreholes to the tunnel scale. In contrast, reactivations of tectonic structures are highly irregular processes and are therefore difficult to predict without detailed knowledge of the pre-existing fracture patterns, a fact which calls for detailed site characterisation measures ahead of the excavation face.

A mechanistic understanding of the hydro-mechanical and hydro-chemical phenomena associated with the self-sealing capacity of the Opalinus Clay has been developed. In this context, a long-lasting packer test campaign in short radial boreholes allowed to bracket the time scales and magnitudes of EDZ fracture self-sealing, indicating a continuous decrease of fracture transmissivities by several orders of magnitudes within a time period of three years. Furthermore, a dedicated in situ experiment on a hydraulic fracture revealed the hydro-mechanical controls, essentially determining the hydraulic significance of the EDZ fractures. In this context, a hyperbolic fracture closure law was derived, expressing for a functional relationship between fracture transmissivity and the prevailing pore pressure (respectively, effective normal stress) when the fracture is subjected to a normal (total) stress component.

The comprehensive experimental data base of the Mont Terri research programme formed the basis for the development of a versatile heuristic modelling approach, aimed at simulating flow and transport processes along the EDZ and capable to estimate the spatial-temporal evolution of hydraulic conductance of the EDZ after tunnel closure. The model was benchmarked with a data set from the HG-A experiment, demonstrating the ability of the approach to mimic the evolution of the hydraulic conductance of the EDZ around a backfilled tunnel section during the entire re-saturation phase. In addition, a two-phase flow model was successfully applied for the back-analysis of gas injection



(a)



(b)

◀ **Fig. 20** Back analysis of a long-term water injection and a gas injection test at the HG-A experiment (from Alcolea and Kuhlmann 2017): **a** simulation of a long-term water injection test with the fracture network models “HG-A” and “HG-A-F”. The pressure fits at observation borehole HG-A2 above the tunnel are displayed; **b** simulation of gas injection test GI-2 with the fracture network model HG-A-F. The preferential gas path along the EDZ at the time of the gas breakthrough is indicated by enhanced gas pressures

tests, giving evidence for the high gas transport capacity of the EDZ along a sealed tunnel section. The suggested methodology provides an abstracted single-shell model of the EDZ, able to mimic the relevant functional features of the EDZ in a traceable manner. Such abstracted model is a requirement for radionuclide release calculations in support of long-term safety analyses of a geological repository.


Acknowledgements This work was supported by ANDRA, BGR, Nagra and NWMO via the Mont Terri Consortium. The authors would like to thank Dr. Paul Bossart, Mr. T. Theurillat, Dr. D. Jäggi of the Mont Terri consortium together with the many contractors who have supported the experiments for their invaluable assistance in the technical planning and performance of the experiment. The valuable review comments and suggestions by Prof. D. Martin (University of Edmonton, Canada) and Prof. T.S. Nguyen (Canadian Nuclear Safety Commission, Ottawa) for improving the technical quality of this paper are highly appreciated.

References

- Alcolea, A., Kuhlmann, U. (2017). Mont Terri HG-A experiment (phase 21). Inverse flow modelling of the hydraulic properties of the EDZ. Mont Terri Technical Note 2016-76 (*in prep.*).
- Alcolea, A., Kuhlmann, U., Marschall, P., Lisjak, A., Grasselli, G., Mahabadi, O., de La Vaissière, R., Leung, H., & Shao, H. (2016). A pragmatic approach to abstract the EDZ around tunnels of a geological radioactive waste repository—Application to the HG-A experiment in Mont Terri. *Geological Society, London, Special Publications*, 443, SP443–8.
- Alcoverro, J., Olivella, S., & Alonso, E. E. (2014). Modelling fluid flow in Opalinus Clay excavation damage zone. A semi-analytical approach. *Geological Society, London, Special Publications*, 415(1), 143–166.
- Alheid, H. J., Aranyosy J. F., Blümling P., Hoteit N., & Van Geet M. (2007). EDZ Development and Evolution (RTDC 4). EDZ development and evolution. State of the art. *NF-PRO. Contract Number F16W-CT-2003-02389*. European Commission, Luxembourg.
- Aranyosy, J. F., Mayor, J. C., Marschall, P., Plas, F., Blümling, P., Van Geet, M., Armand, G., Techer, I., Alheid, A. J., Rejeb, A., Pinettes, P., Balland, C., Popp, T., Rothfuchs, T., Matray, J. M., De Craen, M., Wiczorek, K., Pudewills, A., Czaikowski, O., Hou, Z., & Fröhlich, H. (2008). EDZ Development and Evolution (RTDC 4). In *nuclear science and technology. Understanding and Physical and Numerical Modelling of the Key Processes in the Near Field and their Coupling for Different Host Rocks and Repository Strategies NF-PRO Final Synthesis Report (D. 4.5.3)*. FP6-EURATOM/NF-PRO, F16W-CT-2003-02389 (pp. 150–197). European Commission, Luxembourg.
- Armand, G., Leveau, F., Nussbaum, C., De La Vaissiere, R., Noiret, A., Jaeggi, D., et al. (2013a). Geometry and properties of the excavation-induced fractures at the Meuse/Haute-Marne URL drifts. *Rock Mechanics and Rock Engineering*, 47(1), 21–41.
- Armand, G., Noiret, A., Zghondi, J., & Seyed, D. M. (2013b). Short- and long-term behaviors of drifts in the Callovo-Oxfordian claystone at the Meuse/Haute-Marne underground research laboratory. *Journal of Rock Mechanics and Geotechnical Engineering*, 5(3), 221–230.
- Blümling, P., Bernier, F., Lebon, P., & Martin, C. D. (2007). The excavation damaged zone in clay formations time-dependent behaviour and influence on performance assessment. *Physics and Chemistry of the Earth, Parts A/B/C*, 32(8), 588–599.
- Bossart, P., Bernier, F., Birkholzer, J., Bruggeman, C., Connolly, P., Dewonck, S., Fukaya, M., Herfort, M., Jensen, M., Matray, J.-M., Mayor, J. C., Moeri, A., Oyama, T., Schuster, K., Shigeta, N., Vietor, T., & Wiczorek, K. (2017). Mont Terri rock laboratory, 20 years of research: introduction, site characteristics and overview of experiments. *Swiss Journal of Geosciences*, 110. doi:10.1007/s00015-016-0236-1 (this issue).
- Bossart, P., Meier, P. M., Moeri, A., Trick, T., & Mayor, J. C. (2002). Geological and hydraulic Characterization of the excavation disturbed zone in the Opalinus Clay of the Mont Terri Rock Laboratory. *Engineering Geology*, 66, 19–38.
- Bossart, P., Trick, T., Meierand, P. M., & Mayor, J. C. (2004). Structural and hydrogeological Characterization of the excavation-disturbed zone in the Opalinus Clay (Mont Terri Project, Switzerland). *Applied Clay Science*, 26, 429–448.
- Diederichs, M. S., & Kaiser, P. K. (1999). Stability of large excavations in laminated hard rock masses: the Voussoir analogue revisited. *International Journal of Rock Mechanics and Mining Sciences*, 36(1), 97–118.
- DIT-UPC. (2000). *CODE_BRIGHT, A 3-D program for thermo-hydro-mechanical analysis in geological media. User's guide*. Barcelona: CIMNE.
- Einstein, H. H. (2002). Tunnels in Opalinus Clayshale. A review of case histories and new developments. *Tunnelling and Underground Space Technology*, 15(1), 13–29.
- Ferrari, A., Favero, V., Marschall, P., & Laloui, L. (2014). Experimental analysis of the water retention behaviour of shales. *International Journal of Rock Mechanics and Mining Sciences*, 72, 61–70.
- Harrington, J., Volckaert, G., Jacobs, E., Maes, N., Areias, L., Charlier, R., & Granet, S. (2013). Summary report: experiments and modelling of excavation damage zone (EDZ) behaviour in argillaceous and crystalline rocks (Work Package 4). *EC FORGE Project Report D, 4*.
- Itasca. (2012). *FLAC3D (Fast Lagrangian Analysis of Continua)*. Version 5.01. Itasca Consulting Group Inc., Minnesota, USA.
- Labiouse, V., & Vietor, T. (2014). Laboratory and in situ simulation tests of the excavation damaged zone around galleries in Opalinus Clay. *Rock Mechanics and Rock Engineering*, 47(1), 57–70.
- Lanyon, G. W. (2011). Excavation damaged zones assessment. *Report NWMO DGR-TR-25 2011-21*. (p. 111).
- Lanyon, G. W., Marschall, P., Trick, T., De La Vaissiere, R., Shao, H., & Leung, H. (2009). Hydromechanical Evolution and Self-Sealing of Damage Zones around a Microtunnel in a Claystone Formation of the Swiss Jura Mountains. In *43rd U.S. Rock Mechanics Symposium & 4th U.S.—Canada Rock Mechanics Symposium* (pp. 652–663). American Rock Mechanics Association.
- Lanyon, G. W., Marschall, P., Trick, T., De La Vaissiere, R., Shao, H., & Leung, H. (2014). Self-sealing experiments and gas injection tests in a backfilled microtunnel of the Mont Terri URL. *Geological Society, London, Special Publications*, 400(1), 93–106.
- Lanyon, G. W., & Senger, R. (2011). A Structured approach to the derivation of effective properties for combined water and gas flow in the EDZ. *Transport in Porous Media*, 90(1), 95–112.

- Lisjak, A., Garitte, B., Grasselli, G., Müller, H., & Vietor, T. (2015). The excavation of a circular tunnel in a bedded argillaceous rock (Opalinus Clay): short-term rock mass response and FDEM numerical analysis. *Tunnelling and Underground Space Technology*, 45, 227–248.
- Lisjak, A., Tatone, B. S. A., Mahabadi, O. K., Grasselli, G., Marschall, P., Lanyon, G. W., et al. (2016). Hybrid finite-discrete element simulation of the EDZ formation and mechanical sealing process around a microtunnel in Opalinus Clay. *Rock Mechanics and Rock Engineering*, 49(5), 1849–1873.
- Marschall, P., Distinguin, M., Shao, H., Bossart, P., Enachescu, C., & Trick, T. (2006). Creation and evolution of damage zones around a microtunnel in a claystone formation of the Swiss Jura Mountains. In *International Symposium and Exhibition on Formation Damage Control*, Society of Petroleum Engineers.
- Marschall, P., Horseman, S., & Gimmi, T. (2005). Characterisation of gas transport properties of the Opalinus Clay, a potential host rock formation for radioactive waste disposal. *Oil & Gas Science and Technology*, 60(1), 121–139.
- Marschall, P., Trick, T., Lanyon, G. W., Delay, J., & Shao, H. (2008). Hydro-Mechanical Evolution of Damaged Zones around a Microtunnel in a Claystone Formation of the Swiss Jura Mountains. In *The 42nd US Rock Mechanics Symposium (USRMS)*, American Rock Mechanics Association.
- Martin, C. D., Christiansson, R., & Söderhäll, J. (2001). Rock stability considerations for siting and constructing a KBS-3 repository. *SKB Technical Report*, TR-01-38 (p. 94). Swedish Nuclear Fuel and Waste Management Co, Stockholm, Sweden. <http://www.skb.se>.
- Martin, C. D., & Lanyon, G. W. (2003). EDZ in clay shale: Mont Terri. *Mont Terri Technical Report*, TR 01-01 (p. 207). Federal Office of Topography (swisstopo), Wabern, Switzerland. <http://www.mont-terri.ch>.
- Nagra. (1997). Geosynthese Wellenberg 1996-Ergebnisse der Untersuchungsphasen I und II. *Nagra Technical Report*, NTB 96-01 (p. 511). Nagra, Wettingen, Switzerland. <http://www.nagra.ch>.
- Nagra. (2002). Projekt Opalinuston. Synthese der geowissenschaftlichen Untersuchungsergebnisse. Entsorgungsnachweis für abgebrannte Brennelemente, verglaste hochaktive sowie langlebige mittelaktive Abfälle. *Nagra Technical Report*, NTB 02-03 (p. 659). Nagra, Wettingen, Switzerland. <http://www.nagra.ch>.
- Nagra. (2008). Effects of post-disposal gas generation in a repository for low- and intermediate-level waste sited in the Opalinus Clay of Northern Switzerland. *Nagra Technical Report*, NTB 08-07 (p. 175). Nagra, Wettingen, Switzerland. <http://www.nagra.ch>.
- Nagra. (2016). Production, consumption and transport of gases in deep geological repositories according to the Swiss disposal concept. *Nagra Technical Report*, NTB 16-03, Nagra, Wettingen, Switzerland. <http://www.nagra.ch>.
- Nguyen, T. S., & Le, A. D. (2015). Simultaneous gas and water flow in a damage-susceptible bedded argillaceous rock. *Canadian Geotechnical Journal*, 52(1), 18–32.
- Nussbaum, C., Kloppenburg, A., Caër, T., & Bossart, P. (2017). Tectonic evolution around the Mont Terri rock laboratory, northwestern Swiss Jura: constraints from kinematic forward modelling. *Swiss Journal of Geosciences*, 110. doi:10.1007/s00015-016-0248-x (this issue).
- Poller, A., Smith, P., Mayer, G., & Hayek, M. (2014). Modelling of Radionuclide Transport along the Underground Access Structures of Deep Geological Repositories. *Nagra Technical Report*, NTB 14-10 (p. 166). Nagra, Wettingen, Switzerland. <http://www.nagra.ch>.
- Pruess, K., Oldenburg, C., & Moridis, G. (2012). TOUGH2 user's guide, Version 2.1 Lawrence Berkeley Laboratories, Report LBL-43134, Berkeley, CA, USA.
- Rejeb, A., Slimane, K. B., Cabrera, J., Matray, J. M., & Savoye, S. (2008). Hydro-mechanical response of the Tournemire argillite to the excavation of underground openings: Unsaturated zones and mine-by-test experiment. In *Thermo-hydromechanical and chemical coupling in geomaterials and applications: proceedings of the 3 international symposium GeoProc'2008* (pp. 649–656). Wiley.
- Senger, R. K., Lanyon, G. W., & Marschall, P. (2013). Modeling the Hydraulic and Two-phase Flow Behaviour of the Heterogeneous, Fractured EDZ in the Opalinus Clay during the HG-A Experiment at the Mont Terri URL. In *Proceedings of the Fourth European Association of Geoscientists & Engineers (EAGE) Shale workshop. Shales: what do they have in common?* (pp 148–152). European Association of Geoscientists & Engineers.
- Shao, H., Xu, W., Marschall, P., Kolditz, O., & Hesser, J. (2015). Numerical interpretation of gas-injection tests at different scales. *Geological Society, London, Special Publications*, 415(1), 203–212.
- Steiner, W. (1996). Tunnelling in squeezing rocks: case histories. *Rock Mechanics and Rock Engineering*, 29(4), 211–246.
- Suckling, P., Avis, J., Calder, N., Humphreys, P., King, F., & Walsh, R. (2012). T2GGM Version 3.1: gas generation and transport code. *Nuclear Waste Management Organization Report NWMO TR-2012-23*. Toronto, Canada.
- Tsang, C. F., Bernier, F., & Davies, C. (2005). Geohydromechanical processes in the Excavation Damaged Zone in crystalline rock, rock salt, and indurated and plastic clays in the context of radioactive waste disposal. *International Journal of Rock Mechanics and Mining Sciences*, 42(1), 109–125.
- Walsh, R., Nasir, O., Leung, H., & Avis, J. (2015). Numerical Characterization of the Excavation Damaged Zone in the HG-A Experiment. In *Proceedings: International High-Level Radioactive Waste Management*, Charleston, SC.
- Wilson, C. R., Witherspoon, P. A., Long, J. C. S., Galbraith, R. M., DuBois, A. O., & McPherson, M. J. (1983). Large-scale hydraulic conductivity measurements in fractured granite. *International Journal of Rock Mechanics and Mining Sciences & Geomechanics Abstracts*, 20(6), 269–276.
- Xu, W., Shao, H., Marschall, P., Hesser, J., & Kolditz, O. (2013). Analysis of flow path around the sealing section HG-A experiment in the Mont Terri Rock Laboratory. *Environmental Earth Sciences*, 70(7), 3363–3380.
- Yong, S. (2007). A three-dimensional analysis of excavation-induced perturbations in the Opalinus Clay at the Mont Terri Rock Laboratory. *Ph.D dissertation*, Swiss Federal Institute of Technology in Zürich, Zürich, Switzerland, p. 167.

Coupled hydraulic-mechanical simulation of seasonally induced processes in the Mont Terri rock laboratory (Switzerland)

Gesa Ziefle¹  · Jean-Michel Matray² · Jobst Maßmann¹ · Andreas Möri³

Received: 3 March 2016 / Accepted: 9 December 2016 / Published online: 17 February 2017
© The Author(s) 2017. This article is published with open access at Springerlink.com

Abstract This paper focuses on hydraulic-mechanical effects in the Mont Terri rock laboratory (Switzerland) and investigates their impact on pore pressure, the convergence of a niche and the evolution of pre-existing cracks in the wallrock of the niche. A comparison of measurements with numerical simulation results is conducted. The presented in situ measurements include long-term data on temperature, relative humidity, and niche convergence, as well as crackmeter and jointmeter measurements determining the aperture of a bedding-parallel crack. Furthermore, time-domain-reflectometry measurements were carried out in a borehole located in the niche wall close to the crack. They provide information on the water content of the claystone. The numerical simulation is carried out with OpenGeoSys. It contains a 2-dimensional coupled hydraulic-mechanical model considering orthotropy, swelling and shrinkage effects, linear elastic material behaviour and an excavation damaged zone characterized by a zone of lower rock strength. An additional focus is laid on the evolution of cracks in the wallrock of the niche. The presented model approach allows a prediction of the temporal evolution of a

desaturated zone incorporating a seasonally influenced part. The comparison with measured water contents yields good agreement. Simulation results and measurements consistently predict a convergence of the niche. The evolution of the crack aperture is influenced by long-term as well as seasonally influenced effects. Due to the convergence of the niche, the long-term trend is characterized by closure of the crack. Furthermore, the seasonally influenced desaturation in winter results in opening of the crack, while the resaturation in the warm and wet summer months leads to closure of the crack. Finally, the comparison of simulation results with measurements indicates qualitative agreement. As a matter of fact, the numerical model seems to represent significant effects concerning the evolution of the crack aperture of a single crack.

Keywords Cyclic deformation (CD) experiment · Long-term monitoring of pore parameters (LP-A) experiment · OpenGeoSys · Desaturation process · Atmospheric influences · Crack evolution · Nuclear waste disposal

Editorial handling: P. Bossart and A. G. Milnes.

This is paper #9 of the Mont Terri Special Issue of the Swiss Journal of Geosciences (see Bossart et al. (2017), Table 3 and Fig. 7).

✉ Gesa Ziefle
gesa.ziefle@bgr.de

¹ Federal Institute for Geosciences and Natural Resources (BGR), Stilleweg 2, 30655 Hannover, Germany

² Institut de Radioprotection et de Surete Nucleaire, BP 17, 92262 Fontenay-aux-Roses Cedex, France

³ Federal Office of Topography Swisstopo, Seftigenstrasse 264, 3084 Wabern, Switzerland

1 Introduction

This article is based on the CD (cyclic deformation) experiment which is carried out in the Mont Terri rock laboratory, located in the Opalinus Clay formation in Switzerland. Figure 1 presents the cross section through the Mont Terri anticline and the location of the rock laboratory. The CD experiment is located in the EZB-niche of the underground laboratory (see Bossart et al. 2017). It focuses on the seasonally induced hydraulic-mechanical coupling at the wallrock of the uncovered niche in the claystone. In this context, the investigations focus on the desaturation and resaturation process, swelling and

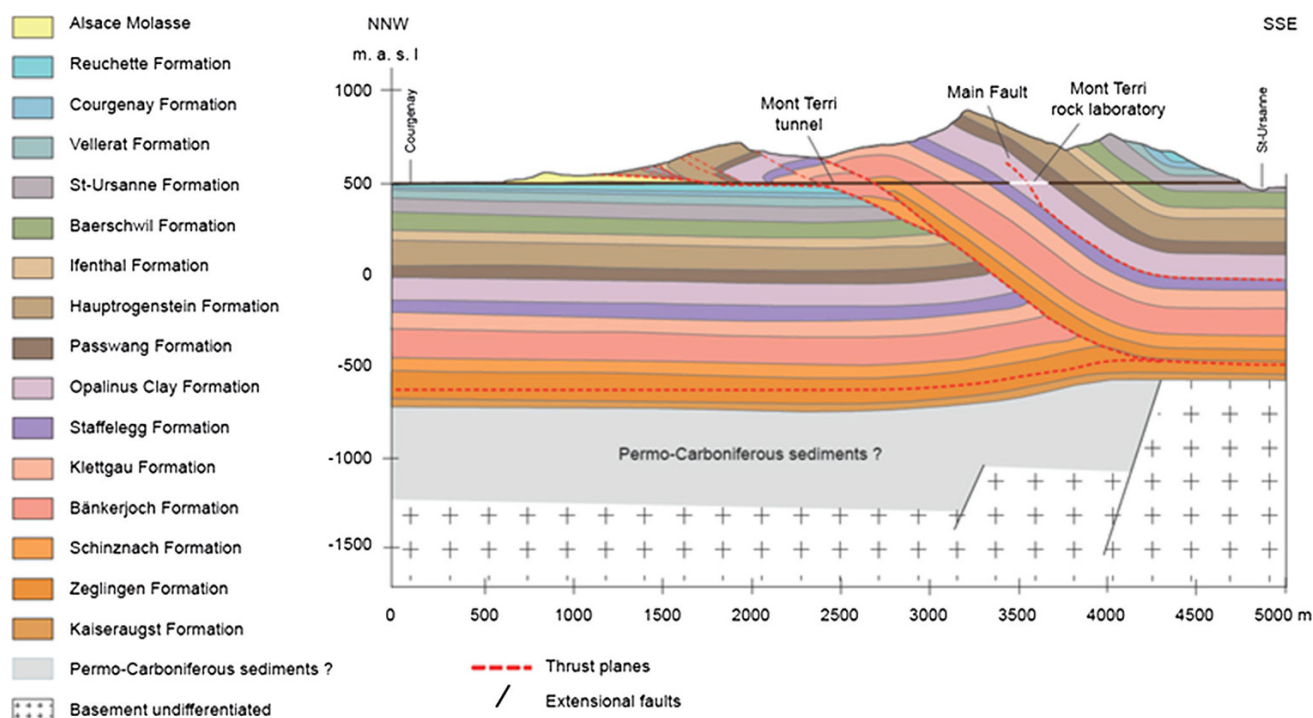


Fig. 1 Geological cross-section of the Mont Terri anticline and location of the Mont Terri rock laboratory (Nussbaum et al. 2017, this volume)

shrinkage, the excavation damaged zone (EDZ), and orthotropic material conditions. The aim of the presented work is to obtain an increased process understanding of the observed effects. Since 2006, the temporal evolution of the water content, the convergence of the niche as well as apertures of a crack were continuously measured and the derived values compared with numerical simulation results. The measurements conducted in the context of the CD experiment are continued in the LP-A (long-term monitoring of pore parameters) experiment. The numerical model approach considers strictly defined effects and enables the determination of significant processes.

The following article starts with a description of the experimental set-up in the niche. Additionally, the measurements are briefly summarized. After that, a numerical model approach is presented. Here, the physical effects are transferred to a mathematical description of the model. The investigated effects concern three different points: (1) the hydraulic process, (2) the mechanical process and (3) the phenomenological investigation of one single crack. The derived results are presented and compared with the measurements in the subsequent sections. Finally, the results are discussed, followed by conclusions and an outlook.

Similar aspects have been investigated in the Underground Research Laboratory in Tournemire (France) [discussed in Maßmann (2009)] and Meuse-Haute-Marne (France) (Yildizdag et al. 2014) which are also located in claystone.

Maßmann (2009) introduced hydraulic-mechanically coupled numerical simulations with the finite element code

RockFlow. Sensitivity studies point to the permeability being the significant input parameter; comparisons with various measurements are carried out (see also Maßmann et al. (2008)) and the differentiation of a fully saturated, a desaturated and a seasonally influenced desaturated zone is introduced. The measured saturation profiles in Tournemire are wide spread, indicating an inhomogeneous distribution of permeabilities which might be induced by desaturation fissures.

Yildizdag et al. (2014) investigated related effects in the context of the mine-by experiment carried out in Meuse-Haute-Marne (France). He proposes different finite element models and uses the simulation tool RockFlow involving coupled hydraulic-mechanical effects, shrinkage, partial saturation, damage and sensitivity studies concerning permeability, and Young's modulus. Yildizdag et al. (2014) states that the mechanical response in the near-field could not be reproduced while the investigation of the pore pressure evolution leads to acceptable results.

Finally, the literature review indicates that the mechanical effects in indurated clay are not yet fully understood and that there exist various uncertainties concerning the measured and simulated saturation profiles—especially in the near-field of the niche. This work deals with the hydraulic-mechanically coupled simulation of the considered effects. It focuses on a relatively simple mechanical approach in combination with a complex hydraulic-mechanical coupling, with the aim of identifying significant effects.

2 Experimental set-up in the niche and measurements

In-situ measurements are carried out in the EZB-niche (Fig. 2), where the claystone is not covered with shotcrete. Here, the atmospheric changes in temperature and relative humidity directly affect the wallrock. The effects which are generated due to these “open conditions” are monitored by various long-term, as well as one-time, measurements.

Long-term measurements of temperature, relative humidity and the convergence of the niche are carried out. The measurements of the relative humidity and

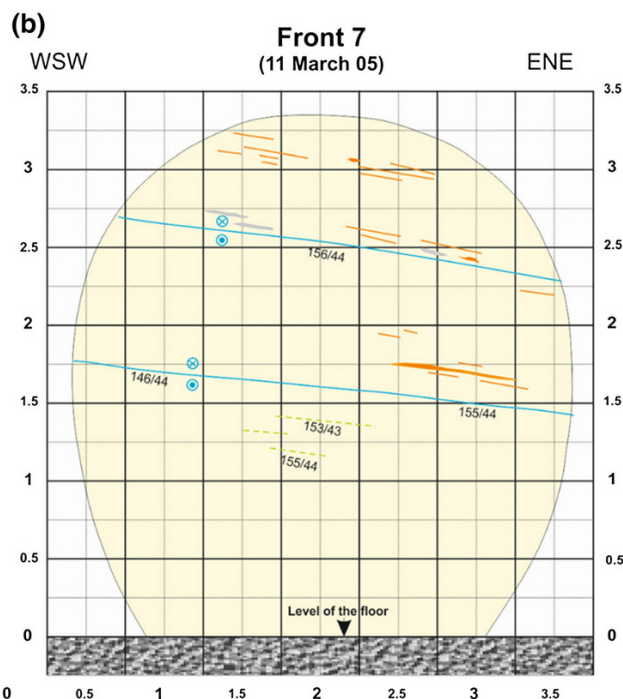
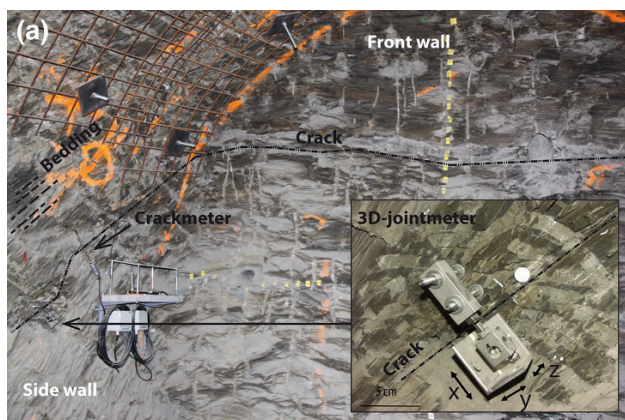


Fig. 2 The EZB-niche in the Mont Terri rock laboratory is not covered with shotcrete. Various measuring devices are installed. The upper picture indicates the location of the crackmeter and the jointmeter [taken from Möri et al. (2010)]. The lower picture is taken from Nussbaum et al. (2005) and indicates the bedding trace, as well as the location of pre-existing fractures in the wallrock of the niche

temperature are presented in Fig. 3, the convergence measurements are given in Fig. 15. More information can be found in e.g. Möri et al. (2010), and Matray and Möri (2012).

The temporal evolution of the fracture apertures suggests a correlation between variations in crack aperture and the variation in the tunnel climate conditions. Consequently, the long-term crack aperture, and the associated shear displacements of selected shrinkage cracks at a bedding-parallel plane in the rock matrix, have been measured by a crackmeter and a 3D-jointmeter (Girardin and Nussbaum 2006; Jaeggi and Gisiger 2012). The crackmeter measures its own deformation and is located perpendicular to an existing crack. The time series is acquired automatically using an independent data acquisition system (DAS). The jointmeter measures relative movements in three directions at two different measurement blocks located on two sides of a selected shrinkage crack. The displacements are manually acquired every 5/7 days.

Additional laboratory experiments with drill cores under controlled initial and boundary conditions are summarized in Matray and Möri (2012). The investigations determine profiles of the porosity, the gravimetric and volumetric water content, the degree of saturation, and the grain density over the length of the 3.28 m BCD-3 borehole drilled in June 2012. The results indicate characteristic values for the undisturbed rock, as well as modified values resulting from various kinds of rock damage: such as shrinkage cracks, natural fractures, or fractures induced by excavation and/or handling.

The long-term measurements, as well as laboratory investigations, started in 2006. They are supplemented by the installation of a so-called TDR probe (Time Domain Reflectometry) in the BCD-3 borehole in 2012. This modular packer system consists of five modules, each

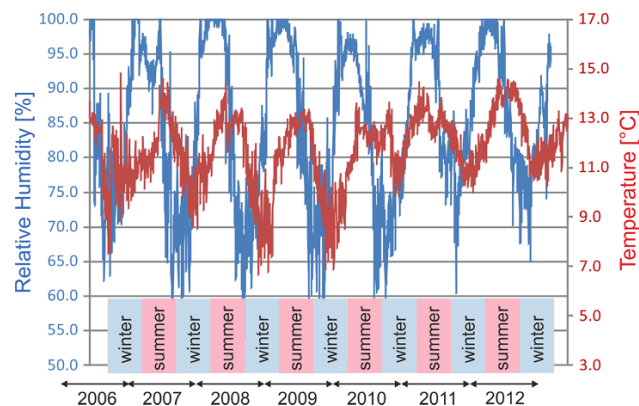


Fig. 3 Measurements of relative humidity (blue) and air temperature (red) in the EZB-niche. The measurements are presented for a time period of 6 years, and indicate the seasonal oscillations of relative humidity and temperature

containing a TDR sensor located behind a latex rubber cover to avoid water intrusion. This TDR probe and related measurements produce profiles of matrix saturation, swelling and pore-water pressures from the niche surface towards the saturated rock matrix. Petrophysical and volumetric water content probe results and a discussion of the results are presented in Matray and Móri (2012) and Matray and Bailly (2014).

Additional measurements of the water content, as well as the convergence of the niche and the crack aperture, are depicted in Figs. 10, 11 and 19.

3 Model approach

3.1 Definition of the problem

The described experiment focuses on coupled hydraulic-mechanical processes in the low permeability, orthotropic claystone formation with significant swelling and shrinkage behaviour. The flow process in the hydraulically orthotropic claystone is simulated using Darcý's law modified for unsaturated media, and a two-phase flow model simplified by the Richard's approach. The mechanical behaviour is described by transversal isotropic, linear elasticity.

The presented model focuses on the effects resulting from the contact of the claystone with the seasonally varying air humidity—neglecting effects induced directly by the excavation. It can be assumed that the excavation of the niche in the claystone with nearly horizontal bedding plane and an orthotropic initial stress field leads to a decrease of the pore volume in some distance sideways the niche. This results in an increase of pore pressures. The opposite effect might appear at the top and bottom combined with a decrease of pore pressures. These effects have been investigated in Maßmann (2009) amongst others. However, there exist no pressure measurements that could confirm these assumptions—but desaturation in the horizontal direction is definitely indicated. It is assumed that the effect of desaturation dominates the evolution of the desaturated area.

The seasonal change of desaturation and resaturation in the Opalinus Clay implies shrinkage and swelling behaviour. This effect is incorporated in the model by an isotropic, linear swelling model, proposed by Rutqvist et al. (2001). Information about the swelling behaviour of the claystone can be found in Bock (2000) and Martin and Lanyon (2003). A general overview of the presented coupled hydraulic-mechanical model is given in Fig. 4. The HM coupling effects are considered using the Biot constant α and the Bishop coefficient χ , reducing the effective stress approach to saturated conditions only. The Bishop coefficient is given by:

$$\chi = \begin{cases} 0, & \text{if } S < 1 \\ 1, & \text{else} \end{cases}.$$

This leads to the following formulation of the mechanical problem:

$$\nabla \cdot (\boldsymbol{\sigma} - \alpha\chi(p - p_0)\mathbf{I} - Sp_{sw,max}\mathbf{I}) = 0$$

where the effective stress tensor $\boldsymbol{\sigma}$, the water pressure p , the initial water pressure p_0 , the identity tensor \mathbf{I} , the water saturation S , and the maximal swelling pressure $p_{sw,max}$.

The formulation of the hydraulic problem is given by:

$$\nabla \cdot \mathbf{q} + n \frac{\partial S}{\partial t} + S\alpha \nabla \cdot \frac{\partial \mathbf{u}}{\partial t} + S_p \frac{\partial p}{\partial t} = 0$$

with: the fluxes due to Darcý's law \mathbf{q} , the porosity n , the time t , the deformation vector \mathbf{u} , and the storage term due to pressure changes S_p .

This model approach implies that classical Terzaghi coupling effects are restricted to the fully saturated case. For the unsaturated case, the coupling is mainly caused by the swelling and shrinkage behaviour. Gravity and the process of excavation are not incorporated in the presented model.

3.2 Model set-up

The coupled simulation is carried out with the finite element code OpenGeoSys (OGS). Further information concerning OGS can be found in e.g. Kolditz (2002), Wang et al. (2009), Kolditz et al. (2012b), Wang et al. (2013), and Kolditz et al. (2012a). The model set-up is performed for a 2D-model with plane strain conditions, representing a vertical slice of the niche. The model domain has an extent of 20 m times 20 m and is presented in Fig. 5. The modelled area is divided into a domain that represents the EDZ and a zone which is characterized by intact Opalinus Clay. Both areas are depicted in Fig. 6. The EDZ is assumed to have an extent of 70 cm at the top and at the side walls of the niche; at the bottom it is reduced to an extent of 25 cm. Further information about the EDZ can be found in Alheid et al. (2002), Matray and Bailly (2014), Nussbaum et al. (2005), and Yong et al. (2010). In comparison to the intact claystone (index OPA), the EDZ is assumed to have a reduced strength. Yong (2007) presents a first approximation to determine the rock mass modulus in comparison with intact rock moduli for a niche located in Mont Terri and surrounded by multiple tectonic shears. The derived reductions vary between more than 75 and 50%. The model presented here focuses on the reduction of the EDZ compared to the surrounding rock mass. For this case, the following properties are assumed:

$$E_{||,EDZ} = \frac{1}{2} E_{||,OPA}$$

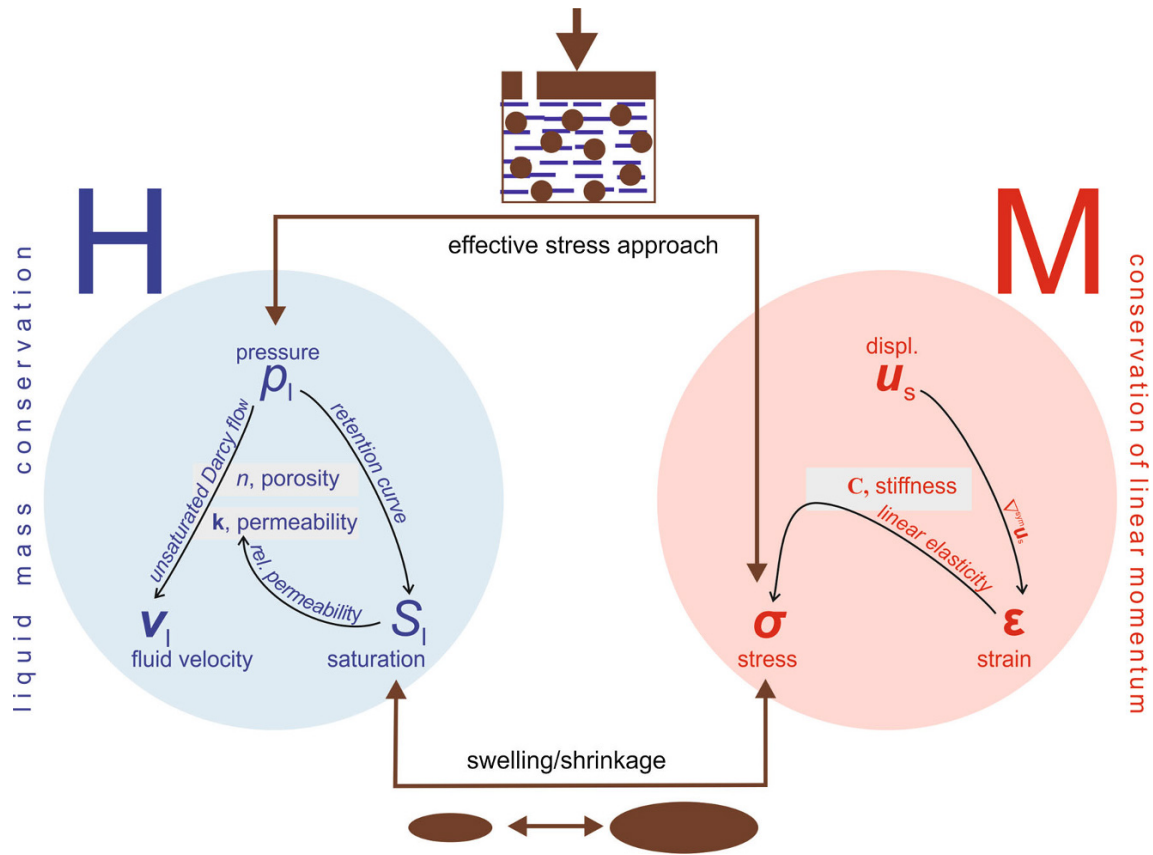


Fig. 4 Model approach for the coupled hydraulic-mechanical system [modified after Maßmann (2009)]. The simulation of the hydraulic process is based on the conservation of the liquid mass which states an interaction between pressure, fluid velocity and saturation. The mechanical process is based on the conservation of linear momentum,

which incorporates interactions between stresses, strains and displacements. A coupling of both processes is implemented due to the classical Terzaghi effective stress approach, as well as a linear swelling/shrinkage model

$$E_{\perp,EDZ} = \frac{1}{2}E_{\perp,OPA}$$

All other material parameters are assumed to be identical for the intact Opalinus Clay and the EDZ. They are summarized in Table 1. More information can be found in e.g. Wild et al. (2015) and Bock (2009). The initial conditions imply a fully saturated area of Opalinus Clay. The boundaries are assumed to remain fully saturated. The detailed model set-up is presented in Fig. 5.

The far-field stresses are specified as initial compressive stresses and assumed to be 7 MPa in the vertical direction and 5 MPa in the horizontal direction. More information about the in situ stress field at the Mont Terri rock laboratory can be found in Martin and Lanyon (2003). The bedding plane has an inclination of 10° in this part of the laboratory and the displacements are prevented in the horizontal direction at the left boundary and in the vertical direction at the bottom of the presented area. Furthermore, a pressure boundary condition at the niche represents the seasonal changes in the temperature and the relative

humidity in the niche. This boundary condition is characterized by negative pore pressures (suction) and is based on the measurements as depicted in Fig. 3. As presented in Maßmann (2009), Andra (2005a) and Bond et al. (2013), the Kelvin equation is used to derive the pressure boundary condition. It is given by

$$p = \frac{\rho_l RT}{M_v} \cdot \ln h_{rel}$$

with: the liquid density ρ_l , the perfect gas constant R , the absolute temperature T , the molecular weight of water M_w , and the relative humidity h_{rel} .

The relation between capillary pressure and saturation is defined by the van Genuchten model

$$S = \left[1 + \left(\frac{p}{P_0} \right)^{1/(1-\beta)} \right]^{-\beta}$$

with: the van Genuchten fitting parameters P_0 and R according to Wild et al. (2015). The relationship between the relative permeability and the saturation is defined by:

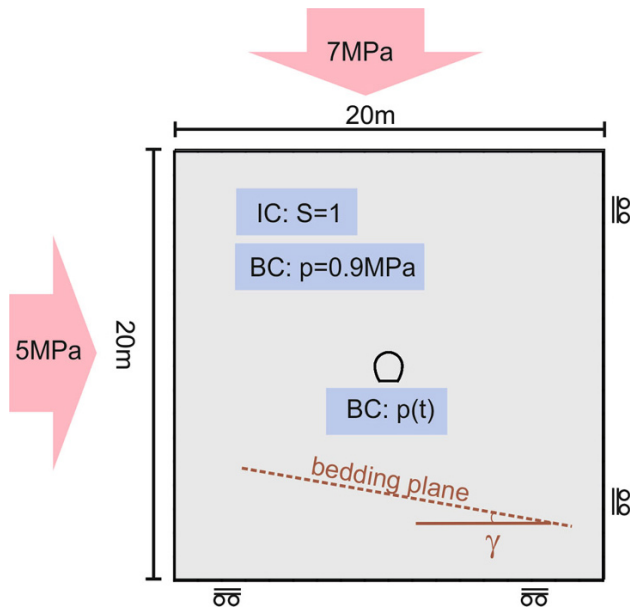


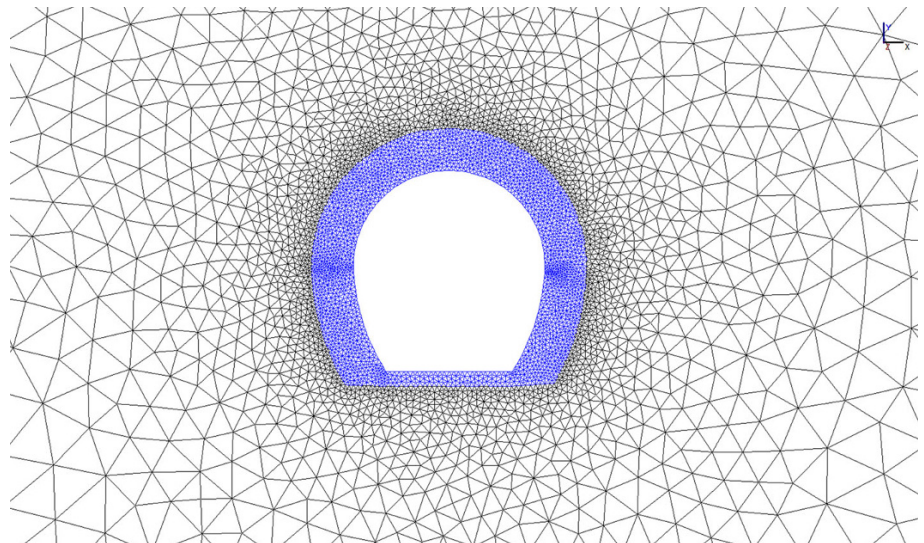
Fig. 5 Geometry and model set-up. The 2-dimensional model has an extent of 20 times 20 m. The bedding plane in this area of the Mont Terri rock laboratory has an inclination of 10° . The boundaries of the numerical model are fixed in the horizontal direction at the *right side*, and in the vertical direction at the *bottom*. The far-field stresses are given by 7 MPa in the vertical direction and 5 MPa in the horizontal direction. Initially, the model domain is assumed to be fully saturated in the whole domain, and it is assumed to remain fully saturated at the boundaries. The pore pressure in this area is set to 900 kPa

$$k_{rel,S} = S_{eff}^{0.5} \left[1 - \left(1 - S_{eff}^{\frac{m}{m-1}} \right)^{\frac{m-1}{m}} \right]^2$$

where the shape factor m and the effective saturation are given by:

$$S_{eff} = \frac{S - S_{res}}{S_{max} - S_{res}}$$

Fig. 6 Part of the finite element mesh incorporating the EDZ. The numerical simulation with OpenGeoSys (OGS) is carried out on a triangle mesh with an extent of 20 times 20 m. The figure represents the central part of this mesh. The blue area represents the excavation damaged zone (EDZ), while the black parts constitute the intact claystone



with: the effective saturation S_{eff} , the residual saturation S_{res} , and the maximal saturation S_{max} . The hydraulic and mechanical parameters are taken from Bock (2009), Wild et al. (2015), and Xu et al. (2014). The permeability is calibrated with respect to the measurements of the water content. All parameters are summarized in Table 1.

4 Hydraulic results

The proposed model represents a desaturation of the claystone due to the exposure of the wallrock to the tunnel atmosphere. While the desaturated zone increases during the cold and dry winter, there exists a temporary resaturation close to the tunnel during the warm, wet summer months. The desaturated zone for the summer, as well as the winter, is presented in Fig. 7 seven years after the excavation. The extent of the desaturated zone reaches its maximum in the direction of the bedding, and has an extent of nearly 1.4 m at this time.

A validation of the depicted effect is carried out by means of a comparison of measurements and simulation results concerning the temporal progression and the degree of desaturation. The desaturated zone can be divided into two parts: the seasonally influenced desaturated zone and the long-term influenced desaturated zone. In this context, the desaturated zone is defined by a saturation of less than 99.5%. The seasonally influenced zone is defined by oscillations of the water content of more than 0.2%—lower deviations are not mandatory connected with seasonal effects.

Table 1 Hydraulic and mechanical parameters which are used in the numerical model

Parameter	Value	Unit
Angle of inclination, γ	10.0	°
Porosity, n	0.16	–
Hydraulic conductivity, K	4.0e–13	m/s
Permeability in the plane of isotropy, k_{\parallel}	6.8e–20	m ²
Permeability normal to the plane of isotropy, k_{\perp}	1.36e–20	m ²
Liquid density, ρ_l	1000	kg/m ³
Perfect gas constant, R	8.314	J/(K mol)
Molecular weight water, M_w	0.018	kg/mol
Biot constant, α	1.0	–
Bishop coefficient, χ	0.0–1.0	–
Grain density claystone, ρ_s	2500	kg/m ³
Poisson number in the plane of isotropy, ν_{\parallel}	0.18	–
Poisson number normal to the plane of isotropy, ν_{\perp}	0.16	–
E in the plane of isotropy, E_{\parallel}	3.6e9	N/m ²
E normal to the plane of isotropy, E_{\perp}	1.1e9	N/m ²
G normal to the plane of isotropy, G_{\perp}	1.2e9	N/m ²
Maximal swelling pressure, $p_{sw,max}$	7.0e7	N/m ²
Van Genuchten parameter, P_0	44.4e6	Pa
Van Genuchten parameter, β	0.54	–
Van Genuchten parameter, m	2	–
Residual saturation, S_{res}	0.002	–
Maximal saturation, S_{max}	1.0	–

4.1 Comparison of the simulation results with measurements of the TDR probe

In summer 2012 (7 years after the excavation of the niche), a TDR probe was installed in borehole BCD-3 which is located along the horizontal line shown in Fig. 7 (bottom). Figure 8 presents measurements of the volumetric water content over a time period of nearly 4 years. These results are compared with simulated water contents which are presented over the distance away from the niche.

The measurements of the water content (Fig. 8) are presented for five locations determined by the geometry of the TDR probe. Initially, results indicate an influence of the drilling at the borewall which lead to a significant decrease of the water contents in the vicinity of the borehole. In addition, a step-like increase/decrease and a subsequent decrease/increase in the water content can be seen between January and April 2013, June 2014, and November/December 2014. These steps as well as the decrease of the water content, that can be observed since November 2015 for all five positions, are artefacts which result from technical reasons concerning the design of the TDR probe. In addition, the volumetric water content indicates—location dependent—that it is part of either the seasonally influenced desaturated zone, the desaturated zone or the saturated zone. TDR 5 is located at a distance of 0.38 m from

the niche. The water content indicates seasonal variations with an amplitude of 0.5%. This location belongs to the seasonally influenced desaturated zone. TDR 4 is located at a distance of 0.99 m from the niche. The volumetric water content indicates desaturated conditions but no significant seasonal influence. TDR 3, which is located at a distance of 1.61 m from the niche, yields similar results. For this location, the measurements indicate even lower water contents than for the location of TDR 4. TDR 2 and TDR 1 are located at distances of 2.22 and 2.83 m respectively from the niche. They are not characterized by seasonal influences, but by a minor saturation process. The material at these locations seems to be under nearly saturated conditions.

The simulation results presented in Fig. 9 indicate volumetric water contents between 13.4 and 13.8% at the location of TDR 5. This equals an amplitude of 0.4%, and an association with the seasonally influenced zone—matching the result of the measurements. Both investigation methods indicate seasonal influences at this location. Furthermore, the numerical simulation indicates that the output location of TDR 4 belongs to the long-term influenced desaturated zone—again matching the result of the measurements. The numerical simulation suggests that the location of TDR 3 belongs to the saturated zone, which does not agree with the measurements. Regarding the

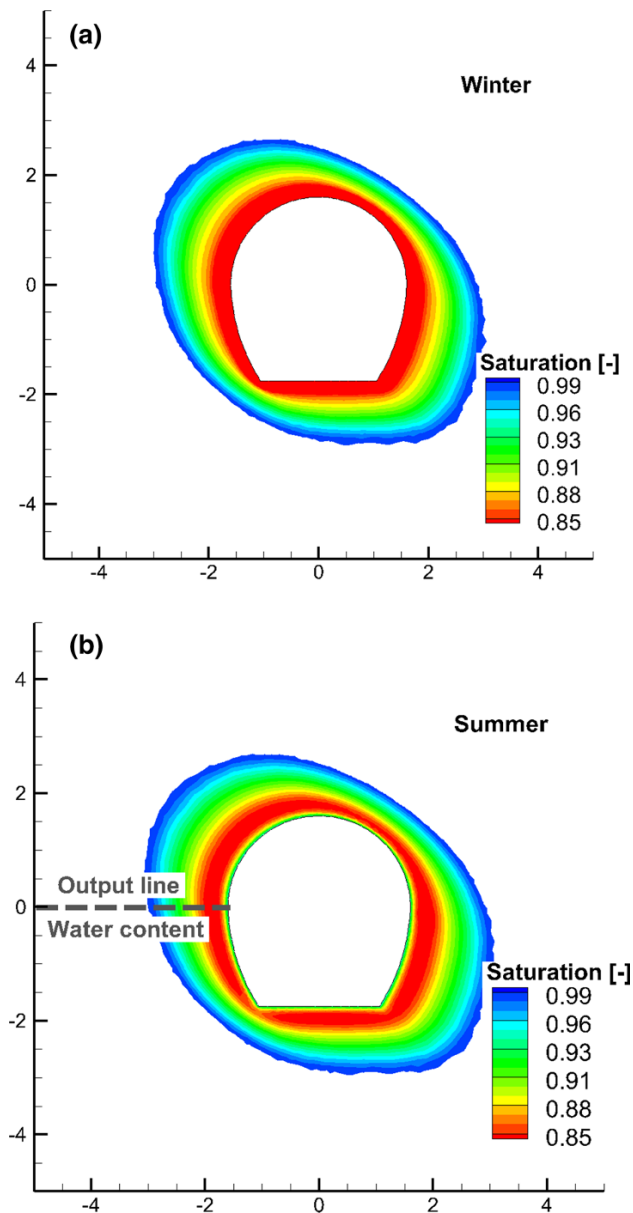


Fig. 7 Desaturated area in winter (*top*) and summer (*bottom*) after 7 years under atmospheric influence. The *coloured* area represents the zone where the saturation is lower than 99%. The comparison of the winter and summer cases indicates a seasonal influence in the vicinity of the niche. The influence of the orthotropic material properties can be seen. Furthermore, the *picture at the bottom* contains the identification of the output location for the following investigations of the water content

unexpectedly low measured water contents at this location, reasons for this difference might be a heterogeneity of the claystone and/or an irregular borehole shape at this position. Please refer also to the results of the petrophysical measurements on core samples (presented in section 4.2, Fig. 10), which also indicate heterogeneities at this location. For the locations of TDR 4 and TDR 5, both investigation methods indicate fully saturated conditions 7 years

after excavation. Finally, the measured water contents are lower than the simulated ones, but the comparison of the investigation methods shows good agreement concerning the extent of the desaturated zone, the extent of the seasonally affected zone, and the seasonal oscillations of the water content, which are also presented in Table 2.

4.2 Comparison of the simulation results with petrophysical measurements on core samples

In combination with the drilling of borehole BCD-3, core samples were taken and investigated in the laboratory. The derived volumetric water content is presented in Fig. 10 over the distance from the niche, along the output line which is defined in Fig. 7 (right). A comparison of these measurements with simulation results for the summer and winter is depicted. The simulation indicates that the seasonally-influenced desaturated zone is characterized by the ongoing change between desaturation and resaturation, while the water content in the long-term desaturated zone undergoes only minor changes. The core samples were taken in summer, and give the summer cycle extent of the water content. The comparison of both investigation methods shows good agreement of the water content 7 years after excavation. The numerical simulation results significantly depend on the assumed permeabilities and the saturation-dependent relative permeabilities. The measurements indicate the existence of heterogeneous areas resulting in deviant behaviour. Finally, the measurements as well as the simulation indicate an extent of the desaturated zone of about 1.4 m after 7 years. Lower water contents which are measured at greater distances are interpreted as heterogeneities of the material. The simulation indicates an extent of the seasonally influenced zone of about 50 cm. The results are summarized in Table 2.

4.3 Long-term evolution of the desaturated zone

In this article, the comparison of measurements and simulation results is used to verify the model approach. Incorporating the model set-up, the results of a long-term simulation can also be interpreted. Here they do not incorporate damage or plastic effects, nevertheless they indicate that an equilibrium stage will hardly be reached in 15 years due to an ongoing, very low desaturation process. However, the hydraulic (please refer to Fig. 11) and mechanical (see Fig. 15) long-term results seem to converge on an equilibrium stage, and most of the convergence as well as most of the desaturated area, already develops in the first 10 years. 15 years after the excavation of the niche, the extent of the seasonally influenced desaturated zone is given as 50 cm (as already stated as a result after

Fig. 8 Measured volumetric water contents over the time. The measurements represent the evolution of the water content over a time period of nearly 4 years. Initially, a decrease in water content due to the drilling of the borehole takes place. The *red curve* shows the water content in the vicinity of the niche and is characterized by seasonal oscillations. The *pink* and the *green curves* are located in the desaturated zone, while the output locations given by the *blue lines* seem to be located in nearly saturated conditions

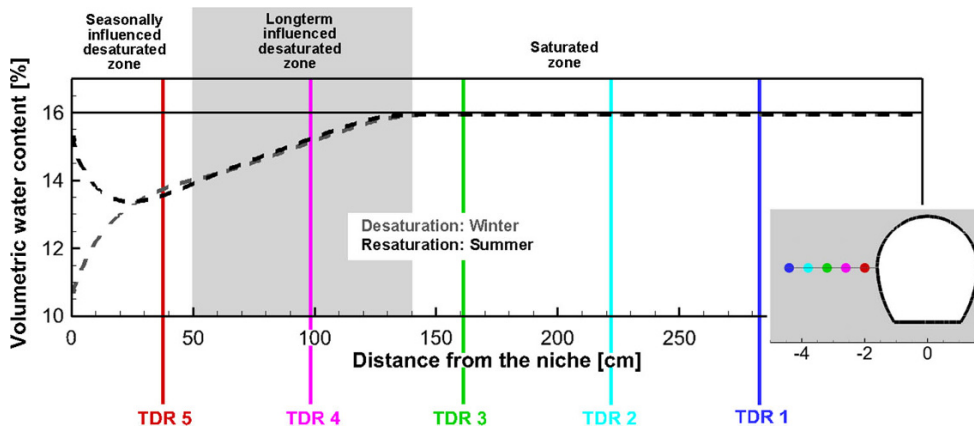
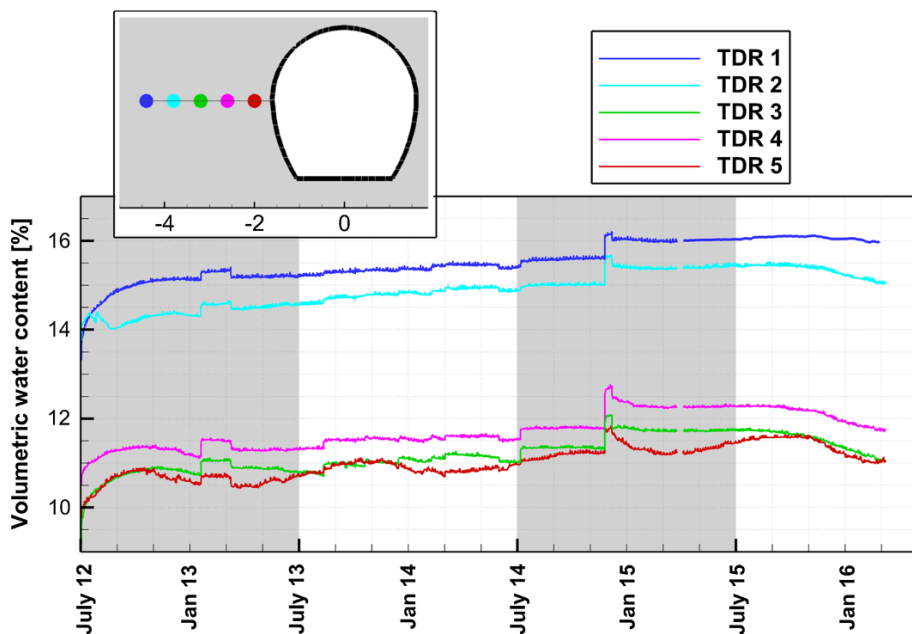


Fig. 9 Simulated water content (7 years after excavation) versus the distance from the niche for the horizontal line given in Fig. 7 (right). Lines represent the desaturation case in winter (grey) and the resaturation case in summer (black). The comparison allows for the

7 years) and the long-term desaturated zone has an extent of 2.2 m.

4.4 Summarizing the results

The presented results regarding the comparison of the numerical simulation with the measurements are summarized in Table 2. Here, a classification of the different locations with respect to the saturation state is presented. It can be stated that the results concerning the extent of the desaturated zone show good agreements. Only the measurements at the location of TDR 3 indicate heterogeneous material behaviour or some kind of fractured zone, which is not considered in the homogeneous numerical model.

definition of a seasonally influenced desaturated zone, a long-term influenced desaturated zone and a saturated zone. The coloured lines mark the output locations of the TDR-measurements

The results from the TDR at the drilling date do not provide any information regarding the seasonal variation, because they are not time-dependent. Consequently, the output location TDR 1 is only classified as “DZ” (desaturated zone).

5 Mechanical results

Concerning the mechanical processes, the desaturation implies an area of compaction due to the shrinkage of the material. The resulting stress state is given in Fig. 12 for the winter. Here, a decrease of the compressive stresses can be observed in the near-field of the niche. The related

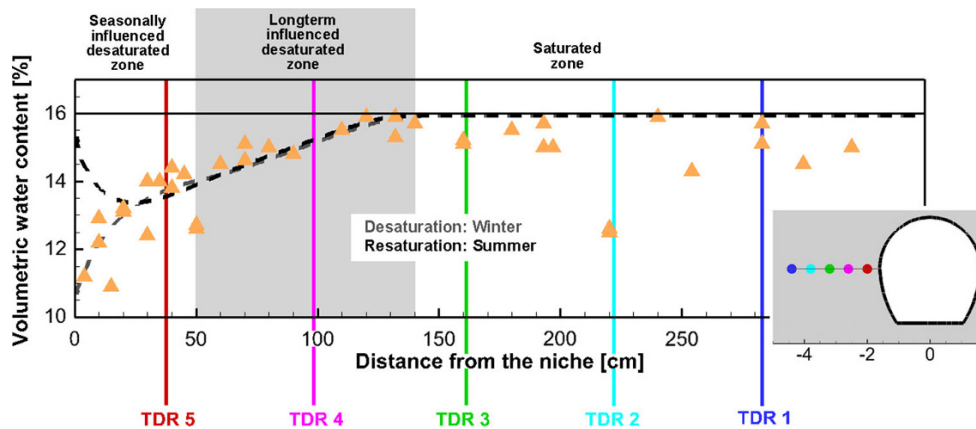


Fig. 10 Comparison of the measured and simulated water contents (7 years after excavation) versus distance from the niche for the horizontal line given in Fig. 7 (bottom). Measured values from core samples are shown by the *orange triangles*. Simulated results as displayed in Fig. 9 are given for comparison

Table 2 Classification of different locations based on measurement and simulation

Investigation method	Output location				
	TDR 1: 38.5 cm	TDR 2: 99.5 cm	TDR 3: 160.5 cm	TDR 4: 221.5 cm	TDR 5: 282.5 cm
TDR probe	SIDZ	DZ	DZ	SZ	SZ
Core samples	DZ ^a	DZ	DZ	SZ	SZ
Simulation (7 years)	SIDZ	DZ	SZ	SZ	SZ
Simulation (15 years)	SIDZ	DZ	DZ	DZ	SZ

SIDZ seasonally influenced desaturated zone, *DZ* desaturated zone, *SZ* saturated zone

^a The investigation of the core samples does not provide any information on seasonal changes. TDR 1 lies in the desaturated zone, however it is not possible to state whether this zone is seasonally influenced

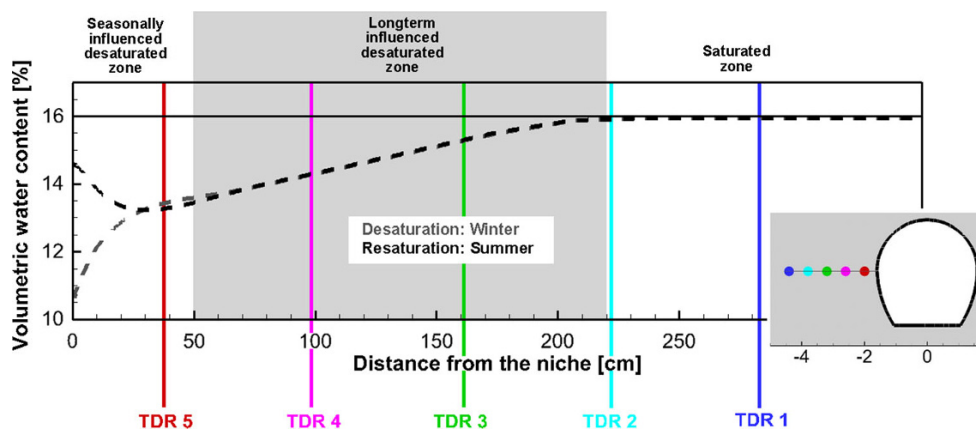


Fig. 11 Simulated water content (15 years after the excavation) versus distance from the niche for the horizontal line given in Fig. 7 (bottom). The simulation indicates an extent of the desaturated zone

of approximately 2.2 m after 15 years. The seasonally influenced desaturated zone is quasi-stationary and has an extent of 50 cm 7 years after excavation in accordance with the results

vertical and horizontal displacements are given in Fig. 13 for the winter and indicate a comparatively large affected zone with movement towards the desaturated area. Due to the seasonal change between desaturation and resaturation,

the displacements at the tunnel surface may be characterized by opposite effects than the displacements at a distance of some decimetres. While movement towards the claystone can be observed at the surface of the niche,

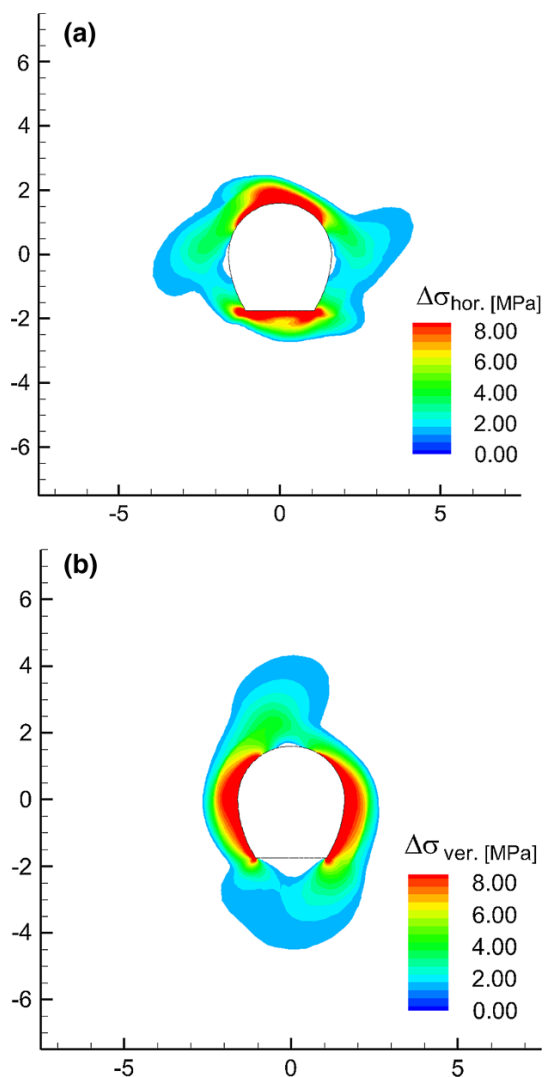


Fig. 12 Decrease in the compressive stresses after 7 years of atmospheric influence (*top* horizontal stresses; *bottom* vertical stresses) in the winter. Zones are shown where the change in the stresses is more than 1 MPa. The results in winter in this context represent the worst case. The resaturation in summer will lead to lower values

movement towards the niche can be observed at a greater distance from the tunnel. This effect significantly depends on the season. It is also presented in Fig. 14 because it leads to significant differences between the results observed at the niche surface and at locations a few cm away from the surface. This area is characterized by significant seasonal oscillations which are restricted to the vicinity of the niche. Measurements with regard to the anchor location (25 cm away from the niche surface) may indicate a lower impact of the seasonal variation of the climatic conditions than measurements at the niche surface.

A comparison of the numerical results with the convergence measurements of the niche is given in Fig. 15. Presented are the vertical, the horizontal and the diagonal

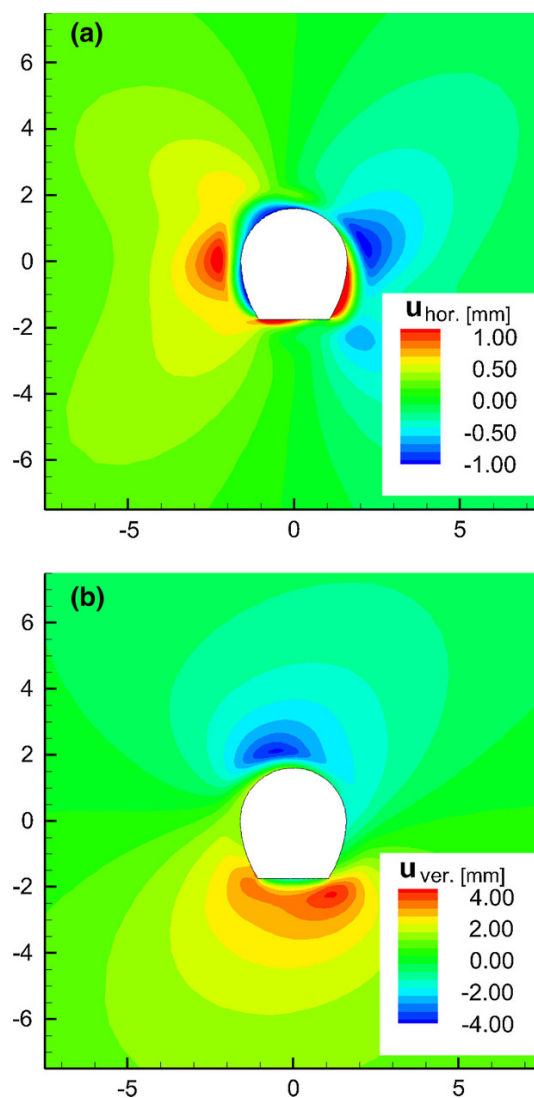


Fig. 13 Horizontal (*top*) and vertical (*bottom*) displacements after 7 years of atmospheric influence in the winter. The results indicate movements towards the niche at a distance of more than 1 m away from the niche. In the vicinity of the niche, these movements significantly depend on the season as is shown in Fig. 14

movement of the niche over the time. The comparison indicates good agreement of the qualitative trend. The quantitative comparison indicates an underestimation of the convergence of the niche by the numerical model. Comparative analyses indicate better results assuming a higher permeability of the claystone. Seasonal oscillations, which are indicated by the model due to the swelling and shrinkage effects, cannot be seen as clearly in the measured results. The presented convergences lead to the deformation of the niche profile as presented in Fig. 16. The measurements, as well as the numerical simulation, indicate a closure of the niche combined with a slight horizontal extension.

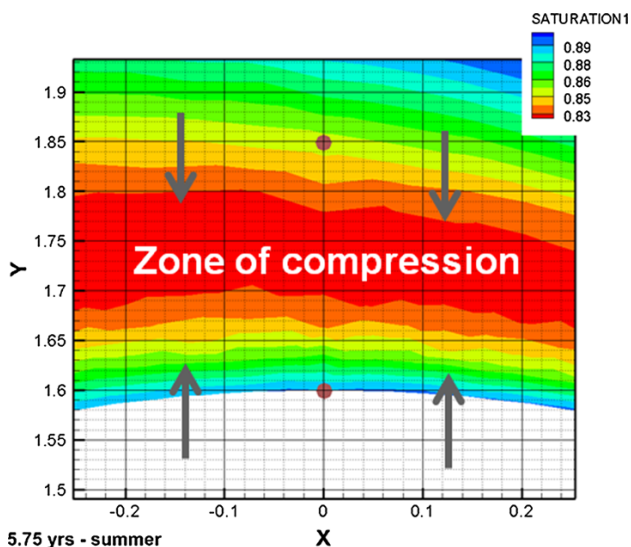


Fig. 14 Influence of the output location on the results. Due to the seasonally induced change between desaturation and resaturation, the first decimetres of claystone are characterized by manifold, seasonal effects. The saturation here—in the vicinity of the niche—varies significantly depending on the time and the location. Consequently, numerical as well as measured results depend on the output location. Results from the surface vary significantly from results e.g. at a distance of 25 cm away from the niche (this equals the depth of an anchor). The *brown* points in the figure mark the output location at the surface of the niche and at the depth of the anchor

6 Phenomenological investigation of a single crack

A special focus of this experiment is laid on the evolution of existing cracks at the surface of the niche. As already mentioned in Sect. 2, crackmeter as well as jointmeter

Fig. 15 Comparison of convergence results from measurements and simulation. Measured and simulated displacements of the presented distances are shown over time. The *blue symbol* (measurements) and *line* (simulation) present the displacements of the diagonal distance between points 3 and 4; the *green symbols and line* reflect displacements of the vertical line between points 2 and 4, the *grey symbols and line* indicate horizontal displacements between points 1 and 3. Measurements were carried out for 10 years. Keeping the differences between measurement and simulation results in mind, the numerical simulation allows for a prediction of the convergence of the niche over a longer time period

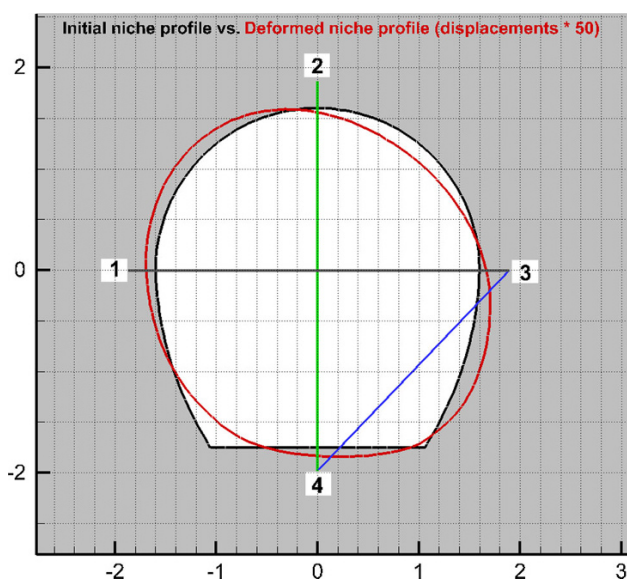
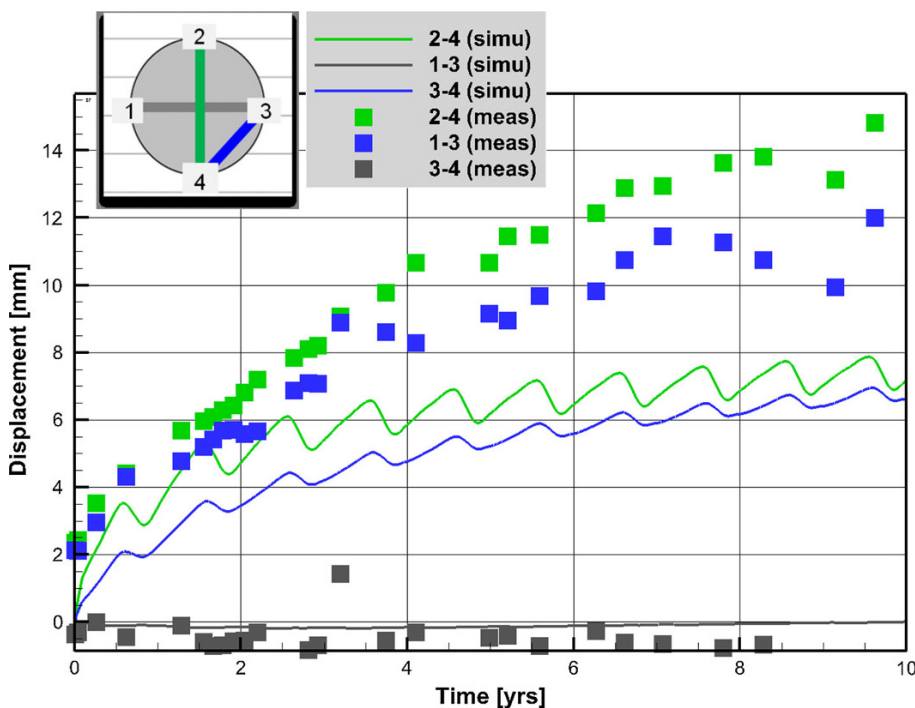


Fig. 16 The initial tunnel profile—shown by the *black line* in combination with the *grey background*—in comparison with the deformed niche which is represented by the *red line*. The deformed niche is scaled by a factor of 50. The results are given for the winter 7 years after the excavation

measurements are carried out over a time period of more than 7 years. Observations concerning the tectonic and artificial (EDZ) fracture network in the vicinity of the EZB niche are presented in Nussbaum et al. (2005). To better understand the effects in the vicinity of these cracks, a first approach incorporates one single crack in the finite element model. Comparative studies were carried out with different

crack geometries, and do not indicate any influence of the crack geometry on the general results. The resulting mesh is presented in Fig. 17 and presents the crack which is assumed to be filled. The parameters of the filling material are supposed to be isotropic. As the significant deformations appear vertical to the bedding, the reference value for the Young's modulus is perpendicular to the bedding. The significant flow velocity is in the bedding direction—consequently, the reference value for the permeability is chosen in the bedding plane. The parameters of the crack are defined by a higher permeability and a lower strength than the Opalinus Clay. They are given by:

$$E_{crack} = \frac{1}{10} E_{OPA,\perp}$$

$$k_{crack} = 10k_{OPA,\parallel}$$

where the designation “crack” means the property of the filling material, and the designation “OPA” means the property of the intact claystone. A different factor between these parameters will influence the quantitative results but not the effect in general. In contrast to that, different effects would be observed if the crack is assumed to have a higher strength and a lower permeability than the OPA. The presented model set-up does not incorporate the EDZ. It indicates an increase of the surface of the niche due to the crack. Consequently, the same effects that can be observed at the surface of the niche are observed at the surfaces of the crack, which can be seen in Fig. 18. In the vicinity of the crack, a seasonally affected zone occurs. Due to the swelling and shrinkage of the claystone, the crack opens while the desaturation process takes place, and closes due to the resaturation of the claystone. But it has to be kept in mind that a long-term affected zone also exists. As already described in Sect. 4, this zone is characterized by a long-term desaturation process. This effect causes a shrinkage of

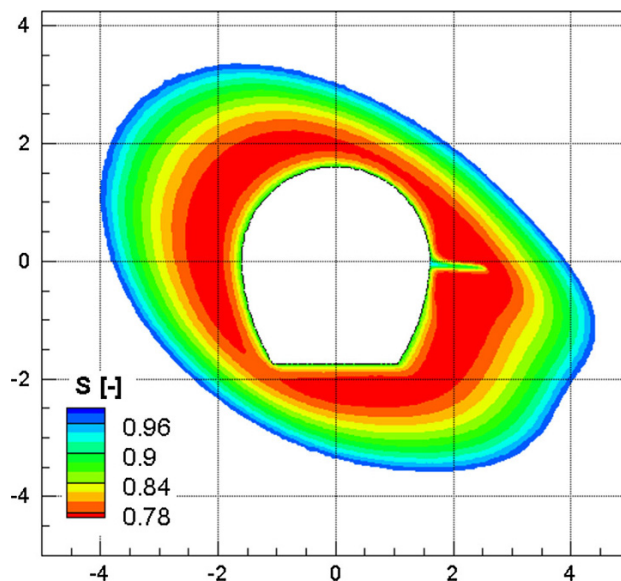


Fig. 18 The effect of resaturation (*summer*) and desaturation (*winter*) takes place in the vicinity of the niche, as well as in the vicinity of the crack. The resulting saturation for the summer 7 years after excavation is presented here

the material in the concerned area. Due to this effect, the long-term behaviour of the crack is characterized by closure of the crack. Both coexisting effects are presented schematically in Fig. 20. They can be observed in the measurements (detailed information can be found in Móri et al. (2010)) as well as in the results of the numerical simulation, and are depicted in Fig. 19. The measured relative humidity as presented in Sect. 2 is here transformed to the absolute humidity, while the displacements are taken from the crackmeter data. The changes in the saturation/absolute humidity and the aperture/displacements are given over a time period of 3 years. The seasonal oscillation of the saturation/absolute humidity leads to

Fig. 17 Part of the mesh for the phenomenological investigation of one single crack. The finite element mesh is characterized by a very fine discretization in the vicinity of the crack. The black areas represent the intact claystone, while the blue areas represent the filling material of the crack. This model does not incorporate any excavation damaged zone (EDZ)

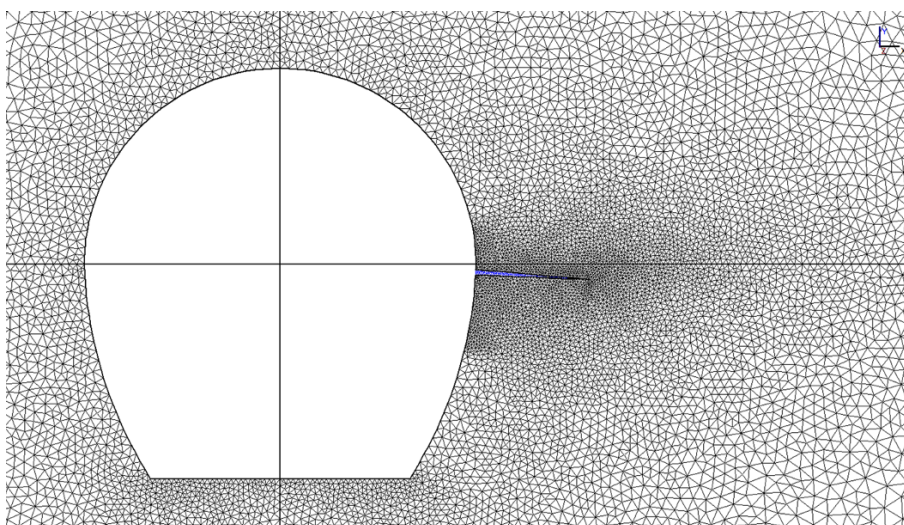


Fig. 19 The evolution of the saturation/absolute humidity and the aperture/displacements of the crack are given here over a time period of 3 years. Measurements are presented in the *upper picture*, simulation results in the *lower picture*. Both result types indicate a seasonal behaviour as well as a long-term influenced trend of the crack. The seasonally affected behaviour is characterized by opening of the crack due to desaturation of the crack in the vicinity of the crack, and closure of the crack due to resaturation in the vicinity of the crack. The long-term trend is characterized by closure of the crack in combination with the desaturation of the nearfield of the niche. The presented results are only phenomenological results—due to the simplicity of the numerical model quantitative comparisons are not yet possible

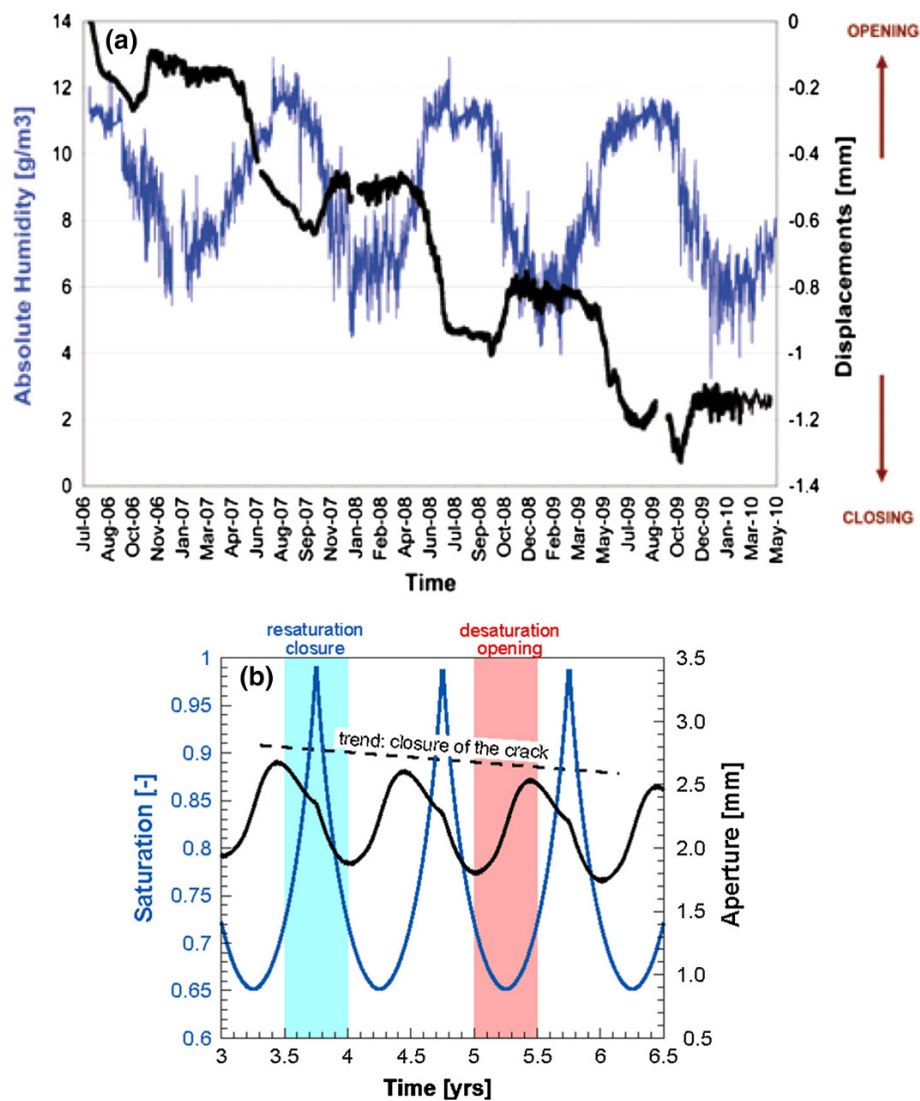
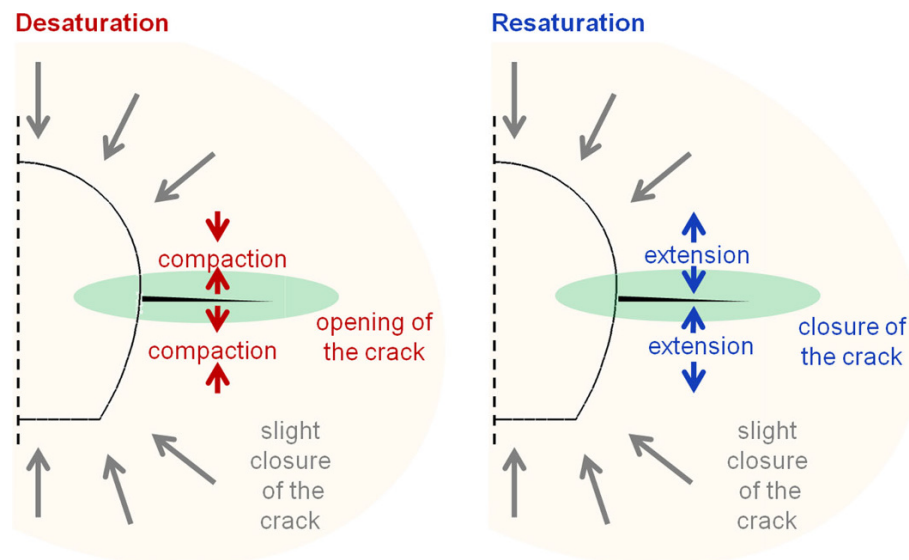


Fig. 20 Simplified scheme of processes occurring in the claystone in the near-field and far-field of the crack due to desaturation and resaturation. As also presented in the discussion of the hydraulic results, the area is divided into two zones: the seasonally influenced zone which is the near-field of the crack and the long-term influenced zone which is the far-field of the crack. The effects due to desaturation and resaturation are presented schematically for both zones. The resulting behaviour of the crack is pointed out



movement of the crack. While the desaturation indicates opening of the crack, the resaturation is combined with closure of the crack. Following the description of the hydraulic process in Sect. 4, this effect is called the seasonally influenced aperture of the crack. Furthermore, a long-term trend is observed in the measurements, as well as in the simulation. This trend indicates closure of the crack due to the ongoing desaturation, which leads to convergence of the niche. This effect coincides with the long-term influenced desaturated zone. The presented results reflect the described processes qualitatively.

7 Discussion of the results

7.1 Hydraulic effects

Concerning the hydraulic process, it can be stated that the desaturation and resaturation lead to three different zones in the claystone. In the vicinity of the niche, a seasonally influenced, desaturated zone develops. The extent of this zone is quasi-stationary after the first 3 years and has an extent of about 50 cm. In addition, a long-term influenced desaturated zone arises. This zone is characterized by a desaturation which is not significantly affected by the seasonal oscillations of the atmospheric conditions in the niche. This zone has an extent of about 1.40 m after 7 years. The long-term simulation indicates that after 10 years the process develops slowly, because minor changes are still observed after 15 years. The extent of the desaturated zone is about 2.2 m at this time. The main material property affecting these results is the permeability of the claystone.

Andra (2005a) came to a similar result for the Callovo-Oxfordian formation at the Meuse/Haute-Marne site in France, and states that the stationary extent of the desaturated zone is 1.5 times the radius of the drift, which results in 2.48 m in the case of the EZB-niche. Following Andra (2005a), a permanent pattern is reached after about 10 years. Additional investigations by Andra are summarized in e.g. Andra (2005b, c, d).

Related results can be found in Maßmann (2009). He investigates hydraulic-mechanically coupled effects at the Tournemire site (France) and defined the seasonally influenced zone as the zone where the saturation varies by more than 0.01%. This leads to an extent of the seasonally influenced zone of about 1–2 m around the opening. Following Maßmann (2009), the desaturated zone (saturation less than 99.9%) strongly depends on the assumed permeability and has an extent of 2–27 m after 100 years.

Concerning the desaturated zone Alcolea et al. (2014) and Lanyon et al. (2014) state that the extent of this zone is about 2 m around an excavation in Opalinus Clay; this

zone is found to depend significantly on the seasonal influences, and correlates with the evolution of temperature and relative humidity. The long-term effective hydraulic conductivity of the 2 m thick EDZ is expected to increase by approximately one order of magnitude relative to the undisturbed rock.

A comparison of the presented simulation results with the discussed temporal TDR measurements indicates good agreement concerning the water content, the extent of the desaturated zone, the extent of the seasonally affected zone, and the seasonal oscillation of the water content.

7.2 Mechanical effects

The mechanical effects in the vicinity of the niche are quite complex. The comparison of the numerical results with the measurements indicates qualitative agreement. The results suggest a closure of the niche combined with a slight horizontal extension, which is significantly affected by the orthotropic conditions. However, the quantitative comparison shows an underestimation of the mechanical effects. A reason for this might be the lack of a viscous material model or a damage model in the simulation, which incorporates the effect of rock strength reduction due to the seasonal oscillations. The increase in the rigidity of the argillite due to the desaturation would lead to the opposite effect. It is also not incorporated in the model, although it is proposed by Andra (2005a). The long-term simulation does not indicate an equilibrium stage after 15 years due to the ongoing but very weak desaturation process. It should not be forgotten that the results significantly depend on the output location. As many processes affect the immediate vicinity of the niche, the resulting displacements, water content, and other parameters at the surface of the niche are significantly different from the values at a distance of e.g. 25 cm (which is the depth of the anchors).

7.3 Investigation of a single crack

The phenomenological investigation of one single crack indicates the influence of seasonally changing atmospheric conditions as well as an impact of the long-term desaturation process. The simulation results match the measurements qualitatively. They indicate seasonal opening (due to the desaturation) and closure (due to the resaturation) of the crack, as well as a trend which is characterized by closure of the crack due to the long-term desaturation process, causing convergence of the niche. Both effects are illustrated in Fig. 18. As already presented in the discussion of the hydraulic results, the area is divided into the seasonally influenced zone—which is the near-field of the crack—and the long-term influenced zone, which is the far-field of the crack. The near-field is characterized by the seasonal

change between desaturation and resaturation, which directly results in opening or closure of the crack. The same behaviour is found in the rock laboratory in Tournemire (France) (Rejeb and Cabrera 2006).

Due to the simplicity of the discussed model, quantitative statements are not yet possible. In order to obtain quantitative results, more information on the properties of the cracks is required. In addition, the numerical model has to be extended to incorporate more cracks as well as crack evolution.

Xu et al. (2014) conclude that the swelling and shrinkage behaviour of various claystones is strongly anisotropic. The deformation perpendicular to the bedding plane is higher than in the direction of the bedding, and shrinkage appears more quickly than swelling. The second statement concerning the velocity of shrinkage and swelling fits the simulation results presented here. Figure 19 clearly shows, that the opening of the crack (caused by the shrinkage effect) appears faster than the closure of the crack (caused by the swelling effect). More information about drying and cracking initiation can be found in Peron et al. (2010). Future investigations could focus on a more detailed description of the behaviour of cracks. Furthermore, the numerical model could be extended regarding plastic as well as damage effects, and regarding a more detailed description of the swelling model.

8 Conclusions and outlook

The seasonally induced desaturation and resaturation process, and its impact on the pore-water pressure, the convergence of the niche and the evolution of the aperture of one pre-existing crack in the wallrock of the niche are investigated. The associated measurements and simulation results, as well as the comparison of both, lead to the following conclusions which can be subdivided into three aspects concerning (1) the hydraulic processes, (2) the mechanical processes and (3) the evolution of a crack aperture.

First of all it can be stated that the relatively simple model approach enables a representation of a large number of measurements with acceptable results. This indicates that the considered effects such as swelling and shrinkage, introduced by a linear swelling model, 2-phase flow using the Richards approach, saturation-dependent material parameters, an elastic material model and orthotropic material conditions, are significant aspects concerning the discussed research question.

Focusing on the hydraulic results, the measurements, as well as the simulation, indicate the evolution of three different zones: a seasonally influenced zone, a long-term influenced zone, and a saturated zone. The seasonal

changes of the atmospheric conditions in the niche induce cycles of desaturation and resaturation. This leads to a long-term desaturation process in combination with seasonal influences around the niche. The measurements and the numerical simulation show a good agreement concerning the volumetric water content of the claystone in the near-field of the niche, the extent of the desaturated zone (about 2.2 m after 10 years), as well as the extent (about 50 cm) and amplitude of the seasonally influenced desaturated zone. Similar results can be found in the cited literature.

The mechanical results indicate a qualitative agreement concerning the trend of the convergence of the niche. Quantitatively, the simulated convergence underestimates the measured values. Furthermore, the simulation suggests significant seasonal oscillations in the convergence of the niche. This effect does not appear in the same clarity in the measurements. An improvement of the mechanical results might be achieved if plasticity, viscosity and/or damage effects are considered in the numerical model. However, the measurements, as well as the numerical simulation, indicate a convergence of the niche combined with a slight horizontal extension.

A phenomenological approach is chosen to identify processes in the vicinity of a single crack. The seasonal evolution of the crack aperture is characterized by an opening of the crack due to desaturation, and a closure of the crack due to resaturation. The long-term trend indicates a slight closure of the crack due to the convergence of the niche, which is driven by the long-term desaturation process. It can be stated that the model succeeds in representing the qualitative behaviour of the crack aperture. Consequently, the evolution of the crack aperture results from the coexistence of two effects: the seasonally induced desaturation and resaturation process in the near-field of the crack, as well as the long-term desaturation process of the niche. The impact of swelling and shrinkage on the displacements seem to play an important role in the seasonal evolution, as well as in the long-term evolution of the crack aperture.

Acknowledgements The Mont Terri Project comprises a great variety of experiments, conducted by the 14 project partners. These partners contribute technical and scientific knowledge as well as financial support. Without these partners it would not be possible to generate such a comprehensive and diverse set of field measurements as well as laboratory and numerical data to obtain an increased understanding of the complex processes in claystone. Therefore we would like to extend our sincere gratitude to all of them. The CD experiment was initiated in 2006 by swisstopo (Paul Bossart). The following partners contributed considerably to this experiment: BGR (Hans-Joachim Alheid and Kristof Schuster), ENSI (Erik Frank and Martin Herfort), IRSN (Jean-Michel Matray), Nagra (Peter Blümling and Tim Vietor), and swisstopo (A. Möri). We would like to take this opportunity to express our particular gratitude to all of them. We are also grateful to Dr. Susanne Stadler for her English proof reading and

Dr. Peter Vogel for the fruitful discussions. Furthermore, special thanks go to Herbert Kunz for the great support concerning the preparation of the finite element mesh with his GINA software and to David Jaeggi who provided the measured data. Finally, very special thanks goes to the reviewers Dr. Alain Millard, CEA, Paris-Saclay, France and Dr. Alex Bond, Quintessa, Warrington, UK for many constructive and helpful comments and suggestions.

Open Access This article is distributed under the terms of the Creative Commons Attribution 4.0 International License (<http://creativecommons.org/licenses/by/4.0/>), which permits unrestricted use, distribution, and reproduction in any medium, provided you give appropriate credit to the original author(s) and the source, provide a link to the Creative Commons license, and indicate if changes were made.

References

- Alcolea, A., Kuhlmann, U., Lanyon, G. W., & Marschall P. (2014). *Hydraulic conductance of the EDZ around underground structures of a geological repository for radioactive waste—A sensitivity study for the candidate host rocks in the proposed siting regions in Northern Switzerland*. Nagra Arbeitsbericht, NAB 13–94, 101 pp. Nagra, Wetingen, Switzerland. www.nagra.ch.
- Alheid, H.-J., Kruschwitz, S., Schuster, K., & Yaramanci, U. (2002). Charakterisierung der Auflockerungszone um Strecken im Opalinuston mit seismischen und geoelektrischen Verfahren. *Angewandte Geologie*, 48, 48–55.
- Andra. (2005a). *Dossier 2005 Argile, Tome—Phenomenological evolution of a geological repository*.
- Andra. (2005b). *Dossier 2005 Argile, synthesis—Evaluation of the feasibility of a geological repository in an argillaceous formation*. France: Meuse/Haute-Marne Site.
- Andra. (2005c). *Dossier 2005 Argile, Tome—Savety evaluation of a geological repository*.
- Andra. (2005d). *Dossier 2005 Argile, Tome—Architecture and management of a geological repository*.
- Bock, H. (2000). *RA experiment rock mechanics analyses and synthesis: Data report on rock mechanics*. Mont Terri Technical Report, TR 00-02, 52 pp. Federal Office of Topography (swisstopo), Wabern, Switzerland. www.mont-terri.ch.
- Bock, H. (2009). *RA experiment: Updated review of the rock mechanics properties of the Opalinus Clay of the Mont Terri rock laboratory based on laboratory and field testing*. Mont Terri Technical Report, TR 08-04, 68 pp. Federal Office of Topography (swisstopo), Wabern, Switzerland. www.mont-terri.ch.
- Bond, A., Millard, A., Nakama, S., Zhang, C., & Garritte, B. (2013). Approaches for representing hydro-mechanical coupling between sub-surface excavations and argillaceous porous media at the ventilation experiment, Mont Terri. *Journal of Rock Mechanics and Geotechnical Engineering*, 5, 85–96.
- Bossart, P., Bernier, F., Birkholzer, J., Bruggeman, C., Connolly, P., Dewonck, S., Fukaya, M., Herfort, M., Jensen, M., Matray, J.-M., Mayor, J. C., Moeri, A., Oyama, T., Schuster, K., Shigeta, N., Vietor, T., & Wiczorek, K. (2017). Mont Terri rock laboratory, 20 years of research: introduction, site characteristics and overview of experiments. *Swiss Journal of Geosciences*, 110. doi:10.1007/s00015-016-0236-1 (this issue).
- Girardin, C., & Nussbaum, C. (2006). *CD experiment (cyclic deformations): Installation and procedures of measurement*. Mont Terri Technical Note, TN 2006-64, 9 pp. Federal Office of Topography (swisstopo), Wabern, Switzerland. www.mont-terri.ch.
- Jaeggi, D., & Gisiger, J. (2012). *CD (cyclic deformation) experiment: Data report of Phase 17 (July 2011–June 2012)*. Mont Terri Technical Note, TN 2012-68, 34 pp. Federal Office of Topography (swisstopo), Wabern, Switzerland. www.mont-terri.ch.
- Kolditz, O. (2002). *Computational methods in environmental fluid mechanics*. Berlin: Springer.
- Kolditz, O., Bauer, S., Bilke, L., Böttcher, N., Delfs, J. O., Fischer, T., et al. (2012a). OpenGeoSys: An open22source initiative for numerical simulation of thermo-hydro-mechanical/chemical (THM/C) processes in porous media. *Environmental Earth Sciences*, 67(2), 589–599.
- Kolditz, O., Görke, U.-J., Shao, H., & Wang, W. (2012b). *Thermo-hydro-mechanical-chemical processes in fractured porous media*. Berlin: Springer.
- Lanyon, G. W., Martin, D., Giger, S., & Marschall, P. (2014). *Development and evolution of the Excavation Damaged Zone (EDZ) in the Opalinus Clay—A synopsis of the state of knowledge from Mont Terri*, Nagra Arbeitsbericht, NAB 14–87, 204 pp. Nagra, Wetingen, Switzerland. www.nagra.ch.
- Martin, C. D., & Lanyon, G. W. (2003). Measurement of in situ stress in weak rocks at Mont Terri Rock Laboratory, Switzerland. *International Journal of Rock Mechanics and Mining Sciences*, 40, 1077–1088.
- Maßmann, J. (2009). *Modeling of excavation induced coupled hydraulic-mechanical processes in claystone*. Ph.D. dissertation, Leibniz Universität Hannover, Germany, 77 pp.
- Maßmann, J., Uehara, S., Rejeb, A., & Millard, A. (2008). Investigation of desaturation in an old tunnel and new galleries at an argillaceous site. *Environmental Geology*, 57(6), 1337–1345.
- Matray, J.-M., & Bailly, D. (2014). *LP-A experiment: Phase 20, statistical analysis of time series acquired in the EZ-B Niche and at the Main fault*. Mont Terri Technical Note, TN 2014-59, 77 pp. Federal Office of Topography (swisstopo), Wabern, Switzerland. www.mont-terri.ch.
- Matray, J.-M., & Möri, A. (2012). *CD (Cyclic deformation) experiment, petrophysical measurements on BCD-3 core samples from the Mont Terri rock laboratory*. Mont Terri Technical Note, TN 2013-49, 27 pp. Federal Office of Topography (swisstopo), Wabern, Switzerland. www.mont-terri.ch.
- Möri, A., Bossart, P., Matray, J.-M., Frank, E., Fatmi, H., & Ababou, R. (2010). Mont Terri Project, Cyclic deformations in the Opalinus Clay. In *Proceedings of the international meeting of clay in natural and engineered barriers for radioactive waste confinements, Nantes* (pp. 103–124).
- Nussbaum, C., Bossart, P., von Rütte, J., Meier, O., & Badertscher, N. (2005). *EZ-B experiment: Small-scale mapping of tectonic and artificial (EDZ) fractures of the EZ-B niche*. Mont Terri Technical Note, TN 2005-30rev, 24 pp. Federal Office of Topography (swisstopo), Wabern, Switzerland. www.mont-terri.ch.
- Nussbaum, C., Kloppenburg, A., Caer, T., & Bossart, P. (2017). Tectonic evolution around the Mont Terri rock laboratory, northwestern Swiss Jura: constraints from kinematic forward modelling. *Swiss Journal of Geosciences*, 110. doi:10.1007/s00015-016-0248-x (this issue).
- Peron, H., Eichenberger, J., Laloui, L., & Salager, S. (2010). *Modelling of drying and cracking initiation in a gallery excavated in shale*. European Rock Mechanics Symposium-EUROCK 2010, pp. 771–774. International Society for Rock Mechanics.
- Rejeb, A., & Cabrera, J. (2006). Time-dependent evolution of the excavation damaged zone in the argillaceous Tournemire site (France). In *The GeoProc international conference on coupled*

- THMC processes in geosystems: fundamentals, modelling, experiments and applications (invited lecture)* (pp. 22–25).
- Rutqvist, J., Börgesson, L., Chijimatsu, M., Kobayashi, A., Jing, L., Nguyen, T. S., et al. (2001). Thermohydromechanics of partially saturated geological media: Governing equations and formulation of four finite element models. *Rock Mechanics and Mining Sciences*, 38, 105–127.
- Wang, Q., Cui, Y.-J., Tang, A.-M., Barnichon, J.-D., Saba, S., & Ye, W.-M. (2013). Hydraulic conductivity and microstructure changes of compacted bentonite/sand mixture during hydration. *Engineering Geology*, 164, 67–76.
- Wang, W., Kosakowski, G., & Kolditz, O. (2009). A parallel finite element scheme for thermo-hydro-mechanical (THM) coupled problems in porous media. *Computers & Geosciences*, 35(8), 1631–1641.
- Wild, K. M., Wymann, L. P., Zimmer, S., Thoeny, R., & Amann, F. (2015). Water retention characteristics and state-dependent mechanical and petro-physical properties of clay shale. *Rock Mechanics and Rock Engineering*, 48, 427–439.
- Xu, W.J., Shao, H., Hesser, J., & Kolditz, O. (2014). Numerical modelling of moisture controlled laboratory swelling/shrinkage experiments on argillaceous rocks. In: S. Norris, J. Bruno, M. Cathelineau, P. Delage, C. Fairhurst, E.C. Gaucher, et al. (Eds.), *Clays in natural and engineered barriers for radioactive waste confinement* (pp. 359–366). Geological Society London Special Publication.
- Yildizdag, K., Shao, H., Hesser, J., Noiret, A., & Sönnke, J. (2014). Coupled hydromechanical modelling of the mine-by experiment at Meuse–Haute–Marne underground rock laboratory France. In: S. Norris, J. Bruno, M. Cathelineau, P. Delage, C. Fairhurst, E. C. Gaucher, et al. (Eds.), *Clays in natural and engineered barriers for radioactive waste confinement* (pp. 265–278). Geological Society London Special Publication.
- Yong, S. (2007). *A three-dimensional analysis of excavation-induced perturbations in the Opalinus Clay at the Mont Terri rock laboratory*. Ph.D. dissertation, Swiss Federal Institute of Technology in Zurich (ETH Zurich), Zurich, Switzerland, 167 pp.
- Yong, S., Kaiser, P. K., & Loew, S. (2010). Influence of tectonic shears on tunnel-induced fracturing. *International Journal of Rock Mechanics and Mining Sciences*, 47, 894–907.

High-resolution mini-seismic methods applied in the Mont Terri rock laboratory (Switzerland)

Kristof Schuster¹ · Florian Amann² · Salina Yong^{2,3} · Paul Bossart⁴ · Peter Connolly⁵

Received: 1 June 2016 / Accepted: 9 December 2016 / Published online: 22 February 2017
© The Author(s) 2017. This article is published with open access at Springerlink.com

Abstract We present several mini-seismic methods developed and applied in recent years in the Mont Terri rock laboratory. All these applications aimed at correlating and interpreting seismically derived parameters with relevant rock-mechanical parameters and findings. The complexity of the local site setting always required very high spatial and parameter resolution. Both, seismic P- and S-wave velocities and dynamic elastic parameters, such as the dynamic Poisson's ratio ν_{dyn} and the Young's modulus E_{dyn} , are used to characterise the Opalinus Clay under real in situ conditions. We were able to establish a correlation between static and dynamic elastic Young's moduli. We describe the extremely large, small-scale variability of seismic parameters normal and parallel to the bedding plane orientation and address the question of fracture detection. We also present examples of the characterization of excavation-damaged zones with

seismic parameters, including extent as well as degree of damage, and compare these to geological and structural mapping. The evolution of borehole-disturbed zones (BdZ) was deduced from repeating high-resolution borehole measurements. Finally, we quantify seismic anisotropy at dimensions between several cm and tens of m.

Keywords Seismic velocities · Dynamic and static elastic parameters · Seismic anisotropy · Fracture detection · EDZ · BdZ · Opalinus Clay · Nuclear waste disposal

1 Introduction

The term “high-resolution mini-seismic methods” (HR-MSM) comprises all seismic, sonic, and ultrasonic in situ methods that the German Federal Institute for Geosciences and Natural Resources (BGR) has developed and continues to develop for underground investigations. This involves a broad variety of seismic, sonic, and ultrasonic methods with high spatial resolution in the centimetre to dekametre range associated with a high dynamic-parameter resolution. We applied all of these methods at the Mont Terri rock laboratory. Figure 1 shows the location of the laboratory within the Opalinus Clay Formation and its complex structural context. The lithological and structural overview of the Opalinus Clay at Mont Terri, its mineralogy, and key parameters is given in Bossart et al. (2017a).

The Opalinus Clay at the Mont Terri rock laboratory can be differentiated into three facies (shaly, sandy, and carbonate-rich sandy), all of which possess different petrophysical properties (Bock 2002; Bossart and Thury 2008). For example, each facies has a pronounced bedding-related anisotropy resulting in transverse isotropic (TVI) seismic parameters and significant small-scale variations of rock

Editorial handling: P. Bossart and A. G. Milnes.

This is paper #10 of the Mont Terri Special Issue of the Swiss Journal of Geosciences (see Bossart et al. 2017, Table 3 and Fig. 7).

✉ Kristof Schuster
kristof.schuster@bgr.de

- ¹ Federal Institute for Geosciences and Natural Resources BGR, Stilleweg 2, 30655 Hannover, Germany
- ² Earth Science Department, Swiss Federal Institute of Technology, Sonneggstrasse 5, 8092 Zurich, Switzerland
- ³ Present Address: Knight Piésold Ltd., Suite 1400, 750 West Pender, Vancouver, BC V6C 2T8, Canada
- ⁴ Federal Office of Topography Swisstopo, Seftigenstrasse 264, 3084 Wabern, Switzerland
- ⁵ Rock Mechanics Team, CHEVRON, Chevron Exploration Technology Company, 1500 Louisiana Street, Houston, TX 77002, USA

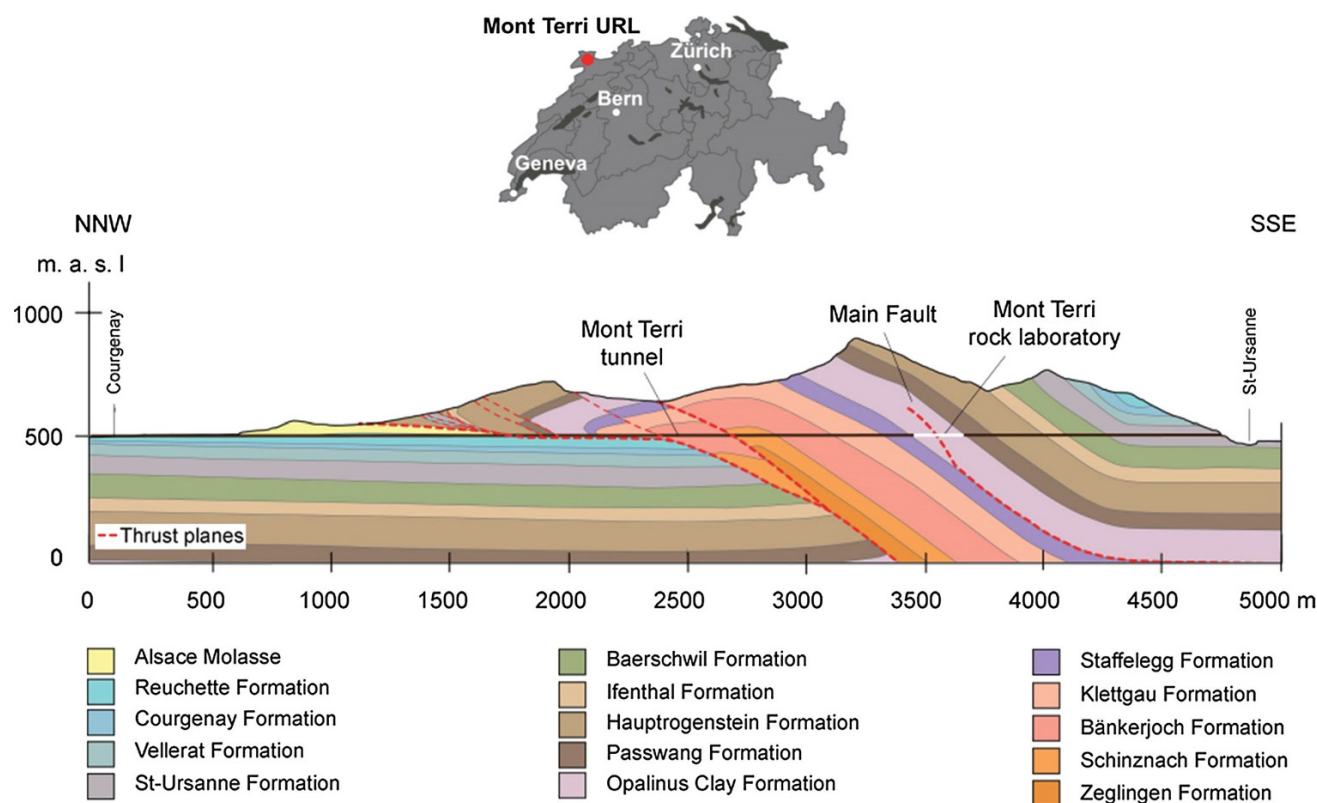


Fig. 1 The Mont Terri rock laboratory, located in the Canton of Jura, northwestern Switzerland, lies in the Opalinus Clay. The geological setting of the Opalinus Clay and the mini-seismic experiment sites in the rock laboratory are shown in Bossart et al. (2017a)

properties of different intensities at several sites due to small-scale heterogeneities. To address these inherent complexities with an appropriate spatial resolution, we need high-resolution mini-seismic measurements (MSM).

Since 1996, BGR has carried out MSM in the Mont Terri rock laboratory in close cooperation with experiment partners. Most of the experiments were closely linked to questions concerning geological, geotechnical, or rock-mechanical questions. The mutual inspiration and open discussions between experiment partners has enabled comprehensive interpretation of the mini-seismic results and furthered continuous development of MSM. Out of all the numerous results achieved during the last years, this present contribution focuses on the following issues:

1. Seismic and dynamic elastic parameters,
2. Small-scale variability of the Opalinus Clay,
3. EDZ and fracture detection,
4. BdZ characterization, and
5. Seismic anisotropy measured at different scales.

Other aspects appropriate for study using our MSM methods and concepts, such as detection and characterization of fault structures, seismic long-term monitoring to characterise evolution of the EDZ (generation and self-

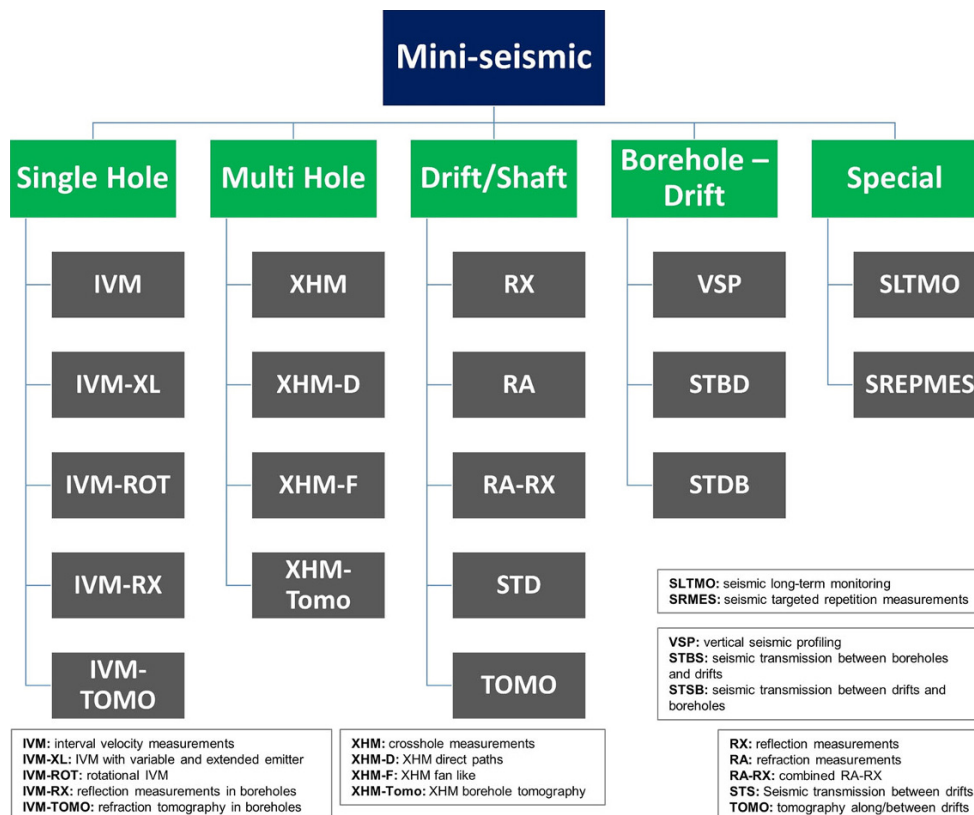
sealing), and evolution of backfill material (sand-bentonite), are presented in other papers in this issue (e.g., Jaeggi et al. 2017; Wiczorek et al. 2017).

Our main objective here is to draw attention to in situ, high-resolution mini-seismic methods and their ability to provide real in situ results for a better understanding of in situ rock-mechanical properties. In addition, combining results from MSM with those derived under laboratory conditions (mostly static tests) on cores can improve our understanding and interpretation of rock-mechanical modelling. Bossart et al. (2017a), this issue) present an overview of the experiments and sites where the MSM have been applied.

2 Methods

The in situ investigations were conducted in single boreholes, between boreholes, non-destructively along and between drifts, and in combinations of these situations. In addition, we used a wide range of seismic monitoring tasks and targeted repetition of measurements to assess evolution of the rock mass with respect to seismic characteristics. The interdependence/applicability of the methodologies is given in Fig. 2. We consider the MSM to be a suitable tool to bridge

Fig. 2 BGR mini-seismic methods (MSM) according to their application: (1) single hole, (2) multi-hole, (3) shaft/drift, (4) borehole—drift, (5) special (monitoring and targeted repetition of measurements)



in situ rock-mechanical results, results from laboratory testing, and results stemming from thermo- and hydro-mechanical modelling. Results from MSM closely sample the actual local in situ conditions. In particular, signals from disturbances caused by the borehole, such as identified BdZ, can be corrected for or, with wide enough separation between emitters and receivers, even neglected. Due to local conditions (stress field, damage, pore space connectivity, ventilation, degree of saturation) rock parameters change with time. Therefore, any measurement, especially in the near-field of an excavation, is a snapshot in time. Thus, the results reflect the state of petrophysical parameters at that specific time. To quantify time-dependent processes in the targeted rock, we repeat a set of measurements or install automatic long-term monitoring with a fixed emitter-receiver system (e.g., Wiczorek et al. 2017).

The frequency range of BGRs mini-seismic data lies in the general range 0.1–100 kHz, depending on local site situations and rock properties. This spans three different frequency bands, namely seismic, sonic, and lower ultrasonic frequencies. In several applications these bands overlap, but the principles are the same for each frequency band. To simplify discussions, we use the term “mini-seismic” or simply “seismic” to cover all these applications.

The basic principle of the mini-seismic measurements is shown schematically in Fig. 3. For all methods, a seismic wave-field is emitted into the rock at a certain location,

which is then recorded with seismic receivers at several other locations, and subsequently analysed. We use various piezoelectric transducers or a selection of mechanical impulse sources (emitters). Seismic wave-field receivers are always piezoelectric transducers registering both 1-and/or 3 components. Typically, we installed between seven (e.g., borehole tools) and 160 (e.g., sensors glued along drifts) receivers for a single shot (excitation). Distances between emitters and receivers range from 5 to 80 cm (borehole tools) and from 5 to 100 m for mini-seismic transmission measurements between drifts. Generally, we analyse refracted, transmitted, and partly reflected P- and S-wave phases. For recording, we use a modified electronic laboratory transient recorder and amplifier system comprising up to 160 channels (Schuster 2002).

For each situation, we choose an appropriate method (Fig. 2) depending on the scientific questions and the desired spatial and parameter resolution. All measurements are necessarily a compromise between spatial and seismic-parameter resolution (Schuster 2012). Generally, as distances between emitters and receivers increase, the spatial resolution decreases. For applications at the Mont Terri rock laboratory, the centre frequency range for the emitters lies in general between 1 and 100 kHz, corresponding to wavelengths between 270 cm (e.g., measurements between drifts) and 2.7 cm (e.g., measurements in boreholes) for

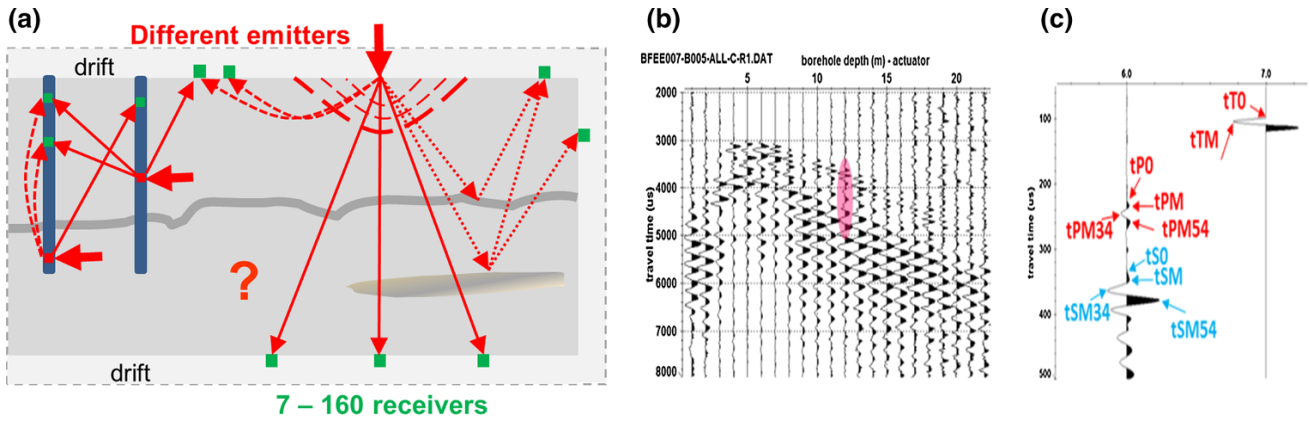


Fig. 3 Basic principle of MSM. **a** Emitted wave-field represented by seismic ray-paths. **b** Derived seismic section with a marked seismic trace, which is used for the extraction of seismic attributes. **c** Marked seismic attributes, which are used for seismic parameter calculation

P-waves and between 140 and 1.4 cm for S-waves. For this appraisal we chose a typical mean P-wave velocity of 2700 m/s and a v_p/v_s ratio of 1.92 for Opalinus Clay. As a first approximation, we assume two-dimensional wave propagation in a plane containing the emitter and the line of receivers. All the boreholes needed or used for our investigations at the Mont Terri rock laboratory were drilled with air. The most common diameters for our boreholes were 86, 101 and 131 mm. The lengths of the different boreholes ranged from 3 to 32 m.

3 Results from in situ applications of mini-seismic methods

We present representative results from mini-seismic measurements performed in the framework of experiments that provided data relevant to answer questions on rock mechanics, lithology, and structure.

3.1 Seismic and dynamic elastic parameters

Using seismic attributes determined from phase correlations in seismic sections, such as travel times, amplitudes, and polarities of different P-wave and S-wave phases, we calculated appropriate seismic parameters for each trace (Fig. 3c). In general, the boreholes used for our measurements are oriented perpendicular, parallel, or at 45° with respect to the bedding plane. Therefore, the measurements record a specific transversely isotropic (TVI) behaviour of the rock and the evaluation of the dynamic elastic parameters along these orientations is done by applying isotropic formulas (no TVI correction) to account for the orientation. Additionally, no differentiation between quasi and “pure” P- or S-waves is made, due to the short travel paths and the specially selected orientations of boreholes or profile layouts with respect to orientation of the bedding plane. Knowing the

coordinates of the emitter and receiver locations, we calculated the P-wave velocity (v_p) and S-wave velocity (v_s). Furthermore, we determined the v_p/v_s ratio, the absolute and normalised amplitudes of several phases, the frequency content, and the dynamic Poisson’s ratio ν_{dyn} . By using a site-specific value for the mean bulk density with respect to the three facies, we can also calculate additional dynamic elastic parameters such as Young’s modulus E_{dyn} , shear modulus G_{dyn} , and bulk modulus K_{dyn} . Thus, we obtain a set of parameters useful to characterise the rock mass and, in certain cases, structural information that can, for example, help differentiate lithologies.

We used the following formulas to derive the parameters mentioned above and also the seismic and dynamic elastic parameters that we will discuss below.

Seismic velocities: $v = \frac{l}{t}$ (v stands for apparent P-wave, or S-wave velocities, in certain cases apparent velocities).

Dynamic elastic Poisson’s ratio: $\nu_{dyn} = \frac{v_p^2 - 2v_s^2}{2(v_p^2 - v_s^2)}$.

Dynamic elastic Young’s modulus: $E_{dyn} = 2 \cdot \rho \cdot v_s^2 (1 + \nu_{dyn})$.

Dynamic elastic bulk modulus: $K_{dyn} = \rho \cdot \left(v_p^2 - \frac{4}{3} v_s^2 \right)$.

Dynamic elastic shear modulus: $G_{dyn} = \rho \cdot v_s^2$.

Seismic anisotropy coefficient: $Av = \frac{(v_{max} - v_{min})}{v_{min}}$.

Average seismic velocity anisotropy: $Av_p = \frac{v_{pmax} - v_{pmin}}{v_{pmean}}$.

100%. Furthermore, distance l , travel time t and bulk density ρ .

At several IVM tests, we registered velocity dispersion in the range 20–120 kHz. In the present contribution we will not further discuss this frequency dependence of seismic velocities and, consequently, of dynamic elastic parameters. Most of the IVM were performed with 50 kHz, which was found to be a good compromise between spatial resolution and coverage.

In the HE-B heater experiment (formerly HE) at the Mont Terri rock laboratory, nine vertical boreholes were drilled around the central vertical borehole where the heater was placed (Göbel et al. 2007). A section of these boreholes with diameters of 86 mm were used for dilatometer measurements and IVM. Here, we used a 4-channel ultrasonic borehole probe. The principle of IVM is described briefly in Sect. 3.2 and in more detail in Schuster et al. (2001) and Schuster (2012). Figure 4a–e presents the derived v_p , normalized amplitudes of first-arrival P-wave phases, and the dynamic elastic parameters v_{dyn} and E_{dyn} obtained with IVM in borehole BHE-25 (location: HE niche, borehole drilled -90° down into the floor, approximately 45° with respect to the bedding planes).

Three apparent v_p (app. v_p) for receivers R1 (10 cm), R2 (20 cm), R3 (30 cm) and the BdZ corrected $v_{p\text{-corBdZ}}$ are plotted on Fig. 4a. The differences between the three app. v_p indicate the existence of a BdZ (see also Sect. 3.4). The $v_{p\text{-corBdZ}}$ allows us to capture the rock parameters that are not affected by the BdZ (i.e. to “look behind the BdZ”). Furthermore, the reduced v_p and normalised amplitudes obtained are below average for features that extend up to 2.4 m and are attributed to the EDZ. The distinct v_p peaks at 2.9 and 5.7 m and the variations in between are interpreted as sandy lenses and structural changes.

To determine dynamic elastic parameters, we used R2 data (distance of 20 cm between emitter and receiver), since the vertically polarized Sv-wave phase could be best resolved for this subset. The Sv-wave phases for R3 data could not be distinctly identified over the complete

section. Where direct comparison was possible between R2 and R3 Sv-phases, it was found that R2 and R3 parameters are very similar. Note that at some locations these R2 data may be slightly influenced by the BdZ. Calculation of the dynamic elastic parameters used an isotropic approach accounting for the measurements being oriented towards bedding. The derived v_{dyn} varies between 0.3 and 0.38 along the profile whilst E_{dyn} shows a gradual increase from 6 to 10 GPa, except at the two peaks around 2.9 and 5.7 m. These two peaks correspond to the v_p -peaks associated with sandy lenses and structural changes mentioned above. Young’s moduli derived from dilatometer measurements at four depths are plotted on Fig. 4d (blue dots, right y-axis) and are considered to represent static values. Similarly to the dynamic values they increase gradually from 3.18 to 3.97 GPa. Comparison between dilatometer and seismically derived data at these depths result in $E_{\text{dyn}} = (2.29, \dots, 2.49) \times E_{\text{stat}}$. These correlation factors (which are labelled in Fig. 4d) are close to the factor 2.5 found by Corkum (2006) at another location in the laboratory. Corkum (2006) derived E_{stat} from core-sample laboratory tests and compared these results with E_{dyn} derived from IVM performed in the same borehole (Schuster 2002).

The dynamic and static E-modulus correlation factor of 2.3–2.5 yields important bounds for the determination of dynamic elastic parameters under in situ conditions with MSM and is crucial to account for when characterising the rock mass.

The main advantages of using MSM for the determination of dynamic elastic parameters can be summarised as follows:

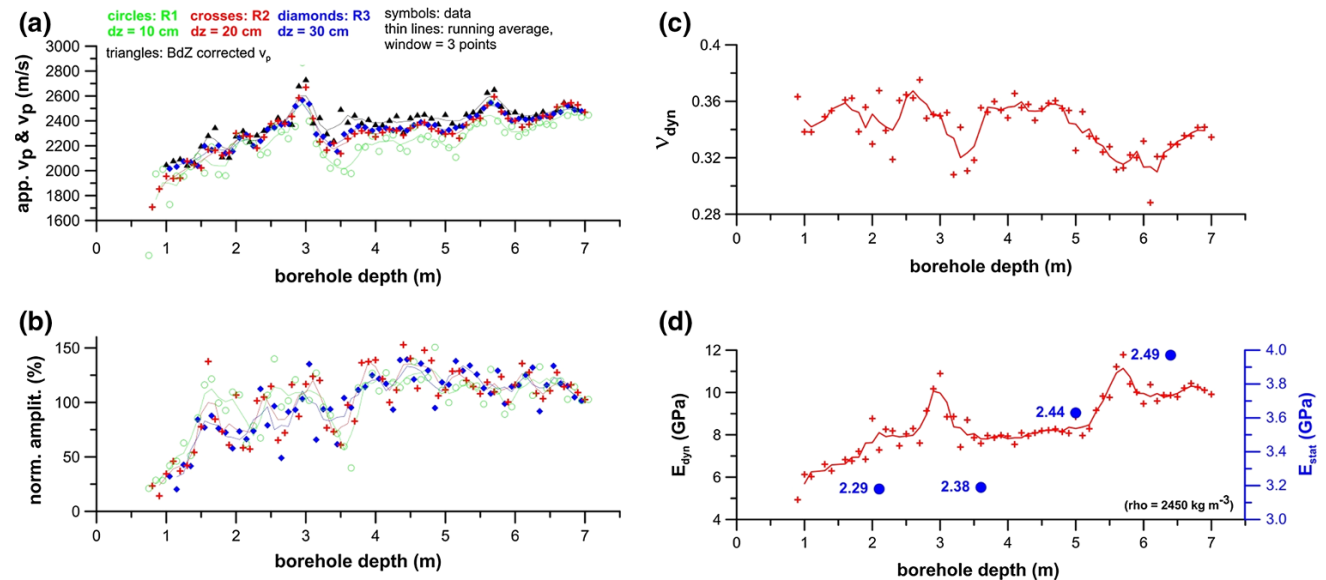


Fig. 4 Seismic parameters derived with IVM in borehole BHE-25. **a** Apparent and BdZ-corrected v_p . **b** Normalised P-wave onset amplitudes. **c** Dynamic Poisson’s ratio (R2-data). **d** Dynamic Young’s

(left y-axis) and static Young’s moduli derived with dilatometer tests (right y-axis). The labels represent the correlation factors between E_{stat} and E_{dyn}

- Dynamic elastic parameters are measured in situ under real site conditions, without taking the risk of specimen alteration during extraction, transport and/or conditioning, especially when the technique chosen provides insight into the properties of the undisturbed rock mass,
- The dynamic Poisson's ratio is, for example when using IVM data, available along the complete borehole length in increments of 5 cm,
- Mini-seismic excitations induce only small displacements of the rock mass and avoid risk of producing non-linear elastic effects that could lead to inaccurate results,
- Continuous borehole measurement avoids missing relevant parts for the characterisation associated with the rock heterogeneity when compared to a selective core-sampling method. Especially in regions with core loss, it is a simple way to obtain dynamic elastic parameters, and
- As a by-product of continuous IVM, cracks can be detected in the rock mass. In many cases a clear correlation between cracked cores and seismic-parameter anomalies (reduced v_p , v_s and amplitudes) at the borehole wall at corresponding depths can be observed.

In summary, the results discussed in this section show that MSM provide a large number of attributes and parameters for the seismic and dynamic elastic characterisation of the Opalinus Clay. Furthermore, we could establish a relationship between static and dynamic elastic parameters.

3.2 Small-scale heterogeneity of the Opalinus Clay

Excavation work and analyses of core samples have exposed the existence of a pronounced variability in rock parameters due to heterogeneities in the Opalinus Clay at the Mont Terri rock laboratory. Boreholes are indispensable to characterise these variations quantitatively using seismic and dynamic elastic parameters with very high spatial and parameter resolution, even when they alter the rock mass (Schuster 2012). To enable a high spatial resolution in the cm range, BGR developed ultrasonic borehole probes. These borehole probes use piezoelectric transducers serving as emitters or receivers of ultrasonic waves at distances of 5 cm (8KUBS-05, Fig. 5b) and 10 cm (8KUBS-10) between emitter (S1) and the first receiver (R1). Between the receivers (R1–R7) the distances are 5 cm (8KUBS-05) or 10 cm (8KUBS-10). The piezoelectric transducers are particularly sensitive to ultrasonic wave energy emerging with vertical or near-vertical incidence angles. Therefore, mainly P-waves and Sv-waves are recorded, no horizontally polarised S-waves. The transducers are coupled pneumatically against the

borehole wall. Outside the boreholes we use 3-component piezoelectric transducers to capture the ultrasonic wave-field with three components. The probes can be applied in boreholes with diameters starting from 86 mm. Greater diameters can be used by assembling temporarily appropriate adapters. The largest diameters used for IVM in the Mont Terri rock laboratory were 300 mm (location: SB niche, borehole orientation -90° down). Using a special adapter, a horizontal borehole with a diameter of 740 mm (Alveole) was measured in the French Meuse/Haute-Marne Underground Research Laboratory. Both types of borehole probes, and the associated software tools, allow us to characterise the local rock mass to a very high spatial and parameter resolution. The principle is shown in Fig. 5a. The emitted seismic-wave energy from source S1 is represented by seismic rays traveling along the borehole wall as refracted waves with different penetration depths. These depths depend on degree of disturbance in the borehole wall. Figure 5c depicts a typical common shot (CSP) section with the correlated P- and Sv-wave phases. The exact distribution of travel paths depends upon the shape of the BdZ. Our IVM enables us to investigate behind the BdZ into the undisturbed rock (see Sect. 3.4). For several CSP data sets, we performed finite-difference ray-tracing simulations to confirm the wave propagation (P- and Sv-waves with refracted propagation paths). After the probe is moved through the borehole, recording incremental measurements in steps of 5 or 10 cm as CSP-sections, the data are re-sorted into seven constant-offset (COF) sections. Figure 5d (borehole BEZ-B03, see Sect. 3.3) shows an example for a distance of 20 cm between source and receivers. In such COF sections, extraction of seismic attributes, estimation, and presentation of seismic parameters are very beneficial.

We installed a high-resolution photo camera on both sonic probes. Taking photographs of details of the borehole wall at every shot point is part of any IVM. These photographs support the interpretation of IVM data. The camera can also be used in selected boreholes without performing IVM. Figure 6a illustrates the principle. The 86 mm diameter borehole wall is unrolled and covers an area 58mm by 63 mm. Figure 6b shows a photograph taken in the shaly facies, containing a single tectonic thrust. Figure 6c belongs to the carbonate-rich sandy facies, where in the central part breakouts can be identified at the borehole wall. Figure 6d shows the sandy facies, where sedimentary bioturbation structures are visible.

On several occasions, detailed and well-resolved small-scale sedimentary and tectonic structures could be captured with the help of the borehole camera photos of unrolled borehole walls. Figure 7 shows a small detail of a disturbed zone ca. 6 m behind the Main Fault at a depth of 12.15 m in borehole BSO-37. This borehole was drilled from the

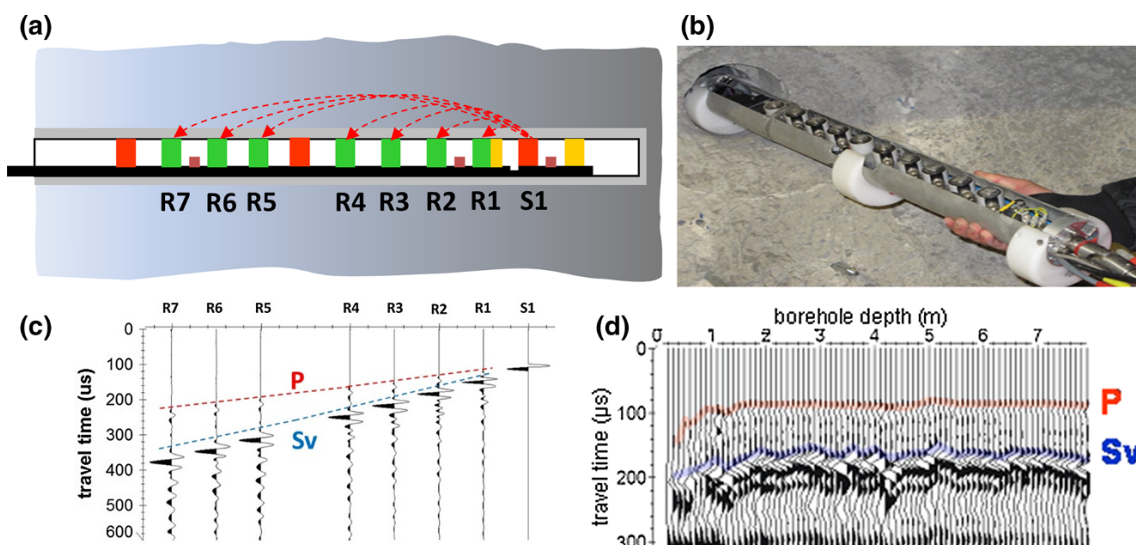
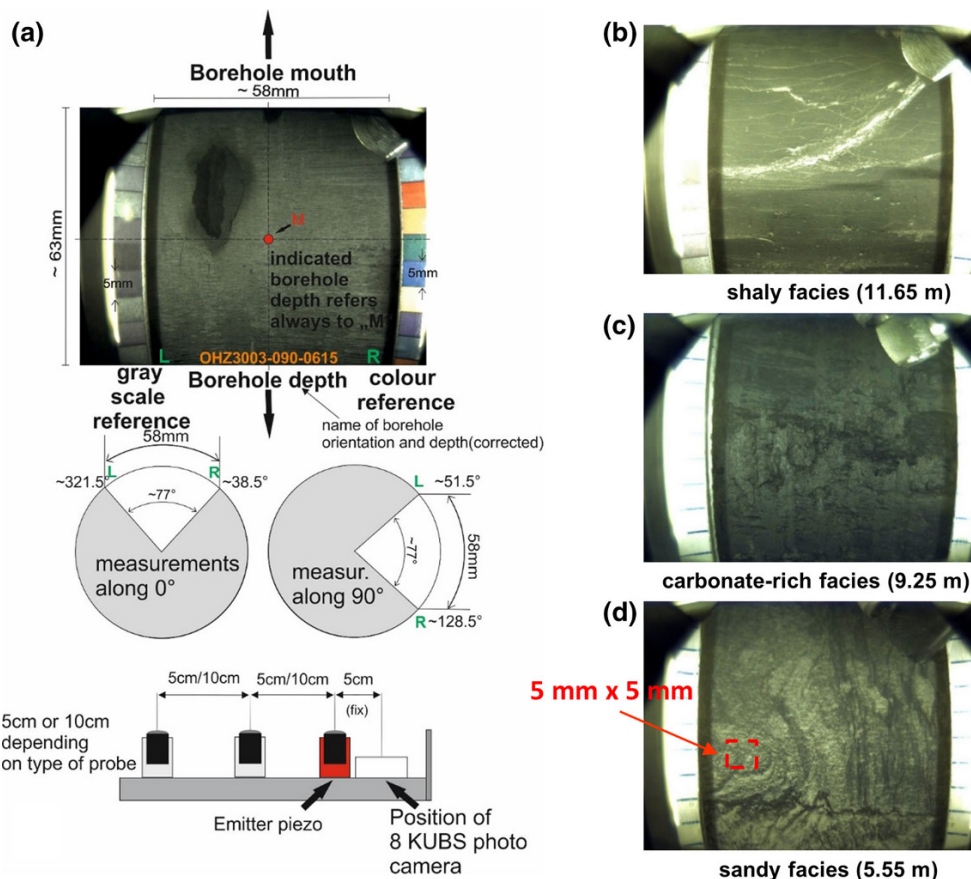


Fig. 5 Principle of seismic interval-velocity measurements (IVM). **b** BGR 8-channel ultrasonic borehole probe (8KUBS-05). **a** Principle of IVM with simplified ray-paths. The simultaneous full wave recording at seven receivers (5–80 cm) allows characterisation of

both the BdZ and the host rock. **c** Single seismic record, excitation signal (S1) and seven seismic traces with marked onsets of P- and Sv-wave phases (receivers R1–R7). **d** Seismic COF section for one receiver distance (R2, 20 cm) with marked P- and Sv-onsets

Fig. 6 a Principle of IVM measurements with the 8KUBS borehole camera. Details of the borehole wall captured in an 86 mm diameter borehole covering an area of 58 mm by 63 mm of the unrolled borehole wall; examples: **b** shaly facies from MI niche, borehole BSO-37 at a depth of 11.65 m, oriented normal to bedding with an azimuth 330°, dip -40° downwards; **c** carbonate-rich sandy facies from MI niche, borehole BDM-B2 at a depth of 9.25 m, oriented normal to the bedding, with an azimuth of 150°, dip +44° upwards; **d** sandy facies from the TT niche, borehole BLT-A8 at a depth of 5.85 m, oriented parallel to the bedding, azimuth 240°, dip 0°. Location of the niches are shown in Figure 6 of Bossart et al. (2017a)



hanging wall of the Main Fault, penetrating this 1-m-thick fault zone and ending in the footwall at a depth of 16 m. Nicely visible in Fig. 7 are calcite-filled shear-veins within

an S- (schistosité) and C (cisaillement) shear-band. The derived seismic parameters at ca. 12.15 m clearly confirmed this disturbed structure.

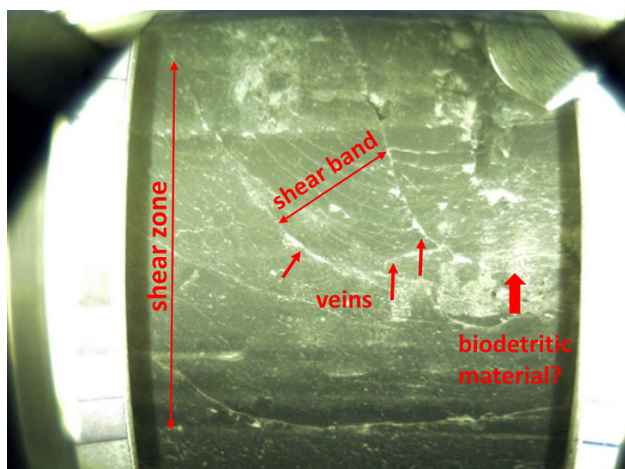


Fig. 7 Borehole camera photograph with small-scale structures from the shaly facies (MI niche, unrolled borehole wall of BSO-37 at a depth of 12.15 m, oriented normal to bedding with azimuth 330°, dip -40° downwards, area of 58 mm by 63 mm), showing a highly tectonically deformed zone approximately 6 m behind the Main Fault, consisting of calcite shear-veins and a S- (schistosité) and C (cisaillement) shear-band. The location of the MI niche and the Main Fault is shown in Figure 6 of Bossart et al. (2017a)

The high potential of IVM for resolving substantial spatial variations is demonstrated in three examples (see Figs. 8, 9, 10, 11). First, IVM were performed in a 28-m-long borehole (location: MI niche, drilled 45° up towards S) running perpendicular to the bedding through three facies of the Opalinus Clay (shaly, carbonate-rich sandy, and sandy). Second, in a 16-m-long borehole (BWS-12) with identical orientation only a few m further W, in addition to IVM we also performed geoelectrical and gamma ray measurements. For comparison and discussion of results, see Fig. 10 and text below. For the third example, we show results from a borehole orientated parallel to bedding strike solely within the sandy facies (location: TT niche, drilled horizontally towards W at the

heading face of the TT niche). A further small-scale variability aspect, namely the detection of fractures, is addressed in Sect. 3.3.

In the 28-m-long borehole, BDM-B2, we performed IVM with an 8-channel ultrasonic borehole probe in 5 cm steps. This resulted in 548 excitation points (CSP) and a total of 4384 seismic traces. Figure 8, representing R4 data (distance of 20 cm from the emitter), shows a COF section consisting of 548 single R4 recordings in a colour-coded amplitude point mode display. The data are plotted ensemble-normalized, meaning that the highest amplitude value (corresponding to 100%) over the complete seismic section, is used to normalise all other amplitudes. This allows direct comparison of all amplitudes within a section and enables direct observation of seismic energy attenuation along a profile. For example, strong local seismic wave-energy attenuation is mostly related to the occurrence of faults or fractures. It is clear from Fig. 8 that the seismic amplitudes up to 7.5 m borehole depth are weaker than those at greater distances. Furthermore, several locally confined amplitude attenuations are obvious for example at 5.5, 13.4 and 26 m borehole depth. The rock between 7.5 and 26 m borehole depth seems to be more competent than other borehole sections. This is the part of the Opalinus Clay that we interpret as the carbonate-rich sandy and sandy facies.

The derived apparent v_p along the total depth for receiver 1 is plotted on Fig. 9 (emitter–receiver distance is 5 cm). The app. v_p covers a range of about 3000 m/s. At this receiver 1, the app. v_p is still influenced by the existence of a BdZ but yields the highest spatial resolution due to the shortest distance between emitter and receiver R1. Up to 20 cm, the app. v_p of the shotcrete is measured, followed by a reduced app. v_p within the EDZ. At around 1.5 m an app. v_p of 2550 m/s for the shaly facies (perpendicular to bedding) starts with a positive anomaly at

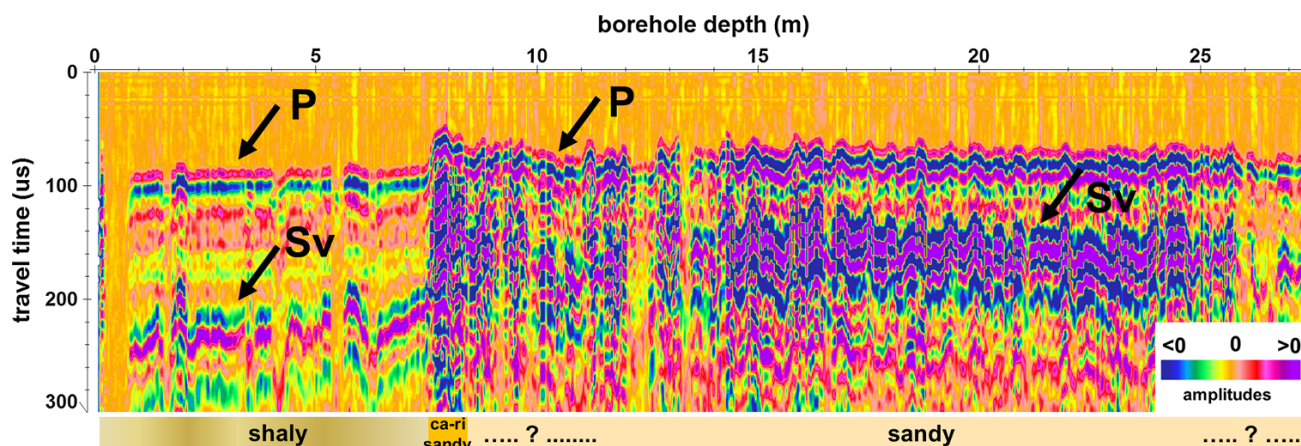


Fig. 8 IVM data from borehole BDM-B2 crossing three facies of the Opalinus Clay. Ensemble-normalised seismic section comprising all traces recorded at a distance of 20 cm from the emitter (constant offset (COF)) with marked P- and Sv-wave phases. Amplitudes are colour coded

Fig. 9 Derived apparent v_p data from IVM in borehole BDM-B2 (see also Fig. 8) for receiver R1 (5 cm). The large dynamic range of v_p is remarkable. For selected sections, a mean v_p is plotted and selected photographs from the borehole wall are shown. Note the close similarity of v_p distribution compared with borehole BWS-I2, which has the same orientation and is located several meters further W (Fig. 10)

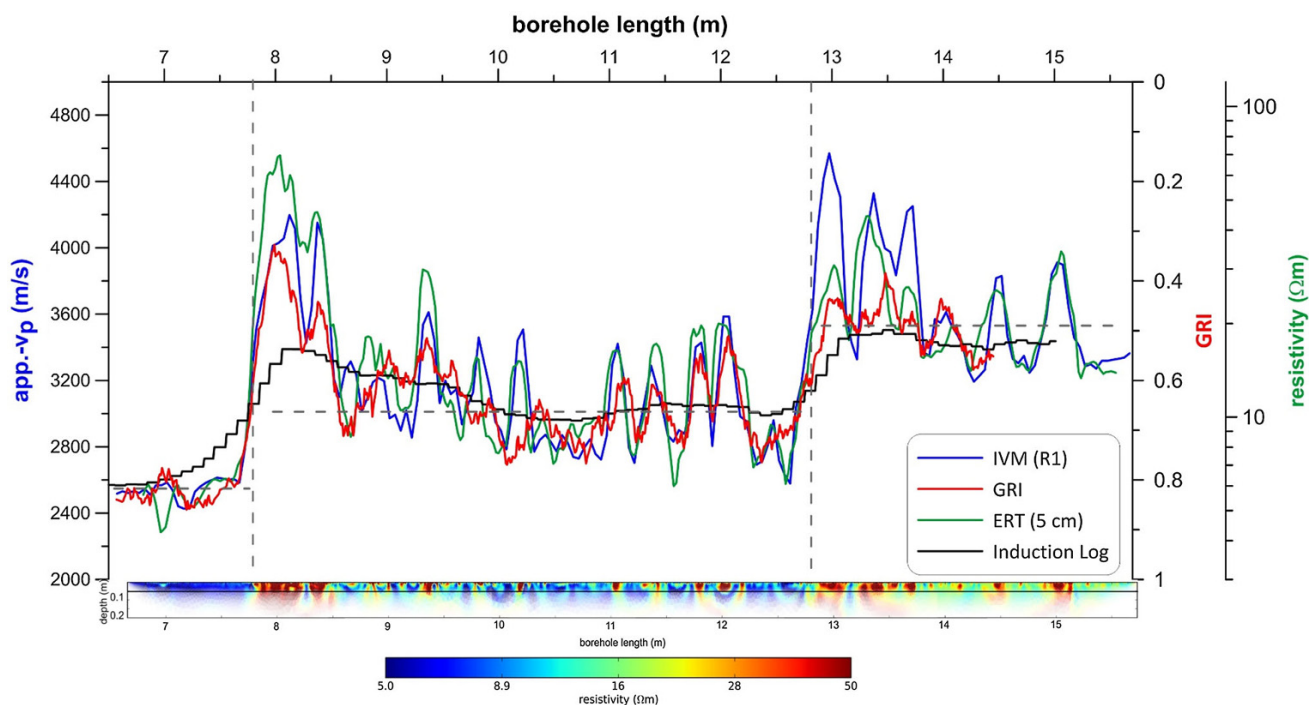
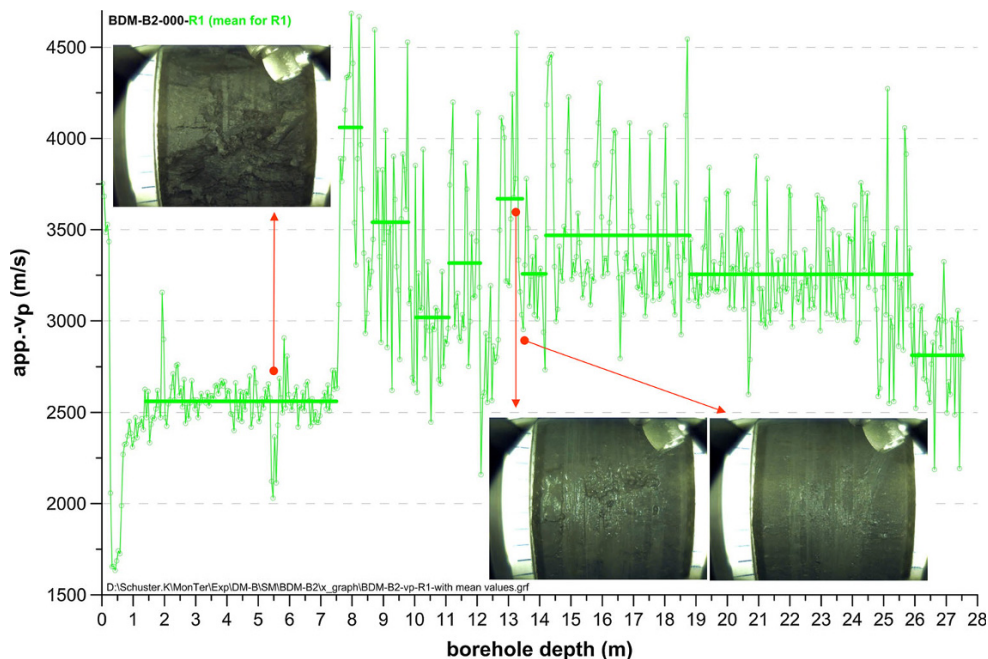


Fig. 10 Comparison of IVM-, ERT-, GRI and conventional induction log data derived in borehole BWS-I2. Note the close similarity of v_p distribution in comparison with borehole BDM-B2, which has the same orientation and is located several m further E (Fig. 9)

1.9 m and a major disturbances at 5.5 m. Very clearly at 7.5 m, the transition into the carbonate-rich sandy facies with an app. v_p of 4700 m/s can be seen followed by a gradual app. v_p decrease until 10.5 m, then the app. v_p varies between 3000 and 4000 m/s. The continuous app. v_p periodicity with ups and downs seems to be interrupted/disturbed at certain depths, e.g., around 10.8, 12.4, 13.7 and

15.5 m. Slight disturbances at these locations can be seen in the photographs taken during the IVM. Figure 9 shows three representative photographs.

From this distribution of derived app. v_p , a distinct transition from the carbonate-rich sandy into the sandy facies can hardly be distinguished. Notable is the app. v_p distribution at the end, between 25.9 and 27.5 m, where the

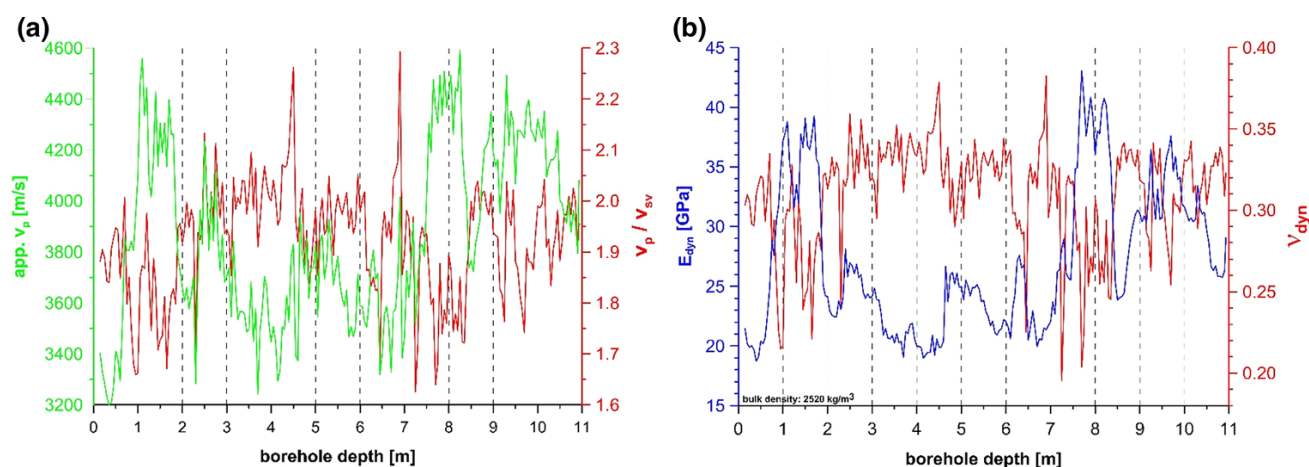


Fig. 11 Derived seismic parameters from IVM in borehole BLT-A8 (sandy facies, parallel with respect to bedding strike) for receiver R4 (20 cm). **a** Apparent v_p (left y-axis) and v_p/v_{sv} ratio (right y-axis). **b**

Estimated dynamic Young's modulus (left y-axis) and Poisson's ratio (right y-axis)

average v_p lies somewhere between the mean v_p for the shaly and sandy facies. A hand-picked differentiation between different “segments” at the disturbances was made in order to calculate mean app. v_p values. These mean values allow for an apparent differentiation within the sandy facies, including the carbonate-rich sandy facies (Fig. 9). The v_p distribution appears highly variable. It clearly reflects the known small-scale heterogeneity of the Opalinus Clay. Comparable v_p distributions are observed in several neighbouring boreholes where the parameter variability is similar.

In the nearby borehole BWS-I2, the v_p and specific electrical resistivity distribution could be correlated with clay content interpreted via the derived gamma-ray index distribution (Fig. 10). This 16 m long borehole begins also in the MI niche only several m further west at a comparable location (drilled 45° upwards towards S). A clear correlation was found with high-resolution electrical resistivity tomography measurements (ERT) results. ERT measurements were performed with a BGR borehole probe comprising 50 electrodes at distances of 1.5 cm. Results from an ERT with Wenner- α configuration were inverted and the specific electrical resistivity distribution were taken from the 2D-modell at a depth of 5 cm for comparison with R1 app. v_p data from IVM (same borehole, nearly same orientation of sensors and electrodes). The correlation between the geophysical parameters (IVM and ERT) is very clear, except at some locations where the results are in contrast (e.g., at 8.5 m). Such findings must be investigated in more detail. More remarkable is the generally very clear correlation between the gamma-ray index (GRI) and both geophysical parameter distributions. The GRI can be interpreted as a measure of the clay content (GRI = 1 equates pure clay and GRI = 0 indicates absence of clay). Higher specific electrical resistivities, which correlate very

well with higher v_p , are interpreted to indicated greater contents of carbonates and/or silica (sand) (Furche and Schuster 2015). The general trend of the ERT results is confirmed by results from a conventional induction log performed by a contractor in the same borehole (Fig. 10). Furthermore, comparing v_p data from borehole BDM-B2 (Fig. 9) with the results discussed here show a clear similarity in the v_p distribution. For example, the sharp transition between the shaly facies and the carbonate-rich facies around 7.5 m is reflected in both representations as well as the individual v_p distributions. We interpret this as a characteristic geological structure that can be detected and followed over a larger distance. This indicates that the methods yield repeatable and reliable results and can support stratigraphical site investigations.

The inferred small-scale heterogeneity in app. v_p can be directly related to the dynamic elastic parameters, e.g. E_{dyn} . These spatial heterogeneities must be accounted for when geomechanically characterising such mechanically variable rock packages.

On close analysis, the data from borehole BDM-B2 (Fig. 9) seem to reveal a second phenomenon (e.g., in the depth range 16 to 19 m), namely, a periodicity of the app. v_p distribution. In the related R4 app. v_p data, this periodicity is even more clearly quantifiable because the plot is smoother due to the greater emitter–receiver distance of 20 cm. The periodic app. v_p variation between 3000 and 4000 m/s is significant. A full cycle contains between 5 and 10 measuring points corresponding to “wave-lengths” between 0.25 and 0.5 m. Whether this periodicity can be related to sedimentation cycles should to be investigated further.

The third example shows results from an IVM investigation in the sandy facies. The 11-m-long sub-horizontal borehole, BLT-A8, starts at the heading face of the TT-

niche and was drilled parallel to the bedding strike. The cores show no signs that there is deviation from a parallel to bedding-strike orientation, however, all derived parameters show very strong variations. This is illustrated here by the R4 data in Fig. 11. The app. v_p and the app. v_p/v_{sv} ratio is depicted in Fig. 11a. It is important to note the particularly high v_p and low v_p/v_{sv} ratio between 1 and 2 m, and around 8 m. The derived dynamic Poisson's ratio ν_{dyn} varies between 0.22 and 0.31 in this range and between 0.20 and 0.38 along the total depth range (Fig. 11b). A bulk density of 2520 kg/m^3 was chosen for the calculation of E_{dyn} . Consequently, the E_{dyn} distribution is similar to the derived velocities (Fig. 11b) with three significant local maxima of E_{dyn} at around 1.5, 8 and 9.5 m. The rate of penetration (ROP) during drilling decreased at these depth significantly due to the unexpected high resistance/strength. Whether the E_{dyn} variation with values between 18 and 42 GPa is solely associated with mineralogical variations along the borehole or other changes, such as variability of porosity or different saturation of pore space, requires further investigation. Similar significant bedding-parallel variations of seismic parameters was also observed in the 4-m-long borehole BED-C2 drilled from the access gallery into the sandy facies, but with lower minimum and maximum v_p (2600–4000 m/s).

Summarizing the results of this section: (1) the Opalinus Clay at the Mont Terri rock laboratory can be very heterogeneous in terms of P- and S-wave velocities and dynamic elastic properties. (2) The scale of these heterogeneities is on the order of cm to dm and suggests a layered macro-structure/mechanical stratigraphy. (3) This is particularly relevant when dealing with stress redistributions around tunnels and other excavations where major stress concentration must be anticipated in the stiffer layers.

3.3 Excavation damaged zones (EDZ) and fracture detection

Underground excavations inevitably lead to an excavation-damaged/disturbed zone (EDZ/EdZ). If the stresses exceed the strength of the material, an EDZ characterised by fractures and micro-cracks will develop. EDZ are present at the Mont Terri rock laboratory in different forms (Bossart et al. 2017b). IVM is very sensitive to the existence of fractures and micro-cracks and therefore this method is preferentially used to characterise the extent as well as the degree of rock mass perturbation. The method is discussed in Sect. 3.2 (see also Fig. 5). We will now discuss an example from the EZ-B (Fracture Generations) experiment (Yong 2007) performed in the shaly facies. The stepwise excavation of a 5-m-long niche (diameter 3.8 m) in the shaly facies of the Opalinus Clay was followed with, amongst other techniques, IVM. The central axis of the EZ-

B niche is oriented normal to the bedding strike. The bedding planes dip 45° . We discuss the first of fifteen IVM repetitions in the central borehole BEZ-B3. This borehole coincides with the central axis of the niche. The first measurements were performed about three months after the excavation of Gallery 04. Figure 12a, b shows the derived v_p , v_{sv} and normalized P-wave onset phase-amplitude distribution along the borehole for a 90° (3 o'clock) orientation of the piezoelectric transducers, corresponding to 45° with respect to the bedding planes. The pronounced small-scale variability in all parameters for depths greater than 2 m reflects the heterogeneity of the rock. It applies also to the dynamic elastic parameters ν_{dyn} and E_{dyn} that we calculated using BdZ-corrected velocities (Fig. 12c). A comparison of dynamic moduli for depths greater than 6 m with BHE-25 data (see Fig. 4, both boreholes oriented 45° with respect to bedding planes) shows that E_{dyn} in the side-wall situation (BEZ-B3) is slightly higher than E_{dyn} in the floor derived from BHE-25 data.

The significantly reduced v_p and v_{sv} in the first 1.45 m and the deviation of the normalized amplitude values from the mean value (=100%) are used to determine the extent of the EDZ. In addition, we use several COF section data plots, each ensemble-normalised. The extent of the EDZ derived from seismic parameters, was assessed to be 1.45 m. Shortly after any excavation step, a structural and geological mapping along the side-walls of the niche was performed (Yong et al. 2010). Visual mapping shows the extent of fractures and cracks up to 1.3 m (left side) and 1.5 m (right side) as a consequence of the excavation of Gallery 04. Accounting for the variability of the Opalinus Clay and the different mapping and measurement locations, the seismically-derived EDZ extent of 1.45 m agrees well with the observations. The notch in the v_p graph at 1.15 m can be attributed to a higher density of pre-existing fractures (see also Fig. 13).

The degree of damage can be assessed using the degree of deviation, e.g., for v_p , from a known representative mean value for this locality and specific borehole orientation towards bedding; or a mean value estimated from the same measurement, but outside the EDZ and away from major anomalies. Figure 12d shows the deviation of the measured values from the mean v_p outside the EDZ (2700 m/s) starting from 0.25 m [data from the shotcrete (0–0.15 m) are excluded]. The plotted data correlates with the intensity of the damage within the EDZ. For distances between 0.15 and 0.25 m the damage of the rock resulted in a very strong attenuation of signals implying relatively high damage. From 1.5 m onwards, the deviations are in the range of the estimated standard deviation for the mean v_p , implying relatively low damage. Note the higher values around 1.15 m that are explained by the v_p -notch discussed above.

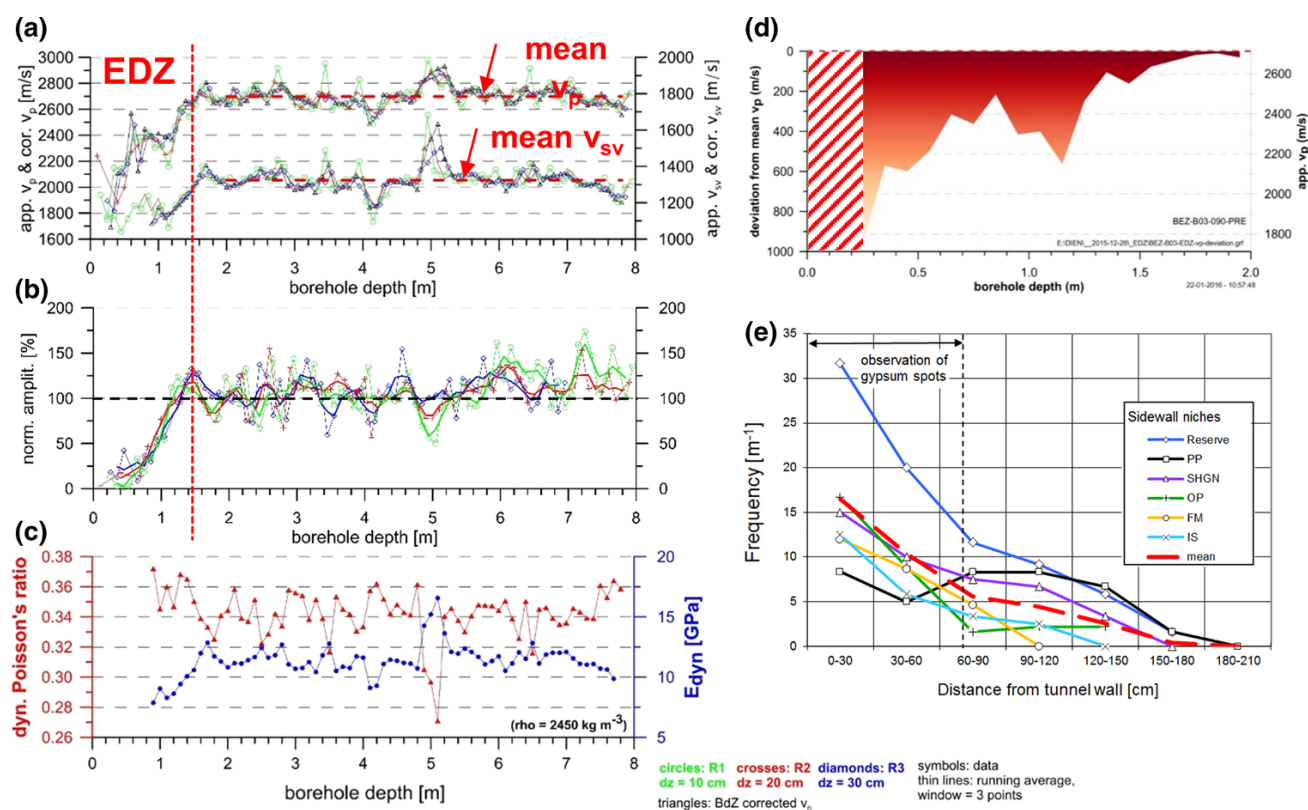


Fig. 12 Derived seismic parameters from first IVM along borehole BEZ-B3. **a** Apparent v_p (left y-axis) and v_{sv} (right y-axis) distribution for receivers R1, R2 and R3 (10, 20 and 30 cm) and BdZ corrected v_p and v_{sv} . **b** normalised P-wave amplitudes for receivers R1, R2 and R3. The derived extent of the EDZ is marked at 1.45 m. **c** Dynamic Poisson's ratio (left y-axis) and dynamic Young's modulus (right y-axis). Both are derived via BdZ-corrected velocities. **d** Degree of

damage within the EDZ calculated as local deviation of v_p from a mean reference v_p . **e** Fracture frequency in the excavation damaged zones. Extension fractures were mapped by line-counts in newly excavated side-wall niches of the Mont Terri security gallery. Gypsum spots were observed up to 0.7 m into the tunnel wall of the security gallery, indicating an interconnected fracture network in the first 0.7 m around the security gallery

The local findings presented in Fig. 12d can be compared with a more general dataset presented in Fig. 12e (Bossart et al. 2017b), where extension fractures were systematically mapped in newly excavated side-wall niches constructed perpendicular to the security gallery (diameter of 5 m). The observed fractures in these side-wall niches mirror directly the EDZ of the security gallery. In addition to fracture frequencies, we measured trace lengths and orientations. The fracture frequencies obtained are shown in Fig. 12e, varying between 32 and 0 fractures/m in a radial distance from 0 to 2 m in the tunnel wall. The highest frequencies were observed in the first 70 cm of the tunnel wall, which corresponds to locations where small gypsum spots were observed on fracture surfaces. This phenomenon is interpreted as an interconnected fracture network in the first 0.5 m of the tunnel wall, where fractures are filled with air and framboidal pyrites were oxidised to gypsum.

Figure 12e reflects the rock damage/disturbance in terms of extension fractures that were observed and mapped by visual inspection after excavation. In contrast, the mini-seismic results (Fig. 12d) reflect rock alteration

caused mainly by fractures at different scales (visible macro- and invisible micro-cracks). Furthermore, at other sites (Schuster 2012) and in other boreholes used for IVM within the EZ-B experiment (Yong 2007), results show very strong seismic-energy attenuation even along visually assessed perfect borehole walls that cannot be explained by visible cracks. We explain this by the existence of micro-cracks below visual resolution. At several locations from borehole depths of about 0.5 m onwards, the borehole walls show borehole breakouts in certain orientations. Both plots (Fig. 12d, e) have strong similarities in the extent and the lateral distribution of these features.

We attempted to correlate individual excavation advances with extent of EDZ delineated by the IVM data, but this proved unsuccessful as the excavation rate was found to have no relation. The six excavation steps with advances of 0.58, 1.12, 0.78, 1.32, 0.6 and 0.7 m resulted in EDZ extents of 0.88, 0.59, 0.26, 1.51, 0.96 and 0.95 m. This was unexpected. Damage ahead of the niche face is best attributed to local relaxation provided by intersecting tectonic shears as well as the proximity to a previously

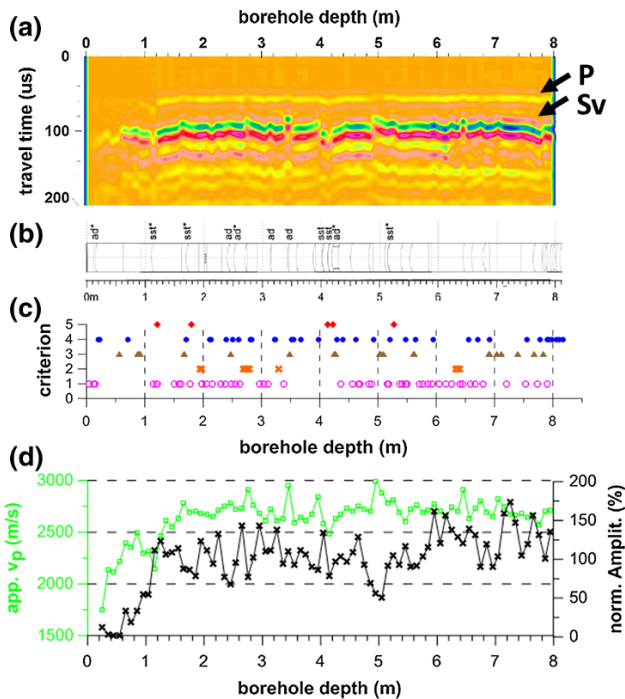


Fig. 13 Comparison of core-mapping attributes with parameters derived from IVM in borehole BEZ-B3. **a** Seismic COF section (R1 data, ensemble-normalised, amplitudes colour coded). **b** Core map. **c** Attributes derived from core mapping, criterion 1 sandy lenses (pink circles), 2 sandy nodules (orange crosses), 3 brownish oxidised lenses, siderite, 4 artificial fractures (blue dots), 5 fractures by way of tectonic structures (red diamonds). **d** Apparent v_p and normalised amplitudes for R1 data

damaged volume of rock due to excavation of an intersecting excavation. Tectonic shears assist in the damage process as they most easily facilitate stress relief, as suggested by the low v_p and normalized amplitudes near the shears. In Fig. 13, several parameters are summarised that support this explanation.

The ensemble-normalised COF section for receiver R1 data indicates, especially in the Sv-wave phase (Fig. 13a), several anomalies and discontinuities that could result from tectonic structures (i.e., shears and/or fractures). Figure 13b shows a core map and Fig. 13c shows, in more detail, several attributes derived from on-site core mapping. Five clearly identified fractures/tectonic structures (dipping fault plane with striae, criterion 5, red diamonds) at 1.21, 1.80, 4.14, 4.23 and 5.27 m and many core features attributed to artificial origins (criterion 4, blue dots) are present. Furthermore, criterion 2 (sandy nodules, orange crosses), criterion 1 (sandy lenses, pink circles) and criterion 3 (brownish oxidised lenses, siderite) are shown. Several of these features correlate well with reduced or higher app. v_p or normalised amplitudes (Fig. 13d). The undulations in the app. v_p and normalised amplitude distributions can be best explained by lateral transitions to sandy lenses or sandy nodules, or to discontinuities. For

example, at 1.21, 4.14 and 4.23 m the fractures (i.e., tectonic shears) found clearly in the cores fit well with reduced app. v_p and reduced normalised amplitudes. Further explanations are given in Yong et al. (2013). An uncertainty in the depth location of some cm has to be taken into account because core removal was not oriented. Furthermore, the IVM borehole data stems from a small location compared with the excavated front of nearly 11 m².

In summary, the results discussed in this section show that EDZ features are resolved with high spatial resolution with respect to the extent and the degree of damage. Furthermore, fractures and tectonic structures outside the EDZ are detectable.

3.4 Borehole disturbed zones (BdZ)

In order to adequately characterise or sample a rock volume, a high density of boreholes is almost always needed. These boreholes themselves may induce significant perturbations in the formation and its response to seismic methods. Experience gained from many measurement campaigns in various underground laboratories where different BdZs have developed has shown that they can be identified using radial velocity gradients deduced from individual apparent velocities derived from IVM. Examples of results from IVM with a 4-channel probe with an apparent v_p distribution is given in Figs. 4a and 12a. Three simplified variants of borehole-wall situations are shown in Fig. 14. For differentiation, we use the radial v_p distribution. A laterally developed BdZ can clearly be distinguished by the different app. v_p when compared to an undisturbed borehole wall, which is characterised by a constant v_p starting from the borehole wall (Fig. 14a). The most commonly encountered case of $v_{pR1} < v_{pR2} < v_{pR3}$ indicates a positive radial v_p -gradient (Fig. 14b). The rarer “egg-like shell” borehole wall with higher v_p near the borehole wall and decreasing v_p with distance until the v_p of the undisturbed rock is reached is shown in Fig. 14c.

The following example shows how a BdZ changes with time. Drilling of the 29-m-long borehole (location: RC niche, borehole BRC2 drilled horizontally towards SE, orientated at 45° with respect to bedding strike) was interrupted for operational reasons at 7.2 m. The first IVM was performed immediately after this initial drilling phase. After completing drilling to 29 m, IVM were resumed the next day, starting at 6.5 m so that the overlapping section between 6.5 and 7.2 m was measured twice. The quality of both data sets is very good. The derived v_p are displayed in Fig. 15. Velocities from the first measurement indicate an unusual velocity gradient of $v_{pR1} > v_{pR2} \geq v_{pR3}$ (Fig. 15a) often attributed to a thin high-velocity layer at the borehole wall (egg-like shell). This sort of BdZ could be caused by

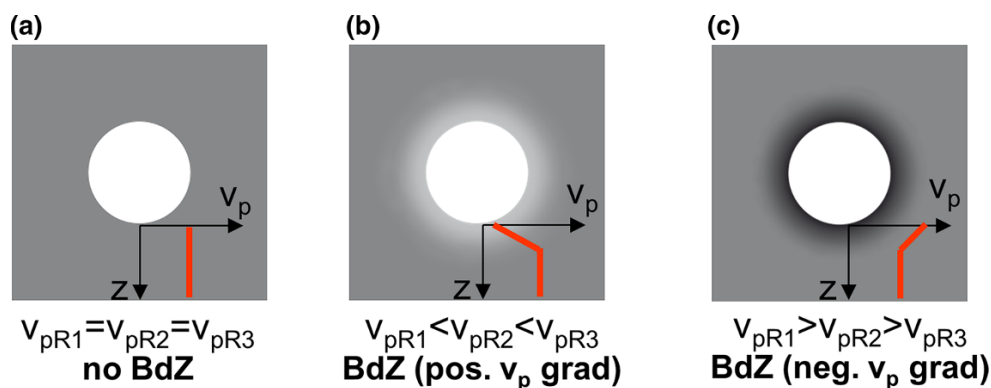


Fig. 14 Three simplified variants of a borehole wall characterised by radial v_p gradients. **a** Intact borehole wall, no BdZ. **b** BdZ with positive v_p gradient, the most common case, less competent near the borehole wall. **c** BdZ with negative v_p gradient, more competent near the borehole wall

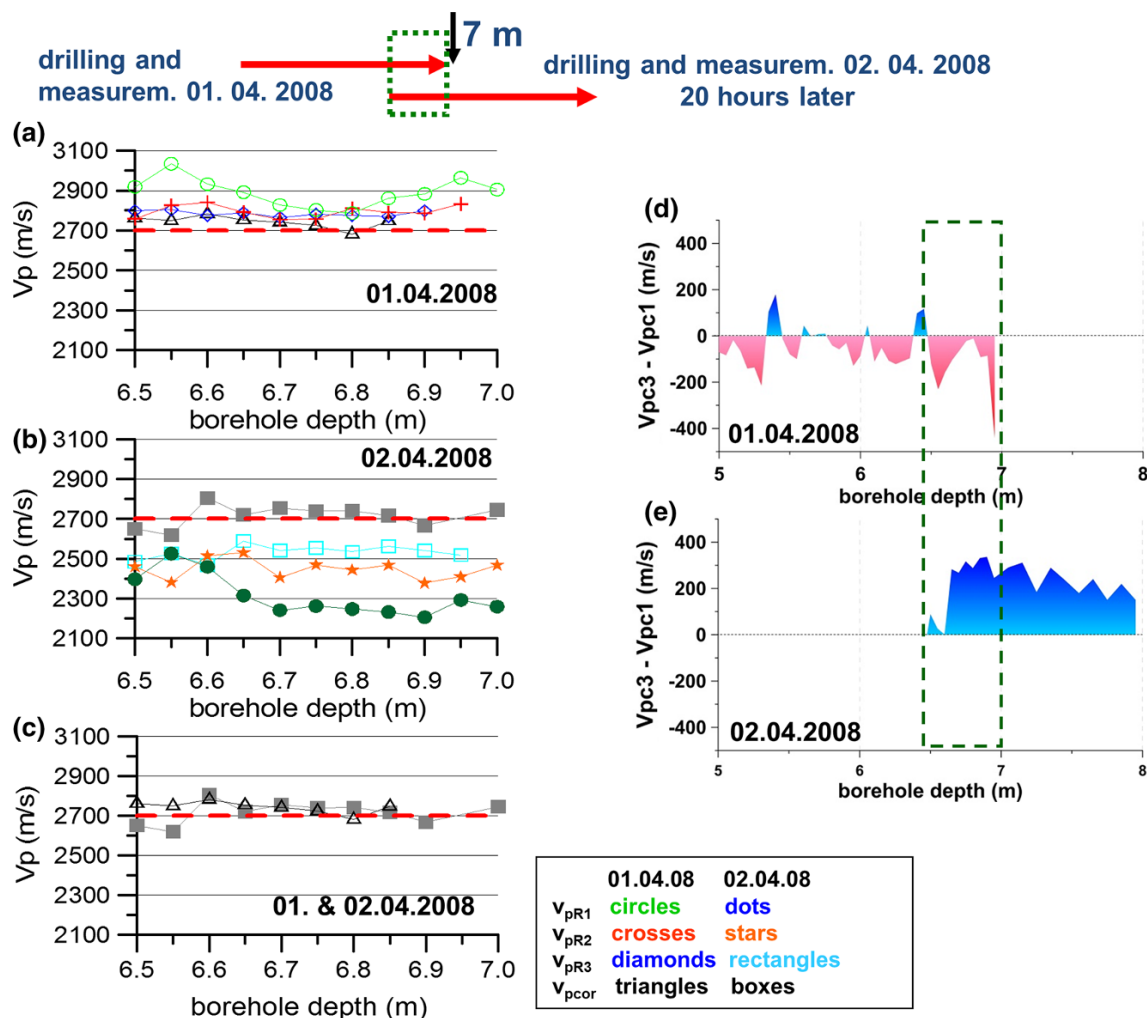


Fig. 15 Evolution of a BdZ derived from IVM in borehole BRC2. Apparent v_p distribution for receivers R1–R3 and BdZ corrected v_p . **a** $V_{pR1} > V_{pR2} \geq V_{pR3}$ indicate a negative radial v_p gradient (egg-like shell). **b** Repetition of IVM 20 h later shows $V_{pR1} < V_{pR2} < V_{pR3}$

the drilling process itself as a result of air drilling, desiccation, and/or increased temperature led to a strengthening of the wall (Wild et al. 2015). The calculated $v_{p-corBdZ}$,

indicative of a disturbed borehole wall. **c** BdZ corrected v_p for both cases are similar. **d** Qualitative visualisation of the BdZ via CMP related $v_{pR3} - v_{pR1}$. **e** As **d** but 20 h later

which represents the velocity outside the BdZ, varies around 2700 m/s, similar to the average value for an undisturbed Opalinus Clay (shaly facies) with a 45°

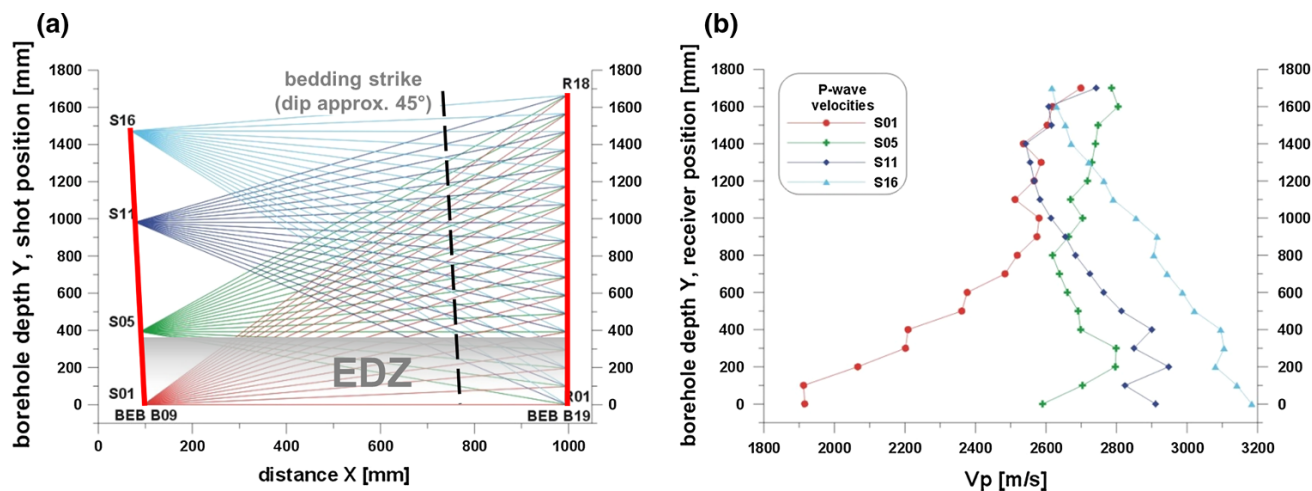


Fig. 16 Seismic anisotropy study between boreholes BEB-B09 and BEB-B19. **a** Seismic ray-paths for selected emitters and receivers R01–R18. **b** Derived v_p distribution for the emitter–receiver combinations shown in **a**)

borehole orientation towards the bedding planes. Note the similar mean v_p found in borehole BEZ-B3 for depth greater 2 m (see Fig. 12a).

The calculated velocity outside the BdZ ($v_{p\text{-corBdZ}}$) obtained 20 h later is in the range of the average value. Both corrected velocities ($v_{p\text{-corBdZ}}$) are very similar in the overlapping section (Fig. 15c). This shows that the correction procedure works well and we are able to “look behind the BdZ”. The v_p derived from this second measurement show a completely different appearance (Fig. 15b). In this case we observe $v_{pR1} < v_{pR2} < v_{pR3}$, similar to many other measurements, and representing a significant change in the BdZ. The borehole video analysis also revealed a change in the state of the borehole wall. Between 0.8 and 2.7 m, 5.4 and 6.1 m and 7.0 and 7.2 m, the quality changed from an intact wall to weak sheeting after 20 h. This development is consistent with results reported by Kupferschmied et al. (2015) who investigated the time development of a BdZ around a borehole in the Mont Terri rock laboratory.

Qualitatively, the extent of the BdZ can be visualized by calculating the differences $v_{pR3} - v_{pR1}$ via CMP-related data (Fig. 15d, e). Quantitatively, the extent of the BdZ was calculated for similar data sets using finite-difference ray-tracing methods (Schuster 2012). From these experimental results, the extent of the BdZ discussed here varies in the range of several centimeters.

The results discussed in this section show that IVM provides an excellent tool to characterise a BdZ and its evolution in time.

3.5 Seismic anisotropy measured in different dimensions

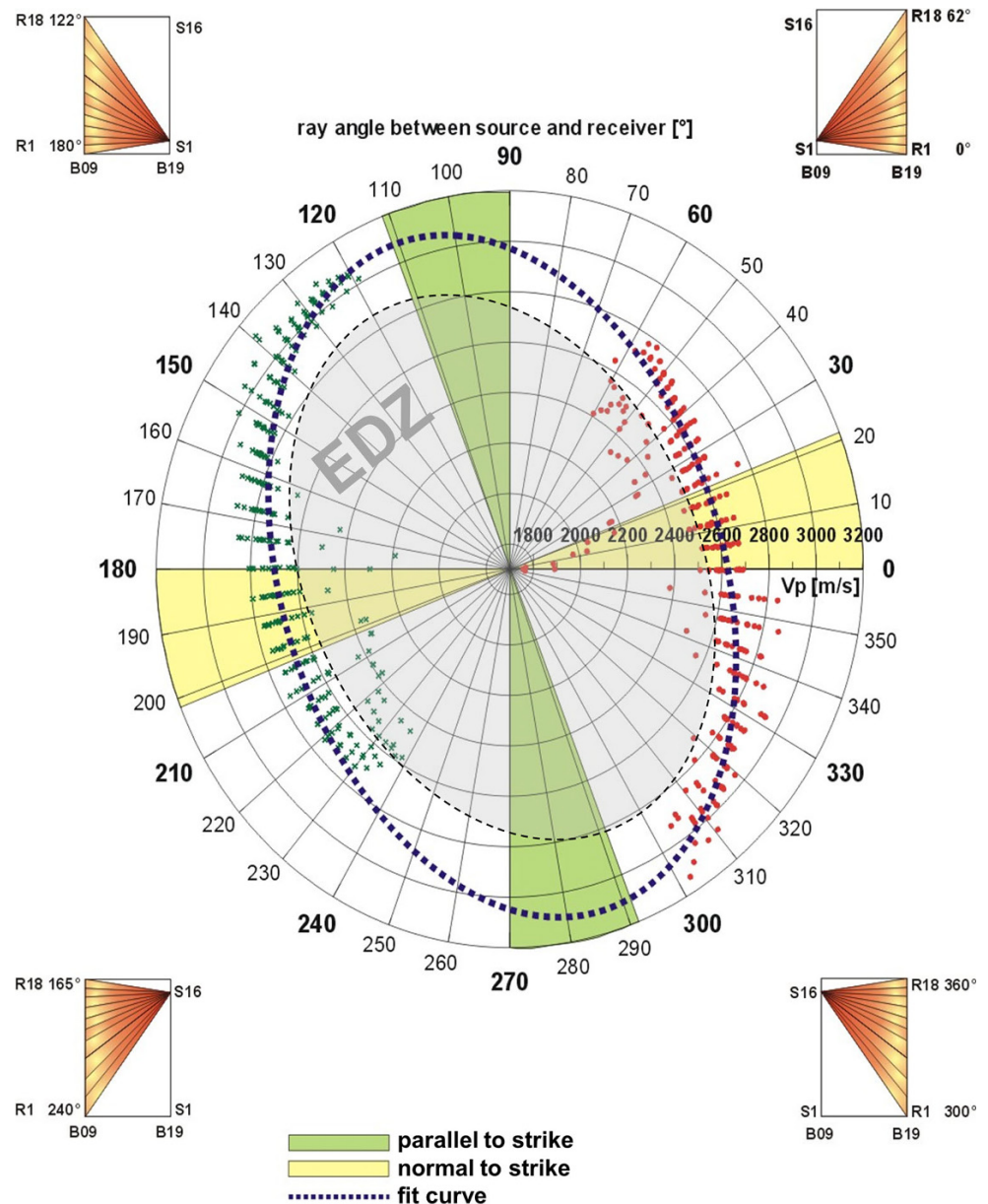
Anisotropic petrophysical parameters are expected in the Mont Terri rock laboratory due to the fine bedding of the

Opalinus Clay. It is important to quantify these values for subsequent rock-mechanical analyses. Seismic anisotropy directly influences the dynamic elastic performance of rock. We typically assume that the biggest contribution to seismic anisotropy is directly related to bedding orientation (extrinsic or effective portion of the anisotropy) and that the intrinsic portion (mineral fabric and orientation of minerals) is part of the bedding orientation itself. In addition, anisotropy can be influenced by the local stress field. We investigated seismic anisotropy using several different MSM that span a very broad distance range. The smallest are IVM at several cm, then come fan-like crosshole measurements (XHM-F) covering distances of several m, and finally, seismic transmission measurements between drifts (STD) with distances between 10 and 60 m.

From IVM results of the shaly facies and several boreholes with orientations parallel and perpendicular to bedding strike, we deduced a seismic anisotropy coefficient A_v . In total, we could use nine boreholes with a normal, and five boreholes with a parallel orientation with respect to the bedding strike. We considered only v_p values outside the EDZ and not influenced by obviously disturbed borehole regions. The mean v_p were 2469 m/s (± 51.3 m/s) for the normal and 3026 m/s (± 141.1 m/s) for the parallel orientations towards bedding planes (standard deviation in parentheses). For the IVM parallel to bedding strike, the sensors were not in all cases aligned along the bedding strike. The estimated seismic anisotropy coefficient $A_v = 0.23$.

For the anisotropy analyses with XHM-F, two 1.8-m-long sub-horizontal boreholes at the eastern side-wall of the EB-niche were used (boreholes were drilled 10° upwards with an orientation nearly parallel to the strike of the bedding). Figure 16a depicts the layout with some seismic ray-paths (Schuster and Alheid 2002). The red

Fig. 17 Seismic anisotropy in a horizontal plane. Angle-dependent v_p variation of all 576 emitter–receiver combinations in a polar diagram. Note the limited angle coverage. Nevertheless, the data fits well with an elliptical fit, after the EDZ-related v_p values were excluded. Four ray coverages are shown as small inserts



lines represent both boreholes with 16 emitting and 18 receiver positions (left to right). The same array was used in the reverse direction resulting in 576 different ray-paths. Some results are shown in detail in Fig. 16b.

For example, for emitting point S01 (red travel paths) and receiver positions R01–R04, the seismic wave-field travels through the EDZ and nearly perpendicular to bedding. This results in a very low v_p of 1900–2200 m/s. For the other receiver positions (R05–R18), the seismic wave field travels progressively more outside of the EDZ and the angle of incidence with bedding strike extenuate gradually. The v_p converges to intermediate values around 2700 m/s. For emitting point S16, the opposite is true. The compilation of all derived v_p is shown as a polar diagram in Fig. 17. The ellipse with violet squares is a simplified fit

using only values not influenced by the EDZ. The four small inserts represent selected travel path distributions. The seismic anisotropy coefficient A_v derived from this anisotropy ellipse is 0.20, close to the value obtained from single borehole measurements using IVM.

Finally, we use data from a seismic transmission experiment (ST experiment) for an anisotropy analysis. Fifty piezoelectric 3-component transducers were deployed along the western side-wall of the access gallery (Fig. 18b). Due to the limited number of emitters and receivers and logistical constraints, this is a much more approximate approach to analyse anisotropy compared to the other two methods discussed above. Figure 18a depicts some of the relevant derived v_{pz} (z-component) results for three emitting points in Gallery 98. The numbers 1–50

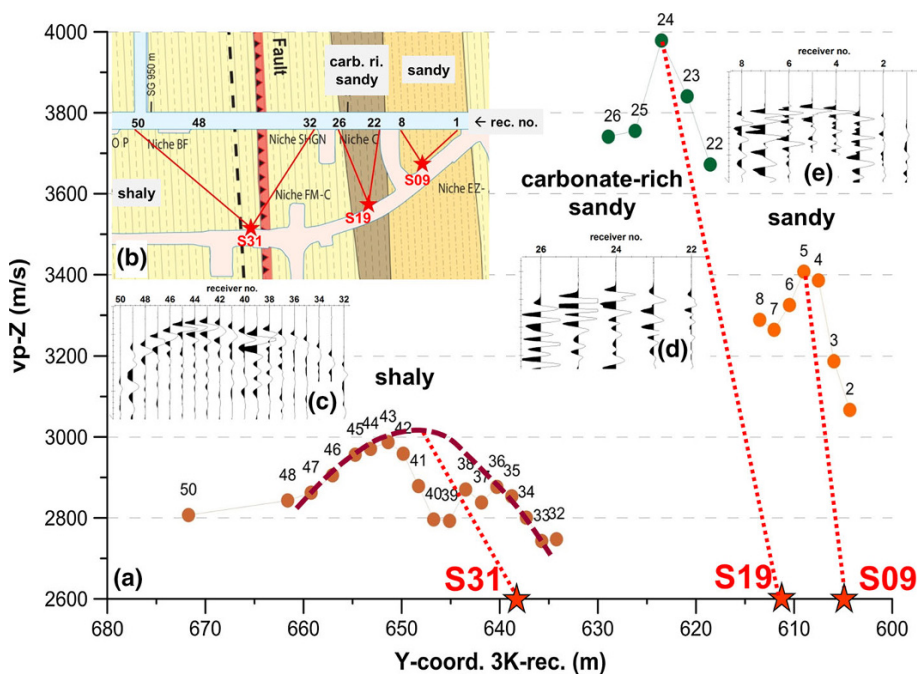


Fig. 18 Results from a seismic transmission experiment were used for an anisotropy study along the three facies types of the Opalinus Clay. **a** Derived v_{p-z} (z-component). The $v_{p-z-max}$ direction for each facies is interpreted to be the bedding-strike parallel orientation (sandy facies: $v_{p-z} \approx 3410$ m/s, carbonate-rich sandy facies: $v_{p-z} \approx 3990$ m/s and shaly facies: $v_{p-z} \approx 3010$ m/s). For the shaly

facies, the v_{p-z} distribution was disturbed, most probably by the Main Fault. **b** The ray coverage for emitter positions S09, S19 and S31. Three-component receivers R1–R50 were deployed in the access gallery and some niches. **c–e** Ensemble-normalised seismic subsections focusing on the first arrival phases for each facies of the Opalinus Clay

above the dots correspond to the numbering of the 3 K-piezos deployed in the access gallery (Fig. 18b). Emitters and receivers were placed on top of the shotcrete, which is assumed to have thicknesses between 10 and 25 cm. Therefore all derived seismic parameters are influenced by the transition through the intersection and the shotcrete itself. Derived travel times are corrected with an average v_p value for shotcrete but the impact is negligible due to the long travel paths (10–60 m). The bond between shotcrete and Opalinus Clay was assessed via light hammer strokes and rated to be strong enough for good signal transmission.

For clarity, this discussion is limited to emitters and receivers with travel paths running primarily through one of the three known facies of the Opalinus Clay. The high quality of the seismic data is compiled in three inserts (Fig. 18c–e) focusing on first arrival phases. These are ensemble-normalised seismic sub-sections from the three facies. In the sandy and carbonate-rich sandy facies (emitters S09 and S19), the highest v_{p-z} encircled by lower v_{p-z} is found. This is attributed to the travel path between emitter and receiver with the highest v_{p-z} coinciding approximately with the orientation of the bedding planes (highest v_{p-z} parallel to the

bedding planes). In the shaly facies, the v_{p-z} distribution is more complex with two local maxima. In this case, the seismic wave-field is probably influenced by the Main Fault, resulting in a local v_{p-z} reduction. In order to find the fastest direction, the v_{p-z} distribution curve was fitted and the apex was taken as the maximum v_{p-z} direction.

Due to logistic constraints, we could not span the angular range necessary for high quality results. The maximum aperture that could be measured in the shaly facies under undisturbed conditions was 55° . A range of at least 90° is necessary to identify the fastest or slowest direction. The seismic anisotropy coefficient A_v derived from the 55° range was extrapolated to the 90° range by considering local site information and assuming an elliptical anisotropy distribution, similar to that derived nearby at a smaller scale (cf. Figure 17). This analysis resulted likewise in an A_v of 0.2, in good agreement with the other results, but with higher uncertainty.

The main result of this section is that we could determine a seismic anisotropy coefficient A_v of 0.2 for the shaly facies of the Opalinus Clay using different methods at different scales.

4 Conclusions

We have applied mini-seismic methods (MSM) in situ in the framework of rock-mechanic, geological, and geotechnical site investigations with high spatial and seismic parameter resolution. These methods offer a good set of powerful tools for real in situ site characterisation through seismic parameters. Especially in cases when core extraction fails or laboratory results are unsatisfactory, MSM are very beneficial to obtain rock properties that can be attributed to real in situ properties. The rock mass can be characterised over scales of several cm to several dekametres. Even when boreholes are required for high resolution and the drilling can disturb the surroundings, we can correct for these affects. MSM can resolve the heterogeneity of the Opalinus Clay in the cm range, supporting structural interpretation. We derived a number of seismic and dynamic elastic parameters that are appropriate for rock characterisations. Furthermore, we could establish a relation between the static and dynamic Young's modulus and quantify seismic anisotropy at different scales. It was also possible to resolve small-scale variations within the Opalinus Clay. We investigated EDZ features, including extent and degree of damage, and could characterise the evolution of BdZ with seismic parameters. Furthermore, fractures outside the EDZ are detectable with these seismic methods. The size of the rock volume investigated ranges from several cm up to several dam. Depending on the desired spatial resolution, non-destructive measurements are performed along or between drifts, between boreholes, or within a single borehole. MSM can therefore accurately capture local in situ conditions for a rock characterization, particularly when the effects resulting from EDZ and BdZ features can be excluded or corrected.

The concepts and applications presented here include many examples that illustrate the power of the techniques and their consistency in the obtained results. Similar results have been gained from measurements that BGR has performed at other locations within the Mont Terri rock laboratory and elsewhere.

Improvements in the techniques are certainly possible; we expect the forthcoming use of 3-component seismic mini-vibrators and 3-component receivers will yield further interesting findings. For a better understanding of the relationship between static and dynamic elastic parameters, controlled experiments that take, for example, porosity and pore-space saturation into account, are necessary. Furthermore, the parallel application of other geophysical methods, as partly demonstrated here, will continue to enhance the interpretations.

Acknowledgements Over the years many colleagues participated in development and measurements. Many thanks to (in alphabetical

order): Hendrik Albers, Hans-Joachim Alheid, Dieter Böddener, Christoph Czora, Werner Hökendorff, Peter Eichhorn, Friedhelm Schulte, Wilfried Stille and Torsten Tietz. We thank colleagues from swisstopo, Christophe Nussbaum, David Jaeggi, Thierry Theurillat and Senecio Schefer, for their straightforward local site support. We also thank both reviewers, Till Popp (IFG Leipzig) and Pierre Dick (IRSN Fontenay-aux-Roses), for their very helpful concerted comments that improved the paper. Roy Freeman reviewed the English for readability. Research leading to the results presented here has received funding from the German Federal Ministry of Economics and Energy.

Open Access This article is distributed under the terms of the Creative Commons Attribution 4.0 International License (<http://creativecommons.org/licenses/by/4.0/>), which permits unrestricted use, distribution, and reproduction in any medium, provided you give appropriate credit to the original author(s) and the source, provide a link to the Creative Commons license, and indicate if changes were made.

References

- Bock, H. (2002). RA experiment: Rock mechanics analyses and synthesis: conceptual model of Opalinus clay. *Mont Terri Technical Report*, TR 01-03. Federal Office of Topography (swisstopo), Wabern, Switzerland. www.mont-terri.ch.
- Bossart, P., Bernier, F., Birkholzer, J., Bruggeman, C., Connolly, P., Dewonck, S., Fukaya, M., Herfort, M., Jensen, M., Matray, J.-M., Mayor, J. C., Moeri, A., Oyama, T., Schuster, K., Shigeta, N., Vietor, T., & Wiczorek, K. (2017a). Mont Terri rock laboratory, 20 years of research: introduction, site characteristics and overview of experiments. *Swiss Journal of Geosciences*, 110. doi:10.1007/s00015-016-0236-1 (this issue).
- Bossart, P., Nussbaum, C., & Schuster, K. (2017b). *Generation and self-sealing of the excavation-damaged zone (EDZ) around subsurface excavation in a claystone*. Wiley (submitted).
- Bossart, P., & Thury, M. (2008). Mont Terri Rock Laboratory. Project, Programme 1996 to 2007 and Results. Reports of the Swiss Geological survey No. 3. Federal Office of Topography (swisstopo), Wabern, Switzerland. www.mont-terri.ch.
- Corkum, A. G. (2006). Non-linear behavior of Opalinus Clay around underground excavations. Ph.D. dissertation, University of Alberta, Edmonton, Alberta, Canada.
- Furche, M., & Schuster, K. (2015). Neuartige Kombination von Geoelektrik (ERT)- und Miniseismik-Messungen zur Charakterisierung von Tongesteinen erfolgreich getestet. BGR online: http://www.bgr.bund.de/DE/Themen/Endlagerung/Methoden/In_situ/neuartige_kombination_ert_miniseismik_messungen.html?nn=1550002.
- Göbel, I., Alheid, H.-J., Alonso, E., Ammon, Ch., Bossart, P., Bühler, C., Emmerich, K., Fernandez, A. M., García-Siñeriz, J. L., Graf, A., Jockwer, N., Kaufhold, St., Kech, M., Klubertanz, G., Lloret, A., Mayor, J. C., Meyer, T., Miehe, R., Muñoz, J. J., Naumann, M., Nussbaum, C., Pletsch, T., Plischke, I., Plöetzle, M., Rey, M., Schnier, H., Schuster, K., Sprado, K., Trick, T., Weber, H., Wiczorek, K., & Zingg, A. (2007). Heater Experiment: rock and bentonite thermo-hydronechanical (THM) processes in the near field of a thermal source for development of deep underground high level radioactive waste repositories. In P. Bossart, & C. Nussbaum (Eds.), *Mont Terri Project—Heater experiment, engineered barriers emplacement and ventilation tests*. Reports of the Swiss Geological Survey No. 1 (pp. 7–16). Federal Office of Topography (swisstopo), Wabern, Switzerland. www.mont-terri.ch.

- Jaeggi, D., Laurich, B., Nussbaum, C., Schuster, K., & Connolly, P. (2017). Tectonic structure of the “Main Fault” in the Opalinus Clay, Mont Terri rock laboratory (Switzerland). *Swiss Journal of Geosciences*, 110. doi: [10.1007/s00015-016-0243-2](https://doi.org/10.1007/s00015-016-0243-2) (this issue).
- Kupferschmied, N., Wild, K. M., Amann, F., Nussbaum, C., Jaeggi, D., & Badertscher, N. (2015). Time-dependent fracture formation around a borehole in a clay shale. *International Journal of Rock Mechanics and Mining Sciences*, 77, 105–114.
- Schuster, K. (2002). Seismic in situ Methods for the Characterisation of Excavation Damaged Zones—Final Report. Projektträger des BMBF und BMWi für Wassertechnologie und Entsorgung, Contract-No. 02E9098.
- Schuster, K. (2012). Detection of borehole disturbed zones and small scale rock heterogeneities with geophysical methods. In Proceedings of the EC-TIMODAZ-THERESA International Conference, Impact of thermo-hydro-mechanical chemical (THMC) processes on the safety of underground radioactive waste repositories (pp. 135–145). Luxembourg.
- Schuster, K., & Alheid, H.-J. (2002). Engineered Barrier (EB) Experiment and Geophysical Characterisation of the Excavation Disturbed Zone (ED-C) Experiment: Seismic Investigation of the EDZ in the EB niche. Mont Terri Technical Report, TR 02-03. Federal Office of Topography (swisstopo), Wabern, Switzerland. www.mont-terri.ch.
- Schuster, K., Alheid, H.-J., & Böddener, D. (2001). Seismic investigation of the excavation damaged zone in Opalinus Clay. *Engineering Geology*, 61, 189–197.
- Wieczorek, K., Gaus, I., Mayor, J. C., Schuster, K., García-Siñeriz, J.-L., & Sakaki, T. (2017). In-situ experiments on bentonite-based buffer and sealing materials at the Mont Terri rock laboratory (Switzerland). *Swiss Journal of Geosciences*, 110. doi: [10.1007/s00015-016-0247-y](https://doi.org/10.1007/s00015-016-0247-y) (this issue).
- Wild, K. M., Wymann, L. P., Zimmer, S., Thoeny, R., & Amann, F. (2015). Water retention characteristics and state-dependent mechanical and petro-physical properties of a clay shale. *Rock Mechanics and Rock Engineering*, 48, 427–439.
- Yong, S. (2007). A three-dimensional analysis of excavation-induced perturbations in the Opalinus Clay at the Mont Terri Rock Laboratory, Ph.D. dissertation, Swiss Federal Institute of Technology, Zürich, Switzerland.
- Yong, S., Kaiser, P. K., & Loew, S. (2010). Influence of tectonic shears on tunnel-induced fracturing. *International Journal of Rock Mechanics and Mining Sciences*, 47, 894–907.
- Yong, S., Kaiser, P. K., & Loew, S. (2013). Rock mass response ahead of an advancing face in faulted shale. *International Journal of Rock Mechanics and Mining Sciences*, 60, 301–311.

Seismotectonic analysis around the Mont Terri rock laboratory (Switzerland): a pilot study

Martinus Abednego¹ · Patrick Blascheck² · Senecio Schefer³ · Christophe Nussbaum³ · Manfred Joswig² · Paul Bossart³ · Jon Mosar¹

Received: 12 September 2016 / Accepted: 17 January 2017 / Published online: 17 February 2017
© Swiss Geological Society 2017

Abstract For this pilot study we used recorded seismic events from the SED permanent network and data from a dedicated SNS network to improve the seismotectonic understanding of very weak seismicity in the vicinity of the Mont Terri underground laboratory. We combined field data on faults with microseismic events and modelling of stress and focal mechanisms. Eighty-six events with very low magnitudes ($M_L \approx -2.0$ to 2.0) recorded between July 2014 and August 2015 were located within a radius of 10 km of the underground laboratory and used for modelling. We compiled 234 fault/striation data from laboratory tunnels and regional geology, and also from seismic/borehole data on basement faults. With this database we defined seven groups of main faults in the cover and four groups in the basement. For each of these groups we computed a synthetic focal mechanism that was subsequently used to determine a synthetic P-phase waveform. The synthetic waveforms were then correlated with the microseismic events of the cover and the basement respectively. Of these, 78 events yielded satisfactorily correlation coefficients that we used for a regional

seismotectonic interpretation. The synthetic focal mechanism can be linked to the main regional structural features: the NNE–SSW-oriented reactivated faults associated with the Rhine Graben development, and the NE–SW-oriented reverse faults related to the thrust development of major folds such as the Mont Terri anticline. The results for this pilot study confirm that our affirmative method can be used to augment local and regional seismotectonic interpretations with very weak-intensity earthquake data.

Keywords Underground and surface seismic mini-arrays · Microseismic activity · Focal mechanisms · Fault data · Synthetic P-phase waveform · Rhine Graben development

1 Introduction

The objective of this pilot study was to gain a better understanding of the seismotectonics and the link between different tectonic structures and seismicity of the Mont Terri region. We explored the potential of generating synthetic earthquake waveforms based on discrete observed fault families and using these to constrain existing but poorly defined microseismic earthquake data. These waveforms can be further utilised to determine focal mechanisms and hypocentre locations. We can then use these parameters to synthesize focal mechanisms for weak-intensity seismic events by correlating recorded and synthetic waveform data from synthetic focal mechanisms.

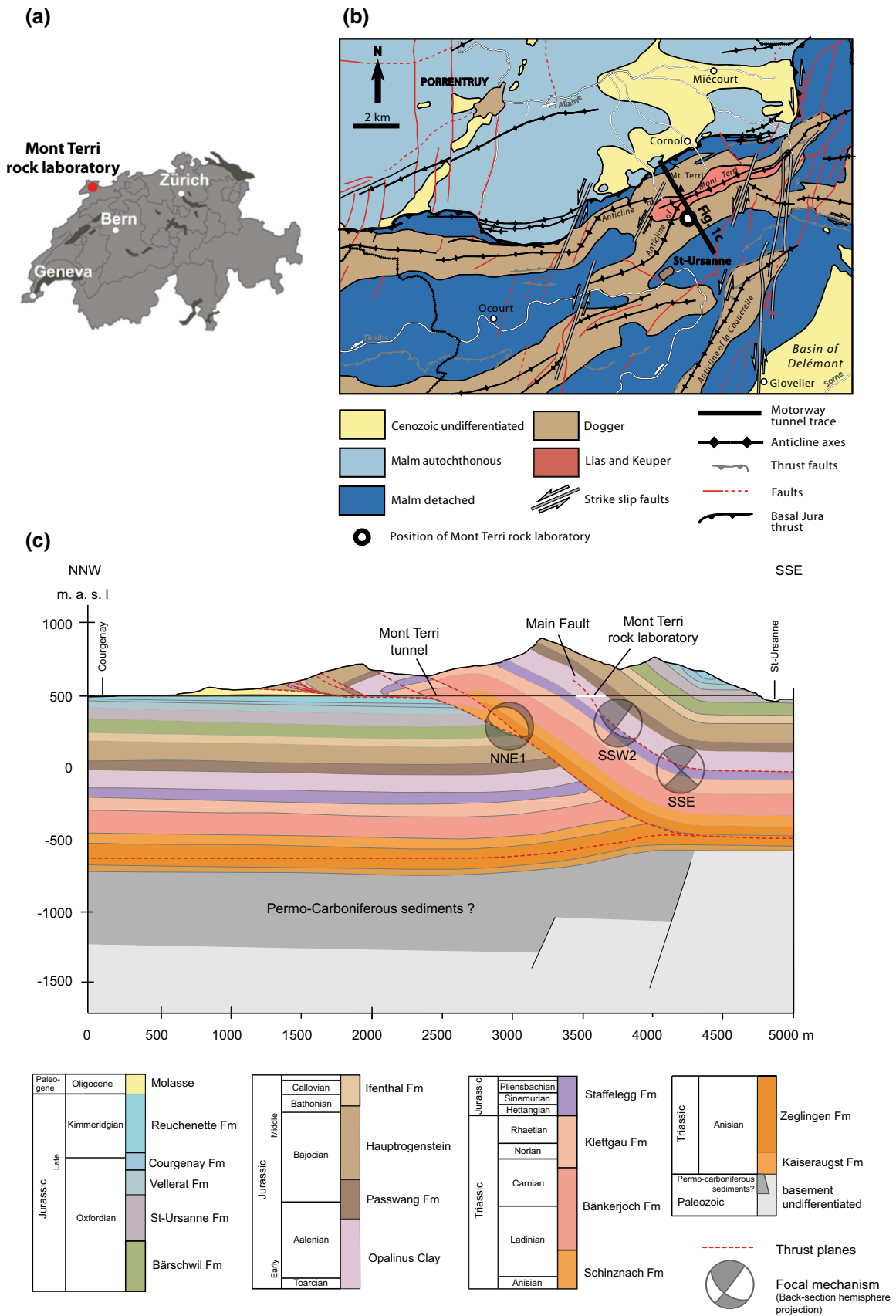
The Mont Terri rock laboratory just north of St-Ursanne in the canton of Jura, Switzerland (Fig. 1) is a geoscience research facility located in the northernmost part of the Jura fold- and-thrust belt and dedicated to research on the hydrogeological, geochemical, and geotechnical properties focused on characterising the Opalinus Clay Formation.

Editorial handling: P. Bossart and A.G. Milnes.

This is paper #11 of the Mont Terri Special Issue of the Swiss Journal of Geosciences (see Bossart et al. 2017, Table 3 and Fig. 7).

✉ Martinus Abednego
martinussatiapurwadi.abednego@unifr.ch

- ¹ Earth Sciences, Department of Geosciences, University of Fribourg, Chemin du Musée 6, 1700 Fribourg, Switzerland
- ² Institut für Geophysik, Universität Stuttgart, Azenbergstr. 16, 70174 Stuttgart, Germany
- ³ Federal Office of Topography swisstopo, Seftigenstrasse 264, 3084 Wabern, Switzerland



◀**Fig. 1** **a** Location of Mont Terri rock laboratory in the northwest of Switzerland. **b** Tectonic map indicating the rock laboratory situated in the Jura fold-and-thrust belt. The dominant structures are NNE–SSW-trending faults with NE–SW and EW fold axes. **c** Cross-section of the Mont Terri anticline (modified after Nussbaum et al. 2017) with back-section hemisphere projection of focal mechanisms of microseismic events in the vicinity of the Mont Terri rock laboratory corresponding to the sub-groups in Fig. 4

This clay formation is being considered as potential host rock for the deep geological repository of radioactive waste (NEA 1999; Thury and Bossart 1999). Structurally, Mont Terri corresponds to the Early Jurassic part of the detached, thrust, and folded Mesozoic Jura series. The structural background to the underground laboratory is a large non-cylindrical NE–NW-oriented ramp-related anticline and a major thrust fault, the Main Fault.

To better understand the seismic hazard in the Mont Terri area and its impact on a possible repository, we implemented a microseismic monitoring project. Instrumental monitoring of seismicity by the Swiss Seismological Service (SED) began in 1975 through the Swiss Digital Seismic Network (SDSNet) and the Swiss Strong Motion Network (SSMNet) (Cauzzi and Clinton 2013). Up to the end of 2008, the SED catalogued 133 events in the vicinity (radius of 20 km) of the Mont Terri rock laboratory in their Earthquake Catalog of Switzerland (ECOS-09) (Fäh et al. 2011) (Fig. 2).

The data in this study are from four permanent SED stations in addition to a newly implemented local network (Seismic Navigation System—SNS). The SED stations are either very close to or within the rock laboratory itself (Fig. 3): two stations in galleries recording since May 19, 2014: the accelerometer MTI01 and the velocimeter MTI02; and two stations at the surface: the accelerometer MTI03 recording since October 1, 2014 and the velocimeter BOURR recording since April 26, 2000. In April 2014, two Seismic Navigation Systems (SNS), operating as seismic mini-arrays (Joswig 2008), were installed at the Mont Terri rock laboratory to increase the density of the existing seismic network in order to optimize monitoring of seismic activity in the vicinity. One station is located inside the rock laboratory and the other near the main south entrance to the safety gallery of the motorway tunnel. Additional SNS were installed at the surface in July 2015 at the locality of Monnat, and in September 2015 near La Combe. A temporary SNS was installed between May and November 2015 close to the Main Thrust within the rock laboratory to monitor any in situ fault slip during repeated hydraulic stimulation testing (FS Experiment, Guglielmi et al. 2016) (Fig. 3).

For this pilot study we considered the two-year monitoring-period between April 1, 2014 and December 31, 2015. During this time, the SED detected and located a total of 94 events within a radius of 30 km around the rock

laboratory, of which 20 were located within a radius of 10 km of the rock laboratory (Table 1).

Microseismic event detection was performed with the NanoSeismicSuite. This software uses an auto-adaptive frequency dependence and noise-muting spectrogram called the sonogram of the seismic records (Joswig 2008; Sick et al. 2012) that are applied to the data sets from SED and SNS. Hypocentre location was done with HypoLine, an analyst-guided location software, combining network and array techniques (Joswig 2008; Vouillamoz et al. 2016) and additional constraints from records of permanent SED stations. The SNS monitoring has been running continuously since April 2014. Due to initial testing performed for the SNS with GPS calibrations, a consistent catalogue exists only as of July 2014. In all, 198 microseismic events were catalogued near the rock laboratory over the period July 2014 to August 2015, of which 86 events are within a radius of 10 km around the laboratory (Table 2; Fig. 3). Of these events, 10 were also catalogued by the SED (Table 1). The 198 events have local magnitudes ranging between $ML = -2.0$ and $ML = 2.0$. These magnitudes are calculated based on horizontal maximum peak-to-peak amplitude readings of the stations and epicentral attenuation functions applied in HypoLine to the datasets from the SED and SNS network (Vouillamoz et al. 2016). Since these events have low local magnitude that were detected by only a few stations, we did not perform magnitude calibration for this specific area. However, using the entire magnitude range (EMR) method (Woessner and Wiemer 2005), we calculated the magnitude of completeness (M_c) to be $M_c = 0.5$, based on local magnitudes in a 20 km area around the Mont Terri rock laboratory.

2 Focal mechanism analysis

We used focal mechanism analysis to determine the orientation, slip direction, and sense of slip of the calculated nodal planes as defined by strike, dip, and rake (Aki and Richards 1980) and implicitly, the fault plane generating the seismicity. Focal mechanisms were calculated based on first-motion or waveform observation of seismograms recorded by the seismic stations. Using these two datasets there are two approaches for determining the focal mechanism of an earthquake: the unsupervised grid search approach, and the supervised synthetic waveform-correlation approach (Oppenheimer et al. 1988; Kobayashi and Nakanishi 1994; Zoback and Harjes 1997; Hardebeck and Shearer 2002).

In first-motion observations, signals generated by a seismic source have to be clearly recorded with a low noise level at the recording stations in order to determine polarity of the first arrival of the P-phase. A high number of

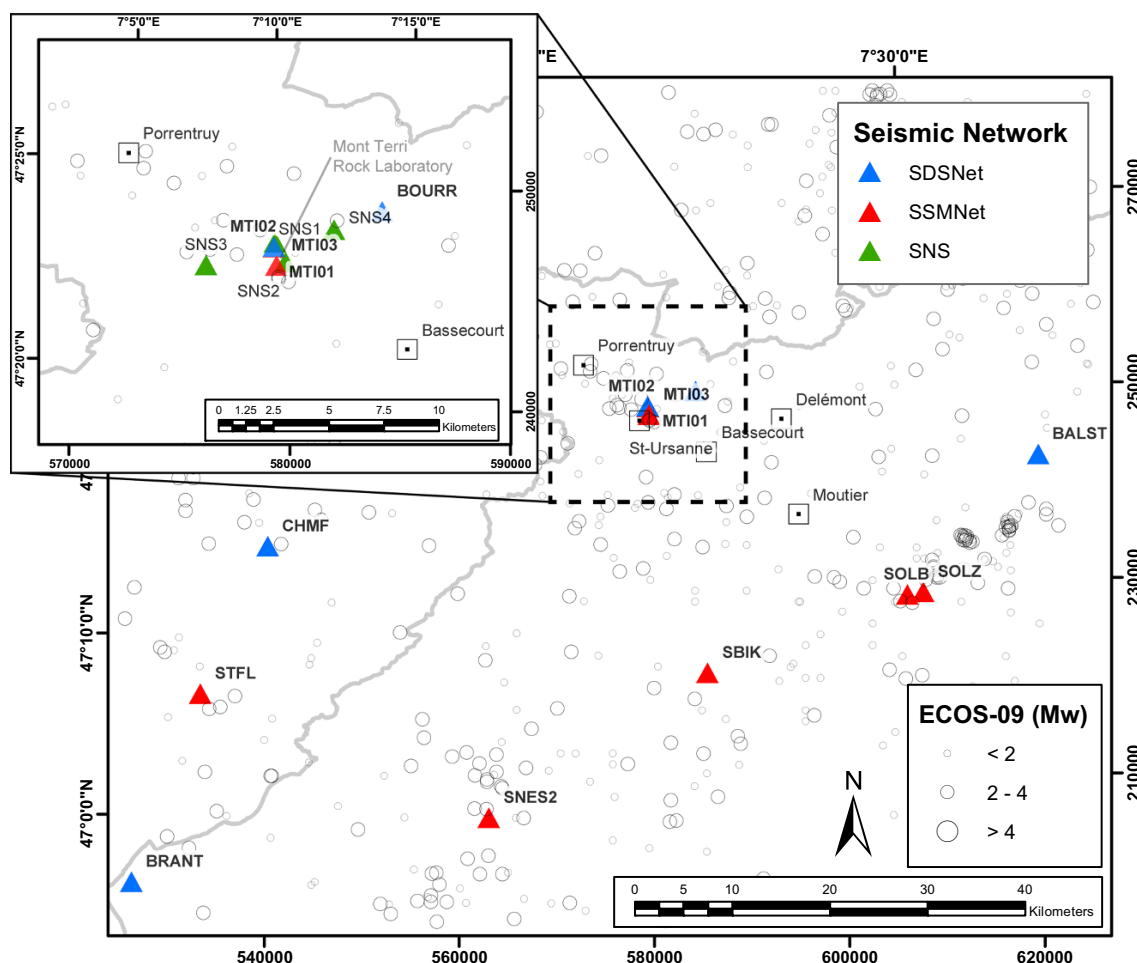


Fig. 2 Instrumentally recorded seismicity catalogued by the Swiss Seismological Service (SED) in the Earthquake Catalog of Switzerland (ECOS-09 (Fäh et al. 2011) from 1975 until 2008 in the vicinity of the Mont Terri rock laboratory. The SED monitors this area using the Digital Seismic Network (SDSNet) and the Swiss Strong Motion

Network (SSMNet) (Cauzzi and Clinton 2013). Seismic Navigation Systems (SNS) are mini-arrays installed in the vicinity of the Mont Terri rock laboratory since April 2014 for microseismic monitoring. The map is in the Swiss coordinate system CH1903

recording stations and a spatial distribution with a good radial coverage will considerably improve constraining the focal mechanism solution using the unsupervised grid search approach. This condition is commonly found for seismic events with magnitude (ML) >1.5–2.0 (Plenefisch and Bonjer 1997).

Since the spatial distribution of the stations around the rock laboratory in our pilot study was irregular and the magnitudes (ML) of the events in the vicinity of the Mont Terri rock laboratory were below 2.0, the grid-search approach yields unconstrained focal mechanism solutions. Therefore, we decided to apply the supervised approach on waveform observations using synthetic waveform correlation to determine the focal mechanisms.

If we assume that an earthquake is generated on a given fault plane with known slip direction and sense then we can determine the two possible nodal planes (one being the active seismic fault plane) of the focal mechanism. This

approach can also be applied to inherited faults for which the slip direction, and hence the paleostress, are known and could be reactivated in the present regional stress field.

3 Synthetic focal mechanisms

3.1 In-situ measurements of faults in the Mesozoic cover

Fault planes and striations were systematically measured and documented during the excavation of the galleries in the Mont Terri rock laboratory (Nussbaum et al. 2011). These were re-analyzed here in order to discriminate fault families and paleostress direction using the Stereonet and FaultKin software packages (Allmendinger et al. 1989a, b, 2012). For this re-analysis we used the “right-hand-rule” convention to record orientations of

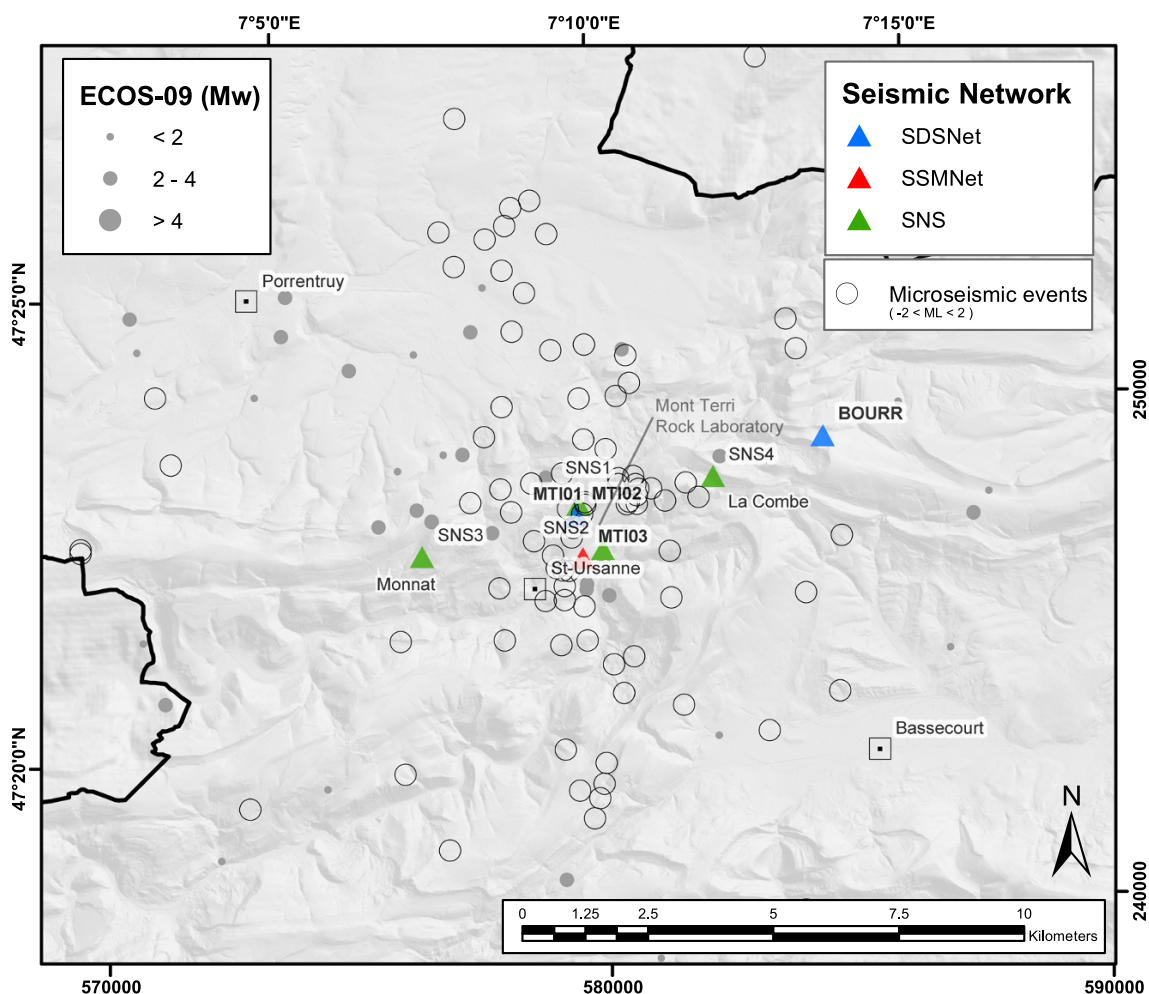


Fig. 3 Map of the Digital Seismic Network (SDSNet) and the Swiss Strong Motion Network (SSMNet) monitoring the seismicity and the Seismic Navigation System (SNS) mini-arrays monitoring the microseismicity in the vicinity of the Mont Terri rock laboratory.

The map shows 86 detected and located microseismic events around the Mont Terri rock laboratory catalogued between July 2014 and August 2015. The map is in the Swiss coordinate system CH1903

slickenlines (or slip direction) and surfaces on which they occur. The slickenline rake is the angle measured clockwise between the strike direction and the slickenline on the surface of interest. We discriminated several groups of faults (Fig. 4). In total, 234 fault-striation pairs, mostly reverse faults (Nussbaum et al. 2011), were available to calculate the paleostress axes using the kinematic pressure-tension (PT-axes) method (Marrett and Allmendinger 1990). The resulting main stress axis has P-axis $337^{\circ}/06^{\circ}$, T-axis $163^{\circ}/84^{\circ}$, and B (intermediate)-axis $067^{\circ}/01^{\circ}$. Taken together, all the axes show a rather consistent distribution with maximum horizontal compression (SH_{max}) oriented NNW $337^{\circ} \pm 28^{\circ}$ (Fig. 5). We have used this mean paleostress axis to represent the present regional stress field. This choice is supported by the lack of any clear and reliable regional present-day stress indicator in the sedimentary cover. All measurements of paleostress in the cover have more or less the same orientation as the

derived horizontal paleostress (SH_{max} NNW). Only one in situ measurement is known from the literature (Heidbach and Reinecker 2013) and it has almost the same orientation as the general one that we proposed here. Therefore we applied this mean stress field (SH_{max} NNW) to all subsequent parametric analyses of groups and sub-groups of faults (in the cover and basement) to generate synthetic focal mechanisms of earthquakes.

This stress inversion approach on fault/striation pairs can be further refined by sorting the data into 4 main groups based on direction and fault dip (Fig. 4): (1) NNE-trending, (2) SSE-dipping, (3) SSW-dipping, and (4) sub-horizontal. Each group can be further subdivided into sub-groups based on orientation of the slip lineation (Fig. 4). Each group can be represented by the simplified fault plane/auxiliary plane projection (equivalent to the nodal plane solution). It is thus possible to determine an ideal stress orientation for each respective group: (1) NNE-

Table 1 List of 94 events detected by the Swiss Seismological Service (SED) within a radius of 30 km around the Mont Terri rock laboratory during the monitoring period between April 1, 2014 and December 31, 2015

Time	Lat	Lon	Depth (km)	ML	Location	
2014/04/01 05:29:20	47.53	6.99	7.8	–	Boncourt JU	
2014/04/03 09:00:00	47.36	7.37	–0.4	1.2	DELEMONT JU	
2014/04/05 04:25:58	47.48	7.42	18.7	1.2	Laufen BL	
2014/04/07 10:08:16	47.23	7.38	–1.0	1.3	Grenchen SO	
2014/04/08 13:28:46	47.28	7.06	–0.9	1.4	Saignelegier JU	
2014/04/11 11:18:09	47.33	7.17	0.4	1.2	St-Ursanne JU	*
2014/04/22 11:02:21	47.23	7.15	8.1	1.7	Tavannes BE	
2014/04/24 11:18:51	47.42	7.18	2.7	–	St-Ursanne JU	*
2014/05/12 13:13:07	47.19	7.44	–0.4	1.4	Grenchen SO	
2014/05/16 04:21:39	47.47	7.19	10.4	2.1	Porrentruy JU	
2014/05/21 02:10:58	47.16	7.16	7.0	1.7	Biel BE	
2014/05/28 19:43:21	47.15	7.17	6.6	1.0	Biel BE	
2014/05/31 14:24:14	47.40	7.25	17.5	1.5	St-Ursanne JU	*
2014/05/31 15:44:55	47.40	7.26	17.3	0.9	DELEMONT JU	*
2014/06/03 13:25:04	47.28	7.14	–0.8	1.3	Tavannes BE	
2014/06/27 09:33:15	47.29	7.14	0.0	1.8	St-Ursanne JU	*
2014/07/01 15:49:08	47.23	7.25	2.6	1.6	Tavannes BE	
2014/07/02 07:28:42	47.22	7.16	3.2	1.4	Tavannes BE	
2014/07/03 10:24:56	47.65	7.28	1.0	1.5	Mulhouse F	
2014/07/04 09:55:48	47.63	7.50	24.3	–	BASEL	
2014/07/08 13:36:28	47.42	7.14	2.8	–	Porrentruy JU	*
2014/08/12 08:01:10	47.33	7.17	2.6	1.3	St-Ursanne JU	*
2014/08/19 03:44:50	47.29	7.56	4.7	1.1	Welschenrohr SO	
2014/08/19 03:47:23	47.28	7.56	6.4	1.8	Welschenrohr SO	
2014/08/22 05:25:59	47.16	7.14	10.9	1.6	Tavannes BE	
2014/08/24 01:39:07	47.29	7.56	5.5	1.2	Welschenrohr SO	
2014/08/26 07:35:12	47.25	7.21	–1.0	1.4	Tavannes BE	
2014/09/11 00:12:29	47.15	7.16	10.2	1.4	Biel BE	
2014/09/30 17:27:15	47.32	7.20	17.9	1.1	St-Ursanne JU	*
2014/10/06 07:32:54	47.24	7.21	–0.7	1.4	Tavannes BE	
2014/10/28 15:16:37	47.33	7.20	–0.4	1.4	St-Ursanne JU	*
2014/11/14 13:40:48	47.32	7.18	–0.7	1.2	St-Ursanne JU	*
2014/11/19 08:32:36	47.20	7.25	31.7	1.3	Tavannes BE	
2014/11/22 13:03:31	47.19	7.05	0.0	–	St-Imier BE	
2014/12/30 08:29:25	47.22	7.14	10.2	1.1	Tavannes BE	
2015/01/06 23:31:21	47.33	7.09	21.5	1.2	St-Ursanne JU	*
2015/01/10 08:12:24	47.28	7.24	18.2	1.0	Tavannes BE	
2015/01/31 21:23:29	47.15	7.14	10.3	1.6	Biel BE	
2015/01/31 21:54:02	47.15	7.15	9.7	3.1	Biel BE	
2015/01/31 22:20:56	47.15	7.14	10.9	2.1	Biel BE	
2015/02/01 00:20:57	47.15	7.14	10.5	1.1	Switzerland	
2015/02/01 12:26:39	47.15	7.14	9.2	1.6	Biel BE	
2015/02/01 16:50:31	47.23	7.10	20.4	1.2	Tavannes BE	
2015/02/01 18:04:06	47.19	7.00	5.0	–	St-Imier BE	
2015/02/01 19:57:51	47.23	7.11	23.4	1.0	Tavannes BE	
2015/02/02 04:05:18	47.15	7.15	10.1	2.6	Biel BE	
2015/02/05 13:42:39	47.23	7.10	20.1	0.8	Tavannes BE	
2015/02/05 15:42:23	47.17	7.12	11.6	0.7	Tavannes BE	

Table 1 continued

Time	Lat	Lon	Depth (km)	ML	Location	
2015/02/20 12:33:11	47.43	7.02	-0.2	1.7	Porrentruy JU	
2015/02/23 00:52:09	47.15	7.14	9.9	1.1	Biel BE	
2015/03/14 19:35:55	47.35	6.85	4.9	-	Saignelegier JU	
2015/03/15 08:21:38	47.18	7.11	7.0	1.0	Tavannes BE	
2015/03/18 15:03:28	47.37	7.16	7.0	1.5	St-Ursanne JU	*
2015/03/31 12:34:33	47.23	7.38	6.9	-	Grenchen SO	
2015/04/09 00:05:01	47.15	7.14	10.6	1.3	Biel BE	
2015/04/14 11:02:10	47.20	7.24	-1.0	1.6	Tavannes BE	
2015/04/18 23:16:25	47.57	7.33	7.0	2.0	Mulhouse F	
2015/04/22 11:40:53	47.39	7.03	-0.2	-	Porrentruy JU	
2015/04/28 12:16:28	47.37	7.12	10.3	1.5	St-Ursanne JU	*
2015/04/30 02:39:50	47.65	7.42	14.8	1.4	Mulhouse F	
2015/05/09 18:34:52	47.15	7.15	9.8	2.4	Biel BE	
2015/05/09 22:18:29	47.15	7.16	9.5	1.2	Biel BE	
2015/05/10 03:03:49	47.15	7.15	10.4	1.2	Biel BE	
2015/05/14 16:28:18	47.15	7.17	6.0	1.0	Biel BE	
2015/05/20 12:19:19	47.33	7.20	-0.4	-	St-Ursanne JU	*
2015/05/22 13:31:29	47.64	6.93	3.1	2.3	Belfort F	
2015/06/08 21:47:10	47.34	6.93	4.1	1.4	Saignelegier JU	
2015/06/12 09:48:33	47.38	7.19	-0.7	1.3	St-Ursanne JU	*
2015/06/28 13:27:22	47.59	7.42	14.4	0.9	BASEL	
2015/06/28 13:38:13	47.58	7.46	14.8	0.4	BASEL	
2015/07/08 11:17:38	47.20	7.20	-1.0	1.7	Tavannes BE	
2015/07/21 07:27:16	47.17	7.17	-1.2	1.4	Tavannes BE	
2015/07/22 07:18:56	47.19	7.24	-0.6	1.6	Tavannes BE	
2015/08/03 07:30:35	47.18	7.21	3.9	1.3	Tavannes BE	
2015/08/07 05:12:13	47.36	7.05	6.2	1.7	Porrentruy JU	*
2015/08/09 12:31:21	47.36	7.05	6.1	1.6	Porrentruy JU	*
2015/08/14 11:33:50	47.27	7.15	-0.7	1.0	Tavannes BE	
2015/08/17 23:31:45	47.36	7.05	3.7	0.8	Porrentruy JU	*
2015/08/18 13:40:27	47.34	7.20	0.0	-	St-Ursanne JU	*
2015/09/09 03:01:49	47.28	7.28	11.4	1.0	Moutier BE	
2015/09/18 12:30:47	47.32	7.18	-0.8	1.2	St-Ursanne JU	*
2015/09/20 21:48:37	47.45	7.49	9.6	0.5	Laufen BL	
2015/09/20 21:50:31	47.45	7.49	8.5	0.5	Laufen BL	
2015/10/02 07:24:02	47.24	7.19	-0.8	1.4	Tavannes BE	
2015/10/21 10:56:44	47.18	7.26	-0.8	1.1	Biel BE	
2015/10/26 08:31:43	47.22	7.21	-0.8	1.6	Tavannes BE	
2015/11/06 08:28:22	47.20	7.16	-0.7	1.4	Tavannes BE	
2015/11/10 15:01:31	47.17	7.22	-1.2	1.7	Biel BE	
2015/11/16 02:08:23	47.61	7.28	8.0	1.8	Mulhouse F	
2015/11/27 08:33:18	47.20	7.20	15.2	1.5	Tavannes BE	
2015/12/03 14:01:06	47.53	7.06	-0.1	-	Boncourt JU	
2015/12/08 22:34:32	47.63	7.30	8.2	0.7	Mulhouse F	
2015/12/10 08:33:46	47.18	7.19	-0.9	1.5	Tavannes BE	
2015/12/21 12:22:22	47.20	7.35	17.1	1.4	Grenchen SO	

The rows marked with a star show the 20 events within a radius of 10 km around the laboratory

Table 2 List of 198 detected and located microseismic events around the Mont Terri rock laboratory monitored in this study from July 2014 until August 2015 using NanoSeismicSuite and HypoLine software (Joswig 2008; Sick et al. 2012; Vouillamoz et al. 2016)

Time	Lat	Lon	Depth (km)	ML	
2014/07/02 01:12:33	46.78	6.07	6.3	0.6	
2014/07/02 07:28:43	47.24	7.14	7.3	0.7	
2014/07/03 10:24:57	47.63	7.28	7.3	0.8	
2014/07/03 15:26:10	47.57	8.32	6.1	–	
2014/07/04 19:36:13	47.26	7.06	12.3	0.0	
2014/07/04 19:42:58	47.34	7.22	4.5	–	*
2014/07/08 13:36:28	47.40	7.18	1.3	0.8	**
2014/07/08 13:36:28	47.40	7.15	1.5	0.9	*
2014/07/09 07:32:05	47.17	7.22	9.8	0.9	
2014/07/09 10:58:35	48.05	7.80	4.4	–	
2014/07/09 12:56:01	47.07	8.22	6.3	–	
2014/07/10 09:56:10	47.52	6.64	9.7	1.5	
2014/07/14 04:40:54	47.99	7.04	7.4	0.8	
2014/07/14 10:42:39	47.04	7.63	9.0	0.6	
2014/07/16 16:12:15	48.49	6.92	8.9	1.4	
2014/07/17 15:08:51	47.03	6.86	8.6	–	
2014/07/18 09:33:08	48.11	6.58	9.0	1.6	
2014/07/18 10:02:14	48.40	6.84	9.1	1.5	
2014/07/22 10:13:32	48.48	6.82	8.9	1.6	
2014/07/24 08:55:53	47.56	7.33	9.0	1.7	
2014/07/24 08:55:55	47.45	7.16	8.5	1.2	*
2014/07/24 10:17:14	48.53	6.76	8.9	1.4	
2014/07/24 14:10:22	47.24	8.24	9.0	–	
2014/07/25 10:15:16	48.51	6.81	8.9	1.5	
2014/07/25 15:35:23	47.48	7.17	6.8	–0.3	
2014/07/27 04:37:16	47.31	7.23	3.0	–	*
2014/08/01 09:56:00	48.38	6.82	11.1	1.3	
2014/08/01 10:03:44	47.69	7.29	10.2	0.9	
2014/08/01 14:39:55	46.57	6.78	11.6	0.9	
2014/08/01 16:10:04	46.61	6.82	7.5	–	
2014/08/03 18:26:02	47.36	7.14	–0.1	–1.3	*
2014/08/04 10:02:14	48.41	6.85	17.7	1.5	
2014/08/06 14:23:46	47.69	5.80	8.6	1.3	
2014/08/07 09:11:18	46.49	7.36	10.6	–	
2014/08/08 08:59:35	47.17	8.16	8.1	–	
2014/08/12 08:01:10	47.32	7.17	2.1	–	**
2014/08/12 09:07:22	47.80	6.85	6.5	1.6	
2014/08/14 13:44:13	47.08	7.36	–0.3	–	
2014/08/15 00:44:56	47.25	7.58	7.9	0.2	
2014/08/15 08:59:26	47.11	8.16	10.9	–	
2014/08/16 11:40:20	47.94	7.23	7.4	0.7	
2014/08/19 10:06:43	48.38	6.84	9.1	1.2	
2014/08/21 10:18:59	48.50	6.76	8.9	1.6	
2014/08/22 12:07:03	47.09	6.92	9.1	1.4	
2014/08/26 08:05:28	47.37	7.35	0.3	1.3	
2014/08/26 08:14:55	48.45	6.67	9.0	1.6	

Table 2 continued

Time	Lat	Lon	Depth (km)	ML	
2014/08/26 08:15:56	47.38	7.19	–0.3	–1.5	*
2014/08/26 18:46:12	47.49	7.53	11.6	0.3	
2014/08/29 11:41:38	47.24	7.10	8.5	0.6	
2014/09/05 10:12:00	48.39	6.72	19.6	1.7	
2014/09/09 11:30:16	47.38	7.18	2.3	–0.9	*
2014/09/09 13:44:02	47.25	7.47	6.2	–	
2014/09/11 13:21:11	47.26	7.11	17.2	0.9	
2014/09/15 08:24:46	47.25	7.16	6.0	–	
2014/09/19 08:32:13	47.58	7.32	8.4	1.7	
2014/09/23 09:00:27	47.55	6.88	6.0	1.5	
2014/09/25 10:04:38	48.54	6.83	8.9	1.8	
2014/09/30 10:16:41	47.83	6.19	13.8	–	
2014/09/30 17:27:15	47.28	7.20	14.6	0.7	**
2014/10/01 09:31:29	47.51	7.41	10.4	1.7	
2014/10/01 13:05:06	47.41	7.01	8.5	–	
2014/10/02 10:21:58	47.38	7.14	0.4	–1.1	*
2014/10/06 07:58:16	47.46	7.21	3.9	1.4	*
2014/10/09 15:05:56	48.14	6.43	24.5	1.4	
2014/10/09 17:48:01	47.37	7.19	–0.3	–	*
2014/10/10 04:31:46	47.41	6.26	14.6	0.9	
2014/10/10 08:22:26	47.34	7.16	1.2	0.9	*
2014/10/11 21:36:43	47.36	7.17	–0.3	–	*
2014/10/12 23:31:03	47.35	7.16	0.1	–1.4	*
2014/10/13 07:30:31	47.17	7.23	7.9	1.0	
2014/10/13 09:37:33	47.19	6.01	8.4	1.4	
2014/10/13 13:59:29	47.18	7.24	9.7	0.9	
2014/10/13 23:13:36	47.37	7.16	0.9	–1.2	*
2014/10/17 07:12:41	47.11	7.15	10.7	1.4	
2014/10/20 10:08:36	48.38	6.85	15.7	1.2	
2014/10/22 01:46:22	47.35	7.23	–0.3	–	*
2014/10/22 01:46:22	47.36	7.22	1.4	–0.9	*
2014/10/23 09:03:28	47.69	6.88	3.9	–	
2014/10/23 13:31:37	47.38	7.40	5.3	0.6	
2014/10/27 15:23:03	46.21	7.20	9.4	–	
2014/10/28 15:16:37	47.35	7.18	2.9	–	**
2014/10/31 14:56:49	47.26	6.44	7.9	1.5	
2014/10/31 22:31:12	47.41	7.22	7.0	–0.8	*
2014/11/03 16:30:22	47.51	6.63	10.0	1.3	
2014/11/05 16:53:31	48.41	6.86	10.9	1.5	
2014/11/06 01:45:57	47.06	7.03	7.3	–	
2014/11/07 11:59:41	47.12	8.15	7.7	–	
2014/11/09 21:11:50	47.65	6.22	8.7	–	
2014/11/13 08:44:16	47.31	7.24	7.7	0.3	
2014/11/14 09:52:21	47.38	7.15	0.0	–1.0	*
2014/11/14 10:29:34	47.38	7.14	–0.3	–0.9	*
2014/11/14 13:40:48	47.33	7.17	–0.3	–	**
2014/11/18 12:12:37	47.17	7.49	11.5	1.1	
2014/11/21 14:34:45	47.45	6.74	6.3	–	

Table 2 continued

Time	Lat	Lon	Depth (km)	ML
2014/11/22 13:03:29	47.55	6.90	3.4	0.6
2014/11/25 14:40:32	47.39	6.96	9.2	1.2
2014/11/26 08:26:33	47.56	7.35	2.3	1.7
2014/12/01 11:12:09	47.25	7.01	10.7	0.2
2014/12/01 15:11:02	46.94	6.68	-1.1	-
2014/12/02 11:48:27	47.15	7.12	6.2	-
2014/12/02 13:52:06	47.49	7.01	0.0	1.2
2014/12/05 11:40:09	47.41	7.17	1.6	0.0 *
2014/12/08 01:07:49	47.39	7.17	-0.3	-1.5 *
2014/12/09 07:51:59	48.14	6.51	23.7	1.4
2014/12/11 15:28:55	47.37	7.23	-0.3	-0.9 *
2014/12/11 18:17:24	46.75	6.93	17.8	1.0
2014/12/13 13:51:28	47.38	7.18	-0.3	-1.4 *
2014/12/13 14:18:16	47.38	7.18	-0.3	-1.3 *
2014/12/14 07:25:54	47.39	7.16	-0.3	-2.0 *
2014/12/14 17:59:06	47.37	7.16	0.0	-1.8 *
2014/12/17 13:47:11	48.23	8.22	10.8	1.9
2014/12/20 13:36:58	47.38	7.18	-0.3	-1.2 *
2014/12/23 00:19:35	46.93	7.14	6.4	0.2
2014/12/24 15:03:03	47.17	7.60	5.1	0.2
2014/12/27 20:39:03	47.38	7.15	-0.3	-1.9 *
2015/01/04 01:29:04	47.40	7.17	2.9	-1.4 *
2015/01/04 06:32:06	47.38	7.16	0.8	-2.0 *
2015/01/06 09:48:52	47.51	7.36	16.8	1.8
2015/01/06 13:31:44	47.39	7.17	1.8	-0.8 *
2015/01/08 14:12:11	47.38	7.18	2.4	-
2015/01/08 14:17:35	47.38	7.18	2.4	-1.0 *
2015/01/13 09:30:46	47.43	7.15	0.4	0.5 *
2015/01/14 12:57:21	47.38	7.19	-0.2	-0.5 *
2015/01/17 11:35:45	47.54	7.21	5.0	0.3
2015/01/26 17:39:46	47.39	7.14	0.0	-0.9 *
2015/01/27 00:58:02	47.40	7.16	5.5	-0.6 *
2015/01/28 01:26:03	47.36	7.16	0.8	-1.4 *
2015/02/01 04:02:48	47.18	7.11	15.4	-
2015/02/01 11:23:52	47.17	7.12	7.7	0.2
2015/02/01 18:04:05	47.13	7.15	6.4	0.6
2015/02/17 08:48:12	47.43	7.37	21.4	1.8
2015/02/22 13:58:28	47.15	7.13	4.0	0.4
2015/02/26 14:59:43	47.15	7.24	6.0	1.1
2015/03/05 10:13:36	47.41	7.22	-0.3	-
2015/03/06 12:37:10	47.37	7.03	0.3	1.0 *
2015/03/12 10:29:22	47.37	7.03	0.3	0.7 *
2015/03/18 15:03:28	47.33	7.17	2.0	1.1 **
2015/03/23 14:30:47	47.37	7.03	0.3	0.8
2015/03/24 12:12:19	47.43	7.15	2.0	1.2 *
2015/04/02 09:24:38	47.27	7.38	9.7	0.7
2015/04/04 04:11:28	47.37	7.15	-0.3	-1.8 *
2015/04/07 12:37:01	47.43	7.16	1.1	1.2 *

Table 2 continued

Time	Lat	Lon	Depth (km)	ML
2015/04/07 18:40:30	47.34	7.19	-0.3	- *
2015/04/08 14:22:16	47.42	7.14	0.9	-0.1 *
2015/04/09 05:54:22	47.16	7.12	5.9	0.4
2015/04/13 12:02:21	47.40	7.05	2.5	- *
2015/04/16 02:45:47	47.37	7.16	-0.3	- *
2015/04/16 09:27:40	47.40	7.14	4.2	0.0 *
2015/04/17 09:22:58	47.38	7.02	0.3	1.2
2015/04/17 12:58:06	47.36	7.15	-0.3	-0.9 *
2015/04/20 13:23:49	47.41	7.15	2.4	0.1 *
2015/04/22 07:12:02	47.37	7.16	-0.3	- *
2015/04/28 12:16:28	47.32	7.13	4.8	1.2 **
2015/05/05 00:19:42	47.38	7.16	-0.3	- *
2015/05/05 09:47:06	47.52	7.40	2.0	1.7
2015/05/07 08:37:39	47.57	7.29	1.7	1.7
2015/05/08 09:48:27	47.45	6.95	3.6	1.7
2015/05/12 13:00:29	47.43	7.13	0.0	1.0 *
2015/05/15 07:30:27	47.24	7.16	13.6	0.8
2015/05/18 18:09:14	47.15	7.17	8.9	0.5
2015/05/20 12:19:18	47.33	7.17	1.5	0.9 **
2015/05/22 13:31:33	47.43	7.14	1.1	0.9 *
2015/05/27 09:28:41	47.42	7.13	3.3	1.1 *
2015/06/01 09:50:49	47.15	7.15	10.7	0.4
2015/06/01 10:58:35	47.55	6.89	6.2	1.5
2015/06/01 11:59:51	47.38	7.18	-0.3	0.0 *
2015/06/01 21:26:52	47.16	7.12	5.9	-0.2
2015/06/03 10:06:30	47.38	7.18	-0.3	0.8 *
2015/06/05 09:36:59	47.56	7.32	3.5	1.7
2015/06/06 11:40:20	47.37	7.16	0.1	1.7 *
2015/06/08 21:47:09	47.36	6.92	6.5	1.1
2015/06/11 11:59:39	47.33	7.17	1.7	1.1 *
2015/06/12 09:48:32	47.38	7.18	0.2	0.9 **
2015/06/19 10:01:12	47.38	7.18	-0.3	0.5 *
2015/06/22 07:29:19	47.19	7.22	9.9	1.2
2015/06/27 13:37:08	47.45	7.13	0.8	-0.6 *
2015/06/29 11:09:59	47.41	7.16	6.1	0.4 *
2015/06/30 12:23:30	47.42	7.15	0.8	-0.2 *
2015/07/01 08:50:10	47.55	7.33	10.6	1.5
2015/07/07 05:05:06	47.38	7.20	0.8	- *
2015/07/07 08:46:14	47.41	7.18	2.8	-0.8 *
2015/07/08 08:06:19	47.06	7.17	10.5	-
2015/07/09 21:25:47	47.38	7.17	-0.3	- *
2015/07/14 12:54:04	47.33	7.12	2.8	0.0 *
2015/07/16 05:33:19	47.43	7.14	2.0	0.6 *
2015/07/18 07:14:14	47.36	7.19	-0.3	- *
2015/07/26 05:35:00	47.36	7.17	-0.3	- *
2015/07/26 06:42:55	47.36	7.12	2.5	-1.0 *
2015/08/06 13:13:39	47.38	7.17	-0.3	- *
2015/08/09 09:41:43	47.32	7.08	2.3	-0.4 *

Table 2 continued

Time	Lat	Lon	Depth (km)	ML	
2015/08/11 11:55:23	47.47	6.91	1.8	1.7	
2015/08/13 10:17:09	47.38	7.17	-0.3	-2.7	*
2015/08/14 00:27:27	47.35	7.17	-0.3	-	*
2015/08/14 11:00:39	47.19	7.25	20.0	0.8	
2015/08/15 00:53:29	47.44	7.37	15.2	-0.2	
2015/08/15 11:18:49	47.39	7.06	5.3	-0.1	*
2015/08/18 13:40:28	47.35	7.18	0.5	0.7	**
2015/08/28 09:10:03	47.44	7.41	13.2	1.8	

The starred rows show the 86 events within a radius of 10 km around the laboratory. The rows marked with 2 stars indicate the events catalogued by the SED (Table 1)

trending, (2) SSE-dipping, (3) SSW-dipping, and (4) Sub-horizontal. Each main group is composed of sub-groups based on their striation orientations. Another sub-group of synthetic focal mechanism (not shown in Fig. 4) is added to each main group by applying the regional stress orientation (defined in Fig. 5) to the respective fault orientation of the main groups.

3.1.1 NNE-trending

Based on the measurement of 19 fault orientations, this main group is trending NNE 015° with an average dip direction of 42° . The orientation of these faults can be linked to the reactivation of NNE-SSW-striking normal faults associated with the Rhine Graben (Ustaszewski and Schmid 2007). On the basis of striation measurements, this main group can be further divided into sub-groups.

(a) NNE1

The NNE1 sub-group is based on 12 striation measurements with a plunge orientation of $149^\circ/40^\circ \pm 12^\circ$. These orientations give a focal mechanism with a strike, dip, and rake of $018^\circ/42^\circ/043^\circ$. This focal mechanism represents a NNE-trending predominantly thrust-dominated fault system with a left-lateral strike-slip component.

(b) NNE2

The NNE2 sub-group is based on 7 striation measurements with a plunge orientation of $043^\circ/6^\circ \pm 12^\circ$. These orientations give a synthetic focal mechanism with a strike, dip, and rake of $008^\circ/34^\circ/142^\circ$. This focal mechanism represents a NNE-trending predominantly thrust-related fault system with a right-lateral strike-slip component.

(c) NNEreg

If the average regional paleostress field based on the integration of the whole dataset (SH_{\max} NNW) is applied to the NNE-trending fault orientation, we can derive a third synthetic focal mechanism (not shown in Fig. 4). This NNEreg sub-group has a focal mechanism orientation with a strike, dip, and rake of $015^\circ/51^\circ/052^\circ$. This focal

mechanism represents a NNE-trending predominantly thrust-related fault system with a left-lateral strike-slip component similar to NNE1.

3.1.2 SSE-dipping

The 157 fault orientations of this main group show a general dip direction and dip of $156^\circ/44^\circ \pm 2^\circ$. This orientation is parallel to the axis of the Mont Terri anticline (Laubscher 1977).

(a) SSE

The SSE-group, based on 157 fault/striation measurements is consistent with a synthetic focal mechanism with a strike, dip, and rake of $060^\circ/44^\circ/085^\circ$. This focal mechanism represents a SSE-dipping thrust-fault system.

(b) SSEreg

Applying SH_{\max} NNW to the SSE-dipping faults, we calculate a synthetic focal mechanism with a strike, dip, and rake of $061^\circ/43^\circ/084^\circ$. This focal mechanism represents a SSE-dipping thrust fault, almost identical to the SSE group.

3.1.3 SSW-dipping

Based on the measurement of 32 fault orientations, we find a mainly SSW-dipping main group with a dip direction and dip of $199^\circ/39^\circ \pm 6^\circ$. Here also we can differentiate several sub-groups.

(a) SSW1

The SSW1 sub-group is based on 16 striation measurements with a plunge orientation of $132^\circ/15^\circ \pm 8^\circ$. These orientations yield a synthetic focal mechanism with a strike, dip, and rake of $112^\circ/38^\circ/157^\circ$. This focal mechanism represents a SSW-dipping predominantly thrust-related fault with a right-lateral strike-slip component.

(b) SSW2

The SSW2 sub-group is based on 9 striation measurements with a plunge orientation of $172^\circ/9^\circ \pm 11^\circ$. These orientations give a synthetic focal mechanism with a strike, dip, and rake of $103^\circ/41^\circ/107^\circ$, and represents a SSW-dipping thrust fault.

(c) SSW3

The SSW3 sub-group is based on 7 striation measurements with a plunge orientation of $236^\circ/5^\circ \pm 15^\circ$. These orientations yield a synthetic focal mechanism with a strike, dip, and rake of $109^\circ/41^\circ/060^\circ$, and represents a SSW-dipping predominantly thrust-related fault system with a left-lateral strike-slip component.

(d) SSWreg

Applying SH_{\max} NNW to the SSW-dipping faults, we find a synthetic focal mechanism orientation with a strike, dip, and rake of $109^\circ/40^\circ/117^\circ$. This focal mechanism represents a SSE-dipping thrust fault similar to SSW2.

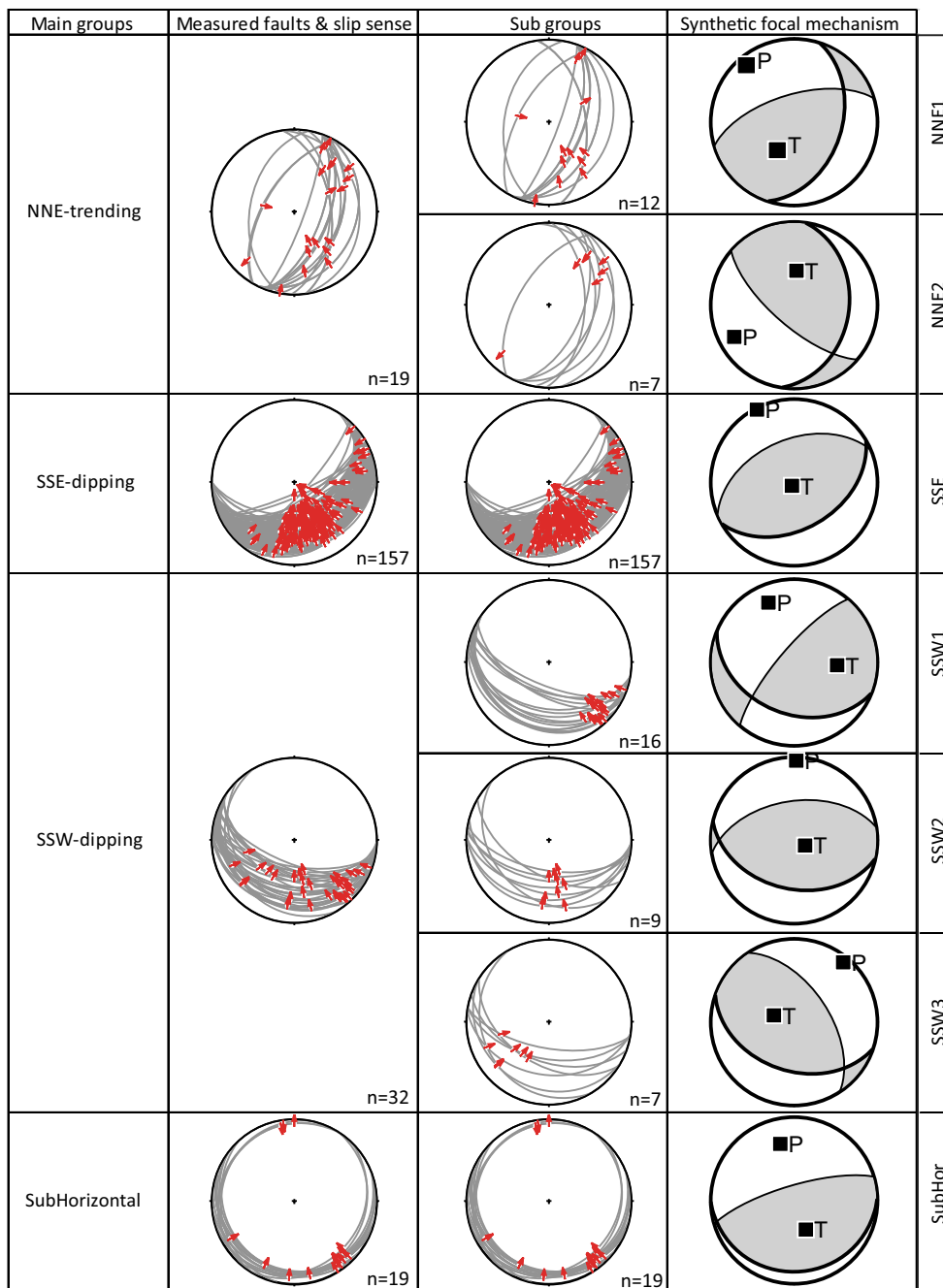


Fig. 4 Synthetic focal-mechanism main groups and sub-groups for microseismic events in the sedimentary cover. The orientation of 234 faults and striations in the sedimentary cover were measured during the excavation of the Mont Terri rock laboratory (Nussbaum et al. 2011). Out of a total dataset of 234 fault/striation pairs, 227 were used

to determine different main groups and sub-groups. These sub-groups determine the synthetic focal mechanisms composed of two nodal planes in which the bold great circle indicates the fault plane and the thin great circle shows the auxiliary plane

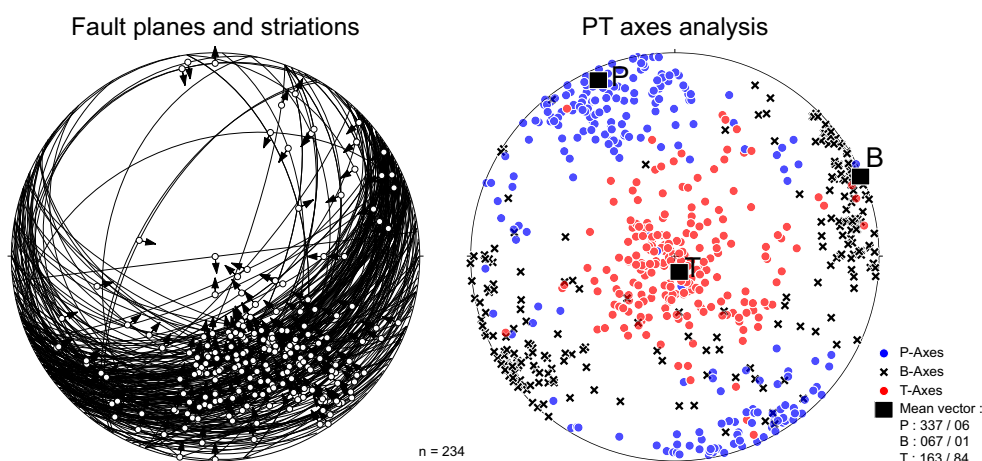
3.1.4 Subhorizontal

A group of 19 subhorizontal faults has a general dip direction and dip of $179^{\circ}/15^{\circ} \pm 4^{\circ}$. This orientation is parallel to the décollement surface at the basal Jura fold-and-thrust belt (Laubscher 1997; Sommaruga 1999; Ustaszewski and Schmid 2007).

(a) SubHor

The SubHor group is based on 19 striation measurements with a plunge orientation of $179^{\circ}/5^{\circ} \pm 4^{\circ}$. The synthetic focal mechanism with a strike, dip, and rake of $089^{\circ}/15^{\circ}/105^{\circ}$ and is related to a subhorizontal thrust fault.

Fig. 5 Regional paleostress-field orientations using 234 measurements of fault orientations, striations, and slip sense in the Mont Terri rock laboratory (Nussbaum et al. 2011) plotted on a lower hemisphere stereoplots. The mean stress field (SH_{max} NNW) has an orientation of maximum horizontal compression towards the NNW with the P-axis $337^\circ/06^\circ$, T-axis $163^\circ/84^\circ$, and B-axis $067^\circ/01^\circ$



Source	Structure	Focal mechanism	Source	Structure	Synthetic focal mechanism
Deichmann - NTB90-46	(a) Earthquake in Glovelier (1987)		Ustaszewski & Schmid (2007)	(c) Permo-carboniferous Trough	
Deichmann (Report for Mont Terri 2015)	(b) Earthquake in St-Ursanne (2000)			(d) Rhine Graben	
		Glov87			PCWereg
		StUr2000			NNEsWdreg

Fig. 6 Focal mechanisms and synthetic focal mechanisms for the microseismic events in the basement: **a, b** The focal mechanisms based on earthquakes analysed in Deichmann (1990), Baer et al. (2001), and Deichmann (2015). **c, d** Synthetic focal mechanisms

produced based on the orientation of interpreted faults by Ustaszewski and Schmid (2007) by applying the regional stress orientation (Fig. 5). The synthetic focal mechanisms have two nodal planes in which the bold great circle indicates the fault plane

(b) SubHorreg

Applying SH_{max} NNW to the SubHor fault orientation yields a focal mechanism orientation with a strike, dip, and rake of $107^\circ/11^\circ/113^\circ$. This focal mechanism represents a subhorizontal thrust fault.

3.2 Focal mechanisms from strong earthquakes in the basement

One strong earthquake and one series of strong earthquakes, catalogued by the SED, were registered in the vicinity of the Mont Terri rock laboratory: (a) in Glovelier (1987) and (b) the series in St-Ursanne (2000). The hypocentre of these earthquakes is located in the basement beneath the main décollement.

3.2.1 Glov87 and Glov87reg

An earthquake of ML 3.7 occurred on December 11th 1987 02:25:58.2 (UTC) in Glovelier (Lat/Lon: $47.313^\circ\text{N}/7.161^\circ\text{E}$) at a depth of 9 km. The associated focal mechanism (Glov87) shows an orientation with a strike, dip, and rake of $008^\circ/79^\circ/020^\circ$ (Deichmann 1990), and represents a strike-slip fault. Depending on the nodal plane considered to be the fault plane, the fault mechanism is sinistral strike-slip on the NS-trending nodal plane, or dextral strike-slip on the W–E-trending nodal plane (Fig. 6).

If we apply SH_{max} NNW to the Glov87 fault orientation to calculate the Glov87reg focal mechanism, we obtain a strike, dip, and rake of $008^\circ/79^\circ/016^\circ$, which is almost identical to the present-day situation of Glov87.

3.2.2 *StUr2000; StUr2000reg1; and StUr2000reg2*

A series of four earthquakes with a magnitude $ML \leq 3.0$ occurred on March 28, 2000, and an earthquake of ML 3.2 on April 6, 2000 in St-Ursanne (Lat/Lon 47.367°N/7.168°E) at a depth of 1 km. The focal mechanism orientation (StUr2000) has a strike, dip, and rake of 074°/65°/089° if the SSE-dipping nodal plane is the fault plane, and 256°/25°/092° if the NNW-dipping nodal plane is the fault plane (Deichmann 1990, 2015). This focal mechanism represents either a SSE-dipping steep reverse fault or a NNW-dipping back thrust (Fig. 6).

When applying SH_{\max} NNW to the two nodal planes of the earthquake, we obtain two synthetic focal mechanisms differing by 30° in orientation: StUr2000reg1 and StUr2000reg2. The focal mechanism StUr2000reg1 has an orientation of strike, dip, and rake of 266°/30°/098°, while the focal mechanism StUr2000reg2 has an orientation of strike, dip, and rake of 236°/31°/075°. These focal mechanisms (not shown in Fig. 6) have the same geological representation as the StUr2000 focal mechanism within a small variation of orientation.

3.3 Synthetic focal mechanisms derived from published data on faults

In the vicinity of the Mont Terri rock laboratory several structures indicating earthquake occurrences are known in the basement and can be related either to a Permo-Carboniferous trough or the Rhine Graben structure (Ustaszewski and Schmid 2007). We used these structures to apply the regional paleostress field SH_{\max} NNW to derive synthetic focal mechanisms for each structure.

3.3.1 *PCWEreg*

Based on Ustaszewski and Schmid (2007), the Permo-Carboniferous trough in northern Switzerland has an W-E orientation with a dip direction and dip of the border fault of 357°/02°. If we apply SH_{\max} NNW to the WE-trending fault orientation this yields a PCWEreg synthetic focal mechanism with strike, dip, and rake of 056°/32°/063°. This represents a SSE-dipping sub-horizontal thrust fault or a NNW-dipping thrust fault (Fig. 6).

3.3.2 *NNEsWdreg*

Following Ustaszewski and Schmid (2007), the Rhine Graben structure is NNE-trending and dipping to the W (285°/79°). Applying SH_{\max} NNW to the NNE-trending W-dipping fault orientation results in a focal mechanism with strike, dip, and rake of 195°/79°/041° (NNEsWdreg), and a NNE-trending, left-lateral strike-slip component.

3.3.3 *Sub-horizontal*

Due to uncertainty of the hypocentral depth near the basement-cover interface, and because some focal mechanism solutions of seismicity in the basement suggest very shallow-dipping faults, we have added a group of sub-horizontal faults to the basement groups (same as in the cover, see Fig. 4).

4 Synthetic waveforms

Microseismic events detected in the vicinity of the Mont Terri rock laboratory exhibit weak intensities and have been recorded by only a few stations near the source. It is, therefore, not possible to satisfactorily constrain a focal mechanism solution using first-motion analysis. An additional uncertainty arises from the interference of ambient noise with the signal of very weak events.

In order to overcome these pitfalls, we used synthetic waveforms in a wave-correlation approach to determine synthetic focal mechanisms for very weak events. Our procedure was as follows: we use synthetic focal mechanisms based on existing fault groups in the investigation area to generate synthetic waveforms that, subsequently, can be correlated with the recorded seismograms of the SNS and the Swiss permanent stations (Figs. 2, 7) in the vicinity of the Mont Terri rock laboratory. The highest correlation factor between the naturally generated waveform and the synthetic waveforms represents the maximum likelihood estimate of the possible focal mechanism solution. The locations of the earthquakes from the microseismic catalog are further evaluated for their depth in relation to the geological context (see Freivogel and Huggenberger 2003; Nussbaum et al. 2017). Subsequently, we determine in which major geological unit (sedimentary cover or basement) each earthquake is located.

Groups of focal mechanisms that are in the sedimentary cover are identified through in situ measurements of fault orientations and striations. Another group of focal mechanisms is allocated to events arising in the basement. This latter group is composed of focal mechanisms from strong earthquakes that were located in the basement and synthetic focal mechanisms generated from structural interpretations of deep structures in the Mont Terri region based on data from the literature.

We generated synthetic waveforms for the stations near the source of the earthquake based on the synthetic focal mechanism defined from the corresponding groups of synthetic focal mechanisms. The waveforms were computed with WaveformTools, a modeling and moment-tensor inversion tool using an algorithm based on Green's functions

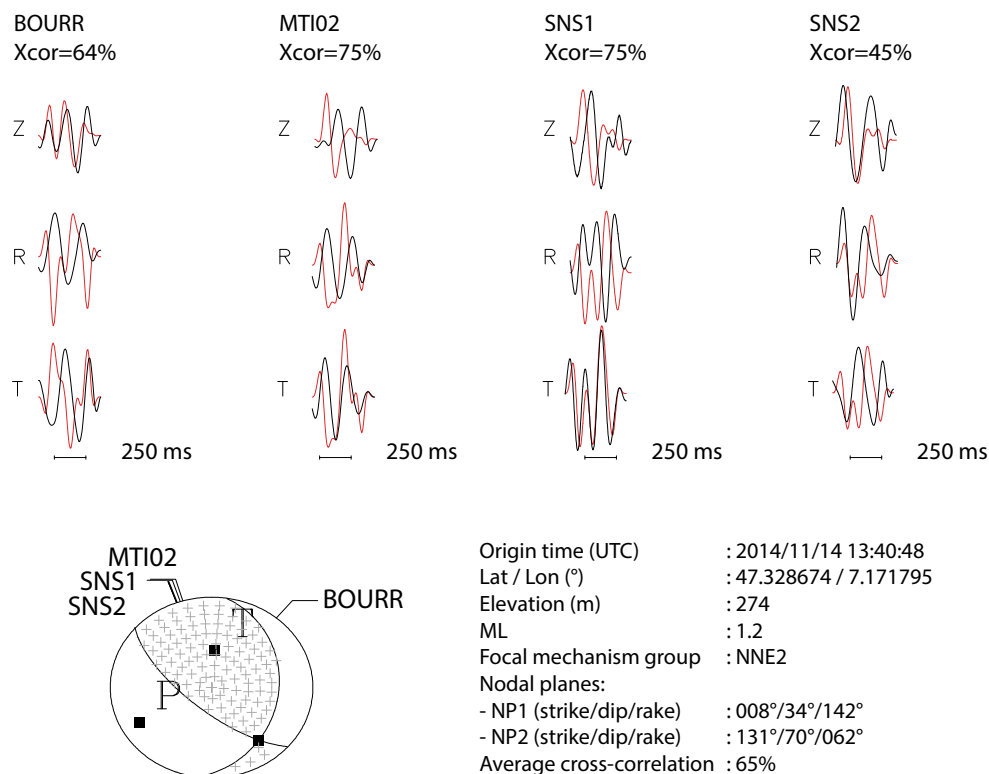


Fig. 7 Cross-correlation of recorded waveforms (*black* seismogram) with synthetic waveforms (*red* seismogram) at four stations generated from the synthetic focal mechanism group NNE2 (Fig. 4) for the

seismic event of 2014/11/14 13:40:48 (UTC) showing an average cross-correlation of 65%

(Zeng and Anderson 1995; Ichinose et al. 2003; Helffrich et al. 2013). Fault orientations, direction, and sense of the movement are used as input to generate synthetic waveforms (see example in Fig. 7). The software also provides an algorithm for performing grid search to determine focal mechanisms based on waveform analysis. However, since the earthquakes that we considered evidenced very weak intensity, only the synthetic waveform generator algorithm is used to cross-correlate existing seismograms from surrounding stations.

We compute the waveforms and compare these using a 500 ms sampling window that contains the P-phase of the signal arriving at the stations in the vicinity of the Mont Terri rock laboratory. The sampling duration is chosen based on the average distance between the source of the earthquake and the stations, which has a complete waveform of the P-phase. The complete synthetic P-phase waveform is generated using the P-phase 3D velocity model of Switzerland (Husen et al. 2003).

4.1 Layered velocity model

To generate synthetic P-phase waveforms at the stations in the vicinity of the Mont Terri rock laboratory for seismogram correlation, a P-wave 1D-layered velocity model

(Fig. 8) derived from a 3D velocity model of Switzerland (Husen et al. 2003) has been input into the WaveformTools software. Devising a more sophisticated and detailed local velocity model was beyond the scope of this pilot study. We therefore used the more regional, but robust, 3D velocity model of Switzerland (Husen et al. 2003) and applied the same parameters to all our dataset, being aware of the possibility of introducing errors due to changes in local geology and therefore in seismic velocity.

4.2 Synthetic waveform correlations

We correlated synthetic waveforms generated by the WaveformTools software with recorded seismograms from stations in the vicinity of the Mont Terri rock laboratory and applied these to 86 selected earthquakes (Table 2). The synthetic waveform correlation is done in two steps. The first step consists of performing an origin time scan based on the time given in the catalog (origin time and location) and the traveltime calculated by the synthetic waveform process depending on the respective layered velocity model. Due to the difference of methodology in locating earthquakes using Hypoline and the traveltime calculation using WaveformTools, a time lag of up to 2 s can occur. Based on the results of this first step, we could fit the origin

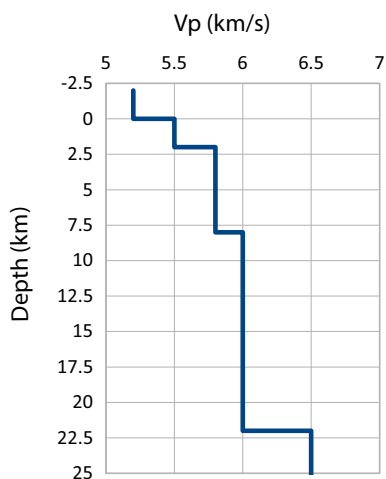


Fig. 8 1D P-wave velocity (V_p) model of Switzerland at the location of Mont Terri rock laboratory to the depth of 25 km derived from the 3D complex velocity model of Switzerland (Husen et al. 2003)

time to the maxima within ± 2 s. We then input the origin time maxima obtained from the first step as the origin time for the second step.

The second step consists in calculating the correlation coefficient of the synthetic waveform compared with the seismogram for each station in the vicinity of the Mont Terri rock laboratory, based on the sub-groups of predefined focal mechanisms. We calculate the average correlation coefficient from the stations for a focal mechanism sub-group and chose the maximum average as the best-fit focal mechanism for the analyzed earthquake. A maximum average correlation coefficient below 50% was taken to be no result. Average correlation coefficients for waveforms of 86 earthquakes correlated with the synthetic waveforms from the seven groups of synthetic focal mechanisms derived from the different fault groups ranged from 50 to 71%. In 7 instances the coefficient was $<50\%$ and these were not considered further.

5 Results

Many earthquakes from the catalog correlated well with the NNE-trending synthetic focal mechanisms constructed from mapped and known faults. Their epicentres agree with NNE-trending faults represented on geological maps where these structures are correlated with the reactivation of pre-existing normal faults related to the Rhine Graben (affecting both basement and/or cover). Hypocentres associated to the SSE-dipping focal mechanisms are also coherent with thrust faults of the anticline structure in the vicinity of the Mont Terri rock laboratory. The SSW-dipping focal mechanisms are associated with faults conjugate to the NNE-trending faults related to reactivation of the

pre-existing NNE-SSW-striking Rhine Graben normal faults (Fig. 9).

To gain a better understanding on the seismotectonics related to structures in the vicinity of the Mont Terri rock laboratory, the focal mechanisms are represented as back-section hemisphere projection beachballs (Fig. 10) and displayed at their hypocentre depth on a geologic section (Fig. 1). Thus, based on our analysis it was possible to determine three synthetic focal mechanisms from the microseismic events near the Mont Terri rock laboratory. These are linked with the major thrust faults interpreted in the Mont Terri ramp-related anticline, especially with the basal ramp and the Main Fault known from the tunnel system (Nussbaum et al. 2017).

6 Discussion

In this pilot study we used 86 from a total of 198 recorded seismic events from the SED permanent network and data from a dedicated SNS network between July 2014 and August 2015, to improve the seismotectonic understanding of very weak seismicity, magnitude (ML) between -2.0 and 2.0 , in the vicinity of the Mont Terri underground laboratory. Microseismicity in the detected magnitude range has a weak intensity, and therefore the seismic signal interferes with ambient noise. Thus, focal-mechanism inversion using first-motion analysis and a waveform grid search method results in solutions with large uncertainty. By correlating recorded seismograms with synthetic waveforms based on synthetic focal mechanism derived from fault orientation and striation measurements, we can associate a constructed (synthetic) focal mechanism to the weak-intensity microseismic events. This procedure is an affirmative methodology to associate existing in situ measured fault orientations and striations with detected very weak-intensity microseismicity in the vicinity of the Mont Terri rock laboratory.

Since the procedure works on the basis of known and in situ measured structures, the computational solution uncertainties that yield average correlation coefficients comparing synthetic to recorded waveforms ranging from 50 to 71% are considered qualified. These rather low values of correlation coefficients are primarily due to the weak-intensity seismic signal interfering with ambient noise.

Being based on predefined (synthetic) focal mechanisms, our methodology does not allow us to investigate new or unknown structures. However, using map and section-view observations, we can correlate the location, orientation, and focal mechanism of microseismic events with the location and orientation of geological structures in the vicinity of the Mont Terri rock laboratory. The NNE-trending focal mechanisms of the microseismic

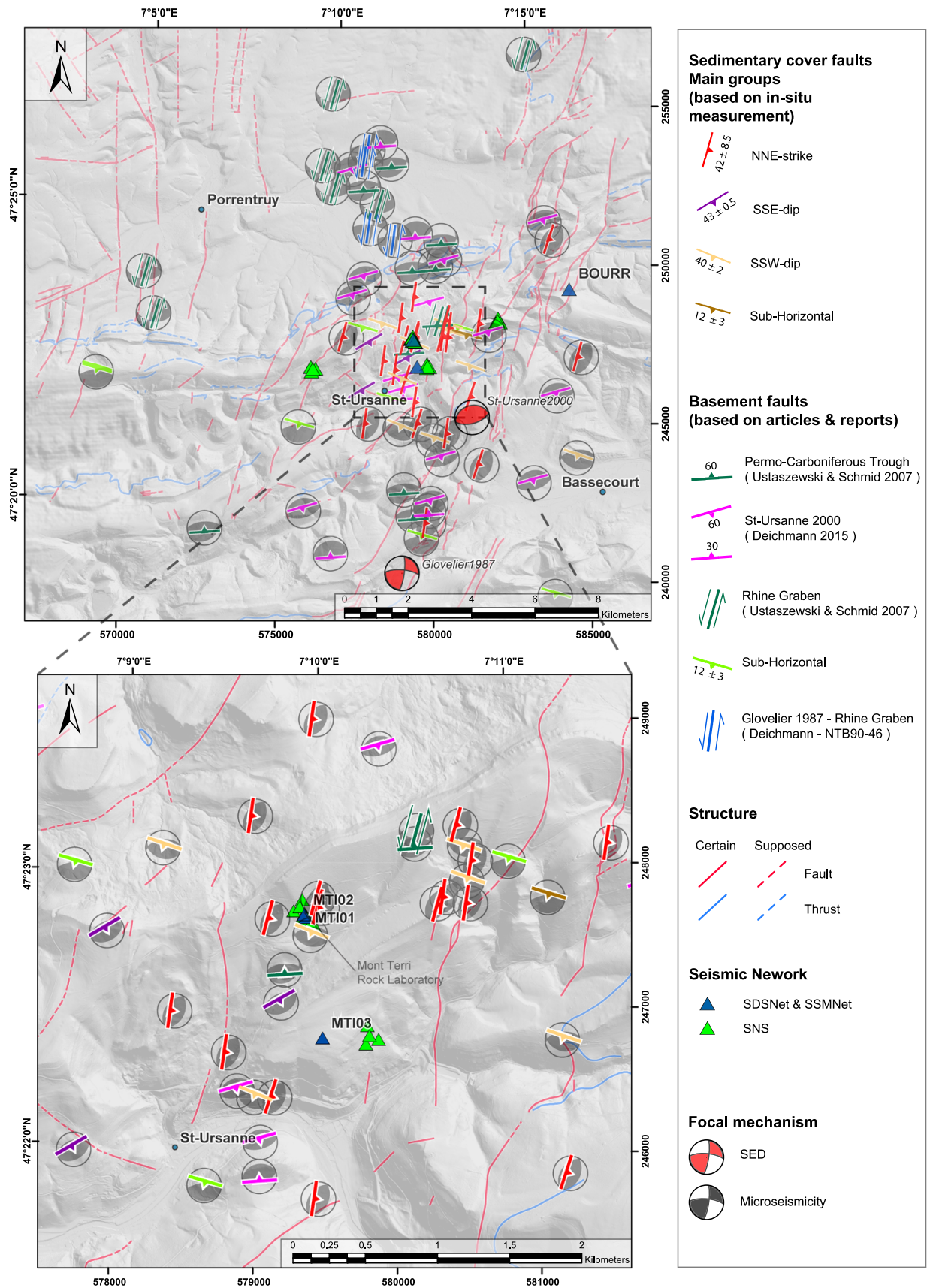


Fig. 9 Focal mechanisms of microseismic events in the vicinity of the Mont Terri rock laboratory represented as beachballs and fault orientations compared with known fault and thrust structures from the Geological Atlas of the Federal Office of Topography swisstopo. Two focal mechanisms determined by the Swiss Seismological Service (SED) are based on earthquakes analysed by Deichmann (1990, 2015) and Baer et al. (2001). The map is in the Swiss coordinate system CH1903

events are associated to existing NNE–SSW-striking mapped faults. We also observe that the SSW-dipping focal mechanisms are associated to conjugate faults with NNE-trending focal mechanisms. During the monitoring period, only a few events occurred that correlated with the SSE-dipping synthetic focal mechanisms. This synthetic focal mechanism could be related to thrusting of the Mont Terri anticline towards NNW. Thus on a regional scale, the synthetic focal mechanism solutions make it possible to use otherwise unconstrained seismic events to correlate with known structures in the basement and/or the cover.

7 Suggestions for future application of our procedure

To improve the results of focal mechanism attribution of a microseismic event, acquiring a complementary dataset of fault orientation and striation measurements in the vicinity of the Mont Terri rock laboratory would open the possibility to refine the orientation of the main group focal mechanism. Further, if we defined a more complex stress field with local/regional changes in the stress-field orientation and applied this to known fault orientations we could then better define the associated focal mechanism with an earthquake. Supervised and guided local grid search methods on the main groups of focal mechanism could also enable us to refine the determination of the focal mechanism of a seismic event. The WaveformTools software gives the possibility to attribute a specific velocity model for each station. This option could be used for further analysis to introduce local specific structure into the interpretation.

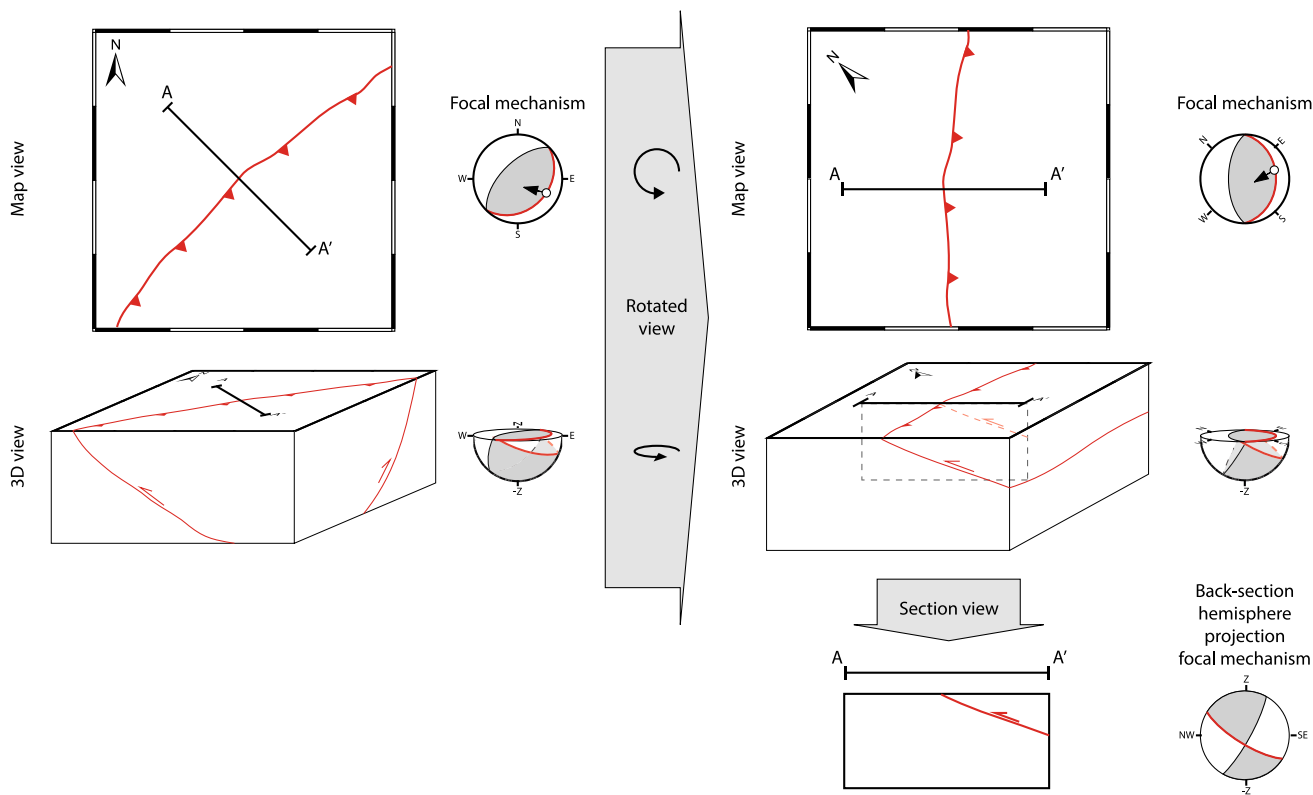


Fig. 10 Scheme for converting a lower-hemisphere projection focal mechanism in map view to a back-section-hemisphere projection focal mechanism in section view linked to the geometrical aspect of a fault


Acknowledgements Thanks to the two reviewers, Prof. Guido Schreurs (Institute of Geological Sciences, University of Bern), and Dr. Marian Hertrich (Nagra), for significantly improving the manuscript. We also would like to thank Roy Freeman for helping with the English of the manuscript. UNIFR and swisstopo are thanked for financial support.

References

- Aki, K., & Richards, P. G. (1980). *Quantitative seismology: Theory and methods* (pp. 801–802). New York: W. H. Freeman and Co.
- Allmendinger, R., Cardozo, N., & Fisher, D. (2012). *Structural geology algorithms: Vectors and tensors*. Cambridge: Cambridge University Press.
- Allmendinger, R. W., Gephart, J. W., & Marrett, R. A. (1989a). Notes on fault slip analysis. *Geol. Soc. Am. Short Course* (pp. 66).
- Allmendinger, R., Marret, R., & Cladoulos, T. (1989b). *Fault kinematics: a program for analysing fault slip data for Macintosh computer*. Ithaca: Cornell University.
- Baer, M., Deichmann, N., Braunmiller, J., Ballarin Dolfin, D., Bay, F., Bernardi, F., et al. (2001). Earthquakes in Switzerland and surrounding regions during 2000. *Eclogae Geologicae Helvetiae*, 94, 253–264.
- Bossart, P., Bernier, F., Birkholzer, J., Bruggeman, C., Connolly, P., Dewonck, S., Fukaya, M., Herfort, M., Jensen, M., Matray, J.-M., Mayor, J. C., Moeri, A., Oyama, T., Schuster, K., Shigeta, N., Vietor, T., Wiczorek, K. (2017). Mont Terri rock laboratory, 20 years of research: introduction, site characteristics and overview of experiments. *Swiss Journal of Geosciences*, 110. doi:10.1007/s00015-016-0236-1 (this issue).
- Cauzzi, C., & Clinton, J. (2013). A high- and low-noise model for high-quality strong-motion accelerometer stations. *Earthquake Spectra*, 29(1), 85–102.
- Deichmann, N. (1990). Seismizität der Nordschweiz, 1980-1988, und Auswertung der Erdbebenserien von Günsberg, Läuelfingen und Zeglingen. *Nagra Technischer Bericht*, 90-46. Nagra, Wettingen. <http://www.nagra.ch>.
- Deichmann, N. (2015). Re-evaluation of the earthquake sequence of 2000 in the area of St-Ursanne and in the Mont Terri rock laboratory. *Mont Terri Technical Note, TN 2013-99*. Federal Office of Topography (swisstopo), Wabern, Switzerland. <http://www.mont-terri.ch>.
- Fäh, D., Giardini, D., Kästli, P., Deichmann, N., Gisler, M., Schwarz-Zanetti, G., Alvarez-Rubio, S., Sellami, S., Edwards, B., Allmann, B., Bethmann, F., Wössner, J., Gassner-Stamm, G., Fritsche, S., & Eberhard, D. (2011). ECOS-09 Earthquake Catalogue of Switzerland Release 2011. *Report and Database. Public catalogue, 17.4.2011. Report SED/RISK/R/001/20110417*, Swiss Seismological Service ETH Zürich, Switzerland.
- Freivogel, M., & Huggenberger, P. (2003). Modellierung bilanzierter Profile im Gebiet Mont Terri–La Croix (Kanton Jura). In P. Heitzmann & J.-P. Tripet (Eds.), *Mont Terri Project—Geology, paleohydrogeology and stress field of the Mont Terri region. Reports of the Federal Office for Water and Geology No. 4*, (pp. 7–44). Federal Office of Topography (swisstopo), Wabern. <http://www.mont-terri.ch>.
- Guglielmi, Y., Birkholzer, J., Rutqvist, J., Jeanne, P., & Nussbaum, C. (2016). Can fault leakage occur before or without reactivation? Results from an in situ fault reactivation experiment at Mont Terri. In *13th International Conference on Greenhouse Gas Control Technologies*, November 14–18, 2016, Lausanne.
- Hardebeck, J. L., & Shearer, P. M. (2002). A new method for determining first-motion focal mechanisms. *Bulletin of the Seismological Society of America*, 92(6), 2264–2276.
- Heidbach, O., & Reinecker, J. (2013). Analyse des rezenten Spannungsfelds der Nordschweiz. *Nagra Arbeitsbericht (NAB 12-05)*. Nagra, Wettingen. <http://www.nagra.ch>.
- Helfrich, G., Wookey, J., & Bastow, I. (2013). *The seismic analysis code: A primer and user's guide*. Cambridge: Cambridge University Press.
- Husen, S., Kissling, E., Deichmann, N., Wiemer, S., Giardini, D., & Baer, M. (2003). Probabilistic earthquake location in complex three-dimensional velocity models: Application to Switzerland. *Journal of Geophysical Research: Solid Earth*, 108(B2).
- Ichinose, G. A., Anderson, J. G., Smith, K. D., & Zeng, Y. (2003). Source parameters of eastern California and western Nevada earthquakes from regional moment tensor inversion. *Bulletin of the Seismological Society of America*, 93(1), 61–84.
- Joswig, M. (2008). Nanoseismic monitoring fills the gap between microseismic networks and passive seismic. *First Break*, 26, 121–128.
- Kobayashi, R., & Nakanishi, I. (1994). Application of genetic algorithms to focal mechanism determination. *Geophysical Research Letters*, 21(8), 729–732.
- Laubscher, H. (1977). Fold development in the Jura. *Tectonophysics*, 37, 337–362.
- Laubscher, H. (1997). The décollement hypothesis of the Jura folding after 90 years. *Bulletin of Applied Geology*, 2(2), 167–182.
- Marrett, R., & Allmendinger, R. (1990). Kinematic analysis of fault-slip data. *Journal of Structural Geology*, 12, 973–986.
- NEA (1999). *Geologic disposal of radioactive waste: Review of developments in the last decades*. OECD Nuclear Energy Agency, Paris.
- Nussbaum, C., Bossart, P., Amann, F., & Aubourg, C. (2011). Analysis of tectonic structures and excavation induced fractures in the Opalinus Clay, Mont Terri underground rock laboratory (Switzerland). *Swiss Journal of Geosciences*, 104(2), 187–210.
- Nussbaum, C., Kloppenburg, A., Caër, T., & Bossart, P. (2017). Tectonic evolution around the Mont Terri rock laboratory, northwestern Swiss Jura: constraints from kinematic forward modelling. *Swiss Journal of Geosciences*. doi:10.1007/s00015-016-0248-x (this issue).
- Oppenheimer, D. H., Reasenber, P. A., & Simpson, R. W. (1988). Fault plane solutions for the 1984 Morgan Hill, California, Earthquake Sequence: Evidence for the state of stress on the Calaveras Fault. *Journal of Geophysical Research: Solid Earth*, 93, 9007–9026.
- Plenefisch, T., & Bonjer, K.-P. (1997). The stress field in the Rhine Graben area inferred from earthquake focal mechanisms and estimation of frictional parameters. *Tectonophysics*, 275(1), 71–97.
- Sick, B., Walter, M., & Joswig, M. (2012). Visual event screening of continuous seismic data by superonograms. *Pure and Applied Geophysics*, 171, 549–559.
- Sommaruga, A. (1999). Décollement tectonics in the Jura foreland fold-and-thrust belt. *Marine and Petroleum Geology*, 16, 111–134.
- Thury, M., & Bossart, P. (1999). The Mont Terri rock laboratory, a new international research project in a Mesozoic shale formation, in Switzerland. *Engineering Geology*, 52, 347–359.
- Ustaszewski, K., & Schmid, S. (2007). Latest Pliocene to recent thick-skinned tectonics at the Upper Rhine Graben—Jura Mountains junction. *Swiss Journal of Geosciences*, 100(2), 293–312.
- Vouillamoz, N., Wust-Bloch, G. H., Abednego, M., & Mosar, J. (2016). Optimizing event detection and location in low-seismicity zones: case study from western Switzerland. *Bulletin of the Seismological Society of America*, 106(5), 2023–2036.
- Woessner, J., & Wiemer, S. (2005). Assessing the quality of earthquake catalogues: estimating the magnitude of

- completeness and its uncertainty. *Bulletin of the Seismological Society of America*, 95(2), 684–698.
- Zeng, Y., & Anderson, J. G. (1995). A method for direct computation of the differential seismogram with respect to the velocity change in a layered elastic solid. *Bulletin of the Seismological Society of America*, 85(1), 300–307.
- Zoback, M. D., & Harjes, H.-P. (1997). Injection-induced earthquakes and crustal stress at 9 km depth at the KTB deep drilling site, Germany. *Journal of Geophysical Research: Solid Earth*, 102(B8), 18477–18491.

In-situ experiments on bentonite-based buffer and sealing materials at the Mont Terri rock laboratory (Switzerland)

Klaus Wiczorek¹  · Irina Gaus² · Juan Carlos Mayor³ · Kristof Schuster⁴ · José-Luis García-Siñeriz⁵ · Toshihiro Sakaki²

Received: 5 April 2016 / Accepted: 9 December 2016 / Published online: 20 February 2017
© Swiss Geological Society 2017

Abstract Repository concepts in clay or crystalline rock involve bentonite-based buffer or seal systems to provide containment of the waste and limit advective flow. A thorough understanding of buffer and seal evolution is required to make sure the safety functions are fulfilled in the short and long term. Experiments at the real or near-real scale taking into account the interaction with the host rock help to make sure the safety-relevant processes are identified and understood and to show that laboratory-scale findings can be extrapolated to repository scale. Three large-scale experiments on buffer and seal properties performed in recent years at the Mont Terri rock laboratory are presented in this paper: The 1:2 scale HE-E heater experiment which is currently in operation, and the full-scale engineered barrier experiment and the Borehole Seal experiment which have been completed successfully in 2014 and 2012, respectively.

Editorial handling: P. Bossart and A. G. Milnes.

This is paper #12 of the Mont Terri Special Issue of the Swiss Journal of Geosciences (see Bossart et al. 2017, Table 3 and Fig. 7).

✉ Klaus Wiczorek
klaus.wiczorek@grs.de

- ¹ Gesellschaft für Anlagen- und Reaktorsicherheit (GRS) gGmbH, Theodor-Heuss-Strasse 4, 38122 Braunschweig, Germany
- ² Nationale Genossenschaft fuer die Lagerung radioaktiver Abfälle (Nagra), Hardstrasse 73, 5430 Wettingen, Switzerland
- ³ Empresa Nacional de Residuos Radiactivos, S.A. (ENRESA), C. Emilio Vargas 7, 28043 Madrid, Spain
- ⁴ Bundesanstalt fuer Geowissenschaften und Rohstoffe (BGR), Stilleweg 2, 30655 Hannover, Germany
- ⁵ Amberg Infraestructuras, Av. de la Industria 37-39, 28108 Alcobendas, Madrid, Spain

All experiments faced considerable difficulties during installation, operation, evaluation or dismantling that required significant effort to overcome. The in situ experiments show that buffer and seal elements can be constructed meeting the expectations raised through small-scale testing. It was, however, also shown that interaction with the host rock caused additional effects in the buffer or seal that could not always be quantified or even anticipated from the experience of small-scale tests (such as re-saturation by pore-water from the rock, interaction with the excavation damaged zone in terms of preferential flow or mechanical effects). This led to the conclusion that testing of the integral system buffer/rock or seal/rock is needed.

Keywords Engineered barrier system · In-situ experiments · Bentonite · Sand–bentonite mixture · Nuclear waste disposal

1 Introduction

Operation of nuclear power plants creates heat-generating radioactive waste which, according to international consensus (OECD-NEA 2008) and to the concepts most countries using nuclear power are developing, should be disposed of in deep geological formations. In different countries, different host rocks are considered owing to their respective geological situations. The geological disposal concepts for radioactive waste are generally based on a multi-barrier system, which comprises the host rock formations and engineered barrier systems (EBS), such as sealing structures for boreholes, galleries, and shafts, as well as the backfill of remaining voids and the waste containers or canisters themselves. The overall objective of nuclear waste disposal in geological formations is to ensure permanent containment

of the waste, concentrating and isolating it for a very long time from the biosphere. Owing to the different types of host rock (clay, salt, or crystalline rock) and repository concepts, the roles and requirements of the engineered barriers are different. In the existing concepts for clay or crystalline host rock, bentonite-based materials are widely used for buffer or sealing purposes. For constructing a repository and for ensuring the safe containment of the nuclear waste over a very long time period, profound knowledge about the material behaviour of the coupled system of waste containers, EBS, and the rock is indispensable. In addition to theoretical and laboratory-scale work, some countries run underground rock laboratories (URLs) in order to obtain this knowledge, following the guidelines of OECD-NEA (2001).

The Mont Terri rock laboratory is a unique facility where international repository research is performed in a claystone environment. It is located in the Jurassic Opalinus Clay in the Swiss Canton of Jura. Figure 1 shows a geological cross-section including the rock laboratory.

Besides many other experiments, large-scale investigations on the combined system of EBS and clay rock have been performed in recent years. Some of the respective experiments are presented here. These comprise

- The HE-E heater experiment
- The EB engineered barrier experiment
- The SB borehole seal experiment

A key project addressing the long-term performance of the engineered barrier system was the European

Commission co-financed PEBS project (“Long-term performance of the engineered barrier system”, Schäfers et al. 2014), which used a comprehensive approach of experimental, modelling and evaluation exercises to address the issue. The HE-E experiment and the final phase of the EB experiment were performed in the frame of PEBS. An overview of the experiment locations and the geological setting is given by Bossart et al. (2017).

2 The role of bentonite-based buffer and sealing materials

Some of the disposal concepts in clay or crystalline rock (e.g., the Swiss, Swedish, or Spanish concepts) involve a so-called buffer which surrounds the waste containers and fills the void between the containers and the host rock. The buffer generally consists of bentonite or bentonite-bearing material and is re-saturated over time by water from the host rock. This results in the development of a swelling pressure, an increase in thermal conductivity and a decrease in hydraulic conductivity. Thus, the buffer provides containment of the waste, limits advective flow, and enables heat dissipation into the rock. It also provides chemical buffering and long-term retardation of radionuclides in case of a leak. The detailed safety functions of the buffer in various disposal concepts are compiled in Deliverable D1.1/D1.2 of the PEBS project (PEBS 2012). Despite the differences in the concepts, they can be summarized as follows:

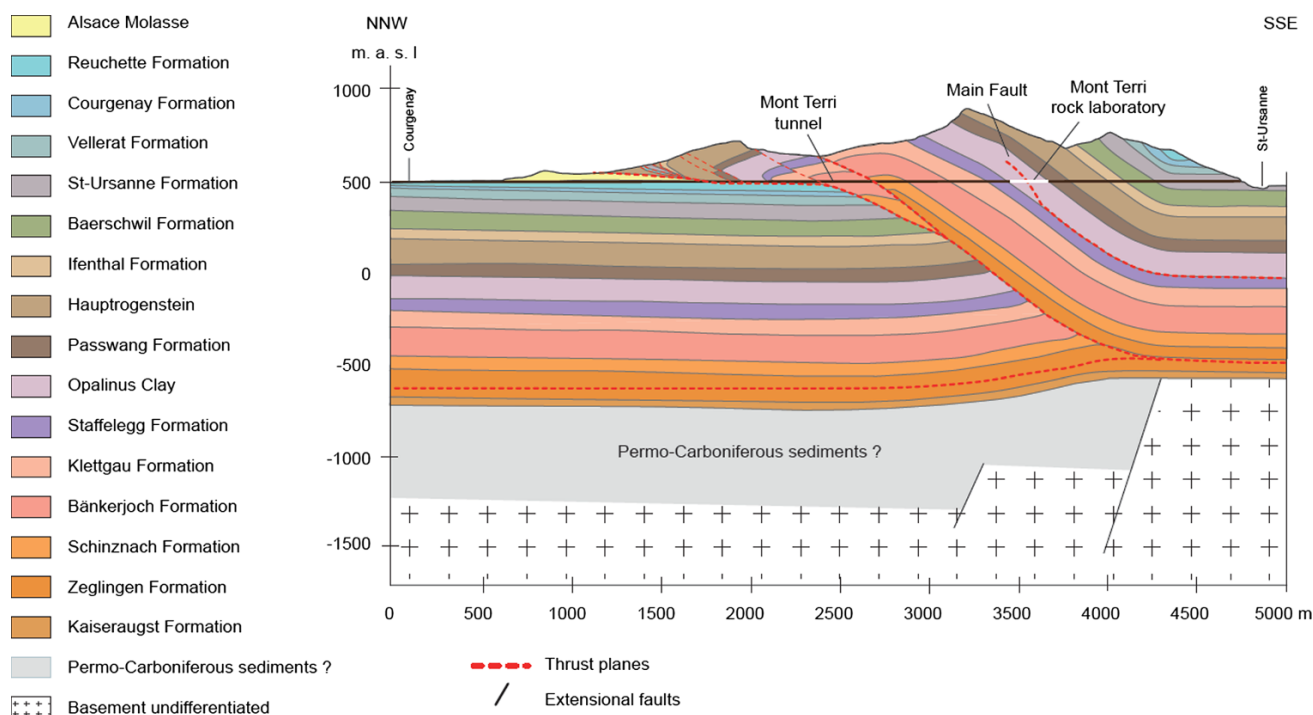


Fig. 1 Geological cross-section of the Mont Terri anticline and location of the Mont Terri rock laboratory (Nussbaum et al. 2017)

- Limitation of advective transport by achieving a low hydraulic conductivity after re-saturation
- Limitation of deformation of the host rock and reduction of the excavation damaged zone (in clay host rock) by achieving sufficient swelling pressure
- Prevention of canister sinking and damping of shear movements in the rock (in crystalline host rock)
- Suitable heat conduction to avoid excessive temperature
- Reduction of microbial activity and related corrosion by high buffer density
- Sorption of radionuclides
- Filtering of colloids
- Resistance to mineral transformation to maintain required properties

Seal elements for boreholes, galleries and shafts are part of all repository concepts. Their safety functions are very similar to those listed for the buffer, although they can also be less stringent. Heat conduction and, obviously, prevention of canister sinking play a minor role for these components. Depending on the concept, the backfill of the remaining voids in the repository provides mechanical support and may also take the role of a barrier in the long term. Currently, in all concepts clay-bearing materials are candidate materials for seal elements and backfill taking a barrier function.

While bentonite has the fundamental properties to fulfil the requirements for the buffer or seal, its coupled thermo-hydro-mechanical–chemical (THMC) behaviour under repository conditions is highly complex. A thorough understanding of buffer and seal evolution is required to provide evidence that the safety functions are fulfilled in the short term and the long term. Especially with respect to the thermo-hydro-mechanical (THM) evolution, experiments in the real or near-real scale under relevant conditions, taking into account the interaction with the host rock, are necessary to identify and better understand the safety-relevant processes as well as to show that laboratory-scale findings can be extrapolated/upscaled to the repository scale.

3 The HE-E heater experiment

The HE-E experiment was started in 2011 as part of the 7th Framework EURATOM project “Long-term Performance of Engineered Barrier Systems” (PEBS). The idea of PEBS was to evaluate the sealing and barrier performance of the EBS with time, through development of a comprehensive approach, involving experiments, model development, and consideration of the potential impact on safety functions (Schäfers et al. 2014). The main objective of the HE-E was

to gain insight in the early non-isothermal re-saturation period of the buffer and its impact on the THM behaviour. Particular objectives were to provide the experimental database required for the calibration and validation of existing thermal–hydraulic–mechanical models of the early re-saturation phase and to verify upscaling of the thermal conductivity of the partially saturated buffer from laboratory to field scale for two types of candidate buffer materials: pure bentonite and sand-bentonite mixture. The HE-E experiment is the first near-real scale in situ experiment involving granular buffer at high temperature.

The experiment was set up in a microtunnel of 1.3 m diameter which had been used earlier for the Mont Terri ventilation experiment VE (Mayor et al. 2007b), with the benefit of a comprehensive rock instrumentation that could be re-used. The location of the microtunnel in the Mont Terri rock laboratory can be found in the paper of Bossart et al. (2017). After completion of the PEBS project in 2014, the experiment partners Nagra, ENRESA, BGR, and GRS decided to continue the HE-E experiment with national funding. Detailed information about the HE-E, as available at the end of the PEBS project, is given in the HE-E final report (Gaus et al. 2014).

3.1 Design and construction

An overview of the HE-E configuration is given in Fig. 2. The experiment is set up in a 10 m long section of the 1.3 m diameter VE microtunnel. It consists of two sections separated by a concrete plug. Both sections are equipped with an electrical heater bedded on highly compacted bentonite blocks. The remaining void is backfilled with granular bentonite buffer (Sect. 1) or 65/35 sand/bentonite mixture (Sect. 2). Especially Sect. 1 represents Nagra’s

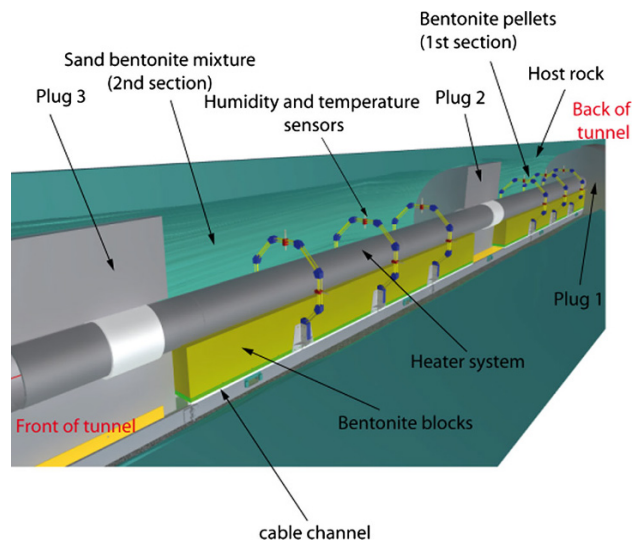


Fig. 2 Overview of the HE-E configuration (Teodori and Gaus 2012)

emplacement concept in a near 1:2 scale. The sand/bentonite mixture was chosen as an alternative potential buffer material after the experiences of the SB experiment (see Sect. 5). In the HE-E experiment, the bentonite used for all buffer types was sodium bentonite (Wyoming bentonite).

The Opalinus Clay around the microtunnel had already been instrumented for the VE experiment; sensors had been installed in different cross sections (Fig. 3): Temperature and pore pressure sensors (SA and SD), temperature and humidity sensors (SB), and extensometers (SD). In 2010/11, the rock instrumentation was completed by additional temperature and pore pressure sensors and a seismic array.

The spatial restrictions of the microtunnel proved a challenge for the installation of heaters, buffer, and instrumentation. The solution was to construct a unit of bentonite block support, heater liner, and sensor carrier outside the microtunnel which was then inserted into the tunnel as a whole (Fig. 4). The sensor carriers support temperature and humidity sensors at defined radial distances from the heater liner in six cross sections (Fig. 3). After installation of each block/liner/carrier package the heater was inserted and the remaining void backfilled with granular buffer material using an auger system (Fig. 5, left). An additional compaction of the buffer was not possible. The three buffer materials (blocks, granular bentonite, and sand/bentonite) were characterised in the laboratory in terms of their petrophysical, thermal and hydraulic properties. Table 1 summarizes the basic properties. On-site measurements gave slightly different values for the granular materials. Emplacement density was estimated by comparison to the total emplaced buffer mass and the microtunnel volume obtained from a 3D scan of the microtunnel geometry (Fig. 5, right).

Installation of the HE-E was finished by mid 2011, and on June 30, 2011 the heaters were started. Since then, the

experiment has been running without major problems. Three main heating phases can be distinguished: A first phase of 3 months with a linear liner temperature increase to 80–90 °C, a second phase with linear temperature increase of another 9 months to reach 140 °C on the liner, followed by the third phase with a constant liner temperature which has been maintained to date.

3.2 Monitoring results to date

An example of the temperature evolution in the buffer is shown in Fig. 6. The results shown have been measured in the heater midplane of the sand/bentonite section; temperature evolution in the pure bentonite section is very similar due to similar thermal properties of the two granular materials. The temperatures in the bentonite blocks (7Bt and 5B1) are slightly higher than those at comparable distance from the heater in the granular buffer (12C and 12M) because of the higher thermal conductivity of the blocks. Due to the overall low thermal conductivity of the dry buffer the thermal gradient is quite high (from 140 °C on the heater surface to 45 °C on the microtunnel surface, 12H). Heating results in a drying of the buffer close to the heater, illustrated by a drop in relative humidity as depicted in Fig. 7 for the sand/bentonite section. Water vapour is expelled to the outer and cooler parts of the buffer, where full saturation and 100% relative humidity are reached after 5 months of heating. Similar results are obtained for the pure bentonite buffer, although it takes about one year to reach 100% humidity.

With the seismic long-term monitoring the evolution in the Opalinus Clay as well as in the sand/bentonite (S/B) buffer is characterised with seismic parameters (Schuster 2014b). One focus is on the evolution of the S/B, where three piezoelectric transducers are located, one emitter, 5 cm from the S/B-Opalinus Clay interface and two

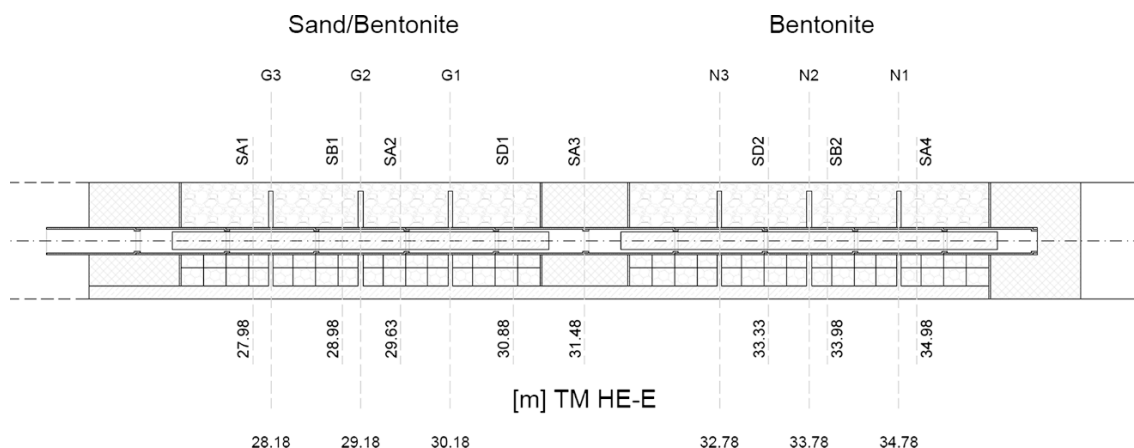


Fig. 3 Longitudinal section of the microtunnel showing the instrumentation cross sections (Gaus et al. 2014). Sections SA, SB, SD denote rock instrumentation, sections N1–N3 and G1–G3 denote buffer instrumentation

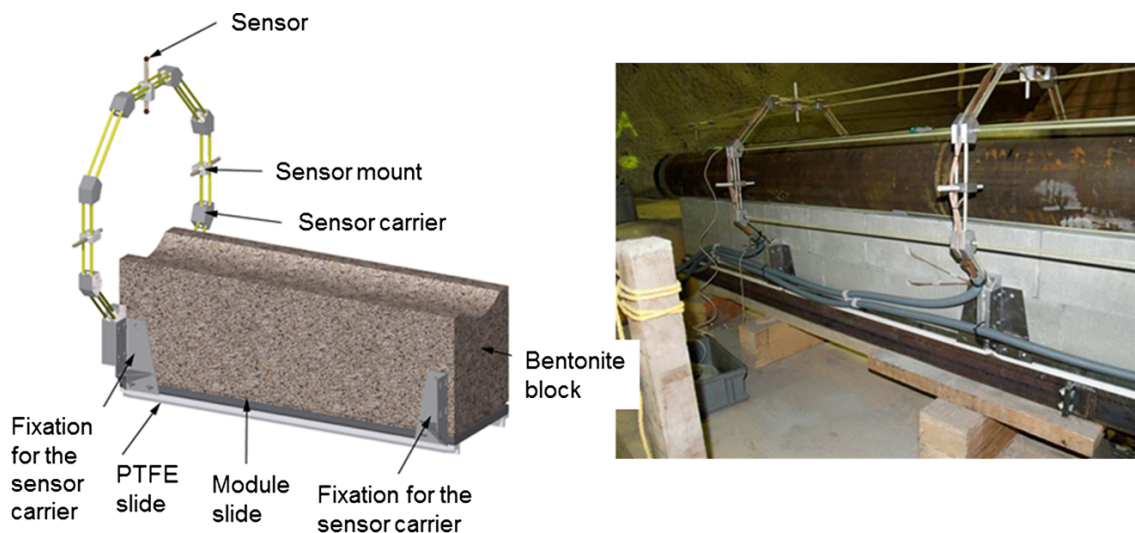


Fig. 4 Integrated buffer installation and instrumentation. *Left* design of a buffer instrumentation module, *right* complete bentonite block/liner/sensor carrier module before insertion into the microtunnel (Gaus et al. 2014)



Fig. 5 *Left* Granular buffer emplacement using an auger system, *right* 3D image of the microtunnel test section before installation for volume calculation (Gaus et al. 2014)

Table 1 Basic properties of HE-E buffer materials (Gaus et al. 2014)

	Bentonite blocks	Granular bentonite	Sand/bentonite
Water content (% by mass)	10.34	5.4	4.1
Bulk density (kg/m ³), preceding laboratory measurement	1993	1595	1440
Dry density (kg/m ³), preceding laboratory measurement	1806	1513	1383
Bulk density (kg/m ³), samples prepared as during emplacement		1543	1500

receivers at 5 and 10 cm distance from the interface. In Fig. 8 the evolution of the derived and normalised P-wave velocities (v_p) for the first 550 days is illustrated. The normalised v_p evolution reflects changes of material parameters of the S/B at different stages and with different gradients. In general, a higher v_p indicates a more competent (more compacted) material.

The first recognisable P-wave phases could be observed immediately after backfilling and closure of the

microtunnel on day 52 for the distance 7.5 cm (emitter at 5 cm, receiver at 10 cm) and 50 days later for the 5 cm distance. This difference could be related to the denser initial compaction of the S/B (small initial gap in the roof). Heating started on day 109. There are at least four pronounced bending points in both graphs as a result of different compaction/saturation stages of the S/B (for the 7.5 cm distance: around days 100, 190, 290, and 490). The latest one was 20 days after the heater reached the

Fig. 6 Temperature evolution in the buffer at the heater midplane of the sand/bentonite section (G2). Data from the granular buffer (12H, 12M, 12C) and from the bentonite blocks (7Bt, 5BI)

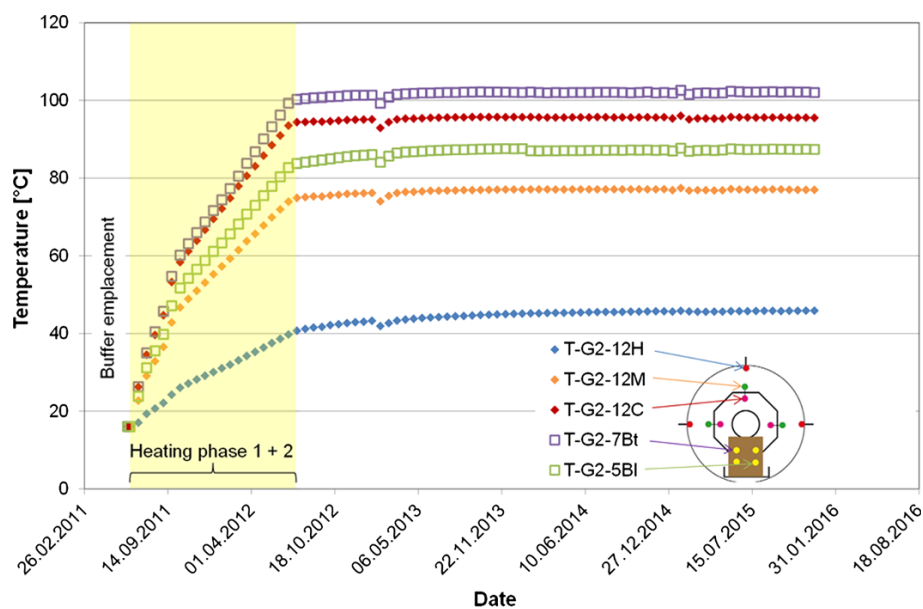
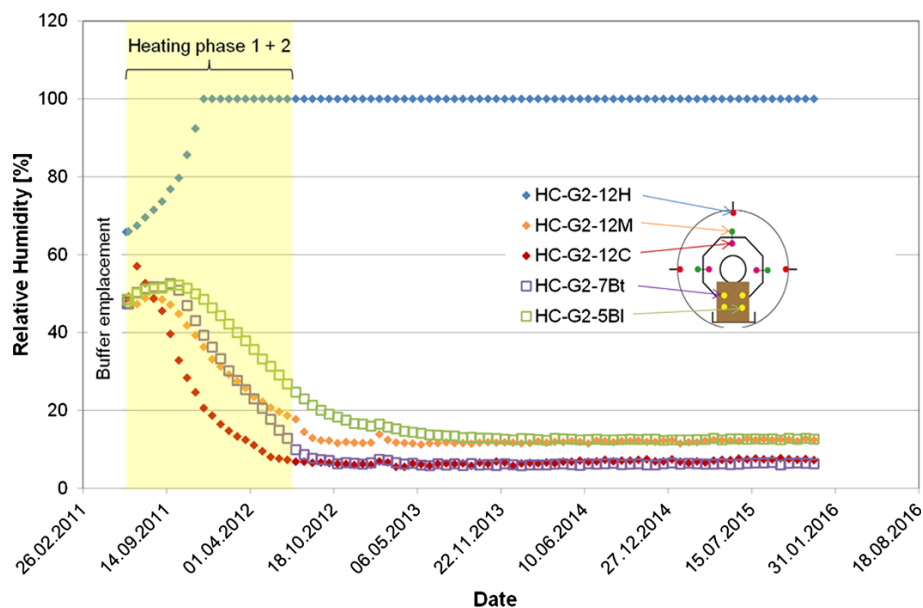


Fig. 7 Relative humidity evolution in the buffer at the heater midplane of the sand/bentonite section (G2). Data from the granular buffer (12H, 12M, 12C) and from the bentonite blocks (7Bt, 5BI)



maximum temperature. Between days 200 and 290, when the RH sensors at the interface reached 100% relative humidity, a constant stage for the 7.5 cm distant travel paths is observed. For the 5 cm distance, closer to the interface, this trend is slightly negative between days 200 and 280, whereas for the following 20 days a remarkable decrease in v_p is observed. Due to the heating a vapour front moves towards the interface. A temporary accumulation of vapour/water close to the interface could reduce the v_p . This interpretation is supported by slight variations in the frequency content of the first arrival phases. Between days 260 and 280 the centre frequency of the sum spectrum is slightly higher than for day 281 to day 300. A further

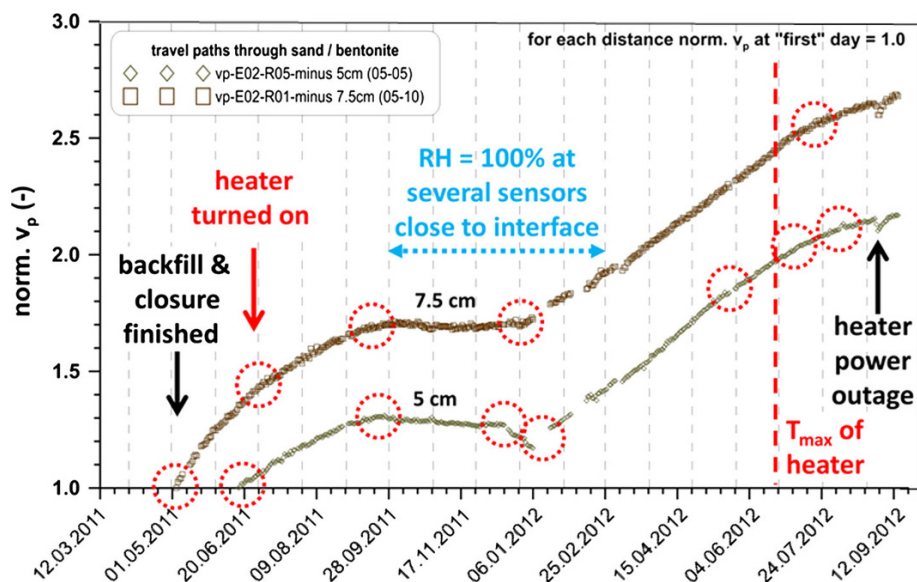
conspicuity is the v_p notch around day 539 which results from a 14 h power failure of the heaters (summer storm).

Monitoring is continued and a continuous gradual increase of normalised v_p between days 800 and 1200 was observed in a first analysis, meaning compaction/swelling of the material is progressing.

3.3 Interpretation

Integral part of the measurement interpretation is model simulation, which was performed in different cycles. During designing the HE-E, scoping calculations (Czajkowski et al. 2012) were performed for planning the

Fig. 8 Normalised P-wave velocity evolution in the sand/bentonite material



experiment execution and to make sure the instrumentation met the requirements. Parallel to performing the experiment, TH- and THM-coupled model calculations were performed with the actual material parameters and boundary conditions of the experiment (Gaus et al. 2014) to reproduce the observed behaviour and to predict future evolution. Despite the conceptual and geometrical restrictions of the different models, the modelling results showed that the temperature and humidity evolution in the buffer could be well reproduced. More detail regarding the modelling of the HE-E and other experiments is given in by Gens et al. (2017).

Re-saturation of the buffer is slow, as it is governed by pore-water supply from the surrounding clay. As mentioned earlier, the microtunnel was not excavated for the HE-E, but had undergone a complex de-saturation/re-saturation history during the preceding ventilation test. Pore pressure measurements in the rock close to the microtunnel show that the near-field was and still is in suction, and only at distances over 1 m from the tunnel surface positive pore-water pressures are observed. Therefore, more time will be needed until a significant re-saturation inside the buffer can be expected. With increased saturation, on the other hand, the thermal conductivity of the buffer will increase and attenuate the temperature gradient.

The hydraulic conductivity and swelling pressure of the buffer materials cannot be evaluated in the in situ test, since the buffer is still very dry. Still, some information is gathered from the seismic measurements. The pure granular bentonite buffer could be installed with a density of more than 1500 kg/m^3 , which makes acceptable hydro-mechanical (HM) properties after re-saturation probable. The emplacement density of the sand/bentonite buffer, however, is very poor (1383 kg/m^3). This is a result of the

narrow grain distribution of the material which was chosen to avoid segregation during the emplacement, and of the impossibility of additional compaction after emplacement. Consequently, laboratory measurements showed insufficiently low permeability (Wieczorek and Miehe 2013) and too low swelling pressure (Villar et al. 2014b) of this material at the density achieved on site, making modifications necessary.

4 The EB experiment

The HE-E focuses on the early post-closure phase with high temperature gradients and low buffer saturation. The buffer evolution at a later stage, when heat production has diminished and the buffer is re-saturated and pore pressure evolves, was addressed by the Engineered Barrier emplacement experiment (EB) which started in 2002. The experiment location is shown in Bossart et al. (2017).

The objectives of this experiment (Mayor et al. 2007a) were to

- Define a buffer material and demonstrate its production at semi-industrial scale
- Characterise HM properties of the buffer
- Design and demonstrate the emplacement and backfilling technique
- Assess the quality of the buffer after emplacement
- Characterise the excavation damaged and/or disturbed zone in the rock and determine its influence on the HM behaviour of the system
- Investigate the evolution of the HM parameters in the buffer and the EDZ as a function of progressing hydration

- Develop a HM model of the complete system

Similar to the HE-E experiment, a dummy canister (in this case without heat production) was placed on highly-compacted bentonite blocks and the remaining space was backfilled with pure granular bentonite buffer (Fig. 9). In contrast to HE-E, the bentonite is a calcium bentonite from Serrata de Nijar in Spain. In order to achieve full saturation of the buffer in a realistic experimental duration, an artificial hydration system was installed. Regarding the tunnel and canister dimensions, the EB experiment is a full-scale experiment.

4.1 Construction

A new niche was excavated for the experiment in 2001, and geophysical and hydraulic measurements were performed for EDZ characterisation. Afterwards, the bentonite blocks and the dummy canister were emplaced. A hydration system consisting of a pipe system of 37 pipes (Fig. 9) and sensors for buffer monitoring in different cross sections (Fig. 10) were installed. Finally, the granular buffer was emplaced using an auger system which had proven to be the most suitable technique, and the experiment setup was sealed off with a concrete plug (Mayor et al. 2007a).

The bentonite blocks had a dry density of 1.69 g/cm^3 and an initial water content of 14%. The dry density of the granular backfill as determined from the total mass emplaced and the total available volume amounted to an average of 1.36 g/cm^3 . Preceding laboratory tests had shown that at full saturation, hydraulic conductivities in the range of 10^{-12} m/s and a swelling pressure of about 1.3 MPa could be expected for such a dry density value (Mayor et al. 2007a).

4.2 Re-saturation phase and monitoring results

In May 2002, the injection of artificial pore-water (Pearson water) into the buffer via the hydration pipes was started. A

total of about 19 m^3 were injected until June 2007. Afterwards, the buffer was only subject to further natural water uptake from the surrounding Opalinus Clay until October 2012, when dismantling of the experiment started.

The evolution of relative humidity as an indicator for suction/saturation in the buffer was monitored in different cross sections (Fig. 10). As an example, Fig. 11 shows the results in cross section B1. One year after start of water injection the granular buffer can be considered almost fully saturated, in the sense that relative humidity reached 100%, which means suction has disappeared. Only one sensor (WB1/2) takes longer to reach 100% humidity.

4.3 Dismantling and evaluation

An important part of the investigation programme was the dismantling and evaluation operation of the EB, which was performed in the frame of the PEBS project.

Between October 2012 and January 2013 the whole experiment was excavated and more than 500 samples of the buffer were taken from different cross sections (Fig. 12) for on-site and laboratory analyses of dry density and moisture content, suction, pore size distribution, basal spacing, thermal conductivity, hydraulic and gas conductivity, swelling strain and swelling pressure, and microbial analyses.

From on-site measurements taken directly after sampling, it was found that the average water content of the buffer (granular bentonite and blocks) was 36%, the average dry density 1.34 g/cm^3 , and the average degree of saturation 95.5% (Palacios et al. 2013). As shown for cross section B1 as an example (Fig. 13), there is some degree of inhomogeneity in terms of dry density and water content distribution, although the large initial density contrast between blocks and granular buffer has practically vanished. Water content is lower and dry density is higher in the upper part of the granular buffer. Laboratory tests on

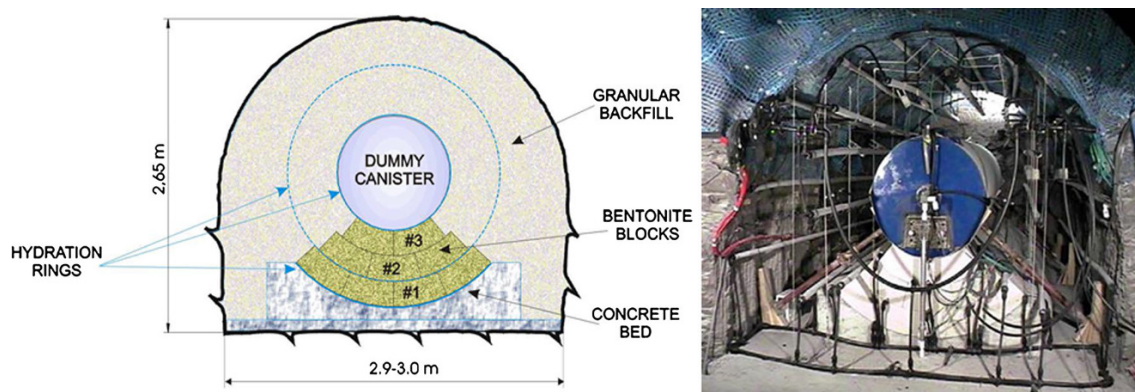


Fig. 9 EB experiment layout. Hydration pipes are arranged in rings around the central dummy canister (Mayor et al. 2007a, b)

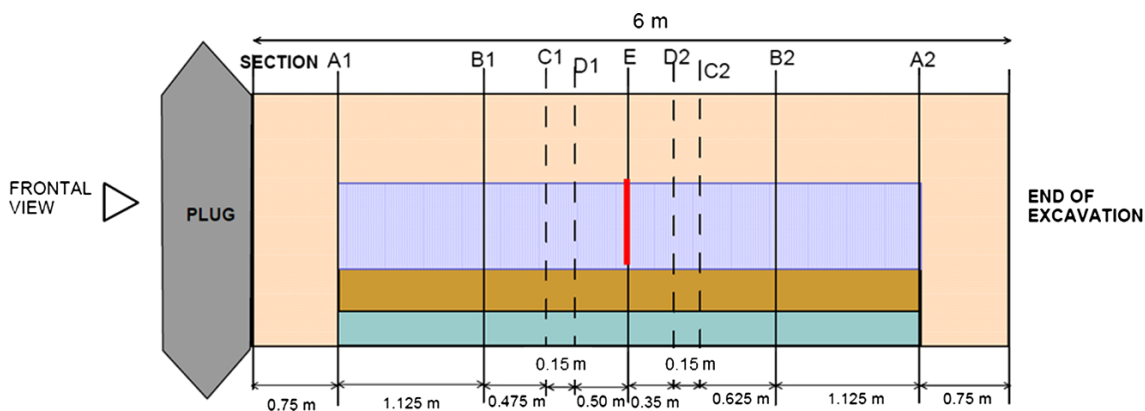
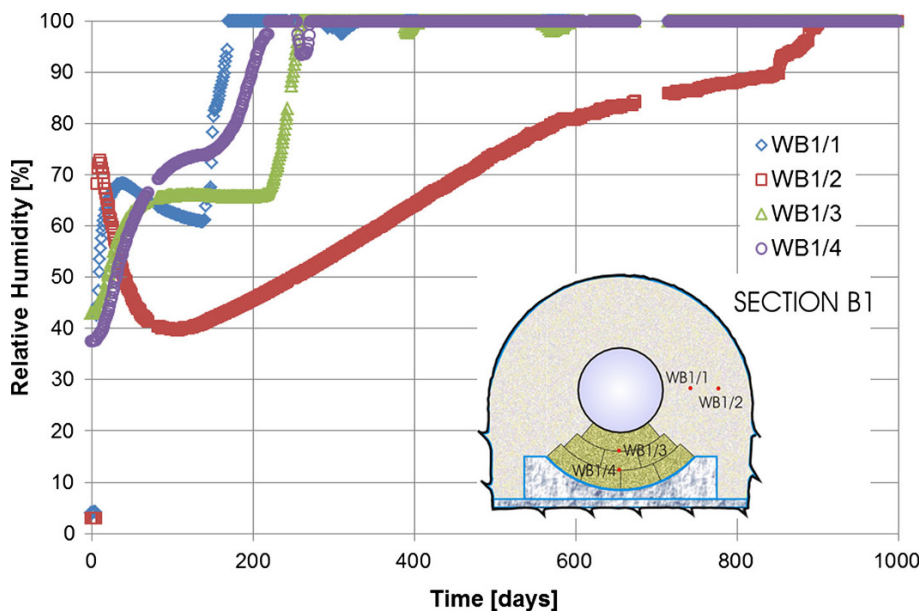


Fig. 10 EB longitudinal section showing the instrumentation cross sections (Vasconcelos et al. 2014)

Fig. 11 Evolution of relative humidity in measurement cross section B1



buffer samples (Villar et al. 2014a) further confirmed an average degree of saturation of approximately 98%, a range of water content between 33 and 44%, and a dry density variation between 1.24 and 1.42 g/cm³. The hydraulic conductivity proved to be in the range of 10⁻¹² m/s for all of 15 tested samples.

4.4 Seismic long-term monitoring during the early phase of the EB and during dismantling

A total of 24 seismic sensors had been installed in the rock and in the buffer to monitor the performance of the system by P-wave velocity (v_p) measurements. The measurements were performed during the first 19 months of operation of the EB (between April 2002 and November 2003). More than eight years later, prior to dismantling of the experiment, the seismic array was reactivated (Schuster 2014a). The results of the measurements are discussed on the

example of the normalised P-wave velocity evolution on a travel path of 1 m length parallel to the left wall of the niche, 38 cm in the Opalinus Clay (Fig. 14).

Reliable P-wave phases could only be detected from day 342 after closure of the niche. Earlier, strong attenuation due to a pronounced EDZ as a consequence of the construction of the EB niche precluded any reliable phase correlation. After that, v_p increased gradually by nearly 10%, which is interpreted as EDZ re-compaction/sealing. The total pressure at the interface between buffer and tunnel wall measured in the vicinity, which is also shown for comparison in Fig. 14, shows a similar evolution.

During the monitoring pause v_p increased further by 6% and continued increasing until start of dismantling. When the dismantling front approached the seismic sensors (buried 38 cm from the wall) v_p first increased slightly due to the stress concentration in the wall and then decreased with different gradients until it nearly reached the starting

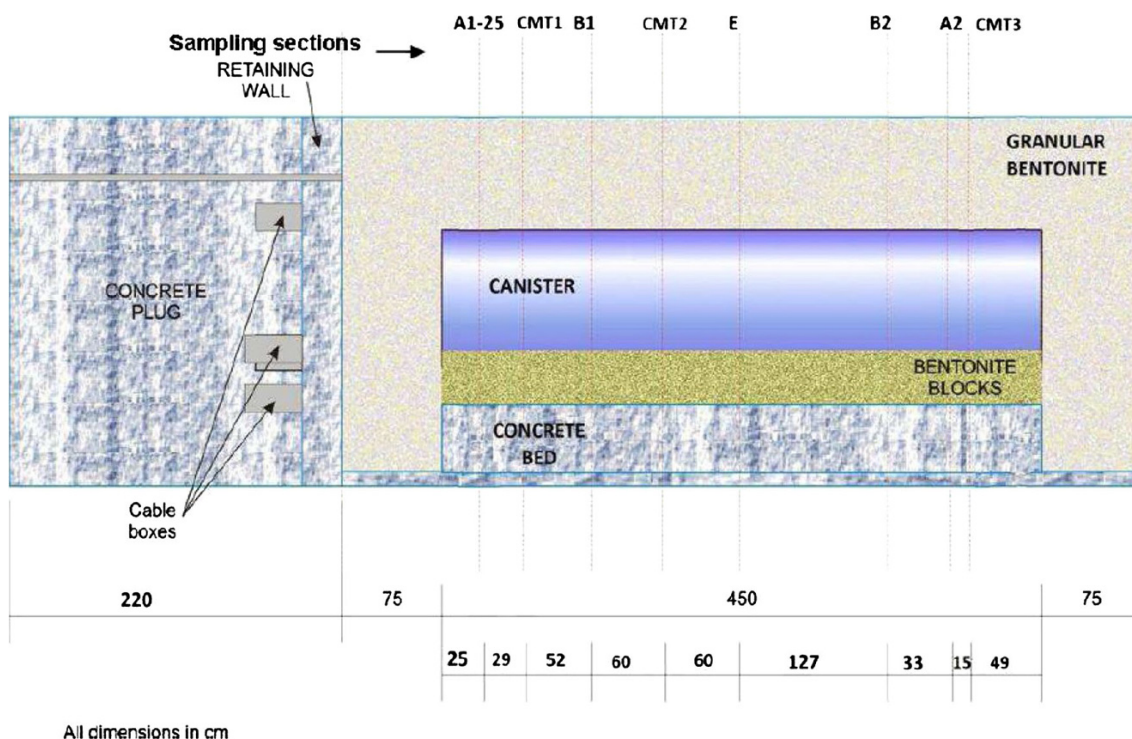


Fig. 12 EB longitudinal section showing the sampling cross sections (Palacios et al. 2013)

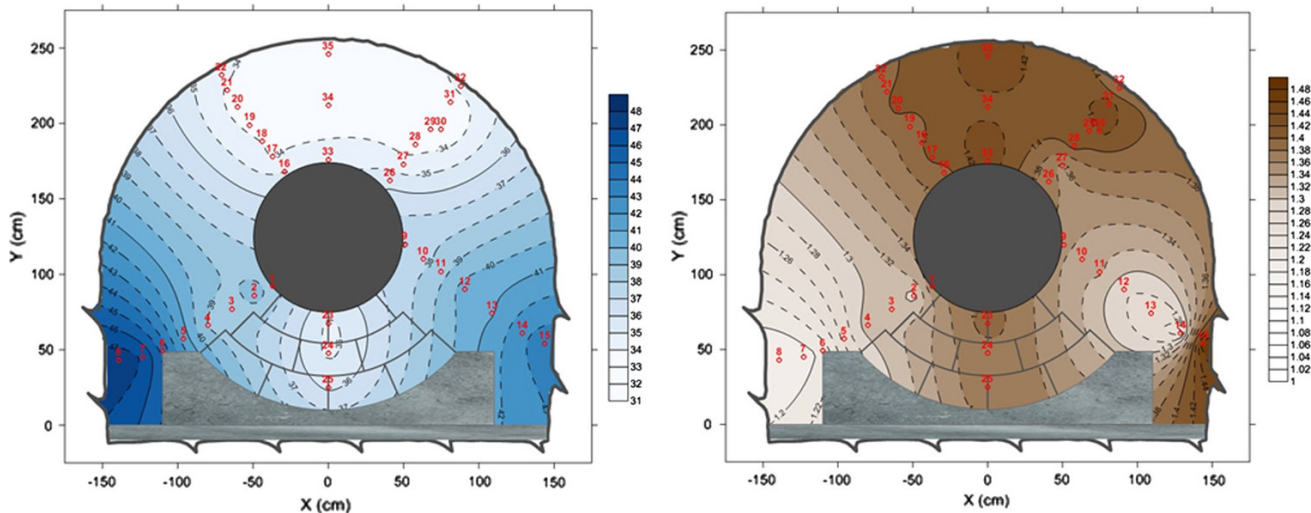


Fig. 13 Water content (left) and dry density (right) after dismantling in EB cross section B1. Red marks show the sampling locations (Palacios et al. 2013)

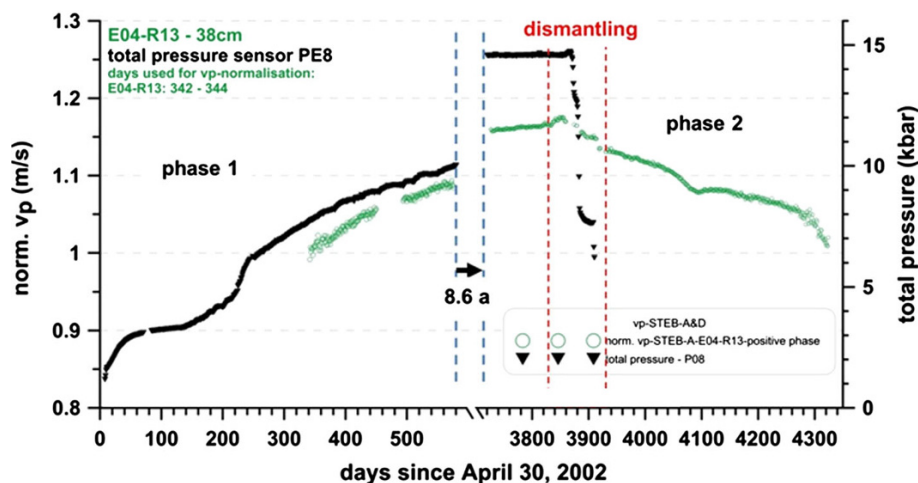
value around day 4320. This can be interpreted as a recreation of an EDZ. A similar evolution can again be observed for the total pressure which expectedly dropped when the excavation front approached.

A full cycle of a creation, sealing and recreation of an EDZ could be visualised with seismic methods. Swelling of the bentonite, together with the hydration process, resulted in a strong mechanical support of the neighbouring rock.

4.5 Conclusions of the EB

The dismantling works of the EB experiment have clearly confirmed the following significant information about a bentonite barrier (emplaced using bentonite blocks and granular bentonite) hydrated under isothermal conditions (Mayor and Velasco 2014):

Fig. 14 Normalised P-wave velocity evolution and total pressure in the EB experiment



- The hydraulic conductivity of the saturated granular bentonite is low enough (less than 5×10^{-12} m/s), even if emplaced with a relatively low average dry density (1.36 g/cm^3 in this experiment), to fall between the acceptable limits considered for this key safety indicator in the Performance Assessment of the repository concepts.
- Homogenization between the two types of bentonite emplaced (blocks and pellets) has taken place. Nevertheless, after the experiment life of more than ten years, still some heterogeneities persist through the bentonite mass: the moisture content tends to increase (and the dry density to decrease) towards the bottom of the experiment niche. This is probably due to the fact that emplacement of the granular bentonite was difficult in this case, due to the existing hydration tubes.
- The measured values of the thermal conductivity of the saturated bentonite (from 0.90 to 1.35 W/m K) are high enough to dissipate the heat generated by the waste.
- Self-sealing of the EDZ in the Opalinus Clay has been observed during the experiment, due to the swelling pressure developed in the barrier. As it could be expected, the seismic data do suggest the gradual recreation of the EDZ after dismantling.
- The dismantling has provided the opportunity to perform microbial analyses of the bentonite emplaced more than ten years before. Samples analyzed had water activities higher than 0.96; they showed relatively high culturability levels for heterotrophic aerobes and low culturable levels of sulphate reducing bacteria.
- In general, the obtained gas permeability values of the saturated bentonite are low and homogeneous (from 1×10^{-22} to $6 \times 10^{-22} \text{ m}^2$).

The controlled dismantling of the EB experiment has allowed to complement and improve the previously gained knowledge (through the available monitoring data) of the

isothermal saturation process of a full-scale bentonite barrier. It has been fully confirmed that the use of a granular bentonite material is a good option to construct bentonite barriers.

5 The SB borehole seal experiment

Depending on emplacement density and initial saturation, pure bentonite can develop very high swelling pressures and very low hydraulic conductivities after re-saturation. While these are favourable sealing properties, gas entry pressure may also be high. The idea of looking into sand/bentonite mixtures as a material for engineered barriers is to reduce cohesion and gas entry pressure to allow for discharge of corrosion gases while maintaining sufficiently low permeability to water and sufficiently high swelling pressure. The SB experiment (Rothfuchs et al. 2012) had the objective to qualify a respective barrier material. It was performed between 2003 and 2012, partially in the frame of the EC-financed ESDRED project.

5.1 The approach was to

- Determine material parameters of candidate sand/bentonite mixtures in the laboratory and select suitable compositions
- Perform scoping calculations for experiment design
- Conduct a large-scale laboratory mock-up experiment for testing installation techniques and instrumentation
- Perform an in situ experiment with four individual borehole plugs
- Perform interpretative modelling
- Dismantle the experiment and conduct post-mortem investigations

5.2 Preceding laboratory and mock-up tests

Laboratory tests were performed on mixtures of sand and calcigel, with sand/bentonite ratios of 30/70, 50/50, and 65/35. Testing comprised the determination of grain and bulk density, permeability to gas (in the dry state) and to water (in the saturated state), gas entry pressure after re-saturation, swelling pressure, saturation time and water retention curves. Favourable results were obtained with mixtures of 65/35 and 50/50 sand/bentonite ratios. At dry densities above 1.8 g/cm^3 (65/35) or around 1.7 g/cm^3 (50/50), water permeabilities at full saturation in the range of 10^{-18} m^2 and swelling pressures above 0.2 MPa were reached. Gas entry pressure for these materials was 0.4–1.1 MPa (65/35) and 0.4–2.8 MPa (50/50), respectively (Rothfuchs et al. 2012).

The mixture with 65/35 sand/bentonite ratio was chosen for two mock-up experiments in steel tubes of 300 mm diameter (Fig. 15), which represents a 1:1 scale with respect to the later in situ experiment. The test procedure was to

- Instrument the test tubes
- Determine initial installation density of the granular sand/bentonite mixture
- Determine the initial gas permeability
- Inject water from the bottom to re-saturate the seal
- Determine seal permeability to water at full saturation
- Inject gas and determine gas entry pressure and permeability after break-through
- Determine the final water content in the seal by post-mortem sampling and analysis

The results of the mock-up tests, in terms of dry density, permeability, swelling pressure, and gas entry pressure were in line with the laboratory values. It was, however, found that the time to reach full saturation was much longer than expected (29 months instead of 6 months) from scoping calculations. Water content was determined after dismantling. An average value of 18.4% was obtained.

5.3 In-situ setup and results

After successful completion of the mock-up tests, the in situ experiment was set up at the Mont Terri rock laboratory in 2005/2006 (Fig. 16). Four boreholes were installed and instrumented similarly to the mock-up tests:

- Boreholes SB1 and SB2 are equipped with 1 m long seal sections of 65/35 sand/bentonite mixture
- Borehole SB15 is equipped with an 0.5 m long seal section of 50/50 sand/bentonite mixture (sealing length was reduced due to an expected slower re-saturation with the higher bentonite content)
- Borehole SB13 is equipped with 0.5 m long seal section of pure granular sodium bentonite for comparison

Figure 17 shows some stages of the construction. The bulk densities of the seals achieved at construction are shown in Table 2. Except for SB2, they are somewhat lower than those obtained in the laboratory.

The experimental procedure followed the one described for the mock-up tests. During re-saturation of the seals it was, however, found that in both boreholes SB1 and SB15 water bypassed the seal element. This can be due to a

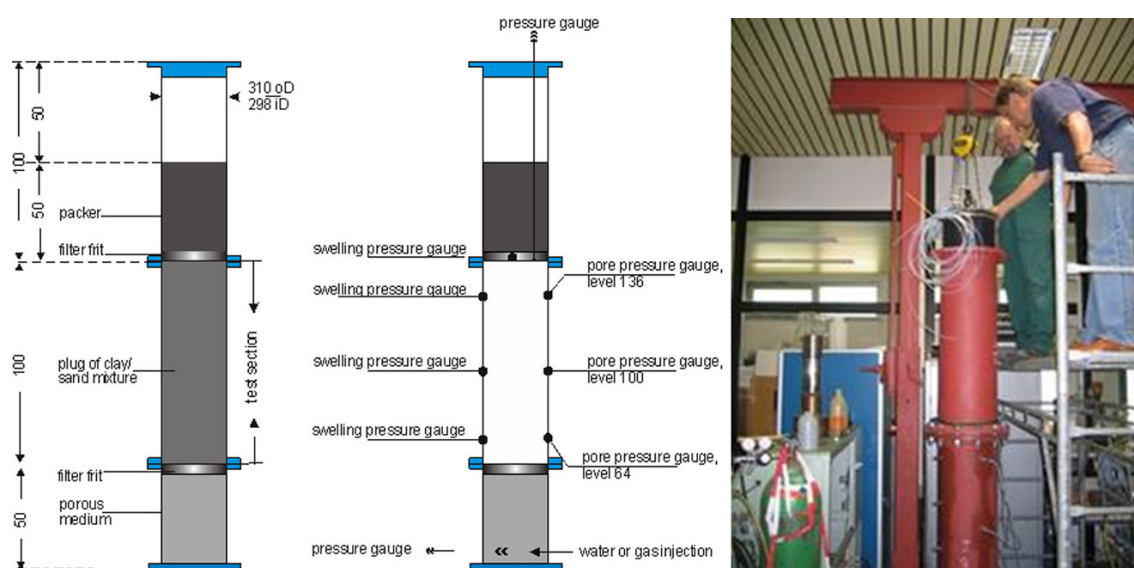


Fig. 15 Overview of SB mock-up design and instrumentation (Rothfuchs et al. 2012)

Fig. 16 Overview of SB in situ configuration. SB1 and SB2: boreholes with 65/35 sand/bentonite seal, SB15: borehole with 50/50 sand/bentonite seal, SB13: borehole with pure bentonite seal

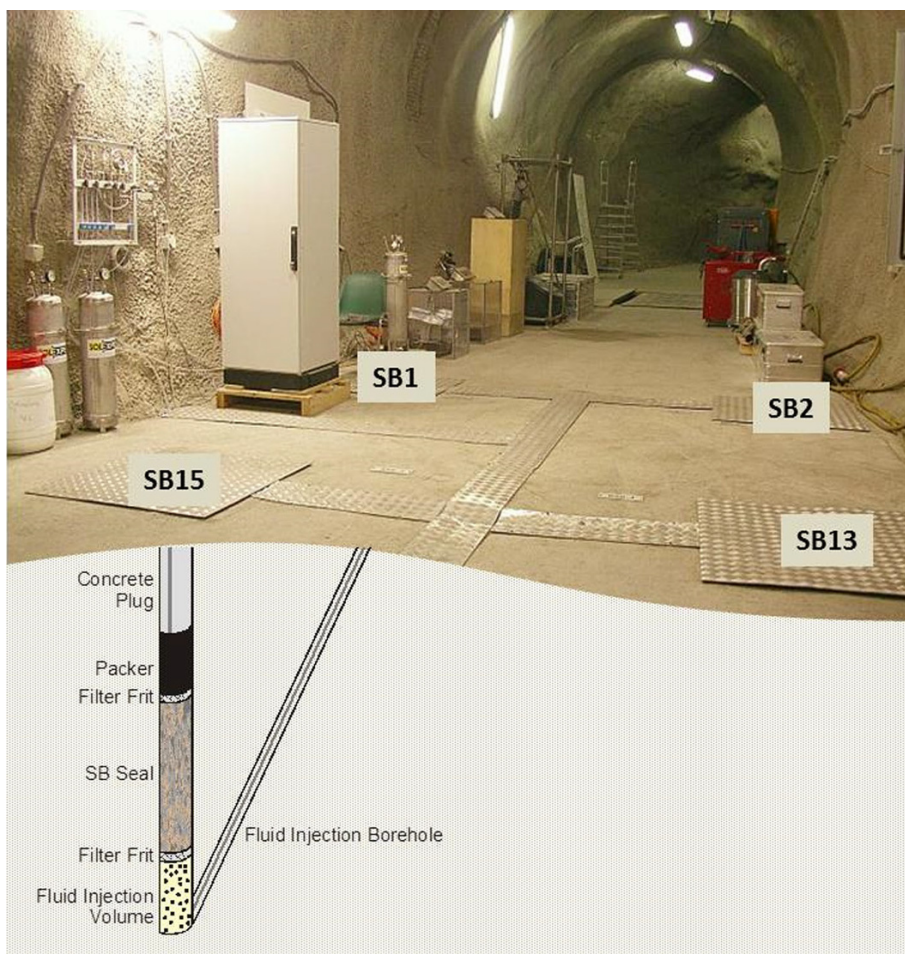


Fig. 17 View into borehole SB2 (diameter 300 mm) after emplacement of sand/bentonite mixture (*left*), after installation of the packer (*centre*), and after grouting of the borehole cellar (*right*) (Rothfuchs et al. 2012)

pronounced borehole disturbed zone (BdZ) around the boreholes and is aided by the low installation density in these boreholes—the swelling pressure is not high enough to re-compact the EDZ. Since the swelling pressure sensors in these boreholes failed, too, they could not be evaluated further.

The test in SB2 ran more successful. Between February and April 2006 the injection pressure was increased stepwise to 0.38 MPa (Fig. 18). Swelling pressure showed a

quick response and reached final values between 0.15 and 0.19 MPa within less than one year after start of injection. No outflow of water could, however, be observed even after more than 5½ years of re-saturation.

In order to investigate this problem and find a way to successfully complete the experiment, a new model simulation was performed taking into account a desaturation/pore pressure reduction in the gallery near-field which could be quantified by adjacent pore pressure

Table 2 Installation densities of the SB buffer materials (Rothfuchs et al. 2012)

	Bulk density achieved in situ (kg/m ³)	Bulk density achieved in the laboratory (kg/m ³)
SB1 (65/35)	1720	1870–1930
SB2 (65/35)	1910	1870–1930
SB13 (50/50)	1640	n. d.
SB15 (0/100)	1690	1730–1820
Mock-up Test 2 (65/35) (for comparison)		2070

measurements. The result was that the applied injection pressure was not sufficient to induce an outflow at the top of the borehole. Increasing the injection pressure to 1.1 MPa led to measureable outflow at the seal top, and a water permeability of $4.2 \times 10^{-18} \text{ m}^2$ was determined. Afterwards, gas injection resulted in a gas entry pressure of 0.45 MPa and a gas permeability at break-through around 10^{-16} m^2 . All in all, the results of this test were quite in line with the preceding laboratory and mock-up tests, showing that the sand/bentonite mixture fulfilled the requirements.

The fourth test, SB13, involved pure granular bentonite as sealing material. As could be expected, much higher swelling pressures (>3 MPa) were obtained here, although it was not possible to completely re-saturate the sealing element within the experiment time.

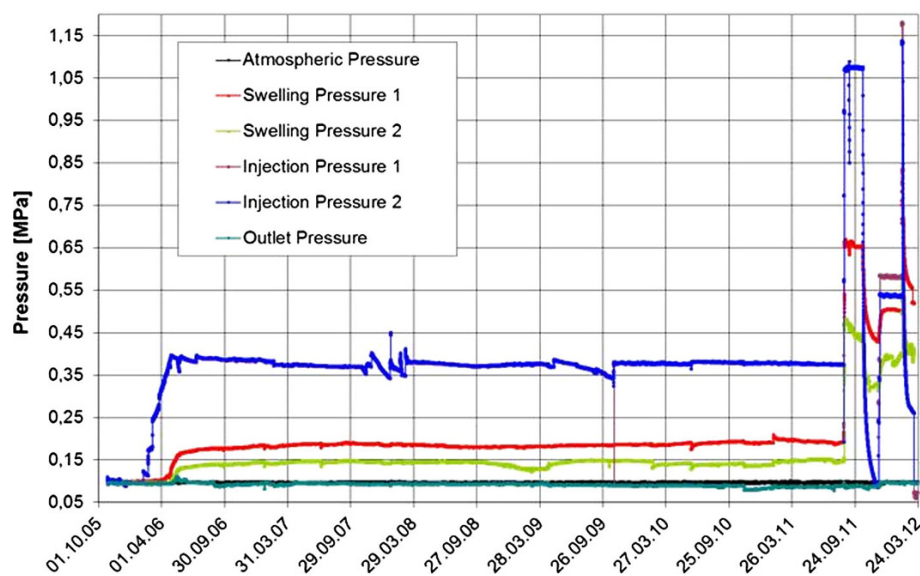
After finishing the experiment, samples were taken from all boreholes between November 2011 and March 2012. This involved retrieving of the concrete plug and the packer and drilling core holes into the seal and the

surrounding rock (Fig. 19). The samples were evaluated in terms of water content. For the samples from SB2, the water content ranges between 16.1 and 20.5%, except for the sample with higher water content. This is in good agreement with the mock-up test. For SB1 and SB15, the water content values are much higher (23–35%), as a consequence of their low emplacement density. Water content measurement of SB13 (29.8% in average) showed that the pure bentonite seal was close to full saturation.

6 Conclusions and perspective

The experiments described here illustrate the effort that is put into in situ testing of bentonite-based buffer and sealing materials. All experiments faced considerable difficulties in installation, operation or evaluation. Still, in connection with laboratory and simulation work they either were successfully completed (EB and SB) or are on a very good way (HE-E).

It was shown that the experiments could mostly be set up at the required conditions and that, if so, both the bentonite and, in case of SB, the sand/bentonite material meet the requirements and perform as expected. Thus, the in situ experiments clearly show that buffer and seal elements can be constructed in a way to meet the expectations raised by small-scale testing. It was, however, also shown that interaction with the host rock causes additional effects in the buffer or seal that cannot always be quantified or even anticipated from the experience of small-scale tests (such as re-saturation by pore-water from the rock, interaction with the excavation damaged zone in terms of preferential flow or mechanical effects), so that testing of the integral system buffer/rock or seal/rock is required.

Fig. 18 Injection pressure and swelling pressure evolution at SB2 (Rothfuchs et al. 2012)

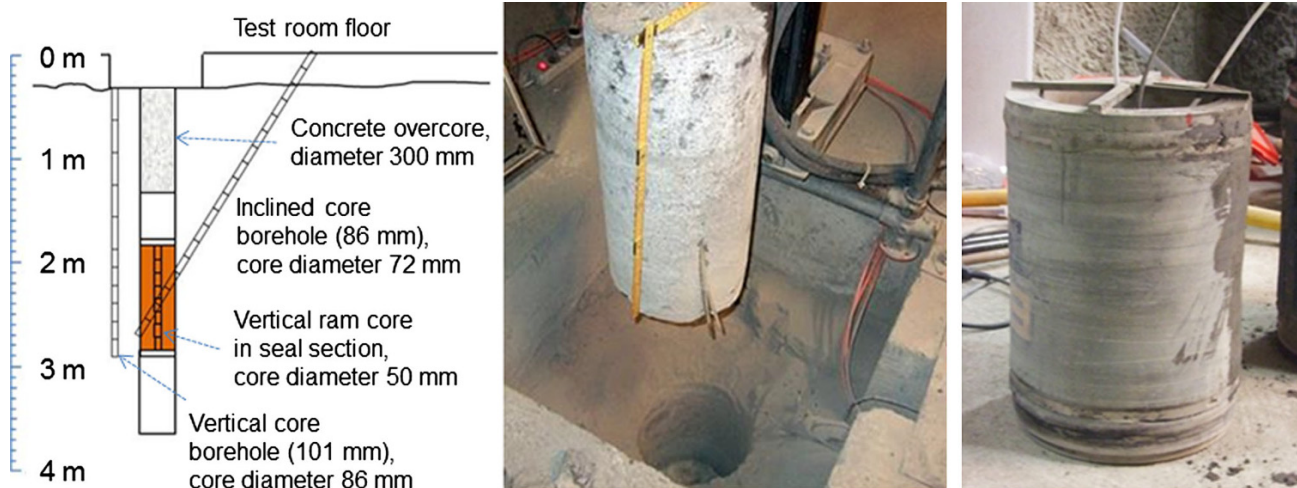


Fig. 19 Sampling overview of borehole SB2 (left), retrieved concrete plug (centre) and packer (right) (Rothfuchs et al. 2012)

All experiments show that for an adequate design and a successful evaluation, reliable model simulations are necessary. Modelling is not a topic of this paper, but detailed information can be found in another paper of this volume (Gens et al. 2017).

In-situ testing of bentonite-based materials is going on: The HE-E is still running in order to follow the slow natural buffer re-saturation, but it is also complemented by Nagra's Full-Scale Emplacement Experiment (FE) which is reported by Mueller et al. (2017). And borehole or shaft seals are planned to be further investigated at the Mont Terri rock laboratory in a new in situ experiment implementing a borehole seal in sandwich architecture, a system which was already tested in mock-up experiments (Emmerich et al. 2012).


Acknowledgements Research leading to the results presented here has received funding from the European Atomic Energy Community's fifth Framework Programme (1998–2002) under contract FIKW-CT-2000-00017, from the European Atomic Energy Community's Sixth Framework Programme (2002–2006) under contract FI6 W-CT-2004-07-20-508851, from the European Atomic Energy Community's Seventh Framework Programme (2007–2011) under grant agreement No. 249681, from the German Federal Ministry of Economics and Energy, and from the Swiss Federal Office for Education and Science. This paper has been reviewed by Michael Jobmann, DBE Technology GmbH, Peine, Germany, and by Dr. Elie Valcke, SCK.CEN, Mol, Belgium.

References

- Bossart, P., Bernier, F., Birkholzer, J., Bruggeman, C., Connolly, P., Dewonck, S., Fukaya, M., Herfort, M., Jensen, M., Matray, J.-M., Mayor, J. C., Moeri, A., Oyama, T., Schuster, K., Shigetani, N., Vietor, T., & Wiczorek, K. (2017). Mont Terri rock laboratory, 20 years of research: introduction, site characteristics and overview of experiments. *Swiss Journal of Geosciences*, 110. doi:10.1007/s00015-016-0236-1 (this issue).
- Czaikowski, O., Garitte, B., Gaus, I., Gens, A., Kuhlmann, U., & Wiczorek, K. (2012). Design and predictive modelling of the HE-E test. *PEBS Deliverable D3.2-1*. <http://cordis.europa.eu/pub/fp7/euratom-fission/docs/design-and-predictive-modeling-of-the-he-e-test.pdf>. Accessed 17 July 2014.
- Emmerich, K., Königer, F., Kemper, G., Gruner, M., Gaßner, W., Hofmann, M., et al. (2012). Semi-technical scale experiments proofed the functionality of a multi-layer hydraulic sealing system in horizontal alignment. In *5th International meeting on Clays in Natural and Engineered Barriers for Radioactive Waste Confinement*, Montpellier, France.
- Gaus, I., Garitte, B., Senger, R., Gens, A., Vasconcelos, P., García-Siñeriz, J.-L., et al. (2014). The HE-E Experiment: Lay-out, Interpretation and THM Modelling, Combining D2.2-11 and D3.2-2 of the PEBS Project. *Nagra Arbeitsbericht NAB 14-53*, Nagra, Wettingen, Switzerland. <http://www.nagra.ch>.
- Gens, A., Wiczorek, K., Gaus, I., Garitte, B., Mayor, J.C., Schuster, K., et al. (2017). Performance of the Opalinus Clay under thermal loading. Experimental results from Mont Terri rock laboratory (Switzerland). *Swiss Journal of Geosciences*, 110. doi:10.1007/s00015-016-0258-8 (this issue).
- Mayor, J. C., García-Siñeriz, J. L., Alonso, E., Alheid, H.-J., & Blümling, P. (2007a). Engineered barrier emplacement experiment in Opalinus Clay for the disposal of radioactive waste in underground repositories. In P. Bossart, & C. Nussbaum (Eds.), *Mont Terri Project—Heater Experiment, Engineered Barrier Experiment and Ventilation Experiment* (pp. 115–179). Report of the Swiss Geological Survey No. 1, Federal Office of Topography (swisstopo), Wabern, Switzerland. <http://www.mont-terri.ch>.
- Mayor, J. C., García-Siñeriz, J. L., Velasco, M., Gómez-Hernández, J., Lloret, A., Matray, J.-M., et al. (2007b). Ventilation Experiment in Opalinus Clay for the disposal of radioactive waste in underground repositories. In P. Bossart, & C. Nussbaum (Eds.), *Mont Terri Project—Heater Experiment, Engineered Barrier Experiment and Ventilation Experiment* (pp. 115–179). Report of the Swiss Geological Survey No. 1, Federal Office of Topography (swisstopo), Wabern, Switzerland. <http://www.mont-terri.ch>.
- Mayor, J. C. & Velasco, M. (2014). EB dismantling synthesis report. *PEBS Deliverable D2.1-8*. http://www.pebs-eu.de/PEBS/EN/Downloads/downloads_node_en.html.
- Mueller, H.R., Garitte, B., Vogt, T., Koehler, S., Sakaki, T., Weber, H., et al. (2017). Implementation of the full-scale emplacement

- (FE) experiment at the Mont Terri rock laboratory (Switzerland). *Swiss Journal of Geosciences*, 110. doi:10.1007/s00015-016-0251-2 (this issue).
- Nussbaum, C., Kloppenburg, A., Caër, T., & Bossart, P. (2017). Tectonic evolution around the Mont Terri rock laboratory, northwestern Swiss Jura: constraints from kinematic forward modelling. *Swiss Journal of Geosciences*, 110. doi:10.1007/s00015-016-0248-x (this issue).
- OECD-NEA (2001). The role of underground laboratories in nuclear waste disposal programmes. Nuclear energy agency, NEA No. 6433, Paris, France.
- OECD-NEA (2008). Moving Forward with Geological Disposal of Radioactive waste—A collective Statement by the OECD/NEA Radioactive Waste Management Committee (RWMC). *Nuclear energy agency, NEA No. 6433*, Paris, France.
- Palacios, B., Rey, M., & García-Siñeriz, J. L. (2013). Engineered barrier experiment in opalinus clay: “EB” experiment—as-built of dismantling operation. *PEBS Deliverable D2.1-4*. http://www.pebs-eu.de/PEBS/EN/Downloads/downloads_node_en.html.
- PEBS (2012). The early evolution of the EBS in safety assessments. *PEBS Deliverable D1.1/D1.2*. http://www.pebs-eu.de/PEBS/EN/Downloads/downloads_node_en.html.
- Rothfuchs, T., Czaikowski, O., Hartwig, L., Hellwald, K., Komischke, M., Mieke, R., et al. (2012). Self-sealing Barriers of sand/bentonite mixtures in a clay repository - SB Experiment in the Mont Terri Rock Laboratory. *Final Report, Gesellschaft für Anlagen- und Reaktorsicherheit (GRS) MbH, GRS-302*. Gesellschaft für Anlagen- und Reaktorsicherheit (GRS) mbH, Köln, Germany.
- Schäfers, A., Gaus, I., Johnson, L., Liu, Y., Mayor, J. C., Sellin, P., et al. (2014). PEBS final scientific report. *Deliverable D5-16 of the PEBS project*. http://www.pebs-eu.de/PEBS/EN/Downloads/downloads_node_en.html.
- Schuster, K. (2014a). Engineered barrier emplacement experiment in opalinus clay: “EB” experiment. EDZ seismic results—Seismic transmission measurements. *PEBS Deliverable D2.1-6*. http://www.pebs-eu.de/PEBS/EN/Downloads/downloads_node_en.html.
- Schuster, K. (2014b). Seismic data report on EDZ and EBS evolution (HE-E). *PEBS Deliverable D2.2-10*. http://www.pebs-eu.de/PEBS/EN/Downloads/downloads_node_en.html.
- Teodori, S.-P., & Gaus, I. (2012). Report of the construction of the HE-E experiment. *PEBS Deliverable D2.2-3*. http://www.pebs-eu.de/PEBS/EN/Downloads/downloads_node_en.html.
- Vasconcelos, R., Pinyol, N., Alonso, E., & Gens, A. (2014). Modelling and interpretation of the EB experiment hydration & Interpretation of the final state of the EB experiment barrier. *Deliverable D3.1-1 and D3.1-2*. http://www.pebs-eu.de/PEBS/EN/Downloads/downloads_node_en.html.
- Villar, M. V., Campos, R., Gutiérrez-Nebot, L. (2014a). EB experiment—laboratory post-mortem analyses report. *PEBS Deliverable D2.1-7*. http://www.pebs-eu.de/PEBS/EN/Downloads/downloads_node_en.html.
- Villar, M. V., Martín, P. L., & Romero, F. J. (2014b). Long-term THM test reports: THM cells for the HE-E test: update of results until February 2014. *PEBS Deliverable D2.2-7.3*. http://www.pebs-eu.de/PEBS/EN/Downloads/downloads_node_en.html.
- Wiczorek, K., Mieke, R. (2013). Thermal Characterisation of HE-E Buffer. *Deliverable D2.2-9*. http://www.pebs-eu.de/PEBS/EN/Downloads/downloads_node_en.html.

Performance of the Opalinus Clay under thermal loading: experimental results from Mont Terri rock laboratory (Switzerland)

Antonio Gens¹  · Klaus Wiczorek² · Irina Gaus³ · Benoit Garitte³ · Juan Carlos Mayor⁴ · Kristof Schuster⁵ · Gilles Armand⁶ · José Luis García-Siñeriz⁷ · Thomas Trick⁸

Received: 22 April 2016 / Accepted: 22 December 2016 / Published online: 16 February 2017
© Swiss Geological Society 2017

Abstract The paper presents an overview of the behaviour of Opalinus Clay under thermal loading as observed in three in situ heating tests performed in the Mont Terri rock laboratory: HE-B, HE-D and HE-E. The three tests are summarily described; they encompass a broad range of test layouts and experimental conditions. Afterwards, the following topics are examined: determination of thermal conductivity, thermally-induced pore pressure generation and thermally-induced mechanical effects. The mechanisms underlying pore pressure generation and dissipation are discussed in detail and the relationship between rock damage and thermal loading is examined using an additional in situ test: SE-H. The paper concludes with an

evaluation of the various thermo-hydro-mechanical (THM) interactions identified in the heating tests.

Keywords Temperature effects · In situ tests · Coupled THM phenomena · Numerical analyses · Heating tests · Pore pressures · Nuclear waste disposal

1 Introduction

Opalinus Clay has been selected in Switzerland as the preferred host rock for disposal of high-level nuclear waste. In this context, the behaviour of Opalinus Clay is being intensively investigated in the Mont Terri rock laboratory, an international project that has been ongoing since 1996. Figure 1 shows the geological profile of the site. The exothermic nature of high-level radioactive waste requires studies that target the performance of Opalinus Clay under non-isothermal conditions so that the impact of heat on the geological barrier becomes well understood.

The behaviour of an indurated mudstone, such as Opalinus Clay, under thermal loading has to be considered in the framework of thermo-hydro-mechanical (THM) couplings as the various THM phenomena interact. Thus, temperature variations will impact hydraulic behaviour due to the generation of pore pressures and the variation of fluid viscosity and will affect the mechanical behaviour through the development of thermally-induced strains. Hydraulic and mechanical behaviour may interact with the thermal response through induced variations of thermal conductivity. Heat convection is also a potential effect of hydraulic behaviour on the temperature field although it is generally negligible in a low permeability medium. Figure 2 shows a scheme indicating the relationship between the most relevant thermal, hydraulic and mechanical

Editorial handling: P. Bossart and A. G. Milnes.

This is paper #13 in the Mont Terri Special Issue of the Swiss Journal of Geosciences (see Bossart et al. 2017, Table 3 and Fig. 7).

✉ Antonio Gens
antonio.gens@upc.edu

José Luis García-Siñeriz
jgarciasineriz@amberg.es;
<http://www.amberg.es>

- ¹ Universitat Politècnica de Catalunya, Jordi Girona 1-3, 08034 Barcelona, Spain
- ² GRS, Theodor-Heuss-Straße 4, 38122 Brunswick, Germany
- ³ Nagra, Hardstrasse 73, 5430 Wettingen, Switzerland
- ⁴ Enresa, Emilio Vargas 7, 28043 Madrid, Spain
- ⁵ BGR, Stilleweg 2, 30655 Hannover, Germany
- ⁶ Andra, 1 Rue Jean Monnet, 92290 Châtenay-Malabry, France
- ⁷ AMBERG INFRAESTRUCTURAS S.A., Avda. de la Industria 37-39, 28108 Alcobendas, Madrid, Spain
- ⁸ Solexperts, Mettlenbachstrasse 25, 8617 Mönchaltorf, Switzerland

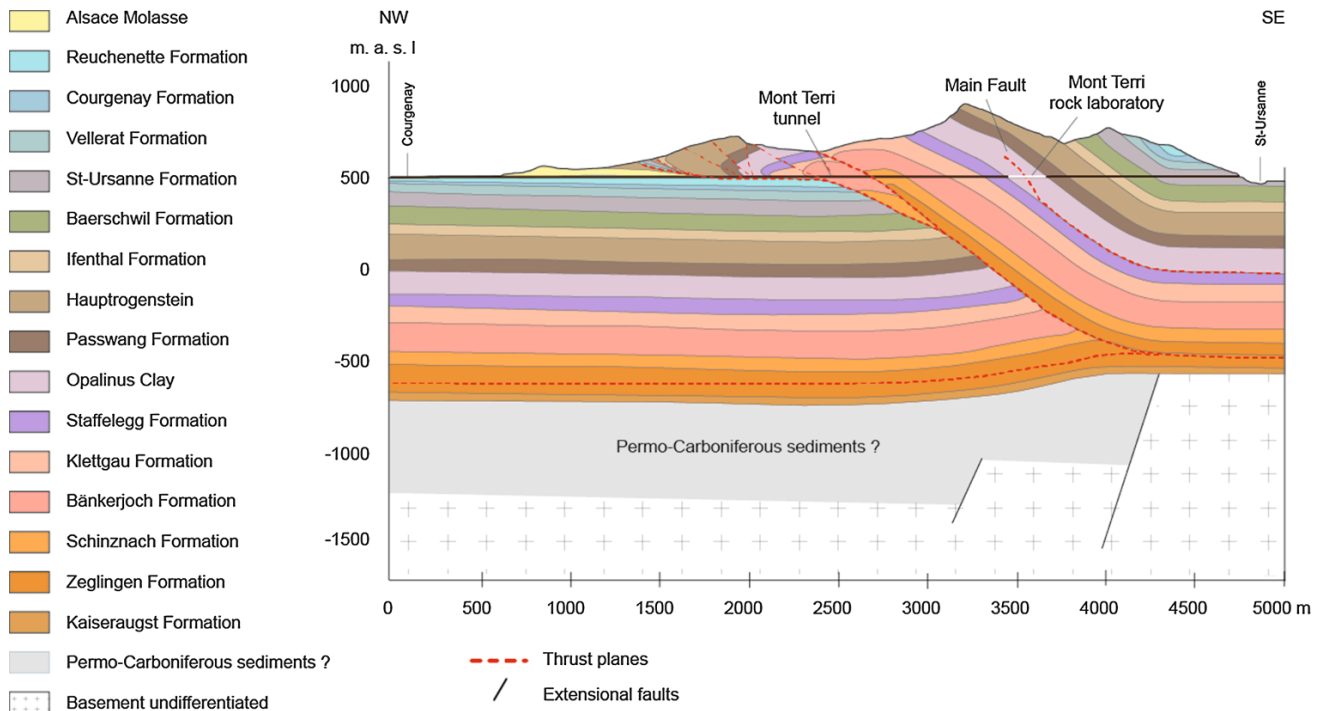
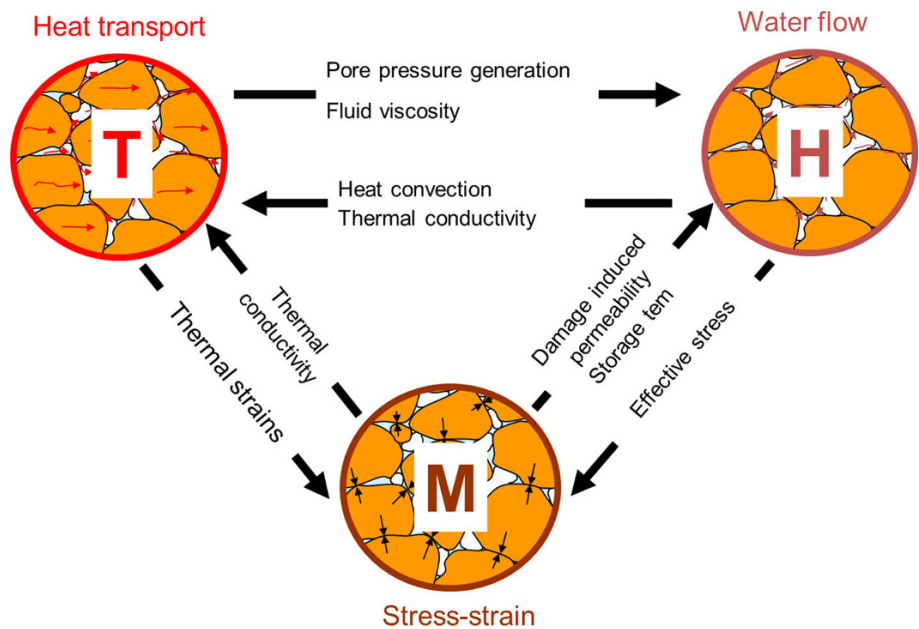


Fig. 1 Geological profile of the Mont Terri rock laboratory site

Fig. 2 Coupled thermo-hydro-mechanical (THM) phenomena



phenomena where the hydromechanical interactions have also been included. As discussed later, not all the interactions have the same level of significance.

To examine the thermal behaviour of Opalinus Clay as well the associated coupled THM effects, a number of thermal in situ tests have been performed in the Mont Terri rock laboratory: HE-B (initially called HE), HE-C, HE-D, HE-S, SE-H, HE-E and FE. Some of them, such as HE-E and FE, are still ongoing. There have also been projects

involving only small-scale tests such as LT (Laboratory temperature testing) and TH-A (microscale THMC). More details are given in Wileveau et al. (2008).

This paper focuses on the behaviour of Opalinus Clay under thermal loading as observed in three main heating field tests: HE-B, HE-D and HE-E that are summarily described first. Afterwards, the results of those in situ tests are reviewed in order to examine more closely the behaviour of Opalinus Clay under thermal loading. Specifically,

the following aspects are discussed: thermal conductivity, pore pressure generation (thermo-hydraulic coupling) and mechanical effects such as strain development and thermally-induced damage. The paper concludes with a discussion on the coupled THM phenomena as observed in Opalinus Clay.

2 The main in situ heating tests

The three Mont Terri rock laboratory in situ heating tests considered are: HE-B, HE-D and HE-E. They encompass a variety of features concerning the geometrical setting, presence and type of backfill, maximum temperature and heating duration. Table 1 contains the main characteristics of the tests whereas Fig. 3 shows their location in the Mont Terri rock laboratory. At the Mont Terri rock laboratory, the overburden height varies between 250 and 320 m. Opalinus Clay is intensively bedded; the closely-spaced bedding planes dip at an angle of approximately 45° at the laboratory location. All tests have been performed in the shaly facies of Opalinus Clay.

2.1 The HE-B experiment

The HE-B experiment involved placing a heater of 0.1 m diameter and 2.02 m long in a 300 mm diameter vertical borehole. The borehole was 7.5 m deep and was drilled in a niche excavated for this purpose. The heater was surrounded by a compacted clay barrier made up of ring-shaped Febex bentonite blocks with a dry density of 1.8 g/cm³. 19 boreholes were drilled in the niche floor to install sensors to measure temperature, relative humidity, total stresses, pore pressures, displacements and electrical resistivity. Devices to determine gas and water release were also installed in the boreholes. The layout of the main

borehole containing the heater and the distribution of the monitoring boreholes in the niche are depicted in Fig. 4.

Before heating was started, the barrier was hydrated artificially for 35 months using synthetic Pearson water (similar in chemical composition to the water present in the Opalinus Clay). Afterwards heating was applied during a 18th month period. Once a maximum temperature of 100 °C was reached in the bentonite, heater power was adjusted in order to keep that maximum temperature constant. The heating period of the experiment spanned from February 2002 to the end of August 2003. At the end of the heating period, the heater was switched off and, after 1 month cooling period, the test was dismantled. Geotechnical, hydraulic and seismic field tests were performed at the end of the test and a number of rock samples were retrieved for testing in the laboratory. A full description of the test has been presented in Göbel et al. (2007), only some representative results are shown here.

Figure 5 shows the distribution of temperatures of the rock (at the central section of the heater) at different times of the heating test. It can be observed that, although a 100 °C temperature was applied by the heater, the maximum rock temperature only reached about 40 °C and dropped rapidly with distance. This is the consequence of the layout of the test (a single heater borehole) and the insulating nature of the bentonite barrier. In spite of the modest increase in temperature, significant pore pressures develop in the Opalinus Clay (Fig. 6). A fast initial development of pore pressures followed by a more gradual dissipation can be observed. The final sudden pore pressure drop is due to the cooling period that followed the switching off of the heater. Higher temperatures in borehole BHE-19 (located at 0.65, from the central borehole axis) give rise to higher pore pressures than those measured in borehole BHE-20 located 2 m away and subjected, therefore, to lower temperatures.

Table 1 Features of the main in situ heating tests performed in the Mont Terri rock laboratory

Experiment	HE-B (HE)	HE-D	HE-E
Borehole/tunnel	Vertical	Horizontal	Horizontal
Borehole/tunnel diameter (m)	0.3	0.3	1.3
Heater/liner diameter (m)	0.1	0.3	0.3
Heater length (m)	2.02	2 × 2	2 × 4
Max. heater temperature (°C)	100	100	140
Backfill thickness (m)	0.1	–	0.5
Backfill material	Compacted blocks (Febex bentonite)	–	Granular bentonite (MX80, MX80 + sand)
Backfill hydration	Artificial	–	Natural
Heating duration	18 months	11 months	Long term
Heating period	February 2002–August 2003	March 2004–February 2005	June 2011–?

Fig. 3 Location of the main heating tests performed in the Mont Terri rock laboratory

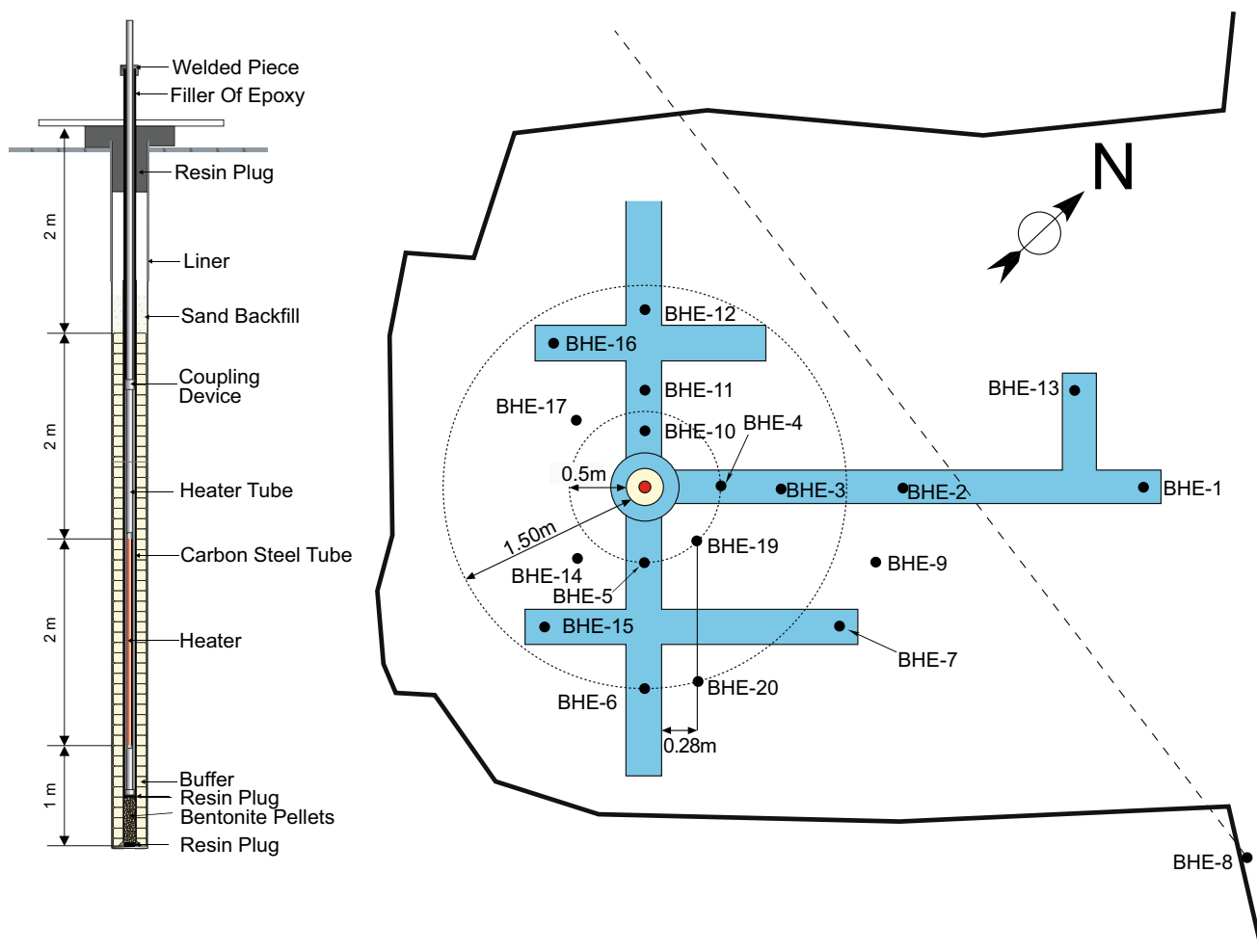
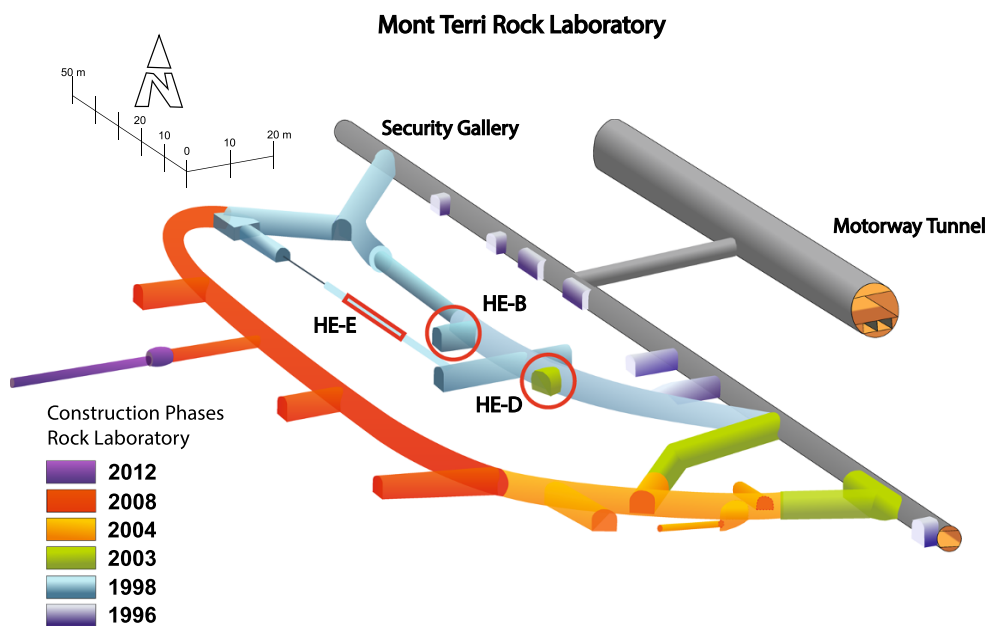


Fig. 4 Central borehole layout and location of the central and instrumentation boreholes in the niche. Experiment HE-B

Fig. 5 Distributions of Opalinus Clay temperatures at various times during the heating period. Experiment HE-B

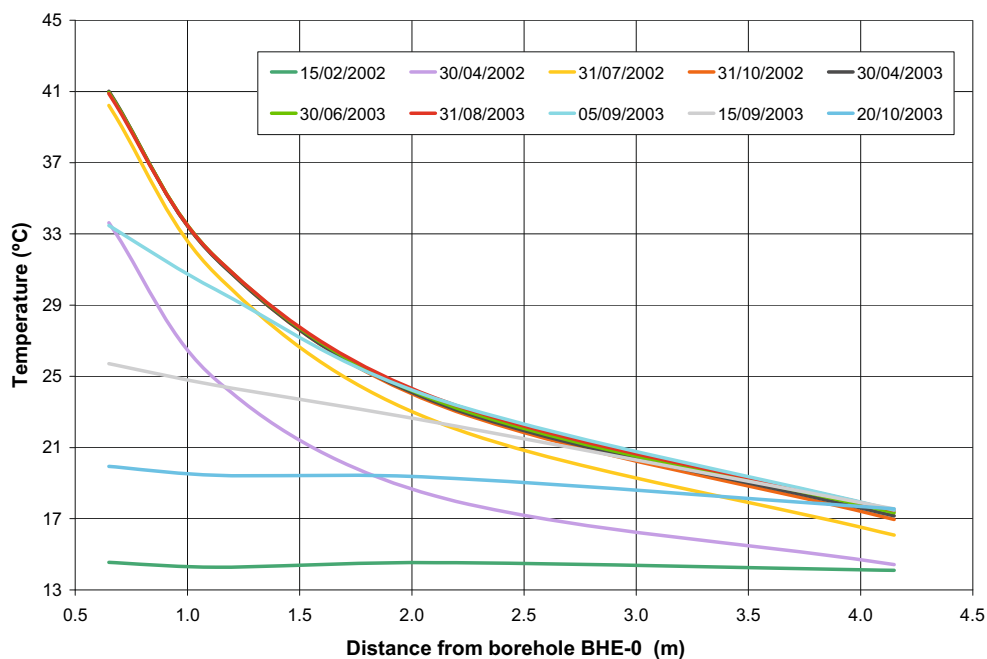
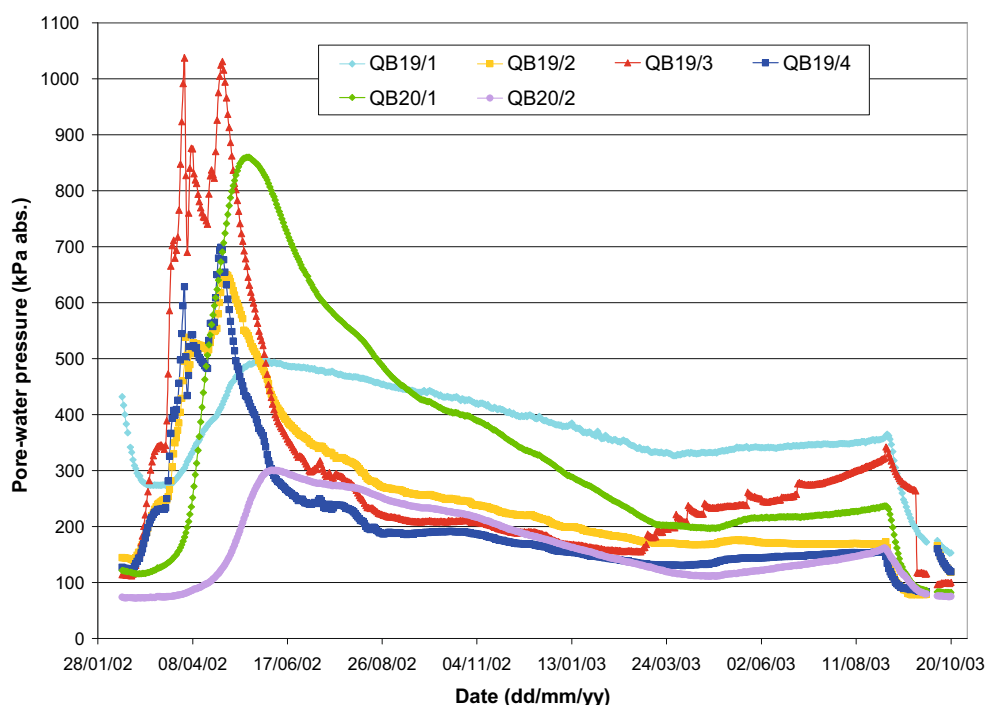


Fig. 6 Thermal-induced pore pressures in Opalinus Clay measured in boreholes BHE-19 and BHE-20 (see Fig. 3). Experiment HE-B



2.2 The HE-D experiment

To perform the in situ heating test HE-D a niche was also excavated off Gallery 98 from which a 30 cm diameter borehole (D0) was drilled horizontally up to a total length of 14 m. A location was selected away from previous experiments in order to test intact rock properties. In the section close to the end of the borehole, two heaters were installed. The heaters were 2 m long

and their separation was 0.8 m. In this case, there was no bentonite barrier and the heaters were in direct contact with Opalinus Clay. To achieve a good contact with the rock, the heaters were pressurized to 1 MPa. In addition, a number of auxiliary boreholes have been constructed to install a variety of instruments for monitoring the test. Figure 7 shows a top view of the test area. A horizontal test layout was chosen in order to have a largely uniform lithology.

Temperatures were measured along two boreholes drilled (D1 and D2) from the niche HE-D. However, perhaps the most relevant observations were those combining measurements of temperatures and pore pressures at the same point in order to relate directly the two variables. This was achieved in borehole D3 (drilled parallel to the heater borehole) and in a series of small diameter boreholes (D7 to D17) drilled from the MI niche. The pore pressure measurements of sensors located below the main borehole were quite successful but the pore pressure probes located above the main borehole exhibited a rather slow response attributed to difficulties encountered in de-airing the sensor area. Finally, sliding micrometer tubing was installed in boreholes D4 and D5 to measure incremental deformations at 1 m intervals. Special care was taken to ensure accuracy in the direction and length of the instrumentation boreholes to guarantee the correct location of the sensors. All instruments were in place before the drilling of the main borehole containing the heaters. In this way, hydro-mechanical effects during excavation could also be recorded. Full information on the test is given in Wileveau (2005).

Approximately 1 month after installation and pressurization, the heaters were switched on with a total power of 650 W (325 W per heater). The heaters were then left

under constant power during 90 days. Afterwards the power was increased threefold, to 1950 W (975 W per heater) and maintained at that level for 248 days more. The heating period lasted from March 2004 to February 2005. At the end of the second heating stage, the heaters were switched off and the clay was allowed to cool down. Temperatures, pore pressures and deformations were measured throughout. Examples of the observations obtained are shown in Figs. 8 and 9 in terms of evolution of temperatures and pore pressures at different distances from the heaters. The pattern of results is similar to that of the HE-B experiment but the increase of pore pressure is now significantly higher as a result of the different test design.

2.3 The HE-E experiment

The HE-E experiment has been installed in a section of the 1.3 m diameter and 50 m long microtunnel excavated in 1999 using the raised-boring technique. The same section of the microtunnel had been used previously for a ventilation test (VE). The layout of the experiment is shown in Fig. 10. Two 4 m-long heaters have been used separated by a plug. Heater 1 is surrounded by an engineer barrier composed of granular MX-80 bentonite made up of pellets with a mean diameter 1 mm approximately and sits on a bed of MX-80 compacted blocks. The dry bulk density of the granular bentonite as placed is 1.46 g/cm^3 and the dry density of the blocks is 1806 g/cm^3 . The arrangement of Heater 2 is the same except that the granular material used in the barrier is a mixture of sand and MX-80 bentonite. The resulting dry density of the granular sand/pellet mixture is 1.50 g/cm^3 . No artificial hydration is used for saturating the engineered barrier, so water uptake by the bentonite will be very limited due to the low permeability of the Opalinus Clay.

Extensive instrumentation was used to monitor the progress of the test in the following locations: (1) the heater surface where the temperature is controlled, (2) the engineered barrier and the interface with the Opalinus Clay (temperature and relative humidity), (3) the Opalinus Clay close to the microtunnel using the sensors from the VE test (temperature, humidity, water pressure and displacement), and iv) the Opalinus Clay at distances ranging from 2 to 6 m from the microtunnel (pore pressures). This test is fully described in Gaus et al. (2014).

The heating stage started at the end of June 2011 and it is still ongoing at present as this experiment is intended as a long-term test. Heating power was gradually raised over a period of one year approximately until reaching a maximum temperature on the heater surfaces of $140 \text{ }^\circ\text{C}$. From that moment on, heater power has been adjusted to keep this control temperature constant. Figure 11 shows the recorded evolution of heater power. The observed difference between

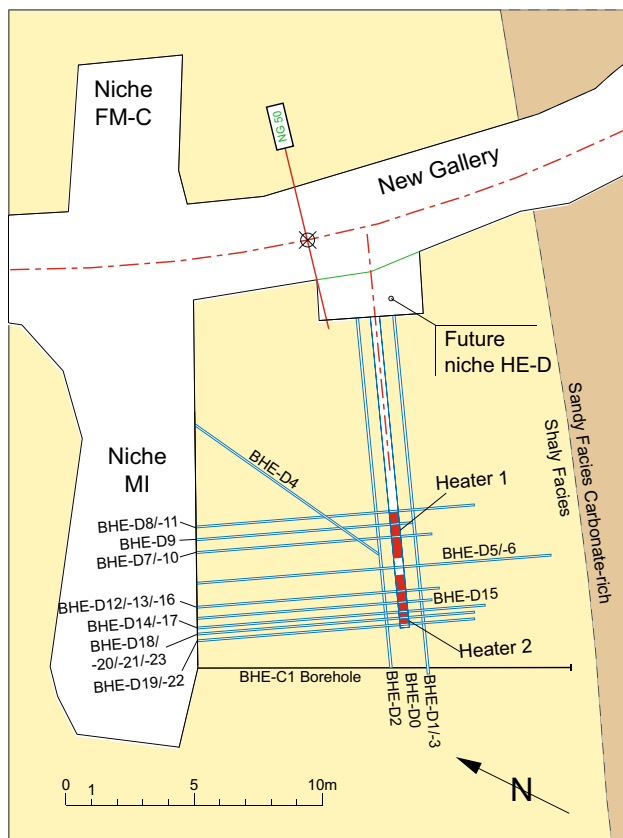


Fig. 7 Schematic layout of the in situ test HE-D. Locations of observations boreholes are shown

Fig. 8 Evolution of temperature at different distances of the heater axis. Experiment HE-D

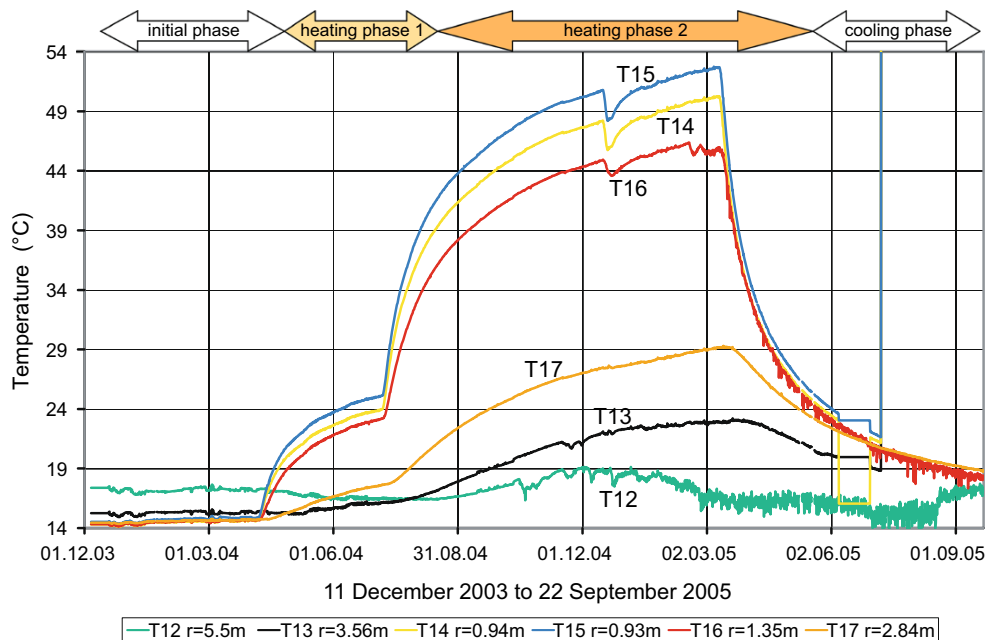
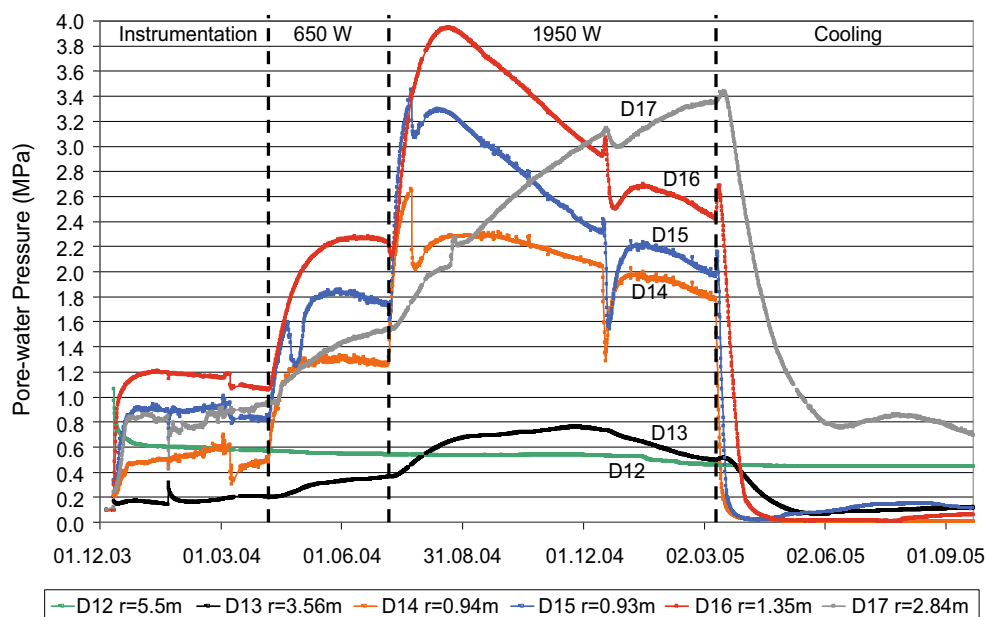


Fig. 9 Evolution of thermally-induced pore pressures at different distances of the heater axis. Experiment HE-D



the two heaters is due to the different thermal conductivities of the two materials used for the engineered barriers. The evolution of the temperatures in Opalinus Clay close to heater 1 is presented in Fig. 12. It can be seen that close to the tunnel/barrier interface, the temperature has reached 90 °C but it drops sharply as the distance to the tunnel increases. Figure 13 shows the evolution of thermally-induced pore pressures at distances ranging from 3.5 to 5.5 m. It can be observed that at the end of the period considered, pore pressure reduction is not apparent yet.

The HE-E test has a number of novel features such as a temperature higher than 100 °C, natural hydration and

granular bentonite used in the engineered barrier, enlarging in this way the range of conditions under which the response of Opalinus Clay has been observed. In spite of the differences between the three tests, the basic characteristics of the response are quite similar so that they can be used to derive some general observations on the non-isothermal behaviour of Opalinus Clay, as described in the following sections. The main effort is placed in the analysis of the HE-D test as it is not affected by the presence of an engineered barrier and the behaviour of the Opalinus Clay can be observed in a more direct manner.

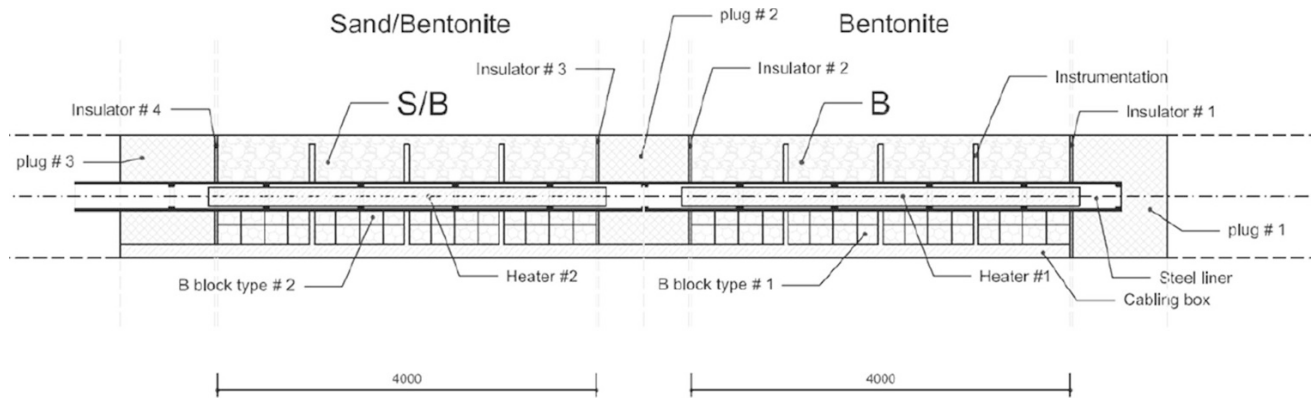


Fig. 10 Schematic layout of the HE-E experiment

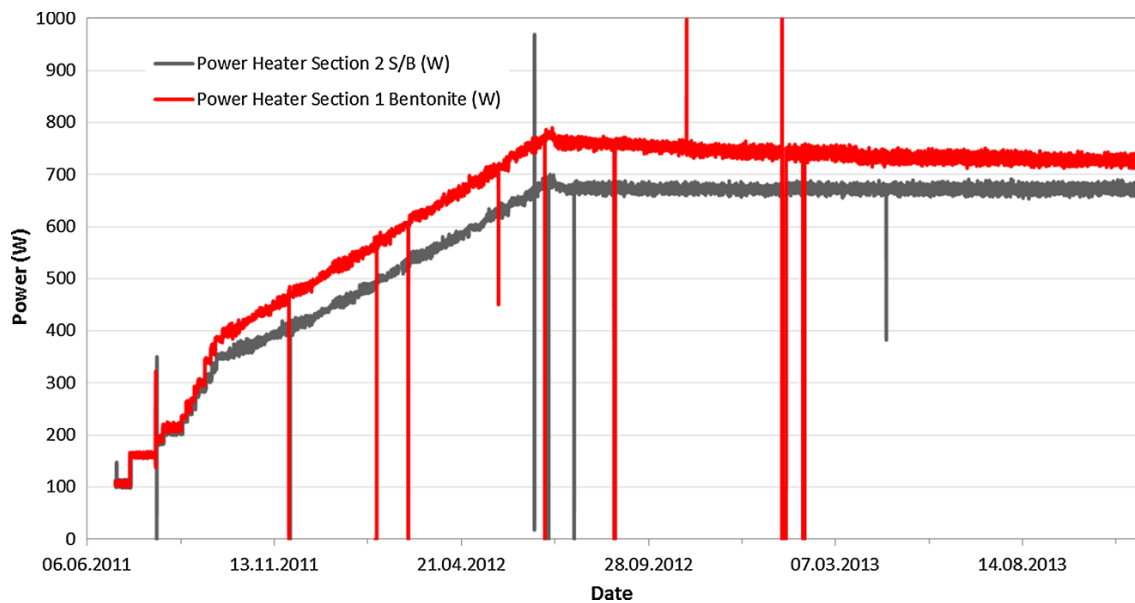


Fig. 11 Evolution of the heater power in HE-E experiment

3 Thermal conductivity

The low permeability of Opalinus Clay ensures that the heat transport by advection is negligible; conduction is the only relevant heat transfer mechanism. Therefore, the thermal field is basically controlled by the value of thermal conductivity, λ , the coefficient that links, in Fourier's law, the conductive flux, \mathbf{i}_c , to the gradient of temperature, T :

$$\mathbf{i}_c = \lambda \nabla T \quad (1)$$

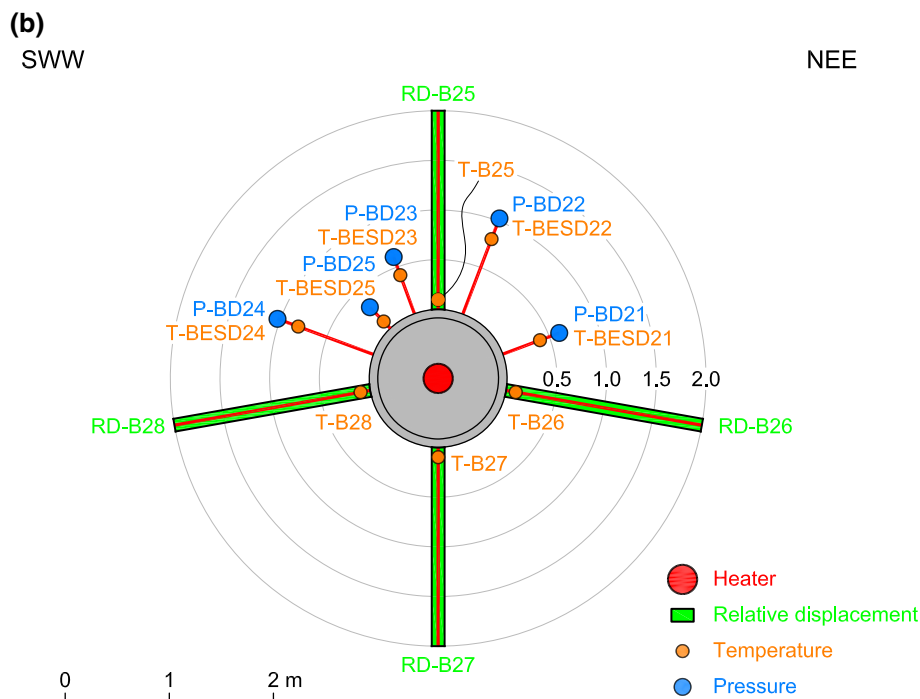
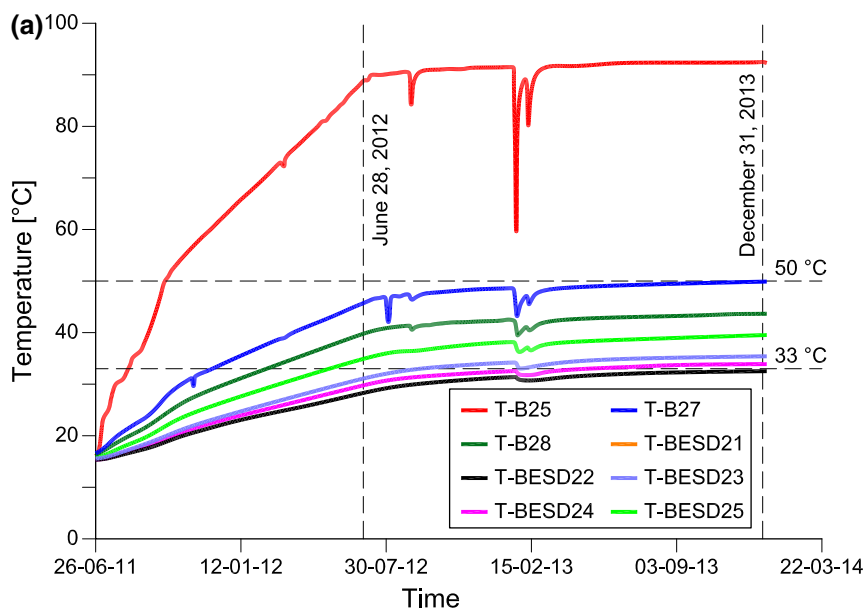
Although tests HE-B and HE-E have been analysed assuming an isotropic thermal conductivity (Göbel et al. 2007; Gaus et al. 2014), it is well established that thermal conductivity of Opalinus Clay is anisotropic (Bossart 2008) exhibiting different values in the directions normal and parallel to bedding. With the coordinates aligned adequately, Eq. (1) becomes:

$$\mathbf{i}_c = \begin{bmatrix} \lambda_{par} & 0 & 0 \\ 0 & \lambda_{par} & 0 \\ 0 & 0 & \lambda_{per} \end{bmatrix} \cdot \nabla T \quad (2)$$

where λ_{par} and λ_{per} are the thermal conductivity values in the bedding plane and in the perpendicular direction, respectively.

If a sufficient number of temperature measurements are available, it is in principle possible to estimate the thermal conductivity values from a backanalysis of an in situ heating test. Because the thermal problem is largely independent of the hydromechanical one, performing a purely thermal analysis suffices. However, as demonstrated by Garitte et al. (2014), there are pitfalls if a conventional backanalysis is performed in which a least square criterion is applied blindly to the ensemble of all the results giving the same weight to all of them. Such conventional analysis can easily provide biased results depending on the sequence of observation times considered as well as on the location of the sensors.

Fig. 12 Evolution of temperatures in Opalinus Clay in the vicinity of Heater 1. HE-E experiment



In this context, the analysis of a synthetic case consisting of a heat point source has provided key insights. This problem has an analytical solution (Booker and Savvidou 1985) that can be applied to anisotropic thermal conductivity conditions using an equivalent thermal conductivity (Carslaw and Jaeger 1946):

$$\lambda_0 = \sqrt[3]{\lambda_{par} \cdot \lambda_{par} \cdot \lambda_{per}} \tag{3}$$

Figure 14 shows the thermal conductivity parameter pairs that provide a good agreement (i.e. an error of less

than 2%) with the analytical solution. It can be noted that the combination of the thermal parameters vary depending on the time at which the backanalysis is performed. The Figure clearly indicates that short term and long term observations provide different information on the combinations of λ_{par} and λ_{per} that provide a good representation of the results. Therefore, to identify independently the two thermal conductivity values, it is essential to combine the short term and the long term observations in an appropriate manner. Building on those observations,

Fig. 13 Evolution of thermally-induced pore pressures in Opalinus Clay. HE-E experiment

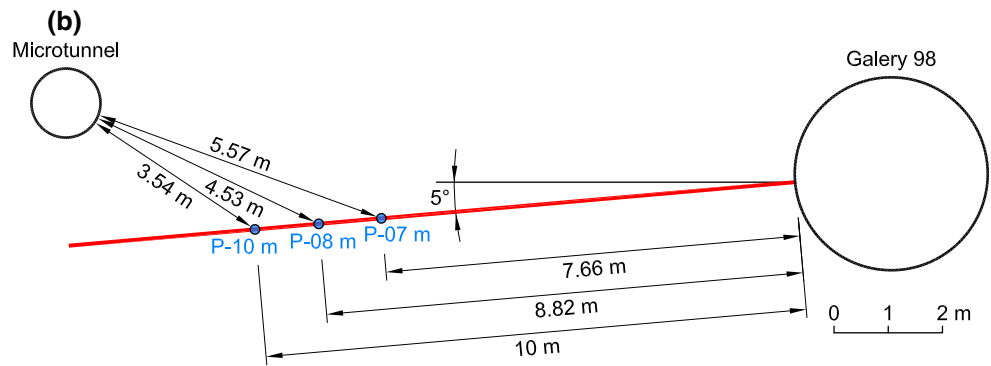
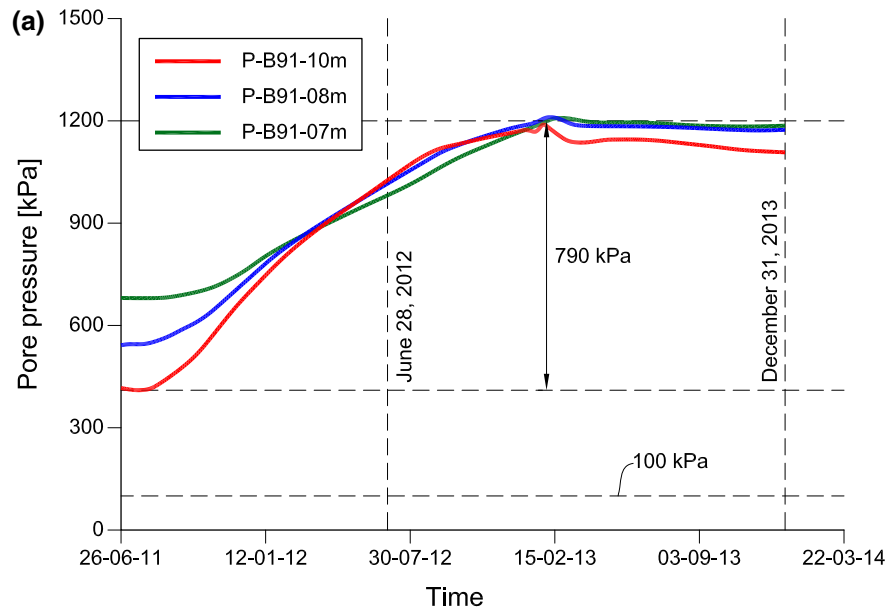
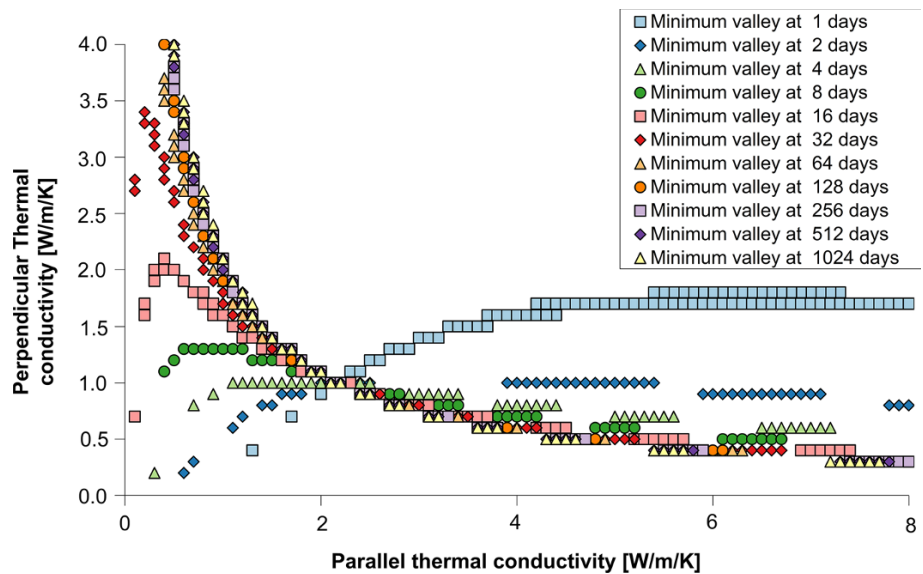


Fig. 14 Thermal conductivity pairs that result in an error of less than 2% computed at different times since the start of heating. Point heat source case



the following procedure was recommended (Garitte et al. 2014):

1. 3D analyses of the experiment considered are performed using different thermal conductivity pairs covering a wide range. 3D analyses are required to take into account anisotropy.
2. Values of thermal conductivity minimizing the difference between observations and calculations are obtained for each individual sensor and for each heating phase. The determination of the pair of thermal conductivity values is performed from the combination of short term and long term data. Outliers are removed from the backanalysis.
3. An overall value of thermal conductivities is obtained from the average of all the sensors. If there are significantly different numbers of sensors aligned parallel and perpendicular to the bedding planes, the average of each orientation will be computed first and a final overall value will be obtained from the average of the sensors at the two different orientations.

The analyses for the synthetic case also allowed identifying the effects of experimental uncertainties in sensor location, power input, temperature measurements and specific heat. For instance, if there is a significant difference between the thermal conductivities computed from sensors parallel and perpendicular to bedding planes, it is an indication of uncertainty in the heating power that may then be adjusted accordingly.

The procedure just outlined has been applied to the observations of the HE-D test. The results are shown in Fig. 15 (Garitte et al. 2014). It can be noted that the parallel sensors and the perpendicular sensors tend to indicate different thermal conductivity pairs. Some power loss was

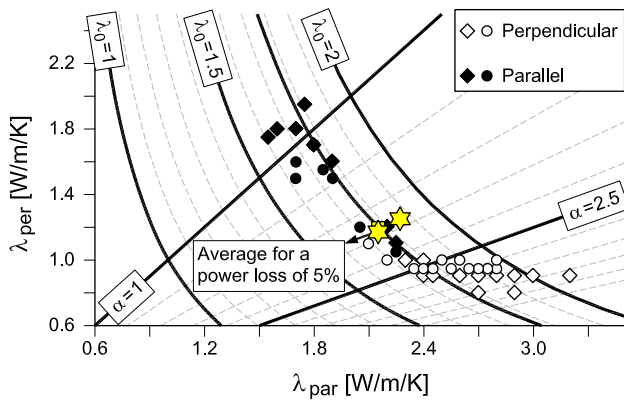


Fig. 15 Best fitting thermal conductivity pairs for different sensors in the HE-D test. The stars indicate the average thermal conductivity values for two different hypotheses of heating power. The parameter α in the figure indicates anisotropy ratio; the curves corresponding to constant values of equivalent thermal conductivity, λ_0 , are also shown

assumed as a possible explanation for this kind of pattern and a second analysis was accordingly performed. Diamond dots indicate the analysis in which no power loss was applied and circle dots indicate the best-fitting thermal conductivity pairs determined in an analysis considering a power loss of 5%. Due to the differences between the two sensor groups and to the fact that more perpendicular sensors were available in the HE-D experiment, the averages of the perpendicular sensors and of the parallel sensors are done first and then the final average is computed. In this way, the best estimates for the thermal conductivity are: $\lambda_{\text{par}} = 2.15 \text{ W/m K}$ and $\lambda_{\text{per}} = 1.2 \text{ W/m K}$, an anisotropy ratio of 1.8. Those values are remarkably close to those obtained in the laboratory (Bossart 2008). It is also interesting that the backcalculated values for all sensors tend to cluster close to a value of equivalent thermal conductivity of about $1.8 \text{ W/m}^{\circ}\text{K}$.

4 Thermally-induced pore pressure generation

In Opalinus Clay, the main hydraulic phenomenon associated with thermal effects is the generation of pore pressure due to changes of temperature. When Opalinus Clay (and other argillaceous rocks) is subjected to a temperature increase, the pore pressure will also increase due to the fact that the thermal expansion of the water is larger than that of the porous skeleton itself. The low permeability of Opalinus Clay ensures that the resulting excess pore pressure does not dissipate rapidly. As a matter of fact, quite a number of interactions underlie this pore pressure generation phenomenon; they are best viewed by considering the water mass balance equation:

$$n \frac{D_s \rho_w}{Dt} + \frac{\rho_w}{\rho_s} \cdot (1 - n) \cdot \frac{D_s \rho_s}{Dt} + \rho_w \cdot \nabla \cdot \frac{d\mathbf{u}}{dt} + \nabla \cdot (\rho_w \cdot q_l) = 0 \quad (4)$$

where n is the porosity, ρ_w and ρ_s are the water and solid densities respectively, t is time, \mathbf{u} are displacements and q_l is Darcy's liquid velocity. D_s denotes material derivative.

Equation (4) can be further developed taking into account the variation of the liquid and solid densities that, with some simplifications, are assumed to be given by:

$$\rho_w = \rho_{w0} \cdot \exp[\beta_w(p_l - p_{l0}) + b_w(T - T_{ref})] \quad (5)$$

$$\rho_s = \rho_{s0} \cdot \exp[\beta_s(p_s - p_{s0}) + 3 \cdot b_s \cdot (T - T_{ref})] \quad (6)$$

where β_w and β_s are the water and solid compressibilities, respectively, and b_w and b_s are the volumetric and linear thermal expansion coefficient for water and the solid phase, respectively. p_l is the liquid pressure, p_s is the solid pressure, and T is temperature.

Then Eq. (4) becomes:

$$[n \cdot b_w + (1 - n) \cdot 3 \cdot b_s] \cdot \frac{D_s T}{Dt} + n \cdot \beta_w \cdot \frac{D_s p_l}{Dt} + (1 - n) \cdot \beta_s \cdot \frac{D_s p_s}{Dt} + \nabla \cdot \frac{d\mathbf{u}}{dt} + \frac{\nabla \cdot (\rho_w \cdot \mathbf{q}_l)}{\rho_w} = 0 \quad (7)$$

The generation and dissipation of pore pressure in the clay due to a temperature change can be more readily understood examining Eq. (7). The first term arises from the differential thermal expansion of solid and liquid phases. The second and third terms are the volume changes of water and solid phase associated with a pore pressure and solid pressure change; the fourth term is the volume change of the material skeleton (that includes contributions from stresses, pore pressures and temperature) and the fifth term corresponds to the flow of water in or out of the clay element considered. The interplay of all those phenomena results in the generation of pore pressure and its evolution with time.

Interesting insights can be obtained examining a typical evolution of temperature and pore pressure as presented in Fig. 16. It was recorded in borehole D3 (Fig. 7) with the sensors located 1.1 m away from the axis of the heater in the direction of the bedding planes. It can be observed that pore pressures react immediately to heating, exhibiting a very strong response. Increments of 2.25 MPa are measured at this particular location; this is a magnitude similar to the estimated minor principal stress in the area. It is also interesting to note that the evolutions of temperature and pore pressures do not coincide. Pore pressure reaches a maximum at a particular time and then it decreases in spite of the fact that temperature continues to rise. This is the result of the interplay between the generation of pore pressures due to thermal action and the dissipation of pore

pressures due to consolidation. At this particular location, dissipation by liquid-flow overcomes the temperature increase effects in the later stages of the experiment.

A numerical three-dimensional coupled THM analysis was performed so that the anisotropy of the material (thermal conductivity and stiffness) and of the in situ stress system could be incorporated in the calculations. Due to the special characteristics of Opalinus Clay, a constitutive model that tries to account for the fact that the microstructure of the material is a combination of clay matrix and cementing bonds have been used (Vaunat and Gens 2003a, b). A full description of the numerical modelling of the in situ test as well as the parameters used is presented in Gens et al. (2007).

Figure 17 presents, for a number of points of the clay, the comparison between the results of the 3D analysis and the observations in terms of pore pressure increases. The results of two companion axisymmetric analyses have also been added for reference. The maximum pore pressure increase is largely well captured and the evolution of pore pressure is also well reproduced with the exception of borehole D17 located further away from the heaters. The pore pressure rise obtained in the computations in the first heating stage is faster than the observed one. This could be due to a slow response of the pore pressure sensors; it can be noted that in the second stage, when the piezometers are likely to be fully saturated, the observed and computed rate of pore pressure increase appear to be the same.

In Fig. 17, it can also be noted that the time at which the maximum pore pressure increase is calculated becomes larger as the distance to the main borehole increases. This is a consequence of the combined effect of the movement of the temperature rise outwards and of pore pressure dissipation from the inner zones. Computed pore pressure distributions on a section perpendicular to the main

Fig. 16 Evolution of temperature and pore pressure in borehole D3 during the HE-D test

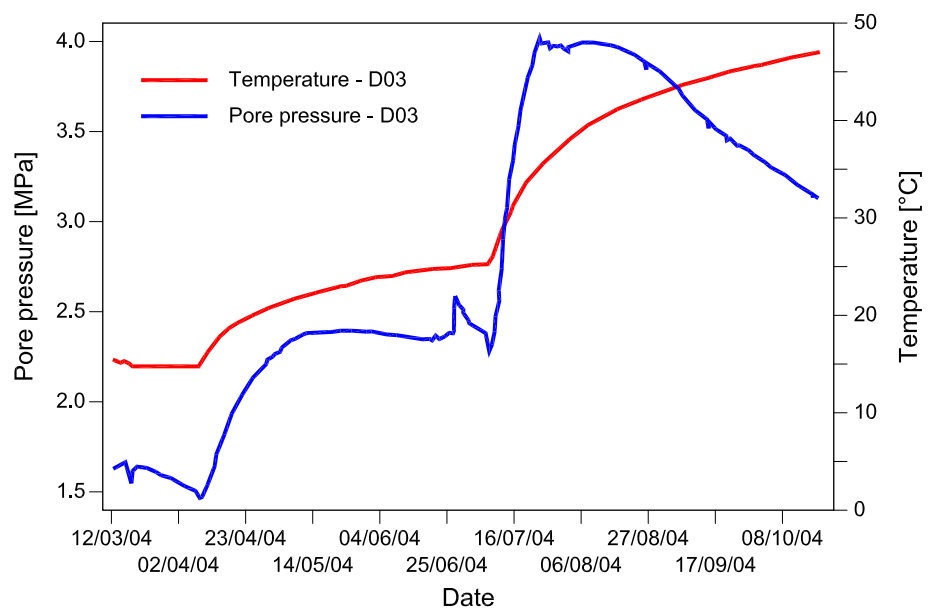
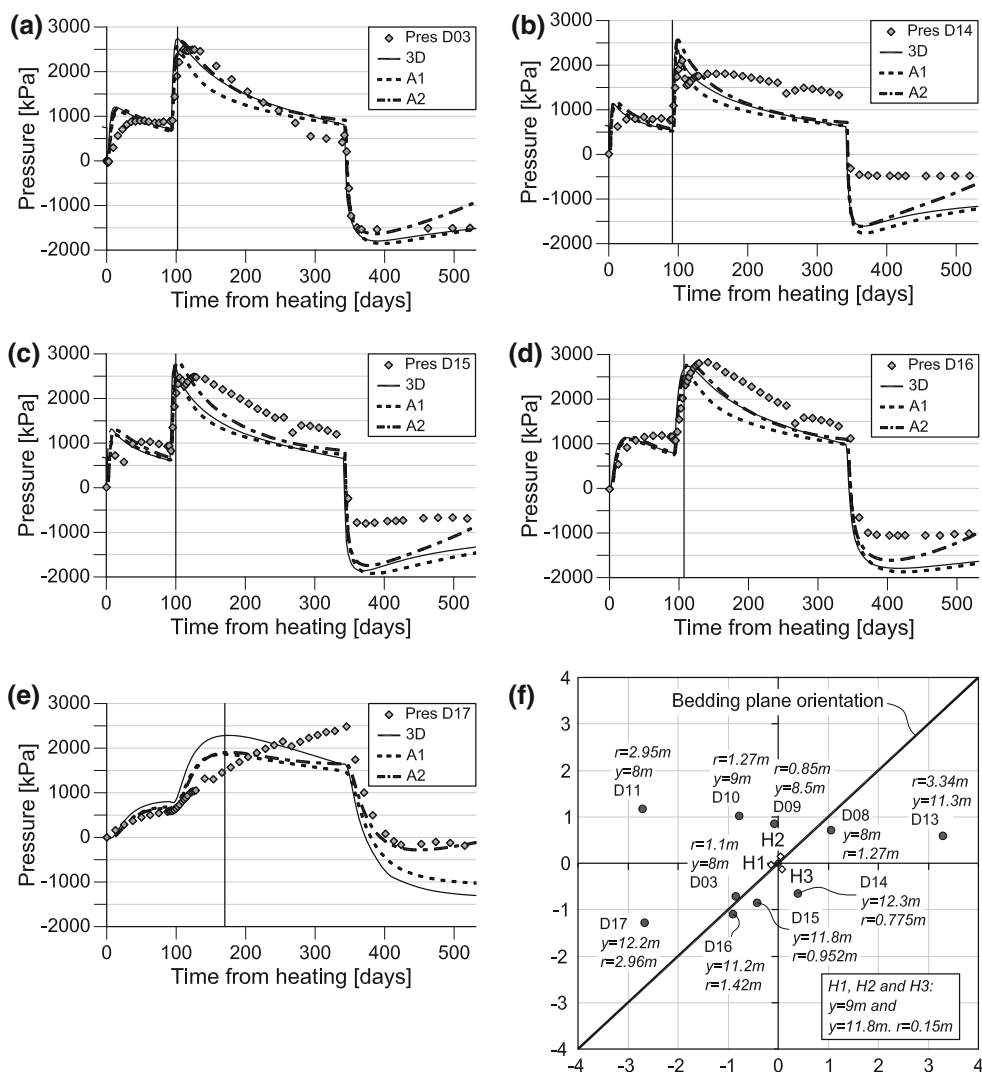


Fig. 17 Evolution of pore pressure increments at various points in the Opalinus Clay during the HE-D test. Observations and computed results **a** Borehole D03, **b** Borehole D14, **c** Borehole D15, **d** Borehole D16, **e** Borehole D17, **f** Sensor location



borehole and located between the two heaters are plotted for various times in Fig. 18. They correspond to two perpendicular directions; one along the bedding plane direction and the other one along a direction normal to the bedding. The differences that can be observed between the distributions in the two directions are not caused by hydraulic effects (permeability was assumed isotropic) but they arise from the different temperature rise brought about by the anisotropy of thermal conductivity.

The anisotropy and the evolution of pore pressures can also be observed in the contours of equal pore pressure presented in Fig. 19 where the displacement with time of the maximum of pore pressure away from the main borehole can be observed. The Figure also shows that the cooling associated with the switching off of the heaters produces a reduction in pore pressure, the counterpart of the pore pressure rise during heating.

Availability of a successfully validated numerical model allows the performance of a series of sensitivity analyses to

explore the potential effects of a number of parameters and, in this way, improve the understanding of the mechanisms causing the thermally-induced generation of pore-water pressures. The values of Young’s modulus, Biot coefficient, solid compressibility, thermal expansion coefficients and thermal conductivity have been varied over a rather wide range. In all cases, the effect on the generated pore pressures was found to be either modest or negligible (Gens et al. 2007).

The effect of intrinsic water permeability is however very significant. This is not surprising because the magnitude of the pore pressure generated results from a competition between the effects of differential thermal expansion of liquid and clay skeleton and the dissipation of pore pressures, the rate of which is controlled basically by the value of rock permeability. The results of sensitivity analyses with values of intrinsic permeability varying in the plausible range (for Opalinus Clay) of 10^{-19} to 10^{-20} m² (the reference value is 5×10^{-20} m²) are shown in Fig. 20a. The

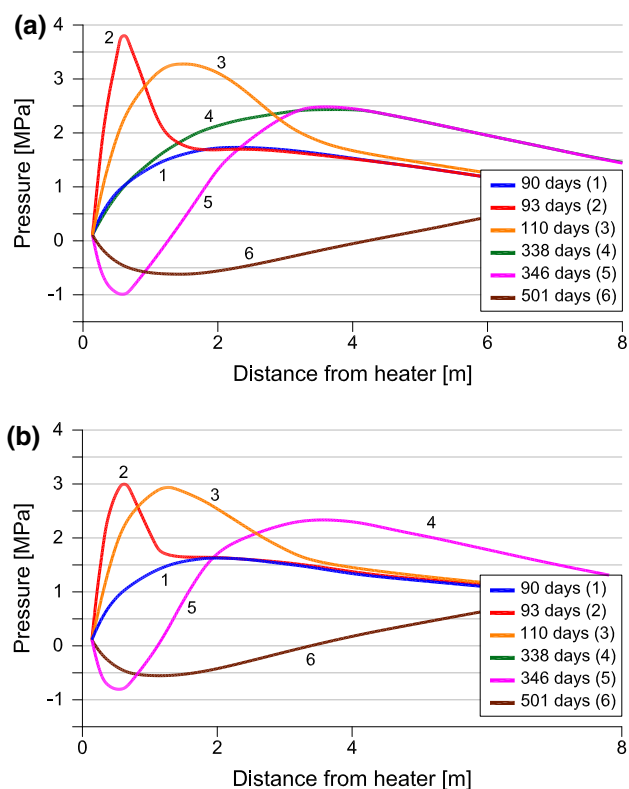


Fig. 18 Computed pore pressure increment distributions at various times on a section across Heater 2 in the HE-D test. **a** Bedding plane direction. **b** Perpendicular to bedding plane direction

effect on generated pore pressures is large. Because of the weight of this parameter in the global behaviour of the test, two additional analyses have been performed using intrinsic permeabilities of 10^{-23} and 10^{-16} m² to correspond to practically undrained and practically drained conditions. As Fig. 20b shows, in the very low permeability case there is an extremely large increase of pore pressures that tracks closely the temperature evolution; dissipation is practically negligible and undrained conditions predominate. In contrast, Fig. 20b also shows that in the very large permeability case no pore pressure generation is observed since pore pressure dissipation dominates throughout. It should be noted that although Opalinus Clay is a low permeability material, pore pressure dissipation plays a critical role with respect to the magnitude of the pore pressures generated by thermal action. If there were no dissipation, pore pressures would reach values above 12 MPa in the rock close to the heater.

5 Thermally-induced mechanical effects

Mechanical effects result from the joint action of temperature changes and pore pressure generation and dissipation. They can be perceived from the measurements of relative displacements in boreholes D4 and D5 performed using a

sliding micrometer (Fig. 7). Borehole D5 was drilled at a direction approximately normal to the main borehole containing the heaters; the deformations measured at various times are plotted in Fig. 21. It can be observed that in the region around the heaters, extension deformations occur, but they become compressive strains at locations further away from the heater. The volume increase of the clay close to the heater, driven by thermal expansion, produces compression in the outer zones. The evolution of strains of some selected intervals of borehole D5 is shown in Fig. 22 together with the computed results from the analyses. A thermal expansion coefficient of $1.4 \times 10^{-5} \text{ K}^{-1}$ has been adopted, following Auvray (2004). A first observation is the very small magnitude of the strains (and hence displacements) measured and computed, consistent with the high stiffness and modest thermal expansion exhibited by Opalinus Clay.

In borehole intervals close to the heater (e.g. intervals 6–7, 7–8 and 8–9 of borehole D-5) dilatant strains are observed in response of the temperature increase; the two heating stages can be easily recognized. In contrast, in borehole intervals away from the heater (e.g. intervals 11–12 and 12–13), compressive strains are measured in the initial stages due to the expansion of the inner regions of the test. As the temperature increase field spreads out with time, the rock expands and dilatant strains are observed and computed. In spite of some scatter of the observations (due to the small magnitudes being measured), the numerical analyses capture satisfactorily the main patterns of behaviour.

Unfortunately, no direct observations of damage in terms of permeability variations were obtained in test HE-D. So, the potential effect of heating on rock damage could not be assessed. However, another in situ heating test, SE-H, was subsequently performed as part of the TIMODAZ project (Li et al. 2001). Heating was applied by circulating water at a high temperature through a packer-isolated section of a 76 mm diameter borehole installed in the shaly facies of Opalinus Clay. A number of hydraulic tests were performed in an adjacent borehole interval. It was found that after a temperature increase to about 65 °C, intrinsic permeability reduced by a factor of 4. So no adverse effects in terms of rock damage appear to result from an increase of temperature, rather the opposite.

6 Concluding remarks

The understanding of the behaviour of Opalinus Clay under thermal loading has been much advanced by the performance and study of a number of in situ heating tests: HE-B, HE-D and HE-E. Those tests cover a wide range of test layouts and conditions. In spite of this, the observed

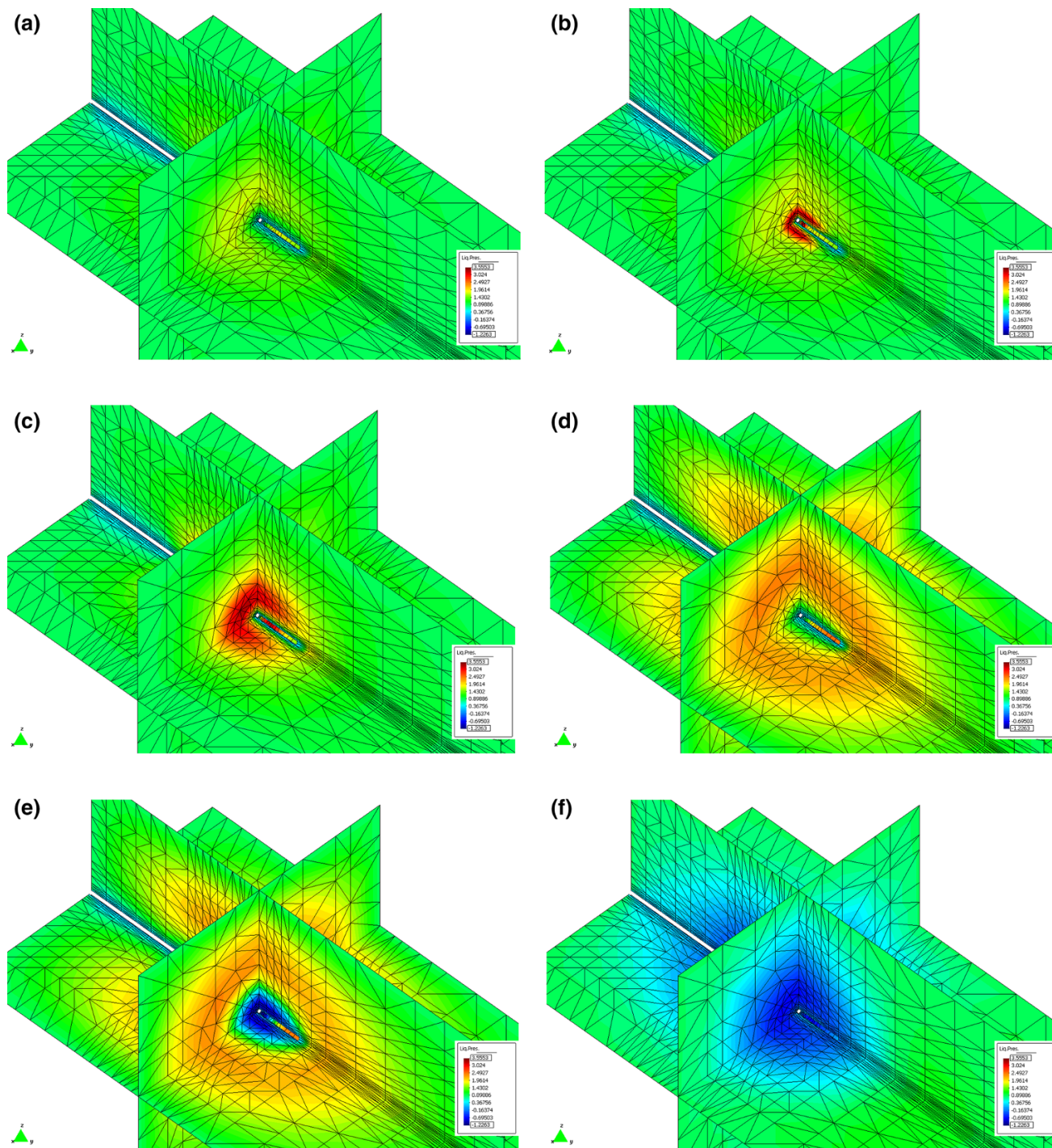
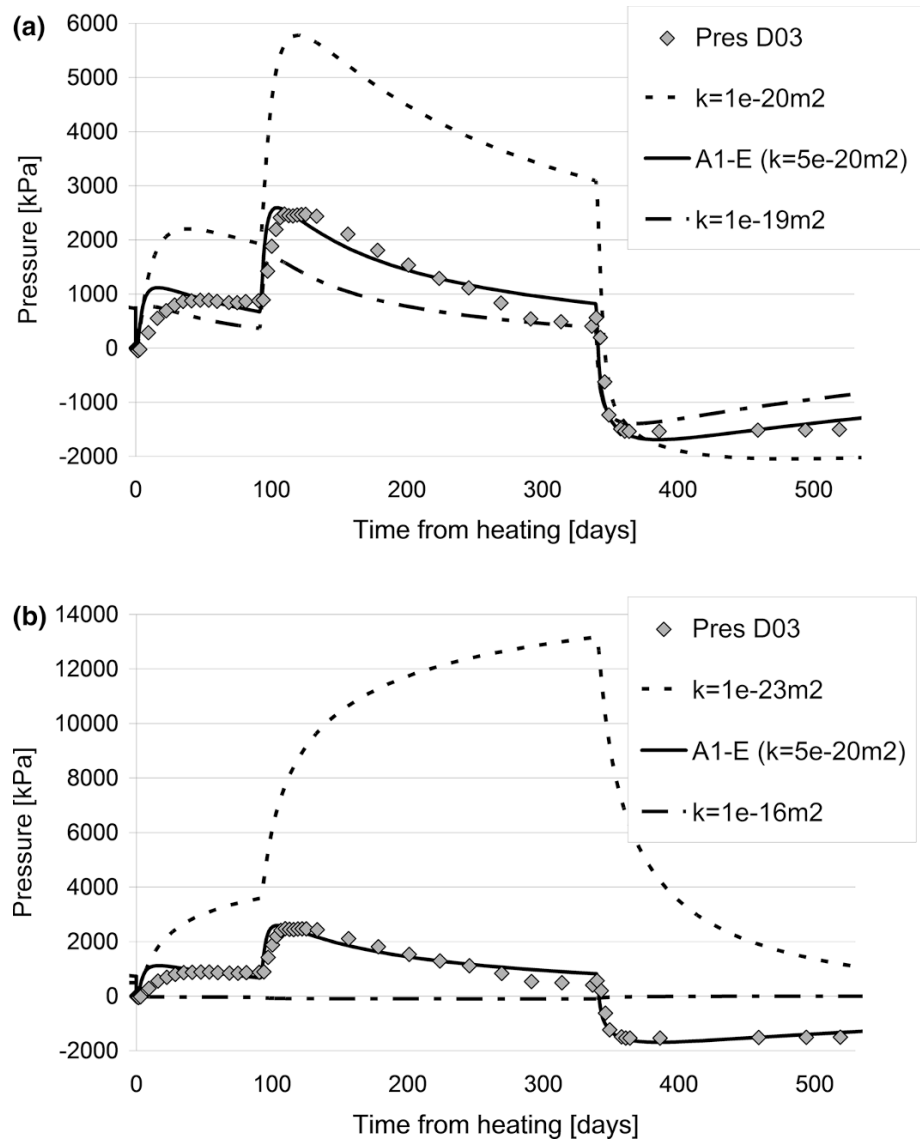


Fig. 19 Computed contours of pore pressure increase in the HE-D test. **a** 90 days (end of 1st heating stage), **b** 93 days, **c** 110 days (pore pressure maxima), **d** 297 days, **e** 346 days (start of cooling phase), **f** 509 days (end of test)

behaviour of Opalinus clay is quite similar in the three cases. Although the temperatures applied by the heaters are rather high, the temperature increases in the Opalinus Clay have been generally moderate because of the rapid thermal attenuation with distance and of the isolating nature of the engineered barriers in tests HE-B and HE-E. In spite of

those modest increases, the generation of pore pressures has been very significant in all cases. The mechanism underlying the generation of pore pressures is well understood; it arises from the combination of the effects of differential rock/water thermal dilation and of pore pressure dissipation, controlled by rock permeability. There is less

Fig. 20 Effect on intrinsic permeability on pore pressure evolution. **a** Permeability parameters in the range of realistic values. **b** Undrained and drained conditions



information on thermal effects on mechanical variables; strains measured in the HE-D test, however, turn out to be quite small. Hydraulic measurements carried out in a different test, SE-H, suggest that heating might be beneficial with respect to rock damage as the intrinsic permeability reduced significantly after an increase of temperature.

The HE-D test has been analysed in more detail because it involves no engineered barrier, so the behaviour of Opalinus Clay under thermal loading can be examined more directly. From those analyses, it is possible to assess the various THM phenomena involved and evaluate their relative importance (Gens 2010):

- The strongest coupling corresponds to the effects of the thermal field on hydraulic and mechanical behaviour. Pore pressure increases are caused by temperature rises whereas thermal expansion is the most important

source of rock deformation and displacements. Deformations and displacements are however small.

- Noticeable but more modest effects result from the coupling of hydraulic phenomena to mechanical behaviour. The dissipation of pore pressures induces additional displacements and strains that, due to the high Opalinus Clay stiffness, are smaller than thermally-induced deformations.
- In principle, mechanical damage could impact the hydraulic observations if a zone of higher permeability develops due to material damage. However no such thermally-induced damaged zone has been observed; in fact a reduction of permeability has been observed in the rock affected by temperature increase
- There is no perceptible coupling from hydraulic and mechanical phenomena to thermal behaviour. Practically all heat transport is by conduction and the thermal

Fig. 21 Distributions of deformation measured at different times in borehole D5, drilled approximately perpendicular to the main borehole. HE-D test

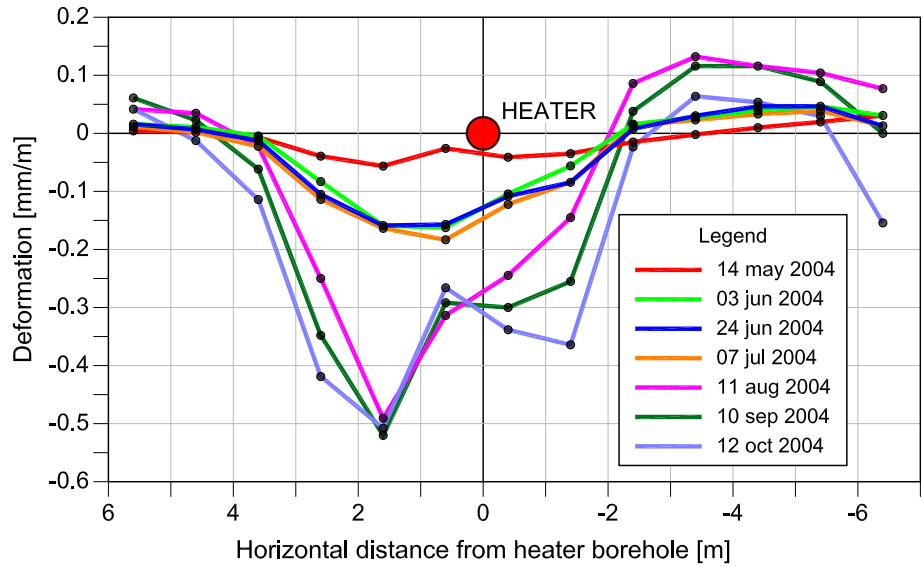
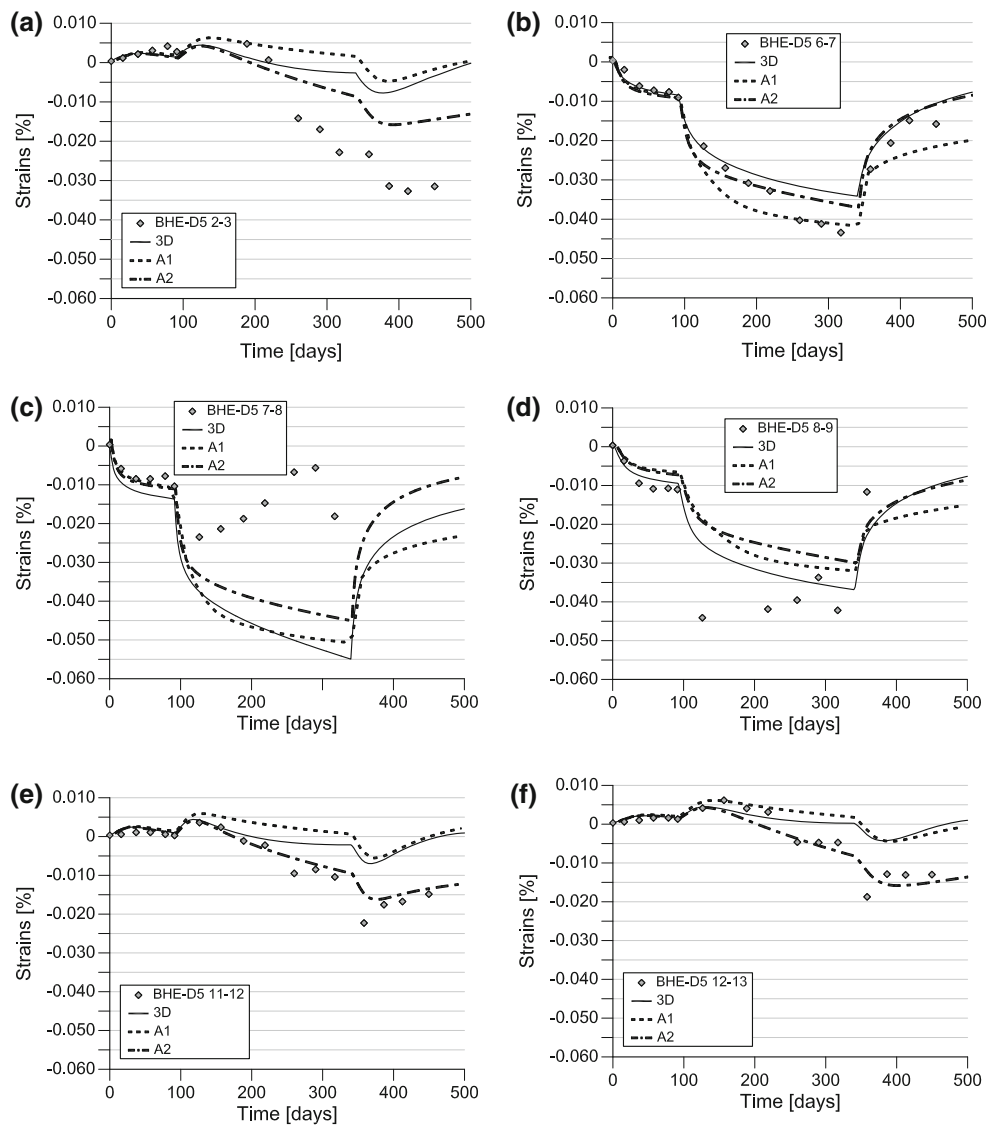


Fig. 22 Evolution of strain increments at various points in the Opalinus clay (Borehole D5). Observed and computed results. HE-D test



conductivity of the material does not change as deformations are small the material remains saturated throughout. In addition, mechanical energy dissipation is negligible in a non-isothermal case.

Acknowledgements The authors are grateful to the reviewers of the Paper, Prof. Pierre Delage, Ecole des Ponts ParisTech, Laboratoire Navier, CERMES, France and Dr. Xiangling Li, Belgian Nuclear Research Centre, Mol, Belgium for their comments and suggestions.

References

- Auvray, C. (2004). Thermomechanical tests on Opalinus Clay of the Mont Terri, *ANDRA internal report, C.RP.OENG.04-0239*. Agence Nationale pour la Gestion des Déchets Radioactifs (ANDRA), Bure. <http://www.andra.fr>.
- Booker, J. R., & Savvidou, C. (1985). Consolidation around a point heat source. *International Journal for Numerical and Analytical Methods in Geomechanics*, 9, 173–184.
- Bossart, P. (2008). Annex 4. Characteristics of the Opalinus clay at Mont Terri. In P. Bossart, & M. Thury (Eds.), *Mont Terri Rock Laboratory. Project, Programme 1996 to 2007 and Results. Reports of the Swiss Geological Survey, No. 3*. Federal Office of Topography (swisstopo), Wabern. <http://www.mont-terri.ch>.
- Bossart, P., Bernier, F., Birkholzer, J., Bruggeman, C., Connolly, P., Dewonck, S., Fukaya, M., Herfort, M., Jensen, M., Matray, J.-M., Mayor, J. C., Moeri, A., Oyama, T., Schuster, K., Shigeta, N., Vietor, T., & Wiczorek, K. (2017). Mont Terri rock laboratory, 20 years of research: introduction, site characteristics and overview of experiments. *Swiss Journal of Geosciences*, 110. doi:10.1007/s00015-016-0236-1 (this issue).
- Carlsaw, H. S., & Jaeger, J. C. (1946). *Conduction of heat in solids*. London: Oxford University Press.
- Garitte, B., Gens, A., Vaunat, J., & Armand, G. (2014). Thermal conductivity of argillaceous rocks: determination methodology using in situ heating tests. *Rock Mechanics Rock Engineering*, 47, 111–129.
- Gaus, I., Garitte, B., Senger, R., Gens, A., Vasconcelos, R., Garcia-Sineriz, J. L. & Mayor, J. C. (2014). The HE-E experiment: Lay out, Interpretation and THM modelling. *Nagra Arbeitsbericht NAB 14-53*, 178 pp. Nagra, Wettingen. <http://www.nagra.ch>.
- Gens, A. (2010). Soil-environment interactions in geotechnical engineering. *Géotechnique*, 60, 3–74.
- Gens, A., Vaunat, J., Garitte, B., & Wileveau, Y. (2007). In situ behaviour of a stiff layered clay subject to thermal loading: observations and interpretation. *Geotechnique*, 57, 207–228.
- Göbel, I., Alheid, H.-J., Alonso, E., Ammon, C., Bossart, P., Brühler, C., Emmerich, K., Fernandez, A. M., García-Siñeriz, J. L., Graf, A., Jockwer, N., Kaufhold, S., Kech, M., Klubertanz, G., Lloret, A., Mayor, J. C., Meyer, T., Miehe, R., Muñoz, J. J., Naumann, M., Nussbaum, C., Pletsch, T., Plischke, I., Ploetze, M., Rey, M., Schnier, H., Schuster, K., Sprado, K., Trick, T., Weber, H., Wiczorek, K., & Zingg, A. (2007). Heater experiment: rock and bentonite thermo-hydro-mechanical (THM) processes in the near field of a thermal source for development of deep underground high level radioactive waste repositories. In P. Bossart, & C. Nussbaum (Eds.), *Mont Terri Project—heater experiment, engineered barriers emplacement and ventilation tests*. Report of the Swiss Geological Survey No. 1 (pp. 7–16). Federal Office of Topography (swisstopo), Wabern. <http://www.mont-terri.ch>.
- Li, X.-L., Arson, C., Bastiaens, W., Bernier, F., Blaser, P., Bésuelle, P., Charlier, R., Chambon, R., Collin, F., Czimerová, A., Delage, P., Dedecker, F., Dizier, A., De Craen, M., Fauriel, S., François, B., Fisch, H., Fierz, T., Fokkens, J., Garitte, B., Gens, A., Gatmiri, B., Gérard, P., Guangjing, C., Gastaldo, L., Honty, M., Reyes-Montes, J.M., Haycox, J. H., Jaap, H., Andrews, J.R., Vincent, L., Laloui, L., Levorova, M., Lebon, P., Li, X. L., Li, Y., Illing, P., Levasseur, S., Monfared, M., Marinelli, F., Meynet, T., Madejová, J., Osacký, M., Pacovsky, J., Radu, J.-P., Rizzi, M., Sieffert, Y., Sillen, X., Sauthier, C., Salager, S., Schroeder, C., Sulem, J., Viggiani, G., Van Marcke, P., Vaunat, J., Vietor, T., Verstricht, J., Vasicek, R., Vigne, L., Wang, L., Weetjens, E., Pettitt, W.S., You, S., & Zhang, Z. (2001). *TIMODAZ. Thermal Impact on the Damage Zone Round a Radioactive Waste Disposal in Clay Host rocks. Final Activity Report. Contract Number FI6 W-CT-2007-036449*. European Commission, Brussels.
- Vaunat, J., & Gens, A. (2003a). Bond degradation and irreversible strains in soft argillaceous rock. In *Proceedings of the 12th Panamerican conference on soil mechanics and geotechnical engineering* (pp. 479–484). Boston.
- Vaunat, J., & Gens, A. (2003b). Numerical modelling of an excavation in a hard soil/soft rock formation using a coupled damage/plasticity model. In Oñate and Owen (Eds.) *Proceedings of the VII international conference on computational plasticity, COMPLAS*. Barcelona: CIMNE.
- Wileveau, Y. (2005). THM behaviour of host rock (HE-D) experiment: Progress Report. Part 1. *Mont Terri Technical Report, TR 05-03*. Mont Terri Project. Federal Office of Topography (swisstopo), Wabern. <http://www.mont-terri.ch>.
- Wileveau, Y., Göbel, I., Huertas, F., Jockwer, N., Schnier, H., Schnier, H., Shimura, T., Weber H. P., Yamamoto, S., & Zhang, C.-L. (2008). Thermal properties and THMC experiments. In P. Bossart, M. Thury (Eds.), *Mont Terri Rock Laboratory. Project, Programme 1996 to 2007 and Results*. Report of the Swiss Geological Survey No. 3 (pp. 145–153). Federal Office of Topography (swisstopo), Wabern. <http://www.mont-terri.ch>.

Implementation of the full-scale emplacement (FE) experiment at the Mont Terri rock laboratory

Herwig R. Müller¹ · Benoit Garitte¹ · Tobias Vogt¹ · Sven Köhler¹ · Toshihiro Sakaki¹ · Hanspeter Weber¹ · Thomas Spillmann¹ · Marian Hertrich¹ · Jens K. Becker¹ · Niels Giroud¹ · Veerle Cloet¹ · Nikitas Diomidis¹ · Tim Vietor¹

Received: 12 March 2016 / Accepted: 9 December 2016 / Published online: 16 February 2017
© The Author(s) 2017. This article is published with open access at Springerlink.com

Abstract Opalinus Clay is currently being assessed as the host rock for a deep geological repository for high-level and low- and intermediate-level radioactive wastes in Switzerland. Within this framework, the ‘Full-Scale Emplacement’ (FE) experiment was initiated at the Mont Terri rock laboratory close to the small town of St-Ursanne in Switzerland. The FE experiment simulates, as realistically as possible, the construction, waste emplacement, backfilling and early post-closure evolution of a spent fuel/vitrified high-level waste disposal tunnel according to the Swiss repository concept. The main aim of this multiple heater test is the investigation of repository-induced thermo-hydro-mechanical (THM) coupled effects on the host rock at this scale and the validation of existing coupled THM models. For this, several hundred sensors were installed in the rock, the tunnel lining, the bentonite buffer, the heaters and the plug. This paper is structured according to the implementation timeline of the FE experiment. It documents relevant details about the instrumentation, the tunnel construction, the production of the bentonite blocks and the highly compacted ‘granulated bentonite mixture’ (GBM), the development and construction of the prototype

‘backfilling machine’ (BFM) and its testing for horizontal GBM emplacement. Finally, the plug construction and the start of all 3 heaters (with a thermal output of 1350 Watt each) in February 2015 are briefly described. In this paper, measurement results representative of the different experimental steps are also presented. Tunnel construction aspects are discussed on the basis of tunnel wall displacements, permeability testing and relative humidity measurements around the tunnel. GBM densities achieved with the BFM in the different off-site mock-up tests and, finally, in the FE tunnel are presented. Finally, in situ thermal conductivity and temperature measurements recorded during the first heating months are presented.

Keywords Opalinus Clay · Excavation · Backfilling · Bentonite · Sensor · Instrumentation · Heat · THM · Nuclear waste disposal

1 Introduction

1.1 Experiment layout

The Swiss repository concept for spent fuel/vitrified high-level waste disposal tunnels (Nagra 2010) foresees the sequential emplacement of waste canisters in several hundred metre long horizontal tunnels in Opalinus Clay (Nagra 2014). The cylindrical waste canisters are to be emplaced in the middle of the tunnel section and separated from the tunnel wall by a bentonite buffer. The term bentonite buffer refers to all bentonite materials in a disposal tunnel. The bentonite buffer is part of the engineered barrier system and thus of the multi-barrier concept contributing to the retardation of radionuclides (Nagra 2002). At every 10th canister position, the concept foresees the installation of an

Editorial handling: P. Bossart and A. G. Milnes.

This is paper #14 of the Mont Terri Special Issue of the Swiss Journal of Geosciences (see Bossart et al. 2017, Table 3 and Fig. 7).

Electronic supplementary material The online version of this article (doi:10.1007/s00015-016-0251-2) contains supplementary material, which is available to authorized users.

✉ Herwig R. Müller
herwig.mueller@nagra.ch

¹ Nagra, National Cooperative for the Disposal of Radioactive Waste, Hardstrasse 73, 5430 Wettingen, Switzerland

‘interjacent sealing section’ (ISS) where the normal (cement-containing) tunnel support is replaced by e.g. steel sets in order to have direct contact between the rock and the ‘bentonite backfill’ and to intercept potential axial flow paths for radionuclides along the tunnel lining (Nagra 2010).

The layout of the ‘Full-Scale Emplacement’ (FE) experiment was designed to simulate these conditions in one single tunnel at the Mont Terri rock laboratory. First, a 50 m long experimental tunnel was constructed (Fig. 1). At the deep end of the FE tunnel an ISS was built using only steel sets for rock support, while the rest of the tunnel is supported by shotcrete. A bentonite block wall was erected manually in a section of the ISS. In the FE tunnel, 3 heaters with dimensions similar to those of waste canisters were emplaced on top of bentonite block pedestals. The first heater emplaced at the deep end of the FE tunnel was named H1, the middle one H2 and the most ‘shallow’ heater (close to the plug) H3. The remaining space was backfilled with a highly compacted ‘granulated bentonite mixture’ (GBM). For the purpose of backfilling the GBM as densely and homogeneously as possible into a horizontal tunnel, a prototype ‘backfilling machine’ (BFM) with 5 screw conveyors was developed. Finally, the experiment was sealed off (towards the FE cavern) with a concrete plug holding the bentonite buffer in place and reducing air and water fluxes.

1.2 Experimental aims

The FE experiment is the latest step in a series of investigations starting with small-scale laboratory tests (Villar et al. 2012), followed by mid-scale in situ heater experiments at the Mont Terri rock laboratory, such as the HE-D experiment (Gens et al. 2007, 2017) and the HE-E experiment (Gaus et al. 2014). With regard to its size and relevance, the FE experiment is comparable to large-scale heater experiments in other rock laboratories, such as the ‘Full-scale Engineered Barrier Experiment’ (FEBEX) at the Grimsel Test Site in Switzerland (Lanyon and Gaus

2013), the ‘prototype repository’ experiment at the ÄSPÖ rock laboratory in Sweden (Johannesson et al. 2004), the PRACLAY experiment in Boom Clay at the HADES rock laboratory in Belgium (Bernier et al. 2007) and the ALC experiment in Callovo-Oxfordian Clay at ANDRA’s rock laboratory in France (Gugala 2015).

The main aim of the FE experiment is the investigation of high-level waste repository induced thermo-hydro-mechanical (THM) coupled effects on the host rock at this scale and the validation of existing coupled THM models (Müller et al. 2015). Further experimental aims are (i) the verification of the technical feasibility of constructing a disposal tunnel using standard industrial equipment, (ii) the optimisation of the bentonite buffer material production and (iii) the investigation of (horizontal) canister and bentonite buffer emplacement procedures for underground conditions (Weber et al. 2012; Bosgiraud et al. 2015).

It is outside the scope of this paper to present all the measurement results from the FE experiment; only a small selection is shown. For more details the reader is referred to Lisjak et al. (2015) on deformation measurements during the tunnel construction and Vogt et al. (2013) on the pore-water pressure development during the tunnel construction.

2 Geological overview

The FE tunnel was constructed in the Mont Terri rock laboratory within the ‘shaly facies’ of the Opalinus Clay. For a detailed description of this strongly over-consolidated silty claystone (‘shale’), the reader is referred to Bossart et al. (2017) and Hostettler et al. (2017).

2.1 Natural discontinuities

Details about the general tectonic setting of Mont Terri and the existing discontinuity network can be found in Bossart et al. (2017) and Nussbaum et al. (2017). The average dip of the bedding in the experimental area is 34° towards the

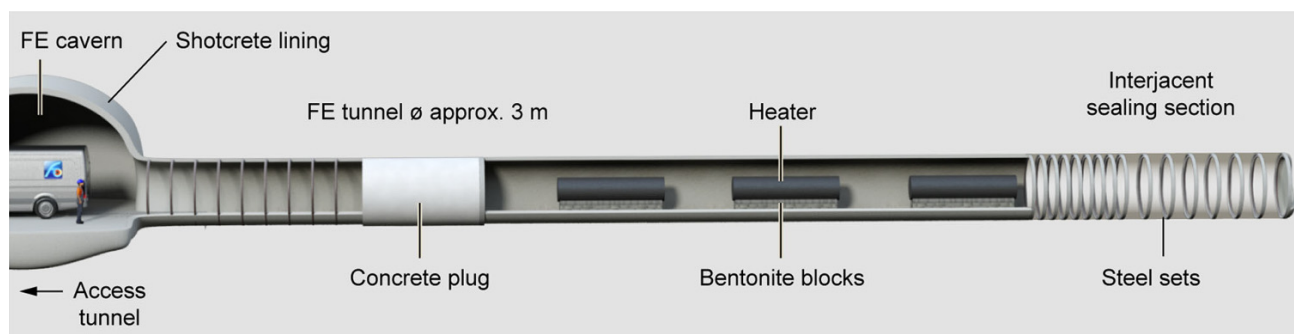


Fig. 1 Visualisation of the general layout of the FE experiment and the 50 m long FE tunnel at the Mont Terri rock laboratory; sensors, bentonite backfill and rock bolts are not shown

south-east. With an excavation direction towards 244°, the axis of the FE tunnel is orientated approximately parallel to the strike of the bedding (Fig. 8).

While the FE cavern was not strongly faulted, a fault zone was encountered with the FE tunnel. This fault zone was oriented subparallel to the bedding and entered the tunnel at the lower right (north-western) side around ‘tunnel metre’ (TM) 14.5. The fault zone remained within the cross-section of the FE tunnel until the tunnel end at TM50. The fault was characterised by a heavily sheared core zone and strongly tectonised damage zone. The normal thickness of the fault zone varied between approximately 0.5–1.5 m. The rock mass adjacent to the fault zone was characterised by countless sheared and polished bedding planes.

2.2 Excavation damage zone

The few ‘excavation damage zone’ (EDZ) features that could clearly be associated with the artificial fracturing process during tunnel excavation (Marschall et al. 2017) did not allow for a conclusive EDZ model, but suggested that the EDZ formation around the FE tunnel was strongly influenced by pre-existing discontinuities, reducing the formation of new EDZ features, for example, by reactivation (mainly shearing) of pre-existing slickensides.

This observation is consistent with the hydraulic conductivities determined in the close vicinity of the FE tunnel, which indicated a rather small EDZ. 8 hydraulic (double packer) tests in the far-field at a distance of 2.4–12.6 m from the FE tunnel wall resulted in a geometric mean of 6.4×10^{-13} m/s. Moreover, 5 hydraulic (double packer) tests performed at a distance of 1.0–2.4 m from the tunnel wall showed slightly increased, but still very low, hydraulic conductivities with a geometric mean of 2.8×10^{-12} m/s. In the very near-field up to 1 m from the tunnel wall, the observed pore-water pressure was less than 0.1 MPa. Only 1 hydraulic test was performed in this zone at a depth of 0.8–0.9 m from the tunnel wall, resulting in a hydraulic conductivity of 1.2×10^{-10} m/s.

Similar observations were made by Shao et al. (2015) by means of gas permeability testing in radial boreholes in the shotcrete section and in the shotcrete-free ISS of the FE tunnel. In the shotcrete section, the extent of the gas-permeable EDZ with a permeability greater than 1×10^{-18} m² was found to be less than 1 m, whereas in the ISS the gas-permeable EDZ was found to be larger than 2 m. This is explained by the fact that the ISS was constructed with steel sets with sliding connections, resulting in a more ‘ductile’ tunnel support (compared to the shotcrete section) allowing long-term convergences and deformation and therefore the opening of discontinuities and EDZ features.

3 Tunnel construction

3.1 FE cavern

Before the start of the FE experiment, the FE cavern was constructed in the extension of the Mine-by (MB) experiment tunnel. This construction work included a local widening of ‘Gallery 08’ (GA08), especially around the portal of the MB tunnel, as well as renovation and reinforcement of the MB tunnel with steel sets and an additional shotcrete layer.

The FE cavern was excavated between November 2010 and May 2011. The size of the FE cavern allowed the use of a 15,000 kg CAT 312 excavator equipped with a rotary drum cutter (‘road-header’). A remotely controlled BROKK 330 excavator was used for the confined spaces. Each of the 11 excavation steps was secured by implementing wire mesh reinforcement, installing and cross-linking steel sets and finally by applying shotcrete.

The reinforcement of the MB tunnel and the FE cavern was designed to ensure safe and long-term access to the FE tunnel. The shotcrete thickness in the FE cavern was more than 30 cm including 2 layers of K196 reinforcement steel mesh. The invert was up to 1.8 m deep and, after being backfilled, was finally covered with an even concrete floor. The resulting maximum (inner) dimensions of the tunnel-shaped FE cavern are approximately 9 m (length) by 12 m (width) by 5 m (height).

3.2 FE tunnel

3.2.1 Construction

The 50 m long FE tunnel was constructed between April 2012 and July 2012 (Daneluzzi et al. 2014). The excavation was done with remotely controlled BROKK 260 and BROKK 90 excavators equipped mainly with a (pneumatically hammering) spade chisel and, for profiling, with a rotary drum cutter type SIMEX TF100 (Fig. 2). The excavation of the FE tunnel with an average external diameter of approximately 3 m and a cross-section of approximately 7 m² was done full-face. Excavation steps were limited to 1.5 m per day in order to allow early rock support to be installed on the same day.

The different types of tunnel support, including the location of the monitoring and deformation measurement sections, can be seen in Fig. 3. From TM0 to TM38, the support in the tunnel consisted of mesh-reinforced shotcrete. The ‘dry application’ method was used for the shotcrete, adding water only at the spraying nozzle. The shotcrete was applied in two layers with a total thickness of at least 16 cm. 1 layer of wire mesh K196 was installed in



Fig. 2 Photo (by COMET) of the excavator (equipped with a small rotary drum cutter) used in the FE tunnel mainly for profiling

the first shotcrete layer. From TM9 to TM18 a third, approximately 10 cm thick layer of shotcrete with a second layer of wire mesh was installed. Due to the uneven rock surface (resulting e.g. from overbreaks), a shotcrete

thickness of up to 50 cm was reached locally. Finally, the inner diameter of the FE tunnel was not perfectly round, varying diametrically between 2.5 and 2.7 m.

At the deep end of the FE tunnel (from TM38 to TM50), an ISS was simulated using only steel sets (and reinforcement mesh) but no shotcrete for rock support (Fig. 4). In the FE tunnel, all steel sets were placed with a spacing of 1 m, except in the ISS close to the shotcrete section where a 0.5 m spacing was chosen for safety and demonstration reasons. Each steel set was composed of several pieces with sliding connections that were tightened by bolts using a 300 Nm torque spanner, allowing some movement after installation. The steel sets were bedded on grout-injected hoses in order to allow early load transfer (after hardening of the grout) and even load distribution from the rock onto the support element.

3.2.2 Tunnel wall deformation monitoring

The tunnel construction was surveyed using a total of 10 convergence measurement sections that were installed with an average spacing of approximately 6 m during the

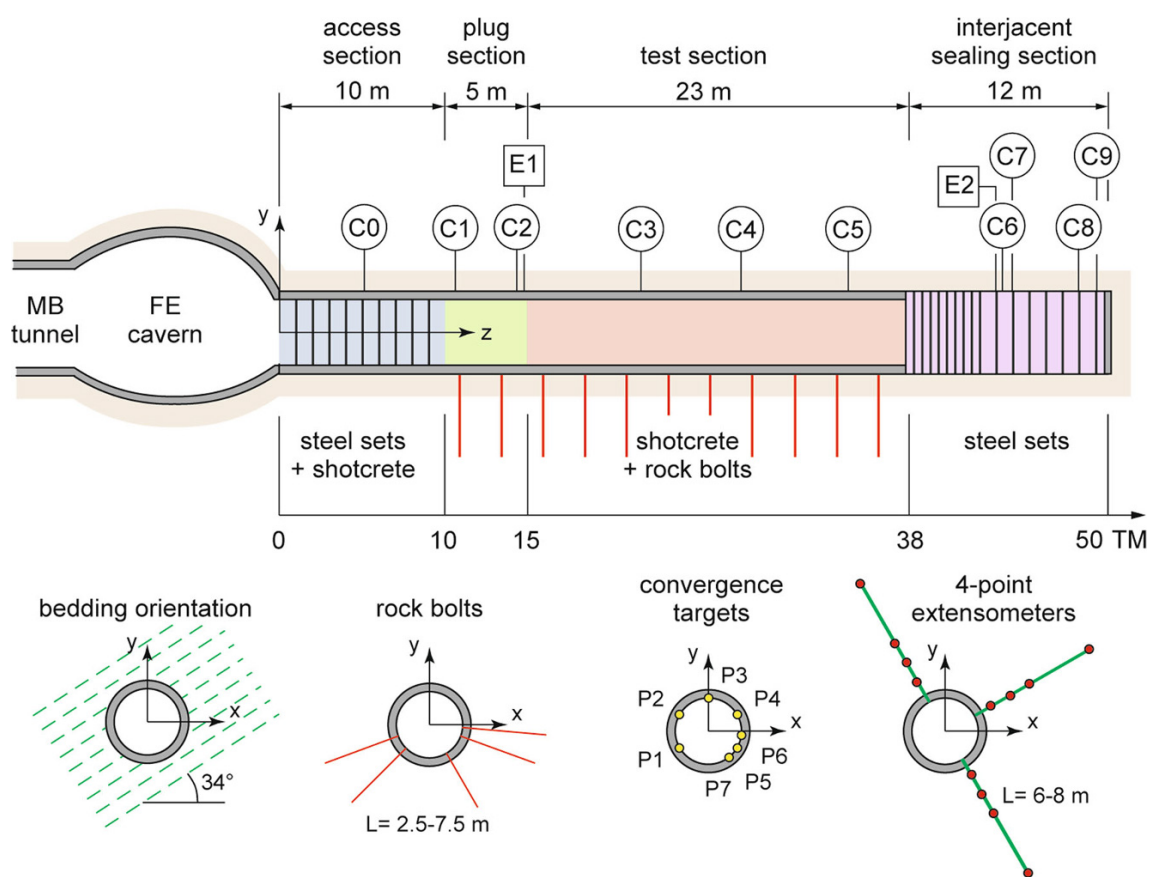


Fig. 3 Simplified longitudinal section (adapted from Lisjak et al. 2015) of the approximately 3 m diameter FE tunnel showing the different support measures, the convergence measurement sections

(C0–C9) and the location of the radial extensometers (E1 and E2) installed during tunnel construction



Fig. 4 The photo on the *left* shows the 12 m long shotcrete-free interjacent sealing section (ISS) at the end of the FE tunnel; the photo on the *right* shows a detail of a steel set bedded on a grout-injected hose for an even load distribution from the rock

excavation within the FE tunnel. In measurement sections C0 to C4 (Fig. 3), the radial configuration consisted of 5 observation targets; in measurement sections C5–C9 the radial configuration consisted of 7 observation targets. In total, 60 observation targets were installed. These targets (prismatic reflectors) were continuously monitored in 3D with a tachymeter during the tunnel construction until backfilling started approximately 30 months later.

All construction work was also monitored by INVAR wire convergence measurements, which showed similar results to the tachymetric tunnel wall deformation measurements. The long-term closing of the non-fixed ('sliding') steel set connections in the ISS was also monitored.

Whereas the steel set section showed normal deformation rates and a more or less symmetric tunnel wall convergence, the shotcrete section was initially characterised by an asymmetric tunnel wall convergence with several centimetres of deformation, particularly at the lower right (north-western) side of the tunnel (Fig. 5).

3.2.3 Invert renovation

Because of the observed deformation rates during the construction, 7.5 m long (steel) rock bolts were installed in the lower right (north-western) side wall of the tunnel in the shotcrete section from TM20 to TM38. Nevertheless, the shotcrete in the invert failed (Fig. 6) and had to be renewed. The renovation of the tunnel section from TM9 to TM38 was completed in September 2012. The old shotcrete in the invert was cut and removed segment by

segment and new (mesh-reinforced) shotcrete was applied. During the renovation, extra 7.5 m long (steel) rock bolts were installed in the right (north-western) side wall of the tunnel. This was done in a pattern designed to prevent failure of the interface between the old and the new shotcrete lining. At the interface on the left side of the tunnel, 2.5 m long (fibre-reinforced plastic) rock bolts were installed in the same pattern.

The failure of the shotcrete invert was mainly caused by an irregular, not perfectly circular excavation profile and by the resulting shear and bending forces in the lining. An intensive coring and lab testing programme showed that the shotcrete in the invert did not have the required quality (although the strength targets were clearly met in the upper part of tunnel). Loose muck and rebound below the invert as well as layering within the shotcrete were detected. The shotcrete in the invert was also partially too unevenly and thinly applied, locally even of crumbling appearance and therefore too weak.

Apparently these circumstances contributed more to the failure of the invert than the properties of the faulted and tectonically weakened rock mass. This hypothesis is supported by the observation that, although constructed in the same geological setting, the steel set section generally showed a more homogeneous tunnel wall convergence and lower deformation rates than the shotcrete section (Fig. 5).

With the renovation work, the deformation rates in the shotcrete section were, if not stopped, reduced to a minimum. Until the concreting of the plug in March 2015 and afterwards, no further problems with the tunnel stability were encountered.

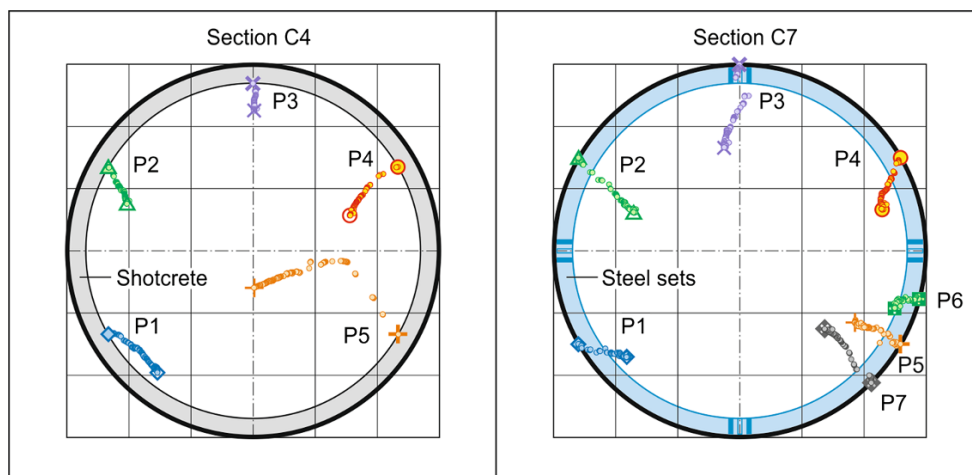


Fig. 5 90 day tunnel wall convergences at 2 example measurement sections C4 (*left graph*) and C7 (*right graph*). C4 was located in the shotcrete section of the FE tunnel at ‘tunnel metre’ (TM) 27.6 and C7 was located at TM44.2 in the shotcrete-free section supported only by

steel sets. The scale of the displacement vectors is amplified by a factor of 20 with respect to the excavated tunnel represented by a *black circle*. The *right side* of each graph represents the north-western side of the FE tunnel

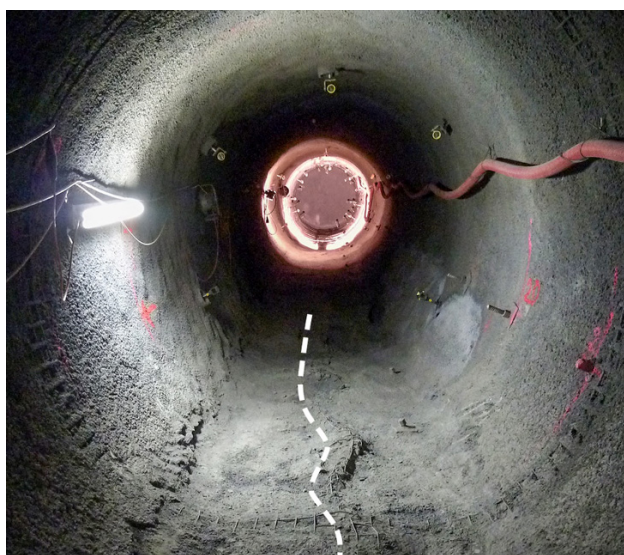


Fig. 6 Photo from the failed shotcrete invert (marked with a *dashed white line*) before the renovation in September 2012

3.2.4 Shotcrete properties

The basis of the shotcrete mixture design for the FE tunnel was the ‘ESDRED mixture’ developed within the framework of another EU project (Wetzig et al. 2011). In this low-pH shotcrete mixture, 40% of the Portland cement was substituted by silica fume. Silica fume reacts with calcium hydroxide (‘pozzolanic reaction’) to lower the pH value of the shotcrete. The reduction of the pH gradient between the (as a bulk) neutral clay minerals and the alkaline shotcrete limits chemical interactions, which is beneficial for the long-term safety of an engineered barrier system (Jenni et al. 2013).

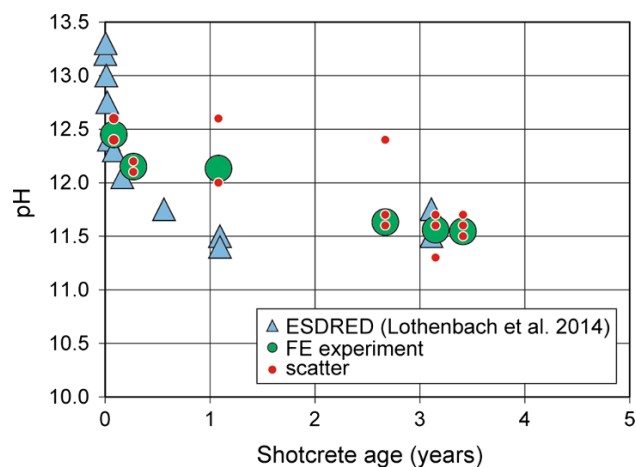


Fig. 7 The filled green circles show the pH values of FE samples measured under laboratory conditions at different shotcrete ages. The *small red circles* are all individual measurements. The values for the ‘ESDRED mixture’ as described in Lothenbach et al. (2014) are represented by *blue triangles*

400 g/m³ of superplasticizer were added to the FE mixture but, differently than in the ‘ESDRED mixture’, no accelerator was used in order to reduce the content of organic matter.

The pH value of the shotcrete samples was measured under laboratory conditions by the ex situ leaching method (Alonso et al. 2012) after 90, 111 days, 1 and 3.4 years. The pH value of the shotcrete samples from the FE tunnel showed an ongoing decrease with time; from an initial value of approximately 12.4, the pH decreased within 3.4 years to a value of approximately 11.5 (Fig. 7). According to modelling results by Lothenbach et al. (2014), the ‘ESDRED mixture’ should reach an

Table 1 Averages of measurement results on shotcrete samples from the FE tunnel

Parameter	Average value
Total porosity	23.1 vol %
Free water content	4.7 wt%
Water permeability	$1.15 \times 10^{-17} \text{ m}^2$
Thermal conductivity	1.7 W/mK
Uniaxial compressive strength	42.4 MPa after 28 days/50.4 MPa after 90 days

equilibrium pH value of 11.5 after 1 year and will slowly decrease to a pH of 11 after a long period of time; the same can be assumed for the FE mixture. Measurement results of selected physical properties of the FE shotcrete are presented in Table 1.

4 Instrumentation

The entire experiment implementation as well as the post-closure THM evolution of this full-scale heater experiment is monitored using several hundred sensors (Table 2). The main monitored parameters are temperature, pressure, deformation and humidity/water content. The sensors are distributed in boreholes, in the tunnel lining, in the bentonite buffer and on the heaters (Fig. 8). Their installation was performed sequentially in the following main phases: (i) instrumentation of the rock mass in the tunnel far-field before the tunnel excavation (November 2011 until April 2012), (ii) instrumentation of the rock mass in the tunnel near-field during the tunnel construction (May until June 2012) and afterwards (December 2012 until February 2014), (iii) instrumentation of the bentonite buffer, where firstly the sensors on the tunnel wall were installed (May until June 2014); finally the sensors on, and in close proximity to, the heaters were emplaced together with the 3 heaters in October 2014, November 2014 and January 2015.

The monitoring environment of the FE experiment is challenging, because a long observation period of at least 10–15 years is envisaged and because high temperatures of up to 130–150 °C at the heater surface and of up to 60–80 °C at the tunnel wall are expected. In addition, the pore-water with a salinity of more than 35 mS/cm might enhance corrosion of metallic sensor components in the rock and in the humid (partially water-saturated) bentonite buffer close to the tunnel wall.

Due to these conditions, besides standard state-of-the-art sensors, fibre-optic sensors as well as modified and prototype measurement systems were also installed. The prototype systems were designed to be more corrosion-resistant. They were also constructed to be less heat-conductive, reducing the impact of the instrumentation on the experiment evolution.

4.1 Tunnel climate

Climate sensors measuring air humidity, air temperature, air pressure and air velocity were installed in the FE cavern and at several locations in the FE tunnel. These sensors monitored the tunnel climate before and during the tunnel excavation, but wherever possible also during the actively ventilated phase until the completion of tunnel backfilling.

4.2 Instrumentation of the rock

In general, the borehole instrumentation was set up parallel, perpendicular and oblique to the bedding, taking the anisotropy of the Opalinus Clay into consideration. The rock mass in the far-field of the FE tunnel was instrumented with up to 45 m long boreholes drilled from the FE cavern (Fig. 8). This instrumentation was completed in April 2012 before the FE tunnel was excavated and therefore allowed a ‘mine-by’ observation of the later excavation. The rock mass in the near-field of the FE tunnel was instrumented with (several metre long) radial boreholes drilled from the FE tunnel partially during, but mainly after, the tunnel construction.

4.2.1 Pore-water pressure

In 6 boreholes drilled from the FE cavern, multi-packer systems with a total of 36 pore-water pressure monitoring intervals were implemented before the start of the tunnel excavation. Additionally, two single packer systems with 1 pore-water pressure monitoring interval each were installed before the start of the tunnel excavation.

For pore-water pressure monitoring in the rock close to the FE tunnel, after the tunnel construction was completed, 8 radial boreholes were instrumented with multi-packer systems and 2 intervals each and, additionally, 11 boreholes were instrumented with single packer systems and 1 interval each.

4.2.2 Deformation

Before the tunnel excavation, horizontal inclinometer chains (with 40 segments each) were installed in two boreholes located above the FE tunnel, drilled sub-parallel

Table 2 Approximate number of sensors installed as part of the FE experiment during the different instrumentation phases

Instrumentation	Phase 1 (tunnel far-field)	Phase 2 (tunnel near-field)	Phase 3 (bentonite buffer)	Total
Temperature	480	140	580	1200
RH, TDR, etc.	0	54	119	173
Deformation	80	44	23	147
Total pressure	36	6	30	72
Pore-water pressure	38	27	0	65
Gas composition	0	0	20	20
Total	634	271	772	1677

Not included in this table are the thermal conductivity sensors, the geophysical sensors, the gas sampling lines, the material samples, the plug instrumentation and some fibre-optic systems

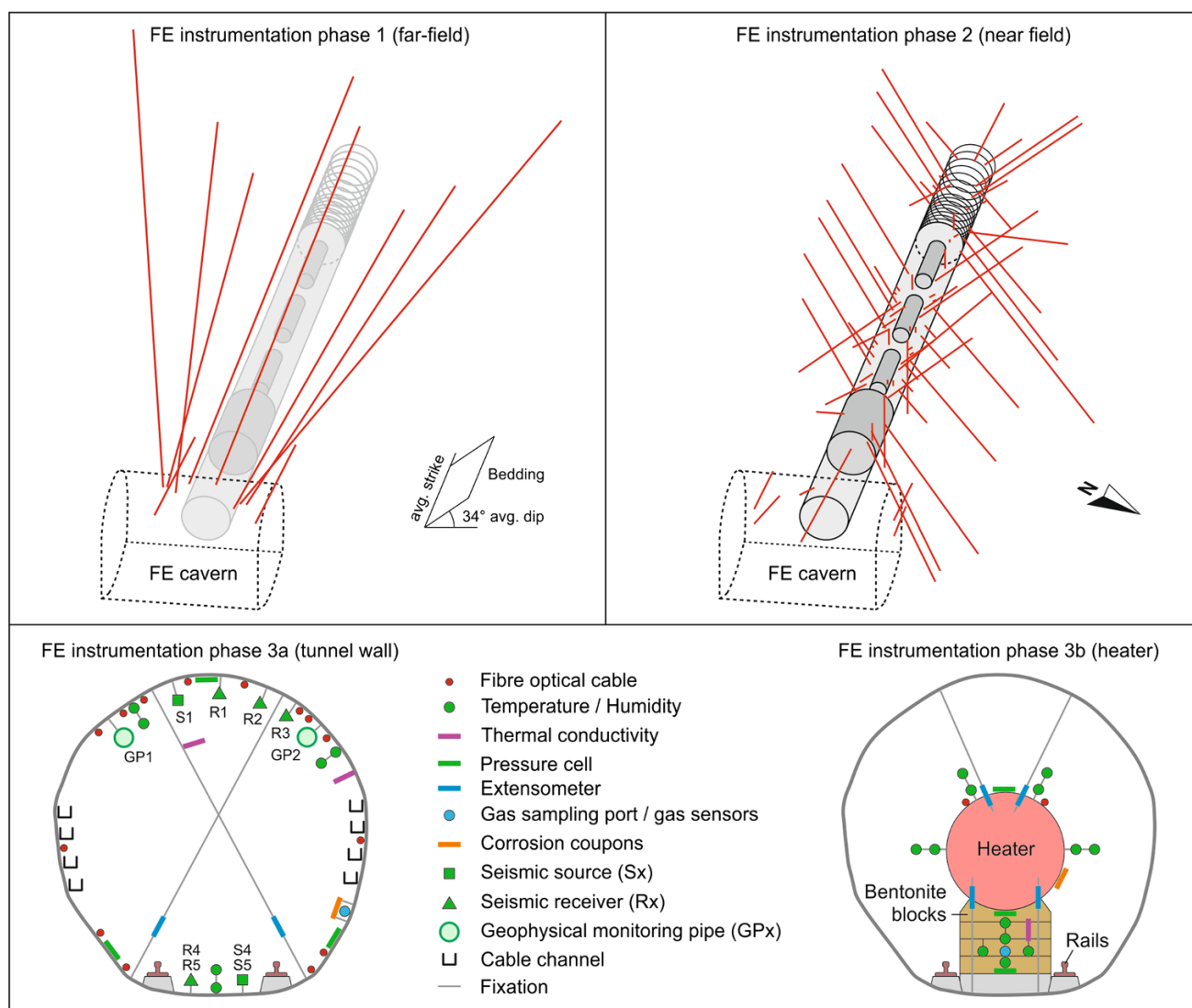


Fig. 8 Overview showing the main instrumentation phases of the FE experiment. The *graphs* at the *top* also indicate the borehole arrangements around the 50 m long FE tunnel. The *graphs* at the

bottom represent strongly simplified summaries of the many different instrumentation cross-sections within the 2.5–2.7 m diameter FE tunnel

to the tunnel axis. During the tunnel construction, five standard rod extensometers each with four displacement sensors and a length of 6–8 m were installed in radial boreholes drilled from within the FE tunnel (sections E1 and E2 in Fig. 3). Thereafter, an additional 6 radial boreholes were instrumented with specially designed long-lasting rod extensometers and seven radial boreholes were equipped with fibre-optic extensometers.

4.2.3 Temperature

In general, most boreholes were equipped with temperature sensors at different depths. In total, 260 conventional temperature sensors (thermocouples and PT1000) were installed as well as 360 m of fibre-optic cable for distributed temperature sensing.

4.2.4 Humidity/water content

The development of the ‘water content’ (WC) of the rock mass around the FE tunnel is being monitored with a commercial dielectric profile probe originally developed for agricultural applications. This dielectric tool has 6 measurement sections within its 1 m length. A total of 5 of these probes were permanently installed in 28 mm diameter boreholes drilled in the ‘cooler’ sections of the FE tunnel.

Figure 9 shows the WC profiles of the Opalinus Clay around the FE tunnel measured using the dielectric profile probes. The data indicate a difference between sections where the rock is covered with shotcrete and the unlined sections. In the profiles without shotcrete, desaturation reaches about 50 cm into the rock, whereas the rock behind the shotcrete seems to be fully saturated, with only minor signs of desaturation in the shotcrete itself.

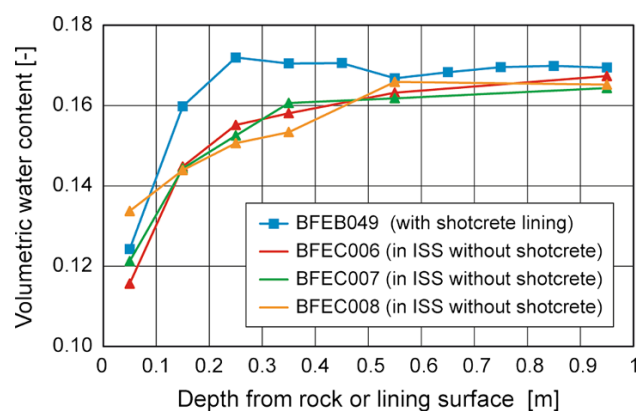


Fig. 9 Water content profiles measured with the dielectric profile probe in selected 1 m long boreholes, drilled radially from the FE tunnel, showing a clear difference between unlined rock and rock covered with shotcrete

The second type of sensor used for the rock moisture monitoring was designed specifically for use in the ‘hotter’ sections in the FE experiment close to the heaters. To withstand long-term use under high temperatures, ‘time domain reflectometry’ (TDR) was selected. The design of the sensor allowed all vulnerable electronic parts to be placed outside the heated tunnel Sect. 6 probes with a total of 24 TDR sensors were installed in a Y-shaped configuration around the middle heater H2 and around the ‘shallow’ heater H3 (Sakaki et al. 2014).

Finally, 17 radial boreholes were equipped with standard and monolithic capacitive ‘relative humidity’ (RH) sensors. The boreholes were 0.2–0.5 m deep and had a diameter of 28 mm.

4.3 Instrumentation of the bentonite buffer

Many sensors on the tunnel wall and on the heaters had to be installed on erectable sensor holders due to the space conflict with the prototype machine developed for backfilling the FE tunnel.

4.3.1 Total pressure and deformation

24 Total pressure cells were installed on the tunnel wall and 2 total pressure cells on the surface of each heater in order to monitor any potential swelling pressure of the bentonite buffer. Furthermore, a total of 23 displacement sensors were installed to track any potential heater movement or tunnel wall deformation after backfilling and during heating. Approximately 120 m of fibre-optic cables were also installed at different positions along the tunnel for distributed strain sensing.

4.3.2 Temperature

Each heater was equipped with 6 internal thermocouples and 18 external thermocouples (fixed to the heater surface). In addition, each heater surface was equipped with 24 fibre-optic point sensors. The spatio-temporal temperature distribution and evolution of the tunnel wall and of the bentonite buffer is monitored by a total of 238 temperature sensors, of which 105 are conventional sensors (thermocouples and PT1000) and the rest are integrated into RH and total pressure sensors. In addition, approximately 300 m of fibre-optic cables were installed at different positions on the tunnel wall for distributed temperature sensing.

4.3.3 Humidity/water content

A total of 99 RH sensors were installed within the bentonite buffer. Additionally, a total of 6 customised TDR

probes were installed around and between heater H2 and heater H3.

4.3.4 Thermal conductivity

Around and between the heaters H2 and H3, a total of 15 thermal conductivity sensors were installed within the GBM and the bentonite blocks. Each of these heat pulse sensors consisted of a single 10 cm long needle. First measurement results show that the initial thermal conductivity of the GBM at the achieved bulk ‘dry density’ (DD) in the backfilled FE tunnel was 0.29 ± 0.05 W/mK and that a slight increase can be observed over the course of the first 12 months after the start of heating (Fig. 10).

4.3.5 Geophysical monitoring

Geophysical methods were selected with the aim of monitoring changes in the bentonite buffer in a quantitative manner with minimal adverse effects on the backfilling procedure or the THM evolution. One monitoring component consists of 2 gas-tight pipes installed approximately 1.7 m apart in the roof of the FE tunnel at a distance of a few centimetres from the shotcrete liner. These pipes facilitate long-term access through the concrete plug and into the bentonite buffer in front of and above the ‘shallow’ heater H3 for a variety of geophysical borehole tools. Measurement campaigns with the focus on bentonite properties in the near-field around the pipes include repeated density and porosity logging as well as single-hole georadar surveys. Tomographic georadar and acoustic surveys are performed to better capture and image the changes in the area between the two pipes. An acoustic ‘borehole’ sensor system (with 1 source and 8 receivers) is typically kept at a fixed position in the pipes for quasi-

continuous monitoring of transients between different measurement campaigns.

The second monitoring component includes two acoustic sensor arrays that were permanently installed before backfilling, one close to the floor and one in the roof of the tunnel (Fig. 8; ‘seismic source’ and ‘seismic receiver’ in lower left graph). These permanent installations allow subtle changes in acoustic waveforms to be captured either within the individual arrays or across the arrays when sensor coupling is sufficient. In combination with the acoustic ‘borehole’ sensor system temporarily installed in the pipes, additional ray paths and imaging capabilities can be tested.

4.3.6 Gas composition

14 Prototype in situ hydrogen and 6 in situ oxygen concentration sensors were installed at different locations along the FE tunnel. The 2 most ‘shallow’ oxygen sensors were located on the GBM side of the plug retaining wall at TM15; the ‘deepest’ one was placed in the ISS at TM43. Additionally, 10 gas sampling lines were installed to allow continuous gas monitoring by mass spectrometry as well as periodic gas sampling. The sampling lines chosen were PEEK with an inside diameter of 1.5 mm. The backfilled sampling points consist of a PVDF housing with either a stainless steel filter or a silver-coated nylon mesh. The silver coating should hinder the development of biofilms, which could lead to clogging of the filters.

At all locations (with the exception of directly behind the plug retaining wall), the oxygen concentrations drop to approximately 0% within 2–3 months after backfilling (Fig. 11).

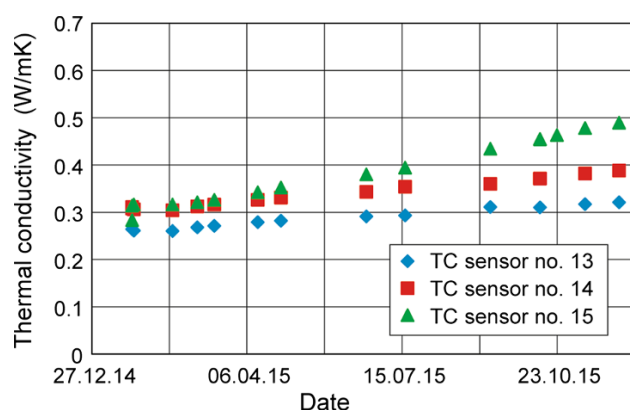


Fig. 10 Time series plot showing how the thermal conductivity of the backfilled GBM increased slightly over time. This example is from three measurement locations close to the tunnel wall around heater H3

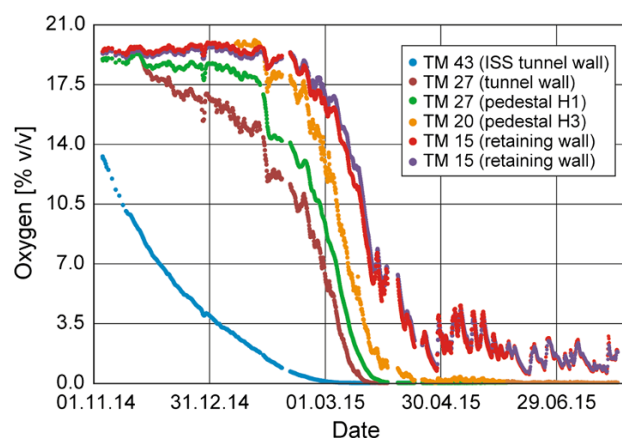


Fig. 11 Oxygen concentrations at different measurement locations along the FE tunnel from November 2014 (shortly after backfilling started) until July 2015

Table 3 Material specifications required for the raw bentonite used in the FE experiment

Criterion	Requirements
Material	Natural (non-activated) sodium bentonite
Smectite content by dried weight, measured by X-ray diffraction using a dried sample	>75%
Additives (magnetite, baryte, binders, etc.)	No additives allowed
CEC (Cation Exchange Capacity), measured by Cu(II)-triethylenetetramine method	>70 meq/100 g
Pyrite content by dried weight, measured by X-ray diffraction using a dried sample	<1%
Sulphur content by dried weight, measured by emission or mass spectroscopy	<0.5% (corresponds to ca. 1% of pyrite)
Organic carbon by dried weight, measured by emission or mass spectroscopy	<1%

4.3.7 Corrosion monitoring

In order to investigate in situ corrosion phenomena in the case of potential future dismantling of the FE experiment, sample holders with different metals were installed on heaters H2 and H3 as well as at two different locations on the tunnel wall in close proximity to the gas sensors and sampling ports. The metals used in the sample holders were carbon steel, wrought copper, electrodeposited copper and cold-sprayed copper. 5 corrosion coupons from each metal were installed at each position. The corrosion coupons were polished and their surface roughness characterised prior to emplacement.

5 Bentonite buffer production

Bentonite is considered as a potential sealing and backfill material in most concepts for geological disposal of radioactive waste. Bentonite is essentially a natural clay mixture consisting mostly of montmorillonite of volcanic, hydrothermally altered origin. There are two main types of bentonite on the market: calcium-rich and sodium-rich depending on the dominant interlayer cation ($\text{Ca}^{2+}/\text{Na}^{+}$). Sodium-rich bentonite was chosen for the FE experiment, based on the requirements specified by Karnland (2010) and Leupin et al. (2014). Table 3 summarises the raw material specifications that had to be fulfilled during the bentonite buffer production for the FE experiment and that were checked by independent laboratories.

5.1 Bentonite blocks

5.1.1 Test production

Compacted bentonite blocks can disintegrate in contact with ambient air. With a test production, a simple novel concept was introduced to estimate the resistance of compacted bentonite to changing climatic conditions. In

November 2012, 90 bentonite blocks compacted at three different water contents (12, 16 and 19%) and three different compaction pressures (70, 100 and 130 MPa) were produced using sodium bentonite (Garitte et al. 2015). Two blocks from each ‘water content’ (WC)/compaction pressure group were emplaced in sealed plastic bags with ‘relative humidity’ (RH) sensors to determine their equilibrium RH. The equilibrium RH was found to lie between 50 and 70% and increased with the WC.

The blocks then were submitted to ‘uniaxial compressive strength’ (UCS) testing in several series. In the first series, the blocks were tested directly after production. In the next series, the blocks were first placed in climate chambers with different relative air humidities of 35, 50, 70 and 90% until the blocks reached equilibrium. The UCS test results clearly show that imposing a RH on a bentonite block higher than its equilibrium RH drastically reduces its strength. On the other hand, imposing a RH on a block lower than its equilibrium RH leaves the block strength unaffected. Blocks with a high equilibrium RH are thus likely to be more resistant to RH variations.

5.1.2 Long-term load test

A long-term load test was set up to verify the previous laboratory test results and to investigate the involved mechanisms phenomenologically. Four groups of blocks with different initial production parameters (WC and compaction pressure) were emplaced in September 2013 at the Grimsel Test Site in Switzerland. The RH in the tunnel air at that time varied around 70%. All block sets were loaded with a pressure similar to the one exerted by a heater on a bentonite block pedestal in the FE experiment.

Blocks compacted at a low WC disintegrated in a short period of time. Only hours after the start of the test cracks appeared, which propagated quickly. The cracks were generated by swelling, caused by water absorption of the relatively dry bentonite from relatively wet air. The support capability of the low WC blocks was lost within only

1 month. Blocks produced with a high WC, and thus characterised by a higher equilibrium RH, on the other hand, took up nearly no water and proved to be very stable over a long period of time (>1.5 years).

The equilibrium RH allows whether or not a compacted bentonite block will disintegrate in ambient conditions to be determined according to the following simple rule: a bentonite block is stable as long as the RH of the ambient air does not exceed its equilibrium RH by more than 5–10%. This concept proved to be successful as no bentonite blocks were affected during the emplacement operations of the FE experiment.

5.1.3 Full-scale load tests

In April 2014 a short-term, full-scale load test was set up at the Grimsel Test Site. This test was performed to check the maximum load a bentonite block pedestal can take and to verify the upscaling results obtained by ‘hybrid finite-discrete element method’ (FEMDEM) modelling using mechanical parameters derived from laboratory tests.

The test set-up for this full-scale load test consisted of a bentonite block pedestal with the same dimensions (in a transversal section) as in the FE experiment, which was loaded vertically (Fig. 12). The test was performed in ambient air RH lower than the block equilibrium RH. It was found that, under these conditions, a FE-sized



Fig. 12 Test set-up of the full-scale load test of a bentonite block pedestal at the Grimsel Test Site

bentonite block pedestal can support loads of more than 1,000,000 kg.

5.1.4 Main block production

After concluding all test productions and pre-tests, the block production parameters for the FE experiment were set to obtain stable blocks that are able to support the 5000 kg heaters under the expected climatic conditions at the Mont Terri rock laboratory. The chosen production parameters were (i) a raw material WC (= mass of water lost during oven drying at 105 °C divided by the dry mass of the material) of 18% and (ii) a compaction pressure of 130 MPa. With these production parameters, around 2500 rectangular blocks (each with a weight of 24.4 kg and dimensions of 40 cm by 20 cm by 14.5 cm) and 500 curved ‘top layer’ blocks (each with a weight of 11.65 kg and dimensions of 40 cm by 10 cm by 10.7–20.5 cm) were produced in March 2014 from the raw material ‘MPC Bentosund WH2’ (Garitte et al. 2015).

The bentonite blocks were produced at a rate of 1 block per minute using a natural sodium bentonite. The selected compaction pressure and WC resulted in an average ‘dry density’ (DD) of 1.78 g/cm³. Besides compaction pressure and WC, the following parameters were submitted to an intensive quality control, acting as rejection criteria during the block production: (i) block dimensions, (ii) density, (iii) no visible cracks/damage and (iv) a minimum UCS of 6 MPa.

5.1.5 Block storage

After production, the bentonite blocks were stacked on pallets and then wrapped tightly with plastic foil to prevent water absorption from the environment, which could have caused damage. 5% of the pallets were equipped with a wireless RH sensor to detect potential leakage of the packaging. All RH sensors showed that the tightness of the pallet packaging was assured throughout the storage period and that the bentonite blocks were unaffected by the RH evolution outside the packaging.

5.2 Granulated bentonite mixture

The raw bentonite material needed for the production of the highly compacted and ‘granulated bentonite mixture’ (GBM) used for backfilling the FE tunnel was obtained through open tender (Garitte et al. 2015). Approximately 350,000 kg of raw bentonite (‘CEBO National Standard’) were transformed into a GBM. The aim of the GBM production process was to increase the bulk DD of the raw bentonite material (approximately 0.9 g/cm³) to an emplaced DD of at least 1.45 g/cm³.

Blümling and Adams (2008) presented a summary of the work carried out on the use of bentonite pellets as backfilling material within the framework of a borehole sealing project. The authors showed in a very systematic way that the emplaced DD is dependent on (i) the DD of individual pellets, (ii) the grain size distribution of the mixture, (iii) the pellet particle shape and (iv) the emplacement method.

The production of a GBM includes several processing steps (Hoffmann et al. 2007). For the FE experiment, the raw material was provided at a WC of about 10–15%. It was then dried by heating to obtain a lower WC in the range of 4–6%, close to the Proctor's optimum, which is associated with a higher pellet DD. The maximum temperature to which the raw bentonite was exposed during the drying process was 80 °C. Considering the upper temperature limit, the drying capacity depended exclusively on the grain size distribution of the raw material and the residence time in the heating chamber. Approximately 1500 kg of raw bentonite were dried per hour in the production for the FE experiment.

The aim during the pelletising process is to increase the pellet DD. For the FE experiment, the pellets were produced by compaction between flat rollers (resulting in pellets of irregular shape). Although alternative methods exist (Pietsch 2004), this method was found to be better from an economic point of view, with a reasonable production rate (1000–2000 kg per h). The negative side of this production method was that the desired maximum grain size could not be reached. The bentonite pellets produced were then mixed in a Kniele mixer, providing enough energy to break some of the pellets, resulting in a mixture with a broad grain size distribution (Fig. 13), the aim being to fill larger pores between large particles with smaller particles at all scales. A specific mixing cycle was



Fig. 13 Photo of the highly compacted ‘granulated bentonite mixture’ (GBM) produced for the FE experiment. For the individual pellets, an average dry density of 2.18 g/cm³ was achieved by compaction between flat rollers

designed to obtain a grain size distribution close to a ‘Fuller distribution’ (Fuller and Thompson 1907). The mixture production rate for the FE experiment was approximately 2000 kg per h.

6 Backfilling machine

6.1 Backfilling concept

A ‘backfilling machine’ (BFM) is needed to backfill a horizontal disposal tunnel with GBM as tightly and homogeneously as possible. Density is considered the key property for ensuring adequate long-term performance of the bentonite-based backfill material in a repository since it directly influences the safety-relevant attributes such as swelling pressure, gas- and water permeability, porosity and suppression of microbial activity. Suppression of microbial activity sets perhaps the most stringent density requirement. Stroes-Gascoyne (2011) reported that microbial activity is clearly suppressed in highly compacted bentonite. Leupin and Johnson (2013) concluded that a saturated density of 1.90 g/cm³ (corresponding to a DD of 1.45 g/cm³) for MX-80 bentonite is a desirable target as it may decrease the likelihood of microbially induced corrosion.

Based on the experience from the EB experiment (Kennedy and Plötze 2004) and the ESDRED project (Plötze and Weber 2007), the decision was made to design and fabricate a BFM with five screw conveyors for the FE experiment. The aim of using five screw conveyors was to improve the backfilling quality in terms of homogeneity, since segregation effects had been observed during previous projects. A staggered alignment of the screw conveyors was chosen with respect to the expected slope angle of the backfilled material. Moreover, an increased compaction was expected as each screw conveyor was designed to remain within the material bulk, building up a conveyance pressure.

6.2 Backfilling pre-tests

Before the BFM was constructed, Two pre-tests were carried out at a test facility close to Flums in Switzerland (Köhler et al. 2015). The first pre-test (performed in September 2012) focused on the coupled effects of (i) the material conveyance, (ii) the resulting backfilling pressure, (iii) the potential to push the material upwards and (iv) the corresponding actuation parameters of the screw conveyors. It was found that the ESDRED screw conveyors had the power to push GBM up to 70 cm upwards, if the resulting push back forces were kept under control by strong brakes.

The second pre-test (performed in March 2013) aimed at (i) a better understanding of the bulk material behaviour as influenced by additional measures (such as slope coverage, insertion of vibration needles, etc.) and (ii) collecting data on the achievable bulk DD with regard to the grain size distribution of the GBM. It was found that, without additional measures (such as a slope coverage), small material avalanches occur at the front of the slope, resulting in ‘fir-tree like’ segregation effects in the backfilled material (Fig. 14).

6.3 Machine construction

In line with the Swiss disposal concept, the backfilling system for the FE experiment was designed to fit into small diameter disposal tunnels. With a view to operational robustness and precision, all machinery was developed rail-bound. An additional benefit of the rail-bound system in the FE experiment was precise manoeuvrability and therefore the reduced risk of collision with the experimental instrumentation.

The backfilling system consists of the BFM with a screw conveyance system and the feeding wagon (Fig. 15). The feeding wagon was designed as a vehicle carrying 4 big-bags (containing the GBM needed for backfilling) hanging on rollers to be pushed forward manually as soon as the bigbag in the front was emptied and removed. The feeding wagon for the FE experiment has no demonstration character with regard to the Swiss disposal concept; it is purely an economical solution for a non-industrial scale experiment.

The core component of the BFM is the conveyance unit. It consists of a horizontal discharging screw conveyor placed below the feeding hopper and a vertical and a horizontal feeding conveyor towards the distribution box. The latter is equipped with level transmitters to adjust the speed of the discharging screw and thus provides optimum conditions for the GBM to flow steadily through the distribution box into the five horizontal screw conveyors. These are aligned in a staggered manner with respect to the (approximately 35°) material slope in the backfilled tunnel. The tips of the screw conveyor tubes are cut obliquely in order to push the conveyed material upwards. During backfilling, all screw conveyors remain in the GBM slope in order to prevent dust formation and to build up a backfilling pressure. This pressure pushes the material upwards, also filling irregular cavities in the upper part of the tunnel profile.

The BFM is held in place by hydraulic brakes (until a repulsive force of 32 kN is reached) in order to maintain a high backfilling pressure. The machine parameters such as each actuator’s power consumption, rotation speed and the hydraulic braking force can be regulated using sophisticated controls (Jenni and Köhler 2015).

6.4 Mock-up backfilling tests

Before acceptance of the prototype BFM, it had to be extensively tested (Köhler et al. 2015). For this purpose, a test site was set up at a workshop in Grono, Switzerland, where all relevant processes related to heater emplacement and backfilling could be tested (Fig. 16). Temporary rails



Fig. 14 ‘Fir-tree like’ segregation effects due to small material avalanches at the slope as seen in the second pre-test (*top pictures*) can easily be avoided by covering the slope, e.g. with a flexible mat (*bottom pictures*)



Fig. 15 Visualisation of the prototype ‘backfilling machine’ (BFM) with its five screw conveyors (driving over an approximately 1 m diameter canister on a bentonite block pedestal) developed for

backfilling the horizontal FE tunnel. The total length of the BFM (including the feeding wagon with the four bigbags containing the GBM) is 17 m



Fig. 16 Photo (by COMET) of the prototype BFM (with the control unit at the back and the feeding unit carrying four bigbags) during the mock-up backfilling test at a workshop in Grono, Switzerland

and a full-scale ‘test tunnel’ (made of industrial steel sheets) with a diameter of 2.5 m and a length of 8 m were installed. The test set-up had the advantage that the back-filled material could be accessed not only through the slope, but also radially through the wall of the ‘test tunnel’. Local density measurements were performed with dielectric sensors and radioactive logging tools as well as horizontal ‘cone penetration testing’ (CPT) equipment.

This ‘test tunnel’ was filled twice within the framework of the FE experiment. During the first mock-up backfilling test performed in May 2014, the focus was on technical functionality and procedural optimisation. During the second mock-up backfilling test performed in August 2014, the backfilling process was optimised in order to achieve higher bulk densities.

Regarding ‘quality control’ (QC) measures, the bulk density was calculated by mass-volume balance (=back-filled weight divided by backfilled volume). In the first mock-up backfilling test, the volume was estimated by combining the known geometry of the ‘test tunnel’ and the application of a 3D camera based on time-of-flight technology to capture the slope geometry. For the second

mock-up backfilling test, the slope was laser scanned with a geodetic total station.

The average bulk DDs achieved with the mock-up backfilling tests are listed in Table 4. The target DD of 1.45 g/cm³ was clearly exceeded, especially around the canister where a bulk DD of approximately 1.53 g/cm³ was reached. At the same time, the required functionality demonstration of the BFM, before using it at the Mont Terri rock laboratory, was performed successfully.

7 Emplacement and backfilling

The backfilling of the FE tunnel was performed in several steps (Köhler et al. 2015). The filling of the deep end of the FE tunnel was done in July 2014 with porous concrete for a potential future artificial saturation of the bentonite block wall.

7.1 Bentonite block wall

In the FE tunnel, a 2 m long bentonite block wall was constructed in the ‘interjacent sealing section’ (ISS)

Table 4 Bulk dry densities calculated from mass-volume measurements in the two full-scale mock-up backfilling tests in Grono, Switzerland

Mock-up backfilling test	No. 1 (overall)	No. 2 (behind canister)	No. 2 (around canister)	No. 2 (overall)
Bulk dry density	1.498 g/cm ³	1.490 g/cm ³	1.525 g/cm ³	1.502 g/cm ³
Deviation	±0.023	±0.013	±0.022	±0.009

between TM44.65 and TM46.65 to (i) investigate what DD can reasonably be expected with bentonite blocks assembled in such a tunnel section, (ii) verify the construction feasibility of a bentonite block wall considering the irregular tunnel surface and (iii) be able to potentially measure the sealing effectiveness of the wall at a later experimental stage.

The construction of the bentonite block wall (Fig. 17) took place in early September 2014, when the RH of the seasonally changing tunnel air in the Mont Terri rock laboratory was at around 80–85%. The bentonite blocks survived the 2 weeks of emplacement without any degradation.

In total, about 14 m³ of bentonite blocks were emplaced manually within Nine working days. The average DD of each block was 1.78 g/cm³; the average WC was 18%. Finally, a global bulk DD of 1.69 ± 0.05 g/cm³ was achieved for the entire bentonite block wall.

7.2 Bentonite block pedestal

As preparation for each heater emplacement and backfilling, a bentonite block pedestal was assembled on a prepared concrete surface. Because of the numerous sensors and cables within this bentonite block pedestal, the work was done manually, not exhibiting any demonstration character with respect to the Swiss disposal concept. Each bentonite block pedestal was 4.4 m long, 0.8 m wide and 0.54 m high. In total, each pedestal consisted of 132



Fig. 17 Photo (by COMET) of the unfinished bentonite block wall in the 'interjacent sealing section' (ISS) at the deep end of the FE tunnel

rectangular bentonite blocks (à 24.4 kg) and 88 curved top layer bentonite blocks (à 11.65 kg).

After the completion of each bentonite block pedestal, the appropriate heater was driven into the FE tunnel with an emplacement wagon specially designed for this purpose. After precisely manoeuvring the 5000 kg heater over the heavily instrumented pedestal, the heater was carefully lowered onto the pedestal with the help of hydraulic cylinders, avoiding any point loads on the bentonite blocks.

In this manner, heater H1 was emplaced in October 2014, heater H2 (Fig. 18) in November 2014 and heater H3 in January 2015. Due to the intensive instrumentation, cable routing and QC work, the construction of one bentonite block pedestal including the associated heater emplacement took between 8 and 13 working days.

7.3 Backfilling

First, the remaining 6.6 m of the ISS were backfilled with the help of the BFM. A total of around 70,000 kg of GBM were emplaced in the ISS within four working days. The large cavities, particularly in the top part of the tunnel, were filled without any problems.

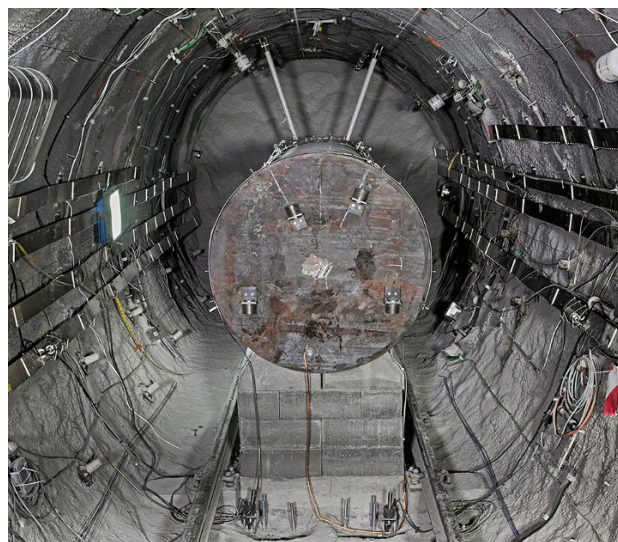


Fig. 18 Photo (by COMET) of a bentonite block pedestal supporting a heavily instrumented heater in the FE tunnel. The greyish mass in the background is a slope of GBM backfilled prior to the construction of the pedestal. The cable routing channels made from stainless steel can be seen on the tunnel wall

After the construction of each bentonite block pedestal and the subsequent emplacement of the associated heater, each section was then backfilled individually. The BFM (Fig. 19) with its 8.5 m long top screw conveyor was designed to be able to drive over the bentonite block pedestal with the emplaced heater so that the screw conveyor tips could still be inserted into the (last) GBM slope (covering the preceding bentonite block pedestal and heater).

Each feeding wagon carried 4 bigbags of GBM, which corresponded to approximately 0.5–0.75 m of backfilled length in the FE tunnel. To complete the whole sequence for each heater, around 60 bigbags (each with a weight of 1000 kg) had to be backfilled, resulting in the feeding wagon being reloaded 15 times. The reloading of bigbags was done at a distance of 75 m from the FE tunnel at the intersection of the MB tunnel with GA08, while the backfilling unit remained in the FE tunnel with the screw conveyor tips inserted in the GBM slope. This sequence was repeated for each of the three heaters. Backfilling one 4.5 m long heater including the 3 m long gap between two heaters took 2–3 working days. Together with the relevant section of the ISS and the volume towards the plug, 29.6 m of the FE tunnel were filled with approximately 255,000 kg of GBM.

Each of the 11 times the BFM was driven out of the FE tunnel, for instrumentation and QC purposes the available GBM slopes were scanned with a 3D laser scanner in order to determine the backfilled volumes. Together with the weighing of each bigbag used for backfilling, the backfilled bulk DD was calculated for each of these 12 sections (Fig. 20). Considering the disturbance by e.g. sensors and cables, the global DD of approximately 1.49 g/cm³



Fig. 19 Photo (by COMET) of the prototype BFM in the FE tunnel at the Mont Terri rock laboratory

achieved in the FE tunnel without any break-downs or accidents can be considered as a very satisfactory result.

8 Plug

The backfilling of the FE tunnel was completed by step-wise construction of a vertical retaining wall in February 2015. This retaining wall consisted of 20 cm thick (according to the tunnel geometry pre-fabricated) concrete segments stacked in five rows. The interface of this retaining wall with the backfilled GBM was located at TM15. Finally, the retaining wall was sealed with two layers of resin in order to reduce vapour and gas transport. In total, approximately 750 sensors and heater cables had to be routed through this retaining wall. They were guided through the plug in two separate tubes which were filled with resin to reduce vapour and gas transport.

After the completion of this preparatory work, the plug was constructed. The FE plug was designed to withstand the potential swelling pressure of a fully saturated bentonite backfill (approximately 3 MPa for an average bulk DD of around 1.45 g/cm³), although full saturation is not expected to occur within the experiment monitoring period (approximately 10–15 years) because of the low permeability of the surrounding rock. The conservative design of this ‘friction controlled’ plug was achieved with the installation of 50 steel dowels inserted perpendicularly into the rock—shotcrete lining—plug interface. On the 17th of March 2015, 31 m³ of self-compacting concrete were pumped into the space between the retaining wall at TM14.8 and the formwork placed at TM9.8. In order to limit the curing temperature to a maximum of 50 °C, a major part of the cement (around 50%) was replaced by fly ash. 40 days after casting, the shrinkage gap at the shotcrete lining—plug interface, estimated to be less than 1 mm and resulting from settlement of the fresh concrete and from drying, was injected with resin with a pressure of 0.5 MPa.

With the plug construction, and particularly with the removal of the formwork, the on-site work in connection with the implementation of the FE experiment at the Mont Terri rock laboratory was completed successfully.

9 Heating

For the FE experiment, three customised heaters each with a length of 4.6 m and a diameter of 1.05 m were manufactured and then emplaced in the FE tunnel. The heaters were designed as hollow carbon steel cylinders in order to allow the installation of electrical resistance heating cables on the inside. This set-up resulted in a heater weight of 5000 kg each.

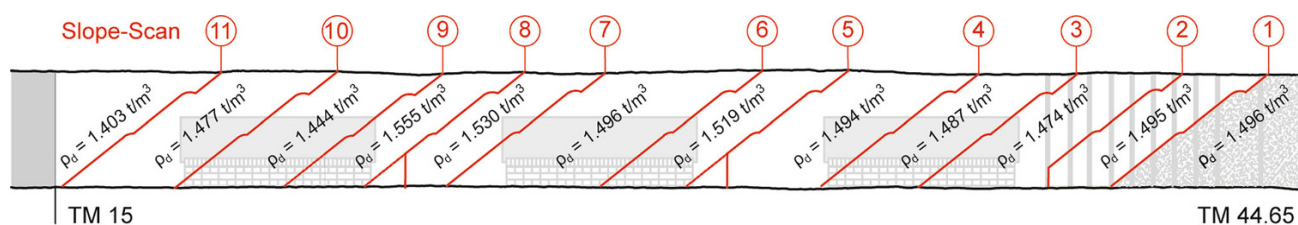


Fig. 20 Longitudinal section of the backfilled FE tunnel indicating the position of the 3D slope scans and the resulting bulk dry densities calculated for each of the sections. Around the five screw conveyor

outlets, the bulk dry density locally reached approximately 1.7 g/cm^3 ; a value comparable to the bulk dry density of a bentonite block pedestal

After the heater emplacement and the subsequent backfilling, the heating phase was started in December 2014 with the ‘deepest’ heater H1 first. Finally, in February 2015, the middle heater H2 and the ‘shallow’ heater H3 close to the plug were turned on (Fig. 21). The heaters are run power-controlled, meaning that the temperature is not fixed and is therefore an experimental outcome. The resulting temperature distribution is influenced mainly by the thermal properties of the (at the beginning relatively dry and therefore poorly heat-conducting) bentonite backfill, but also by the thermal properties of the rock and the boundary conditions at the Mont Terri rock laboratory.

According to current plans, the initial power level of 1350 Watt per heater will be kept constant for at least the first 3 years after the start of heating. Afterwards, it is currently planned to decrease the power according to a decay function typical for spent fuel. The heating and monitoring phase of the FE experiment at Mont Terri is envisaged to last at least 10–15 years. First temperature measurements from the surface of H1 and the comparison to the numerical simulations and predictions are shown in Fig. 22.

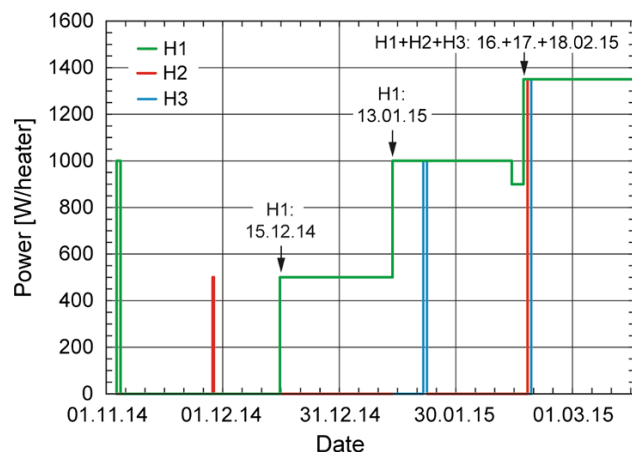


Fig. 21 Time series plot showing how the (power-controlled) heating of the FE experiment at Mont Terri rock laboratory was started. The ‘deepest’ heater H1 was backfilled and turned on first. The first power step at 500 Watt was started on 15th of December 2015. After 1 month the power was increased to 1000 Watt. Finally, on 16th, 17th and 18th of February 2015, all three heaters were turned on successively to a power level of 1350 Watt for each heater

10 Concluding remarks

Within the framework of the FE experiment, the construction of a disposal tunnel in Opalinus Clay using standard industrial equipment and horizontal canister emplacement and backfilling were successfully tested. During the production of the GBM, the material treatment, pelletisation, grinding and mixing were studied in a systematic way and optimised in order to obtain properties that fulfil all requirements. The resistance of the bentonite blocks to varying tunnel climate conditions was improved by optimisation of the production parameters.

Experience from previous experiments led to the design of a prototype BFM with five screw conveyors, allowing the horizontal backfilling of disposal tunnels with GBM as densely and homogeneously as possible. After construction, this machine underwent intensive testing. The minimum bulk DD of 1.45 g/cm^3 , as targeted for the bentonite backfill according to the Swiss repository concept, was exceeded in the mock-up backfilling tests and in the FE tunnel without any break-downs or accidents. The optimisation, industrialisation and automation of these

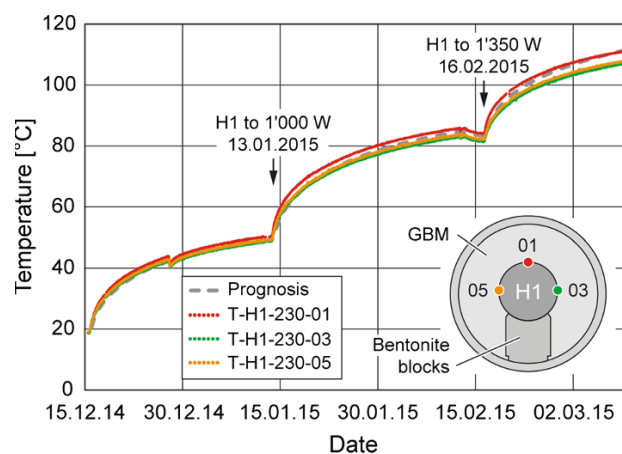


Fig. 22 Time series plot showing how the surface temperature of the ‘deepest’ heater H1 reacted to the selected turn-on sequence. The calculated temperature prediction for an initially (with a water content of approximately 5%) relatively dry GBM with a thermal conductivity of 0.3 W/mK is represented as a dashed grey line in the background

processes can be completed in the decades remaining until the start of repository operation.

The main aim of the FE experiment at the Mont Terri rock laboratory is the investigation of repository-induced effects and validation of existing coupled THM models. Three electrical heaters with dimensions similar to those of future canisters were emplaced in the FE tunnel before backfilling. All heaters were turned on between December 2014 and February 2015 and are planned to constantly emit 1350 Watt each, at least for the first 3 years. Afterwards it is planned to decrease the power according to a decay function typical for spent fuel.

For monitoring the effects of this full-scale heating on the backfill and the host rock, several hundred sensors were installed in and around the FE tunnel. These sensors measure various parameters such as temperature, pressure, deformation, humidity/water content, gas composition, etc. At the end of the continuous heating period, temperatures of approximately 130–150 °C at the surface of the middle heater and approximately 60–80 °C at the rock surface are expected.

The FE experiment can be considered a very important step with a potentially significant outcome for the Swiss disposal concept. It could have a direct influence on the design of future disposal tunnels and also on the loading of the future repository canisters.

Acknowledgements This work is dedicated to the late Peter Blümling, who was one of the main initiators of the FE experiment. The FE experiment was implemented at the Mont Terri rock laboratory, which is operated by swisstopo. The initiator and lead organisation of the FE experiment is Nagra (Switzerland). We thank ANDRA (France), BGR (Germany), DOE/LBNL (USA), GRS (Germany) and NWMO (Canada) for participating in the FE experiment. We also acknowledge our colleagues from swisstopo for their continuous help and efforts during the on-site work. The engineering and demonstration components of the FE experiment were also part of Nagra's participation in the EU project 'Large Underground COncEpt EXperiments' (LUCOEX); parts of the research leading to these results have therefore received funding from the European Union's European Atomic Energy Community's (Euratom) Seventh Framework Programme FP7/2007-2013 under Grant Agreement No. 269905. We are grateful to Bruno Kunz for enhancing the figure quality, Linda McKinley for improving the English of the manuscript and Petra Blaser for the consistency check. Last but not least we thank the reviewers Klaus Wiczorek (Gesellschaft für Anlagen- und Reaktorsicherheit GmbH, Braunschweig, Germany) and Jan Verstricht (Belgian Nuclear Research Centre, Mol, Belgium) for their time and constructive feedback helping to further improve the quality of this publication.

Open Access This article is distributed under the terms of the Creative Commons Attribution 4.0 International License (<http://creativecommons.org/licenses/by/4.0/>), which permits unrestricted use, distribution, and reproduction in any medium, provided you give appropriate credit to the original author(s) and the source, provide a link to the Creative Commons license, and indicate if changes were made.

References

- Alonso, M. C., García Calvo, J. L., Walker, C., Naito, M., Pettersson, S., Puigdomenech, I., et al. (2012). Development of an accurate pH measurement methodology for the pore fluids of low pH cementitious materials. *SKB report, R-12-02*. Swedish Nuclear Fuel and Waste Management, Stockholm, Sweden. www.skb.se.
- Bernier, F., Li, X.-L., & Bastiaens, W. (2007). Twenty-five years' geotechnical observation and testing in the Tertiary Boom Clay formation. *Géotechnique*, 57(2), 229–237.
- Blümling, P., & Adams, J. (2008). Grimsel test site investigation phase IV: Borehole sealing. *Nagra Technical Report, NTB 07-01*. Nagra, Wettingen, Switzerland. www.nagra.ch.
- Bosgiraud, J. M., Nachmilner, L., Hooper, A., Pettersson, S., Fries, T., Verstricht, J., et al. (2015). Expert group report. *EU project LUCOEX, deliverable D1.14*. www.lucoex.eu.
- Bossart, P., Bernier, F., Birkholzer, J., Bruggeman, C., Connolly, P., Dewonck, S., Fukaya, M., Herfort, M., Jensen, M., Matray, J.-M., Mayor, J. C., Moeri, A., Oyama, T., Schuster, K., Shigeta, N., Vietor, T., & Wiczorek, K. (2017). Mont Terri rock laboratory, 20 years of research: Introduction, site characteristics and overview of experiments. *Swiss Journal of Geosciences*, 110. doi:10.1007/s00015-016-0236-1 (this issue).
- Daneluzzi, R., Burrus, F., Küttel, T., Müller, H. R., & Köhler, S. (2014). Report on the construction of the emplacement tunnel. *Nagra working report, NAB 14-54*, Nagra, Wettingen, Switzerland and *EU Project LUCOEX, Deliverable D2.2*. www.lucoex.eu.
- Fuller, W. B., & Thompson, S. E. (1907). The laws of proportioning concrete. *Journal of Transportation Engineering-ASCE*, 59, 67–143.
- Garitte, B., Weber, H. P., & Müller, H. R. (2015). Requirements, manufacturing and QC of the buffer components. *Nagra Working Report, NAB 15-24*, Nagra, Wettingen, Switzerland and *EU Project LUCOEX, Deliverable D2.3*. www.lucoex.eu.
- Gaus, I., Wiczorek, K., Schuster, K., Garitte, B., Senger, R., Vasconcelos, R., et al. (2014). EBS behaviour immediately after repository closure in a clay host rock: HE-E experiment (Mont Terri URL). *Geological Society, London, Special Publications*, 400(1), 71–91.
- Gens, A., Vaunat, J., Garitte, B., & Wileveau, Y. (2007). In-situ behaviour of a stiff layered clay subject to thermal loading. Observations and interpretation. *Géotechnique*, 57(2), 207–228.
- Gens, A., Wiczorek, K., Gaus, I., Garitte, B., Mayor, J.C., Schuster, K., Armand, G., García-Siñeriz, J.-L., Trick, T. (2017). Performance of the Opalinus Clay under thermal loading: experimental results from Mont Terri rock laboratory (Switzerland). *Swiss Journal of Geosciences*, 110. doi:10.1007/s00015-016-0258-8 (this issue).
- Gugala, J. (2015). Final report LUCOEX—WP3. ALC full scale emplacement experiment. *EU project LUCOEX, deliverable D3.4*. www.lucoex.eu.
- Hoffmann, C., Alonso, E. E., & Romero, E. (2007). Hydro-mechanical behaviour of bentonite pellet mixtures. *Physics and Chemistry of the Earth*, 32, 832–849.
- Hostettler, B., Reisdorf, A.G., Jaeggi, D., Deplazes, G., Bläsi, H.-R., Morard, A., Feist-Burkhardt, S., Waltschew, A., Dietze, V., Menkveld-Gfeller, U. (2017). Litho- and biostratigraphy of the Opalinus Clay and bounding formations in the Mont Terri rock laboratory (Switzerland). *Swiss Journal of Geosciences*, 110. doi:10.1007/s00015-016-0250-3 (this issue).
- Jenni, H., & Köhler, S. (2015). Full-scale emplacement (FE) experiment: Report on the construction, testing and commissioning of the emplacement equipment. *Nagra working report*,

- NAB 15-25, Nagra, Wettingen, Switzerland and EU Project LUCOEX, Deliverable D2.4. www.lucoex.eu.
- Jenni, A., Mäder, U., Lerouge, C., Gaboreau, S., & Schwyn, B. (2013). In situ interaction between different concretes and Opalinus Clay. *Physics and Chemistry of the Earth, Parts A/B/C*, 70, 71–83.
- Johannesson, L.-E., Gunnarsson, D., Sandén, T., Börgesson, L., & Karlzén, R. (2004). Äspö Hard Rock Laboratory. Prototype repository. Installation of buffer, canisters, backfill, plug and instruments in Section II. *SKB report, IPR-04-13*. Swedish Nuclear Fuel and Waste Management, Stockholm, Sweden. www.skb.se.
- Karlund, O. (2010). Chemical and mineralogical characterization of the bentonite buffer for the acceptance control procedure in a KBS-3 repository. *SKB Report, TR 10-60*. Swedish Nuclear Fuel and Waste Management, Stockholm, Sweden. www.skb.se.
- Kennedy, K., & Plötze, M. (2004). Engineered barrier emplacement (EB) experiment in Opalinus Clay: Granular material backfill emplacement method evaluation. *EU project deliverable D4*.
- Köhler, S., Garitte, B., Weber, H. P., & Müller, H. R. (2015). FE/LUCOEX: Emplacement report. *Nagra working report, NAB 15-27*, Nagra, Wettingen, Switzerland and EU Project LUCOEX, Deliverable D2.5. www.lucoex.eu.
- Lanyon, G. W., & Gaus, I. (Eds.) (2013). Main outcomes and review of the FEBEX in situ test (GTS) and mock-up after 15 years of operation. *Nagra working report, NAB 13-96*, Nagra, Wettingen, Switzerland. www.nagra.ch.
- Leupin, O. X., & Johnson, L. H. (2013). Buffer requirements for a SF/HLW repository in Opalinus Clay. *Nagra working report, NAB 13-46*, Nagra, Wettingen, Switzerland. www.nagra.ch.
- Lisjak, A., Garitte, B., Grasselli, G., Müller, H. R., & Vietor, T. (2015). The excavation of a circular tunnel in a bedded argillaceous rock (Opalinus Clay): Short-term rock mass response and FDEM numerical analysis. *Tunnelling and Underground Space Technology*, 45, 227–248.
- Lothenbach, B., Rentsch, D., & Wieland, E. (2014). Hydration of a silica fume blended low-alkali shotcrete cement. *Physics and Chemistry of the Earth, A/B/C*, 70, 3–16.
- Marschall, P., Giger, S., De La Vassière, R., Shao, H., Leung, H., Nussbaum, C., et al. (2017). Hydro-mechanical evolution of the EDZ as transport path for radionuclides and gas: Insights from the Mont Terri rock laboratory (Switzerland). *Swiss Journal of Geosciences*, 110. doi:10.1007/s00015-016-0246-z (this issue).
- Müller, H. R., Garitte, B., Köhler, S., Vogt, T., Sakaki, T., Weber, H. P., et al. (2015). FE/LUCOEX: Final report. *Nagra working report, NAB 15-28*, Nagra, Wettingen, Switzerland and EU Project LUCOEX, Deliverable D2.6. www.lucoex.eu.
- Nagra. (2002). Projekt Opalinuston: Konzept für die Anlage und den Betrieb eines geologischen Tiefenlagers: Entsorgungsnachweis für abgebrannte Brennelemente, verglaste hochaktive sowie langlebige mittelaktive Abfälle. *Nagra technical report, NTB 02-02*. Nagra, Wettingen, Switzerland. www.nagra.ch.
- Nagra. (2010). Beurteilung der geologischen Unterlagen für die provisorischen Sicherheitsanalysen in SGT Etappe 2. Klärung der Notwendigkeit ergänzender geologischer Untersuchungen. *Nagra technical report, NTB 10-01*. Nagra, Wettingen, Switzerland. www.nagra.ch.
- Nagra. (2014). SGT Etappe 2: Vorschlag weiter zu untersuchender geologischer Standortgebiete mit zugehörigen Standortarealen für die Oberflächenanlage. Geologische Grundlagen. *Nagra technical report, NTB 14-02*. Nagra, Wettingen, Switzerland. www.nagra.ch.
- Nussbaum, C., Kloppenburg, A., Cae'r, T., & Bossart, P. (2017). Tectonic evolution around the Mont Terri rock laboratory, northwestern Swiss Jura: constraints from kinematic forward modelling. *Swiss Journal of Geosciences*, 110. doi:10.1007/s00015-016-0248-x (this issue).
- Leupin, O. X., Birgersson, M., Karlund, O., Korkeakoski, P., Mäder, U. K., Sellin, P., et al. (Eds.) (2014). Montmorillonite stability under nearfield conditions. *Nagra technical report, NTB 14-12*. Nagra, Wettingen, Switzerland. www.nagra.ch.
- Pietsch, W. (2004). *Agglomeration in industry: Occurrence and applications* (Vol. 1). New York: Wiley.
- Plötze, M., & Weber, H. P. (2007). ESDRED Emplacement tests with granular bentonite MX-80. Laboratory results from ETH Zürich. *Nagra working report, NAB 07-24*, Nagra, Wettingen, Switzerland. www.nagra.ch.
- Sakaki, T., Vogt, T., Müller, H. R., Wörsching, H., & Vrzba, M. (2014). モンテリフェ試験におけるオパリナス粘土岩内含水量モニタリング用TDRプローブの開発 [Development of TDR probes for monitoring water content in Opalinus Clay in the FE experiment at Mont Terri Rock Laboratory.] *Proceedings of the 69th JSCE annual meeting*, September 2014, Osaka, Japan.
- Shao, H., Paul, B., Wang, X. R., Hesser, J., Becker, J., Garitte, B., & Müller, H. R. (2015). Near-field permeability distribution of FE tunnel in the Mont Terri Rock Laboratory—Influence of shotcrete lining on EDZ development. *Proceedings of the 6th international conference on clays in natural and engineered barriers for radioactive waste confinement*, March 2015, Brussels, Belgium.
- Stroes-Gascoyne, S. (2011). Microbiological characteristics of compacted bentonite at a dry density of 1450 kg/m³—A literature review. *Nagra working report, NAB 11-05*, Nagra, Wettingen, Switzerland. www.nagra.ch.
- Villar, M. V., Martín, P. L., Gómez-Espina, R., Romero, F. J., & Barcala, J. M. (2012). Long-term THM tests reports: THM cells for the HE-E test: Setup and first results. *PEBS report D2.2.7.1, CIEMAT technical report CIEMAT/DMA/2G210/02/2012*. Madrid, Spain.
- Vogt, T., Müller, H. R., Sakaki, T., & Vietor, T. (2013). Monitoring THM effects in a full scale EBS/host rock system—First experiences of the FE-experiment in the Mont Terri URL during construction and ventilation phase. MoDeRn international conference and workshop, March 2013, Luxembourg. *Deliverable D5.4.1*, 326–334.
- Weber, H. P., Köhler, S., Teodori, S., Müller, H. R., & Vietor, T. (2012). Work plan, work package 2: Full scale emplacement experiment (FE) at Mont Terri. *Nagra working report, NAB 12-10*. Nagra, Wettingen, Switzerland and EU Project LUCOEX, Deliverable D2.1. www.lucoex.eu.
- Wetzig, V., Fries, T., & Iglesias, E. (2011). Low-pH shotcrete: Application as rock support for radioactive waste disposal. *Proceedings of the world tunnel congress*. Helsinki, Finland.

5-year chemico-physical evolution of concrete–claystone interfaces, Mont Terri rock laboratory (Switzerland)

Urs Mäder¹ · Andreas Jenni¹ · Cathérine Lerouge² · Stephane Gaboreau² · Satoru Miyoshi³ · Yukinobu Kimura³ · Veerle Cloet⁴ · Masaaki Fukaya³ · Francis Claret² · Tsubasa Otake⁵ · Masahito Shibata⁶ · Babara Lothenbach⁷

Received: 8 June 2016 / Accepted: 9 December 2016 / Published online: 16 February 2017
© The Author(s) 2017. This article is published with open access at Springerlink.com

Abstract The Cement–Opalinus Clay Interaction (CI) Experiment at the Mont Terri rock laboratory is a long-term passive diffusion–reaction experiment between contrasting materials of relevance to engineered barrier systems/near-field for deep disposal of radioactive waste in claystone (Opalinus Clay). Reaction zones at interfaces of Opalinus Clay with two different types of concrete (OPC and “low-pH”/ESDRED) were examined by sampling after 2.2 and 4.9 years. Analytical methods included element mapping (SEM, EPMA), select spot analysis (EDAX), ¹⁴C-MMA impregnation for radiography, and powder

methods (IR, XRD, clay-exchanger characterisation) on carefully extracted miniature samples (mm). The presence of aggregate grains in concrete made the application of all methods difficult. Common features are a very limited extent of reaction within claystone, and a distinct and regularly zoned reaction zone within the cement matrix that is more extensive in the low-alkali cement (ESDRED). Both interfaces feature a de-calcification zone and overprinted a carbonate alteration zone thought to be mainly responsible for the observed porosity reduction. While OPC shows a distinct sulphate enrichment zone (indicative of ingress from Opalinus Clay), ESDRED displays a wide Mg-enriched zone, also with claystone pore-water as a source. A conclusion is that substitution of OPC by low-alkali cementitious products is not advantageous or necessary solely for the purpose of minimizing the extent of reaction between claystone and cementitious materials. Implications for reactive transport modelling are discussed.

Editorial handling: P. Bossart and A.G. Milnes.

This is paper #15 of the Mont Terri Special Issue of the Swiss Journal of Geosciences (see Bossart et al. 2017, Table 3 and Fig. 7)

✉ Urs Mäder
urs.maeder@geo.unibe.ch

- ¹ Institute of Geological Sciences, University of Bern, Baltzerstrasse 3, 3012 Bern, Switzerland
- ² French Geological Survey BRGM, 3 Avenue Claude Guillemin, 45100 Orléans, France
- ³ Nuclear Facilities Division, Nuclear Waste Technology Department, OYASHI Corporation, 2-15-2, Konan, Minato-ku, Tokyo 108-8502, Japan
- ⁴ National Cooperative for the Disposal of Radioactive Waste NAGRA, Hardstrasse 73, 5430 Wetingen, Switzerland
- ⁵ Division of Sustainable Resources Engineering, Faculty of Engineering, Hokkaido University, Kita 13 Nishi 8, Kita-ku, Sapporo, Hokkaido 060-8628, Japan
- ⁶ Electric and Nuclear Power Technology Department, Taiheiyō Consultant Co. Ltd., 2-4-2, Ohsaku, Sakura 285-0802, Japan
- ⁷ Swiss Federal Laboratories for Materials Science and Technology EMPA, Überlandstrasse 129, 8600 Dübendorf, Switzerland

Keywords Concrete clay interaction · Long-term experiment · OPC · ESDRED · Opalinus Clay · Deep geological disposal of nuclear waste

1 Introduction

Designs for deep storage of radioactive waste foresee cementitious materials as structural elements, backfill or waste matrix. Interactions take place at interfaces of contrasting materials driven by chemical gradients in pore-water causing diffusive fluxes of dissolved species. This may lead to mineralogical alteration in the barrier system which in turn is expected to locally influence properties like porosity/permeability, swelling pressure or specific retention properties in case of concrete in contact with claystone or compacted bentonite. Laboratory experiments

(Adler 2001; Adler et al. 2001; Dauzeres et al. 2010) and in situ experiments (Read et al. 2001; Tinseau et al. 2006; Gaboreau et al. 2011, 2012; Techer et al. 2012; Jenni et al. 2014) demonstrate alteration of both cement paste and claystone adjacent to interfaces. An increase in porosity in the cement paste close to the interface, and clogging in the claystone adjacent to it are commonly predicted by reactive transport modelling (De Windt et al. 2008; Marty et al. 2009; Kosakowski and Berner 2013; Bradbury et al. 2014). Changes in porosity and its distribution—and therefore also permeability—near such interfaces are an important process governing the long-term physicochemical evolution of the engineered barrier and its geological near-field (Kosakowski and Berner 2013, Bildstein and Claret 2015). Clay-rich rocks that are currently under consideration at an advanced stage of repository planning include Opalinus Clay in Switzerland (Nagra 2002), Callovo-Oxfordian “argillite” in France (ANDRA 2005), and Boom Clay in Belgium (SCK-CEN 2012). Clay-based engineered barrier materials include compacted bentonite and sand/bentonite mixtures, among others.

Early efforts (e.g. ECOCLAY-II, European Commission 2005) established a maximum possible extent of deterioration of the clay barrier (worst case) by cementitious materials based on mass balance considerations (Nagra 2002; Mäder and Adler 2005a) or relatively simplistic reactive transport modelling (e.g. Gaucher et al. 2004; De Windt et al. 2004), reflecting limited numerical model capabilities and availability of thermodynamic data. The conclusion was that this “worst-case” extent of degradation (typically some decimeters) would not impact repository performance significantly in clay formations of ca. 100 m thickness (e.g. a key conclusion of ECOCLAY II, European Commission 2005).

More recently, the topic was re-considered in more detail in the context of potential skin effects, whereby a small extent of alteration (e.g. porosity clogging) might have a large impact on gas transport (escaping waste-generated gas) or pore-water transport (e.g. for bentonite saturation) (Kosakowski et al. 2014). In the absence of reliable predictive models, a focus is thus on field studies at repository-like boundary conditions and over time periods in excess of several years, possibly decades. While early work almost exclusively focused on OPC-type concrete (ordinary Portland cement, initial pore-water pH > 13.5), interest in so-called “low-pH” concretes (or low-alkali cementitious products) increased. These low-pH concretes avoid pH values >12.5 [a value buffered by portlandite, $\text{Ca}(\text{OH})_2$] emanating from cementitious materials and thus potentially reduce uncertainty arising from cement interaction at interfaces. Such blends are based on a reduced OPC proportion in combination with addition of a fly ash/slag component and/or reactive silica (silica fume, nanosilica) that promote rapid consumption of portlandite

by hydration to Ca–(Al–)Si-hydrates and ettringite (Ca–Al-sulfate). This will allow pH to drop below 12, typically after some months. Commonly, superplasticizers are required for improved workability, and shotcrete recipes may further include set accelerators, adding dissolved sulphate/aluminate/calcium and possibly also an organic anion component (e.g. formate).

A pioneering experiment with hyperalkaline fluid in Opalinus Clay was carried out at the Mont Terri rock laboratory from 1998 to 2001 that established suitable materials and equipment for circulation systems, electrodes, sampling and analysis of high-pH fluids (Mäder and Adler 2005b). It demonstrated effective buffering of a hyperalkaline fluid by claystone but failed to provide samples of the fluid/claystone interface region due to a technical failure of overcoring. An Mg-layer silicate, calcite and small amounts of Fe-hydroxide were observed as precipitates in the titanium filter sleeve that separated the test interval from the claystone. Associated laboratory batch experiments also did provide insight into some of the expected mineralogical alterations (Adler et al. 1999; Adler and Mäder 1999).

The Cement–Clay Interaction (CI) Experiment carried out at the Mont Terri rock laboratory aims at reducing uncertainties in process understanding related to cement/clay interfaces by providing a detailed analysis of mineralogical changes over relatively long time periods and under realistic boundary conditions. A time frame of at least 20 years is foreseen for the CI experiment, which was installed in 2007. Sampling campaigns were carried out in 2009 and 2012, and most recently in April 2015 (work in progress). This paper summarizes and compares the main findings regarding mineralogy and porosity alterations observed on 2.2 and 4.9 year-old samples at the interfaces between Opalinus Clay and two different types of concrete—an OPC concrete and a low-alkali (low-pH) concrete (named ESDRED). Key issues are a description of the chemico-physical evolution of reaction zones at the interfaces and its consequences for mass transfer in a repository environment, and a comparison of the OPC-claystone and ESDRED-claystone interface region.

2 Experimental setup and sampling campaigns

The experiment is located in the HE-D niche adjacent to Gallery-98 that was excavated in 1998 (see overview map in Bossart et al. 2017). This niche is located in the shaly facies of Opalinus Clay (174 Ma marine shale), with a clay content of ~60 wt%.

The field experiment comprises two vertical boreholes (368 mm diameter, up to 9 m deep, BCI-6 and BCI-7 in Fig. 1) in Opalinus Clay, filled each with sections of three different concretes and also a section of compacted

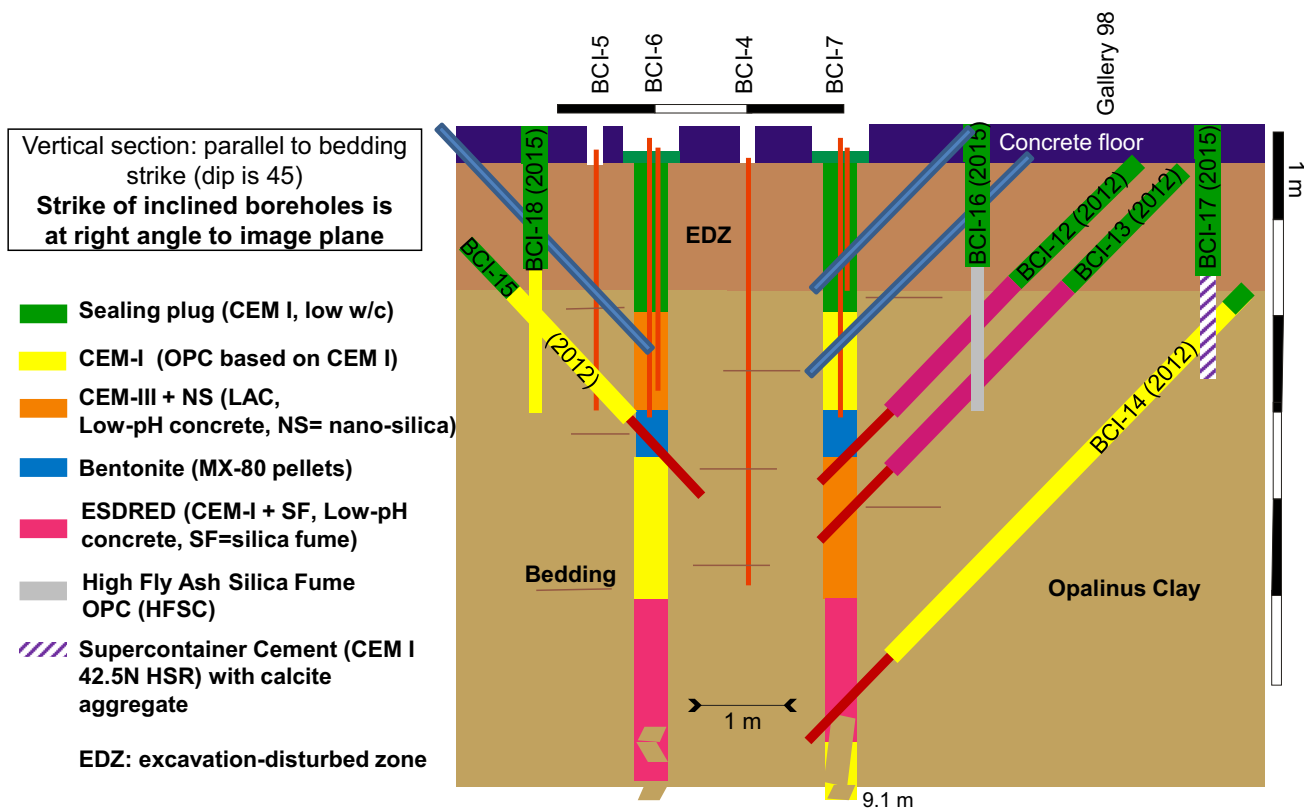


Fig. 1 Layout of CI Experiment at Mont Terri URL (installed 2007). *Dark blue* inclined boreholes: first campaign (2009). *Yellow and purple* inclined boreholes: second campaign (2012). See *text* for further explanations

bentonite. Two monitoring boreholes (BCI-4 and BCI-5, Fig. 1) record pore-water pressure in Opalinus Clay. In order to compare the effect of different cement types on cement–clay interaction, two types of “low-pH” cement (LAC and ESDRED), and an ordinary Portland cement (OPC) were used to prepare the concrete mixtures. Sections containing compacted bentonite pellets were saturated with a built-in system for injection of artificial pore-water (used for ca. 1 year).

During the past 9 years, three sampling campaigns took place. The first campaign (2009) was carried out after 2.2 years (May and July 2009, boreholes BCI-8, BCI-9 and BCI-10, Fig. 1). The interfaces were stabilized by a small central pilot hole in which a reinforcement rod of either threaded steel or an aluminium tube was cemented in (Fig. 2a). This reinforced section was overcored with a single-barrel 86 mm outer diameter (OD) diamond drilling tool equipped with a core catcher and using a simple Hilti drilling machine and compressed air as cooling agent. This operation was only partially successful, and provided only a limited amount of intact LAC and OPC interface samples (Jenni et al. 2014). The interface between ESDRED and Opalinus Clay was recovered from a mock-up experiment of identical age and material and using the same coring technique (Fig. 2c). The mock-up consists of a 284 mm

diameter core of well-preserved Opalinus Clay encased in concrete and kept sealed in a 100 l drum.

An improved interface stabilization technique was developed for the second sampling campaign in February 2012 (Jenni et al. 2014). It involved drilling an approach borehole of 220 mm OD, drilling of 6 small parallel boreholes (46 mm) across the interface in a circular arrangement with a template, and cementing in of fiber glass rods with epoxy resin (Fig. 2b). Overcoring was then performed through the fiber glass armored palisade of the stabilized sample section with 131/101 mm OD/ID double-barrel equipment containing an acrylic liner for additional protection of the core from air circulation. Perfectly preserved samples of the following interfaces could be obtained: OPC-Opalinus Clay (Fig. 2d) and OPC-Bentonite (borehole BCI-15 in Fig. 1), ESDRED-Opalinus Clay (Fig. 2e, borehole BCI-14 in Fig. 1), as well as LAC-Opalinus Clay and LAC-Bentonite (boreholes BCI-12, BCI-13 in Fig. 1).

A third and currently last drilling campaign took place during April 2015. This campaign sampled the interfaces of the backfilled sampling boreholes from the second campaign (BCI-16 to BCI-18, Fig. 1) that contained mortar and paste of OPC and ESDRED. By backfilling boreholes after sampling, new experiments are generated and it will be

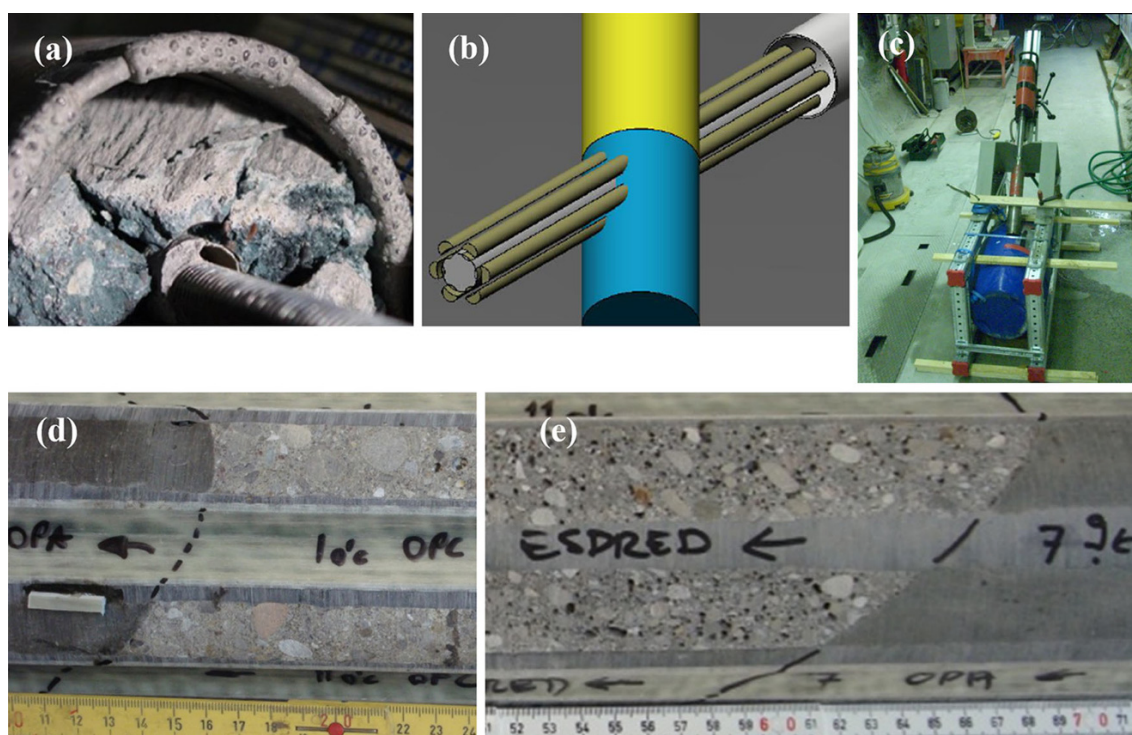


Fig. 2 Sampling technique: first drilling campaign (a); second drilling campaign (b); drilling of ESDRED sample from mock-up (c); drilled core samples from second campaign (lower images): OPC (d) and

ESDRED (e, with abundant former gas pores). Greenish material is fibre glass reinforcement

possible to investigate new cement types, or emplace mortar and paste instead of concrete. The backfills of these latest sampling boreholes include OPC, HSFC (high-silica fume/fly ash concrete developed in Japan) and “super-container cement” (CEM I 42.5 N HSR, calcite aggregate, developed in Belgium), a concrete envisaged for high-level radioactive waste containers encased in a concrete shell.

3 Materials and methods

3.1 Opalinus Clay

Opalinus Clay of the shaly facies comprises ~60 wt% clay minerals (kaolinite \approx illite > illite/smectite mixed layers > chlorite), ~20 wt% calcite, ~12 wt% quartz, ~3 wt% feldspars, ~2 wt% siderite, ~1 wt% dolomite/ankerite, ~1 wt% pyrite and ~1 wt% organic carbon (Pearson et al. 2003; Jenni et al. 2014). The average porosity is 16% (water content of ~6.4 wt%), and the pore-water composition at this location contains ca. 8.4 g/l chloride, 1.13 g/l sulphate, 4.7 g/l sodium, 0.5 g/l calcium, 0.34 g/l magnesium, and 0.022 g/l bicarbonate, a composition adjusted to 10% lower salinity from Koroleva et al. (2011) at the well-studied nearby PC location (see also Table 1). The cation exchange capacity (CEC) ranges from

80-180 meq/kg dry rock depending on clay content (Pearson et al. 2003), and the occupancy is approximately 0.52, 0.21, 0.18, 0.08, 0.01 in equivalent fractions for Na, Ca, Mg, K, Sr, respectively, at the nearby PC location (Koroleva et al. 2011). Samples from the CI location averaged ~120 meq/kg rock for CEC (Jenni et al. 2014, and details below). The clay exchanger includes an inventory of readily available cations of ~120 meq/kg dry rock (260 cation meq/kg_{pw}, 6.4 wt% pore-water) that exceeds the pore-water inventory by a factor of ~7. Illite, illite/smectite mixed layers and kaolinite also contain amphoteric edge sites that can be protonated or deprotonated, and form a pH buffer capacity that may retard the leading (dilute) edge of a high-pH front, for example. The capacity was estimated to be about 0.25% of the CEC, ~0.3 meq/kg, based on a fairly complex derivation from experimental measurements on illite (Bradbury and Baeyens 2000, 2005).

3.2 Concretes (OPC, ESDRED) and cement hydration

The compositions of the two different concrete mixtures are provided in Jenni et al. (2014), including organic additives, and aggregate <16 mm. The main difference between the OPC (CEM I 42.5 R HS) and the low-alkali

Table 1 Approximate initial pore-water concentrations and direction of chemical gradients

Material	Age range	Ca ²⁺	Mg ²⁺	Na ⁺	K ⁺	SO ₄ ²⁻	Cl ⁻	CO ₃ ²⁻	OH ⁻
OPC	0.04–1310	24–2.9	<	26–90	137–209	66–4.5	<	~0.05	>200
ESDRED	0.04–1310	9.2-29	0–0.005	100–22	186–11	2–1.8	<	~0.05	180–7*
Gradient		↑↓ - ↓↑	↑↑	↑↑	↓↓	↑↓ - ↑↑	↑↑	↑↑	↓↓
OPA		12.7	14.3	204	2.3	11.8	237	~0.4	~10 ⁻⁷

Concentrations in mmol/l; age range in days; < indicates below detection; first arrow (or pair) indicates direction of gradient at early time, second arrow at later times; long arrow is for ESDRED, short arrow for OPC

^a Formate is also significant as anionic charge carrier

cementitious product ESDRED (CEM I 42.5 N) is the presence of a substantial amount of silica fume, superplasticizer and set accelerator in the latter. ESDRED was originally developed as a low-pH shotcrete (Alonso et al. 2009). The available samples and their provenance, age and key cement characteristics are summarized in Fig. 3. The interface between ESDRED and Opalinus Clay after 2.2 years was substituted from a mock-up sample cast at the same time as the experiment was installed (Fig. 2c, e). The water/binder ratio of the OPC sample collected after 2.2 years taken from the sealing plug was distinctly lower (0.35) than that used for the OPC sections (0.8) sampled after 4.9 years. Both substitutions were made necessary due to technical difficulties during the first campaign in obtaining samples of sufficient quality. A special feature of the ESDRED concrete is the use of a set accelerator, containing mainly aluminate, sulphate and formate (Andersson et al. 2008; Lothenbach et al. 2014; Wieland et al. 2014).

ment hydration (closed system) was studied experimentally in detail with support from this project and also including thermodynamic modelling of hydration progress. Details and data for the ESDRED mix were published by Lothenbach et al. (2014), Lothenbach (2013) and Wieland et al. (2014), the latter with focus on superplasticizers and its role on radionuclide uptake. OPC hydration and its modelling was published by Lothenbach and Winnefeld (2006) but this was based on a somewhat different cement composition than the one used here, CEM I 42.5 R HS. Experimental results are included in the “Appendix”, adapted from an unpublished Mont Terri Project technical note (Lothenbach 2011).

3.3 Methods

Polished sections and thin sections across the concrete-Opalinus Clay interface were prepared without water contact to avoid rehydration of remaining clinker phases in

Fig. 3 Properties of OPC and ESDRED cement, water/binder ratio, and pictograms of sample provenance. C₃A: tricalcium silicate contained in clinker

	OPC-OPA		ESDRED-OPA	
cement	CEM I 42.5 R HS low C ₃ A (sulfate resistant)		CEM I 42.5 N 40% of cement substituted with silica fume	
age	2.2 y	4.85 y	2.2 y	4.85 y
water/binder	0.35	0.80	0.50	
origin	in-situ 		drum 	in-situ

the cement and dissolution of cement hydrates, and to suppress the swelling of clay minerals and pyrite oxidation in Opalinus Clay. Large differences in hardness and the mechanically weak interfaces posed additional challenges for sample cutting and handling. The samples were first embedded in resin, then the surface to be analysed was chosen at 45° or 90° to the interface plane, and cutting was done with a small diamond saw using petroleum as lubricant. The cut surface was processed using sand paper, oil-based diamond suspensions and petroleum.

Analytical methods except for EPMA (electron probe micro analysis) are described in detail in Jenni et al. (2014) and cater to the fine grained nature of the materials (Opalinus Clay, hydrated cement matrix) and the expected small-scale (mm to μm) multiple mineral alteration zones. In short, the following tools were applied: (1) SEM/EDAX imaging, element mapping and spot analyses in low vacuum mode (University of Bern), (2) transmission light microscopy on polished thin sections, also used for element mapping (University of Bern), (3) EPMA mapping on a JXA-8100 of JEOL (15 keV, $20 \times 20 \mu\text{m}$ and $2 \times 2 \mu\text{m}$ beam size, 40 ms per spot, Obayashi Corp./Taiheiyo Consultant Co.), (4) ^{14}C -doped polymethylmethacrylate (PMMA) impregnation followed by radiography polished surfaces (BRGM), (5) scraping out miniature powder samples from cement matrix and Opalinus Clay for (6) IR measurements, (7) powder XRD, and (8) determination of exchangeable cations and cation exchange capacity (CEC) by the Co-hexamine trichloride method (BRGM), (9) powder XRD on a RIGAKU RINT2500 on thin (mm) slices of sample (Obayashi Corp./Hokkaido University). Synchrotron beamline powder μ -XRD on polished thin sections ($5 \mu\text{m}$) on $200 \mu\text{m}$ thick optical glass carriers (details in Dähn et al. 2014) is selectively quoted, but data has not yet been fully processed.

3.4 Analytical issues and phase identification

Both, cement matrix and clayey matrix do not permit spot analyses (composition, spectroscopy, structure) of pure phases but deliver a signal from a mixture of phases. Resolving such mixtures remains a challenge specifically in case of the presence of amorphous or poorly crystalline phases (e.g. Ca–Si-hydrates, Mg–Si-hydrates, amorphous silica). Element maps combined with spatially resolved methods (EDAX, FTIR, μ -XRD, etc.) are a powerful tool to characterize major bulk mass transfers and some phase identities. This would be the type of information required also for a modelling approach: the scale of alteration, quantitative or semi-quantitative information on mass transfers, and identity or at least restrictions on the participating primary and secondary phases. Further efforts, specifically including μ -XRD are presently on-going. A

quantification of spatially resolved total porosity is also a key issue. Most common methods are hampered by artefacts from sample preparation or by the presence of a large portion of nano-scale and micro-scale porosity. The method applied here using impregnation of ^{14}C -labelled PMMA combined with radiography is thought to be best suited (Gaboreau et al. 2011). The acrylic monomer is a small molecule, mixes with water and has been shown to also penetrate clay-interlayers of smectites (Prêt et al. 2004; Massat et al. 2016). While the pore-geometry cannot be resolved at the relevant small scale, a quantification of local bulk porosity by radiography is possible (quantification involving post-processing of images and calibration is ongoing).

4 Results and discussion

Results of sample analysis from interfaces after 2.2 years were presented in detail by Jenni et al. (2014). Dauzeres et al. (2016) presented details of interfaces between another type of low-alkali cement (LAC) and Opalinus Clay and ESDRED-Opalinus Clay, with focus on the concrete part and Mg–Si-hydrates. Here, we focus on the OPC and ESDRED samples collected after 4.9 years in direct comparison to the samples from the earlier campaign, aiming at a comparison between OPC and low-pH concrete behaviour, and also detailing the claystone part.

4.1 Chemical gradients across interfaces

Transport of dissolved species across the claystone-concrete interface is driven by differences in chemical potentials between the two contrasting pore-waters, and its evolution with time (Table 1, modified from Jenni et al. 2014; ESDRED: Lothenbach 2013, Lothenbach et al. 2014; OPC: “Appendix”). Key gradients in concentrations are opposite for Na and K, large and opposite for Cl and OH, and distinct for Mg and dissolved carbonate from claystone into concrete. Sulphate is being consumed (strongly so in ESDRED) during cement hydration and this leads to a reversal of gradients with time. The gradient in Ca is opposite between OPC (initially high) and ESDRED (initially low) and reverses during hydration. The pore-water evolution in concrete during hydration indicated in Table 1 is valid for closed systems (Lothenbach and Winnefeld 2006; Lothenbach et al. 2014; “Appendix”) but will be different near the interface where dissolved components will exchange with Opalinus Clay and/or are controlled by solubility with respect to different secondary phases than observed in a closed cement system. Specifically, pH may drop due to mineral dissolution (and precipitation) reactions, rather than stay above 13 (OPC) or drop below 12

(ESDRED) after ca. 100 days, as seen during hydration in a closed system. The concentrations of dissolved silica in the hydrating cements are somewhat higher or similar to Opalinus Clay pore-water, and dissolved Al concentrations are about an order of magnitude smaller than Si concentrations. Major components associated with large gradients are therefore OH⁻, Cl⁻, SO₄²⁻, Na⁺, K⁺, Ca²⁺ and Mg²⁺.

More than a third of the anionic charge is initially carried by formate rather than OH⁻ in ESDRED concrete, and formate dominates as charge carrier at later hydration times (Lothenbach et al. 2014). Alkalis diminish rather rapidly in ESDRED concrete after mixing with water, presumably due to incorporation into Ca-Si-hydrate with low Ca/Si, whereas alkalis remain in OPC pore-water during hydration in a closed system (high Ca/Si-ratio Ca-Si-hydrates do not readily incorporate alkalis).

4.2 OPC-Opalinus Clay interface

4.2.1 Zoned interface region: element maps and XRD

The major characteristics (Table 2) of the 2.2- and 4.9-year interfaces were derived from SEM/EDAX images (Figs. 4, 5) and photomicrographs (not shown). Note that bedding trends are inclined at about 45° to the interface, marked for example by shrinkage cracks, best seen on the large-scale false-colour EPMA element maps. The difference in water/binder ratio (w/b) complicates direct comparison of 2.2- and 4.9-year interface characteristics. The very low w/b = 0.35 in case of the 2.2-year sample (sealing plug, Fig. 1) is expected to yield very low capillary porosity in the cement matrix that might significantly reduce diffusive transport. The thicker interaction zones observed after 4.9 years (e.g. sulphur enrichment, carbonate alteration) cannot be attributed solely to longer interaction time, but also to a faster diffusive transport due to a much larger porosity in this w/b = 0.80 OPC. Some specific features

seen in the 2.2 year-old altered cement (details below) are explained by a shortage of water during the earliest hydration stage: despite all precautions, the OPA borehole walls are expected to dry slightly before concrete casting. As soon as the concrete was emplaced, water might have been sucked into the dry margin of OPA and hindered cement hydration. With time, pore-water pressure increased again (as observed in a nearby test interval in Opalinus Clay), and pore-water from claystone was supplied to the cement, leading to a secondary hydration and conversion of remaining alite (Ca-silicate clinker phase) into an otherwise uncommon Mg-hydrate. Carbonate formation in the cement matrix caused by the bicarbonate-rich claystone pore- water further slowed down this secondary hydration by porosity reduction, and a zone of unhydrated clinker remained. This mechanism is considered a special case caused by the low water content of the 2.2-year OPC sample (sealing plug), and this added complexity may not have been experienced by the OPC sampled after 4.9 years, a likely explanation for the simpler zoning pattern observed in this sample, and a lack of evidence for two separate hydration stages.

Zonation of mineral alteration within the cement matrix for 2.2-year samples is detailed in Jenni et al. (2014) and it is also supported by numerous spot EDAX analyses (zone labels refer to Fig. 4, top left):

C1: Ca-rich margin, not continuous, carbonated, unhydrated ferrite, alite transformed to Mg-Al-phase (hydrotalcite?).

C2: Ca-depleted relative to bulk, carbonated, unhydrated ferrite, alite transformed to Mg-Al-phase (hydrotalcite?).

C3: elevated S and increasing Ca (but depleted relative to bulk), not carbonated, Ca-rich patches (portlandite?), unhydrated ferrite, alite transformed to Mg-phase (hydrotalcite?).

Table 2 Summary of characteristics at the OPC-Opalinus Clay interface after 2.2 (2) and 4.9 (5) years

	[μm] [years]	Ca		Mg		S		carbonation		alite & belite		Mg hydrate	
		2	5	2	5	2	5	2	5	2	5	2	5
OPA	-200	Unaltered											
	0	+		(+)		(+)							
OPC		-	-			(+)		✓					✓
	300					+			✓		✓		
	800						+						
	3000	Unaltered											

Empty cells: same characteristics as unaltered material. Approximate thickness of layers in μm is indicated

+, -, ✓ represent “enriched”, “depleted”, and “present”, relative to the unaltered OPA or cement far from interface. (+): Small enrichment

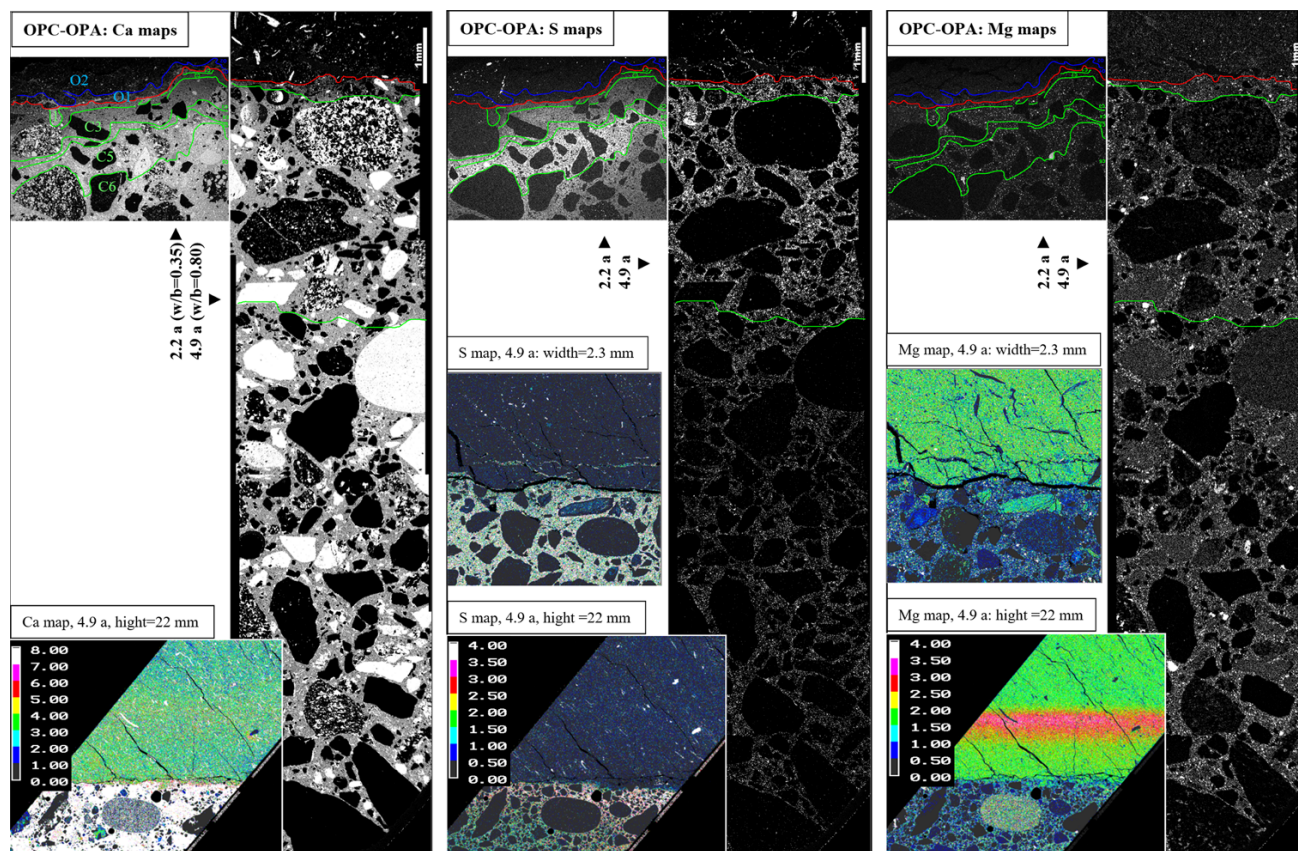


Fig. 4 SEM-EDAX element maps (grey-scale) of Ca (left), Mg (centre), S (right) of 2.2-year samples (small areas) and 4.9-year samples (merged long maps). False-colour inserts are from EPMA element maps in oxide wt% from 4.9-year samples (small and large

areas). The interface OPC-Opalinus Clay is marked in red (SEM maps) or is a resin-filled discontinuity (EPMA). See text for explanation of zones in cement matrix (green lines) and in Opalinus Clay (blue line)

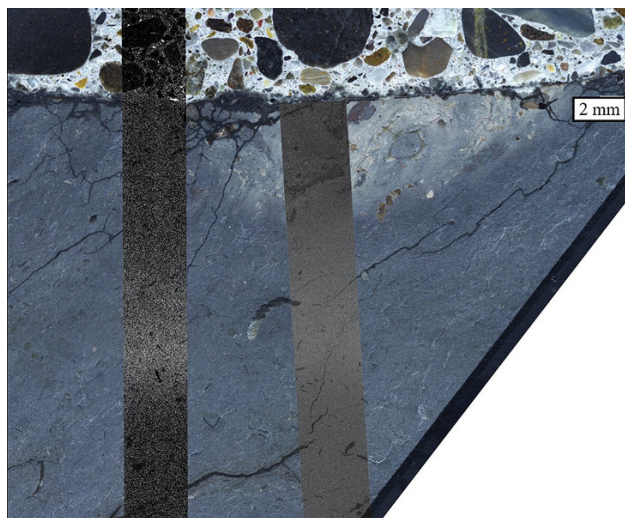


Fig. 5 SEM-EDAX composite Mg-maps (greyscale stripes) superimposed on reflected-light image of interface between OPC concrete (top) and Opalinus Clay. A buff coloured region bordering the interface is rich in phosphate (fossil debris). The width of the image is 26 mm

C4: Ca similar to bulk, increase in S with distance, relict clinker grains, Al-rich domains (*ettringite*, *monosulphate*).

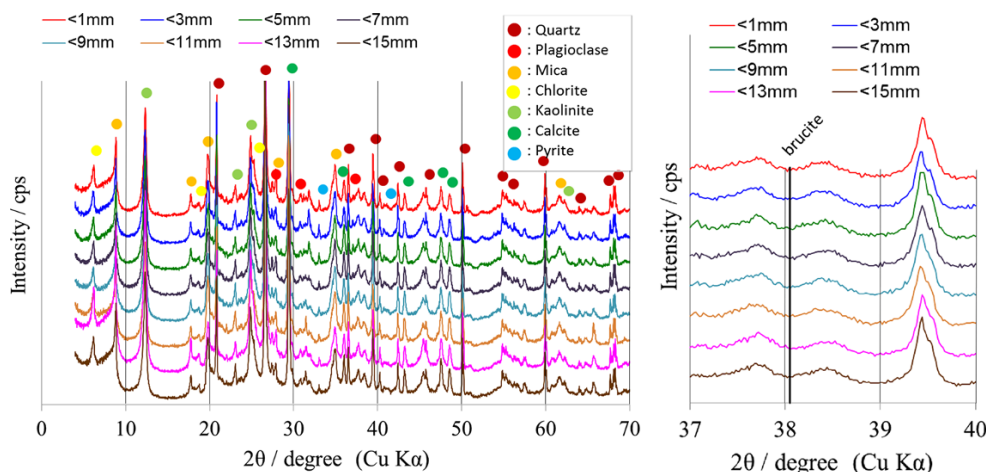
C5: max. S content, Ca above bulk value, Al and Mg-rich patches, increased hydration of clinker.

C6: similar to C5, lower S and *more hydrated*, similar to a “normal” OPC.

The features on the concrete side of the interface that are thought not to be influenced by inferred de-saturation and secondary hydration effects (*italicized* in the list above) include (1) a carbonate-containing margin, locally Ca-enriched right at the interface but Ca-depleted for the most part (100–300 μm), (2) a zone with bulk Ca-content and somewhat elevated sulphur (200–300 μm), and (3) a sulphur-enriched zone (500–1000 μm).

In contrast, the concrete margin observed after 4.9 years is chemically less zoned (Fig. 4; Table 2) and the clinker is fully hydrated (except for minor relict Ca-ferrite), without detectable Mg-rich phases. The extent of the carbonate containing zone is more difficult to distinguish and associated with a Ca-depleted zone (100–300 μm), similar in

Fig. 6 XRD patterns obtained from a profile in Opalinus Clay adjacent to OPC (4.9 year) with 2 mm spatial resolution. *Blow-up* shows region of interest for possible Mg-hydroxide (brucite)



width as observed after 2.2 years. The sulphur-enriched zone is much wider (~4000 μm) compared to 2.2 years, and slightly Ca-depleted at its proximal margin.

The regions where SEM-EDAX element mapping was performed were duplicated and extended by EPMA element mapping on a different 4.9-year core samples. The same wide sulphur-rich zone was observed, but shown more quantitatively in oxide wt% of Ca, Mg and S in false colour images (Fig. 4). Likewise, Ca concentrations measured by EPMA (not visible in Ca map, above range of scale) gradually increase in concrete from 20 to 30 wt% CaO over 7–8 mm from the interface, but remain constant at 4 wt% in the claystone.

There is little evidence for chemical interaction on the claystone side (Fig. 4; Table 2) close to the interface. A narrow zone somewhat enriched in Ca with slightly elevated sulphur is seen after 2.2 years (100–200 μm), but none after 4.9 years, except for some tiny mineralized veinlets that are thought to be associated with a narrow borehole disturbed zone.

The false-colour EPMA Mg-map reveals a striking Mg-enriched zone in the claystone at a distance of 4–6 mm from the interface (not covered by SEM-EDAX maps). The enrichment is ca. 1 wt% MgO from a background value of 2 wt% to ca. 3 wt% in the enriched zone. This Mg zone was also confirmed in a different sample with two extended composite SEM-EDAX maps extending deeper into the claystone (Fig. 5). A Mg-enriched zone is located at ca. 6–8 mm distance from the interface, regardless of rather large heterogeneities in phosphate contents (details on this lithology below). Attempts failed to detect a mineral phase associated with this Mg-enrichment by XRD. A well resolved (2 mm) XRD profile (Fig. 6) did show very little variation in mineral proportions and no newly-formed phases. Specifically, brucite as a likely candidate Mg-phase could not be detected.

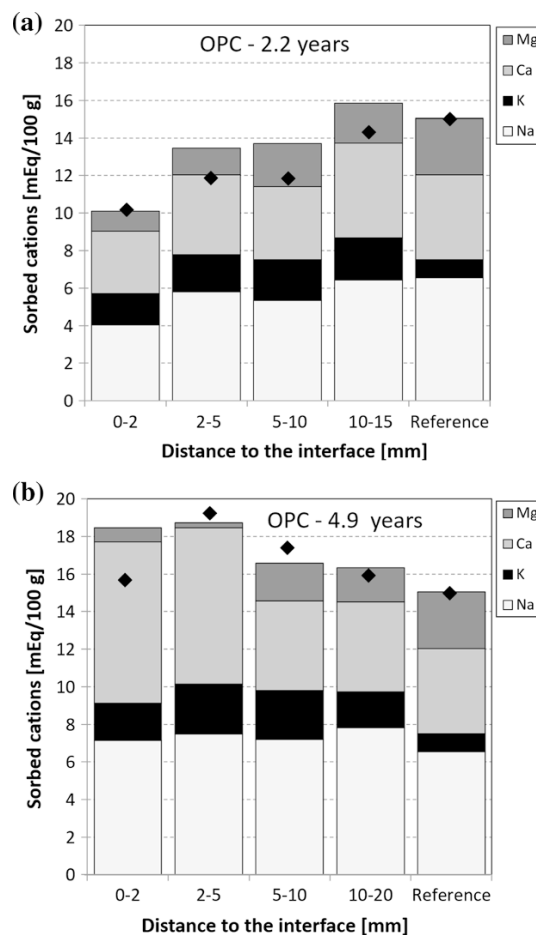


Fig. 7 CEC (diamonds, meq/100 g) and cation occupancy (meq/100 g) on clay exchanger in Opalinus Clay as function of distance from the interface to OPC, after 2.2 (a) and 4.9 years (b)

4.2.2 Zoned interface region: exchangeable cations in Opalinus Clay

Very small samples of powdered claystone were analysed for its cation exchange capacity (CEC) and cation

occupancy (Na, K, Ca, Mg, Sr), but at a coarser spatial resolution (up to 20 mm distance from interface) compared to the SEM/EPMA work presented above. A Mg-depleted zone is evident in the 2.2-year sample from 0 to 5 mm of the interface (or smaller), and relatively little variation in cation occupancy and CEC from there onwards (Fig. 7a). Potassium is relatively enriched up to the limit of measurement at 15 mm distance compared to a more distant bulk sample (reference). After 4.9 years, a Ca-enriched and Mg-depleted zone extends to ca. 5 mm (Fig. 7b). There is generally a somewhat larger error associated with analytical protocols optimized for such small samples, but the qualitative trends are valid.

4.2.3 Effect of phosphate-rich lithology

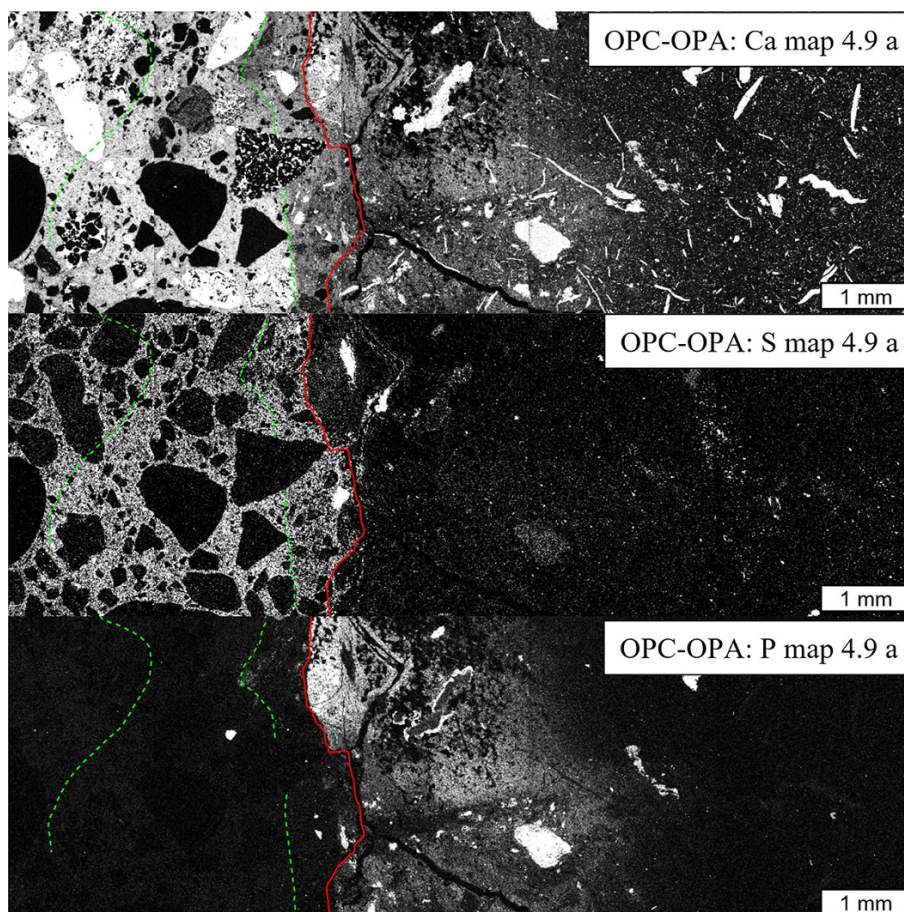
An unusual accumulation of fossil shell fragments in Opalinus Clay exactly at the OPC interface where the 4.9-year sample was taken provided an increased source for S, Fe, and P (Figs. 5, 8). An increased amount of pyrite accumulations (S map; Fe map not shown) was associated with a significantly increased P-content in the clay matrix as well as P-rich particles (P map). Apatite was also identified in the cement matrix by μ -XRD in case of this

specific sample (100 μm^2 beam, work in progress, method in Dähn et al. 2014), indicating that phosphate was mobile and interacted with the cement. The increase of sulphur in the clay matrix (other than associated with pyrite) suggests that a partial oxidation of pyrite was a source for mobile sulphate, also supported by earlier findings (Jenni et al. 2014) where oxidized surfaces of pyrite were documented. This additional sulphate might also have contributed to a larger thickness of the sulphur-enriched layer in concrete in the 4.9-year sample compared to the one after 2.2 years. It is believed that this limited pyrite oxidation occurred during/after drilling the experiment borehole by limited access of oxygen and stopped after concrete casting and oxygen consumption.

4.2.4 Porosity changes across interface region

Porosimetry analysis of the OPC-Opalinus Clay interface after impregnation with ^{14}C -doped MMA resulted in the autoradiograph shown in Fig. 9. Brighter regions represent lower porosity for the 2.2-year samples (less blackened negative film). Segmentation of the concrete part (exclusion of aggregates, cracks and claystone, all shown in black) revealed an obvious zone of lower porosity parallel

Fig. 8 Ca, S, and P SEM-EDAX maps of a section across the OPC-Opalinus Clay interface, 4.9 years after emplacement. Different zones in cement are separated by green lines (see text), the cement/claystone interface is traced in red



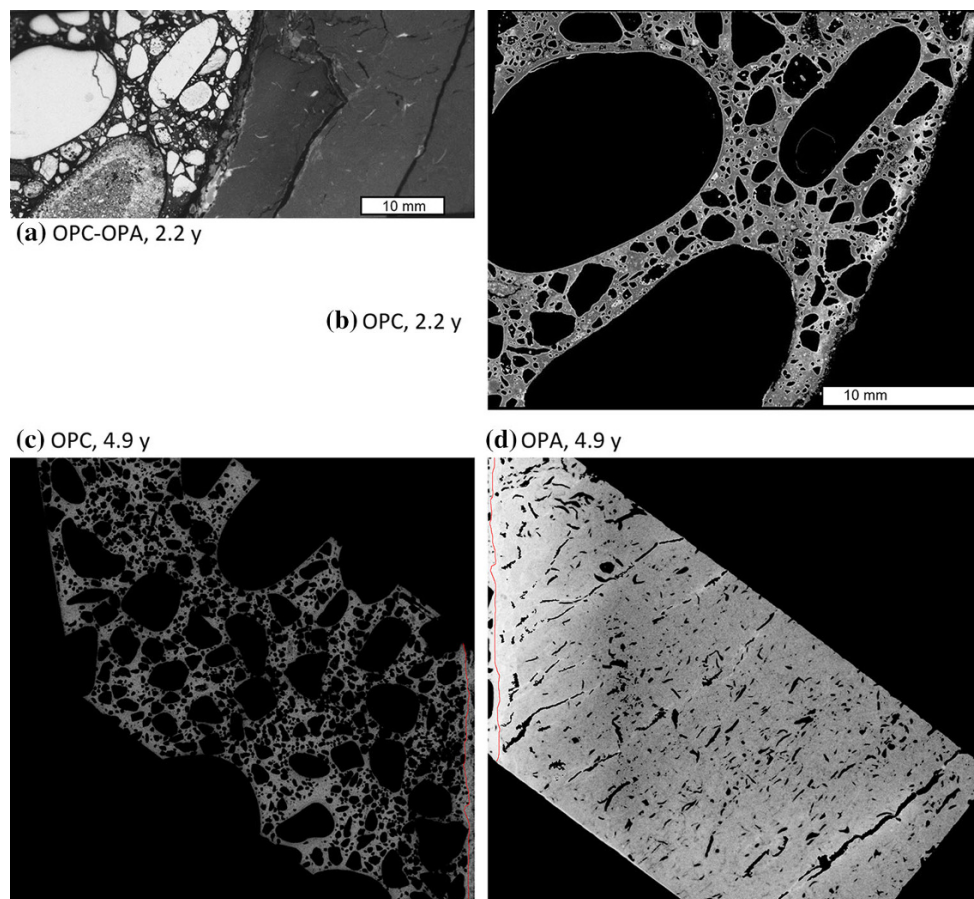


Fig. 9 Autoradiographs of the OPC-Opalinus Clay interface after 2.2 and 4.9 years. Untreated autoradiograph (a, 2.2 year) and processed concrete side of the autoradiograph (b). Processed concrete side (c,

4.9 year) and processed claystone side (d, 4.9 year). The width of the rectangular samples is 22 mm. The interface is marked with a red line

to the interface within the cement matrix, but not directly adjacent to it (Fig. 9b). The thickness of this zone is approximately 1.2 mm, and it is largely coincident with the location of carbonate alteration. The same image treatment applied to the 4.9-year sample (Fig. 9c), but here in reversed grey scale (bright areas are porous) does show less variation in porosity. The claystone side (Fig. 9d) shows somewhat elevated porosity towards the interface but this may also be a result of a mechanically induced drilling-disturbed zone from drilling of the emplacement borehole. MMA-filled cracks induced by sample drying (preferentially parallel to bedding) and fossil fragments with nearly no porosity were segmented and are shown in black. There appears to be a slightly less porous zone at ca. 8–10 mm distance from the interface, and this may correlate with the Mg-enriched zone documented above (Fig. 4).

4.3 ESDRED-Opalinus Clay interface

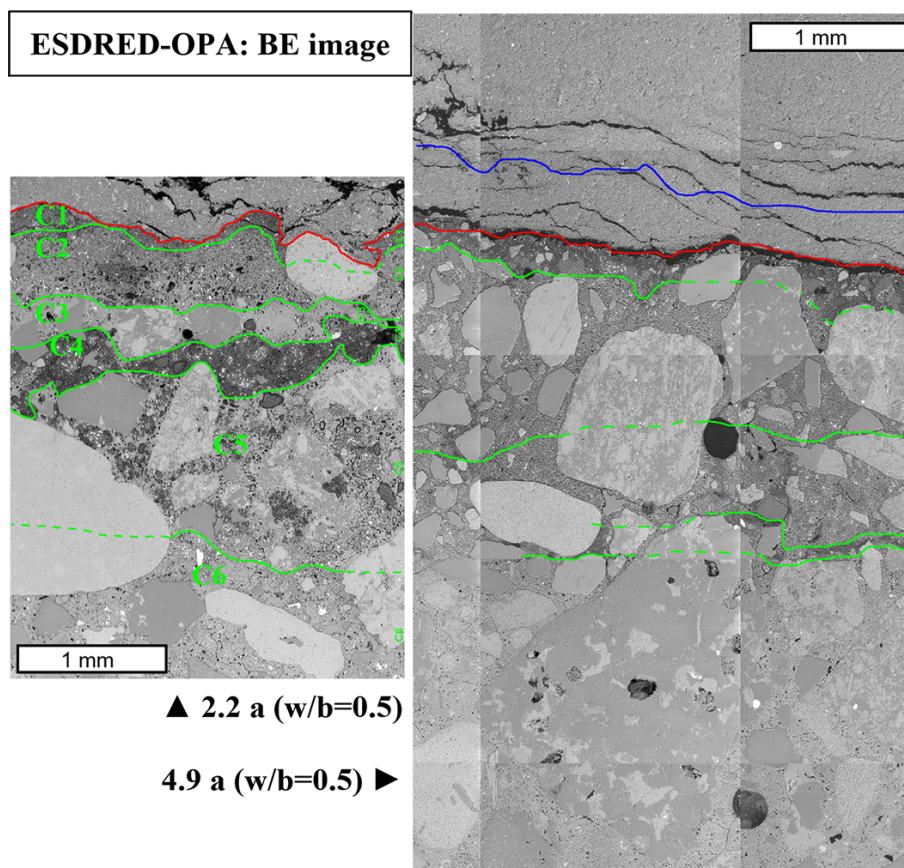
Dauzeres et al. (2016) examined the interfaces between LAC-Opalinus Clay on 4.9-year samples, but also those of ESDRED-Opalinus Clay, with focus on Mg–Si-hydrates

that formed in the cement matrix of both types of “low-pH” concretes close to the interface with claystone. For ESDRED, a ca. 3 mm wide Mg-enriched zone along a 30 mm long interface sample was shown on SEM-EDAX composite element maps that coincided also with a Ca-depleted zone. Small powder samples from this zone were examined by ^{29}Si -MAS-NMR and FTIR and the Mg-bearing phase was identified as mainly Mg–Si-hydrate, also in analogy to spectra obtained from recent characterisation of synthetic Mg–Si-hydrates (Lothenbach et al. 2015; Roosz et al. 2015; Nied et al. 2016). Below, we complement this work and provide also details on the alteration observed on the claystone-side of the interface.

4.3.1 Zoned interface region: element maps

The quality of sample preparation is illustrated in Fig. 10 (back-scattered electron image), where discrete shrinkage cracks in claystone developed during freeze-drying of the sample, but otherwise perfectly polished surfaces represent a section free of artefacts. Also visible is a much higher content of initial gas pores in this shotcrete mix design (a

Fig. 10 SEM back-scattered electron images of ESDRED-Opalinus Clay interface region (2.2 and 4.9 years). See *text* for explanation of zones. *Red line* marks the interface. Opalinus Clay is at the *top*. The width of the *right* composite image is 3 mm, the width of the *left* image 2.3 mm



fairly viscous shotcrete recipe) compared to OPC. Interpretation focuses solely on the clay-rich matrix and the hydrated cement matrix, omitting fossil fragments, silt and aggregate grains.

Compared to OPC, the ESDRED cement matrix contains up to twice the proportion of Si in all zones due to the addition of silica fume. Jenni et al. (2014) distinguished the following zones in a 2.2-year sample (Figs. 10, 11).

C1: contains unhydrated ferrite skeletons; Mg-hydrate replacing alite and belite (Ca-silicate clinkers); Ca-depleted zone; carbonate alteration.

C2: contains unhydrated ferrite skeletons; Mg-hydrate replacing alite and belite; Ca-depleted; carbonate alteration.

C3: most Ca and S enriched zone; almost no ferrite and Mg-hydrate; carbonate alteration.

C4: lowest Ca and S, but highest in Mg; ferrite present; Mg-hydrate abundant; carbonate alteration.

C5: patches of portlandite; patches high in Si; some Mg-hydrate; some relict ferrite and aluminat; carbonate alteration.

C6: less portlandite and Mg-hydrate; some relict belite; close to bulk unreacted cement.

The altered zone in concrete after 4.9 years is similar in width (Fig. 11) but with a slightly simpler zoning pattern

compared to the 2.2-year sample. An almost 2 mm wide Ca and S depleted zone (C1–C5 in Fig. 11) is only slightly wider than a Mg-enriched zone (most Mg-rich in C2–C3, less so next to OPA, C1). Alite and belite were fully hydrated after 4.9 years, and a distinct Ca–Mg-poor but sulphur-rich intermediate zone (C4, 2.2 years, Fig. 11) is not observed.

A distinct and ca. 0.5 mm wide Mg-enriched zone developed in the claystone close to the interface (Fig. 11) after 2.2 and 4.9 years. Other than this, Opalinus Clay appeared unaltered at the resolution of element mapping and XRD (Jenni et al. 2014, Dauzeres et al. 2016). A summary of the alteration zones developed after 2.2 and 4.9 years is given in Table 3. Observations on the degree of enrichment or depletion are additionally supported by numerous EDAX spot analyses (details of 2.2-year samples in Jenni et al. 2014, element-ratio data for 4.9-year sample in Dauzeres et al. 2016).

4.3.2 Zoned interface region: exchangeable cations in Opalinus Clay

A zone of ca. 0.4 mm width and enriched in Mg was observed after 4.9 years (Fig. 11, Mg maps), and this zone correlates with elevated Mg seen also on the exchanger

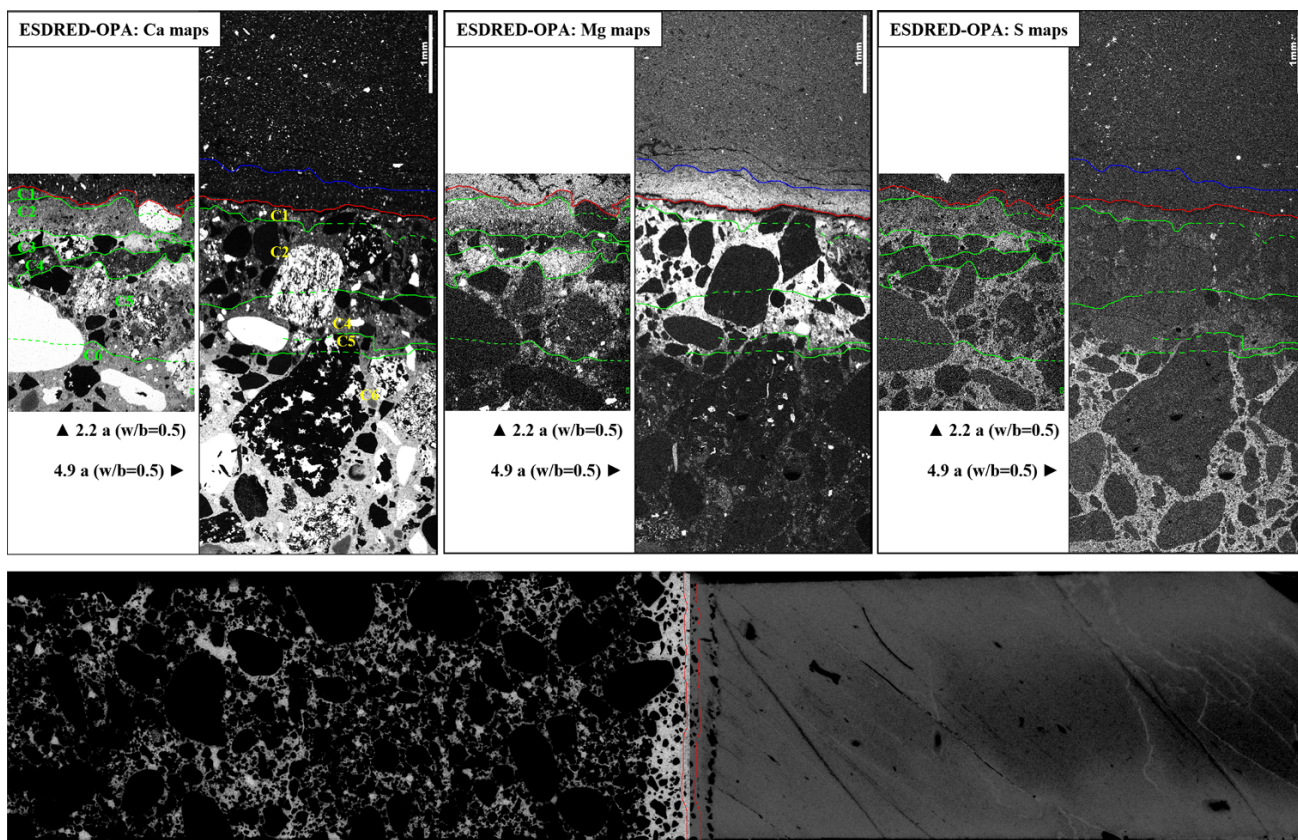


Fig. 11 SEM-EDAX element maps (grey-scale) of Ca (left), Mg (centre), S (right) of 2.2-year samples (smaller areas) and 4.9-year samples (merged long maps). The interface OPC-Opalinus Clay is marked in red. See text for explanation of zones in cement matrix

(green lines) and in claystone (blue line). Lower images radiographic images of ¹⁴C-MMA impregnated samples (see Sect. 4.3.3). Red line marks the interface. The small dimension is 20 mm

Table 3 Characteristics of the zonation at the ESDRD-Opalinus Clay interface after 2.2 (2) and 4.9 (5) years

	[μm]	Ca		Mg		S		carbonation		Mg hydrate	
		2	5	2	5	2	5	2	5	2	5
OPA	-200	Unaltered									
	0			+	+	(+)					
ESDRED	300			+						✓	✓
	450	+		-		+					
	700	-		+		-			✓	✓	
	1400			(+)		(+)					
	?					(+)	+				
		Unaltered									

Empty cells: same characteristics as unaltered material
 +, -, ✓ represent “enriched”, “depleted”, and “present”, relative to the unaltered Opalinus Clay or cement far from interface. (+): Small enrichment

occupancy obtained from a powder sample carefully scraped from the 0–2 mm interface region in Opalinus Clay (Fig. 12). Other than this, the exchanger appears

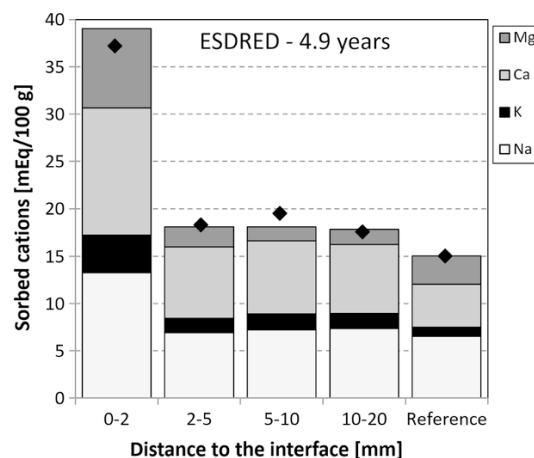


Fig. 12 CEC (diamonds, meq/100 g) and cation occupancy (meq/100 g) on clay exchanger in Opalinus Clay as function of distance from the interface to OPC

undisturbed up to the limit of measurement at 20 mm distance. The unusually large CEC obtained from the sample nearest to the interface may be an artefact from cement material or secondary minerals formed. There is no

CEC/selectivity data available for the 2.2-year sample, but an Mg-enriched zone of comparable width is observed in Opalinus Clay on the Mg element map after 2.2 years (Fig. 11).

4.3.3 Porosity changes across interface region

^{14}C -MMA impregnated samples were imaged (Fig. 11, lower images) and treated as described for OPC, here shown as bright areas meaning elevated porosity. Aggregate, MMA-filled cracks, gas voids, and fossil fragments are all segmented and shown in black. The grey scale is different for the claystone side and the concrete side and was optimized for each material to enhance variations at the different average levels. There is no distinct porosity variation near the interface on the concrete side (Fig. 11, left image), and the grey levels are rather similar to deeper parts, but difficult to see in some regions due to the abundance of fine aggregate, also somewhat enhanced by segmentation. There is no porosity variation evident in the claystone as a function of distance from the interface (Fig. 11, right image), only some less porous patches, and more porous cracks that outline bedding. Porosity quantification is still in progress.

4.4 Interpretation of interaction zones

Figure 13 is a summary schematic of the observed alteration near interfaces. In more detail, the features within the cement matrix adjacent to the OPC-Opalinus Clay interface are a Ca-depleted zone with extensive carbonate alteration and a reduced porosity close to Opalinus Clay (~ 1 mm), followed by a wider sulphur-enriched zone (4–5 mm), before entering almost fully hydrated “normal” OPC. On

the claystone-side of the interface is a conspicuous Mg-enriched zone at 6–8 mm distance, and very minor Ca-rich veinlets representing carbonate precipitation into micro-cracks associated with a borehole-disturbed zone. A more complex zoning pattern in concrete observed after 2.2 years is interpreted to be a result of the low w/c ratio in this sample (from the sealing plug) leading to a two-stage hydration history.

The main features in the cement matrix next to the ESDRED-Opalinus Clay interface are a wider (~ 2 mm) Ca-depleted zone with some sulphur enrichment towards the unaltered cement matrix. A characteristic feature within the cement matrix is a relatively distinct (~ 2 mm) Mg-enriched zone, shown to contain Mg–Si-hydrate by Dauzeres et al. (2016). A distinct Mg-enrichment is also seen in Opalinus Clay adjacent to concrete (0.5 mm wide).

A distinct de-calcification of the cement matrix seen in both reaction zones (OPC and ESDRED) is the result of a decrease in pH that destabilizes earlier formed Ca–Al-sulphate (ettringite, monosulphate), and these components then re-distribute towards the unaltered cement matrix where they re-precipitate at the prevalent higher pH conditions. Transport is towards the cement interior rather than across the interface into claystone due to the prevalent higher water content/porosity in the former more reactive zone. The carbonate alteration zone is overprinted on the de-calcification zone. This carbonate zone is best confirmed by IR spectroscopy as shown in Fig. 14 where abundant calcite is observed in both types of concrete. The features marked by vertical dashed lines indicate different structures and proportions of Ca–Si-hydrates, and contributions from Mg-hydrates in case of ESDRED. Whereas low levels of carbonate contained in the clinker itself are forming monocarbonate (hydrous Ca-aluminate-carbonate)

Fig. 13 Summary of observed alteration features near interfaces of OPC and ESDRED with Opalinus Clay (OPA), and some inferred directions of mass transfer

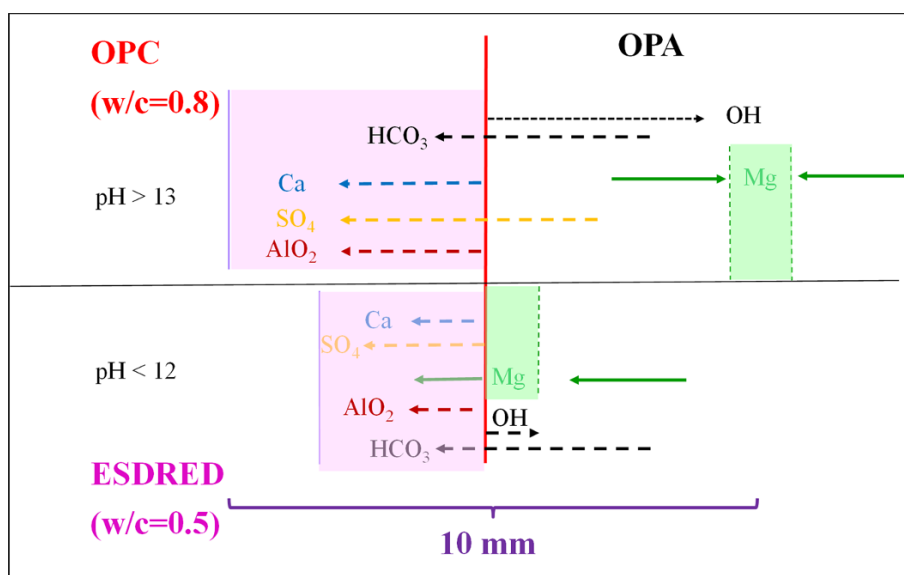
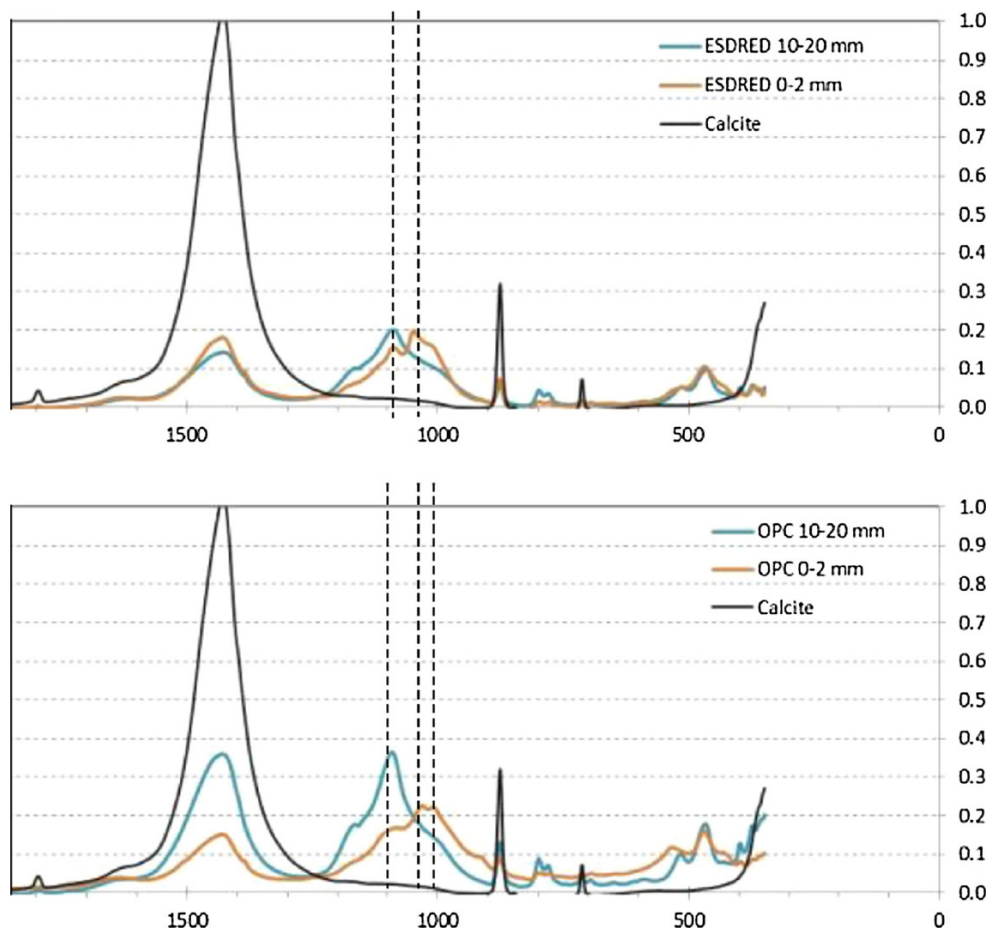


Fig. 14 IR spectra from alteration zones within cement matrix seen on 4.9-year samples of OPC and ESDRED. *X*-axis: wave number, *Y*-axis: intensity normalized to a pure calcite standard. *Vertical dashed lines* indicate features related to Ca–Si-hydrates and Mg-hydrates



during hydration, the calcite in the alteration zone is formed by in-diffusion of bicarbonate from the claystone pore-water, and calcite is replacing mainly Ca–Si-hydrate, and portlandite during early hydration. This type of carbonation was modelled by Matschei et al. (2007) for OPC and the calculated net reduction in porosity is rather small. The zone with reduced porosity observed in the OPC after 2.2 years (Fig. 9) is thought to be due to carbonation but was likely also affected by the complex mineral dissolution and precipitations reactions that caused the observed Ca-aluminate-sulphate re-distribution.

The very minor alteration of Opalinus Clay next to the concrete interface was unexpected. Except for a distinct Mg-enriched zone detached from the interface (OPC) and a diffuse Mg-enrichment towards the interface (ESDRED), there were no mineralogical changes detected (e.g. by XRD of small bulk samples, by IR spectroscopy, EDAX element mapping). A flux of dissolved Mg towards concrete is expected where the solubility of Mg-phases is very small at high pH. This flux was supplied from the pore-water (~ 350 mg/l) and from the clay exchanger (~ 2.6 g/kg_{rock}), representing ca. 12 times the dissolved amount per rock mass. It is therefore plausible that a nearly constant-

concentration boundary was maintained at the interface that supplied Mg to the hydrating cement matrix, initially at a steady rate. This process would have slowed down as hydration proceeded (months), as gradients decreased in the alteration zone and porosity was reduced.

The Mg-enrichment observed in Opalinus Clay adjacent to ESDRED (EDAX, Fig. 10) correlates with an enrichment of Mg on the exchanger determined on mini-samples from 0 to 2 mm of the interface (Fig. 11). Whereas undisturbed Opalinus Clay has a proportion of ca. 10 meq % of Mg on the exchanger, this value was doubled next to the interface, corresponding to ca. 0.5 g/kg_{rock}, or 0.05 wt% Mg. Although we did not quantify the EDAX maps, such a small enrichment solely present on the exchanger is not detectable and it is also difficult to reconcile why the exchanger should become enriched in Mg in the absence of a gradient in dissolved concentration of Mg towards the interface. An alternative mechanism is the precipitation of dispersed Mg-hydroxide (e.g. brucite) triggered by an advancing front of somewhat elevated pH. This rise in pH need not be large because the solubility of Mg-hydroxide phases is strongly decreasing with increasing pH. We consider this latter mechanism a more likely

explanation. The amounts may be too small for detection by mineral-specific analysis methods.

The Mg-enriched zone that developed in Opalinus Clay at some distance from the interface to OPC seen after 4.9-years (Fig. 4) is more difficult to explain. Data from the clay exchanger are not entirely conclusive (Fig. 7): Mg is depleted close to the interface (0–5 mm) but at normal or only slightly elevated levels from 5 to 20 mm. The observed enrichment is ca. 1 wt% MgO (EPMA maps, Fig. 4), compared to a maximum amount of ca. 0.24 wt% that could be accommodated on a fully Mg-exchanged clay matrix. It is more plausible to explain this Mg anomaly by precipitation of a Mg-hydroxide (e.g. brucite) in response to an elevated pH front located at this position after 4.9 years. At earlier times, some Mg may have diffused into the cement matrix but to a much lesser degree compared to ESDRED. As a pH front starts to migrate into Opalinus Clay it would push a Mg-precipitation front at its leading edge, and displace and accumulate earlier precipitated Mg-hydroxide deeper into the claystone. This would only require a relatively weak pH front compared to the full potential of a “fresh” OPC pore-water ($\text{pH} > 13$), whereby mineral dissolution of silicates (quartz, clays) would be too slow/too small to induce detectable other mineralogical changes. This leading edge of a dilute pH-plume would then be mainly retarded by the deprotonation of edge sites (illites) with a total site capacity of ca. 0.3 meq/kg_{rock}. Most of the pH drop would happen within the cement matrix and Opalinus Clay right next to the interface, presumably by a small amount of silicate dissolution (clays). This proposed process is a hypothesis that is probably best tested by some detailed reactive transport modelling. Some spatially highly-resolved modelling work is in progress to better unravel the observed complex interaction zones, and an attempt to characterize the Mg-zone by μ -XRD is in planning, depending on availability of synchrotron beam time.

It appears that at both interfaces—OPC and ESDRED—a sharp pH-drop developed almost immediately right at the interface preventing any further significant OH-attack at the time scale of observation (5 years). It is in fact to be expected that chemical interaction is shifting to the most reactive component, namely the hydrating cement matrix. There, initial water content and porosity are much higher immediately after emplacement of concrete compared to Opalinus Clay, and reaction progress is rapid involving reactive hydrates, sulphates, Ca-aluminates and carbonates. The corollary of this process is that the claystone is being protected from OH-attack mostly by cement-internal processes, enhanced with some influx of Mg, bicarbonate and possibly sulphate from claystone pore-water.

While there is a substantial body of literature that deals with cement leaching (mostly Ca and alkali leaching) the chosen boundary conditions (mostly concrete/mortar/paste against free water) are very different from a cementitious

material in contact with claystone, and thus we did not include a comparison of chemical zoning and textural evolution. We concluded that an analogy based on cement leaching (e.g. Ca leaching) is not of practical relevance for the situation of juxtaposed concrete and claystone.

5 Conclusions and outlook

The CI Experiment at the Mont Terri rock laboratory is a long-term technically simple and passive diffusion–reaction experiment between contrasting materials of relevance to engineered barrier systems and the geological near-field for deep disposal of radioactive waste in claystone. Reaction zones at interfaces of Opalinus Clay with two different types of concrete (OPC and “low-pH”/ESDRED) were examined by sampling after 2.2 and 4.9 years. The presence of aggregate grains posed limits to bulk analytical methods and spot analyses, and element mapping had to be used as key tool to characterize rather small-scale reaction zones at the mm and sub-mm scale. OPC and ESDRED mortars (purified quartz) and pastes were emplaced in 2012 (BCI-12–15, Fig. 1) and first sampled in 2015 exactly for the purpose of applying more precise analytical methods with focus on phase identity (analytical work in progress), also including isotopic methods and μ -XRD powder techniques (some test results can be found in Dähn et al. 2014). The aim is to provide an as complete as possible mineralogical and geochemical description of the early evolution (0–5 years) of claystone-concrete interfaces that can form a sound basis for a detailed reactive transport modelling interpretation.

A key finding was that the extent of reaction in claystone was minimal for both OPC and ESDRED. The reaction zone within the cement matrix was even larger for the low-alkali cementitious product, despite the fact that pore-water pH is much higher in OPC, and that the water/cement ratio was also higher in OPC compared to ESDRED (0.8 vs. 0.5 in 4.9-year samples). While the absolute potential for OH-release is significantly higher for OPC compared to ESDRED, it appears that the increased reactivity of low-alkali cementitious products pushed by reactive silica (silica fume, silica flower, nanosilica) and set accelerators (aluminates, sulphate, Ca) outperform the effect of mainly a high initial KOH component in OPC that apparently was buffered right at the interface to claystone. Because either a distinct zone of decreased porosity may form (2.2 year, OPC) or porosity is decreasing in cement as hydration progresses in both systems, it may be expected that reaction rates will decrease significantly over time. In fact, the reaction zones observed in the 2.2 and 4.9-year samples of ESDRED already do show quite similar widths, indicative of such a behaviour.

An important conclusion is therefore that substitution of OPC by low-alkali cementitious products is not advantageous or necessary solely for the purpose of minimizing the extent of reaction between claystone and cementitious materials. Substitution of OPC by low-alkali cements may add uncertainty associated with the increased amounts of organic additives, and a less well known engineering performance of such more recently developed products.

A substantial effort has been made in modelling cement-clay interaction (see introduction for some references). Our findings indicate that the following processes and capabilities would need to be part of a more realistic modelling effort: (1) a high spatial resolution (10–100 μm), (2) inclusion of the cement hydration phase/processes, (3) kinetic control of reactions (slow vs. fast reactions), and (4) incorporation of sufficient chemical complexity (Mg phases, Ca–Si-hydrates, Ca–Al-sulphates, carbonates, etc.), although the exact phase identities may not necessarily be a decisive factor. Recent developments in reactive transport codes and efforts in the development of thermodynamic data bases for cement systems (CEM DATA 2016, Thermochem 2016) appear to make a realistic modelling approach feasible.

A first-order control on system behaviour is the evolution and re-distribution of porosity—and thus permeability—within the reaction zone. Our efforts with ^{14}C -doped MMA impregnation look promising, but artefacts from sample preparation and data evaluation need to be carefully examined. Ultimately, we would like to know how transport of certain radionuclides (mainly anions) but also water and gas will be affected. A more robust method compared to short-term laboratory experiments might be the implementation of an in situ tracer diffusion test, for example from concrete across an aged interface into claystone, or vice versa. This would provide a direct measure for the

expected decrease of effective diffusion properties as a result of pore clogging (skin effect). Some such efforts (mostly laboratory experiments) were initiated within a European Commission project (CEBAMA 2016).

Planning of a sampling campaign after 10 years of cement-claystone interaction (2017) is initiated. The findings will serve as a robust test for our current state of process understanding, and will extend predictability to several decades (width of reaction zones, porosity evolution) in combination with appropriate modelling.

Acknowledgements The authors like to acknowledge the support by the funding organisations of the CI Project and the Mont Terri Consortium—happy birthday and many happy returns. The on-site team of swisstopo supported the field work. Schützeichel GmbH&Co. KG did an excellent job during all drilling campaigns. Bernhard Schwyn (former principle investigator, Nagra) helped to make this project a success and one of the longest-running field experiments at Mont Terri. Bernd Frieg (Nagra) was instrumental for successful drilling during the implementation phase in 2007. The on-site team of the Grimsel Test Site (Toni Baer, Hans Abplanalp, Nagra) provided expertise during the first drilling campaign and sampling of the mock-up barrels. Many colleagues discussed and disputed ideas and analytical methods at various project meetings. We estimate that ca. 40 specialists were involved in this project over the last 12 years. Detailed comments by Jaime Cuevas (UAM, Spain) and Andreas Leemann (EMPA, Switzerland) are kindly acknowledged; they helped to improve the clarity of the arguments and the presentation.

Open Access This article is distributed under the terms of the Creative Commons Attribution 4.0 International License (<http://creativecommons.org/licenses/by/4.0/>), which permits unrestricted use, distribution, and reproduction in any medium, provided you give appropriate credit to the original author(s) and the source, provide a link to the Creative Commons license, and indicate if changes were made.

Appendix

See Figs. 15, 16, 17 and 18 and Table 4.

Fig. 15 XRD of hydrating OPC paste. A alite, B belite, C calcite, E ettringite, F ferrite, G gypsum, Ht hydrotalcite, Mc monocarbonate, P portlandite

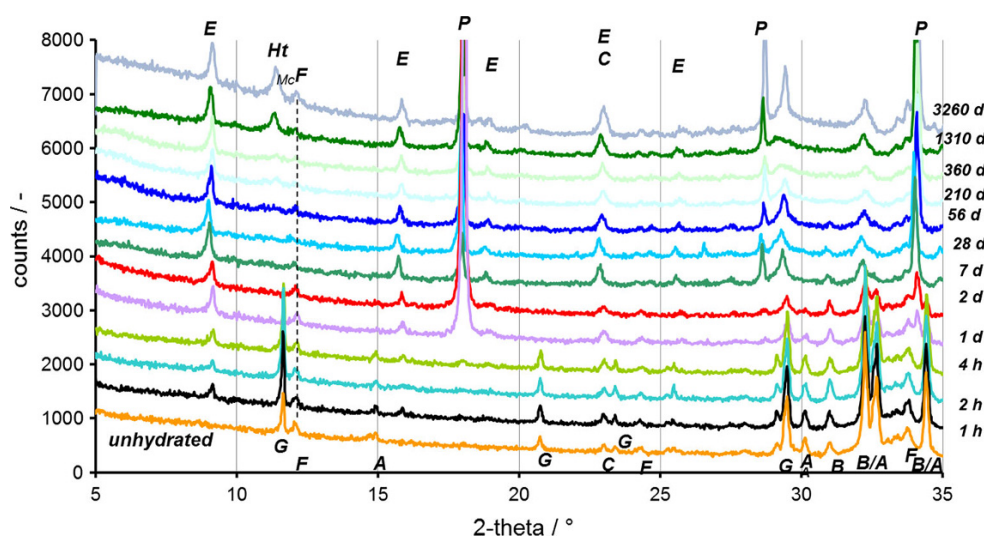


Fig. 16 TGA/DTG of the unhydrated CEM I 42.5 R HS (used to prepare OPC) and the hydrating OPC paste

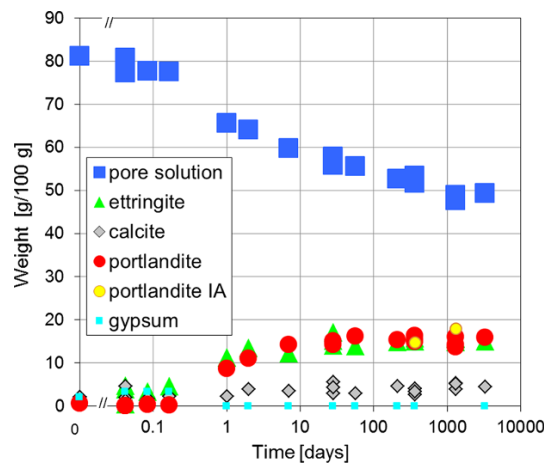
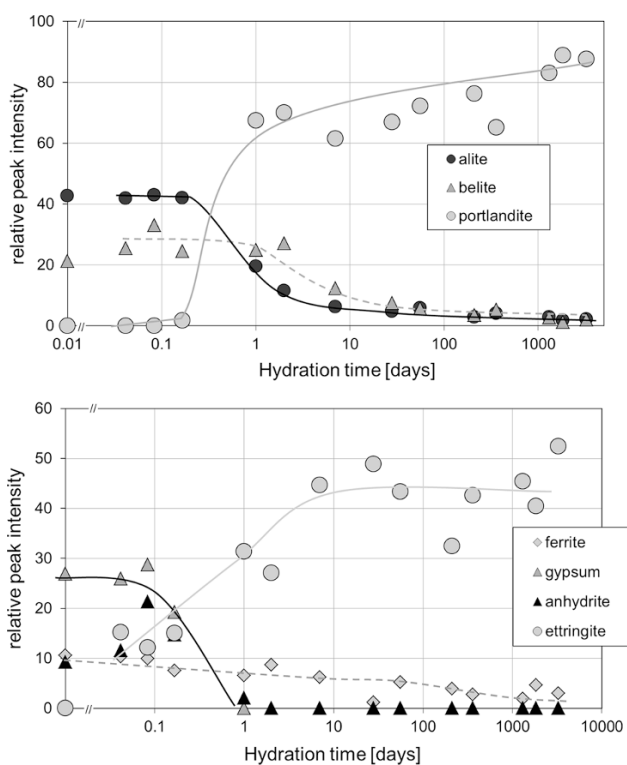
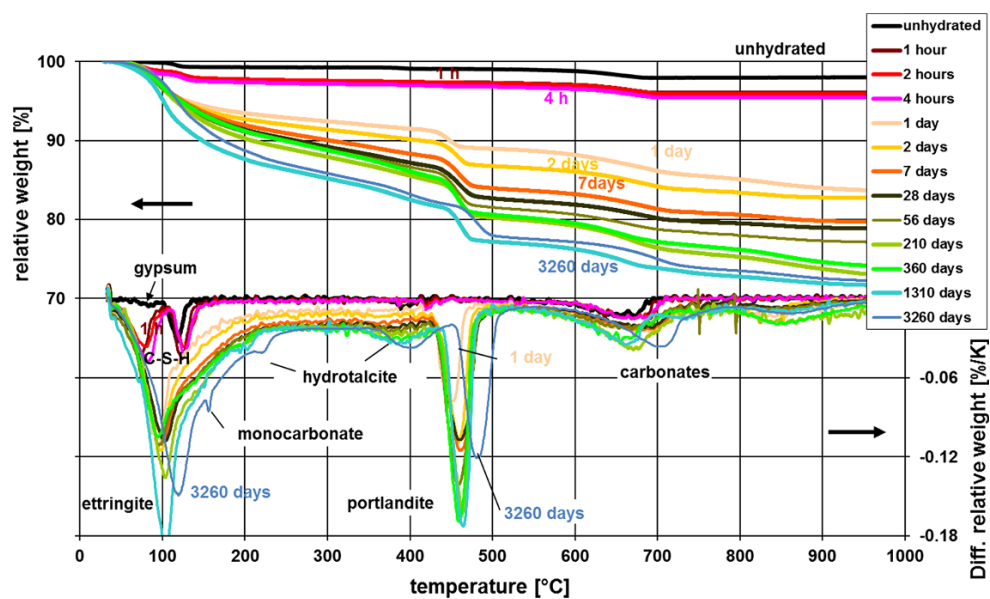


Fig. 18 Amount of pore-solution, calcite, gypsum, ettringite, and portlandite present during the hydration of OPC as determined by TGA. The weight refers to 100 g of dried solid, i.e. the sample weight before being subjected to TGA. IA determined by image analysis

Fig. 17 Semi-quantitative evaluation of XRD patterns of the solid phase after different hydration times. Lines are intended as eye guides

Table 4 Measured total concentrations in pore-solutions gained from OPC

Age (days)	Al	Ba	Ca	Cr	K (mmol/l)	Mo	Na	S	Si	Sr	DOC	OH ^{-a}	pH
0.04	0.002	0.0040	24	0.21	137	0.0093	26	66	0.035	0.12	13	105	13.0
0.08	0.002	0.0036	27	0.19	134	0.0088	26	52	0.023	0.13	13	113	13.0
0.17	0.002	0.0031	25	0.17	134	0.0081	26	53	0.028	0.14	13	118	13.0
0.17	0.004	0.0031	24	0.17	–	0.0080	–	52	–	0.14	–	–	–
0.25	0.002	0.0031	25	0.13	136	0.0062	27	54	0.026	0.17	12	128	13.0
1	0.006	0.0038	9.3	0.0003	149	0.0011	44	44	0.047	0.11	12	140	13.1
2	0.021	0.0053	3.6	<	161	0.0003	53	4.9	0.082	0.09	12	214	13.3
7	0.050	0.010	3.1	<	182	<	67	0.7	0.063	0.12	13	249	13.3
28	0.053	0.010	2.4	0.0008	199	<	79	1.1	0.084	0.10	13	269	13.4
28	0.052	0.0098	2.3	0.0008	–	<	–	1.1	0.085	0.10	–	–	–
56	0.019	0.0089	2.3	0.0017	202	0.0003	82	2.1	0.060	0.08	13	272	13.4
207	0.016	0.0088	2.8	0.0035	207	<	89	2.8	0.047	0.11	15	265	13.4
360	0.010	0.0080	1.9	0.0028	208	0.0003	90	3.4	0.051	0.08	13	258	13.3
1310	0.098	0.0056	2.9	<0.004	209	<0.003	90	4.5	0.052	0.12	13	277	13.3
3260	0.163	–	0.72	–	200	–	9.1	6.6	0.053	–	17	264	13.3
Blank	<	<	0.004	<	<	<	2E–3	<	0.002	5E–6	0.3		
DL	0.002	1E–5	3E–4	0.0002	4E–4	0.0003	1E–3	0.01	0.002	3E–6	0.008		

Measured concentrations of Cs, Fe, and Mg were below a detection limit of 0.2, 0.0002 and 0.001 mM, respectively. Measured values for Zn ranged from 0.0003 to 0.001 mM and were in the range of the detection limit

– Not determined

^a Values for OH⁻ refer to the free concentration as calculated from the measured pH values


References

- Adler, M. (2001). Interaction of claystone and hyperalkaline solutions at 30°C: A combined experimental and modeling study. Ph.D. Dissertation, (p. 120). Bern, Switzerland: University of Bern.
- Adler, M., & Mäder, U. (1999). Laboratory scoping experiments on high-pH water/shale interaction (CW Experiment). In M. Thury & P. Bossart (Eds.), *Mont Terri Rock Laboratory: Results of the hydrogeological, geochemical and geotechnical experiments performed in 1996 and 1997* (pp. 57–59). Bern: OFEG Report, Geology Serie, No. 23. Federal Office of Topography (swisstopo), Wabern, Switzerland. <http://www.mont-terri.ch>.
- Adler, M., Mäder, U. K., & Waber, H. N. (1999). High-pH alteration of argillaceous rocks: An experimental study. *Swiss Bulletin of Mineralogy and Petrology*, 79, 445–454.
- Adler, M., Mäder, U. K., & Waber, H. N. (2001). Core infiltration experiment investigating high-pH alteration of low-permeability argillaceous rock at 30 & #xB0;C. In R. Cidu (Ed.), *Proceedings of the 10th International Symposium on Water-Rock Interaction* (pp. 1299–1302). Amsterdam: Balkema Publishers.
- Alonso, J., García-Siñeriz, J. L., Bárcena, I., Alonso, M. C., Fernández Luco, L., García, J. L., Fries, T., Petterson, S., Bodén, A., & Salo, J. P. (2009). *ESDRED, Module 4 (Temporary Sealing Technology) Final Report (Contract F16 W-CT-2004-508851)*. European Commission, Brussel, Belgium.
- Andersson, M., Ervanne, H., Glaus, M. A., Holgersson, S., Laine, H., Lothenbach B., Puigdomenech, I., Schwyn, B., Snellman, M., Ueda, H., Vuorio, M., Wieland, E., & Yamamoto, T. (2008). *Development of methodology for evaluation of long-term safety aspects of organic cement paste components*. Working Report 2008-28. Posiva Oy, Eurajoki, Finland.
- ANDRA (2005). *Dossier 2005 argile, synthesis: Evaluation of the feasibility of a geological repository in an argillaceous formation. Meuse/Haute-Marne site*. Paris: ANDRA, Agence nationale pour la gestion des déchets radioactifs.
- Bildstein, O., & Claret, F. (2015). Stability of clay barriers under chemical perturbations. In C. Tournassat, C. I. Steefel, I. C. Bourg, & F. Bergaya (Eds.), *Natural and engineered clay barriers* (p. 446). Developments in clay science, vol 6. Amsterdam: Elsevier.
- Bossart, P., Bernier, F., Birkholzer, J., Bruggeman, C., Connolly, P., Dewonck, S., Fukaya, M., Herfort, M., Jensen, M., Matray, J.-M., Mayor, J. C., Moeri, A., Oyama, T., Schuster, K., Shigeta, N., Vietor, T., & Wieczorek, K. (2017). Mont Terri rock laboratory, 20 years of research: introduction, site characteristics and overview of experiments. *Swiss Journal of Geosciences*, 110, doi:10.1007/s00015-016-0236-1.
- Bradbury, M. H., & Baeyens, B. (2000). A generalised sorption model for the concentration dependent uptake of caesium by argillaceous rock. *Journal of Contaminant Hydrology*, 42, 141–163.
- Bradbury, M. H., & Baeyens, B. (2005). Experimental and modelling investigations on Na-illite: Acid-base behaviour and the sorption of strontium, nickel, europium and uranyl. *Nagra Technical Report*, 04-02. Nagra, Wettingen, Switzerland. <http://www.nagra.ch>.
- Bradbury, M. H., Berner, U., Curti, E., Hummel, W., Kosakowski, G., & Thoenen, T. (2014). The Long Term Geochemical Evolution of the Nearfield of the HLW Repository. *Nagra Technical Report*, 12-01. Nagra, Wettingen, Switzerland. <http://www.nagra.ch>.
- CEBAMA. (2016). European Commission Horizon 2020 Research and Training Programme of EURATOM on cement-based materials, properties, evolution, barrier functions. <http://www.cebama.eu/>. Accessed 23 Dec 2016.
- CEMDATA. (2016). Thermodynamic data for hydrated solids in Portland cement system (CaO-Al₂O₃-SiO₂-CaSO₄-CaCO₃-Fe₂O₃-MgO-H₂O). Administered by Barbara Lothenbach,

- EMPA, Switzerland. <https://www.empa.ch/web/s308/cemdata>. Accessed 23 Dec 2016.
- Dähn, R., Popov, D., Schaub, P., Pattison, P., Grolimund, D., Mäder, U., et al. (2014). In-situ X-ray micro-diffraction studies of heterogeneous interfaces between cementitious materials and geological formations. *Physics and Chemistry of the Earth, Parts A/B/C*, 70, 96–103.
- Dauzères, A., Achiedo, G., Nied, D., Bernard, E., Alahrache, S., & Lothenbach, B. (2016). Magnesium perturbation in low-pH concretes placed in clayey environment—solid characterizations and modelling. *Cement and Concrete Research*, 79, 137–150.
- Dauzères, A., Le Bescop, P., Sardini, P., & Cau Dit Coumes, C. (2010). Physico-chemical investigation of clayey/cement-based materials interaction in the context of geological waste disposal: Experimental approach and results. *Cement and Concrete Research*, 40, 1327–1340.
- De Windt, L., Marsal, F., Tinsseau, E., & Pellegrini, D. (2008). Reactive transport modeling of geochemical interactions at a concrete/argillite interface, Tournemire site (France). *Physics and Chemistry of the Earth, Parts A/B/C*, 33, S295–S305.
- De Windt, L., Pellegrini, D., & van der Lee, J. (2004). Coupled modeling of cement/claystone interactions and radionuclide migration. *Journal of Contaminant Hydrology*, 68, 165–182.
- European Commission (2005). *ECOCLAY II, Effects of Cement on Clay Barrier Performance—Phase II, final report (Contract FIKW-CT-2000-00028)*. European Commission, Nuclear Science and Technology.
- Gaboreau, S., Lerouge, C., Dewonck, S., Linard, Y., Bourbon, X., Fialips, C. I., et al. (2012). In-situ interaction of cement paste and shotcrete with claystones in a deep disposal context. *American Journal of Science*, 312, 314–356.
- Gaboreau, S., Prêt, D., Tinsseau, E., Claret, F., Pellegrini, D., & Stammose, D. (2011). 15 years of in situ cement–argillite interaction from Tournemire URL: Characterisation of the multi-scale spatial heterogeneities of pore space evolution. *Applied Geochemistry*, 26, 2159–2171.
- Gaucher, E. C., Blanc, P., Matray, J.-M., & Michau, N. (2004). Modeling diffusion of an alkaline plume in a clay barrier. *Applied Geochemistry*, 19, 1505–1515.
- Jenni, A., Mäder, U., Lerouge, C., Gaboreau, S., & Schwyn, B. (2014). In situ interaction between different concretes and Opalinus Clay. *Physics and Chemistry of the Earth, Parts A/B/C*, 70, 71–83.
- Koroleva, M., Lerouge, C., Mäder, U., Claret, F., & Gaucher, E. C. (2011). Biogeochemical processes in a clay formation in situ experiment: Part B—results from overcoring and evidence of strong buffering by the rock formation. *Applied Geochemistry*, 26, 954–966.
- Kosakowski, G., & Berner, U. (2013). The evolution of clay rock/cement interfaces in a cementitious repository for low- and intermediate level radioactive waste. *Physics and Chemistry of the Earth, Parts A/B/C*, 64, 65–86.
- Kosakowski, G., Berner, U., Wieland, E., Glaus, M., & Degueldre, C. (2014). Geochemical evolution of the L/ILW near-field. *Nagra Technical Report*, 14-11. Nagra, Wettingen, Switzerland. <http://www.nagra.ch>.
- Lothenbach, B. (2011). CI experiment: Hydration experiments of OPC, LAC and ESDRED cements: 1 h to 3.5 years. *Mont Terri Technical Note*, TN 2010-75. swisstopo, Seftigenstrasse 264, 3084 Wabern, Switzerland.
- Lothenbach, B. (2013). Hydration of blended cements. In F. Bart, C. Cau-dit-coumes, C. Frizon, & F. Lorente (Eds.), *Cement-based materials for nuclear waste storage* (pp. 33–41). New York: Springer.
- Lothenbach, B., Nied, D., L'Hôpital, E., Achiedo, G., & Dauzères, A. (2015). Magnesium and calcium silicate hydrates. *Cement and Concrete Research*, 77, 60–68.
- Lothenbach, B., Rentsch, D., & Wieland, E. (2014). Hydration of a silica fume blended low-alkali shotcrete cement. *Physics and Chemistry of the Earth, Parts A/B/C*, 70, 3–16.
- Lothenbach, B., & Winnefeld, F. (2006). Thermodynamic modelling of the hydration of Portland cement. *Cement and Concrete Research*, 36, 209–226.
- Mäder, U., & Adler, M. (2005a). Mass balance estimate of cement—clay stone interaction with application to a HLW repository in Opalinus Clay. In *ECOCLAY II, Effects of Cement on Clay Barrier Performance—Phase II, final report (Contract FIKW-CT-2000-00028)* (pp. 188–192). European Commission, Nuclear Science and Technology.
- Mäder, U., & Adler, M. (2005b). A long-term in situ experiment for the interaction of Opalinus Clay with hyperalkaline fluid at the Mont Terri URL (Switzerland). In *ECOCLAY II, Effects of Cement on Clay Barrier Performance—Phase II, final report (Contract FIKW-CT-2000-00028)* (pp. 192–195.). European Commission, Nuclear Science and Technology.
- Marty, N. C. M., Tournassat, C., Burnol, A., Giffaut, E., & Gaucher, E. C. (2009). Influence of reaction kinetics and mesh refinement on the numerical modelling of concrete/clay interactions. *Journal of Hydrology*, 364, 58–72.
- Massat, L., Cuisinier, O., Bihannic, I., Claret, F., Pelletier, M., Masrouri, F., et al. (2016). Swelling pressure development and inter-aggregate porosity evolution upon hydration of a compacted swelling clay. *Applied Clay Science*, 124–125, 197–210.
- Matschei, T., Lothenbach, B., & Glasser, F. P. (2007). The role of calcium carbonate in cement hydration. *Cement and Concrete Research*, 37, 551–558.
- Nagra. (2002). Project Opalinus Clay—safety report. Demonstration of disposal feasibility for spent fuel, vitrified high-level waste and long-lived intermediate-level waste (Entsorgungsnachweis). *Nagra Technical Report*, 02-05. Nagra, Wettingen, Switzerland. <http://www.nagra.ch>.
- Nied, D., Enemark-Rasmussen, K., L'Hôpital, E., Skibsted, J., & Lothenbach, B. (2016). Properties of magnesium silicate hydrates (M-S-H). *Cement and Concrete Research*, 79, 323–332.
- Pearson, F. J., Arcos, D., Bath, A., Boisson, J. Y., Fernández, A. M., Gäbler, H. E., Gaucher, E., Gautschi, A., Griffault, L., Hernán, P., & Waber, H. N. (2003). *Mont Terri Project—geochemistry of water in the Opalinus Clay formation at the Mont Terri Rock Laboratory*. Bern: OFEG Report, Geology Serie, No. 5. Federal Office of Topography (swisstopo), Wabern, Switzerland. <http://www.mont-terri.ch>.
- Prêt, D., Sardini, P., Beaufort, D., & Sammartino, S. (2004). Porosity distribution in a clay gouge by image processing of ¹⁴C-PolyMethylMethAcrylate (14C-PMMA) autoradiographs. Case study of the fault of St Julien (Basin of Lodève, France). *Applied Clay Science*, 27, 107–118.
- Read, D., Glasser, F. P., Ayora, C., Guardiola, M. T., & Sneyers, A. (2001). Mineralogical and microstructural changes accompanying the interaction of Boom Clay with ordinary Portland cement. *Advances in Cement Research*, 13, 175–183.
- Roosz, C., Grangeon, S., Blanc, P., Montouillout, V., Lothenbach, B., Henocq, P., et al. (2015). Crystal structure of magnesium silicate hydrates (M-S-H): The relation with 2:1 Mg–Si phyllosilicates. *Cement and Concrete Research*, 73, 228–237.
- SCK-CEN (2012). Preparatory safety assessment. Conceptual model description of the reference case. In *External Report of the Belgian Nuclear Research Centre*, ER-215, CCHO—2009-00940000. SCK-CEN, Mol, Belgium. <http://www.sckcen.be>.
- Techer, I., Bartier, D., Boulvais, P., Tinsseau, E., Suchorski, K., Cabrera, J., et al. (2012). Tracing interactions between natural argillites and hyper-alkaline fluids from engineered cement paste and concrete: Chemical and isotopic monitoring of a 15-years

- old deep-disposal analogue. *Applied Geochemistry*, 27, 1384–1402.
- Tinseau, E., Bartier, D., Hassouta, L., Devol-Brown, I., & Stammose, D. (2006). Mineralogical characterization of the Tournemire argillite after in situ reaction with concretes. *Waste Management*, 26, 789–800.
- Thermoddem. (2016). Thermochemical and mineralogical tables for geochemical modeling, developed at BRGM, France. <http://thermoddem.brgm.fr/>. Accessed 23 Dec 2016.
- Wieland, E., Lothenbach, B., Glaus, M.A., Thoenen, T., & Schwyn, B. (2014). Influence of superplasticizers on the long-term properties of cement pastes and possible impact on radionuclide uptake in a cement-based repository for radioactive waste. *Applied Geochemistry*, 49, 126–142.

Corrosion of carbon steel in clay environments relevant to radioactive waste geological disposals, Mont Terri rock laboratory (Switzerland)

Sophia Necib¹  · Nikitas Diomidis² · Peter Keech³ · Masashi Nakayama⁴

Received: 11 March 2016 / Accepted: 22 December 2016 / Published online: 21 February 2017
© The Author(s) 2017. This article is published with open access at Springerlink.com

Abstract Carbon steel is widely considered as a candidate material for the construction of spent fuel and high-level waste disposal canisters. In order to investigate corrosion processes representative of the long term evolution of deep geological repositories, two in situ experiments are being conducted in the Mont-Terri rock laboratory. The iron corrosion (IC) experiment, aims to measure the evolution of the instantaneous corrosion rate of carbon steel in contact with Opalinus Clay as a function of time, by using electrochemical impedance spectroscopy measurements. The Iron Corrosion in Bentonite (IC-A) experiment intends to determine the evolution of the average corrosion rate of carbon steel in contact with bentonite of different densities, by using gravimetric and surface analysis measurements, post exposure. Both experiments investigate the effect of microbial activity on corrosion. In the IC experiment, carbon steel showed a gradual decrease of the corrosion rate over a period of 7 years, which is consistent with the ongoing formation of protective corrosion products. Corrosion product layers composed of magnetite,

mackinawite, hydroxychloride and siderite with some traces of oxidising species such as goethite were identified on the steel surface. Microbial investigations revealed thermophilic bacteria (sulphate and thiosulphate reducing bacteria) at the metal surface in low concentrations. In the IC-A experiment, carbon steel samples in direct contact with bentonite exhibited corrosion rates in the range of 2 $\mu\text{m}/\text{year}$ after 20 months of exposure, in agreement with measurements in absence of microbes. Microstructural and chemical characterisation of the samples identified a complex corrosion product consisting mainly of magnetite. Microbial investigations confirmed the limited viability of microbes in highly compacted bentonite.

Keywords Corrosion layers · Corrosion rate measurements · Microbial activity · Surface micro-characterisations · Opalinus Clay · Bentonite · Nuclear waste disposal

1 Introduction

The international Mont Terri Project aims to investigate the properties of the Opalinus Clay formation from hydrogeological, geochemical and geomechanical points of view. The Mont Terri geological profile is given in Fig. 1, (Nussbaum et al. 2017). Since 1996, international research has been ongoing in the Mont Terri rock laboratory, involving fifteen organisations who consider clay formations as potential host rocks for deep geological disposal of radioactive waste.

Carbon steel (C-steel) alloys are candidate disposal canister materials in many radioactive waste disposal programmes due to their high structural strength and low and predictable corrosion rate, (Andra 2005; Féron et al. 2008; Patel et al. 2012). After sealing of the repository, the

Editorial handling: P. Bossart and A. G. Milnes.

This paper is #16 of the Mont Terri Special Issue of the Swiss Journal of Geosciences (see Bossart et al. 2017, Table 3 and Fig. 7).

✉ Sophia Necib
Sophia.necib@andra.fr

- ¹ Andra, Meuse/Haute-Marne-Centre, RD 960, 55500 Bure, France
- ² Nagra, Hardstrasse 73, 5430 Wettingen, Switzerland
- ³ NWMO, 22 St. Clair Avenue East, Toronto, ON M4T2S3, Canada
- ⁴ JAEA, Hokushin 432-2, Hokkaido, Horonobe-Cho 098-3224, Japan

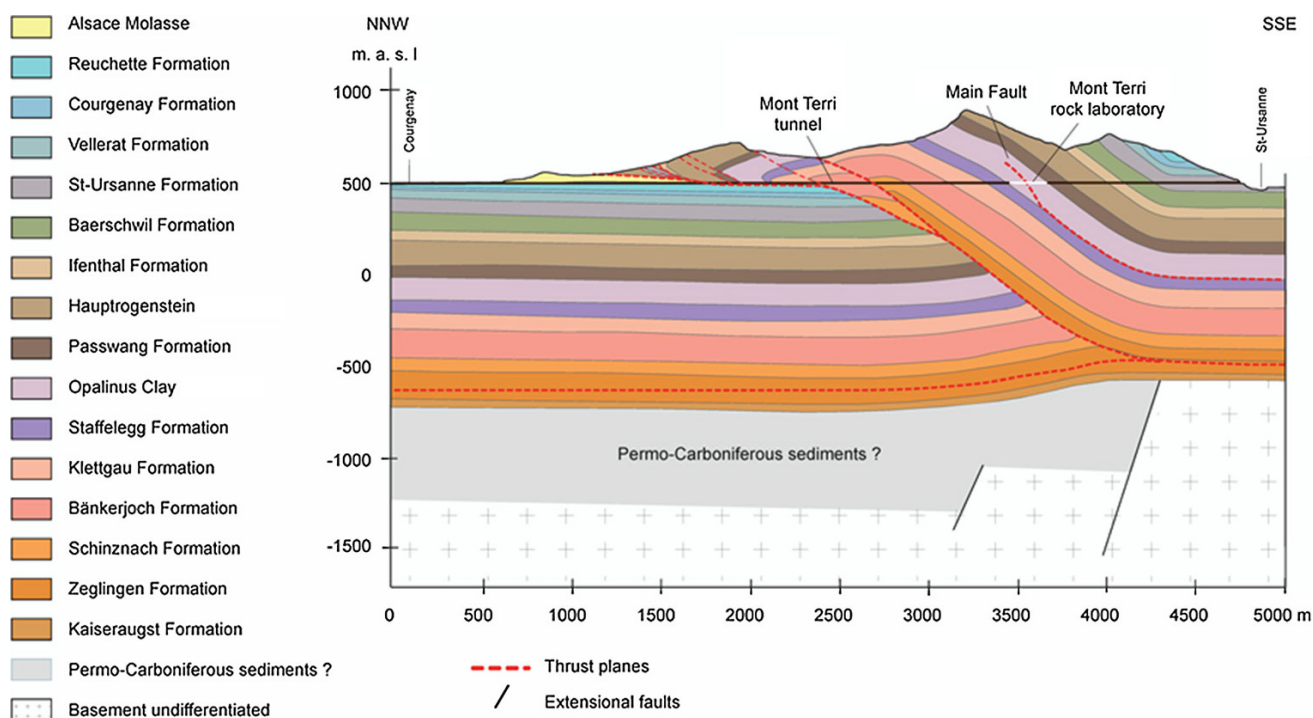


Fig. 1 Geological cross-section of the Mont Terri anticline and location of the Mont Terri rock laboratory

temperature, relative humidity and oxygen concentration at the surface of a disposal canister will vary greatly from the time of emplacement until the end of its lifetime. Upon initial emplacement, the conditions at the canister surface are characterised by high temperatures and readily available oxygen. Gradually, ingress of pore-water from the host rock will induce an increase of relative humidity close to the canister forming an adsorbed water film on the metal surface which is able to sustain electrochemical reactions. In aerated groundwater conditions steel corrosion is generally characterised by the production of a complex mixture of different crystalline and amorphous phases of the oxides and hydroxides of iron. After the consumption of the available oxygen, anoxic conditions will prevail and the canister or casing (for the French concept) will be in direct contact with clay. This final phase dominates the vast majority of the lifetime of the canister.

According to the Pourbaix diagram of Fe in Fe–H₂O–CO₂ system, C-steel should be in the corrosion or passive region at neutral and alkaline pH under anoxic conditions (Chivot 2004). In addition, recent results on the characterisations of archaeological artifacts seem to confirm the long term passive state of C-steel materials in clay soils (Saheb et al. 2013).

In the present paper, the in situ corrosion rate of C-steel materials in clay and bentonite under conditions expected in a deep geological repository has been determined in two distinct experiments. The Iron Corrosion (IC) experiment aims to monitor the instantaneous corrosion rate (CR) of C-steel in contact with Opalinus Clay, by using

electrochemical impedance spectroscopy (EIS) measurements. The iron corrosion in bentonite (IC-A) experiment aims to determine the evolution of the average CR of C-steel in contact with bentonite of different densities by gravimetric and surface analysis measurements. Both experiments aim to gain insight into the relevant corrosion mechanisms by surface analyses and microstructural characterisation of the corrosion products, as well as to define the role of microbes under disposal conditions.

2 Materials and methods

2.1 IC experiment

2.1.1 Experimental module set-up and removal

The test chamber was located in a vertical and descending borehole drilled under nitrogen in Opalinus Clay (Bossart et al. 2017). Due to insufficient air tightness of the packer, the equipment was emplaced about three months after the drilling of the borehole. It contained four 69 cm² metallic electrodes, electrically insulated from each other with alumina, and mounted on a central tubing (Fig. 2). Two electrodes were made of C-steel (grades E24 and S235) with a ferrite–pearlite microstructure, one electrode was made of Inconel 690 and one electrode was made of 316 stainless steel. The whole setup (about 200 mm long, 76 mm diameter) was inserted in a cylindrical Opalinus

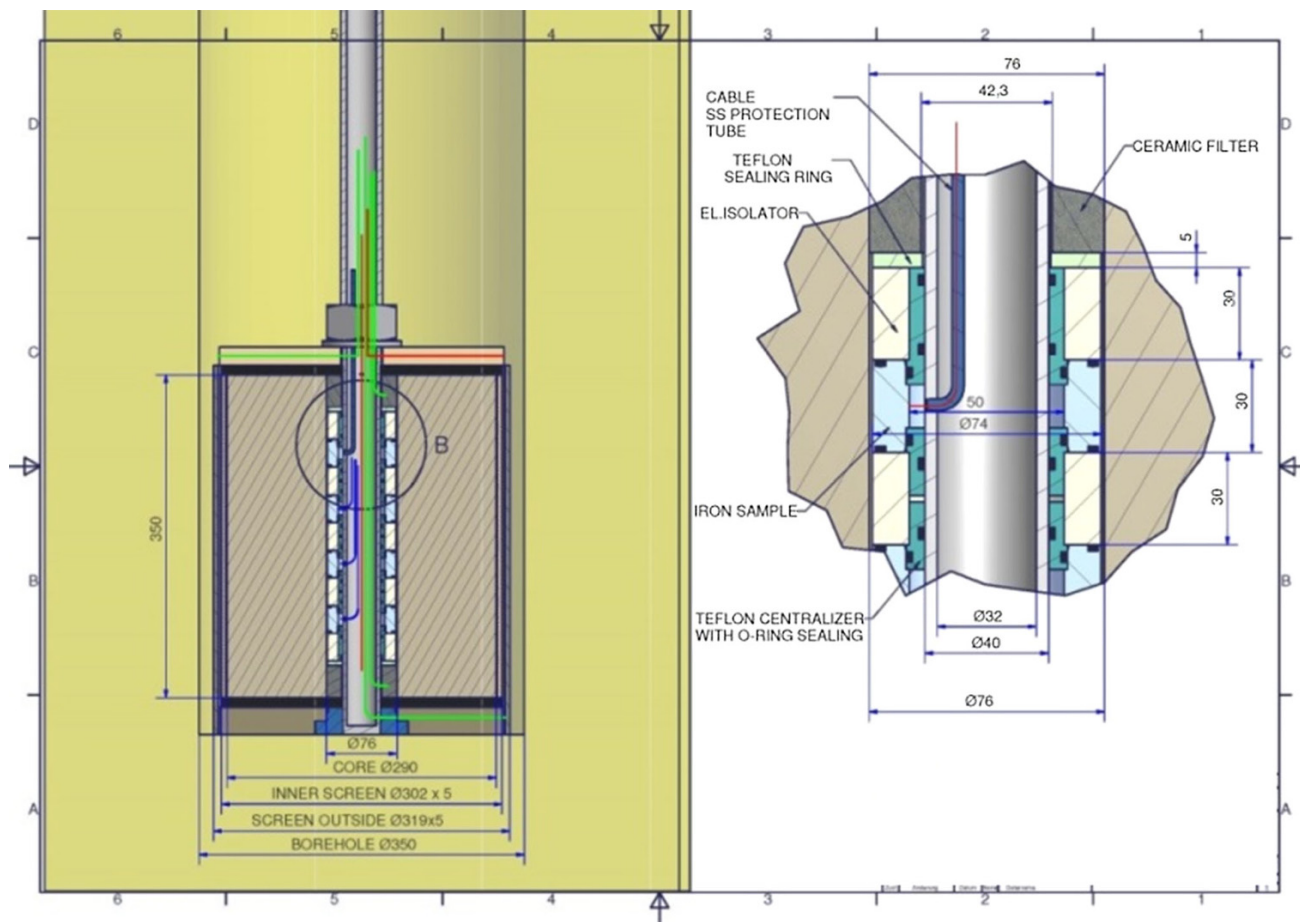


Fig. 2 Experimental set-up showing the test chamber with the metallic electrodes in the IC experiment

Clay borecore (350 mm long, 290 mm in diameter) confined in two stainless steel screens, and introduced at the bottom of the borehole at a depth of approximately 8 m. A packer was placed at the top of the test chamber to isolate it from the environment and ensure anoxic conditions. The temperature was initially kept ambient for two years and then increased to 90 °C using a heating system circulating hot water via the central tubing. The initial space between the metallic electrodes and the Opalinus Clay borecore was limited to 1 mm void so that corrosion occurred in a relatively confined configuration.

The electrolyte, initially a synthetic solution with a composition representative of Opalinus Clay pore-water (Table 1) (Pearson 2002; Pearson et al. 2003), was injected in the test chamber, which was maintained at the pressure of the environment (~ 14 bars). The water flow-rate was manually set to ensure circulation between the metallic

electrodes and the Opalinus Clay borecore, collect water samples and monitor chemical parameters such as the pH, Eh redox potential and Electric conductivity.

After a total period of 7 years, the equipment was dismantled through a careful extraction of the modules from the borehole. The test chamber was maintained under nitrogen until the cutting operation was performed. It aimed to isolate the different electrodes for further characterisation. The electrode made of C-steel (E24 grade) was cut in two halves; one for microbial analyses (E24-a sample) and the other one for surface micro-characterisations (E24-b sample).

2.1.2 Corrosion rate measurements

During the thermal phase, the CR was monitored by performing electrochemical measurements. Two different

Table 1 Composition of the synthetic Opalinus Clay pore-water at 25 °C, initially injected in the IC experiment

Elements	Sr	Na	Cl	K	Mg	Ca	HCO ₃	SO ₄	pH
Contents (mg/L)	44	5530	10,200	53	41	780	29	1350	7.6

three electrode cells were used: a working electrode (C-steel (E24 or S235), a counter electrode (Inconel 690) and a pseudo reference electrode (S235 or E24). Each electrode was connected via a 8-m Cu wire lead. The measurement set up consisted of a potentiostat WMP3 Biologic remotely driven with the EC-lab software. Open circuit potential (OCP) measurements were carried out for 24 h prior and further to performing EIS measurements, in order to verify the stability of the OCP as well as the possible influence the EIS measurements might have on the metal surface. For EIS measurements, a classic equivalent circuit, containing a transfer resistor parallel to a constant phase element (CPE) equivalent circuit in low frequency range, was used to model the EIS results (Fig. 3) (Jonscher 1991). The corrosion rate was estimated from the transfer resistor by using the Stern–Geary method, (Stern and Geary 1957; Roberge and Sastri 1994; Chen and Jepson 1999).

Equation (1) presents the relationship between the corrosion current density and transfer resistor.

Equation (2) presents the relationship between the CR and corrosion current density.

$$J_{corr} = \frac{B}{R_t}, \quad (1)$$

where J_{corr} ($\mu\text{A}/\text{year}$), is the corrosion current density, R_t ($\Omega \text{ cm}^2$) is the transfer resistor, B is a constant.

$$CR = \frac{M_{\text{Fe}} J_{corr}}{\rho_{\text{Fe}} n_a F}, \quad (2)$$

where, CR ($\mu\text{m}/\text{year}$) is the corrosion rate, M_{Fe} (55.85 g/mole) is the atomic mass of iron, ρ_{Fe} ($7.9 \text{ g}/\text{cm}^3$) is the volumic mass of iron, n_a is the number of electrons exchanged in the anodic process, F is the Faraday constant.

EIS spectra were recorded at OCP with a 10 mV amplitude. Frequency ranged from 1 kHz to 10 μHz with 10 frequency values per logarithmic decade. Repeated measurements were done over a period of 5 years.

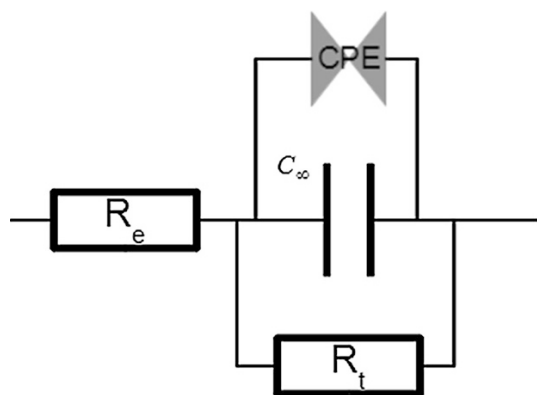


Fig. 3 Equivalent circuit used to calculate the corrosion rate in the IC experiment. R_e resistor, CPE constant phase element, C_∞ condenser, R_t transfer resistor

2.1.3 Surface characterisations

The E24-b sample was prepared in a glove box under N_2 atmosphere. The electrode surface was first covered with a thin layer of resin (Epofix, Struers) to prevent abrasion during manipulation. A block of $\sim 1 \text{ cm}$ was then recovered by sawing the electrode along two planes parallel to the cylinder axis, using a diamond disk saw (Minitom Struers). This block was then impregnated in resin and polished down to $1 \mu\text{m}$ using silicon carbide papers and eventually diamond pastes. Most polishing was performed dry, with absolute ethanol used only for final polishing and surface rinsing.

Optical images of the metal/Opalinus clay interface were obtained with a Zeiss Imager M2m microscope equipped with a CCD camera.

μ -Raman spectra were recorded on a LabRam HR800 microspectrometer with an Olympus BX41 microscope and $50 \times$ long-range objective.

For scanning electron microscopy (SEM), polished cross sections were first coated with a thin carbon layer, then transferred into the microscope. Samples were investigated in Backscattered Electron (BSE) mode using a JEOL JSM7000-F microscope equipped with a field emission gun and operated at 10 kV to improve quantification of oxygen and light elements, and at a current of between 2 and 10 nA. Energy-dispersive X-ray (EDX) spectra were collected using a silicon-drift detector (Bruker XFlash 5010) equipped with a thin beryllium window for the detection and quantification of oxygen. Distribution maps of selected chemical elements were recorded by continuous scanning of the sample and cumulative recording of EDX signal on each pixel.

For micro X-ray diffraction (μXRD), the polished surfaces were glued on glass slides using Canada balsam, then sawed to a thickness of $\sim 1 \text{ mm}$, and polished to obtain a final thickness of about $100 \mu\text{m}$. μXRD data were recorded in transmission mode. Diffraction patterns were collected with a 2D dimensional detector (GE Healthcare image plate) and circularly integrated with the FIT2D software.

2.1.4 Microbial activity investigation

Molecular studies involving PCR–DGGE (polymerase chain reaction—denaturing gradient gel electrophoresis) and PCR SSCP (polymerase chain reaction—single-strand conformation polymorphism) were conducted on water samples from different locations (test chamber and reservoir) and swabs from C-steel surface.

The PCR technique hinges on obtaining enough DNA to make it amplifiable. Two extraction techniques were employed:

- DNA extraction in DNA-rich or DNA-poor samples using commercial PCR kits (a kit for extraction followed by SSCP and a kit for extraction followed by DGGE).
- DNA extraction in DNA-poor samples using phenol-chloroform extraction.

Water samples from the test chamber and the reservoir were taken from the water unit in sterile cells. In addition, swabbing was performed on C-steel metal surface under controlled atmosphere in the glove box. Both, water samples and swabs were investigated by using the most probable number technique (MPN) aiming at determining the concentration of mesophilic and thermophilic sulfurogen bacteria, known to potentially influence the corrosion processes, (Daumas et al. 1993). The mesophilic and thermophilic bacteria grow preferably at temperatures ranging from 20 to 44 °C and above 45 °C, respectively.

Counting the sulphate and thiosulphate-reducing bacteria (SRB and ThRB) was carried out by seeding 2×1 mL of sampled solution on specific anaerobic media (TK Labège BSR and TK Labège BTR), and then diluted several times 10:1 using two flasks per dilution to get the number of bacteria/mL. The positive-testing reactions were seen by the medium turning black after 7 weeks of incubation at 30 °C (for the mesophilic bacteria) and 60 °C (for the thermophilic bacteria) due to the reaction of the sulphide produced during bacterial metabolism with the iron present in the medium.

2.2 IC-A experiment

2.2.1 Experimental setup

The IC-A experiment is conducted within a 15.8 m long vertical and descending borehole sealed with 2.5 m long packer system, (Bossart et al. 2017). The test section is 4.2 m long, between the packer and the bottom of the borehole. The interval is equipped with a slotted stainless steel liner of 6 mm wall thickness which was set without cementing allowing the ingress of pore-water from the host rock (Fig. 4). Within the test section, 12 stainless steel modules were emplaced initially. The modules have holes and a sintered stainless steel filter to allow for the exchange of pore-water with the host rock. Each module contains compacted bentonite and 12 corrosion coupons (Fig. 5). The corrosion coupons were cut from ASTM A694-08 F65 and ASTM 516 Grade 70 carbon steels both from the base alloy and from a 14 cm deep electron beam weld and heat affected zone, and had a diameter of 20 mm and a thickness of 10 mm. Volclay MX-80 bentonite was used for the experiments in four different forms: compacted blocks with a dry density of 1.25 g/cm^3 , compacted blocks with a dry density of 1.45 g/cm^3 , powder-pellet mixture with a dry

density of 1.45 g/cm^3 , and compacted blocks with a dry density of 1.55 g/cm^3 . The corrosion coupons and bentonite were assembled in the modules as shown in Fig. 5, under anoxic conditions. The modules were then partly presaturated ($\sim 90\%$) in anoxic synthetic Opalinus Clay pore-water (Pearson 2002) prior to shipping to the Mont Terri rock laboratory for emplacement.

The time span between drilling of the borehole and emplacement of the 12 test modules was about 10 months. During this period the borehole was kept under anoxic conditions and natural Opalinus Clay pore-water ingressed in the borehole at an average rate of 44 ml/day. During emplacement of the modules an additional 10 L of synthetic anoxic Opalinus Clay pore-water were added to the borehole in order to ensure that all modules were completely immersed.

About 20 months after emplacement, the first sampling campaign took place. During sampling 3 modules were removed from the borehole. Three new modules were emplaced for the continuation of the experiment which is planned to proceed for a total of 10 years. The removed modules contained the following bentonite forms: powder-pellet mixture with a dry density of 1.45 g/cm^3 (Module 1), compacted blocks with a dry density of 1.25 g/cm^3 (Module 2) and compacted blocks with a dry density of 1.55 g/cm^3 (Module 3). Upon removal from the borehole, the modules were emplaced in specially designed stainless steel transfer flasks that were filled with Opalinus Clay pore-water from the borehole and bubbled with argon for 30 min prior to sealing to ensure anoxic conditions during shipping. The transfer flasks were then shipped to the Amec Foster Wheeler laboratories in Harwell, Oxford, UK for dismantling and analyses.

Dismantling of the modules was done in a sterilised argon-purged glovebox. The inner cylindrical filter was cut along its complete length on opposite sides using a hand-held rotating abrasive disc saw. This procedure was carried out in a glovebag to minimise the spread of dust throughout the glovebox. One half of each inner cylindrical filter was removed from the module to expose the inner components of the experiments. Slices of bentonite approximately 1 cm thick were cut manually across the cylinder of bentonite using a large sharp two-handed knife to provide access to the embedded corrosion specimens. After removal from the bentonite, the corrosion specimens and fragments of bentonite were sealed separately under argon in Mylar bags inside the glovebox to maintain an anoxic environment around the samples. The glovebox was cleaned thoroughly after dismantling each module to minimise cross contamination.

2.2.2 Corrosion rate measurements

In order to calculate the corrosion rate of the specimens, two weight loss measurements were carried out

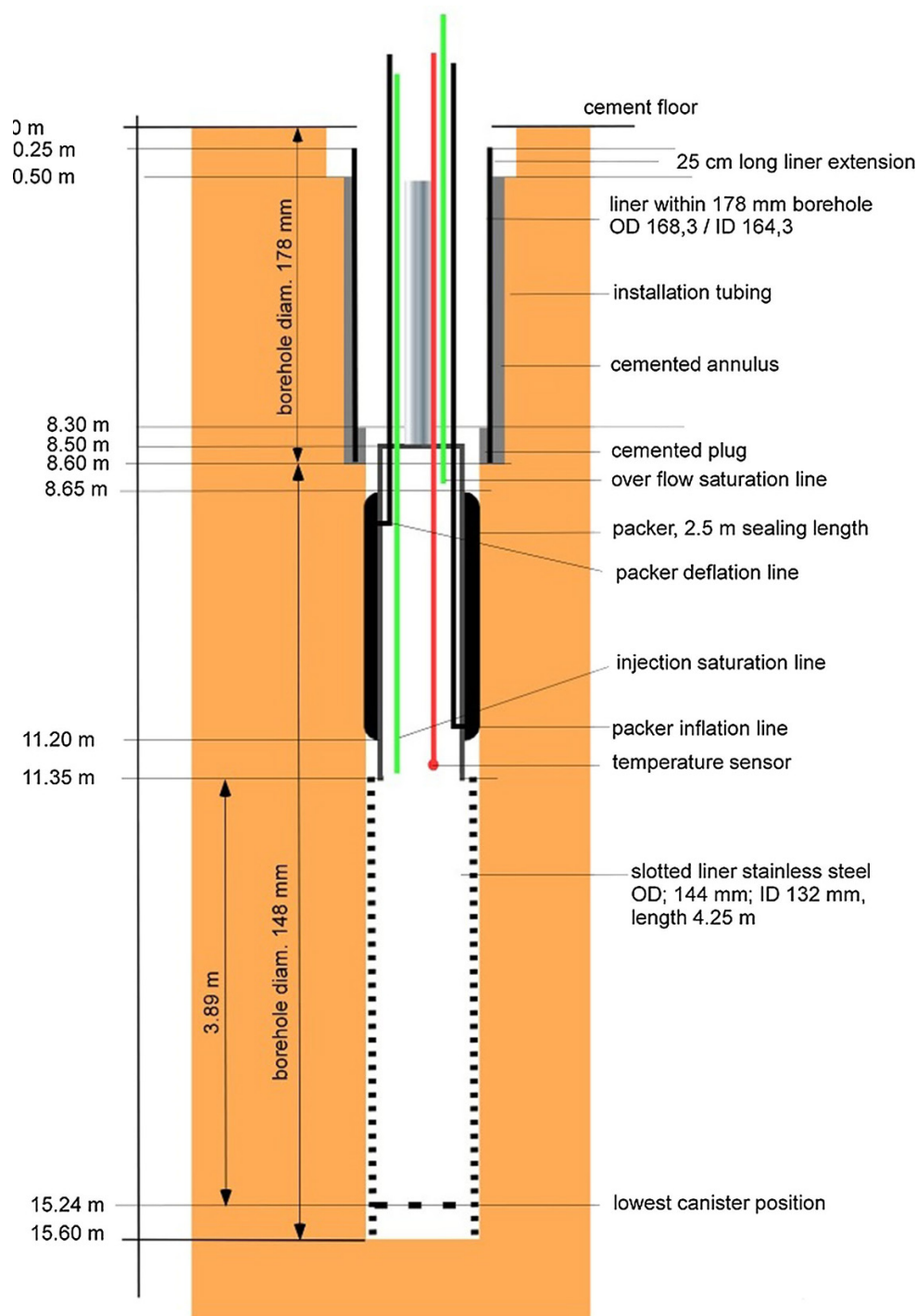


Fig. 4 Borehole layout of the IC-A experiment

on each specimen according to the following procedure. The specimens were cleaned ultrasonically in methanol for 5 min to remove any residual bentonite. After ultrasonic cleaning, the methanol was decanted and the specimens were left to dry naturally in the glovebox for 10 min. Each specimen was then weighed, following the initial drying stage, to measure the weight after

removal of the specimen from the test environment but before any remaining adherent corrosion product scale has been removed. The initial solvent cleaning procedure was followed by descaling the specimens in Clarke's solution (1 litre SG 1.18 HCl, 50 g SnCl₂, 20 g Sb₂O₃) and weighing according to the ASTM G1-03 standard procedure, (ASTM 2011). The weight loss

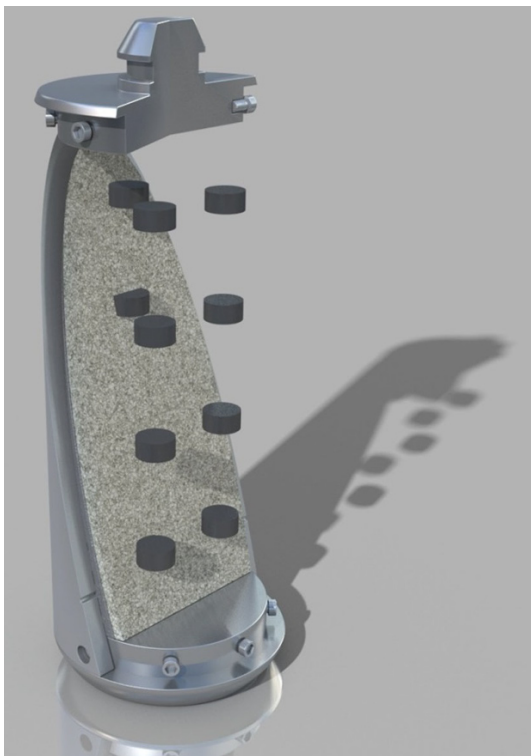


Fig. 5 Illustration of a cutaway of a test module containing bentonite and corrosion coupons in the IC-A experiment

was then converted to a corrosion rate and given in units of $\mu\text{m}/\text{year}$.

2.2.3 Surface characterisation

A number of specimens were examined using SEM and EDX analysis. A Hitachi TM3000 SEM equipped with a Bruker X-ray analysis system was used to image the specimens and perform the analysis using EDX.

Raman spectroscopy was used to analyse the corrosion product, using a Horiba JY LabRam Aramis confocal Raman microscope. The exciting laser wavelength used was 532 nm. A $50\times$ extra-long working distance objective lens was used to collect the 180° backscattered light. The specimens were loaded into sample holders and held in place using Menzel Gläser cover slips attached to the sample holders using Araldite adhesive.

2.2.4 Microbial investigation

The bentonite was cut and sampled with sterile knives and spatulas and packed in sterile sampling bags and then packed in 2 layers of Mylar bags under anoxic conditions and kept at 4°C . Samples were taken at the edge of the bentonite next to the filter as well as from the center of the module. For the determination of the water content and dry density, the samples were measured, weighed and dried in

an oven at 110°C until they reached a constant weight. The sample sections for microbiological analyses were cut into smaller pieces under sterile conditions prior to further processing. A suspension was prepared from the small pieces of sample section destined for cell culturing by adding a weighed amount of sample to a known volume of phosphate-buffered saline solution (PBS, i.e., 0.01 M NaCl buffered to pH 7.6 with $9\text{ mM Na}_2\text{HPO}_4$ and $1\text{ mM NaH}_2\text{PO}_4\cdot\text{H}_2\text{O}$), which was then stirred for 30 min to 1 h. Serial dilutions of the suspensions were used in the enumerations. Aerobic heterotrophs were enumerated on R2A medium, Reasoner and Geldreich 1985. Aerobic plates were poured in a laminar flow hood and incubated at 30°C for 3–3.5 days. Anaerobic heterotrophs were also cultured on R2A medium in an anaerobic glove box, and incubated at 30°C under anaerobic conditions for about 17 to 28 days. Sulphate-reducing bacteria were enumerated by the most-probable number (MPN) method in modified Postgate's B medium, Atlas 1993 and incubated at 30°C under anaerobic conditions for 35–71 days.

3 Results

3.1 IC experiment

The test chamber was initially kept at room temperature for two years and then maintained at 85°C until dismantling occurred, i.e. for about 5 years for a total test duration of 7 years. There was a short interruption of the heating phase (two months) at $t = 6.2$ years due to a breakdown of the heating system. The evolution of the temperature at three different locations is presented in Fig. 6. These results emphasise the temperature gradient both, radially and vertically, as well as between the test chamber and the surface water unit. The temperature differences were taken into consideration for the investigations carried out on the different corrosion layers as well as the microbial activity. The physico-chemical parameters such as the Eh redox potential, pH, electric conductivity, etc. were monitored on water via sensors located in the water unit. The Eh redox potential decreased rapidly due to the oxygen consumption by the host rock and corrosion processes, allowing reducing conditions to prevail (Fig. 7). The occasional increases correspond to the electrode calibration and electricity power cuts.

The pH remained relatively neutral throughout the duration of the experiment (Fig. 8).

From the EIS model of the data, it was evident that the charge transfer resistance increased overtime, and consequently, the CR of both materials, S235 and E24 decreased simultaneously, with initial values around $15\ \mu\text{m}/\text{year}$ and final values estimated below $1\ \mu\text{m}/\text{year}$ (Fig. 9). The

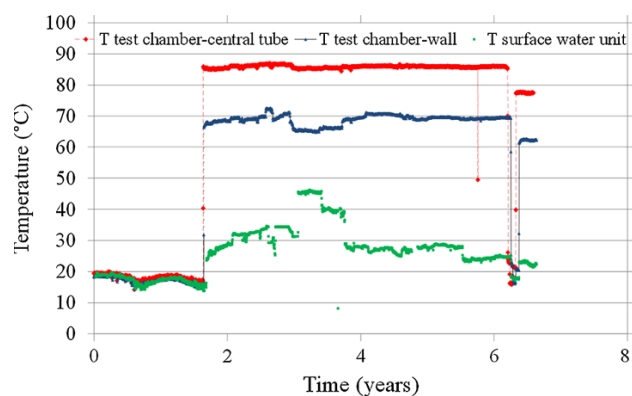


Fig. 6 Temperature evolution at three different locations in the IC experiment: in the test chamber (center and wall) and in the surface water unit

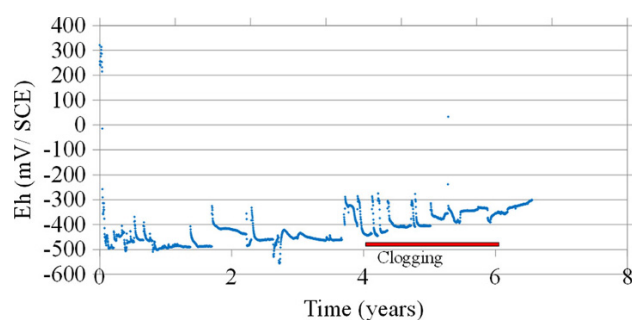


Fig. 7 Evolution of the Eh redox potential measured from the surface water unit in the IC experiment

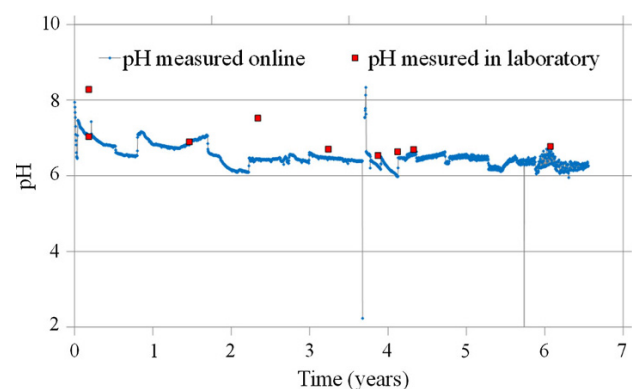


Fig. 8 Evolution of the pH in the IC experiment

equivalent circuit fitted relatively well the experimental data with a maximum error estimated below 10%. The evolution of the water flow-rate shows variations (Fig. 9).

Despite the manual set, the flow-rate tended to decrease due to the clogging of the water circulation loop. N_2 injection was performed when clogging occurred (i.e. at $t = 2.5$ years), which enhanced a congruent increase of the CR (from 4 to 20 and 10 $\mu\text{m}/\text{year}$, respectively, for E24 and S235 materials).

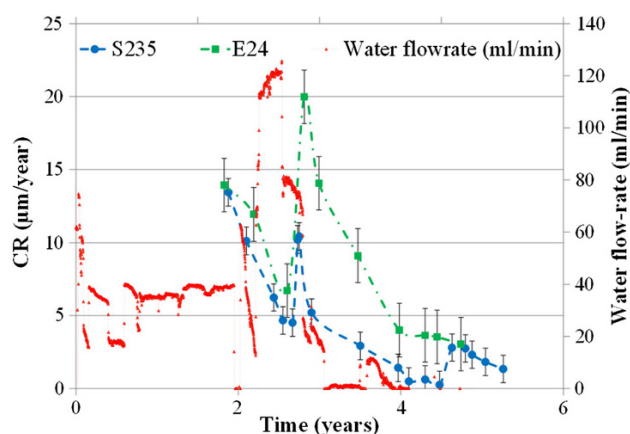


Fig. 9 Evolutions of the CR of C-steel and water flow-rate in the IC experiment: E24 (green squares); S235 (blue circles) and water flowrate (red line)

From $t = 4$ years, the water flow-rate reached 0 ml/min despite declogging tentatives. Further tests carried out in the water loops highlighted that the location of the clogging was at the electrodes/Opalinus Clay borecore interface. Consequently, water circulation was hindered and online monitoring of the Eh redox potential, pH and Electric conductivity was only representative of stagnant water in the water unit.

The characterisation of the E24 metal surface/Opalinus Clay interface revealed mainly non uniform general corrosion with the presence of several layers of corrosion products with distinct compositions identified by EDX analyses, $\mu\text{-XRD}$ and $\mu\text{-Raman}$ techniques (Fig. 10). The metal/Opalinus Clay interface highlighted two main regions: the external corrosion products and the internal corrosion products, which are above and underneath the trace of the original surface, respectively. The innermost layers consisted of mixed magnetite (Fe_3O_4) with two Cl-containing Fe compounds, akaganeite and $\beta\text{-Fe}_2(\text{OH})_3\text{Cl}$. Next, an extended layer of pure chukanovite was determined with a layer mixing Fe silicate, with nodules of chukanovite, and siderite surrounded by fringes of akaganeite. Porosity is visible by the presence of resin. Close to the trace of the original surface, the corrosion products were essentially made by a layer of siderite, containing discrete, extended domains of goethite, lepidocrocite, Fe sulphide at various oxidation states, or sulphur, together with a thin layer enriched in Fe silicate, and even locally a broad agglomerate of goethite. The trace of the original surface corresponded to a layer enriched in iron sulphide. Finally, outer corrosion products were essentially made by siderite forming a layer close to the trace of the original surface, and occurring as more dispersed material further away in the clay.

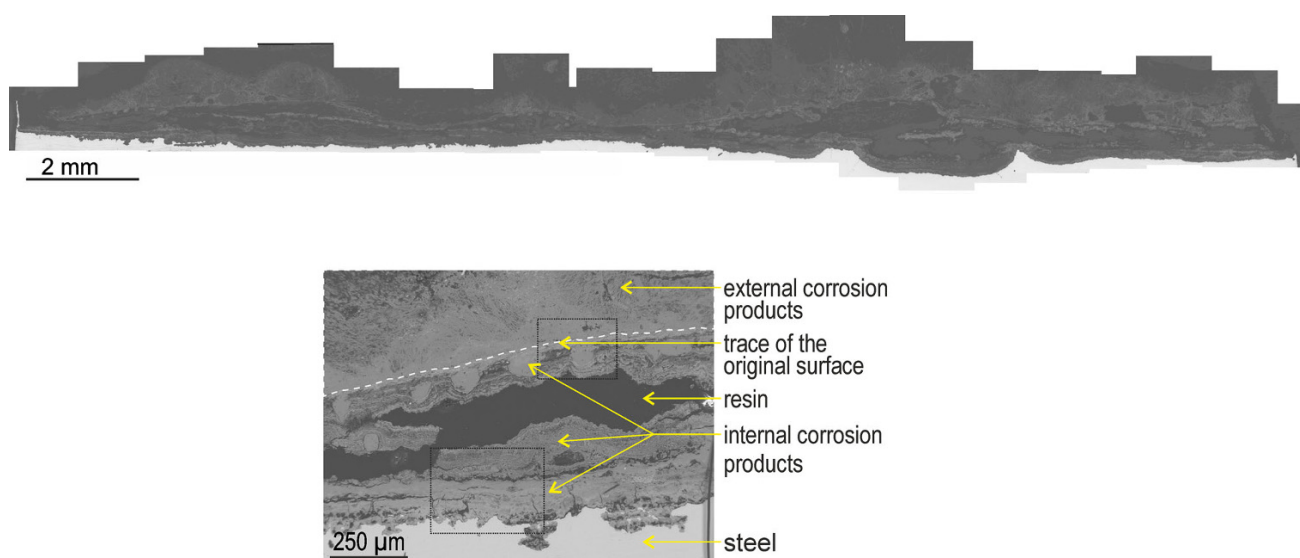


Fig. 10 Characterisations of the E24 metal/Opalinus Clay interface after 7 years in the IC experiment. OM showing the morphology of the interface (*top*); SEM image (BSE mode) showing the different regions of corrosion products (*bottom*)

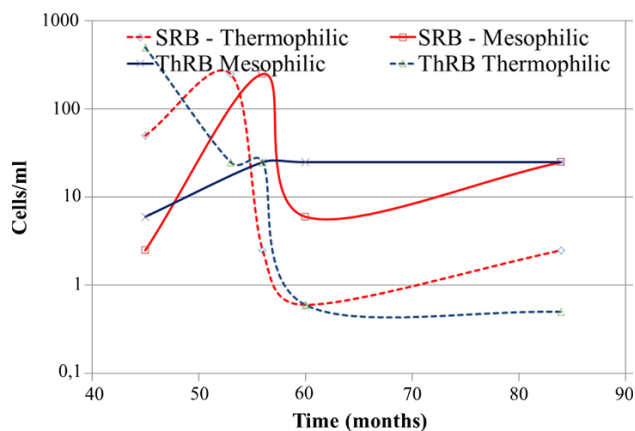


Fig. 11 Evolution of the sulfurogen bacteria (SRB and ThRB) present in pore-water in the IC experiment

Chronologically, chukanovite likely formed first under deaerated conditions. When anoxic conditions took place, Fe-silicate, chukanovite and magnetite formed as inner corrosion layers and siderite formed as the outer corrosion layer. Chloride species might have formed when the temperature dropped suddenly.

Eventually, a second deaerated step occurred as shown with the formation of goethite.

Biomolecular studies performed on water sampled from the test chamber at $t = 5$ years and from the reservoir at $t = 7$ years, revealed the presence of mesophilic and thermophilic bacteria. Moreover, the molecular analyses performed at the C-steel surface showed that bacteria were also present, despite the confined conditions to which the metallic electrodes were exposed.

The results from microbial analyses using the MPN technique, revealed that mesophilic and thermophilic sulfurogen bacteria were present in water sampled from the test chamber throughout the duration of the experiment, at concentrations reaching 150 cells/ml (Fig. 11). After clogging of the water loop, water sampling was performed from the reservoir located on surface and the thermophilic and mesophilic bacteria concentrations decreased to 0.6 and 85 cells/ml respectively. The microbial analyses conducted on the metal surface essentially revealed thermophilic bacteria, which is consistent with the operating temperature in the test chamber. The measured concentration reached 300 cells/cm² (Table 2).

The evolution of the sulphate content shows a first increase compared to the reference value (from 1350 to 3000 mg/L) followed by a progressive decrease over three years and a steady state close to the reference value

Table 2 Microbial activity (SRB and ThRB) at the E24 metal surface (swabs) and in Opalinus Clay pore-water taken from the reservoir in surface in the IC experiment

Samples	Swabs (E24-a)		Stagnant water (reservoir)	
	30 °C bacteria/cm ²	60 °C bacteria/cm ²	30 °C bacteria/mL	60 °C bacteria/mL
Sulphate-reducing bacteria (SRB)	33	3.3 10 ²	25	2.5
Thiosulphate-reducing bacteria (ThRB)	3.3	3.3	25	<0.5

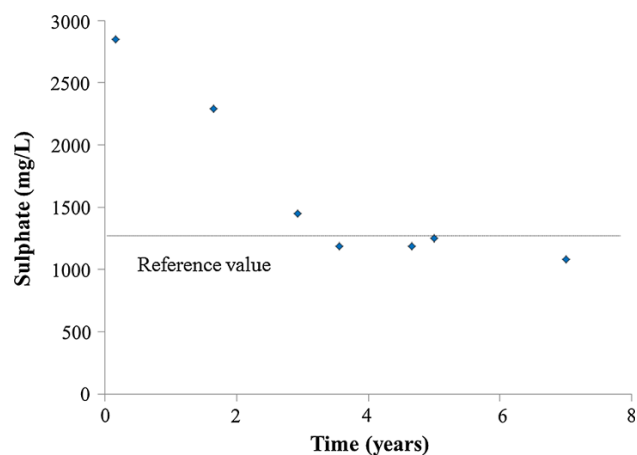


Fig. 12 Evolution of the sulphate content in pore-water in the IC experiment

(Fig. 12). The decrease of the sulphate is congruent with the thermophilic SRB growth (Fig. 11).

3.2 IC-A experiment

The average anaerobic corrosion rate of carbon steel in bentonite of different densities measured after 20 months of exposure in natural Opalinus Clay pore-water is shown in Fig. 13. The measured average corrosion rates ranged between 1.5 and 2.25 $\mu\text{m}/\text{year}$.

The SEM characterisation of the surface of a representative corrosion coupon, prior to sonication in methanol, is shown in Fig. 14. The SEM images indicate that there are some complex structures on the surface of the specimens

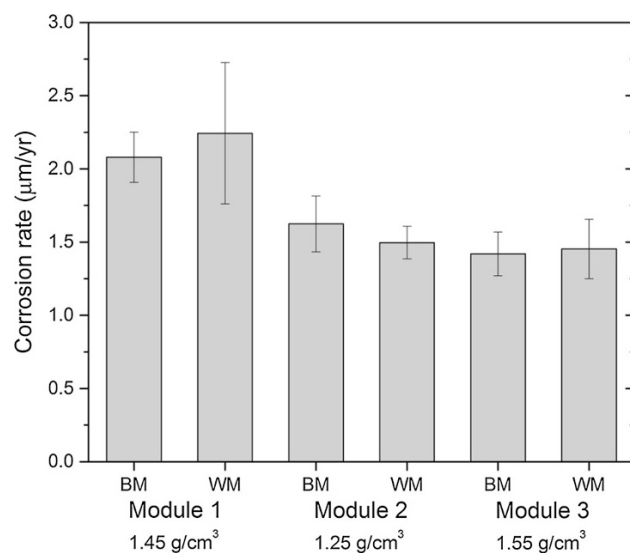


Fig. 13 The average anoxic corrosion rate of carbon steel base metal (BM) and electron beam weld metal (WM) after 20 months of exposure in bentonite of different densities saturated with natural Opalinus Clay pore-water in the IC-A experiment

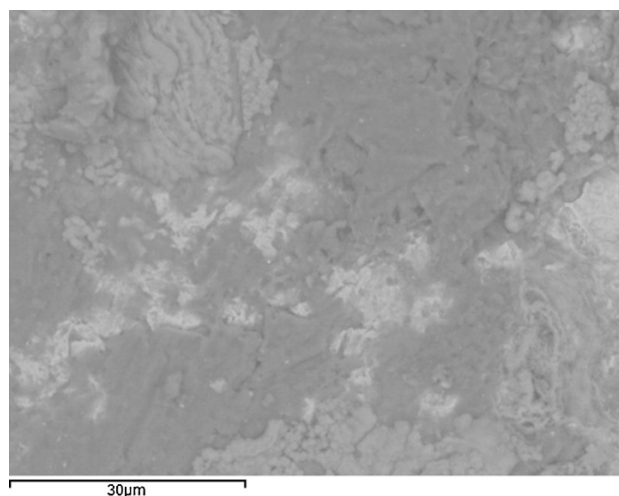


Fig. 14 SEM secondary electron micrograph of the surface of a base metal sample from Module 1 after exposure for 20 months in bentonite saturated with natural anoxic Opalinus Clay pore-water in the IC-A experiment

that vary across the surface of the coupon. EDX plots showed that this complex surface layer consists mainly of Fe and O, as expected for the corrosion product, while the detection of silicon and aluminium is indicative of the presence of residual bentonite on the coupon surface.

Further chemical characterisation of the corrosion products was done with Raman spectroscopy. The main peak was indicative of magnetite but there was a shift in the position of this peak compared to the standard, which may indicate that the actual corrosion product is sub-stoichiometric or a mixed phase spinel, e.g. $\text{Fe}_{3-x}\text{M}_x\text{O}_4$. Additional corrosion products consisting of hematite and an oxyhydroxide phase were identified. The composition of the corrosion products was similar to the one identified in previous ex situ studies, (Smart et al. 2016).

Measurements of the dry density of the bentonite exhibited some differences compared to the target values. For Module 1, the dry density values obtained are consistent, yielding an average value of $1.59 \pm 0.07 \text{ g}/\text{cm}^3$, which is higher than the targeted density of $1.45 \text{ g}/\text{cm}^3$. However, for Module 2, with a targeted density of $1.25 \text{ g}/\text{cm}^3$, the average density obtained was $1.53 \pm 0.08 \text{ g}/\text{cm}^3$. Finally, for Module 3, the average density is $1.74 \pm 0.05 \text{ g}/\text{cm}^3$ for a targeted density of $1.55 \text{ g}/\text{cm}^3$. The measured water content followed the reverse trend compared to the measured dry density (Module 1: 32.1%, Module 2: 40.6%, Module 3: 29.3%). The results indicate that while the measured density decreases in the same order as for the targeted density, the values for the density are significantly higher. Furthermore, there is some variation in the density of bentonite within a single module, suggesting that heterogeneity could be inherent to these systems.

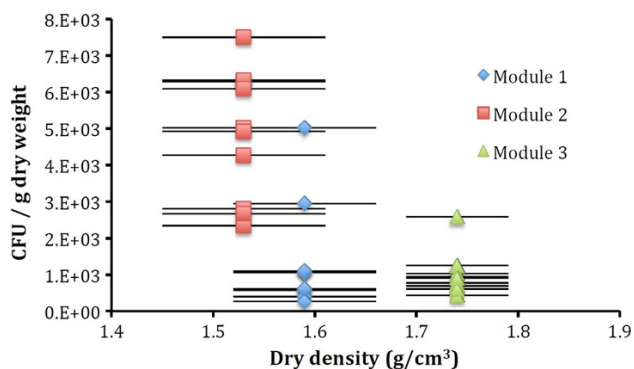


Fig. 15 Summary of cultivation results in the IC-A experiment, for anaerobic heterotrophic microorganisms plotted as a function of measured dry density. CFU colony-forming units

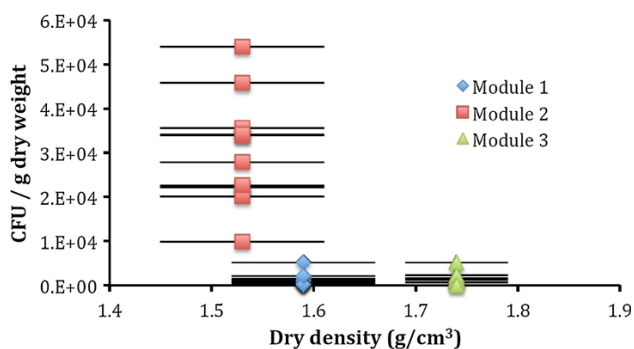


Fig. 16 Summary of cultivation results for aerobic heterotrophic microorganisms in the IC-A experiment, plotted as a function of measured dry density (CFU = colony-forming units)

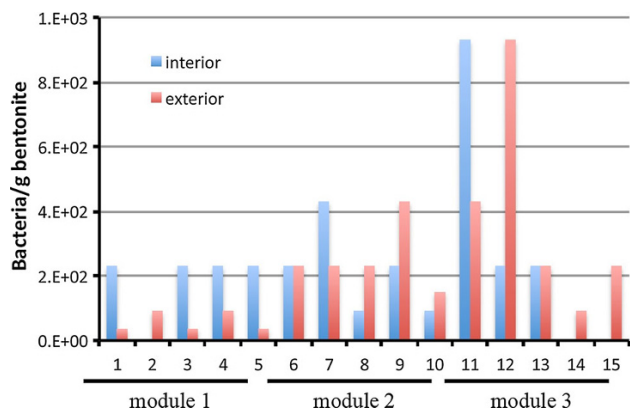


Fig. 17 Summary of cultivation results in the IC-A experiment, for sulphate reducing bacteria in the three modules (Module 1: 1.45 g/cm³, Module 2: 1.25 g/cm³, Module 3: 1.55 g/cm³). The X axis indicates sample numbers

The results of the microbial analyses are shown in Figs. 15, 16 and 17 for anaerobic heterotrophic microorganisms, aerobic heterotrophic microorganisms and sulphate reducing bacteria, respectively. Anaerobic heterotrophic bacteria, i.e. bacteria that use organic

compounds as a source of carbon and that grow in the absence of oxygen, were enumerated using anoxic plate cultivation. When comparing the number of anaerobic heterotrophs amongst the three modules, it appears that, as expected, Module 2, with the lowest measured and targeted dry densities, exhibits the highest numbers of anaerobic heterotrophs. Modules 1 and 3, in contrast, both show lower numbers. Aerobic heterotrophic bacteria, using O₂ as an electron acceptor, exhibit a similar behavior as the anaerobes, with the difference that cell counts are typically greater for the former. While Module 2 exhibited the largest aerobic heterotroph cell counts, Modules 1 and 3 revealed cell counts within an order of magnitude of each other, but with Module 3 showing the larger counts. Sulphate-reducing bacteria numbers were evaluated by the MPN method showing no clear effect of the bentonite density. The SRB counts were generally higher in the interior than the exterior of each subsample, particularly for Module 1. However, there was no specific trend as a function of location in the subsample for the other two modules.

4 Discussion

4.1 IC experiment

Initial oxidation likely occurred in the IC-experiment as confirmed by the evolution of the sulphate content which doubled three weeks after the launch of the experiment. This observation is typical when clay rock, containing pyrite, is exposed to air. Indeed, pyrite oxidation enhances the production of hydrogen sulphate released in clay pore-water, (Vinsot et al. 2014). The oxidation likely occurred between the drilling phase and installation of the equipment. Despite the oxidation stage, reducing conditions were rapidly set according to the Eh redox potential evolution. In other words, the objectives of the IC experiment to perform long term corrosion experiment could be achieved.

Over a period of about 7 years, the metal surfaces of the E24 and S235 electrodes were in a diffusive regime, at the host rock pressure and rapidly covered by protective layers as demonstrated by the low CR measured overtime. The protectiveness is ensured by “the barrier effect” that the corrosion layers enhance at the metal surface.

Despite mechanical removal of the corrosion layers, which followed the N₂ injection, the protectiveness of the metal surface seemed to be maintained thanks to the diffusive regime that was set under limited water circulation first (up to 4 years) and no water circulation (from 4 to 7 years).

The corrosion layers that formed at the metal surface were characteristic of those found in clay environments, which mainly contained magnetite and siderite. Nevertheless, the presence of oxidized species in significant amounts can be quite surprising. In addition they coexist with important amounts of Fe(II) (hydroxyl)carbonate phases indicating that the environmental conditions were mainly reducing, and consistent with corrosion rate measurements. The presence of species such as S(-II) seem to rule out simple post-experimental oxidation, and instead confirms that early oxidative events occurred, likely just after the installation of the equipment in the borehole. Late or post-oxidation can not explain the morphology of all of the observed phases.

Overall, the measured bacteria concentrations remained relatively low, likely due to the confined conditions, which limits the ability of the bacteria to grow, spatially. The available nutrients were probably consumed and were not renewed during the experiment because of the clogging, a situation which was not optimal for bacteria growth. Both, thermophilic and mesophilic bacteria were measured, in agreement with the temperature variations of the water circulated in the test chamber. The presence of Fe-sulfide at the metal/Opalinus clay interface could result from sulphate reducing bacteria (SRB) and thiosulphate reducing bacteria (ThRB) metabolism, which can reduce sulphate and thiosulphate into sulphide, (Remazeilles et al. 2010; Ropital 2010). The location of Fe-sulphide close to the trace of the original surface supports the fact that bacteria had initially nutrients and space to grow. In addition, the evolution of sulphate content in pore-water revealed a decrease between $t = 3$ weeks and $t = 3$ years, which was congruent with the thermophilic sulfurogen bacteria growth. However, the most sensible reason to explain the sulphate content decrease is the dilution effect from pore-water ingress.

4.2 IC-A experiment

The results of the corrosion rate measurements are in good agreement with the anaerobic corrosion rates of carbon steel in bentonite saturated with synthetic pore-waters measured by gas generation, (Smart et al. 2016). In that ex situ experiment, the average corrosion rate of 14 gas cells for a comparable exposure period was $1.9 \mu\text{m}/\text{year}$ and the results varied between 1 and $4.5 \mu\text{m}/\text{year}$. This indicates that the presence of natural Opalinus Clay pore-water containing native microbial populations does not have a considerable effect on the corrosion of steel in bentonite. Furthermore, should the observed trend of the ongoing decrease of the corrosion rate persist with time, lower corrosion rates may be expected in future sampling campaigns. For example, in work that is not dissimilar to this

study, gas cells measuring corrosion rates under anoxic conditions have undergone exposure durations of 5–10 years and reveal corrosion rates of carbon steel that are currently less than $0.5 \mu\text{m}/\text{year}$, (Smart et al. 2016). In the present experiment the corrosion rates of base metal and electron beam welds did not differ considerably. It is important to mention here that the corrosion rates measured in Module 1 containing bentonite pellets and powder at a density of $1.45 \text{ g}/\text{cm}^3$ were higher than those measured in the other two modules that contained bentonite blocks with nominal densities of 1.25 and $1.55 \text{ g}/\text{cm}^3$.

With regards to the microbial analyses of aerobic and anaerobic heterotrophic microorganisms, the sampling was carried out in such a way as to allow the evaluation of the impact of location of individual samples on cell counts. There was no clear systematic trend observed from the data, but it appeared that the exterior location typically harbored higher cell numbers than the interior location for plate counts. Furthermore, the variability in the cell numbers of aerobic and anaerobic microorganisms could be explained by the measured heterogeneity of the bentonite density in the modules. With regards to SRB, the fact that there was no clear effect of sampling location on the number of bacteria could be interpreted as SRB originating from the bentonite rather than the pore-water. The SRB numbers were generally higher than those obtained for the Febex experiment, (Stroes-Gascoyne et al. 2013).

The main finding shows that viable microorganisms are present in bentonite and, depending on the density of the clay in the module, a fraction of those microorganisms remain viable, which is in line with previous work by others, (Stroes-Gascoyne et al. 2010). However, as expected at higher densities, a smaller fraction can grow or even survive (i.e. remain viable for post experimental analysis), while at lower densities, a higher fraction survives.

5 Conclusions

The anaerobic corrosion of carbon steel has been studied in two in situ experiments at the Mont Terri rock laboratory.

The IC experiment confirmed the feasibility of monitoring in situ the CR of C-steel in contact with clay in a diffusive regime. The protective nature of the corrosion product layers and the importance of confinement in order to maintain a CR less than $1 \mu\text{m}/\text{year}$ have been shown. As expected from the literature, non-uniform general corrosion has been identified and the different corrosion layers as well as their chronological order of formation have been highlighted. Sulfurogen bacteria were identified and were likely responsible for the formation of Fe-sulphide at the C-steel surface. The low CR measured indicate that the

impact of SRB on the expected lifetime of C-steel disposal canisters is small in a confined diffusive regime.

On the other hand, the on-going IC-A experiment provided insight into the effect of compacted bentonite on the anaerobic corrosion of C-steel. The measured corrosion rates were in agreement with those measured *ex situ* highlighting the beneficial effect of compacted bentonite in reducing microbially induced corrosion. Furthermore, cell counts indicated that the viability of microbes in bentonite decreases as the dry density increases. The corrosion products after 20 months of exposure mainly consisted of a non-stoichiometric magnetite or mixed phase spinel.

Overall, the corrosion rates of C-steel in contact with clay or bentonite is expected to decrease with time due to the growth of a corrosion product layer under conditions expected in many repository concepts. From a safety assessment point of view, the presented studies have contributed to an increased understanding of corrosion mechanisms and the impact of microorganisms, which can increase the robustness of canister lifetime predictions.

Acknowledgements The authors are grateful to the Mont Terri Consortium for ensuring the success of the IC and IC-A experiments. We thank Paul Bossart, Christophe Nussbaum, Thierry Theurillat, David Jaeggi and Heinz Hauser for their assistance. We would like to thank the experimental partners (Andra, JAEA, Nagra, NWMO) for their financial support. We would also like to thank Solexperts for their significant contributions. S. Necib would like to thank the people who contributed to the IC experiment: Sarah Dewonck from Andra, who initiated the IC experiment; Christian Bataillon for his work on the EIS measurements; Michel Schlegel for his work on the surface characterisation; Sylvie Dumas and Marc Labat for their fruitful work on microbial investigations; Hydroisotop for their remarkable work on the analyses. N. Diomidis would like to thank the people who contributed to the IC-A experiment: Nick Smart, Andy Rance and Bharti Reddy from the Amec Foster Wheeler corrosion team who performed all the analytical work and assembly of the modules; Rizlan Bernier-Latmani, Manon Fruttschi and Alexandre Bagnoud from the Environmental Microbiology Laboratory of the EPFL for their work on microbial investigations. Finally, the authors would like to thank Dr. Fraser King (Integrity Corrosion Consulting Ltd. Nanaimo, BC, Canada) and Dr. Bruno Kursten (Belgian Nuclear Research Centre, Mol, Belgium) for their review and fruitful advice on this work.

Open Access This article is distributed under the terms of the Creative Commons Attribution 4.0 International License (<http://creativecommons.org/licenses/by/4.0/>), which permits unrestricted use, distribution, and reproduction in any medium, provided you give appropriate credit to the original author(s) and the source, provide a link to the Creative Commons license, and indicate if changes were made.

References

- Andra. (2005). Dossier 2005 Argile, *Chapitre 4 "Le stockage—Les installations"*. pp. 121–136.
- ASTM Committee G-1 on Corrosion of Metals. (2011). *Standard practice for preparing, cleaning, and evaluating corrosion test specimens*. ASTM International.
- Atlas, R. M. (1993). *Handbook of microbiological media*. Boca Raton: CRC Press.
- Bossart, P., Bernier, F., Birkholzer, J., Bruggeman, C., Connolly, P., Dewonck, S., Fukaya, M., Herfort, M., Jensen, M., Matray, J.-M., Mayor, J. C., Moeri, A., Oyama, T., Schuster, K., Shigeta, N., Vietor, T., & Wieczorek, K. (2017). Mont Terri rock laboratory, 20 years of research: introduction, site characteristics and overview of experiments. *Swiss Journal of Geosciences*, 110. doi:10.1007/s00015-016-0236-1 (this issue).
- Chen, Y., & Jepson, W. P. (1999). EIS measurement for corrosion monitoring under multiphase flow conditions. *Electrochimica Acta*, 44(24), 4453–4464.
- Chivot, J. (2004). *Thermodynamique des produits de corrosion: Fonctions thermodynamiques, diagrammes de solubilité, diagrammes E-pH des systèmes Fe-H₂O, Fe-CO₂-H₂O, Fe-S-H₂O, Cr-H₂O et Ni-H₂O en fonction de la température*. Chatenay-Malabry: Andra.
- Dumas, S., Magot, M., & Crolet, J. L. (1993). Measurement of the net production of acidity by a sulphate reducing bacterium: experimental checking of theoretical models of microbially influenced corrosion. *Research in Microbiology*, 144(4), 237–332.
- Féron, D., Crusset, D., & Gras, J. M. (2008). Corrosion issue in nuclear waste disposal. *Journal of Nuclear Materials*, 379(1), 16–23.
- Jonscher, A. K. (1991). Low-frequency dispersion in volume and interfacial situations. *Journal of Materials Science*, 26(6), 1618–1626.
- Nussbaum, C., Kloppenburg, A., Caër, T., & Bossart, P. (2017). Tectonic evolution around the Mont Terri rock laboratory, northwestern Swiss Jura: constraints from kinematic forward modelling. *Swiss Journal of Geosciences*, 110. doi:10.1007/s00015-016-0248-x (this issue).
- Patel, R., Punshon, C., Nicholas, J., Bastid, P., Zhou, R., Schneider, C., Bagshaw, N., Howse, D., Hutchinson, E., Asano, R., & King, F. (2012). Canister Design Concepts for Disposal of Spent Fuel and High Level Waste. *Nagra Technical Report*, NTB 12-06. Nagra, Wettingen, Switzerland. www.nagra.ch.
- Pearson, F. J. (2002). PC experiment: Recipe of Artificial pore water. *Mont Terri Technical Note*, TN 2002-17. Switzerland Federal Office of Topography (swisstopo), Wabern, Switzerland. www.mont-terri.ch.
- Pearson, F. J., Acros, D., Bath, A., Boisson, J. Y., Fernandez, A. M., Gabler, H. E., & Gaucher, E. (2003). Geochemistry of water in the Opalinus Clay formation at the Mont Terri Rock Laboratory. *Reports of the Federal Office for Water and Geology (FOWG)*, Geology Series No 5. Switzerland Federal Office of Topography (swisstopo), Wabern, Switzerland. www.mont-terri.ch.
- Reasoner, D. J., & Geldreich, E. E. (1985). A new medium for the enumeration and subculture of bacteria from potable water. *Applied and Environmental Microbiology*, 49(1), 1–7.
- Remazeilles, C., Saheb, M., Neff, D., Guilminot, E., Tran, K., Bourdoiseau, J.-A., et al. (2010). Microbiologically influenced corrosion of archaeological artefacts: characterization of iron (II) sulfides by Raman spectroscopy. *Journal of Raman Spectroscopy*, 41(11), 1425–1433.
- Roberge, P. R., & Sastri, V. S. (1994). On-line corrosion monitoring with electrochemical impedance spectroscopy. *Corrosion Science*, 50(10), 744–754.
- Ropital, F. (2010). *Corrosion et dégradation des matériaux métalliques: compréhension des phénomènes et applications dans l'industrie pétrolière et des procédés*. Paris: Editions TECHNIP.
- Saheb, M., Neff, D., Dillmann, P., Descostes, M., & Matthiesen, H. (2013). Long-term anoxic corrosion of iron. In P. Dillmann, D. Watkinson, E. Angelini, & A. Adriaens (Eds.), *Corrosion and*

- conservation of cultural heritage metallic artefacts* (pp. 260–284). Woodhead Publishing.
- Smart, N. R., Rance, A. P., Reddy, B., & Diomidis, N. (2016). Anoxic corrosion of carbon steel in bentonite in relation to the swiss deep geological repository concept. In *CORROSION 2016*. NACE International, Houston, Texas, United States.
- Stern, M., & Geary, A. L. (1957). Electrochemical polarization. a theoretical analysis of the shape of polarization curves. *Journal of the Electrochemical Society*, *104*(1), 56–63.
- Stroes-Gascoyne, S., Frutsch, M., Hamon, C., Bagnoud, A., Leupin, O., & Bernier-Latmani, R. (2013). MA experiment: Role of moisture, bentonite density and water activity on the development of microorganisms in the bentonite after its dismantling from the EB experiment. *Mont Terri Technical Report*, TR 13-56. Switzerland Federal Office of Topography (swisstopo), Wabern, Switzerland. www.mont-terri.ch.
- Stroes-Gascoyne, S., Hamon, C. J., Maak, P., & Russell, S. (2010). The effects of the physical properties of highly compacted smectitic clay (bentonite) on the culturability of indigenous microorganisms. *Applied Clay Science*, *47*(1), 155–162.
- Vinsot, A., Leveau, F., Bouchet, A., & Arnould, A. (2014). Oxidation front and oxygen transfer in the fractured zone surrounding the Meuse/Haute-Marne URL drifts in the Callovian-Oxfordian argillaceous rock. *Geological Society, London, Special Publications*, *400*(1), 207–220.

Fifteen years of microbiological investigation in Opalinus Clay at the Mont Terri rock laboratory (Switzerland)

Olivier X. Leupin¹ · Rizlan Bernier-Latmani² · Alexandre Bagnoud² · Hugo Moors³ · Natalie Leys³ · Katinka Wouters³ · Simcha Stroes-Gascoyne⁴

Received: 21 April 2016 / Accepted: 17 December 2016 / Published online: 24 February 2017
© The Author(s) 2017. This article is published with open access at Springerlink.com

Abstract Microbiological studies related to the geological disposal of radioactive waste have been conducted at the Mont Terri rock laboratory in Opalinus Clay, a potential host rock for a deep geologic repository, since 2002. The metabolic potential of microorganisms and their response to excavation-induced effects have been investigated in undisturbed and disturbed claystone cores and in pore- (borehole) water. Results from nearly 15 years of research at the Mont Terri rock laboratory have shown that microorganisms can potentially affect the environment of a repository by influencing redox conditions, metal corrosion and gas production and consumption under favourable conditions. However, the activity of microorganisms in undisturbed Opalinus Clay is limited by the very low porosity, the low water activity, and the largely recalcitrant nature of organic matter in the claystone formation. The presence of microorganisms in numerous experiments at the Mont Terri rock laboratory has suggested that excavation activities and perturbation of the host rock combined with additional contamination during the installation of

experiments in boreholes create favourable conditions for microbial activity by providing increased space, water and substrates. Thus effects resulting from microbial activity might be expected in the proximity of a geological repository i.e., in the excavation damaged zone, the engineered barriers, and first containments (the containers).

Keywords Deep geologic repository for radioactive waste · Subsurface microbiology · Sulphate reduction · Water activity · Hydrogen and nitrate amendments

1 Introduction

The concept of deep geological disposal of high level nuclear waste (HLW) is common to most national nuclear energy programs. The radioactive waste will be encapsulated in corrosion-resistant metal containers (e.g., steel, copper, titanium) and buried several hundred meters below ground in a deep geologic repository (DGR), excavated in a stable geological rock formation. Clays are a crucially important part of many DGR designs. On the one hand, clay deposits are being considered as a potential host rock for DGRs in several countries because of the advantageous physical and hydrogeochemical properties of such deposits. On the other hand, bentonite-based barriers and seals are essential components of many DGR designs for a variety of host rocks where they would fulfil multiple specific roles, such as hydraulic, mechanical, thermal, and chemical protection of the containers and ensuring a diffusion-controlled hydrologic environment (e.g., Stroes-Gascoyne et al. 1997; Stroes-Gascoyne and West 1997).

To date, in Europe, four claystone formations have been studied in detail to assess their potential suitability as a host rock for long-lived HLW disposal in a DGR. These are

Editorial handling: P. Bossart and A. G. Milnes.

This is paper #17 of the Mont Terri Special Issue of the Swiss Journal of Geosciences (see Bossart et al. 2017, Table 3 and Fig. 7)

✉ Olivier X. Leupin
olivier.leupin@nagra.ch

¹ National Cooperative for the Disposal of Radioactive Waste NAGRA, Hardstrasse 73, 5430 Wettingen, Switzerland

² École Polytechnique Fédérale de Lausanne EPFL, Route Cantonale, 1015 Lausanne, Switzerland

³ Belgian Nuclear Research Centre SCK-CEN, Boeretang 200, 2400 Mol, Belgium

⁴ University of Saskatchewan, Saskatoon, Canada

Opalinus Clay in Switzerland, Boom- and Ypresian Clay in Belgium and the Callovo-Oxfordian formation and Toarcian argillite, both in France. To investigate engineering-, science-, and safety-relevant issues associated with HLW deep subsurface disposal, underground research laboratories and facilities (URLs and URFs) were established for each of these four clay types (reviewed by Birkholzer et al. 2012). In recent years, a fifth European clay type, Boda Claystone, in Hungary, is being studied for its potential as a host rock for HLW disposal (Lazar and Mathé 2012). Non-clay stable geological formations such as granite, tuff, shale, limestone and salt have also been considered as host rocks for HLW repositories (Delay et al. 2014). In total, 26 URLs/URFs were built worldwide (Blechs Schmidt and Vomvoris 2012).

Opalinus Clay is the candidate host rock for the safe disposal of radioactive waste in Switzerland. It has been studied mainly at the international Mont Terri Underground Research Laboratory (URL) in Switzerland over the past two decades. As for other host rocks, the integrity of the waste and its containment is critical for the safety of its geological disposal in Opalinus Clay. Thus, in addition to chemical and physical disturbances in the repository, it is important to also consider the possible impact of microorganisms on repository engineered barrier integrity.

This paper reviews the current state of knowledge gleaned from microbiological studies at the Mont Terri rock laboratory, which include explorations of the presence and activity of microorganisms in undisturbed and disturbed claystone, both in solid clay cores and in clay pore- (borehole) water. These types of investigations, characterizing the occurrence of microorganisms in Opalinus Clay, their metabolic potential, and their response to repository-induced effects, were started at the Mont Terri rock laboratory shortly after its inception 20 years ago.

Particularly, the potential for microbial activity in the immediate vicinity of waste containers in a HLW repository is of interest for the containers' long-term integrity (e.g., Stroes-Gascoyne et al. 2007). Microbiological activity in the near-field (which includes the Engineered Barrier System (EBS) and those parts of the host rock in contact with, or near, the EBS whose properties have been affected by the presence of the repository) may result in:

- Microbially-influenced corrosion (MIC), which could reduce the longevity of the waste containers. MIC would occur through the formation of corrosion-inducing aggressive environments under biofilms or through the production of corrosive metabolites. For the latter, sulphate-reducing bacteria (SRB), that produce sulphide, are of specific concern.
- Microbial gas production (mainly CO₂ and CH₄) may contribute to the build-up of a gas phase in a repository,

potentially reducing the effectiveness of the bentonite-based barriers and/or natural barriers.

- Microbial activity may lead to dissolution of minerals in the clay, or leaching of specific elements from those minerals, with possible deleterious effects on the integrity and the effectiveness of this barrier.
- Microbes may adsorb radionuclides released from breached containers and either immobilize these in biofilms; or (motile) microbes may act as colloids to enhance radionuclide migration through unsealed (or incompletely sealed) fractures in the near-field.
- Microbial activity could reduce the gas pressure build-up resulting from anoxic corrosion of the waste containers by oxidizing H₂ gas anaerobically, or possibly by the formation of CH₄ from H₂ and CO₂ which would reduce the volume of gas up to four-fold.

There are several ways for microorganisms to become part of a DGR environment. By far, the most likely way is (unavoidable) external contamination, i.e., introduction of microorganisms as a result of anthropogenic activities related to DGR construction. In addition, physico-chemical changes may occur during construction and operation that could stimulate any microorganisms that managed to survive in niches of the geological host rock or engineered barriers.

An extensive study was carried out to investigate the occurrence of indigenous microbes and their community size and structure in an Opalinus Clay core (Mauclair et al. 2007; Stroes-Gascoyne et al. 2007; Poulain et al. 2008). This core was drilled while applying stringent aseptic techniques to avoid or at least severely minimize external contamination. The aseptic measures employed included (a) steam- and ethanol-cleaned drilling equipment; (b) handling of all equipment with ethanol-treated gloves; and (c) cooling with filtered air and nitrogen (instead of drill water) during drilling. Additionally, latex microspheres (in the size range of microbes) were placed near the drill bit to assess the extent of their intrusion into the core, mimicking possible intrusion of microbes (from the air or nitrogen gas used for cooling) into the core. The results from this study provided limited evidence that a small, viable but most likely largely dormant, microbial community may be present in Opalinus Clay, which was corroborated by a second, more limited set of analyses (Stroes-Gascoyne et al. 2008), on large diameter Opalinus Clay cores, drilled using air-cooling.

Although the earlier microbial characterization of Opalinus Clay (Stroes-Gascoyne et al. 2007, 2008) suggested that unperturbed Opalinus Clay appeared to contain only a small viable microbial community (that is probably metabolically inactive (i.e., dormant cells and spores), due to water, space and nutrient restrictions), it has not been resolved how old such surviving microorganisms might be. The Opalinus Clay

formation was deposited 174 Ma ago, but survival of microbes (in spore or dormant form) beyond 0.6–3 Ma in ancient geological formations has been disputed (e.g., Susina et al. 2004; Johnson et al. 2007; Takeuchi et al. 2009). Another possible source of indigenous microbes, therefore, could be a much more recent (<3 Ma) intrusion of water along fractures in the Opalinus Clay formation, although studies by Mazurek et al. (2007, 2009) have suggested that diffusion alone can explain the hydrogeological features of the Opalinus Clay formation, without having to invoke advective flow. Intrusion of microbes along existing but sealed (i.e., through mineral precipitation) fractures could be another possibility as such mineral-filled fractures could have a slightly higher porosity than the intact clay matrix. Stroes-Gascoyne et al. (2008) discuss these possibilities in more detail.

This review summarizes results from studies that addressed the question of microbial presence and activity in the Opalinus Clay host rock, in borehole water, and in experiments mimicking repository-relevant conditions. First, factors affecting microbial activity in Opalinus Clay in general will be considered followed by microbial detection and activity findings in what is considered as undisturbed Opalinus Clay core and un-amended borehole water. Finally experiments will be reviewed in which borehole water was amended with compounds able to stimulate microbial activity that, depending on the type of radioactive waste, may be unavoidable in a DGR (e.g., organics, H₂, nitrate).

2 General factors restricting microbial activity in Opalinus Clay

Even if bacteria that would have been trapped during the sedimentation of Opalinus Clay 174 Ma ago had survived, there would be several more reasons why Opalinus Clay is not a favourable environment for microorganisms to thrive.

First, the *low porosity* of this rock formation is likely to seriously restrict microbial replication and mobility. It has been suggested (Chapelle 1993) that in aquifers, the most consistent predictor of microbial abundance is sediment texture. The diversity of bacteria seems to correlate with sediment type, with the greatest diversity being found in the sandiest sediments. There are probably many mechanisms that contribute to this effect, but the most important factor is the small size of pore throats in clays relative to sands (Chapelle 1993). The average pore throat diameter in clays, as measured by mercury injection porosimetry (MIP), is less than 0.05 µm. A recent study performed by Hemes et al. (2015) determined, with a combination of X-ray, micro Computer Tomography (µ-CT), two dimensional broad ion beam- and focused ion beam scanning electron microscopy (BIB- and FIB-SEM), that the average

size of pore throats in Boom Clay is smaller than 0.01 µm. Senger et al. (2013) reported that most pores in Opalinus Clay are in the meso-pore range (0.001–0.025 µm). In sand, on the other hand, average pore throat diameters are much greater, in the 2–20 µm range (Chapelle 1993). Because bacteria in general have diameters ranging from 0.1 to several µm, the small pore throats in clay will make it physically impossible for bacteria to move freely. Similarly, MIP analysis of sediments has shown that 90–95% of the porosity in sands is interconnected, whereas this percentage is much lower in clays. Again, this low pore interconnectivity will additionally restrict the transport of substrates by diffusion to, and the removal of waste products from metabolically active cells. Additionally, the pore size distribution likely also impacts the ability of organisms to proliferate.

Second, the *very low amount of available water* in Opalinus Clay is another major impediment to microbial life. The free water available to microbes is reduced by interactions with solute molecules (the osmotic effect) and by adsorption to the surface of solids (the matrix effect) (Brown 1990). Microbiologists generally use the term water activity (a_w) to express quantitatively the degree of water availability. The water activity of a solution (or a material containing water) is 0.01 times the relative humidity (in %) of air in equilibrium with that solution (or material). This corresponds to the ratio of the solution's (or material's) vapour pressure (P_{sol}) to that of pure water (P_{water}) at a fixed temperature:

$$a_w = P_{sol}/P_{water}$$

Low a_w values are well-known deterrents for bacterial growth in the food industry (e.g., drying, high sugar, or salt concentrations) and the relationship between a_w and microbial growth limits is well established (Brown 1990). Most Gram-negative bacteria are not able to grow below a_w values of 0.96, and most Gram-positive bacteria are not able to grow below a_w values of 0.90. Select, specialized osmotolerant and halophilic organisms can grow at lower a_w . With the exception of bacterial endospores, most prokaryotes cannot survive at $a_w < 0.6$, but a few can survive at extremely low a_w (a_w as low as 0.30) (Lin et al. 2007).

Water activity in clays is determined by the salt content of the pore-water but also by the suction potential, especially in expanding (smectite) clays such as bentonites, which are often part of the EBS in DGR designs. Opalinus Clay contains 40–80% clay minerals, is a mixture of kaolinite, chlorite, illite and illite/smectite mixed layer phases, and is expected to have significant swelling capacity (swelling pressure perpendicular to stratification is 0.8–1.4 MPa) and suction potential (Ferrari et al. 2014). The latter causes the clay to take up water until it is saturated, at which point the suction potential is zero. The

water activity measured in an Opalinus Clay core sample with a water content of 8.6% was 0.962 (Stroes-Gascoyne et al. 2011) and for Opalinus Clay samples with water contents of 7.93 and 7.90%, a_w values were 0.946 and 0.931, respectively (Stroes-Gascoyne et al. 2008).

Third, the apparent lack of easily accessible and easily degradable energy sources in Opalinus Clay may further restrict microbial activity. Opalinus Clay contains organic matter ($\sim 1.5\%$ w/w (Courdouan et al. 2007 and Courdouan-Metz 2008)) and this carbon could serve potentially as a carbon source and/or electron donor to microorganisms. However, the fact that this organic carbon is present in the rock may indicate that microbes either: (a) are not present in undisturbed Opalinus Clay, (b) are present but not active due to lack of space and available water, or (c) are present but not active due to the inaccessible and/or recalcitrant nature of the organic matter available.

Courdouan et al. (2007) and Courdouan-Metz (2008) concluded that most of the total organic matter in Opalinus Clay is very strongly attached to the mineral phases. They also concluded that synthetic or artificial pore-water (APW) represented the most suitable extractant and yielded extracts most similar to borehole water with respect to low molecular weight organic acids content as well as the size distribution of the hydrophilic dissolved organic matter (DOM). They further found that strictly anoxic conditions during rock sampling, sample storage and analysis (after anoxic extraction) were required to properly evaluate the nature and reactivity of DOM in Opalinus Clay under as close to in situ conditions as possible. Only a very small fraction (about 0.5%) of the total organic carbon (TOC) could be extracted into APW under anoxic conditions and about two-thirds of the dissolved organic carbon (DOC) exhibited hydrophilic properties with a molecular size of less than 500 Da. About half of the extracted hydrophilic DOC consisted of low molecular weight organic acids such as acetate, propionate, lactate and formate; the other half consisted of higher molecular weight organic matter, while the rest consisted of unknown hydrophobic matter. It is expected that most of the hydrophilic organic matter in Opalinus Clay can be respired or fermented under suitable conditions for microbial activity, i.e., in borehole water where low porosity and low water activity would not be limiting. Whether the extracted hydrophobic matter and the large fraction ($>99\%$) of non-extractable TOC can be respired or fermented is not clear.

3 Microbes in solid Opalinus Clay cores

Mauclaire et al. (2007) reported that phospholipid fatty acid (PLFA) extracts from Opalinus Clay core samples yielded on average 64 ng of PLFA per g of dry claystone

which, using a standard conversion factor, would translate to the presence of 5×10^6 microbial cells per gram of clay. The PLFA profiles obtained clearly revealed lipid biomarkers specific for anaerobic Gram-negative bacteria and SRB, with lipid profiles indicative of *Desulfobulbus* and *Desulfovibrio*.

Stroes-Gascoyne et al. (2007) also studied the occurrence of indigenous microbes, and their population size, community structure and metabolic activity, in Opalinus Clay core from the Mont Terri rock laboratory. A clay core was recovered from a 15 m long borehole drilled aseptically (as discussed in the introduction) in the exploration gallery of the Mont Terri rock laboratory in early 2004 (known as the PP niche borehole, or BPP-1). Subsamples of this clay core were sent to various microbial laboratories in Europe where the samples were probed for microbial presence using various types of microscopy, molecular biology techniques (PLFA, q-PCR, PCR-DGGE), and cultivation (MPN and enrichment culturing). However, no microbial cells could be identified using acridine orange direct counting (AODC), or fluorescence in situ hybridization (FISH). All attempts to extract PCR-amplifiable DNA from the clay samples failed, and the vast majority of lipids detected by PLFA analysis was indicative of cell debris, rather than viable cells. Cultivation attempts were slightly more successful with a single positive enrichment result for SRB and a few other successful enrichment cultures for aerobic and anaerobic heterotrophs. Stroes-Gascoyne et al. (2007) concluded from these results that the unperturbed Opalinus Clay environment thus may harbour – if at all – a very limited viable microbial population. Renewed efforts to directly extract DNA from the aforementioned samples remained unsuccessful (Poulain et al. 2008). Nonetheless, the limited number of successful enrichment cultures resulted in the isolation and characterization of seven strains, two of which could be identified at genus level, i.e., belonging to *Sphingomonas* and *Allicyclobacillus* (Poulain et al. 2008). No further analysis of these strains was performed.

More recently, further attempts to characterize the microbial community in undisturbed Opalinus Clay were made. In particular, a multi-investigator, international round-robin study, in which samples from a single core drilled 50 m into the rock formation were distributed to four laboratories, was intended to conclusively settle the question of whether viable indigenous microorganisms could be found in Opalinus Clay (Bagnoud et al. 2015b). The study showed that, in some cases, DNA extraction was successful and pointed to a diverse community including *Sphingomonas*, Procabacteriaceae, *Bdellovibrio*, *Ralstonia*, *Methylophilaceae*, and *Rhizobiales*. However, there was only limited overlap between the results of the four laboratories despite using the same protocols, suggesting the

possibility of extensive heterogeneity in biomass distribution and/or contamination in the samples. Finally, the microbial community uncovered from a core ((Stroes-Gascoyne et al. 2007, 2008) from the HT borehole at the Mont Terri rock laboratory revealed the presence of Firmicutes (Moll et al. 2013). More studies are needed to provide irrefutable proof and representative composition of indigenous microorganisms in the undisturbed rock.

4 Microbes in water from un-amended boreholes in Opalinus Clay

Because of the very tight nature and low content of water in the Opalinus Clay formation, it would take a long time (months or even years) for a borehole to naturally fill with rock formation- (i.e., pore-) water. Therefore, in most but not all experiments at the Mont Terri rock laboratory, boreholes were filled with artificial pore-water (APW). This section reviews experiments in boreholes that were filled naturally with Opalinus Clay formation water or that were filled with APW, to which subsequently no other microbial substrates were added (other than any contamination introduced into the borehole during the drilling process, or organics leaching from the clay formation into the borehole water).

An experiment (IC-A) carried out at the Mont Terri rock laboratory, originally intended to investigate the corrosion of iron under repository-relevant conditions, inadvertently revealed that providing space is a sufficient condition for bacterial activity in Opalinus Clay. The space created (i.e., the borehole) filled up with Opalinus Clay formation water, creating a propitious environment for microbial activity. The experiment involved a borehole drilled under anoxic but non-sterile conditions that was closed for 10 months prior to the deployment of the module for the corrosion experiment. A borehole water sample was obtained after that time and the sulphide concentration found to be 7.4 μM , while there was no detectable sulphide upon drilling. This finding suggested the presence of active microorganisms in the borehole water that can reduce sulphate. Subsequently, the microbial community was characterized through metagenomic sequencing and genome-binning. The results revealed a remarkably simple heterotrophic microbial community, mainly composed of two organisms: (1) a *Pseudomonas* sp., hypothesized to ferment organic macromolecules (either leached from the clay or contributed as contamination during the drilling process) while releasing organic acids and H_2 ; and (2) a sulphate-reducing member of the *Peptococcaceae*, hypothesized to oxidize the organic acids to carbon dioxide while reducing sulphate (Bagnoud et al. 2015a).

Additionally, a survey of the microbial communities in 23 water samples from 8 boreholes across the Mont Terri

rock laboratory was conducted which identified 13 organisms that were present in all boreholes (Bagnoud et al. 2016a). Table 1 shows the contribution of each of the 13 microorganisms ubiquitous in Mont Terri rock laboratory borehole waters to the microbial communities in four anoxic boreholes (BIC-A1, BPC-2, BDR-T1/1 and BDR-T1/2). For instance, ubiquitous microbes represented more than 92% of the microbial community in BIC-A1, the borehole in which the IC-A experiment was conducted.

5 Microbes in water from amended boreholes in Opalinus Clay

This section considers studies in boreholes filled with APW to which amendments were made, either deliberately or inadvertently, affecting microbial activity. Amendments included an organic compound, hydrogen gas or nitrate.

5.1 Organic compound: Glycerol

Early (2003–2006) microbial investigations of Opalinus Clay borehole water from the in situ Porewater Chemistry (PC) experiment using DAPI (4',6-diamidino-2-phenylindole) staining, revealed total cell counts that varied from 6×10^3 to 2×10^6 cells/mL (Battaglia and Gaucher 2003; Ishii 2004; Mauclaire and McKenzie 2006a, b; Mauclaire et al. 2006). Subsequent cultivation and molecular studies of clay and water samples from the PC experiment indicated a diverse and active microbial community in PC borehole water and adjacent clay (accessible in the over-core of the PC experiment) (Stroes-Gascoyne et al. 2011). Sulphate reduction in this experiment was evident with a distinct smell, blackening and visually observable pyrite (and mackinawite) precipitation in sample lines as confirmed by X-Ray Diffraction analysis (Stroes-Gascoyne et al. 2008). Cell counts and quantitative cultivation results were as high as 7×10^8 cells mL^{-1} in these samples. Most probable number (MPN) and agar plate cultivation allowed the enumeration of various physiological groups of microorganisms, including aerobic and anaerobic heterotrophs, sulphate-reducing bacteria, nitrate-utilizing and nitrate-reducing bacteria, iron-reducing bacteria, anaerobic lithotrophs, and methanogens. DNA extractions from PC water, agar plate pure cultures, and enrichment cultures were subjected to quantitative real-time PCR using universal primers for the bacterial and archaeal 16S rRNA genes. The amplicons were separated by DGGE, isolated from the electrophoresis matrix, re-amplified, and sequenced. In addition, SRB were quantified by targeting the dissimilatory sulphite reductase (*dsrA*) gene, while methanogenic *Archaea* were quantified by targeting the methyl coenzyme M reductase gene (*mcrA*). Using a 97%

Table 1 Contribution of ubiquitous Operational Taxonomic Units (OTUs) to the microbial communities from borehole water collected from four anoxic boreholes in the Opalinus Clay at the Mont Terri rock laboratory. Taxonomic affiliation and expected metabolism type

OTU #	Proportion in samples				Taxonomic affiliation	Metabolism type	Reference
	BIC-A1/1	BPC-2/1	BDR-T1/1	BDR-T1/2			
0	1.25E-04	0.5124	1.48E-04	1.08E-04	<i>Desulfocapsa</i>	Sulfate-reducing bacteria	Kuever <i>et al.</i> , 2005
1	1.10E-04	7.05E-05	8.12E-05	7.19E-05	<i>Novispirillum</i>	O ₂ and NO ₃ ⁻ respiring bacteria	Yoon <i>et al.</i> , 2007
2	0.2594	0.0056	0.0007	0.0006	<i>Pseudomonas</i>	O ₂ and NO ₃ ⁻ respiring bacteria	Moore <i>et al.</i> , 2006
3	7.05E-05	1.06E-04	4.43E-05	5.03E-05	Rhodobacteraceae	Metabolically diverse	Garrity <i>et al.</i> , 2005
4	1.57E-05	5.28E-05	7.38E-06	4.31E-05	Xanthomonadaceae	O ₂ respiring bacteria	Saddler and Bradbury, 2005
5	1.57E-05	5.28E-05	0.5684	0.5258	<i>Pleomorphomonas</i>	O ₂ respiring or fermenting bacteria	Xie and Yokota, 2005
6	0.0416	0.0095	0.2667	0.2824	<i>Desulfosporosinus</i>	Sulfate-reducing bacteria	Spring and Rosenzweig, 2006
7	0.0165	1.76E-05	1.48E-05	0.00E+00	<i>Desulfotomaculum</i>	Sulfate-reducing bacteria	Auello <i>et al.</i> , 2013
9	0.5717	0.0184	0.0083	0.0079	<i>Desulfotomaculum</i>	Sulfate-reducing bacteria	Auello <i>et al.</i> , 2013
13	7.84E-06	1.76E-05	7.38E-06	2.87E-05	<i>Methyloversatilis</i>	Metabolically diverse	Kalyuzhnaya <i>et al.</i> , 2006
15	3.92E-05	0.0033	8.86E-05	2.87E-05	<i>Pseudomonas</i>	O ₂ and NO ₃ ⁻ respiring bacteria	Moore <i>et al.</i> , 2006
17	7.84E-06	0.0018	1.48E-05	7.19E-06	<i>Thiobacillus</i>	O ₂ and NO ₃ ⁻ respiring bacteria	Kelly <i>et al.</i> , 2005
36	0.0317	0.1268	0.00E+00	4.66E-04	<i>Desulfosporosinus</i>	Sulfate-reducing bacteria	Spring and Rosenzweig, 2006
SUM	0.9213	0.6781	0.8446	0.8175			



are indicated. Total contribution of the 13 ubiquitous OTU's to each borehole community is indicated for each sample (last row). Colours indicate the fraction of the OTU's in each borehole (green 0.5–1.0; yellow 0.01–0.5; red 0–0.01) (Modified from Bagnoud (2015))

cut-off level of 16S rRNA sequence identity against database references, PC borehole water included *Pseudomonas stutzeri*, *Bacillus licheniformis*, *Desulfosporosinus* sp., and *Hyphomonas*, while overcore samples included *Pseudomonas stutzeri*, three species of *Trichococcus*, *Nostocoida limicola*, *Caldanaerocella colombiensis*, *Geosporobacter subterrenus*, *Kocuria palustris*, and *Desulfosporosinus* sp.

Although the origin of the observed microorganisms in the PC experiment is unknown, it is likely that at least a fraction was introduced for instance through the use of non-sterilized APW during the course of the experiment, despite strict precautions taken during the actual drilling of the PC borehole to avoid microbial contamination (as discussed by Stroes-Gascoyne *et al.* 2007). The PC-experiment also differed from other experiments by the virtual absence of metal construction parts (to avoid the influence of metals on redox conditions in the borehole) and the use instead of many different kinds of plastic and polymer materials. After a careful study of the possible leaching of organic carbon into the PC water from these materials, De Cannière *et al.* (2011) concluded from their analysis results, as well as from geochemical modelling calculations, that the most likely primary organic C source fueling the microbial activity in the PC experiment was glycerol released from the polymeric gel filling in the reference electrodes used. De Cannière *et al.* (2011) further concluded that other sources, such as acetone used to clean some equipment, may also have contributed to microbial processes, but only to a minor extent.

Similarly, the microbial activity observed during an in situ diffusion experiment at the Mont Terri rock

laboratory that was not designed to stimulate the microbial community (the DR experiment; Leupin *et al.* 2012), prompted an investigation into the source of carbon supporting the microbial biomass. One of the possible carbon sources suspected in this experiment was again glycerol leaking from an online pH-probe. The experiment was designed to study the diffusion of tracers into the Opalinus Clay formation and the probe was used to monitor the pH of the circulating borehole water in the experiment (Leupin *et al.* 2012). Laboratory incubations with borehole water from the DR experiment and glycerol amendments were performed to investigate the hypothesis that glycerol was fuelling the microbial community (Fruttschi and Bernier-Latmani 2010a, b). Clear stimulation of microbial activity was observed in the presence of glycerol. Sulphate concentrations were not analysed, but a sulphide smell was associated with the cultures, suggesting that glycerol was an electron donor in sulphate reduction (Fruttschi and Bernier-Latmani (2010a, b)). The compound served either as an electron donor for respiration or as a fermentative substrate.

A detailed microscopic analysis of the laboratory enrichment cultures with glycerol evidenced that the microbes stimulated by glycerol included endospore formers (Fruttschi and Bernier-Latmani 2010a, b). Cells were efficiently stained with DAPI, suggesting the presence of cytoplasmic DNA. The 16S rRNA gene clone library that was obtained from the laboratory enrichment cultures with glycerol was remarkable in its lack of diversity. Essentially, all the clones sequenced from the clone library were representatives of the genus *Desulfosporosinus*, a Gram positive bacterium known to form

endospores. The *Desulfosporosinus* species from this experiment corresponds to OTU 6 (Operational Taxonomic Unit 6) in Table 1 (Bagnoud 2015). The type strains of the species *Desulfosporosinus lacus*, one of the best matches from the clone library, has indeed been reported to use glycerol as a carbon source and electron donor in the presence of sulphate (Ramamoorthy et al. (2006)). However, it can also grow autotrophically with H₂ and CO₂, which is of relevance for DGR safety considering that H₂ and CO₂ gases will be produced in a DGR by anaerobic corrosion of steel and degradation of organics, respectively. Thus, *Desulfosporosinus* species were predominant in the microbial community from the DR experiment borehole water, further stimulated by the addition of glycerol in the laboratory. Therefore, it was concluded that *Desulfosporosinus* species were most likely the main SRB able to utilize glycerol as an electron donor for sulphate reduction in the DR experiment. In fact, *Desulfosporosinus* strains (corresponding to OTU 6 in Table 1) were also identified in the PC experiment discussed above and repeatedly identified in various borehole water samples of the Bitumen-Nitrate (BN) experiment.

5.2 Hydrogen

An experiment (MA) was devised to investigate the impact of H₂ on the microbial community in Opalinus Clay (see Fig. 1). In particular, the salient question was whether the microbial community would be complex enough to allow carbon biogeochemical cycling. MA entailed the repeated (approximately weekly) injection of H₂(g) into the BRC-3 borehole filled with sterile APW at the Mont Terri rock laboratory over a period of 500 days (Bagnoud 2015; Bagnoud et al. 2016a, b). While the borehole was initially aerobic, dissolved oxygen (DO) quickly decreased after initiation of the H₂ injection and, after approximately a month, DO had fallen below the detection limit. Subsequently, the concentration of ferrous iron [Fe(II)] increased, followed by a rapid decrease and the establishment of steady sulphate-reducing conditions starting approximately at day 50. Several approaches were used for the detailed study of the microbial community. First, amplification of the 16S rRNA gene followed by sequencing of 60 samples taken over 500 days yielded a detailed view of the evolution of the microbial community as a function of time and chemical conditions (Bagnoud et al. 2016a). During the oxygen-reducing phase, more than 50% of the microbial community was represented by Gamma-proteobacteria pertaining to the genus *Pseudomonas* and the family Xanthomonadaceae, while the rest were mostly Alpha-proteobacteria such as species from the genus *Novispirillum* and the family Rhodobacteraceae. The latter two persisted throughout the 500 days of the

experiment. While these organisms clearly were instrumental in consuming oxygen by reduction with H₂, they are unlikely to be relevant for repository conditions as anoxic conditions are expected to be established rapidly. Interestingly, the composition of the microbial community during the Fe(II) production phase (presumed to be a microbial iron-reduction phase) was very similar to that of the sulphate-reducing phase, suggesting that the sulphate-reducing bacteria may have reduced Fe(III) before sulphate reduction occurred. Fe(III) was presumably derived from the oxidation of pyrite in the borehole while it was open to the atmosphere for several years. For the majority of the duration of the experiment, a Gram-negative Delta-proteobacterium, belonging to the order *Desulfobacterales* and identified by 16S rRNA sequencing to belong to the genus *Desulfocapsa*, was the most abundant microorganism identified. In addition, Gram-positive SRB were also present throughout.

In order to better unravel the role of the various microorganisms in the oxidation of H₂ and the reduction of sulphate, as well as to attempt the reconstruction of the metabolic web in the borehole, a combined metagenomic and metaproteomic study was carried out (Bagnoud 2015; Bagnoud et al. 2016a). After assembly of the sequencing data for 16 samples, a binning approach was used for assembled contigs, and individual genomes were reconstructed in silico. In particular, seven organisms were identified with sufficient protein to infer their actual metabolic activity in the borehole water. Two autotrophic microorganisms were identified: a member of the *Desulfobulbaceae* family (corresponding to *Desulfocapsa* from the 16S rRNA gene sequencing) and a member of the *Rhodospirillaceae* family (corresponding to *Novispirillum* from the 16S rRNA gene sequencing). Metaproteomic data showed clearly that the *Desulfobulbaceae* strain actively oxidized H₂, reduced sulphate and fixed CO₂ while the *Rhodospirillaceae* strain appeared to also use H₂ as an electron donor while fixing CO₂, but the electron acceptor remained elusive. The former uses the reductive acetyl-CoA pathway for CO₂ fixation, while the latter uses the Calvin-Benson-Bassham cycle for CO₂ fixation.

Further, a *Hyphomonas* species was identified and interpreted to be a fermentative organism, utilizing, most likely, microbial necromass as a source of carbon and energy, and releasing fatty acid intermediates (e.g., acetate) that could be used by other heterotrophic microorganisms in the community (note that *Hyphomonas* sp. was also identified in the PC experiment, Stroes-Gascoyne et al. (2011)). In particular, four heterotrophic SRB were identified and exhibited active sulphate reduction, presumably fuelled by the oxidative acetyl-CoA pathway utilizing acetate (and potentially other organic acids). Three of the four SRB were Firmicutes, while one was a species from

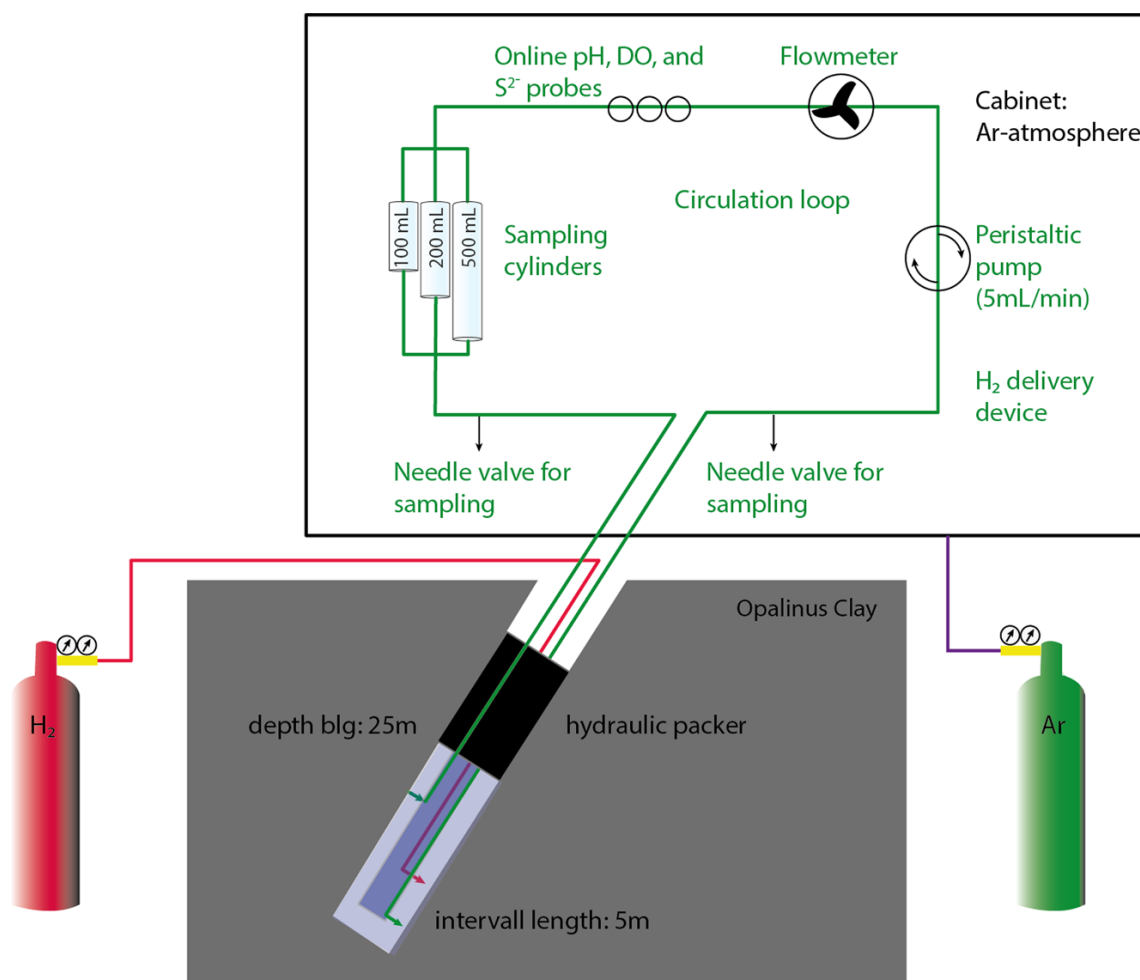


Fig. 1 Schematic of the setup of the MA experiment at the Mont Terri Research Laboratory

the genus *Desulfatitalea*, a *Deltaproteobacterium*. Overall, the metabolic web reconstructed in the borehole water (Bagnoud et al. 2016a) comprised autotrophic growth dependent on H_2 as a source of energy for CO_2 fixation, (suspected) fermentation of necromass, and the oxidation of organic acids back to CO_2 , closing the carbon loop. From the experiment, it was evident that H_2 consumption was rapid and that the presence of this energy source would support a thriving and active sulphate-reducing microbial community (Bagnoud et al. 2016a, b).

Both autotrophic organisms, the *Desulfobulbaceae* (which correspond to OTU 0 in Table 1) and the *Rhodospirillaceae* (which correspond to OTU 1 in Table 1) members, as well as a heterotrophic SRB, a *Desulfotomaculum* member (which corresponds to OTU 7 in Table 1), were identified in the water of all eight boreholes investigated by Bagnoud (2015). Moreover, the fermentative organism belonging to *Hyphomonas* genus, was detected in seven of the eight boreholes investigated by Bagnoud (2015).

5.3 Nitrate

The Bitumen-Nitrate-Clay interaction (BN) experiment was installed in situ in the Opalinus Clay at the Mont Terri rock laboratory, with the aim to clarify the (bio)chemical impact of a spreading nitrate and organic plume on the properties and safety of a potential DGR in clay host rock (Bleyen et al. 2017). In the BN-experiment, the transport and reactivity of nitrate is studied inside saturated packed-off and anoxic intervals, filled with APW, constructed in a borehole drilled in the Opalinus Clay. The current BN-experiment set-up does not take any backfill or cement matrix into account but investigates first a purely aquatic environment in the form of a water-filled borehole. As such, the current BN-experimental setup allows free movement of dissolved macro- and micro-nutrients, electron donors and acceptors, and provides microorganisms a physically non-restricted environment (e.g., open space, maximal a_w). The in situ microbial reduction of added nitrate and/or nitrite is being investigated, in the absence

and/or presence of added electron donors relevant for the disposal concept of nitrate-containing bituminized intermediate level radioactive waste (ILW). The results of the BN tests indicate that microbiological nitrate reduction can occur with electron donors naturally present in Opalinus Clay (e.g., pyrite, DOM, fermentation products, microbiological necromass), but that the rate of nitrate reduction can increase by a factor of 20–70 when an additional electron donor (acetate or hydrogen) is added to the borehole.

The observed evolution of the chemical composition of the borehole water correlated well with the detected shifts in the microbiological populations (analysed by 16S rRNA gene sequencing) observed in the borehole solution. The addition of nitrate inhibited the naturally slowly ongoing in situ microbiological sulphate reduction and induced a shift in the microbial community, with nitrate- and nitrite-reducing microorganism becoming more dominant. These nitrate- and nitrite-reducing microorganism included strains from the genera *Pseudomonas*, *Cupriavidus*, *Pelomonas*, *Undibacterium*, *Acidovorax*, *Phenylobacterium*, *Brevundimonas* and *Corynebacterium*. Once nitrate (and/or nitrite) was completely reduced, the chemical composition and the microbiological community of the interval solution gradually shifted back towards their original state of slow sulphate reduction, showing strains from the genera *Pseudomonas* (Table 2, OTU 2), *Gracillibacter*, and *Desulfosporosinus* (Table 2, OTU 6). This evolution is in agreement with thermodynamic succession in usage of dissolved electron acceptors: nitrate is a more favourable electron acceptor than sulphate, and when nitrate is present it will be used preferentially until depletion, after which sulphate is again next in line to be used as electron acceptor. More details of the BN experiment and specifics of the genomic analysis of the microbial communities encountered during this multi-year, on-going experiment are reported in Bleyen et al. (2017) and by Moors et al. (2012, 2013, 2015).

6 Conclusion from almost 15 years of microbial investigations in Opalinus Clay

It has been considered that a microbial community potentially indigenous to the host rock may become part of a DGR environment. An indigenous community is not necessarily a community that is as ancient as the host rock deposit itself. Natural geological processes such as geological movement, landslides, the formation of cracks and fissures, infiltration of foreign water from aquifers or as a result of flooding, are just a few of the normal processes that can introduce microorganisms into rock formations, and be the source of a more recent or present day indigenous community. However, it has been impossible so far to

demonstrate unambiguously the existence of a viable microbial community originating from the Opalinus Clay itself at the Mont Terri rock laboratory. In addition, physico-chemical evidence rather suggests that the ancient undisturbed Opalinus Clay is far too restrictive (in pore size and water activity) to host microbiological life, except perhaps in areas where those restricting factors are less severe (e.g., fractures). Nevertheless, there is the undisputable involvement of microorganisms in almost every experiment or borehole in the Mont Terri rock laboratory. This indicates that there are, besides possibly the claystone itself, likely many other sources that could introduce microbes in the Mont Terri rock laboratory. The most likely way is the unavoidable external contamination or introduction of microorganisms as a result of anthropogenic activities related to the Mont Terri rock laboratory construction and/or experiment installation. The Mont Terri rock laboratory consists of tunnels drilled and constructed over an extended period of time. During construction, no precautions were taken to avoid microbiological contaminations or the use of (petro-)chemicals or materials beneficial to microbial life. As a result, ubiquitous contamination, resulting in colonization of omnipresent aerobic and/or facultative anaerobic species (such as, for example, *Pseudomonas* or even *Pleomorphomonas* spores), of the tunnel surface is likely. Furthermore, constructing an underground rock laboratory implies anthropogenic activities that may induce physico-chemical changes in the rock environment that might stimulate dormant microorganisms that managed to survive in certain niches of the rock or engineered barriers. Simply drilling a borehole opens up space and, even if no water is used during drilling, drainage of pore-water into that space is sufficient to initiate the establishment of an active microbiological community (c.f., the borehole of the corrosion experiment). In addition, the use of non-sterilized APW in many experiments may have enhanced microbial communities. Microbial metabolic activity can be further enhanced by the presence of exogenous electron donors such as H₂ (from anaerobic corrosion of metals), organics such as glycerol (leaked from electrodes used for monitoring pH), and electron acceptors such as nitrate, in addition to naturally present electron donors, acceptors and organics in the Opalinus Clay. The diversity of the observed microbial communities present in Opalinus Clay borehole water can be surprisingly rich and a specific group of microorganisms is found ubiquitously within the whole Mont Terri rock laboratory, as shown in Table 1 (modified from Bagnoud 2015).

The impact of microbial activity on repository evolution remains incompletely constrained but the considerable research effort that has been invested in this topic has borne fruit. First, it is clear that H₂, produced by anaerobic

corrosion in a HLW DGR, can be readily consumed by bacteria, provided that space and water are present. For repositories that would contain other types of waste, such as bituminized nitrate-containing ILW or abundant organic matter-containing low level radioactive waste (LLW), the availability of additional electron donors and acceptors in these wastes is a further factor that can enhance microbial activity. While this activity can have both positive and negative effects, the full impact is not completely understood and requires considerably more study in the future.

Overall, the results collected to date and discussed here lead to the hypothesis that microorganisms will most likely have an impact on the environment in a repository in Opalinus Clay. Whether this microbial impact is detrimental or beneficial for a given DGR concept for HLW, ILW or LLW, has to be investigated further.

7 Future investigations

Safety assessments for future DGRs disposing of a variety of nuclear waste types will require a clearer understanding of the potential role of microbial communities in a HLW repository. In particular, quantification of microbial effects is needed in order to estimate, for instance, the actual contribution of MIC to the overall corrosion rates of containers in a DGR.

Much remains to be learned about the capacity of microorganisms to alter the minerals that make up the engineered barriers (i.e., those contained in Opalinus Clay and bentonite). Biofilm dwellers are the most likely candidates to catalyse such processes, which almost certainly would take place at interface regions because of the restrictive nature of the intact clay matrix. Nakano and Kawamura (2010) estimated the extent of corrosion of compacted bentonite by microbes in a biofilm on the surface of the bentonite through a conceptual model based on microbial growth dynamics. The model used energy conservation between the Gibbs free energy of formation of products from the elements of bentonite and the energy required for growth and maintenance of micro-organisms. This model predicted a mean population of micro-organisms of 10^6 – 10^7 cells/cm³ on the bentonite surface, with a biofilm thickness of 5–10 µm. The microbial corrosion depth was estimated to be in the range of less than 0.2–5.3 mm per 100,000 years, provided the bentonite density was 1600 kg/m³ while the corrosion depth varied inversely with bentonite density.

In addition, investigations of the potential for methanogenesis in a DGR are needed in order to evaluate whether methane could be produced by biological means from the degradation of organic compounds present in ILW

and LLW that will also be placed in a specially designed geological repository.

From a purely scientific point of view, further microbial investigations to unambiguously prove or disprove the existence of an indigenous, viable microbial community in Opalinus Clay should focus on obtaining DNA from pristine cores. Although such studies would, in principle, not add to the understanding of microbial effects in a DGR, not finding an indigenous population would corroborate strongly the unsuitability of the intact Opalinus Clay matrix to support a viable community, while finding an indigenous viable population may shed further light on possible geological events that could have introduced such a community in Opalinus Clay.

Acknowledgements We thank the Swisstopo crew of St. Ursanne for providing excellent working conditions in the Mont Terri rock laboratory. We also thank the many international researchers involved in the work reviewed in this paper.

We further like to express our gratitude to Professor Darren R. Korber (University of Saskatchewan) and Professor Judy McKenzie (ETH Zürich) for a useful and detailed review.

Open Access This article is distributed under the terms of the Creative Commons Attribution 4.0 International License (<http://creativecommons.org/licenses/by/4.0/>), which permits unrestricted use, distribution, and reproduction in any medium, provided you give appropriate credit to the original author(s) and the source, provide a link to the Creative Commons license, and indicate if changes were made.

References

- Auelo, T., Ranchou-Peyruse, A., Ollivier, B., & Magot, M. (2013). Desulfotomaculum spp. and related Gram-positive sulfate-reducing bacteria in deep subsurface environments. *Frontiers in Microbiology*, 4, 362.
- Bagnoud, A. (2015). Microbial metabolism in the deep subsurface: 1 case study of Opalinus Clay. Ph.D. dissertation, Ecole Polytechnique Fédérale de Lausanne, Lausanne, Switzerland, p 189
- Bagnoud, A., Cherkouk, A., Sergeant, C., Korber, D., & Bernier-Latmani, R. (2015b). Microbiological analysis of the cores of the BFE-A11 drill cores at the Mont Terri Rock Laboratory—Final report. Mont Terri Technical Note, TN 2014-101, 21 pp. Federal Office of Topography (swisstopo), Wabern, Switzerland. <http://www.mont-terri.ch>
- Bagnoud, A., Chourey, K., Hettich, R. L., de Bruijn, I., Andersson, A. F., Leupin, O. X., Schwyn, B., & Bernier-Latmani, R. (2016a). Reconstructing a hydrogen-driven microbial metabolic network in Opalinus Clay rock. Submitted to Nature Communications. (ISSN: 2041-1723).
- Bagnoud, A., de Bruijn, I., Andersson, A. F., Diomidis, N., Leupin, O. X., Schwyn, B., et al. (2015a). A minimalistic microbial food web in an excavated deep subsurface clay rock. *FEMS Microbiology Ecology*. doi:10.1093/femsec/fiv138.
- Bagnoud, A., Leupin, O. X., Schwyn, B., & Bernier-Latmani, R. (2016b). Rates of microbial hydrogen oxidation and sulfate reduction in Opalinus Clay rock. *Applied Geochemistry*, 72, 42–50.

- Battaglia, F., & Gaucher, E. (2003). Mont Terri Project porewater chemistry (PC) experiment: Microbial characterization and particle transport. *Mont Terri Technical Note*, TN 2003-23, 26 pp. Federal Office of Topography (swisstopo), Wabern, Switzerland. <http://www.mont-terri.ch>
- Birkholzer, J., Houseworth, J., & Tsang, C. F. (2012). Geologic Disposal of High-Level Radioactive Waste: Status, Key Issues, and Trends. *Annual Review of Environment and Resources*, 37, 79–106.
- Blechs Schmidt, I., & Vomvoris, S. (2012). Underground research facilities and rock laboratories for the development of geological disposal concepts and repository systems. In J. Ahn, M. J. Apted, (Eds.), *Geological repository systems for safe disposal of spent nuclear fuels and radioactive waste*. Woodhead Publishing Limited
- Bleyen, N., Smets, S., Small, J., Moors, H., Leys, N., Albrecht, A., de Cannière, P., Schwyn, B., Wittebroodt, C., & Valcke, E. (2017). Impact of the electron donor on in situ microbial nitrate reduction in Opalinus Clay. Results from the Mont Terri rock laboratory (Switzerland). *Swiss Journal of Geosciences*, 110 (this issue).
- Brown, A. D. (1990). *Microbial water stress physiology. Principles and perspectives* (328 pp.). John Wiley & Sons.
- Bossart, P., Bernier, F., Birkholzer, J., Bruggeman, C., Connolly, P., Dewonck, S., Fukaya, M., Herfort, M., Jensen, M., Matray, J-M., Mayor, J. C., Moeri, A., Oyama, T., Schuster, K., Shigeta, N., Vietor, T., Wiczorek, K. (2017). Mont Terri rock laboratory, 20 years of research: introduction, site characteristics and overview of experiments. *Swiss Journal of Geosciences*, 110. doi:10.1007/s00015-016-0236-1 (this issue).
- Chapelle, F. H. (1993). *Ground-water Microbiology and Geochemistry* (496 pp.). John Wiley & Sons
- Courdouan, A., Christl, I., Wersin, P., & Kretzschmar, R. (2007). Nature and reactivity of dissolved organic matter in the Opalinus Clay and Callovo-Oxfordian Formations. In: *Proc. Clays in Natural and Engineered Barriers for Radioactive Waste Confinement*, Lille, France.
- Courdouan-Metz, A. (2008). Nature and reactivity of dissolved organic matter in clay formations evaluated for the storage of radioactive waste. Ph.D. dissertation. Swiss Federal Institute of Technology in Zurich, Zurich, Switzerland, 114 pp.
- De Cannière, P., Schwarzbauer, J., Höhener, P., Lorenz, G., Salah, S., Leupin, O. X., et al. (2011). Biogeochemical processes in a clay formation in situ experiment: Part C—Organic contamination and leaching data. *Applied Geochemistry*, 26, 967–979.
- Delay, J., Bossart, P., Ling, L. X., Blechs Schmidt, I., Ohlsson, M., Vinsot, A., et al. (2014). Three decades of underground research laboratories: what have we learned? *Geological Society, London, Special Publications*, 400, 7–32.
- Ferrari, A., Favero, V., Marschall, P., & Laloui, L. (2014). Experimental analysis of the water retention behaviour of shales. *International Journal of Rock Mechanics and Mining Sciences*, 72, 61–70.
- Fruttschi, M., & Bernier-Latmani, R. (2010a). DR Experiment: Evaluation of the role of glycerol in microbial growth at the Mt Terri rock laboratory. *Mont Terri Technical Note*, TN 2009-35, 21 pp. Federal Office of Topography (swisstopo), Wabern, Switzerland. <http://www.mont-terri.ch>
- Fruttschi, M., & Bernier-Latmani, R. (2010b). PC (porewater chemistry) Experiment: porewater microbial community stimulated by glycerol at the Mt Terri rock laboratory—Final report. *Mont Terri Technical Note*, TN 2009-36 26 pp. Federal Office of Topography (swisstopo), Wabern, Switzerland. <http://www.mont-terri.ch>
- Garrity, G. M., Bell, J. A., & Lilburn, T. (2005). Family VII. Rhodobacteraceae. In G. M. Garrity, D. J. Brenner, N. R. Krieg, J. T. Staley, (Eds.), *Bergey's Manual of Systematic Bacteriology*. New-York.
- Geesey, G. G. (1993). A Review of the potential for microbially influenced corrosion of high level nuclear waste containers. Center for Nuclear Waste Regulatory Analyses Report, CNWRA 93-014.
- Hemes, S. S., Desbois, G., Urai, J. L., Schröppel, B., & Schwarz, J. O. (2015). Multi-scale characterization of porosity in Boom Clay (HADES-level, Mol, Belgium) using a combination of X-ray m-CT, 2D BIB-SEM and FIB-SEM tomography. *Microporous and Mesoporous Materials*, 208, 1–20.
- Ishii, K., (2004). Pore water chemistry (PC) experiment: quantification (and qualification) of microbial communities. *Mont Terri Technical Note*, TN 2004-76, 19 pp. Federal Office of Topography (swisstopo), Wabern, Switzerland. <http://www.mont-terri.ch>
- Johnson, S. S., Hebsgaard, M. B., Christensen, T. R., Mastepanov, M., Nielsen, R., Munch, K., et al. (2007). Ancient bacteria show evidence of DNA repair. *Proceedings of the National Academy of Sciences*, 104, 14401–14405.
- Kalyuzhnaya, M. G., Marco, P. D., Bowerman, S., Pacheco, C. C., Lara, J. C., Lidstrom, M. E., et al. (2006). *Methyloversatilis universalis* gen. nov., sp. nov., a novel taxon within the Betaproteobacteria represented by three methylotrophic isolates. *International Journal of Systematic and Evolutionary Microbiology*, 56, 2517–2522.
- Kelly, D. P., Wood, A. P., Stackebrandt, E., Brenner, D. J., Krieg, N. R., & Staley, J. T. (2005). Thiobacillus. In G. Garrity (Ed.), *Bergey's Manual of Systematic Bacteriology* (pp. 764–769). New-York: Springer.
- Kuever, J., Rainey, F. A., & Widdel, F. (2005). Desulfocapsa. In G. M. Garrity, D. J. Brenner, N. R. Krieg, & J. T. Staley (Eds.), *Bergey's Manual of Systematic Bacteriology* (pp. 992–994). New-York: Springer.
- Lazar, K., & Mathé, Z. (2012). Claystone as a potential host rock for nuclear waste storage. Chapter 4 Clay minerals in nature, their characterization, modification and application. INTECH Open Science.
- Leupin, O. X., Wersin, P., Gimmi, T., Mettler, S., Rösli, U., Meier, O., Nussbaum, N. C., Van Loon, L., Soler, J., Eikenberg, J., Fierz, T., van Dorp, F., Bossart, P., Pearson, F. J., Waber, H. N., Dewonck, S., Fruttschi, M., Chaudagne, G., & Kiczka, M. (2012). DR (Diffusion & Retention) Experiment : Synthesis: Field activities, data and modelling. *Mont Terri Technical Report*, TR 11-01, 49 pp. Federal Office of Topography (swisstopo), Wabern, Switzerland. <http://www.mont-terri.ch>
- Lin, L. C., & Beuchat, L. R. (2007). Survival of *Enterobacter sakazakii* in infant cereal as affected by composition, water activity, and temperature. *Food Microbiology*, 24, 767–777.
- Mauclaire, L., & McKenzie, J. (2006a). PC Experiment: Microbial activity and identification within PC, PC-C porewaters. *Mont Project Technical Note*, TN 2006-61, 18 pp. Federal Office of Topography (swisstopo), Wabern, Switzerland. <http://www.mont-terri.ch>
- Mauclaire, L., & McKenzie, J. (2006b). PC and MA Experiments: Microbial activity and identification within PC, PC-C porewaters. *Mont Terri Technical Note*, TN 2006-62, 21 pp. Federal Office of Topography (swisstopo), Wabern, Switzerland. <http://www.mont-terri.ch>
- Mauclaire, L., & McKenzie, J., Schippers, A. (2006). MA-experiment: Microbiological analysis of pore water samples from the PC and PC-C experiments in May 2006. *Mont Terri Technical Note*, TN 2006-56, 22 pp. Federal Office of Topography (swisstopo), Wabern, Switzerland. <http://www.mont-terri.ch>
- Mauclaire, L., McKenzie, J. A., Schwyn, B., & Bossart, P. (2007). Detection and cultivation of indigenous microorganisms in

- Mesozoic claystone core samples from the Opalinus Clay Formation (Mont Terri Rock Laboratory). *Physics and Chemistry of the Earth*, 32, 232–240.
- Mazurek, M., Alt-Epping, P., Bath, A., Gimmi, T., & Waber, H. N. (2009). *Natural Tracer Profiles across Argillaceous Formations: The CLAYTRAC Project* (p. 365). OECD Paris, France: Nuclear Energy Agency report.
- Mazurek, M., Alt-Epping, P., Gimmi, T., Waber, & H. N. (2007). Tracer profiles across argillaceous formations: A tool to constrain transport processes. In T. D. Bullen, & Y. Wang (Eds.), *Proceedings of the 12th International Symposium on Water-Rock Interaction, WRI-12, China 2007 volume 1 & 2* (pp. 767–772). Taylor & Francis Ltd.
- Moll, H., Lütke, L., Bachvarova, V., Steudner, R., Geißler, A., Krawczyk-Bärsch, E., Selenska-Pobell, S., & Bernhard, G. (2013). Microbial diversity in Opalinus Clay and interaction of dominant microbial strains with actinides. *Wissenschaftlich-Technische Berichte, HZDR-036, Helmholtz-Zentrum Dresden-Rosendorf, Dresden*.
- Moore, E. R. B., Tindall, B. J., Dos Santos, V. A. P. M., Pieper, D. H., Ramos, J.-L., & Palleroni, N. J. (2006). Nonmedical: *Pseudomonas*. In M. Dworkin, S. Falkow, E. Rosenberg, K.-H. Schleifer, K.-H., & E. Stackebrandt, (Eds.), *The Prokaryotes* (pp. 646–703). New-York: Springer.
- Moors, H., Cherkouk, A., Mysara, M., Bleyen, N., Boven, P., Selenska-Pobell, S., & Leys, N. (2013). BN Experiment: Intermediate results of the microbiological analyses. Mont Terri Technical Note, TN 2013-38, 68 pp. Federal Office of Topography (swisstopo), Wabern, Switzerland. <http://www.mont-terri.ch>
- Moors, H., Geissler, A., Boven, P., Selenska-Pobell, S., & Leys, N. (2012). BN Experiment: Intermediate results of the microbiological analyses. Mont Terri Technical Note, TN 2011-39, 27 pp. Federal Office of Topography (swisstopo), Wabern, Switzerland. <http://www.mont-terri.ch>
- Moors, H., Mysara, M., Bleyen, N., Cherkouk, A., Boven, P., & Leys, N. (2015). BN Experiment: Results of the microbiological analyses obtained during phase 19&20. Mont Terri Technical Note, TN 2015-72, 34 pp. Federal Office of Topography (swisstopo), Wabern, Switzerland. <http://www.mont-terri.ch>
- Nakano, M., & Kawamura, K. (2010). Estimating the corrosion of compacted bentonite by a conceptual model based on microbial growth dynamics. *Applied Clay Science*, 47, 43–50.
- Poulain, S., Sergeant, C., Simonoff, M., Le Marrec, C., & Altmann, S. (2008). Microbial investigations in Opalinus Clay, an argillaceous formation under evaluation as a potential host rock for a radioactive waste repository. *Geomicrobiology Journal*, 25, 240–249.
- Ramamoorthy, S., Sass, H., Langner, H., Schumann, P., Kroppenstedt, R. M., Spring, S., et al. (2006). *Desulfosporosinus lacus* sp. nov., a sulfate-reducing bacterium isolated from pristine freshwater lake sediments. *International Journal of Systematic and Evolutionary Microbiology*, 56, 2729–2736.
- Saddler, G. S., & Bradbury, J. F. (2005). Xanthomonadaceae. In G. M. Garrity, D. J. Brenner, N. R. Krieg, & J. T. Staley (Eds.), *Bergey's Manual of Systematic Bacteriology*. New-York: Springer.
- Senger R., Papafotiou A., & Marschall, P. (2013). Gas related property distributions in the proposed host rock formations of the candidate siting regions in Northern Switzerland and in the Helvetic Zone. Nagra Arbeitsbericht, NAB 13-083, Nagra, Wettingen, Switzerland. <http://www.nagra.ch>
- Spring, S., & Rosenzweig, F. (2006). The genera *Desulfotobacterium* and *Desulfosporosinus*: taxonomy. In M. Dworkin, S. Falkow, E. Rosenberg, K.-H. Schleifer, K.-H., & E. Stackebrandt, (Eds.), *The Prokaryotes* (pp. 771–786). New-York: Springer.
- Stroes-Gascoyne, S., Pedersen, K., Haveman, S. A., Daumas, S., Hamon, C. J., Arlinger, J., et al. (1997). Occurrence and identification of microorganisms in compacted clay-based buffer material designed for use in a nuclear fuel waste disposal vault. *Canadian Journal of Microbiology*, 43, 1133–1146.
- Stroes-Gascoyne, S., Schippers, A., Schwyn, B., Poulain, S., Sergeant, C., Simonoff, M., et al. (2007). Microbial community analysis of Opalinus Clay drill core samples from the Mont Terri Underground Research Laboratory, Switzerland. *Geomicrobiology Journal*, 24, 1–17.
- Stroes-Gascoyne, S., Sergeant, C., Schippers, A., Hamon, C. J., Nèble, S., Vesvres, M.-H., et al. (2011). Biogeochemical processes in a clay formation in situ experiment: Part D - Microbial analyses - Synthesis of results. *Applied Geochemistry*, 26, 980–989.
- Stroes-Gascoyne, S., Sergeant, C., Schippers, A., Hamon, C.J., Nèble, S., Vesvres, M.-H., Poulain, S., & Le Marrec, C. (2008). Microbial analyses of PC water and overcore samples: Synthesis of results. Mont Terri Technical Note, TN 2006-69 30 pp. Federal Office of Topography (swisstopo), Wabern, Switzerland. <http://www.mont-terri.ch>
- Stroes-Gascoyne, S., & West, J. (1997). Microbial studies in the Canadian nuclear fuel waste management program. *FEMS Microbiology Reviews*, 20, 573–590.
- Susina, N. E., Mulyukin, A. L., Kozlova, A. N., Shorokhova, A. P., Dmitriev, V. V., Barinova, E. S., et al. (2004). Ultrastructure of resting cells of some non-spore-forming bacteria. *Microbiology*, 73, 435–447.
- Takeuchi, M., Komai, T., Hanada, S., Tamaki, H., Tanabe, S., Miyachi, Y., et al. (2009). Bacterial and Archaeal 16S rRNA Genes in late Pleistocene to Holocene muddy sediments from the Kanto Plain of Japan. *Geomicrobiology Journal*, 26, 104–118.
- Xie, C.-H., & Yokota, A. (2005). *Pleomorphomonas oryzae* gen. nov., sp. nov., a nitrogen-fixing bacterium isolated from paddy soil of *Oryza sativa*. *International Journal of Systematic and Evolutionary Microbiology*, 55, 1233–1237.
- Yoon, J. H., Kang, S. J., Park, S., Lee, S. Y., & Oh, T. K. (2007). Reclassification of *Aquaspirillum itersonii* and *Aquaspirillum peregrinum* as *Novispirillum itersonii* gen. nov., comb. nov. and *Insolitispirillum peregrinum* gen. nov., comb. nov. *International Journal of Systematic and Evolutionary Microbiology*, 57, 2830–2835.

Impact of the electron donor on in situ microbial nitrate reduction in Opalinus Clay: results from the Mont Terri rock laboratory (Switzerland)

Nele Bleyen¹ · Steven Smets¹ · Joe Small² · Hugo Moors¹ · Natalie Leys¹ · Achim Albrecht³ · Pierre De Cannière⁴ · Bernhard Schwyn⁵ · Charles Wittebroodt⁶ · Elie Valcke¹

Received: 10 March 2016 / Accepted: 17 December 2016 / Published online: 24 February 2017
© The Author(s) 2017. This article is published with open access at Springerlink.com

Abstract At the Mont Terri rock laboratory (Switzerland), an in situ experiment is being carried out to examine the fate of nitrate leaching from nitrate-containing bituminized radioactive waste, in a clay host rock for geological disposal. Such a release of nitrate may cause a geochemical perturbation of the clay, possibly affecting some of the favorable characteristics of the host rock. In this in situ experiment, combined transport and reactivity of nitrate is studied inside anoxic and water-saturated chambers in a borehole in the Opalinus Clay. Continuous circulation of the solution from the borehole to the surface equipment allows a regular sampling and online monitoring of its chemical composition. In this paper, in situ microbial nitrate reduction in the Opalinus Clay

is discussed, in the presence or absence of additional electron donors relevant for the disposal concept and likely to be released from nitrate-containing bituminized radioactive waste: acetate (simulating bitumen degradation products) and H₂ (originating from radiolysis and corrosion in the repository). The results of these tests indicate that—in case microorganisms would be active in the repository or the surrounding clay—microbial nitrate reduction can occur using electron donors naturally present in the clay (e.g. pyrite, dissolved organic matter). Nevertheless, non-reactive transport of nitrate in the clay is expected to be the main process. In contrast, when easily oxidizable electron donors would be available (e.g. acetate and H₂), the microbial activity will be strongly stimulated. Both in the presence of H₂ and acetate, nitrite and nitrogenous gases are predominantly produced, although some ammonium can also be formed when H₂ is present. The reduction of nitrate in the clay could have an impact on the redox conditions in the pore-water and might also lead to a gas-related perturbation of the host rock, depending on the electron donor used during denitrification.

Editorial handling: P. Bossart and A. G. Milnes.

This is paper #18 of the Mont Terri Special Issue of the Swiss Journal of Geosciences (see Bossart et al. 2017, Table 3 and Fig. 7).

✉ Nele Bleyen
nbleyen@sckcen.be

¹ Belgian Nuclear Research Centre SCK•CEN, Boeretang 200, 2400 Mol, Belgium

² National Nuclear Laboratory NLL, Chadwick House, Birchwood Park, WA3 6AS Warrington, UK

³ Agence Nationale pour la Gestion des Déchets Radioactifs Andra, 1-7, Rue Jean-Monnet, 92298 Châtenay-Malabry Cedex, France

⁴ Federal Agency for Nuclear Control FANC, Rue Ravenstein 36, 1000 Brussels, Belgium

⁵ National Cooperative for the Disposal of Radioactive Waste NAGRA, Hardstrasse 73, 5430 Wettingen, Switzerland

⁶ Institut de Radioprotection et de Sécurité Nucléaire IRSN, 31, Avenue de la Division Leclerc, 92260 Fontenay-Aux-Roses, France

Keywords Nitrite · Redox · Clay · Acetate · Hydrogen · Microorganisms · Nuclear waste disposal

1 Introduction

In several countries such as Belgium and France, clay formations are foreseen as host rocks for geological disposal of bituminized intermediate-level long-lived waste (ILW). Suitable clay formations exhibit several favorable hydromechanical and geochemical characteristics (e.g. low permeability, reducing chemical conditions), which delay and spread in time the migration of released radionuclides (De Craen et al. 2004; Andra 2005; Smith et al. 2009).

Besides radionuclides, the bituminized radioactive waste under investigation here also contains a high amount of NaNO_3 , dispersed inside a hydrophobic bitumen matrix used to immobilize the waste and serving as a highly efficient semi-permeable membrane. After saturation of the disposal gallery, the bituminized waste will slowly start to take up water, resulting in the dissolution and leaching of NaNO_3 (Valcke et al. 2009). In addition, soluble organic compounds, initially present or resulting from bitumen degradation, are expected to be released into the clay pore-water (Valcke et al. 2000a, b). Furthermore, the production of H_2 —by anaerobic metal corrosion and by radiolysis of water and bitumen—will be unavoidable in a repository for this type of waste.

The release of nitrate could initiate several biogeochemical processes in the clay surrounding the waste disposal gallery, possibly affecting some of the favorable characteristics of the host rock. For example, the nitrate plume could affect the redox conditions (initially reducing) of the host rock in the vicinity of the repository due to microbial nitrate reduction using clay components (e.g. organic matter, pyrite or other Fe(II)-containing minerals) as electron donor (Hauck et al. 2001; Jørgensen et al. 2009; Mariën et al. 2011; Zhang et al. 2012, 2013). As the reducing capacity of the undisturbed clay formation will strongly impact the speciation, the solubility, the retention and the transport properties of redox-sensitive radionuclides (Se, Tc, U, Np, Pu, etc.), clay oxidation might favor the migration of these radionuclides in the host rock (e.g. De Cannière et al. 2010). Furthermore, microbial reduction of nitrate would either lead to the generation of nitrite [by dissimilative nitrate reduction to nitrite (DNRN)], nitrogenous gases (by denitrification) or ammonium [by dissimilative nitrate reduction to ammonium (DNRA)] (Fig. 1) (Madigan et al. 2000). The DNRN pathway usually occurs as an intermediate step in the denitrification process, but can also occur without subsequent denitrification, resulting in the accumulation of nitrite (Almeida et al. 1995; Oh and Silverstein 1999). In turn, the produced nitrite can oxidize the clay both

biotically and abiotically (Bleyen et al. 2015, 2016), again possibly resulting in a decrease of the reducing capacity of the clay formation. Continuous denitrification could lead to the formation of a separate gas phase when the concentration of produced N gases would exceed the solubility limit of the gases. This might cause fissuring of the host rock and might thus result in the formation of preferential pathways for radionuclide migration (Mallants et al. 2007; Harrington et al. 2012).

To study the possible geochemical and/or gas-related perturbations induced in the near field of a geological repository for the disposal of nitrate-containing bituminized waste, an in situ experiment, named Bitumen–Nitrate–Clay interaction (BN) experiment, is being performed in the Opalinus Clay in the Mont Terri rock laboratory. This in situ experiment consists of a vertical borehole rigged with downhole equipment containing three packed-off chambers (or intervals) in contact with the surrounding clay and initially filled with artificial pore-water (APW) of the Opalinus Clay. Each interval can be injected, circulated and monitored separately. In this paper, the results of two such injection tests are discussed. For this, two intervals were each injected with APW containing NaNO_3 and were later on given a pulse of either acetate or H_2 . These tests provide insights into the microbial nitrate reactivity (rate and metabolism) in the presence or in the absence of easily biodegradable electron donors, which are expected to be present in a repository for nitrate-containing bituminized ILW.

2 Materials and methods

2.1 Characteristics of the Opalinus Clay at Mont Terri

The Mont Terri Underground rock laboratory is located in the Opalinus Clay, a Mesozoic shale formation (~ 174 Ma)

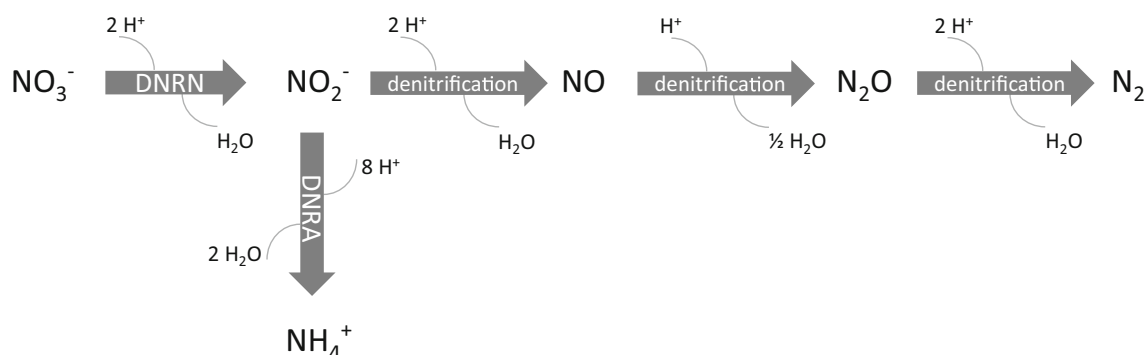


Fig. 1 Biological pathways that reduce nitrate include dissimilative nitrate reduction to nitrite (DNRN), to gaseous N species like NO, N₂O and N₂ (denitrification) and to ammonium (DNRA). Each of these pathways requires specific reductase enzymes

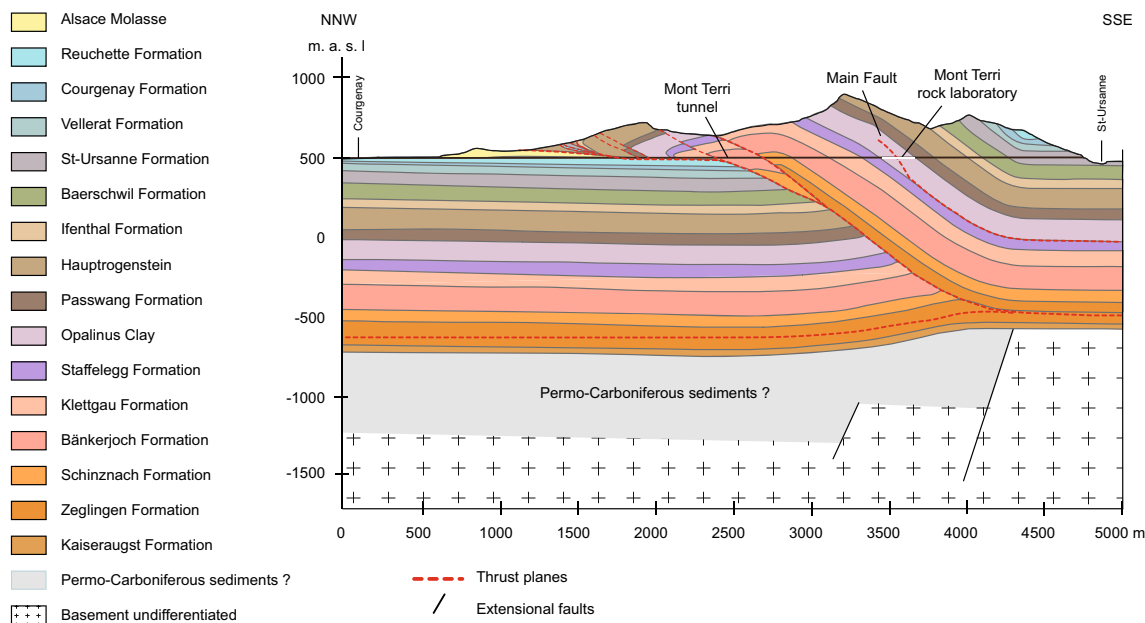


Fig. 2 Geological cross-section of the Mont Terri anticline and location of the Mont Terri rock laboratory (Nussbaum et al. 2017)

in the Jura Mountains of North-Western Switzerland. It transects an anticline structure of the folded Jura Mountains and has an overburden of max 320 m (Fig. 2). A detailed overview of the Mont Terri rock laboratory, including the location of the in situ experiment discussed in this paper, is provided by Bossart et al. (2017). The Opalinus Clay at Mont Terri is subdivided into lithological sub-units with shaly, sandy and carbonate-rich sandy facies (Thury and Bossart 1999). The mineral composition of these subunits is rather similar (though not quantitatively) and comprises mainly of quartz, illite and mixed-layer illite-smectite, kaolinite, chlorite, biotite and muscovite, calcite, aragonite, siderite, dolomite and/or ankerite, albite and/or plagioclase, K-feldspar, pyrite, organic matter (mostly kerogen), and other trace minerals like apatite (Pearson et al. 2003).

The water collected in situ from boreholes at the Mont Terri rock laboratory is of the NaCl type with Cl^- concentrations ranging from less than 28–310 mM and is characterized by a near-neutral pH (7–8). The chloride concentration in a certain borehole of the Mont Terri can be estimated from its location in the Opalinus Clay (Pearson et al. 2003). Other major components of the Opalinus Clay pore-water are sulfate (concentration fixed based on the Cl^- concentration and the $\text{SO}_4^{2-}/\text{Cl}^-$ ratio of present seawater), dissolved carbonate species (corresponding to a $p\text{CO}_2$ ranging from 10^{-1} to $10^{-2.7}$ kPa) and dissolved organic carbon (DOC; usually below $1.7 \text{ mmol C L}^{-1}$). As the concentrations of SO_4^{2-} and cations such as Mg^{2+} and Ca^{2+} , as well as the alkalinity are all linked to the chloride content and the chloride concentration is depending on the location in the Opalinus Clay (Pearson

1999; Pearson et al. 2003), the chemical composition of the pore-water in the clay surrounding the BN borehole could be estimated based on its location in the clay stratigraphy. From this, the composition of the artificial pore-water used in the BN experiment was derived (Table 1).

2.2 Design of the BN experiment

2.2.1 Borehole general configuration and drilling conditions

In 2010, the BN borehole was drilled vertically in the shaly facies of the Opalinus Clay, in the EZ-A niche of the Mont Terri rock laboratory (location shown by Bossart et al. 2017). It is 9.8 m deep with a diameter of 400 or 76 mm, for the first 3.5 m and the next 6.3 m under the gallery floor respectively (Fig. 3). The small diameter borehole (used for the BN experiment) was drilled under continuous nitrogen flushing, to prevent oxidation of clay components as much as possible and to preserve anaerobic microbial communities possibly present in the clay.

2.2.2 BN downhole equipment

The BN downhole equipment consists of three packed-off water chambers (or intervals) of 90 cm long, isolated from each other and from the gallery by inflatable packers. Each interval consists of a cylindrical sintered stainless steel filter screen [porosity 40%; outer diameter (OD) 70 mm, inner diameter (ID) 66 mm] surrounding a central stainless steel casing (OD 60.3 mm). The packer system contains

Table 1 Chemical composition (concentrations in mM) of the artificial pore-water (APW) used to saturate the intervals [target composition derived from Pearson (1999) and Pearson et al. (2003)] and of the interval solutions after saturation of the borehole and equilibration of the surrounding clay for ~8 months

Component	APW	Interval 1	Interval 2	Interval 3
Na ⁺	162	174.0	174.0	174.0
K ⁺	1.05	1.2	1.2	1.2
Ca ²⁺	12.6	11.7	11.0	10.7
Mg ²⁺	8.6	9.7	9.5	9.1
Sr ²⁺	0.4	0.4	0.4	0.4
Total dissolved Fe	–	n.a.	n.a.	<0.0004
Cl [–]	181	203.1	205.9	203.1
SO ₄ ^{2–}	12.28	11.03	11.66	11.66
NO ₃ [–]	–	<0.01	<0.01	<0.01
NO ₂ [–]	–	<0.1	<0.1	<0.1
NH ₄ ⁺	–	n.a.	n.a.	0.083
CHOO [–]	–	<0.0056	<0.0056	<0.0056
CH ₃ COO [–]	–	<0.009	<0.009	<0.009
C ₂ O ₄ ^{2–}	–	<0.006	<0.006	<0.006
TIC	2.8	5.2	2.8	2.8
TOC	–	0.7	0.92	0.8
pH (–)	7.8	7.1	7.2	7.4

The errors on the concentrations are 4% ([SO₄^{2–}]), 5.5% ([NO₃[–]]), 6% ([Cl[–]]), 10% ([Na⁺], [K⁺], [Ca²⁺], [Mg²⁺], [Sr²⁺], [NH₄⁺], [CHOO[–]], [CH₃COO[–]], [C₂O₄^{2–}] and TIC), 15% ([NO₂[–]], [total dissolved Fe]) and 30% (TOC) (95% confidence), while the uncertainty on the pH is estimated to be 0.1 pH unit (95% confidence)

n.a. not analyzed

one 2-m long and two 50-cm long hydraulically inflatable packers (Fig. 3) made of a stainless steel central tube surrounded by sleeves with an inner layer of natural rubber and an outer layer of neoprene and reinforced with stainless steel wires. After installation of the downhole equipment, the packers were inflated individually to a pressure of 5 MPa, by injecting water using dedicated stainless steel lines. At this pressure, the packers successfully isolate the intervals from each other and from the gallery. This was confirmed during later injection tests with nitrate: injection of the middle interval (Interval 2) with 1–25 mM of nitrate did not affect the chemical composition of the other intervals (monitored during max 1 year).

Stainless steel water lines (OD 4 mm and ID 2.4 mm) connect each of the downhole intervals to a water sampling unit and an online chemical monitoring unit in the gallery. To optimize water exchange in the intervals, both the injection and the extraction lines are connected as close as possible (i.e. 25 mm) to the opposite interval ends. The injection line is located at the bottom of the interval while the extraction line is installed at the top (Fig. 3). The water pressure in the intervals is measured by automatic pressure

transducers (Keller AG für Druckmesstechnik, Switzerland), connected to separate water lines that are also positioned 25 mm from the top of each of the chambers of the downhole equipment. On the bottom of Interval 1 (bottom interval), a temperature sensor (PT1000 type; JUMO, Switzerland) has been placed (Fig. 3).

Geological and structural mapping of the BN drill core indicated the presence of one (pre-existing) fault parallel to the bedding plane close to Interval 1, while no fracturing was found for Interval 2. Five bedding parallel faults are located between 4.4 and 5.5 m below the base of the gallery, which is close to Interval 3 (Phister et al. 2010).

2.2.3 BN surface equipment

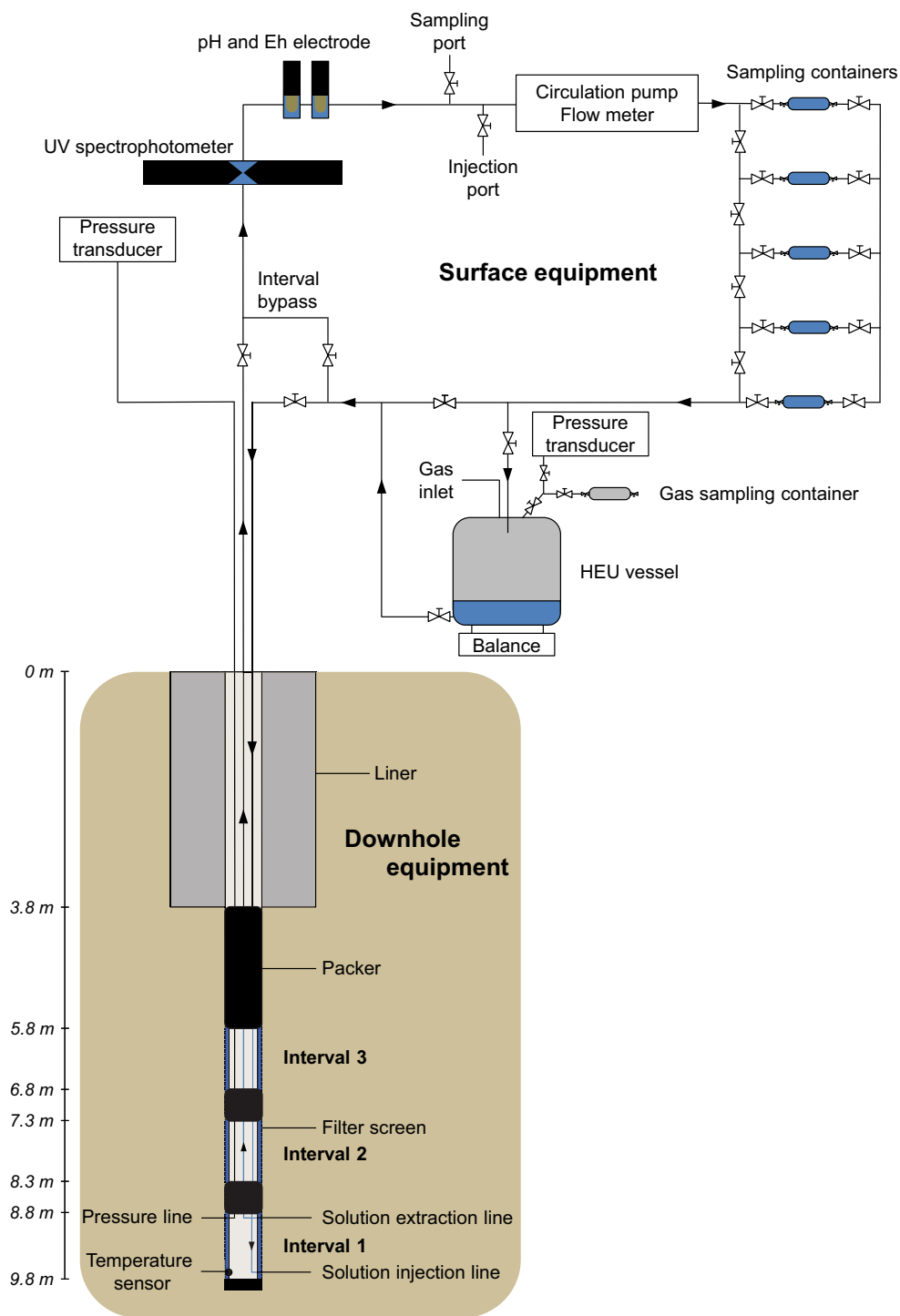
A schematic overview of the BN surface equipment can be found in Fig. 3.

The water in each of the intervals is continuously circulated from the downhole equipment to the surface equipment and back using a circulation pump (Micropump, USA) combined with a flow meter (ABB, Switzerland). This results in a homogenous solution and allows real-time monitoring of its chemical composition. Furthermore, each test circuit is equipped with 5 sampling containers (40 or 150 mL), which can be removed without causing a perturbation when additional chemical and/or microbial analyses are required (Fig. 3). Additional sampling is also possible by collecting the interval solution into an argon-flushed sterile septum bottle via a needle valve positioned in the water sampling unit ('sampling port' in Fig. 3). To prevent fluctuations of the water pressure in the interval as much as possible, the latter sampling method was performed only at the start and at the end of the injection tests, while bypassing the downhole equipment.

To monitor the real-time nitrate and nitrite concentrations, and the redox potential and pH, an UV spectrophotometer and a redox and pH electrode (spectro::lyserTM; redo::lyserTM and pH::lyserTM from S::can Messtechnik GmbH, Austria) have been installed in the circulation of two of the test intervals (Interval 1 and 2). When the interval solution is circulating, it flows continuously through the slit of the spectrophotometer, thereby passing between the UV light source and the detector, and through the housing chambers in which the electrodes are immersed. Further information regarding the spectrophotometer and electrodes is given in Sect. 2.6.3.

To investigate the impact of H₂ on the nitrate reactivity, a Hydrogen Equilibration Unit (HEU) was installed in the circuit of Interval 1 (Fig. 3). In this unit, the circulating interval solution drips into a stainless steel vessel of 10 L, filled with ~1 L of solution and ~9 L of gas. The gas pressure in this vessel is monitored online by a pressure transducer (Keller AG für Druckmesstechnik, Switzerland;

Fig. 3 Schematic overview of the BN experiment, consisting of a vertical borehole rigged with a downhole equipment consisting of three packed-off intervals, each lined with a cylindrical sintered stainless steel filter screen to allow contact with the surrounding clay. Each interval is connected to a stainless steel water circulation unit, equipped with a circulation pump, a flow meter and water sampling containers. In two of the intervals, an online UV spectrophotometer and pH and E_h electrodes are also installed and in the circulation of Interval 1, also a Hydrogen Equilibration Unit (HEU) is available



range 0–1000 kPa) and controls the water pressure in the interval. Dissolution of the gas into the solution is further maximized by slowly but continuously stirring of the solution. The H₂ supply tank rests on a balance in order to monitor the weight of the interval solution within the vessel to determine the volume of the solution and the gas phase in the HEU and as such to ensure that the tank does not completely fill with gas. During the injection test with H₂

(Sect. 2.5), the HEU serves both as a supply of H₂ and as a gas trap, collecting the gases produced by denitrification. To determine the gas composition in the HEU, a gas sampling container is connected to the HEU vessel. During tests in the absence of H₂ (e.g. tests described in Sect. 2.5.1), the HEU was not placed in the circuit of Interval 1.

Based on the individual volumes of the equipment (setup as used for the currently discussed tests) and the

dimensions of the borehole, an estimation of the initial volume of the solution in the circuit of intervals 1 and 2 could be made, i.e. 3.3 L for Interval 1 and 2.8 L for Interval 2, of which 1.4 L is present inside each interval. Note that the total volumes are depending on the number of sampling containers and/or HEU present in the circuit.

2.2.4 Prevention of organic and microbial contamination of the borehole during installation of the experiment

Only stainless steel and neoprene were used as materials for the downhole and gallery surface equipment to avoid biodegradation of the equipment and thus the release and contamination of the borehole water with dissolved organic matter, like was observed in a previous in situ experiment in the Mont Terri rock laboratory (De Canniere et al. 2008, 2011). To prevent additional organic and/or microbial contamination of the borehole as much as possible, all equipment (downhole and in the gallery) was cleaned before installation by rinsing, first with acetone (to remove traces of grease) or ethanol (disinfectant) and later thoroughly with deionized water to remove the cleaning solvents. Before installation, all metallic parts were additionally autoclaved, to prevent microbial contamination as much as possible. Furthermore, the housing chambers of the UV spectrophotometer and electrodes were cleaned with ethanol and subsequent rinsing with deionized water before the start of each new test.

2.3 Saturation and equilibration of the borehole

Immediately after installation of the downhole equipment, the three intervals were injected with APW. Its chemical composition was derived from the location of the BN experiment in the clay stratigraphy and the relationship between sulfate, cations and the chloride content (Pearson 1999; Pearson et al. 2003), though without the organic matter (Table 1). This APW was prepared, stored and injected in the intervals anaerobically (Ar atmosphere with

$[O_2] < 5 \times 10^{-4}$ vol%) to avoid oxidation of the clay surrounding the borehole. It was injected into the intervals at a water pressure of 300–500 kPa (absolute). Note that no special precautions were taken to avoid contamination with exogenous microorganisms during preparation of the APW.

To achieve full saturation and hydraulic equilibrium of the interval with the surrounding clay, APW was reinjected when the water pressure in the interval(s) decreased below atmospheric pressure and until the water pressure in the intervals remained stable. After the initial injection of Interval 1 with APW, the water pressure rapidly decreased and stabilized at ~ 250 kPa (absolute). In Interval 2, three consecutive injections were needed until the water pressure stabilized to a pressure of ~ 130 kPa (absolute). Note that circulation of the solution during the injection tests resulted in a slightly higher water pressure in both intervals.

After static water diffusion into and equilibration with the surrounding clay at a stable water pressure for ~ 7 months, the APW in each interval was homogenized by circulation at a flow rate of ~ 5 mL min^{-1} for 4 weeks. Next, each interval solution was sampled and its chemical composition was determined.

2.4 Study of the diffusion-controlled evolution of anionic and neutral tracers

To assess the diffusion of nitrate into the clay surrounding the BN borehole, the diffusive behavior of non-reactive anionic and neutral tracers in the clay was assessed. For this, the solution in Interval 1 and 2 was replaced completely with an anaerobically prepared APW solution containing two tracers: 15.6 mM bromide and 1600 ‰ $\delta^2\text{H-H}_2\text{O}$ (final concentrations in the interval). At the same time, nitrate and/or acetate were also injected in both intervals during the first series of injection tests with low nitrate concentrations (described in Sect. 2.5.1, test codes INT1_2011 and INT2_2011a in Table 2).

Table 2 Overview of the discussed in situ tests performed for the BN experiment

Test code	Interval	NO_3^-	NO_2^-	CH_3COO^-	H_2 (dissolved)	Start date	Time of e^- donor pulse	Sterility solution injected	Parallel injection of tracers
INT1_2011	1	1.5	–	–	–	2011-03-16	No pulse injection	Not sterile	Br^- and $^2\text{H-H}_2\text{O}$
INT1_2014	1	15	–	–	2.3	2014-10-01	54 days	Sterile	–
INT1_2015	1	15	–	–	1.6	2015-09-23	48 days	Sterile	Br^-
INT2_2011a	2	1.1	0.8	0.8	–	2011-03-16	No pulse injection	Not sterile	Br^- and $^2\text{H-H}_2\text{O}$
INT2_2011b	2	1.1	–	0.3	–	2011-05-31	No pulse injection	Sterile	–
INT2_2013	2	25	–	4	–	2013-11-05	70 days	Sterile	–

The indicated concentrations (in mM) of nitrate, nitrite, acetate and dissolved H_2 are the final concentrations after injection and dilution in the interval

The injected solution was initially pressurized at a higher pressure (~ 400 kPa) compared to the water pressure in the intervals, possibly resulting in some initial advective loss of solution. After injection, the interval solution was equilibrated overnight at a flow rate of ~ 7 mL min^{-1} . The next day, the water pressure was decreased to more or less the in situ pressure while sampling the interval solutions and re-injecting new solution using the needle valves. Since then, the interval solutions were circulated continuously at a flow rate of ~ 10 mL min^{-1} . Throughout this diffusion experiment, the water pressure in the interval remained more or less stable: 256 ± 40 kPa in Interval 1 and 208 ± 30 kPa in Interval 2. Some fluctuations of the water pressure occurred however due to small changes in the flow rate and to a small water pressure increase (by ~ 50 kPa) in Interval 2 caused by denitrification after injection of nitrate and acetate during the first series of injection tests (Sect. 2.5.1). Samples of the interval solutions were taken regularly to monitor the decrease of the tracer concentration.

In September 2015, the diffusive behavior of bromide was re-examined in Interval 1, during a second injection test with nitrate and H_2 (duplicate test for test INT1_2014 but not discussed in this paper; test code INT1_2015 in Table 2). In contrast to the first diffusion test, only the solution in the surface equipment was replaced by a new, sterile APW solution containing NaNO_3 and ~ 29 mM bromide. Dilution and overnight equilibration with the remaining interval solution (at a flow rate of ~ 40 mL min^{-1}) resulted in a final concentration of 17.02 mM bromide. During injection and equilibration, the interval solution was pressurized at ~ 550 kPa, possibly resulting in some advective loss. Afterwards, the water pressure in the interval was decreased to ~ 370 kPa while sampling the solution and re-injecting new solution. Since then, the interval solution was circulated continuously at a flow rate of ~ 10 mL min^{-1} . During the first ~ 10 days, the water pressure increased slightly to 404 ± 15 kPa and remained more or less stable afterwards. At the start of the pulse injection with H_2 , the average water pressure in the interval was not affected, although at the time of the pulse, some water pressure fluctuations were observed due to temporary changes in the pressure of the HEU. At the end of the pulse injection with H_2 , the water pressure had increased slightly (to 472 ± 28 kPa) upon switching to an Ar atmosphere in the HEU vessel (see Sect. 2.5.3). To monitor the decrease of the tracer concentration, samples of the interval solution were taken regularly by disconnecting sampling containers.

The diffusion data of the tracers have been modeled with the Generalized Repository Model (GRM) (Small et al. 2008). This model of the BN experiment represents the geometry of Interval 1 and 2 including the volumes of the circulating fluid, the filter and an assumed void

space adjacent to the borehole with a 1-dimensional finite difference grid. The Opalinus Clay is represented by 20 model cells that increase exponentially in length from 5 mm for the first cell to 730 mm in the last cell. Each successive cell is 1.3 times the length of the preceding cell and the 20 cells cover a total of 3.16 m of clay. This model configuration was compared with a model of shorter length (10 cm) and a radial diffusion model, configured in PHREEQC (Tournassat et al. 2011), which showed that effects of boundary conditions and radial diffusion were not significant over a 100-day time scale. A porosity of 0.17 was assumed for the Opalinus Clay (Pearson et al. 2003; Van Loon et al. 2004a) and pore diffusion coefficients for the clay were fitted to the bromide and $\delta^2\text{H-H}_2\text{O}$ data.

2.5 Injection of Interval 1 and 2 with a nitrate-containing solution

2.5.1 Previous injection tests with low nitrate concentrations

In the first series of tests (not discussed in detail in this paper), the biogeochemical evolution of the solution in the intervals was investigated after injection with low concentrations of nitrate (and/or nitrite) (up to 1.5 mM NO_3^-) with (Interval 2) or without (Interval 1) acetate (details in Table 2, tests INT1_2011, INT2_2011a and INT2_2011b). During the first test in both intervals, tracers were co-injected to perform diffusion tests. Details regarding the injection of the intervals can be found in Sect. 2.4. The C/N ratio of the nitrate and acetate-containing APW solution used in Interval 2 was 0.4 or 0.8 in the 2 consecutive tests in this interval (INT2_2011a and INT2_2011b). The injected APW solutions were prepared anaerobically. In the first test in both Interval 1 and 2 (Table 2), no special precautions were taken to avoid external contamination with microorganisms. For all later tests, a sterile nitrate-containing APW solution was used to inject the intervals, to prevent further externally influenced changes in the microbial community.

The results of these tests indicated that microbial reduction of nitrate and nitrite can occur in the intervals of the BN experiment, using acetate and/or clay components as electron donors. Comparing the evolution in nitrate and nitrite concentrations in the absence or in the presence of acetate, clearly indicates faster reaction rates of microbial nitrate reduction when the system is fueled with acetate. The observed nitrate reduction rates in these preliminary tests are summarized in Table 3. In these tests, nitrate was reduced to nitrite, ammonium and/or nitrogenous gases. Furthermore, high concentrations of nitrate-reducing prokaryotes were detected after injection of the intervals with nitrate, indicating that the nitrate (and nitrite)

Table 3 Summary of the average nitrate reduction rates (in mM day^{-1}) observed in the in situ tests of the BN experiment, either in the absence or in the presence of additional electron donors, i.e. acetate or H_2 , as indicated in Table 2

Test code	NO_3^- reduction rate in absence of additional electron donors	NO_3^- reduction rate in presence of additional electron donors
INT1_2011	0.04	–
INT1_2014	0.02	0.2–0.7
INT2_2011a	–	0.8
INT2_2011b	–	1
INT2_2013	0.02	1.2

reduction, observed during all tests, was microbially mediated. More details are given by Bleyen et al. (2011).

2.5.2 Injection tests with high nitrate concentrations

In the second series of injection tests, which are discussed in this paper, sterile APW with higher nitrate concentrations was injected in Interval 1 and 2 (Table 2). For these tests, injection of the intervals was performed by replacing the solution in the surface equipment with a new APW solution containing NaNO_3 while bypassing the downhole equipment. The solutions for injection of Interval 1 and 2 contained 31 and 59 mM NaNO_3 respectively, and were filter sterilized after preparation. This way, the microbial population present in the intervals would not be disturbed. Care was taken to prevent O_2 and microbial contamination during injection.

After replacement of the solution in the surface equipment, the solution was circulated (at 40 mL min^{-1}) through the interval to mix it with the remaining solution in the downhole equipment, resulting in a dilution of the injected solution. About 10 h after injection (i.e. overnight homogenization of the new with the old solution), samples of the interval solution were taken and the flow rate was decreased to 10 mL min^{-1} . This flow rate was maintained during the remainder of the tests. The nitrate concentration after dilution and overnight homogenization is considered to be the starting concentration of the test, i.e. 15 and 25 mM NO_3^- for Interval 1 and 2 respectively, as indicated in Table 2. The water pressure in Interval 1 and 2 was 308 and 166 kPa respectively, at the start of the injection tests (after overnight equilibration of the injected solution).

2.5.3 Pulse injection with H_2 or acetate

For the tests in Interval 1 and 2 that are subject to further discussion in this paper (see Sect. 2.5.2), a pulse injection

with a certain electron donor (H_2 and acetate) was performed after a few months of circulation with only nitrate. This way, the impact of an additional electron donor on the microbial nitrate reactivity was monitored in one single test. In Interval 1, the addition of H_2 was performed by changing the head space in the HEU vessel from argon to 100% H_2 . For this, the head space was repeatedly evacuated to a pressure of $\sim 4 \text{ kPa}$ and filled with pure H_2 , while keeping the inlet and outlet valves of the HEU closed. The pressure of H_2 in the vessel at the start of the pulse was 320 kPa. After restarting the circulation through the HEU, dissolved H_2 circulated the system together with the interval solution. Based on Henry's law [with $k_H = 0.00073 \text{ M atm}^{-1}$ at $14 \text{ }^\circ\text{C}$ (Lide and Frederikse 1995)], the initial concentration of dissolved H_2 can be calculated: i.e. 2.3 mM dissolved H_2 . This information, combined with the free gas volume in the HEU vessel (9 L) and the total volume of the interval solution at the time of the pulse (estimated to be 2.8 L), allows us to calculate the total initial amount of moles of H_2 present in the circuit after switching to a H_2 atmosphere in the HEU: 1.2 mol H_2 of which 7 mmol H_2 were dissolved in the circulated solution. This dissolved H_2 fraction was replenished each time the solution passed through the HEU, but decreased when the partial pressure of H_2 in the gas phase decreased during the experiment. After $\sim 10 \text{ mM}$ of nitrate was reduced (24 days later) H_2 was removed from the circuit by bypassing the HEU. At this time, the gas phase of the HEU vessel was sampled and subsequently switched again to an argon atmosphere (same method as for the H_2 pulse).

The pulse injection of acetate in Interval 2 was performed after 70 days by reconnecting one of the sampling containers (40 mL) containing freshly prepared APW with nitrate at the concentration present in the interval at the time of reconnection (i.e. 16 mM NO_3^-), and 310 mM sodium acetate. After dilution of the added acetate in the remaining interval solution by circulating the solution for 4 h at 40 mL min^{-1} , the concentration was ~ 80 times diluted to a final concentration of 4 mM acetate. The C/N ratio in the interval solution was 0.4. Afterwards, the flow rate was decreased again to 10 mL min^{-1} .

Throughout the tests, samples of the interval solution were taken regularly by disconnecting sampling containers. All collected samples were stored at $\sim 4 \text{ }^\circ\text{C}$ and under anaerobic conditions prior to the chemical and microbiological analyses, to slow down as much as possible any (microbially mediated) reaction. Furthermore, the nitrate and nitrite concentrations and the pH and E_h were monitored online, enabling sampling of the interval solution at appropriate times.

2.6 Monitoring of the in situ chemical composition

2.6.1 Chemical analyses of sampled solution

The chemical analyses of the sampled solutions were performed as soon as possible after sampling. Subsamples of the solution were taken under an anaerobic atmosphere and analyzed at SCK•CEN by ion chromatography (IC) for SO_4^{2-} , Cl^- , Br^- , acetate, NO_3^- and NO_2^- , by inductively coupled plasma atomic emission spectroscopy (ICP-AES) for Na^+ , K^+ , Ca^{2+} , Mg^{2+} , Sr^{2+} and dissolved Fe(total), by ion selective electrode (ISE) for NH_4^+ and by TOC/TIC analyzer with UV persulfate digestion for TOC (total organic carbon) and TIC (total inorganic carbon). To monitor the diffusion of deuterated water into the surrounding clay, isotope ratio mass spectrometry (relative to the VSMOW standard) was performed by Hydroisotop GmbH (Germany).

2.6.2 Analyses of dissolved gases

To detect the presence of certain dissolved gases (N_2 , N_2O , CO_2 , H_2 , O_2) in the interval solutions during the tests, the solution was equilibrated with a gas phase, either (1) in a sampling container after disconnection from the circuit (for Interval 2) or (2) in the gas phase of the HEU (for Interval 1).

To equilibrate the dissolved and gaseous gas fractions in a sampling container, the headspace method [adapted from (Xiong et al. 2006)] was applied, followed by micro gas chromatography with a thermal conductivity detector at SCK•CEN for analysis of N_2O and N_2 concentrations. For the headspace method, a volume of ~ 10 mL of the solution in the sampling container was removed, while allowing Ar gas to flow into the created headspace. The dissolved gases were equilibrated with the headspace atmosphere during one week at 4 °C (to prevent additional microbial activity) followed by 4 h at 19 °C while sonicating. Afterwards, the gas phase was sampled for analysis. The concentration of dissolved gases in the interval solution was derived using Henry's law [with $k_{\text{H}}(\text{N}_2) = 0.00056 \text{ M atm}^{-1}$ and $k_{\text{H}}(\text{N}_2\text{O}) = 0.021 \text{ M atm}^{-1}$ at 19 °C (Wilhelm et al. 1977)].

To determine the gas composition in the gas phase of the HEU vessel, the head space of the vessel was sampled before replacing the gas in the vessel by argon (at the end of the pulse with H_2). The gas phase was analyzed by gas chromatography with a thermal conductivity detector (for H_2 , O_2 , N_2 , CO_2 , N_2O) at Hydroisotop GmbH (Germany). The concentration of the dissolved gases was calculated using Henry's law applying the following values for k_{H} (at 14 °C): H_2 : $0.00073 \text{ M atm}^{-1}$; O_2 : $0.0010 \text{ M atm}^{-1}$; N_2 : $0.00052 \text{ M atm}^{-1}$; CO_2 : 0.025 M atm^{-1} ; N_2O :

0.018 M atm^{-1} (Wilhelm et al. 1977; Lide and Frederikse 1995).

2.6.3 Online monitoring of nitrate and nitrite concentrations and pH

A multi-parameter UV spectrophotometer (spectro::lyserTM, S::can Messtechnik GmbH, Austria) was used for the high-resolution online measurements of nitrate and nitrite. The spectro::lyserTM records the UV light absorbance in the wavelength range between 200 and 400 nm, and displays the results in real time. The measurement of the nitrate and nitrite concentrations is based on the turbidity-compensated absorbance of 5–7 wavelengths per parameter (between 210 and 245 nm) using an algorithm specifically adapted for BN waters, provided by the manufacturer. Further calibration was performed before each injection test to obtain accurate measurements and long-term stability of the results. In addition, a cross-checked calculation of the nitrite concentration is possible, based on the normalized absorbance at 245 nm. More details are given by Bleyen et al. (in preparation).

To monitor changes in pH and redox potential in the interval solutions, an online pH and E_{h} probe (respectively pH::lyserTM and redo::lyserTM, S::can Messtechnik GmbH, Austria) was used. These probes contain a Reflex reference system (Reflex Sensors Ltd, Ireland), separating the test solution from the Ag/AgCl reference electrode compartment by means of ceramic frit junctions covered with a chemically stable Reflex polymeric interface (consisting of a polyvinyl acetate resin and doped with KCl). The stability and long-term performance of this type of electrodes under in situ conditions are discussed in detail by Bleyen et al. (in preparation).

2.7 Evaluation of the microbial community

Microbiological analyses were performed on the sampled solutions to monitor the evolution of the microbial community upon changes in the water composition and to verify the presence of an active microbial community. These analyses included ATP measurements [method according to Wouters et al. (2013)], cultivation-based techniques and DNA-based molecular biology methods.

2.7.1 Cultivation-based methods

The metabolic versatility of the bacterial community was determined using a 5-log dilution and threefold biological replicates (i.e. Most Probable Number (MPN) determination) in four different anaerobic cultivation media: (1) LB medium (Bertani 1951) for detection of heterotrophic

anaerobic microorganisms; (2) R2A medium (Reasoner and Geldreich 1985) for slow-growing microbes; (3) Medium 63 (Deutsche Sammlung von Mikroorganismen und Zellkulturen) for the cultivation of sulfate-reducing prokaryotes (SRP); (4) N43 medium (Heylen et al. 2006) to detect nitrate-reducing prokaryotes. All media contained activated resazurin (1 mg L^{-1}) as redox indicator to verify anoxicity. The inoculated dilutions were incubated at $30 \text{ }^\circ\text{C}$ for minimally 4 weeks, after which the turbidity and gas formation and/or precipitation of end products in the media was assessed and the microbial concentration was calculated using the method provided by Garthright and Blodgett (2003).

2.7.2 DNA-based microbial community analysis

DNA was extracted from the sampled interval solution applying an in-house developed nucleic acid extraction procedure using potassium ethyl xanthogenate as described by Wouters et al. (2013). This DNA was amplified by polymerase chain reaction (PCR) using universal primers for the bacterial 16S rDNA gene. To be able to detect changes in the microbial community during the different phases of the tests, highly conserved primer sequences were chosen, yielding amplicons covering several variable regions of the 16S rDNA gene. Two types of DNA-based microbial community analyses have been applied for the tests described in this paper: Illumina MiSeq high throughput sequencing (Interval 1) and barcoded 454 FLX + high throughput sequencing (Interval 2) (Moors et al. 2015b).

For the solutions sampled from Interval 1, 464-bp fragments covering the variable regions V3 and V4 of the 16S rDNA gene were first amplified by PCR. For this, the 341F and 785R primers described by Klindworth et al. (2012) and extended with the necessary overhanging adapters were used: 341F 5'-TCGTCGGCAGCGTCAGA TGTGTATAAGAGACAGCCTACGGGNGGCWGCAG-3' and 785R 5'-GTCTCGTGGGCTCGGAGATGTGTA TAAGAGACAGGACTACHVGGGTATCTAATCC-3'. Details regarding the PCR conditions are described by Klindworth et al. (2012). Afterwards, a DNA sequencing library was prepared by performing a second PCR, linking an index to either side of the amplicons, according to the instructions of LGC (United Kingdom) who subsequently performed the MiSeq Illumina DNA sequencing.

For the solutions of Interval 2, DNA was amplified yielding 1151-bp fragments of the 16S rDNA gene, including the variable regions V3–V6. The primers for this PCR were FLX-1492R (5'-ATGGAACAATGCTGAA-3') and a series of forward primers consisting of a DNA-annealing part (5'-CTACGGRAGGCAGCAG-3') linked to a set of barcodes (MID 049-059; according to the

instructions of IMGGM, Germany). The PCR reaction was carried out in $50 \mu\text{l}$ volumes containing 50 vol% Phusion 2 \times master mix (Thermo Fisher Scientific, USA), $0.5 \mu\text{M}$ of each primer and 50–100 ng DNA template. The following PCR conditions were used: initial denaturation at $98 \text{ }^\circ\text{C}$ for 2 min, followed by 30 cycles of denaturation ($98 \text{ }^\circ\text{C}$ for 30 s), annealing ($52 \text{ }^\circ\text{C}$ for 30 s) and elongation ($72 \text{ }^\circ\text{C}$ for 5 min), and a final extension step at $72 \text{ }^\circ\text{C}$ for 5 min. After equimolar pooling of the amplicon mixtures (each with different barcodes), IMGGM (Germany) performed the 454 FLX+ high throughput DNA sequencing.

The obtained raw DNA sequences were treated with an in-house developed bioinformatics pipeline, optimized to preprocess the output of different high throughput sequencing methods. This preprocessing included trimming, denoising (NoDe (Mysara et al. 2015a) or IPED (Mysara et al. 2016)) and chimera removal (CATCH (2015b)). Using this software, sequences were clustered into operational taxonomic units or OTU (Schloss and Westcott 2011). Each OTU contains a number of sequences indicating the abundancy of the OTU in the analyzed sample. Each of the consensus OTU DNA sequences was used to find the closest matching bacterial species by BLAST against the GreenGenes database with a minimum of 90% sequence similarity (DeSantis et al. 2006).

3 Results

3.1 Chemical composition of solution in the BN borehole

After saturation of the intervals with APW and equilibration with the surrounding clay for ~ 8 months, solution was sampled from the intervals. Chemical analyses (Table 1) show that the target composition of the APW and thus the theoretical composition of the pore-water in the Opalinus Clay at the location of the BN experiment do not differ significantly from that of the equilibrated interval solutions, except for the TIC measured in Interval 1. The reason for this difference in TIC is yet unknown, but might be due to an elevated presence of carbonates close to Interval 1. Nevertheless, the chemical composition of the water collected from the three intervals is remarkably similar. The composition of the solutions in Intervals 1 and 2 was determined again before starting the injection tests discussed in this paper. This showed no statistical differences with the composition of the first sampled solution apart from a slight increase in the dissolved iron (up to 0.05 and 0.003 mM for Interval 1 and 2 respectively) and a decrease in the sulfate concentration (by $\sim 1 \text{ mM}$ for both intervals). These small changes are most likely due to some microbial activity ongoing in the interval before the start of

the currently discussed injection tests. Indeed, microbiological analyses confirmed the presence of a large population of sulfate-reducing bacteria (strains from genera *Pseudomonas*, *Gracilibacter*, and *Desulfosporosinus*) in the sampled solution from both intervals before injection with nitrate (Moors et al. 2015b). Furthermore, some ammonium was found in both interval solutions (0.4 mM in Interval 1 and 0.3 mM in Interval 2), which can be explained by biomass degradation (Madigan et al. 2000).

The invariable (main) chemical composition of the interval solutions confirms that geochemical stability was reached in the BN borehole after 8 months of equilibration with the surrounding clay. Furthermore, the composition of the pore-water in the Opalinus Clay can indeed be deduced with an acceptable accuracy based on its location and the relationship between sulfate, cations and the chloride content (Pearson 1999; Pearson et al. 2003).

The results also revealed that some organic matter had diffused into the intervals during saturation, resulting in a TOC concentration of ~ 0.8 mmol C L⁻¹ for each interval, which is similar to the TOC concentrations measured previously in boreholes in the Opalinus Clay at Mont Terri, i.e. 0.3–3.7 mmol C L⁻¹ (Pearson 1999; Courdouan et al. 2007; Eichinger et al. 2011). According to previous studies made on clay aqueous extracts (Courdouan et al. 2007; Eichinger et al. 2011), the low molecular weight (and thus easily biodegradable) organic fraction found in Opalinus Clay water contains highly variable concentrations of acetate (2–31% of DOC), formate (0.2–4% of DOC) and other small organic compounds. In contrast to these studies, no detectable concentrations of acetate, formate or oxalate could be found in the BN interval solutions after the saturation and equilibration period (Table 1) nor before the start of the injection tests discussed here.

3.2 Diffusion-controlled evolution of tracers

The diffusive transport of an anion and a neutral species into the surrounding clay was studied in 2011 by adding bromide and deuterated water to APW injected in Interval 1 and 2 and monitoring the decrease in concentration in the interval solution as a function of time over a period of up to 433 days. Later on, a second bromide injection test was performed in Interval 1 (in 2015), in which the bromide concentration was monitored during 165 days.

The tracers show a steady decrease in relative concentration, which is similar for both intervals. This is consistent with the diffusion of these species in the surrounding clay, as the decrease in relative concentrations in the interval solution is linear with the square root of time after an initial equilibration period (~ 1 day). Furthermore, the evolution of the tracer concentrations in time can be successfully fitted using the GRM and assuming only

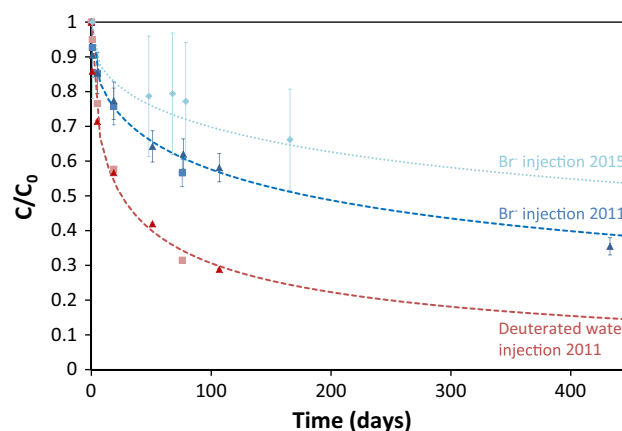


Fig. 4 Evolution of the bromide (blue) and deuterated water (red) concentration (represented in relative concentrations or C/C_0) measured in the water in Interval 1 (triangles) and 2 (rectangles) during the first tracer diffusion tests in 2011. For Interval 1 a second bromide test was performed in 2015 (light blue diamonds). The expanded error (95% confidence) on the relative concentrations of bromide and deuterated water is, respectively, 6–22% and 0.55%. The dashed lines indicate the modeled concentrations based on a pore diffusion coefficient of bromide ($2 \times 10^{-11} \text{ m}^2 \text{ s}^{-1}$) and of deuterium ($1.2 \times 10^{-10} \text{ m}^2 \text{ s}^{-1}$), obtained based on the data from the first tracer diffusion tests in 2011. The dotted line indicates the modeled concentration for bromide based on the pore diffusion coefficient derived from the 2nd bromide diffusion test in 2015 ($1 \times 10^{-11} \text{ m}^2 \text{ s}^{-1}$)

diffusion. This indicates that diffusive equilibration of the interval solution and the pore-water in the surrounding clay occurred without a significant contribution of advective transport [more details by Small (2015)]. The results of the first diffusion test also confirm the expected slower diffusion of bromide into the clay compared to deuterated water (Fig. 4), due to anion exclusion, i.e. the derived pore diffusion coefficient of deuterated water was $1.2 \times 10^{-10} \text{ m}^2 \text{ s}^{-1}$, while that of bromide was 6 times lower ($2 \times 10^{-11} \text{ m}^2 \text{ s}^{-1}$). Both diffusion coefficients are in the range of coefficients for, respectively, neutral and anionic species determined previously for Opalinus Clay, perpendicular and parallel to the bedding plane (Van Loon et al. 2004a, b; Alt-Epping et al. 2008; Wersin et al. 2008). Nevertheless, compared to pore diffusion coefficients estimated for the Pore-water Chemistry (PC) experiment in the Mont Terri rock laboratory, i.e. $2 \times 10^{-10} \text{ m}^2 \text{ s}^{-1}$ for deuterated water and $9 \times 10^{-11} \text{ m}^2 \text{ s}^{-1}$ for bromide (Alt-Epping et al. 2008; Tournassat et al. 2011) the pore diffusion coefficients for bromide and deuterium in the BN experiment appear to be slightly lower. The reason for this difference is not fully understood and may reflect the location of the BN experiment close to the sandy facies of the Opalinus Clay.

A second injection of Interval 1 with bromide in 2015 indicates that the diffusion rate of bromide has slowed down compared to the initial tests (Fig. 4). The pore

diffusion coefficient of bromide derived from this test is $1 \times 10^{-11} \text{ m}^2 \text{ s}^{-1}$. It is possible that this decrease in diffusion coefficient is a result of clogging of the filter screen either by creep of the Opalinus Clay, or as a result of microbial growth or mineral alteration resulting from previous nitrate reactivity in the interval. As the nitrate injection tests discussed in this paper were also performed 2–3 years after the first diffusion test, such clogging could have occurred in the meantime. Moreover, fitting of the nitrate evolution of these injection tests indicated indeed a slower diffusion of nitrate than expected based on the pore diffusion coefficient derived in the first diffusion test with bromide. Therefore, the diffusive behavior of anions in the intervals during the currently discussed tests is assumed to be similar to the behavior of bromide during the second diffusion test. Hence, the pore diffusion coefficient derived for bromide measured in 2015 ($1 \times 10^{-11} \text{ m}^2 \text{ s}^{-1}$) has been used to model the reactive transport behavior of nitrate and nitrite anions in the intervals during these injection tests.

3.3 Nitrate reactivity in the BN borehole

3.3.1 Microbial community

The microbiological analyses performed on the solutions sampled after saturation and equilibration of the intervals have revealed the presence of an active and versatile microbial population in the BN intervals, before the start of the injection tests. As no special precautions were taken to avoid contamination of the APW with exogenous microorganisms, this population could have been introduced during the first injection or installation of the downhole equipment.

ATP measurements suggest that 2×10^5 to 7×10^5 equivalents of active cells (EAC) per milliliter solution were present in all three intervals after saturation (Moors et al. 2012), based on the estimation that most bacterial cells contain 3 mM of ATP (Neidhart 1996). In addition, MPN analyses show the presence of viable microorganisms in every type of tested MPN medium, but especially prokaryotes capable of reducing nitrate (5×10^4 cells mL^{-1} or more). Autotrophic growth capacity is present but oligotrophic heterotrophy appears to be the preferred carbon metabolism of the residing communities in the BN borehole after saturation with APW.

After injection of Interval 1 and 2 with, respectively, 15 and 25 mM NaNO_3 , a large population of nitrate-reducing bacteria had developed in both intervals. These nitrate-reducing microorganisms included predominantly *Pseudomonas* strains but also strains from the genera *Cupriavidus*, *Pelomonas*, *Undibacterium*, *Acidovorax*, *Phenylobacterium*, *Brevundimonas* and *Corynebacterium*. When an easily oxidizable electron donor, such as acetate

or H_2 , was supplied as well, the microbial population changed towards a community consisting predominantly of species who prefer using such electron donor, e.g. species from genera *Acidovorax* (after pulse of acetate) and *Clostridium* (after pulse of H_2) (Moors et al. 2015a). These results indicate that the observed nitrate reduction in the intervals is (mainly) microbially mediated and that changes in the chemical composition of the interval solution are rapidly responded to by a shift in the microbial community.

3.3.2 Evolution of the nitrogenous species

When no additional electron donors were added (stage I in Fig. 5a, b), the nitrate concentration decreased only slowly in time after injection, more or less at the same rate in Interval 1 and 2. This slow decrease in nitrate concentration was mainly controlled by diffusion into the surrounding clay. Indeed, based on the pore diffusion coefficient derived for bromide ($1 \times 10^{-11} \text{ m}^2 \text{ s}^{-1}$; see Sect. 3.2), an estimation of the diffusion of nitrate from Interval 2 could be made (Fig. 6). The modeled data show that for this interval only $\sim 11\%$ of the total decrease of the nitrate concentration after equilibration of the interval solution was due to nitrate reactivity. A similar behavior was observed for Interval 1 (data not shown). Based on these modeled results, the reaction rate during stage I was similar in both intervals, i.e. 0.02 mM NO_3^- per day (Table 3).

The results of the chemical analyses indeed show that some microbial nitrate reduction has occurred during stage I: nitrite was produced in both intervals, though at a different rate. In Interval 1 (Fig. 5a), $\sim 2 \text{ mM NO}_2^-$ was produced through DNRN in the first few days after nitrate injection, with most of it being produced during equilibration of the injected solution with the remaining interval solution. On the other hand, in Interval 2 (Fig. 5b) a slower production of nitrite had occurred: during the first 70 days, 0.5 mM NO_2^- was produced. After this initial reaction in Interval 1, the nitrite concentration decreased slowly ($\sim 0.05 \text{ mM per day}$), until no more nitrite was detected ($< 0.1 \text{ mM}$) in the interval 54 days after injection (Fig. 5a). Similar to nitrate, this decrease can be attributed to diffusion into the clay, combined with nitrite reduction with natural electron donors. In neither of the intervals was ammonium produced, indicating that DNRA did not occur during this stage (Fig. 5a and b).

To assess the effect of easily oxidizable electron donors on the nitrate reduction, a pulse injection with either acetate (Interval 2) or H_2 (Interval 1) was performed (stage II in Fig. 5). About 2 days after pulse injection of Interval 2 with 4 mM acetate (Fig. 5b), the nitrate concentration decreased much faster (1.2 mM NO_3^- per day) than during

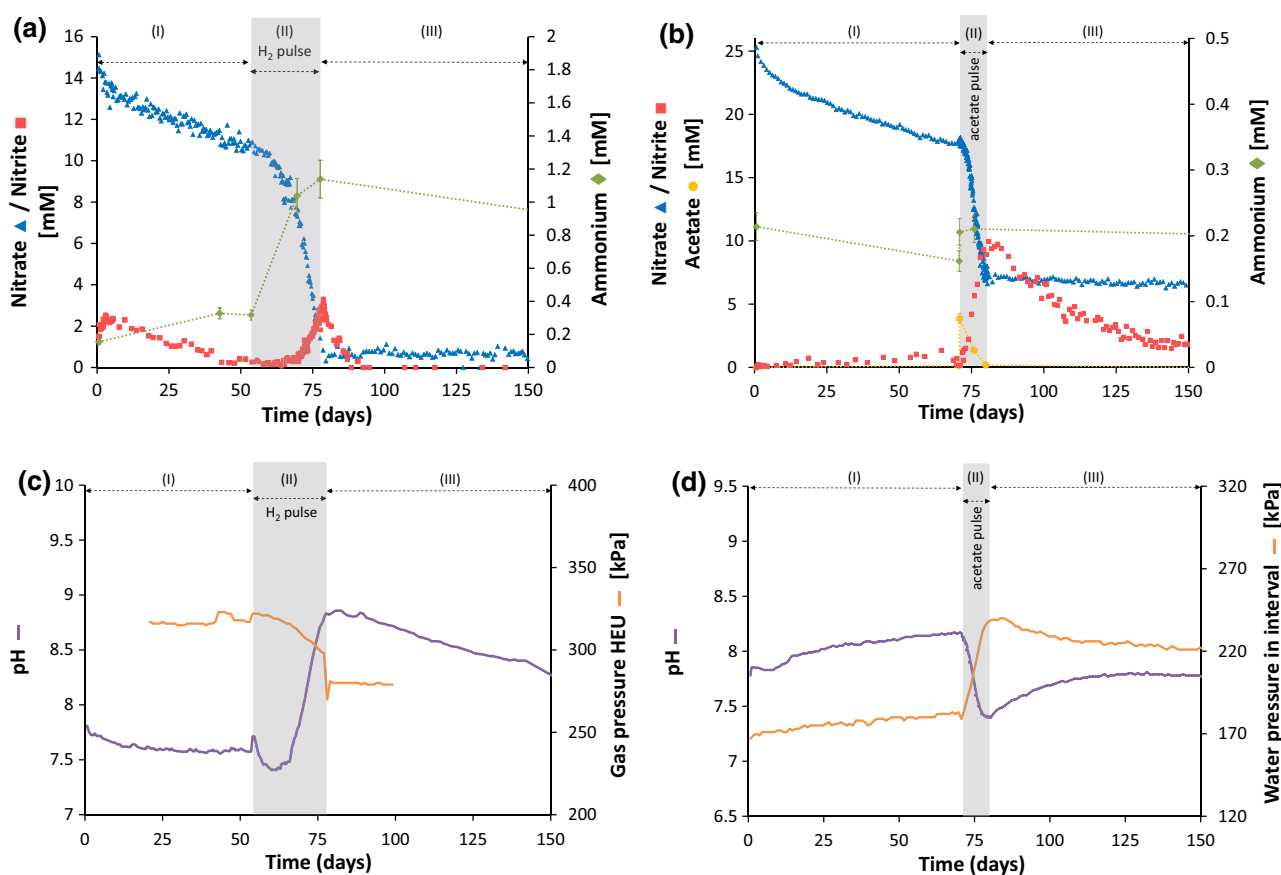


Fig. 5 Evolution of the nitrogenous species, pH and pressures after injection of Intervals 1 and 2 with nitrate during tests INT1_2014 and INT2_2013 (Table 2). **a, b** Evolution of nitrate (blue), nitrite (red) and ammonium (green) concentrations after injection of **a** Interval 1 with 15 mM NO_3^- only and pulse injection with H_2 after 54 days or **b** Interval 2 with 25 mM NO_3^- only and pulse injection with acetate after 70 days. **c** Evolution of the pH (purple) and gas pressure in the HEU (orange) after injection of Interval 1. **d** Evolution of the pH

(purple) and water pressure (green) in Interval 2. Stages I and III: nitrate reactivity without additional electron donor; Stage II: nitrate reactivity during pulse injection with either H_2 (Interval 1) or acetate (Interval 2). The errors on the values are 1% (pH), 10% ($[\text{NH}_4^+]$, $[\text{CH}_3\text{COO}^-]$), 7–15% ($[\text{NO}_3^-]$) and 15–20% ($[\text{NO}_2^-]$) for a 95% confidence interval. The uncertainties (95% confidence) on the pressures are 2 kPa (gas pressure) and 30 kPa (water pressure)

stage I, indicating that the microbial nitrate reduction rate was strongly enhanced due to the addition of acetate. During this fast decrease in nitrate concentration, the nitrite concentration increased strongly and both dissolved N_2O and N_2 were detected in the interval solution (Fig. 5b; Table 4). The observed increase in the water pressure confirms a fast production of gaseous compounds (Fig. 5d). When acetate was completely consumed in Interval 2 (Fig. 5b; end of stage II), $\sim 90\%$ of the nitrate present at the start of the pulse injection was reduced to nitrite (DNRN), while the remainder was likely consumed through denitrification and/or assimilation of N into biomass. Due to the high reaction rate, non-reactive transport of nitrate into the clay is considered to be less important.

After a pulse of H_2 (initially 1.2 mol of H_2 of which 7 mmol dissolved H_2 in interval solution) in Interval 1, no changes in the nitrate decrease rate nor in the concentration of reduced N species were observed during the first few

days (Fig. 5a; stage II). However, after 5 days the nitrate concentration started to decrease at a higher rate: during the first 9 days of the reaction at ~ 0.2 mM NO_3^- per day and later on at a faster rate (~ 0.7 mM NO_3^- per day). This maximum reaction rate is similar, although slightly lower, to the reaction rate in Interval 2 when acetate was injected. The reaction ceased when H_2 was removed from the circuit by bypassing the HEU. At the end of stage II, nitrite, ammonium and N_2 were detected in Interval 1 and in the gas phase of the HEU (Fig. 5a, c; Table 4), indicating that DNRN, nitrate reduction to ammonium, and denitrification had occurred. Production of N_2O during denitrification was not detected in the head space of the HEU vessel (Table 4). After 78 days, when H_2 was removed from the circuit, $\sim 34\%$ of the nitrate present at the start of the H_2 pulse was reduced to nitrite (DNRN) and 8% to ammonium, while the remainder of the fast decrease in the nitrate concentration can be attributed to denitrification and/or assimilation.

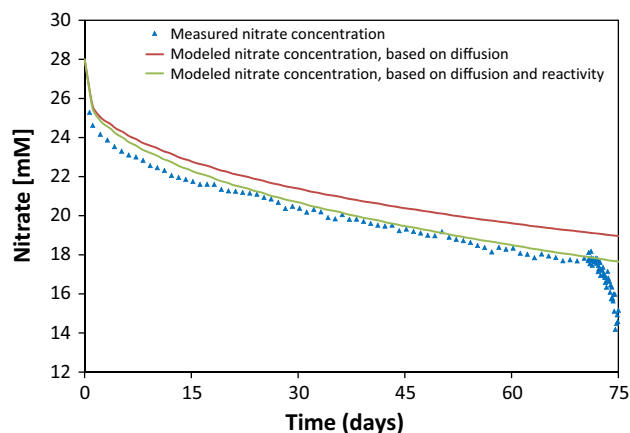


Fig. 6 Comparison of measured (blue triangles) and modeled concentrations of nitrate after injection in Interval 2 during stage I. The modeled results were obtained using the pore diffusion coefficient of bromide ($1.0 \times 10^{-11} \text{ m}^2 \text{ s}^{-1}$), derived from the second bromide tracer diffusion test carried out in 2015. Either only diffusion (red) or a combination of diffusion and nitrate reactivity (green) were taken into account in the model to fit the measured data

Again, non-reactive transport of nitrate into the clay can be considered of less importance due to the high nitrate reduction rate after addition of H_2 .

After complete consumption of H_2 (Interval 1) or acetate (Interval 2), the decrease in the nitrate concentration slowed down considerably (i.e. nearly stopped), as shown in Fig. 5a and b (stage III). At that time, the nitrite concentration had reached its maximal concentration and started to decrease at a rate of 0.2–0.3 mM NO_2^- per day in both Interval 1 and 2. This rate is faster than by diffusion only (based on the diffusive behavior of bromide) and therefore must have been caused by nitrite reduction. As nitrite can also be chemically reduced by dissolved organic matter (DOM) or pyrite (Bleyen et al. 2015, 2016), both a

Table 4 Total amount of gases (in mmoles) present in Interval 2 after complete consumption of acetate (after 78 days) and in Interval 1 after pulse injection with H_2 (after 78 days)

Gas species	Interval 1		Interval 2
	In solution	In gas phase	
N_2	0.012	3.5	1.7
N_2O	<0.2	<0.03	0.37
H_2	5.5	1.1×10^3	n.a.
O_2	<0.004	<0.6	n.a.
CO_2	0.1	0.02	n.a.

For Interval 1, the amount of gases present in solution and in the gas phase of the HEU is given. Due to the absence of a gas phase in Interval 2, the total amount of gases is only represented by the amount of dissolved gases in the interval solution

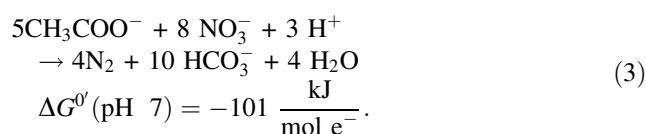
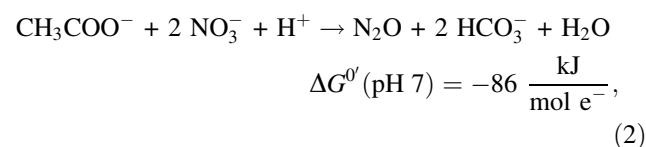
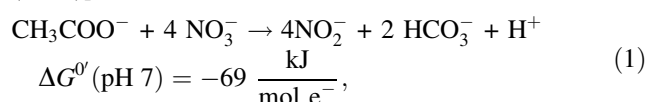
n.a. not analyzed

microbially mediated and a chemical reaction may have occurred simultaneously.

3.3.3 Consumption of electron donors

In the absence of easily oxidizable electron donors added to the intervals, host rock electron donors such as DOM, pyrite and/or other Fe^{2+} containing minerals have likely been oxidized during the observed reduction of nitrate (stage I) and nitrite (stage III). However, the geochemical data currently available do not allow us to select a hypothesis regarding these electron donors: no significant changes in TOC and TIC (Fig. 7) or in total dissolved iron, thiosulfate or sulfate concentration (data not shown) could be observed during these experimental stages.

After pulse injection of Interval 2 with acetate (Fig. 5b; stage II), the acetate concentration started to decrease rapidly, indicating that this compound was used as electron donor for the observed microbial nitrate reduction. This was expected as acetate is readily available for microbial consumption (Madigan et al. 2000) and its oxidation results in a high energy yield. Based on the production of reduced N species, the following reactions likely have occurred in Interval 2 after pulse injection with acetate [Eqs. (1)–(3); derived from Madigan et al. (2000)]:



The consumption of acetate is also confirmed by the evolution of the TIC and TOC concentrations (Fig. 7):

1. The TOC concentration decreased rapidly in Interval 2 during stage II (by $\sim 7.1 \text{ mmol C L}^{-1}$), confirming the consumption of organic C. This decrease is in agreement with the expected TOC decrease based on the acetate consumption ($\sim 7.5 \text{ mmol C L}^{-1}$; Fig. 7b).
2. A fast increase in the TIC concentration ($\sim 3.3 \text{ mmol C L}^{-1}$) can be observed in Interval 2 during acetate consumption, which is in agreement with reactions 1–3. However, based on the decrease in acetate, the TIC should have increased by $\sim 7.5 \text{ mmol C L}^{-1}$. Most likely, the remainder of the inorganic carbon has been released as gas (CO_2) and/or precipitated as

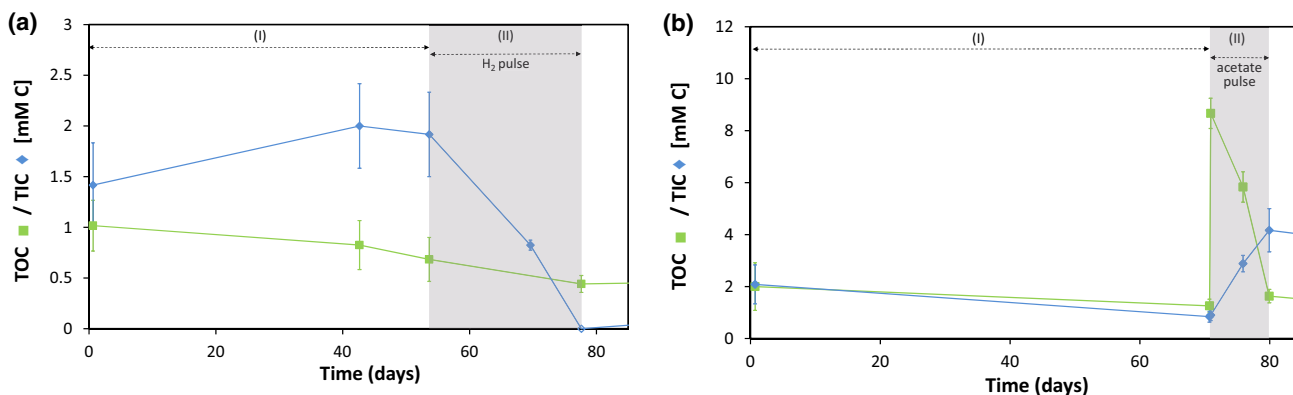


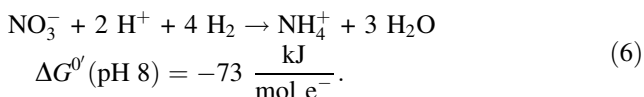
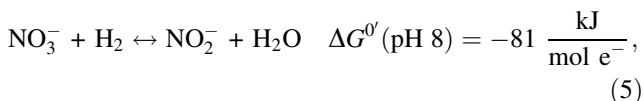
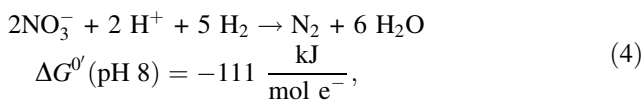
Fig. 7 Evolution of the TOC (green) and TIC (blue) concentrations in Interval 1 and 2 after initial injection with NO_3^- only and pulse injection with H_2 (a Interval 1; pulse after 54 days) or acetate

(b Interval 2; pulse after 70 days). Open markers indicate concentrations below detection limit, i.e. $0.4 \text{ mmol C L}^{-1}$ TIC. The error bars indicate the 95% confidence intervals

calcium carbonate. Indeed, the calcium concentration tended to decrease (by $\sim 1 \text{ mM}$; data not shown) during the consumption of acetate and related production of bicarbonate.

Based on the stoichiometry of the reactions and the amount of nitrite and gaseous N species which have been produced, 3.1 mM acetate (or 82% of the total initial acetate concentration in the interval) was used as electron donor. The remainder of acetate could have been used for biomass production. Non-reactive transport of acetate into the clay is considered to be less important due to the fast reaction rate.

In Interval 1, the gas pressure in the HEU (Fig. 5c; stage II) and the partial pressure of H_2 decreased considerably during the fast nitrate reduction after introduction of H_2 in the circuit, confirming the consumption of H_2 as the electron donor. The preferential use of H_2 compared to naturally present electron donors is also in agreement with the high amount of energy yielded during hydrogenotrophic nitrate reduction. Based on the produced N species, the following microbial reactions are expected to have taken place in Interval 1 after pulse injection with H_2 [Eqs. (4)–(6); derived from Madigan et al. (2000)]:



According to the decrease in the gas pressure (Fig. 5c), the composition of the gas phase in the HEU vessel after

stage II (Table 4) and the amount of dissolved H_2 in the Interval 1 solution, the total amount of H_2 in the interval has decreased by 107 mmol during stage II. Based on the stoichiometry of reactions 4–6, the amount of H_2 that is used as electron donor to produce NO_2^- , N_2 and NH_4^+ , is $\sim 40 \text{ mmol}$. The discrepancy between both values can be explained by either (or both): (1) Some leaks of H_2 in the equipment or borehole; (2) The large combined uncertainty on the amount of H_2 that is used as electron donor, which includes the large uncertainties on the calculated volume of the interval solution and of the gas phase. In addition, part of the produced N species have likely been missed, due to diffusion (nitrite, gaseous N species) or sorption (ammonium) onto the clay.

The hydrogenotrophic metabolism in Interval 1 also seems to be confirmed by the decrease in the TIC concentration (decrease $\geq 1.5 \text{ mmol C L}^{-1}$; Fig. 7a), as hydrogenotrophs are generally autotrophs who fix inorganic carbon into biomass (Madigan et al. 2000).

3.3.4 Evolution of pH and redox potential

During stage I, the evolution of the pH in both intervals seems to differ slightly (Fig. 5c, d), possibly linked to the observed differences in the microbial reactions prevailing in each interval. In Interval 1, the pH decreased in the first weeks after injection until it reached a stable value at a pH of ~ 7.6 when the H_2 pulse was performed (Fig. 5c). On the other hand, in Interval 2, a small but steady increase in pH (total increase of $0.3\text{--}0.4$ pH units) was observed during the first 70 days of the test (Fig. 5).

When easily oxidizable electron donors were added to the intervals, the pH evolution was highly contrasting between Interval 1 and 2 as the pH evolved in opposite directions, depending on the microbial reactions at work. During the fast microbial nitrate reduction with acetate

observed in Interval 2 (stage II), a clear and fast decrease in pH was observed (by ~ 0.75 pH units; Fig. 5d), which is in agreement with the observed dominant microbial reaction, i.e. DNRR [Eq. (1)]. When the gas in the HEU vessel in Interval 1 was replaced by H_2 , the pH first increased by 0.1 pH units (Fig. 5c), most likely because of the CO_2 degassing from the solution upon removal of CO_2 present in the Ar gas phase equilibrated with the interval solution. Afterwards, the pH initially decreased slightly during the lag phase until it reached a new equilibrium. As from the start of the fast hydrogenotrophic reactions, the pH increased significantly (by ~ 1.4 pH units in total; Fig. 5c), which is corresponding to reactions 4 to 6 and with autotrophic CO_2 consumption. After complete consumption of the added electron donors (stage III), the initial pH of the interval solutions was slowly regained.

The redox potential of the interval solutions was monitored online as well, providing data on the evolution of the mixed redox potential, i.e. the resultant potential of all redox couples operating in these solutions (Bohn 1971). After pulse injection with acetate, the measured redox potential of the solution in Interval 2 increased by ~ 100 mV during the fast microbial nitrate reduction to mainly nitrite (from +38 to +140 mV with respect to the standard hydrogen electrode). In contrast, in Interval 1, the addition of H_2 resulted in a severe decrease of the measured redox potential, i.e. a decrease of ~ 470 mV (from +97 to -372 mV with respect to the standard hydrogen electrode). As the theoretical redox potential of the $H_2/2H^+$ redox couple is -489 mV (at pH 8 and at a partial pressure of 320 kPa), the decrease in the measured redox potential can almost entirely be attributed to the addition of H_2 to the system. During the pulse of H_2 , the measured redox potential did not vary significantly (± 20 mV), although also in this test a considerable amount of nitrite was produced. This suggests that the mixed redox potential in the solution of Interval 1 was largely controlled by the $H_2/2H^+$ redox couple due to the rather large quantities of H_2 in the system. Any changes in the redox potential due to microbial nitrate reduction could therefore not be observed.

4 Discussion

4.1 Nitrate reactivity without addition of electron donors

Without addition of electron donors, a slow microbial nitrate reduction was observed, likely using electron donors present in the interval solution or in the surrounding clay (DOM, pyrite, or other Fe^{2+} containing minerals). However, the current chemical data of our experiments do not allow us to determine which electron donor was used

during this slow reaction. As a previous study of the microbial community and metabolic activity in borehole water in the Opalinus Clay using metagenomics suggested the use of sedimentary organic carbon as electron donor by sulfate reducers (Bagnoud et al. 2016), further investigation of the microbial community present in the intervals of the BN experiment might provide more insights into the observed slow microbial nitrate reduction.

The slow nitrate reactivity is in agreement with the results of previously reported lab tests during which nitrate reduction was studied in clay slurries or waters (Boom Clay or Callovo-Oxfordian Clay) or with individual clay electron donors (e.g. pyrite, DOM) (Libert et al. 2011; Mariën et al. 2011; Bleyen et al. 2015, 2016). Furthermore, the observed in situ reaction rate is similar to the rate observed during previous injection tests in the BN experiment, e.g. 0.04 mM NO_3^- per day after injection of Interval 1 with 1.5 mM $NaNO_3$ (code INT1_2011; Tables 2 and 3). In the absence of a sufficient amount of easily oxidizable electron donors, the microbial activity seems thus to be limited by the bioavailability and biodegradability of the electron donors and the rate at which electrons can be provided by the surrounding clay.

In both Interval 1 and 2, nitrate was reduced mainly to nitrite (DNRR), though at a different rate. Furthermore, some nitrite was slowly reduced in Interval 1. The strongly contrasting evolution of the pH in both intervals seems to confirm the previously discussed small differences in metabolic pathways and rates. These differences between Interval 1 and 2 during stage I are likely due to the history of both intervals or to small heterogeneities in the clay formation surrounding each of the intervals, which could have caused small differences in the microbial population present in the interval, and in the availability of electron donors.

4.2 Impact of additional electron donors on the in situ nitrate reactivity

In the presence of acetate and H_2 , which are both bioavailable and energetically favorable electron donors, the microbial populations present in the intervals responded rather quickly, triggering a strong increase in the nitrate reduction kinetics. In Interval 1, introduction of dissolved H_2 resulted in a longer lag phase compared to the addition of acetate in Interval 2 (5 and 2 days respectively) and an initially slower nitrate reduction before the reaction rate picked up. This suggests that the microbial community present in Interval 1 required more time to adapt to the use of H_2 and/or autotrophy compared to the use of acetate as electron donor. As Interval 2 had already been injected with acetate previously during preliminary tests, this

community was already adapted to a heterotrophic metabolism, which explains its faster response.

The maximal reaction rates were however similar for both electron donors and were up to 60 times higher than the rate observed when the in situ available electron donors were used (Table 3). Furthermore, these reaction rates are also similar to the rates observed during previous injection tests (Table 2) with nitrate and acetate in Interval 2 (i.e. 0.8–1 mM NO_3^- per day). The observed stimulation of the nitrate reduction by acetate and H_2 is in agreement with previous lab tests studying nitrate reactivity in sediments (Devlin et al. 2000; Libert et al. 2011).

In both tests with added electron donors, DNRN and denitrification were the dominant metabolic pathways, which was expected as they are thermodynamically favored over DNRA. In Interval 2 (pulse of acetate), this fast nitrate reduction resulted in an increase in the redox potential of the interval solution, which is in agreement with previously reported lab experiments (Percheron et al. 1998), where an increase in redox potential was observed during sulfide-dependent DNRN and denitrification.

Nitrite accumulated in both tests through DNRN, due to limitations in the amount of electron donor compared to that of the electron acceptor, rendering nitrate reduction more favorable compared to nitrite reduction. Indeed, the C/N ratio after pulse injection of Interval 2 with acetate was 0.4, which is lower than the ratio required to prevent nitrite accumulation and stimulate denitrification (i.e. ~ 1.2) as was observed during lab experiments (Almeida et al. 1995; Oh and Silverstein 1999). Furthermore, nitrate reductase is reduced preferentially by electrons derived from acetate oxidation compared to nitrite reductase, which also favors the DNRN reaction over the subsequent denitrification pathway (Almeida et al. 1995; Oh and Silverstein 1999), especially when acetate is limited. Nevertheless, the accumulation of nitrite in the interval (up to ~ 10 mM) did not result in inhibition of the microbial reactivity, as was observed for higher concentrations of nitrite (>20 mM) during lab tests (Almeida et al. 1995; Parmentier et al. 2014).

In Interval 1 (pulse of H_2), nitrite accumulated as well during the fast hydrogenotrophic nitrate reduction, although to a lesser extent than in Interval 2 (pulse of acetate). This accumulation can again be explained by a limitation of the amount of electron donor (i.e. H_2) compared to the available nitrate, due to the solubility (and thus bioavailability) limit of H_2 . Indeed, previously performed studies (Chang et al. 1999; Haugen et al. 2002; Karanasios et al. 2011) indicated that a decrease of the dissolved H_2 concentration below a certain threshold (depending on the microbial species and other environmental conditions) would result in a decrease in denitrification rate. Initially, limitation of the hydrogen availability would only inhibit

nitrite reductase, resulting in accumulation of nitrite. Lowering the dissolved H_2 concentration even further would also inhibit the hydrogenotrophic nitrate reduction (Chang et al. 1999).

4.3 Factors influencing the microbial reactions and their rates

The microbial nitrate reduction rates and dominant metabolic pathways observed in the described experiments do not seem to be dependent on the nitrate concentration: similar rates in both intervals and after injection of 1 to 25 mM NO_3^- were observed during the preliminary and currently discussed injection tests. Rather the bioavailability and energy yielded by oxidation of the electron donor seem to determine the extent of the nitrate reactivity and the metabolic pathways followed. Note that the reaction rates in the near field of a geological repository for nitrate-containing bituminized radioactive waste are likely also controlled by the release rates of nitrate and acetate from the waste and by the production rate of H_2 in the repository (by anaerobic corrosion of steel and radiolysis).

4.4 Implications for geological disposal of nitrate-containing waste

The results presented in this paper indicate that microbial nitrate-dependent oxidation of electron donors naturally present in the Opalinus Clay is possible, though occurs only at a slow rate. Acetate leached from the bituminized waste and H_2 produced by radiolysis of bitumen and water and by anaerobic corrosion of the metallic waste drums could significantly enhance the reaction kinetics. Furthermore, because of the preferential use of these electron donors compared to naturally present electron donors, we do not expect that the reducing capacity of the clay formation would decrease significantly if sufficient amounts of acetate and H_2 are available. However, a substantial microbially mediated reduction of nitrate with acetate has been shown to increase the redox potential of the pore-water. This could result in less reducing conditions in the pore-water, which might hinder the reduction of redox-sensitive radionuclides (e.g. Se, Tc, U, Np, Pu, etc.), in turn favoring the migration of these radionuclides in the host rock (Oremland et al. 1999; De Cannière et al. 2010).

Furthermore, depending on the electron donor (acetate or H_2), the denitrification reaction would lead to either a net gas production (of N_2 in case of heterotrophic reaction with acetate) or gas consumption (of H_2 in case of hydrogenotrophic reaction). In case the gas generation rate would be higher than its dissipation rate by diffusive transport of the dissolved gas, the former pathway with N_2

production would result in the formation of a free gas phase, and might therefore give rise to an overpressure with a (local) gas breakthrough, possibly affecting the radionuclide migration. On the other hand, the consumption of H_2 produced in a repository for bituminized ILW would prevent a gas pressure build-up in the repository and thus a gas-related perturbation of the clay.

5 Conclusions

Upon geological disposal of nitrate-containing bituminized ILW in a clay formation, this type of waste will start to take up water, leading to the dissolution of the hygroscopic salts (e.g. $NaNO_3$) in the bitumen matrix and subsequently to leaching of $NaNO_3$ into the surrounding host rock. Although it remains uncertain whether nitrate-reducing microorganisms can be active under the prevailing harsh conditions for microbes in and around a repository (i.e. high pH, high ionic strength and lack of free space), microbial activity cannot be ruled out. The results obtained by the BN experiment, an in situ experiment in the Opalinus Clay, provide insights in the biogeochemical behavior of nitrate in a clay formation surrounding a repository for nitrate-containing bituminized ILW, in case active microbial species would be present. This paper focused on two injection tests performed in the BN borehole, during which microbial nitrate reactivity was investigated in the presence or in the absence of additional electron donors relevant for such a disposal concept, i.e. acetate (a key bitumen degradation product) and H_2 (originating from radiolysis and anaerobic steel corrosion).

The results of these tests indicate that nitrate reacts quickly at near neutral pH if external sources of bioavailable and energetically favorable electron donors, such as acetate or H_2 , are present and if enough space and water are available in the system. When only naturally present electron donors are available, nitrate mainly diffuses into the surrounding clay, although also some microbial nitrate reduction (mainly to nitrite) occurs at a slow rate. Both in the presence of H_2 and acetate, nitrite and nitrogenous gases were predominantly produced, although some ammonium production could also be observed when H_2 was added. The microbial nitrate reduction rates and dominant metabolic pathways observed in the described experiments are likely depending on the bioavailability and energy-producing capacity of the electron donor present in the system.

The observed reduction of nitrate seems to have an impact on the redox conditions in the pore-water (i.e. an increase of the redox potential), which might affect the migration of radionuclides in the host rock. Furthermore, depending on the electron donor type, denitrification could

lead to either a net gas consumption (i.e. oxidation of H_2) or production (i.e. formation of N_2) in the repository. The latter might cause an additional stress on the clay, which could lead to gas-related perturbations of the host rock. The observed processes of microbially mediated nitrate reduction should be taken into account during future reactive transport modeling of the migration of (redox-sensitive) radionuclides released from bituminized ILW in the host rock.

Further research is necessary to study the impact of the observed microbial nitrate reduction on the redox state of redox-sensitive radionuclides. In addition, the nitrate reduction rates and production of N species should be investigated further under more realistic repository conditions (e.g. high pH imposed by the use of cementitious materials), to determine the effect of such conditions on the microbial activity and the nitrate reactivity.

Acknowledgements This work is undertaken in close co-operation with Swisstopo, the operator of the rock laboratory and the project management team at Mont Terri, namely Christophe Nussbaum and Thierry Theurillat. Financial support was provided by the Mont Terri Consortium. Joe Small acknowledges funding by the U.K. Natural Environment Research Council (NERC) BIGRAD consortium through Grant No. NE/H007768/1 and the National Nuclear Laboratory. Gesine Lorenz (Hydroisotop GmbH) and Elke Jacobs (SCK•CEN) are acknowledged for performing the gas analyses. In addition, the technical assistance of Wim Verwimp and Patrick Boven (SCK•CEN) is greatly appreciated. Finally, we thank Dr. Marc Parmentier (French Geological Survey BRGM, Orléans, France) and Dr. Alexandre Bagnoud (Stream Biofilm and Ecosystem Research Laboratory at EPFL, Lausanne, Switzerland) for their constructive comments and suggestions.

Open Access This article is distributed under the terms of the Creative Commons Attribution 4.0 International License (<http://creativecommons.org/licenses/by/4.0/>), which permits unrestricted use, distribution, and reproduction in any medium, provided you give appropriate credit to the original author(s) and the source, provide a link to the Creative Commons license, and indicate if changes were made.

References

- Almeida, J., Reis, M., & Carrondo, M. (1995). Competition between nitrate and nitrite reduction in denitrification by *Pseudomonas fluorescens*. *Biotechnology and Bioengineering*, 46, 476–484.
- Alt-Epping, P., Gimmi, T., & Waber, N. (2008). Porewater chemistry (PC) experiment: Reactive transport simulations. Mont Terri Technical Report, TR 07-03, Federal Office of Topography (swisstopo), Wabern, Switzerland. www.mont-terri.ch.
- ANDRA (2005). Dossier 2005. ANDRA research on the geological disposal of high-level long-lived radioactive waste. Results and perspectives. ANDRA report, ANDRA, Châtenay-Malabry, France.
- Bagnoud, A., de Bruijn, I., Andersson, A. F., Diomidis, N., Leupin, O. X., Schwyn, B., et al. (2016). A minimalistic microbial food web in an excavated deep subsurface clay rock. *FEMS Microbiology Ecology*, 92, fiv138.

- Bertani, G. (1951). STUDIES ON LYSOGENESIS I: The mode of phage liberation by lysogenic *Escherichia coli*. *Journal of Bacteriology*, *62*, 293–300.
- Bleyen, N., Smets, S., Albrecht, A., De Cannière, P., Schwyn, B., Wittebroodt, C., & Valcke, E. (in preparation) Use of non-destructive on-line spectrophotometric and pH monitoring to assess in situ microbial nitrate and nitrite reduction. *International Journal of Environmental Analytical Chemistry*.
- Bleyen, N., Smets, S., & Valcke, E. (2011). BN Experiment: Status and raw data report of phases 15 and 16. Mont Terri Technical Note, TN 2009-49, Federal Office of Topography (swisstopo), Wabern, Switzerland. www.mont-terri.ch.
- Bleyen, N., Vasile, M., Bruggeman, C., & Valcke, E. (2015). Abiotic and biotic nitrate and nitrite reduction by pyrite. In: *Proceedings of the Clays in Natural and Engineered Barriers for Radioactive Waste Confinement Conference*, P-06-16.
- Bleyen, N., Vasile, M., Marien, A., Bruggeman, C., & Valcke, E. (2016). Assessing the oxidising effect of NaNO₃ and NaNO₂ from disposed EUROBITUM bituminised waste on the dissolved organic matter in Boom Clay. *Applied Geochemistry*, *68*, 29–38.
- Bohn, H. L. (1971). Redox potentials. *Soil Science*, *112*, 39–45.
- Bossart, P., Bernier, F., Birkholzer, J., Bruggeman, C., Connolly, P., Dewonck, S., Fukaya, M., Herfort, M., Jensen, M., Matray, J-M., Mayor, J. C., Moeri, A., Oyama, T., Schuster, K., Shigeta, N., Vietor, T., & Wiczorek, K. (2017). Mont Terri rock laboratory, 20 years: introduction, geology and overview of papers included in the Special Issue. *Swiss Journal of Geosciences*, *110*. doi:10.1007/s00015-016-0236-1 (this issue).
- Chang, C. C., Tseng, S. K., & Huang, H. K. (1999). Hydrogenotrophic denitrification with immobilized *Alcaligenes eutrophus* for drinking water treatment. *Bioresource technology*, *69*, 53–58.
- Courdouan, A., Christl, I., Meylan, S., Wersin, P., & Kretzschmar, R. (2007). Characterization of dissolved organic matter in anoxic rock extracts and in situ pore water of the Opalinus Clay. *Applied Geochemistry*, *22*, 2926–2939.
- De Canniere, P., Schwarzbauer, J., & Van Geet, M. (2008). Leaching experiments and analyses of organic matter released by the materials used for the construction of Porewater Chemistry experiment at Mont Terri Rock Laboratory. *Mont Terri Technical Note*, TN 2005-12. Federal Office of Topography (swisstopo), Wabern, Switzerland. www.mont-terri.ch.
- De Cannière, P., Maes, A., Williams, S., Bruggeman, C., Beauwens, T., Maes, N., Cowper, M. (2010). Behaviour of selenium in Boom Clay. *External Report, SCK•CEN-ER-120*, 328 pp. SCK•CEN, Boeretang 200, 2400 Mol, Belgium.
- De Cannière, P., Schwarzbauer, J., Höhener, P., Lorenz, G., Salah, S., Leupin, O., et al. (2011). Biogeochemical processes in a clay formation in situ experiment: part C—organic contamination and leaching data. *Applied Geochemistry*, *26*, 967–979.
- De Craen, M., Wang, L., Van Geet, M., & Moors, H. (2004). Geochemistry of Boom Clay pore water at the Mol site. Status 2004. *Scientific report, SCK•CEN-BLG-990*, 179 pp. SCK•CEN, Mol, Belgium.
- DeSantis, T. Z., Hugenholtz, P., Larsen, N., Rojas, M., Brodie, E. L., Keller, K., et al. (2006). Greengenes, a chimera-checked 16S rRNA gene database and workbench compatible with ARB. *Applied and Environmental Microbiology*, *72*, 5069–5072.
- Devlin, J., Eedy, R., & Butler, B. (2000). The effects of electron donor and granular iron on nitrate transformation rates in sediments from a municipal water supply aquifer. *Journal of Contaminant Hydrology*, *46*, 81–97.
- Eichinger, F., Lorenz, G., & Eichinger, L. (2011). WS-H Experiment: Water sampling from borehole BWS-H2—Report on physical-chemical and isotopic analyses. *Mont Terri Technical Note*, TN 2010-49. Federal Office of Topography (swisstopo), Wabern, Switzerland. www.mont-terri.ch.
- Garthright, W., & Blodgett, R. (2003). FDA's preferred MPN methods for standard, large or unusual tests, with a spreadsheet. *Food Microbiology*, *20*, 439–445.
- Harrington, J., Milodowski, A., Graham, C., Rushton, J., & Cuss, R. (2012). Evidence for gas-induced pathways in clay using a nanoparticle injection technique. *Mineralogical Magazine*, *76*, 3327–3336.
- Hauck, S., Benz, M., Brune, A., & Schink, B. (2001). Ferrous iron oxidation by denitrifying bacteria in profundal sediments of a deep lake (Lake Constance). *FEMS Microbiology Ecology*, *37*, 127–134.
- Haugen, K., Semmens, M., & Novak, P. (2002). A novel in situ technology for the treatment of nitrate contaminated groundwater. *Water Research*, *36*, 3497–3506.
- Heylen, K., Vanparys, B., Wittebolle, L., Verstraete, W., Boon, N., & De Vos, P. (2006). Cultivation of denitrifying bacteria: optimization of isolation conditions and diversity study. *Applied and Environmental Microbiology*, *72*, 2637–2643.
- Jørgensen, C. J., Jacobsen, O. S., Elberling, B., & Aamand, J. (2009). Microbial oxidation of pyrite coupled to nitrate reduction in anoxic groundwater sediment. *Environmental Science and Technology*, *43*, 4851–4857.
- Karanasios, K., Michailides, M., Vasiliadou, I., Pavlou, S., & Vayenas, D. (2011). Potable water hydrogenotrophic denitrification in packed-bed bioreactors coupled with a solar-electrolysis hydrogen production system. *Desalination and Water Treatment*, *33*, 86–96.
- Klindworth, A., Pruesse, E., Schweer, T., Peplies, J., Quast, C., Horn, M., et al. (2012). Evaluation of general 16S ribosomal RNA gene PCR primers for classical and next-generation sequencing-based diversity studies. *Nucleic Acids Research*, *2012*, 1–11.
- Libert, M., Bildstein, O., Esnault, L., Jullien, M., & Sellier, R. (2011). Molecular hydrogen: An abundant energy source for bacterial activity in nuclear waste repositories. *Physics and Chemistry of the Earth, Parts A/B/C*, *36*, 1616–1623.
- Lide, D. R., & Frederikse, H. P. R. (1995). *CRC handbook of chemistry and physics*. Boca Raton: CRC Press.
- Madigan, M. T., Martinko, J. M., & Parker, J. (2000). *Brock biology of microorganisms*. Upper Saddle River: Prentice-Hall.
- Mallants, D., Jacques, D., & Perko, J. (2007). Modelling multi-phase flow phenomena in concrete barriers used for geological disposal of radioactive waste. *Proceedings of the 11th International Conference on Environmental Remediation and Radioactive Waste Management* (pp. 741–749). American Society of Mechanical Engineers.
- Mariën, A., Bleyen, N., Aerts, S., & Valcke, E. (2011). The study of abiotic reduction of nitrate and nitrite in Boom Clay. *Physics and Chemistry of the Earth*, *36*, 1639–1647.
- Moors, H., Geissler, A., Boven, P., Selenska-Pobell, S., & Leys, N. (2012). BN experiment: intermediate results of the microbiological analyses. *Mont Terri Technical Note*, TN 2011-39. Federal Office of Topography (swisstopo), Wabern, Switzerland. www.mont-terri.ch.
- Moors, H., Bleyen, N., Ahmed, M., Boven, P., Leys, N., Valcke, E., Cherkouk, A., Stroes-Gascoyne, S., Nussbaum, C., Schwyn, B., Albrecht, A., Wittebroodt, C., Small, J., & De Cannière, P. (2015a). The Bitumen-Nitrate-Clay Interaction Experiment at the Mont Terri Rock Laboratory: Response of microbial communities to additions of nitrate and acetate. *Proceedings to the Clays in Natural and Engineered Barriers for Radioactive Waste Confinement Conference*, O-06A-03.
- Moors, H., Mysara, M., Bleyen, N., Cherkouk, A., Boven, P., & Leys, N. (2015b). BN Experiment: Results of the microbiological analyses obtained during phase 19 & 20. *Mont Terri Technical Note*, TN 2015-72. Federal Office of Topography (swisstopo), Wabern, Switzerland. www.mont-terri.ch.

- Mysara, M., Leys, N., Raes, J., & Monsieurs, P. (2015a). NoDe: a fast error-correction algorithm for pyrosequencing amplicon reads. *BMC Bioinformatics*, *16*, 1–10.
- Mysara, M., Saeys, Y., Leys, N., Raes, J., & Monsieurs, P. (2015b). CATCh, an ensemble classifier for chimera detection in 16S rRNA sequencing studies. *Applied and Environmental Microbiology*, *81*, 1573–1584.
- Mysara, M., Leys, N., Raes, J., & Monsieurs, P. (2016). IPED: a highly efficient denoising tool for Illumina MiSeq Paired-end 16S rRNA gene amplicon sequencing data. *BMC Bioinformatics*, *17*, 1–11.
- Neidhart, F. (1996). *Escherichia coli and Salmonella typhimurium: Cellular and molecular biology*. Washington: ASM Press.
- Nussbaum, C., Kloppenburg, A., Caër, T., & Bossart, P. (2017). Tectonic evolution around the Mont Terri rock laboratory, northwestern Swiss Jura: constraints from kinematic forward modelling. *Swiss Journal of Geosciences*, *110*. doi:10.1007/s00015-016-0248-x (this issue).
- Oh, J., & Silverstein, J. (1999). Acetate limitation and nitrite accumulation during denitrification. *Journal of Environmental Engineering*, *125*, 234–242.
- Oremland, R. S., Blum, J. S., Bindi, A. B., Dowdle, P. R., Herbel, M., & Stolz, J. F. (1999). Simultaneous reduction of nitrate and selenate by cell suspensions of selenium-respiring bacteria. *Applied and Environmental Microbiology*, *65*, 4385–4392.
- Parmentier, M., Ollivier, P., Jouliau, C., Albrecht, A., Hadi, J., Greneche, J.-M., et al. (2014). Enhanced heterotrophic denitrification in clay media: the role of mineral electron donors. *Chemical geology*, *390*, 87–99.
- Pearson, F. J. (1999). WS-A experiment: artificial waters for use in laboratory and field experiments with Opalinus Clay. Status June 1998. *Mont Terri Technical Note*, TN 1999-31. Federal Office of Topography (swisstopo), Wabern, Switzerland. www.mont-terri.ch.
- Pearson, F. J., Arcos, D., Bath, A., Boisson, J. Y., Fernández, A. M., Gabler, H. E., Gaucher, E., Gautschi, A., Griffault, L., Hernán, P., & Waber, H. N. (2003). Mont Terri Project - Geochemistry of water in the Opalinus Clay formation at the Mont Terri Rock Laboratory. *Federal Office for Water and Geology Geology Series*, No. 5. Federal Office of Topography (swisstopo), Wabern, Switzerland. www.mont-terri.ch.
- Percheron, G., Michaud, S., Bernet, N., & Moletta, R. (1998). Nitrate and nitrite reduction of a sulphide-rich environment. *Journal of Chemical Technology and Biotechnology*, *72*, 213–220.
- Phister, A., Jaeggi, D., & Nussbaum, C. (2010). Drilling campaign of phase 15: drilling data, photo documentation and drill core documentation. *Mont Terri Technical Note*, TN 2010-38. Federal Office of Topography (swisstopo), Wabern, Switzerland. www.mont-terri.ch.
- Reasoner, D., & Geldreich, E. (1985). A new medium for the enumeration and subculture of bacteria from potable water. *Applied and Environmental Microbiology*, *49*, 1–7.
- Schloss, P. D., & Westcott, S. L. (2011). Assessing and improving methods used in operational taxonomic unit-based approaches for 16S rRNA gene sequence analysis. *Applied and Environmental Microbiology*, *77*, 3219–3226.
- Small, J. (2015). BN Experiment: GRM biogeochemical modelling during Phase 18 and Phase 19 of the Bitumen-Nitrate-Clay interaction experiment. *Mont Terri Technical Note*, TN 2013-44. Federal Office of Topography (swisstopo), Wabern, Switzerland. www.mont-terri.ch.
- Small, J., Nykyri, M., Helin, M., Hovi, U., Sarlin, T., & Itävaara, M. (2008). Experimental and modelling investigations of the biogeochemistry of gas production from low and intermediate level radioactive waste. *Applied Geochemistry*, *23*, 1383–1418.
- Smith, P., Cornélias, B., Capouet, M., Depaus, C., & Van Geet, M. (2009). The long-term safety assessment methodology for the geological disposal of radioactive waste. *SFCI level 4 report*, NIRON-TR 2009-14 E, ONDRAF/NIRAS, Brussels, Belgium.
- Thury, M., & Bossart, P. (1999). The Mont Terri Rock Laboratory, a new international research project in a Mesozoic shale formation in Switzerland. *Engineering Geology*, *52*, 347–359.
- Tournassat, C., Alt-Epping, P., Gaucher, E. C., Gimmi, T., Leupin, O. X., & Wersin, P. (2011). Biogeochemical processes in a clay formation in situ experiment: Part F—reactive transport modelling. *Applied Geochemistry*, *26*, 1009–1022.
- Valcke, E., Sneyers, A., & Van Iseghem, P. (2000a). The effect of radiolytic degradation products of Eurobitum on the solubility and sorption of Pu and Am in Boom Clay. *Proceedings to the Materials Research Society Symposium*, volume 663 (pp. 141–149). Cambridge University Press.
- Valcke, E., Sneyers, A., & Van Iseghem, P. (2000b). The long-term behavior of bituminized waste in a deep clay formation. *Proceedings to the Safewaste Conference*, volume 2 (pp. 562–573). Société française d'énergie nucléaire.
- Valcke, E., Marien, A., & Van Geet, M. (2009). The methodology followed in Belgium to investigate the compatibility with geological disposal of Eurobitum bituminized intermediate level radioactive waste. *Proceedings of the Materials Research Society Symposium*, volume 1193 (pp. 105–116). Cambridge University Press.
- Van Loon, L. R., Soler, J. M., Müller, W., & Bradbury, M. H. (2004a). Anisotropic diffusion in layered argillaceous rocks: a case study with Opalinus Clay. *Environmental Science & Technology*, *38*, 5721–5728.
- Van Loon, L. R., Wersin, P., Soler, J., Eikenberg, J., Gimmi, T., Hernán, P., Dewonck, S., & Savoye, S. (2004b). In-situ diffusion of HTO, $^{22}\text{Na}^+$, Cs^+ and I^- in Opalinus Clay at the Mont Terri underground rock laboratory. *Radiochimica Acta/International Journal for Chemical Aspects of Nuclear Science and Technology*, *92*, 757–763.
- Wersin, P., Soler, J., Van Loon, L., Eikenberg, J., Baeyens, B., Grolimund, D., et al. (2008). Diffusion of HTO, Br^- , I^- , Cs^+ , $^{85}\text{Sr}^{2+}$ and $^{60}\text{Co}^{2+}$ in a clay formation: results and modelling from an in situ experiment in Opalinus Clay. *Applied Geochemistry*, *23*, 678–691.
- Wilhelm, E., Battino, R., & Wilcock, R. J. (1977). Low-pressure solubility of gases in liquid water. *Chemical Reviews*, *77*, 219–262.
- Wouters, K., Moors, H., Boven, P., & Leys, N. (2013). Evidence and characteristics of a diverse and metabolically active microbial community in deep subsurface clay borehole water. *FEMS Microbiology Ecology*, *86*, 458–473.
- Xiong, Z., Xing, G., & Zhu, Z. (2006). Water dissolved nitrous oxide from paddy agroecosystem in China. *Geoderma*, *136*, 524–532.
- Zhang, Y.-C., Slomp, C. P., Broers, H. P., Bostick, B., Passier, H. F., Bottcher, M. E., et al. (2012). Isotopic and microbiological signatures of pyrite-driven denitrification in a sandy aquifer. *Chemical Geology*, *300*, 123–132.
- Zhang, J., Dong, H., Liu, D., & Agrawal, A. (2013). Microbial reduction of Fe(III) in smectite minerals by thermophilic methanogen *Methanothermobacter thermoautotrophicus*. *Geochimica et Cosmochimica Acta*, *106*, 203–215.

Natural gas extraction and artificial gas injection experiments in Opalinus Clay, Mont Terri rock laboratory (Switzerland)

Agnès Vinsot¹ · C. Anthony J. Appelo² · Mélanie Lundy¹ · Stefan Wechner³ · Cristelle Cailteau-Fischbach^{1,4,5} · Philippe de Donato⁴ · Jacques Pironon⁴ · Yanick Lettry⁶ · Catherine Lerouge⁷ · Pierre De Cannière⁸

Received: 28 April 2016 / Accepted: 9 December 2016 / Published online: 23 February 2017
© The Author(s) 2017. This article is published with open access at Springerlink.com

Abstract Two experiments have been installed at Mont Terri in 2004 and 2009 that allowed gas circulation within a borehole at a pressure between 1 and 2 bar. These experiments made it possible to observe the natural gases that were initially dissolved in pore-water degassing into the borehole and to monitor their content evolution in the borehole over several years. They also allowed for inert (He, Ne) and reactive (H₂) gases to be injected into the borehole with the aim either to determine their diffusion properties into the rock pore-water or to evaluate their removal reaction kinetics. The natural gases identified were CO₂, light alkanes, He, and more importantly N₂. The natural concentration of four gases in Opalinus Clay pore-water was evaluated at the experiment location: N₂ 2.2 mmol/L ± 25%, CH₄ 0.30 mmol/L ± 25%, C₂H₆ 0.023 mmol/L ± 25%, C₃H₈ 0.012 mmol/L ± 25%.

Editorial handling: P. Bossart and A. G. Milnes.

This is paper #19 of the Mont Terri Special Issue of the Swiss Journal of Geosciences (see Bossart et al. 2017, Table 3 and Fig. 7).

Electronic supplementary material The online version of this article (doi:10.1007/s00015-016-0244-1) contains supplementary material, which is available to authorized users.

✉ Agnès Vinsot
agnes.vinsot@andra.fr

¹ Agence Nationale pour la Gestion des Déchets Radioactifs ANDRA, Meuse Haute-Marne Center, RD 960, 55290 Bure, France

² Valeriusstraat 11, 1071 MB Amsterdam, The Netherlands

³ Hydroisotop GmbH, Woelkestraße 9, 85301 Schweitenkirchen, Germany

⁴ Université de Lorraine-CNRS-CREGU, GeoRessources Lab, 54506 Vandœuvre-lès-Nancy, France

Retention properties of methane, ethane, and propane were estimated. Ne injection tests helped to characterize rock diffusion properties regarding the dissolved inert gases. These experimental results are highly relevant towards evaluating how the fluid composition could possibly evolve in the drifts of a radioactive waste disposal facility.

Keywords Nitrogen · Alkane · Hydrogen · Noble gases · Diffusion · Nuclear waste disposal

1 Introduction

Opalinus Clay pore-water contains dissolved natural gases: N₂, CO₂, CH₄ and other light alkanes, He and other noble gases. With the exception of N₂, these gases were identified before 2000 in the Mont Terri rock laboratory thanks to measurements on gas samples extracted from cored rock samples or from boreholes (Pearson et al. 2003). Furthermore, in the framework of studies devoted to nuclear waste geological disposal feasibility, intense efforts were made on precise quantification of CO₂ and He content in the pristine pore-water. CO₂ is of key interest regarding the

⁵ Present Address: UPMC Univ. Paris 06, Université Versailles St-Quentin, CNRS/INSU, LATMOS-IPSL, 75252 Paris Cedex 05, France

⁶ Solexperts AG, Mettlenbachstrasse 25, 8617 Mönchaltorf, Switzerland

⁷ French Geological Survey BRGM, 3 Avenue Claude Guillemin, 45060 Orléans Cedex 2, France

⁸ Agence fédérale de contrôle nucléaire AFCN, Rue Ravenstein 36, 1000 Brussels, Belgium

understanding of the processes that control the pore-water composition (Gaucher et al. 2009; Pearson et al. 2011; Tournassat et al. 2015) and He data enables to characterize transport properties of solutes within Opalinus Clay rock (Rübel et al. 2002; Mazurek et al. 2011). More generally, dissolved gases are affected by both reaction and migration processes. As a consequence, data regarding dissolved gas concentration distribution in Opalinus Clay may give some insight on both transport properties of solutes in this argillaceous rock and processes that control the pore-water composition. Regarding light alkanes, data interpretation also meets broader research topics on the relationships between their chemical and isotopic composition and the questions about their origin along with the kinetics associated to their production, their potential migration paths, their potential retention properties on clay minerals etc. (Prinzhofer and Pernaton 1997; Zhang and Krooss 2001; Sherwood Lollar et al. 2008; Prinzhofer et al. 2009; McCollom et al. 2010; Stolper et al. 2015).

In 2004, a new experimental method has been implemented at Mont Terri rock laboratory with the objective to quantify more precisely the CO₂ content at the measurement location. The method is based on gas circulation, at a pressure between 1 and 2 bar, in the packed off interval of a 15-m long ascending borehole (Vinsot et al. 2008). This experiment, named pore-water chemistry (PC-C) gave a series of data on natural Opalinus Clay gases. The same method has been used since 2009 to study transport and reactivity of dissolved hydrogen gas in Opalinus Clay pore-

water. This last experiment, named Hydrogen Transfer (HT), has given data on natural gases over a period of 6.5 years. In 2011, He and Ne were injected together with H₂ in the test interval to study their transport properties in Opalinus Clay pore-water and possible H₂ consumption (Vinsot et al. 2014).

This paper presents the new data regarding natural dissolved gases in Opalinus Clay pore-water obtained in these experiments and the link that may be drawn with available data obtained on core samples.

2 Geological context and rock characteristics

The Mont Terri rock laboratory is located in the security gallery of a motorway tunnel in the Jura Mountains (Fig. 1), in north-western Switzerland at a depth of about 300 m below ground level (Bossart et al. 2017). It is a “methodological laboratory” (Delay et al. 2014) in the Opalinus Clay, which is a well consolidated Jurassic age claystone with a hydraulic conductivity below 3×10^{-12} m/s (Thury and Bossart 1999).

The clay-rocks at the test locations (shaly facies) consist of a dominant clay fraction (~60 wt.%) including illite, kaolinite, chlorite, and illite–smectite mixed layers, associated with quartz (~15 wt.%), calcite (~20 wt.%), feldspar, dolomite, siderite (a few wt.% each), pyrite (~1 wt.%), and organic matter (around 1 wt.% organic C) (Pearson et al. 2003). From thin section microscope observations, the rock displays a fine grain fabric with heterogeneities. The clay

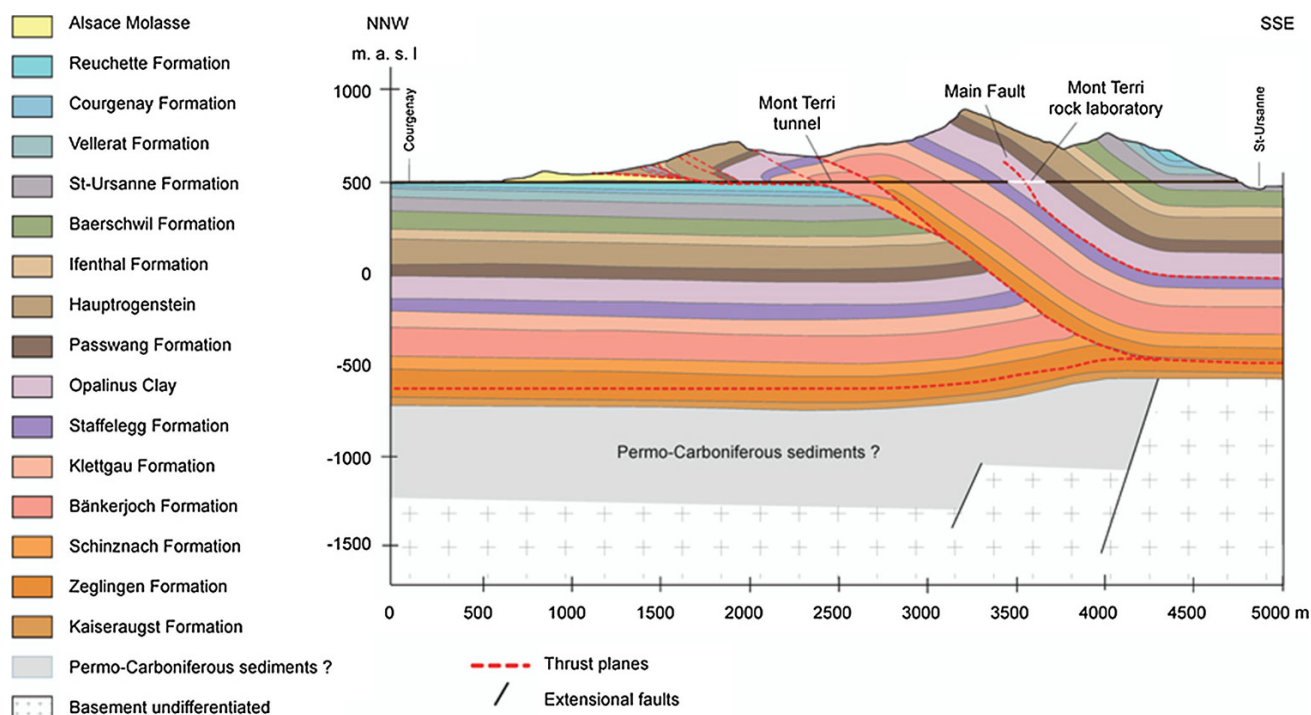


Fig. 1 Geological cross-section of the Mont Terri anticline and location of the Mont Terri rock laboratory (Nussbaum et al. 2017)

matrix is essentially formed of detrital particles of less than $1\ \mu\text{m}$ of illite and illite–smectite mixed layers, with minor $10\text{--}50\ \mu\text{m}$ sized flakes of biotite, muscovite, and chlorite. The carbonate fraction consists of calcite test and shell fragments and diagenetic carbonates including calcite (major micrite, sparite, and rare euhedral grains), dolomite/ankerite (essentially euhedral grains) and siderite (disseminated μm -sized grains, rare clusters). Pyrite occurs as μm -sized framboids of diagenetic origin. The heterogeneities of the clay-rocks are essentially due to the occurrence of the fossil debris ranging in size from $50\ \mu\text{m}$ to few millimetres. The fossil debris include calcite test and shell fragments, but also particles of organic matter and phosphate elements. The water content is around 7 wt.% (with respect to the dry rock mass) and the total porosity is between 16 and 18% by volume.

3 Experiments: setup and methods

3.1 Experimental layout

Two 15 m-long, 101 and 76 mm in diameters respectively, inclined ascending boreholes perpendicular to the bedding

were drilled from the vault of underground drifts in the Mont Terri rock laboratory: BPC-C1 in 2004 in the PP niche from the Security Gallery and BHT-1 in 2009 in Gallery-08. Both boreholes are 20 m far from one another perpendicularly to the Opalinus Clay contact with the limestones of the Passwang Formation. The last 5 m of these boreholes constitute the test intervals in contact with the rock. These zones were drilled using nitrogen in BPC-C1 and argon in BHT-1. The drilling tools were disinfected with chlorinated water and alcohol to minimize the introduction of external micro-organisms in the boreholes.

Immediately after coring, a device comprising an inflatable packer was installed in order to isolate the test intervals from the drift atmosphere. As soon as the packers were set in place, the test intervals were filled with argon in both boreholes. In the test intervals, the equipment took up over 80% of the volume, leaving only a maximum volume of about 5 and 10 litres remaining for fluids in BPC-C1 and BHT-1 respectively. It includes a PFA (per-fluoro-alkoxy)-coated, stainless steel inner tube. BHT-1 equipment comprises ceramic filter screen pieces having a porosity of 42% and a thickness of 14.75 mm, which surround the 40 mm diameter central tubing. However, BPC-C1 equipment does not include a filter screen. The intervals are closed at the

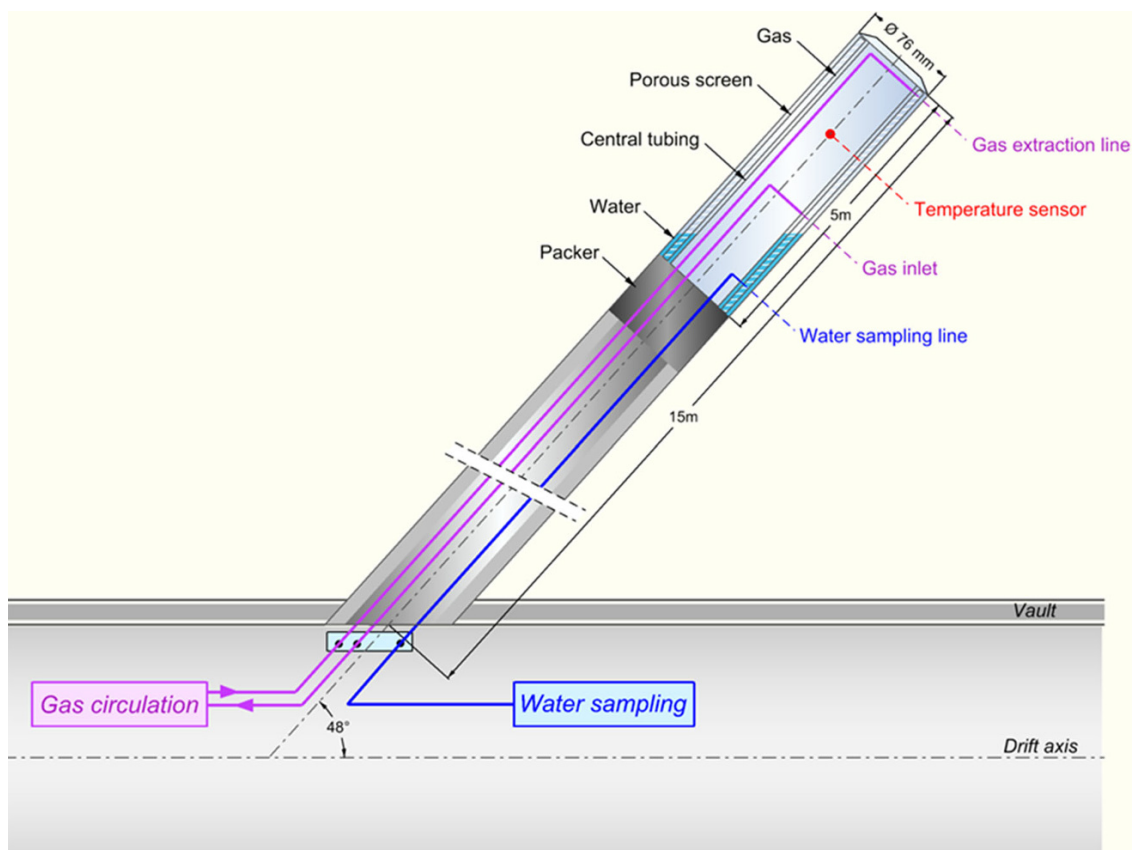


Fig. 2 Experimental layout (BHT-1)

bottom by a packer made of either neoprene-covered natural rubber or polyurethane rubber and inflated with water. In the boreholes, 4 to 6 measurement and circulation lines made of either PEEK (poly-ether-ether-ketone) or stainless steel, pass through the central tubing and connect the test interval with the drift (Fig. 2). Two stainless steel lines are dedicated to gas circulation between the interval and the drift. The gas extraction line enters the filter a few centimetres from the top of the interval, and the gas injection line 40 to 60 cm from the base of the interval. At the top level in BHT-1 borehole, another stainless steel line is dedicated to pressure measurements. Two PEEK lines enter the filter 2 cm from the bottom of the interval; one is for water extraction, the other for pressure measurements. The pressure sensors (Keller LEO 3 pressure gauges) are located in the drift at the far end of the pressure measurement lines.

In the drift, a module comprising a KNF gas-tight pump is used for circulating the gas. This module comprises 10 Swagelok stainless steel sampling cylinders in which the gas circulates continuously. These cylinders (75 or 150 mL) may be disconnected to perform gas sample analyses, without modifying the total gas pressure. Various devices were connected to the gas circuit over several time periods to perform non-destructive in-line analyses of certain gases with an infrared (Cailteau et al. 2011a, b) or a Raman spectrometer (Lundy and Vinsot 2010). In addition, the BHT-1 gas circulation module includes a HY-OPTIMA 740 by H2scan H₂ specific solid detector probe and a Teledyne ISCO D-500 gas injection pump.

In the rock surrounding the test intervals, the water pressure is 15 to 25 bar. In spite of the low hydraulic conductivity value of the rock (below 3×10^{-12} m/s), the difference in pressure between the interval and the rock induces a 3 to 20 mL/day water seepage flow rate from the rock to the interval (Vinsot et al. 2008, 2014). The water seeping into the interval accumulates at the bottom due to gravity. In the drift, a module is used for water extraction. This module includes in-line water sampling cylinders made of either PTFE (poly-tetra-fluoro-ethylene)-coated stainless steel or PEEK. The water lines and the fittings are made of PEEK. The extraction flow rate was adjusted so that the vertical water height in the interval did not exceed 30 cm. In the 4 or more meters above this surface, the available volume was taken up by gas, circulating between the borehole and the drift in a closed loop at a rate of 20 mL/min. This flow induced practically no head loss, thus the pressure was the same at any point of the circuit by ± 5 mbar.

All of the sensors (pressure, gas flow rate, hydrogen, scale etc.) are connected to a central database which acquires and stores the values measured every 5 to 20 min (Tabani et al. 2010).

3.2 Tests chronology

At the beginning of each test, after having filled the test interval and the gas circulation module with pure argon at a pressure of 1.3 ± 0.1 bar, the circulation of this gas and the monitoring of its composition were initiated.

In BPC-C1, the composition of the circulating gas was monitored over almost the entire first year of testing. During this phase, the test interval was purged twice with argon after 44 and 231 days. The most consistent set of data was obtained over 70 days after the second purge, when a uniform gas pressure along the whole gas circuit was obtained (Vinsot et al. 2008). The continuous extraction of seepage water from the test interval had started just before the second purge and the chemical composition of seepage water has been analysed in two water samples before the end of the first year (Vinsot et al. 2008). At the end of the first year, gas circulation and water extraction were stopped. As a result, the water seeping out of the rock filled the test interval. As the gases could not escape during the filling, the gas pressure increased up to a value comprised between 5 and 6 bar. Over the span of approximately a year, water had completely filled the test interval, with the exception of its top far end that contained a gas bubble. At the end of this time period, water extraction resumed. Since then, the dissolved gas concentrations have been analysed in the water samples taken in-line without any contact with the ambient air. The remaining gas bubble was eliminated 2.6 years later by extracting water from the line previously used to extract gas from the top interval.

In BHT-1, the composition of the circulating gas has been monitored continuously since the beginning, except for a period lasting half a year after the first 1.5 year of testing. Since the end of the first year, seepage water has been continuously extracted from the borehole and its composition has been regularly analysed (Vinsot et al. 2014). The dissolved gas concentrations have not been measured in the water samples. After 2 years of testing, the gas from the test interval was replaced by a mixture of gases containing 5 vol% H₂, 5 vol% He, 5 vol% Ne, and 85 vol% Ar at a total pressure close to 1.5 bar. The objective was to study the hydrogen transport and potential hydrogen consumption processes in Opalinus Clay (Vinsot et al. 2014). The non-reactive gases He and Ne served as references as changes in their content should only depend on dissolution and diffusion processes in the rock pore-water. As a consequence, they can help to calibrate the transport part in a reactive transport model. The gas pressure value was set as low as possible, in order to maximize the water flow towards the borehole, but not below the atmospheric pressure, in order to prevent air intrusion in the gas circuit.

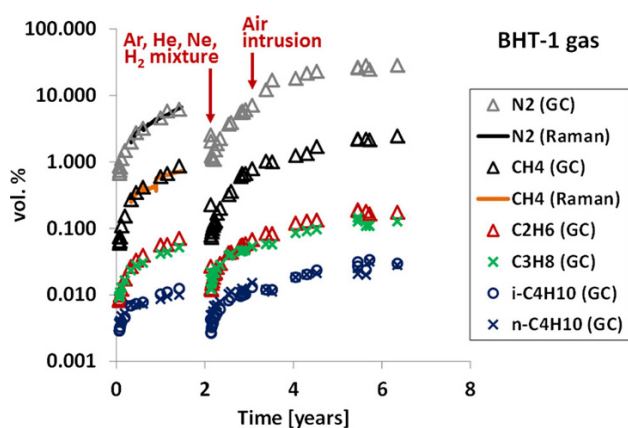


Fig. 3 N_2 , CH_4 , C_2H_6 , C_3H_8 , $i\text{-C}_4\text{H}_{10}$, and $n\text{-C}_4\text{H}_{10}$ content measured in the gas circulating in BHT-1 borehole; logarithm scale; GC gas chromatography; analytical uncertainty is included within the symbol size

Half a year later, a semi-continuous hydrogen injection phase was launched. It consisted in regularly injecting pure hydrogen in order to maintain a partial pressure close to 0.06 bar in the test interval. This phase lasted 1.5 year.

In spite of the preventive maintenance, the BHT-1 experiment encountered two leakage events over the 6.5 years of its duration. The first one occurred after 1.5 year of testing. Damage to the gas circulation pump led to air being admitted into the test interval over a period of 26 h. Then, the test interval was filled with pure argon again and closed off 9 days later for a period of 0.6 year. The second leakage event took place after approximately 3.4 years and induced an introduction of atmospheric air into the gas circuit detectable in the N_2 content (Fig. 3). Air could be introduced into the gas circuit in spite of its overpressure with respect to the surrounding air because the circuit was locally depressed between the gas flow controller and the pump and a leak occurred at this location.

3.3 Chemical analyses

In the laboratory, the gas composition was analysed using a Shimadzu GC17A gas chromatograph equipped with two capillary columns: (a) Plot Fused Silica, Molsieve 5A, $50\text{ m} \times 0.53\text{ mm}$, $df = 50\text{ }\mu\text{m}$ (Varian); (b) Plot Fused Silica, CP Poraplot Q-HT, $25\text{ m} \times 0.53\text{ mm}$, $df = 10\text{ }\mu\text{m}$ (Varian) and two detectors: Detector 1: micro-TCD (Micro-Volume Thermal Conductivity Detector, VICI Instruments Inc.); Detector 2: FID (Flame Ionization Detector, Shimadzu). Sample attachment is carried out with a special quick connection (Swagelok), allowing direct connection of the sample cells with the evacuated inlet system of the gas chromatograph (8 Port Dual External Sample Injector, Valco Europe) without contact with the external

atmospheric gases. The uncertainty affecting the gas content result is $\pm 5\%$.

Carbon-13 content of the alkanes is analysed by a GC-IRMS (IRMS Finnigan Delta S, GC 3400 Varian, resolution (5% valley) 110, abundance sensitivity 2×10^{-5} for 44/45, high voltage stability: 2.1×10^{-5}). The alkanes are completely oxidized to CO_2 in a combustion interface and then measured in the isotope ratio mass spectrometer. Measured results are corrected to carbon standards NBS18–Calcite, IAEA CO–1, NBS23– SrCO_3 , CO_2 –lab standard 1, and CO_2 –lab standard 2.

The water sample cylinders were connected to a special cell to measure the pH without contact with the ambient air. A few mL of the water are immediately used for alkalinity measurement by titration. Another 2 mL are immediately transferred into one arm of a two-armed glass vessel, the second arm containing H_3PO_4 (85%). The vessel is then flushed with pure N_2 and closed. Inclining the vessel causes the H_3PO_4 to mix with the sample and, as a result, the CO_2 from all dissolved inorganic carbon compounds is released into the gas phase. Then, the gas phase is transferred to the evacuated sample loop of the isotope ratio mass spectrometer with dual inlet system for measurement (IRMS: MAT-250, resolution (5% valley): 200, abundance sensitivity: 1.3×10^{-6} for 44/45; high voltage stability: 1×10^{-5}). Measured results are corrected to carbon standards NBS18–Calcite, NBS19–Calcite, NBS23– SrCO_3 , IMEP8– CO_2 , CO_2 –lab standard and Hydroisotop lab standard (DIC). The 1 sigma error for clean standard material is $\pm 0.2\%$. The $\delta^{13}\text{C}$ results are related to VPDB Vienna standard (Vienna Pee Dee Belemnite) in the delta-notation.

3.4 Volume of the gas circuits

The values of total pressure, total volume and temperature of the circulating gas are required in order to quantify the fluxes of gas that are exchanged with the rock pore-water. In both BHT-1 and BPC-C1, the total gas pressure was continuously measured; its uncertainty value was $\pm 0.1\%$ and its maximum variation along the gas circuits was 0.3%. The theoretical volumes available for fluids in the test intervals have a value of 4.7 L in BPC-C1 and 9.3 L in BHT-1. This is based on the characteristics of the borehole equipment, assuming perfectly cylindrical boreholes. In reality, the boreholes may be deformed and, as a result, their volumes may be reduced. Moreover, the volume between the equipment and the borehole top is not precisely known. In BHT-1, two types of operations provided opportunities to estimate the actual volumes available for fluids in the test intervals at a given date by using the ideal gas law: (1) addition of empty parts (gas module or gas sampling cylinders) of known volume on the gas circuit

inducing gas expansion; (2) extraction of known volumes of water inducing gas expansion. Such operations led to an estimation of the volume of the BHT-1 test interval of $9.5 \text{ L} \pm 3\%$. This volume is close to the theoretical one. In the case of BPC-C1, the volume available for the gases in the test interval was supposed to be the theoretical one.

During the course of the experiments, each time a gas sampling cylinder was disconnected, both the total volume available for the gases and the total mass of circulating gas decreased, whereas neither the pressure nor the gas content were modified. On the other hand, the cylinders that were added onto the gas circuit were filled with pure argon at a pressure around 20 mbar. As a result, each time a gas sampling cylinder was added, the gas pressure decreased and the total volume available for the gases increased, whereas the total mass of circulating gas and the content of each gas were nearly not affected. Furthermore, the gas volume varied inversely with the water level in the borehole interval, which depended on both the seepage and the water extraction flow rates. The water level is deduced from two absolute pressure measurements and its uncertainty value is $\pm 2 \text{ cm}$. In BHT-1, the water extraction flow rate was controlled by a pressure controller and measured by a weight scale. The seepage flow rate has been estimated at a value of 12 mL/day . In the case of BPC-C1, the water extraction flow rate was controlled by a syringe-pump and the seepage flow rate was evaluated at around 3 mL/day during the first year. Unfortunately, the exact volume of the BPC-C1 gas circuit was not precisely known because a tank was inline on the gas circuit, and its volume, which had been modified for the purge operations, could not be precisely controlled. Consequently the tank volume, which maximum value was 5.4 L , was considered as a variable parameter in the calculations.

4 Experimental results

4.1 Natural gas content

The composition monitoring of the gas circulating in boreholes BPC-C1 and BHT-1 showed the inflow of N_2 , light alkanes up to C_6 and CO_2 . Helium was also detected, whereas oxygen was not. N_2 and alkane contents increased continuously over the experiment time duration (Figs. 3, 4; Electronic Appendix-Table 1, Electronic Appendix-Table 2). N_2 apart, the occurrence of these gases in the Opalinus Clay pore-water has been described by Pearson et al. (2003).

In the case of BPC-C1, an uncertainty subsisted regarding the origin of N_2 because the test interval of this borehole had been cored with N_2 (Vinsot et al. 2008). In the case of borehole BHT-1, for which argon was used when coring, the increase of N_2 content in the circulating gas over time showed that this gas arises from pore-water.

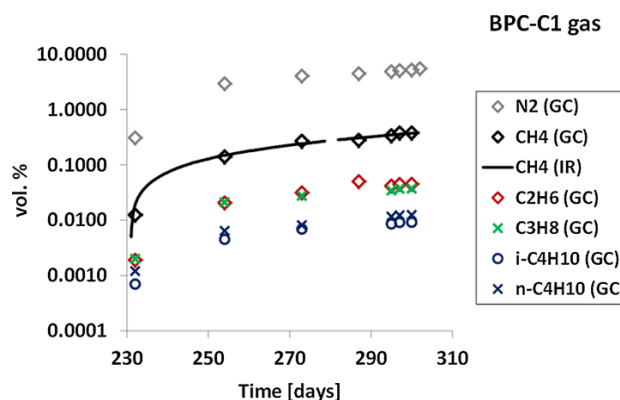


Fig. 4 N_2 , CH_4 , C_2H_6 , C_3H_8 , $i\text{-C}_4\text{H}_{10}$, and $n\text{-C}_4\text{H}_{10}$ content measured in the gas circulating in BPC-C1 borehole from the second argon purge onwards; logarithm scale; *GC* gas chromatography; *IR* infrared spectrometry; analytical uncertainty is included within the symbol size

In borehole BPC-C1, the CO_2 concentration in the gas was lower by 0.5 log unit than those at equilibrium with the pore-water calculated from the measurements of pH, alkalinity, and total inorganic carbon and this discrepancy was not understood (Vinsot et al. 2008). In borehole BHT-1, the CO_2 concentrations in the gas are very variable, unexpectedly low and far lower than those at equilibrium with the pore-water calculated from the measurements of pH, alkalinity, and total inorganic carbon (Vinsot et al. 2014). The measurements of the gases have been checked and are not an issue. The current hypothesis for explaining the large deviations is that one of the items of equipment in the HT experiment (borehole BHT-1) and not in the PC-C experiment (borehole BPC-C1) might contain an adsorbing material acting as a CO_2 trap. The equipment in question is currently thought to be the ceramic screen. Indeed, large pieces of this type of screen ($\approx 3 \text{ dm}^3$) are present in BHT-1, while pieces only measuring a few cm^3 were used in BPC-C1 to protect the line ends at the place where they exit the central tubing. This hypothesis is supported by similar observations in Andra's Meuse/Haute-Marne Underground Research Laboratory at Bure. In an experiment based on the same experimental layout, with the ceramic screens being replaced by PTFE (Lundy et al. 2013), the measured CO_2 content in the gas phase was less than 0.5 log unit lower than the CO_2 partial pressure that was deduced from speciation calculations based on the water chemical analysis results. Laboratory tests and numerical modelling calculations are underway to assess the validity of this hypothesis.

4.2 Natural gas content in seepage water

Chemical compositions of dissolved gases were also measured on ten BPC-C1 water samples after the borehole

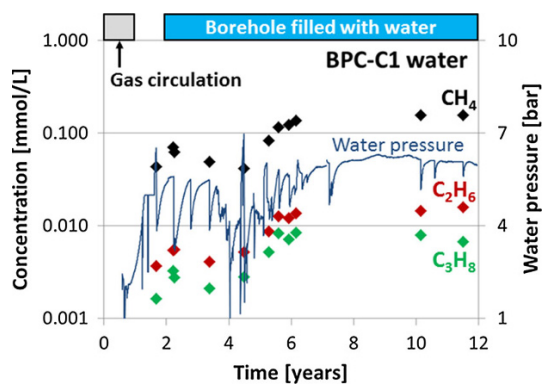


Fig. 5 Dissolved CH_4 , C_2H_6 , and C_3H_8 concentrations measured in BPC-C1 seepage water; logarithm scale; analytical uncertainty is included within the symbol size; water pressure of the test interval measured in the drift at a vertical distance of 9.6 and 12.9 m from the bottom and from the top of the test interval, respectively; the water pressure into the test interval is 1.0 to 1.3 bar lower than the measured one

interval had been filled with water (Fig. 5; Electronic Appendix-Table 3). In the test interval, the water pressure varied over a range of several bar until the 7th year of the experiment. Then, it stabilized at a value larger than 5 bar. If this value was lower than the total pressure of the gases dissolved in the water, than gas bubbles should form and the dissolved gases should escape the water. If the opposite was true, the dissolved gases should remain in the water. In that case, measured values of dissolved gas concentrations should tend towards those that are representative of pristine pore-water. After 10 years of water composition monitoring, the measured methane concentration was 0.16 mmol/L, the measured ethane concentration was between 0.015 and 0.016 mmol/L, and the measured propane concentration was between 0.007 and 0.008 mmol/L. If they were stable, these values could be representative of the alkane concentrations in undisturbed pore-water. However, as they were still increasing, these values indicate the minimum concentrations of these three alkanes in Opalinus Clay pore-water at this location.

4.3 Natural gas isotopes

The isotopic composition of alkanes, up to C3, was measured in the gas and water samples. In both boreholes BPC-C1 and BHT-1, the isotope contents of methane are scattered while those of heavier gases evolve more smoothly (Fig. 6; Electronic Appendix-Tables 1 to 3). The largest methane $\delta^{13}\text{C}$ variations are observed when gas was added to or removed from the test interval. These operations induced gas fractionation between the lighter and the heavier gases. For all the alkanes, the $\delta^{13}\text{C}$ values tend to decrease after a flushing of the test interval and to stabilize afterwards. Rayleigh fractionation could explain this

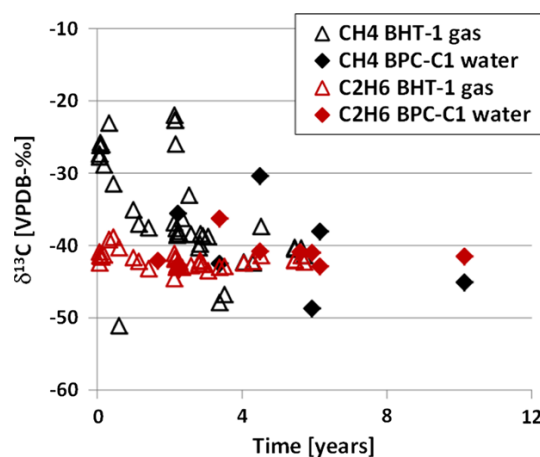


Fig. 6 $\delta^{13}\text{C}$ of CH_4 and C_2H_6 measured in the gas circulating in BHT-1 and in BPC-C1 seepage water; analytical uncertainty is included within the symbol size

observation. The stabilized values are between -30 and -45‰ VPDB for all alkanes in both boreholes.

4.4 Injected gases

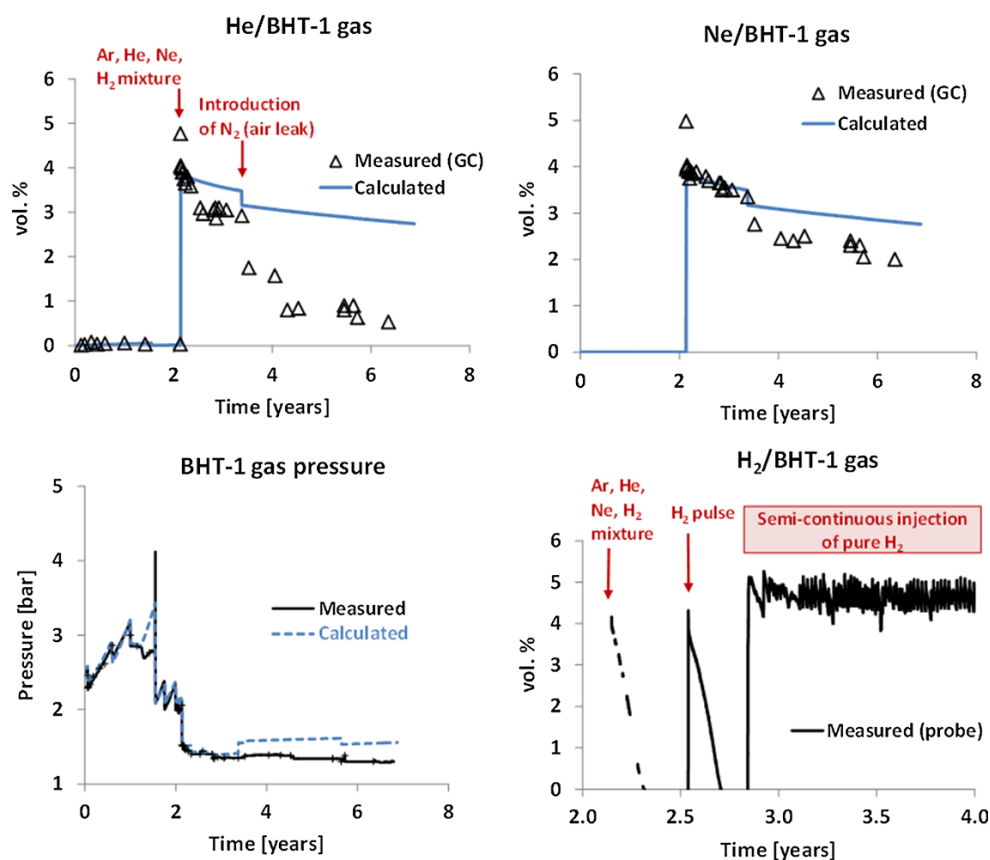
After replacing the gas from the test interval with the mixture of gases containing 5 vol% H_2 , 5 vol% He, and 5 vol% Ne in argon, all the injected gas concentrations decreased, H_2 much faster than He and Ne (Vinsot et al. 2014; Fig. 7). The evolution of Ne concentration could be reproduced over the first year with a diffusion model, considering dissolution and diffusion in pore-water. The difference observed between the evolution of the He concentration and the evolution of the Ne concentration was interpreted as being due to a leak of He because He has a smaller atomic size than Ne. In contrast, even with the possibility of a hydrogen leak, its concentration evolution was much faster than the leak rate.

5 Modelling

5.1 Model description

The model which had been constructed with PHREEQC-3 (Parkhurst and Appelo 2013) to describe the transport of the gas injected in the borehole to the surrounding rock (Vinsot et al. 2014) has also been used to simulate the transport of natural gases in the opposite direction in BHT-1. The model calculates diffusional transport of the gases through the Opalinus Clay by explicit finite differences in a radial one-dimension configuration. Each dissolved gas is supposed to access the entire water-filled porosity but it is given its own diffusion coefficient in pure water (Appelo and Wersin 2007; Appelo et al. 2010). The effective

Fig. 7 Changes in the He and Ne contents and in the gas pressure measured in the gas circulating in BHT-1 and calculated with PHREEQC; changes in the H₂ content measured in the gas circulating in BHT-1 over the time period of H₂ injection



diffusion coefficient D_e of each dissolved gas is related to its diffusion coefficient D_w in pure water by $D_e = \varepsilon D_w / G$ with ε the porosity and G the geometric factor (see for example Van Loon and Mibus 2015). The porosity value is 0.16. A G -value of 7.7 ± 0.2 parallel to bedding was obtained in situ for HTO in the same Opalinus Clay shaly facies at Mont Terri (Appelo and Wersin 2007). This value was used here in the model for all the dissolved gases (neutral species). The solubility values and diffusion coefficients used for the different dissolved gases are presented in Table 1.

Diffusion of gases over the water–gas interface is modelled with the two-film model of Liss and Slater (1974). This model allows obtaining the flux over a general interface by finding the concentration and the pressure at the boundary of water/gas (Appelo and Postma 2005). The gas and water concentrations are considered to be in equilibrium at the gas–water interface. The water-film thickness is assumed to be 0.25 mm (in agreement with calculations for other systems (Appelo and Postma 2005)). However, this value has little influence on the calculations, because the solute concentrations in the cell that borders the borehole are close to equilibrium with the gas concentrations (at the time and space discretization of the model). The wall surface area has been multiplied by a

rugosity factor $R = 10$ to take into account the surfaces created by the drilling in the damaged rock surrounding the borehole. This hypothesis has been previously applied for a very similar experiment performed in Andra's Meuse/Haute-Marne Underground Research Laboratory (Trémosa et al. 2015). The rugosity factor modifies the gas fluxes that are exchanged with pore-water in the first cell of the model. It influences significantly the results when the conditions change rapidly in the gas, i.e. at the beginning of the coring phase or when the interval is flushed with a new gas mixture. Otherwise it does not change significantly the gas content evolution because this one is mainly controlled by the diffusion in the following cells. The sensitivity of the results to the value of the rugosity factor has been looked at. Increasing the value above 10 does not impact the results anymore. The advective part of the transport is not taken into account in the model as previous calculations showed that its impact on the gas content evolution was very small compared to diffusive transport. The geometric characteristics of the model used to describe the BHT-1 borehole are presented in Table 2.

It has been verified that the model radial length was sufficiently large: the maximum distance of influence of the borehole on the dissolved gas contents in the rock pore-water after 7 years is less than 2 m from the borehole

Table 1 Solubilities ($-\log K_H$, K_H being the Henry constant) and diffusion coefficients for the gases in the model

Gas	$-\log K_H$	$-\Delta H_f$ (kJ/mol)	D_w (10^{-9} m ² /s)	D_e (10^{-11} m ² /s)
H ₂ O	-1.506	-44.03	2.24	3.54
H ₂	3.10	(Polynomial)	5.13	8.12
He	3.41	(Polynomial)	7.29	11.53
N ₂	3.19	(Polynomial)	1.96	3.10
Ne	3.35	(Polynomial)	4.04	6.39
Ar	2.86	(Polynomial)	2.45	3.88
CO ₂	1.468	(Polynomial)	1.92	3.04
CH ₄	2.85	(Polynomial)	1.85	2.93
C ₂ H ₆	2.69	-19.5	1.53	2.42
C ₃ H ₈	2.85	-22.2	1.29	2.04

The solubilities (Scharlin et al. 1998) and diffusion coefficients in pure water (D_w) are for 25 °C; value for HTO in water comes from Mills and Harris (1976); values for the gases N₂, Ar, CH₄ and CO₂ were taken from Table 4.4 in Boudreau (1997) and stem from Jähne et al. (1987) and Ohsumi and Horibe (1984). Values for the gases C₂H₆ and C₃H₈ come from Hayduk and Laudie (1974) and (Table 4.3 in Boudreau 1997), but multiplied by 1.1 to be commensurate with the higher diffusion coefficient for CH₄ given by Jähne et al. (1987) compared with Hayduk and Laudie (1974); in the model, solubilities are corrected to 15.6 °C using Van't Hoff's equation with the dissolution reaction enthalpy (ΔH_f) or with a polynomial; effective diffusion coefficients (D_e) are corrected by accounting for the viscosity change of water with temperature at 15.6 °C

Table 2 Geometric characteristics of the PHREEQC model used for the BHT-1 experiment

Initial gas volume	Interval length	Borehole radius	Radial length	Cell number	Cell size
9.5 L	5 m	38 mm	4.9 m	45	20–480 mm

centre; this distance is less than half the model radial length.

The total pressure in the test interval is calculated from the gas masses by using the ideal gas law. It is assumed that the gas mixture in the borehole remains homogeneous while the gases diffuse in-and-out of Opalinus Clay. The effect of the variation in water level is taken into account to evaluate the volume available for the gases and the area of the rock in contact with the circulating gas. The operations or events that occasionally modify either the total volume available for the gases or the total mass of gas are accounted for in the model (Electronic Appendix-Table 4). Operations of interest can be: (1) extracting water; (2) adding empty parts to the gas circuit, such as sampling cylinders containing 20 mbar argon, in which the circulating gas expands; (3) involuntary gas introduction or outflow.

5.2 Modelling results

5.2.1 BHT-1 experiment

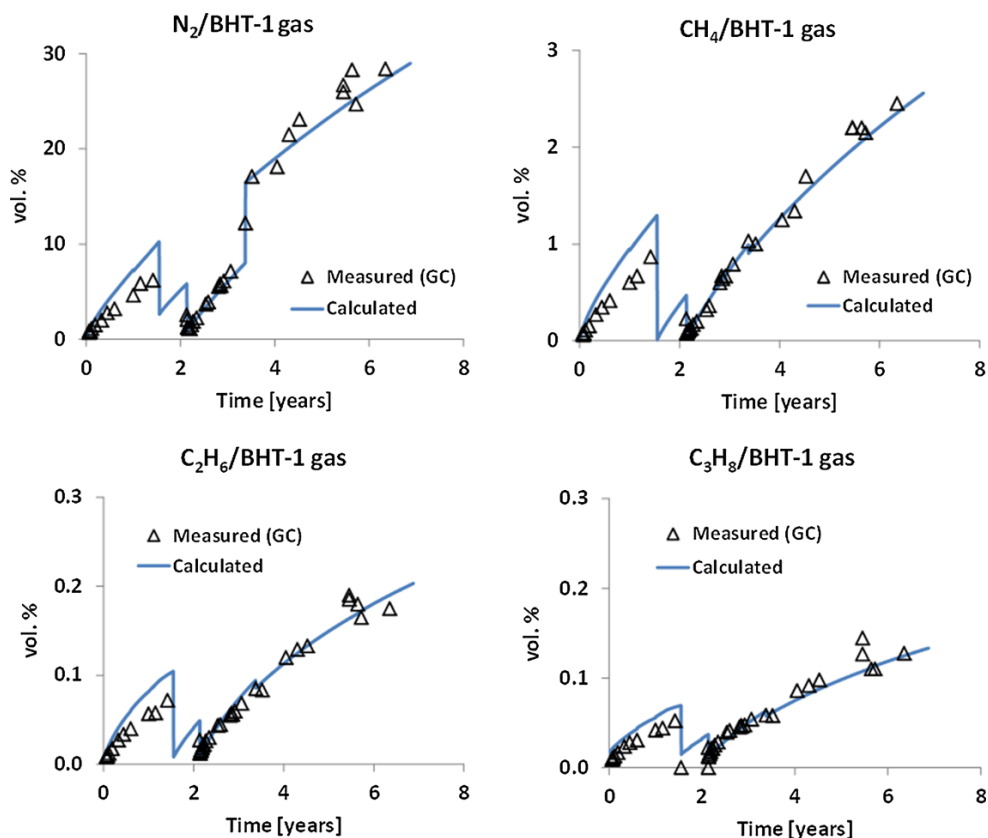
Alkane concentrations in Opalinus Clay pore-water are the unknowns in the model. Furthermore, alkanes may be

adsorbed onto rock solids. As a consequence, both the concentrations and the retention properties of each alkane have to be estimated. For each alkane, a linear retention coefficient K'_d was used in the model, such that the adsorbed alkane concentration $C_{ads} = K'_d \times C_0$; C_0 corresponds to the dissolved alkane concentration; K'_d is dimensionless. The total content of the alkane under consideration is $C_t = C_0 + C_{ads} = C_0 (1 + K'_d)$. By using the bulk dry density value (mass of dry rock over volume of saturated rock, $\rho_d = 2.3$ g/cm³) of Opalinus Clay deduced from both bulk wet density and porosity values (Mazurek et al. 2008), one can calculate K_d (L/kg) = $K'_d \times \varepsilon/\rho_d$ for each alkane. The values obtained for C_0 and K_d are presented in Table 3. Deduced partial pressures at equilibrium with Opalinus Clay pore-water and total concentration (C_t) values are also presented in Table 3. Figures 7 and 8 show the comparison between observed and calculated contents for He, Ne, N₂, methane, ethane, and propane, and the comparison between observed and calculated pressure. Hydrogen and CO₂ contents evolve independently from the other dissolved gases (Vinsot et al. 2008, 2014; Cailteau et al. 2011a); hydrogen evolution involves consumption processes, whereas CO₂ content is controlled by reactions with rock minerals and the ceramic screen in the case of

Table 3 Concentrations, retention coefficients and partial pressures of N₂, CH₄, C₂H₆ and C₃H₈ in the rock surrounding the borehole BHT-1

Parameter	N ₂	CH ₄	C ₂ H ₆	C ₃ H ₈
K' _d (-)	0	0.25	3.98	12.59
K _d (L/kg)	0	0.02	0.28	0.88
K _d ^{OM} (L/kg organic C)	0	2.18	34.62	109.47
C ₀ (mmol/L)	2.2	0.30	0.023	0.0125
C _t (mmol/L)	2.2	0.375	0.115	0.170
Partial pressure at equilibrium with C ₀ (bar)	3.16	0.19	0.01	0.007

C₀ concentration of the dissolved gas in pore-water, C_t total concentration of the gas in the rock (except non-reversibly sorbed gas)

Fig. 8 Changes in the N₂ and alkane contents in the circulating gas measured in BHT-1 and calculated with PHREEQC

BHT-1. H₂ and CO₂ data are not commented here anymore as they do not impact non-reactive gas migration. However, the carbonate species and their equilibrium in solution are taken into account in the model.

On both days 220 (0.60 year) and 365 (1 year), respectively 100 and 160 mL water were extracted from the borehole BHT-1 by opening a water line valve. An unknown mass of gas escaped from the circuit at the end of the water extraction. In the model, the escaped masses of gases have been estimated (Electronic Appendix-Table 4) by adjusting the total pressure at these dates and assuming that all the gases escaped at the same rate, in proportion of their content in the borehole. From day 452 (1.24 year), a failure of the pressure controller prevented the water to be

extracted from the borehole. As a consequence, the water level increased in the borehole interval, inducing a diminution of the volume available for the gases. In spite of this volume decrease, the measured gas pressure decreased, showing that gas was leaking out of the borehole. In the model, the water level increase is simulated however the leak is not giving a discrepancy between the measured and the calculated pressure (Fig. 7). An excess of N₂ and alkanes is also calculated by the model with respect to the measurements during this time period (Fig. 8); the discrepancy may be mainly explained by the leak.

On day 1232 (3.4 years), the air introduction observed is modelled by adding N₂ in the borehole. The mass of added N₂ was adjusted to fit the measured N₂ content (Electronic

Appendix-Table 4). The introduction of air oxygen has not been taken into account, supposing that oxygen was consumed by reaction with components of the rock such as pyrite because it has been previously observed that this reaction is very fast. In spite of these modelling choices, the calculated pressure is larger than the observed one (Fig. 7). This result and also the evolution of Ne content that decreased faster than expected by the model after the air introduction, suggest that gases have escaped out of the circuit when air entered. As a consequence, the alkane concentrations in pore-water used in these simulations may be considered as minimum values.

Over the 4-year time period that began at the moment of the H₂-He-Ne-Ar mixture injection, the calculated contents of N₂ and alkanes and the calculated pressure in the borehole are in relative accordance with the measured ones (Figs. 7, 8). As already mentioned, the calculated Ne content is also in accordance with the measured one up until the air introduction event that occurred at day 1232 (3.4 years). On the other hand, the calculated He content agrees with the measured one only over the first 50 days (Fig. 7). However, from November 2011 until September 2012, the measured He content value was more or less stable, oscillating in the range of 3 ± 0.1 vol%. A possible explanation for this observation is that He escaped out of the gas circuit into the 500 mL hydrogen filled syringe. Subsequently, when the syringe injected hydrogen, it released back its He content at the same time. From the syringe, He could have also diffused into the 3 L-volume hydrogen reservoir. In that case, He recovery in the circulating gas could take several years and it could become undetectable.

The partial pressure of the dissolved N₂ and C1 to C3 alkane estimated with the model is 3.4 bar at 16 °C. This pressure corresponds to the pressure of these gases in a virtual gaseous phase which is in equilibrium with water. Based on this result, while taking into account the other dissolved gases present in the pore-water (i.e. CO₂, heavier alkanes), the value of the total pressure of dissolved gases in Opalinus Clay pore-water, also named the “bubble point”, is larger than 3.4 but it should not reach 4 bar.

5.2.2 BPC-C1 experiment

The model developed for the BHT-1 experiment was applied without any change regarding the parameters of interest (i.e. concentrations in Opalinus Clay pore-water, retention coefficients, diffusion coefficients of the dissolved gases) to calculate the gas content evolution in borehole BPC-C1. The events that affected this experiment are listed in Electronic Appendix-Table 5. For these calculations, the single hypothesis concerned the initial

volume of the test interval and the precise volume of the tank. Assuming that the former was the theoretical one and that the tank volume value was either 0 L or 5.4 L (maximum value), we obtained the calculated curves presented in Fig. 9. The general agreement between measured and calculated data regarding alkane (C1 to C3) contents suggests that alkane contents in Opalinus Clay pore-water could have the same range of values at the BPC-C1 location than at the BHT-1 location. Measured N₂ content after the second argon purge (from day 231 onwards), was larger than the calculated one. At the beginning of this sequence, between the first two analytical results, the N₂ content increased at an apparent rate close to 0.1% per day. However, the N₂ content increase rate was only 0.05% per day between the second and the following analytical results. Moreover, the CH₄ and the N₂ contents are linearly correlated from the second analytical result onwards, whilst the first result is out of this relationship. These observations suggest that air N₂ could have entered the gas circuit between the first two sampling operations.

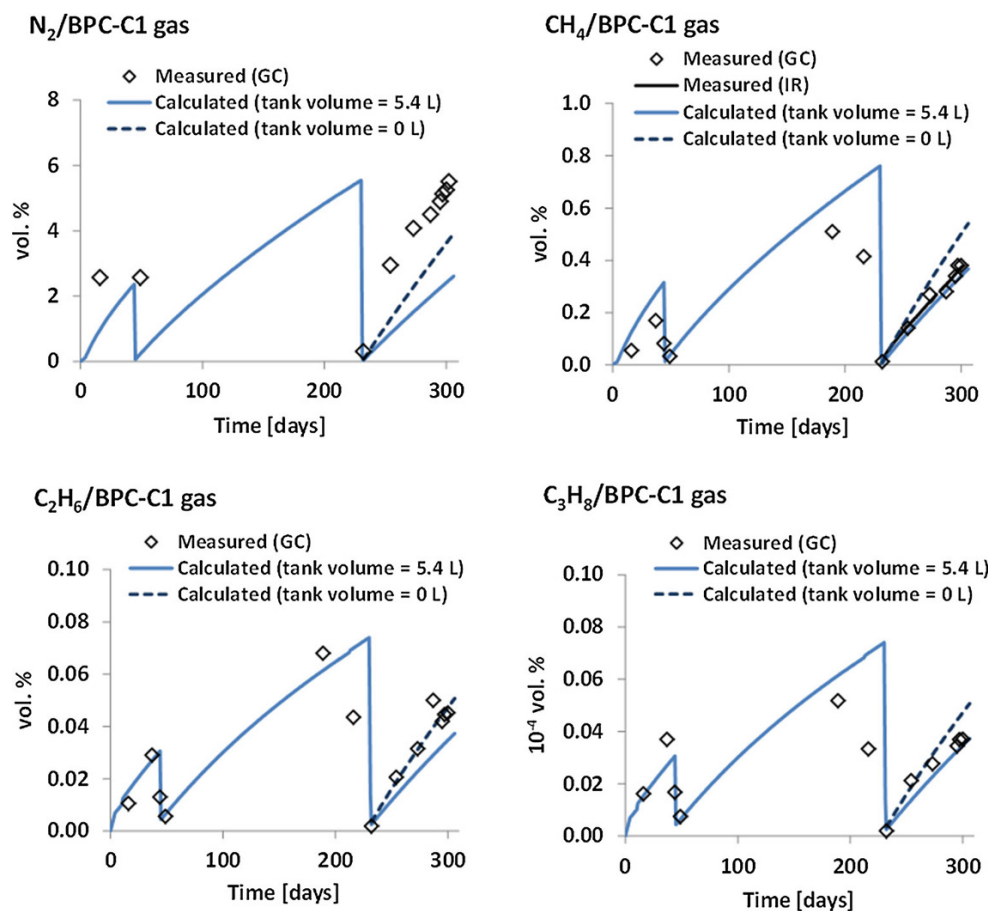
6 Discussion

6.1 Natural gas content and retention properties in Opalinus Clay at Mont Terri

6.1.1 Model sensitivity analysis

Estimated values of N₂ and C1 to C3 alkane concentration in Opalinus Clay pore-water at Mont Terri have been obtained thanks to in situ gas circulation experiments and by modelling diffusion and degassing of these gases with the code PHREEQC-3. The sensitivity of the results to the modelling parameters used (effective diffusion coefficient and volume values) has been checked. The effective diffusion coefficient (D_e) used in the calculations was based on a porosity (ϵ) value of 16% and a geometric factor G value of 7.7 ($\epsilon^{-1.11}$). With this D_e value, the He and Ne evolutions calculated reproduced satisfactorily the measured ones during the early 50 days for He and during more than one year for Ne. However G values could depend on the gas molecule size in clay rich rocks (Jacops et al. 2013). Smaller D_e values than the reference value would have prevented an acceptable fit for these gases, even during the early time period. On the other hand, porosity values close to 18% have been measured on BHT-1 core samples. D_e values up to 22% larger than the reference value have been taken into account in the model. The maximum D_e value considered corresponds to a G factor of 6.2 (ϵ^{-1}). This increase of the diffusion coefficient does not significantly modify the calculated gas content evolution. The influence of the initial interval volume value within its uncertainty

Fig. 9 Changes in the N_2 and alkane contents measured in the gas circulating in BPC-C1 and calculated with PHREEQC



range on the gas content evolution is also minor. On the contrary, reducing the discrepancy between the measured and the calculated gas content values over the first 1.5 years of the BHT-1 experiment leads to a significant change in the natural gas contents of about -25% . This adjustment also leads to calculated values lower than the measured ones during the latest phase of the experiment (over the last 5 years). This difference in the N_2 and alkane content values was assigned as being the uncertainty affecting them.

6.1.2 Comparison with measurements on core samples

Alkane total concentrations in Opalinus Clay rock have been measured in several Mont Terri cores, including a core from the borehole BHT-1 (Lerouge et al. 2015). Results are given in units of volume per mass of pore-water and may be compared to the C_1 values (mmol/L) obtained in the current study (Table 3). Regarding methane total concentration, the agreement is very good between the value obtained on the BHT-1 core (0.009 ± 0.0005 ccSTP/g pore-water $\approx 0.37 \pm 0.02$ mmol/L) and the value deduced from the gas circulation experiment (0.375 ± 0.10 mmol/L). Regarding ethane and propane, the values obtained by modelling the borehole

experiment (0.115 ± 0.03 mmol/L for ethane and 0.170 ± 0.05 mmol/L for propane) are only 56% and 33% by mass respectively of the values obtained from the analysis of the core gases (0.005 ± 0.0005 ccSTP/g pore-water $\approx 0.21 \pm 0.02$ mmol/L for ethane and 0.0125 ± 0.0005 ccSTP/g pore-water $\approx 0.52 \pm 0.02$ mmol/L for propane). These discrepancies are larger than the uncertainties attached to the borehole values. On the other hand, the borehole values represent both the dissolved part and the reversibly adsorbed part of the alkanes, whereas the values measured in the core should really represent the alkane total concentrations. The latest could include a fraction of the alkanes that is non-reversibly adsorbed on the rock. Further investigations are necessary to assess this hypothesis.

6.1.3 Alkane measurement on BPC-C1 borehole water

Alkane concentrations measured in the BPC-C1 water are lower than those estimated from gas measurement in BHT-1; i.e. the BPC-C1 values represent half to two thirds of the BHT-1 values. On the other hand, the comparison between the alkane concentrations measured in BPC-C1 gas and the alkane concentrations calculated in BPC-C1 based on the BHT-1 model showed that the alkane concentrations could

have the same range of values at the BPC-C1 location than at the BHT-1 location. As a consequence, the total pressure of dissolved gases in pristine pore-water should be comprised between 3.4 and 4 bar at the BPC-C1 location. In the BPC-C1 test interval, the water pressure has exceeded this value for about 4 years. Alkane content in the BPC-C1 water samples could still be affected by the last sampling operations that induced a pressure decrease down below the pore-water bubble point. As a result, the alkane concentrations would not have reached the pore-water pristine values yet.

6.1.4 Alkane retention properties in Opalinus Clay

Within the Opalinus Clay solid phase, organic matter has probably the largest affinity for alkanes when compared to the inorganic solids. We calculated K_d^{OM} (L/kg) as being the retention coefficient of a given alkane on Opalinus Clay solid organic matter, by dividing the K_d value of this alkane by the organic carbon content of the rock (0.8 wt.%; Mazurek et al. 2008). These K_d^{OM} values (Table 3) were then compared with octanol/water partition coefficients K_{ow} (Fig. 10). Methane, ethane, and propane K_{ow} values were calculated by using the linear relationship between K_{ow} and the carbon number described for alkane up to C10 (Molyneux 2014). The linear relationship between $\log K_d^{OM}$ and $\log K_{ow}$ for the first three alkanes reinforce the confidence in the data interpretation proposed.

6.1.5 Summary of the results regarding N_2 and alkane contents

The natural content of four gases in Opalinus Clay pore-water was evaluated at the experiment location: N_2 2.2 ± 0.5 mmol/L, CH_4 0.30 ± 0.075 mmol/L, C_2H_6

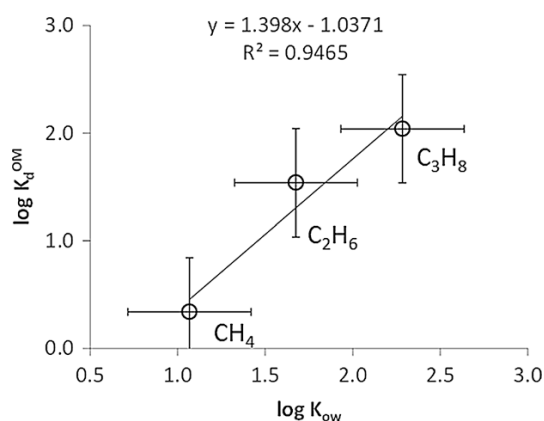


Fig. 10 Alkane C1–C3 retention coefficients on Opalinus Clay organic matter (L/kg organic carbon) deduced from the BHT-1 experiment versus octanol/water partition coefficients (K_{ow})

0.023 ± 0.005 mmol/L, C_3H_8 0.012 ± 0.003 mmol/L. These results provide a minimum value of 3.4 bar for the “bubble point” of Opalinus Clay pore-water at this location by using a thermodynamic equilibrium calculation and the gas solubility values presented in Table 1. Retention coefficients of alkanes on Opalinus Clay have been estimated. The values obtained for methane, ethane, and propane are linearly correlated on a log/log diagram with their octanol/water partition coefficient values, supporting the hypothesis that the alkanes are adsorbed on Opalinus Clay organic matter.

6.2 Origin of Opalinus Clay N_2 and alkanes

In the BHT-1 circulating gas, amongst the alkanes up to C6 observed, methane represents between 67 and 87% by mass; ethane represents between 6 and 12% and propane represents between 4 and 12%. These ratio values evolved over time as the result of distillation-type processes (Fig. 11). The ratio values deduced from the analyses performed on the last gas samples from BPC-C1 and from other borehole headspaces (BWS-A1, BWS-A2, and BWS-A3) at Mont Terri (Pearson et al. 2003) are in the same range (Fig. 12). In the rock, the methane fraction of the alkanes obtained on a BHT-1 core sample (Lerouge et al. 2015) was 34%. In the present study, the methane fraction of the alkanes calculated in the rock surrounding the BHT-1 borehole is 56%. However, a fraction of the alkanes non-reversibly adsorbed on the rock could be missing in the alkane inventory. As a consequence, the methane fraction of the alkanes is probably smaller than 50% in Opalinus Clay at the BHT-1 experiment location. The $\delta^{13}C$ isotopic compositions of the C2–C4 alkanes are similar in all the boreholes and in the BHT-1 core (Fig. 13), although methane $\delta^{13}C$ values are more scattered. These results are consistent with the hypothesis of a thermogenic origin of the alkanes already proposed by Pearson et al. (2003). As

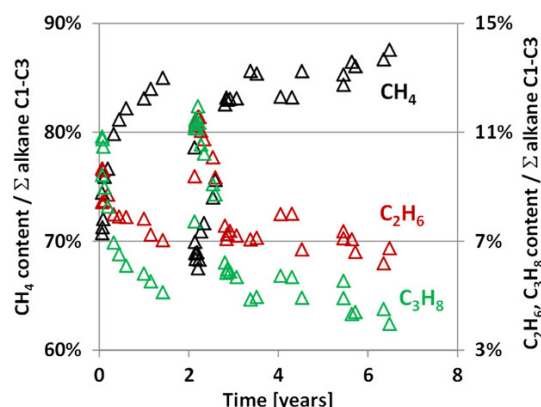


Fig. 11 Evolution of alkane C1–C3 relative proportion by mass observed in the BHT-1 circulating gas

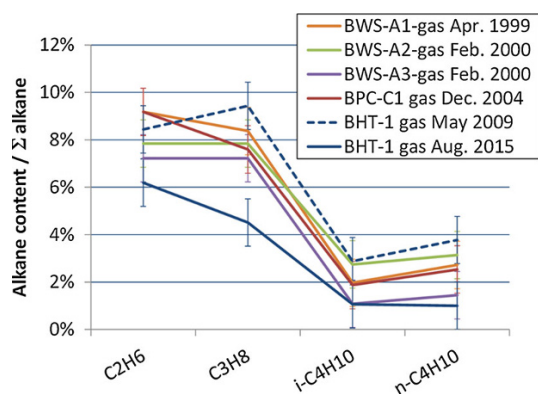


Fig. 12 Alkane C1–C4 relative content in gas sampled in several Mont Terri boreholes (data from Pearson et al. 2003 and this study)

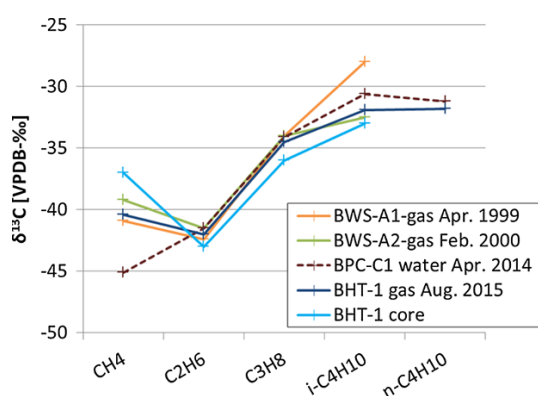


Fig. 13 Alkane C1–C4 carbon isotopic composition in gas sampled in several Mont Terri boreholes (data from Pearson et al. 2003 and this study) and extracted from a BHT-1 core sample (data from Lerouge et al. 2015); analytical uncertainty is included within the symbol size

complementary information, Opalinus Clay burial history indicates that it was exposed at temperature up to 85 °C (Mazurek et al. 2006) during several millions years. Moreover, the evaluation of a lower methane fraction in total alkanes than previously estimated from gas sampling tends to reinforce this hypothesis (Whiticar 1999). Furthermore, the chemical and carbon isotopic compositions of alkanes appear to be similar from one another location within Opalinus Clay at Mont Terri. This observation suggests that all the alkanes encountered in Opalinus Clay at Mont Terri arise from a common source, that they were produced at the same rate and that they have undergone similar migration chronicles. Regarding N₂, it may originate from the alteration of organic and/or inorganic sedimentary matter during diagenesis (Krooss et al. 1995, 2005; Grishina et al. 1998). Both N₂ and alkanes could have been produced either inside or outside the Opalinus Clay, for example in underlying formations that are rich in organic matter.

6.3 Transport properties of dissolved gas in Opalinus Clay at Mont Terri

The dissolved N₂ and alkane concentration values in Opalinus Clay pore-water were estimated with a diffusion model calculation. The diffusion coefficients used in this calculation were taken from the literature. The geometric factor value for the dissolved gases was the one which had been determined for HTO parallel to bedding in the same environment. It made it possible to reproduce with the model the evolution of Ne concentration observed in the borehole BHT-1 over the first year up until an air introduction event. This result confirms that HTO diffusion parameters may be applied to a dissolved gas like neon in Opalinus Clay. Sensitivity of the results to the geometric factor value was studied and a variation within a realistic range did not significantly modify the estimated values of the N₂ and alkane concentrations in Opalinus Clay pore-water. The general consistency between the experimental and modelling results obtained in both gas circulation experiments gives a strong confidence that the processes taken into account in the model represent correctly the actual processes.

7 Conclusion

Two gas circulation experiments in Opalinus Clay at Mont Terri, that have been monitored for 12 and 7 years respectively, made it possible to evaluate the chemical and carbon isotopic compositions of the natural gases dissolved in the pore-water. The latest result of these experiments is that N₂ is the most abundant dissolved gas (2.2 ± 0.5 mmol/L) in Opalinus Clay pore-water at Mont Terri. Together with methane, ethane, propane, and CO₂, dissolved N₂ lead to a total gas pressure value at equilibrium with Opalinus Clay pristine pore-water at the location of the experiments larger than 3.4 bar. As a consequence, gas bubbles may form in the rock surrounding the galleries wherever the total water pressure is smaller than this value.

Retention properties of C1 to C3 alkanes in Opalinus Clay were deduced from the gas circulation experiments. Expressed as distribution numbers, they are 0.02 L/kg for methane, 0.28 for ethane and 0.88 for propane. These values are linearly correlated with K_{ow} values on a log/log diagram, suggesting that the alkanes are adsorbed onto Opalinus Clay organic matter. Alkane proportions and their carbon isotopic compositions obtained are similar to previously published results and they are consistent with the hypothesis of a thermogenic origin. N₂ is thought to arise from the same origin. Regarding dissolved gas diffusion in Opalinus Clay, the geometric factor that has been determined for HTO in the same environment was shown to

apply to neon. As a consequence, it was used to simulate the diffusion of N₂ and alkanes C1 to C3. The gas circulation experiments performed made it possible: (1) to test in situ our description of both the gas exchange processes at the interface between the saturated rock and a gas phase and the gas migration processes into a clay rich rock; (2) to evaluate the natural dissolved gas concentration and their retention properties in the host rock.

Acknowledgements We appreciate the fruitful discussions with Andreas Gautschi, Christophe Tournassat, Urs Mäder, Elie Valcke, Nick Waber, Paul Wersin, Hans-Eike Gäbler, Ana Maria Fernandez, Jennifer McKelvie, Dani Traber, and many other partners during the Mont Terri geochemical meetings. We gratefully thank Gesine Lorenz, Thomas Fierz, Thierry Theurillat, Patrick Delage, and Philippe Tabani for their involvement in the realization of the experiments, Karen Fournier for English advice and Jacques Delay, Sarah Dewonck, Christophe Nussbaum, and Paul Bossart for their continuous support of the project. We warmly acknowledge Thomas Gimmi and Martin Mazurek for their very accurate reading of the manuscript. PC-C and/or HT experiments benefited from financial support by Andra (France), Nagra (Switzerland), CEN-SCK (Belgium), BGR (Germany), and NWMO (Canada).

Open Access This article is distributed under the terms of the Creative Commons Attribution 4.0 International License (<http://creativecommons.org/licenses/by/4.0/>), which permits unrestricted use, distribution, and reproduction in any medium, provided you give appropriate credit to the original author(s) and the source, provide a link to the Creative Commons license, and indicate if changes were made.

References

- Appelo, C. A. J., & Postma, D. (2005). *Geochemistry, groundwater and pollution* (2nd ed.). Boca Raton: CRC Press.
- Appelo, C. A. J., Van Loon, L. R., & Wersin, P. (2010). Multicomponent diffusion of a suite of tracers (HTO, Cl, Br, I, Na, Sr, Cs) in a single sample of Opalinus Clay. *Geochimica et Cosmochimica Acta*, 74(4), 1201–1219.
- Appelo, C. A. J., & Wersin, P. (2007). Multicomponent diffusion modeling in clay systems with application to the diffusion of tritium, iodide, and sodium in Opalinus Clay. *Environmental Science and Technology*, 41(14), 5002–5007.
- Bossart, P., Bernier, F., Birkholzer, J., Bruggeman, C., Connolly, P., Dewonck, S., Fukaya, M., Herfort, M., Jensen, M., Matray, J.-M., Mayor, J. C., Moeri, A., Oyama, T., Schuster, K., Shigeta, N., Vietor, T., & Wiczorek, K. (2017). Mont Terri rock laboratory, 20 years: Introduction, geology and overview of papers included in the Special Issue. *Swiss Journal of Geosciences*, 110. doi:10.1007/s00015-016-0236-1 (this issue).
- Boudreau, B. P. (1997). *Diagenetic models and their implementation: modelling transport and reactions in aquatic sediments*. Berlin: Springer.
- Cailteau, C., de Donato, P., Pironon, J., Vinsot, A., Garnier, C., & Barres, O. (2011a). In situ gas monitoring in clay rocks: Mathematical developments for CO₂ and CH₄ partial pressure determination under non-controlled pressure conditions using FT-IR spectrometry. *Analytical Methods*, 3(4), 888–895.
- Cailteau, C., Pironon, J., de Donato, P., Vinsot, A., Fierz, T., Garnier, C., et al. (2011b). FT-IR metrology aspects for on-line monitoring of CO₂ and CH₄ in underground laboratory conditions. *Analytical Methods*, 3(4), 877–887.
- Delay, J., Bossart, P., Ling, L. X., Blechschmidt, I., Ohlsson, M., Vinsot, A., et al. (2014). Three decades of underground research laboratories: What have we learned? *Geological Society, London, Special Publications*, 400(1), 7–32.
- Gaucher, E. C., Tournassat, C., Pearson, F. J., Blanc, P., Crouzet, C., Lerouge, C., et al. (2009). A robust model for pore-water chemistry of clayrock. *Geochimica et Cosmochimica Acta*, 73(21), 6470–6487.
- Grishina, S., Pironon, J., Mazurov, M., Sergey, G., Pustilnikov, A., Fon-Der-Flaas, G., et al. (1998). Organic inclusions in salt. Part 3. Oil and gas inclusions in Cambrian evaporite deposit from East Siberia. A contribution to the understanding of nitrogen generation in evaporites. *Organic Geochemistry*, 28(5), 297–310.
- Hayduk, W., & Laudie, H. (1974). Prediction of diffusion coefficients for nonelectrolytes in dilute aqueous solutions. *AIChE Journal*, 20(3), 611–615.
- Jacops, E., Volckaert, G., Maes, N., Weetjens, E., & Govaerts, J. (2013). Determination of gas diffusion coefficients in saturated porous media: He and CH₄ diffusion in Boom Clay. *Applied Clay Science*, 83, 217–223.
- Jähne, B., Heinz, G., & Dietrich, W. (1987). Measurement of the diffusion coefficients of sparingly soluble gases in water. *Journal of Geophysical Research: Oceans*, 92(C10), 10767–10776.
- Krooss, B. M., Friberg, L., Gensterblum, Y., Hollenstein, J., Prinz, D., & Littke, R. (2005). Investigation of the pyrolytic liberation of molecular nitrogen from Palaeozoic sedimentary rocks. *International Journal of Earth Sciences*, 94(5), 1023–1038.
- Krooss, B. M., Littke, R., Müller, B., Frielingsdorf, J., Schwochau, K., & Idiz, E. F. (1995). Generation of nitrogen and methane from sedimentary organic matter: Implications on the dynamics of natural gas accumulations. *Chemical Geology*, 126(3), 291–318.
- Lerouge, C., Blessing, M., Flehoc, C., Gaucher, E. C., Henry, B., Lassin, A., et al. (2015). Dissolved CO₂ and alkane gas in clay formations. *Procedia Earth and Planetary Science*, 13, 88–91.
- Liss, P. S., & Slater, P. G. (1974). Flux of gases across the air–sea interface. *Nature*, 247(5438), 181–184.
- Lundy, M., Garitte, B., Lettry, Y., & Vinsot, A. (2013). Experimental design for in situ characterization of the Callovo-Oxfordian pore-water composition at 85 °C. *Procedia Earth and Planetary Science*, 7, 533–536.
- Lundy, M., & Vinsot, A. (2010). Implementation of Raman and mass spectrometry for on line measurement of gas composition in boreholes. In Andra (Ed.), *Clays in Natural and Engineered Barriers for Radioactive Waste Confinement, 4th International Meeting, Nantes, France, March 29–April 1st, 2010, Abstracts* (pp. 535–536).
- Mazurek, M., Alt-Epping, P., Bath, A., Gimmi, T., Niklaus Waber, H., Buschaert, S., et al. (2011). Natural tracer profiles across argillaceous formations. *Applied Geochemistry*, 26(7), 1035–1064.
- Mazurek, M., Gautschi, A., Marschall, P., Vigneron, G., Lebon, P., & Delay, J. (2008). Transferability of geoscientific information from various sources (study sites, underground rock laboratories, natural analogues) to support safety cases for radioactive waste repositories in argillaceous formations. *Physics and Chemistry of the Earth, Parts A/B/C*, 33, S95–S105.
- Mazurek, M., Hurford, A. J., & Leu, W. (2006). Unravelling the multi-stage burial history of the Swiss Molasse Basin: Integration of apatite fission track, vitrinite reflectance and biomarker isomerisation analysis. *Basin Research*, 18(1), 27–50.
- McCollom, T. M., Lollar, B. S., Lacrampe-Couloume, G., & Seewald, J. S. (2010). The influence of carbon source on abiotic organic

- synthesis and carbon isotope fractionation under hydrothermal conditions. *Geochimica et Cosmochimica Acta*, 74(9), 2717–2740.
- Mills, R., & Harris, K. R. (1976). The effect of isotopic substitution on diffusion in liquids. *Chemical Society Reviews*, 5, 215–231.
- Molyneux, P. (2014). Octanol/water partition coefficients Kow: A critical examination of the value of the methylene group contribution to log Kow for homologous series of organic compounds. *Fluid Phase Equilibria*, 368, 120–141.
- Nussbaum, C., Kloppenburg, A., Caër, T., & Bossart, P. (2017). Tectonic evolution around the Mont Terri rock laboratory, northwestern Swiss Jura: constraints from kinematic forward modelling. *Swiss Journal of Geosciences*, 110. doi:10.1007/s00015-016-0248-x (this issue).
- Ohsumi, T., & Horibe, Y. (1984). Diffusivity of He and Ar in deep-sea sediments. *Earth and Planetary Science Letters*, 70(1), 61–68.
- Parkhurst, D. L., & Appelo, C. A. J. (2013). *Description of input and examples for PHREEQC version 3: A computer program for speciation, batch-reaction, one-dimensional transport, and inverse geochemical calculations*. US geological survey techniques and methods, 6-A43.
- Pearson, F. J., Arcos, D., Bath, A., Boisson, J. Y., Fernandez, A. M., Gäbler, H.-E., Gaucher, E., Gautschi, A., Griffault, L., Henàn, P. W., & Wabe H. N. (2003). Mont Terri Project-Geochemistry of water in the Opalinus Clay Formation at the Mont Terri rock laboratory. *Bern: OFEG Report, Geology Serie, No. 5*. Federal Office of Topography (swisstopo), Wabern, Switzerland. <http://www.mont-terri.ch>
- Pearson, F. J., Tournassat, C., & Gaucher, E. C. (2011). Biogeochemical processes in a clay formation in situ experiment: Part E—Equilibrium controls on chemistry of pore water from the Opalinus Clay, Mont Terri Underground Research Laboratory, Switzerland. *Applied Geochemistry*, 26(6), 990–1008.
- Prinzhofer, A., Girard, J. P., Buschaert, S., Huiban, Y., & Noirez, S. (2009). Chemical and isotopic characterization of hydrocarbon gas traces in porewater of very low permeability rocks: The example of the Callovo-Oxfordian argillites of the eastern part of the Paris Basin. *Chemical Geology*, 260(3), 269–277.
- Prinzhofer, A., & Pernaton, É. (1997). Isotopically light methane in natural gas: bacterial imprint or diffusive fractionation? *Chemical Geology*, 142(3), 193–200.
- Rübel, A. P., Sonntag, C., Lippmann, J., Pearson, F. J., & Gautschi, A. (2002). Solute transport in formations of very low permeability: Profiles of stable isotope and dissolved noble gas contents of pore water in the Opalinus Clay, Mont Terri, Switzerland. *Geochimica et Cosmochimica Acta*, 66(8), 1311–1321.
- Scharlin, P., Battino, R., Silla, E., Tuii, I., & Pascual-Ahuir, J. L. (1998). Solubility of gases in water: Correlation between solubility and the number of water molecules in the first solvation shell. *Pure Applied Chemistry*, 70(10), 1895–1904.
- Sherwood Lollar, B., Lacrampe-Couloume, G., Voglesonger, K., Onstott, T. C., Pratt, L. M., & Slater, G. F. (2008). Isotopic signatures of CH₄ and higher hydrocarbon gases from Precambrian Shield sites: A model for abiogenic polymerization of hydrocarbons. *Geochimica et Cosmochimica Acta*, 72(19), 4778–4795.
- Stolper, D. A., Martini, A. M., Clog, M., Douglas, P. M., Shusta, S. S., Valentine, D. L., et al. (2015). Distinguishing and understanding thermogenic and biogenic sources of methane using multiply substituted isotopologues. *Geochimica et Cosmochimica Acta*, 161, 219–247.
- Tabani, P., Hermand, G., Delay, J., & Mangeot, A. (2010). Geoscientific Data Acquisition and management System (SAGD) of the Andra Meuse/Haute-Marne research center. In Andra (Ed.), *Clays in Natural and Engineered Barriers for Radioactive Waste Confinement, 4th International Meeting, Nantes, France, March 29–April 1st, 2010, Abstracts* (pp. 253–254).
- Thury, M., & Bossart, P. (1999). The Mont Terri rock laboratory, a new international research project in a Mesozoic shale formation, Switzerland. *Engineering Geology*, 52(3), 347–359.
- Tournassat, C., Vinsot, A., Gaucher, E. C., & Altmann, S. (2015). Chapter 3: Chemical conditions in clay-rocks. In C. Tournassat, C. I. Steefel, I. C. Bourg, & F. Bergaya (Eds.), *Developments in clay science* (Vol. 6, pp. 71–100). Amsterdam: Elsevier.
- Trémosa J., Hadi J., Claret F., Tournassat C., & Vinsot A. (2015). Kinetic experiments in order to determine the rate of oxygen consumption by the Callovo-Oxfordian Argillaceous rock. In *Clays in Natural and Engineered Barriers for Radioactive Waste Confinement, 6th International Meeting, Brussels, Belgium, March 23–26, 2015, Abstracts* (pp. 116–117).
- Van Loon, L. R., & Mibus, J. (2015). A modified version of Archie's law to estimate effective diffusion coefficients of radionuclides in argillaceous rocks and its application in safety analysis studies. *Applied Geochemistry*, 59, 85–94.
- Vinsot, A., Appelo, C. A. J., Cailteau, C., Wechner, S., Pironon, J., De Donato, P., et al. (2008). CO₂ data on gas and pore water sampled in situ in the Opalinus Clay at the Mont Terri rock laboratory. *Physics and Chemistry of the Earth, Parts A/B/C*, 33, S54–S60.
- Vinsot, A., Appelo, C. A. J., Lundy, M., Wechner, S., Lettry, Y., Lerouge, C., et al. (2014). In situ diffusion test of hydrogen gas in the Opalinus Clay. *Geological Society, London, Special Publications*, 400(1), 563–578.
- Whiticar, M. J. (1999). Carbon and hydrogen isotope systematics of bacterial formation and oxidation of methane. *Chemical Geology*, 161(1), 291–314.
- Zhang, T., & Krooss, B. M. (2001). Experimental investigation on the carbon isotope fractionation of methane during gas migration by diffusion through sedimentary rocks at elevated temperature and pressure. *Geochimica et Cosmochimica Acta*, 65(16), 2723–2742.

Exploring diffusion and sorption processes at the Mont Terri rock laboratory (Switzerland): lessons learned from 20 years of field research

Olivier X. Leupin¹ · Luc R. Van Loon² · Thomas Gimmi^{2,3} · Paul Wersin³ · Josep M. Soler^{4,5}

Received: 19 April 2016 / Accepted: 17 December 2016 / Published online: 7 March 2017
© The Author(s) 2017. This article is published with open access at Springerlink.com

Abstract Transport and retardation parameters of radionuclides, which are needed to perform a safety analysis for a deep geological repository for radioactive waste in a compacted claystone such as Opalinus Clay, must be based on a detailed understanding of the mobility of nuclides at different spatial scales (laboratory, field, geological unit). Thanks to steadily improving experimental designs, similar tracer compositions in different experiments and complementary small laboratory-scale diffusion tests, a unique and large database could be compiled. This paper presents the main findings of 20 years of diffusion and retention experiments at the Mont Terri rock laboratory and their impact on safety analysis.

Keywords Nuclide transport · Sorption · Porosity · Porous media · Claystone · Opalinus Clay · Nuclear waste disposal

Editorial handling: P. Bossart and A. G. Milnes.

This is paper #20 of the Mont Terri Special Issue of the Swiss Journal of Geosciences (see Bossart et al. 2017, Table 3 and Fig. 7).

✉ Olivier X. Leupin
olivier.leupin@nagra.ch

¹ National Cooperative for the Disposal of Radioactive Waste NAGRA, Hardstrasse 73, 5430 Wettingen, Switzerland

² Paul Scherrer Institut PSI, 5232 Villigen, Switzerland

³ Institute of Geological Sciences, University of Bern, Baltzerstrasse 3, 3012 Bern, Switzerland

⁴ Institute of Environmental Assessment and Water Research IDAEA-CSIC, Calle Jordi Girona 18-26, 08034 Barcelona, Spain

⁵ Associated Unit: Hydrogeology Group (UPC-CSIC), 08034 Barcelona, Spain

1 Introduction

Claystone formations are considered worldwide as potential host rocks for the deep geological disposal of radioactive waste. They generally act as aquitards or aquicludes because of their very low hydraulic conductivities, which result from the very small pore and particle sizes. Thus, molecular diffusion is the dominant transport mechanism in these formations under natural conditions (Van Loon et al. 2003; Patriarche et al. 2004; Lavastre et al. 2005; Hendry and Wassenaar 2005; Gimmi et al. 2007; Savoye et al. 2008; Koroleva et al. 2011; Mazurek et al. 2011). Claystone formations also exhibit a large retention potential for sorbing solutes due to the large reactive surface areas of the clay minerals. These properties have triggered an intensive research programme at both laboratory and field scales in the last years. In this regard, the international Mont Terri Project with its underground research laboratory in the Swiss Jura Mountains near St-Ursanne offers a unique platform for improving the understanding of the transport and retention properties of indurated clays. This paper aims to review the main findings and the progress made in the understanding of diffusion and retention processes in Opalinus Clay at the Mont Terri rock laboratory.

Several field diffusion experiments have been performed in the Mont Terri rock laboratory (see Fig. 1; Table 1). The main motivations for conducting diffusion experiments at field scale to complement laboratory-scale experiments, in addition to the large volume of rock that can be investigated, are (a) the very low water/rock ratio leading to a better control of the chemical conditions by the rock and (b) the in situ head pressure which is closer to the disposal situation.

The experiments all served to investigate the in situ transport properties of Opalinus Clay (e.g. Palut et al. 2003; Van Loon et al. 2004b; Wersin et al. 2004; Yllera et al.

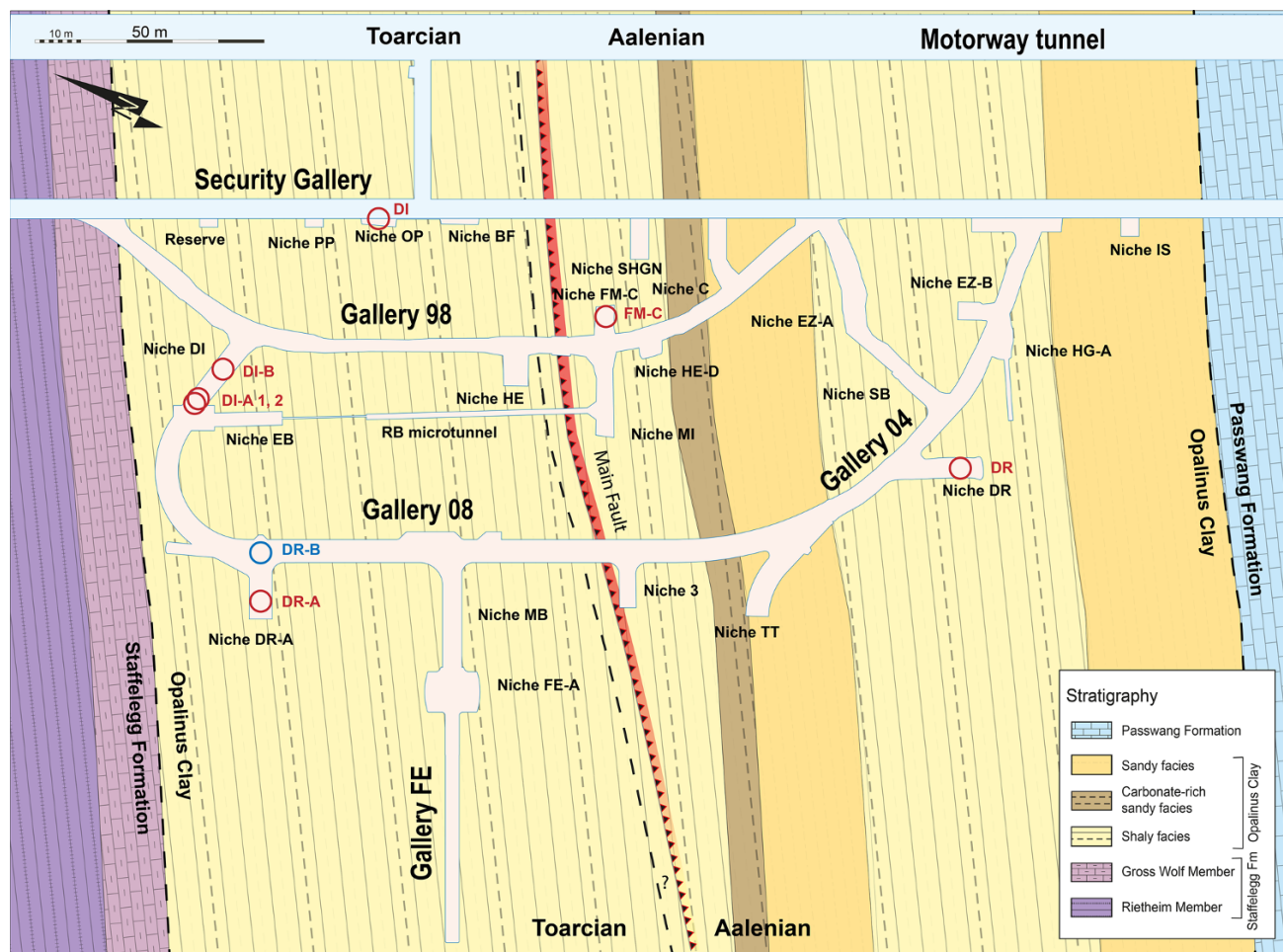


Fig. 1 Map of the Mont Terri rock laboratory indicating the location of the different diffusion experiments

2004; Wersin et al. 2008; Gimmi et al. 2014). A main interest was the comparison of results with those from laboratory experiments performed on small samples (in the order of a few cm) of the same material. For instance, small laboratory samples may be strongly affected by stress release, meaning that the obtained parameters are not representative for in situ conditions. Representativeness was also an issue for the in situ tests. One of the field studies (Palut et al. 2003) suggested the existence of a borehole disturbed zone (BdZ), but all the other studies (Van Loon et al. 2004b; Wersin et al. 2004; Soler et al. 2008; Wersin et al. 2008; Gimmi et al. 2014) did not report such an effect. Even though some differences in transport and retention properties were observed, the laboratory values obtained in smaller-scale diffusion experiments could generally be confirmed. For instance, similar diffusion coefficients to those in laboratory studies were obtained in the FM-C, DI, DI-A1,¹ DI-A2 and DI-B

¹ DI-A1 and DI-A2 were two distinct experiments that were administrated within the Mont Terri DI-A project.

experiments (for locations see Fig. 6 in Bossart et al. 2017) for tritiated water HTO, I^- and $^{22}Na^+$ (Palut et al. 2003; Gómez-Hernández and Guardiola-Albert 2004; Tevissen et al. 2004; Van Loon et al. 2004b; Wersin et al. 2008; Soler et al. 2008). Most of the field experiments in Opalinus Clay used relatively long injection intervals (~ 1 m) and were thus dominated by diffusion parallel to the bedding plane of the clay formation. Only the more recent DR experiment (Gimmi et al. 2014) focused on diffusion perpendicular to bedding and on the anisotropy of diffusion.

2 Concept and modelling of the diffusion experiments

The general concept of most field diffusion experiments at the Mont Terri rock laboratory is based on the layout used in the first DI experiment (Palut et al. 2003), which was a variation of the decreasing source concentration method used in laboratory column experiments (Rowe et al. 1988; Shackelford 1991). The same general principle was followed

in earlier in situ large-scale experiments in the Boom Clay Formation in Belgium (Put et al. 1993; De Cannière et al. 1996; Aertsens et al. 2013). In those experiments, tracers (HTO, $^{125}\text{I}^-$) were injected in a borehole interval and their concentrations monitored in other intervals of the same borehole. In the experiments at Mont Terri, a tracer cocktail is circulated into a hydraulically packed-off borehole from where the tracers diffuse through a filter screen into the Opalinus Clay. The pressure head of the fluid is maintained at a value close to that of the surrounding pore-water to avoid any advective transport. The decrease in the concentration of the tracers in the circulation system of the borehole is monitored over time until the end of the experiment. At that time, a volume of rock around the borehole interval is overcored and tracer distribution profiles in the rock are measured. The two sets of independent data (temporal evolution in the borehole and spatial distribution profiles in the rock) allow determination through modelling of (a) a transport parameter (effective diffusion coefficient) and (b) an accessible porosity (conservative tracers) or sorption parameter (sorbing tracers). Figure 2 shows results from the DI-A2 experiment (Wersin et al. 2008).

In general, the models used to interpret the measured data solve the diffusion-sorption equation

$$\frac{\partial C_{\text{tot}}}{\partial t} = \nabla \cdot (\mathbf{D}_e \nabla C) \quad (1)$$

with C_{tot} the total solute concentration (including the sorbed fraction), C the aqueous solute concentration, t the time, and \mathbf{D}_e the effective diffusion coefficient tensor. Models for sorbing tracers often assume a linear isotherm (Van Loon et al. 2004b; Wersin et al. 2008, 2010; Gimmi et al. 2014), leading to a constant distribution coefficient K_d and a constant rock capacity factor α according to

$$\alpha = \varepsilon + \rho_{\text{bd}} K_d \quad (2)$$

and

$$C_{\text{tot}} = \alpha C \quad (3)$$

with ε the (accessible) porosity and ρ_{bd} the bulk dry density of the rock. A Freundlich type isotherm or multi-site ion exchange was considered in other cases (above references and Soler et al. 2013, 2014; see also below). The decrease in tracer concentration in the borehole depends directly on both \mathbf{D}_e and α (ε for conservative tracers), while transport distances in the rock depend on the magnitude of the apparent diffusion coefficient $D_a = \mathbf{D}_e/\alpha$. In this way, both \mathbf{D}_e and α can be determined for each tracer by simultaneously adjusting the model to both sets of data.

The geometrical and conceptual complexity of the models used to analyse and interpret the data from the field experiments have evolved with time. The simulations for the DI, FM-C and (partly) DI-A1 and DI-B experiments were set up in 3D, but it was then recognised that, for the comparably long injection intervals in these experiments, diffusion parallel to bedding dominated the behaviour. Accordingly, later models for the same geometrical setup (DI-A1, DI-A2, DR-A) considered a 1D radial system with diffusion parallel to bedding only, which considerably facilitates simulations. In order to account for the oblique angle of bedding with respect to the vertical borehole axis, a corrected borehole radius had to be adopted.

The borehole for the DR experiment was drilled perpendicular to the bedding. In this case, a 1D radial representation would also be appropriate, but diffusion parallel and perpendicular to bedding had to be considered explicitly for the comparably short intervals, leading to ellipsoidal tracer plumes.

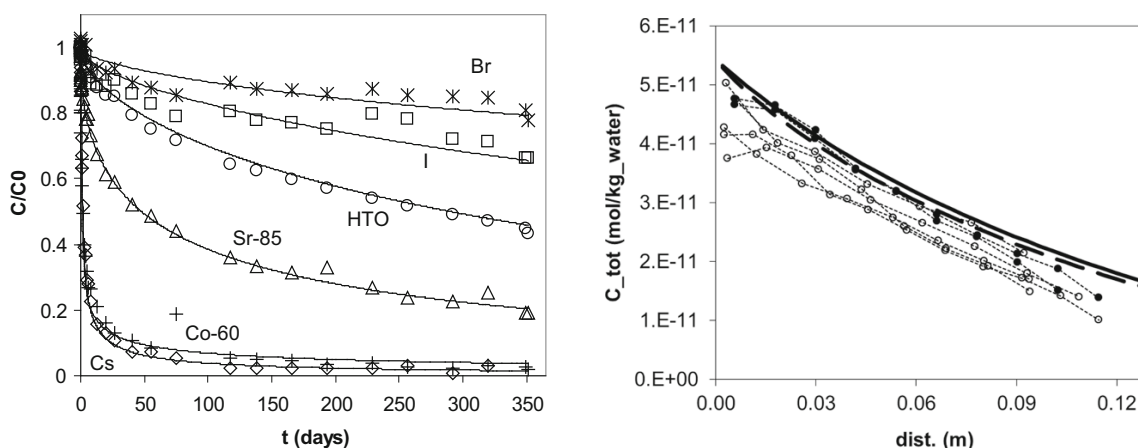


Fig. 2 Experimental and model results from DI-A2 (after Wersin et al. 2008). Evolution of the concentration of the tracers (Br, I, HTO, ^{85}Sr , ^{60}Co , Cs) in the injection system (relative concentration vs. time) (left). Experimental data (symbols) and modelled concentrations (lines). HTO profiles in the rock (concentration vs. distance from

borehole wall) (right). Thin lines and circles represent experimental data; thick line correspond to model results. The 2 uppermost measured profiles (solid circles) were measured around the central part of the circulation interval

Conceptually, the models for the earlier experiments considered single tracer diffusion only (e.g. Palut et al. 2003; Tevissen et al. 2004; Van Loon et al. 2004b; Yllera et al. 2004; Wersin et al. 2004; Soler et al. 2008; Wersin et al. 2008). That is, transport of a tracer (neutral, anion and/or cation) was assumed to be independent of that of any other solute. This approach was justified for these experiments because the tracers were introduced at low concentrations and the background chemical composition of the pore-water remained practically unaffected.

Stable Cs^+ in the DI-A1 and DI-A2 experiments, which was injected at concentrations large enough to experience non-linear sorption, was also initially modelled as a single tracer. Non-linear sorption was included through Freundlich sorption isotherms (Van Loon et al. 2004b; Wersin et al. 2004, 2008). Later, a multi-component approach allowed the use of a more mechanistic cation-exchange model (Appelo and Wersin 2007; Appelo et al. 2010; Soler et al. 2013, 2014).

A multi-component approach with interrelated species-specific diffusion of anions and cations (Appelo and Wersin 2007; Appelo et al. 2010) can be considered as more appropriate from a scientific point of view, even though it was not strictly required for the earlier experiments. The strength of such a multi-component approach lies in the fact that the effect of the negatively charged clay surfaces can also be included. These later models considered a diffuse layer region, from which anions are (partly) excluded and where cations are enriched (and contribute to “surface diffusion”) compared to bulk pore-water. Inevitably, this multi-porosity approach introduces additional parameters such as the width of the diffuse layer region. These parameters are typically unknown, but there are attempts to determine them from independent data. The DR-A experiment was explicitly set up to test the predictive capability of such multi-component approaches. The strong perturbation of the pore-water chemistry in this experiment requires the coupling between transport and sorption of different ions to be considered and a single-component approach is no longer feasible.

3 Evolution of the experimental setup

Table 1 gives an overview of the Mont Terri diffusion experiments performed to date together with the tracers used. The early FM-C experiment was originally planned as a cross-hole tracer test to investigate flow mechanisms in a fracture zone of the main fault area at Mont Terri, but it was then turned into a series of diffusion experiments. In the latest FM-C test (Gómez-Hernández and Guardiola-Albert 2004), diffusion of HTO and I^- through the fracture

zone was investigated, starting from a packed-off borehole section around 0.97 m long.

The main objective of the DI experiment, the pioneer diffusion test, was to develop an experimental concept that would allow a comparison between laboratory and in situ results. It was constructed with two intervals of 0.6 m length. The lower one was used to inject the tracers (HTO and I^-) and the upper one was intended as an observation interval to detect any leakage of tracers along the borehole and packer system. No tracers were detected in the upper interval, meaning that the packer seal was tight and no bypass transport occurred. The setup of the subsequent DI-A1, DI-B and DI-A2 experiments consisted of a single interval from which tracers diffused into the rock.

In the DI-A1, DI-B and DI-A2 experiments, the studies were extended to include different sorbing tracers. In addition, DI-B explored the possibility of performing such experiments using only non-active tracers. The setup of these experiments consisted of a single interval from which tracers diffused into the rock.








Two short injection intervals (top and middle, each 0.15 m long) and a pressure monitoring interval at the bottom (0.13 m long) were installed in the DR experiment. The short injection intervals were chosen to be able to determine the diffusion anisotropy in situ and the larger fluid volume in the circulation loop allowed a longer duration of the test (slower decline of tracer concentrations).

The setup of the recent DR-A experiment was a copy of that of the DI-A2. The DR-A experiment aimed at testing multi-component reactive transport models by inducing a strong salinity perturbation after a first half year of tracer indiffusion. The soon to be started diffusion test DR-B is planned as a very long-term, low-maintenance experiment and requires a fundamentally different experimental design in which no fluid would circulate and no active tracers would be needed. The main focus of this diffusion test is to validate diffusion process understanding by using an alternative experimental setup, longer diffusion periods and larger rock volumes. A central borehole was drilled with sufficiently large dimensions to allow emplacement of a source containing a 2 M NaI solution that will provide a diffusion gradient that can be followed over at least a decade from observation boreholes placed at different distances. For this purpose, a highly sensitive, comparably small and mobile XRF probe was developed to follow the diffusion of iodide and other tracers that may be injected in the future.

4 Analytical methods

All experiments except DR-B involved the circulation of a solution through the injection interval. Samples of the circulated solutions were regularly taken from the return-

Table 1 Summary of the setups of the different in situ diffusion experiments

Experiment	DI	FM-C	DI-A1 (DI-B*)	DI-A2	DR	DR-A	DR-B
Setup (about to scale)							
Source type	circulated fluid ^a , partly re-doped	circulated fluid, single pulse	circulated fluid, single pulse	circulated fluid, single pulse	circulated fluid ^b , three pulses	circulated fluid, pulses	stagnant fluid, single pulse
Source volume, L	9	~6.6	~10.5	~9.6	~20 (per interval)	~10	~85
Interval length, m	0.6	0.97	1	1	0.15	1	1
Bh diameter, m	0.076	0.056	0.076	0.076	0.076	0.076	0.6
Angle bed-bh, °	34	50 (fracture-bh)	31	30	90	33	ca. 35
Main diffusion direction	par (+ perp)	HTO	par	par	perp + par	par	par (+ perp)
Uncharged tracers	HTO	HTO	HTO	HTO	HTO, HDO, H ₂ ¹⁸ O	HTO	
Anion tracers	I ⁻	I ⁻	I ⁻	I ⁻ , Br ⁻	I ⁻ , Br ⁻ , SeO ₄ ²⁻	I ⁻ , Br ⁻	
Cation tracers			²² Na ⁺ , Cs ⁺ , ⁶ Li, ⁸⁷ Rb)	⁸⁵ Sr ²⁺ , Cs ⁺ , ⁶⁰ Co ²⁺	¹³⁷ Cs ⁺ , Cs ⁺ , ¹³³ Ba ⁺ , ⁶⁰ Co ²⁺ , ¹⁵² Eu ³⁺ , Eu ³⁺ , ²² Na ⁺ , ⁸⁸ Sr ²⁺	⁸⁸ Sr ²⁺ , Cs ⁺ , ⁶⁰ Co ²⁺ , Eu ³⁺	
Duration/Exp. phases, a	~1/1997-2001	~0.7/1998-2003	~1/2000-2005	~1/2003-2007	~4/2004-2012	~2/2011-2014	>10/2014-..
Data type ^d	bh, pro	bh, pro	bh, pro	bh, pro	bh, pro	bh, pro	pro
References	e	f	g	h	i	j	

* The setup of DI-B was very similar to that of DI-A1, with interval length 0.6 m, source volume ~30 L, bedding at 32° and duration ~1/2001-2006. Only stable isotopes were used as tracers: HDO, I⁻, ⁶Li⁺ and ⁸⁷Rb⁺ (Soler et al. 2008)

^a Tracers added in lower interval; no tracers detected in upper interval

^b Tracers added in upper two intervals; bottom interval only for pressure monitoring

^c No consistent simulations for borehole and profile data of iodide could be obtained (bh data seem to be affected by sorption), so iodide data were not presented in Palut et al. (2003)

^d bh: circulated borehole fluid time series; pro: rock profiles

^e Palut et al. (2003), Tevissen and Soler (2003)

^f Gómez-Hernández and Guardiola-Albert (2004), Tevissen and Soler (2003)

^g Van Loon et al. (2004b)

^h Wersin et al. (2008, 2010), Soler et al. (2013)

ⁱ Gimmi et al. (2014)

^j Soler et al. (2014)

flow lines and analysed for tracers and partly for major components. Usually no fluid was replaced after sampling, which led to a reduction of the total fluid volume in the circulation loops (e.g. by 6–7% in the case of the DR experiment) by the end of the experiment. In the DI experiment, it was first attempted to keep the HTO activity approximately constant by regularly re-spiking the circulated solution. However, this procedure turned out to be impractical and it was abandoned after three re-spiking events. In addition to the sample data, time series of radioactive tracer activities within the circulated solutions were obtained by γ spectrometry (Wersin et al. 2008) in the DI-A2 and the DR experiments.

4.1 Major element chemistry of water samples

In most experiments, the major element and tracer composition of collected borehole water was analysed by ion chromatography (IC), inductively coupled plasma-optical emission spectroscopy (ICP-OES) and/or inductively coupled plasma-mass spectrometry (ICP-MS). Details of the determination of ions are given in Palut et al. (2003), Van Loon et al. (2004b), Wersin et al. (2004, 2008), Soler et al. (2008) and Gimmi et al. (2014). Most of the samples were filtered (0.45 or 0.2 μm) prior to analysis. Using these techniques, analytical uncertainties are in the range of $\pm 10\%$ for Cl^- and Na^+ and $\pm 5\%$ for all other tracers and solutes. Alkalinity was generally determined for selected samples by potentiometric titration. In some experiments, pH was measured in the laboratory and in-line with a combined glass electrode (high-pressure resisting KCl-type gel electrolyte containing glycerol) and E_h was obtained in-line with an Ag/AgCl electrode (3 M KCl gel type, reference potential of +0.210 V).

4.2 Off-line analyses of radiotracers in water samples

Samples of the water circulating through the borehole interval were taken at different times during the experiments to monitor the decrease in tracer concentrations. Activities of $^{75}\text{SeO}_4^{2-}$, $^{22}\text{Na}^+$, $^{85}\text{Sr}^{2+}$, $^{133}\text{Ba}^{2+}$, $^{137}\text{Cs}^+$, $^{60}\text{Co}^{2+}$ and $^{152}\text{Eu}^{3+}$ in filtered (0.45 μm) borehole water samples were determined by γ -ray counting with two high-resolution intrinsic p-type coaxial Ge-detectors at the radio-analytical laboratory of the Paul Scherrer Institute. The HTO activity concentrations of the same solutions were obtained by liquid scintillation counting (LSC) at the same laboratory. The analytical uncertainties were estimated to be about $\pm 3\%$ for HTO, between ± 5 and $\pm 15\%$ for $^{22}\text{Na}^+$ (β -emitter) and $\pm 5\%$ for the other radiotracers.

4.3 In-situ analyses of radiotracers in reservoir tanks

In the DI-A2 and DR experiments, the depletion of radiotracers in the circulating fluid was also measured in situ using a solid-state intrinsic high-purity Ge-detector with an electric cryo-cooling system (Wersin et al. 2008) which was placed in between (DR) or juxtaposed (DI-A2) to the tracer reservoirs. The following tracers could be tracked in the circulating fluid: $^{75}\text{SeO}_4^{2-}$, $^{22}\text{Na}^+$, $^{85}\text{Sr}^{2+}$, $^{133}\text{Ba}^{2+}$, $^{137}\text{Cs}^+$, $^{60}\text{Co}^{2+}$ and $^{152}\text{Eu}^{3+}$. The Ge-detector had to be regularly dismantled for maintenance, which resulted in small gaps in the time series and slight shifts in the measurements after re-installation; these were attributed to slightly different sensitivities and measurement geometries of the device. The ^{40}K background signal was used to recalibrate the data after re-installation.

4.4 Profile data

Tracer profiles in the claystone were essential in order to estimate transport parameters (e.g. HTO, I^- , Br^- , $^{22}\text{Na}^+$ and others) and water content unambiguously. The behaviour of the different mobile tracers could be compared directly when plotting the radial and axial profiles using normalised concentrations.

Therefore, after termination of the experiments the diffusion test intervals were usually overcored to analyse tracer distribution in the rock. The overcoring technique itself evolved over time and had to be adapted to the diffusion test geometries and boundary conditions (e.g. the inclined central borehole in the DR experiment required an oblique overcoring and the long duration of DR-A required an excentric overcore to maximise the sampling distance). The overcore was typically obtained a few days after taking the last sample from the circulation loop. The overcore was then sub-sampled immediately on site, as far as possible, by cutting disks parallel (e.g. DR experiment) or oblique (e.g. FM-C experiment) to the bedding or by drilling sub-cores (DI-A1, DI-A2). These disks and sub-cores were then further dimensioned to a practical size for the specific analyses. Detailed information on the analytical programme for the sub-samples can be found in e.g. Gimmi et al. (2014). In general, and depending on the specific composition of the circulating fluid, water content, stable water isotopes, active tracers and major element composition of the aqueous extracts were analysed.

5 Compilation of experimental results

The diffusion and sorption parameters obtained from numerical modelling exercises in the DI, DI-A1, DI-B, DI-A2 and DR experiments are compared with diffusion data

from oriented small-scale samples parallel to the bedding plane (Van Loon and Soler 2003; Van Loon et al. 2004b) and with laboratory batch sorption data (Van Loon et al. 2005a). As shown in Table 2, this comparison shows an overall consistent picture between laboratory and in situ results (details discussed below).

For all diffusion experiments carried out so far, except for DR-A, the circulating artificial water was prepared to match approximately the in situ pore-water composition. The borehole waters, which were sampled regularly, indicated fairly constant compositions, consistent with that expected for the pore-water. This confirms that the added artificial pore-water affected chemical conditions to only a small extent, thus ensuring stable chemical conditions. It is noteworthy that most of the added tracers (i.e. HTO, I^- , Br^- , Na^+ , Sr^{2+} , Cs^+) were not, or only barely, sensitive to pH or Eh, and thus perturbation of the pH or redox conditions should not have altered their diffusion behaviour. However, disturbance of salinity will affect cationic and anionic tracers to some extent and this was demonstrated in the DR-A experiment. A redox disturbance was unintentionally caused in the upper borehole section of the DR experiment by leakage of glycerol from the pH electrode (Gimmi et al. 2014). This resulted in microbially induced sulphate reduction and sulphide generation. Tracer data indicated that this led to the precipitation of CoS but did not affect the diffusion of the other injected tracers (Gimmi et al. 2014).

5.1 Water tracer diffusion

For HTO (and HDO in the DI-B and DR experiments, with D being 2H), the derived values for effective diffusivity and porosity show good agreement between in situ and laboratory data, well within the uncertainty of these parameters. A more detailed analysis of the HTO profiles in the DI-A2 experiment shows that the concentrations in the profiles measured around the upper and lower parts of the injection interval are slightly smaller than those in the central part of the interval (length = 1 m; Fig. 2). This fact may suggest that transport distances for HTO were large enough to start noticing the effect of diffusion in the direction normal to bedding. This trend was not obvious for I^- , Br^- or $^{85}Sr^{2+}$. In DI-A2, some evidence was found related to erosion of the borehole wall in the upper and lower parts of the borehole that could also result in the observed differences in the diffusion profiles (Wersin et al. 2008).

Most HTO profiles in the DI, DI-A1, DI-A2 and DR experiments (and HDO in DI-B) show a slightly flatter region (low concentrations compared to model curves) next to the injection borehole (Fig. 2). This feature could in principle be related to (1) a BdZ, with somewhat increased diffusion coefficients and porosity; (2) evaporation of HTO during the overcoring procedure; (3) back-diffusion of

HTO into the resin while it was hardening,² possibly supported by the increased temperature. The occurrence of a BdZ was reported only in the DI experiment, mainly based on a higher rate of out-diffusion at earlier times compared to later times. It was not reported in any of the other experiments, where the drilling disturbance was kept to a minimum by installing the packer system and filling the interval section quickly after drilling. Also, a BdZ would in fact lead to slightly higher HTO concentrations close to the borehole interface compared to model results for uniform rock properties, in contrast to what was observed. Thus, process (1) is not a likely cause of the observed feature of the HTO profiles. Evaporation of water close to the borehole wall would also lead to a potential increase in the HTO concentrations due to the fractionation of 3H into the remaining liquid phase. Moreover, the external rims of the overcores, which were exposed to air for the longest times, did not show any noticeable anomaly. Accordingly, evaporation can also not explain the observation. A slight out-diffusion of HTO into the (not yet hardened) resin was therefore considered as a possible cause for the observed slight flattening of the HTO profiles near the borehole interface and the overestimation of the concentrations when modelling the data. It is possible that HTO shows a higher solubility in the resin compared to other tracers, which would make HTO more sensitive to such out-diffusion. Unfortunately, no resin was sampled to test its HTO content in any of the experiments.

5.2 Anionic tracer diffusion

The effective diffusion coefficients for the anionic tracers I^- and Br^- are systematically smaller than those for the water tracers HTO and HDO. The same trend is manifested for the diffusion-accessible porosities. The diffusion coefficients obtained for Br^- and I^- in the DI-A2 experiment were somewhat higher than those from other in situ experiments (DI-A1, DR, DI-B, FM-C) and laboratory diffusion tests (Table 2). In the case of Br^- , this observation may be related to the higher uncertainty in experimental data arising from the low ratio between tracer to background concentrations. Note that identical parameters were obtained for Br^- and I^- in spite of the slightly slower decrease of bromide concentration in the borehole. This difference is fully explained by the smaller concentration gradient due to the higher background concentration of Br^- in the pore-water. Note also that, for DI, the derived diffusivities and porosities show a large uncertainty, which is related to the BdZ created during borehole construction and

² Immediately after the dismantling of the packer system, the central borehole was filled with sand and resin to stiffen the borehole before overcoring.

Table 2 Modelled diffusion data for the different tracers and comparison with laboratory results

Tracer	Parameter D_e (10^{-11} m ² /s) K_d (L/kg)	In-situ test FM-C ^{ab}	In-situ test DI ^{b,c}	In-situ test A1 ^{a,d}	In-situ test DI-B ^e	In-situ test A2 ^{a,f,g,h}	In-situ test DR ⁱ	Lab data diffusion	Lab data batch sorption
HTO	$D_{e, par}$ anisotropy ratio ϵ	6.8 1, assumed 0.12	5 7, assumed 0.15	5.4–6.5 nc or 6.5 0.17–0.20	4–5 ⁱ nc or 4 (lab value) 0.15–0.16 ⁱ	6.0 nc 0.15	5.4 5.1 0.164	5.4–5.7 ^{ok,l,m} ~4 0.10–0.17 ^{l,m}	
I ⁻	$D_{e, par}$ anisotropy ratio ϵ	2.5 1, assumed 0.05	1–1.5 4.4, assumed 0.07–0.125	1.2–2.0 nc or 6.25 0.09–0.15	0.83–1.2 ⁱ nc or 4 (lab value) 0.08–0.09	3.0 nc 0.08	1.6 3.8 0.08	1.44 ^{l,m} 1.7 (³⁶ Cl ⁻) ^{l,m} ~4 (³⁶ Cl ⁻) 0.058–0.082 ^{l,m}	
Br ⁻	$D_{e, par}$ anisotropy ratio ϵ					3.0 nc 0.10	2.6	1.7–4.5 ⁿ , 1.6 ⁿ 0.078–0.15 ^{n,m}	
²² Na ⁺	$D_{e, par}$ anisotropy ratio α			7.2–8.2 nc or 8 0.45–0.62			7.7 5.1 0.5	7.2–9.4 ^{ok,l,m} 4–6.7 0.33 ^o	
⁸⁵ Sr ²⁺	$D_{e, par}$ anisotropy ratio α			0.12–0.20		7.0 nc 2.4 1.0	0.15	0.09–0.24 ^{o, m} 6.5 ^e , 7.5 ^m 1.9–2.0 ^d 0.64–0.75 ^d , 1.4 ^e , 1.7 ^m	0.15–0.21 ^o
Cs ⁺ , ¹³⁷ Cs ⁺ , ¹³⁴ Cs ⁺	$D_{e, par}$ anisotropy ratio Freundlich isotherm	30		$S = 0.186C^{0.53}$		20.0 (Freundlich) 20–40 (ion exch.) Nc $S = 0.186C^{0.53}$	33(–82)(stable) exchange 3-site ion exchange ^m	26 ⁿ , 18 ^r (¹³⁴ Cs ⁺ , low conc.), 23 ⁿ (Cs ⁺ , stable 1 mM) 2.2–8.7 $S = 0.45C^{0.65h}$ 3-site ion exchange ^m	$S = 0.85C^{0.65h}$ $S = 0.372C^{0.53p}$ 3-site exchange site ^q
⁶⁰ Co ²⁺	$D_{e, par}$ anisotropy ratio α K_d					2–20 Nc 115–918 50–400			420 ⁿ

Effective diffusion coefficients (parallel to bedding), anisotropy ratios ($D_{e, par}/D_{e, perp}$), porosities and sorption parameters. Temperatures for the in-situ and laboratory experiments were about 16 °C and 22–25 °C, respectively. According to published activation energies (20 kJ/mol, Van Loon et al. 2005b), D_{16C} should be about 0.78 D_{25C}

* Modelling using PHREEQC implementing laboratory-based parameters also obtained satisfactory results (Wersin et al. 2010)

nc: not considered (only diffusion parallel to bedding taken into account)

^a Gómez-Hernández and Guardiola-Albert (2004), ^bTevisson and Soler (2003), ^cPalut et al. (2003), ^dWersin et al. (2006), ^eSoler et al. (2008), ^fWersin et al. (2008), ^gWersin et al. (2010), ^hSoler et al. (2013) 'modelling in progress, ⁱVan Loon et al. (2004a), ^kVan Loon and Soler (2003), ^lVan Loon et al. (2004a), ^mNagra (2014), ⁿAppelo et al. (2010), ^ounpublished results, ^pVan Loon et al. (2005a), ^qLauber et al. (2000), ^rVan Loon et al. (2009), ^sVan Loon and Müller (2014)

installation (Tevissen et al. 2004). The smaller effective diffusion coefficients and diffusion-accessible porosities of anions compared to water tracers and cations is explained by repulsion of anions from the negatively charged clay surfaces, which leads to a deficit of anions relative to cations in the electric double layers (EDLs). This anion exclusion effect is commonly approximated by the concept of anion-accessible porosity (Pearson 1999; Pearson et al. 2003), although in reality the decrease towards the negatively charged surface is a continuum rather than a step function. The anion-accessible porosity fraction calculated from the ratio of the porosities of I^- and HTO (HDO in DI-B) for DI-A1, DI-A2, DI-B, FM-C and DR is 0.55 ± 0.014 . This value is in good agreement with porosities obtained in laboratory experiments and indicates the good quality of the derived porosities and a relatively small variation in the anion porosity fraction at Mont Terri. Similar anion-accessible porosities were obtained from a previous compilation of Mont Terri data (Pearson et al. 2003) and also for Opalinus Clay in north-east Switzerland (Gimmi and Waber 2004; Wersin et al. 2013). According to the double layer theory, this parameter should vary with ionic strength; thus, at lower ionic strength the thickness of the EDL should increase, which would lead to a decrease in the anion-accessible porosity fraction. This effect is not observed in the in situ diffusion experiments. The difference in ionic strength seems to be too small (maximum of a factor of roughly 2 (Gimmi et al. 2014)) to be able to observe any effect, given the experimental uncertainty.

5.3 Cation diffusion coefficients

As illustrated in Table 2, the diffusion coefficients of Na^+ , Sr^{2+} or Cs^+ tracers from the field experiments are relatively large when compared to those of HTO. This is in agreement with laboratory studies on montmorillonite, bentonite and other clay-rich rocks (e.g. Glaus et al. 2010; Gimmi and Kosakowski 2011; Tachi et al. 2011; Tachi and Yotsuji 2014). The comparably large values may be explained by the so-called surface diffusion of sorbed cations (including cations in the diffuse layer and in interlayers), which leads to an additional driving force for diffusion besides the pore-water gradient (e.g. Glaus et al. 2013). From a normalisation of a large number of published tracer cation diffusion data, Gimmi and Kosakowski (2011) could show that normalised effective cation diffusion coefficients D_{erw} generally increase with a normalised sorption capacity of the cation. The latter was calculated as $\kappa = \rho_{bd} K_d / \varepsilon$ and $D_{erw} = D_e \tau_w / (D_0 \varepsilon_w)$, with τ_w the tortuosity and ε_w the porosity obtained for a water tracer. Values of D_{erw} larger than 1 point to a contribution of surface diffusion. They also derived average surface mobilities (surface diffusion coefficient

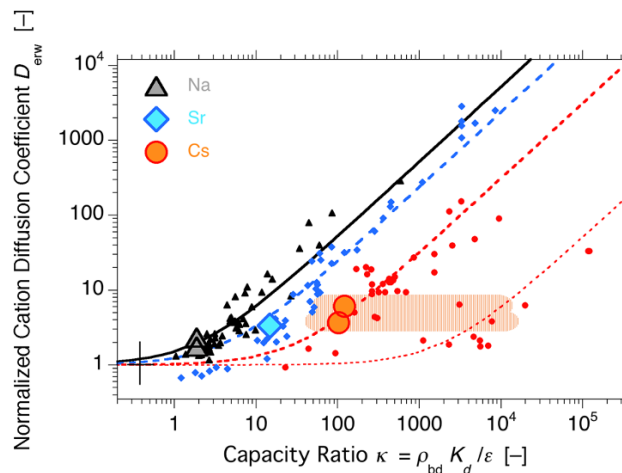


Fig. 3 Normalised cation diffusion coefficients D_{erw} for Na^+ , Sr^{2+} and Cs^+ plotted as a function of the normalised sorption capacity $\kappa = \rho_{bd} K_d / \varepsilon$. *Small symbols* literature values for tracers compiled by Gimmi and Kosakowski (2011); *lines* model (Gimmi and Kosakowski 2011). For Cs, *two lines* are drawn according to two subsets of the data as identified in Gimmi and Kosakowski (2011): *thicker line* for data obtained at comparably high (but constant) Cs background concentrations or for samples without illite, *thinner line* for data obtained at Cs trace concentrations in samples containing illite (thus probably strongly influenced by frayed edge sites). *Large symbols and shaded area* D_{erw} derived from results of Mont Terri field experiments (Van Loon et al. 2004b; Wersin et al. 2008, partly re-analysed). In the field experiments, the Cs concentration was not constant: initially comparably high, then quickly decreasing to lower values. This leads to K_d values varying in time and space due to non-linear (multi-site) sorption. The large symbol for Cs is drawn at the average K_d value, the shaded area encompasses the relevant K_d range

on a flat surface normalised to bulk water diffusion coefficient) for various cations. Different surface mobilities, which represent averages for all relevant sorption sites in multi-site sorption, were derived for Na^+ , Sr^{2+} , Ca^{2+} and Cs^+ . Figure 3 shows a plot of normalised Na^+ , Sr^{2+} and Cs^+ cation diffusion coefficients D_{erw} against the normalised sorption capacity $\kappa = \rho_{bd} K_d / \varepsilon$. The literature values compiled by Gimmi and Kosakowski (2011) are shown as small symbols and their modelled curves as lines; the results of the Mont Terri field experiments for Na^+ , Sr^{2+} and Cs^+ (Van Loon et al. 2004b; Wersin et al. 2008; partly re-analysed) are shown as large symbols. From this Figure, the following can be concluded: (1) Firstly, the normalised diffusion coefficients for Na^+ , Sr^{2+} and Cs^+ derived from the values obtained in the Mont Terri field experiments are in accordance with the trends of other published (mostly laboratory) data, for instance those of Melkior et al. (2005) (for all references see Gimmi and Kosakowski 2011). (2) Secondly, the normalised diffusion coefficients for Na^+ , Sr^{2+} and Cs^+ in the field experiments are somewhat increased ($D_{erw} > 1$), which points to a contribution from surface diffusion. The extent of this

increase is, however, relatively small compared to some of the other (laboratory) data for other materials. This is mainly related to the in situ pore-water composition in the field experiments, with an ionic strength in the order of 0.2–0.4 M (the ionic strength was usually adjusted to the specific location of the test in the Mont Terri rock laboratory). The largest normalised effective cation diffusion coefficients shown in Fig. 3 (see references in Gimmi and Kosakowski 2011) are typically observed for relatively dilute solutions (with low ionic strength). (3) Thirdly, the Cs^+ field diffusion coefficients cannot be uniquely represented in such a plot that depends on a single K_d value. This is because the Cs^+ concentration varied considerably during the field experiments, which affects the degree of sorption in a non-linear way and leads to a K_d that varies in the experiment with space and time. Figure 3 shows the D_e for Cs^+ plotted at the capacity ratio obtained from an average K_d , with a shaded area covering the possible range of K_d values. In the DR experiment, caesium showed different penetration distances for the stable Cs^+ added at high concentrations in the upper interval and for the $^{137}\text{Cs}^+$ added at trace concentrations in the lower interval. This behaviour confirms the non-linear nature of Cs^+ sorption in Opalinus Clay also observed in e.g. the DI-A1 and DI-A2 experiments and in laboratory sorption experiments (Lauber et al. 2000). Cs^+ sorption was first assumed to follow a Freundlich isotherm (Lauber et al. 2000; Van Loon et al. 2004b) in DI-A1 and DI-A2, or a 3-site cation-exchange process (Bradbury and Baeyens 2000; Van Loon et al. 2009; Jakob et al. 2009) later in DI-A2 and DR (Soler et al. 2013; Gimmi et al. 2014). The sorption behaviour could be well described by a Freundlich-type adsorption isotherm in DI-A1 and DI-A2, although there was a clear tendency towards a decreased sorption capacity in the field diffusion experiments relative to the batch sorption data. This tendency, however, may be the result of an inconsistent treatment of diffusion through the filter in the model of the DI-A1 and DI-A2 field experiments, even though other reasons (uncertainty in selectivities, incomplete initial mixing) may also apply (Soler et al. 2013). For cobalt, so far there are no other diffusion data with which to compare the field results. Given the different profiles measured in the rock in the DI-A2 experiment, different combinations of D_e and K_d are possible. However, the K_d values tend to be smaller than those obtained from batch sorption experiments for similar geochemical conditions (420 L/kg, unpublished results, see Table 2). When D_e and ε for Co^{2+} are set to the same values as for HTO, a K_d value of about 90 L/kg is obtained. Thus, the sorption of this tracer may be smaller in intact rock than in crushed rock (batch experiments) but, in view of the large scatter in the rock

profiles for DI-A2 and the scarce laboratory data, it is not possible to draw definite conclusions.

5.4 Porosities

A Cl^- -accessible porosity of 0.09 (0.55 of the average water-loss porosity of 0.164) was reliably estimated from a comparison of the equilibrated Cl^- concentrations in the rock and in the borehole fluid in the DR experiment. The same value was also applicable for Br^- and I^- . The value seems to be unaffected by the lower ionic strength at the location of the DR experiment compared to the earlier DI-A and DI-B experiments.

5.5 Anisotropy factor

Anisotropy ratios were obtained in situ for the first time in the DR experiment. They were found to be slightly larger for HTO and $^{22}\text{Na}^+$ ($\sim 5.1 \pm 0.5$) as compared to the anions ($\sim 3.8 \pm 0.4$ for I^- and $\sim 2.6 \pm 0.4$ for Br^-), which may be related to the exclusion of anions from the narrowest, well oriented pores. The design of the other in situ experiments did not allow anisotropy factors to be derived. The diffusion anisotropy ratios are slightly larger than (HTO), similar to (I), or slightly lower (Br) than values obtained in the laboratory (Van Loon et al. 2004a) for $^{36}\text{Cl}^-$ and HTO in Opalinus Clay from Mont Terri (Gimmi et al. 2014).

5.6 Borehole disturbed zone

The profile data in the DI-A1, DI-B, DI-A2 and DR experiments did not indicate the presence of a BdZ, in contrast to the data from the DI experiment. In the DR experiment, the model of tracer fluid data only suggested the possibility of a BdZ in the range of 1 to 1.5 cm around the lower interval. Such a strongly disturbed zone was, however, clearly not visible in the profile data.

6 Conclusions

Due to steadily evolving experimental designs, similar tracer compositions in different experiments and complementary small laboratory-scale diffusion tests, a unique and comprehensive database for diffusion and sorption of both chemically conservative and reactive nuclides under in situ conditions could be compiled for an indurated argillaceous rock. Such a database is a key component of the safety case for a repository for radioactive waste in claystone.

It could be shown that the sorption and diffusion data from in situ experiments are consistent and also

comparable with the results obtained from small-scale laboratory experiments.

Values for diffusion-accessible porosities for anions turned out to be consistent within the field experiments and also with the results from laboratory experiments. Anion-accessible porosity seemed to be unaffected by the salinity gradients (0.22–0.39 M) in the Mont Terri rock laboratory and the anisotropy factor (3–4 for anions, 5 for HTO and Na⁺) agrees well with the values measured in the laboratory. This factor is smaller than that obtained for samples from the Benken borehole in north-east Switzerland (Nagra 2014).

Field experiments have also shown that phenomena such as textural and/or mineralogical heterogeneities, or processes such as the formation of a BdZ do not jeopardise the interpretation of diffusion data as previously feared. Based on the profile data, the DI-A1, DI-B, DI-A2 and DR experiments did not indicate the presence of a BdZ, in contrast to the BdZ deduced in the DI experiment. The presence of the latter BdZ was due to technical issues during the realisation of the borehole (problems with packer installation led to a longer time when the borehole was open to the atmosphere).

The number and duration of the different experiments allowed suitable rock profiles to be obtained, also for strongly sorbing tracers. The observed sequence of penetration depths of the tracers (HTO > Br⁻ ≥ I⁻ ≥ SeO₄²⁻ > ²²Na⁺ > ¹³³Ba²⁺ > Cs⁺ > ¹³⁷Cs⁺ > ⁶⁰Co²⁺ > ¹⁵²Eu³⁺) is as expected for the small pore diffusion coefficients of the anions compared to HTO and the increasing retardation by sorption for the cations. Penetration depths for the strongly sorbing tracers did not extend beyond a few centimetres.

Finally, the field diffusion experiments at the Mont Terri rock laboratory not only allowed a good scientific understanding of diffusion processes in claystones to be acquired, but also the development and testing of technological skills required for performing underground diffusion tests. This know-how has been successfully transferred to other underground laboratories (e.g. Delay et al. 2014; Naves et al. 2010).

The field diffusion experiments are of great relevance for the safety case of deep geological repositories. The reasons for this are not related primarily to the parameters derived from such experiments but are as formulated in the introduction, namely (a) complementing laboratory-scale experiments, in addition to the large volume of rock investigated, (b) the very low water/rock ratio leading to better control of the chemical conditions by the rock, and (c) the in situ head pressure being closer to the disposal case. In summary, the diffusion experiments conducted at the Mont Terri rock laboratory have greatly improved the understanding of transport and retention processes and the

modelling of these and thus our confidence in Opalinus Clay as a host rock with outstanding safety barrier qualities.

Acknowledgements We thank the swisstopo personnel at St-Ursanne for providing excellent working conditions in the Mont Terri rock laboratory and the many researchers from numerous organisations involved in the work presented in this paper. We also like to express our gratitude to Dr. Christophe Tournassat, French Geological Survey BRGM, Orléans, France and Dr. Sebastien Savoye, CEA, Gif-sur-Yvette for a critical review of the manuscript.

Open Access This article is distributed under the terms of the Creative Commons Attribution 4.0 International License (<http://creativecommons.org/licenses/by/4.0/>), which permits unrestricted use, distribution, and reproduction in any medium, provided you give appropriate credit to the original author(s) and the source, provide a link to the Creative Commons license, and indicate if changes were made.

References

- Aertsens, M., Maes, N., Van Ravestyn, L., & Brassinnes, S. (2013). Overview of radionuclide migration experiments in the HADES Underground Research Facility at Mol (Belgium). *Clay Minerals*, 48, 153–166.
- Appelo, C. A. J., Van Loon, L. R., & Wersin, P. (2010). Multicomponent diffusion of a suite of tracers (HTO, Cl, Br, I, Na, Sr, Cs) in a single sample of Opalinus Clay. *Geochimica et Cosmochimica Acta*, 74, 1201–1219.
- Appelo, C. A. J., & Wersin, P. (2007). Multicomponent diffusion modeling in clay systems with application to the diffusion of tritium, iodide, and sodium in Opalinus Clay. *Environmental Science and Technology*, 41, 5002–5007.
- Bossart, P., Bernier, F., Birkholzer, J., Bruggeman, C., Connolly, P., Dewonck, S., Fukaya, M., Herfort, M., Jensen, M., Matray, J.-M., Mayor, J. C., Moeri, A., Oyama, T., Schuster, K., Shigeta, N., Vietor, T., & Wiczorek, K. (2017). Mont Terri rock laboratory, 20 years of research: introduction, site characteristics and overview of experiments. *Swiss Journal of Geosciences*, 110. doi:10.1007/s00015-016-0236-1 (this issue).
- Bradbury, M. H., & Baeyens, B. (2000). A generalised sorption model for the concentration dependent uptake of caesium by argillaceous rocks. *Journal of Contaminant Hydrology*, 42, 141–163.
- De Cannière, P., Moors, H., Lolivier, P., De Preter, P. & Put, M. (1996). Laboratory and in situ migration experiments in the Boom clay. *Nuclear Science and Technology*, Report EUR 16927 EN, 74 pp. European Commission, Brussels, Belgium.
- Delay, J., Bossart, P., Ling, L. X., Blechschmidt, I., Ohlsson, M., Vinsot, A., et al. (2014). Three decades of underground research laboratories: what have we learned? *Geological Society, London, Special Publications*, 400, 7–32.
- Gimmi, T., & Kosakowski, G. (2011). How mobile are sorbed cations in clays and clay rocks? *Environmental Science & Technology*, 45, 1443–1449.
- Gimmi, T., Leupin, O. X., Eikenberg, J., Glaus, M. A., Van Loon, L. R., Waber, H. N., et al. (2014). Anisotropic diffusion at the field scale in a 4-year multi-tracer diffusion and retention experiment-I: Insights from the experimental data. *Geochimica et Cosmochimica Acta*, 125, 373–393.
- Gimmi, T. & Waber, H.N. (2004). Model of tracer profiles in pore water of argillaceous rock in the Benken borehole: stable water isotopes, chloride and chlorine isotopes. *Nagra Technical*

- Report, 04–05, 105 pp. Nagra, Wettingen, Switzerland. <http://www.nagra.ch>
- Gimmi, T., Waber, H. N., Gautschi, A., & Rubel, A. (2007). Stable water isotopes in pore water of Jurassic argillaceous rocks as tracers for solute transport over large spatial and temporal scales. *Water Resources Research*, 43(4), W04410.
- Glaus, M. A., Birgersson, M., Karnland, O., & Van Loon, L. R. (2013). Seeming steady-state uphill diffusion of $^{22}\text{Na}^+$ in compacted montmorillonite. *Environmental Science and Technology*, 47, 11522–11527.
- Glaus, M. A., Frick, S., Rossé, R., & Van Loon, L. R. (2010). Comparative study of tracer diffusion of HTO, $^{22}\text{Na}^+$ and $^{36}\text{Cl}^-$ in compacted kaolinite, illite and montmorillonite. *Geochimica et Cosmochimica Acta*, 74, 1999–2010.
- Gómez-Hernández, J. J. & Guardiola-Albert, C. (2004). Flow Mechanism (FM-C) Experiment: Three dimensional model predictions of tracer evolution of HTO and iodine in the main fault. *Mont Terri Technical Report*, TR 2000-08, 21 pp. Federal Office of Topography (swisstopo), Wabern, Switzerland. <http://www.mont-terri.ch>.
- Hendry, M. J. & Wassenaar, L. I. (2005). Origin and migration of dissolved organic carbon fractions in a clay-rich aquitard: C-14 and delta C-13 evidence. *Water Resources Research* 41(2)
- Jakob, A., Pfingsten, W., & Van Loon, L. (2009). Effects of sorption competition on caesium diffusion through compacted argillaceous rock. *Geochimica et Cosmochimica Acta*, 73, 2441–2456.
- Koroleva, M., Alt-Epping, P., & Mazurek, M. (2011). Large-scale tracer profiles in a deep claystone formation (Opalinus Clay at Mont Russelin, Switzerland): implications for solute transport processes and transport properties of the rock. *Chemical Geology*, 280, 284–296.
- Lauber, M., Baeyens, B. and Bradbury, M. H. (2000). Physico-Chemical Characterisation and Sorption Measurements of Cs, Sr, Ni, Eu, Th, Sn and Se on Opalinus Clay from Mont Terri. *Paul Scherrer Institut Bericht 00-10*, 78 pp. Villigen, Switzerland. <http://www.psi.ch>.
- Lavastre, W., Jendrzewski, N., Agrinier, P., Javoy, M., & Evrard, M. (2005). Chlorine transfer out of a very low permeability clay sequence (Paris Basin, France): Cl-35 and C-37 evidence. *Geochimica et Cosmochimica Acta*, 69, 4949–4961.
- Leupin, O., Wersin, P., Gimmi, T., Mettler, S., Rösli, U., Meier, O., Nussbaum, C., Van Loon, L., Soler, J., Eikenberg, J., Fierz T., van Dorp, F., Bossart, P., Pearson, F. J., Waber, H. N., Dewonck, S., Fruttschi, M., Chaudagne, G. & Kiczka, M. (2013). DR (Diffusion & Retention) Experiment. *Mont Terri Technical Report*, TR 11-01, 49 pp. Federal Office of Topography (swisstopo), Wabern, Switzerland. <http://www.mont-terri.ch>.
- Mazurek, M., Alt-Epping, P., Bath, A., Gimmi, T., Waber, H. N., Buschaert, S., et al. (2011). Natural tracer profiles across argillaceous formations. *Applied Geochemistry*, 26, 1035–1064.
- Melkior, T., Yahiaoui, S., Motellier, S., Thoby, D., & Tevissen, E. (2005). Cesium Sorption and Diffusion in Bure Mudrock Samples. *Applied Clay Science*, 29, 172–186.
- Nagra (2014). SGT Etappe 2: Vorschlag weiter zu untersuchender geologischer Standortgebiete mit zugehörigen Standortarealen für die Oberflächenanlage: Geologische Grundlagen Dossier VI Barriereigenschaften der Wirt- und Rahmengesteine. *Nagra Technischer Bericht*, NTB 14-02 (Dossier VI), 190 pp. Nagra, Wettingen, Switzerland. <http://www.nagra.ch>.
- Naves, A., Dewonck, S. & Samper J. (2010). In situ diffusion experiments: effect of water sampling on tracer concentrations and parameters. *Physics and Chemistry of the Earth*, 35, 242–247.
- Palut, J. M., Montarnal, P., Gautschi, A., Tevissen, E., & Mouche, E. (2003). Characterisation of HTO diffusion properties by an in situ tracer experiment in Opalinus clay at Mont Terri. *Journal of Contaminant Hydrology*, 61, 203–218.
- Patriarche, D., Ledoux, E., Michelot, J. L., Simon-Coincon, R., & Savoye, S. (2004). Diffusion as the main process for mass transport in very low water content argillites: 2. Fluid flow and mass transport modelling. *Water Resources Research*, 40(1), W01517.
- Pearson, F. J. (1999). What is the porosity of a mudrock? *Geological Society, London, Special Publications*, 158, 9–21.
- Pearson, F. J., Arcos, D., Bath, A., Boisson, J. Y., Fernández, A. M., Gäbler, H.-E., Gaucher, E., Gautschi, A., Griffault, L., Hernán, P. & Waber, H. N. (2003). Geochemistry of water in the Opalinus clay formation at the Mont Terri Rock Laboratory. Federal Office for Water and Geology No. 5. Federal Office of Topography (swisstopo), Wabern, Switzerland. <http://www.mont-terri.ch>.
- Put, M. J., De Cannière, P., Moors, H. & Fonteyne, A. (1993). Validation of performance assessment model by large scale in situ migration experiments. Proceedings of an International Symposium on Geological Disposal of Spent Fuel and High Level and Alpha Bearing Wastes 1992 (pp. 319–326). International Atomic Energy Agency, Vienna, Austria.
- Rowe, R. K., Caers, C. J., & Barone, F. (1988). Laboratory determination of diffusion and distribution coefficients of contaminants using undisturbed clayey soils. *Canadian Geotechnical Journal*, 25, 108–118.
- Savoye, S., Michelot, J. L., Bensenouci, F., Matray, J. M. and Cabrera, J. (2008). Transfers through argillaceous rocks over large space and time scales: insights given by water stable isotopes. *Physics and Chemistry of the Earth*, 33, S67–S74.
- Shackelford, C. D. (1991). Laboratory diffusion testing for waste disposal: A review. *Journal of Contaminant Hydrology*, 7, 177–217.
- Soler, J.M., Leupin, O. X., Gimmi, T. & Van Loon, L. R. (2014). The DR-A in situ diffusion experiment at Mont Terri: Effects of changing salinity on diffusion and retention properties. In *Proceedings of the Materials Research Society Symposium, Volume 1665* (pp. 63–69). Cambridge University Press.
- Soler, J. M., Samper, J., Yllera, A., Hernández, A., Quejido, A., Fernández, M., et al. (2008). The DI-B in situ diffusion experiment at Mont Terri: Results and modeling. *Physics and Chemistry of the Earth*, 33, S196–S207.
- Soler, J. M., Wersin, P., & Leupin, O. X. (2013). Modeling of Cs^+ diffusion and retention in the DI-A2 experiment (Mont Terri). Uncertainties in sorption and diffusion parameters. *Applied Geochemistry*, 33, 191–198.
- Tachi, Y., & Yotsuji, K. (2014). Diffusion and sorption of Cs^+ , Na^+ , I^- and HTO in compacted sodium montmorillonite as a function of porewater salinity: Integrated sorption and diffusion model. *Geochimica et Cosmochimica Acta*, 132, 75–93.
- Tachi, Y., Yotsuji, K., Seida, Y., & Yui, M. (2011). Diffusion and sorption of Cs^+ , I^- and HTO in samples of the argillaceous Wakkanai Formation from the Horonobe URL, Japan: Clay-based modeling approach. *Geochimica et Cosmochimica Acta*, 75, 6742–6759.
- Tevissen, E. & Soler, J.M. (2003). In situ diffusion experiment (DI): synthesis report. *Mont Terri Technical Report*, TR 01-05, 56 pp. Federal Office of Topography (swisstopo), Wabern, Switzerland. <http://www.mont-terri.ch>.
- Tevissen, E., Soler, J. M., Momtarnal, P., Gautschi, A., & Van Loon, L. R. (2004). Comparison between in situ and laboratory diffusion studies of HTO and halides in Opalinus Clay from the Mont Terri. *Radiochimica Acta*, 92, 781–786.
- Van Loon, L. R., Baeyens, B., & Bradbury, M. H. (2005a). Diffusion and retention of sodium and strontium in Opalinus Clay: Comparison of sorption data from diffusion and batch sorption measurements, and geochemical calculations. *Applied Geochemistry*, 20, 2351–2363.

- Van Loon, L. R., Baeyens, B., & Bradbury, M. H. (2009). The sorption behaviour of caesium on Opalinus Clay: a comparison between intact and crushed material. *Applied Geochemistry*, *24*, 999–1004.
- Van Loon, L. R., & Eikenberg, J. (2005). A high-resolution abrasive method for determining diffusion profiles of sorbing radionuclides in dense argillaceous rocks. *Applied Radiation and Isotopes*, *63*, 11–21.
- Van Loon, L. R., & Müller, W. (2014). A modified version of the combined in-diffusion/abrasive peeling technique for measuring diffusion of strongly sorbing radionuclides in argillaceous rocks: A test study on the diffusion of caesium in Opalinus Clay. *Applied Radiation and Isotopes*, *90*, 197–202.
- Van Loon, L. R., Müller, W., & Iijima, K. (2005b). Activation energies of the self-diffusion of HTO, $^{22}\text{Na}^+$ and $^{36}\text{Cl}^-$ in a highly compacted argillaceous rock (Opalinus Clay). *Applied Geochemistry*, *20*, 961–972.
- Van Loon, L. R. & Soler, J. M. (2003). Diffusion of HTO, $^{36}\text{Cl}^-$, $^{125}\text{I}^-$ and $^{22}\text{Na}^+$ in Opalinus Clay: Effect of Confining Pressure, Sample Orientation, Sample Depth and Temperature. *Nagra Technical Report*, 03-07, 145 pp. Nagra, Wettingen, Switzerland. <http://www.nagra.ch>.
- Van Loon, L. R., Soler, J. M., & Bradbury, M. H. (2003). Diffusion of HTO, $^{36}\text{Cl}^-$ and $^{125}\text{I}^-$ in Opalinus Clay samples from Mont Terri. Effect of confining pressure. *Journal of Contaminant Hydrology*, *61*, 73–83.
- Van Loon, L. R., Soler, J. M., Müller, W., & Bradbury, M. H. (2004a). Anisotropic diffusion in layered argillaceous rocks: a case study with Opalinus Clay. *Environmental Science and Technology*, *38*, 5721–5728.
- Van Loon, L. R., Wersin, P., Soler, J. M., Eikenberg, J., Gimmi, T., Hernan, P., et al. (2004b). In-situ diffusion of HTO, $^{22}\text{Na}^+$, Cs^+ and I^- in Opalinus Clay at the Mont Terri Underground Rock Laboratory. *Radiochimica Acta*, *92*, 757–763.
- Wersin, P., Appelo, C. A. J., Baeyens, B., Bossart, P., Dewonck, S., Eikenberg, J., Fierz, T., Fisch, H. R., Gimmi, T., Grolimund, D., Leupin, O. X., Möri, A., Soler, J. M., Van Dorp, F. & Van Loon, L. (2010). Long-Term Diffusion (DI-A) Experiment: DI-A2: Diffusion of HTO, Br^- , I^- , Cs^+ , $^{85}\text{Sr}^{2+}$ and $^{60}\text{Co}^{2+}$: Field activities, Data and Model. *Mont Terri Technical Report*, TR 09-04, 187 pp. Federal Office of Topography (swisstopo), Wabern, Switzerland. <http://www.mont-terri.ch>.
- Wersin, P., Baeyens, B., Bossart, P., Cartalade, A., Dewonck, S., Eikenberg, J., Fierz, T., Fisch, H. R., Gimmi, T., Grolimund, D., Hernán, P., Möri, A., Savoye, S., Soler, J., van Dorp, F. & Van Loon, L. (2006). Long-Term Diffusion Experiment (DI-A): Diffusion of HTO, I^- , $^{22}\text{Na}^+$ and Cs^+ : Field activities, data and models. *Mont Terri Technical Report*, TR 03-06, 195 pp. Federal Office of Topography (swisstopo), Wabern, Switzerland. <http://www.mont-terri.ch>.
- Wersin, P., Mazurek, M., Waber, H.N., Mäder, U.K., Gimmi, T., Rufer, D. & De Haller, A. (2013). Rock and porewater characterisation on drillcores from the Schlattingen borehole. *Nagra Arbeitsbericht*, NAB 12-54, 343 pp. Nagra, Wettingen, Switzerland. <http://www.nagra.ch>.
- Wersin, P., Soler, J. M., Van Loon, L., Eikenberg, J., Baeyens, B., Grolimund, D., Gimmi, T. & Dewonck, S. (2008). Diffusion of HTO, Br^- , I^- , Cs^+ , $^{85}\text{Sr}^{2+}$ and $^{60}\text{Co}^{2+}$ in a clay formation: results and modelling from an in situ experiment in Opalinus Clay. *Applied Geochemistry*, *23*, 678–691.
- Wersin, P., Van Loon, L. R., Soler, J. M., Yllera, A., Eikenberg, J., Gimmi, Th, Hernán, P. & Boisson, J.-Y. (2004). Long-term diffusion experiment at Mont Terri: First results from field and laboratory data. *Applied Clay Science*, *26*, 123–135.
- Yllera, A., Hernández, A., Mingarro, M., Quejido, A., Sedano, L. A., Soler, J. M., Samper, J., Molinero, J., Barcala, J. M., Martín, P. L., Fernández, M., Wersin, P., Rivas, P. & Hernán, P. (2004). DI-B experiment: Planning, design and performance of an in situ diffusion experiment in the Opalinus Clay Formation. *Applied Clay Science*, *26*, 181–196.

Twenty years of research at the Mont Terri rock laboratory: what we have learnt

Paul Bossart¹ 

Received: 3 February 2017 / Accepted: 20 February 2017 / Published online: 7 March 2017
© Swiss Geological Society 2017

Abstract The 20 papers in this Special Issue address questions related to the safe deep geological disposal of radioactive waste. Here we summarize the main results of these papers related to issues such as: formation of the excavation damaged zone, self-sealing processes, thermo-hydro-mechanical processes, anaerobic corrosion, hydrogen production and effects of microbial activity, and transport and retention processes of radionuclides. In addition, we clarify the question of transferability of results to other sites and programs and the role of rock laboratories for cooperation and training. Finally, we address the important role of the Mont Terri rock laboratory for the public acceptance of radioactive waste disposal.

Keywords Opalinus Clay · Deep geological disposal of radioactive waste · Safety relevant processes · Transferability of results · Cooperation and training · Public acceptance

1 Summarizing the key results of the 20 papers in this Special Issue

1.1 Development of investigation techniques

Numerous methods and investigation techniques have been developed in the Mont Terri rock laboratory, mainly for the

characterization of claystone like the Opalinus Clay (Bossart and Thury 2007; Delay et al. 2014). Examples are: a methodology for geochemical characterization of porewaters (Pearson et al. 2003), a new technique for in situ diffusion and retention of radionuclides (Wersin et al. 2004), and new geophysical methods for testing the generation and self-sealing of the excavation disturbed and damaged zones in argillaceous rocks (Schuster et al. 2017). One of the major benefits for the Mont Terri Project Partners is the experience gained from these investigations in the Mont Terri rock laboratory. This can be used for the development and planning of new site investigations and characterization programs. Furthermore, these techniques and methodologies can be also transferred for development of new underground rock facilities in other countries.

1.2 Properties of Opalinus Clay at Mont Terri

The following properties are a somewhat arbitrary selection. They are important for the Swiss deep geological disposal concept, but may not have the same relevance in other countries with different disposal concepts.

- Lithology and tectonics: Opalinus Clay as exposed in the region of the Mont Terri rock laboratory is a homogeneous, extended claystone formation with a pronounced bedding anisotropy. It is an over-consolidated claystone exhibiting shaly, sandy, and carbonate-rich facies. The shaly and sandy facies evidence a mineral composition of 30–80% clay minerals (where about 10% consist of smectite-illite mixed-layer minerals), 10–44% quartz, and 4–35% carbonates. The sedimentary age is of Toarcian/Aalenian age (ca. 174 Ma, Hostettler et al. 2017). The whole 130 m-thick sequence was deposited in a shallow sea in less

Editorial handling: A. G. Milnes.

✉ Paul Bossart
paul.bossart@swisstopo.ch

¹ Federal Office of Topography swisstopo, Seftigenstrasse 264, 3084 Wabern, Switzerland

than 1 million years. Numerous tectonically deformed zones at different scales result from fault-bend fold thrusting with a shortening of almost 3 km (Nussbaum et al. 2017).

- Hydrogeological properties: Opalinus Clay is considered as an aquiclude, over- and underlain by aquifers. Total physical porosity is on the order of 18 vol%. The mean pore diameter is ca. 40 nm. The pore-space in pristine Opalinus Clay is water-saturated and hydraulic conductivity varies between 2×10^{-14} and 7×10^{-12} m/s (Yu et al. 2017). Under normal hydraulic gradients, the free pore-water does not flow (Pearson et al. 2003). Permeability in Opalinus Clay seems not to be affected by tectonic deformations due to the partial self-sealing of open fractures with calcite, quartz, celestine, and fault-gouge material (Jaeggi et al. 2017).
- Geochemical properties: Opalinus Clay pore-water is of Na–Cl–SO₄ type and, according to measured Cl⁻/Br⁻ ratios, evidences a seawater signature (Pearson et al. 2003). The age of this marine pore-water is younger than the 174 Ma sedimentation age, and is associated with the upper Eocene and Oligocene/Miocene marine incursions into the region of the future folded Jura (Clauer et al. 2017; Mazurek and de Haller 2017). Reducing conditions occur in pristine Opalinus Clay. There is a considerable sorption potential, which is based on the high total specific surface (mean of 130 m²/g) and on the reactivity of the clay minerals. Thus Opalinus Clay considerably retards the transport of radionuclides.
- Rock-mechanical properties: Opalinus Clay behaves as a mechanically transverse isotropic material. Deformation mechanism is cataclastic flow at low effective confining pressures, low temperatures, and high strain rates (e.g. conditions as they might be at a real repository in the Opalinus Clay) (Nüesch 1991). The claystone swells on contact with water, with swelling-expansion and pressures perpendicular to the bedding of up to 10% and 1 MPa respectively. The uniaxial compressive strength of saturated Opalinus Clay varies between 10 (shaly facies) and 35 MPa (sandy and carbonate rich facies). Desaturated Opalinus Clay shows shrinkage cracks and significantly increased compressive strengths and stiffness (Ziefle et al. 2017). Rheologically, the shaly facies behaves as a “soil-like” clay shale (Amann et al. 2017).

1.3 Generation of the excavation damaged zone (EDZ) and processes related to self-sealing

- Permeabilities and transmissivities of newly generated EDZ fractures are orders of magnitudes higher

compared to those of the undisturbed Opalinus Clay (Bossart et al. 2004; Marschall et al. 2017).

- Mini-seismic investigations in radial boreholes around the tunnel yielded reduced seismic P-wave velocities and amplitudes compared with undisturbed claystone (Schuster et al. 2017).
- Self-sealing of the EDZ fracture network occurs during re-saturation of tunnel walls, where pore-water driven by hydraulic gradients is flowing into the fracture network. Both swelling of clay minerals (mainly smectite-illite mixed layers) in the EDZ fractures and mechanical fracture closure by the swelling bentonite contribute to self-sealing. Simultaneously, hydraulic transmissivities decrease and P-wave velocity increases (Bossart et al. 2004; Marschall et al. 2017; Schuster et al. 2017).
- The road header technique without water has shown to allow for a precise and smooth excavation, minimizing development of the EDZ.

1.4 Thermo-hydro-mechanical (THM) processes

- Although temperatures applied in the heater experiments are in the order of 100 °C and thus rather high, temperature and pore-water increases in the Opalinus Clay are moderate due to rapid thermal attenuation with distance and the isolating nature of the artificial bentonite barrier (Gens et al. 2017; Mueller et al. 2017). A thermally induced damaged zone (TDZ) in the Opalinus Clay is theoretically possible (e.g. increased hydraulic conductivities). So far, there is no evidence for such a TDZ, even though in one experiment the Opalinus Clay was exposed to temperatures >100 °C.
- Interaction of buffer with host rock causes additional effects (e.g. heterogeneous saturation of granular bentonite by preferential flow paths through the EDZ) that cannot always be quantified or even anticipated from small-scale laboratory tests. THM in situ testing of the integrated buffer/rock or seal/rock system is an important element contributing to an integrated system understanding (Wieczorek et al. 2017).
- Conceptual models and coupled constitutive equations for adequate design and prediction calculations have been developed (Laloui 2013; Gens et al. 2017). These give useful insights into the THM system response.

1.5 Corrosion-related processes

- Corrosion rates of different steels in contact with clay or bentonite decrease with time due to growth of corrosion products on the steel surfaces (Necib et al. 2017).

- Anaerobic corrosion of steel occurs as a result of redox reactions that generate molecular hydrogen. After hydrogen is experimentally injected into Opalinus Clay, its concentration decreases sharply, most probably due to sulphate-reducing bacteria that foster reduction of sulphates to sulphides (Vinsot et al. 2014, 2017).

1.6 Microbial activity

- Microbial reproduction in pristine Opalinus Clay is strongly limited due to the very small mean pore-diameter (ca. 40 nm), low water activity, and the recalcitrant nature of the organic matter.
- Compacted bentonite also limits microbial activity. Thus, microbially induced corrosion can be controlled by the dry density of the bentonite buffer (Necib et al. 2017; Mueller et al. 2017).
- Microorganisms in a clay environment will affect geochemical conditions and processes in a repository (e.g. the redox and pH conditions, anaerobic steel corrosion, and production and consumption of reaction products (Leupin et al. 2017a; Bleyen et al. 2017) if the conditions allow for it (e.g. water availability, sufficient pores space and nutrients).

1.7 Interaction of Opalinus Clay with high-pH cement fluids

- The CI experiment shows that the extent of the alteration zone within Opalinus Clay is limited (mm- to cm-range). There is a well-defined reaction zone within the cement matrix, the latter is more extensive in low-alkali cement. The interfaces show de-calcification and overprint a carbonate alteration, resulting in a porosity reduction (Maeder et al. 2017).
- First results indicate that low-alkali cementitious products do not minimise the extent of reactions between Opalinus Clay and cementitious materials. Currently there is no clear advantage of substituting OPC (ordinary Portland cement) by low-alkali cements (Maeder et al. 2017).

1.8 Diffusion processes in Opalinus Clay

- Diffusion is the main transport process in the Opalinus Clay at Mont Terri, even in tectonically deformed fault zones and self-sealed EDZ. This has been evidenced by interpreting natural tracer profiles in and around the Mont Terri rock laboratory (assessing the kilometre scale, and timescale of several millions of years), and

by field experiments (assessing the centimetre to decimetre scale, and timescale of 1–5 years) (Mazurek and de Haller 2017; Leupin et al. 2017b).

- Due to anion exclusion, the diffusive flux of anions (e.g. I^- , Br^-) is lower than that of water tracers (HTO, HDO), while that of cations (e.g. Sr^{2+} , Cs^+) tends to be higher (Leupin et al. 2017b).
- There is a significant anisotropy effect: diffusion coefficients parallel to bedding planes are 3–5 times higher than normal to bedding planes.
- There seems to be no scale effect: diffusion and sorption parameters of in situ experiments are consistent with those obtained from small-scale laboratory tests.

2 Transferability of results

2.1 What can, and what cannot, be transferred?

A good discussion of what is transferable and not has been presented by Mazurek et al. (2008). In Sect. 2.1, we refer mainly to their findings and conclusions.

The mineralogy, porosity and pore size distributions at many claystone sites are similar and comparable (e.g. Opalinus Clay at Mont Terri and the Callovian-Oxfordian claystone at Meuse/Haute Marne, in the Paris basin of France). The same is true for the chemical type and evolution of their pore-waters. Hydraulic conductivities and diffusion coefficients are often in comparable ranges. Many claystone-formations are compacted and even over-consolidated, and thus rockmechanical parameters show similar ranges.

However, we have to be prudent when comparing clay sites, or transferring information from one site to another. Discrepancies at different claystone sites may be more pronounced than similarities, i.e. when Opalinus Clay is compared with the Toarcian–Domerian claystone at the rock laboratory in Tournemire, southern France (higher over-consolidation, exposed to higher temperatures than Opalinus Clay), or when it is compared with the more plastically behaving Boom Clay of the Hades rock laboratory in Mol, Belgium. Different sedimentary conditions leading to different coarser- or finer grained clastic material and thus to different clay mineralogy, different diagenetic histories, all leading to different degrees of cementation, followed by different burial depth and uplift histories. In turn, these lead to different degrees of compaction and pore-size distributions. Finally, different tectonic evolutions of the claystones at different sites can lead to different deformation fabrics and present-day stress fields. When we want to transfer processes and even individual parameters

to other claystone sites, a good knowledge of mineralogy, of the diagenetic evolution, burial and erosion history, and the tectonic and metamorphic development of a site are essential to assess the transferability.

Finally, we conclude that transferability to other claystone sites is possible among weakly consolidated formations with similar mineralogy and porosity distributions. Highly compacted and highly over-consolidated claystone formations limit the transferability from lesser compacted formations, such as the Opalinus Clay. Transferability may also be restricted among formations with different mineralogical compositions and porosities, and with different pore-water chemistries and different present-day stress fields.

2.2 Transferability to the potential sites of Northern Switzerland

In the framework of the Swiss Sectorial Plan, Nagra proposed three locations where high-level radioactive waste could be stored in the Opalinus Clay (Nagra 2010): Jura-Ost, Nördlich Lägern, and Zürich Nordost in the Cantons of Aargau, Thurgau, and Zurich in northern Switzerland. The siting depth of these sites ranges between 400 and 900 m below the surface, which is considerably deeper than the overburden at Mont Terri rock laboratory (280 m). The Opalinus Clay at Mont Terri has a unique burial geology (the formation was subjected to two burial stages, and maximum burial to ca. 1350 m below surface occurred in the late Cretaceous, see Mazurek et al. 2006), a different uplift and erosion history, and a present-day stress field, all of which differ from the situation in northern Switzerland. Thus, results from the Mont Terri rock laboratory cannot be transferred and applied without restriction to the proposed sites of Northern Switzerland.

On the other hand, hydrogeological, geomechanical, and geochemical processes identified at Mont Terri are indeed at least partially transferrable; for example, processes related to the formation of an excavation damaged zone when tunneling in Opalinus Clay, or the processes related to the diffusion and retention of radionuclides. Based on different consolidation histories, present-day depths and stress fields at the different sites, some characteristic parameters may be different, such as the total physical porosity, hydraulic conductivity, mechanical strength and elastic moduli, and diffusion coefficients. However, when borehole and test data at proposed disposal sites are available, it will be possible to correlate and adapt parameters. For instance, effective porosity and hydraulic conductivity values derived from the Benken borehole in the Zürich Nordost region are systematically lower than those found at Mont Terri due to deeper burial of the Opalinus Clay in Northern Switzerland. Modelling plays an important role when applying results to other potential

sites. Critical to such modeling are clear definitions and good estimates of model parameters for the different sites with their different geological consolidation histories.

3 Cooperation and training

Over the last 20 years scientists, engineers, technicians and contractors from the Mont Terri project partners have planned, financed, and realised experiments in the Mont Terri rock laboratory. Universities and research organisations from different countries are largely involved in the experimental programmes. Their students and trainees are co-funded by the Mont Terri project partners. Up to date, a total of 9 master theses and 22 PhDs were completed or are still going on (in situ experiments, laboratory experiments on clay samples, modelling). The EU and SERI (Swiss State Secretariat for Education, Research and Innovation) financially supported parts of the experiments. The Mont Terri project partners and research institutions have gained extensive knowledge and know-how, and have developed standards for quality and control.

Transfer of information and knowledge among scientists over two decades of experiments in underground argillaceous research laboratories such as Meuse/Haute Marne in France, Hades in Belgium, and Mont Terri in Switzerland, can only be done properly through direct interaction among partners over extended periods of time and by allowing the teams to develop their own expertise (Delay et al. 2014). One can document processes, parameters, and even procedures on how to carry out different kinds of tests. However, such documentation is not enough: tacit knowledge is the kind of know-how that is difficult to transfer to another person by means of documenting or reporting on it. Rock laboratories are thus key elements to perpetrate valuable tacit knowledge. Junior staff receive apprenticeships and are trained by experienced senior scientists and technicians who have worked for many years in rock laboratories. The IAEA (International Atomic Energy Agency) offers and finances fellowships in rock laboratories where scientists and technicians from other countries can learn and achieve their skills.

Thus all rock laboratories have created working groups for exchanging information and seeking international cooperation, either at the level of programme strategies, evaluation of results, or scientific topics. Within that process, the Mont Terri Project has played a major role through the creation of working groups, especially in geochemistry and rock mechanics.

We conclude that rock laboratories provide (i) privileged access to specific information (ii) partners that share resources needed to run in situ experiments (iii) interesting opportunities for the education and formation of students.

Rock laboratories will prevail in the future to train students, junior staff and specialists that are needed, for instance, to realise safe geological disposal systems, CO₂ storage projects, or other related topics that rely on the unique properties of indurated clay rocks.

4 Public acceptance

Rock laboratories are also essential elements in the dissemination of information and communication policy among implementers, safety authorities, and regulators. People visiting these facilities get an impression of the underground works and the different types of scientific and engineering experiments. Especially important are open days allowing stakeholders to contact scientist and engineers, ask detailed questions about repository concepts and technical issues, and also discuss phenomena and time scales that cannot easily be comprehended. During such visits, people can build an educated opinion about geological disposal in a neutral and informed manner. As in all of the communications from Mont Terri rock laboratory, we express what has been learnt and the domains within which these apply in an understandable, neutral, and scientific fashion.

Since 2011, swisstopo, Nagra, and ENSI have been operating the Mont Terri visitors center. About 4000–5000 persons visit the Mont Terri rock laboratory each year. These visits contribute essentially to the acceptance and credibility of the research in the context of deep geological disposal of radioactive waste. Critics and supporters of deep geological disposal will be informed about the national and international developments of deep geological disposal and they can exchange their ideas and opinions.

5 Conclusions

The Mont Terri rock laboratory has considerably contributed to the safety and technical feasibility of geological repositories and process understanding related to e.g. formation of the Opalinus Clay, its properties as cap rock, etc. In view of long-term safety of geological repository in a clay rock environment, the advantages of claystone formations such as the Opalinus Clay are threefold: (1) claystone formations exhibit an extensive retention potential for sorbing radionuclides due to the large reactive surface areas of clay minerals. The major part of radionuclides will be sorbed onto clay mineral surfaces. (2) Non- or weakly-sorbing radionuclides are transported through Opalinus Clay by molecular diffusion (in undeformed Opalinus Clay and tectonic fault zones). (3) Opalinus Clay reveals distinct self-sealing properties due its smectite-illite mixed-layer clay minerals. Interconnected fracture networks, which are formed in the

EDZ during repository construction or possibly generated in the future by earthquakes, will self-seal in relatively short time spans. Thus rapid advective radionuclide transport along preferential flow paths (e.g. through EDZ fracture network) out of the repository into the biosphere is unlikely.

The weaknesses of Opalinus Clay are twofold. (1) Heat-conductivity of Opalinus Clay is rather small when compared to other host rocks. Heating of Opalinus Clay >100 °C in a high-level waste repository might create a thermally induced damaged zone and/or reduce the sorption capacity. (2) Construction of a repository at greater depths (e.g. at 800 m depth) could result in a more extended EDZ and high tunnel convergences. Both weaknesses can be reduced with adequate measures, such as ensuring enough distance between emplacement galleries to avoid overheating, and engineered lining measures that guarantee short term stability of the access galleries.

In conclusion, the methodologies developed, experience gained, and experimental results achieved in the Mont Terri rock laboratory have increased our general knowledge of the complex behaviour of argillaceous formations in response to coupled hydrogeological, mechanical, thermal, chemical, and biological processes. The research we have carried out at Mont Terri over the last 20 years provides invaluable information on repository evolution and yields strong arguments supporting a sound safety case for a repository in argillaceous formations (Bossart et al. 2017). Although extrapolating results to similar potential sites elsewhere must always be applied with care, many general findings from Mont Terri may also be valid at other potential sites in other countries for the deep geological disposal of radioactive waste.

Acknowledgements Olivier Leupin (Nagra), Martin Herfort (ENSI), and Geoffrey Milnes (Scientific Editor of SJG) are kindly thanked for their constructive review of this manuscript. Roy Freeman is thanked for improving the English.

References

- Amann, F., Wild, K.M., Loew, S., Yong, S., Thoeny, R., & Frank, E. (2017). Geomechanical behaviour of Opalinus Clay at multiple scales. Results from Mont Terri rock laboratory (Switzerland). *Swiss Journal of Geosciences*, 110, 1–21. doi:10.1007/s00015-016-0245-0 (this issue).
- Bleyen, N., Smets, S., Small, J., Moors, H., Leys, N., Albrecht, A., De Cannière, P., Schwyn, B., Wittebroodt, C., & Valcke, E. (2017). Impact of the electron donor on in situ microbial nitrate reduction in Opalinus Clay. Results from the Mont Terri rock laboratory (Switzerland). *Swiss Journal of Geosciences*, 110, 1–20. doi:10.1007/s00015-016-0256-x (this issue).
- Bossart, P., Bernier, F., Birkholzer, J., Bruggeman, C., Connolly, P., Dewonck, S., Fukaya, M., Herfort, M., Jensen, M., Matray, J-M., Mayor, J. C., Moeri, A., Oyama, T., Schuster, K., Shigeta, N., Vietor, T., & Wiczorek, K. (2017). Mont Terri rock laboratory, 20 years of research: introduction, site characteristics and

- overview of experiments. *Swiss Journal of Geosciences*, 110. doi:10.1007/s00015-016-0236-1 (this issue).
- Bossart, P., & Thury, M. (2007). Research in the Mont Terri Rock laboratory: quo vadis? *Physics and Chemistry of the Earth*, 32, 19–31.
- Bossart, P., Trick, T., Meier, P.M., & Mayor, J.-C. (2004). Structural and hydrogeological characterization of the excavation-disturbed zone in the Opalinus Clay (Mont Terri Project, Switzerland). *Applied Clay Science*. [Online] 26(1–4), 429–448. doi:10.1016/j.clay.2003.12.018.
- Clauer, N., Techer, I., Nussbaum, C., & Laurich, B. (2017). Geochemical signature of paleofluids in microstructures from “Main Fault” in the Opalinus Clay of the Mont Terri rock laboratory, Switzerland. *Swiss Journal of Geosciences*, 110, 1–24. doi:10.1007/s00015-016-0253-0 (this issue).
- Delay, J., Bossart, P., Ling, L. X., Blechschmidt, I., Ohlsson, M., Vinsot, A., et al. (2014). Three decades of underground research laboratories: what have we learned? *Geological Society, London, Special Publications*, 400(1), 7–32.
- Gens, A., Wiczorek, K., Gaus, I., Garitte, B., Mayor, J. C., Schuster, K., Armand, G., García-Siñeriz, J.-L., & Trick, T. (2017). Performance of the Opalinus Clay under thermal loading. Experimental results from Mont Terri rock laboratory (Switzerland). *Swiss Journal of Geosciences*, 110, 1–18. doi:10.1007/s00015-016-0258-8 (this issue).
- Hostettler, B., Reisdorf, A. G., Jaeggi, D., Deplazes, G., Bläsi, H.-R., Morard, A., Feist-Burkhardt, S., Waltschew, A., Dietze, V., & Menkveld-Gfeller, U. (2017). Litho- and biostratigraphy of the Opalinus Clay and bounding formations in the Mont Terri rock laboratory (Switzerland). *Swiss Journal of Geosciences*, 110, 1–15. doi:10.1007/s00015-016-0250-3 (this issue).
- Jaeggi, D., Laurich, B., Nussbaum, C., Schuster, K., & Connolly, P. (2017). Tectonic structure of the “Main Fault” in the Opalinus Clay, Mont Terri rock laboratory (Switzerland). *Swiss Journal of Geosciences*, 110, 1–18. doi:10.1007/s00015-016-0243-2 (this issue).
- Laloui, L. (2013). *Mechanics of Unsaturated Geomaterials*, p. 381. UK: Wiley-ISTE. ISBN: 978-1-118-61676-5.
- Leupin, O. X., Bernier-Latmani, R., Bagnoud, A., Moors, H., Leys, N., Wouters, K., & Stroes-Gascoyne, S. (2017a). Fifteen years of microbiological investigation in Opalinus Clay at the Mont Terri rock laboratory (Switzerland). *Swiss Journal of Geosciences*, 110, 1–12. doi:10.1007/s00015-016-0255-y (this issue).
- Leupin, O. X., Van Loon, L. R., Gimmi, T., Wersin, P., & Soler, J. M. (2017b). Exploring diffusion and sorption processes at the Mont Terri rock laboratory: lessons learned from 20 years of field research. *Swiss Journal of Geosciences*, 110. doi:10.1007/s00015-016-0254-z (this issue).
- Mäder, U., Jenni, A., Lerouge, C., Gaboreau, S., Miyoshi, S., Kimura, Y., Cloet, V., Fukaya, M., Claret, F., Otake, T., Shibata, M., & Lothenbach, B. (2017). 5-Year chemico-physical evolution of concrete-claystone interfaces, Mont Terri rock laboratory (Switzerland). *Swiss Journal of Geosciences*, 110, 1–21. doi:10.1007/s00015-016-0240-5 (this issue).
- Marschall, P., Giger, S., De La Vassière, R., Shao, H., Leung, H., Nussbaum, C., Trick, T., Lanyon, B., Senger, R., Lisjak, A., & Alcolea, A. (2017). Hydro-mechanical evolution of the EDZ as transport path for radionuclides and gas: insights from the Mont Terri rock laboratory (Switzerland). *Swiss Journal of Geosciences*, 110, 1–22. doi:10.1007/s00015-016-0246-z (this issue).
- Mazurek, M., & de Haller, A. (2017). Pore-water evolution and solute-transport mechanisms in Opalinus Clay at Mont Terri and Mont Russelin (Canton Jura, Switzerland). *Swiss Journal of Geosciences*, 110, 1–21. doi:10.1007/s00015-016-0249-9 (this issue).
- Mazurek, M., Gautschi, A., Marschall, P., Vigneron, G., Lebon, P., & Delay, J. (2008). Transferability of geoscientific information from various sources (study sites, underground rock laboratories, natural analogues) to support safety cases for radioactive waste repositories in argillaceous formations. *Physics and Chemistry of Earth, Parts A/B/C*, 33, 95–105.
- Mazurek, M., Hurford, A. J., & Leu, W. (2006). Unravelling the multi-stage burial history of the Swiss Molasse Basin: integration of apatite fission track, vitrinite reflectance and biomarker isomerisation analysis. *Basin Research*, 18, 27–50.
- Mueller, H. R., Garitte, B., Vogt, T., Köhler, S., Sakaki, T., Weber, H., Spillmann, T., Hertrich, M., Becker, J. K., Giroud, N., Cloet, V., Diomidis N., & Vietor, T. (2017). Implementation of the full-scale emplacement (FE) experiment at the Mont Terri rock laboratory (Switzerland). *Swiss Journal of Geosciences*, 110, 1–20. doi:10.1007/s00015-016-0251-2 (this issue).
- Nagra (2010). Beurteilung der geologischen Unterlagen für die provisorischen Sicherheitsanalysen in SGT Etappe 2. Klärung der Notwendigkeit ergänzender geologischer Untersuchungen. *Nagra Technical Report*, 10-01, 44 pp. Nagra, Wettingen, Switzerland. <http://www.nagra.ch>.
- Necib, S., Diomidis, N., Keech, P., & Nakayama, M. (2017). Corrosion of carbon steel in clay environments relevant to radioactive waste geological disposals, Mont Terri rock laboratory (Switzerland). *Swiss Journal of Geosciences*, 110, 1–14. doi:10.1007/s00015-016-0259-7 (this issue).
- Nüesch, R. (1991). Das mechanische Verhalten von Opalinuston. *Ph.D. dissertation* No. 9349, ETH Zurich, Switzerland, 294 pp.
- Nussbaum, C., Kloppenburg, A., Caër, T., & Bossart, P. (2017). Tectonic evolution around the Mont Terri rock laboratory, northwestern Swiss Jura: constraints from kinematic forward modelling. *Swiss Journal of Geosciences*, 110, 1–28. doi:10.1007/s00015-016-0248-x (this issue).
- Pearson, F. J., Arcos, D., Bath, A., Boisson, J.-Y., Fernandez, A., Gaebler, H.-E., Gaucher, E., Gautschi, A., Griffault, L., Hernan, P., & Waber, H. N. (2003). Geochemistry of water in the Opalinus Clay formation at the Mont Terri Rock Laboratory (Synthesis Report). *Geological Report*, No. 5, 321 pp. Federal Office of Topography (swisstopo), Wabern, Switzerland. <http://www.mont-terri.ch>.
- Schuster, K., Amann, F., Yong, S., Bossart, P., & Connolly, P. (2017). High-resolution mini-seismic methods applied in the Mont Terri rock laboratory. *Swiss Journal of Geosciences*, 110, 1–19. doi:10.1007/s00015-016-0241-4 (this issue).
- Vinsot, A., Appelo, C. A. J., Lundy, M., Wechner, S., Cailteau-Fischbach, C., de Donato, P., Pironon, J., Lettry, Y., Lerouge, C., & De Cannière, P. (2017). Natural gas extraction and artificial gas injection experiments in Opalinus Clay, Mont Terri rock laboratory (Switzerland). *Swiss Journal of Geosciences*, 110, 1–16. doi:10.1007/s00015-016-0244-1 (this issue).
- Vinsot, A., Appelo, C. A. J., Lundy, M., Wechner, S., Lettry, Y., Lerouge, C., et al. (2014). In situ diffusion test of hydrogen gas in the Opalinus Clay. *Geological Society, London, Special Publications*, 400(1), 563–578.
- Wersin, P., Van Loon, L. R., Soler, J. M., Yllera, A., Eikenberg, J., Gimmi, T., et al. (2004). Long-term diffusion experiment at Mont Terri: first results from field and laboratory data. *Applied Clay Science*, 26, 123–135.
- Wiczorek, K., Gaus, I., Mayor, J.C., Schuster, K., García-Siñeriz, J.-L., & Sakaki, T. (2017). In-situ experiments on bentonite-based buffer and sealing materials at the Mont Terri rock laboratory (Switzerland). *Swiss Journal of Geosciences*, 110, 1–16. doi:10.1007/s00015-016-0247-y (this issue).
- Yu, C., Matray, J.-M., Gonçalves, J., Jaeggi, D., Gräsele, W., Wiczorek, K., Vogt, T., & Sykes, E. (2017). Comparative study of methods to estimate hydraulic parameters in the

hydraulically undisturbed Opalinus Clay (Switzerland). *Swiss Journal of Geosciences*, 110, 1–20. doi:[10.1007/s00015-016-0257-9](https://doi.org/10.1007/s00015-016-0257-9) (**this issue**).

Ziefle, G., Matray, J-M., Maßmann, J., & Moeri, A. (2017). Coupled hydraulic-mechanical simulation of seasonally induced

processes in the Mont Terri rock laboratory (Switzerland). *Swiss Journal of Geosciences*, 110, 1–18. doi:[10.1007/s00015-016-0252-1](https://doi.org/10.1007/s00015-016-0252-1) (**this issue**).

Author Index

- Martinus Abednego** Earth Sciences, Department of Geosciences, University of Fribourg,
Chemin du Musée 6, 1700 Fribourg, Switzerland
First author: paper # 11
- Achim Albrecht** Agence Nationale pour la Gestion des Déchets Radioactifs ANDRA,
Centre de Meuse Haute-Marne, RD 960, 55290 Bure, France
Co-author: paper # 18
- Andrés Alcolea** TK Consult AG, Mainaustrasse 30, 8008 Zurich, Switzerland
Co-author: paper # 8
- Florian Amann** Institute of Geology, Engineering Geology, Swiss Federal Institute of
Technology ETH, Zurich, Sonneggstrasse 5, 8092 Zurich, Switzerland
First author: paper # 7
Co-author: paper # 10
- C. Anthony J. Appelo** Valeriusstraat 11, 1071 MB Amsterdam, The Netherlands
Co-author: paper # 19
- Gilles Armand** Agence Nationale pour la Gestion des Déchets Radioactifs ANDRA,
Centre de Meuse Haute-Marne, RD 960, 55290 Bure, France
Co-author: paper # 13
- Alexandre Bagnoud** Ecole Polytechnique Fédérale de Lausanne EPFL, Route Cantonale, 1015
Lausanne, Switzerland
Co-author: paper # 17
- Jens K. Becker** National Cooperative for the Disposal of Radioactive Waste NAGRA,
Hardstrasse 73, 5430 Wettingen, Switzerland
Co-author: paper # 14
- Frédéric Bernier** Federal Agency for Nuclear Control FANC, Rue Ravenstein 36, 1000
Brussels, Belgium
Co-author: introductory paper
- Rizlan Bernier-Latmani** Ecole Polytechnique Fédérale de Lausanne EPFL, Route Cantonale, 1015
Lausanne, Switzerland
Co-author: paper # 17
- Jens Birkholzer** Lawrence Berkeley National Laboratory, Berkeley, CA 94720, USA
Co-author: introductory paper
- Patrick Blascheck** Institut für Geophysik, Universität Stuttgart, Azenbergstr. 16, 70174
Stuttgart, Germany
Co-author: paper # 11
- Hansruedi Bläsi** Institute of Geological Sciences, University of Bern, Bern, Switzerland
Co-author: paper # 1

-
- Nele Bleyen** Belgian Nuclear Research Centre SCK CEN, Boeretang 200, 2400 Mol, Belgium
First author: paper # 18
- Paul Bossart** Swiss Geological Survey, Federal Office of Topography Swisstopo, Seftigenstrasse 264, 3084 Wabern, Switzerland
First author: introductory paper, paper # 21
Co-author: papers # 2, 10, 11
- Christophe Bruggeman** Belgian Nuclear Research Centre SCK.CEN, Boeretang 200, 2400 Mol, Belgium
Co-author: introductory paper
- Typhaine Caër** Géosciences et Environnement Cergy (GEC), Université de Cergy-Pontoise, rue Descartes, 95031 Cergy-Pontoise Cedex, France
Co-author: paper # 2
- Cristelle Cailteau-Fischbach** UPMC Univ. Paris 06, Université Versailles St-Quentin, CNRS/INSU, LATMOS-IPSL, 75252 Paris Cedex 05, France
Co-author: paper # 19
- Pierre De Cannière** Federal Agency for Nuclear Control FANC, Rue Ravenstein 36, 1000 Brussels, Belgium
Co-author: papers # 18, 19
- Francis Claret** French Geological Survey BRGM, 3 Avenue Claude Guillemin, 45100 Orléans, France
Co-author: paper # 15
- Norbert Clauer** Laboratoire d'Hydrologie et de Géochimie de Strasbourg (CNRS-UdS), 1 rue Blessig, 67084 Strasbourg, France
First author: paper # 5
- Veerle Cloet** National Cooperative for the Disposal of Radioactive Waste NAGRA, Hardstrasse 73, 5430 Wettingen, Switzerland
Co-author: papers # 14, 15
- Peter Connolly** CHEVRON, Rock Mechanics Team, Chevron ETC, 1500 Louisiana Street, Houston, TX 77002, USA
Co-author: introductory paper, papers # 3, 10
- Gaudenz Deplazes** National Cooperative for the Disposal of Radioactive Waste NAGRA, Hardstrasse 73, 5430 Wettingen, Switzerland
Co-author: paper # 1
- Sarah Dewonck** Agence Nationale pour la Gestion des Déchets Radioactifs ANDRA, Centre de Meuse Haute-Marne, RD 960, 55290 Bure, France
Co-author: introductory paper
- Volker Dietze** Meraner Straße 41, 86720 Nördlingen, Germany
Co-author: paper # 1

- Nikitas Diomidis** National Cooperative for the Disposal of Radioactive Waste NAGRA, Hardstrasse 73, 5430 Wettingen, Switzerland
Co-author: papers # 14, 16
- Philippe de Donato** Université de Lorraine-CNRS-CREGU, GeoRessources Lab, 54506 Vandoeuvre-lès-Nancy, France
Co-author: paper # 19
- Susanne Feist-Burkhardt** SFB Geological Consulting and Services, Odenwaldstraße 18, 64372 Ober-Ramstadt, Germany;
Department of Earth Sciences, University of Geneva, 13 Rue des Maraîchers, 1205 Geneva, Switzerland
Co-author: paper # 1
- Erik Frank** Swiss Federal Nuclear Safety Inspectorate ENSI, Industriestrasse 19, 5200 Brugg, Switzerland
Co-author: paper # 7
- Masaaki Fukaya** Nuclear Facilities Division, Nuclear Waste Technology Department, OBAYASHI Corporation, 2-15-2, Konan, Minato-ku, Tokyo 108-8502, Japan
Co-author: introductory paper, paper # 15
- Stephane Gaboreau** French Geological Survey BRGM, 3 Avenue Claude Guillemin, 45100 Orléans, France
Co-author: paper # 15
- José-Luis García-Siñeriz** Amberg Infraestructuras, Av. de la Industria 37-39, 28108 Alcobendas, Madrid, Spain
Co-author: papers # 12, 13
- Benoit Garitte** National Cooperative for the Disposal of Radioactive Waste NAGRA, Hardstrasse 73, 5430 Wettingen, Switzerland
Co-author: papers # 13, 14
- Irina Gaus** National Cooperative for the Disposal of Radioactive Waste NAGRA, Hardstrasse 73, 5430 Wettingen, Switzerland
Co-author: papers # 12, 13
- Antonio Gens** Universitat Politècnica de Catalunya, Jordi Girona 1-3, 08034 Barcelona, Spain
First author: paper # 13
- Silvio Giger** National Cooperative for the Disposal of Radioactive Waste NAGRA, Hardstrasse 73, 5430 Wettingen, Switzerland
Co-author: paper # 8
- Thomas Gimmi** Paul Scherrer Institut PSI, 5232 Villigen, Switzerland
Co-author: paper # 20

-
- Niels Giroud** National Cooperative for the Disposal of Radioactive Waste NAGRA,
Hardstrasse 73, 5430 Wettingen, Switzerland
Co-author: paper # 14
- Julio Gonçalves** Aix Marseille Université UMR 6635 CEREGE Technopôle Environnement
Arbois-Méditerranée, BP80, 13545 Aix-en-Provence Cedex 4, France
Co-author: paper # 4
- Werner Gräsle** Federal Institute for Geosciences and Natural Resources BGR, Stilleweg 2,
30655 Hannover, Germany
Co-author: paper # 4
- Antoine de Haller** Earth and Environmental Sciences, University of Geneva, Geneva,
Switzerland
Co-author: paper # 6
- Martin Herfort** Swiss Federal Nuclear Safety Inspectorate ENSI, Industriestrasse 19, 5200
Brugg, Switzerland
Co-author: introductory paper
- Marian Hertrich** National Cooperative for the Disposal of Radioactive Waste NAGRA,
Hardstrasse 73, 5430 Wettingen, Switzerland
Co-author: paper # 14
- Bernhard Hostettler** Naturhistorisches Museum der Burgergemeinde Bern, Bernastrasse 15,
3005 Bern, Switzerland
First author: paper # 1
- David Jaeggi** Swiss Geological Survey, Federal Office of Topography Swisstopo,
Seftigenstrasse 264, 3084 Wabern, Switzerland
First author: paper # 3
Co-author: papers # 1, 4
- Andreas Jenni** Institute of Geological Sciences, University of Bern, Baltzerstrasse 3, 3012
Bern, Switzerland
Co-author: paper # 15
- Mark Jensen** Nuclear Waste Management Organization (NWMO), 22 St. Clair Ave. E.,
Toronto, ON, Canada
Co-author: introductory paper
- Manfred Joswig** Institut für Geophysik, Universität Stuttgart, Azenbergstr. 16, 70174
Stuttgart, Germany
Co-author: paper # 11
- Peter Keech** Nuclear Waste Management Organization NWMO, 22 St. Clair Ave. E.,
Toronto, ON, Canada
Co-author: paper # 16
- Yukinobu Kimura** Nuclear Facilities Division, Nuclear Waste Technology Department,

- Japan
Co-author: paper # 15
- Armelle Kloppenburg** 4D Geo/Structural Geology, Daal en Bergselaan 80, 2565 AH The Hague, The Netherlands
Co-author: paper # 2
- Sven Köhler** National Cooperative for the Disposal of Radioactive Waste NAGRA, Hardstrasse 73, 5430 Wettingen, Switzerland
Co-author: paper # 14
- Bill Lanyon** Fracture Systems Ltd., Tregurrian, Ayr, St Ives, Cornwall, UK
Co-author: paper # 8
- Ben Laurich** Federal Institute for Geosciences and Natural Resources BGR, Stilleweg 2, 30655 Hannover, Germany
Co-author: papers # 3, 5
- Catherine Lerouge** French Geological Survey BRGM, 3 Avenue Claude Guillemin, 45100 Orléans, France
Co-author: papers # 15, 19
- Yanick Lettry** Solexperts AG, Mettlenbachstrasse 25, 8617 Mönchaltorf, Switzerland
Co-author: paper # 19
- Helen Leung** Nuclear Waste Management Organization NWMO, 22 St. Clair Ave. E., Toronto, ON, Canada
Co-author: paper # 8
- Olivier X. Leupin** National Cooperative for the Disposal of Radioactive Waste NAGRA, Hardstrasse 73, 5430 Wettingen, Switzerland
First author: papers # 17, 20
- Natalie Leys** Belgian Nuclear Research Centre SCK CEN, Boeretang 200, 2400 Mol, Belgium
Co-author: papers # 17, 18
- Andrea Lisjak** Geomechanica Inc., 90 Adelaide St W, Toronto, ON M5H 4A6, Canada
Co-author: paper # 8
- Simon Loew** Institute of Geology, Engineering Geology, Swiss Federal Institute of Technology ETH, Zurich, Sonneggstrasse 5, 8092 Zurich, Switzerland
Co-author: paper # 7
- Luc R. Van Loon** Paul Scherrer Institut PSI, 5232 Villigen, Switzerland
Co-author: paper # 20
- Babara Lothenbach** Swiss Federal Laboratories for Materials Science and Technology EMPA, Überlandstrasse 129, 8600 Dübendorf, Switzerland
Co-author: paper # 15

-
- Mélanie Lundy** Agence Nationale pour la Gestion des Déchets Radioactifs ANDRA,
Centre de Meuse Haute-Marne, RD 960, 55290 Bure, France
Co-author: paper # 19
- Urs Mäder** Institute of Geological Sciences, University of Bern, Baltzerstrasse 3, 3012
Bern, Switzerland
First author: paper # 15
- Paul Marschall** National Cooperative for the Disposal of Radioactive Waste NAGRA,
Hardstrasse 73, 5430 Wettingen, Switzerland
First author: paper # 8
- Jobst Maßmann** Federal Institute for Geosciences and Natural Resources BGR, Stilleweg 2,
30655 Hannover, Germany
Co-author: paper # 9
- Jean-Michel Matray** Institut de Radioprotection et de Sûreté Nucléaire, 31 Allée du Général
Leclerc, 92260 Fontenay-aux-Roses, France
Co-author: introductory paper, papers # 4, 9
- Juan Carlos Mayor** Empresa Nacional de Residuos Radiactivos S.A.ENRESA, Calle de Emilio
Vargas, 7, 28043 Madrid, Spain
Co-author: introductory paper, papers # 12, 13
- Martin Mazurek** Institute of Geological Sciences, University of Bern, Baltzerstrasse 3, 3012
Bern, Switzerland First author: paper # 6
- Ursula Menkveld-Gfeller** Naturhistorisches Museum der Burgergemeinde Bern, Bernastrasse 15,
3005 Bern, Switzerland
Co-author: paper # 1
- Satoru Miyoshi** Nuclear Facilities Division, Nuclear Waste Technology Department,
OBAYASHI Corporation, 2-15-2, Konan, Minato-ku, Tokyo 108-8502,
Japan
Co-author: paper # 15
- Hugo Moors** Belgian Nuclear Research Centre SCK CEN, Boeretang 200, 2400 Mol,
Belgium
Co-author: papers # 17, 18
- Alain Morard** Swiss Geological Survey, Federal Office of Topography Swisstopo,
Seftigenstrasse 264, 3084 Wabern, Switzerland Co-author: paper # 1
- Andreas Möri** Swiss Geological Survey, Federal Office of Topography Swisstopo,
Seftigenstrasse 264, 3084 Wabern, Switzerland
Co-author: introductory paper, paper # 9
- Jon Mosar** Earth Sciences, Department of Geosciences, University of Fribourg,
Chemin du Musée 6, 1700 Fribourg, Switzerland
Co-author: paper # 11

- Herwig R. Müller** National Cooperative for the Disposal of Radioactive Waste NAGRA, Hardstrasse 73, 5430 Wettingen, Switzerland
First author: paper # 14
- Masashi Nakayama** Japan Atomic Energy Agency JAEA, 432-2 Hokushin, Horonobe-cho, Hokkaido 098-3224, Japan
Co-author: paper # 16
- Sophia Necib** Agence Nationale pour la Gestion des Déchets Radioactifs ANDRA, Centre de Meuse Haute-Marne, RD 960, 55290 Bure, France
First author: paper # 16
- Christophe Nussbaum** Swiss Geological Survey, Federal Office of Topography Swisstopo, Seftigenstrasse 264, 3084 Wabern, Switzerland
First author: paper # 2
Co-author: papers # 3, 5, 8, 11
- Tsubasa Otake** Division of Sustainable Resources Engineering, Faculty of Engineering, Hokkaido University, Kita 13 Nishi 8, Kita-ku, Sapporo, Hokkaido060-8628, Japan
Co-author: paper # 15
- Takahiro Oyama** Geosphere Environmental Science Department, Abiko Research Laboratory, Central Research Institute of Power Industry CRIEPI, 1646, Abiko, Chiba 270-1194, Japan
Co-author: introductory paper
- Jacques Pironon** Université de Lorraine-CNRS-CREGU, GeoRessources Lab, 54506 Vandoeuvre-lès-Nancy, France
Co-author: paper # 19
- Achim G. Reisdorf** Geologisch-Paläontologisches Institut, Universität Basel, Bernoullistrasse 32, 4056 Basel, Switzerland
Co-author: paper # 1
- Toshihiro Sakaki** National Cooperative for the Disposal of Radioactive Waste NAGRA, Hardstrasse 73, 5430 Wettingen, Switzerland
Co-author: papers # 12, 14
- Senecio Schefer** Swiss Geological Survey, Federal Office of Topography Swisstopo, Seftigenstrasse 264, 3084 Wabern, Switzerland
Co-author: paper # 11
- Kristof Schuster** Federal Institute for Geosciences and Natural Resources BGR, Stilleweg 2, 30655 Hannover, Germany
First author :paper # 10
Co-author: introductory paper, papers # 3, 12, 13
- Bernhard Schwyn** National Cooperative for the Disposal of Radioactive Waste NAGRA, Hardstrasse 73, 5430 Wettingen, Switzerland

- Co-author: paper # 18
- Rainer Senger** Intera Incorporated, 1933 Jadwin Avenue, Suite 130, Richland, WA 99354, USA
Co-author: paper # 8
- Hua Shao** Federal Institute for Geosciences and Natural Resources BGR, Stilleweg 2, 30655 Hannover, Germany
Co-author: paper # 8
- Masahito Shibata** Electric and Nuclear Power Technology Department, Taiheiyo Consultant Co. Ltd., 2-4-2, Ohsaku, Sakura 285-0802, Japan
Co-author: paper # 15
- Naokata Shigeta** Japan Atomic Energy Agency JAEA, 432-2 Hokushin, Horonobe-cho, Hokkaido 098-3224, Japan
Co-author: introductory paper
- Joe Small** National Nuclear Laboratory NLL, Chadwick House, Birchwood Park, WA3 6AS Warrington, UK
Co-author: paper # 18
- Steven Smets** Belgian Nuclear Research Centre SCK CEN, Boeretang 200, 2400 Mol, Belgium
Co-author: paper # 18
- Josep M. Soler** Institute of Environmental Assessment and Water Research IDAEA-CSIC, Calle Jordi Girona 18-26, 08034 Barcelona, Spain
Co-author: paper # 20
- Thomas Spillmann** National Cooperative for the Disposal of Radioactive Waste NAGRA, Hardstrasse 73, 5430 Wettingen, Switzerland
Co-author: paper # 14
- Simcha Stroes-Gascoyne** University of Saskatchewan, Saskatoon, Canada
Co-author: paper # 17
- Erik Sykes** Nuclear Waste Management Organization, 22 St. Clair Ave. E., Toronto, ON, Canada
Co-author: paper # 4
- Isabelle Techer** Equipe Associée 7352 CHROME, Université de Nîmes, rue du Dr. Georges Salan, 30021 Nîmes, France
Co-author: paper # 5
- Reto Thoeny** Grundwasserschutz und Entsorgung, AF-Consult Switzerland AG, Täfernstrasse 26, 5405 Baden, Switzerland
Co-author: paper # 7
- Thomas Trick** Solexperts AG, Mettlenbachstrasse 25, 8617 Mönchaltorf, Switzerland
Co-author: papers # 8, 13

- Thomas Trick** Solexperts AG, Mettlenbachstrasse 25, 8617 Mönchaltorf, Switzerland
Co-author: papers # 8, 13
- Elie Valcke** Belgian Nuclear Research Centre SCK CEN, Boeretang 200, 2400 Mol, Belgium
Co-author: paper # 18
- Rémi De La Vassière** Agence Nationale pour la Gestion des Déchets Radioactifs ANDRA, Centre de Meuse Haute-Marne, RD 960, 55290 Bure, France
Co-author: paper # 8
- Tim Vietor** National Cooperative for the Disposal of Radioactive Waste NAGRA, Hardstrasse 73, 5430 Wettingen, Switzerland
Co-author: introductory paper, paper # 14
- Agnès Vinsot** Agence Nationale pour la Gestion des Déchets Radioactifs ANDRA, Centre de Meuse Haute-Marne, RD 960, 55290 Bure, France
First author: paper # 19
- Tobias Vogt** National Cooperative for the Disposal of Radioactive Waste NAGRA, Hardstrasse 73, 5430 Wettingen, Switzerland
Co-author: papers # 4, 14
- Anton Waltschew** Steinplattenweg 55a, 90491 Nuremberg, Germany
Co-author: paper # 1
- Hanspeter Weber** National Cooperative for the Disposal of Radioactive Waste NAGRA, Hardstrasse 73, 5430 Wettingen, Switzerland
Co-author: paper # 14
- Stefan Wechner** Hydroisotop GmbH, Woelkestraße 9, 85301 Schweitenkirchen, Germany
Co-author: paper # 19
- Paul Wersin** Institute of Geological Sciences, University of Bern, Baltzerstrasse 3, 3012 Bern, Switzerland
Co-author: paper # 20
- Klaus Wiczorek** Gesellschaft für Anlagen- und Reaktorsicherheit (GRS) GmbH, Process Analysis Department, Final Repository Safety Research Division, Theodor-Heuss-Strasse 4, D-38122 Braunschweig, Germany
First author: paper # 12
Co-author: introductory paper, papers # 4, 13
- Katrin M. Wild** Institute of Geology, Engineering Geology, Swiss Federal Institute of Technology ETH, Zurich, Sonneggstrasse 5, 8092 Zurich, Switzerland
Co-author: paper # 7
- Charles Wittebroodt** Institut de Radioprotection et de Sûreté Nucléaire, 31 Allée du Général Leclerc, 92260 Fontenay-aux-Roses, France
Co-author: paper # 18

- Katinka Wouters** Belgian Nuclear Research Centre SCK CEN, Boeretang 200, 2400 Mol, Belgium
Co-author: paper # 17
- Salina Yong** Knight Piésold Ltd., Suite 1400 - 750 West Pender, Vancouver V6C 2T8, British Columbia, Canada
Co-author: papers # 7, 10
- Catherine Yu** Institut de Radioprotection et de Sûreté Nucléaire, 31 Allée du Général Leclerc, 92260 Fontenay-aux-Roses, France; Aix Marseille Université UMR 6635 CEREGE Technopôle Environnement Arbois-Méditerranée, BP80, 13545 Aix-en-Provence Cedex 4, France
First author: paper # 4
- Gesa Ziefle** Federal Institute for Geosciences and Natural Resources BGR, Stilleweg 2, 30655 Hannover, Germany
First author : paper # 9